TUBULAR STRUCTURES XIV

EDITOR:
LEROY GARDNER

CRC Press
Taylor & Francis Group
A BALKEMA BOOK

TUBULAR STRUCTURES XIV

PROCEEDINGS OF THE 14TH INTERNATIONAL SYMPOSIUM ON TUBULAR STRUCTURES, LONDON, UK, 12–14 SEPTEMBER 2012

Tubular Structures XIV

Editor

Leroy Gardner
Department of Civil and Environmental Engineering, Imperial College London, UK

CRC Press
Taylor & Francis Group
Boca Raton London New York Leiden

CRC Press is an imprint of the
Taylor & Francis Group, an **informa** business

A BALKEMA BOOK

CRC Press
Taylor & Francis Group
6000 Broken Sound Parkway NW, Suite 300
Boca Raton, FL 33487-2742

Version Date: 2012919

International Standard Book Number-13: 978-0-203-07310-0 (eBook - PDF)

Tubular Structures XIV – Gardner (Ed.)
© 2012 Taylor & Francis Group, London, ISBN 978-0-415-62137-3

Table of contents

Connections

Elliptical hollow sections

Fatigue and fracture

Stainless steel

Fire

Trusses and arches

Structural behaviour

Materials and section forming

Tubular Structures XIV – Gardner (Ed.)
© 2012 Taylor & Francis Group, London, ISBN 978-0-415-62137-3

Preface

This book contains the papers presented at the *14th International Symposium on Tubular Structures* (ISTS14) held in London, UK, from September 12th to 14th, 2012. The Symposium, now regarded as the key international forum for the presentation and discussion of research, developments and applications in the field of tubular structures, was organised by Imperial College London in collaboration with the International Institute of Welding Subcommission XV-E and the Comité International pour le Développement et l'Étude de la Construction Tubulaire (CIDECT). The 13 previous symposia, held between 1984 and 2010, are described in the "Publications of the previous symposia on tubular structures" section of this book. Throughout its 28-year history the frequency, location and technical content of all the symposia has been determined by the IIW Subcommission XV-E on Tubular Structures.

The Symposium was sponsored by CIDECT, Tata Steel Tubes, Vallourec & Mannesmann Tubes (V&M), s^2 (space solutions) and Stalatube OY. It is their generous support that enabled the Symposium to take place and made it possible to continue the tradition of allowing presenting authors of papers to attend the Symposium without payment of registration fees.

A total of 95 technical papers, each of which has been reviewed by two international experts in the field, are included in the proceedings. One of these papers relates to the invited 'Kurobane Lecture', given, at this Symposium, by Prof. Xiao-Ling Zhao from the Monash University, Australia. Prof. Zhao was selected by the IIW Subcommission XV-E. The Kurobane Lecture is the International Symposium on Tubular Structures Keynote Address which was inaugurated at the ISTS8 in 1998. The Symposium also featured a special session to mark the 50th Anniversary of CIDECT, with structural and architectural contributions.

The editor would like to express his sincere gratitude to the reviewers of the papers for their hard work and expert opinions. The editor also wishes to thank the international programme committee and the local organising committee. Particular thanks are owed to Katherine Cashell, Jeanette Abela, Ulrika Wernmark, Stephanie O'Mahony and Betty Yue for their much appreciated efforts.

The information provided in this publication is the sole responsibility of the individual authors. It does not reflect the opinion of the editor, supporting associations, organisations or sponsors, and they are not responsible for any use that might be made of information appearing in this publication. Anyone making use of the contents of this book assumes all liability arising from such use.

The editor hopes that the contemporary applications, case studies, concepts, insights, overviews, research summaries, analyses and product developments described in this book provide some inspiration to architects, developers, contractors, engineers and fabricators to build ever more innovative and competitive tubular structures. This archival volume of the current "state of the art" will also serve as excellent reference material to academics, researchers, trade associations and manufacturers of hollow sections in the future.

Leroy Gardner
Editor
Imperial College London
2012

Publications of previous international symposia on tubular structures

B. Young (Ed.) 2010. *Tubular Structures XIII*, 13th International Symposium on Tubular Structures, Hong Kong, China, 2010. Boca Raton/London/New York/Leiden: CRC Press/Balkema.

Z.Y. Shen, Y.Y. Chen & X.Z. Zhao (Eds.) 2009. *Tubular Structures XII*, 12th International Symposium on Tubular Structures, Shanghai, China, 2008. Boca Raton/London/New York/Leiden: CRC Press/Balkema.

J.A. Packer & S. Willibald (Eds.) 2006. *Tubular Structures XI*, 11th International Symposium and IIW International Conference on Tubular Structures, Québec, Canada, 2006. London/Leiden/New York: Taylor & Francis (including A.A. Balkema Publishers).

M.A. Jaurrieta, A. Alonso & J.A. Chica (Eds.) 2003, *Tubular Structures X*, 10th International Symposium on Tubular Structures, Madrid, Spain, 2003. Rotterdam: A.A. Balkema Publishers.

R. Puthli & S. Herion (Eds.) 2001. *Tubular Structures IX*, 9th International Symposium on Tubular Structures, Düsseldorf, Germany, 2001. Rotterdam: A.A. Balkema Publishers.

Y.S. Choo & G.J. van der Vegte (Eds.) 1998. *Tubular Structures VIII*, 8th International Symposium on Tubular Structures, Singapore, 1998. Rotterdam: A.A. Balkema Publishers.

J. Farkas & K. Jármai (Eds.) 1996. *Tubular Structures VII*, 7th International Symposium on Tubular Structures, Miskolc, Hungary, 1996. Rotterdam: A.A. Balkema Publishers.

P. Grundy, A. Holgate & B. Wong (Eds.) 1994. *Tubular Structures VI*, 6th International Symposium on Tubular Structures, Melbourne, Australia, 1994. Rotterdam: A.A. Balkema Publishers.

M.G. Coutie & G. Davies (Eds.) 1993. *Tubular Structures V*. 5th International Symposium on Tubular Structures, Nottingham, United Kingdom, 1993. London/Glasgow/NewYork/Tokyo/Melbourne/Madras: E & FN Spon.

J. Wardenier & E. Panjeh Shahi (Eds.) 1991. *Tubular Structures*, 4th International Symposium on Tubular Structures, Delft, The Netherlands, 1991. Delft: Delft University Press.

E. Niemi & P. Mäkeläinen (Eds.) 1990. *Tubular Structures*, 3rd International Symposium on Tubular Structures, Lappeenranta, Finland, 1989. Essex: Elsevier Science Publishers Ltd.

Y. Kurobane & Y. Makino (Eds.) 1987. *Safety Criteria in Design of Tubular Structures*, 2nd International Symposium on Tubular Structures, Tokyo, Japan, 1986. Tokyo: Architectural Institute of Japan, IIW.

International Institute of Welding 1984. *Welding of Tubular Structures/Soudage des Structures Tubulaires*, 1st International Symposium on Tubular Structures, Boston, USA, 1984. Oxford/New York/Toronto/Sydney/Paris/Frankfurt: Pergamon Press.

Tubular Structures XIV – Gardner (Ed.)
© 2012 Taylor & Francis Group, London, ISBN 978-0-415-62137-3

Organisation

This volume contains the Proceedings of the 14th International Symposium on Tubular Structures – ISTS14 held in London, UK, from 12th to 14th September 2012. ISTS14 has been organised by Imperial College London, the International Institute of Welding (IIW) Subcommission XV-E and Comité International pour le Développement et l'Étude de la Construction Tubulaire (CIDECT).

INTERNATIONAL PROGRAMME COMMITTEE

J.A. Packer, *Chair*
University of Toronto, Toronto, Canada

M.A. Bradford
University of New South Wales, Sydney, Australia

Y.Y. Chen
Tongji University, Shanghai, China

S.P. Chiew
Nanyang Technological University, Singapore

Y.S. Choo
National University of Singapore, Singapore

L. Gardner
Imperial College London, UK

S. Herion
Karlsruhe Institute of Technology, Germany

G. Iglesias
Instituto para la Construccion Tubular, Spain

J.P. Jaspart
University of Liège, Belgium

M. Lefranc
Force Technology Norway, Sandvika, Norway

S. Maddox
The Welding Institute, Cambridge, UK

G. Marquis, *Chair of IIW Commission XIII*
The Aalto University School of Science and Technology, Finland

P.W. Marshall
MHP Systems Engineering, Houston, US

A.C. Nussbaumer
Ecole Polytechnique Fédérale de Lausanne, Switzerland

R.S. Puthli
Karlsruhe Institute of Technology, Germany

T. Schlafly
American Institute of Steel Construction, US

G.J. van der Vegte
Delft University of Technology, The Netherlands

J. Wardenier
Delft University of Technology and National University of Singapore, The Netherlands and Singapore

B. Young
The University of Hong Kong, Hong Kong, China

X.L. Zhao, *Chair of IIW Subcommission XV-E*
Monash University, Melbourne, Australia

LOCAL ORGANISING COMMITTEE

L. Gardner, *Chair*
Imperial College London, UK

J.M. Abela
Flint and Neill, UK

K.A. Cashell
The Steel Construction Institute, UK

T.M. Chan
University of Warwick, UK

A.Y. Elghazouli
Imperial College London, UK

D. Lam
University of Bradford, UK

T. Mustard
TATA Steel, UK

D.A. Nethercot
Imperial College London, UK

M.L. Romero
Universidad Politécnica de Valencia, Spain

M.A. Serrano
Universidad de Oviedo, Spain

M.A. Wadee
Imperial College London, UK

Y.C. Wang
University of Manchester, UK

P. Watson
TATA Steel, UK

S. Welch
TATA Steel, UK

S. Whitfield
TATA Steel, UK

Tubular Structures XIV – Gardner (Ed.)
© 2012 Taylor & Francis Group, London, ISBN 978-0-415-62137-3

Acknowledgements

The Organising Committee wish to express their sincere gratitude for the financial assistance from the following organisations: IIW (International Institute of Welding), CIDECT (Comité International pour le Développement et l'Étude de la Construction Tubulaire), Tata Steel Tubes, Vallourec & Mannesmann Tubes (V&M), s^2 (space solutions) and Stalatube OY.

The technical assistance of the IIW Subcommission XV-E is gratefully acknowledged. We are also thankful to the International Programme Committee as well as the members of the Local Organising Committee. Finally, the editor (who also served as a reviewer) wants to acknowledge the kind assistance of the following reviewers:

J.M. Abela
M.A. Bradford
D. Camotim
K.A. Cashell
R. Chacon
S. L. Chan
T.M. Chan
Y.Y. Chen
S.P. Chiew
Y.S. Choo
M. Eekhout
A.Y. Elghazouli
S. Herion
G. Iglesias
J. Krampen
D. Lam
M. Lefranc
R. Liew
P.W. Marshall
O. Mirza
T. Mustard
D.A. Nethercot
A.C. Nussbaumer
K. Ochi
J.A. Packer
R.S. Puthli
P. Ritakallio
M.L. Romero
B. Rossi
T. Schlafly
M.A. Serrano
N. Silvestre
M.A. Wadee
Y.C. Wang
P. Watson
J. Wardenier
S. Welch
S. Whitfield
T. Wilkinson
B. Young
X.L. Zhao

Leroy Gardner
Editor
Imperial College London

ISTS Kurobane lecture

Tubular Structures XIV – Gardner (Ed.)
© 2012 Taylor & Francis Group, London, ISBN 978-0-415-62137-3

Hybrid hollow structural sections

X.L. Zhao
Department of Civil Engineering, Monash University, Clayton, Australia

ABSTRACT: This paper gives a summary of recent developments in Hybrid Hollow Structural Sections (HSS). They are in the form of: concrete filled HSS; concrete filled double skin HSS; FRP (fibre reinforced polymer) strengthened HSS with/without concrete filling; FRP, concrete and HSS double skin sections. The existing research, main findings and future work are presented.

1 INTRODUCTION

Different abbreviations were used in the literature to describe various types of metal profile with a hollow tubular cross-section, such as SHS for Square Hollow Section, RHS for Rectangular Hollow Section, CHS for Circular Hollow Section, EHS for Elliptical Hollow Section, OHS for Oval Hollow Section and HSS for Hollow Structural Section. The abbreviation "HSS" is adopted in this paper to represent the general term **H**ollow **S**tructural **S**ection.

HSS could be used together with other materials to form hybrid HSS. For example, they could be in the form of concrete filled HSS, concrete filled double skin HSS, FRP (fibre reinforced polymer) strengthened HSS with/without concrete filling, FRP-concrete-HSS double skin sections.

There is an increasing trend in using concrete-filled HSS in recent decades, such as in industrial buildings, structural frames and supports, electricity transmission poles, spatial construction, high-rise or super high-rise buildings and bridge structures (Zhao et al. 2010a).

It is well known that hollow structural sections have many advantages over conventional open sections, such as excellent strength properties (compression, bending and torsion), lower drag coefficients, less painting area, aesthetic merits and the potential of void filling (Wardenier et al. 2010). Compared with unfilled tubes, concrete-filled tubes demonstrate increased load carrying capacity, ductility, energy absorption during earthquakes as well as increased fire resistance. For example, for a column with an effective buckling length L_e of 5 m, mass of steel section of 60 kg/m and concrete core strength of 40 MPa, the compression capacity increases about 50% due to concrete-filling. The increase in rotation capacity under pure bending due to concrete filling was found to be 300% (Zhao and Grzebieta 1999). For concrete-filled RHS subjected to large deformation cyclic bending the failure modes changed from localized cracking to an outward folding mechanism. The fire resistance of unprotected CHS or RHS columns is normally found to be less than 30 minutes (Twilt et al. 1996). Concrete filling can increase the fire resistance up to 2 or 3 hours (Han et al. 2003a, Lu et al. 2010).

FRP (fibre reinforced polymer) has high strength to weight ratio, resistance to corrosion and usually to environmental degradation (Hollaway and Teng 2008). While FRP has been widely used in strengthening aircraft and more recently concrete structures (e.g. Teng et al. 2002, Baker et al. 2002, Rizkalla et al. 2003, Oehlers and Seracino 2004), it has not been widely applied to steel structures. The knowledge of repairing aircraft cannot be directly applied to steel structures in the Civil, Offshore and Mining industry because the materials used are very different. The existing knowledge of CFRP-concrete composite systems may not be applicable to CFRP-steel systems because of the distinct difference between the debonding mechanism of a CFRP-steel system and a CFRP-concrete system, and the unique failure modes for steel members and connections.

It has been shown (Hollaway and Cadei 2002, Zhao and Zhang 2007, Schnerch et al. 2007) that FRP has great potential to strengthen steel structures including HSS. The benefit of using FRP together with hollow structural sections is summarized in Table 1. It is clear that FRP can improve the performance of HSS in terms of strength, ductility, energy absorption and fatigue life.

The existing research, main findings and future work on hybrid HSS are presented in this paper.

2 HOLLOW STRUCTURAL SECTIONS AND CONCRETE

2.1 *Concrete filled HSS*

2.1.1 *Existing research and main findings*

2.1.1.1 *General*

The major research on CFST members and connections was summarized in CIDECT Design Guides No.4 (Twilt et al. 1996), No.5 (Bergmann et al. 1995),

Table 1. Improved performance of HSS due to FRP strengthening.

Configuration and FRP used (Young's Modulus)	Improved performance	Reference
CHS and RHS beams in bending, CFRP sheet (from 50 GPa to 270 GPa)	• Increased moment capacity and ductility in general • For circular hollow sections, slender sections (which cannot reach first yield due to local buckling) could become non-compact sections (which can reach plastic moment capacity)	Haedir et al. (2009), Photiou et al. (2006), Seica and Packer (2007)
CHS and RHS columns in compression, CFRP sheet (230 GPa) and GFRP sheet (80 GPa)	• Compression strength increases about 20% to 70% if CFRP is used • Compression strength increases about 5% to 10% if GFRP is used • Increased energy absorption under large deformation compression force	Shaat and Fam (2006), Bambach and Elchalakani (2007), Teng and Hu (2007), Haedir and Zhao (2011)
RHS subject to concentrated forces through a bearing plate, CFRP Plate (165 GPa)	• Web buckling capacity of cold-formed rectangular hollow sections (RHS) increases about 1.5 to 2.5 times • Web buckling capacity of aluminium RHS increases up to 3.5 times • Web buckling capacity of stainless steel RHS increases up to 50%	Zhao et al. (2006), Wu et al. (2012), Islam and Young (2010, 2011)
RHS subject to concentrated forces through a welded branch, GFRP plate (12.4 GPa)	Web buckling capacity increases about 50%.	Fam and Aguilera (2012)
Welded VHS tubes in tension, CFRP sheet (230 GPa)	Recovered the full yield capacity, which was 50% lost due to HAZ softening, of welded very high strength steel tubes.	Jiao and Zhao (2004)
Welded aluminium K-joints under static load, GFRP sheet (30 GPa) and CFRP sheet (79 GPa)	• Recovered the full connection capacity of aluminium K-joints if CFRP is used or about 80% connection capacity if GFRP is used. • The retrofitted connection with GFRP reinforcement achieved 1.17 to 1.25 times the capacity of the welded aluminum connection without any visible cracks.	Fam et al. (2006) Pantelides et al. (2003)
Welded cross-beam connections subject to fatigue loading, CFRP sheet (230 GPa)	Fatigue life extends to twice the original fatigue life.	Xiao and Zhao (2012)
Welded aluminium K-joints subject to fatigue loading, GFRP sheet (30 GPa)	The repaired connections exceeded the fatigue limit of the aluminium welded connections with no known cracks. The repaired connections with 90% of the weld removed satisfied the constant amplitude fatigue limit threshold.	Nadauld and Pantelides (2007)
CFST columns, CFRP sheet (65 GPa)	• The static strength increased by 55% and 140% when the number of CFRP layers was 2 and 4 respectively • Increased ductility to resist cyclic loading	Xiao et al. (2005)
CFST columns, CFRP sheet (247 GPa)	Recovered certain compression strength of concrete-filled tubes after exposure to fire	Tao et al. (2007a, 2008)
Hybrid FRP–concrete–steel double skin columns, GFRP tube (80 GPa)	The local buckling of the inner steel tube is either delayed or suppressed by the surrounding concrete, leading to a very ductile response.	Teng et al. (2007)

No.7 (Dutta et al. 1998) and No.9 (Kurobane et al. 2005), Wang (2002), Nethercot (2003), Wardenier et al. (2010) and Zhao et al. (2010a). A list of comprehensive references has been given in Zhao et al. (2010a). A brief summary of the design of CFST members using different standards is given in this section in terms of bending, compression, combined actions and fire resistance.

2.1.1.2 *CFST members in bending*

The nominal moment capacity given in the following standards BS5400 (2005), AS5100 (2004),

EC4 (2004), DBJ13-51 (2003) is based on simple plastic theory although slightly different stress distributions are adopted. The difference in the nominal moment capacities among the 4 standards mentioned above is found to be less than 2.5% for some typical HSS and concrete (Zhao et al. 2010a). The design capacity difference varies from 7% to 24%, which is mainly due to different material property factors or capacity factors adopted in different standards. The nominal moment capacity for concrete filled CHS and RHS beams can be estimated as follows:

$$M_{CFST,CHS} = 4 \cdot f_y \cdot t \cdot r_m^2 \cdot \cos\gamma_0 + \frac{2}{3} \cdot f_c \cdot r_i^3 \cdot \cos^3\gamma_0 \quad (1a)$$

$$r_m = \frac{d - t}{2} \quad (1b)$$

$$r_i = \frac{d - 2 \cdot t}{2} \quad (1c)$$

$$\gamma_0 = \frac{\pi}{2} \cdot F_{CHS} \quad (1d)$$

$$F_{CHS} \approx \frac{\frac{1}{8} \cdot \frac{f_c}{f_y} \cdot \frac{d}{t}}{1 + \frac{1}{4} \cdot \frac{f_c}{f_y} \cdot \frac{d}{t}} \quad (1e)$$

$$M_{CFST,RHS} = f_y \cdot t \cdot \left[B \cdot (D - t) + \frac{1}{2} \cdot (D - 2 \cdot t)^2 \right] + f_y \cdot t \cdot \frac{1}{2} \cdot (D - 2 \cdot t)^2 \cdot (1 - F_{RHS})^2 + \frac{1}{2} \cdot (B - 2 \cdot t) \cdot d_n^2 \cdot f_c \quad (2a)$$

$$d_n = \left(\frac{D - 2 \cdot t}{2} \right) \cdot F_{RHS} \quad (2b)$$

$$F_{RHS} \approx \frac{1}{1 + \frac{1}{4} \cdot \frac{f_c}{f_y} \cdot \frac{B}{t}} \quad (2c)$$

where f_y is the yield stress of HSS, f_c is concrete cylinder strength, d, D, B and t are defined in Figure 1.

2.1.1.3 *CFST members in compression*

Different standards (e.g. AIJ 1997, AISC 2010, ACI 2002, BS5400, EC4, DBJ13-51) have different approaches in dealing with the design of CFST compressive section capacity, as shown in Table 2.

It was found by Zhao et al. (2010a) that the nominal section capacity predicted by BS5400 is slightly higher than those from AS5100 (2004), EC4, DBJ13-51, whereas the difference in nominal capacities among the other 3 standards is within 4% for some typical sections. The difference between the design section capacities varies from 1% to 20% among the standards due to different material property factors or capacity factors adopted in different standards.

For CFST column design the approach is very similar, i.e. section capacity (N_s) multiplied by a reduction factor (φ).

$$N_c = \varphi N_s \quad (3)$$

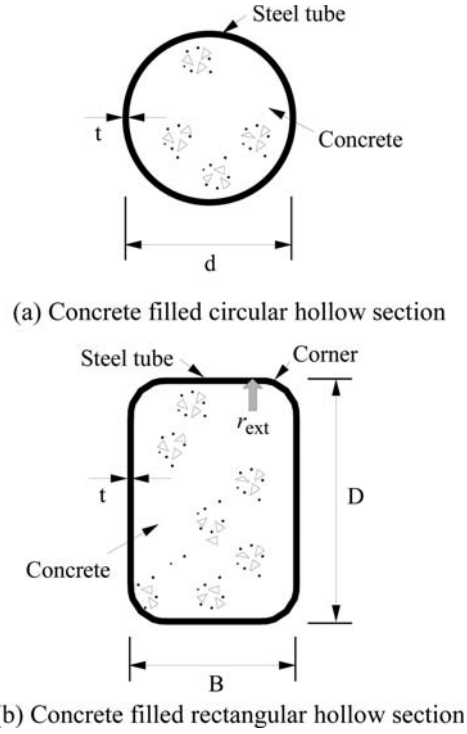

Figure 1. Concrete filled Hollow Structural Section (HSS).

Different column curves are adopted in different standards to determine the reduction factor φ which is basically a function of column slenderness, except for BS5400 where an extra reduction factor of 0.85 needs to be considered. The column slenderness depends mainly on the column length, boundary conditions at column ends and yield stress. Some typical column curves are summarized in Zhao et al. (2010a). The maximum difference in column design capacity among the four standards mentioned above is about 10% to 20% for some typical sections.

2.1.1.4 *CFST members subject to combined bending and compression*

The stress distribution in CFST members subjected to combined bending and compression (also called CFST beam-columns) has four typical cases corresponding to various level of axial force versus the level of bending moment. The four typical stress distributions determine four typical locations of the neutral axis in CFST beam-columns, which in turn correspond to the four key points (A, B, C and D) in the interaction diagrams defined in Figure 2. The interaction diagram for an unfilled HSS beam-column is also shown in Figure 2 as a dashed line connecting points A and B. The part CDB in the interaction diagram is unique for CFST members due to the contribution of concrete.

Three straight lines (AC, CD and DB) are adopted in Eurocode 4 to simplify the interaction diagram. In DBJ13-51, a combination of a straight line (AC)

Table 2. Design approaches for section capacity of CFST HSS.

Code	Method	Confinement considered (Yes or No)	Concrete strength (Cube or Cylinder)
AIJ	Superposition	No	Cylinder
AISC	Equivalent steel section with modified yield stress	No	Cylinder
ACI	RC method by converting steel tube into equivalent "reinforced bars".	No	Cylinder
BS5400	Composite section with modified concrete strength	Yes	Cube
EC4	Composite section with modified concrete strength	Yes	Cylinder
DBJ13-51	Treat the whole section as one material with modified stress	Yes	Cube

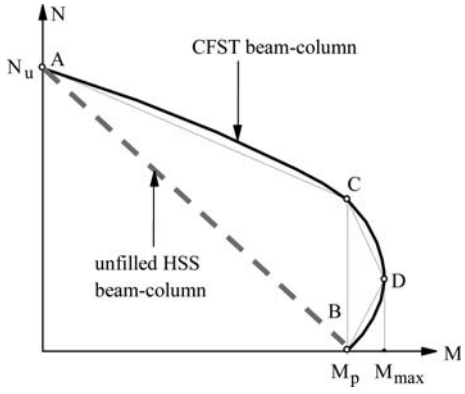

Figure 2. Schematic view of interaction diagram.

and a curve (CDB) is adopted. In BS5400 it is specified that the maximum bending moment should not exceed the ultimate moment capacity of CFST members subject to pure bending. Therefore the interaction diagram in BS5400 only consists of two parts (AC which is a straight line for CFST RHS and a curve for CFST CHS, and CB which is a vertical cut-off line). The turning point C in EC4 and BS5400 has the same value, whereas a different value is adopted in DBJ13-51. DBJ13-51 also gives two separate interaction diagrams, one for section capacity and the other for member capacity in a non-dimensional format. Design examples can be found in Zhao et al. (2010a).

2.1.1.5 *Fire resistance of CFST columns*

Three levels of assessment of fire resistance of unprotected CFST columns were presented in CIDECT Design Guide No. 4 (Twilt et al. 1995). Level 1 assessment utilizes a simple design table to determine the minimum cross-sectional dimensions, reinforcement ratios and location of reinforcement bars to satisfy a certain degree of utilization (μ) and fire resistance (R30 minutes to R180 minutes). Level 2 assessment utilizes the concept of a buckling curve for CFST columns for different fire classes. It recommends a buckling curve for given values of tube size, steel grade, fire class, concrete grade and the amount of reinforcement. The effective buckling length factor of columns in braced frames is between 0.5 and 0.7 depending on the boundary conditions (Twilt et al. 1995). A conservative value of 0.7 may be used for estimating the bucking length of columns on the top floor and for the columns at the edge of a building with only one adjacent beam. The validity range of level 2 assessment can be summarised as follows: Fire classes are R60, R90 and R120, Concrete grades C20, C30 and C40, CHS diameter d = 219 to 406 mm and thickness t = 4.5 to 6.3 mm, SHS width B = 180 to 400 mm and thickness t = 6.3 to 10 mm. Level 3 assessment includes a complete thermal and mechanical analysis with real boundary conditions. This is the most sophisticated level. It requires expert knowledge and time in handling necessary computer programs.

The preferred solution in China to achieve sufficient fire resistance is to use plain concrete-filled tubes with external fire protection rather than using steel bar or fibre reinforced concrete. The formulae in DBJ13-51 to calculate the thickness of fire protection materials are based on the research by Han et al. (2003a, 2003b), which can be expressed as a function of fire load ratio, fire resistance, perimeter of the column and column slenderness. It was demonstrated by Han and Yang (2007) that the protection thickness could be reduced from 50 mm (based on conventional code for fire protection of steel columns) to 10 mm (based on DBJ13-51) for two high rise buildings: SEG Plaza (291.6 m in height) and Wuhan International Stock Centre (242.9 m in height) requiring 180 minutes of fire resistance, due to concrete-filling.

An extensive research program was carried out in North America on CFST HSS columns under fire (Lie and Chabot 1990, Kodur and Lie 1996, Lie and Stringer 1994, Kodur 1998, 1999), with three types of concrete-filling, namely plain concrete, steel bar-reinforced concrete and steel fibre-reinforced concrete. A formula was proposed (Lie and Stringer 1994,

Kodur 1999) to calculate the fire resistance of CFST columns as shown in Eq. (6).

$$R = f\frac{(f_c' + 20)}{(KL - 1000)}D^2\sqrt{\frac{D}{P}} \quad (4)$$

where R is the fire resistance in minutes, f_c' is the specified 28-day cylinder concrete strength in MPa, D is the outside diameter or width of the column in mm, P is the applied axial load in kN, K is the effective length factor, L is the column length in mm and f is a parameter that depends on the type of concrete filling (plain, bar-reinforced or fibre-reinforced), the cross-sectional shape (circular or square), the type of aggregate (carbonate or siliceous), the percentage of steel reinforcement (p_r) and the thickness of concrete cover. Values of the parameter f are summarized in Table 7.5 of Zhao et al. (2010a).

2.1.2 *Future work*

The future work in CFST HSS is needed in the following areas: (i) new materials such as stainless steel tubes, high strength steel tubes filled with self-consolidating concrete, geopolymeric recycled concrete and ultra high strength concrete (e.g. Uy 2008, Lu et al. 2009, Uy et al. 2011, Shi et al. 2012, Liew et al. 2012); (ii) new structural elements such as EHS, very slender CFST columns, tapered CFST columns and CFST fabricated section utilizing very high strength steel tubes as corners (e.g. Yang et al. 2008, Zhao and Packer 2009, Espinos et al. 2011, Han et al. 2010, An et al. 2012, Mashiri et al. 2011); (iii) connections and frames (e.g. Kurobane et al. 2005, Nie et al. 2006, Herrera et al.2008, Han et al. 2008, 2009, Wang et al. 2009); (iv) fatigue resistance of CFST joints (e.g. Udomworarat et al. 2000, Gu et al. 2008, Tong et al. 2008, Mashiri and Zhao 2010); (v) earthquake followed by fire (e.g. Song et al. 2012); and (vi) CFST subject to impact and blast loading as well as progressive collapse (e.g. Bambach et al. 2008, Fujikura et al. 2008, Remennikov et al. 2011, Qu et al. 2011, Kang et al. 2012, Nethercot 2009).

2.2 *Concrete filled double skin HSS*

2.2.1 *Existing research and main findings*

Concrete filled double skin hollow structural sections have four possible combinations of CHS and RHS as the outer and inner tubes. Two examples are shown in Figure 3.

Most of the existing research on CFDST has been summarized in Zhao and Han (2006) and Chapter 9.4 of Zhao et al. (2010a).

The ultimate moment capacity of CFDST (M_{CFDST}) can be estimated using the sum of the section capacity of an unfilled inner tube (M_{inner}) and that of an outer tube with concrete component, i.e.

$$M_{CFDST} = M_{inner} + M_{outer-with-concrete} \quad (5)$$

where $M_{outer\text{-}with\text{-}concrete}$ can be derived in a similar manner as that for CFST, i.e. adopting simple plastic

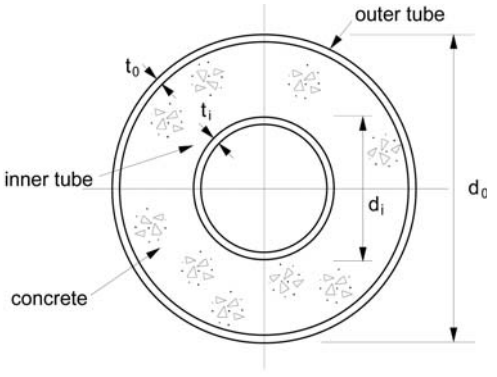

(a) CFDST with CHS outer and CHS inner

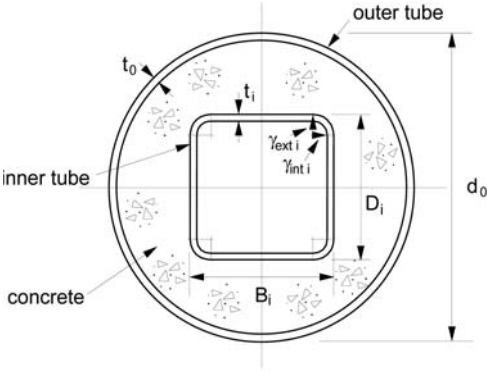

(b) CFDST with CHS outer and RHS inner

Figure 3. Concrete filled double skin Hollow Structural Section (HSS).

theory to find out the position of the neutral axis, then adding the moment contribution of each force through the cross-section. Formulae for M_{CFDST} were given in Zhao and Choi (2010) for four possible combinations of CHS and RHS as the outer and inner tubes.

For CFDST sections in compression, local buckling is delayed or eliminated, with a significant increase in load carrying capacity and ductility compared with those of the outer tube alone, as shown in Figure 4. The section capacity of a CFDST can be estimated using the superposition method; i.e. a sum of capacities of the outer tube, inner tube and concrete.

For CFDST subject to combined bending and compressive forces, the interaction formulae were derived by Han et al. (2004), Tao et al. (2004). They are similar to those given by Han et al. (2001) for concrete-filled beam-columns. They were summarised in Chapter 9.4.2.3 of Zhao et al. (2010a).

If other conditions are kept the same, the fire endurance of CFDST columns was found to be slightly better than tubular columns fully filled with concrete

(i) CHS outer with d_o/t_o of 55

(ii) CFDST with d_o/t_o of 55

(a) Failure mode

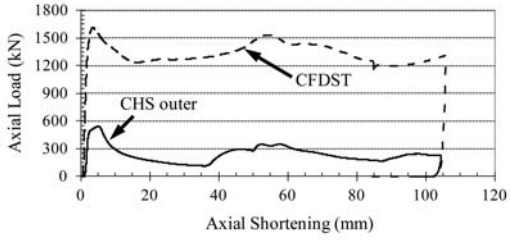

(b) Axial load versus shortening curve (with d_o/t_o of 55)

Figure 4. Typical behaviour of CFDST in compression versus that of outer steel tube (adapted from Zhao et al. 2010b).

(Yang and Han 2008, Lu et al. 2010). This is mainly because of the relatively low temperature in the inner steel tube. Therefore the fire resistance of a CFDST column could be conservatively estimated by treating it as a CFST column.

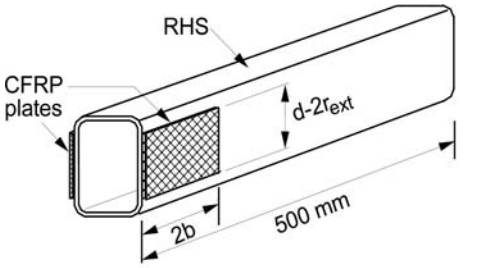

(a)Type O (Outside web strengthening)

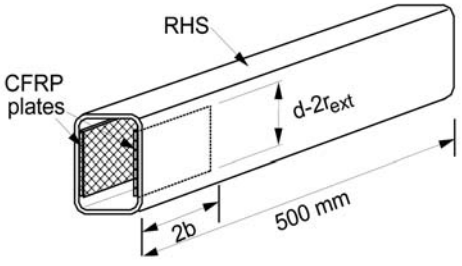

(b) Type I (Inside web strengthening)

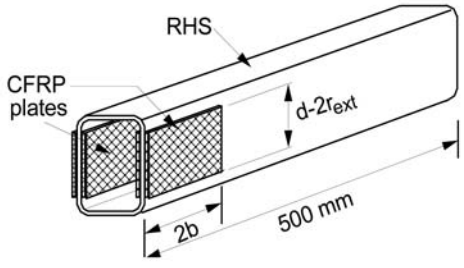

(c)Type B (Both sides strengthening)

Figure 5. Types of strengthening for Rectangular Hollow Section (RHS) webs (adapted from Zhao et al. 2006).

2.2.2 *Future work*

The future work described in Section 2.1.2 for CFST HSS equally applies to CFDST HSS with additional references relevant to CFDST subject to dynamic loading shown below: e.g. Nakanishi et al. (1999), Han et al. (2006) and Corbett et al. (1990).

3 HOLLOW STRUCTURAL SECTION MEMBERS AND FRP

3.1 *CFRP strengthened RHS webs*

Web crippling failure becomes critical at the loading points or supports of beams where concentrated forces are applied. Zhao et al. (2006) conducted a study on FRP strengthening of cold-formed rectangular hollow sections (RHS) subject to an end bearing force. Three types of strengthening scheme were adopted as shown in Figure 5.

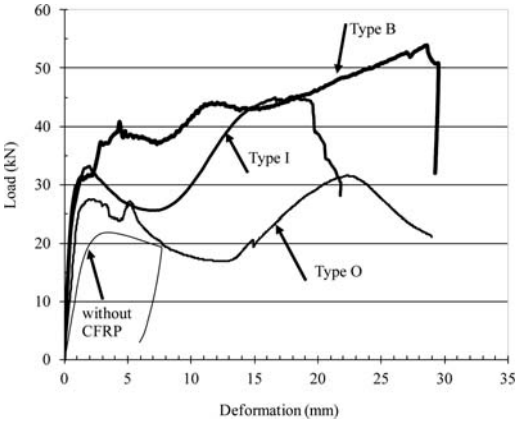

Figure 6. Typical load deformation curves for cold-formed RHS $100 \times 50 \times 2$ with various types of strengthening (adapted from Zhao et al. 2006).

Typical load-deformation behaviour is presented in Figure 6, which clearly demonstrates the increased web crippling capacity and ductility. The main reasons for the improved behaviour are the increased restraint against web rotation and the change of failure mode from web bucking to web yielding. Design formulae were proposed (Zhao et al. 2006) to predict the improved web buckling capacity, which are similar to those for un-strengthened webs, but with reduced effective length factor. Similar research was also conducted on aluminium RHS and stainless steel RHS by Wu et al. (2012) and Islam and Young (2010, 2011). Recently Fam and Aguilera (2012) carried out tests on GFRP (glass fibre reinforced polymer) strengthened RHS webs in a welded T-joint.

3.2 *CFRP strengthened HSS in compression*

Hybrid GFRP-CHS columns were studied by Teng and Hu (2007), whereas CFRP-CHS columns were investigated by Haedir and Zhao (2011). The "elephant foot" buckling mode in CHS is delayed or eliminated by FRP. More increase in ultimate load carrying capacity was found with CFRP than that with GFRP.

Tests were carried out on hybrid CFRP-SHS columns by Shaat and Fam (2006). Failure of retrofitted SHS columns was via overall buckling followed by secondary local buckling associated with delamination and crushing of the CFRP. Bambach and Elchalakani (2007) conducted quasi-static tests on CFRP reinforced SHS under large deformation axial compression. Multiple folding mechanisms were observed (see Figure 7) with an increased ultimate strength and energy absorption. The FE work by Shaat and Fam (2007) revealed that the axial strength of CFRP-SHS columns is not sensitive to initial imperfection of SHS. Bambach and Elchalakani (2007) applied a plastic mechanism analysis to reasonably predict the unloading curves of such hybrid columns.

Figure 7. Typical failure mode of SHS and CFRP-SHS subject to large deformation axial loading (Bambach and Elchalakani 2007).

It should be noted that different combinations of longitudinal and transverse fibres were adopted in the above studies.

The design of CFRP-SHS and CFRP-CHS columns was presented in Bambach et al. (2009a) and Haedir and Zhao (2011).

3.3 *CFRP strengthened HSS in bending*

Haedir et al. (2009) carried out tests on CFRP-CHS beams in pure bending. Both longitudinal and transverse CFRP sheets were applied. It was found that the longitudinal CFRP layers contributed more to the increase in moment capacity, whereas the hoop layers played a more important role in restraining or delaying the local buckling. Slender CHS could become a non-compact CHS when strengthened by CFRP. The rotation capacity of non-compact CHS also increased significantly. Analytical models for determining the ultimate moment capacity and for predicting the moment-curvature response of CFRP-reinforced steel CHS beams were developed by Haedir et al. (2011). The nonlinear model accounted for material properties of the steel and CFRP, volume fractions of the fibre and adhesive, amount of CFRP, and a wider range of section slenderness. Design rules for predicting the strength of composite CHS under bending were also proposed (Haedir and Zhao 2012). Similar work was done by Seica and Packer (2007), where curing of the specimens was performed both in air and in seawater. A slightly lower increase in the ultimate moment capacity was observed for specimens cured in seawater.

Photiou et al. (2006) conducted a study on CFRP and GFRP strengthening of artificially degraded steel RHS beams. The degrading was done through machining the thickness of the tension flange. All the upgraded beams reached the plastic collapse load of the original undamaged RHS beams. It was recorded that the steel beams can be deformed well into their plastic regions. However it is difficult to quantify the achieved rotation capacity since the non-dimensional moment-curvature curves were not reported in the paper.

3.4 *Future work*

There is a need to conduct more tests to cover wider ranges of parameters, such as steel tubular section sizes, CFRP modulus, adhesive types and thickness. There is a lack of detailed FE simulation of web buckling with FRP strengthening (Fernando et al. 2009). More research is needed to understand the behaviour of FRP strengthened HSS subject to impact and blast loading (Bambach et al. 2009b), as well as harsh environmental conditions (Seica and Packer 2007).

4 HOLLOW STRUCTURAL SECTION JOINTS AND FRP

4.1 *CFRP strengthened welded VHS joints*

There is a significant (up to 50%) strength reduction in the HAZ (heat affected zone) of very high strength (VHS) tubes after welding. Jiao and Zhao (2004) investigated the behaviour of CFRP strengthened butt-welded VHS tubes. Significant strength increase was obtained for CFRP strengthened butt-welded VHS tubes. The full yield capacity of VHS steel tubes was recovered when the bond length reachedabout 50 mm.

4.2 *FRP strengthened aluminium CHS K-joints*

Welded aluminum K-joints with different damage levels (e.g. about 25%, 65% and 100% of the total welded length) were repaired by using GFRP (Pantelides et al. 2003). The repaired joints with a damage level up to 65% reached capacities about 20% higher than those without cracks, whereas the repaired joints with a damage level of 100% recovered 95 to 99% of the original capacity. A similar study was carried out by Fam et al. (2006) on using CFRP and GFRP to repair cracked welded aluminum K-joints with a damage level of 90%. The full strength of the welded joints could be restored if CFRP was used, whereas about 80% of the capacity was restored by using GFRP.

Nadauld and Pantelides (2007) studied the fatigue performance of GFRP-strengthened aluminium K-joints with partially fractured branch-to-chord welds. The repaired joints exceeded the fatigue limit of the welded aluminium K-joints without damage. The same type of K-joints with 90% of the weld removed were repaired using GFRP. Such repaired joints satisfied the constant amplitude fatigue limit threshold. A cumulative damage index was established which led to a fatigue reduction factor for the rehabilitation design of cracked aluminum connections using GFRP composites.

4.3 *Future work*

There is a need to develop strengthening techniques for various types of welded HSS joints subject to fatigue loading, such as cross-beam joints (Xiao and Zhao 2012), cast steel to HSS joints. Theoretical modeling and numerical simulation are also necessary.

5 HOLLOW STRUCTURAL SECTION, CONCRETE AND FRP

5.1 *CFRP strengthened CFST*

Xiao et al. (2005) studied CFST columns confined by CFRP at critical locations to avoid plastic hinges, hence soft storey behaviour, under earthquake loading. A gap (made with 1-mm-thick soft foam tapes affixed on the surface of the steel tube) was introduced between the CFRP and the tubular column to delay the engagement of the CFRP, to achieve both increased strength and ductility. The work on using CFRP to strengthen CFST SHS and CHS columns is still very limited although attempts were made by some researchers (Tao et al. 2007b, Sun et al. 2008, Park et al. 2010). Research has been undertaken (Tao et al. 2008) to determine the effectiveness of using FRP composites to repair damaged CFST columns, particularly for damage due to fire exposure. These results revealed that CFRP gave reasonable repair for specimens with a low level of exposure to fire.

5.2 *Hybrid double skin section*

Teng et al. (2007) developed a hybrid FRP–concrete–steel double-skin tubular column (see Figure 8 for an example). The test results confirmed that the concrete in the new column is very effectively confined by the two tubes and the local buckling of the inner

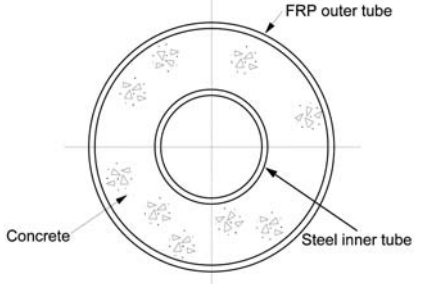

(a) FRP-concrete-steel hybrid double skin section (without eccentricity)

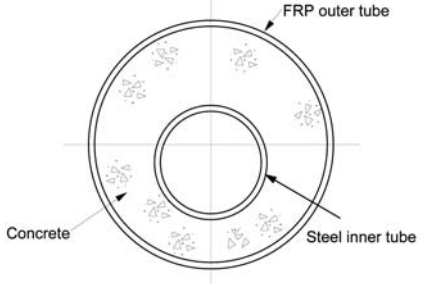

(b) FRP-concrete-steel hybrid double skin section (with eccentricity)

Figure 8. Schematic view of FRP-concrete-steel double skin section, e.g. CHS FRP as outer tube and steel CHS as inner tube (adapted from Teng et al. 2007).

steel tube is either delayed or suppressed by the surrounding concrete, leading to a very ductile response. When such hybrid sections are used as beams, the inner steel tube could be shifted towards the tensile side (see Figure 8(b)). Such beams were found to have a very ductile behaviour. The GFRP tube enhances the structural behaviour by providing both confinement to the concrete and additional shear resistance.

5.3 *Future work*

More tests are needed on FRP-CFST columns and FRP-concrete-HSS hybrid columns with wider ranges of parameters. There is a need to develop analytical models, numerical simulation and a design guide for such hybrid sections under static and dynamic loading (Shan et al. 2007).

6 CONCLUSIONS

This paper has presented a summary of recent developments in hybrid hollow structural sections (HSS) in the form of: concrete filled HSS; concrete filled double skin HSS; FRP strengthened HSS with/without concrete filling; FRP, concrete and HSS double skin sections. The benefits of hybrid HSS include increased strength, ductility, fire resistance, energy absorption and fatigue life. The existing research, main findings and future work for each type of HSS have been described. A comprehensive list of references in this field has been given.

ACKNOWLEDGEMENT

The author wishes to thank the following professors in the field of hollow structural sections and FRP strengthening for their advice, collaboration and friendship: Prof. Greg Hancock at the University of Sydney, Prof. Jeff Packer at the University of Toronto, Prof. Jaap Wardenier at Delft University of Technology, Prof. Lin-Hai Han at Tsinghua University, Prof. Le-Wei Tong at Tongji University, Prof. Qing-Yuan Wang at Sichuan University, Prof. Jin-Guang Teng at Hong Kong Polytechnic University, Prof. Sami Rizkalla at North Carolina State University and Prof. Len Hollaway at Surrey University. The encouragement and support from members of IIW XV-E subcommission and CIDECT are deeply appreciated. The author wishes to dedicate this paper to the late Professor Yoshi Kurobane who made such a significant contribution to the research into hollow structural sections.

REFERENCES

ACI. 2002. *Building code requirements for structural concrete and commentary*. ACI 318M-02, Michigan: American Concrete Institute.

AIJ. 1997. *Recommendations for design and construction of concrete filled steel tubular structures.* Tokyo: Architectural Institute of Japan.

AISC. 2010. *Specification for structural steel buildings*. ANSI/AISC 360-10, Chicago: American Institute of Steel Construction.

An, Y.F., Han, X.L. & Zhao, X.L. 2012. Behaviour and design calculations on very slender thin-walled CFST columns. *Thin-Walled Structures* 53(6): 161–175.

AS5100. 2004. *Bridge design – Steel and composite construction*. Australian Standard AS 5100, Sydney: Standards Australia.

Baker, A.A., Rose, L.R.F. & Jones, R. 2002. *Advances in the bonded composite repair of metallic aircraft structure*. Amsterdam: Elsevier.

Bambach, M.R. & Elchalakani M. 2007. Plastic mechanism analysis of steel SHS strengthened with CFRP under large axial deformation. *Thin-Walled Structures* 45(2): 159–170.

Bambach, M.R., Jama, H., Zhao, X.L. & Grzebieta, R.H. 2008. Hollow and concrete filled steel hollow sections under transverse impact loads. *Engineering Structures* 30(10): 2859–2870.

Bambach, M.R., Jama, H. & Elchalakani, M. 2009a. Axial capacity and design of thin-walled steel SHS strengthened with CFRP. *Thin-Walled Structures* 47(10): 1112–1121.

Bambach, M.R., Elchlakani, M. & Zhao, X.L. 2009b. Composite steel–CFRP SHS tubes under axial impact. *Composite Structures* 87(3): 282–292.

Bergmann, R., Matsui, C., Meinsma, C. & Dutta, D. 1995. *Design guide for concrete filled hollow section columns under static and seismic loading*. Köln: TÜV-Verlag.

BS5400. 2005. *Steel, concrete and composite bridges*. BS5400, Part 5: Code of practice for design of composite bridges. London: British Standards Institution.

Corbett, G., Reid, S. & Al-Hassani, S. 1990. Resistance of steel-concrete sandwich tubes to penetration. *International Journal of Impact Engineering* 9(2): 191–203.

DBJ13-51. 2003. *Technical specification for concrete-filled steel tubular structures*. Fuzhou: The Construction Department of Fujian Province.

Dutta, D., Wardenier, J., Yeomans, N., Sakae, K., Bucak, Ö & Packer, J.A. 1998. *Design guide for fabrication, assembly and erection of hollow section structures*. Köln: TÜV-Verlag.

EC 4. 2004. *Design of composite steel and concrete structures – Part 1.1: General rules and rules for buildings.* EN 1994-1-1:2004, December 2004, Brussels: European Committee for Standardization.

Espinos, A., Gardner, L., Romero, M.L. & Hospitaler, A. 2011. Fire behaviour of concrete filled elliptical steel columns. *Thin-Walled Structures* 49(2): 239–255.

Fam, A., Witt, S. & Rizkalla, S. 2006. Repair of damaged aluminum truss joints of highway overhead sign structures using FRP. *Construction and Building Materials* 20(10): 948–956.

Fam, A. & Aguilera, J. 2012. Strengthening T-joints of thin-walled rectangular hollow steel sections (HSS) using GFRP plates. *FRP International* 8(6): 3–6.

Fernando, D., Yu, T., Teng J.G. & Zhao X.L. 2009. CFRP strengthening of rectangular steel tubes subjected to end bearing loads: effect of adhesive properties and finite element modelling. *Thin-Walled Structures* 47(10): 1020–1028.

Fujikura, S., Bruneau, M., & Lopez-Garcia, D. 2008. Experimental investigation of multihazard resistant bridge piers having concrete-filled steel tube under blast loading. *Journal of Bridge Engineering* 13(6): 586–594.

Gu, M., Tong, L.W., Zhao, X.L. & Lin, X.G. 2008. Stress intensity factors of surface cracks in welded T-joints between CHS brace and concrete-filled chord. *Proceedings of the 12th International Symposium on Tubular Structures*, Shanghai, China, October, pp. 359–366.

Haedir, J., Bambach¸M.R., Zhao X.L. & Grzebieta R.H. 2009. Strength of circular hollow sections (CHS) tubular beams externally reinforced by carbon FRP sheets in pure bending. *Thin-Walled Structures* 47 (10): 1136–1147.

Haedir J. & Zhao, X.L. 2011. Design of short CFRP-reinforced steel tubular columns. *Journal of Constructional Steel Research* 67(3): 497–509.

Haedir J., Zhao, X.L., Grzebieta,R. H. & Bambach, M. 2011. Non-linear analysis to predict the moment-curvature response of CFRP-strengthened steel CHS tubular beams. *Thin-Walled Structures* 49(8): 997–1006.

Haedir J. & Zhao, X.L. 2012. Design of CFRP-strengthened steel CHS tubular beams. *Journal of Constructional Steel Research* in press, doi: 10.1016/j.jcsr.2011.12.004

Han, L.H., Zhao, X.L, Yang, Y.F. & Feng, J.B. 2003a. Experimental study and calculation of fire resistance of concrete-filled hollow section columns. *Journal of Structural Engineering* 129(3): 346–356.

Han, L.H., Yang, Y.F. & Xu, L. 2003b. An experimental study and calculations on the fire resistance of concrete-filled SHS and columns. *Journal of Constructional Steel Research* 59(6): 427–452.

Han, L.H., Tao, Z. & Zhao, X.L. 2004. Concrete-filled double skin (SHS outer and CHS inner) steel tubular beam-columns. *Thin-Walled Structures* 42(9): 1329–1355.

Han, L.H., Huang, H., Tao, Z. & Zhao, X.L. 2006. Concrete-filled double skin steel tubular (CFDST) beam-columns subjected to cyclic bending. *Engineering Structures* 28(12): 1698–1714.

Han, L.H. & Yang, Y.F. 2007. *Modern technology of concrete-filled steel tubular structures*. Beijing: China Architecture and Building Press.

Han, L.H., Wang, W.D. & Zhao, X.L. 2008. Behaviour of steel beam to concrete-filled SHS column frames: Finite element model and verifications. *Engineering Structures* 30(6): 1647–1658.

Han, L.H., Li, W. & Uy, B. 2009. Seismic behaviour of concrete-filled steel tubular frame to RC shear wall high-rise mixture structures. *Journal of Constructional Steel Research* 65(7): 1249–1260.

Han, L.H., Ren, Q.X. & Li, W. 2010. Tests on inclined, tapered and STS concrete-filled steel tubular (CFST) stub columns. *Journal of Constructional Steel Research* 66(10): 1186–1195.

Han, L.H., Zhao, X.L. & Tao, Z. 2001. Test and mechanics model for concrete-filled SHS stub columns, columns, and beam-columns. *Steel and Composite Structures* 1(1): 51–74.

Herrera, R.A., Ricles, J.M., & Sause, R. 2008. Seismic performance evaluation of a large-scale composite MRF using pseudodynamic testing. *Journal of Structural Engineering* 134(2): 279–288.

Hollaway, L.C. & Cadei, J. 2002. Progress in the technique of upgrading metallic structures with advanced polymer composites. *Progress in Structural Engineering and Materials* 4(2): 131–148.

Hollaway, L.C. & Teng., J.C. 2008. *Strengthening and rehabilitation of civil infrastructures using fiber-reinforced polymer (FRP) composites*. Cambridge: Woodhead Publishing.

Islam, S.M.Z. & Young, B. 2010. Effects of different adhesive and FRP on strengthening of stainless steel tubular structural members. *Proceedings of the 13th International Symposium on Tubular Structures*, Hong Kong, China, December, pp.273–280.

Islam, S.M.Z. & Young, B. 2011. FRP Strengthened aluminium tubular sections subjected to web crippling. *Thin-Walled Structures* 49(11): 1392–1403.

Jiao, H. & Zhao, X.L. 2004. CFRP strengthened butt-welded very high strength (VHS) circular steel tubes. *Thin-Walled Structures* 42(7): 963–978.

Kang, K.W., Lee, S.C. & Liew, J.Y.R. 2012. Analysis of steel-concrete composite column subject to blast. *Structures and Buildings*, ICE Proceedings, in press.

Kodur, V.K.R. & Lie, T.T. 1996. Fire resistance of circular steel columns filled with fibre-reinforced concrete. *Journal of Structural Engineering* 122(7): 776–782.

Kodur, V.K.R. 1998. Design equations for evaluating fire resistance of SFRC-filled HSS columns. *Journal of Structural Engineering* 124(6): 671–677.

Kodur, V.K.R. 1999. Performance-based fire resistance design of concrete-filled steel columns. *Journal of Constructional Steel Research* 51(1): 21–36.

Kurobane, Y., Packer, J.A., Wardenier, J. & Yeomans, N. 2005. *Design guide for structural hollow section column connections*. Köln: TÜV-Verlag.

Lie, T.T. & Chabot, M. 1990. A method to predict the fire resistance of circular concrete filled hollow steel columns. *Journal of Fire Protection Engineering* 2(6): 111–126.

Lie, T.T. & Stringer, D.C. 1994. Calculation of the fire resistance of steel hollow structural section columns filled with plain concrete. *Canadian Journal of Civil Engineering* 21(3): 382–385.

Liew, J.Y.R., Xiong, D.X. & Xiong, M.X. 2012. Experimental investigation on ultra-high strength concrete filled steel tube columns. *Proceedings of the 14th International Symposium on Tubular Structures*, London, UK, September.

Lu, H., Zhao, X.L. & Han, L.H. 2009. Fire behaviour of high strength self-consolidating concrete filled steel tubular stub columns. *Journal of Constructional Steel Research* 65(10–11): 1995–2010.

Lu, H., Han, L.H. & Zhao, X.L. 2010. Fire performance of self-consolidating concrete filled double skin steel tubular columns: Experiments. *Fire Safety Journal* 45(2): 106–115.

Mashiri, F.R. & Zhao, X.L. 2010. Square hollow section (SHS) T-joints with concrete-filled chords subjected to in-plane fatigue loading in the brace. *Thin-Walled Structures* 48(2): 150–158.

Mashiri, F.R., Uy, B. & Naderloo, H. 2011. Concrete-filled VHS-to-mild steel plate fabricated section stub column tests. *Proceedings of the 6th International Symposium on Steel Structures*, Seoul, Korea, November, pp. 913–918.

Nadauld, J. & Pantelides, C.P. 2007. Rehabilitation of cracked aluminium connections with GFRP composites for fatigue stresses. *Journal of Composite Construction* 11(3): 328–335.

Nakanishi, K., Kitada, T. & Nakai, H. 1999. Experimental study on ultimate strength and ductility of concrete filled steel columns under strong earthquakes. *Journal of Constructional Steel Research* 51(3): 297–319.

Nethercot, D.A. 2003. *Composite construction*, London: Spon Press.

Nethercot, D.A. 2009. Enhancing the robustness of steel and composite buildings. *Proceedings of the 6th International Conference on Advances in Steel Structures*, Hong Kong, China, December, pp.105–122.

Nie, J.G., Qin, K. & Xiao, Y. 2006. Push-over analysis of the seismic behavior of a concrete-filled rectangular tubular

frame structure. *Tsinghua Science and Technology* 11(1): 124–130.

Oehlers, D.J. & Seracino, R. 2004. *Design of FRP and steel plated RC structures – retrofitting beams and slabs for strength, stiffness and ductility*. Oxford: Elsevier.

Pantelides, C.P., Nadauld, J. & Cercone, L. 2003. Repair of cracked aluminium overhead sign structures with glass fiber reinforced polymer composites. *Journal of Composite Construction* 7(2): 118–126.

Park, J.W., Hong, Y.K. & Choi, S.M. 2010. Behaviors of concrete filled square steel tubes confined by carbon fiber sheets (CFS) under compression and cyclic loads. *Steel & Composite Structures* 10(2): 187–205.

Photiou, N.K., Hollaway, L.C. & Chryssanthopoulos, M.K. 2006. Strengthening of an artificially degraded steel beam utilizing a carbon/glass composite system. *Construction and Building Materials* 20(1–2): 11–21.

Qu, H.Y., Li, G.Q., Chen, S.W., Sun, J.Y. & Sozen, M.A. 2011. Analysis of circular concrete-filled steel tube specimen under lateral impact. *Advances in Structural Engineering – An International Journal* 14(7): 941–952.

Remennikov, A.M., Kong, SY. & Uy, B. 2011. Response of foam- and concrete-filled square steel tubes under low-velocity impact loading. *Journal of Performance of Constructed Facilities* 25(7): 373–381.

Rizkalla, S., Hassan, T. & Hassan, N. 2003. Design recommendations for the use of FRP for reinforcement and strengthening of concrete structures. *Progress in Structural Engineering and Materials* 5(1): 16–28.

Schnerch, D., Dawood, M., Rizkalla, S. & Sumner, E. 2007. Proposed design guidelines for strengthening steel bridges with FRP materials. *Construction and Building Materials* 21(7): 1001–1010.

Seica, M.V. & Packer, J.A. 2007. FRP materials for the rehabilitation of tubular steel structures, for underwater applications. *Composite Structures* 80(3): 440–450.

Shaat, A. & Fam, A. 2006. Axial loading tests on CFRP-retrofitted short and long HSS steel columns. *Canadian Journal of Civil Engineering* 33(6): 458–470.

Shaat, A. & Fam, A. 2007. Fiber-element model for slender HSS columns retrofitted with bonded high-modulus composites. *Journal of Structural Engineering* 133(1): 85–95.

Shan, J.H., Chen, R., Zhang, W.X., Xiao, Y., YI, W.J. & Lu, F.Y. 2007. Behavior of concrete filled tubes and confined concrete filled tubes under high speed impact. *Advances in Structural Engineering – An International Journal* 10(2): 209–218.

Shi, X.S., Wang, Q.Y., Zhao, X.L. & Collins, F. 2012. Experimental study on strength and ductility of steel tubular stub columns filled with geopolymeric recycled concrete. *Proceedings of the 14th International Symposium on Tubular Structures*, London, UK, September.

Song, Q.Y., Heidarpour, A., Zhao, X.L. & Han, L.H. 2012. FE modelling of flexible I-beam to square hollow section column connections subjected to earthquake and subsequent fire. *Proceedings of the 14th International Symposium on Tubular Structures*, London, UK, September.

Sun, G.S., Zhao, Y.H. and Gu, W. 2008. Stability of concrete filled CFRP-steel tube under axial compression. *Proceedings of the 12th International Symposium on Tubular Structures*, Shanghai, China, October, pp. 111–116.

Tao, Z., Han, L.H. & Zhao, X.L. 2004. Behaviour of concrete-filled double skin CHS steel tubular stub columns and beam-columns. *Journal of Constructional Steel Research* 60(8): 1129–1158.

Tao, Z., Han, L.H. & Wang, L.L. 2007a. Compressive and flexural behaviour of CFRP-repaired concrete-filled steel tubes after exposure to fire. *Journal of Constructional Steel Research* 63(8): 1116–1126.

Tao, Z., Han, L.H. & Zhuang, J.P. 2007b. Axial loading behaviour of CFRP strengthened concrete-filled steel tubular stub columns. *Advances in Structural Engineering – An International Journal* 10(1): 37–46.

Tao, Z., Han, L.H. & Zhuang, J.P. 2008. Cyclic performance of fire-damaged concrete-filled steel tubular beam-columns repaired with CFRP wraps. *Journal of Constructional Steel Research* 64(1): 37–50.

Teng, J.G., Chen, J.F., Smith, S.T. & Lam, L. 2002. *FRP – strengthened RC structures*, West Sussex: John Wiley & Sons, Ltd.

Teng, J.G. & Hu. Y.M. 2007. Behaviour of FRP-jacketed circular steel tubes and cylindrical shells under axial compression. *Construction and Building Materials* 21(6): 827–838.

Teng, J.G., Yu, T., Wong, Y.L & Dong, S.L. 2007. Hybrid FRP–concrete–steel tubular columns: Concept and behaviour. *Construction and Building Materials* 21(6): 846–854.

Tong, L.W., Sun, C.Q., Chen, Y.Y, Zhao, X.L., Shen, B. & Liu, C.B. 2008. Experimental comparison in hot spot stress between CFCHS and CHS K-joints with gap. *Proceedings of the 12th International Symposium on Tubular Structures*, Shanghai, China, October, pp. 389–395.

Twilt, L., Hass, R., Klingsch, W., Edwards, M. & Dutta, D. 1996. *Design guide for structural hollow section columns exposed to fire*. Köln: TÜV-Verlag.

Udomworarat, P., Miki, C., Ichikawa, A., Sasaki, E., Sakamoto, T., Mitsuki, K. & Hasaka, T. 2000. Fatigue and ultimate strengths of concrete filled tubular K-joints on truss girder. *Journal of Structural Engineering* (Japan Society of Civil Engineers) 46(3): 1627–1635.

Uy, B. 2008. Stability and ductility of high performance steel sections with concrete infill. *Journal of Constructional Steel Research* 64(7–8): 748–754.

Uy, B. Tao, Z & Han, L.H. 2011. Behaviour of short and slender concrete filled stainless steel tubular columns. *Journal of Constructional Steel Research* 67(3): 360–378.W

Wang, W.D., Han, L.H. & Zhao, X.L. 2009. Analytical behaviour of frames with steel beams to concrete-filled steel tubular column. *Journal of Constructional Steel Research* 65(3): 497–508.

Wang, Y.C. 2002. *Steel and composite structures: Behaviour and design for fire safety*. London: Taylor & Francis.

Wardenier, J., Packer, J.A., Zhao, X.L. & van der Vegte, G.J. 2010. *Hollow sections in structural applications*, Delft: Bouwen met Staal.

Wu, C., Zhao, X.L., Duan, W.H. & Phipat, P. 2012. Improved end bearing capacities of sharp-corner aluminium tubular sections with CFRP strengthening. *Journal of Structural Stability and Dynamics* 12(1): 109–130.

Xiao, Y., He, W.H. & Choi, K.K. 2005. Confined concrete-filled tubular columns. *Journal of Structural Engineering* 131(3): 488–497.

Xiao, Z.G. & Zhao, X.L. 2012. CFRP repaired welded thin-walled cross-beam connections subject to in-plane fatigue loading. *International Journal of Structural Stability and Dynamics* 12(1): 195–211.

Yang, H., Lam, D. & Gardner, L. 2008. Testing and analysis of concrete-filled elliptical hollow sections. *Engineering Structures* 30(12): 3771–3781.

Yang, Y.F. & Han, L.H. 2008. Concrete-filled double-skin tubular columns under fire. *Magazine of Concrete Research* 60(3): 211–222.

Zhao X.L. & Grzebieta R. 1999. Void-filled SHS beams subjected to large deformation cyclic bending. *Journal of Structural Engineering* 125(9): 1020–1027.

Zhao, X.L. & Han, L.H. 2006. Double skin composite construction.*Progress in Structural Engineering and Materials* 8(3): 93–102.

Zhao, X.L., Fernando, D. & Al-Mahaidi, R. 2006. CFRP strengthened RHS subjected to transverse end bearing force. *Engineering Structures* 28(11): 1555–1565.

Zhao, X.L. & Zhang, L. 2007. State of the art review on FRP strengthened steel structures. *Engineering Structures* 29(8): 1808–1823.

Zhao, X.L. & Packer, J.A. 2009, Tests and design of concrete-filled elliptical hollow section stub columns. *Thin-Walled Structures* 47(6–7): 617–628.

Zhao, X.L. & Choi, A. 2010. Moment capacity of concrete filled double skin tubes. *Proceedings of the 13th International Symposium on Tubular Structures*, Hong Kong, China, December, pp. 583–590.

Zhao, X.L., Han, L.H. & Lu, H. 2010a. *Concrete filled tubular members and connections*. London: Taylor & Francis.

Zhao, X.L., Tong, L.W. & Yang, X.Y. 2010b. CFDST stub columns subjected to large deformation axial loading. *Engineering Structures* 32(3): 692–703.

CIDECT 50th anniversary session papers

Tubular Structures XIV – Gardner (Ed.)
© 2012 Taylor & Francis Group, London, ISBN 978-0-415-62137-3

Tubular steel structures in architecture

M. Eekhout
Faculty of Architecture, Delft University of Technology, Director of Octatube, Delft, The Netherlands

ABSTRACT: The aesthetics of tubular structures are a major contribution to their architectural image, but as designers strive for a heightened spatial enlightenment, designs are requiring ever more complex structural solutions and high standards in their elements and components. New designs are helped by combinations of intelligent detailing, by the application of computerized 3D design, by engineering improvements in materials, by fabrication techniques and by assembly procedures. More attention is now paid to the integration with other components of the building, such as roof cladding, glass façades, panelled walls, climate installations, etc. The building as a technical artefact becomes increasingly complicated in its making and in its functioning. In the last decades Western European architectural ideas have been received with high expectations around the world. The computer and the internet have changed the behaviour and potentialities of architects. In earlier days it were books only to stimulate getting acquainted with foreign architecture, assisted by glossy magazines. The internet sites have even accelerated this. But the core of the developments is forced by design in tubular structures. When seen over a longer period, certain changes are apparent.

1 1991 STANSTED AIRPORT TERMINAL BUILDING, NORMAN FOSTER

The design of the Stansted Airport Terminal building is overwhelmed by the spreading arms of the roof structure, which is based on 36 modules in tubular structure. The outside modules are standing trees of tubular structure, which keep up intermediate roof modules of the same size that are connected along their edges. The 4 spreading arms carry the perimeter of a tubular triangulated framework shell visible as a vaulted ceiling. During the construction the 4 arms were held together by ties, which are connected in a very crucial joint, on the site called the 'Jesus joint'. The primary tubular structure module is concentrated on ground level of the terminal in 4 CHS columns, welded in a majestic framework, which penetrates the lower stories through voids. The roof structures are clad in metal, but the tops are covered in glass to obtain overhead daylight of the terminal space, softened by perforated metal sheeting. The large overhead volume gives the building the feeling of one unifying space with smaller activities.

Figure 1. Stansted Airport, London.

2 1991 AIRPORT PASSENGER TERMINAL STUTTGART, GERKAN, MARG UNDER PARTNER

The sloped roof of this terminal building is supported by a forest of steel trees, which are composed of circular tubes in a tree-like arrangement of stems, thicker

Figure 2. Passengers Terminal, Stuttgart.

and thinner branches that finally hold up the roof. The structure is characterised by welded intermediate steel castings to make a streamlined and natural transition from the smaller tubes into the thicker tubes and finally into the lower stems.

3 1992 EL ALAMILLO BRIDGE, SEVILLE, CALATRAVA

The prominent harp-like suspension bridge by Santiago Calatrava was built for the Olympic games of 1992 in Barcelona. The bridge was held up by 13 guy cables attached to the prominent and purpose made steel tubular section. The actual counterbalance to the cables and loads from the deck and cables is formed by filling the steel mast with concrete. Mainly the upper half acts as a counter ballast. Dutch architect Ben van Berkel would later (1996) design a similar cable stayed bridge in Rotterdam, the Erasmus bridge or 'The Swan', which is more facetted in form, made as a purpose made hollow section and instead of deadweight the counter balance was brought by two mayor stabilising cables at the back.

4 1993 WATERLOO INTERNATIONAL TRAIN TERMINAL, LONDON, NICOLAS GRIMSHAW

The high speed terminal train station nears the centre of London was designed by Nicolas Grimshaw as a large urban shed and inaugurated in 1993. The form the the structure had to follow the rails, which are in London partly historic and partly quite condensed and unavoidable curved in plan. In cross section the structure is a truss with three pins. The left truss has a suspended cladding, the other half an upper cladding. Cladding is in metal decking and glass. The form of the roof circular in plan with a large radius and the cross section with many different corners resulted in a construction system that had flexibility in form to allow for all possible geometrical deviations. Recently the Eurostar ceased to frequent Waterloo.

Figure 3. El Alamillo Bridge, Seville.

5 1994 KANZAI AIRPORT TERMINAL, OSAKA, RENZO PIANO, OVE ARUP

This airport in an densely populated urban area has been built on an artificial island, of which the underground was expected to deform considerably. This has been taken into account in the engineering plans of layout, schemes and details.

The architect's plan for a long building and overviewable terminal volume resulted in a king-size hall where departure and arrivals are separated horizontally. The tubular steel structure in an elegant arched form hovers over space. The structure itself has elegant details, some of them were made in cast steel and welded.

The three-dimensional trusses govern space, and between them are ceiling membranes in a similar shape, which lead the flow of air through the volume. The details of the building have been set on rubber bearings. Other precautions were taken as compensations against earthquakes. The Kobe earthquake of 1995 did no damage at all and the terminal complex emerged unscathed.

Figure 4. Waterloo station, London.

Figure 5. Partial façade Kanzai Airport.

6 1996 NEUE MESSE LEIPZIG, GERKAN MARG UND PARTNER, IAN RITCHIE

A 90 meters span tubular structure in which the main trusses span in the 90 m span direction above the glass cladding below. The cladding is suspended via tubular purlins in 2 directions from which the spiders are connecting the laminated clear glass panels. The height of 30 m caused a natural flow of air to ventilate as a chimney through space. Lower entrance ventilation, upper ridge exhaust ventilation.

7 1997 FREMONT STREET EXPERIENCE, LAS VEGAS, JON JERDE

A glass clad regular space frame in the form of a cylindrical barrel vault that easily could have span with the space frame alone.

The lower chord of the space frame has been enriched with a light penetrating sun screen, which unifies the space frame, takes the technical character down a bit. One wonders why tubular columns are at all positioned underneath a cylindrical space frame vault? The reason is more architectonical than functional/technical. The indoor atmosphere increased.

Figure 6. Interior passenger Terminal Kanzai Airport.

Figure 7. Neue Messe, Leipzig.

8 1997, STADE DE FRANCE, PARIS, MZRC

This tubular structures roof acts structurally as a saucer which is suspended upward and stabilised downward. From the outside it is a flat saucer. The interior displays a grid of CHS profiles, interconnected. the grid of flat trusses continues over the free playing field and hardly gives any shadow and covering. The floating character of this stadium overwhelms the A1 drivers alongside the building.

9 1998 LAW COURTS BORDEAUX, RICHARD ROGERS

A rather traditional set-up of trusses on columns with barrel-vaulted undulating roofs in between tem, mainly in tubular structures but now is a complex late-modern building with stone covered lower floors in concrete and upper volume in tubular steel enveloped with glass. Detailing is modern and state of the art. The conical space contains a court room. High Tech in an urban environment.

Figure 8. Fremont Street, Las Vegas.

Figure 9. Interior State de France, Paris.

Figure 10. Law Courts, Bordeaux.

Figure 11, 12. Oriente station & shopping centre, Lisbon.

10 1998 ORIENTE TRAIN STADIUM, LISBON, CALATRAVA

This train station has a minority in circular tubes and a majority of specially made steel ribs. Visually very much attraction looking and at the time of the Expo of Lisbon it was the entrance to the world. The welcoming gesture speaks for itself. The adjacent shopping centre continues the spatial experience.

11 2000 EDEN PROJECT, NICOLAS GRIMSHAW

The covering of the Eden project in Bodelva, Cornwall UK, contains two large greenhouses where public botanical gardens are located. The geometry of the domes is derived from regular polyhedra, intersecting in this case as giant soap bubbles. The space frames used are quite regular thanks to the Pre-High-Tech studies of the late Richard Buckminster Fuller. The

Figure 13. Eden Project, Cornwall.

Figure 14. British Museum, London.

lengths of the space frame members varies around 4 to 5 metres. The cushions have a diameter of 4 to 9 metre diameter. Cushions are made as triple layered ETFE cushions, with two air-inflated chambers.

12 2000 BRITISH MUSEUM ATRIUM ROOF, LONDON, NORMAN FOSTER

The inner courtyard of 92 × 72 metres with the elliptical, slightly asymmetrically positioned Library. In this building Karl Marx wrote his 'Das Kapital' as he could not afford a private writing place. This atrium covering has the form of a squared asymmetrical donut and has been designed, engineered and made on site as a shell grid of a triangulated single skin space frame.

Because of the visual flow of material elements and glass panels, the path was chosen for a strong bur simple single layer of RHS square hollow sections. They

Figure 15. Millenium Dome/O2 Dome, London.

were welded on site on the RHS profiles, after having been positions exactly in situ by 3D surveying apparatus. Quite in contradiction to the development in space frame world, this space frame was not regular or repetitive. That is the reason why all corners were snubbed off in a workshop off-site, coded and positioned and clicked on place. Only after the positioning of all tubes the welding could begin, which had to take care of many distortions in the overall shell.

13 2000 MILLENIUM DOME, LONDON, RICHARD ROGERS, BURO HAPPOLD

The Millennium Dome was a public project to show British awareness of the turn of the century. Like the Millennium bridge it attracted a lot of attention. It became world's largest tent structure. Prominent features are the tubular mast poles sticking out of the Teflon coated membrane fabric. Diameter of the dome is 365 meter. Long after the change of millennium the dome got another function: called the O2 dome after the sponsoring telecom company, it serves now as the temple for pop artists. Michael Jackson contracted 50 shows 'This is it' here, but deceased some weeks before the start.

14 2001 MEDIATHEQUE SENDAI, MIYAGI, JAPAN, TOYO ITO

A five stories public building made of steel structures by a ship building company, with characteristic tubular columns, all in a different but outstanding form. Through these tubular circles of columns stairs and elevators are designed. This vertical traffic gives a unobstructed view of the different stories.

15 2003 TOWN HALL ALPHEN AAN DE RIJN, NL, ERICK VAN EGERAAT

This first official Dutch and permanent Free Form building has a very irregular shape, yet almost all elements and components in its geometry are geometrically defined as they are part of a torus, cone, cylinder etc. In the beginning of the Free Form technology it caused a struggle between the designing parties and

Figure 16. Mediatheque, Japan.

Figure 17. Town Hall Alphen aan de Rijn.

the producing and building parties as the designers overlooked the geometrical complexities.

Yet the lessons were learned within an additional year of design development and the building from then on was only built up of similar elements in different form, positioned in different click points. The architect requested individualized screened glass panels. All elliptical façade tubes had a different height, some even in a crooked form near a prominent stair (wedding stair): *'industrialisation in lots of one'*. (Janssen & Boorn, 2002)

16 2004 FEDERATION SQUARE MELBOURNE, LAB ARCHITECTURE

An open environment on a well known place in the city amidst older 'heritage' buildings often accumulates tensions amongst the public. It becomes a topic of intense debate. Such was the case with the 'Fed' Square. The total assembly positions itself counter to the conservative parties. The theatre is the most outspoken part of those buildings in a fuzzy tubular network geometry with an even more complex glass covering. Fuzzy networks in 'down under'. For the 2008 Olympic Games in Beijing architect PTW Architects, CSCEC and Arup would design an indoor swimming pool stadium with a similar roof and façade

Figure 18. Interior Town Hall, Alphen.

Figure 19. Federation Square, Melbourne.

system with 'fuzzy logic' in tubular structures covered with inflatable cushions.

17 2006 BARAJAS AIRPORT TERMINALS, MADRID, RICHARD ROGERS / ANTONIO LAMELA

The new Barajas Terminals form together the international airport of Madrid, one of the largest in Europe and certainly one of more spacier airports to date. The construction exists of tapered tubular columns in changing colours indicating the gates, on concrete frames in a very smoothened design modus. The steel roof plane with bamboo ceiling undulates over the long double Y-stilts construction. The length of the terminals, the wideness, the gentle gestures of the columns

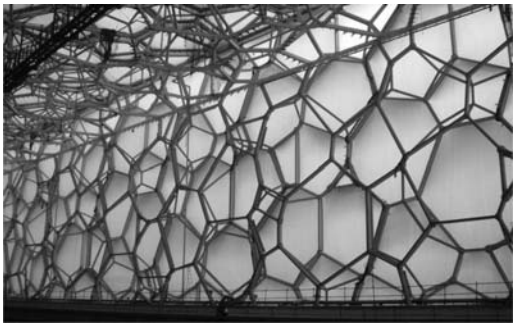

Figure 20. Swimming stadion, Beijing.

Figure 21. Terminal 4 Barajas Airport, Madrid.

and the changing colours of the stilts make these terminals almost a modern version of grand cathedral spaces and unique in the world.

18 2005 NATURAL MUSEUM, LEEUWARDEN, NL, JELLE DE JONG

This museum of Natural History was housed in a 17th/19th century building in the city centre and had to be covered to extend its museum collection and public meeting possibilities. After a design competition the architect made a design based on an experienced lightweight steel tubular grid, clad with insulated glass panels, stabilized by stainless steel rods from 4 long masts, penetrating trough the glass plane.

The masts stabilize the roof plane upward or downward snow, deadweight and wind forces and downward for upwind. The roof scheme is a table structure, independent form the existing buildings. The roof edges are chosen on the top of the tiled roofs, but only a thin rubber flap makes the cover, no forces are allowed on the existing building, the edges around have ventilating windows. The roof structure of the horizontal glass plane and the 4 prominent masted poles were accepted by the monument commission as an extreme structural state of the art positioning to the old buildings.

Figure 22. Natural Museum, Leeuwarden, NL.

Figure 23. The Cockpit, Utrecht.

19 2005 SOUND BARRIER / 'COCKPIT' CAR SHOWROOM A2 UTRECHT, NL, KAS OOSTERHUIS

This 1.500 meters long sound barrier along the A2 near Utrecht, NL and 180m long car Hessing showroom of exclusive cars has a fluent Free Form design which blends well in the short time this building is seen from driving the highway. The cross sectional shape changes during the entire length, is triangulated in a space frame and only the cockpit has a tubular space frame with clearly over-designed tubular members. Glazing follows the triangulation of the design grid.

20 2005 ALLIANZ STADIUM, MÜNCHEN, HERZOG + DE MEURON

This lightweight showing stadium is covered with EFTE cushions along all of its facades, illuminating in different colours: White for neutral football games, red when Bayern München plays and blue when 1860 München plays. The light is an integral message for the stadium that often is used in the darker hours of the day. The tubular structure of the football stadium functions as it should, serving the function of roof without attracting much attention.

Figure 24. Allianz Arena, Munich.

Figure 25. Evo Restaurant, Barcelona.

21 2006 EVO RESTAURANT, HOTELES HESPERIA, BARCELONA, RICHARD ROGERS

The Evo restaurant sits as a gigantic diamond on the high Hesperia Hotel in Barcelona and has been designed as an expensive icon in the silhouette of the high rise building. The menus are suited for the elite. The view out is phantastic. The restaurant has a diameter of 22 m and has a network geometry dome structure made of slender RHS tubes, welded on site, that is to say: on the ground level. The entire diamond shaped restaurant has been lifted with a giant crane in its position.

Figure 26. BMW World, Munich.

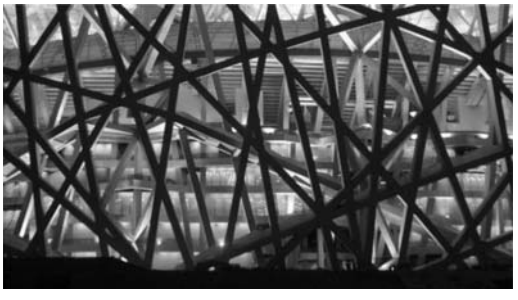

Figure 27, 28. Olympic Stadium, Beijing.

22 2007 BMW WELT MUNICH, COOP HIMMELBLAU

This building serves mainly as a rich environment from which the lucky owners of new BMW cars can get their brand new cars and drive into the future. The building has some prominent sides. One of them is the double cone, made of a tubular network which by its turning movement twists the entire building visually. (Himmelblau, 2010)

23 2008 BIRD NEST INDOOR SPORT STADIUM, BEIJING, HERZOG + DE MEURON / OVE ARUP

The Bird nest stadium is the apotheosis of the use of tubular structures to date in the world. It used 8x more steel than an average stadium of the same size, elsewhere causing the world's price of steel to skyrocket for a while. The design was very outspoken, had the looks of a giant Chinese woven reed basket, and is considered as a prime example of a Free Form building. It was mainly used 14 days in its life in the summer of 2008, but it was on all television sets over the entire world and had a function as public advertisement of China as a country organising the 2008 Olympics.

24 CONCLUSION

While the first 15 years, half a professional generation, of tubular structures were mainly colored by high tech architecture, the latter 15 years after that were colored by prominent free form architecture projects. Kanzai Airport was the turning point: both high tech and free form. This was the time that the computer penetrated design offices and that accurate designing and engineering of complicated structures and free form structures became possible. Before that it was only confined to a few specialists who had advanced computer programs and were used to deal with components in large variety of form and dimensions. Since then, however, computer programs are commercially available for designers and engineers. What stays is the wish of the architect to make surprising buildings with 3-dimensional structures to make the spatial gestures. Tubular structures have proven to be flexible and versatile enough for this purpose.

REFERENCES

Jansen, J & Boorn, 2002, Stadhuis Alphen aan de Rijn, TU Eindhoven.

Mönninger, M., 2010, Coop Himmel(b)lau Complete Works 1968–2010, Taschen.

Eekhout, M., 2011, Tubular Structures in Architecture, Cidect Geneva & TU Delft.

Tubular Structures XIV – Gardner (Ed.)
© 2012 Taylor & Francis Group, London, ISBN 978-0-415-62137-3

Design and erection of the London Eye and the Wembley National Stadium arch

A.P. Mann
Senior Consultant, Jacobs, UK

ABSTRACT: Since the Millennium, the London skyline has acquired two prominent structures: the London Eye and the Wembley Stadium arch. Both are very large lattice structures and both are made up of tubular element substructures. Although serving quite different functions, both structures posed similar design challenges not least in the need to consider global buckling modes. Partly because of that demand, the need to assure tolerances was also very important for each. Given their huge sizes, these was an especial need to consider processes of node fabrication, sub-assembly and final erection into position.

1 LONDON EYE

1.1 *Introduction*

Since the Millennium, the London skyline has acquired two prominent and now well known structures: the London Eye and the Wembley arch. Although serving very different purposes, both structures share certain features. Firstly, and generically, they are both large span tubular structures acting primarily in compression. Secondly, they both support or incorporate cables and thirdly, considerations of fabrication, sub assembly and erection were highly significant for both projects and there was a certain commonality between their construction approaches.

The London Eye rim was designed, fabricated and erected by Hollandia based in Rotterdam. The Wembley Arch was designed by Mott MacDonald and fabricated by Cleveland Bridge (Darlington). Cleveland Bridge were also responsible for the erection engineering. The paper's author acted as third party for site works on both projects and acknowledges here the great skill of the design and construct teams.

1.2 *London Eye function*

Figure 1 shows the Eye. The Eye's rim (about 132 m across) is a triangular lattice using tubes for all its members. On the outside, the rim supports 32 passenger capsules and the total self weight is transmitted down from the rim via cables to the central hub and thence to ground. Laterally, wind acts on the capsules plus the exposed surface of the rim and this load is also carried via the spoke cables back to the hub. To transmit lateral loading, the spoke cables are inclined out of plane (Figure 2). Moreover, for efficiency and to avoid cable slackening, all cables are pre stressed. By this means the 'tension cables' carry tension and the

Figure 1. London Eye rim.

'compression cables' carry compression, by relief of tension. One down side is of course the inevitability of placing the rim in a permanent state of circumferential compression (though this does confer some advantages). Arithmetically, the cable prestress is quite large such that the total compression induced in the rim is also large; this being the summation of prestress plus gravity and wind loads with the prestress contribution being dominant.

The rim's mode of failure is then one of global buckling having the classic four quadrant mode shape buckling form under excess axial load. For stability and to limit interaction it was essential to compute the elastic critical buckling load and keep it high in relation to individual member capacities.

Figure 2. Eye rim with spoke cables.

An interesting question in assessing capacity is to consider what the partial load factor on prestress loading should be. Self evidently there is uncertainty in both gravity and wind loads which partly justifies their relevant factors: it is conceivable that either of them in practice (especially the wind load) could be higher than computed. However, the prestress load is put in to a defined and measured amount and can actually only reduce with time – the reduction being linked to losses via by cable creep although the spoke cables are periodically 'tuned up'. Philosophically, if the rim were to buckle, the dominant driving force (the prestress) would be shed, whereas of course gravity loading remains always active which again brings into question what partial load factor is appropriate. Although these are interesting asides, in practice the prestress was treated as dead load though arguably this was conservative.

Given that the dominant loads are axial and that global buckling is a significant issue, it also follows that the global structural tolerances (out of plane) are matters to be addressed positively. During design, active consideration was given to tolerances. There are several sources of dimensional variation: the rim might not be plane, and the wheel might not be round and the hub might not be in the centre of whatever shape the rim ended up. All of these separate tolerance topics have implications not only for rim structural capacity but also for wheel functionality. The concern was compounded because building the rim was a 'one off' so pragmatically no one could be totally sure what tolerances were achievable. There is little point in any design demanding a tight tolerance if the contactor struggles to enforce it. Moreover following construction, the team would have the problem of determining what to do if the tolerances had not been achieved.

To investigate alignment effects during the design stage, various simulations were run with cables at differing prestress values to see what possible misalignments might be generated, these included variation on absolute prestress values, plus tension variations between individual spoke cables. Thereafter, other simulations were run with different misalignments to assess global buckling sensitivity. Fortunately these studies suggested firstly that alignment would not be overly affected by variations in cable prestress and secondly (again fortunately) that buckling capacity was not much affected over a range of sensible misalignment presumptions or of cable stress variations.

There are however other practical consequences of tolerance. A key point to note is that functionally the Eye works by being in continuous motion and requiring passengers to board a continually moving wheel (it is in fact the safety and practicality of that boarding process which governs wheel speed). Thus a key interface is that between the Boarding Platform surface and the steps of the capsules both vertically and laterally. Excess vertical steps would create a trip hazard, while excess horizontal gaps would create foot trap hazards. The target therefore was to keep the gap between the Boarding Platform edge and the capsule steps not so tight as to risk a clash and not so wide as to risk a foot trap hazard. For both these reasons, rim planarity, rim circularity and rim concentricity were important objectives.

To further assure horizontal alignment, the rim is guided through horizontal restraint rollers set either side of the Boarding Platform. Consequently, the structural implication of this is that the wheel is 'forced' into line during each rotation to a degree linked to its out-of-plane tolerance. Hence there is a fatigue loading case with a cycle of loading (in and out) once for each revolution. Acceptable alignment in the vertical direction was to some extent achieved by controlling wheel circularity (and assuring the hub was in the centre) via control of the cable tensioning (and the assembly/erection methodology was important in this respect) and partly by providing some adjustability in the attachment points of the capsules to the rim. In practice, step variations are not very much. There is also a height variation between summer and winter due to thermal changes but as the thermal mass of the structure is so high, this has not, in practice, been a problem. If necessary, the Boarding Platform surface can be adjusted up and down since it is supported on jacks but this is rarely done.

As the rim rotates, it does ovalise to some extent and this also creates some fatigue loading in plane. That is not a major problem, not least since the entire rim is permanently in compression. Fatigue cracking

can initiate in welded zones even when steel is in compression (cracks being propagated by residual stress) but as the rim is in high imposed compression any consequences would not be so important and cracks would be unlikely to propagate. In practice no cracking has been detected (there are annual inspections). As the rim rotates, the forces in the cables do change though not to a huge amount but such changes also impose fatigue cycling on the cable end node supports so these too are designed for local stress fluctuations.

Local fatigue issues occur at the capsule attachment points because these structural parts undergo one complete reversal of load with each wheel rotation. It will be observed (Figure 1) that each capsule has four support points and that there is bracing between the separate support points. This is deliberate for although the structure is designed for fatigue, very high assurance is required against potential capsule loss. Hence the philosophy was to provide a highly redundant attachment structure such that any single support could be lost with the capsule still remaining in position.

Generally then the structural design of the rim is fairly complex. There is a global buckling problem to be resolved taking the dominant loads as pre stress. Then superimposed on that there are global and local fatigue issues linked to a number of causes. The design also has close links to functionality in that tolerances are important for a number of reasons. Finally, taking account of erection methodology, there is a key erection load case to consider.

1.3 *Interface with drive system and electrical pick up*

The rim has an interface with the wheel drive system which is shown in Figure 3. Fixed to the side of the rim there is a running strip coated with a friction surface (see also Figure 4). This strip is gripped by the drive wheels top and bottom and as these wheels are turned by their motors so the sandwiched strip is pushed along and the whole wheel rotates. Neither the rim nor the running strip are circular but are instead made up of a series of straights. The implication of this is that the drive wheel sets have to move up and down (and be capable of moving in and out) with wheel rotation. To do this, they are fixed to articulated arms. As this movement capability is in all circumstances necessary, the actual rim circularity tolerance is not that important from a drive perspective; tolerances being much less than the movements inherent in having a segmental driving surface. There is a separate interface with the electrical pick up system and the horizontal and vertical rim tolerances governed the amount of articulation that had to be built into the pick up supports.

1.4 *Detailing*

A key requirement of the rim design was aesthetics. The intention was always that whatever was built had to look good. For this reason, the bulk of connections

Figure 3. Eye rim interface with drive system.

Figure 4. Eye rim nodes and running strip.

on the truss are fully welded with the architect taking a keen interest in their appearance. The design of the nodes required considerations of:

- Appearance
- Strength
- Fatigue resistance
- Practicality
- Facilities for mass production in jigs

There are different types of nodes, normal types accommodating triangular bracing and the type that anchors the cables. A typical truss junction can be seen in Figure 4.

1.5 *Assembly*

As the contractor Hollandia was based in Rotterdam, the entire structure was shop fabricated there and shipped direct to the London site. The rim itself came in four quadrants each of these coming over the sea and up the Thames on barges. Figure 5 shows a rim section on the quay in Holland ready to be loaded onto its barge. These four segment were then fitted together on site. At site, the inner chord remained bolted between quadrants whilst the outer chord was site welded. Thereafter, the spoke cables were added and tensioned up. How this was achieved whilst maintaining

Figure 5. Eye rim segment ready to be loaded onto a barge.

circularity will be appreciated from a description of the erection methodology.

1.6 *Erection*

A significant imperative for the project was rapid completion for the wheel had to be in place by Millennium eve. As time was really short, this was a significant factor in the thinking devoted to the erection method. Other considerations were that site space for assembly was extremely restricted. It is possible to erect wheels vertically but this requires some significant temporary works to maintain alignment and traditionally vertical erection methodology has been used where rims have rigid spokes rather than cables. Moreover, a vertical erection method in London would have meant a large amount of working at height along with the risk of dropping tools onto rights of way below. Given that space was available on the river, Hollandia decided to assemble the rim flat over the water surface and then jack the whole rim up into its vertical plane from that position.

Of course there are pros and cons with any erection method. In favour, fortunately the Thames happens to be about twice the rim diameter opposite Jubilee gardens and also fortunately, the navigable passage runs along the opposite bank. Thus it was possible to pile into the river on the garden's side to form temporary support platforms to hold the rim temporarily. The four segments of rim were supported on these platforms (Figure 6). Whilst in this horizontal plane, cables were added and tensioned up so this was much easier than it would have been to add cables in the vertical plane with all the added risk of uncertainty in achieving circularity. On the down side, to match the erection methodology, it was necessary to articulate the A frame (column support) top and bottom and to adjust the hinge support position upwards at the A frame bottom so as to allow the frame to be in an alignment that cleared the river wall and fitted up to the rim on its river supports. This demand may be appreciated from Figure 7. Structurally, it will also be appreciated from

Figure 6. Eye rim temporarily supported above the river.

Figure 7. Eye erection.

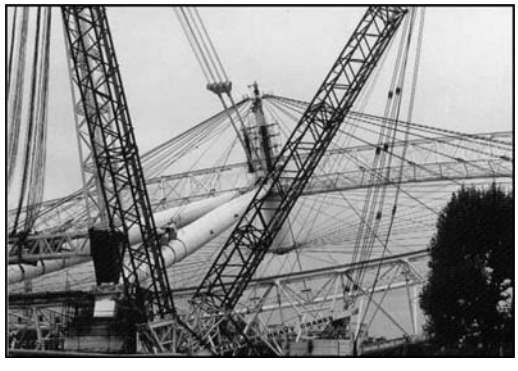

Figure 8. Eye rim out of plane umbrella of support cables.

the erection picture of Figure 7 that at the moment of lift off, the rim weight was at its most eccentric relative to the foundations and therefore this moment dictated the maximum up lift imposed on the rear foundation and the foundation design was actually governed by that condition. Additionally, at the moment of lift off, the rim was loaded out of plane and to counteract this was restrained out of plane by an umbrella of temporary cables anchored onto a disc mounted at the rear of the spindle: this array can be seen in Figure 8.

Figure 9. Wembley arch over the stadium.

Figure 10. Arch with roof hanging below and over pitch trusses.

Erection of the rim from horizontal to vertical was a spectacular event and took place in one day hence part of the justification for its adoption. Technically the moment of lift was the moment of greatest stress for much of the structure though this ran counter to popular instinct which probably thought higher elevations would be more critical.

2 WEMBLEY ARCH

The Wembley arch spanning 315 m purports to be one of the longest in the world for a building. Overall, the arch is 140 m high (about the same as the Eye) and the 'tube' is ∼7 m diameter. Total self weight is about 1,750 tonnes of steel. The arch is spectacular, visible from a long way off and a signature for the stadium (Figure 9). Its function is to support the roof below (hung on cables) but perhaps surprisingly, it supports not only the roof directly below but a good proportion of the roof on the opposite side of the pitch since that roof is partly supported on trusses which span right across the pitch to carry a moving roof (these trusses can be seen in Figure 10).

Figure 11. Arch before erection with 5 turning masts in position.

Structurally, as for the Eye, the arch is a lattice structure made up of tubular sub elements. It is mostly in compression so again, as for the Eye, global buckling is a major consideration as is buckling of the individual tubes from which it is made. Out of plane wind load is carried again via inclined cables and they have enough gravity stress for wind generated 'compression' to be carried by relief of tension. As the arch is obviously in high compression it has the standard potential buckling modes of failure. Restraint out-of-plane is partly provided by orthogonal cable restraint but there is also an in – plane, side sway, buckling mode resisted by arch in plane stiffness. Because buckling is a dominant design factor, out of plane alignment tolerance was also a significant factor and the contract specification dictated limits for that. During erection, measures had to be deployed to keep the planarity alignment acceptable. Unlike the Eye rim, there are no significant fatigue issues to counter.

2.1 *Nodes*

Aesthetics was clearly important so became a significant influence on the nodal form adopted: all nodes are welded with considerable geometrical complexity belied by their smooth clean appearance post fabrication (some of the complexity is linked to sequence of assembly such that access is retained to complete internal welding).

There were four broad groups of nodes:

- Standard node intersections tube to tube
- Interface with cross arch diaphragms
- Nodes to attach to cables which support the roof
- Nodes to attach cables used for erection purposes

Many of these can be seen in Figure 11.

- Nodes which attach to temporary cables

2.2 *Assembly*

As with all large structures, the practicalities of assembly are key for planning and inseparable from the

Figure 12. Arch assembly: Sub units being lifted into position.

Figure 13. Arch erection with base pinned.

adopted erection methodology. As for the Eye, the plan was to assemble the arch on the ground and then hoist it up. Thus the strategy was for the arch to be made up of sub units which were then assembled into an arch shape (laid out horizontally) on stillages in a position ready for hoisting. Because even the sub units were large, fabrication shops had to be built on site.

This assembly process involved first of all making up 41 diaphragms partly factory welded but then delivered to site in thirds for final assembly (these diaphragms can be seen as the 'verticals' in Figure 11). Thereafter, these were erected in jigs (one diaphragm at each end) and the tubes in between were welded into place. These tubes had been pre cut and profiled in Cleveland Bridge's Darlington factory. These completed sub units were then moved by crawler crane (Figure 12) onto the pitch stillages in hit and miss patterns for the other tubes completing the arch to be welded in between.

Figure 14. Erection pin at arch base.

Figure 15. Strand jacks for pulling up turning masts.

2.3 *Erection*

Figures 11 and 13 shows the erection methodology. Although in principle this followed the same strategy as lifting the Eye there were differences. But firstly there are similarities: a key one was the need to introduce a proper pin at the arch base to allow articulation out of plane. The was quite complicated since in the final condition, the arch was required to be pin based so as to be capable of articulation *in-plane* (i.e. at 90° to the erection rotation). The base detail to permit this can be seen in Figure 14. Another similarity is the need to be hauled up on cables so nodal attachment points were required for temporary cables detailed so as to be geometrically clear of the cables used finally for supporting the roof. Again, and like the Eye rim, there were erection load cases of in-plane and out-of-plane loading, a need to maintain alignment consistent with the buckling mode of failure and a critical load case just at lift off.

A difference to the Eye erection is that significant temporary works were required to facilitate the lift. Figures 11 and 13 show the use of five turning masts each of which pulled on the arch to raise it. The cables pulling the turning mast up were rotated by shortening attachment cables through strand jacks (Figure 15). Noting there are five turning masts, each with different cable lengths from their heads down to the arch (Figures 11 and 13), it may be appreciated that at any stage of the lift, the amount of force in each cable differed to a degree linked to the system stiffness. It was not possible to pull all five masts in unison and even if they had been so pulled, differing cable stresses and hence differing cable extensions would have created

Figure 16. Arch going 'over the top'.

an arch out of plane deviation. To overcome this, there had to be a sequence of incrementally defined steps. Moreover as the force in each mast system varied, the increment at each point varied. The consequence of this is that cable pulling was a selected mixture of both applied force and applied displacement with the driver for displacement being to keep the arch in plane at all stages or at least within tolerance limits of misalignment. To control this a mathematical model of the whole process was developed and from this a defined sequence of jacking steps was evaluated for each of the five turning masts.

For both the Arch and the Eye rim, the whole erection process was monitored continuously in terms of predicted force on the lifting system(s) and predicted displacement at defined points with survey checks made at each increment to assure that the lifting forces and measured displacements were what was expected against the mathematical models. The whole operation had to be controlled in this manner with a personnel command and control strategy.

A further difference between lifting the arch and lifting the Eye rim is that on the arch, the tilt went further than vertical and as the arch went 'over the top' loads were transferred at that point from pulling cables to restraining cables. (Figure 16).

Both the rim and the arch underwent changes of shape between their unstressed position on the ground and their erected position in the air. As part of the pre-erection engineering it was necessary in both cases to study what those shape changes would be (say under self weight) and determine if preset was required to offset the changes so that the as-built structures conformed to design intent shape.

3 CONCLUSIONS

These are two iconic tubular structures and both presented great challenges in terms of design, fabrication, assembly and erection. A key observation from each is that any design overall needs to consider all the practicalities of assembly and erection if it is to be complete. The reason is obviously that structural capacity is linked to the ability to detail the nodes and the ability to achieve sensible alignments. Furthermore the manner of erection in both these case studies had a significant effect on the detailing, and the manner of erection in both cases imposed significant stresses during the erection phase. In both cases, those erection conditions were enough to influence sizing i.e. the erection condition was at least as important as the permanent condition.

Tubular structures offer great advantages when appearance is a major demand and they offer major advantages when dominant loads are compressive. However, as experienced designers understand, the completeness of design, the practicalities of assembly and costs are all very strongly influenced, if not dominated, by the practicability of making the nodes not least the amount of welding within them. That in turn is very strongly influenced not just by the apparent demands of achieving strength but by the simple geometric demands of weld length and weld volume enforced by the geometry of the tube intersections. It is really the nodes and their configuration that govern the overall design of the members and not the other way around. Altogether, if a design is to achieve a satisfactory outcome in terms of material, functionality, appearance, ease of assembly and erection then there must be an iterative process of development involving skill inputs from several specialists

FURTHER READING

Berenbak J, Lanser A, Mann AP. 2001. The British Airways London Eye. Parts 2 Structure. *The Structural Engineer* 79 (2): 19–28.

Mann AP, Thompson N, Smits C. 2001. Building the British Airways London Eye. *ICE Proceedings, Institution of Civil Engineers,* 144(2): 60–72.

Composite construction

Tubular Structures XIV – Gardner (Ed.)
© 2012 Taylor & Francis Group, London, ISBN 978-0-415-62137-3

Local buckling in Concrete-Filled circular Tubes (CFT)

R. Chacón, E. Mirambell & E. Real
Technical University of Catalonia UPC, Barcelona, Spain

ABSTRACT: Local buckling phenomena in Concrete-Filled Tubes (CFT) is prevented in EN1994 by limiting the slenderness of the steel tubes (D/t) to $90 \cdot \varepsilon^2$. This limitation is inherited from EN1993-1-1 in which slenderness limits are defined for Circular Hollow Sections (CHS). This approach has been tackled by researchers for the case of CHS but has not been studied for CFT to the same extent. This paper describes a series of three-dimensional numerical simulations of CFT subjected to both flexural and axial loads. The three-dimensional simulations provide a phenomenological insight concerning the complex mechanical phenomena involved in local buckling. The results obtained show discrepancies between the EN1994 limitations and the pinpointed phenomenological observations for the case of CFT.

1 INTRODUCTION

Concrete-filled tubes (CFT) are widely used in civil engineering and building construction and consist of a steel tube with a concrete core casted inside. The behavior of CFT has been widely studied and hundreds of tests on CFT subjected to axial and flexural loads are nowadays available in the literature (Goode 2008). Most of the studies have pointed out the beneficial effects of CFT when subjected to different types of loading by comparing their cross-sectional resistance and ductility to pure steel or pure concrete elements. Consensus concerning this matter has been achieved among researchers: due to an enhancement of the confined concrete strength, the resistance of CFT is quite higher than the addition of the resistances of each material when considered separately. The compressive strength is increased due to tri-axial confinement of the concrete core. The susceptibility to local buckling of the steel tube is decreased since the concrete core provides to the steel plate an additional constraint. This constraint prevents the plate to undergo inwards buckling and thus, the critical buckling load of the plate is increased.

Several models of resistance prediction have been proposed (Hatzigeorgiou 2008, Susantha et al. 2001, Johansson 2002) for members with relatively thick steel plates. These models have been compared by several authors (Beck et al. 2009, Oliveira et al. 2010, Chacón et al. 2011) with relevant codes (EN1994 2004, AISC 2005). These comparisons have pinpointed the adequacy of the prediction of the confinement effect onto the ultimate strength of CFT subjected to combined bending and compressive loads.

Moreover, it is understood that CFT columns subjected to bending and/or compressive loads might be prone to local buckling when the D/t ratio of the steel tube is high. The critical buckling loads of the plates belonging to CFT may condition the cross-sectional capacity of the members. The critical buckling mode associated with local instability of a steel plate of a CFT might be labeled as "outwards buckling" since the steel plate is not able to develop inwards waves. As far as known by the authors, no information concerning mathematical developments or eigenvalue analyses of such phenomenon are available in the literature. The cross-sectional resistance of CFT has been traditionally decoupled from the local buckling phenomenon by limiting the D/t ratio of the tube to certain limits.

On the other hand, researchers have pinpointed an existing post-local-buckling strength of slender steel plates which contributes to the ultimate strength of the whole section (Kwon et al. 2011). Several formulae are provided by these authors for the sake of predicting the ultimate strength of the steel plate. These formulae do not require the computation of the effective area of the plate and are derived empirically from a series of experimental tests.

In this paper, the potential local buckling of CFT is studied by means of a fully three dimensional FE-based numerical model in which: i) the concrete core is modeled with solid finite elements and the confinement effect is accounted for and ii) the steel tube is modeled with shell elements and the potential local buckling is taken into account.

The model includes a contact-based formulation in which both entities interact realistically. Full material and geometrical nonlinearity is included. Results concerning the susceptibility to local buckling of the steel plate as well as comparisons with the European code EN1994 are provided at the end of the paper.

In addition, experimental results of CFT subjected to pure compression gathered from the literature are used for comparison purposes.

2 EN1994. DESIGN OF COMPOSITE STEEL AND CONCRETE STRUCTURES

2.1 *General*

EN1994 provides with guidelines for the design of composite columns and compression members with steel grades S235 to S460 and normal weight concrete of strength classes C20/25 to C50/60. These guidelines apply to isolated columns and columns in framed structures where the other structural members are either composite or purely metallic. The steel contribution ratio δ (eq. 1) should fulfill the condition $0{,}2 \leq \delta \leq 0{,}9$.

$$\delta = \frac{A_s \cdot f_y}{A_s \cdot f_y + A_c \cdot f_{ck}} \tag{1}$$

Two methods of design are given: i) a general method whose scope includes members with non-symmetrical or non-uniform cross-sections over the length, ii) a simplified method for members of doubly symmetrical cross-sections.

2.2 *Simplified method*

Only the simplified method is discussed herein. The members must be checked for: cross-sectional resistance, resistance to local buckling and resistance to shear between steel and concrete elements. The cross-sectional resistance must be verified with the well known interaction diagram. The plastic resistance to compression $N_{pl,Rd}$ of a CFT cross-section should be calculated by adding the plastic resistances of its components. Account may be taken of increase in strength of concrete caused by confinement.

The resistance of a cross-section to combined compression and bending and the corresponding interaction curve may be calculated assuming rectangular stress blocks as shown qualitatively in Fig. 1. This diagram can be constructed by varying the neutral axis throughout the cross-section and satisfying the cross-sectional equilibrium with the pair of resulting forces N and M.

Account may be taken of increase in strength of concrete caused by confinement (point A in Fig. 1) This allowance is valid if and only if the relative slenderness of the structural element does not exceed 0,5 and the relative eccentricity of the applied load e/D does not exceed 0,1, being e the eccentricity of loading given by the applied forces M_{Ed}/N_{Ed} and D the diameter of the tube.

2.3 *Local buckling*

Local buckling should be accounted for if the diameter-to-thickness ratio D/t in CFT is greater than $90 \cdot 235/f_y$. The effects of local buckling may be neglected for a steel section if the given limit is not exceeded. If $D/t > 90 \cdot 235/f_y$, full account of local buckling is necessary in all calculations (the designer is recommended to approach this calculation as in shell structures, EN1993-1-6) and the simplified model is no longer valid.

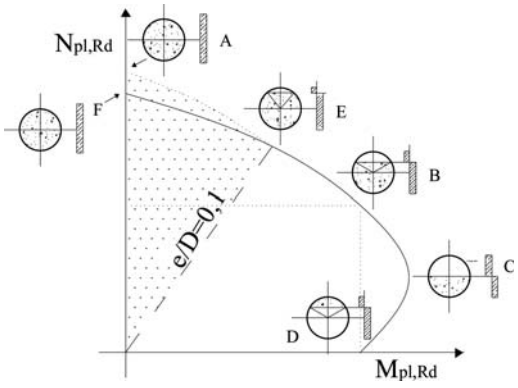

Figure 1. Cross-sectional interaction diagram of a CFT according to EN1994.

3 NUMERICAL MODEL

3.1 *Geometrical modelling*

The structural response of the CFT is modeled by means of the three-dimensional, multi-physics, FE-based Software (Abaqus v10.3, 2011). The concrete core is modeled by using C3D8R solid elements whereas the steel tube is modeled with S4R shell elements.

Both geometries are put together by means of a surface-based contact formulation and meshed separately. This contact formulation reproduces both normal and tangential behaviors between surfaces. For the former, the model allows separation (but no penetration) of adjacent nodes of both entities whereas for the latter, the model is based upon a linear force-slip tangential behavior with a friction coefficient $\mu = 0{,}3$. For both cases tangential and normal stresses are transmitted from one entity another. Thus, the steel tube might induce a certain level of confinement to the concrete or alternatively, the steel plate might undergo local buckling if it is separated from the concrete core. Moreover, it is worth pointing out that symmetries were employed for the sake of reducing the computational cost of the simulations.

3.2 *Constitutive equations*

The concrete core is characterized by a plasticity-based damage model. It assumes that the main two failure mechanisms are tensile cracking and compressive crushing of the concrete material. On the one hand, the model assumes that under uni-axial compression the response is initially linear until the value of failure stress is reached. The maximum stress corresponds to the onset of micro-cracks in the material. The plastic response is characterized by a nonlinear path until the value of f_{ck} is attained and a strain-softening response

Figure 2. Mesh and numerical modelling.

characterizes the material beyond this point. Beyond this stress, the behavior is represented macroscopically with a softening response. On the other hand, the model assumes that the uniaxial tensile response is linear until the value of $f_{ctk} = 0{,}09 \cdot f_{ck}$ is reached (a user-tuneable magnitude). The post-cracking response is characterized by means of values of fracture energy (GFI $\approx$ 0,15 N/mm). The multi-axial behavior is reproduced by means of a scalar damage elasticity set of equations. The uni-axial resistance is increased up to $1{,}16 \cdot f_{ck}$ if the material is subjected to multi-axial stress (also a tuneable magnitude).

The steel tube is characterized by means of elastic-perfectly plastic material. Uni-axially, the material yields once f_y is attained. Multi-axially, the von Mises criterion determines the onset of yielding. No strain hardening is considered in this study.

3.3 *Type of analysis*

The studied phenomenon is strongly nonlinear. Tensile cracking of the concrete, local buckling of the steel plate together with a contact-based formulation must be dealt with coupled. For making the simulations computationally tractable, it has been decided to use an explicit analysis. The procedure solves the equation of motion which relates the inertial forces, the viscous forces and the elastic forces into the same equilibrated system (either static or dynamic).

The rate of load-introduction as well as the mass-scaling of the system is set in such a way the structural problem may be assumed as quasi-static rather than dynamic.

3.4 *Numerical simulations*

The numerical simulations consisted of two load-steps (Fig. 3). It is important to point out that these numerical simulations belong to a vaster study on CFT belonging to integral bridges. Therefore, the numerical simulations were aimed at reproducing the type of forces that the piers from integral bridges are usually subjected to (Chacón et al. 2011). In any case, the internal forces may be summarized in: compressive, bending or a combined action of bending and compression.

- At the first step, an axial load was centrically applied to the CFT. This axial load represents a percentage of the squash load $N_{pl,Rd}$ of the CFT. Eight different values ranging from 0% to 100% of $N_{pl,Rd}$ are included (for the case of 100% of $N_{pl,Rd}$, the CFT fails and the analysis finishes).

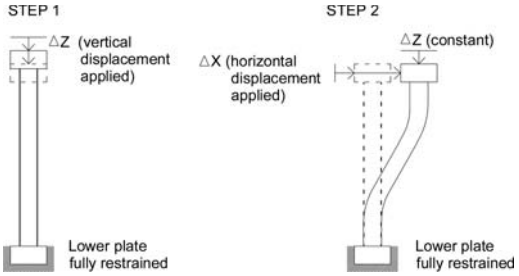

Figure 3. Loading steps in the numerical simulations.

- At the second step, a lateral displacement was applied on the upper cross-section. These displacements assumingly reproduce the non-mechanical (creep, shrinkage, etc) and mechanical deformation (braking, seismic loads) from the bridge deck. The upper cross-section remains horizontal during the whole analysis.
- The resulting internal forces of the CFT can be obtained by applying equilibrium conditions (eq. 2 to 4).

$$\Sigma F_{ver} = 0 \rightarrow N_A = N_B = N \tag{2}$$

$$\Sigma F_{hor} = 0 \rightarrow V_A = V_B = V \tag{3}$$

$$\Sigma M = 0 \rightarrow M_A = M_B = \frac{V \cdot L}{2} + N \cdot \Delta \tag{4}$$

4 NUMERICAL DATABASE

4.1 *Experimental database*

A vast experimental database of 1819 experimental tests is available in the literature (Goode 2008). This database includes tests performed by several authors and provides geometrical, material and ultimate loads information of circular, square and rectangular CFT subjected to axial and/or flexural loads. In this paper, a sample of 526 circular CFT subjected to pure compression excerpted from this database is used for comparison purposes. The sample is chosen in such a way the specimens are not prone to global buckling according to the EN1994 criteria.

4.2 *Numerical database*

A numerical database provided in the present study consists of 192 circular CFT prototypes of total length L = 10,0 meters and outer diameter D = 1,0 meter (L/D = 10) and 112 CFT prototypes with L = 10,0 meters and D = 2,0 meters (L/D = 5). A set of parametric variations of the steel contribution ratio was developed. These specimens were numerically subjected to various combinations of axial and flexural loads. This database has been useful in other studies performed by the authors concerning the ultimate load

Table 1. Geometry of the numerically simulated prototypes.

Element	D (m)	Thickness (mm)	f_y (N/mm^2)	N (%N_{plRd})	Simulations
L10D1M	1	10-15-20 25-30-35	235–275 355–460	8 cases [0–100]	192
L10D2M	2	20-30-40 50-60-70-80	355–460	8 cases [0–100]	112
				Total	304

Table 2. Additional numerical simulations.

Element	D (m)	Thickness (mm)	f_y (N/mm^2)	Total cses
L10D1M	1	6	235–275	4
	1	8	355–460	4

capacity and ductility of CFT subjected to bending and compressive loads (Chacón et al. 2011) for the particular case of integral bridge piers. Table 1 summarizes the geometrical and material properties of the studied CFT. The steel tube presents variations in thickness as well as in yield strength f_y whereas the concrete core is characterized with an invariable compressive strength $f_{ck} = 30$ N/mm^2 for all cases. In this study, additional simulations were performed in elements subjected to pure compression with very high D/t ratios. Table 2 depicts the geometries of such prototypes. The length is set to L = 10,0 meters and the outer diameter D = 1,0 meter (L/D = 10).

5 EXPERIMENTAL RESULTS

The sample depicted in sub-section 4.1 includes prototypes subjected to purely compressive loads. The ultimate load capacity of those specimens is provided though information concerning the failure mode of such prototypes is not fully documented.

Figure 4 shows the ultimate load capacity of 526 CFT subjected to pure compression standardized to the EN1994 (in this case, the formulation is applied without accounting for the effect of confinement). The results are plotted against the ratio $(D/t)/(90\cdot\varepsilon^2)$. These plots should be read as follows: i) If $N_{exp}/N_{EN1994} < 1{,}0$, the results are not on the safety side, ii) If $(D/t)/(90\cdot\varepsilon^2) > 1{,}0$, the CFT should be labeled as susceptible to local buckling (and thus the simplified method would not be valid in the present form). Bold lines indicate the boundaries of the aforementioned regions.

Close inspection of the results leads to twofold conclusions:

– The vast majority of the results are on the safety side (regardless of the susceptibility to local buckling).
– The ultimate load capacity of the allegedly prone to local buckling specimens is generally greater than the EN1994 prediction.

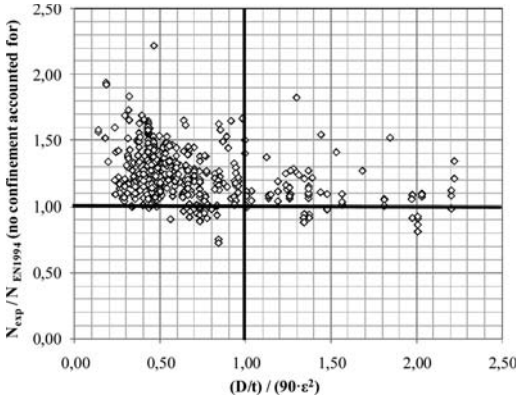

Figure 4. Experimental results as a function of their susceptibility to local buckling (no confinement accounted for).

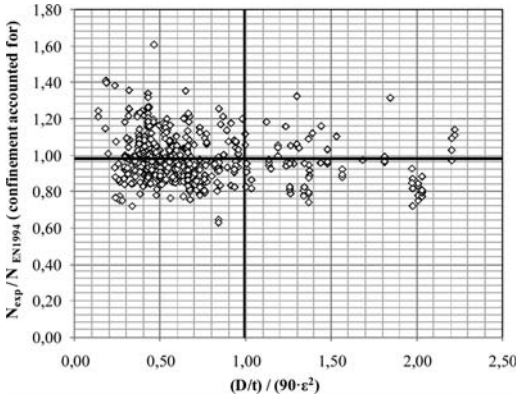

Figure 5. Experimental results as a function of their susceptibility to local buckling (confinement accounted for).

– The D/t limitation provided in EN1994 does not seem to represent the pivotal point beyond which local buckling occurs. However, this plot does neither give information about the possibility that these prototypes undergo local buckling nor, about their potential post-buckling reserve.

Figure 5 shows the ultimate load capacity of 526 CFT subjected to pure compression standardized to the EN1994 (in this case, the formulation is applied accounting for the effect of confinement, point A in Fig 1).

In this case, the vast majority of the results are not on the safety side (regardless of the susceptibility to local buckling). The plot suggests a warning about the validity of the confinement effect provided by EN1994. Similar results have been pinpointed by other authors (Beck et al 2009, Chacón et al 2011).

6 NUMERICAL RESULTS

The experimental results presented in previous sections pinpoint that the susceptibility to local buckling is not reproduced adequately with the limiting ratio D/t. This section provides further information related to the physical phenomenon that clarifies the structural problem to some extent. The results are separated in two sub-sections, namely, pure compression and pure bending. Due to space constraints, the combined bending and compression phenomenon is not treated herein.

6.1 *Pure compression*

CFT subjected to pure compression show different structural response depending on the D/t ratio. Expectedly, the prototypes with high D/t undergo local buckling at early load stages whereas prototypes with low D/t show considerable yielding at failure load. The "axial force" – "longitudinal displacement" curve of the prototype $L = 10\,m$, $D = 1\,m$ and $t = 10\,mm$ is given in Fig. 6 for various values of steel yield strength f_y. All prototypes presented in this plot should be labeled as "prone to local buckling" according to EN1994. The structural response show different branches. First, all prototypes exhibit an identical linear response. After awhile its slope changes suddenly. This change is identified as a bifurcation point.

At this point, for the prototype with $f_y = 235\,N/mm^2$, the steel plate has already reached its yield strength. The slope of the post-bifurcation point branch is very low compared to the linear branch.

For the prototype with $f_y = 460\,N/mm^2$, the steel plate has not yet reached its yield strength at the bifurcation point. The slope of the post-buckling branch is considerably high. Eventually, the steel plate yields and the post-buckling slope is degraded to the same level as for the prototype with $f_y = 235\,N/mm^2$. For high values of longitudinal displacement, the concrete core crushes (the longitudinal strain reaches $\varepsilon = 0{,}35\%$).

Fig. 7 shows the axial load as a function of the radial displacement of a node located nearby the area of local buckling (Fig. 8 shows this area). The bifurcation point is noticeable (labeled as "buckling" in Fig. 6 and Fig. 7). The change of slope is particularly sharp for the prototype with $f_y = 235\,N/mm^2$.

Fig. 8 shows the von Mises stresses of the steel plate in a deformed shape obtained from the numerical simulations. The figure shows a detail of the fully restrained bottom plate of the prototype. The buckling mode is noticeable and additionally, according to the color scale, it is observed that at buckling, the prototype has undergone severe yielding (the units of the von Mises stresses are in N/m^2).

On the other hand, Fig 9 shows the axial force-longitudinal displacement curve of the prototype $L = 10\,m$, $D = 1\,m$ and $t = 30\,mm$ for various values of steel yield strength f_y. All prototypes presented in this plot should not exhibit local buckling according to EN1994. In this case, the structural response shows different stages. First, all prototypes exhibit an

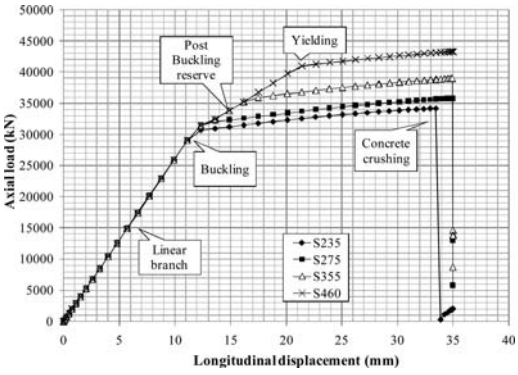

Figure 6. Axial load-longitudinal displacement plot of prototypes with high D/t ratio (D/t = 100).

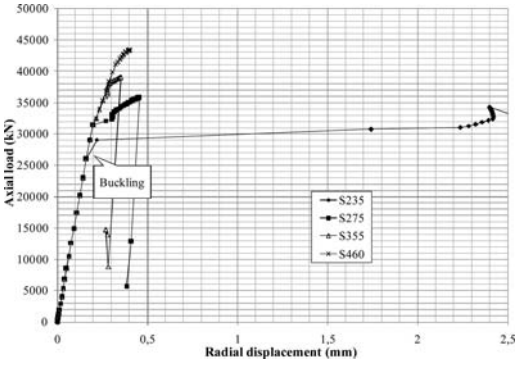

Figure 7. Axial load-radial displacement plot of prototypes with high D/t ratio (D/t = 100).

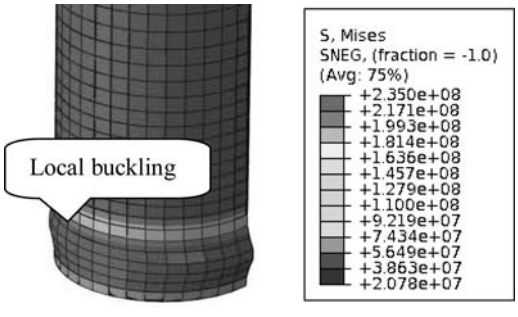

Figure 8. von Mises stresses at bifurcation point for a prototype with high D/t ratio (D/t = 100) and $f_y = 235\,N/mm^2$.

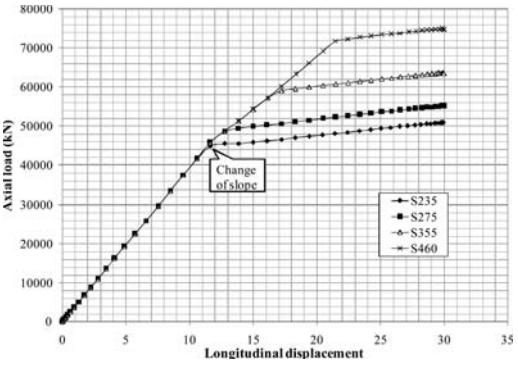

Figure 9. Axial load-longitudinal displacement plot of prototypes with low D/t ratio (D/t = 33.33).

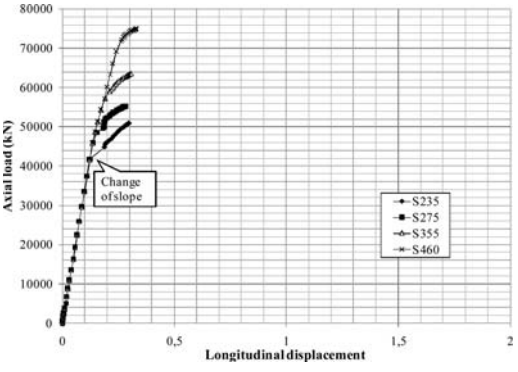

Figure 10. Axial load-radial displacement plot of prototypes with low D/t ratio (D/t = 33.33).

identical linear response. Secondly, the initial linear slope changes. This change is sharper for prototypes with $f_y = 235\ N/mm^2$ than for prototypes with $f_y = 460\ N/mm^2$ in which it is almost unnoticeable.

The main difference between high and low D/t ratios stems in the axial force-radial displacement curve. This radial displacement is shown in Fig. 10 and also exhibits a change of slope. This occurs at considerable higher values than in prototypes with high D/t ratio. Moreover, the change of slope is not as sharp as the one observed with more slender prototypes.

Fig. 11 shows the von Mises stresses (N/m^2) of the steel plate in a deformed shape obtained from the numerical simulations at the point at which the slope changes. No out-of-plane deformation is noticeable. It is also observed that at buckling, the prototype has not yet undergone any noticeable yielding ($f_y = 460\ N/mm^2$).

6.2 *Pure bending*

The numerical simulations of a prototype subjected to pure bending are developed in CFT subjected to lateral displacements at the upper cross-section as shown in Fig. 3. No previous axial force is applied for these cases. A lateral displacement Δ of an element with

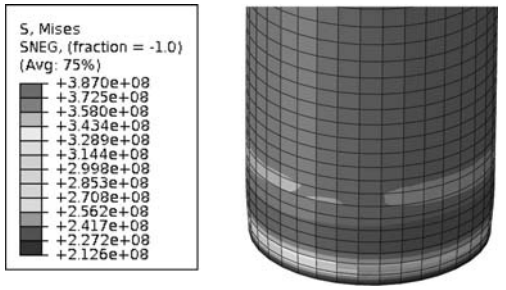

Figure 11. von Mises stresses at the change-of-slope point for a prototype with low D/t ratio (D/t = 33.33) and $f_y = 460\ N/mm^2$.

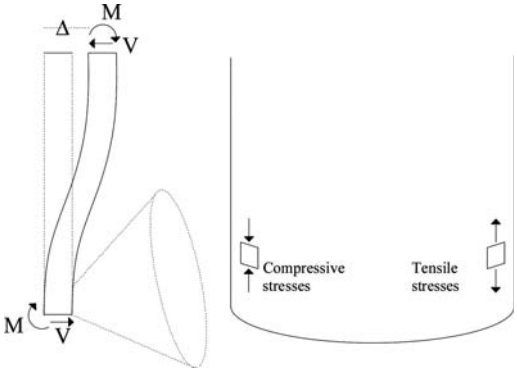

Figure 12. Resulting internal forces.

fully restrained end cross-sections develops internal forces as shown in Fig. 12. The resulting bending moments generate both compressive and tensile stresses in the CFT. These compressive stresses may cause buckling of the steel plate.

In an incremental process, the relationship between the displacement Δ and the resulting bending moment M is initially linear. At high load stages this process might become considerably nonlinear due to various reasons (buckling, yielding, cracking). Fig 13 shows a render from a process of a CFT subjected to an incremental Δ displacement. The render shows a view cut detail of the fully restrained bottom cross-section at which local buckling occurs. The chosen prototype has dimensions L = 10 m, D = 1 m, t = 10 mm. Clear separation between materials is observable.

As a matter of fact, the relative displacement between the concrete core and the steel plate varies throughout the incremental process. Fig. 14 shows the absolute displacement of two nodes (whose position is indicated in Fig. 13) as a function of the step-time of the incremental process. The first node belongs to the concrete core and the second node belongs to the steel plate. Both nodes are adjacent and in absence of local buckling, both nodes are expected to undergo the same level of displacement. In Fig. 14, it is observed that the displacement of both nodes may be separated in three different zones. Zone A, at which both nodes exhibit identical displacement. Zone B, at which

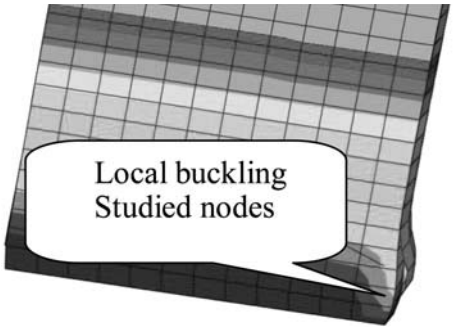

Figure 13. Separation between concrete and steel in the compressed area of the bottom cross-section.

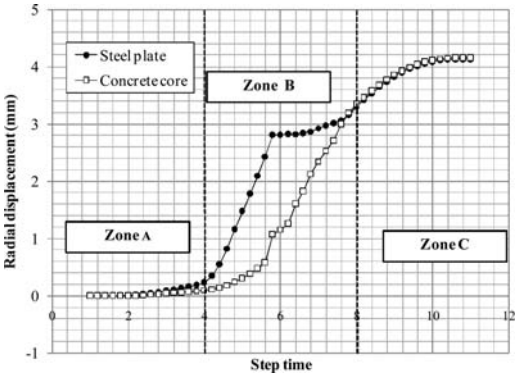

Figure 14. Radial absolute displacement of the nodes located at adjacent positions of the steel plate and concrete core.

there is a clear separation between both nodes (local buckling zone) and Zone C, the post-buckling zone, at which the concrete core exhibits a greater radial deformation (there is no steel plate confining it) and eventually, it reaches again the steel plate. An analysis of such behavior has been performed for all specimens belonging to the database presented in table 1.

Fig. 15 shows the difference between the absolute displacements between both nodes. This difference is labeled as the "relative" displacement between entities. It is observed that at Zone A, the difference is null. At Zone B, the relative displacement reaches a maximum value (1,85 mm for this particular prototype) and eventually, the relative displacement decreases to zero at Zone C.

The magnitude of the maximum relative displacement does not give further information about the potential local buckling of the prototype. If, however, this magnitude is expressed in terms of the plate thickness, further information may be extracted from this measure. Fig. 16 shows the maximum relative displacement between nodes expressed as a percentage of the plate thickness for different CFT ($L = 10$ m, $D = 1$ m, varying t [10,15,20,25,30,35] mm). The results are plotted as a function of the D/t ratio. The

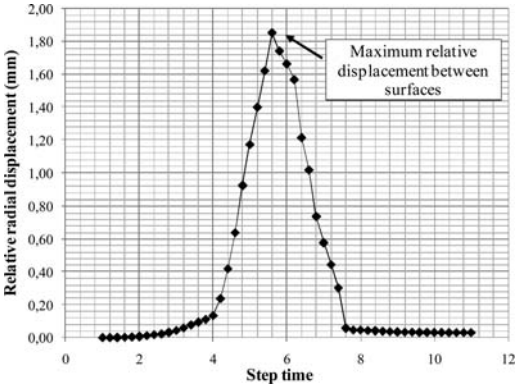

Figure 15. Relative displacement between the nodes located at adjacent positions of the steel plate and concrete core.

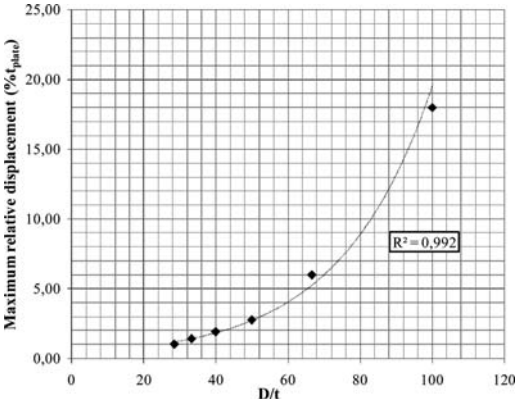

Figure 16. Relative displacement as a function of D/t. $L = 10$ m. $D = 1$ m. $f_y = 235$ N/mm^2.

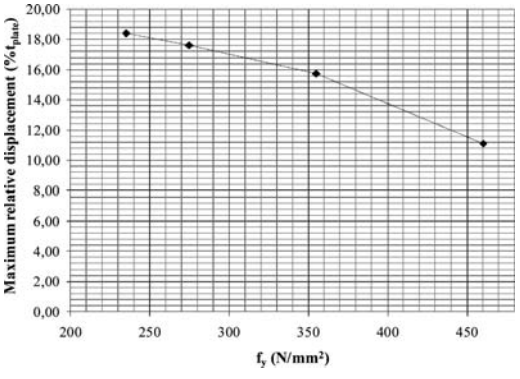

Figure 17. Relative displacement as a function of f_y. $L = 10$ m. $D = 1$ m. $t = 10$ mm. $D/t = 100$.

relationship between both magnitudes is clearly exponential. A best fit curve is also plotted with the results. This fit is quite accurate according to the regression coefficient R^2=0,992. Noticeably, the higher the D/t ratio, the higher relative displacement between the concrete core and the steel plate is. In terms of the

plate thickness, the results vary ranging from 1% to 18% of t.

Expectedly, the prototype that exhibits a greater separation between materials presents a $D/t = 100$. Unexpectedly though, this relative displacement is dependent on the yield strength of the tube f_y in such a way that the higher the f_y, the lower the separation.

This observation contradicts the EN1994 limitation $D/t < 90 \cdot \varepsilon^2$ but is in fully accordance with the results presented in sub-section 6.1 for compressed members.

7 CONCLUSIONS

On the one hand, the experimental results presented in this paper show that the ultimate load capacity of CFT subjected to compressive loads is not particularly sensitive to the susceptibility to local buckling that is defined in EN1994.

On the other hand, the numerical results presented provide a phenomenological insight concerning local buckling in CFT. Failure modes and structural responses of CFT subjected to both compressive and bending loads are described. This insight gives hints about the pre- and post buckling behavior of CFT. Preliminary results show that the EN1994 limitation concerning the susceptibility to local buckling is contradictory to the hitherto observed trends. A more detailed research program concerning this important topic is being performed by the research team.

ACKNOWLEDGMENT

The authors acknowledge the financial support provided by the Spanish Ministerio de Ciencia e Innovación as part of the project 7004/T07-51 "Seguridad y funcionalidad de los puentes integrales frente a acciones accidentales. Investigaciones para el establecimiento de criterios de diseño y construcción".

REFERENCES

Abaqus Simulia V 6.10. Dassault Systemes. RI. USA. 2011

American Iron and Steel Construction (AISC). Specification for steel structural buildings. 2005

Beck A., Oliveira W., Nardim S., El Debs A. 2009. Reliability-based evaluation of design code provisions for circular concrete-filled steel columns. Engineering Structures, Vol 31 (10): 2299–2308.

Chacón R., Mirambell E., Real E. 2011 Strength and Ductility of Concrete-Filled Tube Piers. 6th European Conference on Steel and Composite Structures, Budapest. Eurosteel.

European Committee for Standardisation (ECS). 2004. Eurocode 4: design of composite steel and concrete structures, Part 1-1: general rules and rules for buildings.

Goode C. 2008. Composite columns – 1819 tests on concrete-filled steel tube columns compared to EN1994. *The Structural Engineer.* 18(16): 33–38.

Hatzigeorgiou, G., 2008. Numerical model for the behaviour and capacity of circular CFT columns, Part I: Theory, Engineering Structures, Vol. 30 (6): 1573–1578.

Johansson, M. The efficiency of passive confinement in CFT columns. 2002. Steel and Composite Structures, Vol. 2 (5): 379–396.

Kwon Y., Seo S., Kang D. 2011. Prediction of the squash loads of concrete-filled tubular section coluns with local buckling. Thin-Walled Structures, Vol 49 (1): 85–93.

Oliveira W., Nardim S, El Debs A, El Debs M. 2010. Evaluation of passive confinement in CFT columns. Journal of Constructional Steel Research, Vol 66 (4); 487–495.

Susantha, K., Ge, H., Usami, T. 2001. A capacity prediction procedure for concrete-filled steel columns. Journal of Earthquake Engineering, Vol. 5 (4): 483–520.

Tubular Structures XIV – Gardner (Ed.)
© 2012 Taylor & Francis Group, London, ISBN 978-0-415-62137-3

Concrete filled circular hollow sections under cyclic axial loading

T. Sheehan & T.M. Chan
University of Warwick, UK

ABSTRACT: This paper describes investigations into the structural response of concrete-filled Circular Hollow Sections (CHSs) under cyclic axial loading. The research is based primarily upon laboratory testing. A series of tests on both hot-formed and cold formed concrete-filled CHSs with a non-dimensional global slenderness in the region of 1 were conducted to investigate key structural responses including first cycle peak load, post buckling resistance, reserve strength, ductility level and energy dissipation. Measurements were taken of cross-section geometry, geometric imperfections and material properties. Key test results and sample load-deformation histories are presented. The generated structural performance data will be exploited to calibrate the numerical finite element models which will be used for further parametric studies.

1 INTRODUCTION

A variety of structural systems are used in seismic buildings to provide lateral stability and dissipate energy. Among these, concentrically braced frames are often favoured for simplicity of design. Furthermore, they are more susceptible to ductile failure modes, in contrast to moment frames, which often undergo brittle failure at the connection. Rectangular hollow steel sections are usually selected as bracing members and a significant amount of research has been carried out on these to date, such as Nip et al. (2010), comparing the response of hot-rolled carbon, cold-formed steel and stainless steel sections under cyclic axial loading. In addition to this, several researchers have explored the behavior of concrete-filled steel rectangular sections, such as Broderick et al. (2005), Lee et al. (2000) and Liu & Goel (1988). Concrete-filled tubular braces are becoming increasing popular for this application owing to their excellent strength and ductility in comparison with hollow steel sections. The contribution of concrete enhances the strength of these slender braces in compression, delaying the onset of local buckling and reducing the difference in resistance between compressive and tensile loading.

In practice, circular hollow sections are often overlooked, since more intricate connections are required. However, research to date, such as Elchalakani et al. (2003) and Martinez-Saucedo et al. (2008) have demonstrated that hollow circular steel members are also highly suitable for use as bracing members, as they are not as sensitive to local buckling as rectangular sections owing to the more uniform shape. The advantages of this section could be utilized further by using concrete-filled circular hollow sections as bracing members. The homogeneity of confining pressure on the concrete core and outward pressure on the steel tube provides the optimum cross-section.

Hence, this research will compare the resistance of hollow and concrete-filled circular tubes of both hot-rolled and cold-formed steel. A series of laboratory tests will be carried out, applying a cyclic axial load to each specimen in accordance with ECCS guidelines (1986). Intermediate-length bracing members will be tested, having a non-dimensional slenderness in the region of 1.0 in accordance with BS EN-1993-1-1 (2005) and BS EN 1994-1-1 (2004).

2 EXPERIMENTAL STUDY

2.1 *Introduction*

A series of tensile steel material tests, compressive concrete material tests and column tests under cyclic axial loading were carried out to investigate the structural behaviour of concrete-filled circular hollow sections under cyclic axial loading. All tests were performed in the Structures Laboratory of the School of Engineering, University of Warwick.

2.2 *Tensile coupon tests*

Tensile coupon tests were performed to establish the basic material stress-strain response; this was subsequently utilised during the analysis of the member test results and in the development of numerical models. The tests were carried out in accordance with BS EN ISO 6892-1 (2009).

Two types of steel section were employed for this research: A hot-finished circular tube with a nominal yield stress of 355 N/mm^2 and wall thickness of 3.2 mm (Celsius 355) and a cold-formed tube with a nominal 0.2% proof stress of 355 N/mm^2 and a wall thickness of 3.0 mm (Hybox 355). Both sections had an outer diameter of 48.3 mm. For each material,

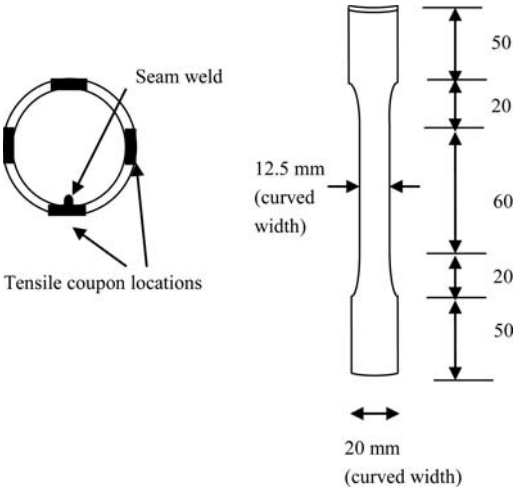

Figure 1. Tensile coupon locations and dimensions.

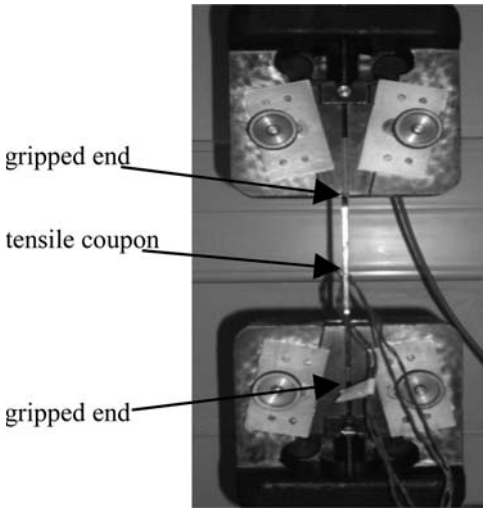

Figure 2. Tensile testing set-up.

4 longitudinal coupons were taken from different locations around the cross-section circumference. The coupon locations and dimensions are shown in Figure 1.

The test set-up is shown in Figure 2. The coupon ends were flattened prior to testing in order to fit inside the grips of the testing machine. While this process is thought to have locally work-hardened the end portions, the coupons were dimensioned so as to mitigate the effect of this hardening on the central region.

Typical stress-strain relationships obtained for both hot-rolled and cold-formed steel coupons are presented in Figure 3. The results correlate closely to those expected, with the hot-rolled steel exhibiting reasonably linear behaviour up to yield, followed by a plateau before advancing to the strain hardening region. The cold-formed steel on the other hand is

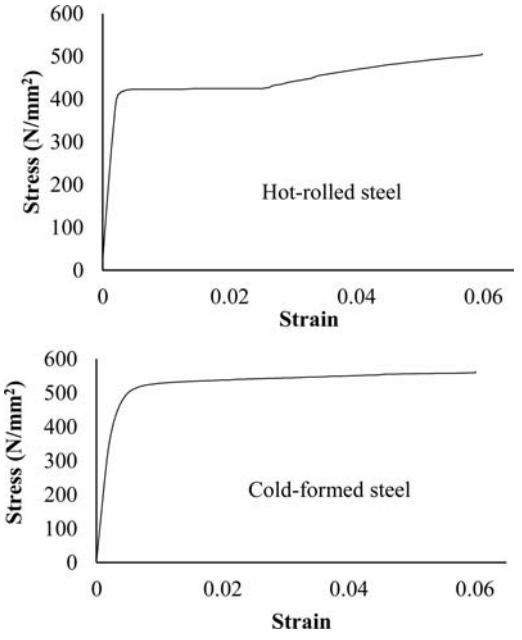

Figure 3. Stress-strain relationships from tensile coupon tests.

Table 1. Results of tensile coupon tests.

Steel	Yield stress/ 0.2% proof stress (N/mm^2)	Ultimate tensile Stress (N/mm^2)	Young's modulus (N/mm^2)	% elongation after fracture
Hot-rolled	415	546	206000	37
Cold-formed	499	573	184000	30

significantly more non-linear in the initial stages and does not display the same plateau as the hot-finished coupons.

The average yield stress (hot-rolled)/0.2% proof stress (cold-formed), ultimate stress, Young's modulus and percentage elongation after fracture are presented in Table 1 for both types of steel. In determining the values, the seam weld-coupon results were omitted.

2.3 *Concrete material tests*

A number of trial concrete mixes were carried out. Water-cement ratios and proportions of coarse and fine aggregate were varied in order to meet two objectives. The first objective was a compressive strength in the region of 20–25 MPa. This is to meet the minimum strength requirement of Grade 20 for seismic applications, specified in BS EN 1998-1. Also, it has been found that higher concrete strengths do not provide much benefit – this was shown by Broderick et al. (2005) for strengths greater than 28 MPa. The second objective was to achieve satisfactory compaction

Table 2. Concrete mix proportions by weight.

Water	Cement	Coarse aggregate	Fine aggregate
0.72	1	2.3	2.86

Table 3. Compressive strength and static elastic modulus.

7 day strength N/mm^2	28 day strength N/mm^2	Test date strength N/mm^2	Static elastic modulus N/mm^2
17.14	25.1	29.4	20100

for the long, slender tubes. Various methods of vibration were investigated and an effective procedure was developed using a beam-vibrator and a rubber mallet. Specimens were cast vertically, with the vibrator clamped onto a loosely bolted steel frame which was in direct contact with the test specimen. This arrangement was found to provide ample pulsation without leading to segregation and the method was aided by gently tapping the sides of the tube with the mallet. The tubes were filled in layers, with continuous vibration of the frame during casting and application of the mallet after each layer. After casting, the tops of the tubes were sealed with plastic to prevent the escape of moisture during curing. The design concrete mix is shown in Table 2.

The concrete mix used a maximum aggregate size of 6.35 mm had a high percentage of water and fine aggregate. The compressive strength was obtained in accordance with BS EN 12390-3 (2003) at 7 days, 28 days and the day of testing. In addition to this, the static elastic modulus on the test date was also measured. The values for these are given in Table 3.

2.4 *Column tests*

Cyclic axial tests were performed on six tubular columns, three of which consisted of hot-finished steel and the remaining three of cold-formed steel. For each steel type, one specimen was hollow, while the remaining two were filled with concrete.

2.4.1 *Specimen preparation*

All specimens were circular sections, with an outer diameter of 48.3 mm and a length of 1500 mm. All concrete-filled specimens were cast with the concrete mix given in Table 2 and compacted as described in Section 2.3. Following casting, both hollow and concrete-filled tubes were welded onto 25 mm thick steel end plates, and two outer stiffeners of dimensions 125 mm × 50 mm × 8 mm were welded onto each end as shown in Figure 4.

A small hole was drilled in the centre of the end-plates, in order to facilitate the escape of water vapour from the tube during welding. After manufacture,

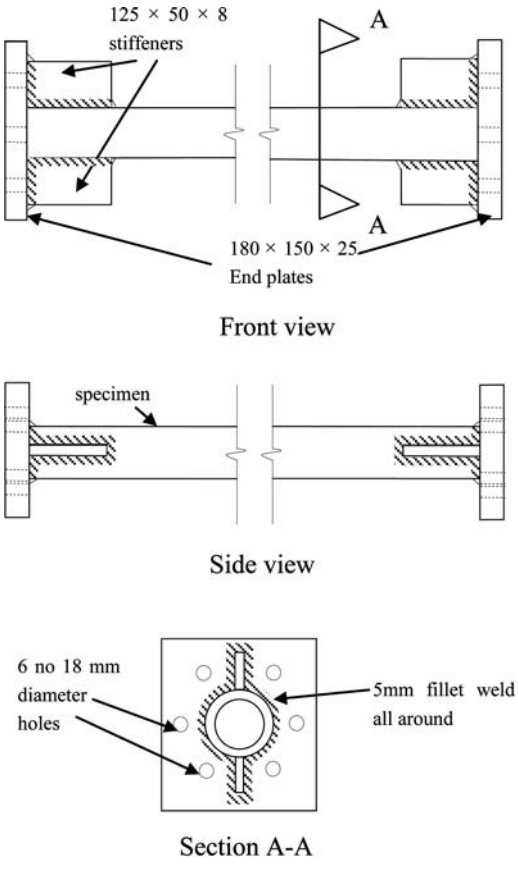

Figure 4. Cyclic test specimen details.

Table 4. List of test specimens and global imperfections.

Label	Steel	Infill	Global imperfection mm
HR-H	hot-finished	hollow	0.58
CF-H	cold formed	hollow	0.73
HR-F1	hot-finished	concrete	0.37
HR-F2	hot-finished	concrete	0.38
CF-F1	cold formed	concrete	0.73
CF-F2	cold formed	concrete	0.67

plaster was injected through the hole to fill the gap between the top surface of the concrete and the end-plate.

Specimen imperfections were measured at 30 mm intervals along each of four faces, in order to obtain the maximum global imperfection. A list of test specimens and corresponding maximum global imperfections is given in Table 4.

2.4.2 *Test procedure*

Specimens were tested in a purpose-built test rig, illustrated in Figure 5. The end plates were bolted

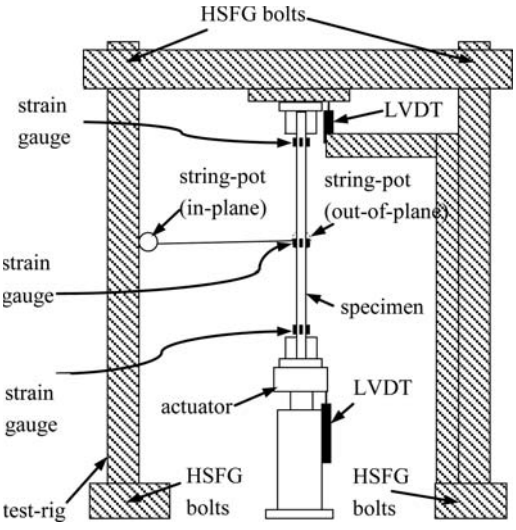

Figure 5. Test-rig and instrumentation.

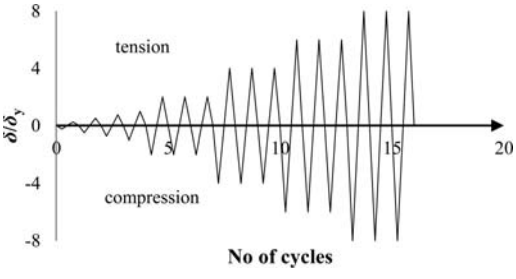

Figure 6. Cyclic loading protocol.

into the test-rig using six M16 bolts at each end and a cyclic load was applied using a 50-tonne hydraulic actuator.

The loading protocol used (Fig. 6) was that outlined in ECCS (1986), in which one compression and tension cycle is applied at each of the following displacement amplitudes: $0.25\delta_y$. $0.5\delta_y$. $0.75\delta_y$. $1.0\delta_y$. followed by three displacement amplitudes at each of the following $2\delta_y$. $4\delta_y$. $6\delta_y$. $8\delta_y$, etc. up to failure, where δ_y is the yield displacement of the specimen obtained from tensile coupon tests.

The axial load and displacement were monitored throughout the tests and in addition to this, the lateral displacement at mid-height was measured in two orthogonal directions, and axial strains at 12 points on the tube – four strain gauges on the four faces (Fig. 7), at the top, middle and bottom of the specimen. Some measures were taken to account for slip at connections and the flexibility of the test rig: HSFG bolts were utilized at the four corners, and the vertical displacement of the top beam was monitored throughout the test using an LVDT. This enabled axial displacement measurements to be adjusted accordingly.

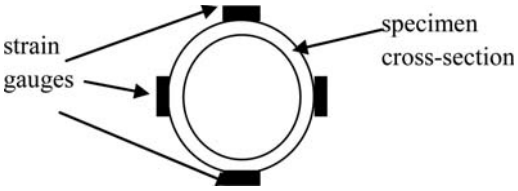

Figure 7. Strain gauge locations.

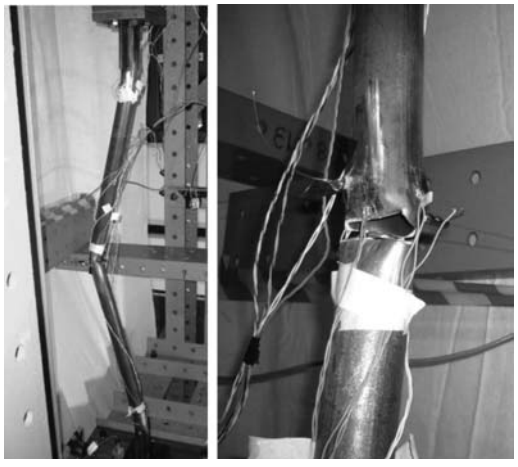

Figure 8. Deformation and failure of HR-H.

2.4.3 *Test results*

2.4.3.1 *Deformation and failure*

All specimens buckled predominantly about the unstiffened axis, regardless of the direction of the maximum imperfection. The hollow specimens, HR-H and CF-H exhibited overall member buckling during the 5th loading cycle, followed by local inward buckling at mid-height during greater displacement amplitudes. The extent of this local deformation increased as cycles progressed, until finally a crack propagated across this region during a tensile loading. Local buckling was mainly concentrated at the mid-height, with no noticeable buckling at the end regions, for either HR-H or CF-H. The failure of HR-H is depicted in Figure 8.

In the case of the concrete-filled tubes, overall buckling occurred in the 5th cycle, similarly to the hollow tubes. However, as the axial displacement increased, local inward buckling was delayed by the presence of the concrete. Curvature at the mid-height was less severe and distributed over a greater distance, as shown in Figure 9, allowing it to undergo larger displacement cycles. In contrast to the hollow tubes, in which the plastic hinge was confined to the mid-height, significant bending was also observed at the ends of the unstiffened length. Specimen HR-F1 showed both inward and outward local buckling at the mid-height and base, and eventually ruptured at these locations. In addition to the buckling, considerable necking was

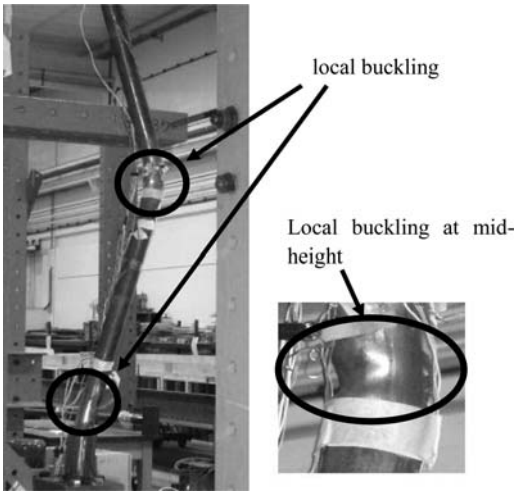

Figure 9. Deformation of HR-F1.

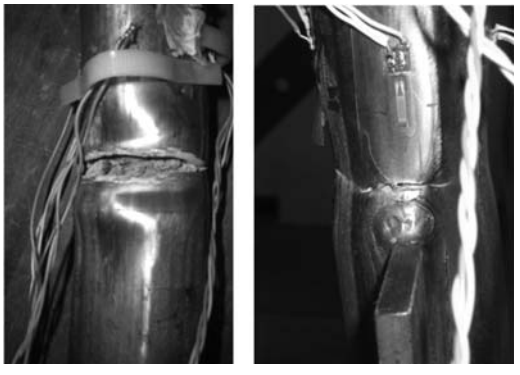

Figure 10. Failure at mid-height and base of HR-F1.

observed at the base of HR-F1, which can be seen in Figure 10.

Specimens HR-F2, CF-F1 and CF-F2 responded in a similar manner to HR-F1, developing plastic hinges near the top, middle and base of the specimens. The severity of local buckling and location of ultimate steel rupture varied from specimen to specimen, with HR-F2 failing near the top, and CF-F1 and CF-F-2 failing close to the base. Figure 11 shows the central and base regions of CF-F2. Here, the local bucking at mid-height (left) was not as severe as for HR-F1 and hence rupture occurred at the base.

A summary of the maximum compressive and tensile loads and number of cycles to failure is given in Table 5. Tensile forces ($N_{t,max}$) are normalized with respect to the expected yield force from the tensile coupon tests ($N_{t,y}$). The first cycle peak buckling loads ($N_{c,max}$) are normalized with respect to the predicted buckling loads ($N_{b,Rd}$) given in BS EN 1993-1-1 and BS EN 1994-1-1 for the hollow and filled specimens respectively. Non-dimensional slenderness ($\bar{\lambda}$) and buckling loads were calculated for hot-rolled and

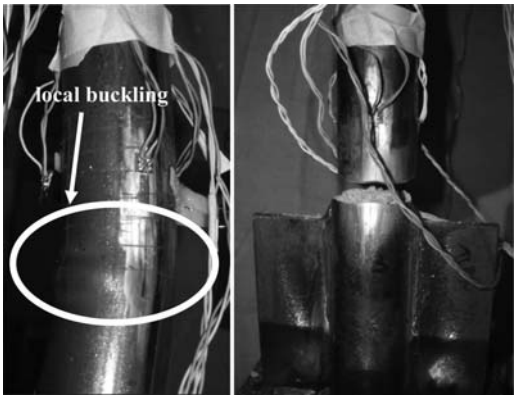

Figure 11. Mid-height region and base of CF-F2 at failure.

Table 5. Maximum numbers of cycles and loads.

ID	No of cycles to fracture	N_{tmax} kN	$N_{t,max}/N_{t,y}$	N_{cmax} kN	$\bar{\lambda}$	$N_{c,max}/N_{b,Rd}$ (EC3/EC4)
HR-H	17	180	0.96	155	0.78	1.17
CF-H	14	209	0.98	151	0.90	1.43
HR-F1	28	198	1.05	174	0.81	1.14
HR-F2	19	198	1.05	175	0.81	1.15
CF-F1	15	220	1.03	174	0.92	1.18
CF-F2	16	216	1.01	164	0.92	1.11

concrete-filled tubes using buckling curve 'a' and for the hollow cold-formed tube using buckling curve 'c'.

The maximum tensile loads for both hot-rolled and cold-formed hollow sections are slightly less than those predicted from the material tests, possibly owing to softening of the material from previous cycles, or from the residual out-of-straightness following elongation during buckling. The maximum tensile loads for concrete-filled specimens slightly exceed the predicted yield load, with the concrete infill providing average improvements of 9.4% and 4.1% for hot-rolled and cold formed filled tubes respectively in comparison with their hollow counterparts.

The first cycle buckling loads also exceed BS EN 1993-1-1 (2005)/BS EN 1994-1-1 (2004) predictions in all cases, with the hollow cold-formed section CF-H displaying a more noticeable increase than the hot-rolled or filled tubes.

2.4.3.2 *Ductility level and energy dissipation*

Load-displacement hysteresis curves for each specimen are presented in Figures 12–17.

Hot-rolled and cold formed members produced similar hysteresis curves, showing significant decreases in compressive and tensile peak loads during the second and third cycles at each displacement amplitude, and gradual degradations in compression and tension loads with increasing axial displacements. Concrete-filled tubes displayed noticeably

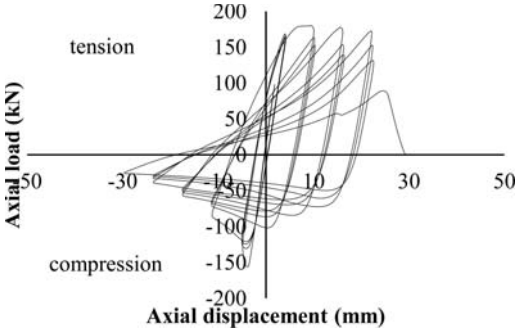

Figure 12. Load-displacement response for HR-H.

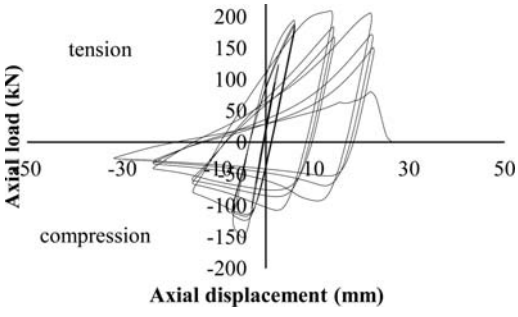

Figure 13. Load-displacement response for CF-H.

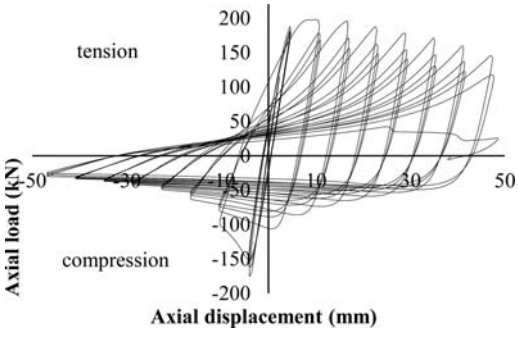

Figure 14. Load-displacement response for HR-F1.

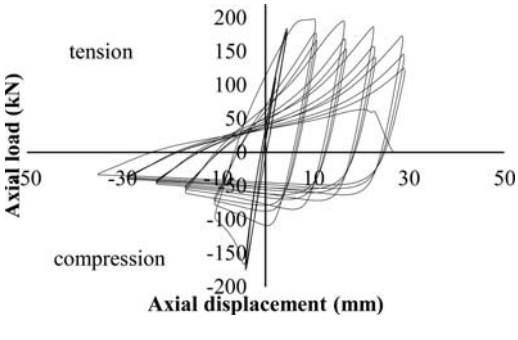

Figure 15. Load-displacement response for HR-F2.

fuller shaped curves than hollow members, and the curve for hot-rolled members was also a more rounded shape than for cold-formed. Also, concrete-filled tubes maintained a higher compressive resistance and more stable behaviour up to the maximum compressive displacement amplitude than hollow tubes. This is illustrated in Figures 18 and 19 for hot-rolled and cold-formed members respectively in their 13th cycles.

The load-displacement relationships show a low stiffness when loading in tension and a possible explanation for this is the elongation of specimens during compression cycles, which are then restraightened during tensile loading. Test data shows that a residual lateral deflection was always present after the initial buckling, which supports this explanation.

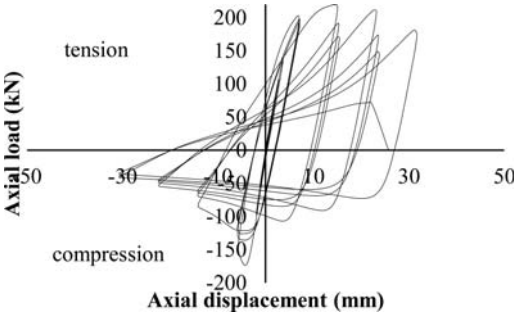

Figure 16. Load-displacement response for CF-F1.

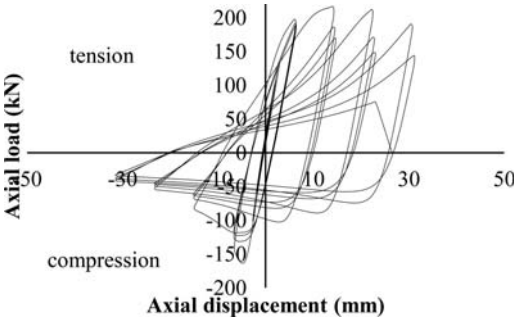

Figure 17. Load-displacement response for CF-F2.

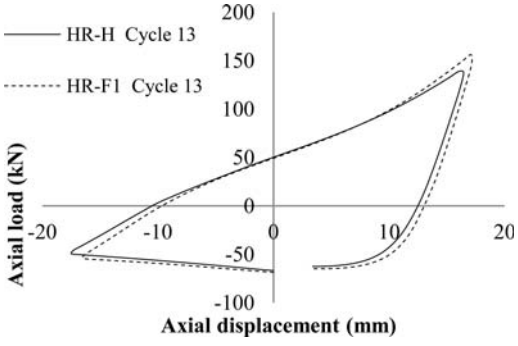

Figure 18. Load-displacement hysteresis for HR-H and HR-F1 in the 13th cycle.

Displacement ductility ratios are presented in Table 6 for each specimen, which is defined as $\mu_\Delta = \delta_{max}/\delta_y$, where δ_{max} is the maximum axial displacement.

Specimen HR-F1 exhibited significantly better ductility than the other five specimens. With the exception of this specimen, values for μ_Δ did not differ between hollow and concrete-filled specimens. Comparing hot-rolled and cold-formed steels, it is found that the former gave a superior performance to the latter in terms of ductility.

The energy dissipation for each member was evaluated using the area under the hysteresis curve and values are presented in Table 6 for the energy dissipated during the 8th, 11th and 14th cycles, and for the total energy dissipated per specimen up to failure.

Generally, cold-formed members dissipated more energy per cycle, as a results of a having a higher yield stress but did not endure as many cycles as the hot-rolled specimens, leading to lower overall amounts of energy dissipation. This is illustrated in Figure 20.

The presence of concrete does not appear to increase the energy dissipated per cycle, but prolongs the duration of the specimen enabling it to withstand a greater number of cycles prior to failure. This is particularly noticeable for specimen HR-F1, which dissipated a total of 96 kNm – almost three times greater than the hollow equivalent, HR-H. Figures 21 and 22 compare the energy dissipated between filled and hollow specimens for hot-rolled and void-formed steels respectively.

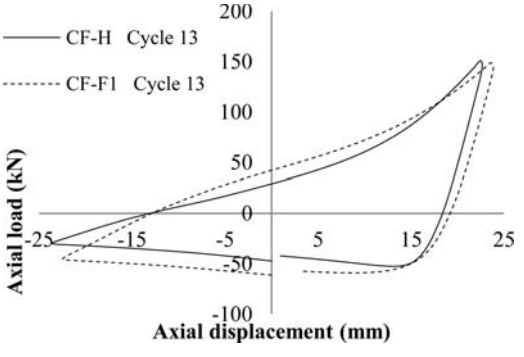

Figure 19. Load-displacement hysteresis for CF-H and CF-F1 in the 13th cycle.

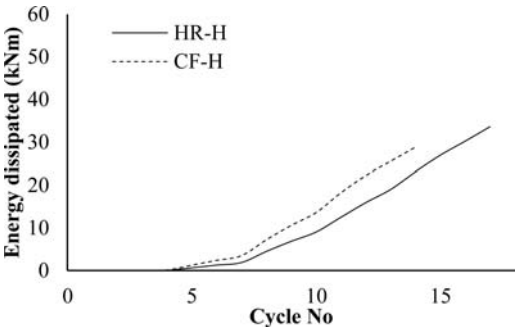

Figure 20. Energy dissipation for HR-H and CF-H.

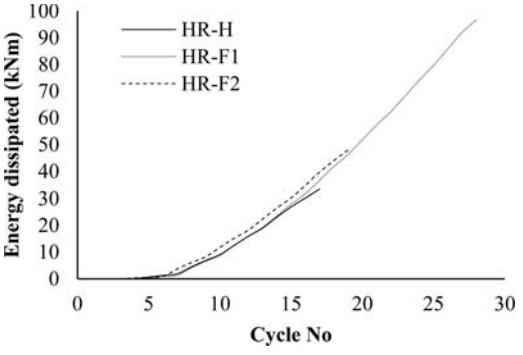

Figure 21. Energy dissipation for hot-rolled test specimens.

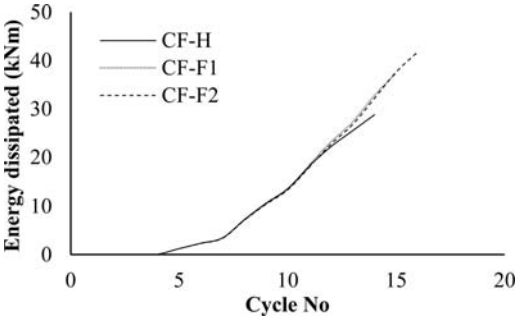

Figure 22. Energy dissipation for cold-formed test specimens.

Table 6. Energy dissipated at various stages of testing.

specimen	μ_Δ	Energy dissipated in 8th cycle kNm	Energy dissipated in 11th cycle kNm	Energy dissipated in 14th cycle kNm	Total energy kNm
HR-H	10	2.6	3.5	4.1	33.6
CF-H	8	4.4	5.3	2.5	28.8
HR-F1	16	3.2	4.1	4.8	96.7
HR-F2	10	2.4	3.3	4.0	48.0
CF-F1	8	4.5	5.5	6.1	37.4
CF-F2	8	4.4	5.4	6.1	41.8

3 CONCLUSIONS

It has been shown that concrete-infill enhances the performance of circular tubular steel members, although perhaps not to the same extent as rectangular hollow members. The uniformity of the cross-section ensures a more stable response, and provides superior durability under seismic loading.

Now that intermediate-length specimens have been tested, there is scope for further research looking at the resistance of longer members, with a non-dimensional slenderness in the region of 2. The effect of infill and cross-section shape for more slender circular members will need to be explored in a similar manner to establish relationships between non-dimensional slenderness and a variety of parameters, such as ductility, strength degradation and energy dissipation.

ACKNOWLEDGEMENT

The authors wish to thank TATA steel and Mr. Trevor Mustard for their support in this project. The authors would also like to thank Professors Roger Johnson and Toby Mottram from the University of Warwick and Professor Ahmed Elghazouli from Imperial College London for their technical guidance in carrying out this research.

REFERENCES

Broderick, B.M., Goggins, J.M. & Elghazouli, A.Y. 2005. Cyclic performance of steel and composite bracing members, *Journal of Constructional Steel Research* 61(4): 493–514.

Elchalakani, M., Zhao, X.L. & Grzebieta, R. 2003. Tests of cold-formed circular tubular braces under cyclic axial loading, *Journal of Structural Engineering* 129(4): 507–14.

Lee, C., Grzebieta, R.H. & Zhao, X.L. 2000. The importance of further studies on the capacity evaluation of concrete-filled steel tubes under large deformation cyclic loading, *Structural Failure and Plasticity*: 685–690, Oxford: Pergamon.

Liu, Z. & Goel, S.C. 1988. Cyclic load behavior of concrete-filled tubular braces, *Journal of Structural Engineering* 114(7): 1488–1506.

Martinez-Saucedo G., Tremblay, R. & Packer, J.A. 2008b. Seismic response if circular hollow section braces with slotted end connections. *Proceedings of the 12*th*International Symposium on Tubular Structures*: 227–233, Shanghai.

Nip, K.H., Gardner, L. & Elghazouli, A.Y. 2010. Cyclic testing and numerical modelling of carbon steel and stainless steel tubular bracing members, *Engineering Structures* 32(2): 424–41.

BS EN-1993-1-1. 2005. Design of steel structures, Part 1-1: General rules and rules for buildings. European Standard, CEN.

BS EN-1994-1-1. 2004. Design of composite steel and concrete structures, Part 1-1: General rules and rules for buildings. European Standard, CEN.

BS EN 1998-1. 2004. Design of structures for earthquake resistance – Part 1: General rules, seismic actions and rules for buildings. European Standard, CEN.

BS EN ISO 6892-1. 2009. Metallic materials – Tensile testing – Method of test at room temperature. European Standard, CEN.

BS EN 12390-3. 2002. Testing hardened concrete: Part 3: Compressive strength of test specimens. European Standard, CEN.

ECCS. 1986. Recommended Testing Procedure for Assessing the Behaviour of Structural Steel Elements under Cyclic Load. Brussels.

Tubular Structures XIV – Gardner (Ed.)
© 2012 Taylor & Francis Group, London, ISBN 978-0-415-62137-3

An experimental study of high-strength CFST columns subjected to axial load and non-constant bending moments

D. Hernández-Figueirido
Dpt. Ing Mecánica y Construcción, Universitat Jaume I, Castellón, Spain

M.L. Romero, J.L. Bonet & A. Hospitaler
Instituto de Ciencia y Tecnología del Hormigón, Universitat Politècnica de València, Valencia, Spain

ABSTRACT: This paper describes 49 experimental tests conducted on rectangular and square tubular columns filled with high strength concrete subjected to a non-constant bending moment distribution. The test parameters were the length (2, 3 and 4 m), the cross-section aspect ratio (square or rectangular), the wall thickness (4 or 5 mm), and the ratio of the top and bottom first order eccentricities $r = e_{top}/e_{bottom}$ (1, 0.5, 0 and −0.5). The effect of slenderness combined with the influence of variable curvature is compared with the design loads from Eurocode 4. The results show that for the slender elements of this experimental campaign the code presents an error close to 4%. It proves that this standard is applicable to high strength concrete, although the concrete tested is outside the upper bound of Eurocode 4 specifications.

1 INTRODUCTION

The use of normal strength concrete-filled tubular (CFT) columns has been widespread for some decades due to their high stiffness, ductility, and fire resistance, and has been well summarized by Shams & Saadeghvaziri (1997), Shanmugam & Lakshmi (2001), Gourley et al. (2008), and more recently by Zhao et al. (2010). Moreover, the use of high-strength concrete ($f'_c > 50$ MPa) has become more frequent due to advances in technology, mainly those affecting elements subjected to high compression. However, it was concluded from previous studies that further experimental tests for high strength concrete-filled (HSC) columns were necessary, Gourley et al. (2008).

Different authors stated that as high strength concrete is characterized by low dilatation, a substantial confinement effect does not occur (Johansson & Gylltoft 2001, Zeghiche & Chaoui 2005). Furthermore, for rectangular CFT columns the confinement is generally neglected due to non-uniform lateral pressure distribution across the section.

Several authors have presented studies for slender rectangular CFT columns where an axial load is applied in combination with an eccentricity in the load. In most cases the eccentricity is the same at both ends, producing a constant bending moment distribution, i.e. constant curvature. The first tests were performed by Knowles & Park (1969), followed later by Bridge (1976). Han (2000) studied tubular columns with a high slenderness ratio but with normal strength concrete, concluding that the strength of the concrete has very little influence on the ultimate capacity given that the failure load is governed by the flexural rigidity. Recently Yu et al. (2008) published the results of research on circular, square, short and long CFTs filled with high performance self-consolidating concrete. The results were in agreement with design values calculated using different design codes. Also, Han & Yao (2003, 2004), Lee (2007) and Zhang & Guo (2007) have performed experimental tests combining slender rectangular CFT columns with HSC and eccentricity.

Though a large body of research for CFT columns exists, it was found that cases where the eccentricity is different at both ends of the columns, producing a non-constant bending moment, were not well studied in the bibliography. Besides, if one of the eccentricities is positive and the other negative a double curvature in the element occurs. This problem directly affects slender, but not stub, columns as it changes the values of second order bending moments. Eurocode 4 (2004) provide an equivalent moment factor (β and C_m respectively) that depends on the type of bending diagram. Goode (2008) compiled the results of several tests, and compared them with Eurocode 4 (2004) provisions, reaching the conclusion that although for circular sections the provisions could be extended to a strength of concrete of 75 MPa, more tests are needed mainly for long circular tubular columns in combination with a bending moment. He did not present any results regarding double curvature.

For circular columns, only Kilpatrick & Rangan (1999), and Zeghiche & Chaoui (2005) have performed tests with different eccentricities at both ends. In the latter, the test parameters were slenderness,

eccentricity, and single and double curvature. The comparison with EC4 provisions results on the unsafe side for variable curvature. They stated that more numerical and experimental tests should be performed to check the validity of the buckling design methods of Eurocode 4 (2004) in the case of high strength concrete for single and double curvature.

The authors compiled and updated the databases of Kim (2005) and Goode (2008) totaling close to 1400 rectangular experimental tests. From this new database, it was concluded that there is a lack, both for normal and high strength concrete, of tests for columns with non-constant bending moment.

For rectangular columns, Wang (1999) presented an experimental study where eight tests on normal strength concrete-filled columns were carried out with end eccentricities which produced moments other than constant curvature bending. He concluded that Eurocode 4 was safe but very conservative in some cases.

The authors (Hernandez-Figueirido et al. 2011) presented previously the first results of an experimental campaign for rectangular CFT columns for both constant and variable curvature with normal and high strength concrete but for columns with a length of 2 m and a medium slenderness.

This paper supplements this previous research with the results of the variable curvature tests for rectangular columns for cases with different lengths (L = 2, 3 and 4 meters) studying the effect of the slenderness on high strength concrete-filled columns. The test parameters were the length, the type of cross-section, the thickness (4 or 5 mm) and the ratio of the top and bottom first order eccentricities $r = e_{top}/e_{bottom}$ (1.0, 0.5, 0.0 and −0.5). In these tests the load eccentricity at the ends is fixed and the maximum axial load of the column is evaluated and compared with the design loads from Eurocode 4 (2004).

2 EXPERIMENTAL TESTS

2.1 *Introduction*

In this experimental program forty-six tests were carried out on high strength concrete-filled columns, referring to Table 1. Tests were repeated on three additional columns to demonstrate the reliability of the experiments, cases 2, 8 and 41, adding up to a total of forty-nine tests.

The aim of this test matrix was to investigate the effect that the slenderness of the column in combination with a variable bending moment has on their behavior, focusing on HSC. The effective buckling lengths of the columns (L_b) are the length of the tubes plus 135 mm, since to obtain the exact distance between the hinges it is necessary to add the special assembly length. The nominal cross-section of the tubes (height h × width b × thickness t) measured 100 × 100 × 4 mm, 100 × 150 × 4 mm, 100 × 150 × 5 mm, respectively. The thicknesses of the tubes were selected in order to avoid local buckling following Eurocode 4 (2004).

In this paper the nominal strengths of concrete are always 90 MPa and the axial load is applied with two different eccentricities at the top (20 or 50 mm) to strong axis bending to avoid any possible interaction between the strong and weak axes. The initial out-of-straightness of the steel tubes was not measured due to its difficulty. However, they accomplish the European fabrication standard EN 10219 what limits the maximum value to L/333.

All of the tests were performed in the laboratory of the Department of Mechanical Engineering and Construction of the Universitat Jaume I in Castellon, Spain.

2.2 *Material properties*

The hollow steel tubes were cold formed and supplied by a manufacturer. The nominal yielding strength of the steel was 275 MPa with an ultimate nominal strength of 330 MPa. However, the real strength (f_y) of the empty tubes was obtained by coupon test and compression stub section, referring to Table 1. The modulus of elasticity Es of the steel was set by European standards with a value of 210 GPa.

All columns were cast using concrete batched in the laboratory obtaining an approximate nominal concrete strength of 90 MPa (HSC). The concrete compressive strength f_c (termed also f'_c in ASIC code) was determined from a mean of three 150 × 300 mm cylinders using standard tests. All samples were tested on the same day as the column tests, 28 days, and the results are given in Table 1.

2.3 *Manufacture of the columns*

A 350 mm × 350 mm × 10 mm steel plate was welded to the bottom of each empty steel tube to facilitate the casting of the fresh concrete and to join the element to the pinned support assembly. The elements were then cast in a vertical position and the concrete was vibrated every 0.5 m with a needle vibrator. The tubes were overfilled with 1 cm of concrete and later covered with wet cloth. Prior to the test, the residual layer of concrete was smoothed and the columns were sealed off with another similar welded plate to ensure perfect contact between the plates and the steel and concrete core.

2.4 *Test setup and procedure*

The specimens were tested in a special 5000 kN capacity testing machine in a horizontal position, Figure 1.

The eccentricity of the compressive load applied was equal at both ends in some cases (20 mm or 50 mm), so the columns were subjected to constant curvature bending, whereas in the remaining cases a non-constant bending moment was produced.

Table 1. Tests properties and results.

Test	b	h	t	L (mm)	e_{top} (mm)	e_{bot} (mm)	r	f_y (MPa)	f_c (MPa)	N_{exp} (kN)
1	100	100	4	2135	20	−10	−0.5	346	92	737
2	100	100	4	2135	20	−10	−0.5	371	93	758
3	100	100	4	2135	20	0	0	363	89	652
4	100	100	4	2135	20	10	0.5	280	93	525
5	100	100	4	2135	20	20	1.0	375	88	490
6	100	100	4	2135	50	25	0.5	358	87	383
7	100	100	4	2135	50	50	1.0	358	91	321
8	100	100	4	2135	50	50	1.0	371	93	323
9	100	100	4	3135	20	−10	−0.5	353	97	502
10	100	100	4	3135	20	0	0	363	92	410
11	100	100	4	3135	20	10	0.5	280	86	363
12	100	100	4	3135	20	20	1.0	375	74	381
13	100	100	4	3135	50	−25	−0.5	358	96	357
14	100	100	4	3135	50	0	0	346	92	316
15	100	100	4	3135	50	25	0.5	358	90	218
16	100	100	4	3135	50	50	1.0	292	87	230
17	100	100	4	4135	20	−10	−0.5	280	88	367
18	100	100	4	4135	20	10	0	280	96	254
19	100	100	4	4135	20	20	1.0	280	94	220
20	100	100	4	4135	50	25	0.5	369	92	184
21	150	100	4	2135	20	−10	−0.5	268	93	945
22	150	100	4	2135	20	0	0	280	90	926
23	150	100	4	2135	20	10	0.5	342	90	850
24	150	100	4	2135	20	20	1	298	86	804
25	150	100	4	2135	50	25	0.5	424	90	463
26	150	100	4	2135	50	50	1	341	77	466
27	150	100	4	3135	20	−10	−0.5	280	91	690
28	150	100	4	3135	20	0	0	280	84	562
29	150	100	4	3135	20	10	0.5	342	89	501
30	150	100	4	3135	20	20	1.0	298	84	460
31	150	100	4	3135	50	−25	−0.5	308	92	502
32	150	100	4	3135	50	0	0	362	91	430
33	150	100	4	3135	50	25	0.5	312	91	287
34	150	100	4	3135	50	50	1	341	89	309
35	150	100	5	2135	20	−10	−0.5	304	93	104
36	150	100	5	2135	20	0	0	370	89	106
37	150	100	5	2135	20	10	0.5	424	86	981
38	150	100	5	2135	20	20	1.0	459	83	935
39	150	100	5	2135	50	25	0.5	293	85	526
40	150	100	5	2135	50	50	1.0	368	84	528
41	150	100	5	2135	50	50	1	336	92	458
44	150	100	5	3135	20	−10	−0.5	336	91	692
43	150	100	5	3135	20	0	0	370	79	690
44	150	100	5	3135	20	10	0.5	424	85	622
45	150	100	5	3135	20	20	1.0	459	91	573
46	150	100	5	3135	50	−25	−0.5	306	85	548
47	150	100	5	3135	50	0	0	396	87	456
48	150	100	5	3135	50	25	0.5	332	91	328
49	150	100	5	3135	50	50	1.0	368	82	381

It was necessary to build up special assemblies at the pinned ends to apply the load with different eccentricities while maintaining the column in a horizontal position, Fig 1.b, and c.

This figure presents a general view of the test for a 2-meter-long specimen where a special anti-torsion steel frame was built in order to avoid bottom hinge torsion rotation. Five LVDTs were used to symmetrically measure the deflection of the column at mid length (0.5 L) and also at four additional levels (0.25 L, 0.37 L, 0.625 L, 0.75 L).

Once the specimen was put in place, it was tested using a displacement control protocol in order to measure post-peak behavior.

3 RESULTS

3.1 *Force displacement*

Table 1 lists the maximum axial load (N_{exp}) for the forty-nine tests.

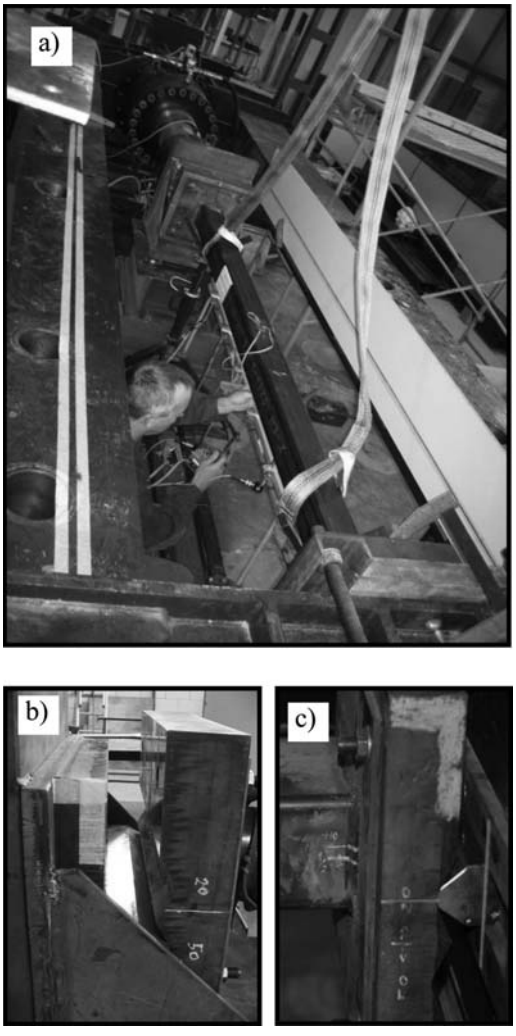

Figure 1. General view of the tests.

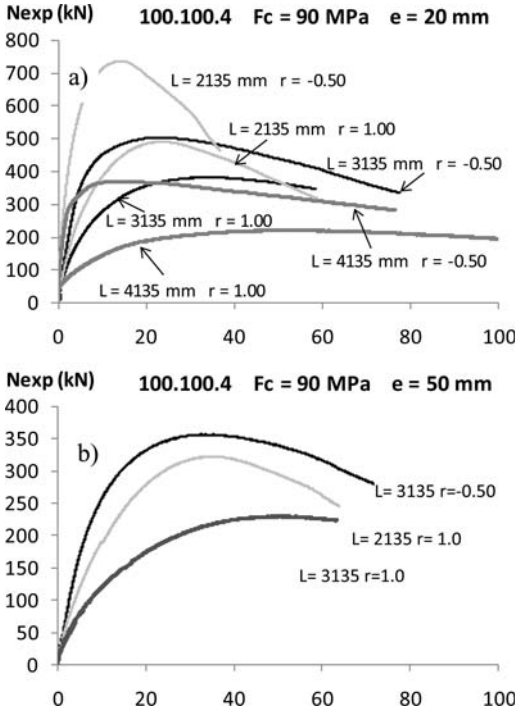

Figure 2. Axial load versus midspan displacement.

For a better understanding of the influence of the second order effects, Fig. 2 presents the force-displacement curves for square cross-section ($100 \times 100 \times 4$) and for tests with different lengths, but only with opposing eccentricity ratios $r = 1.0$ and -0.5 for simplicity.

The top eccentricity $e_{top} = 20$ mm is presented in Fig. 2a and the top eccentricity $e_{top} = 50$ mm is presented in Fig. 2b in order to study the effect of this parameter on global behavior. It is worth noting that there is a lower number of tests with $e_{top} = 50$ mm. In these tests, the general tendency of the curves is as expected: for a given length when the eccentricity at the bottom (minimum) is decreased (from $r = 1$ to $r = -0.5$), therefore producing variable curvature, Fig. 2a, the maximum load is increased (and the midspan lateral displacement reduced) because the second order bending moment is reduced. Also, if cases with the same eccentricity ratio but different lengths are compared, the maximum axial load is higher if the length is lower.

It is interesting to observe that ductile post-peak behavior is achieved for all cases, but it is always slightly reduced for cases with lower length in comparison to those with higher length, that is, the slope of the descending branch is more pronounced for lower slenderness. Moreover, the cases with $r = -0.5$ differ from the cases with $r = 1.0$ in the descending branch. The slope is more gradual for cases with constant curvature than for those with variable curvature.

From Table 1, it can be observed that the load is obviously increased when the width or thickness of the tube is increased. The results show for the limited cases analyzed that the slenderness of the section, i.e. width to thickness ratio (B/t), has a lesser effect than directly increasing the area of concrete.

To complete the previous graph, Fig. 3 presents the maximum load N_{max} in terms of eccentricity ratio (e_{top}/e_{bot}) for all tests with the smaller section. From this figure it can be noted that the difference in the ultimate axial load is higher among the cases of 2 and 3 meters than among the cases of 3 and 4 meters.

It is also possible to observe that this difference is higher for the cases of $r = -0.5$ than for those where $r = 1.0$. This is because the problem is clearly governed by the second order effects and the variable bending moment has a higher effect in the cases with lower slenderness. A more in-depth examination of this

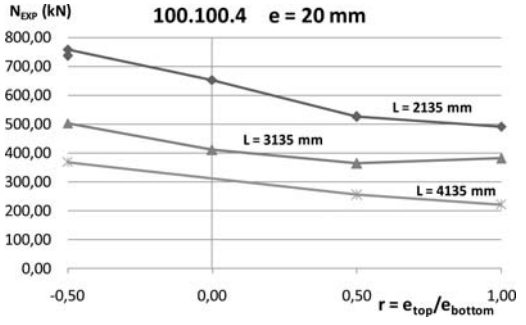

Figure 3. Axial load versus eccentricity ratio.

statement will be presented in the following sections comparing different cases of e_{top}/e_{bottom}.

3.2 *Observation of the deformed shape*

The deformed shape obtained from the 5 LVDTs is not presented in this paper for simplicity. However, from its study, it can be affirmed that the displacements are always in the same direction even in the case of double curvature ($r = -0.5$). It can be noted that for constant curvature the maximum displacement is achieved in the midspan section, producing a symmetrical deformed shape while for double curvature the maximum displacement is located to the left of the midspan section, i.e. closer to the higher eccentricity, producing an unsymmetrical deformed shape.

It is interesting to note that the behavior in terms of the length is different for constant and variable curvature. While for $r = 1$ the maximum displacement is achieved for $L = 4135$ mm and a lower one for $L = 2135$ mm, for $r = -0.5$ the maximum displacement is achieved for $L = 3135$ mm and a lower one for $L = 4135$ mm, which was initially surprising.

It can also be inferred that for the case of $L = 4$ meters with $r = -0.5$ the second order effects are lower and the first order curvature (variable) which depends on the length is higher in comparison with $r = 1.0$. This results in the element trying to bend in the negative direction, drastically reducing the lateral deflection.

4 COMPARISON WITH EUROCODE 4 (CEN 2004)

The design of normal-strength concrete-filled tubular columns has to be carried out in Europe following Eurocode 4 (2004) which limits the cylinder strength of concrete to 50 MPa for columns. The experiments in this study aim to clarify whether Eurocode 4 is still applicable to 90 Mpa, and also whether the second order effects, which depend on the slenderness and the eccentricity ratio, are correctly accounted for. This standard affirms that within the column length, second order effects may be allowed for by multiplying the greatest first order design bending moment ($M_{Ed} = N \cdot e_{top}$) by an amplification factor. In addition,

Table 2. Calculation of second order effects in Eurocode 4.

Eurocode 4 (CEN 2004)
$M_{tot} = k \cdot N \cdot e_{top} + k_2 \cdot N \cdot e_0$
$k = \dfrac{\beta}{1 - \dfrac{N_{Ed}}{N_{cr,eff}}}$ $k_2 = \dfrac{1}{1 - \dfrac{N_{Ed}}{N_{cr,eff}}}$
$\beta = 0.66 + 0.44 \cdot \dfrac{M_{top}}{M_{bot}} \geq 0.44$
$N_{cr,eff} = \dfrac{\pi^2 \cdot EI_{eff,2}}{L^2}$
$EI_{eff,2} = 0.9 \cdot (E_s I_s + 0.6 E_{cm} I_c)$
$e_0 = \dfrac{L}{300}$
$E_{cm} = 22000 \cdot \left(\dfrac{f_c}{10}\right)^{0.3}$ (MPa)

the value of the M_{Ed} is incremented in Eurocode 4 including the influence of the member imperfection, $e_0 = L/300$. Table 2 summarizes a comparison of the equations for calculating the second order effects. The remaining part of the description of the design method (interaction diagrams) is not included for simplicity.

Since these test specimens are rectangular, the increment in the resistance of the cross-section due to the confinement effect is ignored and the partial safety factor for steel and concrete is fixed at 1. Table 3 presents a comparison between the experiments (N_{exp}) and the design load of Eurocode 4 (N_{EC4}).

From Table 3 and Fig. 4 it can be stated that for Eurocode 4 (2004) some of the cases are on the unsafe side ($N_{exp}/N_{AISC} < 1$) and others are on the safe side ($N_{exp}/N_{AISC} > 1$), reaching a mean value of 1.04 and a standard deviation of 0.10 was obtained.

It is worth noting that the concrete tested is outside of the upper bound of Eurocode 4 specification. It can be also observed that the cases with higher axial load are always on the safe side.

From a detailed study of Table 3 it can be inferred that Eurocode 4 is safer for $r = -0.5$ than for $r = 1.0$ if the same length is studied. Also the ratio (N_{exp}/N_{code}) error increases in the unsafe side if the length or the eccentricity increases. However there are particular cases for Eurocode 4 code which present excessive unsafe errors. It corresponds to the cases where the second order effects are more important and are due to an overestimation of the flexural stiffness E·I. This indicates that the equation of the stiffness of the section E·I needs correction. Some authors as for instance Tikka and Mirza (2006) have proposed that

Table 3. Error of Eurocode 4.

T	b	h	t	L (mm)	e_{top} (mm)	e_{bot} (mm)	r	N_{exp} (kN)	N_{EC4} (kN)	N_{exp}/N_{EC4}
1	100	100	4	2135	20	−10	−0.5	737	655	1.12
2	100	100	4	2135	20	−10	−0.5	758	655	1.15
3	100	100	4	2135	20	0	0	652	611	1.06
4	100	100	4	2135	20	10	0.5	525	522	1.00
5	100	100	4	2135	20	20	1.0	490	511	0.95
6	100	100	4	2135	50	25	0.5	383	347	1.10
7	100	100	4	2135	50	50	1.0	321	293	1.09
8	100	100	4	2135	50	50	1.0	323	301	1.07
9	100	100	4	3135	20	−10	−0.5	502	450	1.11
10	100	100	4	3135	20	0	0	410	409	1.00
11	100	100	4	3135	20	10	0.5	363	356	1.01
12	100	100	4	3135	20	20	1.0	381	345	1.10
13	100	100	4	3135	50	−25	−0.5	357	332	1.07
14	100	100	4	3135	50	0	0	316	303	1.04
15	100	100	4	3135	50	25	0.5	218	256	0.85
16	100	100	4	3135	50	50	1.0	230	208	1.10
17	100	100	4	4135	20	−10	−0.5	367	287	1.27
18	100	100	4	4135	20	10	0	254	257	0.98
19	100	100	4	4135	20	20	1.0	220	254	0.86
20	100	100	4	4135	50	25	0.5	184	194	0.94
21	150	100	4	2135	20	−10	−0.5	945	829	1.14
22	150	100	4	2135	20	0	0	926	798	1.16
23	150	100	4	2135	20	10	0.5	850	777	1.09
24	150	100	4	2135	20	20	1	804	669	1.20
25	150	100	4	2135	50	25	0.5	463	503	0.92
26	150	100	4	2135	50	50	1	466	402	1.15
27	150	100	4	3135	20	−10	−0.5	690	576	1.19
28	150	100	4	3135	20	0	0	562	522	1.07
29	150	100	4	3135	20	10	0.5	501	515	0.97
30	150	100	4	3135	20	20	1.0	460	453	1.01
31	150	100	4	3135	50	−25	−0.5	502	431	1.16
32	150	100	4	3135	50	0	0	430	403	1.06
33	150	100	4	3135	50	25	0.5	287	335	0.85
34	150	100	4	3135	50	50	1	309	308	1.00
35	150	100	5	2135	20	−10	−0.5	104	962	1.08
36	150	100	5	2135	20	0	0	106	959	1.11
37	150	100	5	2135	20	10	0.5	981	888	1.10
38	150	100	5	2135	20	20	1.0	935	838	1.11
39	150	100	5	2135	50	25	0.5	526	515	1.02
40	150	100	5	2135	50	50	1.0	528	475	1.11
41	150	100	5	2135	50	50	1	458	475	0.96
44	150	100	5	3135	20	−10	−0.5	692	673	1.02
43	150	100	5	3135	20	0	0	690	615	1.12
44	150	100	5	3135	20	10	0.5	622	593	1.04
45	150	100	5	3135	20	20	1.0	573	581	0.98
46	150	100	5	3135	50	−25	−0.5	548	499	1.09
47	150	100	5	3135	50	0	0	456	485	0.93
48	150	100	5	3135	50	25	0.5	328	404	0.81
49	150	100	5	3135	50	50	1.0	381	359	1.06
									Avg.	1.04

the flexural stiffness E·I must dependent not only on the material and geometry but also on the eccentricity and the slenderness.

5 CONCLUSIONS

The paper describes forty-nine experimental tests conducted on rectangular and square tubular columns filled with high strength concrete subjected to axial load and a non-constant bending moment distribution.

The following conclusions can be summarized:

– For a given length, when the eccentricity at the bottom (minimum) is decreased (from r = 1.0 to r = −0.5), therefore producing variable curvature, the maximum load is increased (and the midspan lateral displacement reduced) since the second order bending moment is reduced. It is interesting

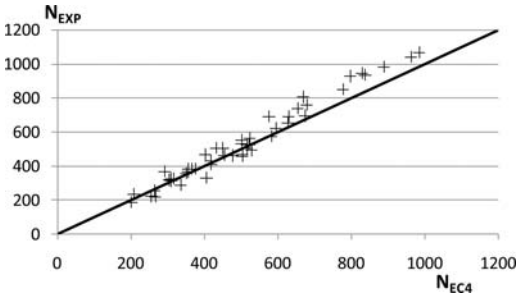

Figure 4. Predicted load of Eurocode 4 versus experimental load.

to observe that ductile post-peak behavior is achieved for all cases, but is always slightly reduced for cases with lower length in comparison with higher length, that is, the slope of the descending branch is more pronounced for lower slenderness. Moreover, the cases with $r = -0.5$ differ from those with $r = 1.0$ in the descending branch. The slope is more gradual for cases with constant curvature than for those with variable curvature.

- For longer elements, the problem is clearly governed by the second order effects and the variable bending moment has a higher effect for lower slenderness.
- It is interesting to observe that the behavior in terms of the length is different for constant and variable curvature. While for $r = 1$ the maximum displacement is achieved for $L = 4135$ mm and the lower one for $L = 2135$ mm, for $r = -0.5$ the maximum displacement is achieved for $L = 3135$ mm and the lower one for $L = 4135$ mm, which was initially surprising. But it can be inferred that for the case of $L = 4$ meters with $r = -0.5$ the second order effects are lower and the first order curvature (double), which depends on the length, is higher in comparison with $r = 1.0$. This results in the element attempting to bend in the negative direction drastically reducing the lateral deflection.
- Second order effects depend not only on the slenderness but also on the eccentricity and the first order bending moment, which agrees with the proposal by other authors (Tikka and Mirza 2006) to combine all the effects together inside the definition of the stiffness E·I, making this dependent not only on the materials and the section, but also on the slenderness and the eccentricity.
- The experimental ultimate load of each test was compared with the design loads from Eurocode 4, presenting an average error close to 5%. The results show for the limited cases tested that this code is applicable to high strength concrete.
- However there are particular cases which present excessive unsafe errors. It corresponds to the cases where the second order effects are more important and are due to an overestimation of the flexural stiffness EI. This result indicates that the equation of the flexural stiffness of the section E·I in combination with the equivalent moment factors (β) need correction.

ACKNOWLEDGEMENTS

The authors wish to express their gratitude to the Spanish Ministry of Science and Innovation for help provided through project BIA2009_9411, to the Spanish Ministry of Education through BIA2005-255, and the European Union for FEDER Funds.

REFERENCES

Bonet, J.L., Miguel, P.F., Fernandez, M.A., Romero, M.L. 2004, Biaxial bending moment magnifier method, Engineering Structures, 26(13): 2007–19.

Bridge, R. Q. 1976, Concrete Filled Steel Tubular Columns, Report No. R283, School of Civil Engineering, University of Sydney, Sydney, Australia.

European Committee of Standardization (CEN). 2004. Eurocode 4: Design of composite steel and concrete structures Part 1-1: General rules and rules for buildings", EN 1994-1-1:2004, Brussels.

Goode, C.D. 2008, Composite columns-1819 tests on concrete filled tube columns compared with Eurocode 4, The Structural Engineer, 86(16): 33-38.

Gourley, B. C., Tort, C., Denavit, M. D., Schiller, P. H., and Hajjar, J. F. 2008. A Synopsis of Studies of the Monotonic and Cyclic Behavior of Concrete-Filled Steel Tube Beam-Columns", Report No. UILU-ENG-2008-1802, Newmark Structural Laboratory Report Series (ISSN 1940-9826), Department of Civil and Environmental Engineering, University of Illinois at Urbana-Champaign, Urbana, Illinois.

Han, L.H., Yao, G.H. 2003, Influence of concrete compaction on the strength of concrete-filled steel RHS columns, Journal of Construction Steel Research, 59(6): 751–67.

Han, L.H, Yao,G.H. 2004, Experimental behaviour of thin-walled hollow structural steel (HSS) columns filled with self-consolidating concrete (SCC), Thin-Walled Structures 42: 1357–1377.

Han, L.H. 2000, Tests on concrete filled steel tubular columns with high slenderness ratio, Advances in Structural Engineering, 3(4): 337–344.

Hernández-Figueirido, D., Romero, M.L., Bonet, J.L., Montalvá, J.M. 2012, Ultimate capacity of rectangular concrete-filled steel tubular columns under unequal load eccentricities", Journal of constructional steel research, 68(1): 107–117.

Johansson, M., Gylltoft, K. 2001, Structural behaviour of slender circular steel-concrete composite columns under various means of load application, Steel and Composite Structures, 1(4): 393–410.

Kilpatrick, A.E., Rangan, B.V. 1999, Tests on High-Strength Concrete-Filled Steel Tubular Columns, ACI Structural journal, 96 (2): 268–275.

Kim, D.K. 2005, A database for composite columns, Ms Thesis. Georgia Tech University. U.S.A.

Knowles, R. B., Park, R. 1969, Strength of Concrete Filled Steel Tubular Columns, Journal of the Structural Division, ASCE, 95(12): 2565–2587.

Lee, S.J. 2007, Capacity and the moment-curvature relationship of high-strength concrete filled steel tube columns under eccentric loads, Steel and Composite Structures, 7(2), 135–160.

Perea, T. 2010. Analytical and experimental study on slender concrete-filled steel tube columns and beam-columns. Ph.D. thesis, Georgia Institute of Technology, Georgia, GA.

Portoles, J.M., Romero, M.L., Bonet, J.L., Filippou, F.C. 2011, Experimental study of high strength concrete-filled circular tubular columns under eccentric loading, Journal of constructional steel research, 67(4): 623–633

Shams, M., Saadeghvaziri, M.A. 1997, State of the art of concrete-filled steel tubular columns, ACI Structural Journal, 94 (5): 558–571.

Shanmugam, N.E., Lakshmi, B. 2001, State of the art report on steel-concrete composite columns, Journal of constructional steel research, 57 (10): 1041–1080.

Tikka, T.K., Mirza, S.A. 2006, Nonlinear equation for flexural stiffness of slender composite columns in major axis bending, Journal of structural engineering, 132 (3): 387–399.

Wang, Y.C. 1999, Tests on slender composite columns, Journal of constructional steel research, 49(1): 25–41.

Yu, Q., Tao, Z., Wu, Y.X. 2008, Experimental behaviour of high performance concrete-filled steel tubular columns, Thin-Walled Struct, 46: 362–370.

Zeghiche, J. and Chaoui, K. 2005. An experimental behaviour of concrete-filled steel tubular columns, Journal of constructional steel research, 61(1): 53–66.

Zhang, S., Guo, L. 2007, Behaviour of High Strength Concrete-Filled Slender RHS Steel Tubes, Advances in Structural Engineering, 10(4): 337–351.

Zhao, X.L., Han, L.H. and Lu, H. 2010. Concrete-filled tubular members. 1st Ed. Oxon: Spon Press.

Tubular Structures XIV – Gardner (Ed.)
© 2012 Taylor & Francis Group, London, ISBN 978-0-415-62137-3

Static behavior of T-shaped concrete-filled steel tubular columns subjected to eccentric compressive loads

H. Yang & S.M. Zhang
Harbin Institute of Technology, Harbin, China

Y.L. Yang
Key Laboratory of Mechanics on Disaster and Environment in Western China Ministry of Education, Lanzhou, China; Lanzhou University, Lanzhou, China

ABSTRACT: Special-shaped column frame structures improve residential architectural space, by eliminating the exposure of column corners to indoor space. Due to improvement in constraint effect for concrete, special-shaped Concrete-Filled Steel Tubular (CFST) columns are expected to have advantages in mechanical behavior. In the meanwhile, steel plates' premature local buckling and concave corner's separation between steel tube and concrete should be given more attention. The tensile bar stiffener, welded on inside tube surfaces, was introduced in this paper. Experimental study of 4 T-shaped columns subjected to eccentric compressive loads was carried out. Parametric impact analysis was emphasized on the constraint effect, the eccentricity and the specimen type. Failure modes and static mechanical properties were investigated. Experimental results showed that: the tensile bar stiffener effectively restrains the deformation at welds of steel plates and concave corners; the CFST specimens are provided with better comprehensive mechanical performance, especially for the stiffened CFST specimens.

1 INTRODUCTION

Columns in traditional frame structures, with corners extended into indoor space, normally have larger cross-sectional depths than those of adjacent infilled walls, leading to the reduction of usable utilization area and disturbance to indoor environment (Figure 1). Recently, special-shaped columns, as an improved architectural approach, have been increasingly introduced into residential and commercial buildings. Smooth jointing of special-shaped columns and adjacent infilled walls guarantees the efficiency of indoor space and useability of corner locations (Figure 2).

Systematic research and extensive engineering practice is mainly on the RC special-shaped column. Early studies focused on the static behavior of T-shaped and L-shaped stubs, subjected to axial compressive load and biaxial eccentric compressive load, based on which, resistance interaction curves for practice were proposedby Joaquin (1979), Cheng & Hsu (1989), Mallikarjuna & Mahadevappa (1992), Dundar & Sahin (1993) and Yau (1993). Since 2000, with the development of housing industry in China, further study carried out extensively by Chinese researchers, such as Zhang & Ye (2003), Cao (2005) and Wang & Shen (2006), has concentrated on the comprehensive static and seismic behavior, especially for members in structural systems, directly for engineering applications.

The irregularity in cross section of special-shaped column brings about disadvantages in mechanical behavior, and leads to limitations in its seismic

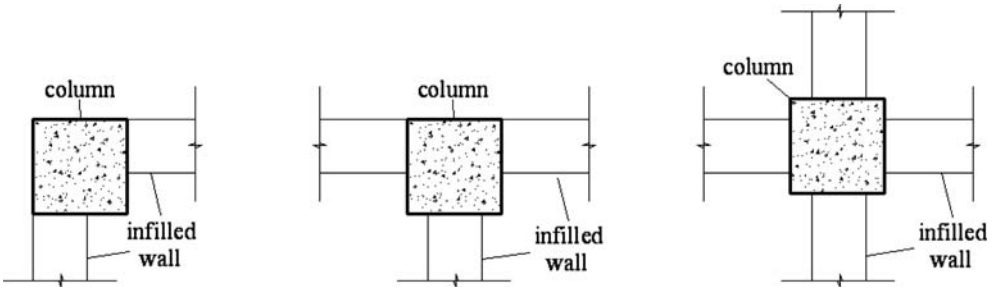

Figure 1. Joints in frame structure with rectangular columns.

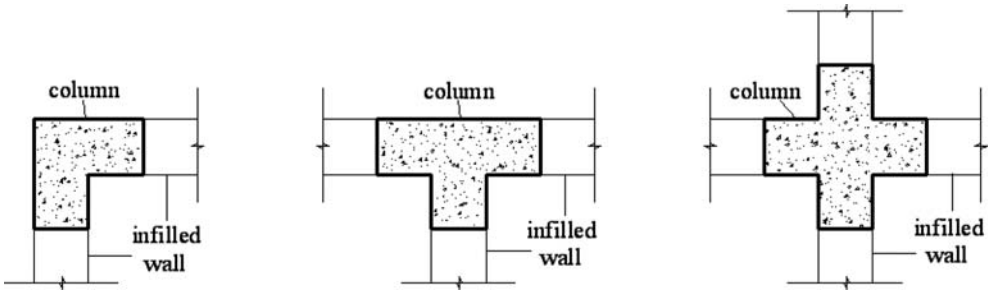

Figure 2. Joints in frame structure with special-shaped columns.

performance: only apply to 8-degree seismic fortification zone (0.2 g) or below, and subjected to rigorous applicable maximum building height restrictions, compared with that of rectangular columns. These limitations are based on the China National code – Technical specification for concrete structures with specially shaped columns (JGJ 149-2006/JGJ 514-2006), which focuses on the special-shaped columns.

Scholars in China have engaged in research and promotion of special-shaped composite columns to improve their seismic behavior, e.g. CFST and steel reinforced concrete (SRC) columns. Research on special-shaped CFST columns have focused on postponing the buckling of steel tubes and the constraint effect for concrete, therefore stiffeners were employed in the special-shaped tube. Pulled binding bars by Cai & He (2008) and ribs by Chen (2003) were adopted in axially loaded test research on T-shaped, L-shaped CFST stubs; bar stiffeners researched by Wang et al. (2009) and Yang et al. (2010) were introduced in static and pseudo static experiments, and preliminary achievements were made. The research mentioned above, nevertheless, is inadequate for engineering application and complementary systematic research should be carried out.

An experiment on T-shaped CFST columns subjected to eccentric compressive load was carried out in this paper. Tensile bar stiffeners were introduced in CFST specimens to postpone the tubes' buckling. Failure modes and static behavior of the specimens were investigated, and mechanical behavior of specimens was properly evaluated.

2 EXPERIMENTAL STUDY

2.1 *Details of specimens*

An experiment on T-shaped columns subjected to eccentric compressive load was carried out. Specimens, basic information of which is summarized in Table 1, consist of 4 eccentrically loaded specimens. Except for specimen type, the eccentricity parameter, deviating toward the web, was investigated. Restricted by loading device and measuring apparatus, specimens were designed with similarity ratio of 1:2, with the length of specimens being 1500 mm. The cross sectional dimensions and constituents are demonstrated in Figure 3.

Table 1. Parameters of specimens.

Specimen	Specimen type	Eccentricity (mm)
TEC	Reinforced concrete	50
TES	Concrete-filled steel tube	50
TESS-1	Stiffened concrete-filled steel tube	25
TESS-2	Stiffened concrete-filled steel tube	50

To postpone or restrain local buckling of T-shaped tubes, tensile bars as stiffeners were welded on the internal tube surfaces and concave corners, with longitudinal weld spacing of 100 mm and with cross sectional distribution shown in Figure 3c. The tensile bar employs straight hot-rolled plane bars. Holes, on the tube, with diameters slightly larger than those of the stiffeners, were drilled and reserved for the stiffeners to pass through and to be welded at both ends.

2.2 *Material properties*

According to the Chinese National standard – Metallic materials-tensile testing at ambient temperature (GB/T228-2002), mechanical properties of the steel plate and reinforcement bar were tested, and their material properties are collected in Table 2 and Table 3.

2.3 *Experimental devices and measuring apparatus*

The experiment was carried out at the Structural and Seismic Test Research Center, Harbin Institute of Technology. A 500t computerised OSD hydraulic pressure press was used as the loading device, with two articulated rigid loading pads at the top and bottom, in which the bottom pad lifted the specimen and the top kept motionless.

In the eccentrically loaded specimen experiment, a knife-edge articulation system was sandwiched between the loading pad and specimen, to simulate articulated boundary conditions. The knife-edge articulation system consists of two close engaged parts: one rigid steel plate with a centered triangular convex

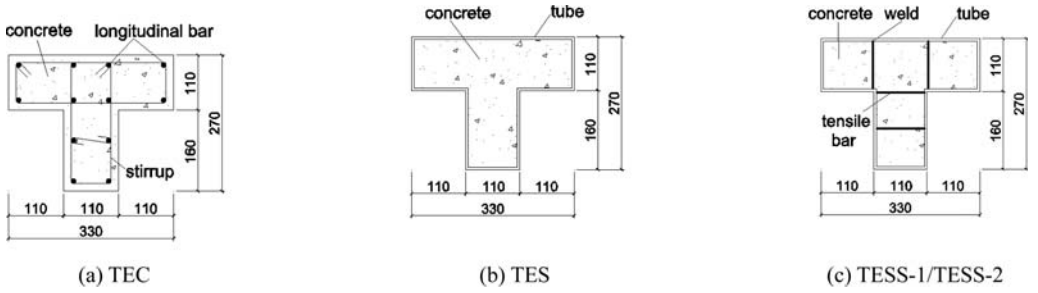

Figure 3. Cross-sectional dimensions of specimens.

Table 2. Material mechanical properties of RC specimens.

Specimen	Longitudinal bar		Stirrup		Concrete
	Yielding strength (N/mm^2)	Diameter (mm)	Yielding strength (N/mm^2)	Diameter (mm)	Prismatic compressive strength (N/mm^2)
TEC	353	12.1	373	6.5	37.5

Table 3. Material mechanical properties of CFST specimens.

Specimen	Steel tube		Stiffener		Concrete
	Yielding strength (N/mm^2)	Thickness (mm)	Yielding strength (N/mm^2)	Diameter (mm)	Prismatic compressive strength (N/mm^2)
TES	315	3.49	—	—	37.5
TESS-1/2	315	3.49	304	8.0	37.5

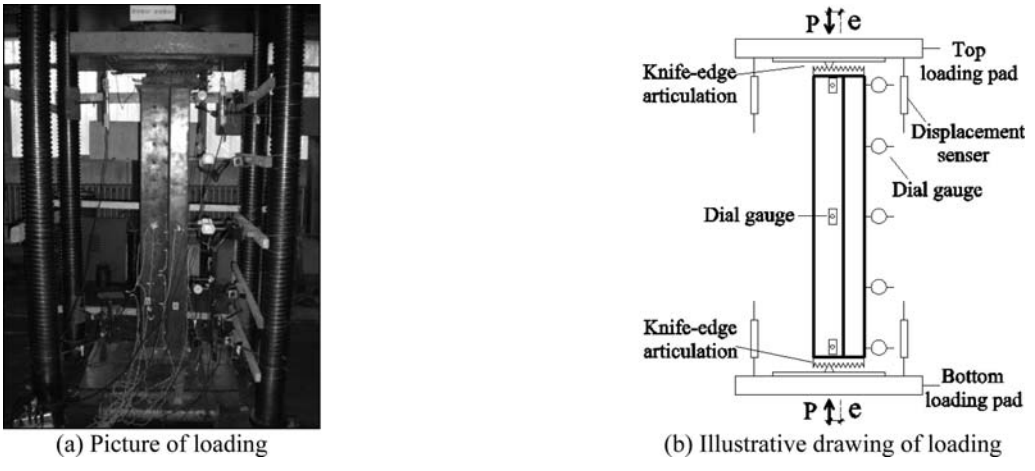

Figure 4. Loading devises and measuring apparatus in eccentric compressive test.

fixed on the loading pad and another rigid steel plate with saw-tooth triangular concaves fixed on the specimen. The magnitude of eccentricity is adjusted with different engaged location of triangular convex on the saw-tooth triangular concaves (shown in Figure 4).

The actual load was real-time monitored on the pressure press and recorded every loading step. Displacement sensors were arranged to measure vertical displacement (shown in Figure 4). Five dial gauges were arranged in a deforming plane, quartering the

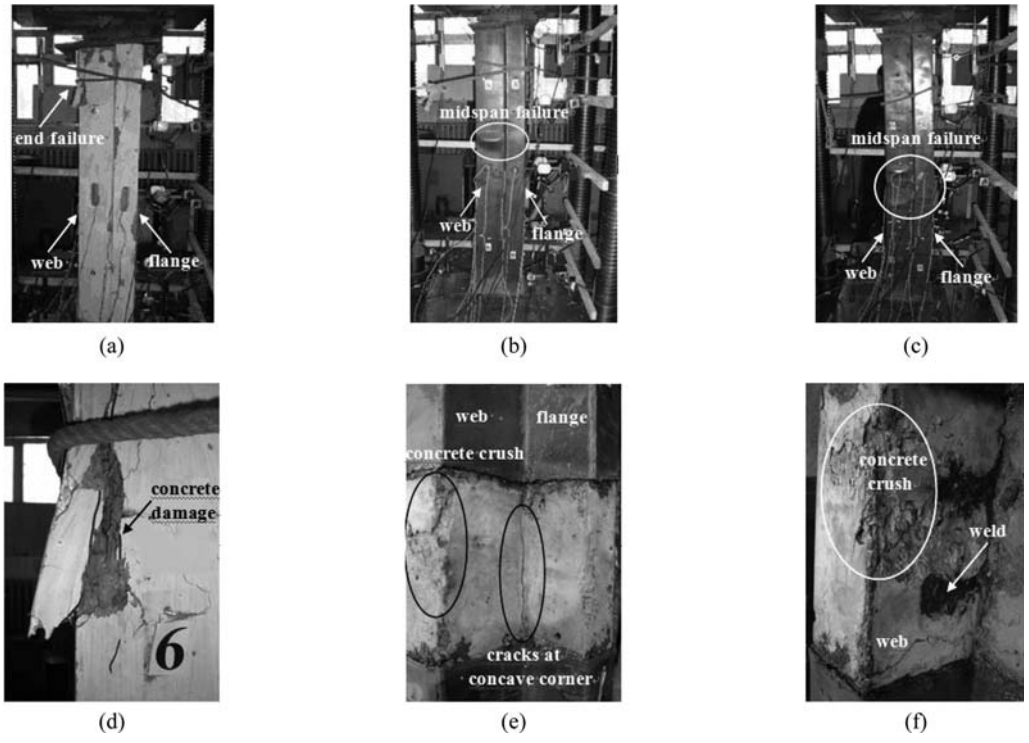

Figure 5. Experimental phenomenon.

specimen length, to measure its lateral displacement at different heights. Three dial gauges were arranged perpendicular to the deforming plane, to verify whether the specimen deformed uniaxially (shown in Figure 4).

2.4 *Test phenomenon*

For the eccentrically loaded CFST specimens, failure regions were mainly located in the mid-span of specimens, where the curvature of deformed axis was larger than any other region, due to articulated boundary conditions.

Depending on the off-center direction of vertical load and boundary conditions, the failure mode of steel tube in CFST specimens is embodied by steel plate buckling near the mid-span of specimens. The steel plates, far away from section center or with large width-to-thickness ratio in compressive web region, buckled at ascending stage and developed severely during descending stage (Figure 5b, c).

In the RC specimen TEC, the web is crushed more severely than the flange. Diagonal cracks occurred in the web, and propagated to the web margin and the concave corner, resulting in concrete spallation in the web margin and vertical cracks in concave corners (in Figure 5a, d).

Compared with RC specimen TEC, the concrete failure mode is alleviated and the confinement provided by tube was relatively large in specimen TES, but the interaction between steel tube and core concrete is still insufficient. Only slightly damaged concrete located in compressive region and superficial cracks in concave corner revealed that the concrete compressive strength was inadequately utilized, especially after steel tube's premature local buckling. By removing the steel tube, it was observed that crushed concrete expansion failed to overcome tubular out-of-plane deformation, resulting in separation between concrete and tube at buckle positions and even at concave corners. The separation resulted in two materials working individually and no complete exploration of material strength can be reached (Figure 5b, e).

For stiffened specimens TESS-1 and TESS-2, concrete was damaged in local crushed mode more seriously than that in non-stiffened specimen TES, i.e. no obvious diagonal cracks but large-area serious cracks. The crushed concrete was located between two adjacent stiffener welds, while concrete near welds showed less damage, which indicates that stiffeners restrain the neighboring steel tube to provide more confinement for concrete. There was rarely separation between concrete and tube and their good interaction improved the exploration of material strength (Figure 5c, f).

3 ANALYSIS OF EXPERIMENTAL RESULTS

There are three points featuring mechanical properties on load-displacement relationship curves. The three points are respectively the yielding point (Uy, Py), the

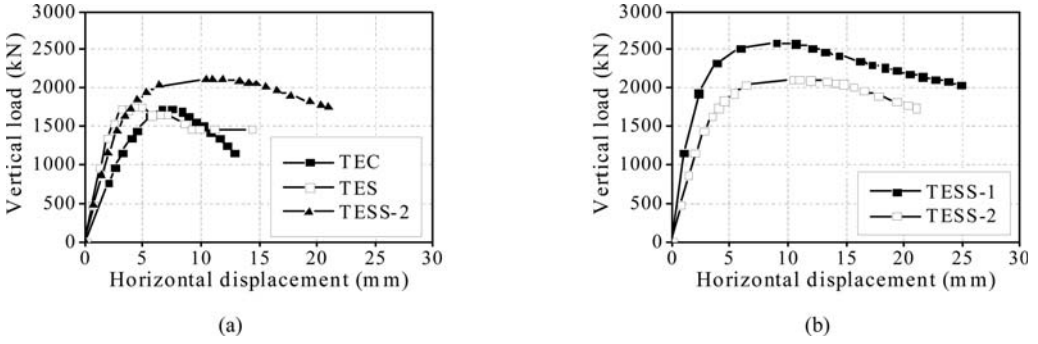

Figure 6. Comparison of vertical load-horizontal displacement curves of specimens.

Table 4. Test results.

Specimen	Yielding displacement (mm)	Yielding resistance (kN)	Peak resistance (kN)	Resistance enhancement	Ultimate displacement (mm)	Ductility factor	Ductility enhancement
TEC	5.34	1603	1740	1.00	10.40	1.95	1.00
TES	2.86	1660	1739	1.00	9.12	3.10	1.59
TESS-1	3.04	2188	2597	1.49	20.01	6.59	3.38
TESS-2	4.39	1818	2120	1.22	19.59	4.46	2.29

peak point (Up, Pp) and the ultimate point (Uu, Pu). The ultimate point is the point with 85% of peak resistance during descending stage. Nominal resistance Pn is the superposition resistance of concrete and steel based on their strengths. Ductility factor μ is defined as the ratio of the ultimate displacement Uu to yielding displacement Uy.

Combining the experimental phenomenon with the mechanical properties, the mechanical behavior of specimens subjected to eccentric load was investigated and analyzed in the Figure 6 and Table 4.

The behavior comparison of specimens with the same eccentricity is presented as below. The stiffened CFST specimen TESS-2, due to its greater confinement for concrete, was provided with an enhancement over the RC specimen TE1: 13% increase in the yielding resistance, 22% increase in the peak resistance and 129% increase in ductility factor.

By arranging stiffeners in T-shaped tube, the confinement and static behavior under eccentric compressive load of specimen TESS-2 is substantially enhanced, compared with that of TES. Figures in Table 4 show the enhancement in peak resistance (22%) and ductility factor (44%), which attributes to the outstanding mechanical efficiency of tensile bar stiffeners.

For stiffened CFST specimens (TESS-1 and TESS-2), with the eccentricity decreasing, the TESS-1 has an increase over TESS-2 in yielding resistance (20%), peak resistance (23%) and ductility factor (48%). Eccentricity's impact can be explained with sectional stress distribution. Due to second-order effect, with the eccentricity increasing, the mid-span sectional stress distribution was transformed from total compression to partial compression and tension, which reduces the elastic stiffness, elastic-plastic stiffness, peak resistance and ductility.

4 CONCLUSIONS

1. The T-shaped CFST specimens are provided with higher resistance and better ductility, compared with that of T-shaped RC specimen.
2. The tensile bar stiffener proposed in this paper can postpone steel tube's buckling and enhance confinement for concrete.

ACKNOWLEDGEMENTS

The project is supported by the Fundamental Research Funds for the Central Universities (Grant No. HIT. NSRIF.2010015), the Project-sponsored by SRF for ROCS, SEM., and the Fundamental Research Funds for the Central Universities "Research on Static Behavior of L-shaped Concrete-filled Steel Tubular Columns" (Grant No. lzujbky-2012-21), which are gratefully acknowledged.

REFERENCES

Joaquin M. 1979. Design Aids for L-shaped Reinforced Concrete Columns. *ACI Structural Journal*:1197–1216.

Cheng T. & Thomas H. 1985. Biaxially Loaded L-shaped Reinforded Concrete Columns. *Journal of Structural Engineering* 111(12):2576–2595.

Mallikarjuna & Mahadevappa P. 1992. Computer Aided Analysis of Reinforced Concrete Columns Subjected to Axial Compression and Bending-I L-shaped Sections. *Computer & Structures* 44(5):1121–1138.

Dundar C. & Sahin B. 1993. Arbitrarily Shaped Reinforced Concrete Members Subjected to Biaxial Bending and Axial Load. *Computer & Structures* 49(4):643–662.

Yau C. Y. & Chan S. L. & So A. K. W. 1993. Biaxial Bending Design of Arbitrarily Shaped Reinforced Concrete Column. *ACI Structural Journal* 90(3):269–278.

Zhang D. & Ye X. G. 2003. Nonlinear Analysis of Special-shaped Reinforced Concrete Columns. *Journal of Hefei Univercity of Technology* 26(4):490–494.

Chen Z. Y. 2003. Research on construction techniques of concrete-filled rectangular steel tube columns and axial bearing capacity of concrete-filled special-shaped steel tube stub. *Dissertation for the Master Degree in Engineering, Tongji University*. Shanghai

Cao W. L. & Huang X. M. & Song W. Y. 2005. Experiment and Non-linear Element Analyses of Seismic Behavior of Short Specially Shaped Columns with Crossed Reinforcing Bars. *Journal of Building Structures* 26(3):30–37.

Wang H. B. & Shen P. S. 2006. Nonlinear Analysis of L-Shaped Column Subjected Cyclic Loads. *Chinese Quarterly of Mechanics* 27(1):124–129.

Cai J. & Sun G. 2008. Experimental Investigation on L-shaped Concrete-filled Steel Tube Stub Columns with Binding Bars under Axial Load. *China Civil Engineering Journal* 41(9):14–20.

Wang Y. Y. & Yang Y. L. & Zhang S. M. 2009. Seismic Behaviors of Concrete-filled T-shaped Steel Tube Columns. *Key Engineering Materials* 400–402: 667–683.

Yang Y. L. & Yang H. & Zhang S. M. 2010. Compressive Behaviour of T-shaped Concrete Filled Steel Tubular Columns. *International Journal of Steel Structures* 10(4): 419–430.

Tubular Structures XIV – Gardner (Ed.)
© 2012 Taylor & Francis Group, London, ISBN 978-0-415-62137-3

Time effects on the static response of concrete filled steel tubular arch bridges

Y. Geng, X.R. Wu & Y.Y. Wang
School of Civil Engineering, Harbin Institute of Technology, Harbin, China

G. Ranzi
School of Civil Engineering, The University of Sydney, Sydney, Australia

ABSTRACT: This paper presents a finite element model implemented in ABAQUS to investiagte the long-term behaviour of CFST arch bridges and to highlight the influence of time effects on the overall structural response considering the construction sequence and geometric nonlinearities. The numerical results presented in the paper are based on a particular case study which consists of the Dong-Guan Waterway bridge. The ability of the proposed approach to predict the long-term response of CFST arch bridges has been validated against site measurements recorded during construction. It has been observed that the time-dependent behaviour of the concrete has a significant effect on displacements, stress distributions, and bending moment diagrams of CFST arches during construction and in service, while highlighting the importance of accounting for the actual times of loading when inserting applied actions in the analyses and for the presence the live loads.

1 GENERAL INSTRUCTIONS

Concrete-filled steel tubular (CFST) arch bridges have been gaining popularity because of their high compressive strength as well as efficiency in construction. Since 1990, there have been more than 300 CFST arch bridges built in China, among which more than 85 have a span longer than 150 m. The world longest one is the He Jiang bridge with a span of 529 m. With the current trend towards longer and slender bridges there is a need to ensure that the time-dependent behaviour does not compromise the design of these structural systems and its influence on the overall response needs to be evaluated.

Extensive research has been carried out to date to study the long-term response of CFST arch bridges. Numerical studies have been performed to evaluate the long-term behaviour of arch bridges, e.g. (Wang et al. 2007; Shao et al. 2010). Zhang (2007) developed a finite element model in ANSYS to predict the long-term response of a CFST arch bridge with considerations on possible loading histories undergone by the core concrete. In his analysis, the bending moment on the arches was assumed to have no contribution on the long-term response. Very recently, Pi et al. (2011) and Bradford et al. (2011) proposed a theoretical formulation to predict the occurrence of creep buckling in CFST arches at service conditions. In particular, these studies focussed on the in-plane behaviour and buckling of shallow/deep CFST circular arches. All these studies concluded that time effects have a significant influence on displacements and stress distributions in CFST arch bridges.

This paper presents the results of a numerical model implemented in ABAQUS to describe the long-term behaviour of CFST arch bridges, using the Dong-Guan Waterway bridge (Figure 1) as a case study, and to highlight the influence of time effects on the

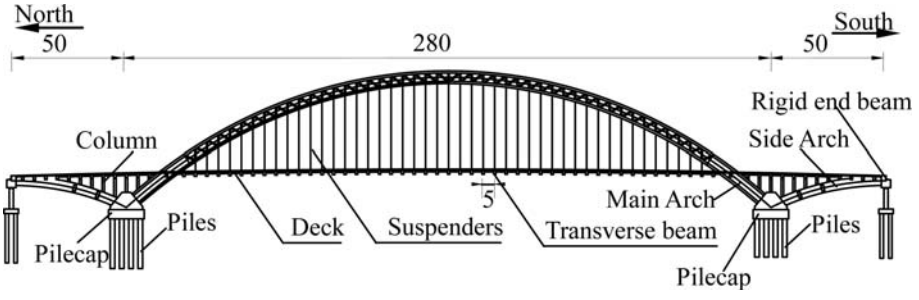

Figure 1. Elevation view for Dong-Guan Waterway Bridge (Unit: m).

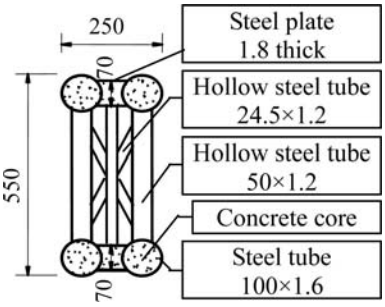

Figure 2. Cross-section of main arch (Unit: cm).

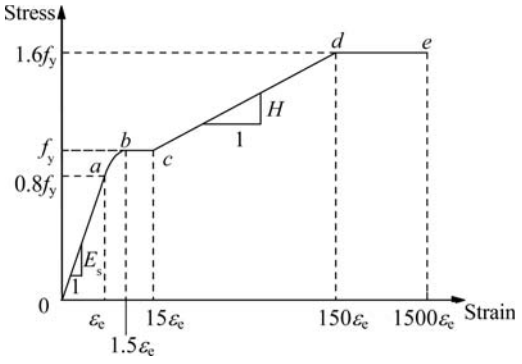

Figure 3. Stress-strain curve for steel under uniaxial stress.

overall structural response considering the construction sequence and geometric nonlinearity. The time-dependent behaviour of the concrete is modelled by means of EC2 (BSI 2004) which is implemented in ABAQUS by means of the UMAT subroutine. The accuracy of the proposed approach is validated against site measurements recorded during the construction of the bridge. A parametric study is then presented to highlight the importance of accounting for the construction sequence and including live loads in the analysis when determining the long-term response of CFST arch bridges.

2 DESCRIPTION OF THE STUDY CASE

The Dong-Guan Waterway Bridge is a half-through CFST arch bridge with main span length of 280 m (Figure 1). The distance between the two arch ribs is 19.5 m. The catenary main arch ribs have the rise over span ratio of 1/5. Thirteen wind braces, i.e. one I-type wind brace at the arch crown and twelve K-type ones located symmetrically with respect to the arch crown, are placed between the arch ribs to ensure the lateral stability of the bridge during construction and service life.

The cross-section of the main arch is illustrated in Figure 2. The top and bottom chords consist of two horizontal dumbbell-shaped CFST members while the truss webs are formed with diagonal and vertical hollow steel tubes.

The yield strength of the steel specified for arch ribs and wind braces is 345 MPa and the encased core concrete has a cylinder characteristic compressive strength (f_{ck}) of 40 MPa. The remaining parts of the bridge are constructed with reinforced concrete.

Flexible ties pass through the springings of the main arch and are anchored to the rigid end beams. These ties are particularly useful during construction to control the displacement of the arch springing.

The arches are supported by bored reinforced concrete piles (Figure 1) embedded in the slightly weathered mudstone. The rigid cast-in-situ end beams at the crown of the side arches are supported by pot rubber bearings.

3 FINITE ELEMENT MODELING

3.1 *Basic assumptions*

A finite element model is developed in ABAQUS to describe the long-term behaviour of CFST arch bridge and is applied in the following for the analysis of the Dong-Guan Waterway Bridge. The numericla model is based on full shear interaction theory with perfect bond between the concrete and steel components. Plane sections remain plane before and after loading (i.e., linear strain distribution).

3.2 *Material properties*

The time-dependent behaviour of the concrete is represented based on the EC2 model (BSI 2004) and included in the analysis based on the step-by-step procedure. The latter has been implemented in ABAQUS using the UMAT subroutine. The time-dependent behaviour of the concrete is assumed to be identical in both compression and tension, usually acceptable for stress levels less than about one half of the strength of the concrete, as recommended in Gilbert & Ranzi (2011). In this study, the stress levels in the arch ribs at service conditions are sufficiently low to remain within the framework of linear creep. No cracking can occur in the core concrete and creep due to shear stresses is ignored. The sealed conditions of the core concrete have been included in the concrete model specifying a nil value for the exposed perimeter. For the nonlinear behaviour of the concrete it is assumed that it carries no tensile stresses. For this purpose, the nonlinear constitutive equations proposed by Han (2007) are adopted on the analysis. Possible confinement effects are considered at a particular cross-section when compressive stresses become greater than 55% of the compressive strength.

The steel response is described by the five-phase stress-strain curve shown in Figure 3 (Han 2007). The material coefficients are based on (Zhong 1994).

3.3 *Structural modelling*

All members of the main arch ribs are represented using Timoshenko beam elements B31 available in ABAQUS, except for the hollow steel tubular webs which are modelled by means of truss elements T3D2. B31 is also adopted to simulate the side arches, the columns supporting the transverse beams at the side arches, the transverse and longitudinal beams, and the piles. The ties and the suspenders are described with truss elements T3D2 while enabling the element to carry only tensile forces. Changes in the axial forces induced in the ties during the construction are implemented by varying the air temperature at each construction step. The deck slabs are built with 4-node shell elements S4.

The 'Model Change' technique is adopted to simulate the variation of the stiffness for arch ribs during the construction. The analysis work carried out by Geng et al. (2010) has shown that the assembling process of the hollow steel arch ribs does not significantly affect the stress and the profile of arch ribs at the completion of construction. Because of this, the construction process considered in the following starts at the closure of the hollow steel tubular arches. In particular, the measurement used as benchmark are related to this time, i.e. closure of the arch, before the loosening of the tiebacks. To model the segmental construction procedure for the pumping of the core concrete in arches, the concrete core and the steel tubes are built separately. The various components of the cross-sections have been connected by means of rigid bars to ensure plane sections remain plane.

Different mesh sizes have been investigated to identify a reasonable mesh that provides accurate results while minimising computational time. Based on this the main arch has been discretised into 56 elements.

The piles are fixed at their bottom ends. During the construction, the soil restrains the lateral deformation of the piles. Such interaction is implemented using the spring element SPRING1, whose positions and stiffness are determined according to the Chinese Code (JTG D63 2007). The simulation of the piles and the restraint effect of the soil to the piles provides an acceptable representation the real situation. The predicted horizontal displacement of the arch springings is $-2\sim +4$ mm during the construction which matches well with the site monitored results of $-2\sim +5$ mm for the arch springings on the upstream side and $-2\sim +3$ mm for those on the downstream side.

The whole bridge model is presented in Figure 4.

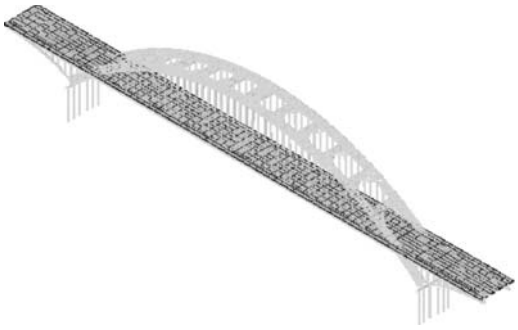

Figure 4. Finite element model for the bridge.

4 VALIDATION OF THE NUMERICAL MODEL

4.1 *Site monitoring*

Extensive site monitoring has been carried out on the Dong-Guan Waterway Bridge. The displacement of the main arch has been monitored using a TCA1800 Total Station. In order to provide an adequate representation of the displacement of the arches, one monitor point was selected for each segment of the steel arch, with a total of 11 monitor points as depicted in Figure 5 (a). The stresses in the steel tubes have been measured with vibrating-wire strain gauges arranged at each cross-section as shown in Figure 5(b).

The stretching forces of the ties have been measured with feed-through sensors. The prestressing forces in the ties are specified in the model based on the measured results.

4.2 *Numerical validation*

The accuracy of the proposed finite element model is validated against the displacements and stresses measured on the arch ribs during construction. Analyses with and without geometric nonlinearities are carried out to study the service behaviour of CFST arch bridges.

Figures 6 and 7 outline typical comparisons between numerical and measured values. Positive (negative) stresses are tensile (compressive), while positive (negative) displacements depict upward (downward) movements. All numerical results are determined at the same location of the arch where the measurements were taken. The reference arch profile for the displacement measurements, i.e. the profile for which the displacements are considered to be zero, is the one possessed by the arch before the tiebacks were loosened. It can be observed that the predicted results match well with the monitored results with maximum deviations of 10.6% and 8.8% for the displacements and stresses, respectively.

During the construction of CFST arch bridges, the time-dependent behaviour of the core concrete significantly influences the static response of the structure. At the end of the construction, the displacement at the arch crown is increased by 21.9% of the instantaneous value, and the maximum increase of the stress in steel tubes is 22.6%.

Geometric nonlinearities have a limited influence on the static response of the CFST arch bridges at service conditions as shown in Figures 6 and 7. Maximum differences between the displacements calculated at the arch crown with and without geometric nonlinearities are 2.8%. Similar differences have been observed

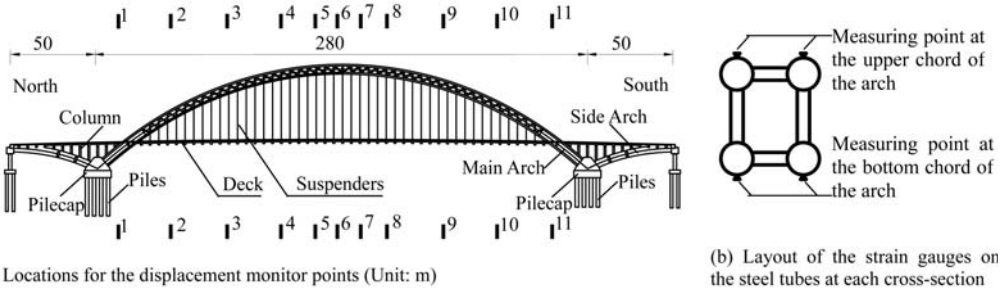

(a) Locations for the displacement monitor points (Unit: m)

(b) Layout of the strain gauges on the steel tubes at each cross-section

Figure 5. Site monitoring system layout.

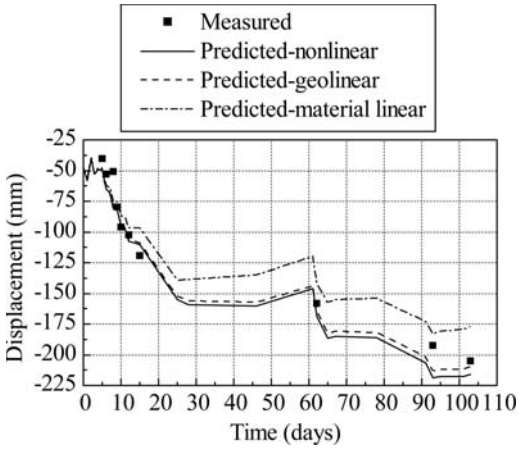

Figure 6. Comparison between numerical and measured values for the displacements at arch crown during construction.

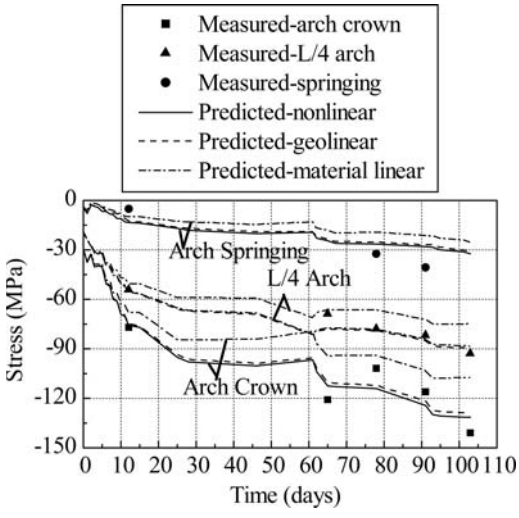

Figure 7. Comparison between numerical and measured values for the stresses in the steel tube of the upper chords during construction.

for the in the upper and lower chords, i.e. in the order of 2.2% and 3.7%, respectively.

5 TIME-DEPENDENT RESPONSE OF CFST ARCH BRIDGES AT SERVICE CONDITIONS

5.1 *Loading condition*

With the consideration of the construction process and the ageing of the concrete, the analysis is performed to investigate how time effects influence the static response of CFST arch bridges at service conditions for their service life (100 years). This is carried out using the Dong-Guan Waterway Bridge as a study case. In the analysis, the bridge is subjected to the long-term load combination specified by Equation 1 (JTG D62-2004), with the live loading applied as the quasi-permanent distributed loads on the whole bridge deck.

$$S_{ld} = S_{Gk} + \sum_{j=1}^{n} \phi_{2j} S_{Qjk} \quad (1)$$

where S_{ld} represents the long-term load combination; S_{Gk} denotes the characteristic dead loads; $\phi_{2j}S_{Qjk}$ depicts the quasi-permanent value for the jth live load; ϕ_{2j} is the quasi-permanent coefficient for the jth live load, 0.4 for the road traffic load, 0.4 for the pedestrian path load, and 0.75 for the wind load; S_{Qjk} defines the jth characteristic live load.

Chinese guidelines (JTG D62-2004) require to include live loads in the long-term calculations to account for the presence of heavy traffic and for the overload conditions at which some bridges are working. Since most of the CFST arch bridges currently in place are in China, the Chinese Code has been adopted for the calculation of the loads.

5.2 *Time effects on the displacement of the arch*

Figure 8 depicts the time-dependent changes produced on the displacement of the main arch rib after 100 years.

It is apparent that time effects in the core concrete significantly increase the displacement of the arch. The

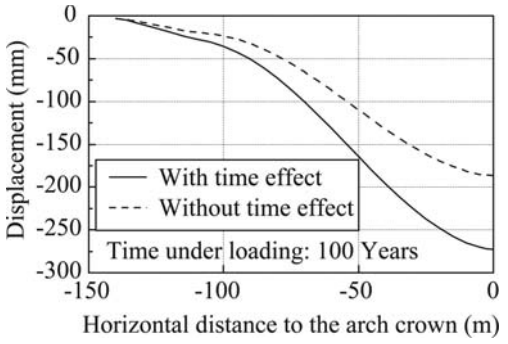

Figure 8. Time effects on the displacement of CFST arches under service loading.

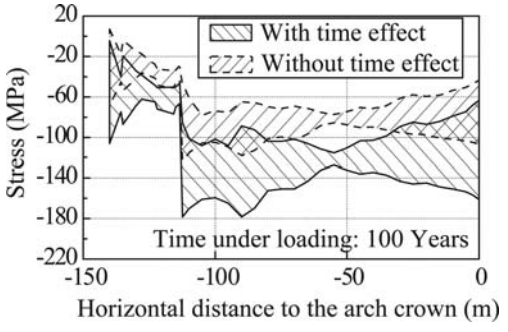

Figure 9. Time effects on the stress envelop in steel tubes of CFST arch ribs under service loading.

long-term displacement at the arch crown is 46.1% of the instantaneous one, indicating the importance of considering time effects when specifying the camber of the arch ribs.

5.3 *Time effects on the stress distribution at the cross section of the arch*

Figure 9 depicts the difference of the stress results in steel tubes predicted with and without the consideration of time effects after 100 years. It can be observed that the time-dependent behaviour of the core concrete enhances significantly the stresses in the steel tube. The most critical stress redistribution occurs at the place of maximum initial stress,(about 100 m from the arch crown where the first wind brace above the deck intersects the arch ribs) which produces a maximum steel stress increase of 51.2% when compared to the instantaneous value.

5.4 *Influence of time effects on the internal actions along the arch ribs*

Figure 10 compares the predicted inner forces in the main arch ribs subjected to service loading for 100 year calculated with and without time effects. In Figure 10(b), positive moments cause the arch to sag. It can be noted that time effects of the core concrete

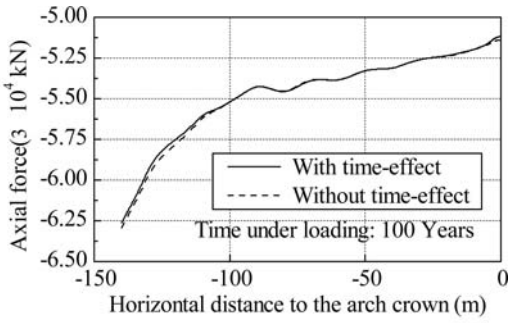

(a) Comparison on the axial forces along the arch ribs

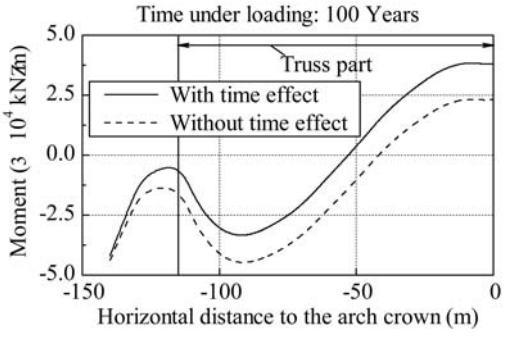

(b) Comparison on the bending moments along the arch ribs

Figure 10. Time effects on the inner forces of CFST arch ribs under service loading.

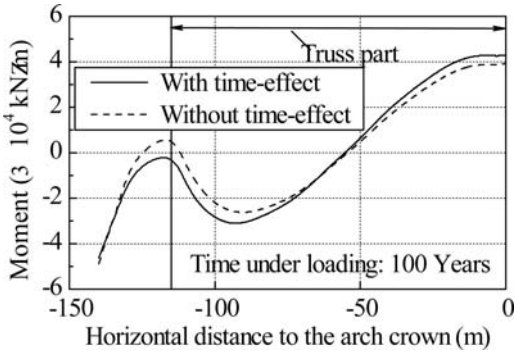

Figure 11. Bending moment curves of CFST arches obtained without the consideration of construction process.

have a negligible influence on the axial force distribution, with a maximum variation taking place over time of 0.7%, and a significant influence on the bending moment diagrams, with maximum time-dependent reductions and increases in the order of 8.3% and 64.7%, respectively.

Figure 11 presents the bending moment diagrams calculated with and without time effects gained by neglecting the construction process. The loads are assumed to be applied at 28 days after concrete casting. The maximum difference between the bending

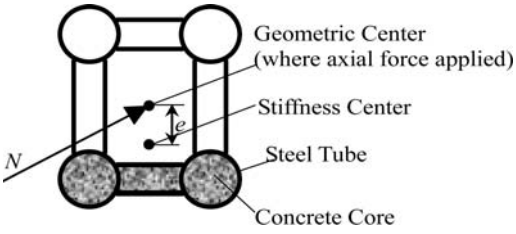

Figure 12. Location of the stiffness centre of the arch rib during construction.

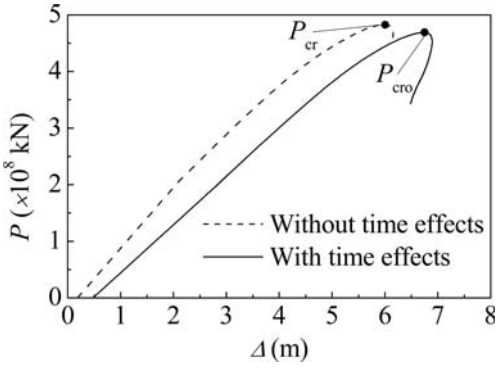

Figure 13. Influence of prebuckling deformations induced by time effects on ultimate capacity of CFST arch bridges.

moments obtained with and without consideration for time effects is 11%, which is much smaller than the value of 64.7% obtained with the consideration of the construction process as presented in Figure 10(b). While during the construction, the bottom chords are pumped first. At that time, the stiffness centre of the cross-section is lower than the geometric centre (Figure 12), leading to a negative additional bending moment ($N \cdot e$) which is almost constant along the arch as it is caused by the change of the cross-sectional properties. Time effects reduce the distance between the stiffness centre and the geometric centre, and hence reduce the negative additional bending moment, increasing the positive moment and reducing the negative moment along the arch. In this context, the construction process needs to be considered in the long-term analysis of trussed CFST arch bridges, otherwise considerably underestimation of the time effects may be obtained.

5.5 *Influence of time effects on the ultimate capacity*

Time effects increase the deflection of the arches, therefore reducing the critical buckling loads of the structure when compared to their instantaneous values. This is investigated numerically for the Dong-guan Waterway bridge considering distributed loads applied on the bridge slab for a duration of 100 years. Figure 13 presents the load-displacement curves of the CFST arches obtained with and without consideration

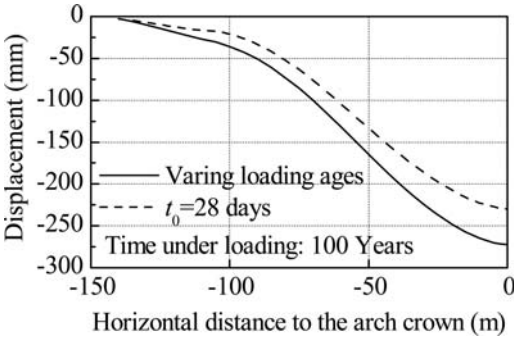

Figure 14. Comparison of the predicted displacement of CFST arch ribs with and without considering varying loading ages.

for time effects. In Figure 13, P represents the equivalent loads in one suspender, Δ denotes the vertical deflection at the arch crown, P_{cro} depicts the instantaneous critical loads, and P_{cr} defines the critical loads obtained accounting for time effects. The initial value of the Δ is the displacement of the bridge after 100 years calculated based on service loads. In the analysis, imperfections are introduced in the model based on the shapes exhibited by critical buckling modes (i.e. the first eigenmode) with the maximum perturbations of 1/1000 of the arch length.

From Figure 13, it can be noted that the prebuckling deformations induced by time effects reduce the critical buckling load of the bridge by 2.9% when compared to the instantaneous value. For CFST arch bridges with the span-to-rise ratio of 5, the prebuckling deformations induced by time effects have limited influence on their static ultimate capacity.

6 NECESSITY OF CONSIDERING THE VARIATION OF LOADING AGES DURING CONSTRUCTION

It is commonly accepted that the segmental construction process needs to be considered when predicting the static response of bridges. The entire construction of CFST arch bridge can be in the order of years. Because of this, the concrete age at the different instants of loading during construction can vary from as early as 3 days to 3 years.

In Figure 13 and 14, the predicted displacement and stress envelops obtained considering the varying loading ages of the core concrete are compared with those calculated based on $t_0 = 28$days. Plotted values have been calculated after 100 years of service. The results determined based on the accurate use of the loading ages higher by 20.2% for the displacement at the arch crown and by 48.9% for the stress in the steel tube when compared to the case of $t_0 = 28$.

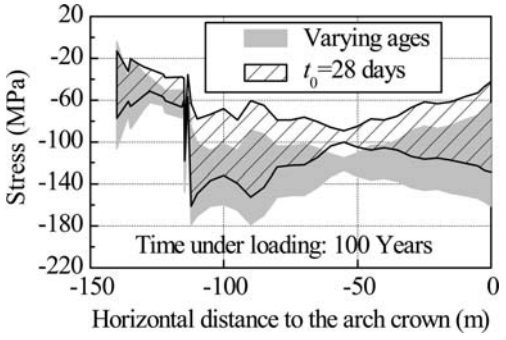

Figure 15. Comparison of the predicted stress in steel tubes of CFST arch ribs with and without the consideration of the varying loading ages.

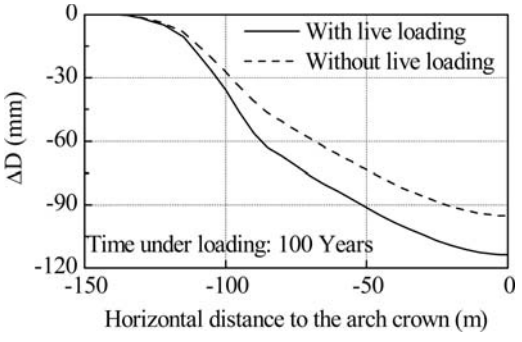

Figure 16. Contribution of live loading to the incremental displacement of CFST arch ribs caused by time-dependent behaviour after construction.

7 INFLUENCE OF LIVE LOADS ON THE LONG-TERM RESPONSE

The live loading is required to be applied on the bridge in the form of quasi-permanent combination during the long-term analysis by the Chinese Code (JTG D62-2004).

Different analyses have been performed with and without the inclusion of live loads to determine their influence on the variations of displacements (ΔD) and stresses in steel tubes ($\Delta\sigma$). In Figures 15 and 16, curves showing the results considering only the bridge self-weight are labelled with 'without live loading', while those that account also for live loads, based on Equation 1 are denoted using 'with live loading'.

The results of Figures 15 and 16 emphasise the increase in deflections and stresses taking place when also accounting for the live loads in the calculations. For example, the incremental time-dependent displacement (ΔD) caused by the inclusion of quasi-permanent live loading represents 16.4% of the total displacement increment at the arch crown, and 22.7% at $L/4$ along the arch. The live loading significantly affects the stress distribution in the arch rib as well, with a maximum increase of 24.7% for the stress in the steel tube near the intersection of the first wind brace above the deck (about 100 m from the arch crown).

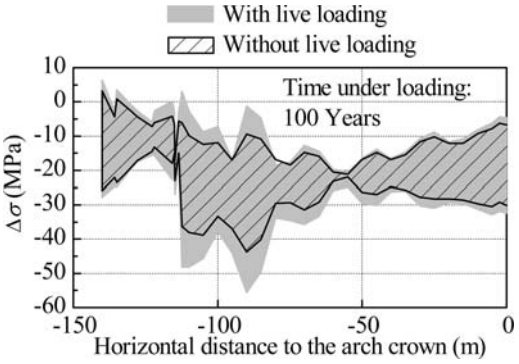

Figure 17. Influence of live loads on the time-dependent stress distribution in the steel tubes after construction.

8 CONCLUSIONS

A finite element model has been developed in ABAQUS to study the long-term behaviour of CFST arch bridges. which has been applied in this paper to the Dong-Guan Waterway bridge as a case study, and to highlight the influence of time effects on the overall structural response considering the construction sequence and geometric nonlinearity. The accuracy of the numerical model has been validated against site measurements recorded during construction. It has been observed that the time-dependent behaviour of the concrete has a significant effect on displacements, stress distributions, and bending moment diagrams of CFST arches during construction and in service. It has also been shown that it is important, for an accurate long-term prediction, to specify the actual time of loading in the analyses and to include considerations for the live loads, because inducing larger deformations.

ACKNOWLEDGEMENTS

The research reported in the paper was supported by the National Natural Science Foundation of China (No. 51178146), by the Project to support Chinese academics (who graduated from overseas universities) in Harbin Institute of Technology and by the Australian Research Council through its Discovery Projects funding scheme (DP1096454).

REFERENCES

Bradford M A, Pi Y L, & Qu W L. 2011. Time-dependent in-plane behaviour and buckling of concrete-filled steel tubular arches. *Engineering Structures*. 33(5), 1781–1795.

European Committee for Standardization, BS EN 1992, Eurocode 2: Design of concrete structures-Part 1-1: general rules and rules for buildings, 2004.

Geng Y., Zhang S. M., Wang Y. Y. & Wang X. L. 2010. Static behaviour of a concrete filled steel tubular double X-shape arch bridge without wind braces under construction. *Proceedings of Ninth Pacific Structural Steel Conference*. *19–22 November 2010.* Beijing, China, 906–910.

Gilbert, R. I. & Ranzi, G. 2011. *Time-dependent behaviour of concrete structures*, Spon Press, London, UK.

Han, L. H. 2007. *Concrete-Filled Steel Tubular Structures — Theories and Applications (2nd ed.)*. Science Press. Beijing, China. (in Chinese)

JTG D62. 2004. *Code for design of highway reinforced concrete and prestressed concrete bridges and culverts.* CCCC highway consultants CO., Ltd., Bei Jing, China, 2004 (in Chinese)

JTG D63. 2007. *Code for Design of Ground Base and Foundation of Highway Bridges and Culverts*, Beijing, China: Ministry of Communications of the People's Republic of China, 2007. (in Chinese).

Pi Y. L., Bradford M. A., & Qu W. L. 2011. Long-term nonlinear behaviour and buckling of shallow concrete-filled steel tubular arches. *International Journal of Non-linear Mechanics*. 46(9), 1155–1166.

Shao X. D., Peng J. X., Li L. F., Yan B. F. & Hu J. H. 2010. Time-dependent behavior of concrete-filled steel tubular arch bridge. *Journal of bridge engineering*. 15(1), 98–107.

Wang Y. F., Han B., Du J. S. & Liu K. W. 2007. Creep analysis of concrete filled steel tube arch bridges. *Structural engineering and mechanics*. 27(6), 639–650.

Zhang Z. C. 2007. Creep analysis of long span concrete-filled steel tubular arch bridges. *Engineering mechanics*. 24(5), 151–160. (in Chinese).

Zhong S. T. 1994. *Concrete-filled steel tubular structures (revised edition)*. Hei Longjiang Science and Technology Press, Hei Longjiang, China. (in Chinese).

Tubular Structures XIV – Gardner (Ed.)
© 2012 Taylor & Francis Group, London, ISBN 978-0-415-62137-3

Experimental study on concrete-filled cold-formed steel tubular stub columns

A.Z. Zhu, L.L. Luo & H.P. Zhu
School of Civil Engineering & Mechanics, Huazhong University of Science & Technology, Wuhan, PR China

ABSTRACT: Cold-formed steel is widely used in modern buildings and bridges. Significant research into the structural performance of Concrete-Filled Cold-Formed Steel Tubular (CFCFST) members with tube thickness not exceed 6 mm has been published. However, research into the performance of CFCFST members with longitudinal inner stiffeners in thicker wall tubes is seldom published. In this paper, a total of 20 CFCFST stub columns with thickness of 6 mm and 10 mm were conducted the axial compression test. Cross-sectional dimension of the square hollow tubes is 200 mm × 200 mm. Length of the stub columns is 600 mm. CFCFST stub columns with unstiffened and inner-stiffened hollow tubes were all tested. Both common concrete and self-consolidating concrete with normal compression strength of 30 MPa were applied. Axial compressive bearing capacities predicted using design methods in the Chinese codes CECS 159 and DBJ, the American specification AISC as well as the British bridge code BS 5400 were all compared with the test capacities of the CFCFST stub specimens. It was found that methods in these codes are much conservative to predict the axial compressive bearing capacity of the CFCFST column specimens.

1 INTRODUCTION

Concrete-Filled Steel Tubular (CFST) members have been playing an increasingly important role in modern buildings and bridges. Meanwhile, as the cold-formed steel members are used more and more popular, the importance of Concrete-Filled Cold-Formed Steel Tubular (CFCFST) members in future structures would never be overestimated.

In recent years, more and more significant research into the structural performance of CFCFST members with tubular thickness not exceed 6 mm has been published. Eight rectangular CFCFST specimens including stub columns, beams and beam-columns with thickness of 3.2 mm were conducted experimental and parametric analytical study by Tao et al. (2006). An experimental and computational study on the behaviors of circular CFCFST columns with tubular thickness less than 3.0 mm was conducted by Gupta et al. (2007). Elchalakani et al. (2004) carried out an experimental investigation of the cyclic inelastic flexural behaviors of circular CFCFST beams with tubular thickness not exceed 3.0 mm.

However, research on performance of both cold-formed steel members as well as the CFCFST members with thicker cold-formed tubes, especially tubes with inner longitudinal stiffeners is seldom published. Tao et al. (2009) studied the performance of a series of CFCFST members with inner longitudinal stiffeners. But the rectangular and square hollow tube built up by welding four plane plates, not cold-formed plates, with tubular thickness of 2.5 mm. Guo et al. (2007) studied the effect of the cold-formed process on the strengths of the cold-formed steel coupons as well as square and rectangular hollow stub columns with thickness of 8 mm, 10 mm and 12 mm. Lv et al. (2010) carried out numerical study on both cold-formed hollow steel stub columns and CFCFST stub columns with inner longitudinal stiffeners. The thickness of the steel tubes includes 8 mm, 10 mm and 12 mm. Zhang et al (2006 & 2007) compared the static and dynamic characteristics of unstiffened and stiffened thin-walled CFCFST columns with thickness no excess 3.0 mm. However, stiffened cold-formed steel tubular section studied in existing research mentioned above (Fig. 1) is different from the new sections studied in this paper (Fig. 2). Compared with the sections shown in Figure 1, the stiffened sections shown in Figure 2 can achieve structural members with the greatest possible cross-sectional dimensions without considering the sectional- dimension limit or common type limit of

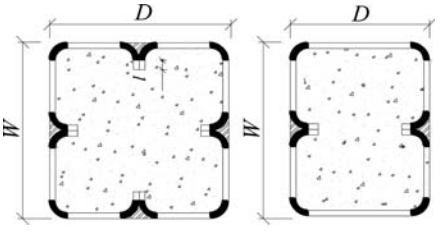

Figure 1. Stiffened sections built up by welding cold-formed lipped section.

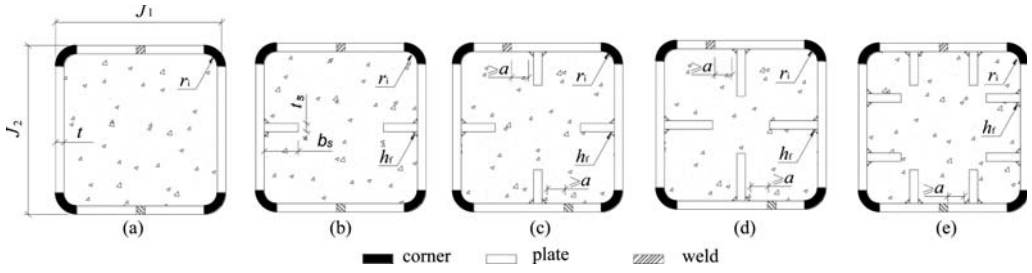

Figure 2. Diagrammatic sketch of the unstiffened and stiffened sections.

the cold-formed lipped steel section. Moreover, the inner stiffeners can also be freely arranged due to the demand of enhancing the bearing capacity or the construction requirements for members.

In this paper, a total of 20 CFCFST stub columns with thickness of 6 mm and 10 mm were conducted the axial compression test. Cross-sectional dimension of the square hollow tubes is 200 mm × 200 mm. Length of the stub columns is 600 mm. CFCFST stub columns with unstiffened and inner-stiffened square hollow tubes shown in Figure 1 were all tested. Common concrete and self-consolidating concrete with normal compression strength at 28 days equals to 30 MPa were used. Meanwhile, steel coupon tensile test were conducted to obtain main material properties of all parts of the hollow steel section. Concrete material test were also conducted to determine the real compressive cube strength ($f_{cu,st}$) and elastic modulus ($E_{c,st}$). Axial compressive bearing capacities predicted using design methods in the Chinese codes CECS 159 (2004) and DBJ (2003), the American specification AISC as well as the British bridge code BS 5400 (Han & Yang 2007), were all compared with the test capacities of the CFCFST column specimens.

2 EXPERIMENTAL INVESTIGATION

2.1 *Test of steel coupons*

A total of 30 steel coupons including plane plates, welded plates and corner plates were conducted axial tensile test in order to obtain real material characteristics. All the tensile coupons were cut from the corresponding plane part, welded part, corner plate as well as inner stiffener part of the section (Fig. 2), respectively, in longitudinal direction. All the plates were made into short standard tensile specimens (Tang 1999 & Zhu 2007). Cross-sectional area (A) and main test results including ultimate tensile strength σ_u, average ultimate tensile strength $\overline{\sigma_u}$, yield stress σ_s and average yield stress $\overline{\sigma_s}$ were listed in Table 1. Since the stress-strain curves in Figures 3 and 4 have no clear yield stages, the yield stress σ_s equals to the 0.2% tensile proof stress $\sigma_{0.2}$ (Tang, 1999) was analyzed in this paper.

In table 1, the label P-6-1 defines the following specimens: the first letter P indicates that the specimen was cut from the plane part of the section. The following figure 6 refers to the nominal thickness of the specimen. The last number 1 refers to the first specimen of this coupon group which totally has 3 specimens. Meanwhile, letters W, C, S and T indicate the coupons were respectively cut from the welded part, the corner part, the inner stiffener part and the top or bottom cover plate of the hollow steel tubes.

As the nominal yield stress of steel Q345 in group 1 and Q235 in group 2 are respectively 345 MPa and 235 MPa, yield strengths of plane plates, welded plates as well as corner plates cut form the 2 groups of cold-formed steel hollow tubes were all enhanced due to the cold-formed process. Moreover, ultimate tensile strengths and yield strengths of both welded plates and corner plates are much higher than corresponding strengths of the plane plates in each group. According to table 1, the yield strengths of the welded plates and corner plates in group 1 are respectively 22.30% and 23.27% higher than the yield strength of the plane plates, while the two strengths in group 2 are respectively 32.31% and 13.59% higher than the yield strength. Test strengths of stiffener plates and top or bottom plates applied in each group were also listed in table 1. It should be noted that tensile test of the last two top plates in group 2 with thickness of 16 mm were failure. Therefore, only the strengths of coupon T-16-1were obtained. Figure 5 shows the typical failure mode of plane plates, welded plates and corner plates.

2.2 *Test of concrete material*

The concrete mix was designed for compressive cube strength (f_{cu}) at 28 days of approximately 30 MPa. Table 2 shows the proportions of common concrete (specimen A) and self-consolidating concrete (specimen B) studied in this paper. The aggregate size ranges from 5 to 25 mm. Small quantity of the UEA cement expansive additive was used in both the common and the self-consolidating concrete. Furthermore, small quantity of the HL-8000 super plasticizer was also used in the self-consolidating concrete. A series of compressive cube (150 × 150 × 150 mm) and prismoid (150 × 150 × 300 mm) specimens were tested to determine the strength $f_{cu,st}$ and modulus $E_{c,st}$ at 28 days of the two kinds of concrete. The strengths $f_{cu,st}$ of specimen A and specimen B are 26.58 MPa and 25.81 MPa, respectively. The elastic modulus $E_{c,st}$ are 3.12×10^4 MPa and 2.84×10^4 MPa, respectively.

Table 1. Measured specimen dimension and test results of steel coupons.

Specimen Group 1	A (mm)	σ_u (MPa)	$\overline{\sigma_u}$ (MPa)	σ_s (MPa)	$\overline{\sigma_s}$ (MPa)	Specimen Group 2	A (mm)	σ_u (MPa)	$\overline{\sigma_u}$ (MPa)	σ_s (MPa)	$\overline{\sigma_s}$ (MPa)
P-6-1	215.32	574.70	537.37	461.41	437.88	P-10-1	340.87	451.00	445.67	424.12	381.68
P-6-2	226.17	495.50		406.91		P-10-2	345.16	442.10		372.09	
P-6-3	223.05	541.90		445.33		P-10-3	338.79	443.90		348.83	
W-6-1	206.58	622.10	582.00	585.87	535.54	W-10-1	352.20	523.10	526.93	507.13	505.00
W-6-2	214.56	566.10		525.73	(22.30%)	W-10-2	359.35	538.30		505.50	(32.31%)
W-6-3	216.58	557.80		495.01		W-10-3	366.05	519.40		502.36	
C-6-1	97.76	562.60	614.00	521.69	539.76	C-10-1	333.30	495.10	495.47	432.04	433.55
C-6-2	96.29	633.50		529.65	(23.27%)	C-10-2	303.23	504.60		435.31	(13.59%)
C-6-2	89.80	645.90		567.93		C-10-3	318.49	486.70		433.30	
S-6-1	186.67	516.40	531.63	409.81	410.79	S-8-1	244.97	579.60	551.07	499.53	453.59
S-6-2	188.85	537.20		411.65		S-8-2	245.51	528.50		410.04	
S-6-3	184.66	541.30		410.92		S-8-3	242.43	545.10		451.18	
T-10-1	285.12	593.10	595.10	482.11	495.17	T-16-1	468.53	402.10	402.10	312.25	312.25
T-10-2	281.22	586.10		499.40		T-16-2	461.63	—		—	
T-10-3	280.53	606.10		504.01		T-16-3	464.81	—		—	

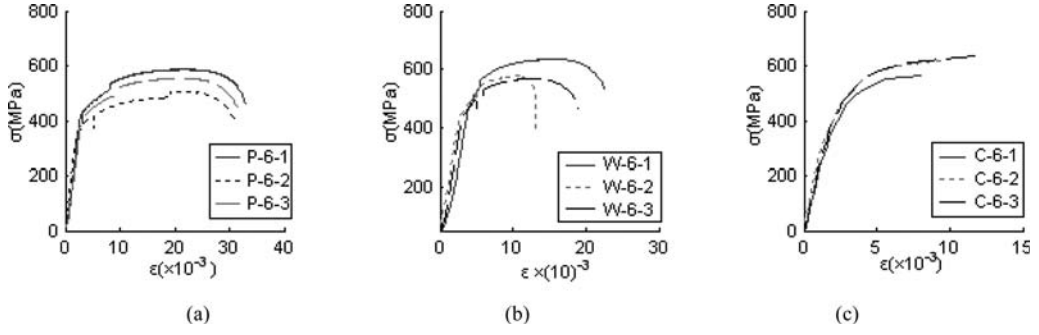

Figure 3. Typical σ-ε curve of steel coupons with thickness of 6 mm.

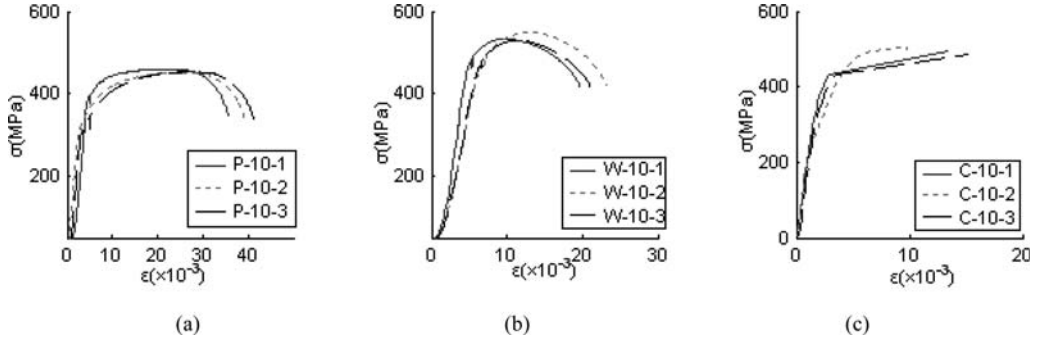

Figure 4. Typical σ-ε curve of steel coupons with thickness of 10 mm.

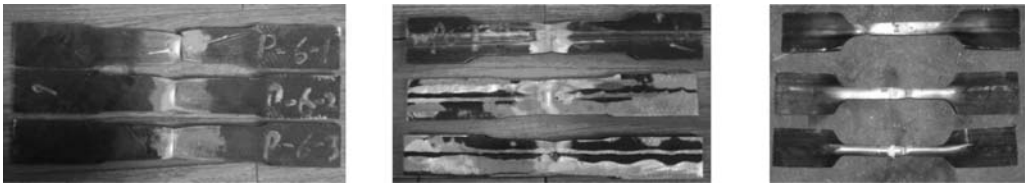

Figure 5. Typical failure mode of steel coupons.

2.3 *Test of CFCFST column specimens*

A total of 20 CFCFST column specimens with thickness of 6 mm and 10 mm were conducted the axial compression test. All these composite column specimens were classified according to the thickness of the hollow tubes and the concrete type. Therefore, a total of 4 groups of columns were tested. All the hollow tubular sections were designed as shown in Figure 2, where the net minimal distance between weld of stiffener and weld of the tube wall was designed as no less than a (double the tube thickness). Design ratio of the inner radius of corner to tube thickness equals 1.5. All hollow tubes weld with a bottom plate were fabricated in rolling steel plant. And the top plate was welded 14 days later than the concrete was filled.

Table 3 shows measured dimensions of the column specimens. Definitions of the measured dimensions were shown in Figure 6. In table 3, the label Pa-6-1 defines the following specimens: the first letter P indicates axial compressive column. The following letter a refers to the first cross section shown in Figure 2. The following number 6 refers to the nominal thickness of the hollow steel tube. The last figure 1 indicates the common concrete was filled while figure 2 refers to the self-consolidating concrete was applied. Therefore, the second letter b, c, d and e refer to the 2nd, the 3rd, the 4th and 5th section shown in Figure 2, respectively. It should be noted that section c is different from section b only in that the nominal width of the inner stiffeners (b_s) is 60 mm in the section c while 40 mm in section b. Moreover, measured dimensions $b_{s,av}$ and $t_{s,av}$ listed in table 3 are calculated average values of all the inner stiffeners in each column specimen. A_s and A_c define the cross-sectional area of steel sections (including stiffeners and corners) and concrete sections, respectively. The area of the corner part is calculated as $A_0 = \pi(R^2 - r^2)$. Where $R = (J_1 + J_2 - B_1 - B_2)/4$ and $r = [(J_1 + J_2 - B_1 - B_2 - 2(t_3 + t_4)]/4$.

A typical CFCFST column test setup is shown in Figure 7. A compression testing machine with capacity of 5000 kN was used to apply axial compressive force to the column specimens. Each column specimen has two plane plates at both ends, namely the bottom plate and the top plate. Nominal dimension of the two end plates is 240 mm × 240 mm.

Table 2. Concrete mix design.

	Content (kg/m^3)	
Material	Specimen A	Specimen B
Sand (%)	50%	50%
Cement	256	256
Flash ash	86	86
Water	200	200
Sand	909	909
Aggregate	909	909
Expansive additive	38	38
Super plasticizer	—	3.8

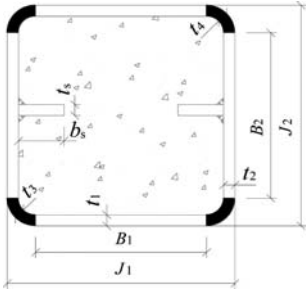

Figure 6. Definition of cross-sectional dimension.

Table 3. Measured dimension of column specimens.

Specimens	H (mm)	B_1 (mm)	B_2 (mm)	t_1 (mm)	t_2 (mm)	t_3 (mm)	t_4 (mm)	J_1 (mm)	J_2 (mm)	$b_{s,av}$ (mm)	$t_{s,av}$ (mm)	A_s (mm^2)	A_c (mm^2)
Pa-6-1	605	170	163	6.39	6.32	6.14	6.18	202	192	–	–	4703.95	33880.41
Pb-6-1	602	167	170	6.08	6.05	6.30	6.34	204	196	40	6.26	5088.47	34682.60
Pc-6-1	603	167	170	6.10	6.30	6.20	6.20	200	195	40	6.09	5597.90	33221.62
Pd-6-1	605	166	170	6.17	6.04	6.32	6.10	200	198	60	6.03	6032.88	33360.89
Pe-6-1	600	166	170	6.13	6.33	6.00	6.00	203	200	40	6.09	6652.92	33706.24
Pa-6-2	601	166	164	6.15	6.05	6.18	6.42	203	194	–	–	4564.54	34576.62
Pb-6-2	600	165	170	6.18	6.02	6.00	6.00	204	197	40	6.08	5081.54	34872.76
Pc-6-2	605	169	168	6.05	6.23	6.22	6.00	200	197	40	6.00	5556.75	33650.11
Pd-6-2	604	166	169	6.10	6.09	6.18	6.18	202	194	60	5.95	5983.79	33004.57
Pe-6-2	590	168	174	6.15	6.23	6.06	6.12	204	200	40	6.28	6603.96	33496.52
Pa-10-1	599	146	150	10.21	10.41	10.22	10.00	203	199	–	–	7466.57	32327.61
Pb-10-1	599	154	148	10.25	10.14	10.18	9.76	200	200	40	8.80	8084.93	31399.82
Pc-10-1	600	150	156	10.00	10.28	10.00	10.10	200	197	40	7.96	8600.23	30355.50
Pd-10-1	601	148	153	10.08	10.00	10.16	10.16	201	196	60	8.20	9219.48	29682.08
Pe-10-1	600	148	151	10.03	10.05	9.86	9.72	200	201	40	8.26	9913.05	29728.78
Pa-10-2	595	150	152	10.00	10.04	10.00	10.40	202	200	–	–	7327.52	32535.98
Pb-10-2	594	150	150	10.29	10.03	10.30	10.00	202	200	40	8.24	8057.79	31784.03
Pc-10-2	603	156	160	10.00	10.10	10.32	9.92	200	201	40	7.90	8645.46	31166.92
Pd-10-2	603	150	153	10.00	10.10	9.78	10.01	200	198	60	7.83	9138.79	29977.01
Pe-10-2	600	150	150	10.08	10.10	10.06	10.20	199	202	40	8.32	9938.63	29632.33

The test ultimate bearing capacity N_u and average ultimate tress σ_u ($\sigma_u = N_u/(A_s + A_c)$) of all specimens were listed in columns 2 and 3 in table 4, respectively.

It should be noted that the ultimate capacities of specimens Pd-10-1, Pe-10-1, Pd-10-2and Pe-10-2 were not obtained because there were no failure phenomena during the loading process, even when the compressive load approached the loading capacity of the testing machine. Thus, tests of these four specimens were stopped as the compressive load approached 5000 kN. However, as the top section of the SHS tube of specimen Pc-6-1 has serious initial defects, it was very difficult to conduct axial compressive load on the specimen after the top plate is welded. Thus the capacity N_u of this specimen is even less than that capacity of specimen Pb-6-1. In order to distinguish the test capacity N_u of specimens Pd-10-1, Pe-10-1, Pd-10-2, Pe-10-2 and Pc-6-1 from other specimens, parentheses are used in table 4.

Figure 7. Test setup of CFCFST column specimen.

From table 4, as far as column specimens filled with the same concrete are concerned, the ultimate capacity N_u and average ultimate stress σ_u increase with the increases of the sectional area or number of the inner stiffeners. Since the ultimate stress σ_u increases, it can be obtained that the sectional carrying efficiency of the composite cross-section also increases. The average ultimate stress σ_u of specimens with sections b and c in groups 2 and 4 are very close, which means the increase of the ultimate capacity wholly depends on the increase of the steel sectional area. However, all specimens with sections b and e have better sectional carrying efficiency than those specimens with sections a and d, respectively, almost in all groups. Otherwise, although the test strength of the compressive cubic specimens of self-consolidating concrete is a little lower than that of the common concrete, the ultimate capacity N_u and stress σ_u of column specimens in groups 2 and 4 are obviously higher than those values in groups 1 and 3, respectively.

Figures 8 and 9 are the stress-strain (σ-ε) curves of CFCFST column specimens with thickness of 6 mm and 10 mm. Where the vertical axis $\sigma = N/(A_s + A_c)$. N is the test load. The horizontal axis ε is average values of four strain gauges positioned on the center point of each outer face of the column specimen. Meanwhile, all the test strain and load N are recorded in pairs. From these curves, only the sectional carrying efficiency in column specimens with section c in group 2 (with thickness of 6 mm) is obviously better than that of the specimens with section b. However, the sectional carrying efficiency of two sections b and c are very close in other 3 groups.

Table 4. Comparison of test bearing capacity with predicted bearing capacities.

Specimen		N_u (kN)	σ_u (MPa)	N_{CECS} (kN)	$\frac{N_{CECS}}{N_u}$	N_{DBJ} (kN)	$\frac{N_{DBJ}}{N_u}$	N_{AISC} (kN)	$\frac{N_{AISC}}{N_u}$	N_{BS} (kN)	$\frac{N_{BS}}{N_u}$
Group1	Pa-6-1	2730	70.75	1942.72	0.71	2062.66	0.76	2305.39	0.84	1999.11	0.73
	Pb-6-1	3020	75.93	2073.39	0.69	2208.63	0.73	2454.20	0.81	2135.96	0.71
	Pc-6-1	(2750)	70.84	2210.42	0.80	2378.63	0.86	2600.52	0.95	2283.20	0.83
	Pd-6-1	4120	104.59	2347.25	0.57	2541.86	0.62	2753.40	0.67	2427.65	0.59
	Pe-6-1	4490	111.25	2544.41	0.57	2780.08	0.62	2974.27	0.66	2635.53	0.59
Group2	Pa-6-2	3010	100.01	1909.45	0.63	2022.00	0.67	2271.31	0.75	1962.81	0.65
	Pb-6-2	3300	114.22	2073.96	0.63	2208.29	0.67	2455.64	0.74	2136.26	0.65
	Pc-6-2	3630	115.52	2203.79	0.61	2367.57	0.65	2594.96	0.71	2275.50	0.63
	Pd-6-2	4030	113.11	2326.94	0.58	2520.48	0.63	2729.29	0.68	2406.75	0.60
	Pe-6-2	4300	118.56	2526.23	0.59	2759.88	0.64	2953.15	0.69	2616.65	0.61
Group3	Pa-10-1	3980	76.90	2067.60	0.52	2351.16	0.59	2405.88	0.60	2103.34	0.53
	Pb-10-1	4510	82.59	2187.28	0.48	2524.22	0.56	2532.51	0.56	2228.86	0.49
	Pc-10-1	4500	92.59	2283.13	0.51	2674.32	0.59	2632.56	0.59	2329.80	0.52
	Pd-10-1	(4400)	103.36	2406.64	0.55	2864.62	0.65	2764.52	0.63	2458.96	0.56
	Pe-10-1	(4700)	107.22	2556.43	0.54	3084.61	0.66	2928.45	0.62	2614.43	0.56
Group4	Pa-10-2	3920	98.34	2040.68	0.52	2313.35	0.59	2377.41	0.61	2075.11	0.53
	Pb-10-2	4330	108.68	2186.94	0.51	2518.17	0.58	2533.87	0.59	2227.99	0.51
	Pc-10-2	4340	109.01	2304.46	0.53	2690.02	0.62	2659.54	0.61	2350.85	0.54
	Pd-10-2	(4550)	116.32	2393.51	0.53	2839.31	0.62	2751.50	0.60	2444.93	0.54
	Pe-10-2	(4625)	116.88	2560.55	0.55	3093.18	0.67	2932.52	0.63	2618.83	0.57

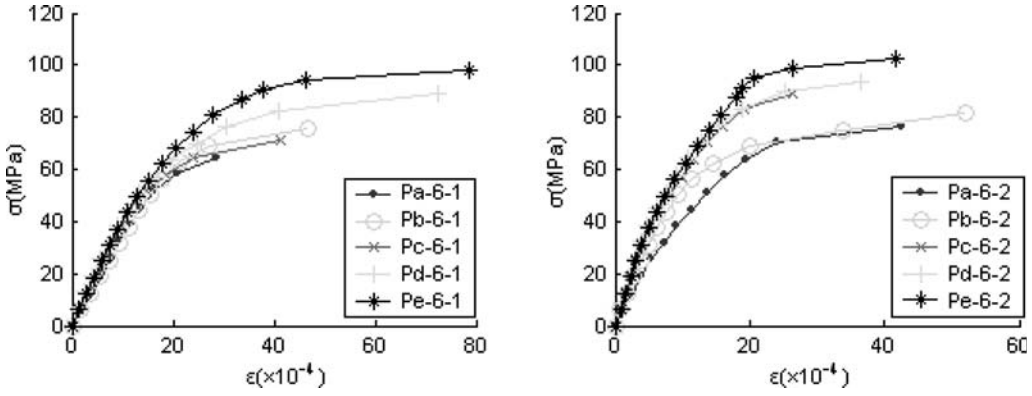

Figure 8. Experimental σ-ε curves of CFCFST column specimen with thickness of 6 mm.

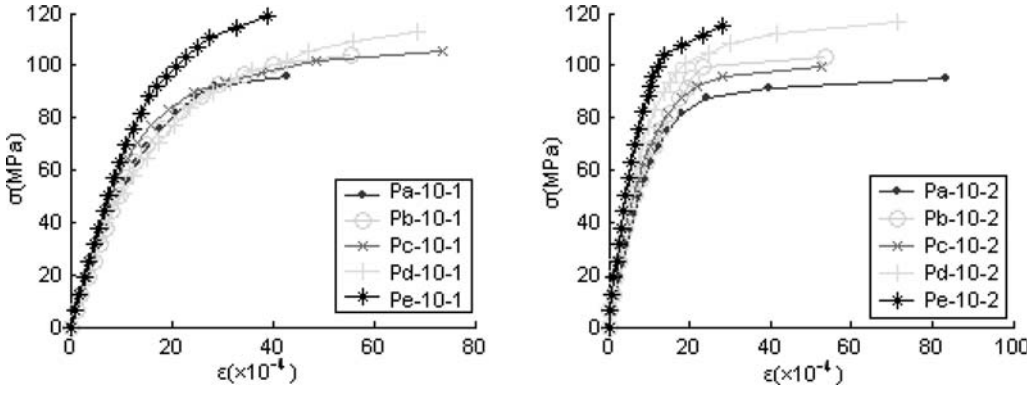

Figure 9. Experimental σ-ε curve of CFCFST column specimen with thickness of 10 mm.

(a) Pa-6-1 (b) Pb-6-1 (c) Pd-6-1 (d) Pe-6-1 (e) Pb-10-1 (f) Pb-10-2

Figure 10. Typical failure mode of CFCFST column specimen.

Figure 10 shows the typical failure mode of the tested CFCFST column specimens.

3 COMPARISON OF TEST BEARING CAPACITY WITH PREDICTED CAPACITIES

The Chinese codes CECS 159 (2004) and DBJ (2003), the AISC specification as well as the BS 5400 code (Han & Yang 2007) provide design methods for axial compressive bearing capacity for CFST columns.

In CECS code, the axial bearing capacity N_{CECS} is given by Eq. (1), where f and f_c are compressive design strengths of steel and concrete. The two strengths can be obtained consulting the Chinese codes GB 50017 (2003) and GB concrete code (2002), respectively. Therefore, design strengths f for steel Q235 and Q345 are given as 215 MPa and 310 MPa, respectively. And f_c is given as 14.3 MPa. Otherwise, A_s and

A_c are respectively cross-sectional area of steel tube and cross-sectional area of concrete filled in the tube, which can be obtained from table 3.

$$N_{CECS}=f\cdot A_s+f_c\cdot A_c \quad (1)$$

In DBJ code, the axial bearing capacity N_{DBJ} can be obtained by multiplying A_{sc} by f_{DBJ}. Where A_{sc} is total sectional area of the CFST section, namely $A_{sc} = A_s + A_c$. f_{DBJ} is given by Eq. (2). f, f_c, A_s and A_c are same values as in Eq. (1). ξ_0 is the confinement factor. $\xi_0 = f \cdot A_s/f_c \cdot A_c$.

$$f_{DBJ}=(1.18+0.85\cdot\xi_0)\cdot f_c \quad (2)$$

According to the AISC specification, simplified axial bearing capacity N_{AISC} analyzed in this paper is given by Eq.(3).

$$N_{AISC} = f_y\cdot A_s + 0.85f_c'\cdot A_c \quad (3)$$

where f_y is the nominal yield strength of the steel. f_c' is the compressive concrete cylinder strength. Therefore, yield strengths of f_y for steel Q235 and Q345 are given as 235 MPa and 345 MPa, respectively. And f_c' is given as strength f_{cu} multiplied by 0.79 (Chen & Wang 2005). f_{cu} is the compressive cube strength of concrete. For concrete C30, nominal strength f_{cu}= 30 MPa.

In BS 5400 code, Eq. (4) is applied to determine the axial bearing capacity N_{BS}. Where f_{cu} is the compressive cube strength of concrete.

$$N_{BS}=0.95f_y\cdot A_s+0.45f_{cu}\cdot A_c \quad (4)$$

All bearing capacities predicted using the design methods mentioned above were also listed in Table 4. As far as the ratios of all predicted capacities to test capacities are concerned, most of the ratios are greater than 0.50 while less than 0.80. Therefore, it could be obtained that these four design methods are much conservative to predict the bearing capacity of the CFCFST column specimens.

Except for the column specimen Pc-6-1 as well as the specimens Pd-10-1, Pe-10-1, Pd-10-2 and Pe-10-2 which have particular test bearing capacities in table 4, ratios N_{CECS}/N_u,N_{DBJ}/N_u,N_{AISC}/N_u and N_{BS}/N_u of all other specimens in each group decrease with the increase of inner stiffeners. Therefore, all these methods are more conservative to predict the bearing capacity of the CFCFST column specimens with inner stiffeners than those columns without inner stiffeners. Moreover, the most conservative design method is the Chinese code CECS while the least one is the AISC specification. Actually, the predicted bearing capacity N_{AISC} using equation (3) is just a simplified capacity, which multiplied by a parameter approximately equals to 0.877 may equals to the real bearing capacity predicted using this code. Thus the AISC specification is likely more conservative than the Chinese CECS code. But the simplified AISC method is better to predict the design bearing capacity of the column specimens although it is still conservative.

Compared column specimens with thickness of 6 mm with column specimens with thickness of 10 mm, values of N_{CECS}/N_u, N_{DBJ}/N_u, N_{AISC}/N_u and N_{BS}/N_u of the latter groups are commonly less than those of the former groups. Therefore, all these design methods are more conservative to predict the bearing capacity of specimens in groups 3 and 4. As far as two kinds of concrete filled in the tube are concerned, all design methods mentioned above are more conservative to predict the bearing capacities of specimens in group 2 than those specimens in group 1. But there is nearly no difference between specimens in groups 3 and 4.

4 CONCLUSIONS

This paper presents an axial compression test study on the CFCFST stub column specimens with new kinds of inner-stiffened section as well as thicker cold-formed steel tubes. Both common concrete and self-consolidating concrete with compressive cube strength (f_{cu}) at 28 days of approximately 30 MPa were applied. Axial tension test of steel coupons and compression test of concrete specimens were conducted to determine main material properties of cold-formed steel and concrete, respectively. Predicted bearing capacities using the Chinese codes CECS 159 and DBJ, the American specification AISC as well as the British bridge code BS 5400 were all compared with the test capacities of the CFCFST column specimens. Main observations and conclusions are made based on the limited test and analysis carried out in this paper.

First of all, the test ultimate tensile strength and yield strength of both the corner and welded plates cut from the steel tube are much higher than strengths of the plane plates due to the fabricate process. The average yield strengths $\overline{\sigma_s}$ of the welded plates and corner plates with nominal thickness of 6 mm are respectively 22.30% and 23.27% higher than corresponding plane plates while two strengths of those plates with nominal thickness of 10 mm are 32.31% and 13.59% higher, respectively.

Secondly, the test compressive cube strength $f_{cu,st}$ (26.58 MPa) and the elastic modulus $E_{c,st}$ (3.12×10^4 MPa) of common concrete are greater than corresponding values (25.81 MPa and 2.84×10^4 MPa) of the self-consolidating concrete. However, the ultimate capacity N_u and average ultimate stress σ_u of column specimens using self-consolidating concrete are obviously higher than those values of specimens using common concrete. Moreover, the capacity N_u and stress σ_u increase with the increases of the sectional area or quantity of the inner stiffener.

Finally, most ratios of all predicted axial compressive bearing capacities to test capacities of the CFCFST column specimens range from 0.50 to 0.80. Meanwhile, all these design methods are more conservative to predict the bearing capacity of specimens with tube thickness of 10 mm than capacity of specimens with thickness of 6 mm. Furthermore, for

specimens with tube thickness of 6 mm, these design methods are more conservative to predict the bearing capacity of specimens filled with self-consolidating concrete than capacity of specimens filled with common concrete.

ACKNOWLEDGEMENTS

The authors are grateful to the supports of National Basic Research Program of China 973 (No. 2011CB013800), National Natural Science Foundation of China (No. 51108204, 50925828) and Doctoral Fund of Ministry of Education of China (No. 20100142120072). Meanwhile, thanks are given to Hankou Rolling Steel Mill in Wuhan Steel Corporation Group for fabricating all specimens and supporting part of the steel material for free.

REFERENCES

CECS (2004). *Technical Specification for Structures with Concrete-filled Steel Tube Members.* In: CECS 159: 2004. Beijing (China): Chinese Plan Press. (in Chinese)

Chen X.R., Wang T.C. (2005) *Concrete structures (Volume One, 3rd version)*. China Architecture & Building Press, 2005. (in Chinese)

Chinese Concrete Code (GB 2002). *Code for Design of Concrete Structures*. In: GB 50010-2002. Beijing (China): China Architecture & Building Press. (in Chinese)

Chinese Standard (GB 2003). *Code for Design of Steel Structures*. In: GB 50017-2003. Beijing (China): Chinese Plan Press. (in Chinese)

DBJ (2003). *Technical Specification for Concrete-filled Steel Tubular.* In: DBJ 13-51-2003. Fuzhou (China): Fujian Department of Housing and Urban-Rural Development. (in Chinese)

Elchalakani M., Zhao X.L., Grzebieta R. (2004). Concrete-filled steel circular tubes subjected to constant amplitude cyclic pure bending. *Engineering structures*, 26: 2125–2135

Guo Y.J., Zhu A.Z. et al. (2007). Experimental study on compressive strengthen of thick-walled cold-formed sections.*Journal of constructional steel research*, 63: 718–723

Gupta P.K., Sarda S.M., Kumar M.S. (2007). Experimental and computational study of concrete filled steel tubular columns under axial loads. *Journal of constructional steel research*, 63: 182–193

Han L.H. Yang Y.F. (2007). *Modern Technical for Concrete-filled Steel Tubular Structures*. Beijing (China): China Architecture & Building Press. (in Chinese)

Lv T., Wang L., Zhu A.Z. et al. (2010). Study on Unstiffened and Stiffened Cold-formed SHS and RHS Stub Columns. *Proceedings of the 11th international symposium on structural engineering*, I: 253–259

Tang Y.Q. Ye W.M. (1999). *A Handbook Of Testing Technique In Civil Engineering*. Shanghai (China): Tongji University Press

Tao Z., Wang Z.B., Han L.H. (2006). Behavior of rectangular cold-formed steel tubular columns filled with concrete. *Engineering mechanics*, 23: 147–155 (in Chinese)

Tao Z., Uy B., Han L.H., et al. (2009). Analysis and design of concrete-filled stiffened thin-walled steel tubular columns under axial compression. *Thin-walled structures*, 47: 1544–1556

Zhu A.Z., Chen, X.C. et al. (2010). Analysis Of Concrete-Filled Unstiffened And Stiffened Cold-Formed Stub Columns. *Proceedings of the 11th International symposium on structural engineering*, I: 246–252

Zhang Y.C., Chen Y. (2006). Experimental Study and Finite Element Analysis of Square Stub Column with Straight Ribs of Concrete-Filled Thin-Walled Steel Tube. *Journal of building structures*, 27: 16–22. (in Chinese)

Zhang Y.C., Xu C., and Lu X.Z. (2007). Experimental Study Of Hysteretic Behaviour For Concrete-Filled Square Thin-Walled Steel Tubular Columns. *Journal of constructional steel research*, 63: 317–32

Tubular Structures XIV – Gardner (Ed.)
© 2012 Taylor & Francis Group, London, ISBN 978-0-415-62137-3

Concrete filled double skin circular tubular members subjected to pure bending and centric compressive loading

K. Uenaka
Dept of Civil Engineering, Kobe City College of Technology, Kobe, Japan

H. Kitoh
Dept of Urban Engineering, Osaka City University, Osaka, Japan

ABSTRACT: A Concrete Filled Double Skin Circular Tubular (CFDST) member consists of double concentric steel tubes and in-filled concrete between the two tubes. The CFDST member with a hollow section is consequently lighter than an ordinary concrete filled steel tubular, so-called CFT member. Twelve specimens of each pure bending test and centric loading test have been prepared. Two of testing parameters are diameter-to-thickness ratio and inner-to-outer diameter ratio, ranging from 70 to 160 and from 0 to 0.70, respectively. As the results, both bending and centric loading strengths of CFDST can be estimated based on a CFT's design formula. Both strengths were also affected by inner-to-outer diameter ratio, D_i/D_o. Discussions being focused on elasto-plastic stress under plane stress condition are given. A comparison of confined stress intensity being induced by the double tubes of two tests is also discussed.

1 INTRODUCTION

A concrete filled double skin circular tubular, CFDST, member consists of double concentric steel tubes and filled concrete between them as shown in Fig. 1 (a). A CFDST with hollow cross section is consequently lighter than an ordinary concrete filled steel tubular, so-called CFT with solid section (see Fig. 1 (b)). When CFDST is applied to high-raised bridge pier, seismic action will be reduced owing to lighter structural members due to hollow section.

Reviewing the past studies on CFDST, we can first find experimental and analytical studies on CFDST with polymer concrete for practical application of marine structures (Mantrala, S. K. 1995a & 1995b). Zhao et al. (2002 & 2010) had conducted series of mechanical behaviors of CFDST members (Zhao, et al.), diameter-to-thickness ratio (D_o/t_o) in which are less than 50. The detailed review on CFDST is also described in Zhao, X. L. et al. (2006).

Under the above-described background, we have conducted two systematic studies on CFDST with large diameter-to-thickness ratio, D_o/t_o being larger than 70. One is the stub column test under centric loading (Uenaka et al. 2010). The other is the pure bending test through four-point loadingtest (Uenaka et al. 2008). These tests were discussed by twelve specimens under selected two parameters, which were diameter-to-thickness ratio (D_o/t_o) and inner-to-outer diameter ratio D_i/D_o, respectively. In the following, systematically three-point loading test on deep CFDST beam also conducted (Uenaka et al. 2011)

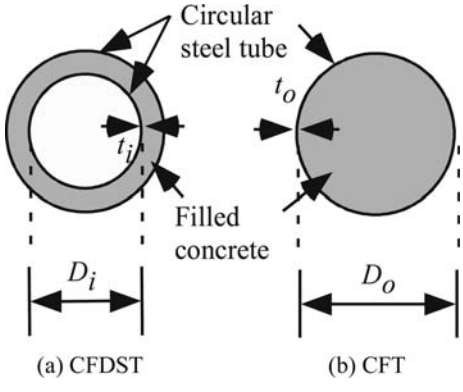

Figure 1. Cross section.

This paper mainly presents the discussions on comparison of above two testing results, namely, those are centric compressive loading (Uenaka et al. 2010) and pure bending tests (Uenaka et al. 2008). Influence of the intensity of confined stress on axially loading and pure bending capacities is also discussed. Furthermore, methods to predict both tests ultimate capacities are given.

2 EXPERIMENTAL

2.1 *Centric Compressive loading (CC) test*

Figure 2 shows the centric compressive loading test specimens. Details of the specimens are summarized from No. 1 to 12 in Table 1. The specimens are commonly 450 mm in height and 160mm in diameter, respectively. Nominal double tube's thickness (t_i, t_o) are 1.0, 1.6 or 2.3 mm. Inner tube's diameter (D_i) is ranging from 0(CFT) to 113 mm. Two main parameters, namely, ratio of diameter-to-thickness (D_o/t_o) and that of inner-to-outer diameter (D_i/D_o) range from 70 to 160 and from 0.0 to 0.70, respectively. Consequently, centric loading test specimens are totally twelve being combinations of three double tube's thicknesses and four inner tube's diameters.

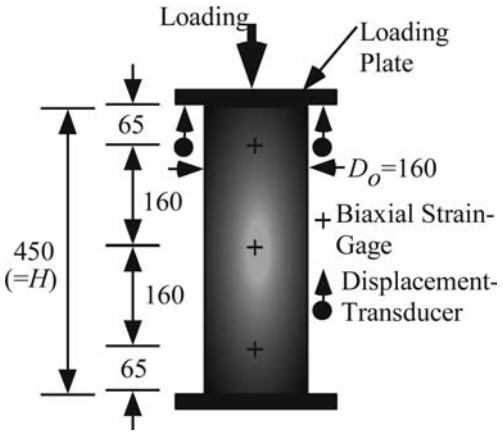

Figure 2. Centric compressive loading test.

Twelve biaxial strain gauges are attached on outside of double tubes on eastern-western direction to obtain stress conditions to be induced by in-filled concrete. Two displacement transducers are also arranged at the top of the specimens.

2.2 *Pure Bending (PB) test*

Pure bending test specimens are illustrated in Fig. 3. The specimens are detailed from No. 13 to 24 in Table 1. Two main parameters, D_o/t_o and D_i/D_o, are the same as above-described centric loading test specimens. Connecting plates are welded on both sides of

Table 1. List of the specimens.

No.	Tag.	Testing Method	Outer and Inner Tubes [1] t_o, t_i (mm)	[2] D_o (mm)	[3] D_i (mm)	Ratio [2]/[1]	Ratio [3]/[1]	Ratio [3]/[2]	Material Properties f_{yo}, f_{yi} (MPa)	f'_c (MPa)
1	c10-000	Compression	1.00	160	0.0	160.0	-	0.00	221	18.7
2	c10-375				37.5		37.5	0.23		
3	c10-750				75.0		75.0	0.47		
4	c10-1125				112.5		112.5	0.70		
5	c16-000		1.60		0.0	100.0	-	0.00	308	
6	c16-375				37.5		23.4	0.23		
7	c16-750				75.0		46.9	0.47		
8	c16-1125				112.5		70.3	0.70		
9	c23-000		2.30		0.0	69.6	-	0.00	286	
10	c23-375				37.5		16.3	0.23		
11	c23-750				75.0		32.6	0.47		
12	c23-1125				112.5		48.9	0.70		
13	b10-000	Bending	1.00		0.0	160.0	-	0.00	286	25.7
14	b10-375				37.5		37.5	0.23		
15	b10-750				75.0		75.0	0.47		
16	b10-1125				112.5		112.5	0.70		
17	b16-000		1.60		0.0	100.0	-	0.00	320	
18	b16-375				37.5		23.4	0.23		
19	b16-750				75.0		46.9	0.47		
20	b16-1125				112.5		70.3	0.70		
21	b23-000		2.30		0.0	69.6	-	0.00	320	
22	b23-375				37.5		16.3	0.23		
23	b23-750				75.0		32.6	0.47		
24	b23-1125				112.5		48.9	0.70		

outer tube to attach strong side beams as shown in Fig. 3. These connections are fixed by high strength bolted joint. Thus, pure bending moment is applied to the specimens by symmetrically four point loading action.

Twelve biaxial strain gauges are also arranged on the same positions of the centric loading test. Three displacement transducers are arranged to measure curvature of specimens.

3 RESULTS AND DISCUSSIONS

3.1 *Failure modes*

Figure 4 shows typically failure modes of centric loading tests specimens. Local buckling of outer tube being associated with shearing failure of in-filled concrete can be found. Furthermore, inner tube's failure is shown in Fig. 5. It can be also observed that local buckling of inner tube is due to shearing failure of in-filled concrete.

Figures 6 and 7 show failure modes of pure bending test. Local buckling of outer tube in compressive region can be found. On the contrary, outer tube's cracking can be also observed near the welded connecting plate in tensile region. This is because local bending moment is observed owing to supporting of inner tube in compressive region as illustrated in Fig. 8.

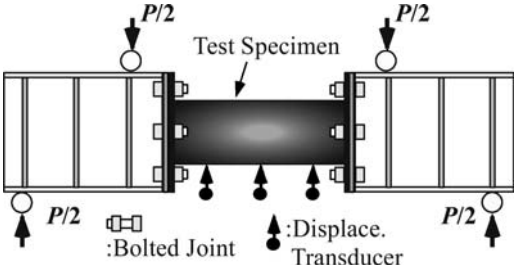

Figure 3. Pure bending test.

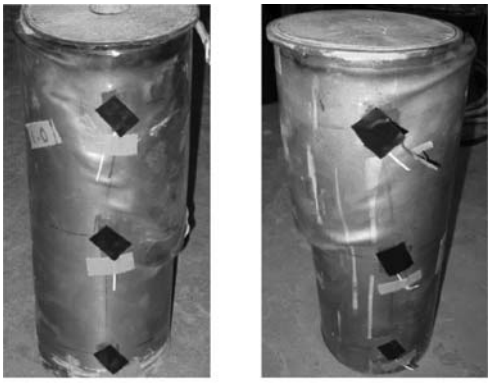

Figure 4. Failure modes of outer tube.

Comparing the failure zones observed in the centric compressive test with those in the pure bending tests, the former were over almost whole member length, while the latter were localized at the member end. It is noted, therefore, that sufficient stiffening at the end portion should be important in case under bending action.

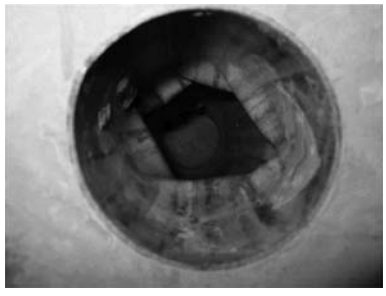

Figure 5. Failure mode of inner tube (c23-750).

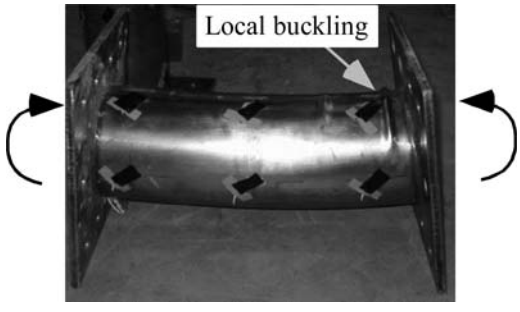

Figure 6. Local buckling of compressive region.

Figure 7. Cracking of tensile region.

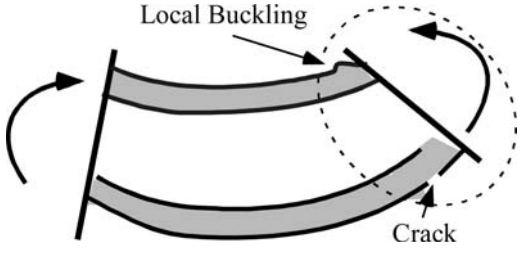

Figure 8. Local moment due to sustaining of inner tube.

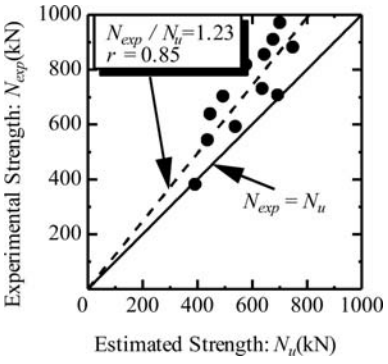

Figure 9. Experiments and estimations (CC test).

3.2 *Ultimate strengths*

3.2.1 *Centric compressive loading test*

Axially loading capacities (N_u) of CFDST is expressed as below

$$N_u = N_{uso} + N_{usi} + N_{uc} \tag{1}$$

where N_{uso}, N_{usi} and N_{uc} are individually axial strengths of outer tube, inner tube and in-filled concrete, namely,

$$N_{uso} = A_{so} \cdot f_y \quad , \quad N_{usi} = A_{si} \cdot f_y \quad , \quad N_{uc} = A_c \cdot f_c'$$

where A_{so}, A_{si} and A_c: cross sectional areas of outer tube, inner tube and in-filled concrete, f_y: yielding point of steel tubes and f_c': concrete cylinder strength, respectively.

Figure 9 and Table 2(a) compare experimental strengths with estimated values. Experimental results agreed with or larger than the estimations, in which the ratio N_{exp}/N_u equivalent to 1.23 and correlation factor is 0.85. Whereas, Fig. 10 shows the relationship between normalized experimental axial strength (N_{exp}/N_u) and inner-to-outer diameter ratio (D_i/D_o). The normalized axial strength N_{exp}/N_u gradually decreased as the ratio D_i/D_o increased. This fact suggested that confinement effect decreased as D_i/D_o increased. The detailed confined effect under centric loading action is given later.

3.2.2 *Pure bending test*

When neutral axis locates inner tube, pure bending strength (M_u) can be obtained as below

$$M_u = \frac{2k f_c'}{3}\left(R_o^3 \cos^3\alpha_o - R_o^3 \cos^3\alpha_i\right) + 4 f_{sy}\left(R_o^2 t_o \cos\alpha_o + R_i^2 t_i \cos\alpha_i\right) \tag{2}$$

where k: reduction factor of concrete (=0.85), R_o, R_i: radii of outer and inner tubes, t_o, t_i: thicknesses of inner and outer tubes. Two degrees, α_o and α_i, between neutral axis and the bottom of compressive zone can be obtained when N_u is equivalent to zero, namely,

$$N_u = \frac{\pi k f_c'}{2} R_o^2\left(1 - \frac{2\alpha_o}{\pi} - \frac{\sin 2\alpha_o}{\pi}\right) - \frac{\pi k f_c'}{2} R_i^2\left(1 - \frac{2\alpha_i}{\pi} - \frac{\sin 2\alpha_i}{\pi}\right) - 4 f_{sy}\left(R_o t_o \alpha_o + R_i t_i \alpha_i\right) \tag{3}$$

The relationship between testing results and estimations is shown in Fig. 11. Experimental values are also good agreement with or larger than estimated ones by Eq. (2). Furthermore, Figure 12 shows the relationship between normalized pure bending strength (M_{exp}/M_u)

Table 2. Test results.

(a) Centric compressive(CC) test

No.	Tag.	$\frac{D_i}{D_o}$	Failure Mode	Axial Strength (kN) [1] Exp.	[2] Est.	[1]/[2]
1	c10-000	0.00	C	699.7	496.6	1.41
2	c10-375	0.23	C	635.0	450.3	1.41
3	c10-750	0.47	C	540.0	440.3	1.23
4	c10-1125	0.70	C	378.3	395.4	0.96
5	c16-000	0.00	C	815.4	580.9	1.40
6	c16-375	0.23	C	851.6	647.5	1.32
7	c16-750	0.47	C	728.1	639.6	1.14
8	c16-1125	0.70	C	589.0	541.9	1.09
9	c23-000	0.00	C	907.5	680.1	1.33
10	c23-375	0.23	C	968.2	704.6	1.37
11	c23-750	0.47	C	879.1	752.0	1.17
12	c23-1125	0.70	C	703.6	697.4	1.01

Note: C: Compressive failure of in-filled concrete

(b)Pure bending test(PB) test

No.	Tag.	$\frac{D_i}{D_o}$	Failure Mode	Bending Strength (kN m) [1] Exp.	[2] Est.	[1]/[2]
1	b10-000	0.00	BT	14.0	9.5	1.47
2	b10-375	0.23	BT	14.8	10.6	1.40
3	b10-750	0.47	BT	14.6	12.3	1.19
4	b10-1125	0.70	BT	13.1	12.7	1.03
5	b16-000	0.00	BT	19.5	16.2	1.20
6	b16-375	0.23	BT	21.6	17.6	1.23
7	b16-750	0.47	BT	23.4	20.0	1.17
8	b16-1125	0.70	BT	20.3	21.5	0.94
9	b23-000	0.00	BT	27.7	22.6	1.23
10	b23-375	0.23	BT	29.6	23.9	1.24
11	b23-750	0.47	BT	28.2	27.3	1.03
12	b23-1125	0.70	BT	32.5	30.2	1.08

Note:BT: Buckling and tensile crack of outer tube

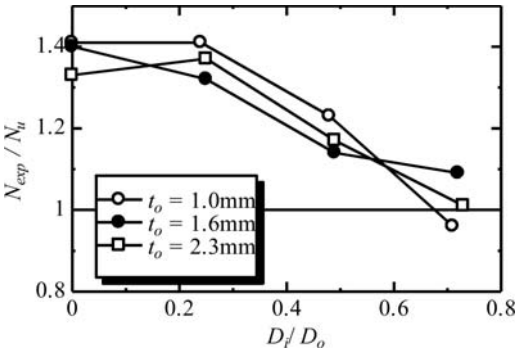

Figure 10. D_i/D_o and N_{exp}/N_u.

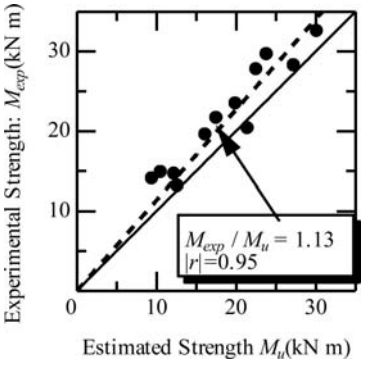

Figure 11. Experiments and estimations.

and D_i/D_o. It can be also found that M_{exp}/M_u decreased as D_i/D_o increased. This is because confined strength decreased as D_i/D_o increased. Obtained test results are similar to above-described centric loading results. Discussion on confined effect subjected to pure bending action is also given later.

3.2.3 *Comparison of two test results*

Increasing D_i/D_o, axial strength ratios N_{exp}/N_u similarly decreased owing to tube thickness as shown in Fig. 10. It can be seen, however, that the difference due to tube thickness for bending strength ratio M_{exp}/M_u as shown in Fig. 12. The reason why the difference may be that thick tubes were easy to rupture at their end under bending action.

3.3 *Deformabilities*

3.3.1 *Centric compressive loading test*

Figure 13 shows the relationship between normalized axial load and axial shortening, which are the ratio of axial displacement to specimen's height (H). The obtained initial stiffnesses up to 0.5% of axial shortening of CFDST agreed with that of CFT. However, the specimen, D_i/D_o of which is equal to 0.7, exhibited smaller deformability in comparison with the specimen with D_i/D_o being less than 0.47.

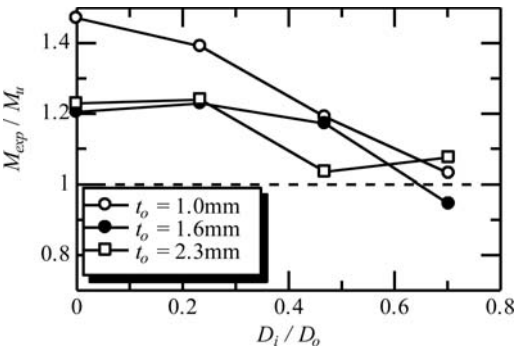

Figure 12. M_{exp}/M_u and D_i/D_o.

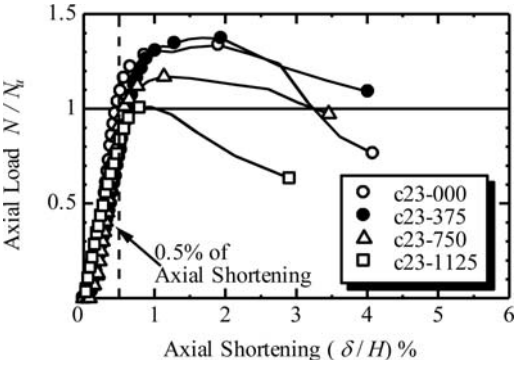

Figure 13. CC test.

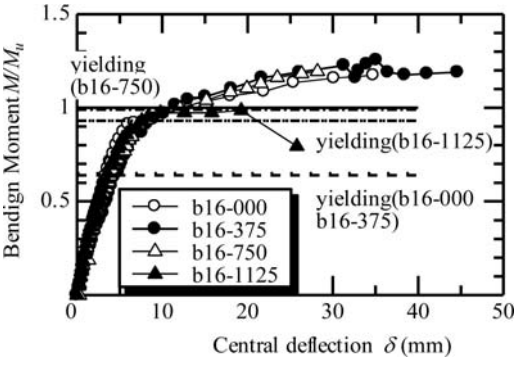

Figure 14. PB test.

3.3.2 *Pure bending test*

The relationship between normalized bending moment (M_{exp}/M_u) and central displacement is provided in Fig. 14, in which broken lines indicate yielding of each specimen. The bending deformability of CFDST specimens almost agree with that of CFT. However, maximum curvature of CFDST with $D_i/D_o = 0.7$ attains to 25 mm, which is the smallest value of all the specimens. This is due to the local bending moment observed at the sustaining of the end plate as described in Failure mode.

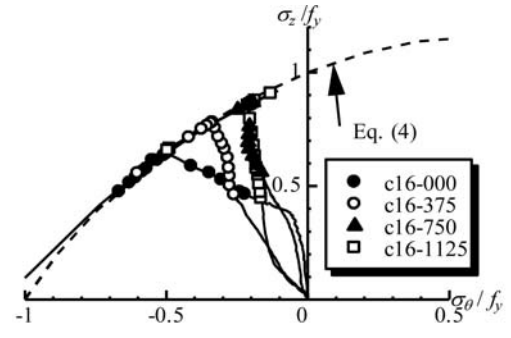

(a) CC test

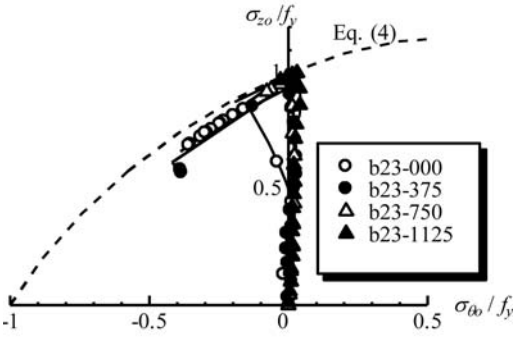

(b)PB test

Figure 15. Stress histories of outer tube.

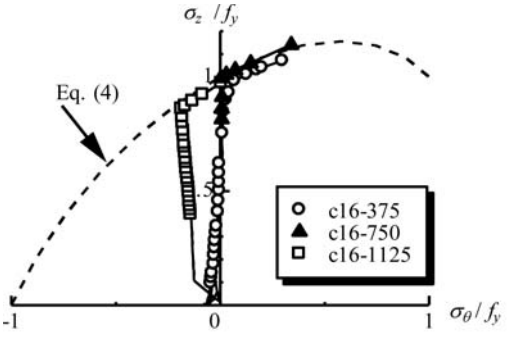

(a) CC test

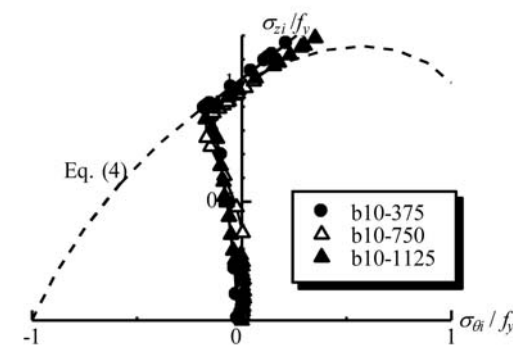

(b)PB test

Figure 16. Stress histories of inner tube.

3.3.3 *Comparison of two test results*

From the two test results, increasing the diameter-to-thickness ratio within 0.47, the deformabilites of two tests are good agreement with those of CFT. For the bending test specimens with largest $D_i/D_o = 0.70$, ultimate deformabilities can not be obtained owing to the local bending moment occurred near the bolted connection after peak behavior.

3.4 *Biaxial stress*

3.4.1 *Calculation of elasto-plastic stress*

When perfectly plastic material subjected to von Mises criterion is applied, yield condition under plane stress is expressed as

$$\sigma_z^2 - \sigma_\theta \cdot \sigma_z + \sigma_z^2 = f_y^2 \tag{4}$$

where σ_z, and σ_θ are axial and circumferential stresses, respectively.

When the tubes enter the elasto-plastic zone, the relationship between two increments of stress, $d\sigma_z$ and $d\sigma_\theta$, and those of strain, $d\varepsilon_z$and $d\varepsilon_\theta$, are expressed as

$$\begin{Bmatrix} d\sigma_z \\ d\sigma_\theta \end{Bmatrix} = \left\{ \frac{E}{1-\nu^2} \begin{pmatrix} 1 & \nu \\ \nu & 1 \end{pmatrix} - \frac{1}{S} \begin{bmatrix} S_1^2 & S_1 S_2 \\ S_1 S_2 & S_2^2 \end{bmatrix} \right\} \begin{Bmatrix} d\epsilon_z \\ d\epsilon_\theta \end{Bmatrix}$$

where S, S_1 and S_2 are expressed as below

$$S = s_z S_1 + s_\theta S_2 \quad ,$$

$$S_1 = \frac{E}{1-\nu^2}(s_z + \nu s_\theta) \quad ,$$

$$S_2 = \frac{E}{1-\nu^2}(s_\theta + \nu s_z)$$

then ν is Poisson's ratio, σ_z, σ_θ are deviatoric stresses of circumferential and axial directions. In this paper, compressive values are treated as positive.

3.4.2 *Comparison of test results*

The stress histories of outer tube under compression and bending-compression are shown in Fig. 15, x and y axes in which are divided into yielding stress f_y. Axial or bending-compression stress σ_z attaining to yield surface, circumferential stress (σ_θ) proceeded into tensile region. This fact can be explained in terms of volumetric dilatation of in-filled concrete. The tensile circumferential stress of the specimen c16-1125 under centric compression took place initially. This is because the test stub column swelled owing to the thinnest thickness between the two walls.

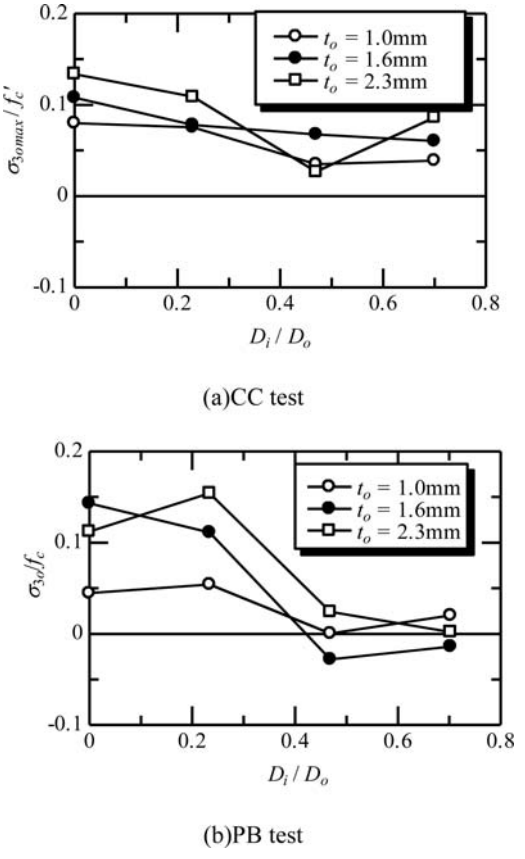

Figure 17. $\sigma_{\theta o}/f_c'$) and D_i/D_o.

Whereas, stress conditions of inner tube are provided in Fig. 16. The circumferential stress arose toward compression after yielding of axial stress or bending-compression stress, σ_z. This is also due to the volumetric dilatation being caused by in-filled concrete.

3.5 *Confined stress intensity*

Confined stress induced by outer tube is expressed as

$$\sigma_{3o}=\frac{2t_o\sigma_{\theta o}}{D_o}$$

where $\sigma_{\theta o}$ is confined strength when maximum load is obtained.

Figure 17 shows the relationship between normalized confined strength being divided into concrete cylinder strength ($\sigma_{\theta o}/f_c'$) and the ratio D_i/D_o. It should be noted that D_i/D_o increases as $\sigma_{\theta o}/f_c'$ decreases. This observation also leads to a conclusion that D_i/D_o increases as both axial and pure bending strength decreases as described in *3.2 Ultimate strength*.

4 CONCLUSIONS

Centric compressive loading and pure bending tests of each twelve specimens of CFDST under two testing parameters, D_o/t_o and D_i/D_o, were conducted respectively. Confined strength of their tests are mainly discussed. The main results obtained are shown below.

- Observed failure mode of centric compressive loading test is local buckling of double tubes associated with shearing failure of in-filled concrete. That of bending test is local buckling and cracking of outer tube in compression and tension due to bending.
- Strengths obtained by two tests are identical or larger than the estimations. However, inner-to-outer diameter ratio, D_i/D_o, increased as both strengths decreased
- Deformabilities of CFDST with D_i/D_o being less than 0.47 obtained by two tests are almost similar to those of CFT.
- Circumferential stress of outer tube proceeded into tensile region after axial stress attains to yielding surface in bending-compression or centric loading. Whereas, that of inner tube proceed into compressive region after yielding.
- Confined strength is meaningfully affected by inner-to-outer diameter ratio D_i/D_o.

ACKNOWLEDGEMENT

The authors thank Prof. Keiichiro Sonoda for a sincere help to this study.

REFERENCES

Architectural Institute of Japan (2002), Standard for structural calculation of steel reinforced concrete structures. (in Japanese)

Wei, S., Mau, S.T., Vipulanandan, C. & Mantrala, S. K.1995a. Performance of new sandwich tube under axial loading: experiment. *Journal of Structural Engineering* 121(12): 1806–1814.

Wei, S., Mau, S.T., Vipulannandan, C. & Mantrala, S. K.1995b. Performance of new sandwich tube under axial loading: analysis. *Journal of Structural Engineering* 121(12): 1815–1821.

Zhao, X. L., Grzebieta, R. H. & Elchalakani, M. 2002. Tests of concrete-filled double skin CHS composite stub columns. *Steel & Composite Structures* 2(2): 129–142.

Zhao, X. L. & Han, L. H. 2006. Double skin composite construction, *Progress in Structural Engineering and Materials* 8(3): 93–102.

Zhao, X. L., Tong, L. W. & Wang, X. Y. 2010. CFDST stub columns subjected to large deformation axial loading, *Engineering Structures* 32: 692–703.

Uenaka, K., Kitoh, H. & Sonoda, K. 2008. Concrete filled double skin tubular members subjected to bending, *Steel & Composite Structures* 8(3): 297–312.

Uenaka, K., Kitoh, H. & Sonoda, K. 2010. Concrete filled double skin circular stub columns under compression, *Thin-Walled Structures* 48(1):19–24.

Uenaka, K. & Kitoh, H. 2011. Mechanical behavior of concrete filled double skin tubular circular deep beams, *Thin-Walled Structures* 49(2): 256–263.

Tubular Structures XIV – Gardner (Ed.)
© 2012 Taylor & Francis Group, London, ISBN 978-0-415-62137-3

Design of concrete filled tubular CHS T-joints under in-plane bending

J. Chen & W.L. Jin
College of Civil Engineering and Architecture, Zhejiang University, Hangzhou, China

Y. Ye & X.H. Sheng
Zhejiang Electric Power Design Institute, Hangzhou, China

ABSTRACT: Experimental investigation was conducted to study the ultimate strengths of concrete-filled tubular CHS (Circular Hollow Section) T-joints under in-plane bending loading. The main chord was loaded in compression while the brace was under in-plane bending loading. Three concrete filled steel T-joints were tested. The failure modes and ultimate strengths of test specimens were obtained. Test results indicate that the filled concrete has significant effect on the ultimate strength of T-joints. Design equations for the concrete-filled T-joints under in-plane bending were proposed. Width of weld, contribution of concrete in compression and variation of thickness at the chord punch shear face were considered in the proposed equations. It is shown that predictions obtained from the proposed equations are generally accurate compared with test results. In addition, simplified equation was also proposed.

1 INTRODUCTION

Tubular truss structures have been widely used in buildings, bridges and offshore structures for their pleasing appearance, light weight, easy fabrication and rapid erection. Concrete-filled steel tubes are increasingly used in the truss structures as the main chords due to its excellent performance in compression. In this type of structures, the chord of the joint is concrete-filled steel tube while the brace is steel tube. There are many researches focused on the behaviour and strengths of concrete-filled steel tubular joints. Tebbett et al. (1979) tested grouted T-joints used in offshore structures. Packer (1995) tested concrete-filled T-, X- and gapped K-connections. Feng & Young (2009)(2010) conducted experiment investigation on concrete-filled stainless steel tubular T- and X-joints.

Experimental investigation indicates that filling the circular hollow section chord member with concrete could effectively improve the strength of the joints. Therefore design equations specified in current AISC (2010) and CIDECT Standard (2000) for hollow steel tubular joint may not applicable. Design methods for concrete-filled hollow structural section (HSS) steel joints are proposed by Packer et al. (1992). However, those design method are only for the square and rectangular section joints. There is still lack of design method for the concrete-filled steel circular hollow section joints. The intersecting curve of brace and chord for circular section joint is a space curve which makes the calculation of circular section joint more complex than that of square and rectangular section. Therefore, new design method should be proposed for concrete-filled tubular CHS joints. In this study, design method was proposed for concrete-filled T- joints under in-plane bending.

2 SUMMARY OF EXPERIMENTAL INVESTIGATION

The test program presented in Chen et al. (2010) provided experimental ultimate loads and failure modes of circular hollow section concrete-filled steel tubular joints under in-plane bending. The T-joints specimens were fabricated from circular hollow section steel tubes. Self-compacting concrete (SCC) was filled in the concrete-filled steel joints. In total three concrete-filled steel T-joints were tested. The dimensions and geometric ratios of the joints were given in Table 1.

Tensile coupon tests were conducted to obtain the steel material properties of the test specimens.

Table 1. Measured dimension of test specimens.

	Chord			Brace		
Specimens	Steel	D (mm)	T (mm)	Steel	d (mm)	t (mm)
CS219-159	20#	219	8.42	Q345	159	5.60
CS219-168	20#	219	8.43	Q345	168	7.82
CS219-203	20#	219	8.42	Q345	203	7.79

D: Outer diameter of chord; T: Wall thickness of chord; d: Outer diameter of brace; t: Wall thickness of brace.

Table 2. Tensile coupons test results.

Steel	Nominal thickness (mm)	Measured			
		E (GPa)	f_y (MPa)	f_u (MPa)	ε_f (%)
20#	8.4	200.1	325	480	29.5
Q345	5.6	199.0	330	485	34.0
Q345	7.8	203.7	375	530	30.0

Table 3. Ultimate strengths and failure mode of test specimens.

Specimens	M_{TEST} (kN · m)	Failure mode
CS-219-159	72.9	Chord punch shear yielding & brace yielding
CS-219-168	99.4	Chord punch shear yielding
CS-219-203	157.7	Chord punch shear yielding

Table 4. Comparison of design strengths with test results.

Specimens	M_{TEST} (kN · m)	M_{AISC} (kN · m)	M_{CIDECT} (kN · m)
CS-219-159	72.9	41.4	40.0
CS-219-168	99.4	46.3	44.7
CS-219-203	157.7	67.5	65.3

The measured material properties obtained from the coupon tests are summarized in Table 2. The compressive strength (f_{cu}) and elastic modulus (E_c) obtained on 150-mm cubes at 28 days were 56.0 MPa and 37420 MPa, respectively. The details of the experimental investigation are presented in Chen et al. (2010). The experimental ultimate loads (M_{TEST}) and failure mode obtained from the column tests are shown in Tables 3.

The test specimens are labeled such that the chord type, outer diameter of chord, and outer diameter of brace could be identified from the label. For example, the labels "CS-219-203" define the specimens as follow:

- The first two letter indicate that the type of the chord, where the prefix "CS" refers to Concrete-filled Steel tube.
- The following three digits indicate the nominal outer diameter of the chord of specimen in mm.
- The last three digits are the nominal outer diameter of the brace of specimen in mm.

The design strengths calculated using current AISC Standard (M_{AISC}) and CIDECT Standard (M_{CIDECT}) are compared with test results in Table 4. It is shown that the design strengths are very conservative. It should be noted that the AISC standard and CIDECT standard are for steel joints instead of concrete-filled steel joints. Therefore, design equations for concrete-filled steel joints are needed.

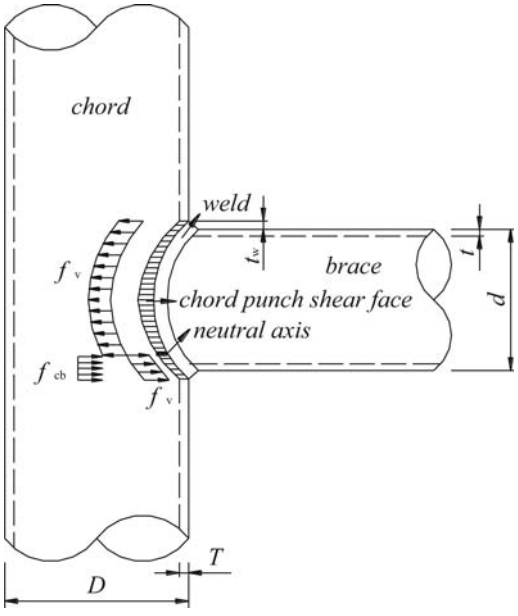

Figure 1. Analytical model of concrete-filled tubular T joint under in-plane bending.

3 PROPOSED DESIGN METHODS

3.1 *Design assumptions*

The analytical mode is presented in Fig. 1. The following design assumptions are made in the proposed design method:

1) Full plastic deformation developed for steel at the chord-brace intersecting curve.
2) An equivalent uniform compressive stress distribution (stress block) is used to replace the more exact concrete stress distribution for concrete in compressive zone.
3) Tensile strength of concrete is neglected.

3.2 *Concrete strengths*

The load area of concrete in compression is surrounded by additional concrete. Packer (1995) has recommended the ratio of bearing stress to the crushing strength of concrete in square or rectangular section concrete-filled joints. It should be noted that the concrete are filled in full length of the chord in this study. In addition, the loaded area of circular section joints mainly near the crown of the chord and is much smaller than the loaded area of square or rectangular section joints. Therefore, the concrete strength is taken as $f_{cb} = 79\sqrt{f_c}\ le\ 5f_c$, as suggested by CEP-FIP(1993). For concrete strength lower than 250 Mpa, $f_{cb} = 5f_c$ is

Figure 2. Crack on the chord of specimen CS-219-203.

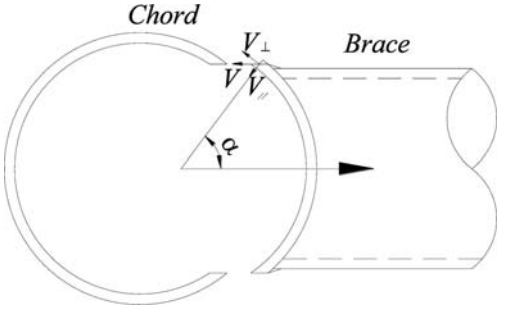

Figure 3. Shear force on the chord punch shear face.

used in the following derivative. f_c is the compressive strength of the filled concrete in the chord.

3.3 *Width of weld*

The crack on the chord (Fig. 2) indicates that width of the weld should be considered in the design. However, the width of the weld around the brace is not constant. Therefore, an effective diameter of the brace (d_e) is proposed in this study and could be calculated as Eq. (1).

$$d_e = d + \frac{4t_w}{\pi} \tag{1}$$

where d is the outer diameter of the brace; t_w is the width of weld at the crown point of the chord.

3.4 *Thickness variation at the chord punch shear face around the brace*

The chord punch shear face around the brace is the face in the chord intersected by the brace outer perimeter (+weld width) and is parallel to the axis of brace. The thickness of the chord punch shear face around the brace varied along the chord-brace intersecting curve, as shown in Fig. 3. The thickness of the chord punch shear face equals to the wall thickness of the chord at the crown point of the chord while it is much thicker than the wall thickness of the chord at the saddle point of the chord. In order to consider the thickness variation of the chord punch shear face, the shear force V at the chord punch shear face is decomposed into $V_{//}$ and $V_\perp$ as shown in Fig. 3, where $V_{//} = V\cos\alpha$ is the force vertical to the chord radius and $V_\perp = V\sin\alpha$ is the force parallel to the chord radius. Thus there are two possible failure modes, $V_{//}$ reach maximum shear force or $V_\perp$ reach maximum tensile force.

When shear failure occurs, Eq. (2) and Eq. (3) should be satisfied:

$$V_\perp \le f_y T \frac{d_e}{2} d\theta \tag{2}$$

and

$$V_{//} = f_v T \frac{d_e}{2} d = \frac{1}{\sqrt{3}} f_y T \frac{d_e}{2} d\theta \tag{3}$$

where f_y is the yield strength of the chord, f_v is the shear yield strength of the chord; T is the wall thickness of the chord.

Thus Eq. (4) could be obtained:

$$\frac{V_\perp}{V_{//}} = \tan\alpha \le \sqrt{3} \tag{4}$$

α should be $\le \pi/3$ and Eq. (5) could be obtained:

$$\sin\alpha = \beta\sin\theta \le \frac{\sqrt{3}}{2} \tag{5}$$

where $\beta = d_e/D$; D is the outer diameter of the chord.

The solutions of Eq. (5) are shown in (a) and (b):

(a) $\beta \le \frac{\sqrt{3}}{2}$; (b) $\beta \ge \frac{\sqrt{3}}{2}$ and $\theta \le \arcsin\left(\frac{\sqrt{3}}{2\beta}\right)$

When conditions (a) or (b) is satisfied, shear failure will occur, and the shear force at the chord punch shear face (V) could be calculated using Eq. (6):

$$V = \frac{V_{//}}{\cos\alpha} = \frac{f_v T d_e d\theta}{2\cos\alpha} = \frac{f_v T d_e d\theta}{2\sqrt{1-(\beta\sin\theta)^2}} \tag{6}$$

When tensile failure occurs, Eq. (7) and Eq. (8) should be satisfied:

$$V_\perp = f_y T \frac{d_e}{2} d\theta \tag{7}$$

$$V_{//} \le f_v T \frac{d_e}{2} d\theta = \frac{1}{\sqrt{3}} f_y T \frac{d_e}{2} d\theta \tag{8}$$

Thus Eq.(9) could be obtained:

$$\frac{V_\perp}{V_{//}} = \tan\alpha = \frac{f_y}{\tau} \ge \sqrt{3} \tag{9}$$

α should be $\geq \pi/3$ and Eq. (10) could be obtained:

$$\sin\alpha = \frac{d_e \sin\theta}{D} = \beta \sin\theta \geq \frac{\sqrt{3}}{2} \tag{10}$$

The solution of Eq. (10) is shown in (c) and (d):

(c) $\arcsin\left(\frac{\sqrt{3}}{2\beta}\right) \leq \theta \leq \pi - \arcsin\left(\frac{\sqrt{3}}{2\beta}\right)$

(d) $\beta \geq \frac{\sqrt{3}}{2}$

When conditions (c) and (d) are satisfied, tensile failure will occur. The shear force at the chord punch shear face (V) could be calculated using Eq. (11):

$$V = \frac{V_\perp}{\sin\alpha} = \frac{f_y T d_e d\theta}{2\beta \sin\theta} \tag{11}$$

From Eq. (2)–(11), it could be seen that the whole chord punch shear face failed in shear when $\beta \leq \sqrt{3}/2$. When $\beta \geq \sqrt{3}/2$, part of the chord punch shear face (near the crown point of the chord) failed in shear while another part (near the saddle point of the chord) failed in tensile.

3.5 *Position of neutral axis*

The thickness variation at the chord punch shear face around the brace is not considered in determining the position of neutral axis (Line AB in Fig. 3) for simplicity. The position of neutral axis could be determined using Eq. (12) and (13) based on the assumptions in 3.1, as illustrated in Fig. 4.

$$f_v \pi d_e T \frac{2\theta_o}{2\pi} = f_v \pi d_e T \frac{(2\pi - 2\theta_0)}{2\pi} + 5 f_c \left(\pi \frac{d_e^2}{4} \frac{(2\pi - 2\theta_0)}{2\pi} + \frac{d_e^2}{4} \sin\theta_0 \cos\theta_0 \right) \tag{12}$$

$$\theta_0 = \frac{P_{ps} + 5P_c\left(1 + \frac{\sin\theta_0 \cos\theta_0}{\pi}\right)}{2P_{ps} + 5P_c}\pi \tag{13}$$

where $P_{ps} = f_v \pi d T$; $P_c = f_c \pi \frac{d^2}{4}$

The distance (y) between the central of brace section (O) and action point of concrete and steel combined compression force (C) could be calculated as Eq. (14):

$$y = \frac{d_e}{2} \frac{\sin\theta_0}{\theta_0} \left(1 + \frac{5}{6} \frac{f_c}{f_v} \frac{d_e}{T} \sin^2\theta_0\right) \tag{14}$$

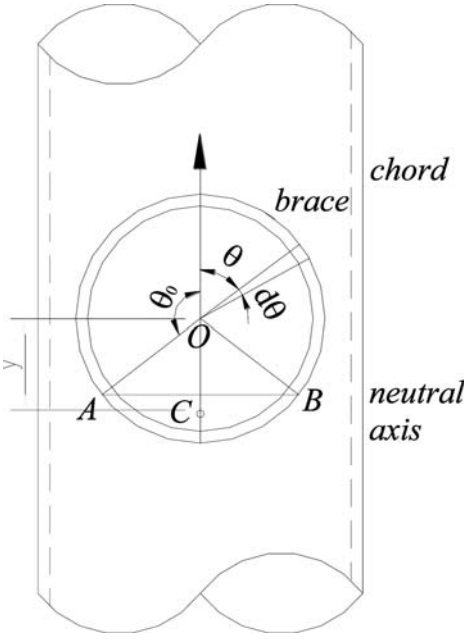

Figure 4. Position of neutral axis.

3.6 *Moment capacity*

When $\beta \leq \sqrt{3}/2$ the chord punch shear face failed in shear and the moment capacity could be calculated using Eq. (15).

$$M_{ps} = 2\int_0^{\theta_0} \frac{f_v T d_e}{2\sqrt{1-(\beta\sin\theta)^2}} d\theta \left(\frac{d_e}{2}\cos\theta + y_0\right) = \frac{1}{2}\left(\frac{1}{\beta}\arcsin(\beta\sin\theta_0) + \xi F(\theta_0|\beta)\right) f_v T d_e^2 \tag{15}$$

When $\beta \geq \sqrt{3}/2$, part of the chord punch shear face failed in tensile and another part failed in shear, thus the moment capacity could be calculated using Eq. (16).

$$M_{ps} = 2\int_0^{\varphi} \frac{f_v T d_e}{2\sqrt{1-(\beta\sin\theta)^2}} d\theta \left(\frac{d_e}{2}\cos\theta + y_0\right) + 2\int_{\varphi}^{\pi-\varphi} \frac{\sqrt{3} f_v T d_e}{2\beta\sin\theta} d\theta \left(\frac{d_e}{2}\cos\theta + y_0\right) + 2\int_{\pi-\varphi}^{\theta_0} \frac{f_v T d_e}{2\sqrt{1-(\beta\sin\theta)^2}} d\theta \left(\frac{d_e}{2}\cos\theta + y_0\right)$$

$$= \frac{1}{2}\left(\frac{1}{\beta}\arcsin(\beta\sin\theta_0) + \xi\left(2F(\varphi|\beta) - F((\pi-\theta_0)|\beta) + \frac{\sqrt{3}}{\beta}\ln\left(\frac{1+\sqrt{1-\left(\frac{\sqrt{3}}{2\beta}\right)^2}}{1-\sqrt{1-\left(\frac{\sqrt{3}}{2\beta}\right)^2}}\right)\right)\right) f_v T d_e^2 \tag{16}$$

where $\phi = \arcsin\left(\frac{\sqrt{3}}{2\beta}\right)$

The design strengths calculated using the measured geometry sizes and material properties are compared

Table 5. Comparison of design strengths with test results.

Specimens	M_{TEST} (kN · m)	M_{ps} (kN · m)	M_{sim} (kN · m)
CS-219-159	72.9	89.1	84.6
CS-219-168	99.4	102.3	93.1
CS-219-203	157.7	155.9	134.7

with the test results in Table 5. It is shown that the design strengths agree with the test results well for specimens CS-219-168 & CS-219-203. For specimen CS-219-159, the design strength is unconservative. The reason is that the brace of specimen CS-219-159 yielded and the load was unable to increase during the test. Therefore, the ultimate strength of the chord is not fully developed.

3.7 *Simplified design method*

It is shown that the proposed method using Eqs. (2)–(16) is very cumbersome. Therefore, a simplified design method was also proposed. The variation of the thickness at the chord punch shear face is not considered in the simplified model. In addition, the distance of the central of brace to the action point of combined force of concrete and steel in compression (y) is assumed to be $d_e/2$. Thus the ultimate strength could be calculated using Eq. (17) as below. The design strengths (M_{sim}) are presented in Table 5. It is shown that the design strengths calculated using the proposed equations are conservative except for specimen CS-219-159.

$$M_{sim} = 2\int_0^{\theta_0} f_v \pi d_e T \frac{d\theta}{2\pi}\left(\frac{d_e}{2}\cos\theta + \frac{d_e}{2}\right) = \frac{1}{2\sqrt{3}}\left(\sin\theta_0 + \theta_0\right) f_y {d_e}^2 T \tag{17}$$

4 CONCLUSIONS

Design equations for the concrete-filled steel tubular T-joints under in-plane bending were proposed. The width of weld, contribution of concrete in compression, variation of thickness at the chord punch shear face were considered. It is shown that the proposed design equations are generally accurate. In addition, simplified design equation is also proposed. The design predictions from the simplified equation are generally conservative.

ACKNOWLEDGMENTS

The research work described in this paper was supported by a grant of National Natural Science Foundation of China (51108409) and research projects from Science and Technology Department of Zhejiang Province (2011C23102) and (2011R10064).

NOTATION

The following symbols are used in this paper:

d = outer diameter of brace;
d_e = effective outer diameter of brace;
D = outer diameter of chord;
E = Young's modulus;
E_c = Young's modulus of concrete;
f_{cu} = concrete compressive strength, by 150-150-150 cubic specimens;
f_c = crush strength of strength, by cylinder tests;
f_{cb} = maximum bearing stress;
f_y = yield stress of steel;
f_u = ultimate stress of steel;
f_v = shear strength of steel;
M_{AISC} = ultimate strength of specimen predicted using AISC standard;
M_{CIDECT} = ultimate strength of specimen predicted using CIDECT standard;
M_{FEA} = ultimate strength of specimen obtained from finite element analysis;
M_{PS} = ultimate strength of specimen predicted using proposed equations;
M_{Sim} = ultimate strength of specimen predicted using simplified equations;
M_{TEST} = ultimate strength of specimen obtained from test results;
t = wall thickness of brace;
t_w = width of weld at the crown point of the chord;
T = wall thickness of chord;
V = shear force at the chord punch shear face;
$V_{\parallel}$ = force vertical to the chord radius on the chord punch shear face;
$V_{\perp}$ = force parallel to the chord radius on the chord punch shear face;
y = distance between the central of brace section and action point of concrete and steel combined compression force;
β = ratio of brace outer diameter to chord outer diameter;
ε_f = elongation (tensile strain) after fracture based on gauge length of 50 mm.

REFERENCES

AISC. (2010) *Specification for structural steel buildings*. American Institution of Steel Construction (AISC), ANSI/AISC 360-10, Chicago, Illinois, 2010.

CEP FIP (1993) Comite Euro-International du Beton. *CEB-FIP Model Code 1990 (Concrete Structures)*. London: Thomas Telford.

Chen J., Chen J., Jin W.L. (2010) Behavior of concrete-filled tubular T-joints under in-plane bending cyclic loading. *Proceedings of 11th International Symposium on Structural Engineering*. Guangzhou, China. 519–524.

Feng R., Young B. (2008) Tests of concrete-filled stainless steel tubular T-joints. *Journal of Constructional Steel Research*. Vol. 64(11), 1283–1293.

Feng R., Young B. (2009) Behavior of concrete-filled stainless steel tubular X-joints subjected to compression. *Thin-Walled Structures*. Vol. 47(2), 365–3740.

Packer J.A., Wardenier J., Kurobane Y., Dutta D., Yeomans N. (1992) *Design Guide for RHS Joints Under Predominantly Static loading*. Verlag TUV Rheinland, Cologne, Germany.

Packer J A. (1995) Concrete-filled HSS connections. *Journal of Structural Engineering-ASCE*. Vol. 121(3), 458–467.

Tebbett I.E., Beckett C.D., Billington C.J. (1979) The punching shear strength of tubular joints reinforced with a grouted pile. *Proceedings of offshore technology conference, offshore technology conference association*. Houston, Texas, 915–921.

Zhao, X.L., Herion, S., Packer, J.A., Puthli, R.S., Sedlacek, G., Weynand, K., Wardenier, J., Wingerde, A. van and Yeomans, N. (2001), *Design guide for circular and rectangular hollow section joints under fatigue loading*, Verlag TUV Rheinland GmbH, Cologne, Germany.

Tubular Structures XIV – Gardner (Ed.)
© 2012 Taylor & Francis Group, London, ISBN 978-0-415-62137-3

Research on the shear transfer mechanism of CFT panel zone

Jiansheng Fan, Xi Cheng & Hui Zhou
Key Laboratory of Civil Engineering Safety and Durability of the Ministry of Education, Dept. of Civil Engineering, Tsinghua Univ, Beijing, China

ABSTRACT: Concrete-filled Tube panel zone behavior is studied in theory. Deformation conversion method that using length changes of the diagonals to calculate the shear angle is derived in both two-dimensional and three-dimensional occasions. Trilinear model for steel tube and elastic-perfectly plastic model are adopted to simulate the panel zone behavior. Based on reasonable shear transfer mechanism assumption, a four-line model is set up by superposition method to calculate the capacity and deformation. The theory is promoted to three-dimensional occasions and establishes contacts between planar and spatial parameters.

1 INTRODUCTION

1.1 *Research background*

Composite tubular connections are widely used in building structures (Kurabane et al. 2004). Shear capacity is one of the main elements of the composite connection design. Technical specification for structures with concrete-filled rectangular steel tube members (2004) shows how to calculate shear capacity of composite plane connections with internal diaphragm. However, with further research, we find that it is inaccurate to follow the existing code. Besides, earthquake always shakes the buildings with bi-directional load. Actually there are little studies on 3D composite connections.

1.2 *Research status*

Normally, during frame structure design, connections are substituted by simply rigid or swing joint. However in order to evaluate a structure more accurately, further features of connections should be take into account. Based on the tests, Rassati & Leon (2004) developed the component modeling of partially restrained composite joints under cyclic and dynamic loading as shown in Figure 1.

For the Spring 1, a variety of models have been put forward. Qin (2006) and Xu (2008) studied CFT planar connections and modified the design formulas. Kanatani (1987) studied on concrete filled RHS column to H-beam connections. Peng (2001), Cheng (2000) and Ricles (2004) also did a lot on CFT column to beam connections. In terms of the shear capacity, all these models use superposition method including both steel tube and core concrete. Von Mises criteria is applied to assess the stress state of steel tube, in contrast, there is no uniform method to calculate the core concrete.

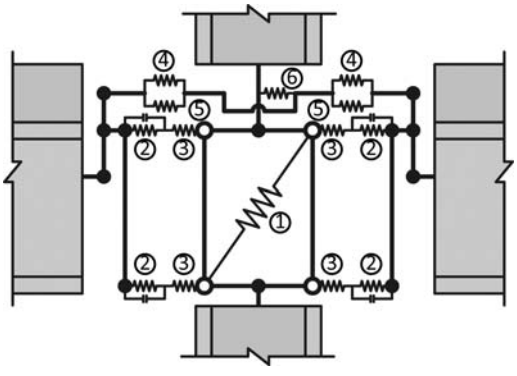

Figure 1. Component modeling for planar connections.

On balance, though lots of research has been done, the shearing transfer mechanism is still puzzled. It is not able to calculate the behavior of panel zone precisely due to a lack of rational theory model.

2 DEFORMATION CALCULATION

2.1 Deformation in plane connections

For plane connections under unidirectional shear loading case, square panel zone changes into parallelogram as shown in Figure 2. Considering cyclic loading, the direction of the parallelogram is changing. Therefore, if we lay displacement gauges along the diagonal to test the relative displacement of the panel zone, we can obtain the shear deformation using Equation 1. Some

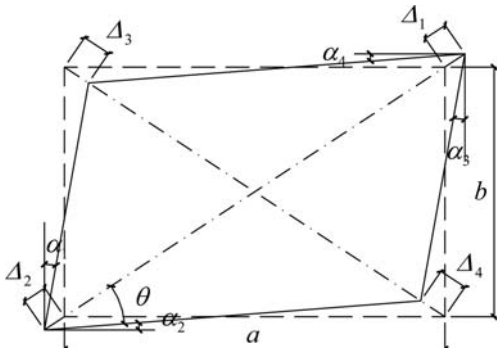

Figure 2. Schematic diagram for 2D shear deformation.

numberings of the accessory equations are neglected for short.

$$\gamma = \alpha_1 + \alpha_2 = \bar{X}\frac{\sqrt{a^2+b^2}}{ab} \tag{1}$$

$$\bar{X} = \frac{\left|\Delta_1 + \Delta_2\right| + \left|\Delta_3 + \Delta_4\right|}{2}$$

$$\sin\theta = \frac{b}{\sqrt{a^2+b^2}}, \quad \cos\theta = \frac{a}{\sqrt{a^2+b^2}}$$

$$\alpha_1 = \alpha_3 = \frac{\bar{X}}{b}\cos\theta, \quad \alpha_2 = \alpha_4 = \frac{\bar{X}}{a}\sin\theta$$

In the above formulas, symbol a stands for the width of the panel zone and b stands for the height. $\Delta_1 + \Delta_2$ and $\Delta_3 + \Delta_4$ are the length changing of the two diagonals. Other symbols' meaning can be comprehended from Figure 2.

Based on the loading conditions in the test (Fig 3), shear force of the panel zone can be calculated by Equation 2.

$$Q_j = \frac{2Q_b L_b}{H_b - t_{bf}} - Q_c = \frac{2Q_b L_b}{H_b - t_{bf}} - \frac{Q_b L}{H} \tag{2}$$

In this formula (2), Q_j stands for the shear force, Q_b stands for the vertical loading at the beam and Q_c stands for the reaction force at end-column. The other symbols are shown in Figure 3.

2.2 *Deformation in 3D connections*

For three-dimensional case, the situation is much more complicated. When subjected by bi-directional shear force, the panel zone is changed into parallelograms in both two directions. Overall, a cuboid is changed into a parallelepiped while ∠AOB retains right angle as shown in Figure 4. Similar with the plane occasion, we can use the displacement gauge to measure relative displacement of diagonals $\Delta_1 + \Delta_2$, $\Delta_3 + \Delta_4$,

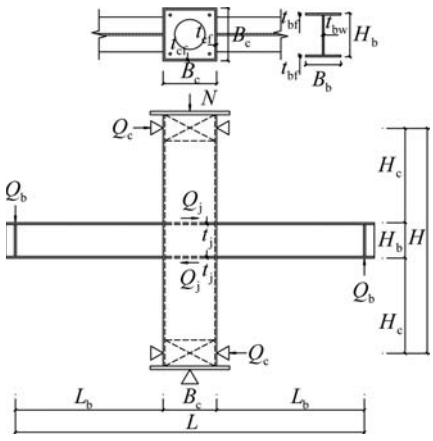

Figure 3. Loadcase for plane connections.

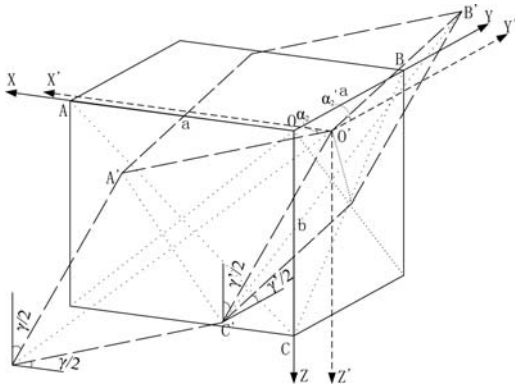

Figure 4. Schematic diagram for 3D shear deformation.

and $\Delta_1' + \Delta_2'$, $\Delta_3' + \Delta_4'$. In this way, we can calculate the shear angle of plane1 & 2 by Equation 3 & 4.

$$\gamma = \bar{X}\frac{\sqrt{a^2+b^2}}{ab} \tag{3}$$

$$\gamma' = \bar{X}'\frac{\sqrt{a^2+b^2}}{ab} \tag{4}$$

$$\bar{X} = \frac{\left|\Delta_1 + \Delta_2\right| + \left|\Delta_3 + \Delta_4\right|}{2}$$

$$\bar{X}' = \frac{\left|\Delta_1' + \Delta_2'\right| + \left|\Delta_3' + \Delta_4'\right|}{2}$$

From the geometry relationship, we can figure out that shear deformation in plane OBC has nothing to do with plane OAC or vice versa. On the other hand, O′A′ is on the XZ plane while O′B′ is on the YZ plane. So we can calculate the angle between O′A′(O′B′) and X(Y) axis following Equation 5.

$$\alpha_2 = \frac{\bar{X}}{a}\sin\theta, \quad \alpha_2' = \frac{\bar{X}'}{a}\sin\theta \tag{5}$$

By solving the projection in the XZ plane and the YZ plane caused by 3D shear angle γ and γ', we can get equivalent 2D shear angle.

There is no harm in marking C′(x_c, y_c, z_c) in coordinate system O′X′Y′Z′. By the projection transformation, C_1 in the XZ plane can be expressed as $C_1(x_c,0,z_c)$ and C_2 in the YZ plane can be expressed as $C_2(0,y_c,z_c)$. According to the geometry, vectors can be expressed as follows.

$$\overline{O'A'} = (a\cos\alpha_2, 0, a\sin\alpha_2)$$

$$\overline{O'B'} = (0, a\cos\alpha_2', -a\sin\alpha_2')$$

$$\overline{O'C'} = (x_c, y_c, z_c)$$

$$\overline{O'C_1} = (x_c, 0, z_c)$$

$$\overline{O'C_2} = (0, y_c, z_c)$$

making that

$$\beta = \frac{\pi}{2} - \gamma, \quad \beta' = \frac{\pi}{2} - \gamma'$$

$$< \overline{O'A'}, \overline{O'C'} >= \beta, \quad < \overline{O'B'}, \overline{O'C'} >= \pi - \beta'$$

$$\overline{O'A'} \cdot \overline{O'C'} = ab\sin\gamma = a\cos\alpha_2 x_c + a\sin\alpha_2 z_c$$

$$\overline{O'B'} \cdot \overline{O'C'} = -ab\sin\gamma' = a\cos\alpha_2' y_c - a\sin\alpha_2' z_c$$

$$x_c = \frac{b\sin\gamma - \sin\alpha_2 z_c}{\cos\alpha_2}$$

$$y_c = \frac{\sin\alpha_2' z_c - b\sin\gamma'}{\cos\alpha_2'}$$

Using the equation,

$$x_c^2 + y_c^2 + z_c^2 = b^2$$

we can find that

$$z_c = b\frac{\sin\gamma\sin\alpha_2\cos^2\alpha_2' + \sin\gamma'\sin\alpha_2'\cos^2\alpha_2 + \cos\alpha_2\cos\alpha_2' K}{\cos^2\alpha_2 + \cos^2\alpha_2' - \cos^2\alpha_2\cos^2\alpha_2'}$$

in this formula

$$K = \sqrt{\begin{matrix}\cos^2\alpha_2 + \cos^2\alpha_2' - \cos^2\alpha_2\cos^2\alpha_2' \\ -\sin^2\gamma - \sin^2\gamma' + 2\sin\gamma\sin\gamma'\sin\alpha_2\sin\alpha_2'\end{matrix}}$$

Though the above method, the projection length of O′C′ in the XZ plane and the YZ plane can be expressed as L_1 and L_2

$$L_1 = |\mathrm{O'C_1}| = \sqrt{x_c^2 + z_c^2} = \frac{1}{\cos\alpha_2}\sqrt{z_c^2 - 2b\sin\gamma\sin\alpha_2 z_c + b^2\sin^2\gamma}$$

$$L_2 = |\mathrm{O'C_2}| = \sqrt{y_c^2 + z_c^2} = \frac{1}{\cos\alpha_2'}\sqrt{z_c^2 - 2b\sin\gamma'\sin\alpha_2' z_c + b^2\sin^2\gamma'}$$

So the shear deformation in 3D occasion can be derived.

$$\gamma_1 = \frac{\pi}{2} - \arccos\left(\frac{b\sin\gamma}{L_1}\right) \tag{6}$$

$$\gamma_2 = \frac{\pi}{2} - \arccos\left(\frac{b\sin\gamma'}{L_2}\right) \tag{7}$$

The meaning of the symbols in Equation 6 & 7 can be found previously.

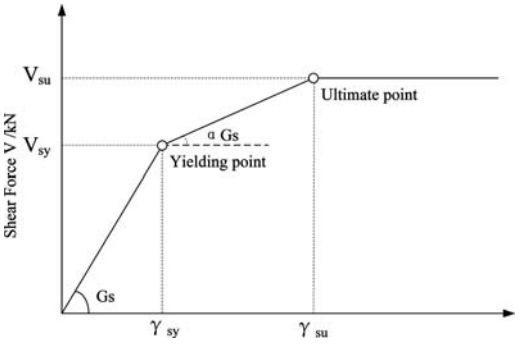

Figure 5. Trilinear model for steel tube in panel zone.

3 MODEL FOR PLANE CONNECTIONS

3.1 *Model for steel tube*

According to the existing research, shear capacity of composite connections is made up of panel zone steel tube and concrete.

In this paper, we use trilinear relations to describe the steel tube in the panel zone. Shear capacity, yield deformation and ultimate deformation caused by steel tube in the panel zone can be expressed as follows.

$$V_{sy} = \frac{A_w}{\sqrt{3}}\sqrt{f_{sy}^2 - \sigma_s^2} \tag{8}$$

$$V_{su} = \frac{A_w}{\sqrt{3}}\sqrt{f_{su}^2 - \sigma_s^2} \tag{9}$$

$$\gamma_{sy} = \kappa_s\frac{V_{sy}}{A_w G_s} \tag{10}$$

$$\gamma_{su} = \kappa_s\frac{V_{su} - V_{sy}}{A_w G_s'} + \gamma_{sy} \tag{11}$$

Here $A_w = A_s/2$ stands for the effective shearing area of steel tube. f_{sy} and f_{su} stand for the yield strength and ultimate strength of steel tube.

$$\sigma_s = \frac{NE_s}{(E_s A_s + E_c A_c)} \tag{12}$$

N stands for the axial force while E_s and E_c stand for the Young's modulus of steel and concrete. A_s and A_c mean the area of steel and concrete. κ_s stands for shearing-shape coefficient, here we take 1.2 for square tube.

As the shear modulus of steel, G_s is usually a constant about 79×10^3 MPa.

G_s' reflects the reduction of shear modulus after yielding as shown in Figure 5. The reduction rate α can be taken for 0.1 as a suggestion.

3.2 *Model for core concrete*

For the sake of simplicity, core concrete can be simulated by elastic-perfectly plastic model. Ultimate shear

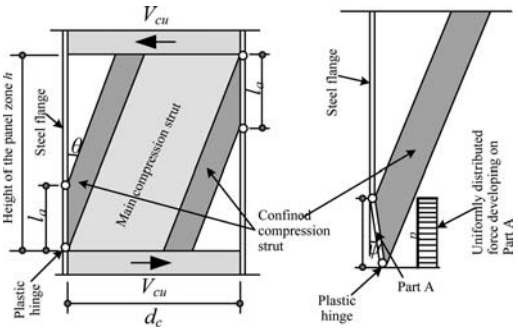

Figure 6. Model for concrete in 2D panel zone.

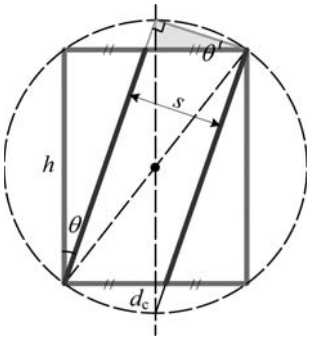

Figure 7. Schematic for angle of compression strut.

capacity can be decomposed into two parts, main compression strut (V_{cu1}) and confined compression strut (V_{cu2}) (Fukomoto 2005) as shown in Figure 6.

Main compression strut is evolved from the arch mechanism observed in reinforced concrete beam shear capacity research as shown in Figure 7. (AIJ 1990) According to Fukumoto (2005), shear capacity and ultimate deformation can be expressed as following.

$$V_{cu} = V_{cu1} + V_{cu2} \tag{13}$$

$$V_{cu1} = \frac{1}{2} d_c \cdot d_c \cdot \sigma_{cB} \cdot \tan\theta$$

$$\tan\theta = \sqrt{1 + \left(\frac{h}{d_c}\right)^2} - \frac{h}{d_c}$$

$$V_{cu2} = 2pl_a = 4\sqrt{\frac{M_{fp}}{d_c \sigma_{cB}}} d_c \sigma_{cB} \sin\theta$$

$$\gamma_{cu} = \kappa_c \frac{V_{cu}}{\alpha_{cu} A_c G_c}$$

Here h is the height of panel zone. For composite beam connection, $h = 0.5h_c + h_b - t_{bf}$, for steel beam connection $h = h_b - 2t_{bf}$. h_c and h_b stands for the thickness of concrete slab and height of steel beam. t_{bf} is the thickness of steel beam flange. $d_c = B_c - 2t_{cf}$ stands for the width of concrete panel zone. B_c and t_{cf} means the width and thickness of steel tube.

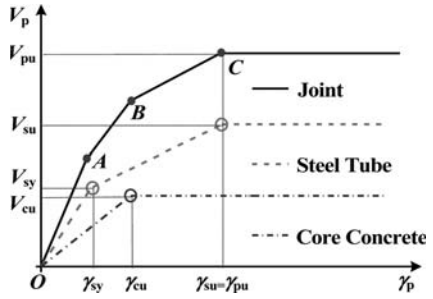

Figure 8. Four-line model for 2D connections.

As shown in Figure 6, the length of part A is l_a. There exists plastic hinges at both ends due to the pressure applied to the flange from concrete. Assuming that the rotation angle is ψ, based on the principle of virtual work, we obtain that

$$\frac{1}{2} p\psi l_a^2 = 2M_{fp}\psi$$

In this formula, $M_{fp} = (d_s t_s^2/4)\sigma_{sy}$ stands for the ultimate moment beard by steel flange.

As for the deformation, κ_c is the shearing-shape coefficient. $G_c = E_c/2(1+\nu_c)$ is the shear modulus of concrete. Symbol ν_c stands for the Poisson's ratio.

Through regression method, reduction coefficient α_{cu} of shear modulus for concrete can be expressed as $\alpha_{cu} = 0.00158 f_c + 0.0411 h/(B_c - 2t_{cf}) + 0.086$

3.3 *Superposition model for 2D connections*

With model for steel tube and core concrete, we can get the four-line model using superposition method as shown in Figure 8. Here point A is the yielding point and C is the ultimate point. The shear capacity of panel zone can be expressed as following.

$$V_{py} = AV_{sy} + BV_{cu} \tag{14}$$

$$V_{pu} = V_{su} + V_{cu} \tag{15}$$

Case 1 $\gamma_{sy} < \gamma_{cu} < \gamma_{su}$,

$$\gamma_{py} = \gamma_{sy}, \quad \gamma_{pu} = \gamma_{su}, \quad A = 1, \quad B = \frac{\gamma_{sy}}{\gamma_{cu}}$$

Case2 $\gamma_{cu} < \gamma_{sy} < \gamma_{su}$

$$\gamma_{py} = \gamma_{cu}, \quad \gamma_{pu} = \gamma_{su}, \quad A = \frac{\gamma_{cu}}{\gamma_{sy}}, \quad B = 1$$

Case 3 $\gamma_{sy} < \gamma_{su} < \gamma_{cu}$

$$\gamma_{py} = \gamma_{sy}, \quad \gamma_{pu} = \gamma_{cu}, \quad A = 1, \quad B = \frac{\gamma_{sy}}{\gamma_{cu}}$$

Normally, during the loading process, the steel tube webs come to yield first, then the core concrete reaches ultimate deformation and at last, steel tube webs fail as what case 1 describes.

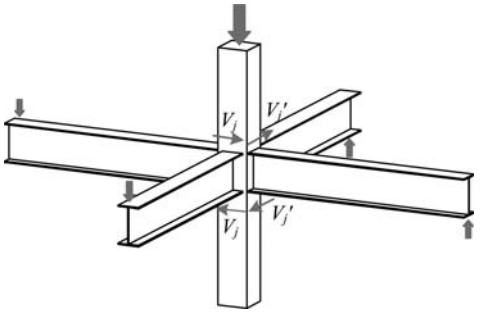

Figure 9. Schematic diagram for 3D shear load case.

4 MODEL FOR 3D CONNECTIONS

4.1 *3D model for steel tube*

Under bidirectional loading, steel tube bears not only axial force but also two-way shear force as shown in Figure 9.

The stress state of steel can be expressed using von Karman notation as

$$\sigma_{ij} = \begin{bmatrix} \sigma_x & \tau_{xy} & \tau_{xz} \\ \tau_{yx} & \sigma_y & \tau_{yz} \\ \tau_{zx} & \tau_{zy} & \sigma_z \end{bmatrix} = \begin{bmatrix} 0 & \tau_1 & 0 \\ \tau_1 & -\sigma_s & -\tau_2 \\ 0 & -\tau_2 & 0 \end{bmatrix}$$

Using von Mises yield criterion, considering that for equally bidirectional load case, making $\tau_1 = \tau_2$ we can obtain that

$$\tau_{\max} = \frac{\sqrt{f_{sy}^2 - \sigma_s^2}}{\sqrt{6}}$$

Similar with the 2D occasion, using τ_{max} calculated before, we can figure out shear capacity contributed by steel tube.

$$V_{sy} = \frac{A_w}{\sqrt{6}}\sqrt{f_{sy}^2 - \sigma_s^2} \tag{16}$$

$$V_{su} = \frac{A_w}{\sqrt{6}}\sqrt{f_{su}^2 - \sigma_s^2} \tag{17}$$

In terms of deformation, assuming that 3D shear deformation angle $\gamma = \gamma'$, according to Equation 6&7, we know that $\gamma_{3D} = \gamma'_{3D}$.

From the expression of z_c, $z_c \approx Kh$ as shear deformation γ is small. Therefore $L_1 = L_2 = z_c \approx Kh$, steel tube yielding shear deformation and ultimate deformation can be expressed as following.

$$\gamma_{sy}^{3D} = \frac{\pi}{2} - \arccos\left(\frac{\sin\gamma_{sy}}{K}\right) \tag{18}$$

$$\gamma_{su}^{3D} = \frac{\pi}{2} - \arccos\left(\frac{\sin\gamma_{su}}{K}\right) \tag{19}$$

In this formula, we can build relationship between 2D shear deformation and the 3D one.

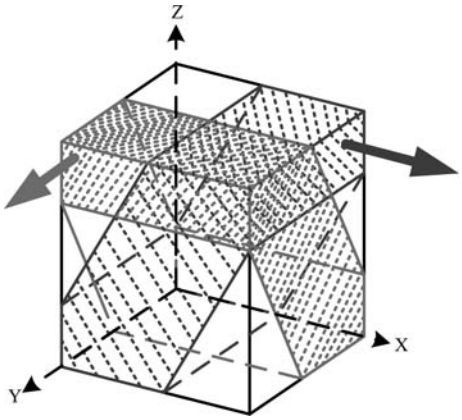

Figure 10. 3D compression strut model for concrete.

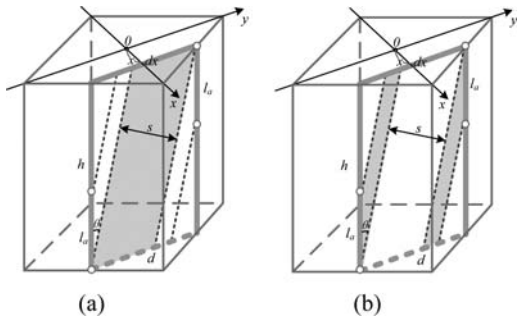

Figure 11. 3D compression strut model for concrete.

4.2 *3D model for core concrete*

Just the like 2D occasion, we can decompose the shear capacity into two parts, the main compression strut and the confined compression strut with 3D stress state as shown in Figure 10.

Similar with plane connection, using calculus theory and considering symmetrical condition, we can obtain the capacity of main compression strut V_{cu1}.

In the infinitesimal plane shown in Figure 11(a),

$$dV_{cu1} = \frac{1}{2} d \cdot d_x \cdot \sigma_{cB} \cdot \tan\theta$$

$$\tan\theta = \sqrt{1 + \left(\frac{h}{d}\right)^2} - \frac{h}{d}$$

$$d = \sqrt{2} d_c - 2x$$

Through integration, we can obtain

$$V_{cu1} = \frac{\sqrt{2}}{4}\sigma_{cB} d_c \sqrt{h^2 + 8d_c^2} + \frac{1}{8}\sigma_{cB} h^2 \operatorname{arcsinh}\frac{2\sqrt{2}d_c}{h} - \frac{\sqrt{2}}{2}\sigma_{cB} d_c h \tag{20}$$

And for the confined compression strut shown in Figure 11(b), in the infinitesimal plane,

$$dV_{cu2} = 2pl_a = 2t_S\sqrt{\sigma_{sy}\sigma_{cB}}\sin\theta dx$$

$$l_a = \sqrt{\frac{4M_{fp}}{p}} = \frac{t_S}{\sin\theta}\sqrt{\frac{\sigma_{sy}}{\sigma_{cB}}}$$

$$\sin\theta = \frac{d}{\sqrt{2}\sqrt{h^2+d^2+h\sqrt{h^2+d^2}}}$$

Through integration, we can also obtain

$$V_{cu2} = \frac{\sqrt{2}}{2}Mt_S\sqrt{\sigma_{sy}\sigma_{cB}} \tag{21}$$

in which

$$M = \sqrt{T^2+hT} - h\ln\left(\sqrt{T}+\sqrt{T+h}\right)$$
$$+\frac{1}{2}h\ln h + h\left[\ln\left(\sqrt{2}+1\right)-\sqrt{2}\right]$$

and

$$T = \sqrt{h^2+8d_c^2}$$

Considering that in the actual project design, shear capacity should be decomposed into x&y direction.

$$V_{cu} = \left(V_{cu1}+V_{cu2}\right)/\sqrt{2} \tag{22}$$

The ultimate shear deformation can be expressed as

$$\gamma_{cu}^{3D} = \frac{\pi}{2} - \arccos\left(\frac{\sin\gamma_{cu}}{K}\right) \tag{23}$$

In which

$$\gamma_{cu} = \kappa_c\frac{V_{cu}}{\alpha_{cu}A_cG_c}$$

stands for the ultimate shear deformation in 2D case. The other symbols' meanings are like before. Normally, γ_{cu} tends to reach 0.05 rad approximately.

4.3 *Superposition model for 3D connections*

Using the results that have been stated, we can get superposition model for 3D connections to calculate the capacity and the deformation.

The basic form (Fig 8) of the model is just like the 2D occasion except that we should use V_{pu}, V_{py} and γ_{cu}, γ_{sy}, γ_{su} obtained in 3D occasion instead of the original ones.

5 CONCLUSIONS

In this paper, trilinear model for steel tube and elastic-perfectly plastic model are adopted to simulate the panel zone behavior. Based on reasonable shear transfer mechanism assumption, this paper sets up the four-line model by superposition method to calculate the capacity and deformation. In order to expand the range of applications, this paper promotes the theory to 3D occasions and builds relationships between planar and spatial parameters.

6 NOTATION

Here is the Notation for this passage.

γ shear angle
a width of the panel zone
b height of the panel zone
$\Delta_1+\Delta_2/\Delta_3+\Delta_4$ length changing of the two diagonals
Q_j shear force
Q_b vertical loading at the beam
Q_c reaction force at end-column
A_s area of steel tube section
A_w effective shearing area of steel tube
f_{sy} yield strength of steel
f_{su} ultimate strength of steel
N axial force
V shear force
γ_{cu} ultimate shear angle for concrete compression strut model
γ_{sy} shear angle reflects yield point of steel
γ_{su} shear angle reflects ultimate point of steel
V_{cu} shear force supported by concrete
V_{sy} shear force supported by steel(with yield strength)
V_{su} shear force supported by steel(with ultimate strength)
V_{pu} calculated shear capacity
E_s Young's modulus of steel
E_c Young's modulus of concrete
A_c area of concrete section
κ_s shearing-shape coefficient
G_s shear modulus of steel
h height of concrete panel zone
d_c width of concrete panel zone
h_c thickness of concrete slab
h_b height of steel beam
t_{bf} thickness of steel beam flange
B_c width of steel tube
t_{cf} thickness of steel tube
M_{fp} ultimate moment beard by steel flange
α_{cu} concrete's reduction coefficient of shear modulus

REFERENCES

Architectural Institute of Japan. 1990. *Design guidelines for earthquake resistant reinforced concrete building based on ultimate strength concept.*

Cheng, C.T., Hwang, P.S., Chung, L.L. 2000. Connection behaviors of steel beam to concrete-filled circular steel tubes. *Composite and Hybrid Structures*:581–589.

China Association for Engineering Construction Standardization. 2004. *Technical specification for structures with concrete-filled rectangular steel tube members*:159

Fukumoto, T., Morita, K. 2005. Elastoplastic behavior of panel zone in steel beam-to-concrete filled steel tube column moment connections. *Journal of Structural Engineering* 131(12): 1841–1853.

Kanatani, H., Tabuchi, M., Kamba, T., et al. 1987. A study on concrete filled RHS column to H-beam connections fabricates with HT bolts in rigid frames. *Composite Construction in Steel and Concrete*: 614-635. New York: American Society of Civil Engineers.

Kurobane, Y., Packer, J.A., Wardenier, J. and Yeomans, N. 2004. *Design guide for structural hollow section column connections*, Köln: Verlag TÜV.

Peng, S.W. 2001. Seismic resistant connections for concrete filled tube column-to-WF beam moment resisting frames. [*Ph.D. Dissertation*]. Bethlehem, Pennsylvania: Leigh University.

Qin Kai. 2006. Research on the performance of connections composed of concrete-filled square steel tubular columns and steel-concrete composite beams. [*Ph.D. Dissertation*]. Beijing: Tsinghua University.

Rassati, G.A., Leon, R.T., et.al. 2004. Component modeling of partially restrained composite joints under cyclic and dynamic loading. *Journal of Structural Engineering* 130(2): 343–351.

Ricles, J.M., Peng, S.W., Lu L.W. 2004. Seismic behavior of composite concrete filled steel tube column-wide flange beam moment connections. *Journal of Structural Engineering* 130(2):223–232.

Xu Guigen. 2008. Experimental and theoretical study on connections of concrete-filled square tubular columns. [*Ph.D. Dissertation*]. Beijing: Tsinghua University.

Tubular Structures XIV – Gardner (Ed.)
© 2012 Taylor & Francis Group, London, ISBN 978-0-415-62137-3

Concrete filled double skin asymmetric tube sections subjected to pure bending

A. Albareda Valls & J. Maristany Carreras
Structures in Architecture. UPC, Barcelona, Spain

ABSTRACT: Concrete filled tubes have been increasingly used in recent decades as columns or beam-columns in tall buildings, due to their excellent mechanical qualities under compression. This is the reason why several investigations have been also focused on their behavior in bending last years, although few real bending applications exist. Derived from this well-known composite sectional typology, concrete filled double skin tubular sections appeared–composed this time by two concentric steel tubes and filled concrete between them. They have been investigated these last years by different structural researchers due to their improved ductility and strength, especially in seismic areas. However, no studies exist related with their bending response. This investigation has developed a numerical model with a damaged plasticity material model for concrete, in order to describe the behavior of concrete filled symmetric and asymmetric double skin tube sections subjected to pure bending. The term "asymmetric" refers to those double skin tubular sections in which the inner tube has been displaced along the "y" axis, so that more steel area is moved far from the centroid. Although it is known that asymmetry is not really effective in sections subjected to pure compression, in bending these sections are capable of improving their resistant response in some cases. To verify that purpose, different specimens with different geometries and material strengths have been analyzed. This text presents general conclusions about their behavior and advantages, and also some basic rules for future civil and architectural structures.

1 INTRODUCTION

1.1 *Concrete filled double skin tubes under bending*

Concrete Filled Tube sections (CFT) have been increasingly used these recent decades as columns or beam-columns in tall buildings, due to their improved ductility and strength. These resistant qualities come from the combination of material properties of steel of the tube and concrete of the core. Concrete in these sections improves considerably its strength, as a result of the lateral pressure caused by confinement effect.

Recently, a new sectional typology has appeared, derived from the mentioned CFT ones: concrete filled double skin tubular sections (CFDST), formed by two concentric steel tubes and filled concrete between them. These new sections improve the resistant capabilities of the first ones, especially in slender columns by virtue of their hollowness.

While numerous investigations have been carried out to describe the behavior of CFDST sections subjected to pure compression (Tao et al., 2004) , (Han et al., 2006) and (Uenaka et al., 2010), no studies exist related with their behavior subjected to pure bending, although they could have a good response also in this case. It is known that the steel disposed near neutral axis of a section is not really effective in resisting bending efforts; in case of double concentric skin tubular sections, the whole inner tube fully coincides with the centroid of the composite section [Fig. 1].

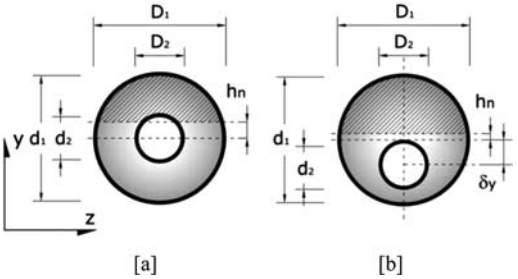

Figure 1. Concrete filled double skin [a] symmetric and [b] asymmetric tube sections.

1.2 *Concrete filled double skin asymmetric tubes subjected to bending*

Different from concentric CFDST sections do behave the asymmetric ones formed also by two steel tubes (outer and inner) –but displaced over the "y" axis- and filled with concrete between them. The fact of displacing the inner tube could enhance its ultimate bending capacity. The effectiveness depends logically on the value of the friction forces developed between both material surfaces.

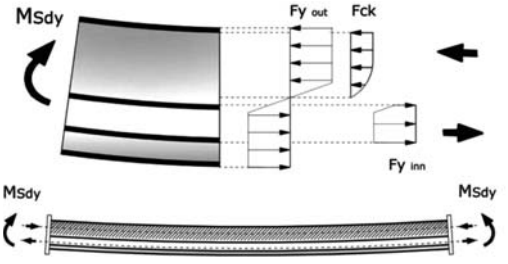

Figure 2. Concrete filled double skin asymmetric tube section under bending.

Concrete filled double skin symmetric and asymmetric tubes could have interesting applications in future architectonical and civil structures, especially in those beam tubular elements with an outer maximum diameter fixed for design reasons. However, the use of asymmetric sections should be only focused on bending elements, since their response under compression is not really advantageous from the one provided by the concentric ones.

This investigation is devoted to describe the behavior and to point out possible applications of symmetric and asymmetric CFDST sections subjected to pure bending. For this purpose, a numerical analysis has been carried out and general design rules are proposed, derived from several analyses with different geometries and material strengths.

The fact of displacing the inner tube along the "y" axis of the section makes better use of the material under pure bending, since more concrete becomes compressed and more steel becomes tensioned [Fig 2]. Furthermore, this new typology is easily suitable for post-tensioning by improving notably its effectiveness.

Several scientists have been investigating about bending of simple CFT sections these recent years: (Chitawadagi et al., 2009), (Lu et al., 2007), (Probst et al., 2010) and (Elchalakani et al., 2001).

2 FINITE ELEMENT MODELLING

Elchalakani et al. (2001) tested several specimens of concrete filled tube sections subjected to pure bending. Five of these sections have been used in this investigation to calibrate the numerical model proposed, in order to be capable of reproducing the flexural behaviour of asymmetric CFDST sections. The specimens reproduced in this numerical analysis are all different to validate the results from a theoretical simplified model, also proposed in Section 6. The numerical modelling has been done using the commercial software ABAQUS/Explicit, version 6.10.

2.1 *FEM model geometry and meshing*

Three-dimensional models have been used in this study to reproduce the steel tubes and the concrete core. For both steel and concrete part instances, element type

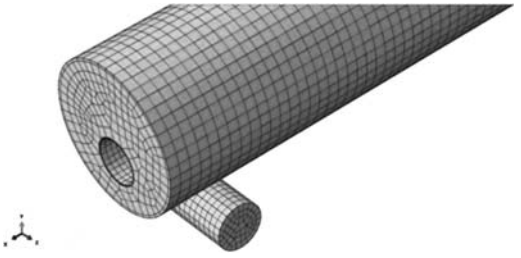

Figure 3. General view of the mesh used for the model.

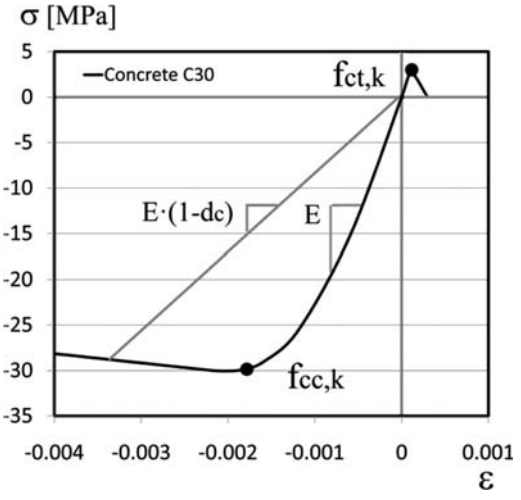

Figure 4. Uniaxial stress-strain curve used for concrete.

C3D8 available in ABAQUS 6.10 library has been chosen. This is a three-dimensional brick element, defined by 8 nodes with three degrees of freedom at each one, and no reduced integration. This is a general purpose linear brick element.

2.2 *FEM material properties*

2.2.1 *Concrete*

The well-known damaged plasticity model for concrete, available in ABAQUS 6.10, has been used to simulate the complex concrete behaviour. This is a three-dimensional continuum plasticity-based damaged model which is capable of simulating both tensile and compressive concrete responses, even in case of high confining pressures.

Two hardening laws (depending on plastic strain rates) are defined separately into tension and compression. Concrete in plastic range behaves really different under tension that under compression (Fig. 4), as it is shown in figure below. Beyond the maximum compressive or tensile yield stress, a damage process starts to degrade the stiffness matrix of the material. The damaged ratio in both states is expressed by the scalar coefficient d_c and it represents the percentage of cracking or crushing as it is explained in the investigation carried out by Castro (2011).

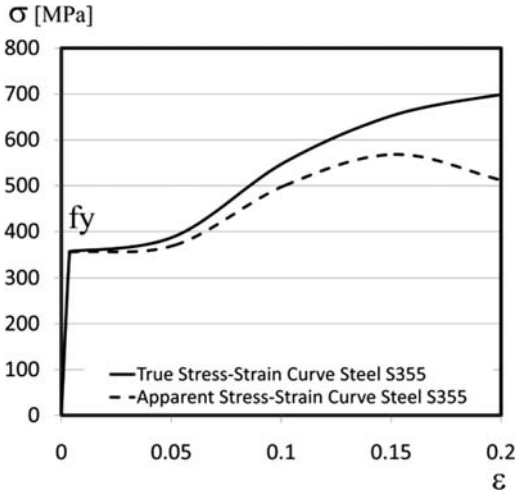

Figure 5. Uniaxial true and apparent stress-strain curves used for steel.

Using the model proposed, no discrete cracks appear beyond the maximum tensile stress due to the assumption of continuity, although they would really exist. When concrete reaches its maximum tensile strength, its stress quickly decreases according to an exponential descent. This behaviour has been reproduced in the material model through a bilinear function. By the contrary, a multi-linear curve has been defined for plastic hardening in compression [see Fig. 4].

This model allows defining the shape of the yield surface by means of the two parameters Kc and σ_{b0}/σ_{c0}: the first one describes the shape of the deviatoric plane, while the latter describes the ratio between the initial equibiaxial to the uniaxial compressive yield stress. A non-associated flow rule is used and the flow potential follows the Drucker-Praguer hyperbolic function. The dilation angle proposed is 31°, and the viscosity parameter is defined small (close to zero) in order to allow stresses outside the yield surface, and this way avoiding convergence difficulties.

The maximum tensile yield stress for concrete is considered as the 9% of the maximum characteristic compressive stress, and for the elastic Poisson's ratio, an initial value of 0.20 has been used. The initial modulus of elasticity has been derived from the following experimental expression:

$$E_0 = 4700 * \sqrt{f_{ck}} \quad [\text{in N/mm}^2] \qquad (2)$$

2.2.2 *Steel*

An elastic-plastic model according to the von Mises yield criterion has been implemented for steel of the tubes. A complete stress-strain curve with hardening effect has been defined, obtained from uniaxial experimental tests. For the elastic Poisson's ratio, a value of 0.30 has been taken, and for the elastic Young modulus, a value of 210000 N/mm^2 has been used.

Table 1. Specimens tested by Elchalakani et al. (2001).

Specimen	D	t	f_c	f_y	E_c	E_y
CBC1	101.83	2.53	23.40	365	22735	2.0e5
CBC2	88.64	2.79	23.40	432	22735	2.1e5
CBC3	76.32	2.45	23.40	415	22735	2.1e5
CBC4	89.26	3.35	23.40	412	22735	2.1e5
CBC5	60.65	2.44	23.40	433	22735	2.1e5

*All values expressed in [mm] and [N/mm^2].

2.2.3 *Interaction properties*

Interaction between the steel tubes and the concrete core is crucial in order to guarantee a correct activation of the inner profile. The option surface to surface contact, available in ABAQUS, has been used in the model; the interaction properties defined are capable of transferring both normal and shear stresses.

For normal stresses, the option "hard contact" has been chosen to reflect the contact status of the different part instances; for tangential stresses a friction coefficient has been calibrated according to Eurocodes, with an initial elastic slip. The friction coefficient has been defined variable depending on normal stresses, but always starting from an initial value of 0.20 (see section 3.1 of this text).

3 VALIDATION OF THE FE MODEL

To validate the numerical model proposed, curves obtained from five real experiments, carried out by Elchalakani et al. (2001), have been compared to the results from the FE analysis. These tests deal with simple concrete filled tubes subjected to pure bending, with different material strengths and geometries. Specimens used for that purpose are listed below in Table 1.

3.1 *Validation of the friction coefficient used*

Due to the importance that have friction forces in CFDST sections to transfer forces in bending, and in order to be capable of quantifying them, three more analyses have been carried out assuming a linear function for the friction coefficient, by using three different initial values of 0.20, 0.25 and 0.30. Full coincidence between experimental results and Eurocodes is detected, since the FE curves match with accuracy with the experimental results in case of assuming an initial friction coefficient of 0.20. In concrete areas with important normal pressures (beyond 5 MPa, considered a standard value in circular CFT sections under compression), the friction coefficient is enhanced up to 0.35 according to the assumptions proposed in EC4 for circular-shaped sections.

Due to the similarity between the specimens proposed, this comparison has been done only for CBC1. An initial friction coefficient of 0.20 has been assumed for all specimens. A linear function has been assumed

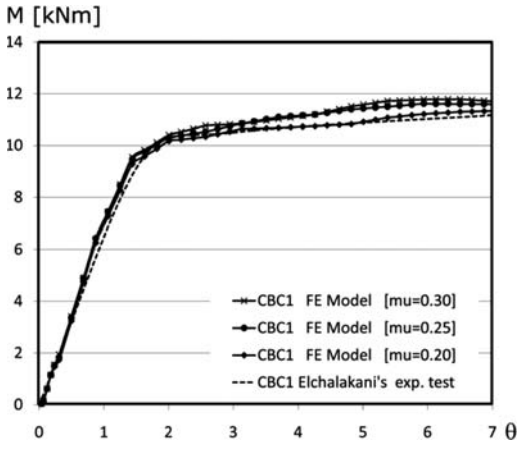

Figure 6. Comparison of FE and experimental results for CBC1, with different initial friction coefficients.

Table 2. Difference between FE and experimental results, in terms of ultimate bending moment.

Specimen	M_u test*	M_u FEM*	M_uFEM/$M_u$test
CBC1	11.33	11.90	1.053
CBC2	10.86	10.38	0.953
CBC3	6.92	6.55	0.946
CBC4	10.47	10.99	1.049
CBC5	3.78	3.83	1.013

*Values expressed in KN · m.

to determine the variation of the friction coefficient, depending on normal stresses and with a maximum value of 0.35 for pressures beyond 5 N/mm^2. In this way, friction forces depend on the normal pressure of the interfaces, and therefore their value can be increased in confined areas.

3.2 *Agreement between numerical and experimental results*

Four more specimens have been analyzed, and results from the FE analysis and the experimental tests have been compared in terms of maximum bending moment. Maximum distortion observed between the finite element models and the experimental tests carried out by Elchalakani et al. (2001) is about 5.4% (see Table 2).

4 NUMERICAL STUDY

With the aim of describing the behaviour of concrete filled double skin tubes subjected to pure bending generally (symmetric and asymmetric), there have been proposed 16 different specimens, with different material strengths and different geometries. Sections which end with letter A are symmetric, while sections which

Table 3. Properties of the CFDST Specimens proposed.

Specimen	D_1	t_1	D_2	t_2	f_c	f_y	δ_y
CC01A	323.90	6.00	114.30	4.00	30	355	0.00
CC01B	323.90	6.00	114.30	4.00	30	355	52.40
CC02A	323.90	6.00	101.60	3.00	30	355	0.00
CC02B	323.90	6.00	101.60	3.00	30	355	55.58
CC03A	323.90	6.00	88.90	3.00	30	355	0.00
CC03B	323.90	6.00	88.90	3.00	30	355	58.75
CC04A	323.90	6.00	76.10	3.00	30	355	0.00
CC04B	323.90	6.00	76.10	3.00	30	355	61.95
CC05A	323.90	6.00	114.30	4.00	50	355	0.00
CC05B	323.90	6.00	114.30	4.00	50	355	52.40
CC06A	323.90	6.00	101.60	3.00	50	355	0.00
CC06B	323.90	6.00	101.60	3.00	50	355	55.58
CC07A	323.90	6.00	88.90	3.00	50	355	0.00
CC07B	323.90	6.00	88.90	3.00	50	355	58.75
CC08A	323.90	6.00	76.10	3.00	50	355	0.00
CC08B	323.90	6.00	76.10	3.00	50	355	61.95

*All values expressed in [mm] and [N/mm^2].

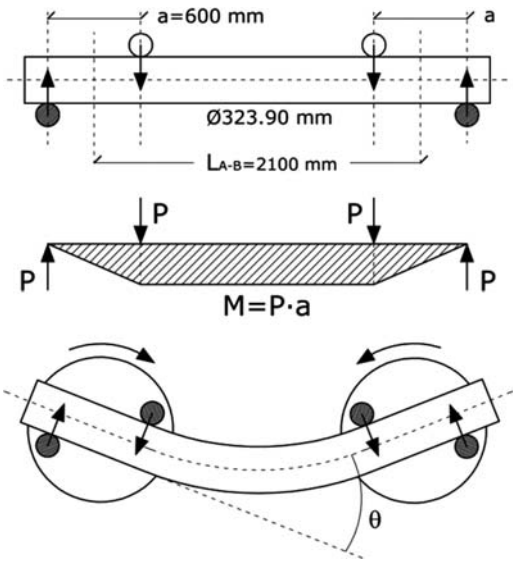

Figure 7. Procedure used for the pure bending test in the FE model and bending moment diagram obtained.

end with B are asymmetric, but equivalent in terms of area. To simplify the analysis, the outer diameter has been considered constant with a value of 323.90 mm obtained from ARCELOR®commercial tables; variations come from displacing and changing the diameter of the inner profile.

Being δ_y the displacement of the inner tube on the "y" axis of the section.

The specimens mentioned have been subjected to a pure bending test, according to the methodology carried out by Elchalakani et al. (2001), as it is shown below:

A sample of the curves obtained from the numerical analysis is shown below [Fig.9] for the specimen

Figure 8. General view of the FE model.

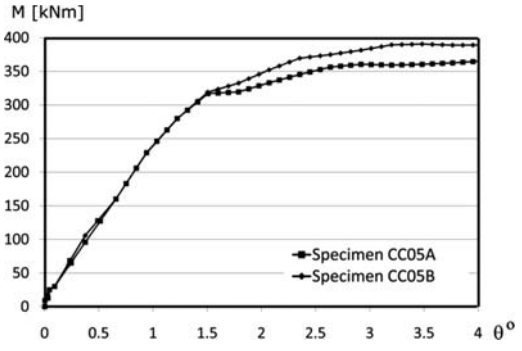

Figure 9. Moment-curvature diagrams for specimens CC05, symmetric [A] and asymmetric [B].

Table 4. Percentage of variation of bending capacity between Symmetric and Asymmetric Specimens.

Specimen	M_u FEM Symm [A]	M_u FEM Asymm [B]	M_u FEM Asymm/Symm
CC01	349.30	365.68	1.046
CC02	331.77	353.57	1.066
CC03	321.68	344.06	1.069
CC04	323.51	335.33	1.036
CC05	365.52	389.17	1.065
CC06	352.60	366.51	1.039
CC07	348.90	360.10	1.032
CC08	345.07	359.99	1.043

*All values expressed in kN · m.

CC05, separated according to the position of the inner tube (A symmetric and B asymmetric).

Full list of results obtained in the analyses is shown in Table 4, by comparing symmetric with asymmetric sections. Percentage of resistance gain is shown on the right column, and it ranges between 3.2 and 6.9%.

5 ANALYSIS OF RESULTS

5.1 *Stress distribution on concrete core*

Several differences related with stress distribution in concrete core have been detected from results of the FE analysis. The position of the inner tube along the "y" axis is decisive in order to determine the neutral axis of the composite section.

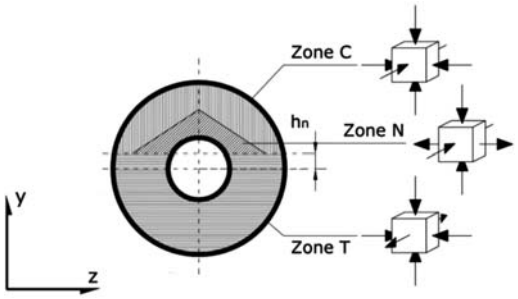

Figure 10. Idealised areas of stress state in concrete core of CFDS symmetric tubes subjected to bending.

It is important to note that the fact of displacing the inner tube in the tensioned area of concrete core tends to regularize the neutral axis of the global section. At the same time, confinement effect appears in compressed regions of the core, with stresses well above the concrete compressive yield stress (stresses about 30–50% higher).

The analysis of longitudinal stresses in the "x" axis must be necessarily compared with the three-dimensional stress state of the core. For that purpose, different stress distributions have been separated into three different areas. The displacement of the inner tube has a clear influence on the global stress state of the core, and at the same time it increases the maximum bending resistance of the whole section.

As it has been mentioned, three different stress state areas have been detected in concrete core, for both cases of symmetric and asymmetric CFDS sections: zones C, N and T. For the first group, Zone C on the one hand is subjected to compressive stresses in all directions, and this is the reason why concrete in this area becomes slightly confined. On the other hand, Zone N corresponds to the neutral axis of the section, and it is subjected to a biaxial compressive stress state in the "y" and "x" axes and a tensile stress in the "z" direction. Finally, the zone called T is clearly determined by a longitudinal tensile stress, combined with a biaxial compressive stress state in the other two axes.

For concrete filled double skin asymmetric tube sections, the three same areas are also detected, but with some important differences. On the one hand, zone N is also triangular shaped, but this time it appears below the neutral axis, by increasing the confining area C. On the other hand, this area is subjected to a biaxial tensile stress state in the "x" and "z" axes, instead of the biaxial compressive state which was pointed before.

Stresses in the "z" and "y" directions [axes of the section plane] are important in order to ensure a correct contact bond between the inner tube and the concrete core. Compressive stress in these axes guarantees the presence of friction forces, and also a correct transfer of stress between the two different instances.

As it has been mentioned before, a confinement effect is detected in specific areas of the core. This three-axial compressive stress state allows increasing the concrete compressive strength, according to the

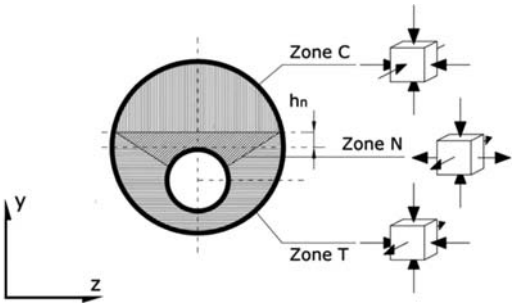

Figure 11. Idealised areas of stress state in concrete core of CFDS asymmetric tubes subjected to bending.

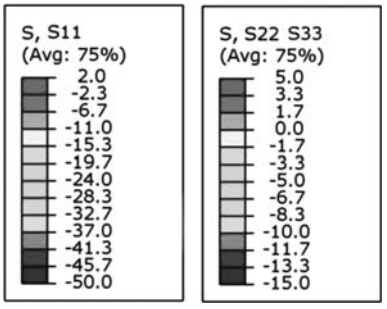

Figure 13. Comparison between three different stress states of the core, depending on the diameter of the inner tube.

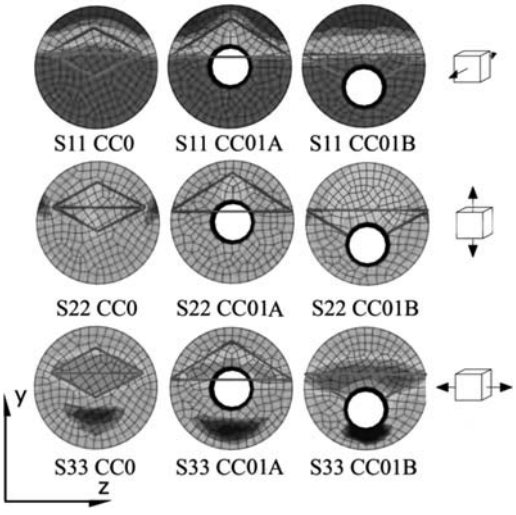

Figure 12. Comparison between three different stress states of the core, depending on the diameter of the inner tube.

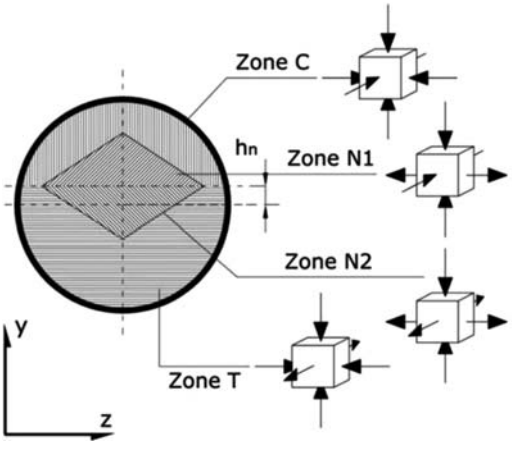

Figure 14. Idealised areas of stress state in concrete core of simple CFT sections subjected to bending.

postulates of (Richart, et al., 1928). It is noted that in asymmetric concrete filled double skin tubes, this confined areas tend to be slightly larger than in symmetric ones.

The fact of introducing an inner profile in the concrete core has a clear effect on its stress state as it is shown in [Fig. 12], where stresses in CFT simple sections are compared with stresses in CFDST ones, but with different positions on the "y" axis.

Designs with large inner tube diameters guarantee more contact surface for transferring stresses from the core. However, at the same time they reduce the compressed area of the tube in the "z" and "y" axes, since more concrete is horizontally tensioned (in zone N).

Finally, and for comparison purpose, stress state areas of concrete core in simple CFT sections under bending have been also analyzed.

Generally, zone N is more important in these last case without inner profile than in concrete filled double skin symmetric and asymmetric tubes (see [Fig. 13]). On the contrary, tensile stresses in neutral areas of the two first typologies are really higher than in CFT ones. In conclusion, the effect of introducing an inner profile in the core reduces considerably the neutral area N, by increasing at the same time the magnitude of its stresses.

5.2 *Stress distribution in steel tubes*

The principal difference of stress distribution in steel tubes between symmetric and asymmetric sections is focused on the inner tube. Its position clearly determines the neutral axis and its stress state: the tube becomes less tensioned as closer it is from neutral axis.

In concrete filled double skin symmetric tubes, the inner tube is subjected to a bending effort only caused by its location, which it is characterized for being close to the neutral axis. On the contrary, in asymmetric CFDST sections, the steel response becomes more effective since 100% of the inner tube can become tensioned.

5.3 *Contact between the concrete core and the steel tubes*

From results obtained, it can be noted that stresses are well transferred from the concrete core to the inner

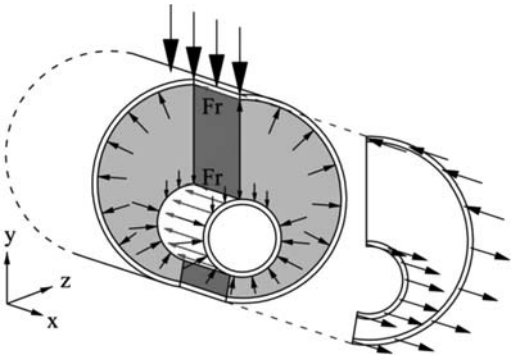

Figure 15. Idealised figure of an asymmetric CFDST section subjected to pure bending. Most part of the core is compressed in "z" and "y" axes, and this fact guarantees the transfer of stress.

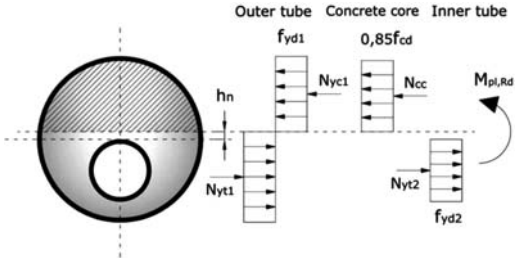

Figure 16. Theoretical rigid-plastic model for CFDS asymmetric tube sections.

tube, in a similar way like between concrete and the outer tube. This is even possible in cracked areas, in part thanks to the biaxial compressive state in the two section "z" and "y" axes. A compressive stress state on these two axes guarantees a correct bond between the two instances, since it fully activates the frictional forces on the interfaces.

6 THEORETICAL MODEL

This paper also proposes a simplified rigid-plastic approach to calculate the ultimate bending capacity (M_u) of symmetric and asymmetric concrete filled double skin tube sections.

According to Elchalakani et al. (2001) local buckling does not appear before reaching the ultimate bending moment in sections with $d/t > 74$ (which it is the case of the specimens tested). Furthermore, from results of the FE analysis and experiments, it has been noted that friction forces between steel and concrete are sufficient to well activate the concrete core.

Before obtaining the ultimate bending moment of the section, neutral axis is required. Analytical process to get this value for asymmetric CFDST sections is very similar to the one referred to symmetric tubes. This is the reason why only approximated expressions

Table 5. Percentage of variation of ultimate bending moment between FEM results and theoretical ones.

Specimen	M_u FEM	M_u Theor.	M_u FEM FEM/Theor.
CC01A	365.68	281.53	1.298
CC01B	365.68	281.53	1.298
CC02A	331.77	273.51	1.213
CC02B	353.57	290.61	1.216
CC03A	321.68	271.64	1.184
CC03B	344.06	288.50	1.192
CC04A	323.51	269.07	1.202
CC04B	335.33	284.13	1.180
CC05A	365.52	281.53	1.298
CC05B	389.17	305.70	1.273
CC06A	352.60	289.36	1.218
CC06B	366.51	307.44	1.192
CC07A	348.90	288.16	1.210
CC07B	360.10	305.06	1.180
CC08A	345.07	283.83	1.215
CC08B	359.99	279.05	1.290

*All values expressed in kN · m.

for asymmetric sections (5–10) are given below, based on the distribution in Figure 16:

$$N_{cc} \approx \left[\frac{\pi}{2} \cdot (R_1 - t_1)^2 - 2 \cdot h_n \cdot (R_1 - t_1)\right] \cdot 0.85 \cdot f_{cd} \tag{5}$$

$$N_{yt2} = \pi \cdot \left[{R_2}^2 - (R_2 - t_2)^2\right] \cdot f_{yd2} \tag{6}$$

$$N_{yt1} - N_{yc1} \approx 2 \cdot h_n \cdot t \cdot f_{yd1} \tag{7}$$

Assuming:

$$\begin{aligned} N_{cc} + N_{yc1} &= N_{yt1} + N_{yt2} \quad \rightarrow \\ N_{cc} - N_{yt2} &= N_{yt1} - N_{yc1} \quad \rightarrow \end{aligned} \tag{8}$$

$$\begin{aligned} &\left[\frac{\pi}{2} \cdot (R_1 - t_1)^2 - 2 \cdot h_n \cdot (R_1 - t_1)\right] \cdot 0.85 \cdot f_{cd} \\ &-\pi \cdot \left[{R_2}^2 - (R_2 - t_2)^2\right] \cdot f_{yd2} = 2 \cdot h_n \cdot t \cdot f_{yd1} \end{aligned} \tag{9}$$

$$-\frac{\pi \cdot \left[{R_2}^2 - (R_2 - t_2)^2\right] \cdot f_{yd2}}{2 \cdot t \cdot f_{yd1} + 2 \cdot (R_1 - t_1) \cdot 0{,}85 \cdot f_{cd}} \tag{10}$$

The distortion between results coming from the FE analysis and results obtained from the theoretical model is about 20–30%. This explicit increase in flexural response of the FE model is really coincident with results coming from real tests (summarized in Table 2).

This is due to different causes: on the one hand the confinement effect experimented by some parts of the core is not contemplated in the theoretical model (concrete in these areas increases its compressive strength, as it is shown in section 5.1). On the other hand, the expression (10) proposed to obtain neutral axis is clearly approximated in the theoretical model, while in the FE analysis it is accurate.

7 DESIGN CRITERIA

In general terms, concrete filled double skin symmetric sections are not very effective subjected to bending as the whole inner tube is located close to the neutral axis. This problem can be partially solved by displacing the inner profile along the "y" axis in concrete filled double skin asymmetric sections. This typology could be very useful for structural designs in which limited outer diameters are required, combined with large bending efforts.

In most cases, as more displaced is the inner tube, higher is the flexural resistance of the global section. However, this increase depends on having a correct bond between materials in order to transfer stresses properly.

One of the most important conditions in order to guarantee a correct bond between the core and the inner tube is to have sufficient pressed contact area in the interfaces. Pressure on contact surfaces guarantees the appearance of friction forces, by being often also capable of enhancing the friction coefficient. In other cases, connectors between different instances would be required.

This contact can be guaranteed even in tensioned areas of the core, due to having a high percentage of concrete subjected to a biaxial compressive state in the two axes of the section plane. However, as larger and thinner is the outer tube, better the contact works.

REFERENCES

Chitawadagi, M.V.; Narasimhan, M.C. 2009. Strength deformation behaviour of circular concrete filled steel tubes subjected to pure bending. Journal of Constructional Steel Research; 1–10.

Castro Medina, J.C. 2011. Modelización numérica del comportamiento Estructural de barras de pandeo restringido (in Spanish). Barcelona. Doctoral Thesis of Polytechnic University of Catalonia.

Cimpoeru, S.J.; Murray, N. 1993. The large deflection pure bending properties of a square thicn-walled tubes. International. J. Mech. Sci. 1993;35(3–4):247–56.

Elchalakani, M.; Zhao, X.; Grzebieta, R.H. 2002. Tests on concrete-filled double skin (CHS outer and SHS inner) composite short columns under axial compression. Thin-walled structures; 40:415–441.

Elchalakani, M.; Zhao, X.L.; Grzebieta, R.H. 2001. Concrete-filled circular steel tubes subjected to pure bending. Journal of Constructional Steel Research, 2001; 57:1141–1168.

Han, L; Zhao, X. 2006. Double Skin Composite Construction. Structural Engineering Materials; 8:93–102.

Hansville, G.; Lippes, M. 2008. Design of composite columns made of concrete filled tubes with inner massive core profiles and high strength materials. Composite Construction in Steel and Concrete IV. Proceedings of the 2008 Composite Construction in Steel and Concrete Conference VI, section Composite Columns: 326–337.

Lu, F.W.; Li, S.P.; Li, D.W.; Sun, G. 2007. Flexural Behavior of concrete filled non-uni-thickness walled rectangular steel tube. Journal of Constructional Steel Research; 63:1051–1057.

Moga, P.; Pacurar, V. 2006. Circular Composite Columns. Mechanism of Shear Transfer. Ovidius University Annals Series: Civil Engineering; 8(1).

Probst, A.D.; Kang, T.H.; Ramseyer, C.; Kim, U. 2010. Composite Flexural Behavior of Full-Scale Concrete-Filled Tubes without Axial Loads. Journal of Structural Engineer, ASCE, ; 1401–1412.

Richart, Brandtzaeg and Brown. 1928. A Study of Failure of Concrete under Combined Compressive Stresses. – [s.l.]: University of Illinois, Eng. Exp. Stn. Bull. 185.

Shanmugam, N.E.; Lakshmi, B. 2001. State of the art report on steel-concrete composite columns. Journal of Constructional Steel Research.; 57:1041–1080.

Shimura, Y.; Okada, T. 2001. Concrete Filled Tube Columns. Nippon Technical Steel Report, Nº 77,78, July 1998; 57–64.

Starossek, U.; Falah, N.; Löhning, T. 2008. Numerical Analyses of the Force Transfer in Concrete-Filled Steel Tube Columns. The 4th International Conference on Advances in Structural Engineering and Mechanics (ASEM'08). Jeju, Korea, May 26–28, 2008.

Tao, Z.; Han, L; Zhao, X. 2004. Behaviour of concrete-filled double skin (CHS inner and CHS outer) steel tubular stub columns and beam-columns. Journal of Constructional Steel Research; 60:1129–1158.

Uenaka, K.; Kitoh, H.; Keiichiro, S. 2010. Concrete filled double skin circular stub columns under compression. Thin-walled structures; 48:19–24.

Zhao, X.; Tong, L.; Wang, X. 2010. CFDST stub columns subjected to large deformation axial loading. Engineering Structures; 32:692–703.

Connections

Tubular Structures XIV – Gardner (Ed.)
© 2012 Taylor & Francis Group, London, ISBN 978-0-415-62137-3

Influence of the angle in the strength of RHS K-joints in galvanized lattice girders

M.A. Serrano-López, C. López-Colina & A. Lozano
Department of Construction, University of Oviedo, Gijon, Spain

G. Iglesias
Grupo Condesa, Vitoria, Spain

J. González
Ideas en metal, Gijón, Spain

ABSTRACT: This paper assesses the influence on the joint strength of the angle between the brace members and the chord in a K or N joint made with rectangular hollow sections. The study is specially focused on the case when those brace members include characteristic holes required for the hot-dip galvanizing process. To accomplish the objective of the proposed work, some tests on full-scale K and N joints, including angles of 35, 45, 55 and 90 degrees, were carried out. The experimental work was complemented by a validated numerical simulation in order to give some design recommendations and to extend the research to other joint configurations, including some non-symmetrical joints.

1 INTRODUCTION

It is known that structural hollow sections are always an excellent choice for trusses. When designing lattice girders, the option of circular hollow sections (CHS) provides a good structural behaviour and good aesthetics. However, joints details require accurate profiling of the ends of CHS brace members and therefore higher fabrication costs. Thus, rectangular hollow sections (RHS) are more cost effective, combining the good structural behaviour with joint details that only require flat cuts at the ends of brace members before welding their perimeters to the chord members.

An important issue with tubular steel structures is corrosion protection. Hot dip galvanization presents several advantages in comparison with other techniques but requires the provision of vent holes in the brace members. These vent holes must be large enough for optimization of the galvanizing process without reducing the strength of the joint. Therefore, an important consideration when using hot-dip galvanized lattice girders has been the uncertainty in the joint behaviour due to a possible reduction in the joint or member resistance produced by the vent holes required for the galvanizing process.

Although there have been no reported failures attributed to vent holes, the lack of proper technical knowledge of this issue could limit the wider use of hot-dip galvanized tubular structures because there are no calculation procedures in design codes such as CEN (2005), for the evaluation of the effect of holes on the joint capacity. In this situation, designers typically would over-size the brace member or maybe they could change their mind and decide to use laminated open sections – whose behaviour is well known – for steel structures that are designed to be hot-dip galvanized.

In order to answer these questions, given the concern of designers involved in this issue, a couple of projects funded by CIDECT (Comité International pour le Development et l'Etude de la Construction Tubulaire) and EGGA (European General Galvanizing Association) have been developed in the last few years.

CIDECT project 14B (Iglesias & Landa 2007) aimed to define how the holes should be executed and to propose some internationally accepted recommendations about the size, shape and position of vent holes. The holes were proposed on the basis of production efficiency and safety in the galvanizing plant hoping that the recommended size (between 20% and 25% of the diagonal of the cross section) and position (in the brace at a maximum distance from the chord of 18 mm) were also structurally appropriate. Following this, CIDECT project 5BX (Serrano et al. 2011) aimed to investigate – through a combination of experimental tests and finite element modelling – whether the above recommended vent holes could have any adverse effect on the performance of the hollow section joints.

One of the main variables taken into account in CIDECT project 5BX was the angle between the brace member and the chord, in order to evaluate its influence on the joint strength. This paper is focussed on

presenting and analyzing the results of this part of the research.

2 EXPERIMENTAL

2.1 *Tested joints*

As above mentioned, rectangular hollow section K and N joints that are widely used in hot dip galvanized steel trusses are considered. For the typical K-joint of a Warren lattice girder, three different angles of 35°, 45° and 55° between the braces and chord have been investigated. Also, the N joint that appears in other lattice girder configurations was considered. In this case, the non-symmetrical joint included a brace that was perpendicular to the chord and a diagonal with a 35° angle.

To address the objectives, joints with and without vent holes were tested. The above-recommended size, shape and position of the vent holes needed for the galvanization process were considered.

Four full-scale joint specimens were tested for each one of the 4 set of joints considered. Two of them included the vent hole and another two did not have holes. This meant a total of 16 tested joints. All the joints had a common gap of 15 mm between the brace members and RHS $150 \times 100 \times 5$ for chords and SHS 100×3 for the braces. The vent holes diameter was 35 mm. Three specific specimens were galvanized prior to testing in order to check if this condition had any influence.

Although the steel grade was the same (S275) for all the hollow sections, in order to take into account the actual material properties, particularly in the later numerical simulation, it was necessary to carry out some standard tensile tests. Three coupons were produced from different faces of all the cold-formed hollow sections.

2.2 *Test procedure*

To carry out the experimental program a purpose-built test frame was used. Some recommendations for tests on these types of connections (Wardenier & Stark 1978; Wardenier & de Koning 1976) were taken into account. Figures 1 and 2 show the test configurations for the K-joints with an angle of 45° and for the N-joints. Several attachments were specially designed and manufactured to accomodate the required angles for the four sets of joints. A hydraulic jack loaded the vertically positioned brace member while one end of the chord was left free, in-plane, and the other two ends were pinned to ensure that predominantly axial forces were transmitted to the members. The displacement in the loaded brace member was measured by a LVDT transducer allowing plotting of the force-displacement curves.

The load through the actuator over the vertical brace member was increased until failure of the joint. The tests were displacement-controlled and the registered

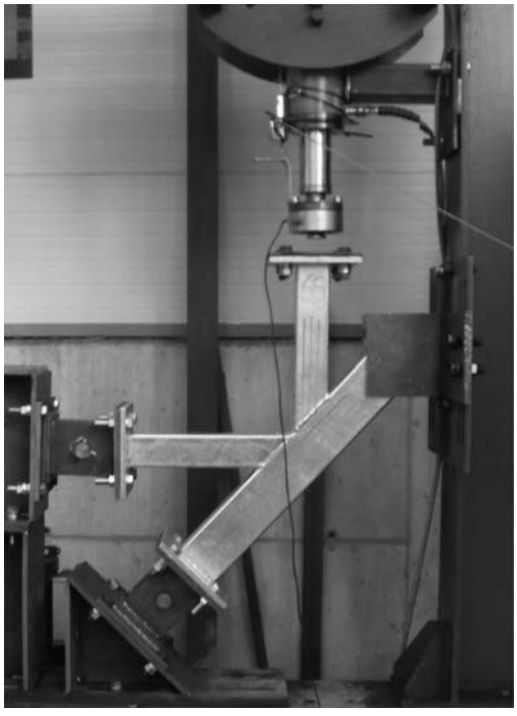

Figure 1. Test configuration for 45° K-joints.

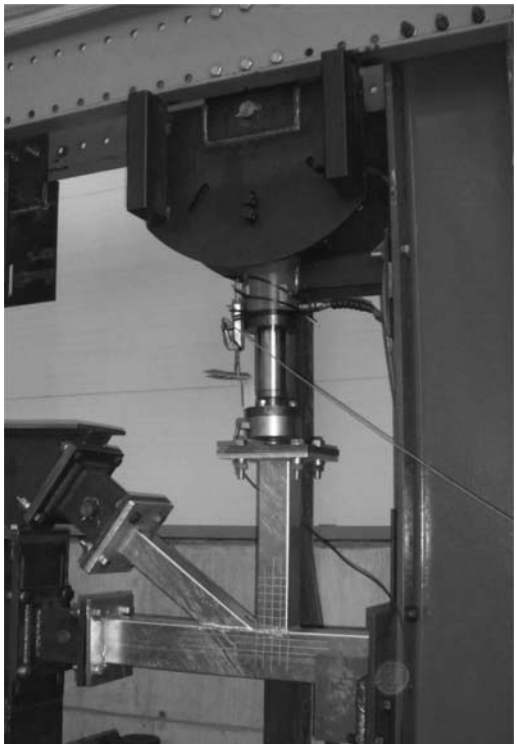

Figure 2. Test configuration for N joints.

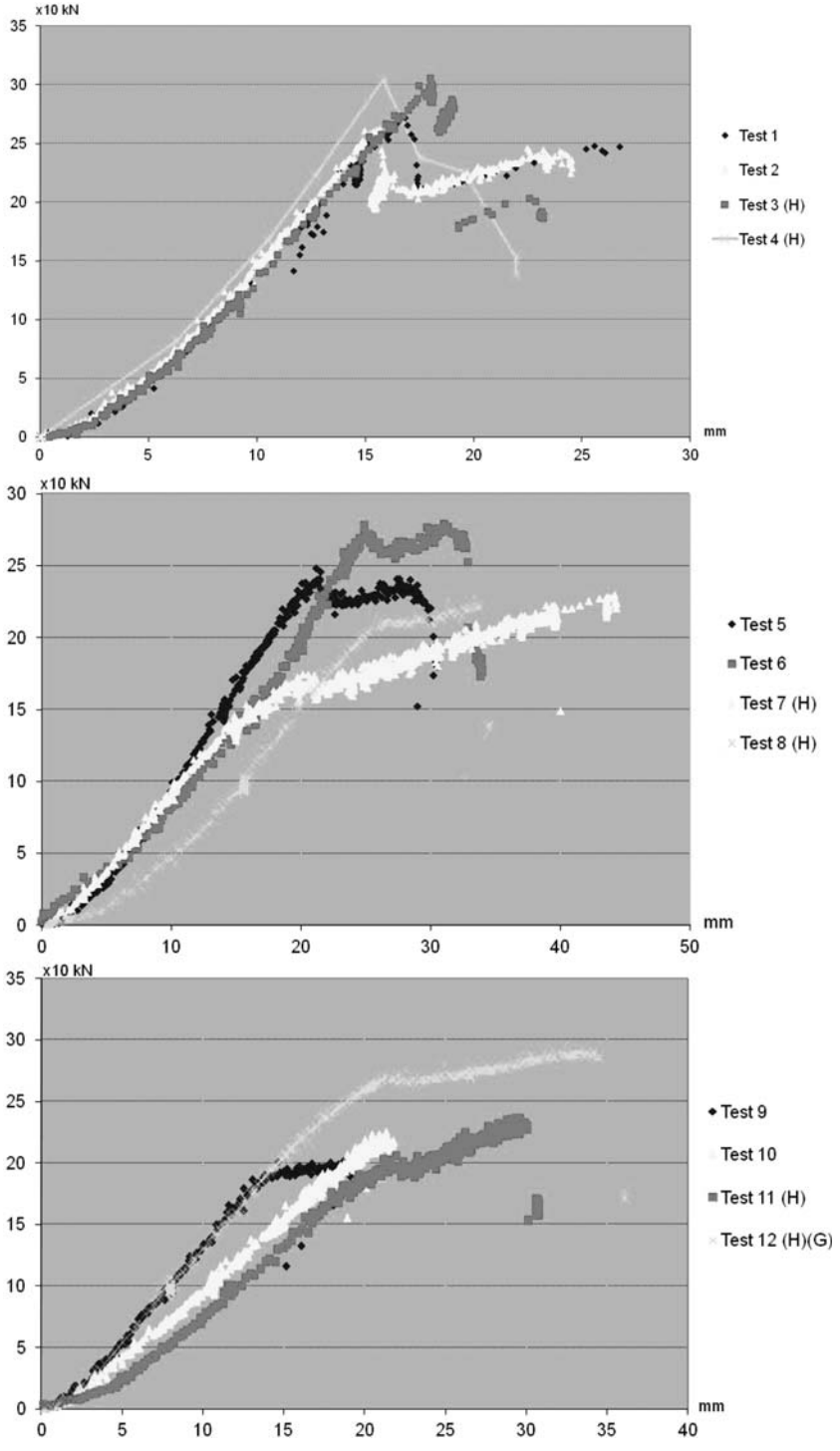

Figure 3. Experimental force-displacement results for K-joints with brace angles of 35°, 45° and 55°.

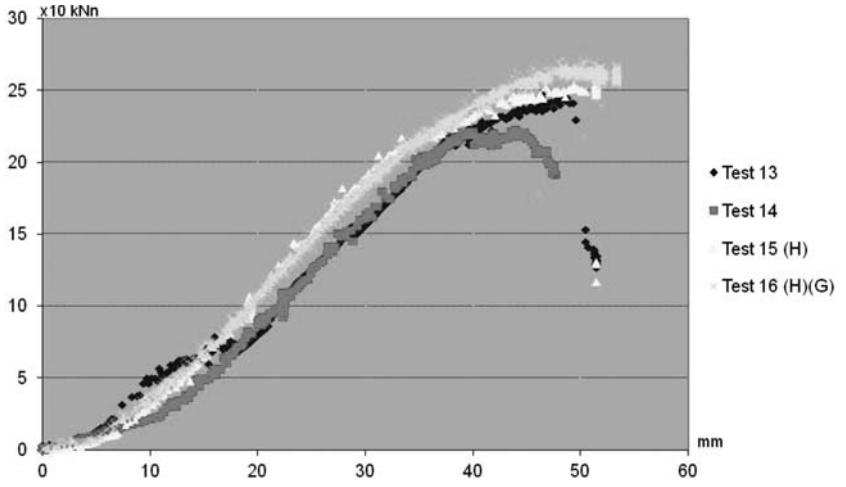

Figure 4. Experimental force-displacement results for N-joints.

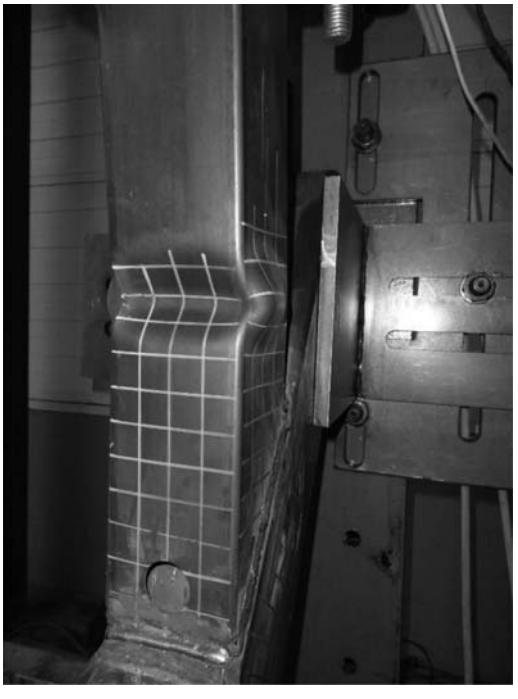

Figure 5. Failure in a 35° K joint with the vent hole.

collapse load was the maximum value of the force-displacement curve.

2.3 *Test results*

Figure 3 shows the experimental force-displacement curves obtained for the three sets of K-joints with angles between braces and chord of 35°, 45° and 55°, respectively. Letter H indicates that the joint tested included a vent hole. Figure 4 shows the curves for the set of N-joints in which the diagonal angle was 35°.

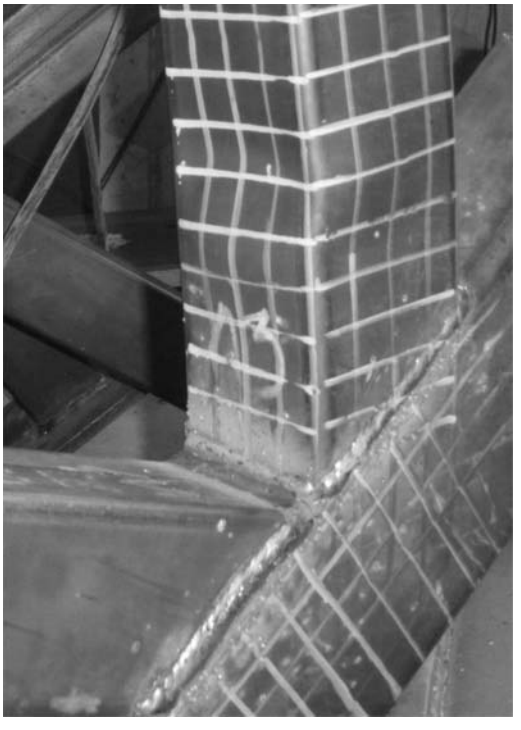

Figure 6. Failure in a 55° K-joint without vent hole.

In these figures the letter G indicates that the joint was galvanized before testing.

Figures 5 and 6 show the most common failure mode that occurred in the tested joints in both situations, with and without the vent hole.

3 NUMERICAL SIMULATION

As well known, laboratory work is expensive and usually the test program must be limited. So a numerical

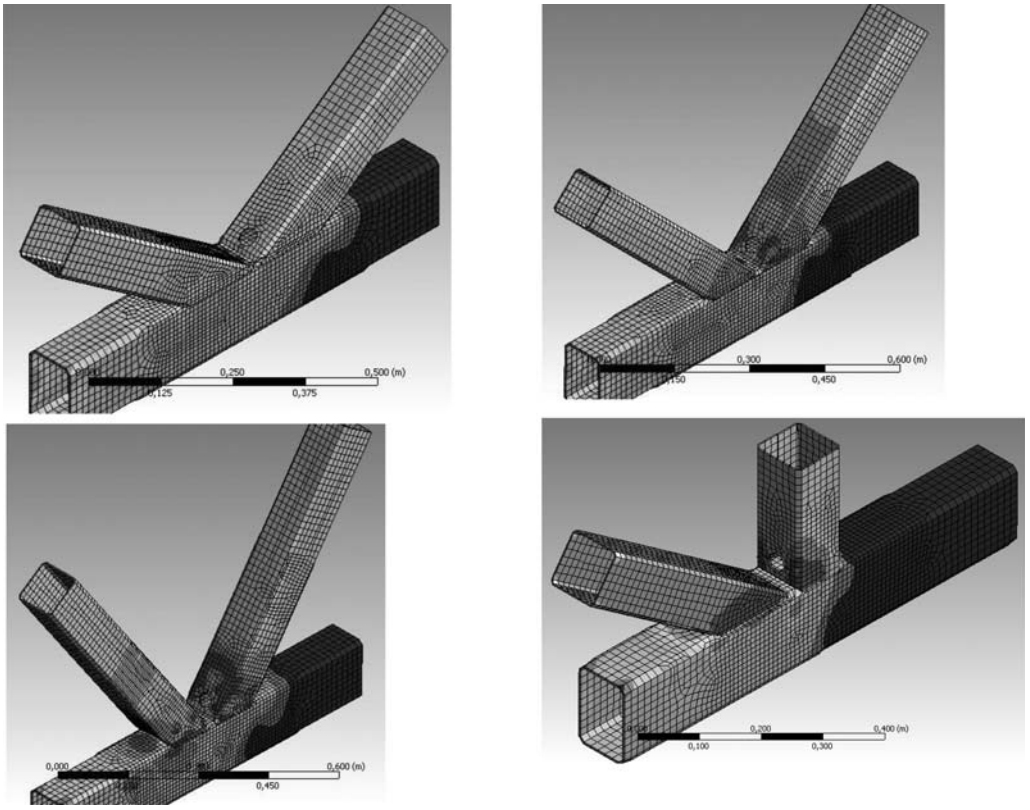

Figure 7. Numerical models for three K-joints (35°, 45° and 55°) and the N-joint.

Table 1. Maximum strength [kN] obtained in the FEM for non-symmetrical joints.

Joints Ref.	Chord	Comp. Brace	Tension Brace	Brace angles	Without hole	With hole
KGP04 Test	150 × 100 × 6	90 × 5	90 × 5	35°	452,46	453,22
KGP04 FEM	150 × 100 × 6	90 × 5	90 × 5	35°	446,89	446,63
Joint 1	150 × 100 × 6	90 × 5	60 × 4	35°	430,82	418,08
Joint 2	150 × 100 × 6	90 × 5	60 × 4	45°	374,81	361,61
Joint 3	150 × 100 × 6	90 × 5	60 × 4	55°	351,43	331,43
Joint 4	150 × 100 × 6	90 × 5	60 × 4	90°–35°	248,96	222,39

simulation followed the experimental tests to complement them. The aim of this part is the validation of the FE analysis in order to be able to extend the research to other joint configurations, including some non-symmetrical joints. The FE software ANSYS Workbench V.13 academic research was used for a parametric study or different joint configurations. The selected elements in the model were a four-noded shell 181 with six degrees of freedom at each node. Two different element sizes of 10 mm in the finer mesh area, and 20 mm outside this area, were taken in order to adjust the size of elements to the necessities of the simulation. Figure 7 shows a meshed model of each set of joints considered in this work: K-joints with 35°, 45° and 55° and N-joints.

Using the actual material properties obtained in the standard tensile test, a non-linear analysis was carried out taking into account geometric non-linearities, non-linear material properties and non-linear buckling. An initial imperfection was selected according to the recommendations by (Schafer & Peköz 1998).

In order to reproduce the laboratory tests as faithfully as possible, the joint was loaded by small steps of displacement on one of the brace members. The other brace member and one end of the chord were pinned. The other end of the chord remained free to move in the load plane. Stresses, buckling modes and ultimate loads were calculated and their results were compared with the experimental tests, allowing validation of the model to extend its application as below.

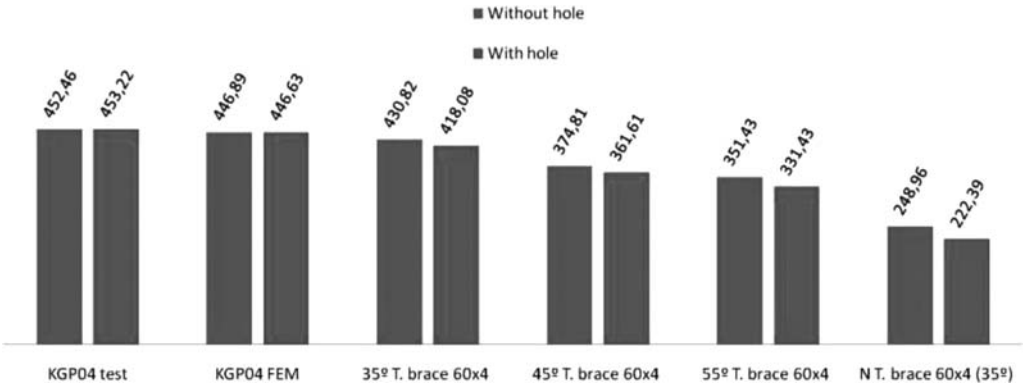

Figure 8. Maximum strength in FE simulation for non-symmetrical joints.

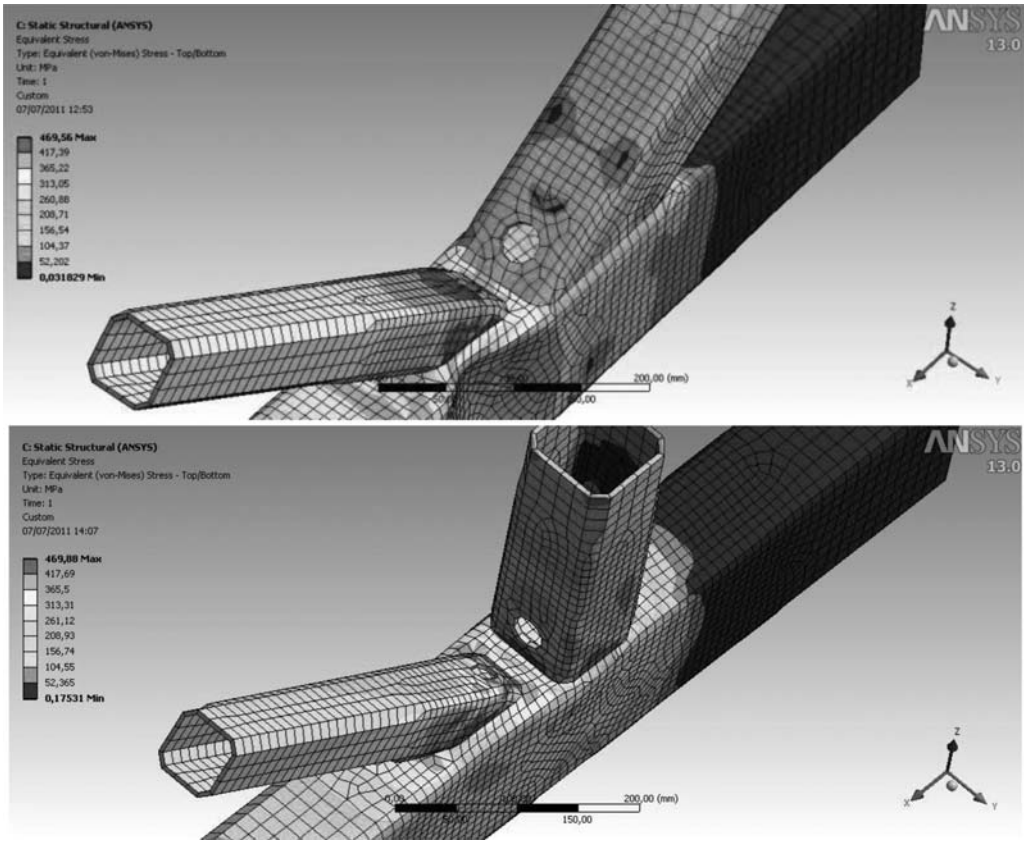

Figure 9. Different angles in FE simulation for non-symmetrical joints.

3.1 *FEM simulation for non-symmetrical joints*

Once the FE model was validated, it was extended to other joint configurations. In this sense, there was a concern about the behaviour of some asymmetric joint configurations.

This part of the study was specifically aimed at non-symmetrical joints of lattice girders in which the size of the tensile brace member is smaller than the compression brace member. Under these circumstances it is possible that the smaller section of the tensile brace member leads to failure in this brace instead of the previously studied failure in the compression member.

For an initial insight into this situation, some numerical simulations were carried out. The considered joint configurations for this part of the research are shown in Table 1. As a starting point, the experimental and numerical results of the set of joints KGP04 from the CIDECT project 5BX (Serrano et al. 2011) were taken

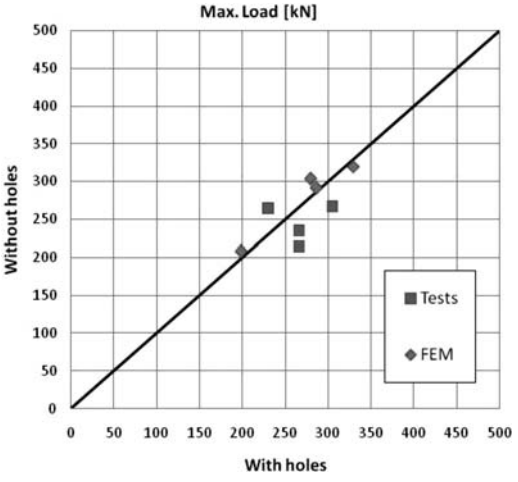

Figure 10. Maximum load in joints without hole vs with hole.

(two first rows of Table 1). For the non-symmetrical simulation, four joint configurations with different brace angles were considered. All of them had the same chord and compression member as in KGP04 but a smaller tensile member of SHS 60 × 4. Table 1 and Figure 8 show the maximum strength obtained for joints with and without the vent holes and Figure 9 shows respectively two meshed models for a K-joint and a N-joint in the non-symmetrical simulation.

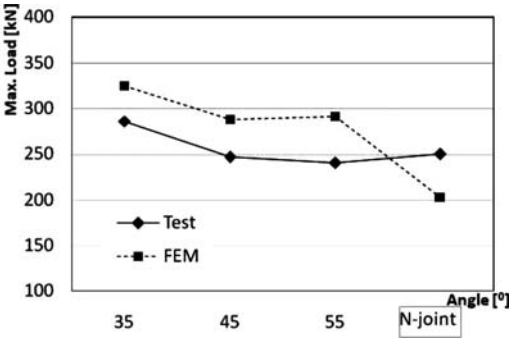

Figure 11. Comparison Test-Numerical simulation.

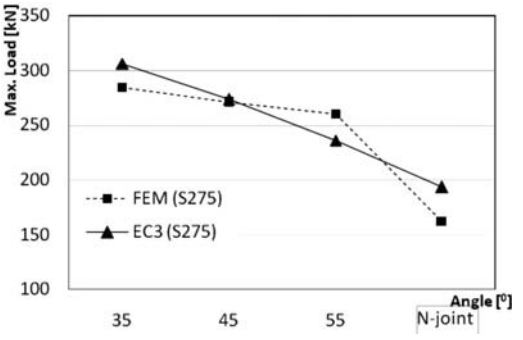

Figure 12. Comparison FEM-EC3 for nominal steel S275.

4 DISCUSSION OF RESULTS

A range of results have been produced for this paper, including experimental tests on four sets of joints with different brace angles, a complete numerical simulation of all the joints and an additional numerical simulation for non-symmetrical joints. These results are presented and compared below in this section. Figure 10 shows the maximum load in joints without any hole against the same joint with the vent hole, for both experimental and numerical simulation results. The vicinity of the plotted points to the diagonal lines concludes that there were not significant differences between both.

Having assumed that there is no influence from the vent holes, Figure 11 shows the maximum load for the joint tested with different brace angles. Every plotted point represents the mean value of the obtained data by FEM or by test. The plotted results allow a clear comparison of tests and simulation and indicate that there is a reasonable agreement and therefore the method for the finite element modelling can be considered validated. From this figure it can be concluded that the resistance of K-joints is lower as the brace angle gets bigger.

Figure 12 presents a comparison of FE results and EC3 equation results for the four sets of joints taken into account in this research when a nominal steel S275 is considered. A good agreement is observed and a clear conclusion indicates the lower resistance in joints when the brace angle gets bigger. It is important to note that when the failure mode is a local buckling in the brace member (BF) the angle has no influence according to EC3 equations. In fact the observed influence of the angle in EC3 is due to the fact that the predicted failure mode by equations is a chord plastification (CP) and in this case the angle would have an influence. However, the results of the experimental tests and numerical simulation indicated for all the tested joints a failure by local buckling in the brace (BF) instead of CP.

The situation is not so clear for N-joints. From FE and EC3 proposals, resistance is even lower than K-joints with the bigger brace angle, nevertheless test results indicate that there is not a significant reduction (Fig. 11).

In the case of non-symmetrical joints with different cross sections for the tension and compression brace members, Figure 8 allows a quick comparison of the results obtained just in the FE simulation.

Again there was no significant influence of vent holes on the ultimate load of the joint. Also, it can be observed that, independently of the joint presented or not a vent hole, the maximum strength that the joint was able to reach decreased as the brace angle increased. Here the analyzed N-joint followed the same pattern observed above by FE and EC3.

5 CONCLUSIONS

Once the experimental and numerical results have been presented and discussed, the following conclusions can be drawn from this work:

- From the experimental programme and from the numerical simulation it can be concluded that there is no influence of vent holes on the behaviour and strength of the tested joints.
- For symmetrical K-joints in Warren lattice girders, the joint resistance decreases as the angle between the brace member and the chord increases. In case of N-joints some more results are needed.
- A reasonably good agreement was obtained when tests and finite element model were compared, allowing to use the numerical model to predict the non-symmetrical joints behaviour.
- EC3 equations predict quite well the strength of the joints but not so well the failure mode. It would be necessary a change in the brace failure equation to take into account the angle between braces and chord in order to predict accurately both resistance and failure mode.
- In case of the studied non-symmetrical joints, it can be said again that there is no influence of vent holes. It can be also concluded that the K-joints present a lower resistance when the angle between braces and chord increases.

ACKNOWLEDGEMENTS

The authors would like to express deep gratitude to CIDECT and EGGA for funding project 5BX. They also would like to acknowledge the Spanish company Ideas en Metal for their contribution in the experimental program and the tube manufacturer CONDESA for supplying the testing material.

REFERENCES

CEN. 2005. *Eurocode 3: Design of steel structures. Part 1–8: Design of joints. EN-1993-1-8:2005.* European Committee for Standardization.

CEN. 2006. *Cold formed welded structural hollow sections of non-alloy and fine grain steels. Tolerances, dimensions and sectional properties. En-10219-2:2006.* European Committee for Standardization.

Del Coz, J.J., García, P.J., Fernández, M., Suárez, J.L. 2007. *Non-linear analysis of the tubular 'heart' joint by FEM and experimental validation.* Journal of Constructional Steel Research, 63(8): 1077–1090.

Iglesias, G. & Landa, P. 2007. *Recommendations for holes needed due to galvanization process.* Final report project 14B. UPV-EHU, ICT, CIDECT.

López-Colina, C., Serrano, M.A., Gayarre, F.L., Suárez, F.J. 2010. *Resistance of the component 'lateral faces of RHS' at high temperature*. Engineering Structures 32 (4): 1133–1139.

López-Colina, C., Serrano, M.A., Gayarre, F.L., del Coz, J.J. 2011. *Stiffness of the component 'lateral faces of RHS' at high temperature.* Journal of Constructional Steel Research 67 (12): 1835–1842.

Packer, J.A., Wardenier, J., Zhao, X.L., van der Vegte, G.J. and Kurabane, Y. 2009. *Design guide for rectangular hollow section (RHS) joints under predominantly static loading, 2nd edition, CIDECT, Switzerland.*

Schafer, B.W. & Peköz, T. 1998. *Computational modelling of cold-formed steel: characterizing geometric imperfections and residual stresses.* Journal of Constructional Steel Research 47: 193–210.

Serrano, M.A., López-Colina C., Iglesias, G. 2011. *Static strength of RHS K-joints in which brace members may be affected by vent holes for truss Hot-Dip Galvanizing.* Final report project 5BX. Universidad Oviedo, ICT, CIDECT.

Wardenier, J. & de Koning, C.H.M. 1976. *Rig comparison tests. Report 5S/76/33. CIDECT.* Delft: TNO-TH.

Wardenier, J. & Stark, J.W.B. 1978. *The static strength of welded lattice girder joints in structural hollow sections.* Revised final report. 5Q/78/4. *CIDECT*. Delft: TNO-TH.

Wardenier, J., Packer, J.A., Zhao, X.L. & van der Vegte, G.J. 2010. *Hollow Sections in Structural Applications. 2nd Edition*, Bouwen met staal, The Netherlands.

Tubular Structures XIV – Gardner (Ed.)
© 2012 Taylor & Francis Group, London, ISBN 978-0-415-62137-3

Over strength criteria of slotted connections with high yield strength steels

S. Iwamoto & K. Ochi
Kumamoto University, Kumamoto, Japan

ABSTRACT: This paper addresses the ultimate strength (P_m) of slotted connections with enough weld lengths (L) for yield capacity of CHS members. The required over strength factor of the full-strength connections was decided by the yield (P_y) and tensile strength of CHS members. The paper presents the results of a various analysis based on finite element models for slotted connections of CHS. The effects of parameters such as material constants of the stress-strain model and yield ratio of materials were shown. The required strength factor (P_m/P_y) for the full-strength connections with conventional steels is compared with the results of FEA for the connections with high yield strength and high yield ratio steels. Including the existing test data with parameters such as material properties, weld length and shape of connections, a required over strength factor for the connections with high yield strength steels is recommended.

1 INTRODUCTION

The ultimate strength of slotted connections as shown in Figure 1 and 2 has been the subject of intensive studies. These studies which covered required weld length and possible failure modes enable national and international design guide (Wardenier et al. 2008) to be developed.

The Japanese Building Code required over strength factor (α) for full-strength connections of brace ends under seismic loads. In the case of brace ends, AIJ (1998, 2006) required as following:

$$P_m \geq \alpha \cdot P_y \tag{1}$$

A typical value of over strength factor recommended in the Japanese Building Code is 1.2. Based on the effects of yield ratio of hot rolled sections, some different values of over strength factors are proposed in AIJ publications varying with the material properties and steel grades.

However, it should be noted that circular hollow sections are usually manufactured by cold formed and hot finished production processes. The difference of the production processes have been shown to affect the material properties.

Steel tubes manufactured by cold-forming and seamed by welding are much more economic and popular for structural applications than seamless tubes. Recently, cold-formed CHS with high strength steels are used which has a higher yield-to-ultimate strength ratio than the conventional steel grades. High yield strength cold formed circular hollow sections cause a complex situation in terms of material properties (Ling et al. 2007a, 2007b).

It was clarified that the material constants of the Ramberg-Osgood equation for high yield strength steels and cold formed CHS are decided by the yield strength and ultimate tensile strength by Ochi (2010).

Using the stress-strain models with the material properties of several yield/tensile strength ratios (YR)

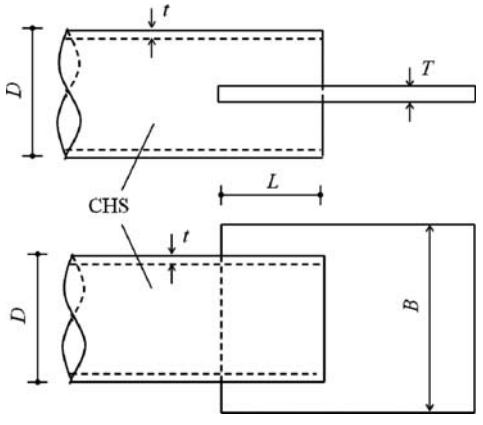

Figure 1. Single gusset plate-to-slotted CHS connections.

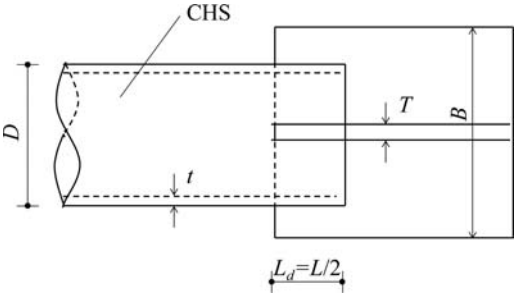

Figure 2. Cross gusset plates-to-slotted CHS connections.

and the application of FE analyses on slotted connections, The aim of this paper is to compare the ultimate strength of connections and the required over strength factors.

2 FE ANALYSES FOR CONNECTIONS

2.1 *General*

In this study, the FE analyses program is comprised of single plate-to-slotted connections with material models on several yield/tensile strength ratio YR, three diameter-to-thickness ratios and weld lengths. These parameters were decided by the existing test results and recommendations.

2.2 *Material stress-strain models*

The Ramberg-Osgood equation is especially useful to describe the non-linear relationship between stress and strain for materials that harden with plastic deformation, showing a smooth elastic-plastic transition.

The Ramberg-Osgood equation, expressed in terms of strain, is:

$$\varepsilon = \frac{\sigma}{E} + 0.002\left(\frac{\sigma}{\sigma_y}\right)^n \tag{2}$$

where ε = logarithmic strain; σ = true stress; σ_y = yield stress (yield strength); E = elastic modulus and n = material constant.

Ultimate tensile strength is

$$\sigma_u = \left(\frac{1}{c \cdot e \cdot n}\right)^{1/n} \tag{3}$$

in which *e*is the mathematical constant.
where:

$$c = \frac{0.002}{\sigma_y^n} \tag{4}$$

Equation 3 is used for determining the material constant (n) in Equation 2. The Ramberg-Osgood Equation 2 requires the yield strength and tensile strength as input parameters (Ochi 2010).

Figure 3(a) shows the true stress-true strain curves generated by the Ramberg-Osgood equation using the yield strengths and tensile strengths as shown in Table 1.

The engineering stress-strain curves of Ramberg-Osgood equation using Equation 5 and 6 are shown in Figure 3(b).

$$\sigma = \sigma_e(1 + \varepsilon_e) \tag{5}$$

$$\varepsilon = \ln(1 + \varepsilon_e) \tag{6}$$

where ε_e = engineering strain; σ_e = engineering stress

Figure 3(b) shows that the tensile strengths of the engineering stress-strain curves keep the constant value of 600 (MPa) changing with the yield strengths as shown in Table 1.

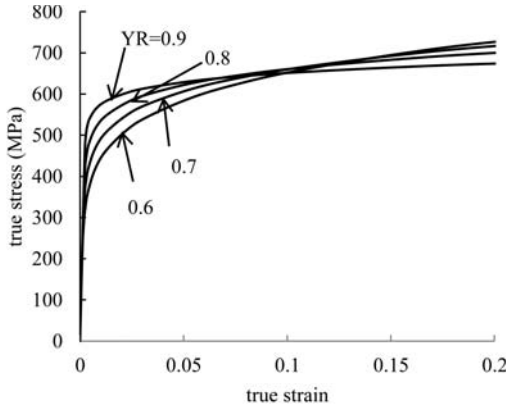

(a) True stress-strain curves

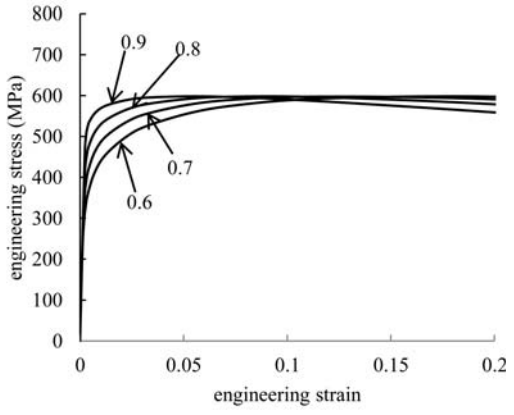

(b) Converted engineering stress-strain curves under tensile loads

Figure 3. Ramberg-Osgood stress-true strain curves.

Table 1. Material properties of stress-strain models.

Material No.	YS MPa	TS	YR
1	360	600	0.6
2	420	600	0.7
3	480	600	0.8
4	540	600	0.9

YS = yield strength; TS = tensile strength; YR = yield ratio

2.3 *Finite element model*

The experimental data (Ochi 1998) was used to calibrate this study for slotted connections under tensile loads. Finite element analyses including the Ramberg-Osgood relation were conducted to evaluate the ultimate strength of the connections. The test results of cold formed CHS connections summarized in Table 2 are selected for FEA.

Table 2. Dimensions and variables of specimens.

D	t	YS	TS			
(mm)		(MPa)		YR	L/D	n
114.3	2.8	380	471	0.806	1.2 and 1.5	12.5
114.3	3.5	396	481	0.824	1.2 and 1.5	13.5
114.3	4.5	407	477	0.853	1.2 and 1.5	15.5

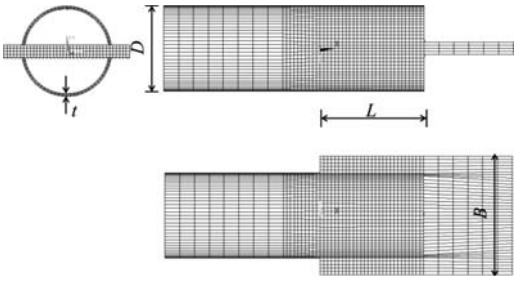

Figure 4. Meshed models of connections.

Finite element analyses (ANSYS 13) with solid elements were carried out to simulate the behaviour of the test specimens. Eight nodded solid elements were used. Figure 4 shows the finite element mesh generated for a connection.

Because that main purpose in this study focusses on over strength factor of the connections, the welds were not modelled in Figure 4. Also, the gusset plate and the circular hollow section elements are fully connected to each other. The Ramberg-Osgood Equation 2 requires the yield strength and tensile strength as shown in Table 2.

Because the Ramberg-Osgood equations could not directly be used as input for ANSYS, the multilinear true stress-true strain relations using Equation 2 were used.

Figure 5 shows the distribution of the Von Mises equivalent stress generated by the finite element models at the ultimate strength.

In Figure 5, the areas of stress concentration around the tube circumference found in the FE analysis agree well with the location of the cracks observed in the test specimen while generating a circumferential tensile failure.

The stresses at the end of the plate due to the weld length and plate thickness were about 10% higher than around the tube circumference. Also, the stress level along the plate was same as at the tube circumference. This means that circumferential tensile failure was the critical mode for the model shape chosen for the specimens as shown in Table 2. Because of $L/D > 1.2$ required for full strength connection with over strength factor (AIJ 2002), the tear-out failure can be neglected in the over strength factor.

Figure 6 shows the typical FE load-deformation curves on the specimens ($L/D = 1.2$) shown in Table 2. Figure 7 plots the predicted ultimate strengths

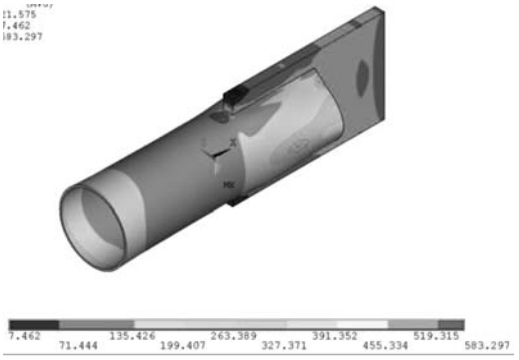

Figure 5. Distribution of the Von Mises equivalent stress.

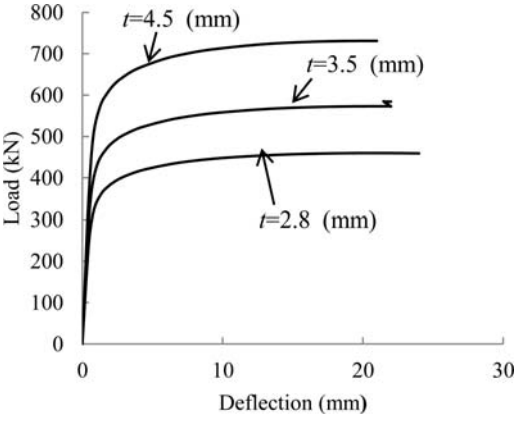

Figure 6. Load-deformation curves ($L/D = 1.2$).

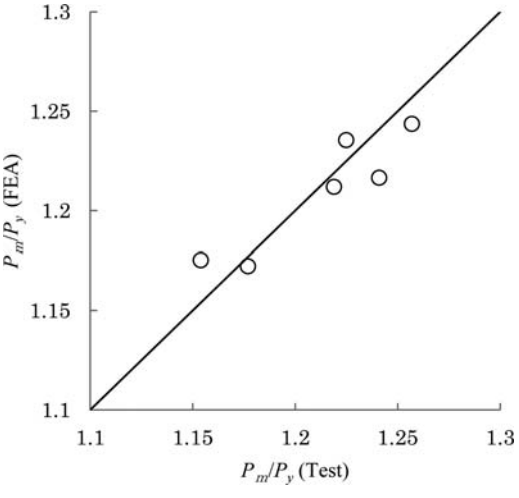

Figure 7. Comparison between FEA and experiments for the connections.

Table 3. Variation ranges for basic variables in data base.

Variables	Single plate	Cross plate
D/t	32.6–72.9	24.2–47.2
L/D	0.98–2.56	0.93–1.51
YR	0.671–0.816	0.667–0.882

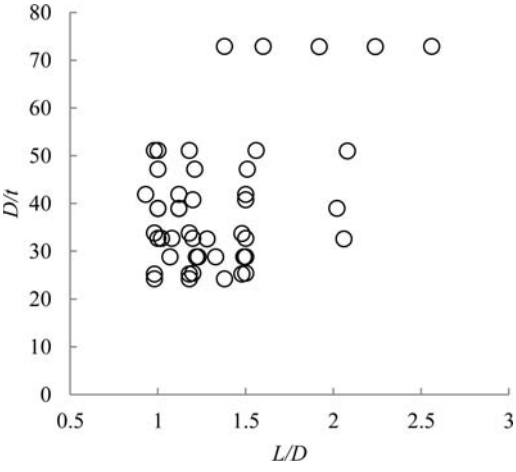

Figure 8. Geometrical variables for the connections.

obtained from the FEA versus test results for all specimens given in Table 2. The ultimate strength is normalized with respect to yield strength of the CHS member. It can be seen that the ultimate strength by FEA provide a reasonable approximation of the test results.

3 PARAMETRIC STUDY AND DISCUSSION

3.1 *Test data base*

For the gusset plate-to slotted CHS connections, the range of the data base is shown in Table 3, Figure 8 and 9.

Based on these data, AIJ (2002) requires a reduced factor (0.9) for axial full tensile strength when the weld length exceed the 1.2 times diameter ($L/D = 1.2$) and full tensile strength when the weld length exceed 1.5 times the diameter ($L/D = 1.5$).

In Figure 8, the data include both of the single plate connections and cross plate connections as shown in Figure 1 and 2. The weld lengths (L) of the cross plate connections are calculated the twice length of actual weld length (L_d).

The Japanese Building Code required over strength factor (α) to the yield strength of members for full-strength connections of brace ends under seismic loads. A typical value of over strength factor in the Japanese Building Code is 1.2. Based on the effects of yield ratio of hot rolled sections, some values of over strength factors are proposed in AIJ publications varying with the material grade.

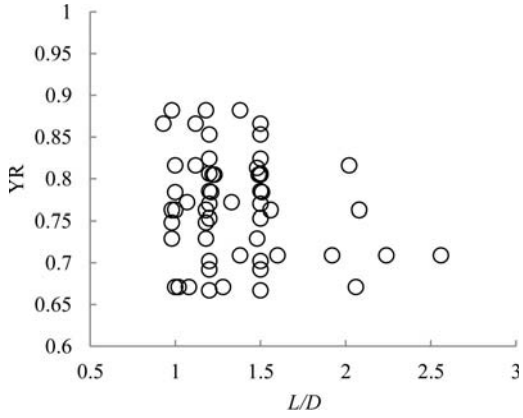

Figure 9. Geometrical variables and material properties for the connections.

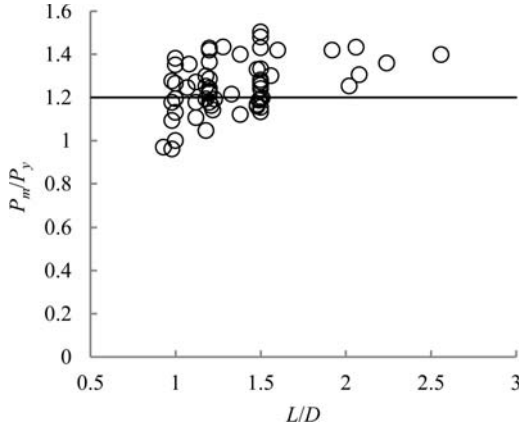

Figure 10. Normalised test results versus weld lengths.

The codes and recommendations use the nominal material properties of yield strength and tensile strength which may be different from the actual values of the yield and ultimate tensile strengths.

The actual yield/tensile strength ratio (YR) are shown in Figure 9. The data base includes the test results for the slotted CHS connections made of various steels ranging from mild steel to high-strength steel grades with cold formed, hot finished including the heat treated sections and hot rolled CHS.

In Figure 10, the ultimate strength (P_m) of the connections is normalized with respect to the actual yield strengths of CHS (P_y). It is well known that the yield strength of cold formed CHS is higher than that of hot formed CHS with the same steel grade.

The AIJ recommend that connections with the sufficient weld lengths ($L/D > 1.5$) satisfy the full section capacity. However, because of the high yield ratio, some tests results ($L/D > 1.5$) under the required over strength factor (1.2) are shown in Figure 10. The ductility of connections due to the actual yield ratio of the tube materials is dependent on the production process.

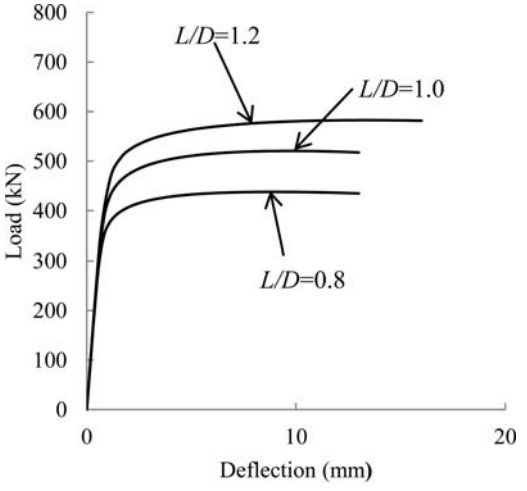

Figure 11. Load-deformation relationships (YR = 0.9; t = 2.8 mm).

3.2 *FEA and discussion*

Using the FE models as shown in Figure 4 for basic model, FE analyses were conducted to evaluate the effects of the parameters such as the weld length (L/D), diameter to thickness ratio (D/t) and yield ratio (YR) for the ultimate strengths of the connections.

Because the main criterion is the over yield strength of the CHS for the ultimate strength of the connections, the FE models were generated with high L/D ratios of 0.8, 1.0, 1.2, 1.3, 1.4 and 1.5. D/t ratios were based on the test three specimens as shown in Table 2. The material stress-strain models as shown in Table 1 and Figure 3 (a) with YR as 0.6, 0.7, 0.8 and 0.9 were used. Typical load-deformation relationships for FEA with YR = 0.9 are shown in Figure 11.

Test data are divided into three ranges as shown in Figure 12. In Figure 12, the dashed lines are upper limits (1/YR) of over strength factor for the connections. The solid lines depict are required over strength factor (1.2) for the seismic design.

Figure 12(a) shows the test data with lower YR ($0.65 < YR < 0.75$) and the FEA results with YR = 0.7. The lower YR test data include cold formed, hot finished and hot rolled sections. There are differences in the stress strain relationships between cold formed sections as shown in Figure 3 and hot rolled sections with a distinct yield plateau. The difference in materials grades affects the relationships between the test data which includes hot-formed sections and FEA results for cold-formed sections. The test data and FEA results with L/D ratio > 1.0 gave the required over strength factor.

Figure 12(b), (c) shows the test data with higher YR. It can be seen that the ultimate strengths of the test results are in good agreement with the FEA results for the cold-formed sections.

In Figure 12(b), the required over strength factor is satisfied in the range of L/D above 1.3.

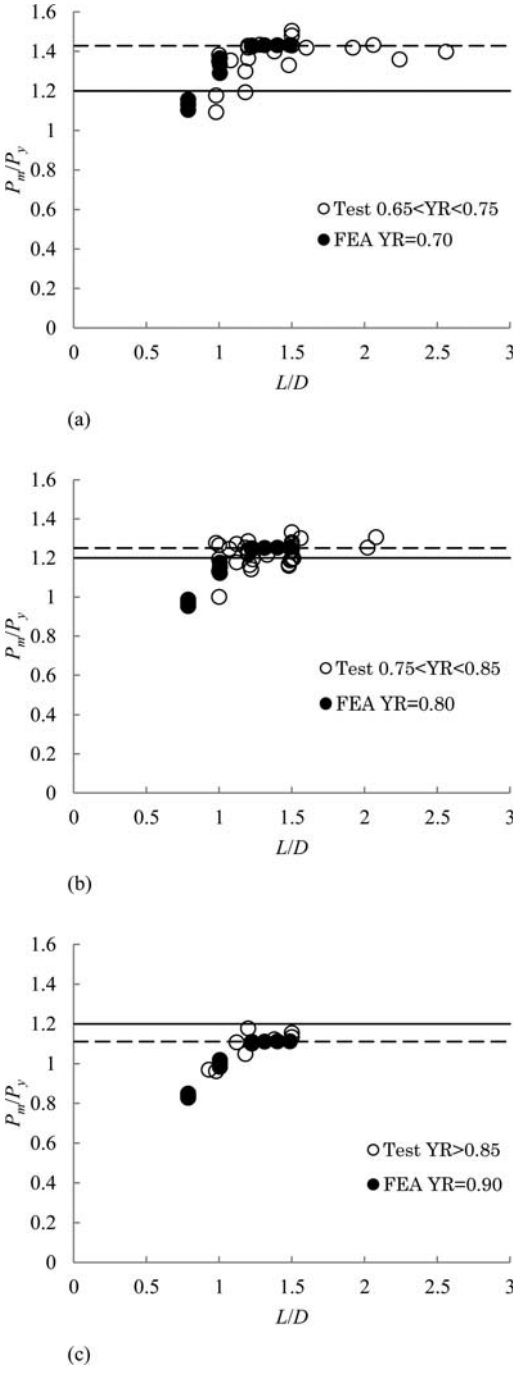

Figure 12. Comparison between FEA results and experimental results for the connections.

In Figure 12(c), the test data which include all the high strength steel sections and all FE results do not exceed the required factor. Basic concepts of the over strength factor for the connections were based upon the deformation capacity and plastic design of the brace members. The plastic designs of the connection

with high strength steel for the lower classifications depend on limitations of deformation capacity of the connections.

4 CONCLUSIONS

The FE analyses carried out indicate that the material properties of the tube had a significant effect on the strength and over strength factor of the slotted connections under axial tensile loads. Using the cold-formed material properties, the material constants of the modified Ramberg-Osgood curves are presented for the parametric FE analysis. Based on the comparison of the FEA ultimate strength of the connections with the several material properties depending on yield ratio, it can be seen that the important parameters are the geometric parameters and the material properties.

Based on the FEA results and experimental data, the effects of the parameters such as the weld length (L/D), diameter to thickness ratio (D/t) and yield ratio (YR) for recommended value of the over strength factor of the connections were discussed. The test data and the FEA results in the case of low to medium yield/tensile strength ratio ($0.65 < \mathrm{YR} < 0.75$) have a higher safety margin against required over strength factor than the connections with medium to high yield strength ratio ($0.75 < \mathrm{YR} < 0.85$) materials. The connections with YR<0.85 materials including conventional cold formed CHS are conservative for the code and the recommendations ($L/D > 1.2$). On the other hand, high yield ratio ($\mathrm{YR} > 0.85$) give the smaller margin for the yield strength of members than the required over strength factor. The connections with slotted CHS should have required values of over strength factors dependent upon the tube manufacturing process or actual yield ratio variation.

REFERENCES

Architectural Institute of Japan 1998, Recommendation for limit state design of steel structures.

Architectural Institute of Japan 2002, Recommendations for the design and fabrications of tubular truss structure in steel.

Architectural Institute of Japan 2006, Recommendations for design of connections in steel structures.

Kurobane, Y., Packer, J.A., Wardenier, J., & Yeomans, N., 2008. Design guide for structural hollow section column connections. CIDECT Series "Construction with hollow steel sections" No. 9, CIDECT, ISBN 978-3-938817-03-2.

Martinez-Saucedo. G., Packer, J.A. & Willibald, S. 2006. Parametric finite element study of slotted end connections to circular hollow sections, *Engineering Structure*s 28, ELSEVIER: 1956–1971.

Ling, T.W., Zhao, X.L., Al-Mahaidi, R. & Packer, J.A. 2007a, Investigation of shear lag failure in gusset-plate welded structural steel hollow section connections, *Journal of Constructional Steel Research* 63, ELSEVIER: 293–304.

Ling, T.W., Zhao, X.L., Al-Mahaidi, R. & Packer, J.A. 2007b, Investigation of block shear tear-out failure in gusset-plate welded connections in structural steel hollow sections and very high strength tubes", *Engineering Structures* 29, ELSEVIER: 469–482.

Ochi & Goya. 1998. Ultimate strength of tube-to-through gusset plate joints – a comparison between cold-formed and hot-finished sections. *Proc. Fifth Pacific Structural Steel Conferences*, Seoul, Korea: 651–656.

Ochi, K. 2010. Material properties of cold formed tubular sections with high yield strength steels. *Proc. 13th Intern. Symp. on Tubular Structures*, Hong Kong, China, Tubular Structures XIII: 429–434.

Wardenier, J., Kurobane, Y., Packer, J.A., Vegte, G.J. van der, & Zhao, X. –L. 2008. Design guide for circular hollow section (CHS) joints under predominantly static loads. 2nd Edition, CIDECT Series "Construction with hollow steel sections" No. 1, CIDECT, ISBN 3-8249-0802-6.

Tubular Structures XIV – Gardner (Ed.)
© 2012 Taylor & Francis Group, London, ISBN 978-0-415-62137-3

Finite element modelling of beam-to-column flush end plate connections utilising blind bolts

O. Mirza & B. Uy
School of Engineering, University of Western Sydney, Penrith, New South Wales, Australia

ABSTRACT: This research presents the experimental investigation on beam-to-column flush end plate connections utilising blind bolts. The test results were used to establish the load-displacement characteristics of the connections under the both static and cyclic loading conditions. The finite element modelling results were compared with the experimental results. The finite element models showed that they were in good agreement with the experimental results. From the results gained, it can be concluded that the improved design has enhanced the performance over the previous experiment for both loading conditions. However, the connection failure still plays a major role in high rise buildings when they are subjected to earthquake in a 1:2500 year return period.

1 INTRODUCTION

Composite steel-concrete construction, particularly for bridge superstructures and multi–storey frames, has achieved a high demand in several countries. This is mainly due to a reduction in depth, savings in steel weight and possibility of rapid construction.

Beam-to-column connections have been found to be of great significance in influencing the structural behaviour under seismic loading. Observations from full-scale seismic tests and from damaged structures, Nie et al. (2008) and Popov and Takhirov (2002) confirmed that beam-to-column connections have a considerable effect on the survival time of structural members due to their ability to distribute forces.

The design of connections has been explored by many researchers including Wu et al. (2005) and De Silvana and El-Debs (2004) to enhance the behaviour of the connection by means of additional fittings through bolted connections. Wu, Chung et al. (2005) and De Silvana and El-Debs (2004) focused on H shaped structural steel beams connected to a concrete-filled steel tubular column that was modified through the use of U-shaped end plates in order to get the required strength. Bolts were used to establish the connection between the welded endplate at the beam ends and the tubular column. These enhancements improved the overall strength of the connections.

However, the connections were considered to be too complicated to construct due to excessive welding and the need to pre-stress the tie-rods. Wang et al. (2009) considered these connection designs to be impractical and requiring high tolerance, and therefore suggested to simplify the connection design. Therefore, the development of blind bolts was considered as one of the solutions to the existing problem.

Mirza and Uy (2011) have undertaken previous research to study the behaviour of blind bolts when subjected to earthquake loading. However, previous research demonstrated that the failure mode in both the connections and on the headed stud shear connectors were severe. This paper provides an experimental study and finite element analysis of a novel joint system used in steel frames to withstand seismic load at a 1 in 2500 year occurrence.

Despite existing research being conducted with regard to the development of robustness of composite connections by Loh et al. (2006a), Loh et al. (2006b) and Wang et al. (2007), it is still imperative to further investigate the performance characteristics of these new and innovative composite connections when subjected severe earthquake loads. Figure 1 illustrates the connection using blind bolts through a steel tube filled with concrete. The main compressive loads are

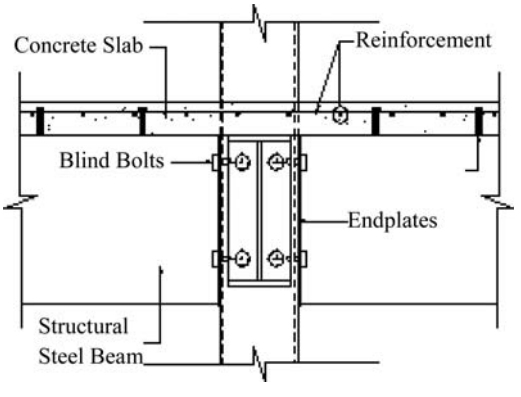

Figure 1. Typical connection detail.

Table 1. Test specimens.

Specimen	Column	Beam	Blind bolt	Loading type
1	SHS300 × 10	610UB101	M20	Static
2	SHS300 × 10	610UB101	M20	Cyclic

therefore transferred in this zone and the longitudinal reinforcement in the slab is thus used to carry the major tension force.

2 EXPERIMENTAL SPECIMENS

The experiments provide a study of novel joint systems used in composite frames to withstand earthquake loading. The test specimens were representative of beam-to-column joints in medium rise buildings. The composite flush endplate connection was designed to provide strength and ductility for earthquake resistance with energy dissipation located in ductile components of beam-to-column joints. The experiment comprises of two specimens, of which one tested under monotonic loading and the other under cyclic loading, as shown in Table 1.

Each specimen consisted of a 2000 mm wide, 3540 mm long and 150 mm deep reinforced concrete composite slab connected to a 610UB101 structural steel beam through shear studs, as shown in Figure 2.

The structural steel beams were connected to a concrete-filled square column of SHS 300 × 10 with flush end plate connections using AJAX M20 blind bolts. The structural steel beams acted as primary and secondary supports for the slab. The slab was reinforced with N12@100 reinforcement in both longitudinal and secondary directions that contributed greatly to the overall performance of the connection region in the negative moment direction, in terms of both stiffness and strength.

The aim of this series of experimental study was to monitor the load-deflection behaviour until the blind bolts reached their ultimate capacity. In the monotonic loaded specimen, an axial load of 1980 kN was applied to the concrete filled tubular column to reduce side sway where EI is the governing factor. At the same time, approximately 35% of monotonic loads were applied at both ends of the structural steel beams until the specimen reached its ultimate capacity.

For cyclic loaded specimen, an axial load of 1963 kN with approximately 35% of the axial capacity of the column was applied to the concrete-filled tubular column. This promotes good earthquake detailing as it will reduce the likelihood of a plastic hinge forming in the column which could cause catastrophic failure, rather the plastic hinge would form within the beam. Both upward and downward cyclic loads were applied simultaneously to both ends according to the AISC, AISC (2005) bi-directional cyclic loading, as presented in Figure 3.

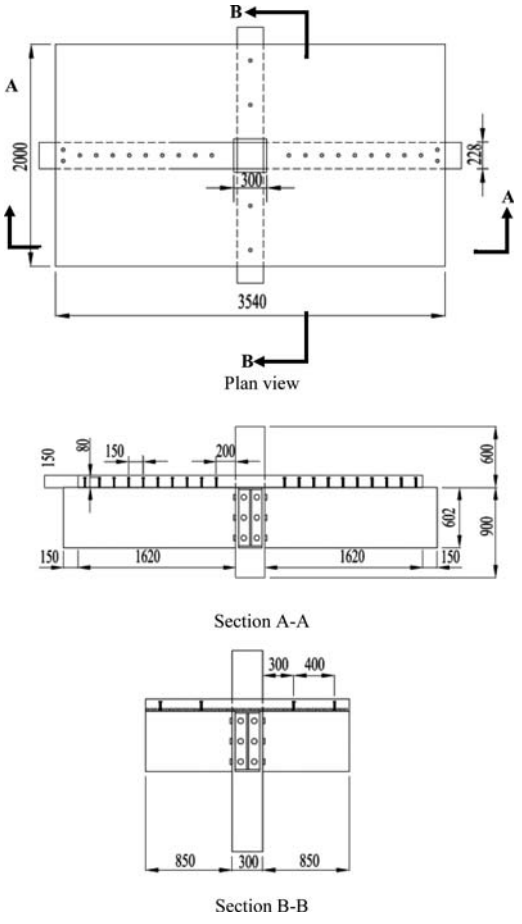

Figure 2. Details of test specimens.

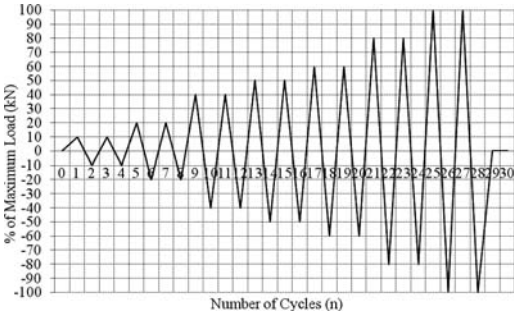

Figure 3. Cycles of earthquake loading according to AISC, AISC (2005).

3 FINITE ELEMENT MODEL

3.1 *Material properties*

In general, constitutive laws are used to define the stress-strain characteristics of a material. The accuracy of the analysis is dependent on the constitutive laws

used to define the mechanical behaviour. In materials such as concrete, structural steel and reinforcing steel, profiled steel sheeting and shear connectors, the constitutive laws are represented by the stress-strain relationships of the materials. In this paper, the mechanical behaviour at static and seismic loadings is considered. For static loading, the material properties are according to Mirza and Uy (2009a), and for seismic loading, the concrete and steel materials are according to Kent and Park (1971).

3.2 *Finite element type, mesh and boundary conditions*

Three-dimensional solid elements were used to model the push off test specimens in order to achieve an accurate result from the finite element analysis. For both the concrete slab and the structural steel beam, a three-dimensional eight-node element (C3D8R) was used because it is a solid element and was also used to improve the rate of convergence. A three-dimensional thirty-node quadratic brick element (C3D20R) for blind bolts and shear connectors was chosen because it is a second order element consisting of 20 nodes and these provide higher accuracy when compared with the first order elements. They also capture stress concentrations more effectively and are better for modelling geometric features. A four-node doubly curved thin shell element (S4R) was used for the profiled steel sheeting because it is the most appropriate type of element to model thin walled steel structures. The S4R element has six degrees of freedom per node and proved to give accurate solutions, and also permits quadratic deformation over four nodal coordinates, membrane action and plain strain behaviour. Finally, a two-node linear three-dimensional truss element (T3D2) for reinforcing steel was adopted, where the axial direction is released using an option of equation provided in ABAQUS.

Figure 4 illustrates the finite element mesh used to represent a quarter model of the experimental specimen. The aim of this was to reduce the simulation cost and computational time. The generated mesh was designed to give an optimal accuracy where the fine mesh surrounds the blind bolts and shear connectors and a coarse mesh was used elsewhere.

All the nodes designated as Surface 1 are restricted to move in the y-direction while all the nodes in Surface 2, are restricted to move in the x-direction. For the application of load, uniformly distributed axial load was applied to the centre of the reinforced concrete tubular column, whilst a concentrated load was applied at 150 mm from the tip of the end of the structural steel beam. The concentrated load was the combination of gravity and base shear load. The load represents maximum deflection on the frame in order to determine the performance of the blind bolts when subjected to different loading. Both the loads were employed using the modified RIKS method, which can be obtained through a series of iterations for each increment for a non-linear structure. The RIKS method was used for the nonlinear analysis to ensure that any unloading was captured.

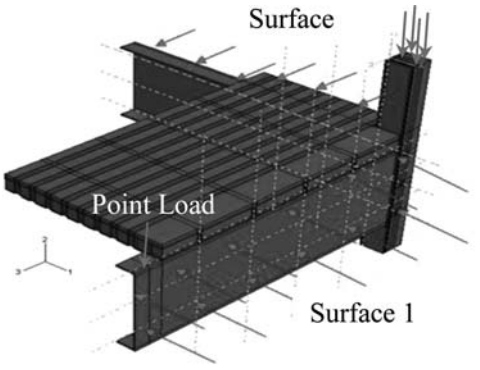

Figure 4. Finite element model layout.

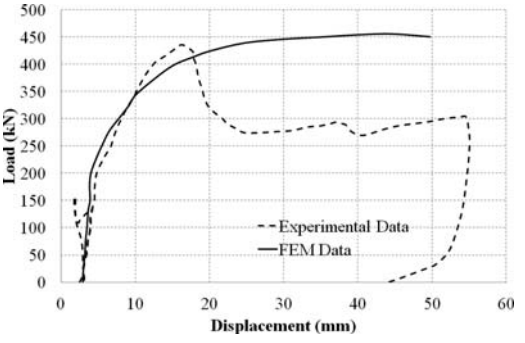

Figure 5. Load versus displacement relationship for static loading.

4 RESULTS AND DISCUSSIONS

4.1 *Static loading*

Figure 5 shows the load versus displacement relationship under static loading. When the load reached 229 kN, fine cracks were observed close to the column support, as shown in Figure 6. This was a significant improvement when compared with previous design, where the first cracking was observed at 168 kN. As loading progressed, more fine cracks appeared at 314 kN with additional cracks at the end of the concrete slab, as in Figure 7. When the load reached 400 kN, bending of the end plate was observed, as shown in Figure 8. A peak load of 425 kN was measured in Figure 5 with a 15 mm displacement. There was a 16% improvement to the peak load from previous design with a peak load of 362 kN.

Figure 5 proves that the finite element model is in good correlation with the experimental data up until the structures collapse. This is because the authors herein used a well-established nonlinear static implicit procedure to analyse the finite element model. This

Figure 6. Fine cracks appeared close to column.

Figure 7. Cracking at the end of concrete slab.

Figure 8. Bending of end plate.

method is not entirely suitable for use in the post-failure range and in complex contact interactions. However, the static implicit method solved the convergence difficulties and the ultimate load can be attained.

Initially, it was observed that the concrete element near the column face reached its cracking stress. This proved that the concrete started to crack near the column surface. With the continuation of the loading,

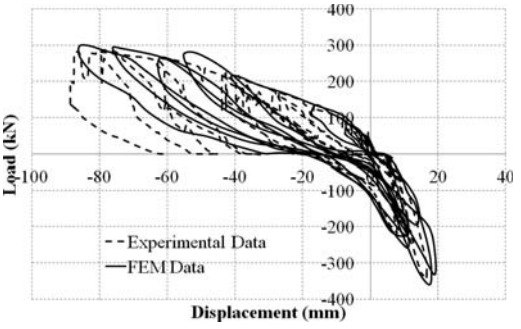

Figure 9. Load versus displacement relationship for cyclic loading.

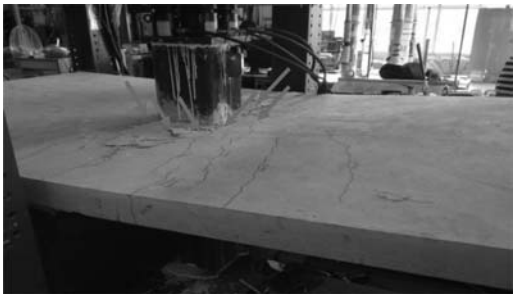

Figure 10. Fine cracks near the column.

it was observed that the end of the concrete element started to crack. Finally, the finite element work illustrated that the column face and end plate exceed their yield stress and started to bend, which caused connection failure.

4.2 *Cyclic loading*

Figure 9 demonstrates the load versus displacement relationship for the specimen subjected to cyclic loading. Initially, fine cracks appeared near the column and towards the centre of the slab when the specimen was subjected to a 170 kN downward load as shown in Figure 10. The cracks became wider with additional cracks opening up at 212.5 kN.

At an upward load of 300 kN at the column face, failure occurred. The failure was caused by the bolts in tension, which occurred at the bottom side. Figures 11 and 12 illustrate that the bottom row of the blind bolts has been pulled out of the concrete-filled steel tube when the specimen was subjected to upward loading.

The maximum gap between the top region of the end plate and column was 5 mm, while the maximum bottom gap was 41 mm. There was a 14% improvement to the peak load from previous design with a peak load of 259 kN.

Figure 9 also demonstrates that the finite element model is in good agreement with the experimental data. The failure showed in the finite element model is similar to the experimental study.

Figure 11. End plate bending.

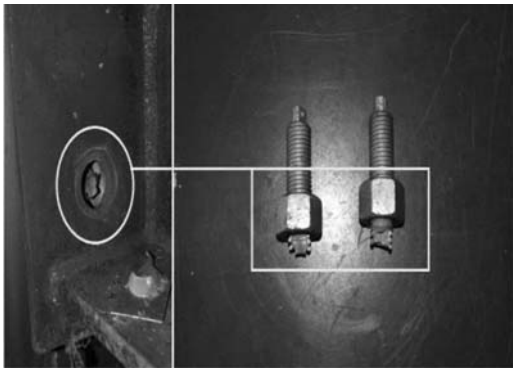

Figure 12. Blind bolts failure due to tension.

4.3 *Beam-to-column earthquake resistance*

The design of beam-to-column connections in the research herein was in accordance with the Australian Standards AS/NZS 1170.4 (2007) and AS 2327.1 (2003). The experimental investigation showed that the maximum load of the beam-to-column connection was 298 kN. When the structure was subjected to a 1:500 year return period, the maximum calculated load of the beam-to-column connections was 240 kN. Therefore, as shown in Figure 13, the designed beam-to-column connection is able to withstand the 1:500 year return period.

The calculated value for 1:2500 year return period was 425 kN. Therefore, the current design still needs improvement in order to be able to withstand a low-probability, high-consequence earthquake loads of a 1:2500 year return period to prevent further structural failures.

A possible solution would be modification of the blind bolts. This could include thickness of the blind bolt heads. This will therefore improve the overall strength of connections. Furthermore, one should bear

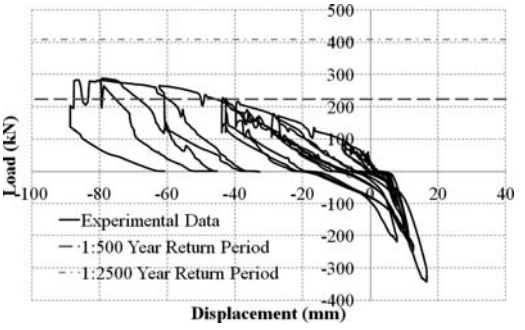

Figure 13. Comparison of experimental result with earthquake return period.

in mind that the reinforced concrete slab has a great impact on the behaviour of the connections and therefore must be designed carefully to achieve the desired semi-rigid connection. In addition, the thickness of the endplates will also need to be modified, which may provide better results.

5 CONCLUSIONS

This paper discussed the behaviour of composite beam-column flush end plate connections subjected to low probability, high-consequences loading. It has been revealed that there is a need to cater for low probability, high-consequence earthquake loads such as those of a 1-in-2500 year return period to prevent further structural failures which can cause catastrophic loss of lives.

It has been asserted that medium-rise buildings are most likely to have an unfavourable behaviour towards an earthquake, and that failure is most likely to occur at the connections of the structure. Hence the focus of this paper is the adequacy of standardising increased earthquake return periods within structural design connections. It is this earthquake return period that has been identified as being one of the main factors in relation to the magnitude of an earthquake.

A reasonably accurate finite element model has been developed to investigate the behaviour of shear connectors and end plate connections in composite steel-concrete beams. The comparison between the finite element models and experimental results gives a good correlation.

Full scale tests on beam-to-column flush end plate connections utilising blind bolts demonstrated the strength and stiffness, which could be utilised in transferring load between the beam and column within low to medium rise structural frames.

Key findings of this research are:

1. The blind bolts connecting the structural steel beam to the concrete-filled steel tube column performed well when subjected to static loading. However, fracture of the bolts was observed when the connection was subjected to cyclic loading;

2. The improved design has increased the strength, stiffness and ductility performance when compared with a previous experiment. However, the connection failure still plays a major role in high-rise buildings when they are subjected to earthquake loading.
3. For the composite flush endplate connections, the strength and stiffness in the negative moment direction is considerably larger than that in the positive moment direction. This was due to the contribution of the slab reinforcement in tension in the negative moment direction. Moreover, the flexible nature of the bottom blind bolts in tension also contributed to the larger negative moment.

ACKNOWLEDGEMENT

The authors would like to acknowledge the generous support of Ajax Engineered Fasteners, Australian Tube Mills and ARC through Linkage Project No. LP0669334. The authors also would like to thank the University of Western Sydney and the technical staff for helping with the experimental investigation.

REFERENCES

AISC 2005. Specification for structural steel building. *American Institute of Steel Construction*.

AS 2327.1, A. S. 2003. Composite structures, Part 1: Simply supported beams.

AS/NZS 1170.4 2007. Australian AS1170.4: 2007, Structural design actions: Part 4: Earthquake actions, Standards Australia International, Ltd.

De Silvana, N. and El-Debs, A. 2004. An experimental study of connections between I-beams and concrete filled steel tubular columns. *Steel & Composite Structures* 4(4): 303–315.

Kent, D. C. and Park, R. 1971. Inelastic behavior of reinforced concrete members with cyclic loading. *Bullentine of the New Zealand Society for Earthquarke Engineering* 4(1): 108–125.

Loh, H. Y., Uy, B. and Bradford, M. A. 2006a. The effects of partial shear connection in composite flush end plate joints Part I: Experimental study. *Journal of Constructional Steel Research* 62(4): 379–390.

Loh, H. Y., Uy, B. and Bradford, M. A. 2006b. The effects of partial shear connection in composite flush end plate joints Part II: Analytical study and design appraisal. *Journal of Constructional Steel Research* 62(4): 391–412.

Mirza, O. and Uy, B. 2009a. Behaviour of headed stud shear connectors for composite steel-concrete beams at elevated temperatures. *Journal of Constructional Steel Research* 65(3): 662–674.

Mirza, O. and Uy, B. 2011. Behaviour of Composite Beam-Column Flush End Plate Connections Subjected to Low-Probability, High-Consequence Loading. *Engineering Structures* 33: 647–662.

Nie, J., Qin, K. and Cai, C. S. 2008. Seismic behavior of connections composed of CFSSTCs and steel-concrete composite beams – finite element analysis. *Journal of Constructional Steel Research* 64(6): 680–688.

Popov, E. P. and Takhirov, S. M. 2002. Bolted large seismic steel beam-to-column connections Part 1: experimental study. *Engineering Structures* 24(12): 1523–1534.

Wang, J. F., Han, L. H. and Uy, B. 2009. Behaviour of flush end plate joints to concrete-filled steel tubular columns. *Journal of Constructional Steel Research* 65(4): 925–939.

Wang, W. D., Han, L. H. and Uy, B. 2007. Experimental behaviour of steel reduced beam section to concrete-filled circular hollow section column connections. *Journal of Constructional Steel Research* 64(2): 493–504.

Wu, L., Chung, L. and Tsai, S. 2005. Seismic behaviour of bolted beam to column connection for concrete filled steel tube. *Journal of Constructional Steel Research* 61: 1387–1410.

Tubular Structures XIV – Gardner (Ed.)
© 2012 Taylor & Francis Group, London, ISBN 978-0-415-62137-3

Shear behaviour of open beam-to-tubular column angle connections

Y. Liu, C. Málaga-Chuquitaype & A.Y. Elghazouli
Department of Civil and Environmental Engineering, Imperial College London, UK

ABSTRACT: Whilst the moment-rotation behaviour of typical connection configurations has been extensively examined in previous studies, there is a relative lack of information on the performance under more generalised loading conditions, particularly in relation to semi-rigid connections to tubular columns under shear loads. To this end, this paper deals with the shear behaviour of open beam-to-tubular column angle connections by means of experimental and numerical investigations. The experimental set-up, connection configurations and material properties are first introduced, followed by an overview of the results and observations from the tests on both blind-bolted angle connections and combined channel/angle details. The main behavioural patterns are identified and their effect on the connection performance is discussed. Subsequently, detailed three-dimensional finite element models are constructed by means of the nonlinear program ABAQUS, and their results are validated against the experimental data. It is shown that the FE model can accurately and efficiently simulate the overall behaviour of bolted angle connections. The experimental and numerical results presented in this paper highlight the main inelastic response characteristics of these forms of connection under shear loading conditions.

1 INTRODUCTION

Hollow structural sections (HSS) represent an effective choice as column members due to both their structural efficiency and architectural appeal. Nevertheless, the difficulties associated with the lack of access for the installation of conventional bolts have often resulted in the under-exploitation of these merits. This situation is aggravated by the relative lack of research and design guidance for bolted angle connections with tubes. Most of the research on open-beam-to-tubular-column connections to date has focused on fully-rigid fully-welded details (Cao et al. 1998, Kosteski & Packer 2003), and current European standards (CEN 2005) incorporate rules for determining the stiffness and resistance of semi-rigid connections that do not extend to connections incorporating tubular columns.

The practical and economical merits offered by bolted angle connections between open beams and open columns have prompted the development of semi-rigid open beam-to-tubular column connection alternatives such as the flowdrill process (Banks 1993) and special bolts with sleeves designed to expand inside the tube (Huck International Inc. 1990, Lindapter International Ltd. 1995). A simpler blind-bolt design is that presented by the Hollo-bolt, proposed by Lindapter International (1995). In particular, the wide availability and ease of use of the Hollo-bolt have motivated a number of experimental studies on Hollo-bolted connections subjected mainly to bending and direct tension (Barnett et al. 2001, Elghazouli et al. 2009). Barnet et al. (2001) performed a review of different blind-bolting alternatives and carried out an experimental study on blind-bolted T-stubs and connections using Hollo-bolts. More recently, Elghazouli et al. (2009) performed an experimental investigation into the monotonic and cyclic behaviour of Hollo-bolted beam-to-tubular column connections. It was shown that the grade of the Hollo-bolt, coupled with the gauge distance between the Hollo-bolt and beam flange, have a most notable effect on the flexural response of this type of connection. Nevertheless, information on the behaviour of blind-bolted connections under other loading conditions is still limited, particularly for angle connections subjected to shear loads.

Another alternative for bolted connections between open beams and tubular columns is that offered by combined channel/angle configurations. This type of connection incorporates a channel section which is shop-welded at the legs to the face of the column hence allowing the use of any conventional bolted detail between the channel and the beam. Despite its versatility, there is a dearth of experimental studies on such 'reverse channel' configurations. Málaga-Chuquitaype & Elghazouli (2010) carried out an experimental study into the flexural behaviour of combined channel/angle connections under monotonic and cyclic loading. It was observed that the flexibility of the reverse channel component has a direct influence on both the initial rotational stiffness and moment capacity of the connection. Nevertheless, as with blind-bolted details, there is a lack of information on the behaviour of combined channel/angle connections under other forms of loading conditions such as shear loads.

Many studies have been carried out on the numerical simulation of semi-rigid connections incorporating conventional bolts (Kishi et al. 2001, Citipitioglu et al. 2002, Pirmoz et al. 2008). However, detailed finite element models for the simulation of blind-bolted or reverse channel joints with angles are still limited. Recently, Wang et al. (2010) developed theoretical and numerical models using ANSYS (2003) to investigate the tension behaviour of Hollo-bolted T-stubs. However, similar detailed models for the simulation of blind-bolted or reverse channel joints with angles are still lacking.

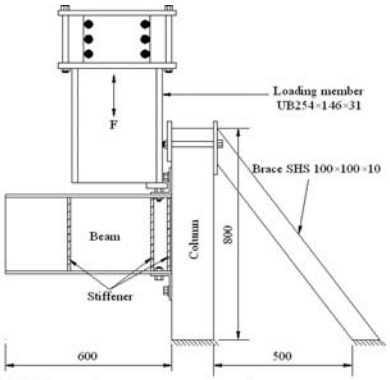

(a) Schematic representation of test set-up.


(b) General view of test arrangement.

Figure 1. Test set-up of bolted connections (dimensions in mm).

This paper examines the shear behaviour of semi-rigid angle connections between open beams and tubular columns through experimental and numerical investigations. Three shear tests on blind-bolted angle connections and three tests on combined channel/angle details are described. The main behavioural patterns are identified and their effect on the connection performance is discussed. Subsequently, detailed three-dimensional finite element models are constructed by means of the nonlinear program ABAQUS, and their results are validated against the experimental data. Good agreement between experimental and numerical results is obtained.

2 TESTING ARRANGEMENT AND SPECIMEN DETAILS

2.1 *Experimental set-up*

The set-up used for testing the beam-to-tubular column connections in shear is shown in Figure 1. Columns of 800 mm height were used in all tests. The column was fixed at both ends by welding it to a 10 mm plate clamped at the base and bolting it to a lateral bracing at the top, as depicted in Figure 1. A hydraulic actuator operating in displacement control was used to apply vertical deformations at the head of the bolts connecting the beam and top angle. The force imposed by the actuator was transmitted through a heavy-section I-beam and a bearing plate of 30 mm thickness in order to achieve an even distribution of stresses over the head of the top angle bolts, as shown in Figure 1. In the case of the web angle connections, a 30 mm plate was placed on the top beam flange in line with the bolts connecting the beam web side of the web angles. The displacement at the head of the top angle bolts (for top and seat angle connections) and at the top beam flange (in the case of web angle connections) was gradually increased up to a maximum vertical displacement of 16 mm, or until the capacity of the actuator was reached (at around 600 kN). The applied vertical displacement and corresponding vertical force were recorded by the load cell and transducer incorporated within the actuator. A more detailed description of the test set-up can be found in Liu (2012).

Table 1. Summary of the test specimens.

Reference	Type	Angle	Reverse channel component	Dimension (mm) (as shown in Figure 2)										
				a	b	c	d	e	f	g	h	i	j	k
Blind-bolted angle connections														
B10-N8-A45-T	A	L100 × 75 × 8	–	45	30	35	65	–	–	–	100	45	–	–
B10-N8-A50-T	A	L100 × 75 × 8	–	50	50	35	40	–	–	–	100	45	–	–
B10-N15-A50-T	A	L150 × 80 × 15	–	50	100	35	45	–	–	–	100	45	–	–
Combined channel/angle connections														
C10-N8-A45-T	B	L100 × 75 × 8	SHS 150 × 70 × 10	45	30	35	65	–	–	–	100	45	70	515
C6.3-N15-A50-T	B	L150 × 80 × 15	SHS 150 × 70 × 6.3	50	100	35	45	–	–	–	100	45	70	465
C10-N8-A50-W	C	L150 × 80 × 8	SHS 150 × 70 × 10	50	50	45	30	40	90	15.5	–	–	–	465

2.2 *Specimen details*

A total of six open beam-to-tubular column angle connections were studied: three blind-bolted connections and three reverse channel details. A summary of the test series is given in Table 1, which includes the geometric details of the connection as well as the characteristics of the angle and reverse channel components. Figure 2 depicts the connection configurations studied (Type A used in Hollo-bolted specimens, and Types B and C utilized in reverse channel configurations). The reference employed for the specimens is expressed by *Pt-Nx-Ay-T* for top and seat angle specimens, whereas *Pt-Nx-Ay-W* is utilized for specimens incorporating web angle components. In this nomenclature, *P* represents the connection type (*B* stands for the blind-bolted angle connection and *C* stands for combined channel/angle connection), *t* is the thickness of the column or channel in mm, *x* is the thickness of angle in mm, and *y* expresses the gauge distance between the centre of the bolt hole in the horizontal angle leg and column flange in mm (i.e. the value of 'a' as indicated in Figure 2).

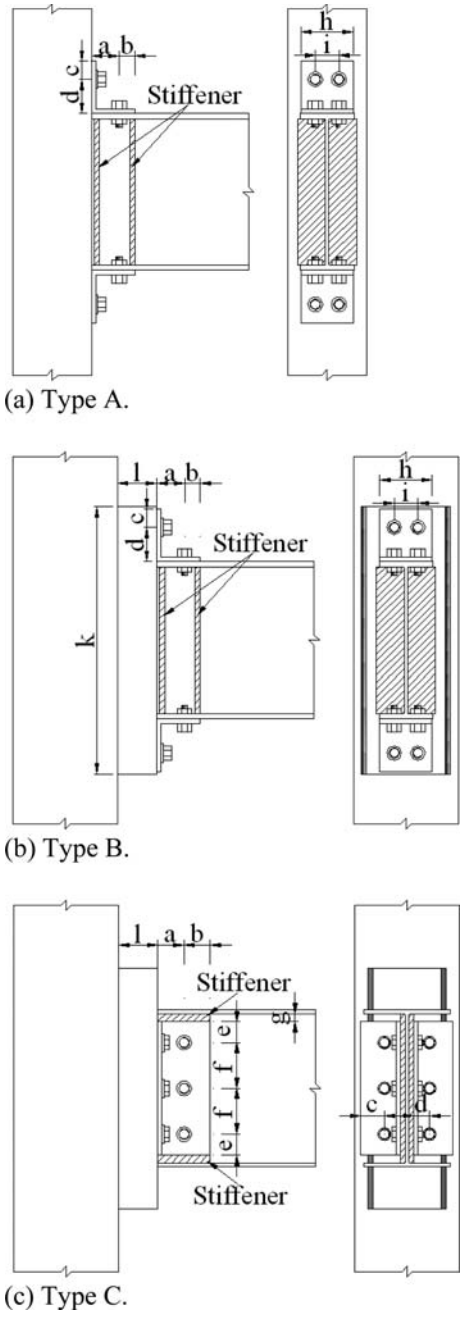

Figure 2. Connection configurations.

It is important to note that Square Hollow Sections SHS 150 × 150 × 10 were used as columns for all blind-bolted specimens whereas SHS 200 × 200 × 10 columns were employed in combined channel/angle details. Also, Universal Beams UB 350 × 102 × 25 and Grade 10.9 M16 standard bolts were employed in all cases. The grade of the steel used for beams, columns and angles was S275. Table 2 presents the mean yield stress values and ultimate strength for the angle, beam and column components as obtained from at least three coupon tests in each case.

Preliminary numerical studies carried out as part of the present research (Liu 2012) have shown that the beam web stiffness plays a vital role in the shear performance of the connection. Buckling of the beam web can prevent the connection from reaching its maximum shear capacity and initiate complex joint interactions. Therefore, web stiffeners were used in order to limit undesirable beam failure modes, as shown in Figure 2. This enabled a better understanding of the basic mechanisms of bolt, angle and column face deformations. To this end, the beam web was stiffened in top and seat angle connections (Figure 2a and Figure 2b) by means of four 10 mm steel plates (two on each side) welded perpendicular to the web along the full beam depth. Similarly, in the case of reverse channel connections with web angles (Specimen C10-A8-A50-W), the beam web was thickened by welding 10 mm-thick plates at each side as depicted in Figure 2c.

Following the recommendations of Elghazouli et al. (2009), Grade 10.9 M16 Hollo-bolts were used for the blind-bolted configurations. Also, as suggested by Málaga-Chuquitaype & Elghazouli (2010), the reverse channel components used for combined channel/angle

Table 2. Material properties of connection elements.

Element	Yield stress (N/mm^2)	Ultimate stress (N/mm^2)
Beam UB 305 × 102 × 25	329	443
Column SHS 150 × 150 × 10	368	498
Column SHS 150 × 150 × 6.3	385	485
Angle L 100 × 75 × 8	312	438
Angle L 100 × 80 × 15	293	449
Hollo-bolt sleeve*	382	512

*Obtained from the mean of three hardness tests.

connections were obtained from SHS by longitudinal cutting. Table 1 summarizes the dimensions of the SHS from which the reverse channels were obtained. Fillet welding with thickness 10 mm was used to connect the column and the reverse channel throughout the length of channel component.

3 EXPERIMENTAL RESULTS AND OBSERVATIONS

3.1 *Blind-bolted angle connections*

Figure 3a presents the shear force-displacement relationships obtained for the three blind-bolted angle connection specimens studied. The influence of the angle horizontal gauge distance (distance 'a' in Figure 2) can be examined by comparing the results of specimens B10-N8-A45-T and B10-N8-A50-T with $a = 45$ mm and $a = 50$ mm, respectively. It can be observed from Figure 3a that the initial stiffness of Specimen B10-N8-A45-T is nearly 25% larger than that of Specimen B10-N8-A50-T. This difference can be largely attributed to the stiffer horizontal angle leg. However, after yielding occurs, at a load of around 122 kN, the stiffer vertical leg of Specimen B10-N15-A50-T (i.e. shorter distance d in Figure 2 and Table 1) seems to offset these initial stiffening effects. This counter-balancing effect is particularly evident for displacements greater than 6 mm.

The results of Specimens B10-N8-A50-T and B10-N15-A50-T in Figure 3a, where the angle was varied from L100 × 75 × 8 in the former to L150 × 80 × 15 in the latter, can be compared to illustrate the influence of angle thickness. As expected, the thickness of the angle has a direct effect on the connection response, including the stiffness, capacity, and deformation modes. The initial stiffness of Specimen B10-N15-A50-T with the thicker angle is around 60% larger than that of Specimen B10-N8-A50-T, while its capacity at a displacement of 8 mm is also 100 kN higher than the corresponding capacity of Specimen B10-N8-A50-T.

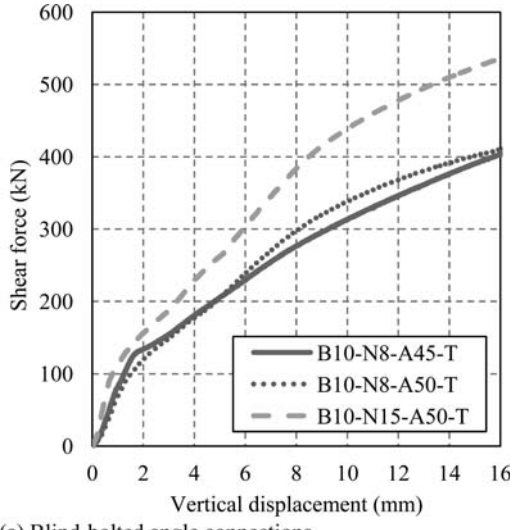

(a) Blind-bolted angle connections.

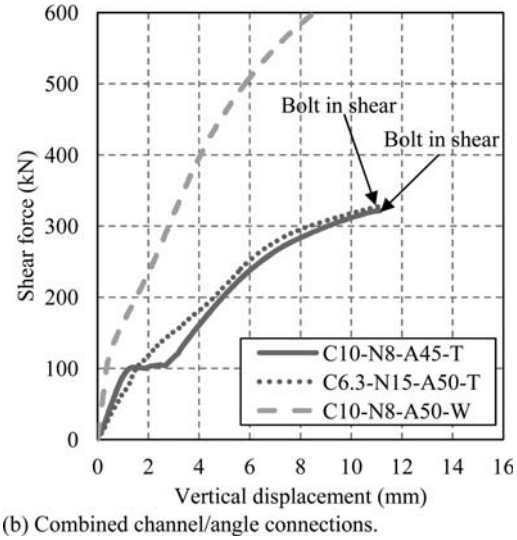

(b) Combined channel/angle connections.

Figure 3. Shear force-displacement relationships.

3.2 *Combined channel/angle connections*

Figure 3b presents the shear force-displacement relationships for the three combined channel/angle connection specimens. The effects of the angle thickness and reverse channel thickness on the shear response of combined channel/angle connections can be explored by comparing the experimental results of Specimens C10-N8-A45-T and C6.3-N15-A50-T. It can be observed from Figure 3b that the stiffness of Specimen C10-N8-A45-T is 37% higher than that of Specimen C6.3-N15-A50-T. This lower initial stiffness of Specimen C6.3-N15-A50-T relative to Specimen C10-N8-A45-T is attributed to the accumulation of bearing deformation in the relatively thinner channel as well as the increased horizontal gauge distance (dimension 'a' in Figure 2). It is important to note that the shear force-displacement response of Specimens C10-N8-A45-T and C6.3-N15-A50-T are similar despite the significant differences in their deformation modes, with the deformation of the reverse channel-bolt assemblage dominating the response of Specimen C6.3-N15-A50-T. Additionally, bolt slip occurred almost instantaneously at a load level of 100 kN in Specimen C10-N8-A45-T whereas a more gradual slip was observed in Specimen C6.3-N15-A50-T. Both specimens failed at a displacement of around 11 mm due to shear fracture of the bolts connecting the bottom angle and the channel components

The response of double web angle connections under shear was studied with reference to Specimen C10-N8-A50-W (Type C). As illustrated in Figure 3b, the web angle configuration offers significantly higher stiffness and post-yield capacity when compared with top and seat angle details.

3.3 *Ductility*

The experimental results show that blind-bolted angle connections provided significant shear-ductility levels exceeding 16 mm of vertical displacement without significant deterioration in stiffness or capacity. This high ductility can be attributed to the Hollo-bolt insert. Indeed, higher ductility has been documented for Hollo-bolts in comparison to standard bolts when subjected to single and double shear loading (Liu 2012). Conversely, the combined channel/angle connection Specimens C10-N8-A45-T and C6.3-N15-A50-T failed by shear fracture of the standard bolts at around 11 mm of vertical displacement. The results also suggest that the addition of a flexible reverse channel component can enhance the ductility of the connections at the expense of some reduction in stiffness and capacity. Also, the ductility capacity of connections incorporating web angle/channel components (i.e. Specimen C10-N8-A50-W) can be improved due to the increased number of bolts in shear.

4 NUMERICAL SIMULATION

4.1 *Modelling details*

Three-dimensional (3D) finite element models were developed using the FE software ABAQUS 6.7 (2003). These models make use of eight-node brick solid elements of Type C3D8I, as shown in Figure 4. Special attention was given to the faithful representation of the geometric and mechanical characteristics of the bolts including the shank, sleeve, head and nut, as illustrated in Figure 4. The stress-strain relationships for the material of all the connection components were defined by a tri-linear kinematic hardening rule with an elastic modulus of 210 GPa and Poisson's ratio 0.3. The models consider the experimentally obtained yield stress and ultimate strength values for the angle, beam and column components, as illustrated in Table 2.

The contact phenomena between each pair of interacting surfaces was taken into account by defining 'hard and friction' surface interaction properties. In the tangential direction, a friction coefficient of 0.3 was defined according to previous experimental studies, while in the normal direction, 'hard' contact pressure-over closure relationship was employed, but the separation was allowed. The more flexible surface was chosen as the slave surface, while the more rigid area was assigned as master. Moreover, slippage between the bolt and hole surfaces was considered by means of the contact definition.

Bolt pretension in standard and Hollo-bolts was introduced by means of two loading steps before external loading. Firstly, pretension forces of 110 kN were applied. The second step involved removing the applied pretension while simultaneously fixing the bolt length as its deformed value. The boundary conditions and loading in the numerical analyses followed the conditions and loading methods employed during the tests and described previously.

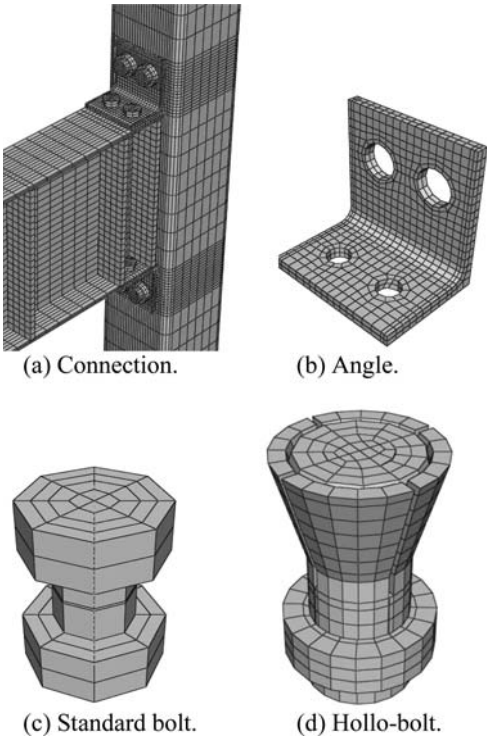

Figure 4. FE representation of connection components.

A number of mesh sensitivity studies were carried out in order to arrive at an optimum representation which involves a comparatively finer mesh for the angles, bolts and the contact areas within the beams and columns, whereas a relatively coarser mesh was employed elsewhere. The dimensions of the adopted mesh ranged between 6 mm within the refined region, and up to 100 mm within the coarser region.

4.2 *Validation*

Specimens B10-N8-A45-T, C10-N8-A45-T and C10-N8-A50-W (web angle) are used herein as typical examples for validation purposes. The shear force-displacement relationships, obtained from the experimental results as well as FE simulation, are compared in Figure 5. It can be noted from Figure 5 that reasonable estimates of stiffness and yield capacity are obtained in all cases.

The differences between the experimental results and numerical simulations observed (between 0.2 mm and 1.2 mm of vertical displacement) for Specimen B10-N8-A45-T in Figure 5a can be attributed to bolt slippage. Importantly, in the FE simulation, slippage of the bolt occurs almost instantaneously once the friction forces are overcome, whereas a more gradual slip displacement was observed during the test. Similarly, good agreement can be observed between the yield capacity estimations of the FE model and the experimental values within a difference of $\pm 10\%$.

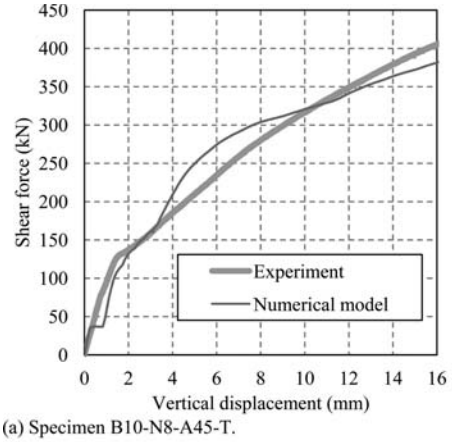

(a) Specimen B10-N8-A45-T.

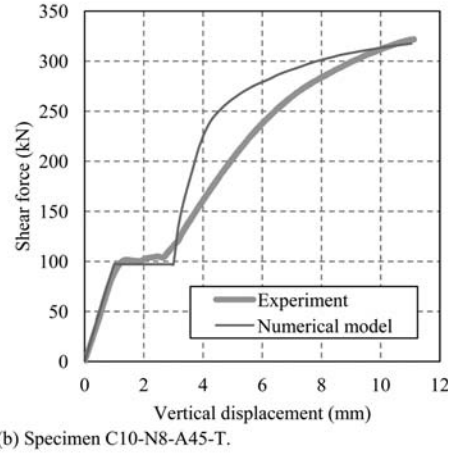

(b) Specimen C10-N8-A45-T.

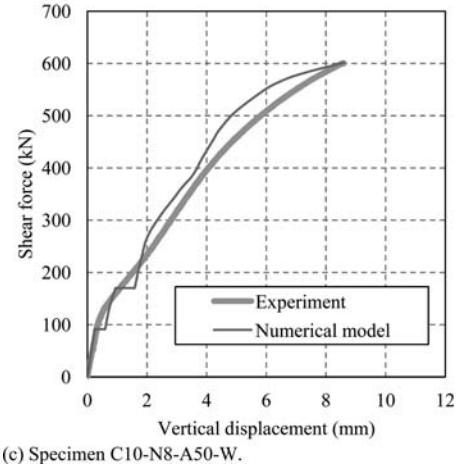

(c) Specimen C10-N8-A50-W.

Figure 5. Comparison of experimental and numerical shear force-displacement response.

On the other hand, the overestimation of post-yield stiffness for Specimen C10-N8-A45-T in Figure 5b is attributed to differences in the evolution of bolt slippage displacement between the FE models and the experimental results. The same is true for Specimen C10-N8-A50-W where the multiple slip paths in the web angle components initiated distinguishable short slip-only deformations at load levels of 100 and 180 kN approximately, while a more gradual accumulation of deformation was observed during the test.


(a) Experiment mode.

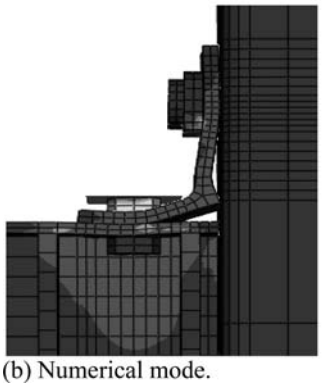
(b) Numerical mode.

Figure 6. FE representation of connection components.

Figure 6 illustrates the deformation pattern observed in the top angle of Specimen B10-N8-A45-T at a vertical displacement of 16 mm and compares it with the FE model prediction at the same displacement level. It is evident from this figure that the deformation and plastic mechanism are replicated by the proposed FE model.

Despite some differences, the FE estimations were found to correlate well with experimental results in the small as well as large levels of displacement demands. This good agreement with the experimental results confirms that the detailed FE models are able to simulate the shear response of bolted angle connections with reasonable accuracy.

5 CONCLUDING REMARKS

This paper has examined the shear behaviour of bolted angle connections between tubular columns and open beams. An experimental programme comprising three

shear tests on blind-bolted angle connections and three tests on combined channel/angle connections has been described. A discussion on the salient response characteristics such as stiffness, yield capacity and failure mechanism has been presented.

From the experimental results, it can be concluded that the inelastic mechanisms exhibited by the connections examined herein under shear loads primarily involve the interaction between the angle components and the column/channel face assemblage. As expected, it has been shown that the angle horizontal gauge distance between the bolt centre and the column face has a direct influence on the initial stiffness with only minor influence on the shear capacity. Importantly, the thickness of the angle is directly proportional to the connection yield capacity and initial stiffness. Similarly, the thickness of the reverse channel stands in direct relationship to the connection yield capacity and stiffness. Besides, it was observed that the overall resistance and stiffness of the connections with double web angles can be significantly increased in comparison with top and seat angle connections.

In terms of ductility, blind-bolted angle connections can provide significant shear-ductility levels exceeding 18 mm of vertical displacement without signs of failure. Conversely, the combined channel/angle connection specimens with top and seat angles exhibited less ductility, failing at around 11 mm of vertical displacement. The results also show that the addition of a flexible reverse channel component may enhance the ductility of the connections at the expense of some reduction in stiffness and capacity. In the case of combined channel/angle connections under shear loads, the ductility development is typically limited by the brittle fracture of the bolts in shear rather than the failure of the other constituent components. Finally, the addition of web angle components was observed to delay the shear failure of the connection due to the increased redundancy offered by the higher number of standard bolts resisting the shear action.

Continuum FE models were proposed which include a number of advanced modelling features such as loading reversal, contact phenomena, bolt slippage definition and bolt pretension application. Models were validated against available experimental results and were found to accurately and efficiently simulate the overall behaviour of bolted angle connections. In particular, the stiffness, load capacity and ultimate failure modes are all very well predicted. Moreover, the detailed characteristics of the models render the observation of key response parameters relatively straightforward, including the stress distribution and deformation patterns.

ACKNOWLEDGEMENTS

The support of Tata Steel Tubes, particularly that of Mr T. Mustard, for the research described in this paper is gratefully acknowledged. The authors would also like to thank the technical staff of the Structures Laboratories at Imperial College London, especially Mr T. Stickland, for their assistance with the experimental work. Additionally, the first author would like to acknowledge the grant provided by The Chinese Scholarship Council and The UK Department for Innovation, Universities & Skills, for her doctoral research studies through a UK/China Scholarship for Excellence.

REFERENCES

ABAQUS 2003. ABAQUS Theory Manual,Version 6.7, Hibbit, Karlsson and Sorensen Inc.

ANSYS 2003. ANSYS Multiphisics 10.0, Canonsbury, Pennsylvania Inc.

Banks, G. 1993. Flowdrilling for tubular structures. Proceedings of the Fifth International Symposium on Tubular Structures. UK.

Barnett, T., W. Tizani & D. Nethercot 2001. The practice of blind bolting connections to structural hollow sections: A review. *Steel and Composite Structures* 1(1): 1–16.

Cao, J., J. Packer & N. Kosteski 1998. Design guidelines for longitudinal plate to HSS connections. *Journal of Structural Engineering* 124(7): 784–791.

CEN 2005.*EN 1993-1-8, Eurocode 3: Design of steel structures, Part 1–8: Design of joints*.

Citipitioglu, A. M., R. M. Haj-Ali & D. W. White 2002. Refined 3D finite element modeling of partially-restrained connections including slip. *Journal of Constructional Steel Research* 58(5–8): 995–1013.

Elghazouli, A. Y., C. Málaga-Chuquitaype, J. M. Castro & A. H. Orton 2009. Experimental monotonic and cyclic behaviour of blind-bolted angle connections. *Engineering Structures* 31(11): 2540–2553.

Huck International Inc. 1990. *Industrial fastening system*. Arizona (USA).

Kishi, N., A. Ahmed, N. Yabuki & W. F. Chen 2001. Nonlinear finite element analysis of top and seat-angle with double web-angle connections. *Structural Engineering and Mechanics* 12(2): 201–214.

Kosteski, N. & J. A. Packer 2003. Longitudinal plate and through plate-to-hollow structural section welded connections. *Journal of Structural Engineering* 129(4): 478–486.

Lindapter International Ltd. 1995. Type HB hollo-bolt for blind connection to structural steel and structural tubes. UK, Lindapter International Ltd.

Liu, Y. 2012. Behaviour of steel connections under extreme loading conditions, PhD Thesis, Department of Civil and Environmental Engineering, Imperial College London, UK.

Málaga-Chuquitaype, C. & A. Y. Elghazouli 2010. Behaviour of combined channel/angle connections to tubular columns under monotonic and cyclic loading. *Engineering Structures* 32(6): 1600–1616.

Pirmoz, A., A. S. Daryan, A. Mazaheri & H. E. Darbandi 2008. Behavior of bolted angle connections subjected to combined shear force and moment. *Journal of Constructional Steel Research* 64(4): 436–446.

Wang, Z. Y., W. Tizani & Q. Y. Wang 2010. Strength and initial stiffness of a blind-bolt connection based on the T-stub model. *Engineering Structures* 32(9): 2505–2517.

Tubular Structures XIV – Gardner (Ed.)
© 2012 Taylor & Francis Group, London, ISBN 978-0-415-62137-3

Residual stress investigation of welded high strength steel box T-joints

S.P. Chiew, J. Jiang & C.K. Lee
School of Civil and Environmental Engineering, Nanyang Technological University, Singapore

ABSTRACT: An experimental investigation to determine the residual stress distributions at the chord weld toe of two welded High Strength Steel (HSS) box T-joints is described in this paper. Two identical specimens with the same geometrical size were fabricated to investigate the influence of preheating on the residual stress magnitude and distribution of HSS welded box T-joint. One specimen was welded at ambient temperature while the other one was preheated to 100°C before the welding. Following the American Welding Society (AWS) standard, the brace and chord boxes were both fabricated from Reheated, Quenched and Tempered (RQT) high strength steel plates with nominal yield stress of 690 MPa using Flux-Cored Arc Welding (FCAW). The residual stress near the chord weld toe of the joints was measured by the incremental hole-drilling method according to the American Society for Testing and Materials (ASTM) standard E837-08. By comparing the measured results obtained from the two specimens, it is found that preheating can effectively reduce the magnitude of residual stress induced by welding. The residual stress magnitude also showed significant variations at different locations along the circumferential direction of the welded joint.

1 INTRODUCTION

High strength steel (HSS), with minimum yield strength of greater than 460 MPa, is increasingly used in construction industry. For example, in bridge engineering, S420 and S460 steel were used in three long span suspension bridges for decks and pylons: Hålogaland Bridge in Norway, Messina Bridge and Yemen-Djibouti Bridge to make a solution to create economical designs (Lars Jensen et al. 2009). Also, applications of HSS can be found in building design. 77 Hudson at Colgate Center in Jersey City is a case that columns of the building are made of A913-Gr65 (S460) instead of Gr50 (S355) (Dan Dubina 2008). By using HSS, the weight of the structure was reduced by 17% compared with the case Gr50 were used. The successful application of HSS can be found in many other examples such as the Yokohama Landmark Tower in Japan, Airbus-Hangar in Frankfurt and Freedom Tower in New York (Dan Dubina 2008). In offshore engineering, the BP Harding jack-up and Siri field production jack-up both are good examples for HSS successful applications (Billingham et al. 2003).

HSS has merits such as economy, architecture, sustainability and safety. By increasing the strength of steel, the size of the structural sections can be reduced. HSS reduces the weight and thus offers more opportunities for architects to improve the aesthetic and elegance of the structure. However, using HSS in buildings has some disadvantages such as reduced capacity for strain hardening after yielding, potential fatigue problems, limitations in design codes and residual stress due to welding for HSS.

In this paper, an experimental study on the residual stress induced by welding for HSS box joint is presented. Two box T-joints with identical dimensions, one welded at ambient temperature while another preheated to 100°C before welding, were fabricated to investigate the influence of preheating on the residual stress magnitude and distribution.

2 EXPERIMENTAL INVESTIGATION

To measure the variations of the residual stress induced by the welding process, the incremental hole-drilling method suggested by the ASTM E837-08 (ASTM 2008) standard was adopted. The hole drilling method measures the residual stress by releasing the localized stress and thus changing the local strain on the surface of the testing material when a small hole is drilled in a residually stressed structure. The design of the specimens, the fabrication procedure of the specimens, the strain gauge scheme, test setup and procedure are presented in the following sections.

2.1 *Overview of design*

In the present experimental investigation, two box T-joints, both of them made of HSS RQT steel plate with minimum yielding stress of 690 MPa, were fabricated by flux-cored arc welding (FCAW). The welding standard AWS D1.1 2008 (AWS 2008) was followed for all full penetration welds used in the joint fabrication. To evaluate the impact of preheating on residual stress, one specimen was preheated to 100°C before

the welding while the other specimen was welded at ambient temperature. Since the HSS RQT steel came only in the form of steel plate, both the chord and the brace of the T-joints were formed by first properly cut steel plates into strips and then welded into box sections. After that, T-joints were created by connecting the brace and the chord together using full penetration butt weld. Figure 1 shows the dimensions of the joints. Figure 2 shows the fabricated specimen.

2.2 *Materials & welding parameters*

The RQT HSS plate used in this study is a type of reheated, quenched and tempered structural steel with improved forming and welding performance by substituting some alloying element with carbon. Electrode type OK Tubrod 15.09 was used during the FCAW welding. It is a type of flux-cored wire electrode suitable for welding high strength steel with minimum yield strength of 690 MPa. Diameter of the electrode is 1.2 mm. Table 1 lists the detailed welding parameters that were used in the specimen fabrication.

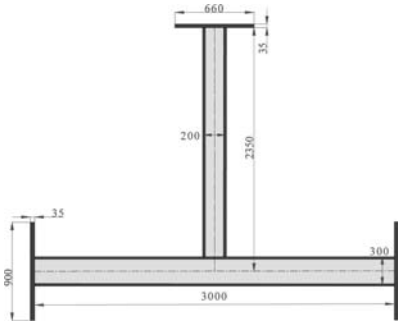

Figure 1. The geometry of the box T joint.

Figure 2. The fabricated specimen.

2.3 *Fabrication procedure*

During the specimen fabrication process, the 12 mm RQT steel plate was first cut and profiled into two pairs of strips with suitable sizes. After that, the brace and the chord were assembled respectively by welding the profiled strips together (Figure 3). Four backing plates were attached to the base plate by spot welding. The role of these backing plates is to sustain the weld filler when welding was carrying out to form the box sections. In order to prevent large deformation of the box section, two end plates were welded into the section by spot welding. After this preparation was done, the weld filler was added pass by pass to form the brace and chord. A T-joint was then formed by welding the chord and the brace together. Finally, connection plates used to fix the joint to the test rig were prepared and the joint was painted to prevent corrosion (Figure 2).

Figure 3 shows the cross section of the box section and the welding pass sequence employed in the fabrication of the brace and chord. Run 1 to Run 4 were added at four corners respectively. After that, welding passes were carried out at each corner one by one until a full penetration weld profile was obtained. The fabrication process was complete in such a sequence so that the box section can be heated evenly to reduce the structural deformation.

Figure 4 shows the welding profile and sequence for the chord-brace intersection part. As shown in Figure 5, each complete weld run around the brace-chord connection consists of four weld steps. The first step adds weld filler from Point 1 to Point 7. The second step adds from Point 7 to Point 13 and the third step from Point 13 to Point 19. The final step starts from Point 19

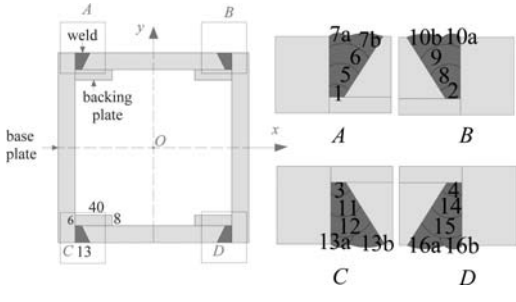

Figure 3. Cross section of the box section and the welding sequence of the box section.

Table 1. The welding parameters used in fabrication.

		Electrode		Current		
Position	Process	Class	Diameter	Type	Amplitude	Volts
Box section	FCAW	E111T1-K3	1.2 mm	DCEP	300–320	30–32
T- joint	FCAW	E111T1-K3	1.2 mm	DCEP	300–320	30–32

and eventually back to Point 1. After the box formation and joint welding, ultrasonic test was conducted to ensure the welding quality.

2.4 *The strain gauge scheme*

Figure 6 shows the strain gauge scheme for the specimen with preheating. 24 measurement points around the brace-to-chord intersection were identified to capture the residual stress distribution near the chord weld toe. Point 1 to Point 18 are points which are located at 10 mm from the weld toe while Point 19 to Point 24 are located at 15 mm from the chord weld toe. The drilling positions were arranged in such a way that spare space was reserved between Point 19 to Point 24 for the installation ACPD probes in the future fatigue testing. The drilling positions in this area are further from the chord weld toe to minimize the impact of the drilled holes on the joint fatigue performance.

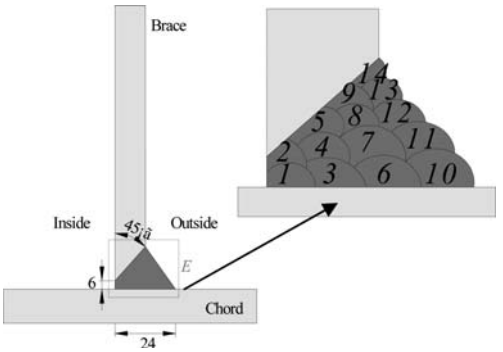

Figure 4. Cross section and welding sequence of the T joint

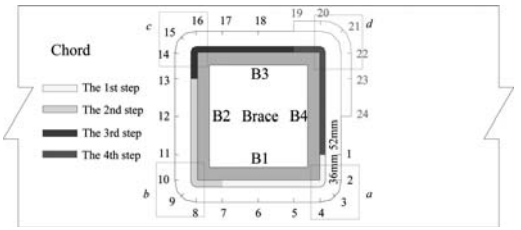

Figure 5. The welding sequence for the box T-joint.

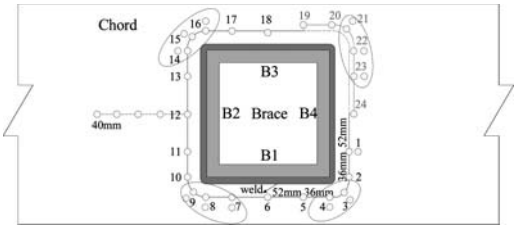

Figure 6. The strain gauges scheme for the specimen with preheating.

In order to use the linear interpolation method to estimate the residual stress at the weld toe, additional measurement points were added at 20 mm from the weld toe for the corners *a*, *b* and *c*. At the corner *d*, additional measurement points were added at 25 mm from the weld toe (Figure 6). To evaluate the residual stress variation with the distance from the weld toe, at Point 12, additional 4 measurement locations were positioned with the spacing of 40 mm between strain gauges, as shown in Figure 6. The spacing from Point 24 to Point 1 and Point 24 to Point 23 is 52 mm. The spacing is 36 mm from Point 1 to Point 2 and Point 23 to Point 22. Similar spacing was adopted for the other three edges. At the corner *a*, the spacing from Point 2 to Point 3 and from Point 3 to Point 4 are 20 mm. Similar spacing was applied for the other three corners.

For the specimen welded at ambient temperature, additions of four strain gauges (Points 25–28) were installed (Figure 7). Fig. 8 shows a photo of the T-joint after the all strain gauges around the brace-chord connection were installed.

2.5 *Test principle and setup*

The standard ASTM hole-drilling method is a common way for measuring residual stress by removing localized stress and measuring strain relief in the adjacent material. It causes relatively little damage to the specimen and allows localized residual stress measurements. The principle of the method is to release the localized stress by introducing a small hole into a residually stressed structure and thus changing the local strain on the surface of the testing, as shown in Figure 9. By comparing the strain at this point before

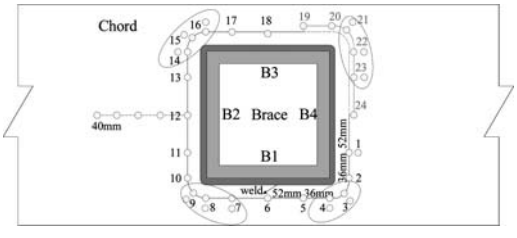

Figure 7. The strain gauges scheme for the specimen welded at ambient temperature.

Figure 8. Strain gauge scheme around one corner.

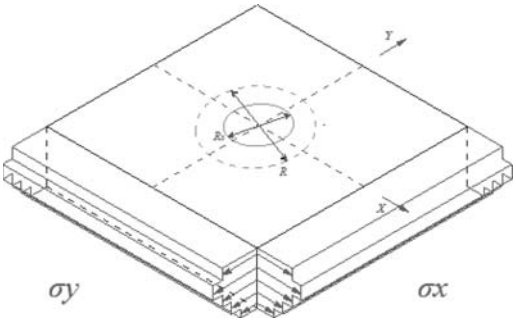

Figure 9. Hole geometry and residual stresses.

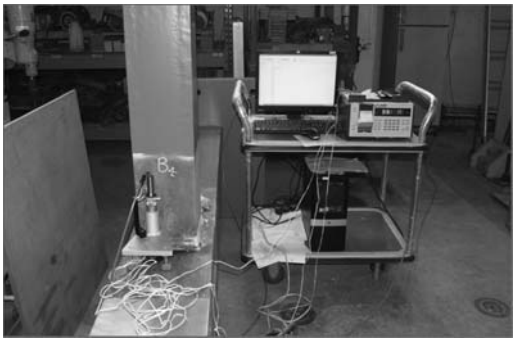

Figure 10. Setup of the residual stress measurement.

and after hole-drilling, stress relaxation due to hole drilling can be determined by Eqn. (1):

$$\varepsilon = \frac{1+\nu}{E}\cdot(\bar{a})\cdot\frac{\sigma_x+\sigma_y}{2} + \frac{1}{E}\cdot(\bar{b})\cdot\frac{\sigma_x-\sigma_y}{2}\cos 2\alpha + \frac{1}{E}\cdot(\bar{b})\cdot\tau_{xy}\cdot\sin 2\alpha \quad (1)$$

In Eqn. (1), E is the Young's modulus, ν is the Poisson's ratio and ε is the relieved strain. σ_x and σ_y are the stresses in the x and the y directions respectively. α is the angle from the x-axis to the maximum principle stress. $\bar{a}$ and $\bar{b}$ are calibration constants. In residual stress measurement, after the three groups of relieved strains are obtained by a strain rosette, σ_x, σ_y and α can be determined.

The RS-200 milling guide was employed for measuring the residual stress in the T-joints by the hole-drilling method through positioning and drilling of a hole in the centre of a special strain gauge rosette. An air pressure with 40 ksi was supplied to drive carbide cutter so that high rotating speed is obtained to drill a hole aligned concentric with the strain gauge. The 'zero' cutter depth is determined by slowly advancing the cutter until it cuts through the rosette backing material and lightly scratches the working surface. At this moment, the strain readings are initiated. After that, strain readings are noted for 20 equal hole depth steps with 0.025 mm gap to capture the stress variation along the hole depth. Figure 10 shows the test setup for the residual stress measurement.

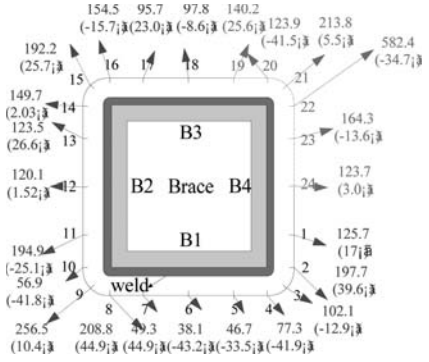

Figure 11. Maximum principle stress distribution for the specimen with preheating (Position: 10/15 mm).

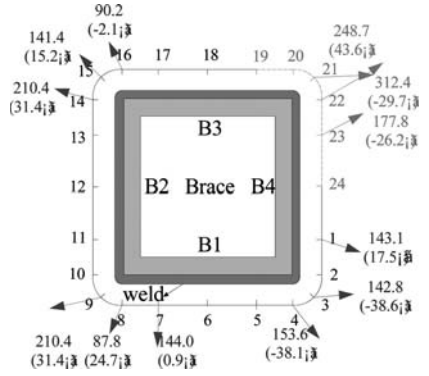

Figure 12. The maximum principle stress distribution for the specimen with preheating (Position: 20/25 mm).

3 TEST RESULTS

3.1 *Preheating specimen*

Figure 11 gives the distribution of the maximum principle residual stress and its direction for 10/15 mm locations. The residual stresses shown in the figure are the average values based on 1 mm hole-drilling. The transverse direction is vertical to weld filler addition path. Negative values in Figure 11 denote counter-clockwise shifting from the transverse direction and positive values denote clockwise shifting from the transverse direction. Note that the magnitude of residual stress is much higher near the corners than the other points. Particularly, at Point 9 and Point 22 (corner *b* and *d*), the principle stresses are 265.5 MPa and 582.4 MPa respectively. For principle stress direction, smaller shifting appeared along the sides B2 and B4 comparing with the sides B1 and B3.

The testing results of 20 mm/25 mm points at four corners are shown in Figure 12. The principle residual stresses at 20 mm/25 mm points are lower than the values at 10 mm/15 mm points for most cases. However, it should be noticed that at Point 3, Point 4 and Point 21, the principle stress at 20 mm/25 mm are higher than at 10/15 mm.

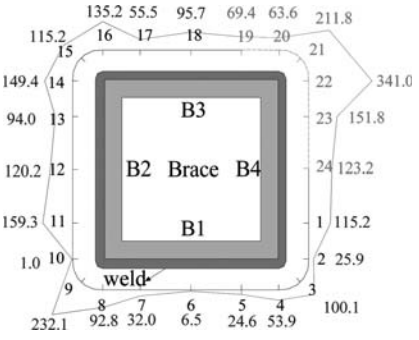

Figure 13. Transverse residual stress distribution for the specimen with preheating (Position: 10/15 mm).

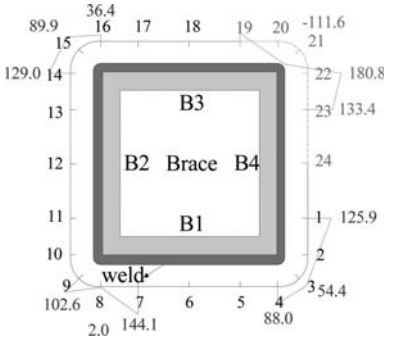

Figure 14. Transverse residual stress distribution for the specimen with preheating (Position: 20/25 mm).

Figure 13 and Figure 14 show the transverse residual stress distributions at 10/15 mm and 20/25 mm positions, respectively. It is obvious for that the transverse stress along the sides B1 and B3 is significantly smaller than that along the sides B2 and B4. Points 9, 21 and 22 should be noticed for their high magnitude of transverse stress. The stresses at the corners *b* and *d* are much higher compared with the other points. In addition, it should be noticed that Point 4 and Point 7 are two points that the transverse stress at 20 mm from the weld toe is higher than that at 10 mm from the weld toe. Compressive stress appeared at Point 21 at 25 mm from the weld toe.

Linear interpolation method is used to estimate the transverse and longitudinal residual stress at the weld toe and the comparison of both values is illustrated in Figure 15. The transverse stress is higher than the longitudinal component when the same position is evaluated. This observation is obvious at the corner *b*, *c* and *d*. Compressive longitudinal stress can be found at some locations while only high tensile transverse stress can be found from the figure. The maximum transverse residual stress at the weld toe in the preheating joint is 530 MPa, which nearly equals to 77% of the yielding stress of the material.

Figure 16 shows the residual stress variations with the distance from the weld toe. The values are shown according to the measurement data at Point 12. It

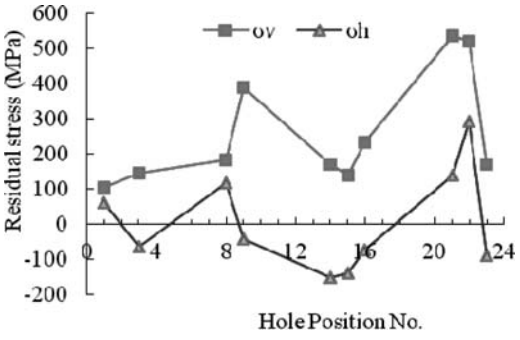

Figure 15. Transverse (σ_v) and longitudinal (σ_h) residual stress along the chord weld toe.

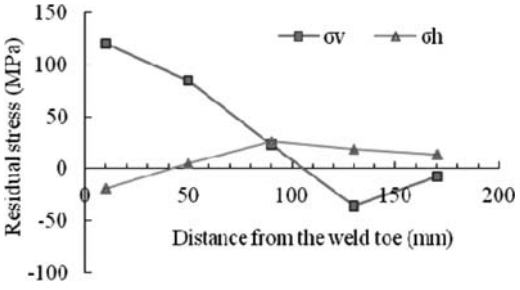

Figure 16. Variations of transverse (σ_v) and longitudinal (σ_h) residual stress with distance from the weld toe.

can been seen that while the transverse residual stress decrease as the distance from the weld toe increase, no noticeable pattern could be observed for the low magnitude longitudinal residual stress component.

3.2 *Ambient temperature specimen*

Figure 17 shows the distribution of the maximum principle stress and its direction for the specimen welded at ambient temperature. Note that the magnitudes of residual stress at corners *b* and *c* are much higher than the other points for this specimen. The principle stresses at Points 10, 11 and 14 are 451.6 MPa, 401.2 MPa and 413.6 MPa, respectively. Similar with the preheating specimen, the residual stresses along the side B2 and B4 are higher than that along the sides B1 and B3. Shifting from the principle stress direction for the points near the corners is larger than the other measurement points. Figure 18 shows the principle residual stress at 20/25 mm at the four corners. Comparing with the residual stress at 10/15 mm points shown in Fig. 17, it can be seen that at Points 2, 4, 8, 9, 16, the principle residual stresses at the 20/25 mm locations are higher. One possible cause for this phenomenon is the superposition of the residual stress field formed during the chord box fabrication with the residual stress field formed during the welding of the brace-chord intersection

The distributions of transverse residual stress at 10/15 mm and 20/25 mm locations are shown in

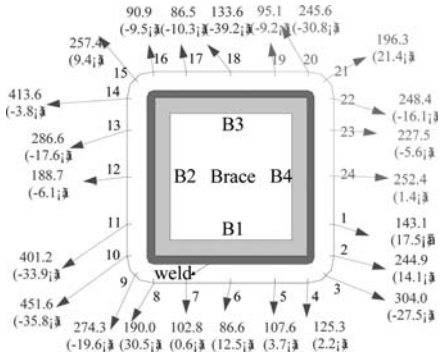

Figure 17. The maximum principle stress distribution for the specimen welded at ambient temperature (Position: 10/15 mm).

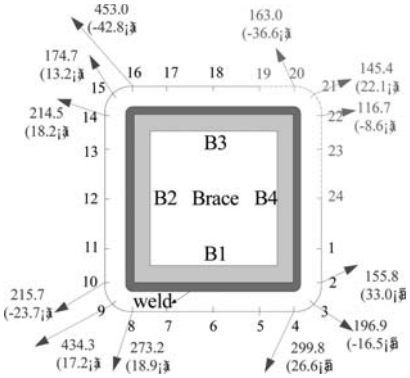

Figure 18. The maximum principle stress distribution for the specimen welded at ambient temperature (Position: 20/25 mm).

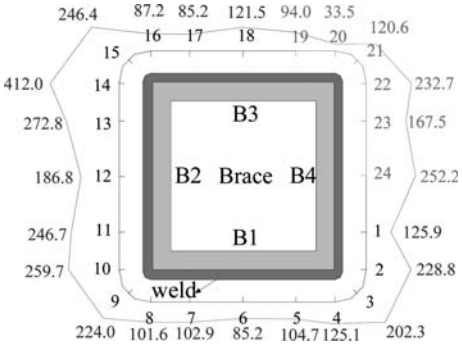

Figure 19. Transverse residual stress distribution for the specimen welded at ambient temperature (Position: 10/15 mm).

Figures 19 and 20. A smaller transverse residual stress turns out along the sides B1 and B3, compared with B2 and B4. The maximum transverse residual stress is 412 MPa at 10 mm from the weld toe is located at Point 14. It should also be noticed that the transverse residual stress at 20/25 mm from the weld toe is higher

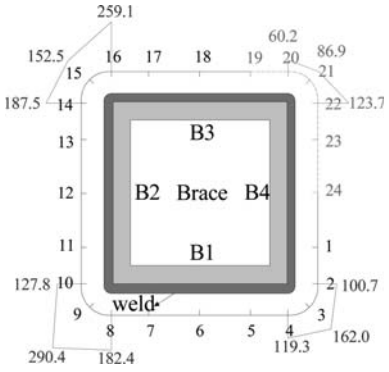

Figure 20. Transverse residual stress distribution for the specimen welded at ambient temperature (Position: 20/25 mm).

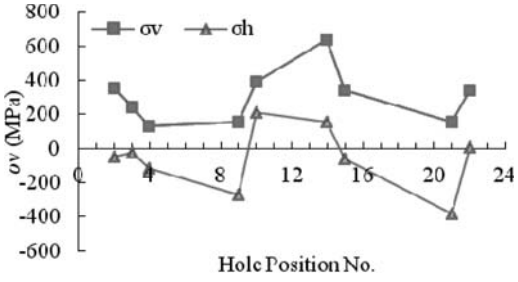

Figure 21. Transverse (σv) and longitudinal residual (σh) stresses at the chord weld toe.

than that at 10/15 mm from the weld toe for Points 3, 8, 9, 16 and 20.

The linear interpolation method was employed to estimate the transverse and longitudinal residual stresses and Figure 21 shows their distributions. Similar with the preheating specimen, the magnitude of transverse stress is higher than the longitudinal component. Furthermore, compressive longitudinal stress can be found at some locations while tensile transverse stress appears along the whole connection.

4 ANALYSIS AND DISCUSSION

4.1 *Preheating effect*

The transverse residual stresses for both specimens are shown in Figure 22. At almost all points, the magnitude of residual stress for the ambient joint is higher than the preheating one. This phenomenon is more obvious at the corners (Points 2, 10 and 14). However, Point 20 to Point 22 (Corner *d*) is the exception. From comparisons for the specimens at Points 2, 10 and 14 (Corners *a*, *b* and *c*), it can be concluded that preheating could effectively eliminate the transverse residual stress. Similar conclusion is obtained by Sanchez-Cabrera et al. (Sanchez-Cabrera et al. 2006) and Xu et al. (Xu et al. 2007). However, at Corner *d*, higher residual stress exists in preheating specimen.

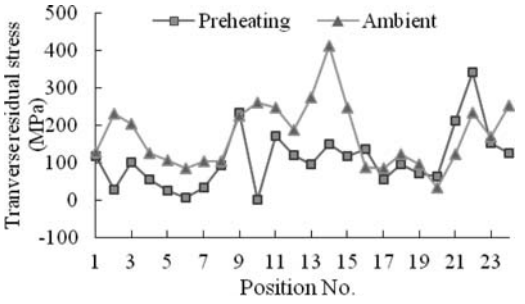

Figure 22. Comparison between the transverse residual stresses for the two specimens.

One explanation is that the preheating rate may not be uniform. Uneven preheating may cause high temperature gradients in the steel, which makes the cooling rate is different. In this case, the residual stress in parts of the preheating joint may be higher than the specimen welded at ambient temperature. Chord edge effect is another possible reason that may change the distribution of residual stress seriously.

4.2 *Chord edge effect*

It should be noticed from Figure 6 and Figure 7 that, along the sides B1 and B3 of the brace, the distance between the edge of the chord to the weld toe is only 25 mm. Such a short distance may cause superposition of the residual stress field formed during the chord box fabrication with the residual stress field formed during the welding of the brace-chord intersection. This explains why for the two specimens, the residual stress magnitudes along the sides B1 and B3 are generally smaller than the stress along the sides B2 and B4. It also explains the phenomenon that for these points, the magnitudes of residual stress are higher at 20/25 mm from the weld toe than at 10/15 mm from the weld toe. To confirm this, four strain gauges (Points 25, 26, 27 and 28, Fig. 7) were added in the specimen welded at ambient temperature to evaluate the differences in residual stress with those points located along the sides B1 and B3. The transverse residual stresses for Points 25 26, 27 and 28 were found to be equal to 212.8 MPa, 237.2 MPa, 187.6 MPa and 194.6 MPa, respectively. Compared with the residual stresses measured at Point 4 to Point 8 and Point 16 to Point 20, the residual stress at Points 25, 26, 27 and 28 is higher. Therefore, a reduction of residual stress could be occurred due to the cancellation of the residual stress fields formed during chord fabrication with that formed during the welding for the joint.

4.3 *Corner effect*

The residual stress distribution in the preheating joint is not uniform around the intersection of the brace and the chord. The residual stresses at the corners are higher than the values from other positions. This corner effect seems more obvious when the measurement points are located at 10/15 mm from the weld toe when comparing with points located at 20/25 mm from the weld toe. In Fig. 11, the maximum residual stress is located at Point 22, where the principle stress is 582.4 MPa, nearly equals to 85% of the nominal yielding stress. Another critical location is Point 9, where the principle residual stress is much higher than Points 8 and 10. For the transverse residual stress, similar conclusion can be obtained from Fig. 13.

5 CONCLUSIONS

Based on the analysis of the test results for both specimens, several conclusions can be drawn. Firstly, preheating is beneficial to reduce the magnitude of residual stress. Secondly, for both specimens, the residual stress magnitudes along sides B1 and B3 are generally smaller than the stress along the sides B2 and B4. Thirdly, due to the chord edge effect, the magnitude of residual stress is not always higher for the position closer from the weld toe than that at the further position.

ACKNOWLEDGMENT

The financial support provided by the Regency Steel Asia Endowment Fund @ NTU in this project and assistance from Yongnam Engineering & Construction Pte Ltd in fabricating the specimens are gratefully acknowledged.

REFERENCES

Lars Jensen, Matthew L. Bloomstine. Application of high strength steel in super long span modern suspension bridge design, Proceeding of NSCC2009, 494–501, 2009

Dan Dubina. Performance and benefits of using high strength steel, ECCS annual meeting, Aalesund, 2008.

Billingham J, Sharp JV, Spurrier J and Kilgallon PJ. Review of the performance of high strength steel used offshore. Bedfordshire, UK, 2003.

ASTM E837-08. Standard Test Method for Determining Residual Stresses by Hole-Drilling Strain-Gage Method. ASTM International, West Conshohocken, PA 19428-2959, United States, 2008.

AWS D1.1. Structural Welding Code-Steel. American Welding Society, Miami, USA, 2008.

Sanchez-Cabrera VM, Rubio-Gonzalez C, Ruiz-Vela JI. Effect of preheating temperature and filler metal type on the microstructure, fracture toughness and fatigue crack growth of stainless steel welded joints, Materials Science and Engineering,V452, P235–243, 2007

Xu Jun, Li We. A finite element analysis of welding-induced distortion control for large box beam structures, Procedures of the Institution of Mechanical Engineers Part B: Journal of Engineering Manufacture, 221(2), P289–301, 2007

Tubular Structures XIV – Gardner (Ed.)
© 2012 Taylor & Francis Group, London, ISBN 978-0-415-62137-3

Branch plate-to-CHS T-connections: Finite element study and design recommendations

A.P. Voth
Yolles, a CH2M HILL company, Toronto, Canada

J.A. Packer
University of Toronto, Toronto, Canada

ABSTRACT: To evaluate the suitability of current international design recommendations for transverse and longitudinal T-type plate-to-CHS connections subjected to branch plate tension or compression, a parametric numerical finite element study was undertaken. Finite element modelling and analysis techniques used in the parametric study were validated against previously tested experimental results. A total of 99 connections with varied geometric properties were modeled and analyzed using commercially available software, ANSYS. An evaluation of current CIDECT partial design strength functions (Q_u) concluded that general conservatism and under-utilization of branch tension-only connection capacity exists. Partial design strength functions are proposed based on a regression analysis of numerical finite element results and existing international experimental data. Lower bound reduction (resistance) factors are applied to these guidelines.

1 INRODUCTION

The fabrication simplicity, cost-effectiveness and aesthetic appeal of axially loaded branch plate-to-hollow structural section (HSS) connections makes them ideal for both enclosed framed structures and for exposed steel work including cable-stayed roof systems and tubular arch bridges. An imposed deformation limit of 3% of the connecting face width for rectangular hollow sections (RHS) or 3% of the diameter for circular hollow section (CHS) connections (Lu et al. 1994, Wardenier et al. 2008a) generally governs the limit states design resistance of plate-to-HSS connections. Though practical and necessary, the strength of the hollow section chord is low and often under-utilized, particularly for heavily loaded tension-only plate-to-CHS connections.

Branch plate-to-CHS connection resistance is currently determined by using the lower of two limit states: chord plastification and chord punching shear, given that both the branch plate and the weld are adequately designed and are non-critical, and is highly dependent on connection geometry (including the orientation and dimensions of the both the branch plate and chord member). Axially loaded T-type branch plate-to-CHS connection design guidelines (CIDECT Design Guide No. 1, 2nd Edition by Wardenier et al. 2008a, IIW design rules 2009 and AISC Steel Design Guide No. 24 by Packer et al., 2010) were developed by adapting existing CHS-to-CHS design guidelines to a very limited database of branch plate-to-CHS experimental results by Washio et al. (1970) and Akiyama et al. (1974) using regression analysis (van der Vegte et al. 2008, Wardenier et al. 2008b). The chord plastification connection resistance, expressed as an axial force in the branch member, is given by CIDECT (Wardenier et al. 2008a) as:

$$N_1^* = Q_u Q_f f_{y0} t_0^2 / \sin\theta_1 \quad (1)$$

where Q_u is a partial design strength function that predicts connection resistance without chord axial stress, and Q_f is a chord stress function that reduces connection resistance based on chord normal stress influence. These functions along with chord punching shear expressions are summarized in Table 1, with the connection types illustrated in Fig. 1.

The partial design strength function found in CIDECT Design Guide No. 1, 2nd Edition (Wardenier et al. 2008a) is based on the partial design strength function developed for T-type CHS-to-CHS connections (van der Vegte et al. 2008), which in its most general form is given as:

$$Q_u = A\left(1 + B\beta^2\right)\left(1 + C\eta\right)\gamma^D \quad (2)$$

where A, B, C and D are regression constants. A recent re-evaluation (Wardenier et al. 2008b, Wardenier et al. 2009) of existing T-type plate-to-CHS experimental results used Eq. 2 as a basis, assumed that the branch plates were relatively thin (η for transverse connections and β for longitudinal connections close to zero), and resulted in the Q_u functions given in

Table 1. CIDECT design resistance of T-type branch plate-to-CHS connections under axial load (Wardenier et al. 2008a).

	Transverse plate	Longitudinal plate
Chord plastification	$Q_u = 2.2(1 + 6.8\beta^2)\gamma^{0.2}$ $Q_f = (1 - \lvert n\rvert)^{C_1}$ where $n = \frac{N_0}{N_{pl,0}} + \frac{M_0}{M_{pl,0}}$ for chord compression stress ($n < 0$), $C_1 = 0.25$ for chord tension stress ($n \geq 0$), $C_1 = 0.20$	$Q_u = 5(1 + 0.4\eta)$
Punching shear	$N_1 * = 1.16 b_1 t_0 f_{y0}$ when $b_1 \leq d_0 - 2t_0$	$N_1 * = 1.16 h_1 \frac{t_0 f_{y0}}{\sin^2 \theta_1}$

Range of validity:
Compression chords must be class 1 or 2, but also $2\gamma \leq 50$
Tension chords must be $2\gamma \leq 50$
Transverse plate: $0.4 \leq \beta \leq 1.0$; longitudinal plate: $1 \leq \eta \leq 4$
$f_{y1} \leq f_{y0}$, $f_y/f_u \leq 0.8$, $f_{y0} \leq 460$ MPa

Note: θ_1 is the angle of the force acting on the plate

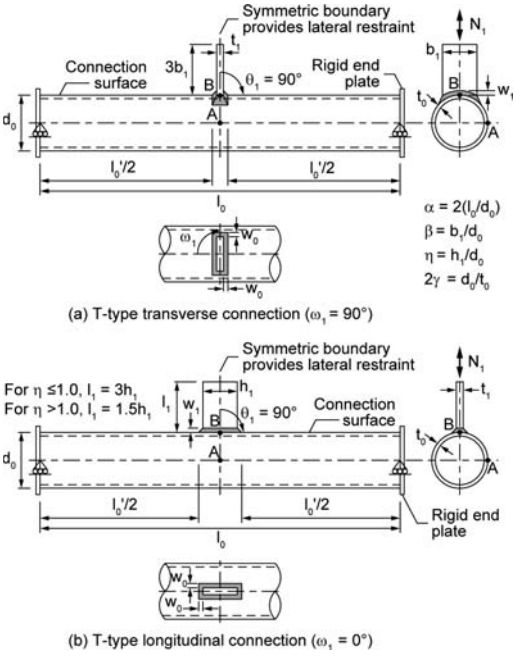

Figure 1. General parametric connection configuration.

Table 1. These guidelines were developed using a lower bound approach where the compression-loaded connection resistance is used for both branch tension and compression; the extra capacity of tension-only connections is therefore not utilized. Also, chord punching shear resistance governs over chord plastification (see Table 1) for transverse plate-to-CHS connections (see Fig. 1) with thick chord walls ($2\gamma = d_0/t_0 \approx 15$ or less) and limited connection width ratios ($\beta = b_1/d_0$), making this limit state potentially unnecessary.

A recent study into the effect of chord normal stress for X-type plate-to-CHS connections (Voth 2010, Voth & Packer 2011b) concluded that the current CIDECT chord stress function (Q_f) formed an acceptable lower bound. Similar studies on CHS-to-CHS X- and T-type connections (van der Vegte & Makino 2006, van der Vegte et al. 2001, Wardenier et al. 2007) on rectangular hollow section X- and T-type connections indicate that the chord normal stress function is very similar for X- and T-type connections. The CIDECT chord stress function shown in Table 1 could therefore also be applied as an acceptable lower bound for T-type plate-to-CHS connections.

To evaluate the aforementioned design guidelines for T-type plate-to-CHS connections, experimental and numerical finite element (FE) research programs have been undertaken. The results of the experimental program (Voth 2010, Voth & Packer 2011a) indicated that connections tested in tension and compression have significantly different behaviour and tension-only connection have considerably more capacity available than indicated by the CIDECT design guideline (Wardenier et al. 2008a). To further investigate the behaviour of transverse and longitudinal T-type plate-to-CHS connections under branch plate compression and tension load, a numerical FE study is presented herein that evaluates the suitability of current design guidelines and separate tension and compression resistance functions.

2 FINITE ELEMENT MODELLING

2.1 *General finite element modelling techniques*

Non-linear finite element modelling techniques have been previously established and validated against eleven experimental X- and T-type connections, with static tensile or compressive branch load (Voth 2010, Voth & Packer 2011a). The modelling techniques used are summarized herein.

All models were constructed and analyzed using commercially available software: ANSYS 11.0 (ANSYS Inc. 2007). Both geometry and measured material properties, including chord end conditions and fillet weld details, were replicated within the FE model. To determine the appropriate element type, mesh layout, the number of chord through-thickness elements and material fracture criterion, a sensitivity analysis was conducted. Eight-node solid brick elements (SOLID45), each with three translational degrees of freedom per node and reduced integration with hourglass control, were ultimately used for each connection model along with three chord through-thickness elements. Uniform mesh density was used, except in locations where large deformations and/or peak stress concentrations leading to cracking and eventually fracture occurred where increased mesh density was used to better capture this behaviour; typically at joint locations between the branch plate and CHS chord. For symmetrical connections with respect

to geometry, restraint and loading, only one quarter or one eighth of T- and X-type connections respectively were modelled with symmetrical boundary conditions. To ensure that plate-to-CHS load transfer was through the fillet weld only and not directly from plate to CHS chord, all FE models were constructed with a 1.0 mm gap between the plate and the CHS at all welded joints.

Multi-linear true stress-strain curves, converted from tensile coupon results of both plate, Grade 300W (CSA 2004) and CHS, ASTM A500 Grade C (ASTM 2010), material were used for FE material properties until the point of coupon necking. The post-necking behaviour was determined by an iterative method developed by Matic (Matic 1985) and modified by Martinez-Saucedo et al. (2006), using FE modelling of experimental coupons directly. The plate material had a yield and ultimate strength of 326 MPa and 505 MPa respectively, and the CHS material had a yield and ultimate strength of 389 MPa and 527 MPa, with the weld material being given the same properties as the plate. A failure criterion was imposed to emulate material ultimate fracture whereby the "death feature" of an element was activated using a previously determined maximum equivalent (von Mises) strain value of $\varepsilon_{ef} = 0.2$ (Voth & Packer 2011a). This failure criterion is specific to the range of parameters investigated. Once the maximum equivalent strain value was reached within an element, the stiffness and the stress in that element were reduced to near-zero allowing the element to freely deform. A non-linear time step analysis was used incorporating non-linear material properties, large deformation allowance and full Newton-Raphson frontal equation solver. Static incremental displacement was applied to the branch plate end with connection load determined using nodal response at that location to reproduce the displacement-control loading.

Connection deformation was defined as the change in distance between point A and a point at the crown of the CHS chord or point B (see Fig. 1). The connection ultimate limit state capacity ($N_{1,u}$) was determined from the load-deformation response as the minimum of: (a) the load at a deformation of $3\%d_0$, $N_{1,3\%}$, if this deformation preceded the deformation at $N_{1,max}$, (b) the maximum connection load, $N_{1,max}$ (either a local maximum prior to CHS shell "snap through" for connections tested in compression or the global maximum load as a result of punching shear failure) and (c) branch plate yielding, $N_{pl,1}$.

2.2 *Numerical parametric connection modelling*

Numerical parametric models of T-type plate-to-CHS connections were constructed using the general finite element modelling techniques established (see Section 2.1 and Voth 2010, Voth & Packer 2011a). The numerical parametric study required the proportions, meshing arrangement and model construction to be altered from the validation models due to changes in connection geometry and restraint. FE models were constructed with constant chord diameter (d_0) of

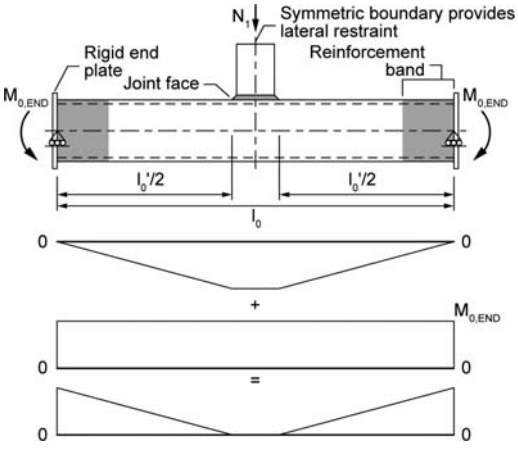

Figure 2. Member end loading to exclude chord normal stress at joint face.

219.1 mm, plate thickness (t_0) of 19.01 mm and branch inclination angle (θ_1) of 90° (see Fig. 1) as one-quarter models. Four CHS chord through-thickness elements were used to more accurately capture chord plastification and fillet welds (w_0 and w_1) were sized to carry the full plate capacity with a leg length of 13.4 mm. The plate yield strength (f_{y1}) and weld strength were increased for high capacity connections only to ensure that branch plate yielding was not critical.

The branch plate length (l_1) for transverse connections (skew angle, $\omega_1 = 90°$) was set to $3b_1$ and for longitudinal connections ($\omega_1 = 0°$) was set to $3h_1$ for $\eta \leq 1.0$, and $1.5h_1$ for $\eta > 1.0$, where η is the branch member depth-to-chord diameter ratio, in an effort to attain a plate uniform stress distribution between the joint the branch plate end (see Fig. 1). Uniform chord normal stress was not applied and the chord ends were capped with a rigid end plate to prevent ovalization of the chord. The preceding connection properties remained constant with all other geometric properties considered as variables within the following parametric studies (see Fig. 1).

As a conservative approach, T-type connections were modelled in three-point bending where, for a one-quarter model, the chord end was supported by a roller at the chord neutral axis (see Fig. 1). To prevent an unstable condition, lateral restraint was provided by the symmetric boundary. High equilibrium-induced chord bending moment (or chord normal stress) at the joint connecting face, which is undesirable for determining connection behaviour without chord stress or design recommendations without a chord stress influence function (Q_f). To remove this chord normal stress due to bending at the joint face, counteracting in-plane bending moments ($M_{0,END} = N_1 l_0'/4$) were applied to the rigid chord end plates (see Fig. 2) thus allowing the chord normal stress influence function (Q_f) to remain independent to the partial design strength function, Q_u (refer to Table 1).

In-plane bending moment applied to the chord end, however, produces two additional problems that must

be addressed. First, connections with high ultimate capacity due to geometric configuration (e.g. thick chords or high plate widths) or longer connection lengths produce higher end moments that may exceed the yield capacity of the chord, as the applied end moment ($M_{0,END}$) is a function of the applied connection load (N_1) and the effective chord length (l'_0). A band of elements with higher yield strength at the CHS chord end (see Fig. 2 – "reinforcement band") was used to prevent chord end failure prior to connection capacity. If reinforcement was required, the band width was determined on an individual connection basis depending on predicted connection capacity and chord length. Second, to prevent non-convergent results which are possible with load-controlled analysis (predominantly for connections loaded in compression during periods of significant plastification and deformation), displacement-controlled analysis was used. Displacement-controlled analysis makes the calculation of the applied end moment difficult as the branch plate load for a given applied displacement is not known until the end of each time step. The applied end moment required for application at the start of each time step was determined by predicting the branch load using a Taylor series approximation and load information from the previous time step, in combination with an end-of-time-step correction and a small displacement rate based in part on the connection load-deformation curve slope.

Table 2. Effective chord length parameter ($\alpha' = 2l'_0/d_0$) for transverse T-type plate-to-CHS connections.

		Nominal plate width ratio, $\beta = b_1/d$									
		0.2		0.4		0.6		0.8		1.0	
t_0 (mm)	2γ	C	T	C	T	C	T	C	T	C	T
15.88	13.80	8	8	8	8	8	8	8	8	8	
11.10	19.74	12	12	12	12	12	8	12	8	8	8
7.95	27.56	12	12	12	12	12	12	12	8	8	8
4.78	45.84	16	16	16	16	16	12	16	12		

Note: C = Branch plate compression; T = Branch plate tension.

3 PARAMETRIC STUDY OF T-TYPE CONNECTIONS

3.1 *Investigated parameters*

A parametric numerical finite element study, consisting of 99 geometric configurations, was used to investigate the behaviour of T-type plate-to-CHS connections subject to both tension and compression branch plate loading. Connection models with four values of 2γ, five nominal width ratios (β) and eight nominal depth ratios (η) were constructed and analysed using the previously validated FE modelling techniques and geometry given in Section 2.2 and in Fig. 1. To minimize boundary condition effects on connection behaviour, an effective chord length parameter ($\alpha' = 2l'_0/d_0$) was determined for each geometric configuration, based on the results of the previous chord length and boundary condition study (Voth 2010) and chord length sensitivity results from each connection model herein. The value of α' for each geometric configuration is presented in Tables 2 and 3 for transverse and longitudinal connection types respectively. Fillet weld size has been incorporated into connection behaviour by converting both η and β to effective values (η' of 0.32, 0.72, 1.12, 1.62, 2.12, 2.62, 3.12 and 4.12 and β' of 0.32, 0.51, 0.69, 0.87 and 1.00). As the weld and the plate were designed to remain non-critical, the combined weld-plate footprint can be considered equivalent to a thicker and wider branch plate without a fillet weld. For the purpose of developing design guidelines, this equivalent plate footprint is used herein.

3.2 *Comparison of CIDECT design guidelines with parametric study results*

All numerical models were governed by the load at the $3\%d_0$ deformation limit ($N_{1,3\%}$), except for two transverse connections that reached a local or global maximum before this limit; a compression model with $2\gamma = 45.84$ and nominal $\beta = 0.2$, and a tension model with $2\gamma = 13.80$ and nominal $\beta = 0.2$. The general behaviour of transverse and longitudinal connections loaded in both branch plate tension or compression is summarized by chord

Table 3. Effective chord length parameter ($\alpha' = 2l'_0/d_0$) for longitudinal T-type plate-to-CHS connections.

		Nominal plate depth ratio, $\eta = h_1/d$															
		0.2		0.6		1.0		1.5		2.0		2.5		3.0		4.0	
t_0 (mm)	2γ	C	T	C	T	C	T	C	T	C	T	C	T	C	T	C	T
15.88	13.80	12	8	12	8	12	8	8	8	8	8	8	8	8			
11.10	19.74	12	12	12	12	12	8	12	12	12	12	8	8	8	8	8	8
7.95	27.56	12	12	12	12	12	12	12	12	12	12	12	12	12	8	12	8
4.78	45.84	16	16	16	16	16	12	16	16	16	16	16	16	16	16	16	16

Note: C = Branch plate compression; T = Branch plate tension.

ovalization at the 3%d_0 deformation limit with stress concentration at branch plate edges preceding crack initiation, indicated by the first killed element. Longitudinal connections generally experienced significantly more chord plastification than comparable transverse connections. Crack initiation occurred at the point of highest stress concentration for all models.

Experimental research by Washio et al. (1970) and Akiyama et al. (1974) on plate-to-CHS connections has been previously complied by Ariyoshi et al. (1998) and Makino et al. (1998) into an international database. Though this database is comprehensive (includes load-deformation curves, connection capacity, etc.) and includes all existing international data, it does not include all geometric or material property information, making its use for behaviour analysis difficult. Further, very few experimental datasets exist; seven experimental tests conducted by Washio et al. (1970) and 29 by Akiyama et al. (1974). The connection capacity of almost all international study results was controlled by the 3%d_0 deformation limit. The current CIDECT design guidelines (Wardenier et al. 2008a), presented in Table 1, are herein evaluated with respect to the numerical finite element study and the international database by examining the ratio of the partial design strength function ($Q_{u,R}$) from test or FE results to the CIDECT partial design strength function ($Q_{u,CIDECT}$). This ratio is plotted for all geometric properties within Figs. 3 to 6. The partial design strength function from numerical FE and international database results ($Q_{u,R}$), is equivalent to the normalized connection capacity ($N_{1,u}/(f_{y0}t_0^2)$) because the chord stress function (Q_f) and the $\sin\theta_1$ term from Eq. 1 both equal unity. It is of note that the CIDECT design guidelines include an embedded resistance factor whereas the results from either the international database or parametric numerical analysis do not.

An examination of transverse connections under branch plate compression load (Fig. 3), indicates that the CIDECT design guideline (see Table 1) is generally conservative for numerical FE results (Voth FE) – values greater than unity, especially for low values of β (see Fig. 3a) and high 2γ values (see Fig 3b) and for all experimental results from Washio et al. (1970). The Voth FE and Washio et al. (1970) data generally fall within the same region with the CIDECT design recommendations over-predicting the connection capacity from numerical FE results (Voth FE) for connections with thick chord walls (low 2γ values). The experimental results of Akiyama et al. (1974) are also generally over-predicted by the CIDECT design guidelines, however these results fall outside the typical size range of members used as structural elements ($2\gamma < 60$) and also outside the current CIDECT design guideline range of validity ($2\gamma < 50$). All results from Akiyama et al. (1974) are outside these ranges and Fig. 3b is shown as an example. Transverse connections with branch plate tension follow a similar trend (see Fig. 4); with almost all parametric numerical (Voth FE) and Akiyama et al. (1974) experimental results being under predicted by the CIDECT design equation. Connection capacity, in some cases, is over two times the current CIDECT design guidelines indicating that these guidelines do not capture the inherent increase

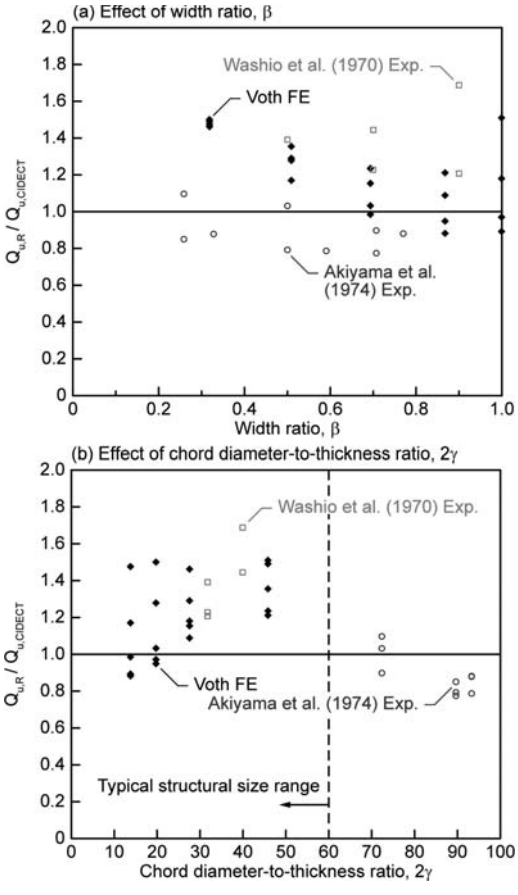

Figure 3. Comparison of CIDECT design guidelines with results database for transverse connections in compression.

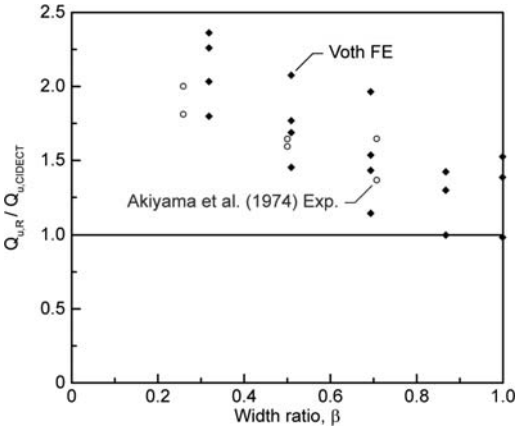

Figure 4. Comparison of CIDECT design guidelines with results database for transverse connections in tension.

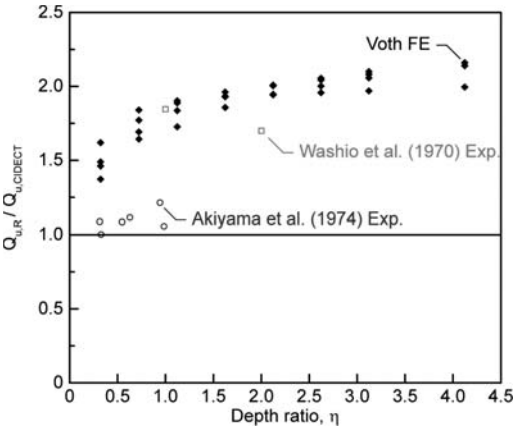

Figure 5. Comparison of CIDECT design guidelines with results database for longitudinal connections in compression.

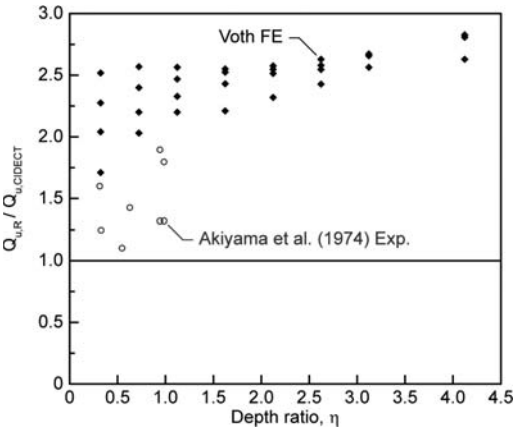

Figure 6. Comparison of CIDECT design guidelines with results database for longitudinal connections in tension.

in capacity of tension-only transverse plate-to-CHS connections.

The CIDECT design guidelines (Wardenier et al. 2008a) for longitudinal connections with branch plate compression load (see Table 1) are also conservative for all numerical parametric results (Voth FE) as well as the experimental results of Washio et al. (1970) as shown in Fig. 5. Additional connection capacity from approximately 30% to over 100% beyond that recommended by CIDECT is available. For longitudinal connections with branch plate tension (see Fig. 6) the CIDECT design guidelines further underpredict the numerical FE analysis results (Voth FE). Most of the datasets have connection capacities 150% greater than that of the CIDECT recommended connection capacity, again demonstrating that the current CIDECT design guidelines do not capture the inherent capacity of branch tension-only T-type plate-to-CHS connections. The current CIDECT design guidelines for both longitudinal and transverse branch plate-to-CHS connections, while forming an acceptable lower bound, do not capture the additional capacity inherent with branch tension-only loaded connections. New partial design strength functions, Q_u, are therefore determined in the following Section 3.3 to address this issue.

Table 4. Statistical comparison of proposed partial design strength functions.

Type	Proposed partial design strength function	$Q_{u,R}/Q_{u,p}$ statistics	Mean	CoV(%)
TC	$Q_u = 2.9\zeta(1+3\beta^2)\gamma^{0.35}$	with $\beta = 1.0$	1.07	12.95
		without $\beta = 1.0$	1.06	12.25
TT	$Q_u = 2.6\zeta(1+2.5\beta^2)\gamma^{0.55}$	with $\beta = 1.0$	1.03	6.77
		without $\beta = 1.0$	1.01	5.17
LC	$Q_u = 7.2\zeta(1+0.7\eta)$		1.01	4.77
LT	$Q_u = 10.2\zeta(1+0.6\eta)$		1.00	7.12

Note: TC = transverse plate in compression; TT = transverse plate in tension; LC = longitudinal plate in compression; LT = longitudinal plate in tension.

3.3 *Regression analysis and design recommendations*

A nonlinear regression analysis was performed using the current CIDECT guidelines equation format as a basis. Similar to a method used by Wardenier et al. (2008b, 2009), Eq. 2 – which is the basis for the function developed for T-type CHS-to-CHS connections (van der Vegte et al. 2008) – was modified by assuming that the branch plates are relatively thin (η for transverse connections and β for longitudinal connections are close to zero) resulting in partial design strength regression functions of:

$$Q_u = A\left(1 + B\beta^2\right)\gamma^D \quad \text{for transverse connections} \qquad (3)$$

$$Q_u = A\left(1 + C\eta\right)\gamma^D \quad \text{for longitudinal connections} \qquad (4)$$

Regression analysis used to evaluate the proposed partial design strength functions ($Q_{u,p}$) was limited to the parametric FE results (Voth FE) and the experimental results by Washio et al. (1970), disregarding results from Akiyama et al. (1974) for reasons given previously. The proposed design recommendations are summarized in Table 4 for the four types of T-type plate-to-CHS connections separating tension and compression behaviour. Though included in Eq. 4, the chord radius-to-thickness ratio term (γ) has limited influence for longitudinal plate-to-CHS connections and is therefore excluded from the recommendations presented in Table 4. An additional reduction factor (ζ) is described later in this section and is set to unity for the statistics presented in Table 4.

To evaluate the effectiveness of the proposed partial design strength functions, the $Q_{u,R}/Q_{u,p}$ ratio for

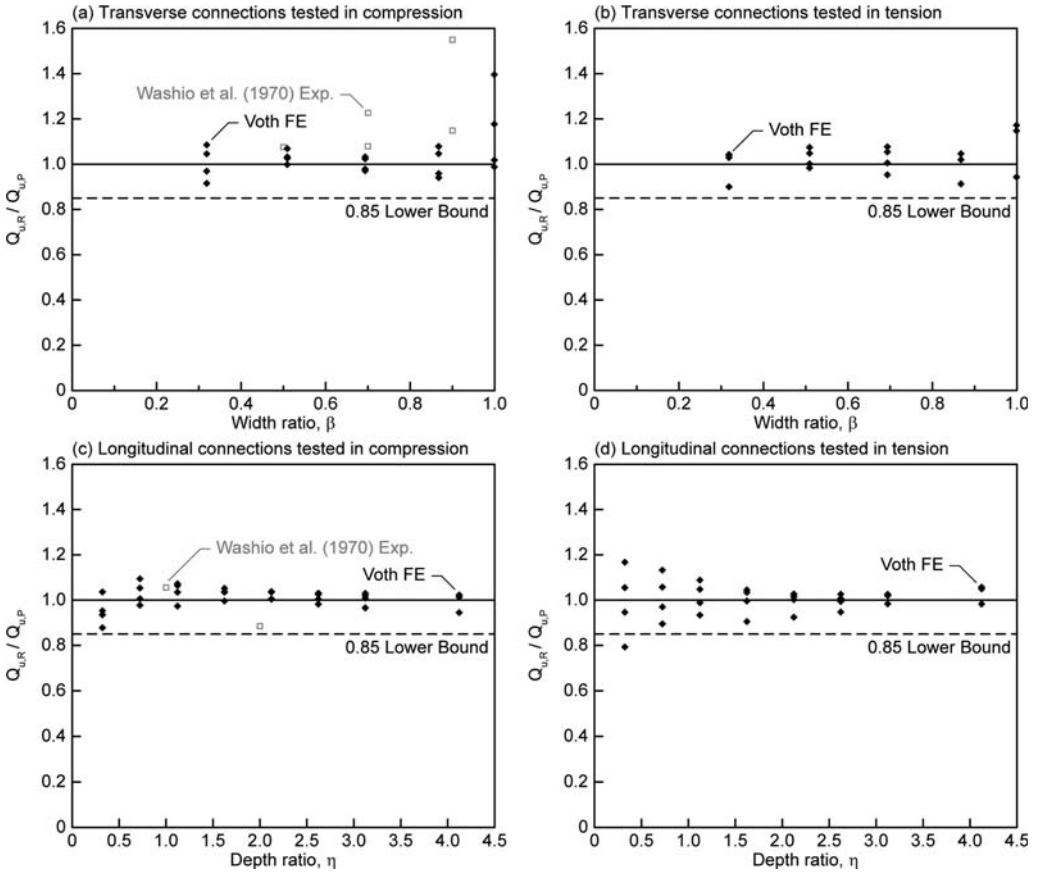

Figure 7. Comparison of proposed partial design strength functions with applicable results for T-type plate-to-CHS connections.

is plotted against β and η in Fig. 7. All of the parametric FE results and Washio et al. (1970) experimental data are well predicted by the proposed design functions except for transverse connections in compression with high β values, where the proposed functions under-predict the connection capacity (see Fig. 7a) subsequently increasing the coefficient of variation (CoV) in Table 4. As the proposed design expressions are conservative for connections with high β values, a reduction in capacity of these connections would not impact the safety of the design recommendations. There is a minimal reduction in the coefficient of variation if the statistical analysis is performed on transverse connections without the $\beta = 1.0$ data (see Table 4). It is clear that for longitudinal connections there is a good coefficient of variation (CoV) and mean close to unity, from the statistical data presented in Table 4.

As the majority of plate-to-CHS connections presented in the preceding sections have significant ductility beyond the deformation at the connection "ultimate" capacity, $N_{1,u}$, the database is generally dominated by a yielding failure mode, allowing for the use of a reduction factor of ζ close to unity. Though the proposed partial design strength functions ($Q_{u,p}$) provide a good statistical fit with connection results, there is some scatter for both transverse and longitudinal connections. To ensure that adequate safety margins are given, a lower bound design approach is adopted herein. Each design expression for T-type plate-to-CHS connections has a $Q_{u,R}/Q_{u,p}$ ratio always greater than 0.85 (except for one point in Fig. 7d) and thus a lower bound reduction factor (analogous to a LRFD resistance factor) of $\zeta = 0.85$ is recommended for the proposed Q_u functions in Table 4. The one point below a $Q_{u,R}/Q_{u,p}$ ratio of 0.85 is for a longitudinal connection tested in tension with a very small plate depth ratio of $\eta = 0.2$, which is currently outside the range of validity used in CIDECT Design Guide No. 1, 2nd Edition (Wardenier et al. 2008a). A wider range of validity ($2\gamma \leq 46$ and $0.2 \leq \eta \leq 4$) can also be used for the proposed design recommendations given in Table 4.

4 CONCLUSIONS

An examination of current design guidelines, for T-type branch plate-to-CHS connections, has been undertaken using a numerical finite element

parametric study consisting of 99 models, under both tension and compression branch plate load. In addition to incorporating previous international research data by Washio et al. (1970), this study has determined that current CIDECT partial design strength functions (Q_u) are generally conservative for T-type branch plate-to-CHS connections and they under-utilize connection capacity of tension-only loaded connections. Using regression analysis, improved partial design strength functions are proposed (Q_u values in Table 4) with lower bound reduction factors ($\zeta = 0.85$) that alleviate concerns with the existing expressions. Further, the proposed design expressions given in Table 4 have a wider range of validity (represented by the β, η, 2γ and t_0 ranges in Tables 2 and 3) than currently used in international design expressions (see Table 1) and the number of limit states checks is reduced from two to one for all connection types covered.

NOTATION

A_i = cross-section area of member i
b_1, b_1' = nominal, effective branch width ($b_1' = b_1 + 2w_0$): 90° to chord longitudinal axis
d_0 = external diameter of CHS member
f_u = ultimate stress
f_{yi} = yield stress of member i
h_1, h_1' = nominal, effective branch depth in plane with chord longitudinal axis
i = denotes member (i = 0 for chord, i = 1 for branch)
l_0, l_1 = chord length, branch length
M_0 = chord bending moment
$M_{0,END}$ = applied in-plane bending moment
$M_{pl,0}$ = chord plastic moment capacity
N_i = axial force in member i
$N_{1,3\%}$ = branch load at 3% d_0 connection deformation
$N_{1,u}$ = connection ultimate limit state capacity
N_1* = connection resistance expressed as an axial force in branch member
$N_{pl,i}$ = yield capacity for member i ($= A_i f_{yi}$)
Q_f = chord stress influence function
Q_u = partial design strength function,
$Q_{u,R}$ = partial design strength function from experimental or numerical results
$Q_{u,p}$ = proposed partial design strength function
t_i = thickness member i
w_0, w_1 = measured weld leg length along chord, branch
α, α' = chord length parameter ($\alpha = 2l_0/d_0$), effective chord length parameter ($\alpha' = 2l_0'/d_0$)
β, β' = nominal, effective connection width ratio $\beta = b_1/d_0$, $\beta' = b_1'/d_0$, $\beta = t_1/d_0$ for longitudinal
γ = chord radius-to-thickness ratio ($\gamma = d_0/2t_0$)
ε_{ef} = maximum equivalent strain
ζ = reduction factor
η, η' = nominal, effective branch member depth-to-chord diameter ratio ($\eta = h_1/d_0$ and $\eta' = h_1'/d_0$ for longitudinal; $\eta = t_1/d_0$ for transverse)
θ_1 = included inclination angle between branch and chord
ω_1 = included skew angle of branch to chord axis

REFERENCES

Akiyama, N., Yajima, M., Akiyama, H. & Ohtake, A. 1974. Experimental study on strength of joints in steel tubular structures. *J. Society of Steel Construction*, (10)102, 37–68 (in Japanese).

ASTM. 2010. *Standard specification for cold-formed welded and seamless carbon steel structural tubing in rounds and shapes, ASTM A500/A500M-10*. ASTM International, West Conshohocken, USA.

ANSYS Inc. 2007. ANSYS. ver. 11.0, Cononsburg, PA, USA.

Ariyoshi, M., Wilmshurst, S. R., Makino, Y., van der Vegte, G. J. & Choo, Y. S. 1998. Introduction to the database of gusset-plate to CHS tube joints. *Proc. 8th intern. Symp. on tubular structures.* Singapore, A.A. Balkema, 203–211.

CSA. 2004. *General requirements for rolled or welded structural quality steel/ structural quality steel, CAN/CSA-G40.20-04/G40.21-04.* CSA, Toronto, Canada.

IIW. 2009. *Static design procedure for welded hollow section joints: recommendations.* IIW Doc. XV-1329-09, IIW, Paris, France.

Lu, L.H., de Winkel, G.D., Yu, Y. & Wardenier, J. 1994. Deformation limit for the ultimate strength of hollow section joints. *Proc. 6th intern. Symp. on tubular structures*. Melbourne, Australia, A.A. Balkema, 341–347.

Makino, Y., Ariyoshi, M., Minehara, Y., van der Vegte, G.J., Wilmshurst, S.R. & Choo, Y.S. 1998. Database of test and numerical analysis results for gusset-plate to CHS tube joints. *IIW Doc. XV-E-98-237*, Kumamoto University, Kumamoto, Japan.

Martinez-Saucedo, G., Packer, J.A. & Willibald, S. 2006. Parametric finite element study of slotted end connections to circular hollow sections. *Engineering Structures*, (28)14, 1956–1971.

Matic, P. 1985. Numerically predicting ductile material behavior from tensile specimen response. *Theoretical and Applied Fracture Mechanics*, (4)1, 13–28.

Packer, J.A., Sherman, D.R. & Lecce, M. 2010. Hollow structural section connections. *Steel Design Guide No. 24,* American Institute of Steel Construction (AISC), Chicago, USA.

van der Vegte, G.J. & Makino, Y. 2006. Ultimate strength formulation for axially loaded CHS uniplanar T-joints. *Inter. J. Offshore and Polar Engineering*, (16)4, 305–312.

van der Vegte, G.J., Makino, Y., Choo, Y.S. & Wardenier, J. 2001. The influence of chord stress on the ultimate strength of axially loaded uniplanar X-joints. *Proc. 9th intern. Symp. on tubular structures.* Düsseldorf, Germany, A.A. Balkema.

van der Vegte, G.J., Wardenier, J., Zhao, X.-L. & Packer, J.A. 2008. Evaluation of new CHS strength formulae to design strengths. *Proc. 12th intern. Symp. on tubular structures*. Shanghai, China, Taylor & Francis Group, 313–322.

Voth, A.P. 2010. *Branch plate-to-circular hollow structural section connections.* Ph.D. thesis, University of Toronto, Toronto, Ontario, Canada.

Voth, A.P. & Packer, J.A. 2011a. Branch plate-to-circular hollow structural section connections: Experimental investigation and finite element modeling. *J. of Structural Engineering*, DOI 10.1061/(ASCE)ST.1943-541X.0000505 (Sept. 22, 2011).

Voth, A.P. & Packer, J.A. 2011b. Branch plate-to-circular hollow structural section connections: X-type parametric numerical study and design. *J. of Structural Engineering*, DOI 10.1061/(ASCE)ST.1943-541X.0000545 (Nov. 30, 2011).

Wardenier, J., Kurobane, Y., Packer, J.A., van der Vegte, G.J. & Zhao, X.-L. 2008a. *Design guide for circular hollow section (CHS) joints under predominantly static loading, 2nd Edition.* CIDECT, Geneva, Switzerland.

Wardenier, J., van der Vegte, G.J. & Liu, D.K. 2007. Chord stress function for rectangular hollow section X and T joints. *Proc. 17th intern. offshore and polar engineering conf.* Lisbon, Portugal, International Society of Offshore and Polar Engineers (ISOPE), (IV), 3363–3370.

Wardenier, J., van der Vegte, G.J. & Makino, Y. 2008b. Joints between plates or I sections and a circular hollow section chord. *Proc. 18th intern. offshore and polar engineering conf.* Vancouver, Canada, International Society of Offshore and Polar Engineers (ISOPE), (IV), 319–326.

Wardenier, J., van der Vegte, G.J. & Makino, Y. 2009. Joints between plates or I sections and a circular hollow section chord. *Inter. J. Offshore and Polar Engineering*, (19)3, 232–239.

Washio, K., Kurobane, Y., Togo, T., Mitsui, Y. & Nagao, N. 1970. Experimental study of ultimate capacity for tube to gusset plate joints – part 1. *Proc. annual conf. of the AIJ.* Japan.

Tubular Structures XIV – Gardner (Ed.)
© 2012 Taylor & Francis Group, London, ISBN 978-0-415-62137-3

Response of beam-to-tubular column angle connections subjected to combined flexure and axial loading

Y. Liu, C. Málaga-Chuquitaype & A.Y. Elghazouli
Department of Civil and Environmental Engineering, Imperial College London, UK

ABSTRACT: In some design situations, such as those involving extreme loading conditions, steel connections can play a vital role in arresting structural disproportionate collapse, and therefore should be designed to resist significant moments, axial loads, shear forces, or a combination of these actions. While the moment-rotation behaviour of semi-rigid and fully-rigid connections has been studied comprehensively by previous investigators, there is a relative lack of information on the connection performance under other loading conditions, particularly in relation to semi-rigid connections to tubular columns. This paper is concerned with the behaviour of open beam-to-tubular column angle connections subjected to axial and combined axial/flexural actions. It focuses on two types of semi-rigid connections to tubular columns, including blind-bolted as well as reverse channel angle configurations. To this end, an experimental study on the full component characterization of angle connections to tubular columns under tension and compression actions is summarized. The main behavioural patterns are briefly discussed and the salient response characteristics such as stiffness, capacity and failure mechanisms are examined. Based on the experimental results, detailed component models are described with due account for flexural and axial load interactions.

1 INTRODUCTION

The structural and architectural advantages of Hollow structural sections (HSS) make them an ideal choice as column members. However, these merits may sometimes be underexploited due to the perceived difficulties and available connection details between open beams and tubular columns. Most of the research on open-beam-to-tubular-column connections has focused on fully-rigid fully-welded details (Cao et al. 1998, Kosteski & Packer 2003) and rules for determining their resistance have been incorporated in current European standards (CEN 2005). However, there is a dearth of information and design guidance in relation to the behaviour of semi-rigid bolted angle connections for tubes.

The costs associated with the construction, inspection and maintenance of fully welded details has motivated the development of other connection alternatives such as the flowdrill process (Banks 1993) and special bolts with sleeves designed to expand inside the tube (Huck International Inc. 1990, Lindapter International Ltd. 1995). A simpler blind-bolt design is that proposed by Lindapter International (1995) through the development of the Hollo-bolt. In particular, the avoidance of close tolerance holes and specialized installation equipment renders the use of Hollo-bolts attractive. Another alternative for bolted connections between open beams and tubular columns is that offered by combined channel/angle configurations, in which a channel section is shop-welded at the legs end to the face of the column. The channel face is then connected on-site to the open beam by means of any conventional bolted detail. Given their practical and economical advantages, these two connection alternatives (blind-bolted angle connection and combined channel/angle details) are examined in this paper.

A number of experimental studies have been carried out on Hollo-bolted T-stubs and connections subjected mainly to bending (France et al. 1999, Barnett et al. 2000, Barnett et al. 2001, Elghazouli et al. 2009). More recently, work at Imperial College London (Elghazouli et al. 2009, Málaga-Chuquitaype & Elghazouli 2010) included an experimental investigation into the monotonic and cyclic behaviour of top and seat as well as top, seat and web angle connections Hollo-bolted or connected via reverse channels to structural hollow columns. Nevertheless, a comprehensive characterization of the full axial force-displacement relationship of blind-bolted angle and combined channel/angle connections to tubes has not been performed, particularly under compressive loads.

A number of studies have also been carried out on the analytical modelling of semi-rigid connections incorporating conventional bolts (Angerskov 1976, Kishi & Chen 1990). In comparison, analytical research on the response prediction of bolted connections to tubular columns is limited, despite the recognition that the behaviour of the tubular column flange is significantly different from that of open sections (Elghazouli et al. 2009,

Málaga-Chuquitaype & Elghazouli 2010). Ghobarah et al. (1996) suggested a model for the estimation of the initial stiffness and capacity of blind-bolted end-plate connections between open beams and tubular columns. Wang et al. (2010) investigated the behaviour of Hollo-bolted T-stubs and proposed an analytical model for the evaluation of their initial stiffness. Component-based mechanical models were also proposed for blind-bolted (Málaga-Chuquitaype & Elghazouli 2010) and reverse channel (Málaga-Chuquitaype 2011) angle connections able to trace their full monotonic and cyclic moment-rotation response. Although general in form, none of these models have been validated against significant tensile or compressive joint deformations.

It has been noted that under extreme loading conditions such as those represented by idealized column removal scenarios (Vlassis et al. 2008), significant levels of axial action are imposed onto the connections and that this has a strong influence on the structure survivability. Accordingly, there is a clear need for characterising the response of connections between open beams and tubular columns subjected to direct axial forces. This paper deals with the behaviour of two cost-effective and practical connections subjected to direct tension and compression by means of experimental and simplified mechanical analyses. It summarizes and discusses the results of seven tension tests and six compression tests on Hollo-bolted angle connections and combined channel/angle details. The experimental set-up, connection configurations and material properties are first introduced followed by an overview of the results and observations from the tests. Finally, the component-based method is extended to open beam-to-tubular column angle connections employing Hollo-bolts or reverse channel components subjected to combined flexure and axial loads.

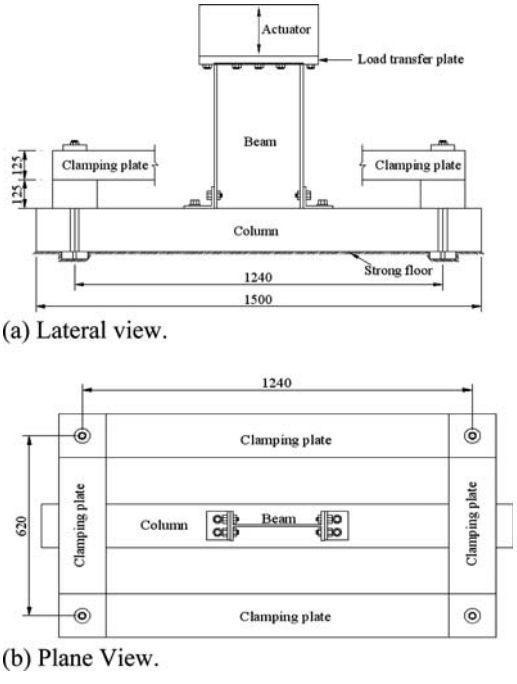

Figure 1. Tension test set-up (dimensions in mm).

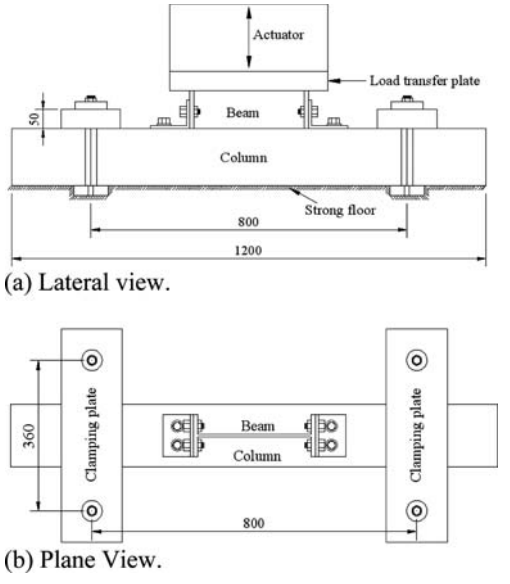

Figure 2. Compression test set-up (dimensions in mm).

2 EXPERIMENTAL ARRANGEMENT AND SPECIMEN DETAILS

2.1 *Testing set-up*

Figure 1 shows the experimental set-up used for testing bolted angle connections under tension. A 1500 mm length column was used in all tensile specimens. The column was fixed at both ends by means of four 125 mm thickness clamping plates, as depicted in Figure 1. A hydraulic actuator operating in displacement control was connected to the beam top end in order to apply vertical deformations. The displacement at the top of the beam was gradually increased up to failure of the specimen or until the actuator capacity was reached at around 700 kN.

Similarly, the test set-up used for the bolted angle connections under compression is depicted in Figure 2. The tubular column was fixed at both ends by two 50 mm clamping plates. To prevent buckling effects within the beam, a short beam of 125 mm length was employed. Displacements were applied to the specimen via a vertical actuator connected to the top surface of the beam. A maximum displacement of 25 mm was applied to all compression specimens.

The applied vertical displacement and corresponding vertical force were recorded by the load cell and transducer incorporated within the actuator. Strain gauges were used to monitor the strains at expected inelastic regions within the angles and columns. The

Table 1. Summary of the tension test specimens.

Reference	Type	Angle	Column	Channel	Dimensions (mm) (as shown in Figure 3)								
					a	b	c	d	h	i	j	k	l
Blind-bolted angle connections													
T1	A	L100 × 75 × 8	SHS 150 × 150 × 10	–	45	30	35	65	100	45	45	–	–
T2	A	L100 × 75 × 8	SHS 150 × 150 × 6.3	–	45	30	35	65	100	45	45	–	–
T3	A	L100 × 75 × 8	SHS 150 × 150 × 10	–	50	50	35	40	100	45	45	–	–
T4	A	L100 × 80 × 15	SHS 150 × 150 × 6.3	–	50	100	35	45	100	45	45	–	–
Combined channel/angle connections													
T5	B	L100 × 80 × 15	SHS 200 × 200 × 10	SHS 150 × 150 × 6.3	50	100	35	45	100	45	45	475	70
T6	B	L100 × 80 × 15	SHS 200 × 200 × 10	SHS 150 × 150 × 10	50	100	35	45	100	45	45	475	70
T7	C	L100 × 75 × 8	SHS 200 × 200 × 10	SHS 150 × 150 × 10	50	50	35	40	100	80	45	465	70

Table 2. Summary of the compression test specimens.

Reference	Type	Angle	Column	Channel	Dimensions (mm) (as shown in Figure 3)								
					a	b	c	d	h	i	j	k	l
Blind-bolted angle connections													
C1	A	L100 × 75 × 8	SHS 150 × 150 × 10	–	50	50	35	40	100	45	45	–	–
C2	A	L100 × 75 × 8	SHS 200 × 200 × 10	–	50	50	35	40	100	45	45	–	–
C3	A	L100 × 75 × 8	SHS 150 × 150 × 10	–	50	50	35	40	100	45	45	–	–
Combined channel/angle connections													
C4	B	L100 × 75 × 8	SHS 200 × 200 × 10	SHS 150 × 150 × 10	45	30	35	65	100	45	45	515	70
C5	B	L100 × 75 × 8	SHS 200 × 200 × 10	SHS 150 × 150 × 10	50	50	35	40	100	45	45	465	70
C6	B	L100 × 80 × 15	SHS 200 × 200 × 10	SHS 150 × 150 × 6.3	50	100	35	45	100	45	45	475	70

verticality of the load was monitored through displacement transducers, while other transducers were employed to measure displacements at selected points within the column and angle components.

2.2 *Specimen details*

Seven tension tests were performed: four blind-bolted connection specimens and three reverse channel details. Similarly, six specimens were tested under compression action: three blind-bolted angle details and three combined channel/angle specimens. Table 1 summarizes the tension specimens while Table 2 presents the same information for the compression tests. These tables include the geometric details of the connections as well as the column and beam sizes. 'T' is used to refer to Tension specimens (T1 to T7) and 'C' to Compression specimens (C1 to C6). Figure 3 depicts the connection configurations studied (Type A, Type B and Type C).

Tables 1 and 2 give the dimension of the SHS from which the reverse channels were obtained. It is important to note that Universal Beams UB 305 × 165 × 25 were employed for Specimen T7 and C3, while Universal Beams UB 305 × 105 × 25 were used for other specimens. Additionally, the dimensions of 'e', 'f' and 'g' for Specimen T7 (with web angles as shown in Figure 3c) are 35 mm, 95 mm and 12.5 mm, respectively.

Grade 10.9 M16 standard bolts were employed to connect the beam flange and angle as well as the reverse channel and angle components, while Grade 10.9 M16 Hollo-bolts were utilized between the tubular column and angles. All bolts were preloaded to 110 kN. The angles were made of Grade S275 steel whilst S375 was adopted for beams and columns. The mean yield stress values and ultimate strength for the angle, beam and column components as obtained from at least three coupon tests are presented in Tables 1 and 2. The axial capacity of Grade 10.9 M16 Hollo-bolts can be considered as 78 kN and its initial stiffness as 195 kN/mm based on the experimental tension-deformation relationships presented by Elghazouli et al. (2009). Also, hardness tests were employed to determine the material characteristics of the Hollo-bolt sleeves and the results are presented in Table 3. Fillet welding with a throat thickness of 10 mm was used to connect the column and the reverse channel throughout the length of the channel external face.

3 RESULTS AND OBSERVATIONS FROM TENSION TESTS

3.1 *Blind-bolted angle connections*

The tensile force-displacement relationships for the four blind-bolted specimens are depicted in Figure 4

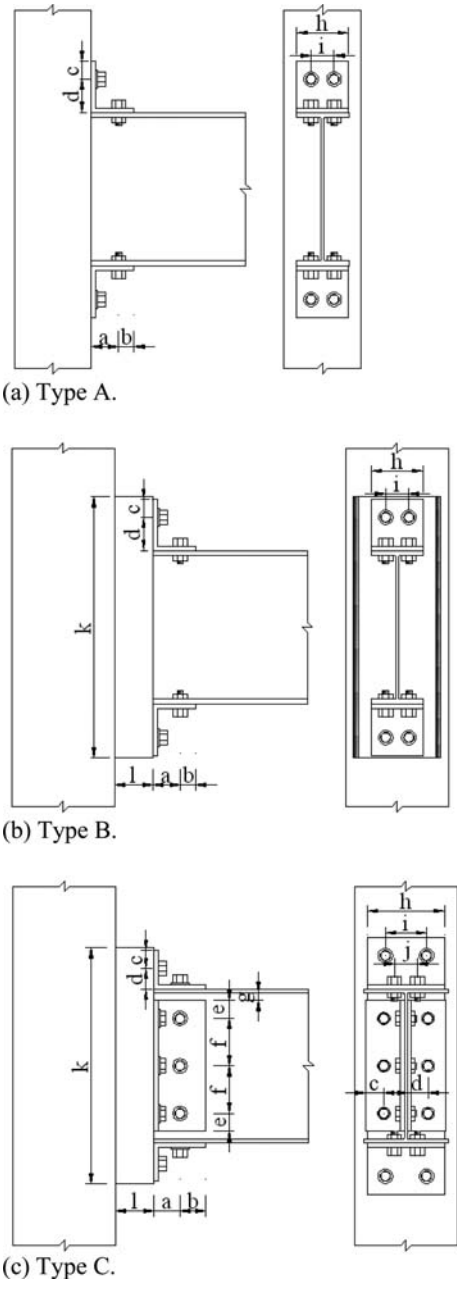

Figure 3. Connection configurations.

together with an indication of their corresponding failure mechanisms. The influence of the angle horizontal gauge distance (*d* in Figure 3) can be examined by comparing the results of Specimens T1 and T3 with d = 65 mm and d = 40 mm, respectively. It can be observed that the initial stiffness of Specimen T3 was 25% larger than that of Specimen T1 due to the shorter horizontal gauge distance (i.e. stiffer angle leg). Moreover, Specimen T3 developed 65% higher tensile yield forces than Specimen T1. However,

Table 3. Material properties of connection elements.

	Yield stress (N/mm^2)	Ultimate stress (N/mm^2)
UB 305 × 165 × 25	329	443
UB 305 × 102 × 25	400	490
SHS 200 × 200 × 10	433	487
SHS 150 × 150 × 10	334	433
SHS 150 × 150 × 6.3	385	485
L 100 × 75 × 8	312	438
L 100 × 80 × 15	293	449
Hollo-bolt sleeve*	382	512

*Obtained from the mean of three hardness tests.

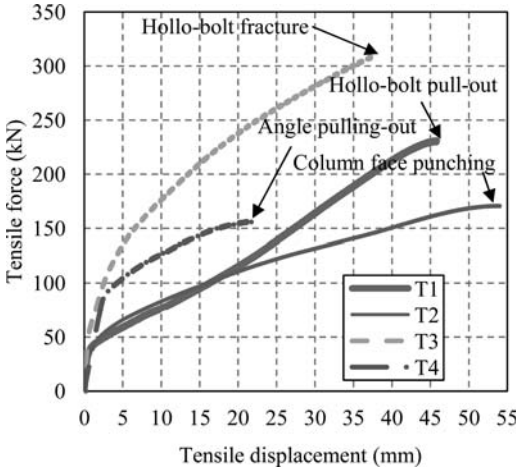

Figure 4. Tensile force-displacement relationships for blind-bolted angle connections.

Specimen T3 failed at a smaller displacement than Specimen T1 due to the fracture of the Hollo-bolt connecting the top angle and the column.

The influence of column thickness on the tensile behaviour of Hollo-bolted connections can be studied by comparing the results of Specimens T1 and T2. The thickness of the column was reduced from 10 mm in Specimen T1 to 6.3 mm in Specimen T2, while all other geometric and material characteristics were retained. It can be noted from Figure 4a, that the initial stiffness of Specimen T1 was about 28% larger than that of Specimen T2 due to the thicker column. This level of difference is maintained up to the attainment of the connection yield capacity (i.e. 35 kN). After yielding, the tensile force-displacement responses for both specimens follow a similar path for displacements of up to 17 mm.

As expected, the reduction in the column wall thickness of Specimen T4 in conjunction with stiff angles (L100 × 80 × 15) resulted in significant deformation around the Hollo-bolts in the thin column leading to a modest joint stiffness of around 38 kN/mm as

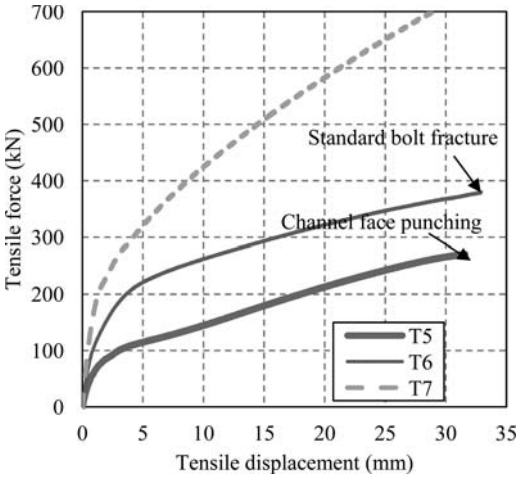

Figure 5. Tensile force-displacement relationships for combined channel/angle connections.

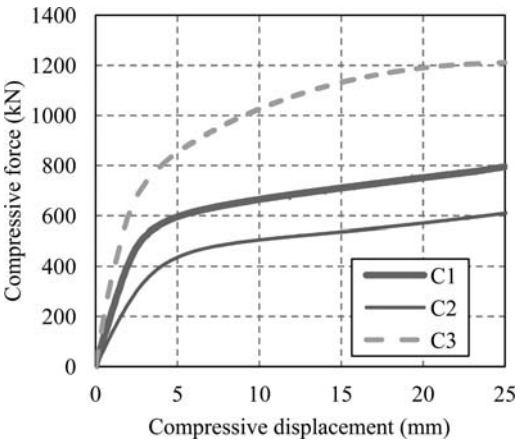

Figure 6. Compressive force-displacement relationships for blind-bolted angle connections.

shown in Figure 4a. Moreover, a reduced connection ultimate capacity was also observed (157 kN) caused by pulling-out of the Hollo-bolts connecting the angles and the column starting at a displacement of around 22 mm. Specimen T4 also had less ductility capacity in comparison with the other blind-bolted configurations.

3.2 *Combined channel/angle connections*

The tensile force-displacement relationships for Specimens T5, T6 and T7 are depicted in Figure 5. The effect of reverse channel thickness on the response of combined channel/angle connections can be examined by comparing the experimental results of Specimens T5 (with channel thickness = 6.3 mm) and T6 (with channel thickness = 10 mm).

It can be observed from Figure 5 that the increase in channel thickness leads to a proportional increase in the stiffness and capacity which were about 40% and 55% higher for Specimen T6 in comparison with Specimen T5, respectively. The response of bolted connections with top and seat as well as web angles subjected to tension load can be illustrated with reference to Specimen T7. The initial stiffness of Specimen T7 increased to 242 kN/mm, and the tensile force reached 700 kN (the actuator capacity) at a displacement of 29 mm. Further discussion of the experimental results can be found elsewhere (Liu 2012).

4 RESULTS AND OBSERVATIONS FROM COMPRESSION TESTS

4.1 *Blind-bolted angle connections*

The compressive force-displacement relationships for blind-bolt angle specimens are illustrated in Figure 6. It is evident from the figure that the provision of beam/angle widths smaller than the corresponding column face width leads to proportional reductions in the connection stiffness and capacity. In the case of Specimen C1 (with column SHS 150 × 150 × 10), the initial stiffness was about 40% higher than that of Specimen C2 (with column SHS 200 × 200 × 10) for the same beam/angle width (i.e. 102 mm). Moreover, Specimen C1 yielded at a load about 100 kN higher than that of Specimen C2 and this difference increased to 180 kN for compressive capacities at 20 mm of displacement.

The effects of providing angle/beam components wider than the column face width can be illustrated by comparing the results of Specimens C1 and C3 in Figure 6 where the beam width is increased from 102 mm in the former to 165 mm in the latter, while retaining all other geometric and material characteristics. This increment in the angle/beam width led to enhancements of around 70% and 60% in stiffness and capacity, respectively. The capacity of the connection under compression at 10 mm of compressive displacement also increased by 60% in Specimen C3 with respect to the corresponding capacity of Specimen C1.

4.2 *Combined channel/angle connections*

Three combined channel/angle connections were examined with emphasis on the influence of the stiffness of the reverse channel as well as the geometry and thickness of the angle components; the corresponding compressive force-displacement relationships are presented in Figure 7. It can be observed that the stiffness of Specimen C4 was only 5% higher than that of Specimen C5 due to the slightly higher angle leg length in Specimen C5. Likewise, both Specimens C4 and C5 reached compressive capacities in the order of 650 kN. In contrast, the thinner channel employed in Specimen C6 lead to a reduction of nearly 30% in stiffness and 50% in yield capacity when compared with the observed values for Specimens C4 and C5.

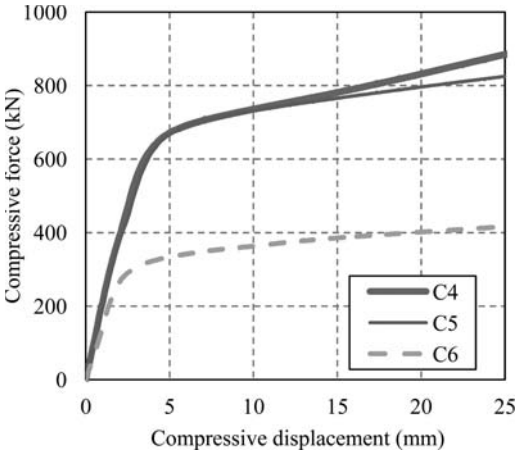

Figure 7. Compressive force-displacement relationships for combined channel/angle connections.

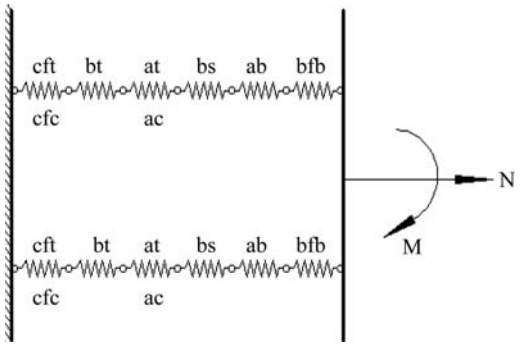

Figure 8. Component-based model for bolted angle connections under bending loadings.

5 COMPONENT-BASED MODEL

5.1 *Constitutive components*

The component-based model used for examining the response of semi-rigid open beam-to-tubular column angle connections is illustrated in Figure 8. The model is composed of two rigid bars, representing the column centreline and the beam end, connected by a series of nonlinear springs at each bolt-row level. The following components have been considered in assembling the response of the bolted angle connections:

1) Bolts in tension (F_{bt},K_{bt})
2) Bolts in shear (F_{bs},K_{bs})
3) Column/channel face in bending (F_{cft},K_{cft})
4) Angle in bending (F_{at},K_{at})
5) Column/channel face in compression (F_{cfc},K_{cfc})
6) Angle leg in compression (F_{ac},K_{ac})
7) Angle leg in bearing (F_{ab},K_{ab})
8) Beam flange in bearing (F_{bfb},K_{bfb})
9) Beam web in bearing (F_{bwb},K_{bwb})

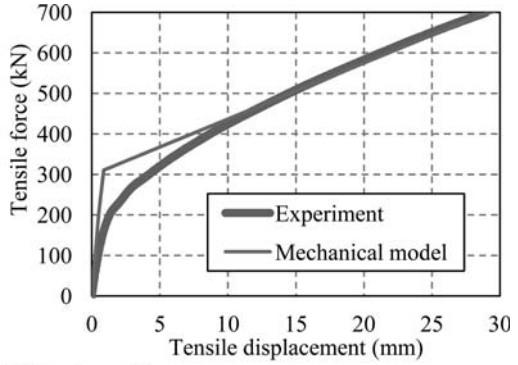

(a) Specimen T7.

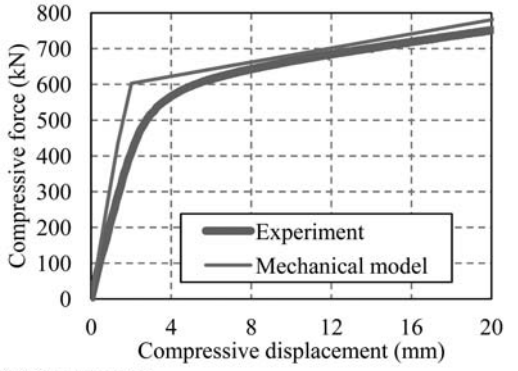

(b) Specimen C1.

Figure 9. Comparison of axial force-displacement relationships between the tests and the mechanical models.

A bilinear model is used to represent the response of each individual component and a detailed mechanical characterization of their stiffness and capacities can be found elsewhere (Liu 2012). Also, after yielding, a strain hardening coefficient in the range of 1%–5% is employed to define the post-elastic stiffness, in line with typical values found by other researchers (Simões da Silva et al. 2002).

5.2 *Validation*

The simplified model proposed above was validated against the results of the axial tests. Specimens T7 (tension specimen with web angles) and C1 (compression specimen) are selected in Figure 9 as typical examples. As demonstrated in Figure 9a, the initial stiffness based on the component response matches the experimental results well within an accuracy of 5% for Specimen T7. Similarly, the obtained yield forces closely resemble the experimental values within 10% for Specimen T7. As in the case of compression action, it is evident from Figure 9b that the simplified model provides a close prediction of the connection compressive response including the initial stiffness and yield capacity for Specimen C1. Overall, it is shown that the

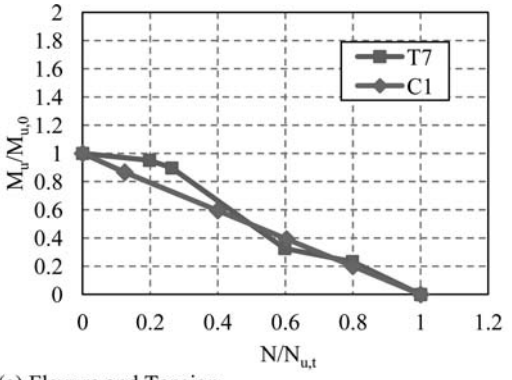

(a) Flexure and Tension.

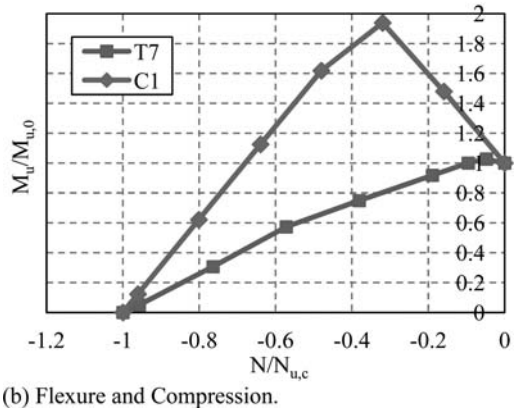

(b) Flexure and Compression.

Figure 10. Ultimate M-N interaction from component-based models for Specimens T7 and C1.

simplified model can capture the main features of the connection response subjected to axial actions.

5.3 *Interaction between bending and axial loads*

High axial forces can be induced in the connection under extreme loading conditions such as those involving sudden column removal due to severe blast or impact loads or under fire scenarios. Therefore, the component-based model suggested and described above is employed in this section to exemplify the response of the connections subjected to combined bending and axial loads. Specimens T7 and C1 are selected for the interaction assessment herein. Figure 10 presents the interaction curves between the ultimate moment capacity and the corresponding applied axial force for Specimens T7 and C1. In this figure, tension is represented by positive values of the axial force ratio ($N/N_{u,t}$), while negative values of $N/N_{u,c}$ represent compression action, where $N_{u,t}$ and $N_{u,c}$ are the connection ultimate capacity under pure tension or compression action, respectively. Similarly, $M_{u,0}$ is the connection ultimate bending capacity under direct moment load.

It is observed from Figure 10a that the yield moment capacity ratio ($M_u/M_{u,0}$) decreases as the applied tension force increases. On the other hand, in the case of Specimen C1, the ultimate moment ratio ($M_u/M_{u,0}$) reaches its maximum value (about 2) when the compression force (N) is about 35% of its ultimate compression capacity ($N_{u,c}$). Afterwards, the ultimate moment ratio starts to decrease with the increasing compression load, but it is still larger than one until the applied compression force is up to around 70% of its compression capacity. However, for Specimen T7 with top and seat as well as double web angles, the maximum moment ratio ($M_u/M_{u,0}$) is only 1.03 and this occurs at a compression load of 5% of its ultimate compression capacity. Also, the moment ratio is lower than 1 when the applied compression ratio is higher than 10%. In general, the application of higher tensile force results in lower ultimate moment values, while a modest compression force leads to improved ultimate moment capacities.

6 CONCLUDING REMARKS

The behaviour of bolted angle connections between tubular columns and open beams under axial force has been examined by means of experimental and simplified analytical models. An experimental programme comprising seven tensile tests and six compressive tests on blind-bolted angle connections and combined channel/angle configurations has been summarised. The main behavioural patterns were identified, and the key response characteristics such as stiffness, capacity and failure mechanism were discussed. The experimental results provide necessary information for the validation and calibration of complementary component-based models.

The inelastic mechanisms exhibited by blind-bolted angle and combined channel/angle connections under tensile force originate from the interaction between the angle components and Hollo-bolt/column face assemblage. It was shown that the angle gauge distance, between the column bolt centre and the beam flange, has a significant effect on the initial stiffness and tensile capacity of the connection. Besides, the thickness of the column wall also has a notable influence on the connection capacity, in particular when thicker angles are employed. Furthermore, the addition of web angles was shown to significantly enhance the overall connection tensile resistance.

In the case of Hollo-bolted connections subjected to compression, the inelastic mechanisms were largely determined by the relative widths of the column and the beam/angle components. Large plastic deformations accumulated in the column face in the case of specimens with angle/beam widths smaller than the column face width. Moreover, the provision of beam/angle widths smaller than the corresponding column faces lead to proportional reductions in the connection stiffness and capacity. The flexibility of the reverse channel component relative to the stiffness of the angles was shown to have a direct influence on both the initial stiffness and capacity of the connection.

A component-based model was developed to simulate the response of bolted angle beam-to-tubular column connections subjected to direct tension and compression actions as well as combined axial and bending loads. Results obtained by means of this representation were compared with the experimental response in terms of stiffness and capacity. It was found that the proposed component models produce reliable estimates of blind-bolted and combined channel/angle connections. Furthermore, these component-based models were employed to examine the response of the connections subjected to combined bending and axial loads. It was observed that the application of higher tensile force results in lower ultimate moment values, while a modest compression force leads to improved ultimate moment capacities.

ACKNOWLEDGEMENTS

The support of Tata Steel Tubes, particularly that of Mr T. Mustard, for the research described in this paper is gratefully acknowledged. The authors would also like to thank the technical staff of the Structures Laboratories at Imperial College London, particularly Mr T. Stickland, for their assistance with the experimental work. Additionally, the first author would like to acknowledge the grant provided by The Chinese Scholarship Council and The UK Department for Innovation, Universities & Skills, for her doctoral research studies through a UK/China Scholarship for Excellence.

REFERENCES

Angerskov, H. 1976. High strength bolted connections subjected to prying. *Journal of the Structural Division-ASCE* 102(1): 161–175.

Banks, G. 1993. Flowdrilling for tubular structures. Proceedings of the Fifth International Symposium on Tubular Structures. UK.

Barnett, T., W. Tizani & D. Nethercot 2000. Blind bolted moment resisting connections to structural hollow sections. Connections in Steel Structures IV, Virginia, USA.

Barnett, T., W. Tizani & D. Nethercot 2001. The practice of blind bolting connections to structura hollow sections: A review. *Steel and Composite Structures* 1(1): 1–16.

Cao, J., J. Packer & N. Kosteski 1998. Design guidelines for longitudinal plate to HSS connections. *Journal of Structural Engineering* 124(7): 784–791.

CEN 2005. *EN 1993-1-8, Eurocode 3: Design of steel structures, Part 1–8: Design of joints*.

Elghazouli, A. Y., C. Málaga-Chuquitaype, J. M. Castro & A. H. Orton 2009. Experimental monotonic and cyclic behaviour of blind-bolted angle connections. *Engineering Structures* 31(11): 2540–2553.

France, J. E., J. Buick Davison & P. A. Kirby 1999. Strength and rotational stiffness of simple connections to tubular columns using flowdrill connectors. *Journal of Constructional Steel Research* 50(1): 15–34.

Ghobarah, A., S. Mourad & R. M. Korol 1996. Moment-rotation relationship of blind bolted connections for HSS columns. *Journal of Constructional Steel Research* 40(1): 63–91.

Huck International Inc. 1990. *Industrial fastening system*. Arizona (USA).

Kishi, N. & W. F. Chen 1990. Moment-rotation relations of semi-rigid connections with angles. *Journal of Structural Engineering* 116(7): 1813–1834.

Kosteski, N. & J. A. Packer 2003. Longitudinal plate and through plate-to-hollow structural section welded connections. *Journal of Structural Engineering* 129(4): 478–486.

Lindapter International Ltd. 1995. Type HB hollo-bolt for blind connection to structural steel and structural tubes. UK, Lindapter International Ltd.

Liu, Y. 2012. Behaviour of steel connections under extreme loading conditions, PhD Thesis, Department of Civil and Environmental Engineering, Imperial College London, UK.

Málaga-Chuquitaype, C. 2011. Seismic behaviour and design of steel frames incorporating tubular members, PhD thesis, Department of Civil and Environmental Engineering, Imperial College London, UK. PhD.

Málaga-Chuquitaype, C. & A. Y. Elghazouli 2010. Behaviour of combined channel/angle connections to tubular columns under monotonic and cyclic loading. *Engineering Structures* 32(6): 1600–1616.

Málaga-Chuquitaype, C. & A. Y. Elghazouli 2010. Component-based mechanical models for blind-bolted angle connections. *Engineering Structures* 32(10): 3048–3067.

Simões da Silva, L., A. Santiago & P. V. Real 2002. Post-limit stiffness and ductility of end-plate beam-to-column steel joints. *Computers and Structures* 80: 515–531.

Vlassis, A. G., B. A. Izzuddin, A. Y. Elghazouli & D. A. Nethercot 2008. Progressive collapse of multi-storey buildings due to sudden column loss-Part II: Application. *Engineering Structures* 30(5): 1424–1438.

Wang, Z. Y., W. Tizani & Q. Y. Wang 2010. Strength and initial stiffness of a blind-bolt connection based on the T-stub model. *Engineering Structures* 32(9): 2505–2517.

Tubular Structures XIV – Gardner (Ed.)
© 2012 Taylor & Francis Group, London, ISBN 978-0-415-62137-3

Capacity of CFRHS X-joints made of double-grade S420 steel

T. Björk & H. Saastamoinen
Lappeenranta University of Technology, Lappeenranta, Finland

ABSTRACT: This study considers the ultimate capacity of X-joints manufactured from Ruukki double grade S420MH/S355J2H Cold-Formed Rectangular Hollow Sections (CFRHS). The goal of the investigation was to define the validity of the current design rules for the used double grade steel with yield strength level of 420 MPa. The main parameters in this study were the geometry of the joints, size of welds, and heat inputs during welding. The X-joints were subjected to axial tensile loading and experimental test were carried out at −40°C degrees. Some compression loaded tests were also performed at room temperature. The results showed good strength and deformation capacities and they did not support in Eurocode suggested reduction factor of 0.9 for the capacity of X-joints made of this steel grade. In addition, the few available results did not support the requirement in Eurocode to increase the throat thickness of a fillet weld for this strength level. Numerical analyses were carried out in order to find proper material models for nonlinear behaviour of the joint. The use of A_{gt} as a limit strain value in the material model showed good agreement with the experimental results.

1 INTRODUCTION

The rectangular hollow section (RHS) has several advantages as a structural member compared to profiles with an open cross section. The simple geometry of RHS also makes it easy to join the members by welding and therefore building aesthetically pleasing structures. The ultimate strength and deformation capacity of cold-formed RHS-joints made of S355-steel have been studied widely by using experimental tests and a finite element method (FEM) e.g. by Soininen, Björk & al. [1–4]. The recently developed Ruukki double grade S420MH/S355J2H steel for rectangular hollow section by Rautaruukki Oyj combines the properties of S420MH and S355J2H grades. Ruukki double grade RHS is made from hot-rolled steel by cold-forming and HF-welding. According to current design rules [5–7] the weld dimensions and the static design load reduction factor of strength class S420 must be applied to Ruukki double grade if its strength class S420 properties are to be utilized. The applicability of these design rules for Ruukki double grade steel has been studied in a Master's Thesis by Saastamoinen [8]. Herion, Puthli & al. have also recently studied similar topics using steel grades up to S690 level and found arguments for the proposed reduction factors but also a need to adjust the current design rules for fillet welds [9, 10].

2 GOAL

The primary goal of this research is to prove the validation of the current design rules for welded RHS joints made of Ruukki double grade steel with nominal yield strength of 420 MPa. The validation is evaluated based on capacity of the joint and the strength of fillet welds. Even if the design code does not set any requirements for the deformation capacity of the joint, it should fulfil some unofficial requirements.

3 MATERIALS AND METHODS

Ruukki double grade S420MH/S355J2H combines the properties of steel grades S420MH and S355J2H and meets the requirements of EN 10219 standard. The nominal mechanical properties and chemical compositions of Ruukki double grade are presented in tables 1 and 2 where $f_{y0.2}$ references to the yield strength, f_u to the ultimate strength and A_5 to the ultimate elongation. The true mechanical properties of the RHS used in joints are presented in table 3.

In this paper, the CFRHS- joint capacities are defined by laboratory tests and analytical calculations. Based on this comparison the necessary requirements for the static design resistance reduction factor (0.9) or increased throat thickness in case of S420 steel grade, are evaluated. The finite element method (FEM) is also used to evaluate the capacity of one joint.

4 EXPERIMENTAL TESTS

4.1 *Test specimens*

The research is focused on X-joints, because in the corners of the chord members the stresses from external loads are coalesced into residual stresses due to

Table 1. Nominal mechanical properties of Ruukki Double Grade, S355J2H and S420MH.

Grade	$f_{y0.2}$ [MPa]	f_u (t < 3) [MPa]	f_u (3 ≤ t ≤ 16) [MPa]	A_5 [%]	T [°C]
Ruukki Double Grade S420MH/S355J2H	420	510–630	500–630	20	−40
S355J2H EN 10219	355	510–680	470–630	20	−20
S420MH EN 10219	420	500–630	500–630	19	−20

Table 2. Nominal chemical compositions of Ruukki Double Grade, S355J2H and S420MH.

Grade		C	Si	Mn	P	S	CEV
Ruukki Double Grade	Typical [%]	0.08	0.18	1.40	0.010	0.006	0.32
S420MH/S355J2H	Maximum [%]	0.16	0.25	1.60	0.020	0.012	0.39
S355J2H EN 10219	Maximum [%]	0.22	0.55	1.60	0.035	0.035	0.45
S420MH EN 10219	Maximum [%]	0.16	0.50	1.70	0.035	0.030	0.43

Table 3. The mechanical properties of the RHS used in joints.

$b \times h \times t$ [mm]	Sample ID	$f_{y,true}$ [MPa]	$f_{u,true}$ [MPa]	A_5 [%]	Joints
80 × 80 × 5	4H95590	516	559	24	XA4, XA5
100 × 100 × 6	4H83980	495	528	29	X3, X3B, X13
120 × 120 × 4	4H84330	519	570	25	X4, X5, X5B, X5C
120 × 120 × 4	20747041858	451	542	32	X12C braces
120 × 120 × 6	4H84450	516	566	24	X1, X1B, X2, X2B, X2, X3B, X2
120 × 120 × 10	11492031069	483	519	23	X4, X9
50 × 150 × 5	11516011347	506	583	23	X11
150 × 150 × 6	13108021776	475	541	25	X5, X5B, X5C
150 × 150 × 10	25054031429	526	558	21	XA4, XA5
150 × 150 × 12.5	21666021958	470	506	24	X13
200 × 100 × 4	10519010315	506	578	26	X6
200 × 100 × 6	13107021800	466	525	26	X8
200 × 200 × 5	10403098220	479	568	25	X7, X10, X11
200 × 200 × 6	11237041223	473	558	26	X6, X7, X8

cold forming. In the corners, the degree of cold forming is highest which can, especially in the case of high strength steel, reduce the deformation capacity of the joint. The true cross section dimensions of the RHS used in X-joints are presented in tables 4, 5, and 6, where b_1, h_1 and t_1 reference the width, height, and wall thickness of brace member and b_0, h_0 and t_0 to the chord members, respectively. Table 4 consists of joints welded with a throat thickness requirement of $a = 1.11t_1$. The joints seen in table 4 were welded using overmatching filler material, except joints X5C and X12C, which were welded using matching weld filler material as well as undersize throat thicknesses compared to current design rules. The preliminary goal was to study the effect of base material on the joint behaviour, not the properties of the welds. Overmatching of the filler material strengthens the weld and localizes the strain in the base material next to the weld. This can reduce the deformation capacity of the joint compared to a joint with a matching filler material, where the yielding also takes place in weld and decreases the strain concentration in the base material. This was studied experimentally by test specimens X5/X5C and X12/X12C and also numerically in chapter 6.

Table 5 consists of joints welded with a throat thickness of $a = 1.48t_1$ in which the test ID is denoted by the letter B. The test series of table 6 concerns the investigation of the minimum required, weld throat thickness. The joint geometries were selected to allow yielding and failure to take place either in brace members, in chord members or partly in both, which is called a general type joint failure. The welding was performed by an SMAW-process and all the welding parameters used (WPS) are documented in reference [8]. In order to find the weakest link of a joint consisting of the parent material, the weld and heat affected zone (HAZ), the coupon test specimens were cut out of joints with brace-chord with a width ratio $\beta = 1$ so that all these adjacent zones could be included in the

Table 4. The true cross section dimensions of joints with nominal throat thickness $a = 1.11t_1$.

Joint ID	Chord $b_0 \times h_0 \times t_0$ [mm]	Brace $b_1 \times h_1 \times t_1$ [mm]	β	b_0/t_0	b_1/t_1	a [mm]	a/t_1
X1	119.7 × 120.2 × 5.93	120.0 × 119.8 × 5.98	1	20	20	6.2	1.03
X2	120.1 × 119.9 × 5.90	120.0 × 119.7 × 5.95	1	20	20	6.4	1.07
X3	119.7 × 120.2 × 5.93	100.4 × 100.3 × 6.03	0.83	20	17	6.3	1.04
X4	120.1 × 120.4 × 9.85	120.0 × 120.2 × 4.08	1	12	30	5.9	1.44
X5	150.4 × 149.9 × 6.10	120.0 × 120.2 × 4.08	0.8	25	30	5.9	1.45
X6	200.7 × 200.7 × 6.00	200.9 × 100.3 × 4.00	1	33	50	4.7	1.18
X7	200.7 × 200.7 × 6.00	201.5 × 200.4 × 4.95	1	33	40	5.8	1.17
X8	200.5 × 200.7 × 6.03	199.9 × 99.9 × 6.00	1	33	33	6.6	1.10
X9	120.1 × 120.4 × 9.85	120.1 × 120.1 × 9.88	1	12	12	11.2	1.13
X10	200.7 × 201 × 5.00	200.4 × 201 × 4.95	1	40	40	5.4	1.08
X11	200.7 × 201 × 5.00	150.7 × 150.7 × 4.95	0.75	40	30	5.1	1.03
X12	119.9 × 119.9 × 4.00	120.2 × 120.2 × 3.94	1	30	30	5.6	1.41
X13	150.9 × 150.7 × 12.64	100.3 × 100.3 × 5.90	0.67	12	17	7.1	1.20
X14	200.5 × 200.5 × 4.95	200.63 × 200.43 × 4.91	1	40	40	7.1	1.07
X5C	150.2 × 149.9 × 6.00	119.7 × 120 × 4.00	0.8	25	30	4.9	1.22
X12C	119.7 × 120.6 × 4.04	119.7 × 120.3 × 4.01	1	30	30	4.6	1.14

Table 5. The true cross section dimensions of joints with nominal throat thickness $a = 1.48t_1$.

Joint ID	Chord $b_0 \times h_0 \times t_0$ [mm]	Brace $b_1 \times h_1 \times t_1$ [mm]	β	b_0/t_0	b_1/t_1	a [mm]	a/t_1
X1B	120.1 × 119.9 × 5.90	120.1 × 119.8 × 5.98	1	20	20	7.7	1.30
X2B	120.0 × 119.8 × 5.90	119.8 × 119.8 × 5.96	1	20	20	8.5	1.42
X3B	120.0 × 119.8 × 5.90	100.4 × 100.3 × 5.91	0.83	20	17	8.3	1.40
X5B	150.4 × 149.9 × 6.10	120.2 × 120.3 × 3.95	0.8	25	30	6.2	1.57
X12B	119.9 × 119.9 × 4.00	120.2 × 120.2 × 3.94	1	30	30	6.5	1.64

Table 6. The true cross section dimensions of joints with undersize nominal throat thickness.

Joint ID	Chord $b_0 \times h_0 \times t_0$ [mm]	Brace $b_1 \times h_1 \times t_1$ [mm]	β	b_0/t_0	b_1/t_1	a [mm]	a/t_1
XA4	150.7 × 150.7 × 9.95	80.1 × 79.9 × 4.99	0.53	15	16	4.1	0.83
XA5	150.7 × 150.7 × 9.95	80.1 × 79.9 × 4.99	0.53	15	16	4.9	0.98

same test specimen. The specimen included effects due to cold forming and heat input but not the structural stress concentrations of the complete joint. The billets of tension test specimens were cut out of X-joints used to create welding procedure specifications (WPS) as presented in figure 1. The joint specimens proved to have a higher strength but a smaller elongation than values obtained from the coupon tests presented in table 3. In the table in figure 1 the total uniform elongation A_{gt} references to elongation under maximum load.

4.2 *Test set up*

Brackets were attached to the ends of the brace members in order to fix the joint in the loading rig. Pinned brackets enabled the free rotation only out of the plane of the X-specimens but prevented rotation of brace ends in the specimen plane. The loading and boundary conditions of the joint are shown in figure 2.

The ends of the chord were closed to ensure coolant circulation. In order to discover the potential disposition for brittle behavior of the joints, the tests were carried out at −40°C temperature, which was measured by thermo elements fixed on the top and bottom sides of the joint and adjusted by the dry ice in the ethanol based coolant. The test specimen was wrapped in insulating blanket to prevent extra heat flow from the system. The applied load and displacements of the joint and the ends of braces were measured. The measuring length for estimating the joint deformation was set to $l = h_0 + 2 \cdot 25$ mm in order to include some deformation of the brace members and also enabling space for the insulation blanket. Axial tension loads were applied

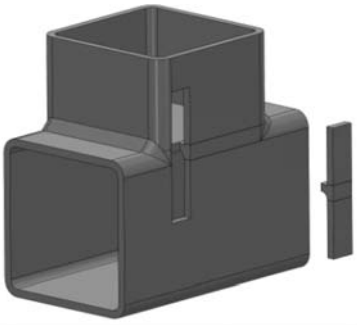

Specimen	$f_{y0.2}$ [MPa]	f_u [MPa]	Total elongation [%]	A_{gt} [%]
X1	597	663	15.4	3.8
X1B	582	654	12.7	3.3
X2	567	659	14.9	4.2
X4	568	697	14.8	3.7
X9	537	621	12.3	3.5
X12	558	641	16.9	6.3

Figure 1. Mechanical properties of coupon test specimens including base material, weld and HAZ [8].

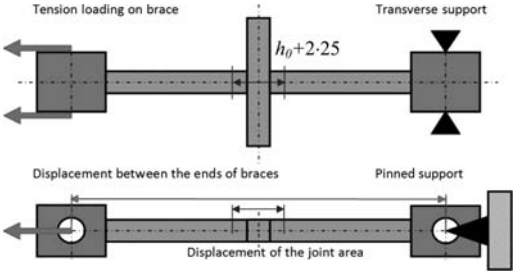

Figure 2. The loading and constrains of the X-joint [8].

to all specimens except X10, X11 and X14 which were tested by compression loads.

4.3 *Experimental test results*

A typical experimental force-displacement curve is plotted in figure 3. Yield load F_y, ultimate load F_u and load $F_{3\%}$, based on 3% plastic deformation of joint ($2\delta_{3\%}$), were defined from the force-displacement curve of the joint. The yield load is defined by approximating the load-displacement curve as a bilinear model consisting of elastic and plastic portions. If the load $F_{3\%}$ was available, it was used in the calculations instead of F_u. The load $F_{3\%}$ is used to make joints with different elasticity comparable to each other [11].

The most common failure modes are presented in figure 4. The typical failure mode for joints with $\beta = 1$ was chord web failure (denoted as W). Although the fracture was initially ductile, it was followed by a secondary brittle fracture in joints X1B, X2 and X2B. However, joints X1 and X12 fractured by a general failure mode (denoted as G), where the yielding takes place in the chord flange and the brace member

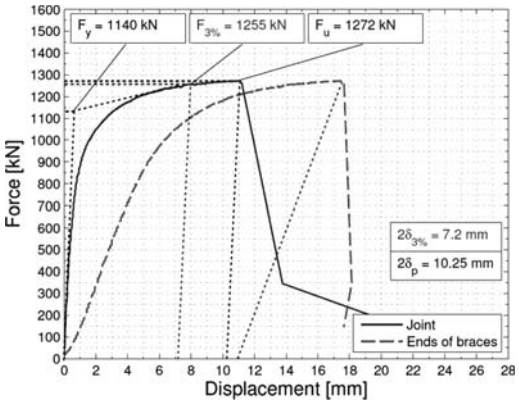

Figure 3. The force-displacement curves of joints X2 [8].

simultaneously. The failure mode was the most common among joints with $\beta < 1$. Punching shear failure (denoted as S) took place only in joint X3B. In joint X4 the necking started in the brace member outside the joint area denoted as B. The buckling failure of the chord web was denoted as C and took place in the all compression loaded joints.

5 ANALYTICAL CALCULATIONS

5.1 *Calculations using Eurocode 3 and yield line theory*

The joint capacities were calculated according to Eurocode 3, Part 1–8 and yield line theory (YLT) proposed by Björk [2, 12]. Design rules according to Eurocode 3 are valid when the yield strength of the RHS is not more than 460 MPa. When RHS yield strength is more than 355 MPa, a static design load reduction factor of 0.9 should be applied to calculations according to the Eurocode design rules. A safety factor of $\gamma_{M5} = 1.0$ was used in the calculations. The YLT introduces a brace-flange mechanism where yielding takes place in both the brace and the flange of the chord as illustrated schematically in figure 5. The failure mechanism is described in more detail in references [2, 12].

5.2 *Throat thickness*

Welds can be designed for an external force or to match the weakest capacity of the joining components. It is common practise to use the latter principle in order to ensure sufficient deformation capacity of the structure. When the static strength of the weld, divided by the peripheral length of the RHS-joint is set equal to the plastic tension strength of RHS wall, the required throat thickness can be defined. The secondary bending moment due to eccentricity e of weld can be neglected, because the rotation of the brace flanges is prevented by the adjacent flanges of the cross section. The required throat thickness a can be

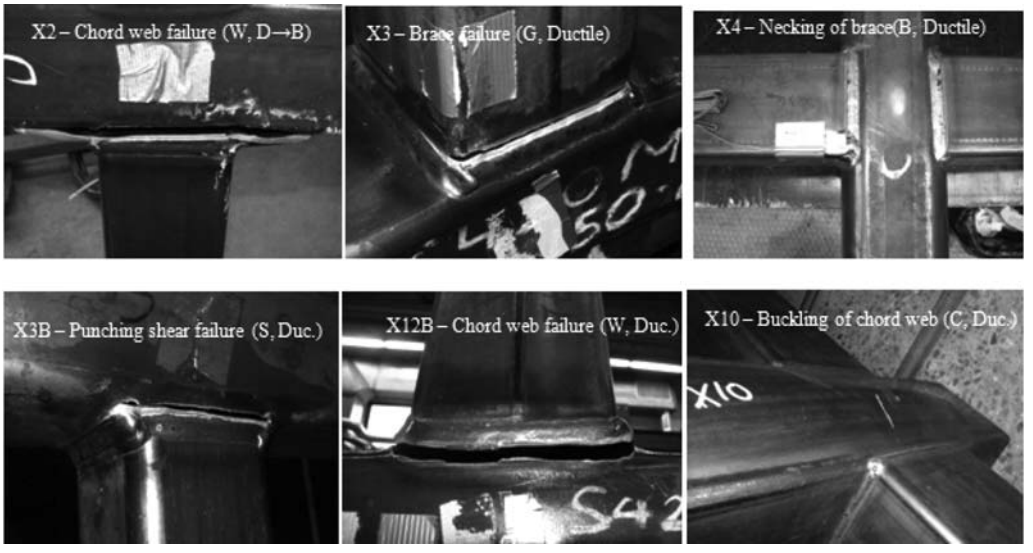

Figure 4. Common fracture types of X-joints.

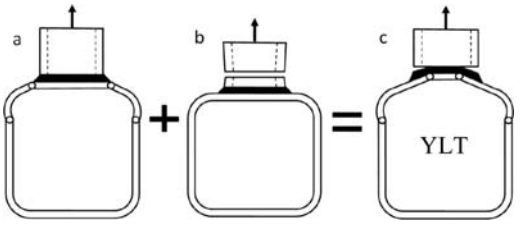

Figure 5. The difference of failure mechanisms between conventional and applied yield line theory.

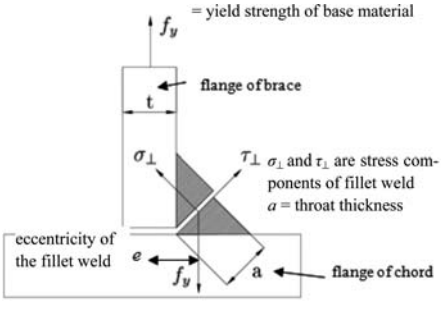

Figure 6. Equilibrium of stresses on fillet weld calculation cross-section.

defined based on the equilibrium of stresses in the critical section of fillet weld as illustrated in figure 6.

$$a \leq \sqrt{2}\beta_w \frac{\gamma_{M2} f_y}{\gamma_{M0} f_u} t\,. \tag{1}$$

Values for a/t, where a is calculated from Equation (1), are presented in table 7.

Table 7. Values for a/t in different strength classes.

Strength class	γ_{M0}	γ_{M2}	β_w	f_y [MPa]	f_u [MPa]	a/t
S355	1.0	1.25	0.9	355	510	1.11
S420	1.0	1.25	1.0	420	500	1.48

5.3 *Deformation capacity*

The sufficiency of deformation capacity of joints was assessed by measuring the plastic displacement δ_p related to chord's width b_0. In this work, the minimum required deformation capacity was set to the value proposed by Björk and argued in reference [2]. The proposed value for minimum required deformation capacity was derived from the analysis of plastic hinges in a finite element model. The proposed deformation limit is for joints with $\beta \leq 0.8$

$$\frac{\delta_p}{b_0}(1-\beta). \tag{2}$$

For joints with $0.8 \leq \beta \leq 1$ the deformation limit is

$$\frac{\delta_p}{b_0} \geq 0.005. \tag{3}$$

Plastic displacement δ_p refers primarily to the brace member's deformation perpendicular to the chord's flange in the T-joint. As the X-joint is actually two T-joints in series, the deformation of the X-joint is required as the double plastic displacement $2\delta_p$, assuming the deformation is distributed equally on both sides of the joint. In practice, however, the plastic deformation does not take place symmetrically yielding conservative results.

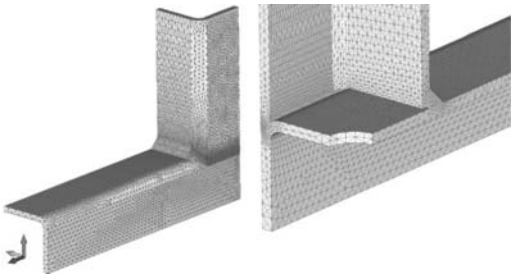

Figure 7. The mesh of the joint geometry [8].

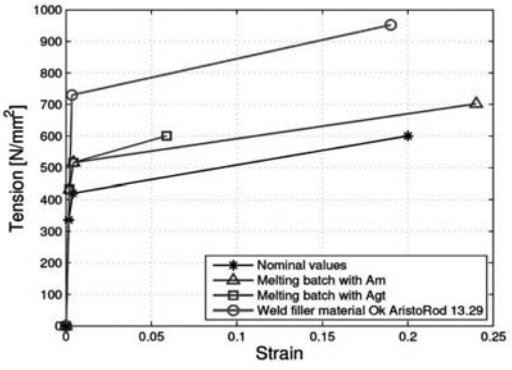

Figure 8. Material models plotted without conservative strain hardening [8].

6 FEA

The joint geometry was modelled using the true dimensions of RHS and the weld throat thickness of the joint. The joint geometry was created by SolidWorks and FEMAP 10 was used as a pre-processor for the NASTRAN solver. It was necessary to model only a 1/8-part of the full joint utilizing the available symmetry. Quadratic tetrahedral elements were used to mesh the joint geometry containing the fillet weld with root gaps, bevel groove weld, and varying wall thicknesses. The mesh is presented in figure 7. The material models were generated for RHS and the weld filler material and are seen in figure 8, where A_{gt} is the total uniform elongation and A_m marks the fracture strain. Young's modulus was set to $E = 210000$ MPa and Poisson's ratio to $\nu = 0.3$.

The results of the analysis are presented as force-displacement curves where the reference distance l for displacements was the same as that used in corresponding experimental test. Values for A_{gt} and A_m are presented also in table 8.

Table 8. FEA results for material models.

Material model	f_y [MPa]	$f_{y0.2}$ [MPa]	f_u [MPa]	A_{gt}	A_m
Nominal values	–	420	500	–	0.20
Melting batch	–	516	566	0.06	0.24
Weld filler AristoRod 13.29	730	–	800	–	0.19

7 DISCUSSION

7.1 *The results of the experimental tests*

The loads, deformation capacities, failure mechanisms, and fracture types of the joints tested are presented in table 9. The deformation capacity is sufficient, if the ratio of the measured deformation to the required capacity is ≥ 1. The notations used in the failure mechanisms column are presented in figure 4. In the fracture type column, a ductile fracture is denoted as d and a brittle fracture as b. It can be seen from table 9 that full width joints had unexpectedly better plastic deformation capacity than joints with $\beta \leq 1$. Most of the joints with $\beta \leq 1$ did not reach the 3% plastic displacement of the chord's width $\delta_{3\%}$. Even the total deformation is greater in joints with $\beta \leq 1$, in joints with $\beta = 1$ the loading from brace member transfers directly to the web of the chord resulting in smooth membrane stress and thus large plastic deformation capacity. Nevertheless, all the joints met the requirements set for the deformation capacity according to equations 2 and 3. The reason for small plastic deformation in joints X10 and X14 is the lack of compression load capacity after the elastic buckling has taken place in the chord web.

Joints welded with throat thicknesses of $a = 1.11t_1$ and $a = 1.48t_1$ are compared in table 10. The criteria for the comparison are the number of weld passes, the heat input, the throat thickness, the deformation capacity and the ultimate strength. Heat input for multi-pass welds were calculated only pass-wise and are presented in reference [8]. The numbers of passes concerning fillet and bevel groove welds are indicated with corresponding welding symbols It can be seen from table 10 that increasing throat thickness did not significantly affect the deformation capacity and the ultimate strength of the joints. It can be also noticed that the true values of throat thickness were distinguished from nominal values, especially in joints X5 and X12. The differences in the deformation capacity of ultimate strength were not significant between joints X1, X2, X1B and X2B, which had the same RHS dimensions but a different number of weld passes. The greatest increase in the ultimate strength was only 5.8% which seems quite small taking into account increased welding costs resulted from the multi-pass fillet welds needed to reach adequate throat thickness. However, based on comparisons #3 and #4 a slight indication of the effect of the heat input into deformation capacity can be noticed. In joints X2 and X2B bevel groove welds were welded with one full penetration pass. These joints had lower deformation capacity than joints X1 and X1B which had more weld passes in the bevel groove welds. Reducing the number of weld passes to one also contributed to the change of

Table 9. Results obtained from laboratory tests.

Joint ID	F_y [kN]	$F_{3\%}$ [kN]	F_u [kN]	β	$2\delta_{p,measured}$ [mm]	b_0 [mm]	$\frac{2\delta_{p,measured}}{2\delta_{p,required}}$	Failure mechanism	Fracture Type
X1	1080	1262	1262	1	11.91	120	9.93	G	d
X1B	1140	1320	1335	1	11.84	120	9.87	W	d → b
X2	1140	1255	1272	1	10.25	120	8.54	W	d → b
X2B	1160	1300	1321	1	10.33	120	8.61	W	d → b
X3	530	–	793	0.83	5.85	120	4.88	G	d
X3B	545	–	820	0.83	6.69	120	5.58	S	d
X4	965	1020	1069	1	–	120	–	B	d
X5	415	–	696	0.8	7.39	150	4.93	G	d
X5B	435	–	718	0.8	7.32	150	4.88	G	d
X5C	425	–	696	0.8	7.98	150	5.32	G	d
X6	730		980	1	8.38	200	4.19	G	d
X7	1245		1511	1	7.18	200	3.59	G	d
X8	895		1118	1	7.67	200	3.84	W	d
X9	1860	–	2075	1	3.42	120	2.85	G	d → b
X10	–		642	1	0.29	200	0.15	C	d
X11	151		229	0.75	11.29	200	6.02	C + F	d
X12	715	810	820	1	9.51	120	7.93	G	d
X12B	720	820	828	1	8.09	120	6.74	W	d
X12C	690	–	776	1	7.16	120	5.97	G	d
X13	945	–	1167	0.67	6.41	150	2.59	G	d
X14	–		637	1	0.52	200	0.26	C	d
XA4	355	–	540	0.53	7.35	150	2.09	G	b
XA5	490	625	690	0.53	13.55	150	3.84	G	d

Table 10. A comparison of joints welded with throat thicknesses $a = 1.11t_1$ and $a = 1.481t_1$.

Comparison #	Joint ID	Passes √	Passes ◣	Heat input Q [kJ/mm]	Heat input Diff. [%]	Throat thickness a/t_1	Throat thickness Diff. [%]	Deformation capacity $2\delta_p$ [mm]	Deformation capacity Diff. [%]	Ultimate strength F_u [kN]	Ultimate strength Diff. [%]
1	X1	2	1	–	–	1.03	+24.3	11.91	−0.6	1262	+5.8
	X1B	3	3	–		1.28		11.84		1335	
2	X2	1	1	–	–	1.06	+33.0	10.25	+0.8	1272	+3.9
	X2B	1	3	–		1.41		10.33		1321	
3	X1	2	1	–	–	1.03	+2.9	11.91	−13.9	1262	+0.8
	X2	1	1	–		1.06		10.25		1272	
4	X1B	3	3	–	–	1.28	+10.2	11.84	−12.8	1335	−1.0
	X2B	1	3	–		1.41		10.33		1321	
5	X3	–	1	1.16	−2.5	1.04	+32.7	5.85	+14.4	793	+3.4
	X3B	–	1/3	1.13		1.38		6.69		820	
6	X5	–	1	1.15	+28.9	1.48	+4.7	7.39	−0.9	696	+3.2
	X5B	–	1	1.49		1.55		7.32		718	
7	X12	1	1	0.87	+42.9	1.41	+14.9	9.51	−14.9	820	+1.0
	X12B	1	1	1.24		1.62		8.09		828	

fracture mechanism. Joints X2 and X2B fractured at the web of the chord while joints X1 and X1B fractured in the brace member adjacent to the weld toe. However, this particular joint geometry has almost the same expected ultimate load carrying capacity for both previously mentioned fracture mechanisms. Consequently, geometrical and material specific variations may have a sufficient effect in order to change the fracture mechanism. The highest deformation capacity increase was between joints X3 and X3B but this was mostly explained by the manganese sulphide layer of the base material found on the fractured surface. Although the deformation capacity was greater in joint X3B than X3, the ultimate strength did not change correspondingly. Joint X3 fractured in the brace member adjacent to the weld toe, while in joint X3B a punching shear mechanism was the observed fracture mode. The greatest decrease in the deformation capacity was observed between joints X12 and X12B, which also had the largest difference in the heat input in this series of tests. However, the difference in the heat input concerned only fillet welds adjacent to brace members and

Table 11. A comparison of the results of laboratory tests and analytical calculations.

	Eurocode 3					Yield line theory					Failure mechanism		
Joint ID	$F_y/F_{y,420}$	$F_y/F_{y,true}$	$F_u/F_{u,500}$	$F_u/F_{u,true}$	$F_u/F_{y,420}$	$F_y/F_{y,420}$	$F_y/F_{y,true}$	$F_u/F_{u,500}$	$F_u/F_{u,true}$	$F_u/F_{y,420}$	EC3	YLT	experimental
X1	1.45	1.18	1.43	1.26	1.70	1.37	1.11	1.34	1.19	1.60	W	W	G
X1B	1.54	1.25	1.50	1.32	1.78	1.42	1.16	1.38	1.22	1.65	W	W	W
X2	1.54	1.25	1.43	1.26	1.70	1.45	1.18	1.34	1.18	1.59	W	W	W
X2B	1.57	1.28	1.48	1.30	1.76	1.43	1.17	1.35	1.19	1.61	W	W	W
X3	1.77	1.44	2.22	1.96	2.64	1.61	1.31	2.03	1.79	2.42	F	F	G
X3B	1.86	1.51	2.35	2.07	2.79	1.67	1.36	2.10	1.86	2.51	F	F	S
X4	0.81	0.98	0.72	0.95	0.85	1.24	1.01	1.10	0.97	1.31	B	B	B
X5	1.58	1.40	2.23	2.06	2.65	1.48	1.31	2.08	1.93	2.48	F	F	G
X5B	1.65	1.46	2.29	2.11	2.72	1.54	1.36	2.14	1.97	2.54	F	F	G
X5C	1.62	1.43	2.23	2.06	2.65	1.53	1.35	2.11	1.95	2.51	F	F	G
X6	1.19	1.02	1.24	1.10	1.48	1.28	1.08	1.34	1.17	159	B	G	G
X7	1.13	1.00	1.15	1.02	1.37	1.10	0.97	1.12	0.99	1.33	B	G	G
X8	1.37	1.21	1.43	1.29	1.71	1.25	1.12	1.31	1.23	1.56	W	G	W
X9	1.33	1.15	1.24	1.20	1.48	1.28	1.11	1.20	1.16	1.43	W	G	G
X10			3.15	2.77	3.74						C		C
X11	1.06	0.93	1.35	1.19	1.60	1.02	0.89	1.29	1.14	1.54	F	F	C+F
X12	1.52	1.23	1.45	1.27	1.72	1.39	1.12	1.32	1.16	1.57	W	W	G
X12B	1.53	1.24	1.46	1.28	1.74	1.38	1.12	1.32	1.16	1.57	W	W	W
X12C	1.45	1.35	1.37	1.26	1.63	1.35	1.25	1.27	1.17	1.51	W	W	G
X13	1.30	1.16	1.34	1.33	1.60	1.32	1.17	1.37	1.34	1.63	F	G	G
X14			3.11	2.73	3.70						C		C
XA4	1.05	0.84	1.35	1.21	1.60	1.30	1.02	1.66	1.49	1.98	F	G	G
XA5	1.45	1.16	1.56	1.40	1.85	1.77	1.38	1.89	1.73	2.25	F	G	G

chord flanges. Joints X12 and X12B fractured adjacent to the bevel groove weld, which means that the fillet welds did not have as significant a role in the load carrying as bevel groove welds. Contrary to this result, deformation capacity did not change as much between joints X5 and X5B although the difference in heat input concerned the whole fillet weld, which was welded around the brace member.

7.2 *Comparison of calculated and experimental results*

Results obtained from laboratory tests and calculations, ($F_{test}/F_{calcul.}$) are compared in table 11. The joint capacities were calculated using both nominal material strength values ($f_{y0.2}$ and f_u from table 1) and true material strength values ($f_{y,true}$ and $f_{u,true}$ from table 3). The true cross-section dimensions were used to calculate the joint capacities. It can be seen from table 12 that the expected fracture mechanisms were generally in good agreement with the laboratory results. Almost all full-width joints fractured as expected and the difference between tested and calculated capacities was lowest in all of the tested joints. Most of the joints with $\beta < 1$ fractured in a different way than expected and also the experimental results distinguished more from theoretical capacities than in the case of full-width joints. The joints with larger dimensions (X6, X7, X8, X10, X11 and X14) behaved as expected both in the tensile or compression loading. Blanco cells in table 9 denote there is no yield load available from experimental tests or the YLT is not valid. Joints XA4 and XA5 had sufficient ultimate strength and deformation capacity even though they were welded with small throat thicknesses.

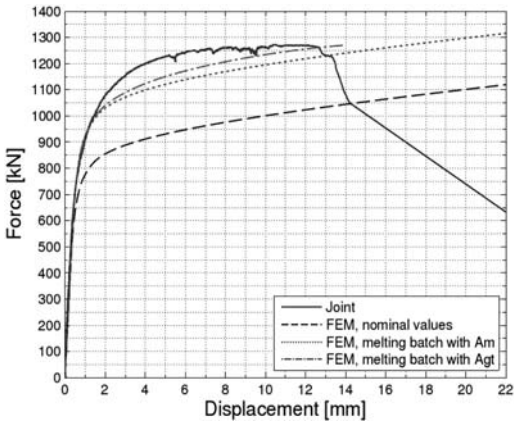

Figure 9. Comparison of the force-displacement curves from the laboratory test and the FE-models with different elongation limits [8].

7.3 *Results from FEA*

The load-displacement curves of an FE-model with different material models are compared to a load-displacement curve obtained from laboratory test X1

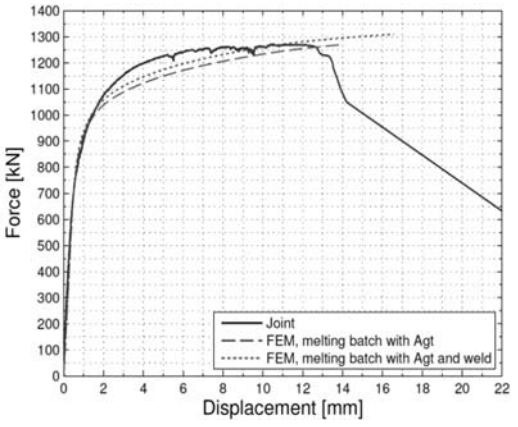

Figure 10. Comparison of the force-displacement curves from the laboratory test and the FE-models with and without weld filler [8].

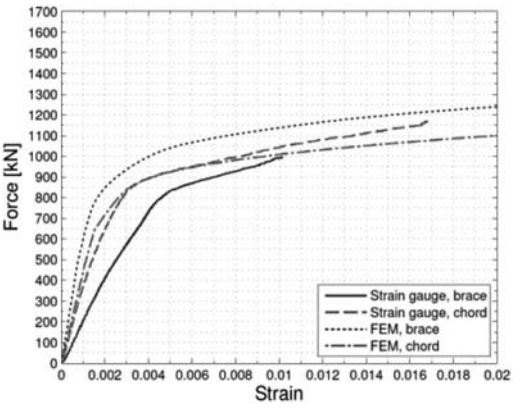

Figure 11. Force-strain curves obtained from the FE-model and strain gauges.

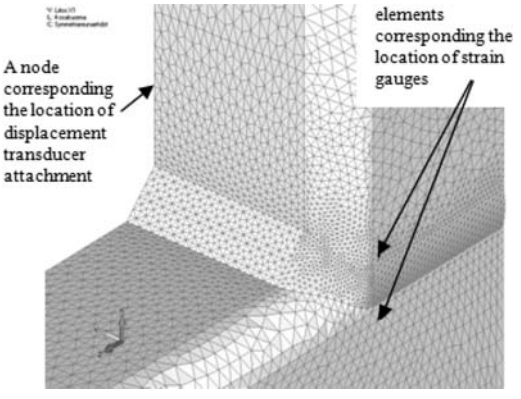

Figure 12. Locations of the displacement transducer attachment and strain gauges in the FE-model.

in figures 9 and 10. The curves in figure 9 are calculated using nominal material strength values and true values applying total uniform elongation (A_{gt}) and fracture strain (A_m) from table 8. In figure 10 the curves are calculated using true material strength values with total uniform elongation. The upper FEM-curve in figure 10 includes the weld filler metal material model contrary to the lower curve It can be seen from figures 9 and 10 that a force-displacement curve based on nominal material strength values significantly underestimates the load carrying capacity of the joint. Curves obtained using melting batch values represent the true joint behavior more accurately. Using a total uniform elongation value instead of the ultimate strain provides a more accurate curve. Using the weld filler material model the FE-model overestimates the true joint load carrying capacity. It should be noticed that the FE-model lacks the material models of RHS corners and HAZ. In theory, RHS corners are stronger than the web and flange of the RHS, this is due to strain hardening caused by the manufacturing process. On the other hand, HAZ may be weaker than the base material due to the heat input caused by welding. Because of these inaccuracies of the FE-model the surprisingly accurate result using the total uniform elongation value in the material model may only be a coincidence. For conservative results, it is more advisable to use the ultimate strain value when creating a material model.

Force-strain curves obtained from the FE-model and strain gauges as well as the location of strain gauges and the displacement transducer are presented in figures 11 and 12. It can be seen that the curves concerning chord strain values are in good agreement but curves relating to the brace strain values are not. It was noticed that the brace was misaligned which made the strain values obtained from the brace and chord differ due to uneven stress distribution caused by the bending moment. The other reason for differences between FEA and strain gauge results can be the local softening effect due the welding, which was not considered precisely in FEA.

8 CONCLUSIONS

Based on 23 experimental X-joint tests and analytical calculations it can be concluded that

- the current design rules seems to be valid for X-joints made from Ruukki double grade S420MH/S355J2H rectangular hollow sections
- however, there seems to be no adequate reason to use a reduction factor of 0.9 for joint capacities made of steel grade S420
- the few performed experimental tests did not prove any significant benefit to use a throat thickness of $a = 1.48t_1$ instead of $a = 1.11t_1$
- the results from the FEA are sensitive to the material model used

REFERENCES

Soininen, R., Fracture Behaviour and Assessment of Design Requirements Against Fracture in Welded Steel Structures Made of Cold Formed Rectangular Hollow Sections. Doctoral Thesis. Lappeenranta University of Technology, Department of Mechanical Engineering. Lappeenranta, 1996

Björk, T., Ductility and Ultimate Strength of Cold-Formed Rectangular Hollow Section Joints at Subzero Temperatures. Doctoral Thesis. Lappeenranta University of Technology, Department of Mechanical Engineering. Lappeenranta, 2005. ISBN 952-514-167-4

Björk T., Marquis G., Kemppainen R.& Ilvonen R., The capacity of cold-formed rectangular hollow section K-gap joints. Proceeding of 10th international symbosium on tubular structures, 2003 Madrid

Björk T, Heinilä S. & Marquis G., Assessment of subzero fracture of welded tubular K-joints. Journal of structural engineering, 2008, vol 134, No 2, pp.181–188

SFS-EN 1993-1-1. Eurocode 3: Design of steel structures. Part 1-1: General rules and rules for buildings. SFS, 2005

SFS-EN 1993-1-8. Eurocode 3: Design of steel structures. Part 1-8: Design of joints. SFS, 2005

SFS-EN 1993-1-12. Eurocode 3: Design of steel structures. Part 1-12: Additional rules for the extension of EN 1993 up to steel grades S700. SFS, 2007

Saastamoinen, H. Ultimate Strength and Deformation Capacity of X-joints Fabricated from Double Grade Rectangular Hollow Sections. Master's Thesis. Lappeenranta University of Technology, Department of Mechanical Engineering. Lappeenranta, 2011, (in Finnish)

Herion S., Fleischer O., Schneider M., Josat O., Reduction of weld sizes. CIDECT Report 5BY-5/11. Draft final report. July 2011

Puthli R., Ummenhofer T., Bucak Ö., Herion S., Fleischer O., Fischl A., Adaption and extension of the valid design formulae for joints made of high-strength steels up to S690 for cold-formed and hot-rolled sections. CIDECT report 5BT-11/11. July 2011

Zhao, X-L., Deformation Limit and Ultimate Strength of Welded T-joints in Cold-Formed RHS Sections. Journal of Constructional Steel Research. 2000, vol. 53, pp. 149–165

Björk, T., Marquis, G., A New Yield Line Theory Based Design Approach for Ultimate Capacity of Welded RHS X-joints. Design, Fabrication and Economy of Welded Structures. International Conference Proceedings, Miskolc, Hungary 24–26 April 2008. Chichester, England: Horwood Publishing Limited, 2008. pp 271–278. ISBN 978-1-904275-28-2

Tubular Structures XIV – Gardner (Ed.)
© 2012 Taylor & Francis Group, London, ISBN 978-0-415-62137-3

Experimental investigation of the static capacity of grade C450 RHS T and X truss joints

J. Becque
The University of Sheffield, Sheffield, South Yorkshire, UK

T. Wilkinson
The University of Sydney, Sydney, New South Wales, Australia

ABSTRACT: The results of an experimental program on X and T truss connections in C450 cold-formed RHS are presented. The aim of the program was to study the effect of the higher material yield strength and reduced f_u/f_y ratio of C450 compared to C350 steel on the various possible failure modes. At the same time the program also included RHS with wall slenderness values outside the current CIDECT geometric limits, since these slender cross-sections typically form part of the range of cold-formed RHS which are commercially on offer. Awaiting the results of comprehensive finite element studies based on the here presented data, the experimental results cautiously indicate that the current CIDECT design rules for T and X connections in grade 350 steel can be applied to C450 with $t < 6$ mm provided that the CIDECT geometric restrictions are met, and the minimum value of f_y and $0.8f_u$ is substituted for f_y when determining the connection strength.

1 INTRODUCTION

This paper presents the results of an experimental program carried out at the University of Sydney with the aim of studying the static capacity of X and T truss joints in grade C450 cold-formed rectangular hollow sections (RHS). A total of 15 connections were tested, including 4 T joints and 11 X joints.

The driving factors behind the research were twofold. First, the large amount of material cold-working received during the manufacturing process of RHS results in an increased material yield stress f_y, while the f_u/f_y ratio is typically reduced. It is thereby noted that, in what follows, the term 'yield stress' should be understood to represent the 0.2% proof stress, while the symbol f_u represents the ultimate tensile strength. The research aimed to investigate the effects of the altered material properties on the connection capacity and to (re)assess the need for reduction factors in the design equations when designing C450 X and T connections.

Second, advances in manufacturing techniques have allowed RHS with wall thicknesses of up to 16 mm to be produced by cold-rolling. However, upon inspection of commercial C450 RHS catalogues it is clear that a significant number of the sections on offer fall outside the geometric restrictions of CIDECT Design Guide 3 (Packer et al. 2009) in terms of their wall slenderness. The program aimed to include these more slender sections and gather experimental data on their connection behaviour and capacity.

2 BACKGROUND

While having evolved over many decades, the CIDECT design guidelines for truss connections have typically been presented with certain restrictions on their applicability. These restrictions themselves have evolved in synch with the design rules and apply to certain geometric parameters of the connections, as well as to the material properties. Earlier versions of CIDECT Design Guide 3 (Packer et al. 1996) limited the material yield stress f_y to 355 MPa, while also imposing the requirement that f_u/f_y had to exceed 1.2. While these restrictions have been maintained in the recently published AISC Design Guide 24 for Hollow Structural Section Connections (Packer et al. 2010), the latest version of the CIDECT Design Guide 3 (Packer et al. 2009) (which is also in accord with the recommendations of the International Institute of Welding, IIW 2009) has extended the range of applicability of the design rules to yield strengths of up to 460 MPa. However, it stipulates to use the minimum of f_y and $0.8f_u$ instead of f_y in the design equations and also imposes an additional reduction factor of 0.9 on the connection capacity. Eurocode 3 EN1993-1-12 (2007) equally imposes a reduction factor of 0.9 for S460.

When researching the origins of the reduction factor of 0.9, it appears that most of the justification for it originates from experimental work specifically conducted on K gap connections. Kurobane (1981) was first to demonstrate that the ultimate capacity of

CHS K gap connections in S460 is in relative terms 18% lower compared to the same joints in S235. Noordhoek et al. (1996) similarly found that CHS K gap connections of S460 had lower joint capacity factors than S235, even when an effective yield stress of $0.8f_u$ was used. However, Puhtli et al. (2010) carried out tests on CHS X-joints in S460 and observed that for nearly all connections tested, the experimentally determined capacity exceeded the capacity calculated without the factor of 0.9. The experiments were followed by numerical analyses which indicated that, while there is some justification for the inclusion of a reduction factor, the current value of 0.9 is conservative for X joints. The parametric studies, however, also revealed a dependence of the results on the f_u/f_y ratio. This dependence is the result of punching shear failures and effective width failures in tension being governed by the tensile strength f_u, while the design equations are based on the yield stress f_y. With respect to RHS connections, Mang (1978) conducted some early research on high strength S690 K-joints and observed a relative reduction in strength of 1/3 compared to S235 joints. Liu & Wardenier (2004) carried out further numerical work on RHS K gap connections in S460 and noticed a 10–16% reduction in capacity compared to S235 joints. Their research considered ultimate capacities, as well as the 3% deformation limit of Lu et al. (1994).With respect to wall slenderness values for X and T joints, earlier versions of Design Guide 3 (Packer et al. 1996) imposed a limit of 35 on chord and brace members, while compressive brace members needed to satisfy at least Class 2 requirements. Various design standards around the world are still based on these recommendations e.g. EC3 EN1993-1-8 (2005) and AISC Design Guide 24 (Packer et al. 2010). However, based on re-evaluation of numerical work by Yu (1997) on T and X joints and by Koning & Wardenier (1976) on K gap joints, while taking into account the 3% deformation limit, CIDECT Design Guide 3 (Packer et al. 2009) has extended the wall slenderness limit to 40. However, compressive chord members, as well as brace members, need to satisfy Class 2 requirements.

3 MATERIAL TESTS

A total of 24 tensile coupons were tested according to the AS/NZS1391 (1991) specifications. The coupons were cut from the same segments of RHS tube as the members of the actual test specimens. For each RHS one coupon was taken from the middle of the face opposite the weld face and one coupon was taken from the middle of a face adjacent to the weld face, as illustrated in Figure 1. All coupons were 20 mm in width and were tested at a strain rate of 5×10^{-4}/s in a 300 kN capacity MTS Sintech machine. It should be noted that the RHS employed in the tests were obtained from two different sources: sizes up to $200 \times 200 \times 6$ were manufactured in Australia by OneSteel Australian Tube Mills, while the larger sizes were imported from Japan.

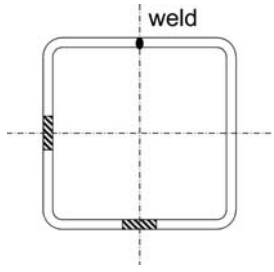

Figure 1. Location of the test coupons.

Table 1. Tensile coupon results.

		Adjacent to weld		Opposite weld	
Section	Source	f_y MPa	f_u MPa	f_y MPa	f_u MPa
$400 \times 400 \times 16$	JAP*	478	527	434	531
$400 \times 300 \times 8$	JAP	446	542	469	550
$350 \times 350 \times 8$	JAP	441	524	443	514
$350 \times 250 \times 10$	JAP	432	534	455	534
$300 \times 300 \times 8$	JAP	471	536	462	510
$250 \times 250 \times 6$	JAP	476	562	504	574
$250 \times 150 \times 5$	AUS*	426	509	449	518
$200 \times 200 \times 6$	AUS	442	516	456	524
$200 \times 100 \times 5$	AUS	425	495	440	534
$200 \times 100 \times 4$	AUS	422	508	453	523
$150 \times 150 \times 6$	AUS	432	499	433	504
125x125x5	AUS	424	503	418	502
Average JAP		457	538	461	536
Average AUS		428	505	441	518

*JAP = Japanese origin; AUS = Australian origin.

While all sizes are sold in Australia as C450 conforming to AS/NZS 1163 (2009), it is recognized that sections from these two origins might generally exhibit somewhat different material properties. Table 1 lists the values of f_y and f_u obtained in the coupon tests. 'Static' lower-bound values are reported, obtained by halting the test near the 0.2% proof stress and near the ultimate load and allowing the load to settle for about 2 minutes, as illustrated by the example provided in Figure 2.

It is seen from Table 1 that the material in the face opposite the weld generally exhibits a slightly higher yield stress than the material in the face adjacent to the weld, while the tensile strengths in both faces are similar. This can be explained by the larger amount of work-hardening undergone by the face opposite the weld during the fabrication process.

Of particular importance is the f_u/f_y ratio. For the Australian made sections, an average yield stress f_y of 435 MPa was found, in combination with a tensile strength f_u of 511 MPa. Consequently, $f_u/f_y = 1.18$. For the Japanese made sections, on average $f_y = 459$ MPa and $f_u = 537$ MPa, and thus $f_u/f_y = 1.17$. The materials narrowly fail the CIDECT requirement that f_u/f_y has to exceed 1.2.

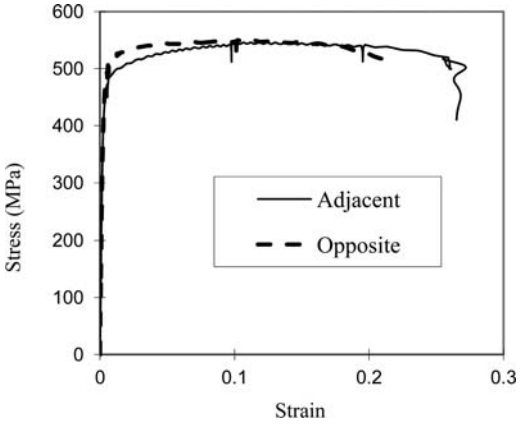

Figure 2. Results of RHS200 × 200 × 6 coupon tests.

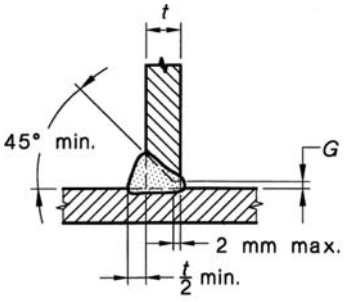

Figure 3. Compound weld (taken from AS/NZS 1554.1 2000).

4 WELDING

All connections were welded according to AS/NZS 1554.1 (2000) by a certified welder. Gas metal arc welding with W503 electrode wire was selected for all welds and Argon UN1006 was used as a shielding gas. Before welding the brace members were purged using Argon UN1956. Weld failures were outside the scope of the project and undesirable, since the aim of the research was to investigate the implications of using grade C450 on the connection capacity. Therefore, full penetration butt welds with superimposed fillet welds were selected whenever possible. Figure 3, taken from AS/NZS 1554.1 (2000), shows the prequalified weld detail which was used. The decision to select a compound weld was reinforced by findings that it is difficult to obtain full penetration at the root of the weld (Wardenier et al. 2009), a conclusion which was also drawn from slicing through and visually inspecting two practice connections.

5 TESTS ON T AND X CONNECTIONS

A total of 15 tests were carried out, including 4 T joints and 11 X joints. An overview of the test program is provided in Table 2. Keeping in mind the driving factors behind the research, which are on the one side the increased yield stress but reduced f_u/f_y ratio of the C450 steel and on the other side the increased wall slenderness of many of the cold-formed products, the experimental program was designed to include two types of sections in a balanced way:

1. sections with a nominal yield stress of 450 MPa which satisfied the geometric constraints of the CIDECT design guidelines (Design Guide 3, Packer et al. 2009). These tests investigated the effect of the altered material properties only.
2. sections with a nominal yield stress of 450 MPa which, due to their increased cross-sectional slenderness, fell outside the scope of the CIDECT design guidelines. These tests are highlighted in Table 2.

A wide range of geometries were included in the test program, with section sizes ranging from 75 × 75 × 5 to 400 × 400 × 16. The geometric parameters β, 2γ, τ and α are listed in Table 2 for each connection. The parameter β is equal to the ratio of the width of the brace member to the width of the chord member, 2γ is the ratio of the chord width to the chord thickness, τ is the ratio of the thickness of the brace member to the thickness of the chord member, and α is the angle included between the axes of the brace member and the chord member. Table 2 also indicates whether the connection was loaded in tension (T) or in compression (C).

The test program was designed with the aim of including the complete range of possible failure modes, as identified in the CIDECT references (e.g. Packer et al. 2009), into the experiments: chord face plastification, chord side wall failure, punching shear and effective width failures.

A strong frame with a 1000 kN jack was used to test the smaller size X-joints in compression (X1, X2, X3, X5, X7 and X8). The set-up is illustrated in Figure 4. The specimens were tested between universal hinges, which were fitted onto the 320 × 320 × 32 mm end plates of the specimen. This test configuration was chosen because it ensured a centered entry of the load into the specimens. The hinges allowed for end rotations to develop, mimicking the flexibility of the omitted parts of the brace members in the actual truss. In particular, the set-up allowed the increasing in-plane misalignment of the brace members to occur as a result of the chord shear deformations typically observed in X-joints with $\alpha \neq 90°$. This is illustrated for specimen X8 in Figure 4. On the other hand, the specimens were short enough to avoid overall Euler buckling.

Specimens X9, X10 and X11 included RHS of unprecedented size and were tested in the 2000 kN capacity DARTEC machine (Fig. 5). All three specimens were right angle X joints ($\alpha = 90°$) and were tested between fixed end conditions, a practice which has been common place with various other researchers (e.g. Feng & Young 2010, Rasmussen & Young 2001). After being fitted with cap plates, the specimens were

Table 2. Test results.

Test	Chord	Brace	β	2γ	τ	α	T/C[1]	Predicted failure mode	Observed failure mode	P_{cr} [2]	P_u [3]	$P_{3\%}$ [4]	$P_{pred,1}$ [5]	$P_{pred,2}$ [6]	Ratio1 [7]	Ratio2 [8]
-	-	-	-	-	-	°	-	-	-	kN	kN	kN	kN	kN	-	-
T1	200×200×6	100×100×8	0.50	33	1.33	90	C	Chord face plastification	Chord face plastification	-	Not reached	171	110	132	1.55	1.30
T2	200×200×6	75x75x5	0.38	33	0.83	90	T	Chord face plastification	Chord face plastification	-	191	118	88	106	1.34	1.11
T3	125x125x5	100×50×6	0.80	25	1.20	90	T	Chord face plastification	Punching shear	-	217	Not reached	117	136	1.85	1.60
T4	400×400×16	200×200×12.5	0.50	25	0.78	90	C	Chord face plastification	Chord face plastification	-	1797	1075	822	983	1.31	1.09
X1	250×150×5	125x125x5	0.83	30	1.00	90	C	Chord face plastification	Chord side wall buckling +chord face plastification	164	251	181	202	239	0.90	0.76
X2	250×150×5	150×150×5	1.00	30	1.00	90	C	Chord side wall buckling	Chord side wall buckling	250	413	365	94	105	3.88	3.48
X3	150×150×6	150×150×6	1.00	25	1.00	90	C	Chord side wall buckling	Chord side wall buckling	628	831	Not reached	341	390	2.44	2.13
X4	200×100×4	200×100×4	1.00	50	1.00	45	T	Side wall shear failure	Punching shear	-	588	Not reached	266	314	2.21	1.87
X5	200×100×5	150×100×5	0.75	40	1.00	45	C	Chord face plastification	Chord face plastification	-	226	223	191	223	1.17	1.00
X6	200×200×6	200×100×4	1.00	33	0.67	90	T	Effective width failure	Effective width failure	-	659	Not reached	582	692	1.13	0.95
X7	150×150×6	125x125x4	0.83	25	0.67	90	C	Chord face plastification	Side wall failure +effective width failure	200	356	350	275	329	1.27	1.06
X8	250×250×6	150×150×6	0.60	42	1.00	60	C	Chord face plastification	Chord face plastification	-	202	181	193	231	0.94	0.78
X9	350×350×8	300×300×8	0.86	44	1.00	90	C	Chord side wall buckling + chord face plastification	Chord side wall buckling + chord face plastification	465	848	735	548	646	1.34	1.14
X10	350×250×10	250×250×10	1.00	25	1.00	90	C	Chord side wall buckling	Chord side wall buckling	1336	>1770	>1770	601	672	>2.22	>1.99
X11	400×300×8	300×300×8	1.00	38	1.00	90	C	Chord side wall buckling	Chord side wall buckling	670	1291	1270	284	316	4.47	4.02

[1] T/C = Tension/Compression
[2] P_{cr} = Experimentally measured buckling load of the chord side wall
[3] P_u = Experimentally measured ultimate load
[4] $P_{3\%}$ = Experimentally measured load where the chord deformations exceed 3% of the chord width
[5] $P_{pred,1}$ = Predicted capacity using the minimum value of f_y and $0.8f_u$ and an additional reduction factor of 0.9
[6] $P_{pred,2}$ = Predicted capacity using only f_y without an additional reduction factor of 0.9
[7] Ratio1 = $\min(P_u, P_{3\%}) / P_{pred,1}$
[8] Ratio2 = $\min(P_u, P_{3\%}) / P_{pred,2}$

placed directly on the bed of the testing machine. To bridge the slightly uneven gap between the top cap plate and the plate at the underside of the jack, 70 MPa plaster was mixed up and sealed inside a plastic bag. The ram of the testing machine was then brought down until it made even contact with the bag and the plaster was left to set.

The X joints in tension (X4 and X6) were tested as illustrated in Figure 6. Cap plates were welded to the ends of the brace members and fitted with perpendicular plates which could be held by the jaws of the 2000 kN DARTEC testing machine.

Specimens T2 and T3 were tested in tension using the set-up illustrated in Figure 7. A plate slotted into the brace member was placed in the jaws of the 2000 kN capacity DARTEC testing machine. Eight 24 mm high-strength threaded rods, doweled into the bed of the machine and connected to RHS100 × 50 × 6 cross members, held the specimen down while a tensile force was applied. It is clear that the applied load has to dissipate into the side walls in shear before being transferred to the rods and that the joint therefore qualifies as a T connection. Buckling of the chord side walls at the location of the dowels was determined not to be a limiting issue. The nuts on the eight rods were just loosely tightened without applying force, in order to avoid the specimen being clamped down with prying action developing during the test. Instead, the specimen was seen to 'float' off the bed during the test with a gap of about 2 mm opening up between the underside of the specimen and the base of the machine. This ensured a simple flow of forces.

Specimens T1 and T4 were tested in compression. With $\beta = 0.50$, the expected (and observed) failure mode was plastification of the top chord face with very little participation of the side walls. Therefore, the set-up illustrated in Figure 8 was deemed acceptable. The specimens were placed flat on the bed of the testing machine to prevent any bending moments from developing in the chord and introducing extra compression into the chord top face. The compressive load was introduced into the specimen through a universal hinge to ensure uniform bearing contact with the brace member.

Figures 9–12 illustrate various failure modes encountered in the test specimens: plastification of the chord face (Fig. 9, showing T4), punching shear (Fig. 10, showing T3), chord side wall buckling (Fig. 11, showing X3) and effective width failure of the brace (Fig. 12, showing X6).

6 TEST RESULTS: DISCUSSION

Table 2 lists the ultimate loads P_u obtained in the tests. Consideration was also given to a deformation limit which, in accordance with Lu et al. (1994), was set at 3% of the chord width. The corresponding load $P_{3\%}$

Figure 4. X joint in compression (X8).

is listed in Table 2. Whenever applicable, the load at which side wall buckling was first observed, P_{cr}, is also shown.

The current CIDECT design guidelines (CIDECT Design Guide 3, Packer et al. 2009) were used to obtain a prediction of the connection capacity. It is thereby noted that some of the connections tested (in particular, the connections highlighted in Table 2) did not satisfy the geometric constraints imposed by the CIDECT rules in terms of the wall slenderness values of the chord and/or brace members. While the CIDECT rules must not be applied to these connections, a prediction is nevertheless given. Predictions were obtained in two different ways:

1. by applying the design rules of CIDECT Design Guide 3 (Packer et al. 2009) as stated, i.e. with limiting f_y to $0.8f_u$ and applying an extra modification factor of 0.9. Actual values of f_y and f_u, as determined from coupon tests, were used. This prediction is listed as $P_{pred,1}$ in Table 2.

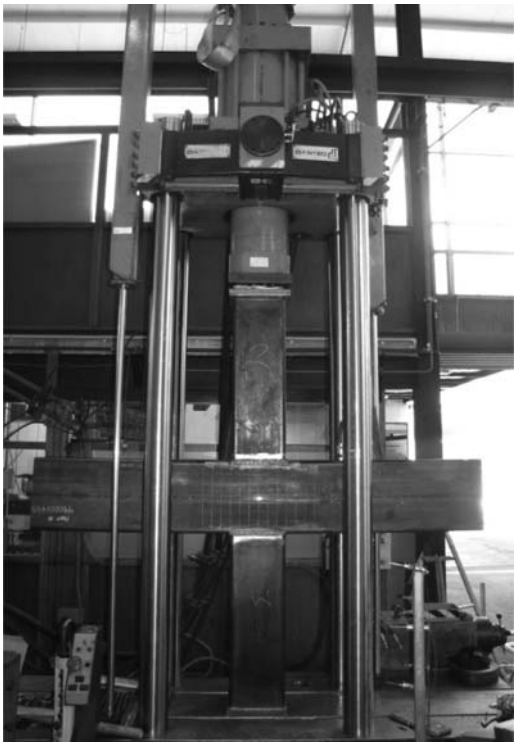

Figure 5. Large X joint in compression (X11).

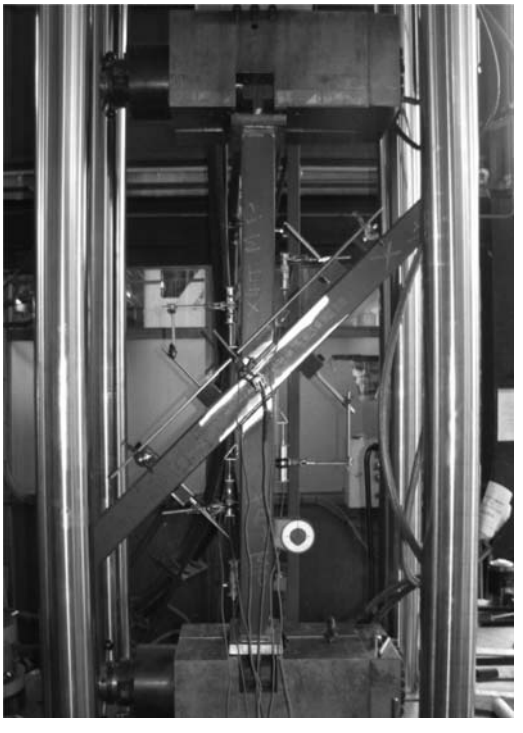

Figure 6. X joint in tension (X4).

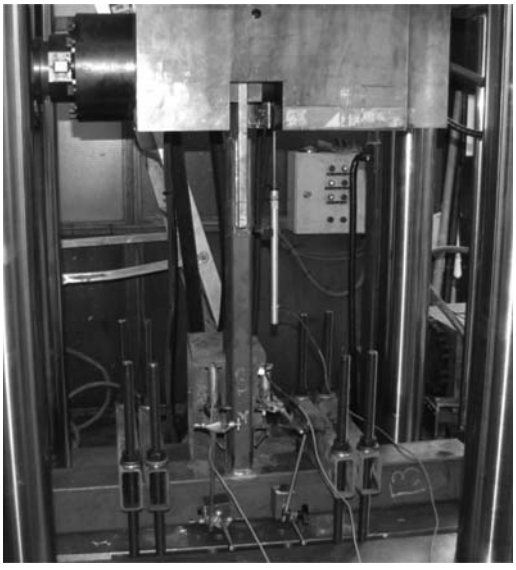

Figure 7. T joint in tension (T3).

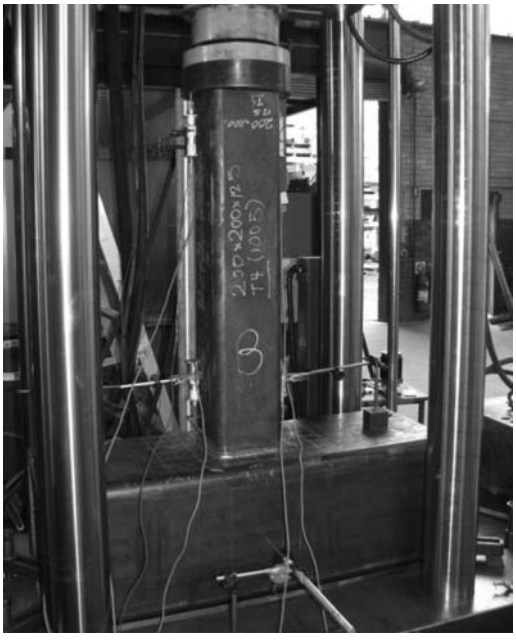

Figure 8. T joint in compression (T4).

2. the CIDECT rules valid for $f_y = 355$ MPa were applied, without modification, to the C450 connections. Actual values of f_y as determined from coupon tests, were used. This prediction is listed as $P_{pred,2}$ in Table 2.

In either case it was taken into account that the CIDECT rules yield *factored* capacities, implicitly including a partial safety factor of 0.9. The factor of 0.9 was divided away to allow an objective comparison between the experiment and the prediction.

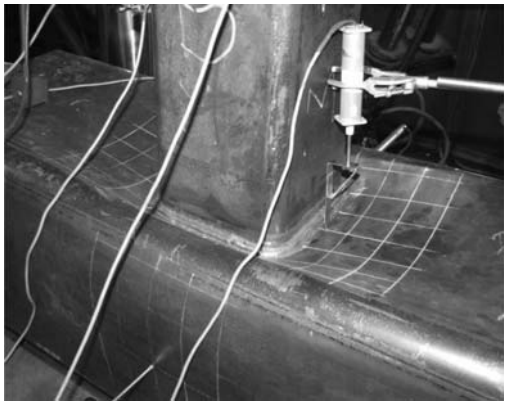

Figure 9. Chord face plastification (T4).

Figure 10. Punching shear (T3).

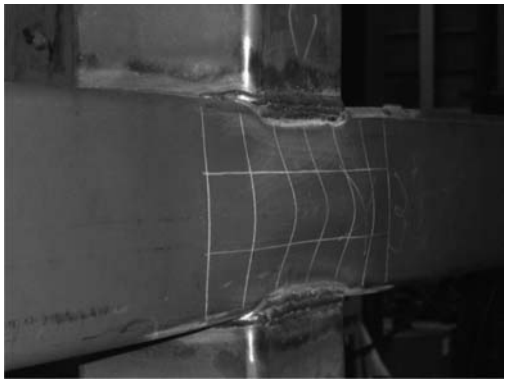

Figure 11. Chord side wall buckling (X3).

In Table 2, Ratio1 indicates the ratio of the experimentally determined capacity (including the 3% deformation limit) to the predicted capacity $P_{pred,1}$. Ratio2 is the ratio of the experimentally determined capacity (again including the 3% deformation limit) to the prediction $P_{pred,2}$.

When considering only those connections which satisfied the geometric constraints of the current CIDECT rules (i.e. the connections not highlighted in Table 2), it is seen that Ratio2 is consistently above 1.0. However, connection T3, where the predicted

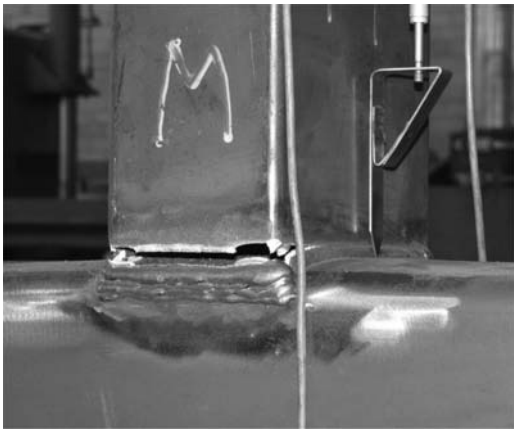

Figure 12. Effective width failure of the brace (X6).

failure mode is different from the actual, observed failure mode, requires further consideration. The discrepancy results from the fact that $\beta < 0.85$ and that, consequently, a punching shear check is not explicitly required by the CIDECT rules. In reality, however, due to the particular geometry of the connection the brace side walls sat directly adjacent to the rounded corner zones of the chord (Fig. 10) and punching shear became the governing failure mode. If a punching shear check were carried out according to the CIDECT rules, this would result in: $P_{pred,1} = 193$ kN and $P_{pred,2} = 224$ kN, and consequently: Ratio1 = 1.12 and Ratio2 = 0.97. The fact that Ratio2 comes in slightly below unity is not entirely surprising, since the punching shear capacity is in effect governed by f_u (while the design equation is based on f_y), and since the f_u/f_y ratio is slightly less than the required value of 1.2. A similar observation can be made for specimen X6, where Ratio2 = 0.95. X6 fails by an effective width failure of the brace wall in tension, a phenomenon equally governed by f_u. The experimental results therefore provide evidence in support of the recommendation to limit f_y to $0.8f_u$, especially seen the brittle nature of punching shear and effective width failures.

Apart from the punching shear and effective width failures, connections which satisfied the CIDECT geometric limits exhibited the lowest Ratio1 and Ratio2 values for chord face plastification failures, while still exceeding unity: Ratio2 = 1.00 for X5, 1.09 for T4, 1.11 for T2 and 1.30 for T1. Based on these test, no conclusive evidence is currently present to support the introduction of an additional safety factor of 0.9. However, numerical studies are underway to provide additional data.

Equal-width X-joints which failed by chord side wall buckling and which satisfied the CIDECT limits, exceeded the predicted capacity by at least a factor of two (X3 and X10). In the case where $\beta < 1.0$ and the specimen failed in combined side wall buckling and chord face plastification, Ratio2 dropped to 1.06 (X7).

Specimens X2 and X11 were equal-width X-joints with a side wall slenderness of 50, which is well outside the CIDECT limits. Nevertheless, these specimens exceeded the CIDECT predicted capacities by factors of 3.5–4.0, the largest margins in the test program. This prompts the conclusion that the CIDECT design rules for chord side wall buckling of equal-width joints become more conservative for higher side wall slenderness values.

The applicability of the CIDECT design rules becomes significantly more problematic for joints with $\beta < 1.0$ which exhibit high chord side wall slenderness values (>40) and which fail in combined chord face plastification and side wall buckling. In these cases, the formation of a chord face plastification mechanism is considerably facilitated by the slender side walls, which, due to their relatively low bending stiffness, participate in the failure mechanism. Participation of the side walls was observed for β ratios well below 0.85. The CIDECT rules in their current form must not be applied to these connections. While Ratio2 = 1.14 for X9, Ratio2 = 0.78 for X8 and Ratio2 = 0.76 for X1.

7 CONCLUSIONS

The results of an experimental program investigating the static capacity of cold-formed C450 RHS X and T truss joints are here presented. A total of 15 tests are described, including 4 T joints and 11 X joints. The program will serve as the starting point of detailed finite element simulations, but points towards some preliminary conclusions. In particular, it indicates a need to limit f_y in the design calculations to a certain fraction of f_u, while it does not provide supporting evidence for the complete elimination of an additional modification factor of 0.9. The scope of the specimens tested do not include thicknesses above 6 mm, or for K-joints, so the initial conclusions have not been verified against a full range of connection options.

ACKNOWLEDGMENT

The authors would like to extend their sincere gratitude towards CIDECT and OneSteel Australian Tube Mills for their financial patronage of the program. The donation of the materials used in the experiments by the latter sponsor is also greatly appreciated.

REFERENCES

AS/NZS 1163 2009. "Cold-formed structural steel hollow sections." Australian Standard/New Zealand Standard, Standards Australia, Sydney, Australia.

AS/NZS 1391 1991. "Methods for Tensile Testing of Metals." Australian Standard/New Zealand Standard 1391:1991, Standards Australia, Sydney, Australia.

AS/NZS 1554.1 2000. "Structural steel welding: Part 1: Welding of steel structures." Australian Standard/New Zealand Standard, Standards Australia, Sydney, Australia.

EN 1993-1-8 (EC3) 2005. “Eurocode 3: Design of steel structures – Part 1.8: Design of joints.” EN1993-1-8, European Committee for Standardization, Brussels, Belgium.

EN 1993-1-12 (EC3) 200). “Eurocode 3: Design of steel structures – Part 1.12: Additional rules for the extension of EN 1993 up to steel grades S700.” EN1993-1-12, European Committee for Standardization, Brussels, Belgium.

IIW 2009. “Static design procedure for welded hollow section joints – Recommendations.” 3rd edition, International Institute of Welding, Sub-commission XV-E, Annual Assembly, Singapore, *IIW Doc. XV-1329-09*.

Feng, R., & Young, B. 2010. “Tests and behaviour of cold-formed stainless steel tubular X-joints.” *Thin-Walled Structures* 48(12), pp. 921–934.

Koning, C.H.M., de, & Wardenier, J. 1976. “Supplement with test results of welded joints in structural hollow sections with rectangular boom.” *TNO-IBBC Report No. BI-76-122/35.3.51210. Stevin Report No. 6-76-5.*

Kurobane, Y. 1981. “New developments and practices in tubular joint design.” *IIW Doc. XV-488-81* and *IIW Doc. XIII-1004-81*.

Liu, D.K., & Wardenier, J. 2004. “Effect of the yield strength on the static strength of uniplanar K-joints in RHS (steel grades S460, S355 and S235).” *IIW Doc. XV-E-04-293*, Delft University of Technology, Delft, the Netherlands.

Lu, L.H., de Winkel, G.D., Yu, Y., & Wardenier, J. 1994. “Deformation limit for the ultimate strength of hollow section joints.” *Proceedings of the 6th International Symposium on Tubular Structures*, Melbourne, Australia, Tubular Structures VI, Balkema, Rotterdam, The Netherlands, pp. 341–347.

Mang, F. 1978. “Untersuchungen an Verbindungen von geschlossenen und offenen Profilen aus hochfesten Stählen.” AIF-Nr. 3347. Universität Karlsruhe, Germany.

Noordhoek, C., Verheul, A., Foeken, R.J., Bolt, H.M., & Wicks, P.J. 1996. “Static strength of high strength steel tubular joints.” *ECSC agreement number 7210-MC/602*.

Packer, J.A., Wardenier, J., Kurobane, Y., Dutta, D., & Yeomans, N. 1996. *Design guide for rectangular hollow section (RHS) joints under predominantly static loading.* First edition, CIDECT series “Construction with hollow steel sections” No. 3, Verlag TUV Rheinland, Köln, Germany.

Packer, J.A., Wardenier, J., Zhao, X.-L., van der Vegte, G.J., & Kurobane, Y. 2009 *Design guide for rectangular hollow section (RHS) joints under predominantly static loading.* Second edition, CIDECT series “Construction with hollow steel sections” No. 3, Verlag TUV Rheinland, Köln, Germany.

Packer, J.A., Sherman, D., & Lecce, M. 2010. Hollow Structural Section Connections, AISC Steel Design Guide 24, American Institute of Steel Construction, USA.

Puthli, R., Bucak, O., Herion, S., Fleischer, O., Fischl, A., & Josat, O. 2010. “Adaptation and extension of the valid design formulae for joints made of high-strength steels up to S690 for cold-formed and hot-rolled sections.” *CIDECT report 5BT-7/10* (draft final report), Germany.

Rasmussen, K.J.R., & Young, B. 2001. “Tests of X- and K-joints in SHS stainless steel tubes.” *Journal of Structural Engineering* 127 (10), pp.1173–1182.

Wardenier, J., Packer, J.A., Choo, Y.S., van der Vegte, G.J, & Orton, A. 2009. “Axially loaded T and X joints of elliptical hollow sections” *CIDECT report 5BW-6/09*.

Yu, Y. 1997. “The static strength of uniplanar and multiplanar connections in rectangular hollow sections.” PhD thesis, Delft University Press, Delft, the Netherlands.

Tubular Structures XIV – Gardner (Ed.)
© 2012 Taylor & Francis Group, London, ISBN 978-0-415-62137-3

FEA of T & X joints in Grade C450 steel

M. Mohan & T. Wilkinson
University of Sydney, Australia

ABSTRACT: Finite element modelling of higher strength Rectangular Hollow Sections (RHS) at 450 MPa yield have been benchmarked against a set of 6 T & X experiments. The main aim to date is to benchmark finite element models against test results at 3% deformation and ultimate loads. The FEA approach that provides the best simulation of results incorporates elements that are 20 noded hexahedral elements, von Mises yield criterion with kinematic hardening rules and an arc length method using modified Riks-Ramm technique. The paper will examine various parameters including β, 2γ, τ; alternate geometries; geometric imperfections, chord length and chord loads.

1 INTRODUCTION

CIDECT Design Guides have material strength and geometric limitations on the applicability of many of their design rules. The reasons are twofold: higher strength materials often have less ductility, and experience greater deformations before yield; and more slender sections may experience plate local buckling failures not necessarily considered in the background research. Design Guide 3 (2009) extended the applicability to yield strengths up to 460 MPa, but has a requirement to use the minimum of $[0.8f_u, f_y]$ plus an additional correction factor of 0.9 based on extra deformation for high strength steel, rather than f_y alone. These modification factors reduce the design capacity by the order of 10–15% compared to using 460 MPa alone.

The aim of this project is to assess the joint behaviour of higher strength and slightly less ductile Grade C450 rectangular tubular joints, with regards to applicability to Grade C450 (or similar) and the need for the additional reduction factors that apply at this stage. Some of the numerical simulation work done to date is provided in this paper.

Finite element analyses have been conducted to benchmark a number of T and X joint experimental tests with regards to maximum load, 3% deformation limit load, initial elastic stiffness and structural ductility/deformation capacity at maximum load/ failure. The test parameters and test results for which benchmarking have been carried out are as provided in Table. 1. Parametric analysis for a range of chord axial loads has been studied. A more elaborate discussion on the tests is provided by Becque et al. 2011.

The process and methodology followed includes assessing the behavior of models for the following:

- Element type (shell vs solid vs hybrid combination model; nodes per element (8-noded vs 20 noded brick))
- Material properties (isotropic and kinematic hardening)
- Investigation of a damage model for tensile failure (LeMaitre)
- Analysis type (arc length, large deformation and strain options).

2 METHODOLOGY

2.1 *Finite element model*

A quarter of the T joint was modelled taking into account symmetry of the joint. In the case of X joints, one-eighth joint models were developed. The fabrication of these joints had minimum rotational/ translational joint eccentricity and justifies this assumption. Finite element geometry/mesh was developed using MSC.Patran 2010/MSC.Mentat. Physical representation of the joint was done using various element topologies. These include linear/quadratic shell and solid elements.

Finite element models for experimental tests conducted on four T and two X joints reported in Table 1 have been generated. The solid element model incorporates four elements through the thickness of chord, brace and welds. Typical finite element models with solid elements are as shown in Figures 1 and 2. The geometry of the butt welds in these models is assumed to be uniform with 100% penetration and at a footprint of 45 degrees angle from the face of the brace to the chord. Geometric FE imperfections, tube thickness and corner radii closely reflect measured values. The finite element models incorporate slotted gusset plates/cover plates at the loading (restraint) ends of tensile/compressive tests in accordance with the fabrication drawings. The results for mesh with linear hexahedral solid elements (hex8) have been compared with quadratic hexahedral elements (hex20) in all these analyses.

Table 1. Geometrical parameters, failure modes and test results of T and X joint.

Test ID	Chord size Brace size/ Brace Load	Geometry	Failure Mode, test	P_{test} 3% (kN)	$P_{test,ult}$ (kN)
T1	$200 \times 200 \times 6$ $100 \times 100 \times 8$ Compressive	$\beta = 0.5$ $2\gamma = 33$ $\tau = 1.33$	Chord Face Plasticfication	171	Large
T2	$200 \times 200 \times 6$ $75 \times 75 \times 5$ Tensile	$\beta = 0.38$ $2\gamma = 33$ $\tau = 0.83$	Chord Face Plasticfication	118	191
T3	$125 \times 125 \times 5$ $100 \times 50 \times 6$ Tensile	$\beta = 0.8$ $2\gamma = 25$ $\tau = 1.2$	Punching Shear	Not reached	217
T4	$400 \times 400 \times 16$ $200 \times 200 \times 12.5$ Compressive	$\beta = 0.5$ $2\gamma = 25$ $\tau = 0.78$	Chord Face Plasticfication	1075	1797
X6	$200 \times 200 \times 6$ $200 \times 100 \times 4$ Tensile	$\beta = 1.0$ $2\gamma = 33$ $\tau = 0.67$	Effective Width Failure	Not reached	659
X9	$350 \times 350 \times 8$ $300 \times 300 \times 8$ Compressive	$\beta = 0.86$ $2\gamma = 44$ $\tau = 1.0$	Chord side wall Buckling & Chord face Plastification	735	848

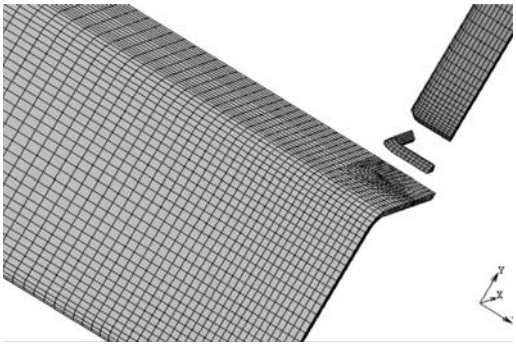

Figure 1. Finite element mesh used for test T2.

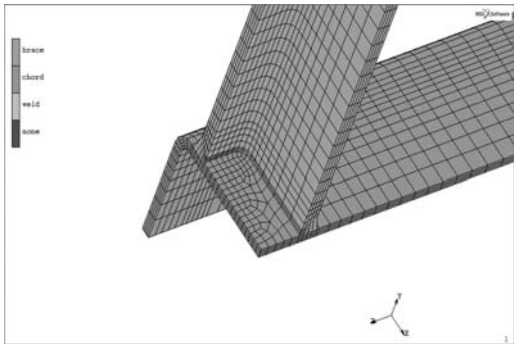

Figure 2. Finite element mesh for Test T3.

Parametric studies for variations to chord length in these joint tests have been simulated. In order to evaluate differences between X and T joints, finite element studies were conducted on T joints converted to X joints. One of these converted X joints has been modelled for various element types. These include quadratic shell elements (quad8) and a hybrid model with hex20 solid elements at the chord/brace interface and with quad8 shell elements away from the interface. Finite element mesh plots for these element variations are provided in Figs. 3 and 4.

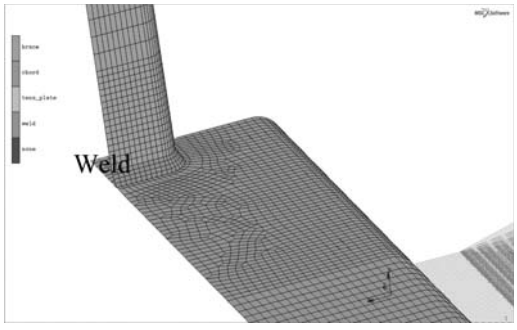

Figure 3. Finite element mesh plate element models.

2.2 *Material*

Tensile coupon tests for $200 \times 200 \times 6$ were previously conducted. The true stress strain curves obtained from the engineering stress strain results is as shown in Figure 5. This stress strain curve has been adopted for all elements in the analyses. Von Mises yield criterion with kinematic hardening rule was used in most analyses. In compression test simulations, kinematic hardening was required to better represent loading effects in the inelastic region. In tensile test simulations, isotropic hardening is adequate to represent loading effects. However kinematic hardening was required to simulate unloading effects.

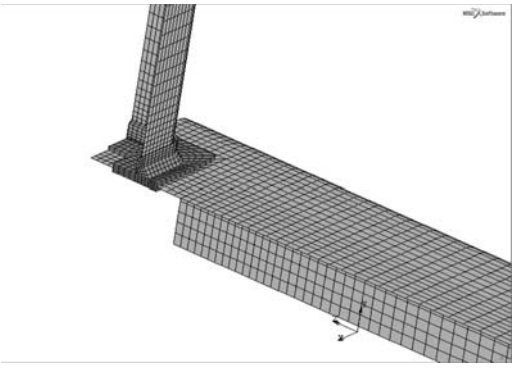

Figure 4. Finite element mesh for hybrid model with plate and solid elements.

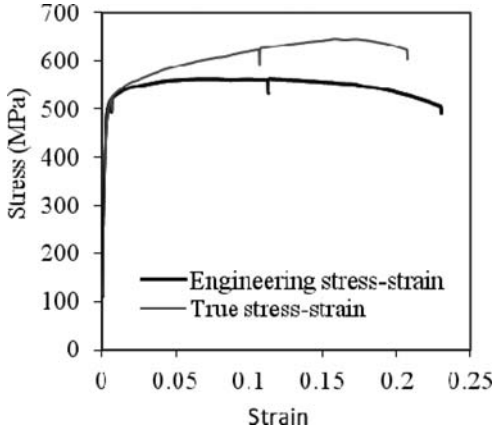

Figure 5. Material stress strain curve.

A phenomenological approach to ductile damage has been done through Lemaitre damage model (MSC.Marc 2010, Lemaitre et.al 1990). The damage model requires as inputs plastic strain threshold, critical damage Dc, corrected ultimate stress and damage resistance parameter, S. The critical damage is used to compare the ductile damage D with the state of the material. When D reaches Dc the damage probability tends to be 1. The comparison is done by the relative damage value. Simulation of tensile coupon test results has been used to define damage values in Lemaitre model.

2.3 *Loads and boundary conditions*

Loads and restraints for T and X joints with tensile brace/compressive loads closely follow the experimental test setup. Relevant boundary conditions at planes of symmetry have been adopted.

2.4 *Analyses*

Non linear large displacement analyses were conducted using MSC.Marc 2010. Predictions and

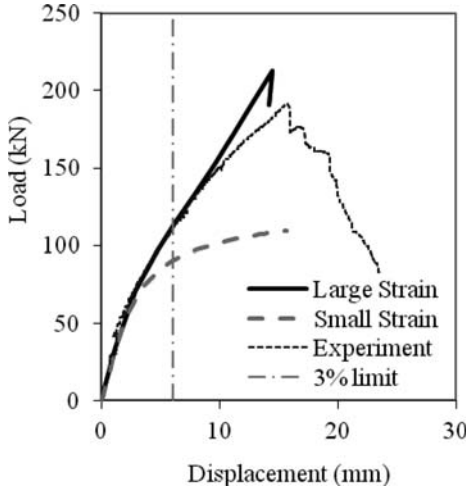

Figure 6. Small Strain vs. Large Strain.

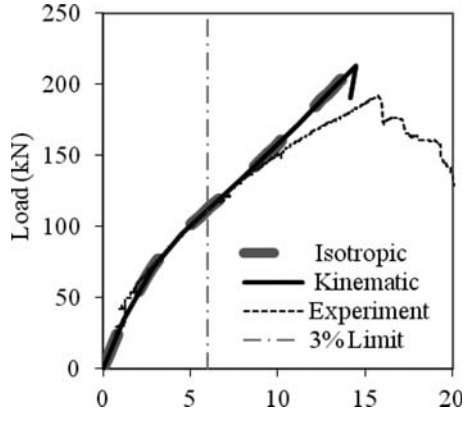

Figure 7. Kinematic Hardening vs. Isotropic Hardening for tensile test T2.

experimental results have been compared for a range of analyses parameters. These include large displacement large strain, large displacement small strain, adaptive arc length techniques such as Crisfield, and modified Riks-Ramm. Relative displacement/force convergence tolerance of 0.01 have been specified in these analyses.

Large displacement small strain plasticity method was compared to large displacement large strain plasticity methods. The latter approach gave better correlation to experimental results. A comparison between the two approaches and measured experimental results is provided in Figure 6 for test t2.

Results for isotropic and kinematic hardening are shown in Figs. 7 and 8 for tensile test T2 and compressive test X9. Kinematic hardening model is found to be more reliable in simulating loading and unloading effects.

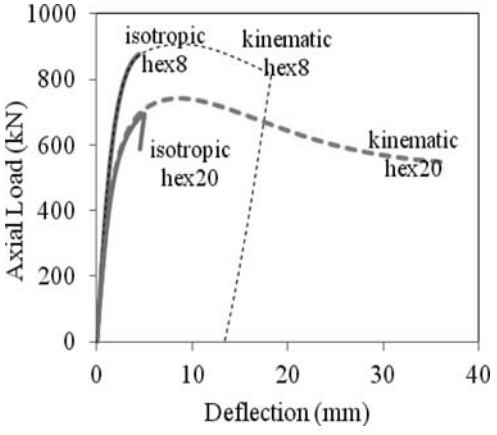

Figure 8. Kinematic Hardening vs. Isotropic Hardening for compressive test x9.

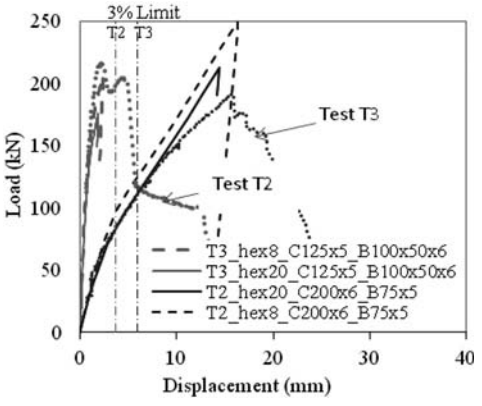

Figure 9. Load Displacement Response for T type joint in Tension at the chord to brace interface: FE vs. Experimental.

3 TENSILE BRACE LOADS

3.1 *Numerical results*

The measured load displacement response for T joint tests T2, T3 at the chord brace interface and results obtained from numerical simulations adopting hex8 and hex20 elements are compared in Figure 9. Similar comparison for X joint test X6 with additional load displacement response at ends of the brace is provided in Figure 10. In an analyses variation, test X6 was analysed without imperfection to study the effect of imperfection on ultimate load capacity. These results are as shown in Figure 11 along with insets showing failure locations during test.

3.2 *Influence of chord restraints on T joints*

Tests T2, T3 have bolts loosely tightened at 145/150 mm (Figure 12.1). It was felt that the T joint may be constrained due to its close proximity with the brace in both FEA and experimental tests, FEA

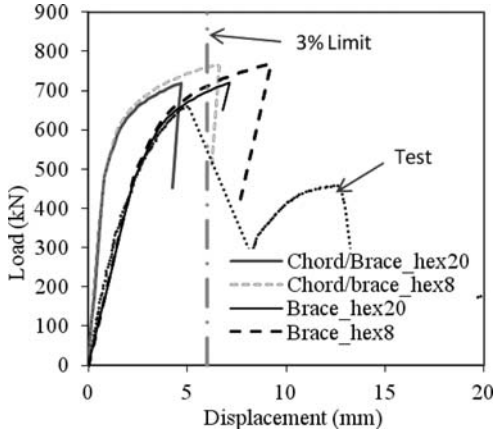

Figure 10. Load Displacement Response for lower vs. higher order elements.

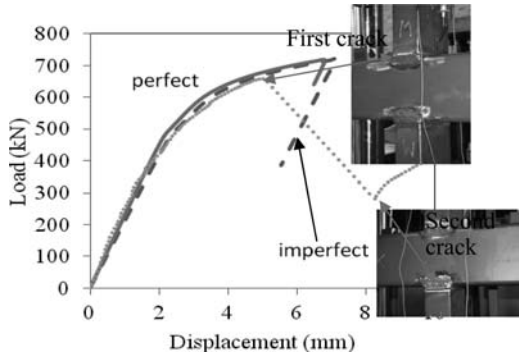

Figure 11. Load Displacement Response for perfect and imperfect elements: FE vs. Test.

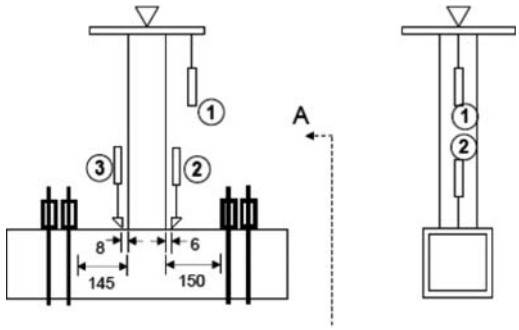

Figure 12.1. Experimental test set up for Test T2.

assumptions possibly being greater than the experimental test set up. A sensitivity study was therefore conducted by moving the location of these constraints away from the joints. The base FEA model adopts the nearest vertical constraint at 140 mm from the face of the weld (Figure 12.2). Nearest vertical constraints were modified to locations 160 mm, 370 mm and to ends of the chord.

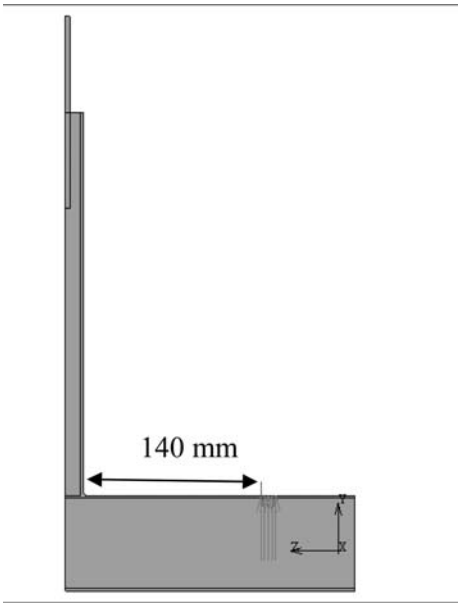

Figure 12.2. Model Variations to clamp locations.

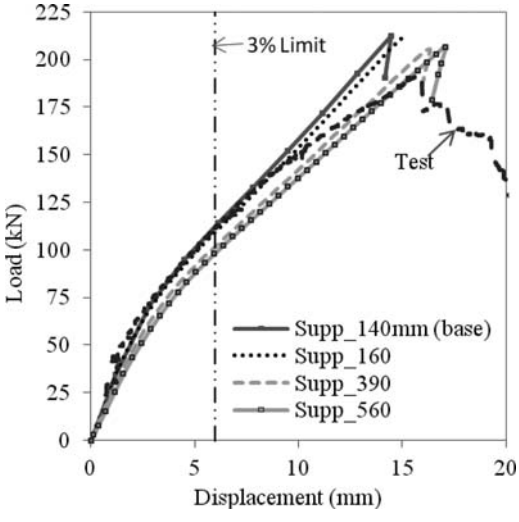

Figure 13. Parametric FEA results for chord restraints in joint type T2.

The load displacement curves simulated using hexahedral 20 elements, von Mises yield with kinematic hardening and for large strain and large displacement formulation for test T2 is provided in Figure 13. The analyses confirm that load displacement response is sensitive to the location of constraints.

3.3 *Comparisons between T and X joints*

Current CIDECT rules are the same for T, X and Y joints. Test T2 has been designed to fail in chord face plastification with little participation from the chord. Test T3 has been designed to fail in punching shear. In order to verify whether X joints satisfy the load limits derived for the T joint, Test T2 described in Section 3.2 and test T3 have been converted to X joints. Load displacement response comparing T and T modified as X is provided in Figure 14. In both scenarios, ultimate loads predicted in T joints are higher than an equivalent X joint.

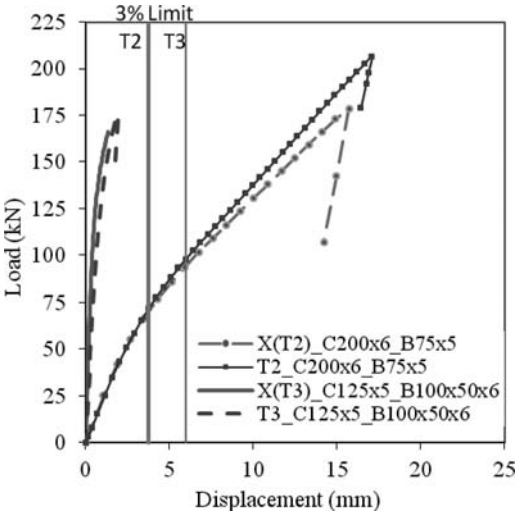

Figure 14. Comparison of FE results for T and X joints.

3.4 *Shell vs solid elements*

Test T2 modified to X joint configuration has been modelled with different shell, solid and hybrid shell/solid models (ref to Figs. 1, 3 and 5 of Section 2.1). Load displacement response results for these models at the junction of the chord and brace are provided in Figure 14. These modified models have been compared against analyses results for hex20 solid element model. Representation of joint with both thin and thick shell elements could not properly and accurately predict joint deflections. Also, it tended to underpredict the joint capacities. A comparison between results obtained for the different element types and CIDECT predicted loads are provided in Table 2.

As seen by previous researchers, finite element weld profile is required for accurately predicting load capacities of joint. Modelling chord, brace and welds with thick plate element formulations gave lower estimates for end loads. A hybrid element model with hex20 at the brace/chord interface and quad8 elements compares well with hex20 elements. Such a methodology can result in substantial reduction in solve times.

3.5 *Lemaitre damage model*

Load displacements for Test T2 with hex20 elements with Lemaitre damage fracture criteria are provided

Table 2. Predicted load capacities for shell and solid elements.

Element Type	Simulations			
	Load at 3% P_{s3} (kN)	End Load P_{us} (kN)	Ratio R1 P_{s3}/P_{p1}*	Ratio R2 P_{s3}/P_{p2}*
Hex 20	95	179	1.08	0.90
Quad8; Thin shell; no weld	51	61	0.58	0.48
Thin Shell; welds	143	143	1.63	1.35
Thick Shell; welds	–	78	0.89	0.74
Hybrid (Hex20 and Quad8)	94	180	1.07	0.89

- P_{p1} and P_{p2} are two predictive approaches and equates to 88 kN and 106 kN at 3% deflection limits.
- Pp1 is calculated using min(fy, 0.8fu) with an additional modification factor of 0.9.
- Pp2 is calculated using fy without the modification factor of 0.9.

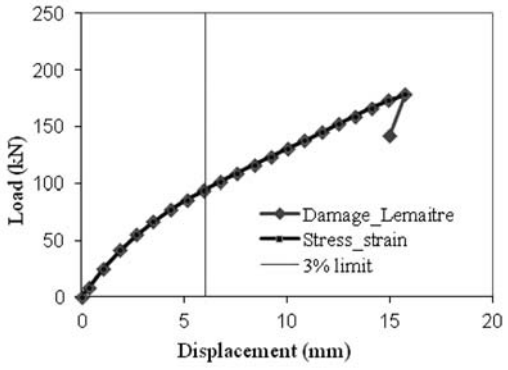

Figure 15. Comparison of Lemaitre Damage Model results and without damage model.

in Figure 15. Differences in results for models with and without damage in these simulations are minimal. The relative damage values predicted have been used to identify the damage location and the load at which ultimate damage occurs. Relative damage values at 159 kN and 179 kN are shown in Figs. 16 and 17. At 179 kN, the probability of damage exceeds 1 showing that the damage has occurred. At 172 kN, the damage is likely to be 100%. The location of failure predicted by the model coincides with those seen in the tests (inset in Figure 17). The failure shown in the tests is at approximately 165 kN.

The probability of damage for simulated test X6 with damage criteria is provided in Figure 18. The location of likelihood of failure in tests X6 is correctly predicted in Test X6. However, relative damage values are within 1 suggesting that damage has not occurred. A potential cause for this mismatch is that the model does not correctly reflect the fabrication details corresponding to β of 1.

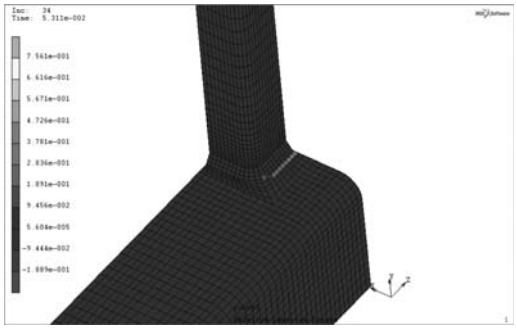

Figure 16. Critical Zones: Damage Value at 159 kN.

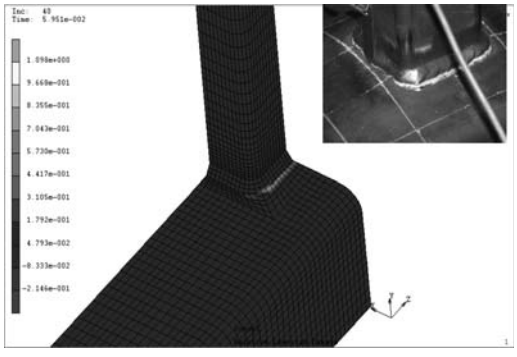

Figure 17. Critical Zones: Damage Value at 179 kN. *Damage Value >1 indicates probability of damage as 1.*

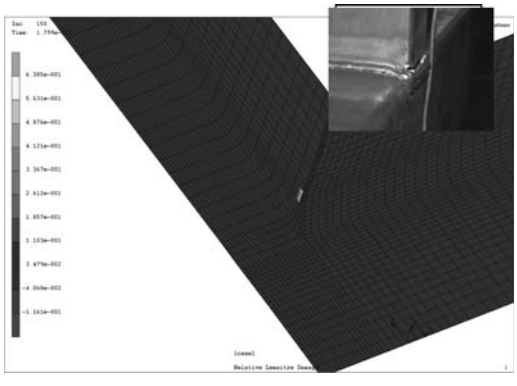

Figure 18. Lemaitre Relative Damage at 717 kN.

3.6 *Influence of chord load on ultimate load capacity*

Compressive or tensile loads have been applied as distributed pressures at the end of the chords. Eight chord pre-load ratios have been applied. Four of these are compressive and at $0.2f_y$, $0.4f_y$, $0.6f_y$ and $0.8f_y$. The directions of these loads have been reversed to provide tensile pre-loads. In the first step of the analyses, ends of the chord are pre-loaded. Axial tensile brace loads have then been applied in the second step. The second

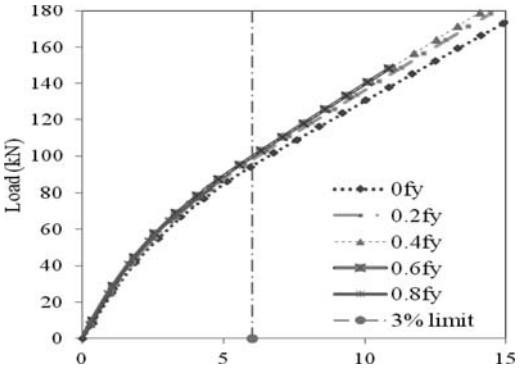

Figure 19. Effect of tensile preload on ultimate capacity.

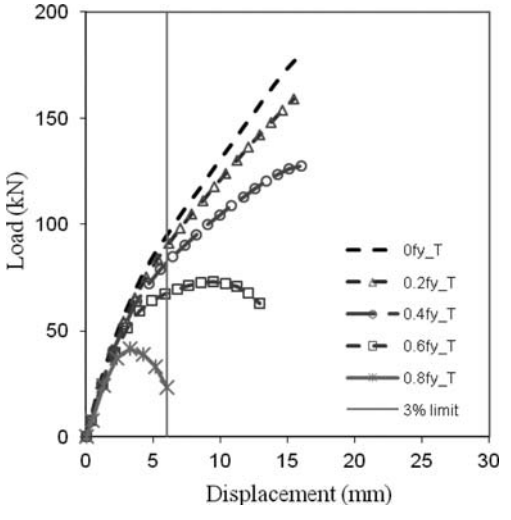

Figure 20. Effect of compressive chord preload on ultimate capacity.

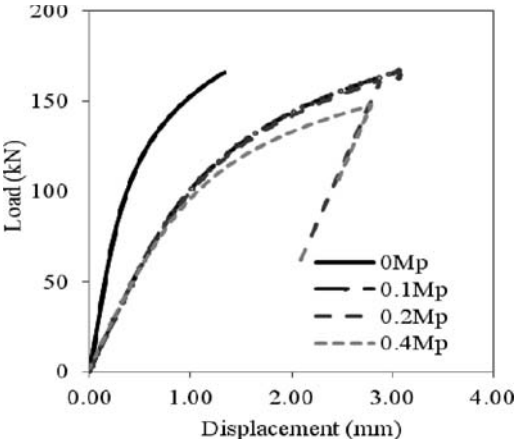

Figure 21. Effect of chord moment on ultimate capacity.

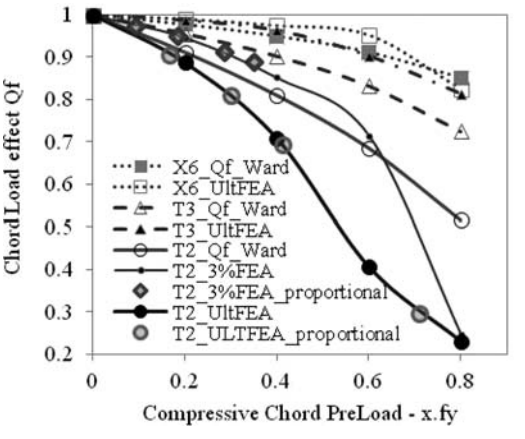

Figure 22. Comparison of parametric chord load effect: FE analyses to current design.

step of the analyses maintains the chord axial loads specified in the first step.

Analyses for preload moments in the chord as a factor of plastic moment capacities were carried out for test T3. Factored moments of $0.1M_p$, $0.2\ M_p$, $0.4\ M_p$ and $0{,}6\ M_p$ was used. These moments result in tensile stresses at the brace footprint. Load displacement plots for T2 under tensile or compressive chord stresses and T3 for chord moments are shown in Figs. 19, 20 and 21.

A plot of chord load effect Q_f as predicted by Wardiener et al. (2010) and as simulated using FEA is provided in Figure 22. In order to verify if proportional loading made a difference to Qf, in test T2 simulations chord loads and brace tensile loads have been applied in a single load event. Qf at 3% deflection and ultimate load limits were derived for a range of compressive chord loads. The results are found to be very similar to the previously simulated dual step load events. These results are also provided in Figure 22.

A comparison between design capacity estimates with factored, un-factored loads and FEA predicted values is provided in Figs. 23 and 24. The differences between results obtained for test T2 and cur rent design equations were minimal. Since tensile loads tend to produce larger capacities than compressive brace loads, the direction of load in this model was reversed. These results are reported in section 4.2.

4 COMPRESSIVE BRACE LOADS

Results for FE joint models representing tests T1, T4 are provided in Figure 25 for lower and higher order elements. It was found that adaptive meshing is required in order to simulate large displacement response for the selected mesh. The lower order elements used for the purposes of analyses however gave increased loads due to larger stiffness and is as shown in Figure 26. Results for FE joint representing X9

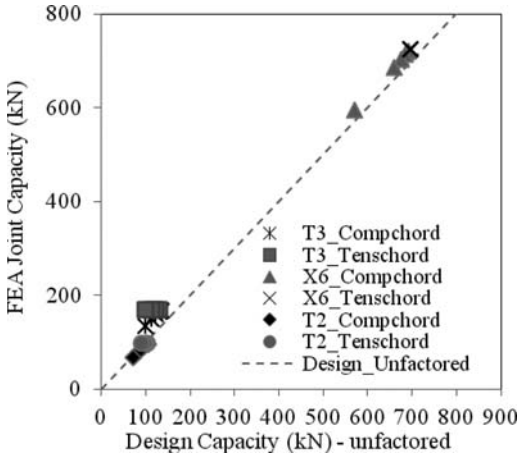

Figure 23. Comparison of parametric FE design capacity to current design for un-factored material properties.

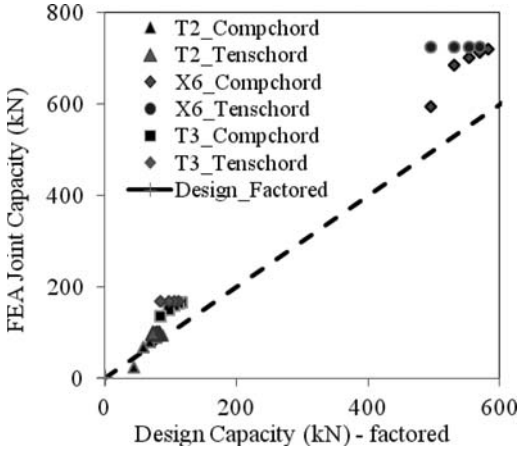

Figure 24. Comparison of parametric FE design capacity to current design for the factored material properties.

is provided in Figure 27. All simulations reported in these figures have weld foot prints which are smaller than those adopted in the experimental tests; larger weld footprint gave higher ultimate load. In general FE results correlated well with experimental tests with respect to load-displacement behavior, stiffness, failure loads and failure modes.

4.1 *Influence of chord loads on ultimate load capacity*

Parametric variations for the model representing X9 joint was studied for compressive and tensile preloads. Results from FE simulations are found to exceed joint capacities for current design rules with and without additional correction factor of 0.9 and is as shown in Figure 28.

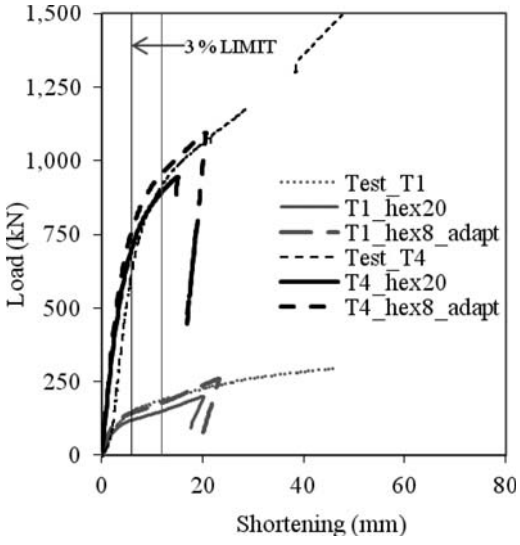

Figure 25. Load Displacement Response at the chord to brace interface for T type joint under compression: FE vs. Experimental.

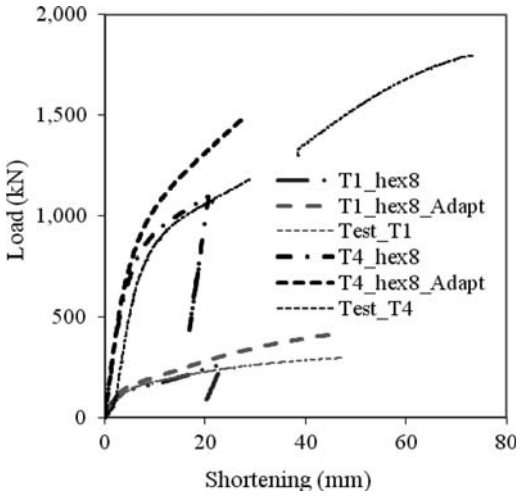

Figure 26. Load Displacement Response at the chord to brace interface for T type joint under compression: FE hex8 vs. FE adaptive mesh.

Loads in previously benchmarked results for tensile test T2 were reversed and the joint was studied for compressive loads with and without chord preloads. The load displacement curve is provided in Figure 29 and a comparison between tensile and compressive brace loads is provided in Figure 30. In this scenario, the current design estimates for both factored and unfactored design was found to be inadequate. Further analyses to verify a range of parameters β, τ and γ is currently being conducted.

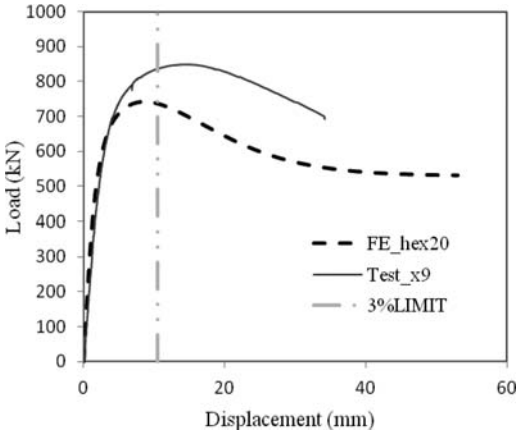

Figure 27. Load Displacement Response at the chord to brace interface for X9 type joint under compression: FE vs. Experimental.

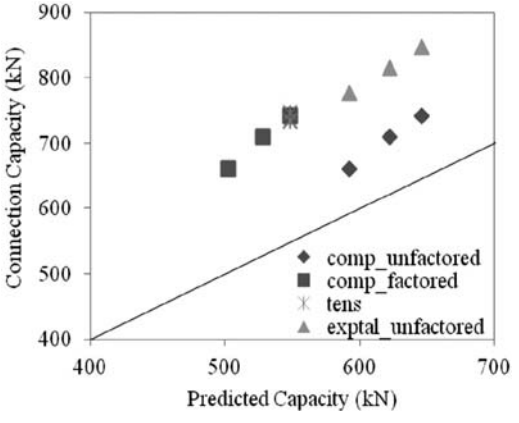

Figure 28. Comparison of parametric FE design capacity under compressive brace load and axial chord load.

5 CONCLUSION

5.1 *Analyses parameters*

Finite element models of six T and X type laboratory joints have been created and analysed using MSC. Marc software. Various parameters in the analysis have been investigated as part of benchmarking against each experimental results; these include load displacement response, maximum load, 3% deformation load, failure and initial fracture location. The following parameters are found to correlate with the measured response:

- Elements are 20 noded hexahedral elements
- von Mises yield criterion with kinematic hardening rules
- Arc length method using modified Riks-Ramm technique.
- A hybrid mesh, replacing the numerically intensive 20 noded bricks with shell elements away from the joint interface, has showed promising results.

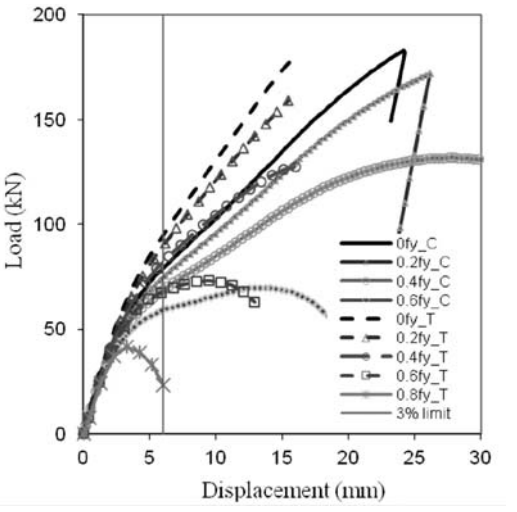

Figure 29. Comparison of parametric FE design capacity for compressive and tensile brace loads with compressive chord loads.

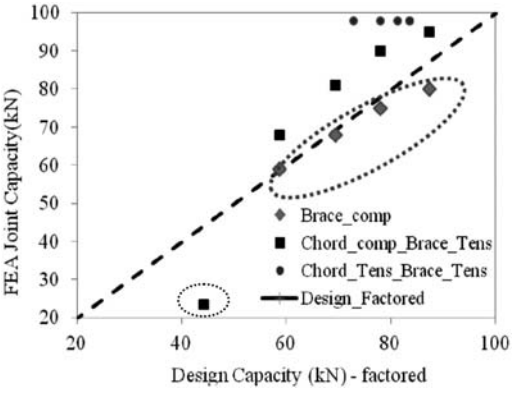

Figure 30. Comparison of parametric FE design capacity for tensile/compressive brace loads to current design rules.

- Fracture prediction through Lemaitre damage criterion.

5.2 *Joint capacity*

The capacity predictions for T, X joints with and without axial chord loads have been found to be in general larger than those calculated without the application of additional correction factor of 0.9 for c450 grade steel required by the current design rules. However parametric simulation studies of tensile test T2 with β of 0.38 and chord to wall slenderness ratio of 35, as converted to a compressive connection gave lower capacities. Simulated results as compared to the calculated capacities with the additional correction factor of 0.9 are also found to be lower when axial chord loads are applied. Results reported for tensile tests are for 6 mm thickness sections. Further work is therefore

currently being carried out for changes to parameters of β, γ and τ.

REFERENCES

AS/NZS 1163. 2009. Cold-formed structural steel hollow sections. *Australian Standard/New Zealand Standard*, Standards Australia.

AS/NZS 1391. 1991. Methods for Tensile Testing of Metals. Australian Standard/New Zealand Standard 1391:1991, Standards Australia.

CIDECT Design Guide 3. 1996. *see* Packer et al. (1996).

CIDECT Design Guide 3 2009. *see* Packer et al. (2009).

IIW. 2009. Static design procedure for welded hollow section joints – Recommendations. 3rd edition, International Institute of Welding, Sub-commission XV-E, Annual Assembly, Singapore, *IIW Doc. XV-1329-09*.

Becque, J. 2011. Experimental investigation of X and T truss connections in C450 cold-formed rectangular hollow sections, CIDECT report 5BV.

Kurobane, Y. 1981. New developments and practices in tubular joint design. *IIW Doc. XV-488-81* and *IIW Doc. XIII-1004-81*.

Lemaitre, J. and Chaboche, J.L. 1990. Mechanics of solid materials. Cambridge University Press, 1990.

MSC.Marc 2010. MSC. Software Corporation.

Packer, J.A. and Henderson, J.E. 1997. Hollow Structural Section Connections and Trusses, A Design Guide. *Canadian Institute of Steel Construction.*

Packer, J.A., Sherman, D., and Lecce, M. 2010. Hollow Structural Section Connections, AISC Steel Design Guide 24, *American Institute of Steel Construction*, USA.

Packer, J.A., Wardenier, J., Kurobane, Y., Dutta, D., and Yeomans, N. 1996. Design guide for rectangular hollow section (RHS) joints under predominantly static loading. *First edition, CIDECT series "Construction with hollow steel sections" No. 3*, Verlag TUV Rheinland, Köln, Germany.

Packer, J.A., Wardenier, J., Zhao, X.-L., van der Vegte, G.J., Kurobane, Y. 2009. Design guide for rectangular hollow section (RHS) joints under predominantly static loading. Second edition, *CIDECT series: Construction with hollow steel sections,* No. 3, Verlag TUV Rheinland, Köln, Germany.

Puthli, R., Bucak, O., Herion, S., Fleischer, O., Fischl, A., and Josat, O. 2010. Adaptation and extension of the valid design formulae for joints made of high-strength steels up to S690 for cold-formed and hot-rolled sections. *CIDECT report 5BT-7/10* (draft final report), Germany.

van der Vegte, G.J., and Makino, Y. 2008. The Effect of Chord Length and Boundary Conditions on the Static Strength of CHS T- and X-joints. *Proceedings of the Fifth International Conference on Advances in Steel Structures, Vol. III*, ed. Liew, J.Y., and Choo, Y.S., Singapore.

Wardenier, J., Packer, J.A., Zhao, X.-L. and van der Vegte, G.J. 2010. *Hollow Sections in Structural Applications*. 2nd edition, Bouwen met staal, The Netherlands.

PREFERENCES, SYMBOLS AND UNITS

b_0 = chord width
b_1 = brace member width
d_0 = chord diameter of CHS connection
h_0 = chord depth
h_1 = brace member depth
$f_{0.01}\%$ = proportionality limit (0.01% proof stress)
f_y = yield stress or 0.2% proof stress
f_u = tensile strength
t_0 = chord member thickness
t_1 = brace member thickness
α = angle between the centre lines of the chord and the brace members
$\beta = b_1/b_0$ = ratio of the brace member width to the chord member width
$\gamma = b_0/2t_0$
Δ = elongation after fracture (%)
$\tau = t_1/t_0$ = ratio of the brace member thickness to the chord member thickness

Tubular Structures XIV – Gardner (Ed.)
© 2012 Taylor & Francis Group, London, ISBN 978-0-415-62137-3

Measurements vs. estimation of nominal and local strain in a tubular K-joint of a stinger

N.S. Ermolaeva, Y. Yu, X. Chen & H. Ren
Allseas Engineering, Delft, The Netherlands

ABSTRACT: This paper covers the comparison of estimated data and data obtained through real-time measurements at a K-type tubular joint of a space frame, called a "stinger", used as a support for a pipeline during its installation on the seabed. Data used for comparison with the calculated strain range are obtained from statistical analysis of the measured nominal and local strain in the braces of the joint. It is shown that the statistical distribution of strain ranges derived from the measurements is sometimes different from what is considered in the fatigue analysis of stinger tubular joints, while the maximum strain ranges are still within the range of data used for stinger design.

1 INTRODUCTION

A subsea pipeline for gas or oil transfer can be installed on the seabed by different methods. One of the installation methods is called "S-lay". This method is characterized by horizontal assembly of a pipeline on board of a specially designed pipe lay vessel. Step by step, after an extra pipe joint is welded to the pipeline, the vessel moves forward and the pipeline slides in the sea in a form of "S" shape (see Fig. 1). More details on the S-lay and other methods of pipeline installation can be found elsewhere (Palmer, 2008).

A stinger is an indispensable part of the S-lay installation method, which supports and guides a pipeline from the lay vessel to the seabed in a pre-designed curvature. Usually it is constructed as a space frame tubular structure. An example of a stinger section is shown in Figure 2. Though the stinger structure might resemble the structure of an offshore platform jacket or a boom of a crane and other lifting equipment used in harsh sea environments, the load pattern of the stinger is quite different. An offshore crane boom is operated above water, thus, no direct wave loads are applied to it. Although an offshore platform jacket is continuously subjected to wave loads, there is no vessel induced motion on the structure. Thus, its dynamic response will be quite different from that of a stinger. It is expected that the methods of fatigue calculations widely used for cranes and offshore platforms cannot be applied directly to a stinger structure, and require further development. In order to understand the dynamic behavior of the stinger, real-time strain measurements were performed at one of the K-joints (see the highlighted joint in Fig. 2). For non-operational (no pipe lay) vessel activities the preliminary processed data has been reported earlier (Ermolaeva et al. 2010).

This paper will focus on the measurements performed in the pipe lay mode. The measurements will be then compared with the estimated strain ranges used for the fatigue analysis of the considered joint in the stinger design phase. There are several possibilities to validate the method used for fatigue estimation of the joint, which are discussed in the paper:

- checking the assumed statistical distribution of nominal and local stress ranges;
- direct comparison of nominal and local strain ranges in calculations and measurements;
- derivation of local stress/strain ranges, based on the equations used in fatigue calculations, and their comparison with the local strain ranges obtained through measurements.

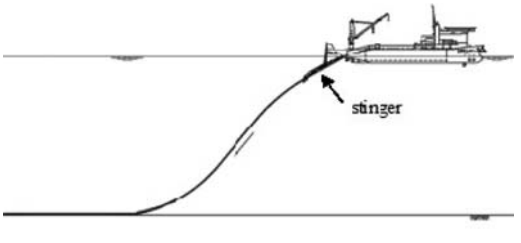

Figure 1. Pipeline in S-lay configuration.

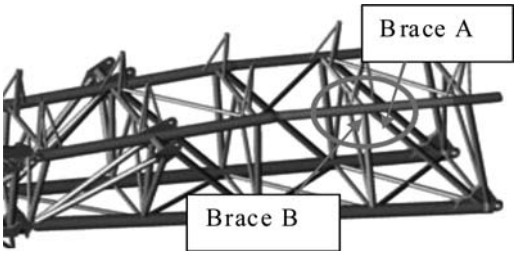

Figure 2. Stinger section.

2 FATIGUE ASSESSMENT METHODOLOGY

2.1 *General*

Some aspects of a tubular joint fatigue resistance are usually addressed as early as in a stinger design phase. A designer chooses the ratio of geometry parameters giving the lowest possible stress concentration factors (SCFs) at the intersection of braces and a chord. For example, a fatigue friendly connection will be with a smaller chord radius over wall thickness ratio (γ) and with a smaller brace over chord wall thickness ratio (τ) for specific nominal stresses in the chord and the braces. The effect of geometry parameters has been investigated by many researchers and implemented into different design guides and recommendations (Wardenier, 2001; DNV, 2008). When the static design of the stinger structure is ready, the fatigue assessment of joints may be performed. As mentioned earlier, the stinger structure is neither a crane nor a jacket structure. That is why it does not directly fall under recommendations for fatigue calculations available for lifting appliances or offshore units. However, a DNV approach for offshore steel structures (DNV, 2008) for fatigue estimation of tubular joints can be used as the basis. The procedure is outlined in the following Sections.

2.2 *Sea environment conditions*

A stinger, being an attachment to a vessel operating in sea environment, is subject to loads originating from sea waves and loads from a pipeline which it supports. These loads are of stochastic nature and their statistics follow the statistics of the sea state, which is specified by a wave frequency spectrum with a given significant wave height, a representative frequency, a main (dominant) propagation direction, and a spreading function. In applications, the sea state is usually assumed to be a stationary random process, i.e. with all its statistical properties not varying with time. Three hours has been introduced as a standard time between registrations of sea states when measuring waves, but the period of stationarity can range from half an hour to 10 hours (DNV, 2007). The time interval, during which a process can be considered stationary, is called a "short term" period further on.

In offshore community it is accepted (DNV, 2007) that in a short-term sea state the wave heights are Rayleigh distributed. When the short terms are combined in a longer time period and the assumption of stationarity is not valid anymore the wave heights are represented by a Weibull distribution function. The same valid to short- and long-term distributions of a response (stress range) in structures operating in sea environment. If the short-term statistics do not comply with the Rayleigh distribution function the process is influenced by the non-linearity of the system and should be treated as non-stationary.

2.3 *Fatigue assessment procedure*

Because the stinger is submerged during pipeline installation and is above water in survival and transit conditions, and, moreover, can be in different radius configurations (in order to serve shallow to deep water pipe-lay projects), the choices for relative duration of one or another vessel activity should be made. For this, the statistics and prognosis on pipe lay projects for Allseas fleet experience is used. Based on these choices, an operational profile of stinger usage and life matrix are constructed, the latter is used further to generate load cases. In combination with wave scatter diagrams, the life matrix gives the number of cycles for each of the load cases comprising a certain stinger geometry (radius and position, up or down), wave height, wave approach angle and frequency. In terms accepted in the offshore community, the parameters characterizing a sea state usually are: a significant wave height (H_S), wave heading (θ), and mean wave zero crossing period (T_Z).

In a stinger fatigue assessment, two typical pipe laying projects are considered: in shallow and deep water locations. The former is characterized by a larger stinger radius, and the latter by a smaller one. The stinger geometry configuration or stinger radius is a composition of stinger sections at certain angles with respect to each other that forms the required radius for the pipe supported by the stinger during pipeline installation.

Hydrodynamic (HD) analysis of a vessel with an attached stinger structure is performed for a 3-hours run in each sea state corresponding to the life matrix, followed by a statistical analysis. Total force in 6 directions corresponding to the probability of exceedance of 10^{-3} is determined. Afterwards, a choice is made of time steps for further hydrodynamic runs and determination of nodal loads to be transferred to FEA programs for structural analysis.

For operational load cases in addition to hydrodynamic loads, loads from the pipeline sliding or lying on the supporting roller boxes (RB loads) should be considered. These loads are usually calculated from roller box reaction forces based on one of the special purpose pipe lay installation FEA programs, for the load cases determined by the life matrix. This analysis is dynamic and results are statistically processed as in the case of HD loads.

Both types of loads (HD and RB) being transferred as an input to FEA for further structural calculations of stinger joints, correspond to the given probability of exceedance (10^{-3}). It is assumed therefore that the stinger structural response follows the same statistical distribution and corresponds to the same probability as the input loads.

For the next step the calculations are split for tubular connections and connections, reinforced with gusset plates or other reinforcements. The former are calculated based on member forces (axial load, in-plane and out-of plane bending moments) and Efthymiou equations (or other parametrical equations for SCF estimation) for 16 points, 8 at the brace and 8 at the chord sides, for each of the considered load cases. It should be noted that because of the specifics of load cases for stinger structure, a stinger tubular joint classification might be changed, that is why for each load

case prior to application of one or another parametrical equation for SCF calculation a certain check should be made. For each location and each load case, a stress range is calculated. Assuming that the determined stress range corresponds to the certain probability of exceedance of the supposed statistical distribution (Rayleigh), this distribution is reconstructed and used further for fatigue damage calculation along with corresponding S-N curve and Palmgren-Miner summation rule. The procedure is compiled into a number of in-house developed computer programs including interfaces with several commercial software packages.

3 MEASUREMENTS

3.1 *Measurement set-up*

A K-joint at the top chord of a stinger section (see Fig. 2) was equipped with a measuring system comprising strain gauges and four portable data loggers of 2H Offshore[1]. The loggers allow a choice of intermittent or continuous measurements, frequencies and interval between measurement sessions within certain available frame, number of channels to be logged etc. Duration of the measurements is limited by this choice and by the capacity of the memory cards and power supply batteries. Before installing the loggers one should determine, using the dedicated software, the measurement parameters and starting time of the measurements (logging). After a measurement session is over, and a vessel operation schedule allows retrieving the memory cards, the data can be processed further using calibration factors supplied along with the data loggers. The measurements analyzed here were performed in an intermittent mode (29 minutes in each half an hour) with a frequency of 10 Hz. Because there was no way to calibrate a zero measurement, only a dynamic strain (strain variation) was measured. This is assumed to be sufficient for fatigue assumptions validation.

Strain gauges were placed around the weld connection of diagonal brace A of the considered K-joint (Figs. 2 and 3) for local strain measurements as close as possible to the weld toe and at about 1-m distance from the weld on both braces, A and B (see Figs. 2 and 3) of the K-joint, to obtain nominal strain values. The strain gauges nearby the weld were positioned on the brace and the chord in a direction normal to the weld and at a distance not greater than 6 mm from the weld toe. The numbering of the strain gauge locations along the intersection line is clockwise starting from the crown toe in the direction of outside through inside of the frame (see Fig. 3). The locations seen on the chord inside the frame from left to right, are 1 (crown toe), 8, 7 (saddle), 6, 5 (crown heel). Points 2, 3 (saddle) and 4 are at the outside. Optional numbering on the brace side is from 9 through 16. As throughout the text the strain gauges IDs are used, their location is

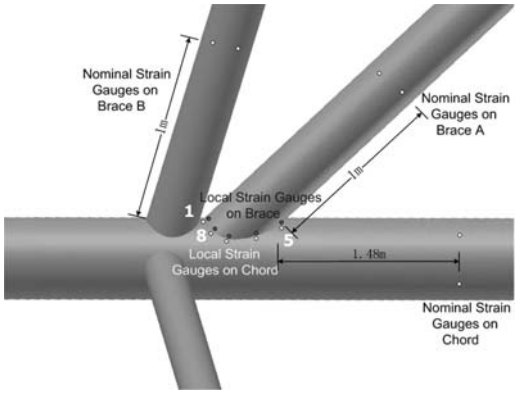

Figure 3. Strain gauge locations shown from the inside the frame.

Table 1. Strain gauge locations and IDs.

		Chord		Brace	
Location	in/outside	No	gauge ID	No*	gauge ID
crown toe	–	1	G5	(9)	E5
	outside	2	F4	(10)	D4
saddle	outside	3	F3	(11)	D3
	outside	4	F2	(12)	–
crown heel	–	5	F1	(13)	–
	inside	6	–	(14)	–
saddle	inside	7	–	(15)	E7
	inside	8	–	(16)	E6

*Optional numbering.

listed in Table 1. Only those gauges that are considered to provide reliable data are given.

3.2 *Stinger loading conditions*

In the fatigue assessment of stinger joints, the loading conditions are typically summarized in a life matrix. Each cell of the life matrix corresponds to a certain combination of a loading condition (stinger geometry and position, and a sea state) and a number of occurrences of this condition during a stinger design life. As described in Section 2.3, for a particular sea state a combination of wave height, H_S, wave period, T_Z, and wave heading, θ, is implied. In the strain measurement sessions, H_S, T_Z, wave direction and vessel heading were obtained from a wave radar system and the vessel main data logger. The wave approaching angle (wave heading, θ) was calculated from the main wave direction and vessel position (vessel heading).

A series of 15 half-hour terms in the same day was chosen for further data processing, with the mean value of H_S in the range of 2.2–3.1 meters, T_Z being 7.9–8.9 s and the wave heading in between 79° and 90°. The variation of the weather parameters above is considered to be consistent with rather stable sea conditions.

Stinger position in measurements was down (submerged) in a pipe lay radius. A pipe lay project during

[1] Currently "Pulse Structural Monitoring Ltd"

the measurements was in shallow waters and with a shorter stinger than had been used in fatigue estimations, later referred to as "short" and "long" stinger, respectively. This distinction is important in the comparison analysis because for the longer stinger the hydrodynamic loads are higher than for the shorter one, due to the following reasons: (a) the center of gravity of the longer stinger is farther from the center of gravity of the vessel than for the shorter one; and (b) the longer stinger with the extra stinger section(s) results in extra weight and consequently extra hydrodynamic load. Theoretical background on hydrodynamic loads for offshore structures can be found elsewhere (Journeé & Massie, 2001).

4 DATA PROCESSING

4.1 *General*

Data processing starts with screening the logged data for bad sectors and their elimination from the data analysis. This operation typically reduces the measurement interval from 29 to 26 minutes. Slow drift removal and band-pass filtering are the next steps. During the data processing analysis it was concluded that the resolution of the strain gauges is 8.15 microstrain (8.15×10^{-6}). This means that a variation of measured strain close to this value will not give a reliable statistical distribution, and can be considered as corresponding to a cut-off frequency in a high frequency range.

Examples of an original and filtered signal are given in Figures 4 and 5, respectively. The latter is ready for processing for cycle counting. The rainflow counting method (Matsuishi & Endo, 1968) is applied further for the derivation of the strain range cycles.

The analysis of the strain ranges showed that the maximum recorded value is small enough to accept a linearity between the strain and stress ranges. Therefore, all conclusions resulted from the measurements for the strain ranges are valid for stress ranges as well.

4.2 *Statistical analysis*

The strain ranges in every strain gauge location and in each of the measurement terms were analyzed with respect to statistical distribution. Both Rayleigh and Weibull distributions were considered. The Rayleigh probability density function (pdf) can be presented as follows,

$$p(x,\sigma) = \frac{x}{\sigma^2} e^{-x^2/2\sigma^2}, \; x \geq 0 \quad , \tag{1}$$

where $\sigma > 0$ is the mode parameter.

While Weibull pdf is given by the following (two-parametrical) equation

$$p(x,\lambda,k) = \frac{h}{\lambda}\left(\frac{x}{\lambda}\right)^{h-1} e^{-(x/\lambda)^h}, \; x \geq 0, \tag{2}$$

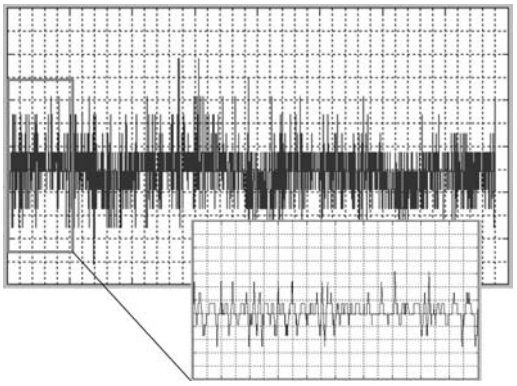

Figure 4. Half an hour original signal example, with a zoom-in of part in the insert.

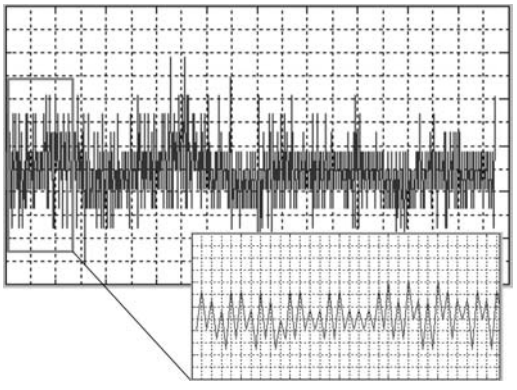

Figure 5. Filtered signal of the original in Figure 4, with a zoom-in of part in the insert.

where $h > 0$ is the shape parameter and $\lambda > 0$ is the scale parameter of the distribution.

It is seen that the Rayleigh distribution can be represented also by Equation 2, if the shape parameter is $h = 2$.

The statistical hypothesis (i.e. an acceptability of an assumed statistical distribution) is checked further using the Chi-square (χ^2) criterion. For more details on statistical distributions and their acceptance the reader is referred to handbooks on statistics.

The strain range cycles (observations) resulting from the measurements were fitted to both the Rayleigh and Weibull probability density functions. An example of the fitting is given in Figure 6 where the observed data is shown as a histogram vs. a theoretical distribution. Certain statistical value of the strain range, corresponding to a probability of exceedance equal to 10^{-3}, was derived from the corresponding distribution. This statistical value is of importance here for comparison purposes, because in the fatigue calculation procedure it is used for reconstruction of (local) stress ranges in the Rayleigh distribution before the fatigue damage can be calculated. Using the value derived from the nominal strain measurements, a separation of the strain range corresponding

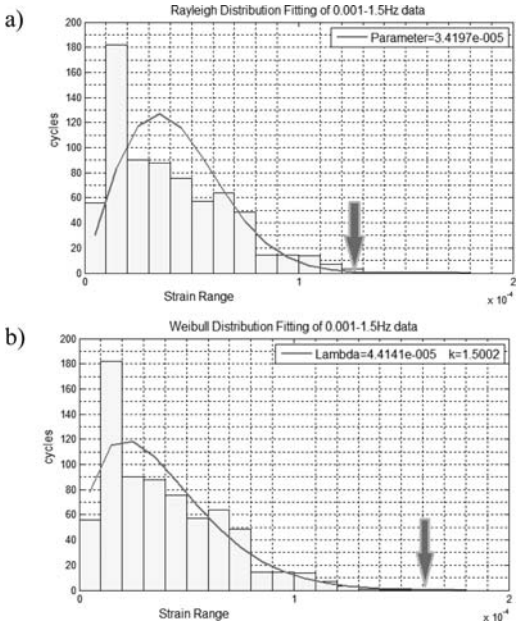

Figure 6. An example of the fitting of the strain range cycles (observations) in a half-hour measurement term in the (a) Rayleigh and (b) Weibull distributions. Bars correspond to the measured data and form a histogram, lines – to theoretical distribution. Arrows point at the strain range value corresponding to the 10^{-3} probability of exceedance.

to different member forces (axial load, in-plane and out-of-plane bending moment) was performed, for further comparison with nominal load conditions applied in calculations.

5 RESULTS AND DISCUSSION

5.1 *Weibull vs. Rayleigh*

Both nominal and local strain ranges resulting from the measurements were checked for statistical distribution. It appeared that the observed nominal strain ranges in both braces can be fitted with Rayleigh distribution. The significance value with which the statistical hypothesis is accepted following a χ^2-criterion is reasonably high, being in between 0.015 and 0.202 as averaged per strain gauge. It should be noted that for engineering application a 0.05 significance threshold is normally accepted, the higher the value the better the fit. By loosening the criterion the significance threshold for statistical hypothesis acceptance/rejection is lowered, as well as the quality of fitting.

The local (near the weld toe) strain ranges, resulting from the measurements, correspond mostly to the Weibull distribution with different parameters of h, see Table 2. It should be noted that the measurement data of the outside locations (F2, F3, F4) has a shape parameter close to unity ($h = 0.9 \ldots 1.4$). The data of the inside locations (E6, E7) is fitted with $h \geq 2$, while the shape parameter for the crown toe locations (E5, G5), though being lower than 2, shows a variation in tendency between the Rayleigh and Weibull distributions. The corresponding significance (averaged through measurement terms per gauge) of the Rayleigh distribution hypothesis acceptance at inside locations is 0.016 and 0.069. For data of other local strain gauges the Weibull distribution fitting is accepted with the significance value in between 0.016 and 0.516, except for outside gauges D3 and D4, where very poor fitting is observed. The reason behind that is yet to be investigated and is outside the scope of this paper.

Table 2. Weibull shape parameter for local strain ranges.

Term	D3	D4	E5	E6	E7	F1	F2	F3	F4	G5
1	1.0	1.0	1.4	2.0	2.1	1.3	1.2	1.3	1.2	1.7
2	1.0	1.1	1.0	2.0	2.1	1.3	1.2	1.4	1.4	1.4
3	1.0	1.0	1.0	2.0	2.1	1.4	1.3	1.4	1.3	1.3
4	1.0	1.0	1.6	2.0	2.1	1.3	1.3	1.3	1.3	1.8
5	1.0	1.1	1.6	2.0	2.2	1.3	1.2	1.3	1.3	1.8
6	1.1	1.1	1.7	2.1	2.3	1.3	1.4	1.3	1.3	1.3
7	1.1	1.2	1.7	2.2	2.4	1.4	1.4	1.4	1.4	0.8
8	1.2	1.2	1.5	2.1	2.3	1.3	1.4	1.4	1.3	0.7
9	1.1	1.2	1.3	2.1	2.4	1.4	1.4	1.4	1.4	1.1
10	1.1	1.2	1.6	2.3	2.5	1.3	1.4	1.4	1.3	1.1
11	1.1	1.2	1.7	2.3	2.7	1.3	1.3	1.4	1.3	1.2
12	1.2	1.3	1.7	2.2	2.5	1.4	1.4	1.4	1.4	1.3
13	1.1	1.1	0.9	2.4	2.5	1.3	1.3	1.3	1.3	2.0
14	1.2	1.2	0.9	2.4	2.6	1.3	1.4	1.4	1.4	1.8
15	1.1	1.1	0.9	2.4	2.4	1.1	1.2	1.2	1.1	1.5

5.2 *Hydrodynamic and pipe load components*

As described above, the total load on a stinger consists of two major components: hydrodynamic (HD) and pipe (or roller box) load (RB). In order to approach better comparison between the measured and estimated data, the RB and HD load ratio is demonstrated here based on intermediate results in stinger fatigue assessment for a shallow water project. Local stress ranges in both braces, A and B, at 90° wave heading without wave spreading are considered. It appeared that the local stress ranges RB/HD ratio is 0.56 and 0.67 for braces A and B, respectively. This means that the vertical brace (B) is more influenced by pipe load than diagonal brace (A) and that the pipe load component is roughly half the hydrodynamic component, at least for a considered wave heading, stinger configuration and typical shallow water pipe lay project. An example of the load components contribution to the total load is shown in Figure 7 for brace A.

5.3 *Wave spreading effect*

The data obtained from measurements is influenced by wave spreading, naturally inherent in the sea environment. In the fatigue estimation wave spreading is accounted for, and the effect thereof is shown here for the considered K-joint. The effect of wave spreading on

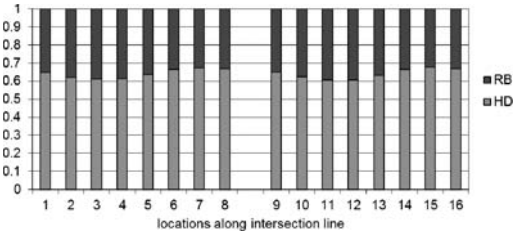

Figure 7. HD and RB load contributions to the local stress ranges of brace A. Positions 1 and 9 are crown toe, 3, 7, 11 and 15 – saddle, 5 and 13 – crown heel; 1 thru 8 is chord side, 9 thru 16 – brace side.

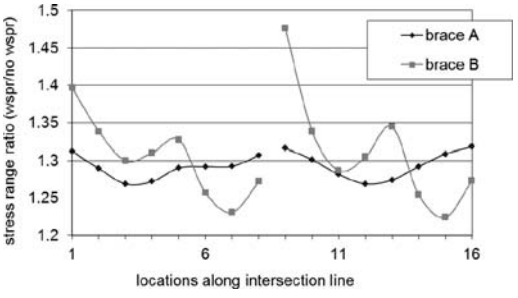

Figure 8. Wave spreading effect around the mean value of 90° for the stress ranges along the intersection line. Positions 1 thru 16 see in Figures 3 and 7, and Table 1.

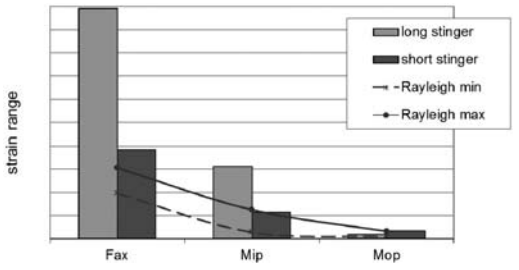

Figure 9. Comparison of estimated and measured nominal strain ranges in brace A represented by the components from member forces.

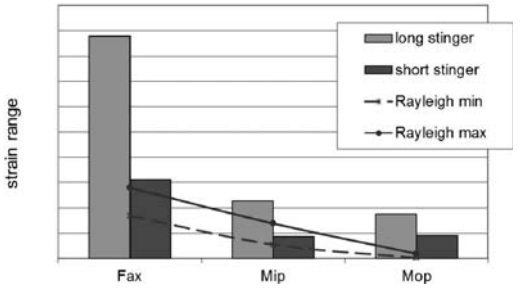

Figure 10. Comparison of estimated and measured nominal strain ranges in brace B represented by the components from member forces.

both braces weld toes locations, along the intersection line for a 90° wave heading, is given in Figure 8.

The effect is presented here by the ratio of estimated stress ranges, with wave spreading and without wave spreading, in the sea state of $H_S = 1$ m and $T_Z = 8.5$ s. For the considered locations the effect is not the same. It is seen that the vertical brace (B) is more influenced by wave spreading, while for the diagonal brace (A) the wave spreading effect can be averaged along the intersection line giving a value of approximately 1.3. This means that for the certain wave heading (90°) considered here, accounting for the wave spreading effect increases the estimated local stress ranges for the diagonal brace by 30% on average. Other main wave headings might have another ratio. It should be also noted that this effect is highly dependent on vessel dynamics, and cannot be directly applied to a stinger at other pipe layers. It is demonstrated here only for the purpose of further comparison with measurement data.

5.4 *Comparison with estimated values*

For a comparison of the measured and estimated data, the following data were available from a fatigue estimation routine for a typical shallow water pipe lay project and a stinger in full design length (long stinger): combined (hydrodynamic and pipe) load, $\theta = 90°$ with wave spreading, $H_S = 2.5$ m and $T_Z = 8.5$ s. Additional calculations were performed for the stinger in the configuration of the pipe lay project at the time of the measurements (short stinger), however, due to time limitations, this was only done for the hydrodynamic load component, 90° wave heading without wave spreading, and the same H_S and T_Z as above. Assuming that the effect of wave spreading and the RB load component is the same as for the long stinger, the stress ranges obtained for the short stinger were increased by 30% for wave spreading effect and by 56% and 67% for the RB load contribution. Both effects are shown in previous sections for braces A and B considered here.

Nominal strain ranges from axial force (F_{AX}), in-plane (M_{IP}) and out-of-plane (M_{OP}) bending moments in braces A and B are shown in Figures 9 and 10, respectively. Data from both estimates (long and short stinger configurations) are given in comparison with the range of statistical values reconstructed from the measured data. Rayleigh min and max values in Figures 9 and 10 refer to the minimum and maximum of the statistical strain range values over the considered measurement terms. It is seen that all nominal strain components are lower than those estimated in both short and long stingers, except for out-of plane bending moment strain in brace A, and in-plane bending moment strain in brace B. In brace A the out-of-plane bending moment nominal strain component is higher than that used for fatigue assessment (long stinger). However considering that it is very small, being at the resolution limit of the strain gauges this component

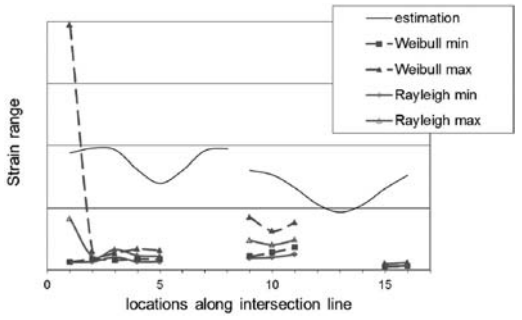

Figure 11. Comparison of local strain ranges at brace A used for fatigue analysis with measured values (represented by different distributions), for locations 1 thru 16 in Figures 3 and 7, and Table 1.

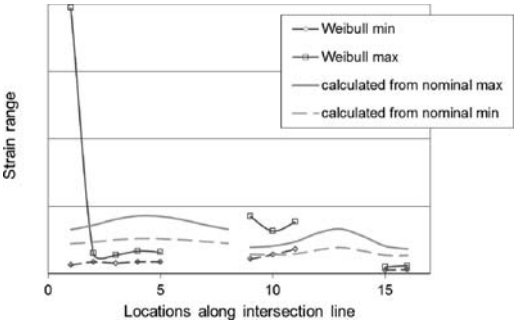

Figure 12. Comparison of local strain ranges estimated from nominal measured values in brace A with local strain ranges from measurements represented by Weibull distribution, for locations 1 thru 16 see in Figures 3 and 7, and Table 1.

will not affect the total strain value much. In brace B, the maximum value of the in-plane bending moment nominal strain component appeared to be slightly higher than estimated for the short stinger, most probably indicating that one or both of the assumptions speculated in the above (wave spreading and RB load effect) might be inaccurate. It should be noted however that the value is far smaller than those taken in fatigue assessment of the joint (long stinger).

A local strain ranges comparison for brace A is given in Figure 11. Rayleigh/Weibull min and max values in Figure 11 refer to the minimum and maximum of the corresponding statistical strain range values, over the considered measurement terms. From the available measurement data it is seen that a wider data spreading corresponds to the crown toe point. It is seen that whatever distribution is chosen for data fitting, most of the measured strain ranges are lower than those taken for fatigue estimation, at the considered locations at the weld toes. The only exception is observed in one measurement term (the terms are not distinguished in Figure 11), where the statistical strain range value corresponding to Weibull distribution at the crown toe chord side location (point 1 in Fig. 11) is twice as high as the estimated strain range used in the joint fatigue assessment. The only difference with other measured data is the lowest shape parameter value ($h = 0.65$), see term 8 and strain gauge G5 in Table 2. In order to figure out the reason for the exception, more information is necessary on vessel movements, which is not available at the moment.

Using the measured nominal strain ranges, the ranges of axial force, in-plane bending moment and out-of-plane bending moment for braces A and B, in their statistical representation, were re-constructed. From these forces and using the parametrical equations for SCFs in an unbalanced K-joint, the local strain ranges were calculated and compared with the measured local strain ranges (Fig. 12). From such a comparison one can evaluate if the procedure used for local stress calculation in fatigue assessment corresponds to reality. It seems that, for most of the points along the weld, the method is conservative. However, this conclusion might not be the same for the crown toe on both the chord and brace sides, and for outside locations on the brace side. It should be noted that for those locations the poorest fit occurred, and the number of cycles from the Rainflow procedure was about twice as high as in other locations. This means that there is some other effect on the local strain, in addition to strain rise because of the structural SCFs. This effect is not traceable in the available data and, in order to be resolved, more measurements need to be done.

6 SUMMARY AND CONCLUSIONS

Measurements of the strain from a K-joint in a stinger structure, during a shallow water pipe lay project, have been analyzed herein and compared with the estimated data from fatigue analysis for environmental conditions applicable during the measurement period. On the basis of estimated stress ranges, the contributions of hydrodynamic and pipe load components to local stress range are shown, as well as the effect of wave spreading around the considered main wave heading, in a representative shallow water project for a particular pipe lay vessel.

The measured data was statistically processed and fitted by Rayleigh and Weibull distributions. It was seen that a Rayleigh distribution can be considered acceptable for nominal strain range, while measurements at locations near the weld toes showed a tendency to Weibull distribution. The strain ranges used in the comparison analysis were based on the statistical values corresponding to 10^{-3} probability of exceedance, and only for those locations for which the measurement data was available.

Nominal strain ranges appear to be generally lower than those used in the fatigue assessment, except for out-of-plane bending moment strain ranges in brace A. Considering that the measured values of this strain range are on the resolution limit of the strain gauges, and their contribution to the total strain is marginal

in comparison with axial force and in-plane bending moment strains, this difference can be considered negligible. In a comparison of nominal strain ranges in brace B, the measured in-plane bending moment strain range is slightly higher than the estimated value. It should be noted that the calculated values were obtained under the assumptions for a pipeline load (RB) contribution corresponding to a longer stinger, heavier pipe and much larger water depth, which made the load conditions in the estimation more severe than during the measurements. In addition, the measured value is far smaller than those taken in the fatigue assessment of the joint (long stinger). Therefore, there is confidence in the conclusion derived for nominal stresses and strains in both braces: the measured values are lower than calculated strain ranges.

The statistically processed measured data at local points was directly compared with the corresponding strain range values used in the stinger joint fatigue estimation. The measured strain ranges appeared to be generally below the estimated values, except for the crown toe chord side location in one of the measurement intervals, which needs further investigation.

In order to evaluate the procedure accepted for estimation of local stresses based on member forces and corresponding (parametrical) SCFs, the local stresses at the weld toes were calculated following this procedure using the measured nominal strain ranges at both braces. It appeared that the procedure is conservative for most of the locations nearby the weld, except for the crown toe and close to the crown toe outside locations on the brace side. At these points the measured values are higher than estimated from nominal measured values. It is suggested that there is some unaccounted for (local) effect at these gauge positions. That is, however, not possible to trace in the available data.

To conclude:

- statistical distribution of stress/strain ranges may not be necessarily Rayleigh and the effect of the distribution on estimated fatigue damage has to be further investigated;
- nominal measured strain ranges are within the expected range, at least for the sea conditions encountered during the measurements;
- local strain ranges measured at some locations are higher than those used in the fatigue assessment and more measurements are advised for further validation of the fatigue damage estimation procedure, in different sea states and vessel operational conditions.

REFERENCES

DNV-RP-C203. 2008. *DNV Recommended Practice DNV-RP-C203. Fatigue design of offshore steel structures. April 2008*. Høvik: DNV.

DNV-RP-C205. 2007. *DNV Recommended Practice DNV-RP-C205. Environmental conditions and environmental loads. April 2007.* Høvik: DNV.

Ermolaeva, N., Yu, Y. & Zhao, L. 2010. Design and fatigue assessment of a stinger. In Young (ed.), *Tubular Structures XIII*; *Proc. intern. symp., Hong Kong, 15–17 December 2010*. Rotterdam: Balkema. 547–555.

Journeé, J.M.J. & Massie, W.W. 2001. *Offshore Hydrodynamics*. 1st Edition, Delft: Delft University of Technology.

Matsuishi, M. & Endo, T. 1968. Fatigue of metals subjected to varying stress. *Proceedings of the Kyushu Branch of Japan Society of Mechanical Engineers*: 37–40.

Palmer, A.C. & King, R.A. 2008. *Subsea Pipeline Engineering*. 2nd Edition. Tulsa: PennWell.

Wardenier, J. 2001. *Hollow Sections in Structural Applications*. 2nd Edition: CIDECT.

Tubular Structures XIV – Gardner (Ed.)
© 2012 Taylor & Francis Group, London, ISBN 978-0-415-62137-3

Lessons learned from testing of tubular steel joints after 30 year in service

Å. Pedersen & P. Decosemaeker
Total Exploration Norge

M. Lefranc
FORCE Technology, Norway

ABSTRACT: Offshore oil industry is a large user of steel structures. In particular the structure supporting the equipment is very often built as a space frame steel structure currently called jacket.

Those structures, located offshore, are subjected to the static load from the equipment placed on the deck and the repetitive action of the environment loadings, also the wind, the current and the waves.

Frigg field is a gas field located in the North Sea and operated by Total. The platforms have been installed in the early 70's and after 30 year exploitation the field has been closed in 2004 and the platforms removed.

In the case of steel structures such as the jackets, it gives the opportunity to study the damages and the alteration of the material after it has been exposed to real loads for a long time.

The investigations focus into three aspects:

1. Inspection: Comparison between the inspection performed in situ (Offshore under water), the non destructive testing performed onshore and the destructive test.
2. Analysis method: Comparison between calculated hot spot damages and findings.
3. Material: Testing of the material: strength, residual fatigue of joints, toughness and comparison with the original data.

The test program has been finalized and a total overview of the findings is presented in this paper.

Conclusive remarks and lessons learned regarding welding quality related to inspection, material deteriorations and fatigue will be presented.

1 INTRODUCTION

The Frigg field has been decommissioned in the years 2004 to 2009.

The three jackets which were part of the field development have been brought to shore at the Stord Yard on the west coast of Norway.

A study of those structures has been initiated by Total and awarded to FORCE Technology.

The aim of the study is to learn about the effects on the structure and its components of the wave action during the life of the platforms.

During the service time of the platforms the steel components have been subject to repetitive loadings, and high stresses at the hotspots. Inspection and testing of those components may give information on the long term behaviour of the steel material and also an indication of the suitability of the design and fabrication rules.

Selected nodes of the jackets have been inspected visually and by NDT methods. Some pieces of those nodes have been cut out and inspected further in laboratory.

2 DESCRIPTION OF JACKETS

A view of the Frigg field is shown in figure 1. The field has been installed in the early 70's and dismantled in the last years. The last items have been shipped to shore summer 2009.

The DP1, DP2 and QP jackets were situated on the Norwegian continental shelf of the North Sea in the Frigg Field. The platforms were used for drilling, treatment of gas and condensates and living quarter.

The jacket DP1 (Figure 2) was installed in 1975.

During the launching operation some of the buoyancy tank collapsed and the jacket touch the ground leading to severe damages. The jacket was never piled and used. It has been resting vertically on the sea bottom in 35 years.

The jacket DP2 (figure 3) was installed 2 years later as a replacement for the DP1.

The design has been slightly modified compared to the one used in DP1: X braces on the sides have been changed to V braces.

Note that the conductor frames arrangement has been kept almost identical. Large cracks have been

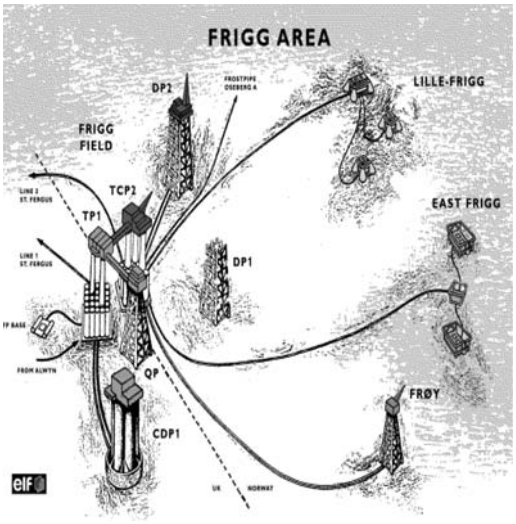

Figure 1. View of Frigg field.

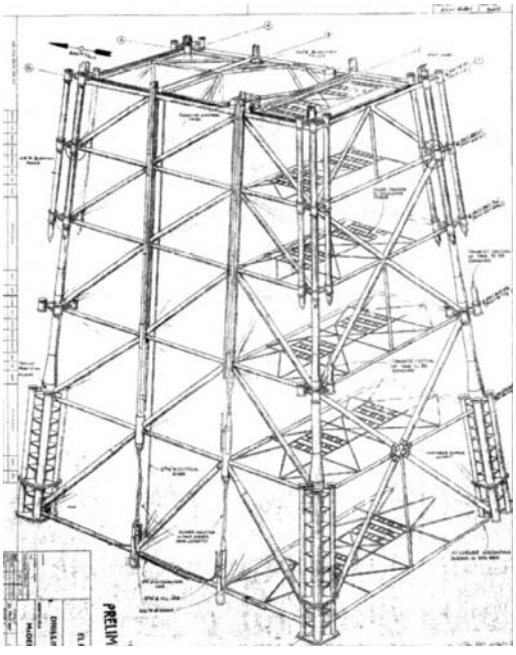

Figure 2. General layout drawing of DP1 jacket.

found quite early after installation in two nodes connecting the frame to the main steel at the first level under the sea surface. Those two nodes have been repaired by grouted clamps. After this repair no further cracking in this area has been observed. Also it appears that the fatigue damage has been reduced after the installation of the conductors.

The QP jacket (Figure 3) is supporting the living quarter. It is a lighter structure supporting fewer appurtenances.

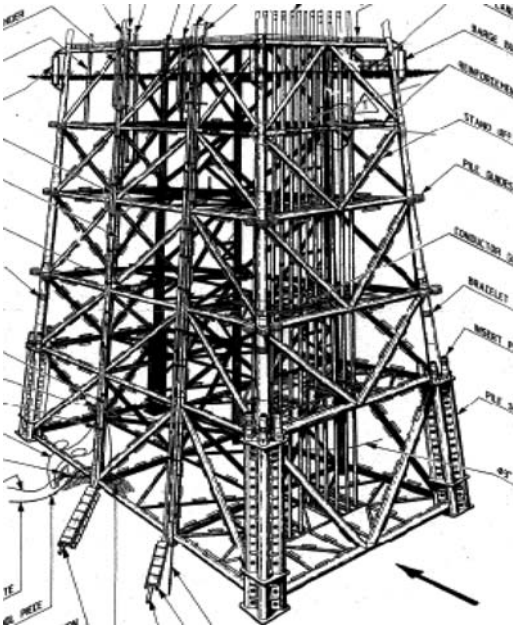

Figure 3. General layout drawing of DP2 jacket.

Table 1. Key figures of the Jackets.

	DP1	DP2	QP
Weight	6480 t	8000 t	3800 t
Water depth	104 m	100 m	104 m
Top Dimension	48 m × 25 m	47.8 m × 24.8 m	26.6 m × 26.6 m
Bottom Dimension	61.6 m × 43.3 m	61.9 m × 43.7 m	54.8 m × 54.8 m

However some nodes have a relatively complex geometry with unusual small angles between the incoming braces which may lead to fatigue damage.

Table 1 presents the key figures of the jackets.

More detailed information is given in reference 1.

The red circles and arrows indicate the locations of the selected nodes.

DP1: two corner nodes just below the sea level.

DP2: one corner node, one on launch frame and two nodes repaired with grout.

QP: two corner nodes, one T node, one V-node, one complex node at launch frame.

Pictures 5 (a to d) show some of the selected nodes.

3 INSPECTION

Both visual inspection and NDT with Eddy current test have been performed.

3.1 *Visual inspection*

All available material on the nodes has been visual inspected with special focus on welds and HAZ.

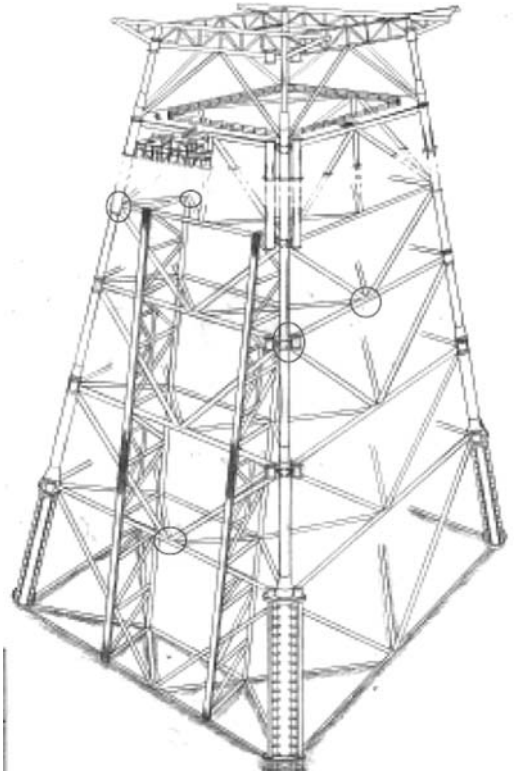

Figure 4. Iso view of QP Jacket.

Figure 5a. Nodes DP1.

Corrosion and pitting where observed on several external and internal welds.

The nodes have been stored onshore outdoor for several months; corrosion may have started or increased during this time.

Example of corroded welds can be seen on photo Figure 6.

The visual inspection shows some bad workmanship as shown in figure 7(a,b,c).

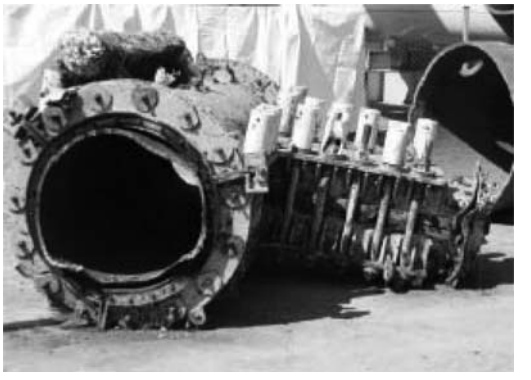

Figure 5b. Repaired node DP2.

Figure 5c. Complexe joint QP.

Figure 5d. Launch frame node DP2.

3.2 *Eddy current inspection*

All available welds were manually scanned with use of Locator II Eddy Current digital equipment together with standard welding probe and standard Hocking Steel Calibration block.

In addition to the welds the HAZ and parent material 5 cm to each side of weld where also included in this Eddy Current Inspection.

The inspection of the DP2 nodes has revealed one 300 mm long crack in the launch node. For the grout

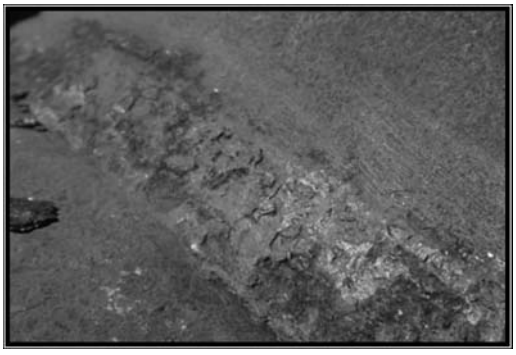

Figure 6. Details of weld corrosion DP1 Jacket.

Figure 7a. Use of electrode wires in the welding groove.

Figure 7b. Undercut and pitting.

Figure 7c. Hanging root.

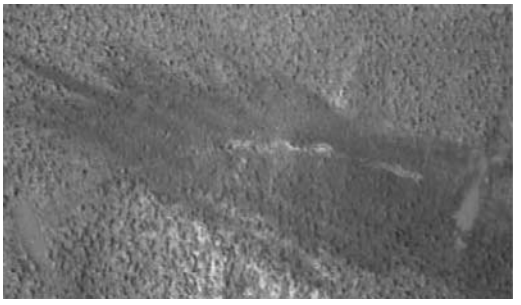

Figure 8. Crack in the grout repair node: no indication of growth since reparation.

repaired nodes, the cracks identified previously seem not to have grown (See picture 8).

For the QP platform cracks have been found only in the corner node: 45 mm long crack indication between plate and upper run of weld and 20 mm long crack indication between weld and base metal. The locations are related to secondary member connections: sharp angle brace to launch frame and connection of a pile guide.

3.3 *Wall thickness measuring*

All parts of the structure wall thickness measurement where carried out using Krautkramer USM35 digital equipment together with single crystal probe and steel step wedge calibration block.

This measurement was done to verify and compare design drawings with installed steel plates.

In general the wall thicknesses were larger than the nominal from drawing, in a range of 5% to 10%.

4 DESTRUCTIVE TESTING

Macro-section examination, microstructure examination, tensile strength, impact testing, hysteresis testing and fatigue tests have been performed by Force Technology laboratory in Denmark.

The following tests have been performed:

- Tensile tests: 16
- Charpy tests: 9
- Cross section examination: 14
- Micro structure examination: 3
- Chemistry: 1
- Hysteresis tests: 5
- Fatigue test: 6
- Bolt pretension: 4

4.1 *Macro-section examination*

The aim of this destructive test is to evaluate the weld quality and especially at the root. The majority of the weld performed in the 3 jackets are one sided. Exceptions are the main nodes on the launch frame in DP2.

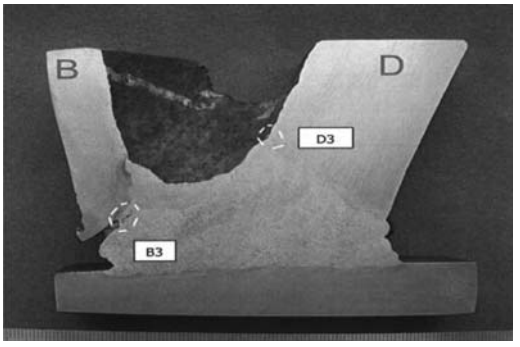

Figure 9a. Macro-section.

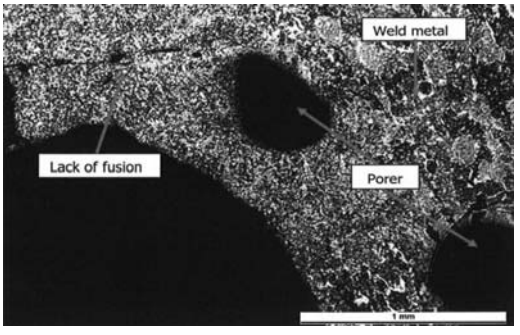

Figure 9b. Macro sample at position B3.

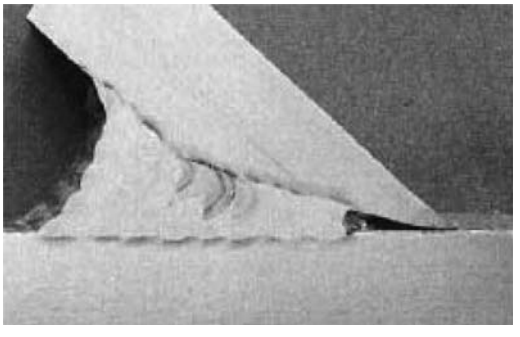

Figure 9c. Macro sample.

The macro-sections have been selected at hot spot locations and where the geometry was difficult: shape angles, thick plate thickness, overlap or connections of three braces.

The investigation does not reveal significant differences between the three jackets.

The welds show a lot of defect especially at the root: lack of fusion, pores, and inclusions.

However none of the observed defects has lead to fatigue damage crack.

Some examples of macro-sections are reproduced in the followings pictures 9 (a to e).

Figure 9d. Macro sample.

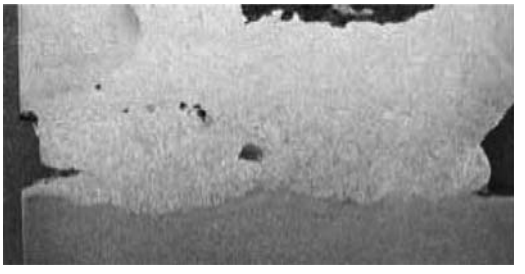

Figure 9e. Macro-section.

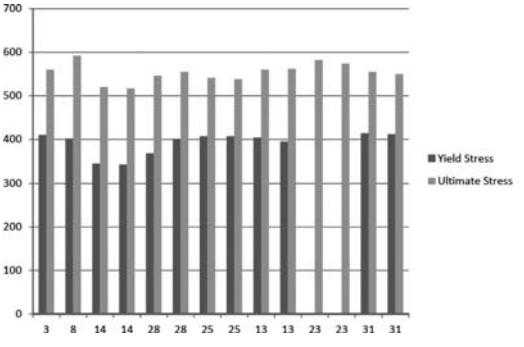

Figure 10. Tensile test, strength.

4.2 *Material tensile test*

The aim of those tests series is to investigate a potential alteration of the mechanical properties of the steel due to repetitive loading and local stress above yielding.

The coupons have been selected from different nodes at hot spot locations in the parent material and in the weld. The results are shown in figure 10.

The elongation of the specimens is presented in figure 11.

From those tests the following remarks may be done:

1. The tensile tests shows good consistency through all type of geometry and structures
2. The material tested is in accordance with a 355 MPA steel quality.

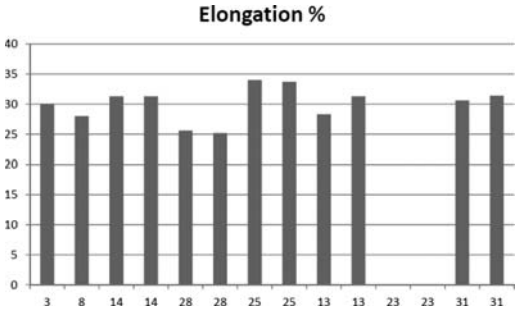

Figure 11. Tensile test, elongation.

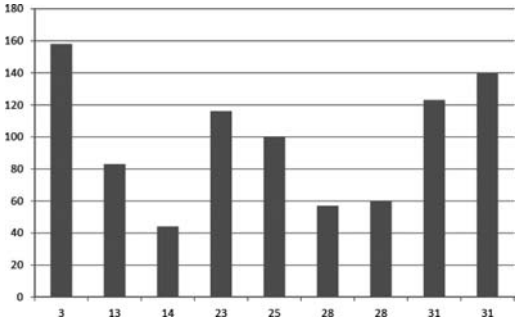

Figure 12. Charpy test.

3. The weld material shows an higher strength compared to parent material.
4. No alteration of the strength of the material can be noted
5. The elongation of the material is above 24%: also no or insignificant effect of the repetitive loading and local yielding of the material.

4.3 *Charpy test*

The Charpy value has been measured for the parent material, the parent material at hot spot locations and for the welded material.

All tests have been performed at −40°C. All given value is an average of 3 tested coupons.

The results show a larger scatter compared to the tensile test results.

The tests in weld material are the tests items 23, 28 and 31. Those values are not different from the others.

The test item 3 is from jacket DP1. The test items 23, 25 and 31 are from DP2. Those two jackets were fabricated at the same yard. The results of those tests are consistent and vary from 100 J to 158 J: also very good values.

However the low value from items 13, 14 and 28, are from the QP which was fabricated at a different yard.

It may therefore be concluded that the variation and the scatter of the results are due to different fabrication procedure for the welding.

Table 2. Results from hysteresis tests.

Item	Node location	Coupon description	Permanent strain
35	QP	In weld	0,1%
34	QP	In weld	0,1%
34	QP	Parent material	0,5%
29	DP2	Parent material underneath weld	0,5%
20	QP	weld	0,1%

4.4 *Hysteresis test*

Hysteresis testing has been performed for 4 nodes at 5 locations. Three tests have been performed in the weld material and two in the parent material adjacent. The tests have been performed as follow:

1. Coupons have been stretch to 7 % elongation
2. The force has been released.
3. 7% elongation has been repeated 10 times
4. The reminding plastic elongation has been measured.

The coupons have been selected from locations where welds are difficult and are subjected to high stresses during the life of the structures. Therefore they are the most promising to reveal any effect on the material.

It is to be noted that no one of the coupons did brake during the test.

No sign of aging for the material may be shown.

4.5 *Fatigue test*

The coupons have been selected at the same locations that the one for the hysteresis tests.

Two of the tests have been stopped before brake of the specimens. The stress range used in the tests was therefore increased to 300 MPa.

In the figure 13 the results are compared with the SN curves B1 (140) and B2 (160). Those curves are considered the most representative since it was not possible to perform fatigue test for a nodes or for a welded detail.

The results of the tests confirm that the fatigue behavior of the material is not changed during the life time of the platform.

4.6 *Measurement of bolt pretension*

An interesting issue is to establish if the pre-tension of the bolts closing the clamps is still unchanged after 25 years in service. The adopted procedure was to measure the variation of strain when the bolts are cut by a torch. However this will induce warm in the material and may damage the strain gauges. In addition the

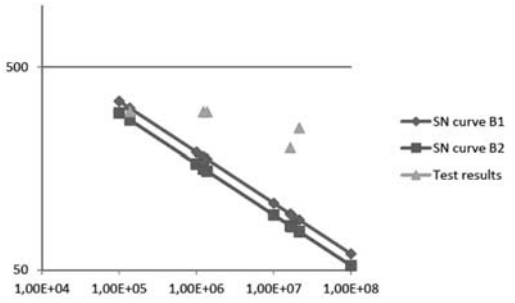

Figure 13. Comparison of fatigue results with SN curves.

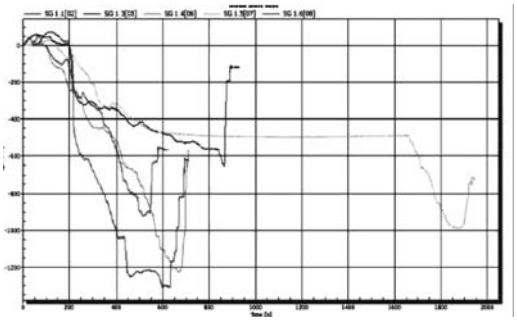

Figure 14. Pre-tension release test on bolts in clamp.

release of the pre-tension force may be sudden and cause damages.

Therefore the procedure was carefully established and a gentile and slow cut operation was adopted.

Six bolts were instrumented. Of those six, four did succeed and gave reliable and consistent results.

The graphs in figure 14 show the output of the measurement.

It appears that the measured pretension is about 60 to 40% of the yield of the bolts. This value is slightly less than the standard pre-tension value of 60%. This relatively low pre-tension may be due to the repetitive loading on the structure or due to incorrect installation.

5 CONCLUSION

From the investigation performed during this campaign some general finding may be done.

The inspection of the nodes at shore did not reveal major cracks which were not identified during the offshore inspection: Only one long crack was identified in addition to some minor indications.

From the inspection and the macro-sections it may be stated that the fabrication quality does vary significantly between the tree structures and between the locations. Many of the macro-sections shows undercut at the root of the weld together with inclusions, pores and lack of fusion.

In the contrary the toes of the welds have been found to be well executed.

The weld type used has been mostly one sided. However at critical locations as for example the diagonals welds to leg of node DP2 double sided welds have been performed.

No one of the specimen investigated shows any sign of fatigue damage crack, even at fatigue sensitive locations with very bad workmanship.

The material has been identified to be in accordance to the fabrication specification. Further toughness, yield and ultimate strength have been tested in parent material and in the weld material to identify a possible deterioration of the mechanical properties.

All specimens have shown a high toughness, and the tensile tests are identical to a new material. No sign of effect of successive yielding on the specimens was found.

Finally the resistance to repetitive loadings has been checked.

Hysteresis test consists of ten cycles of 7% elongation of a specimen. The remaining permanent strain of the specimen was measured to be maximum 0.5%. But no specimen did fail.

Fatigue test has been performed on material taken in hot spot zone of the nodes. The number of cycles to failure has been compared to the SN curve for non welded material. The results show values above this curve.

From the tests it may be concluded that the material has not change its ability to support cyclic loading.

The main conclusion of this study is that the material and the status of the structure are in general as expected. No fatigue crack has started from the weld root even when the geometry of the weld root was very bad.

The material may still be subjected to large elongation in the plastic range in as welded condition.

ACKNOWLEDGEMENT

The Authors thank the yard Aker Stord to have made possible the investigation by adapting the dismantlement schedule to the request from the investigation team.

REFERENCES

Study of the damage on tubular steel structure after 30 years in service, Paper 102, ISTS XIII.

Tubular Structures XIV – Gardner (Ed.)
© 2012 Taylor & Francis Group, London, ISBN 978-0-415-62137-3

Structural performance of TS590 high-strength steel welded tubular joints under extreme bending loading

G.E. Varelis & S.A. Karamanos
Department of Mechanical Engineering, University of Thessaly, Volos, Greece

T. Papatheocharis & P.C. Perdikaris
Department of Civil Engineering, University of Thessaly, Volos, Greece

ABSTRACT: The present work examines the behavior of welded tubular connections made of high- strength steel and subjected to extreme loading conditions focusing on their low-cycle fatigue performance and highlighting the benefits of using high strength steel in structural tube applications. An experimental investigation of tubular X-joints made of high-strength steel is presented first. Experimental testing has been designed in order to examine the joint's behavior under out-of-plane monotonic and cyclic loads in loading levels exceeding the elastic limit of the joint. The second part of the work is numerical aimed at simulating numerically the experiments through a detailed finite element model in ABAQUS. The overall joint behavior and local phenomena at the weld toe are simulated and the numerical results are compared with the experimental measurements. Special attention is given on the evaluation of stress and strain fields at the connection "hot-spot" locations, which are compared with the values found in the literature. The results of this research effort are aimed at proposing static and low-cycle fatigue design methodologies for welded tubular connections made of high-strength steel.

1 INTRODUCTION

The present work examines the behavior of welded tubular connections made of high-strength steel, subjected to extreme loading conditions with emphasis on their low-cycle fatigue performance. It is part of a large European research effort on the structural behavior of tubular structures made of high-strength steel (grade equal or higher than 590 MPa).

The benefits of using high-strength steel on the static strength of welded tubular joints have been reported in a HSE report (HSE, 2004) through a JIP. Nevertheless, the fatigue performance of high-strength steel tubular joints has not been extensively examined. The existing design guidelines (e.g. CIDECT) focus on high-cycle fatigue design of tubular joints with steel grades up to 460 MPa, whereas only limited research effort concerns low-cycle fatigue performance of those joints (Baba et al. 1981, van der Vegte et al. 1989). Recently, in a series of papers, the low-cycle fatigue performance of tubular T-joints has been reported (Waalen & Berge 2005, Boge et al. 2007, Hochman et al. 2010). It should be noted that no experimental information is available for the low-cycle fatigue of tubular joints made of high-strength steel.

The experimental investigation consists of four (4) X-joints tested under monotonic and strong cyclic out-of-plane bending conditions at load levels well beyond the elastic regime. Together with the overall joint performance, local phenomena at the critical regions are monitored. The effect of the weld metal strength on the ultimate and fatigue capacity of the joints is investigated. Furthermore, numerical analyses are conducted, using rigorous finite element simulations of the welded tubular joint, with emphasis on the accurate simulation of the weld region. The numerical results are compared with the experimental measurements. Special attention is given to the evaluation of the stress and strain fields at the so-called "hot-spot" locations, in terms of the stress/strain concentration factors.

2 DESCRIPTION OF SPECIMENS AND EXPERIMENTAL SET-UP

Four X-joint tubular joint specimens are tested and analyzed under out-of-plane bending (OPB). The tubular joint configuration is shown in Figure 1. The steel tubes for the welded tubular joint, i.e. the chord and the two braces, have been provided by Tenaris Dalmine SpA, Dalmine, Italy. The tubes are seamless, and made of high-strength steel (TS590 grade) with a nominal yield stress of 590 MPa. The two braces are 7-inch-diameter CHS tubes (7.625 in or 193.7 mm) with 10 mm nominal wall thickness, whereas the chord is a 14-inch-diameter CHS tube (355.6 mm) with a nominal wall thickness equal to 12.5 mm. The welded specimens were manufactured by Stahlbau Pichler SpA, Bolzano, Italy. The welds has been performed

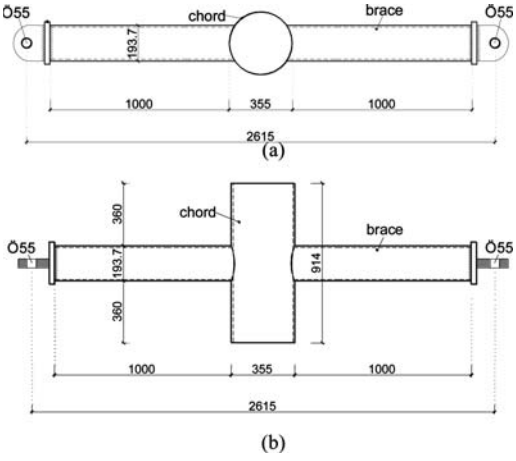

Figure 1. Specimen geometry for the OPB tests: (a) front view, (b) side view (dimensions in mm).

according to the general provisions of AWS D1.1 (AWS, 2004) and EN ISO 15609-1. Two different electrodes have been used for the welds, corresponding to Classes 55 and 79 (i.e. nominal yield strength of 550 MPa and 790 MPa respectively). The two electrodes are referred to as "weld A" and "weld B" respectively.

The experiments are conducted at the laboratory facilities of the Civil Engineering Department, at the University of Thessaly. The experimental set-up consists of a four-point bending loading configuration applied to the joint braces through a steel cross-beam, and appropriate wooden grips. Two special ball-joint hinges are used for connecting the cross-beam with the grips. Both ends of the X-joint specimen braces are hinged, using a double-hinge "roller" system that allows for horizontal movement of the two ends without introducing axial loading, while keeping the symmetry of the specimen set-up at the deformed configuration. The moment lever-arm created by this load-support set-up is 830 mm, and this is used in all calculations thereafter. Details of the overall geometry, loading system for the OPB tests are shown in Figure 2.

Thickness measurements have been conducted in several cross-sections, on the chord and braces to detect possible deviations from the nominal values (12.5 mm and 10 mm respectively). It was found that, despite some small variations of the thickness value around the cross-section of the tubes, the mean value for the chord thickness was measured equal to 12.49 mm, practically equal to the nominal value, while the mean measured thickness for the brace was measured equal to 10.27 mm, slightly greater than the nominal value.

The local strains at the critical parts of the joint were monitored through several strain gages on the top and bottom side of the joint. More specifically, uniaxial five-element strip gages are attached at the tension side of chord, at the weld toe area, in the hoop direction,

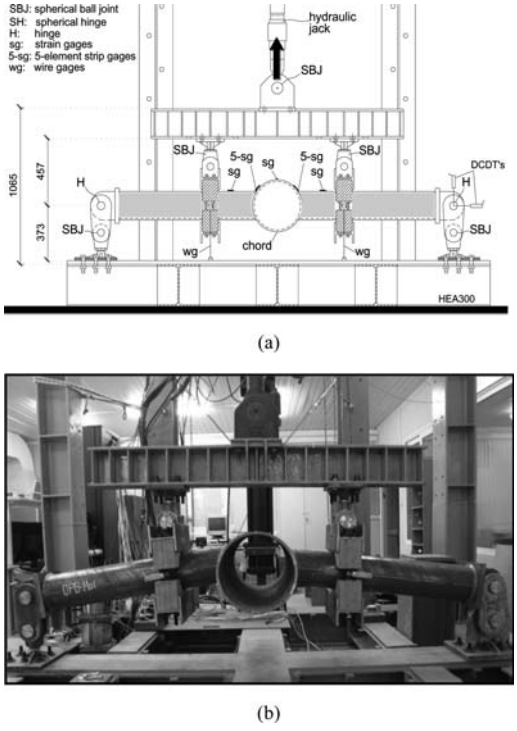

Figure 2. Test setup, loading system for the out-of-plane bending tests: (a) schematic representation (b) deformed specimen.

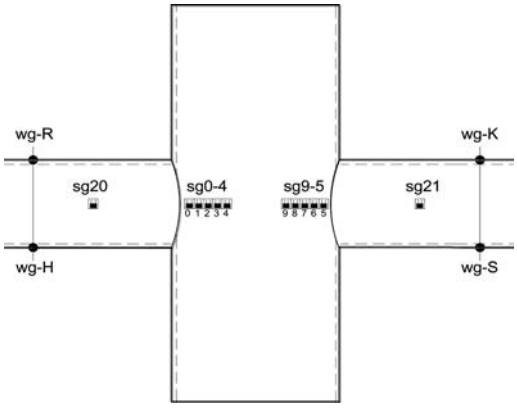

Figure 3. Strain gage location – specimen top side.

i.e. normal to the weld direction, as shown in Figure 3. The strain gage closest to the brace-chord connection area is located at a distance of 5 mm from the weld toe, which is in accordance with the provisions of CIDECT guidelines (CIDECT, 2001) to measure stress/strain concentrations due to the discontinuity of the weld. Moreover, four additional strain gages are placed at both braces (top and bottom side) to study the evolution local strains away from the connection area. Finally, four wire position transducers and DCDT's are used

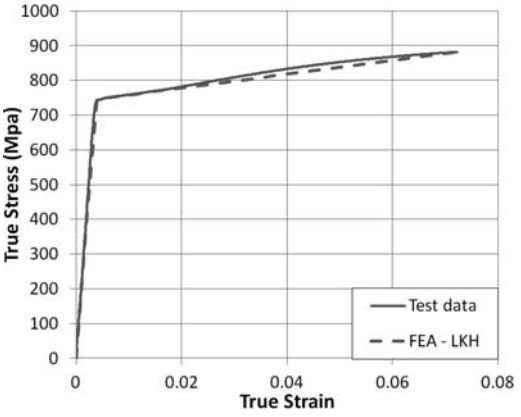

Figure 4. Uniaxial steel material stress-strain curve.

for recording the displacement at the location where the load is applied, and the displacement of the support, as shown in Figure 2. In Figure 3 the exact positioning of all measuring devices on the top side of the specimen is depicted.

The mechanical properties of the steel material have been determined through tensile tests on steel coupon specimens extracted by the tubes before the specimens are manufactured. The tests were conducted by CSM, Rome, Italy. It was found that the actual yield stress of the TS590 steel material is 746 MPa, significantly higher (26.4%) than the nominal value. The stress-strain curve exhibits a small plastic plateau up to 1.5% engineering strain, and the ultimate stress is equal to 821 MPa, reached at a strain of 7.5%. The corresponding material true stress-strain curve from tensile tests on steel coupon specimens is depicted in Figure 4. The mechanical properties of welds A and B have also been examined through tensile testing, by ITMA, Spain. It was found that the actual material properties of weld A material are 866 MPa and 900 MPa for the yield stress and the ultimate stress respectively, whereas the corresponding actual material properties of weld B material are 961 MPa and 1078 MPa. Both weld materials have values of yield and ultimate stress higher than those of the tube steel base material (746 MPa and 821 MPa), so that both welds can be considered as "overmatched". Moreover, fracture toughness tests were also conducted. The specimens examined using the weld A presented increased fracture toughness (136 kJ/m^2) compared to the specimens using the weld B (89 kJ/m^2). Finally, fatigue tests on specimens made of the TS590 material as well as specimens containing both types of welds were conducted in order to examine the effect of the weld on the fatigue performance. The resulting fatigue endurance limit (referring to 2×10^6 cycles) for the base material was found equal to 693 MPa, while the corresponding limits for the specimens using the weld A and B were found equal to 135 MPa and 98 MPa respectively.

Table 1. Summary of experimental results.

Specimen	Weld type	Moment (Max/Min)*	ΔM	N_f
T1	A	M (121.44/-)	–	–
T2	B	M (115.42/-)	–	–
T3	A	C (93.4/9.34)	84.06	240
T4	B	C (93.4/9.34)	84.06	200

* Moment (kNm), ΔM: Moment load difference (kNm), N_f : Number of cycles, M: Monotonic loading, C: Cyclic loading.

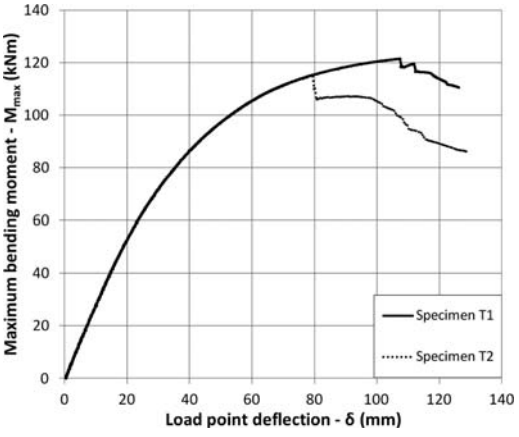

Figure 5. Monotonic OPB loading behavior until failure.

3 EXPERIMENTAL RESULTS

3.1 *Monotonic loading test*

To examine the ultimate capacity and the deformation capacity of the X-joints under consideration subjected to out-of-plane bending, two monotonic tests have been performed, one test for each weld conditions (A and B) named as specimen T1 and specimen T2 respectively (Table 1). The experimental results are presented in Figure 5 in terms of their applied moment – load displacement curves. The specimen with weld A conditions resisted a maximum bending moment equal to $M_{max} = 121.44$ kNm and failure occurred at a value of displacement equal to $\delta = 107.5$ mm. The specimen with weld B conditions exhibited a maximum bending resistance equal to $M_{max} = 115.42$ kNm, which is slightly lower (about 6 kNm) than the one of the previous specimen. The displacement at the maximum bending moment is equal to $\delta = 79.45$ mm, significantly lower than the corresponding displacement of the specimen with weld A conditions. Both specimens failed in the form of fracture at the weld saddle of the joint, on the chord side, as presented in Figure 6. The experimental results indicate that the lower the strength of the weld, the higher the bending capacity, in terms of both maximum moment and – most importantly – deformation capacity. This is in accordance with the fracture toughness test results for both weld types.

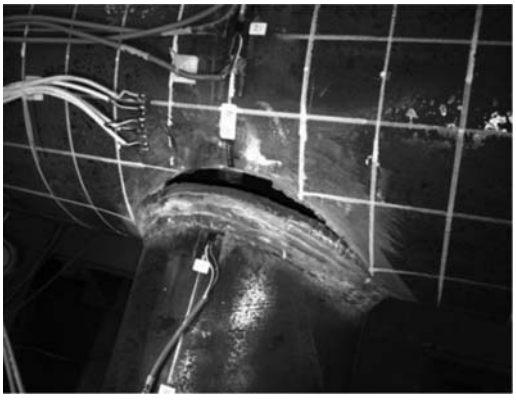

Figure 6. Cracked chord at the weld toe due to monotonic loading – specimen T1.

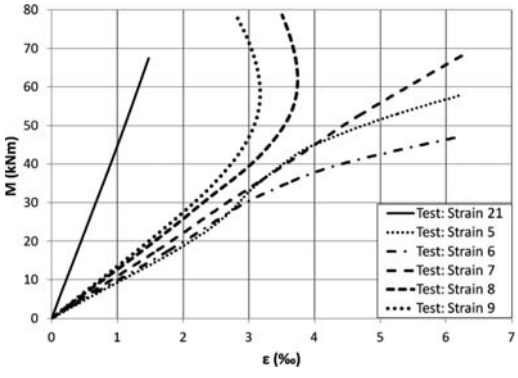

Figure 7. Strain evolution for increasing bending moment.

The evolution of strains at the vicinity of the weld toe on the chord part of the joint under increasing out-of-plane bending load, measured using the five-element strain gages of Figure 3, is depicted in Figure 7. In this figure, the measured value of longitudinal strain measured on the joint brace, away from the weld toe, at a location where the moment distribution is constant (strain gage 21) is also depicted. The strains near the weld toe are used to evaluate the strain concentration factor SNCF at the weld toe area. Based on the test measurements of Figure 7, two main observations can be made. First, for bending moment loading up to 20 kNm the joint deforms elastically, and a value of SNCF equal to 5.69 can be obtained using a linear extrapolation of the measured strains, as suggested by Romeijn (1994) and by the CIDECT No. 8 (2001) design guidelines for circular hollow section joints. The extrapolation of strains is shown in Figure 8.

In addition, when the tubular joint exceeds the elastic region, there is a strain relief in the hoop direction starting in a distance about equal to the thickness of the chord t_0 from the weld toe in the chord saddle area. This will be discussed in more detail in a following paragraph.

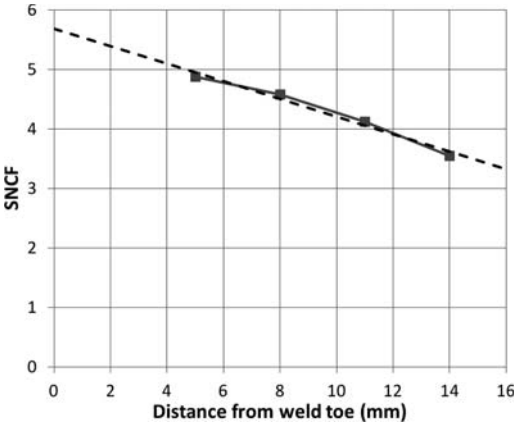

Figure 8. Experimental estimation of SNCF.

3.2 *Cyclic loading tests*

The cyclic behavior of the high-strength steel X-joints is experimentally investigated applying strong cyclic loading on two specimens. More specifically, one joint specimen for each weld condition (weld A/weld B welded joint) has been subjected to cyclic out-of-plane bending, until failure. In both experiments the same loading sequence has been followed; the joints are first subjected to monotonically increasing out-of-plane bending up to 100 kNm and subsequently to a cyclic out-of-plane bending loading sequence at load ratio $R = M_{min}/M_{max} = 0.1$ with $M_{max} = 93.4$ kNm. The moment-deflection diagram of the X-tubular joint with the weld A conditions indicates a rapid accumulation of deformations after the 180th loading cycle, as shown in the closed loops of Figure 9(a), and this is associated with significant degradation of joint resistance. The corresponding behavior of the specimen with the weld B conditions is shown in Figure 9(b). The specimen with weld A conditions failed after 240 loading cycles, while the specimen with weld B conditions under the same loading conditions failed after 200 cycles. Although the specimen with the weld B conditions showed a slightly lower fatigue resistance, its behavior was rather similar. Both failures occurred in the form of through-thickness cracking due to fatigue Figure 10, at the chord saddle location of the weld toe area, at the same location that occurred in the monotonic loading case, presented in Figure 6. Because of the relatively low number of cycles, the fatigue failure of the joints can be regarded within the low-cycle fatigue range. A summary of all the experimental results is presented in Table 1.

4 NUMERICAL SIMULATION

4.1 *Numerical modeling*

The numerical model used for the simulation of the experiment represents the actual dimensions of the welded joint. The weld geometry has been modeled

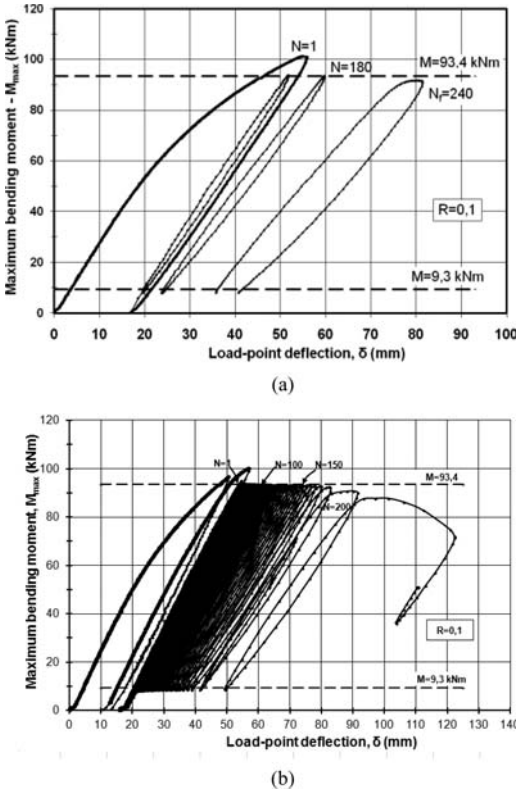

Figure 9. Maximum bending moment – load-point deflection curves: (a) specimen T3, (b) specimen T4.

Figure 10. Fatigue crack at the chord weld toe – specimen T3.

in detail, according to the provisions of the American Structural Welding Code AWS D1.1(AWS, 2004).

The model is developed in ABAQUS (Simulia, 2011) and uses 8-node, quadratic, reduced integration solid elements (C3D8R) for most of the chord, whereas 4-noded solid elements (C3D4) are used in the brace part and the weld region of the joint on the chord. Moreover, the mesh size is denser near the weld region in order to provide accuracy in the simulation results

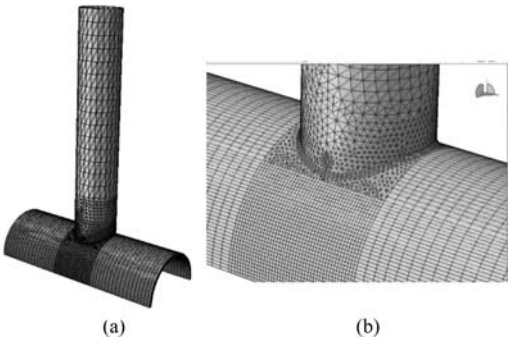

Figure 11. Numerical model developed: (a) General view (b) Weld region.

and time-effective simulations. Only half of the joint is modeled, taking advantage of symmetry and applying the appropriate symmetry conditions. The model is shown in Figure 11.

4.2 *Numerical results and comparison with experimental data*

The numerical results have been initially obtained using a material model of J_2 flow plasticity, accounting for large strains. For the purposes of the present analysis, linear kinematic hardening has been employed. The corresponding bilinear stress-strain curve is plotted in Figure 4, and compares fairly well with the uniaxial tensile test data. The joint geometry was modeled according to the measured dimensions of the tubular members, which are very close to the nominal ones, considering a uniform thickness of the chord and the brace. As displayed in Figure 12, the experimental measurements can be numerically reproduced quite accurately for monotonic and cyclic loading conditions.

It is worth noticing that the overall joint behavior is sensitive to rather small variations of the chord thickness value. This difference is attributed to the earlier initiation of inelastic behavior when the chord thickness becomes smaller, so that the joint resistance is significantly reduced. In any case, the results show that the numerical model is capable of simulating accurately the experimental procedure and representing the experimental results.

The strain concentration factor (SNCF) and the stress concentration factor (SCF) has been also evaluated numerically. The numerical SNCF value is estimated equal to 7.18, higher than the experimentally evaluated value. According to CIDECT guidelines (2001), the corresponding SCF for the joint under consideration is equal to 9.82 and according to Wordsworth and Smedley (1978) it is equal to 10.25, whereas the numerical model results to a SCF value equal to 6.16 using a linear extrapolation and 8.19 using quadratic extrapolation, as shown in Figure 13(b). The above differences are attributed to the sensitivity of the strain/stress field near the weld toe in terms of local conditions (notch effect).

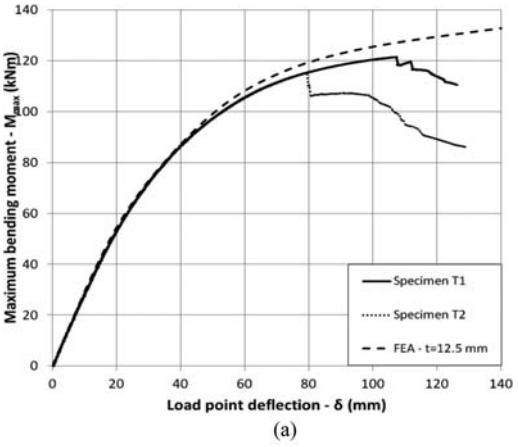

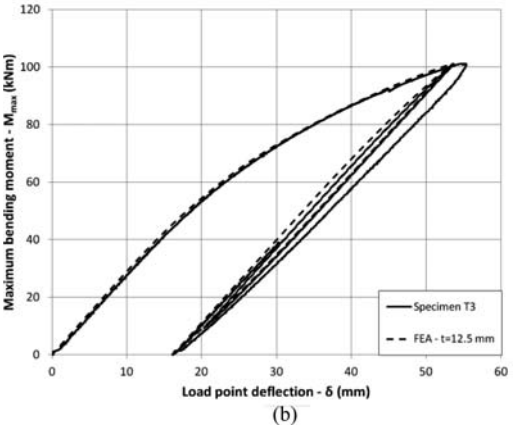

Figure 12. Comparison of the numerical and experimental load – displacement curves: (a) Monotonic, (b) Cyclic loading.

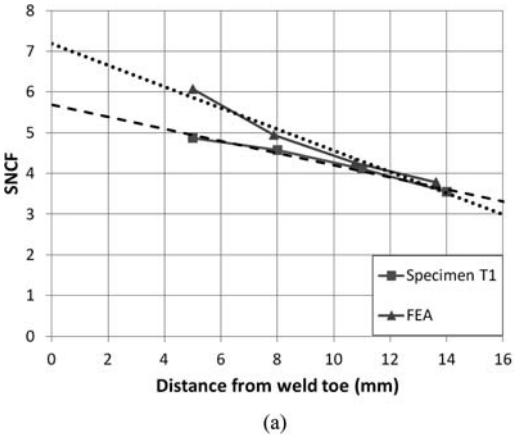

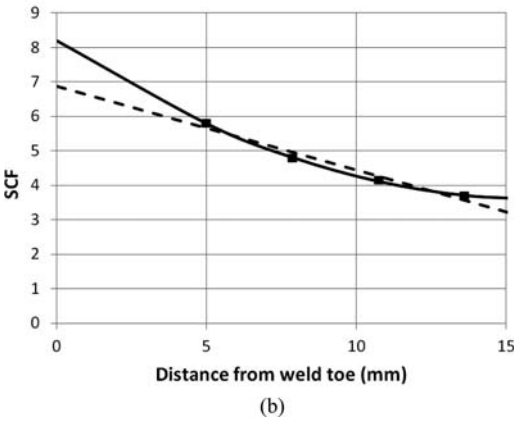

Figure 13. (a) SNCF and (b) SCF evaluation.

Towards better understanding of the chord deformation at the weld area, the deformed chord geometry is shown in Figure 14, corresponding to a joint section at the chord middle plane. The concentration of plastic deformation near the weld-toe area is significantly higher than the one located at the weld of the joint, so that the location of cracking initiation at the weld-toe is verified.

Using the numerical model, the strain evolution was monitored at the locations where the strain-gages were placed on the specimens as shown in Figure 3. Two additional check points, namely "point 1" and "point 2", were added along the chord hoop direction. The numerical predictions indicate the same strain evolution trend observed in the experimental measurements.

It is noticeable that when bending loading is applied, the joint brace (sg 21) as well as the chord area very close to the weld toe (sg 5) are always in tension. At point 1, located 6.55 cm from the weld toe along the chord hoop, the material initially experiences tensile strains which subsequently change to compressive strains as the bending loading is increased. From this location of the chord and towards the chord top (point 2) the strains are always compressive. This indicates that there is a significant change of chord curvature near the weld toe region, which reaches a critical value at a distance of about 5 times the chord thickness.

5 DESIGN IMPLICATIONS

The design provisions of EN 1993-1-8 (2002), which are identical to those proposed by CIDECT (1991) for the ultimate resistance, are used for predicting the joint bending capacity. Using the measured values of joint thickness and the actual yield stress of the steel material, the predicted bending resistance for OPB is equal to $M_{op,Rk} = 116.45$ kNm not taking into consideration any safety factors. In addition, EN 1993-1-12 (2009) introduces a factor equal to 0.8 for the steel grade under consideration. The predicted resistance is in very good agreement with the experimental value for the weld B welded joint and differs only 3.76% from the experimental resistance for the weld A welded joint when the 0.8 factor is not considered. Despite the fact that the proposed formula is valid for joints made of steel

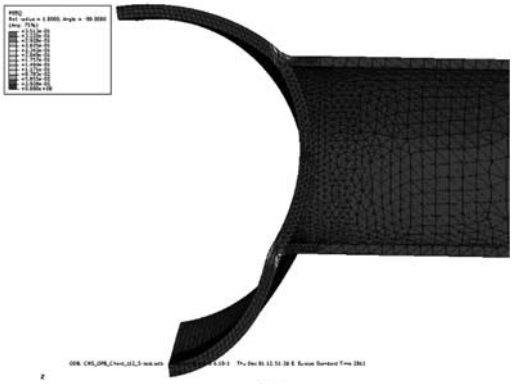

(a)

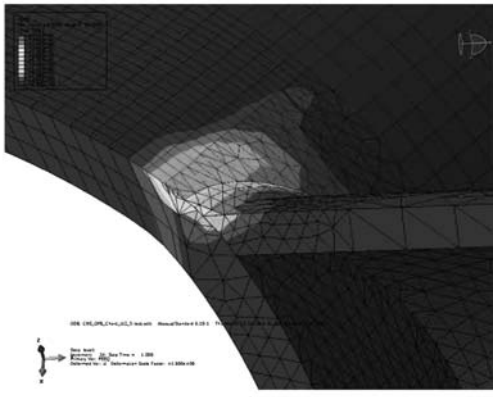

(b)

Figure 14. Mid-span section (a) Deformed chord geometry (b) Equivalent plastic strain distribution at the weld-toe area.

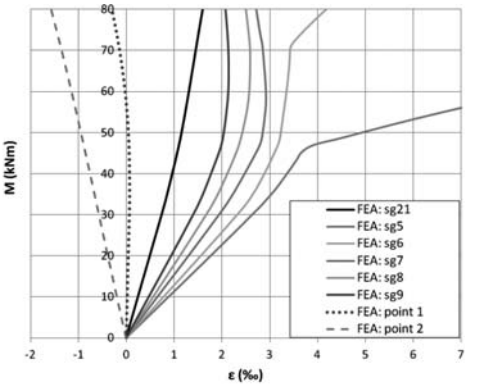

(a)

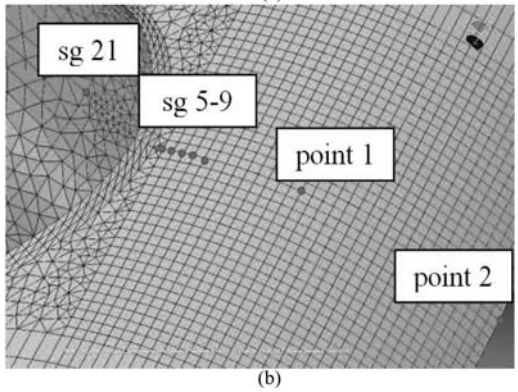

(b)

Figure 15. Numerical strain values at various check points (a) Check point locations (sg 21-meridional, sg 2-5/point 1/ point 2 – hoop) (b) Calculated strain values versus applied moment.

with yield stress no more than 460 MPa, it can be concluded that the proposed design equation is generally in good agreement with the experimental findings and can be used for the bending resistance prediction of high-strength steel joints subjected to OPB, without the 0.8 factor.

The fatigue design of tubular X-joints made of high-strength-steel is not covered by any international design code. Based on the experiments conducted within this study it is possible to evaluate the applicability of the existing fatigue design curves (developed for ordinary steel grades up to 460 MPa) on the fatigue resistance of high-strength steel joints. EN 1993-1-9 (2002) adopts the "classification" method but does not provide any fatigue curves for tubular X-joints of any steel grade. On the other hand, CIDECT (2001) guidelines adopt the "hot spot" stress method, but they are applicable for a number of cycles greater than 10^3. One simple way to extend the high-cycle fatigue curves to the low-cycle regime has been proposed by Ballio et al. (1995), where an "equivalent" elastic stress range" is introduced and a linear extension of the S-N curves in the log-log scale is proposed. Using this approach, the predicted number of cycles for the X-joints under consideration is equal to $N_f = 69$, which is about one third of the experimentally measured fatigue life of the joints. Taking into consideration the inherited safety margins in the design specifications, it can be concluded that the use of this design methodology in the low-cycle fatigue range results in safe predictions and could be adopted for design purposes.

6 CONCLUSIONS

In the present study, experimental and numerical investigation of the behavior of CHS welded joints made of high-strength steel and subjected to out-of-plane monotonic and cyclic bending has been presented. The experimental results indicate that the lower the strength of the weld, the higher the bending capacity, in terms of maximum moment deformation capacity. More tests are required for reaching safer conclusions. The experimental results have been simulated quite accurately by numerical models capable of describing the joint deformation at a rigorous manner and supporting the experimental observations. Finally, shortcomings of the existing design codes for the design of high-strength steel welded joints are highlighted. An

extension of the existing CIDECT design guidance for high-strength steel under static and low-cycle fatigue loading is proposed.

ACKNOWLEDGEMENT

This work was carried out with a financial grant from the Research Fund for Coal and Steel of the European Community, within HITUBES project: "Design and Integrity Assessment of High Strength Tubular Structures for Extreme Loading Conditions", Grant N0 RFSR-CT-2008-00035.

REFERENCES

AWS D1.1/D1.1M:2004, *An American National Standard, Structural Welding Code – Steel*, 550 N.W. LeJeune Road, Miami, Florida, 33126

Baba, S., Arizumi, Y., Naruoka, M. 1981. Low-Cycle Fatigue Test of Welded Tubular joints, *Journal of the Structural Division*, ASCE, Vol. 107, Issue 3:. 487–505.

Ballio, G., Castiglioni, C.A., 1995. AUnified Approach for the Design of Steel Structures under Low and/or High cycle Fatigue. *Journal of Construction Steel Research*, 34: 75–101.

Boge, F., Helland, T.K., Berge, S. 2007. Low cycle fatigue of T-tubular joints with out-of-plane bending loading, *Proceedings of the International Conference on Offshore Mechanics and Arctic Engineering-OMAE*, 4: 107–115.

CIDECT No. 1. 1991. *Design Guide for Circular hollow Sections (CHS) under Predominantly Static Loading,* TUV – Verlag

CIDECT No. 8. 2001. *Design Guide for Circular and Rectangular Hollow Section Welded Joints under Fatigue Loading,* TUV – Verlag

EN 1993-1-8. 2002. *Eurocode 3: Design of steel structures – Part 1–8: Design of joints*, European Committee for Standardization.

EN 1993-1-9. 2002. *Eurocode 3: Design of steel structures – Part 1–9: Fatigue strength of steel structures*, European Committee for Standardization.

EN 1993-1-12. 2009. *Eurocode 3: Design of steel structures – Part 1–12: Additional rules for the extension of EN 1993 up to steel grades S 700*, European Committee for Standardization

HSE 2004. *Review of low cycle fatigue resistance*. Research report 207 by Failure Control Limited. Surrey, UK

Hochman, M., Madshus, M., Berge, S. 2010. Low Cycle Fatigue of T-tubular Joints under Axial Loading. *Proceedings of the Twentieth International Offshore and Polar Engineering (ISOPE)*, Beijing, China.

Romeijn, A.1994: *Stress and strain concentration factors of welded multiplanar tubular joints*, PhD Thesis, Delft, The Netherlands.

Simulia ABAQUS 6.10, Dassault Systèmes, 2011

van der Vegte, G.J., de Back, J., Wardenier, J., 1989. *Low cycle fatigue of welded structures. Analysis of low cycle fatigue on tubulat T-and X-joints*. Stevin report 15.6.89.11/A1, CIDECT report 7H-89/2-E.

Waalen, J., Berge, S. 2005. Low cycle fatigue of T-tubular joints with in-plane bending loading. *Proceedings of the International Conference on Offshore Mechanics and Arctic Engineering- OMAE, 3, art. no. OMAE2005-67468*:. 211–219.

Wordsworth, A.C., and Smedley, G.B., 1978. *Stress concentrations at unstiffened tubular joints*, Loyd's Register of Shipping, Paper 31.

Tubular Structures XIV – Gardner (Ed.)
© 2012 Taylor & Francis Group, London, ISBN 978-0-415-62137-3

Numerical investigation of welding residual stresses in planar bridge trusses made of CHS steel profiles

F. Zamiri, A. Nussbaumer & C. Acevedo
École Polytechnique Fédérale de Lausanne (EPFL), Lausanne, Switzerland

ABSTRACT: The weld-induced residual stresses in a tubular planar K-shaped connection made of construction steel grades S355J2H and S690QH is evaluated using three-dimensional finite element models in thermo-mechanical simulation of welding process. Both lumped single-pass and multi-pass simulation alternatives are examined.

The transversal component is the largest residual stress component at the gap region for all models, with values reaching the yield strength of studied steel grades. The shapes of residual stress profiles evaluated from the multi-pass models for the two steel grades show a similar trend. Although this can change when the effects of phase transformations will be considered. Considerable difference in the residual stress distribution in the gap region is observed between multi-pass welding simulation and equivalent single-pass models for both steel grades studied. For the single-pass models, the effect of using element activation on the residual stresses are negligible.

1 INTRODUCTION

Application of circular hollow sections for bridge structures has increased since the early 90's, especially in Europe (Acevedo and Nussbaumer 2012). Tubular bridges provide aesthetics, structural efficiency, and sustainability and are advantageous compared to other structural solutions, in particular for mid-sized span bridges (Nussbaumer et al. 2010). Similar to the offshore platform structures, two fabrication methods for the tubular bridge joints exist: welding the tubes together, and using cast steel parts in place of joints and connecting them to truss members by girth welds. While the latter has shown a better fatigue performance in the past, the former fabrication method is still interesting for some bridge projects because of cost and aesthetics issues.

Using high-strength low-alloy (HSLA) steels can lead to a more transparent structure with a higher live load to dead load ratio. Part 1–12 of Eurocode 3 which was introduced in 2007 permits the use of steel grades up to grade S700. However, fatigue cracking in the welded joints is a limiting factor for application of higher grade steels in tubular bridge structures. In the current IIW recommendations (Hobbacher 2003) fatigue life is considered the same for the structural steels up to grade S960. Part 1-9 of Eurocode (EN1993 2005a) recommends the use of the same fatigue resistance curves for all structural steel grades. Although experimental fatigue data supports the above fact, the underlying phenomena of evolution of microstructure in the heat affected zone and formation of residual stresses during the welding process are different for various steel grades.

Residual stresses in the HAZ are one of the major factors that influence the fatigue crack growth, and hence, the fatigue life of the welded details (Radaj 2003)s. The tensile residual stresses affect the fatigue response of the detail by keeping the cracks open, even if the external load is compressive. The non-uniform plastic deformations which occur during the welding are the main source for the formation of welding residual stresses (Withers 2007). Several factors affect the residual stress magnitude and distribution in the HAZ, including:

- geometry
- material properties
- mechanical restraints of the connection
- temperature history experienced by the weldment

The temperature history mentioned above is determined by several welding parameters, namely heat input, shape of the heat source and the number of welding passes.

During the welding process many different phenomena occur which can be regrouped into three interacting domains: thermal field, mechanical field, and microstructure field. Figure 1 shows these three domains with the simplified interactions that take place during welding. The dark arrows depict the dominating effects and the dotted arrows indicate that the corresponding effect is of less importance. The thermal field affects both the microstructure and the mechanical field, while the inverse effects are negligible. This is

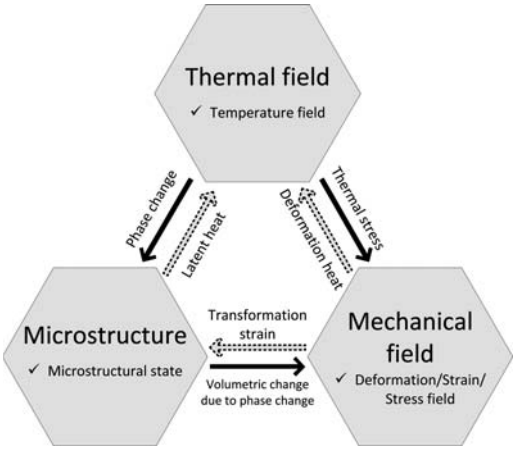

Figure 1. Simplification of interactions between the three domains during the welding process. Dark arrows show the dominant interactions.

Table 1. Profile sizes and non-dimensional geometric parameters of the studied K-Joint.

Nominal dimensions		Non dimensional parameters	
Chord	168.3 × 20 mm	$\beta(d_1/d_0)$	0.53
Brace	88.9 × 8 mm	$\gamma(d_0/2t_0)$	4.21
Eccentricity(e)	49.3 mm	e/d_0	0.29
θ^*	60°	$\tau(t_1/t_0)$	0.4

*Nominal angle between the chord and the braces.

the key to de-coupling of the thermo-mechanical analysis into a sequential procedure which includes solving the thermal field problem, and subsequently solving each of the microstructure and mechanical fields.

2 NUMERICAL SIMULATION

The geometry for the planar K-joint modeled in this study is similar to the joints of full-scale specimens which were tested under constant amplitude fatigue loading in ICOM laboratory (Acevedo & Nussbaumer 2012). The dimensions and non-dimensional geometric parameters of the joint are shown in Table 1. The dimensions are exemplar of tubular bridge trusses in which the value of γ is below the application range of CIDECT (2000) formulas for the stress concentration factors (application range is $12 \leq \gamma \leq 30$). The CIDECT's stress concentration factors are given for the case that no eccentricity exists in the joint, which is not the case for many bridge joints, including the joint investigated here.

The detail of weld gap at the crown toe and the crown heel is presented in figure 2. The welding was done in 7 welding passes, according to the welding procedure specifications from the fabricator. As will be seen later, the number of weld passes was

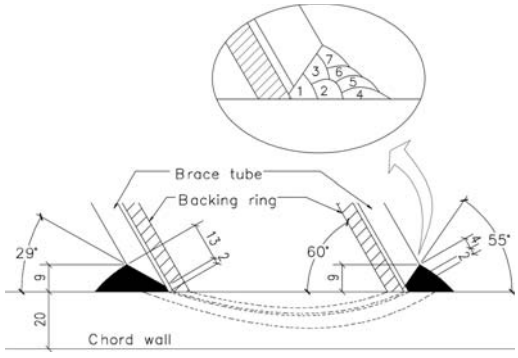

Figure 2. Geometry of the weld gap for the brace-to-chord connection. The detail shows the welding passes according to the welding procedure specifications.

reduced for the numerical analysis. The complex weld geometry was simulated according to the method explained by (Costa Borges 2008). The arc welding was done using flux cored electrodes. The steel backing ring provides more complete weld penetration and hence, a better fatigue performance (Schumacher & Nussbaumer 2006). However, it does not have a significant effect on the thermal or mechanical field for welding simulation. Therefore, it was not included in the model.

2.1 *Material data*

The original truss was made of structural steel S355J2H according to EN:10210-1 2006. To evaluate the effect of material, simulation was carried out with both steel grade S355J2H and grade S690QH. the temperature dependent thermal and mechanical properties were chosen from different sources. The values suggested by Eurocode 3-1-2 fire design recommendations (2005b) were used for the thermal conductivity, specific heat capacity, and latent heat of the steel material. Temperature-dependent Young's modulus values were selected according to Eurocode. Poisson's ratio and coefficient of thermal expansion were chosen as suggested by (Michaleris 2011). For yield strength of S355 steel, the values given by Michaleris were used. Yield strength of S690 was selected from Eurocode values. The rate-independent mechanical properties of the two steel grades are given in Figure 3. The same material properties are assumed for the parent metal and weld material. Transformation plasticity is not considered in this study.

2.2 *Heat source and boundary conditions*

There are several heat source models available in the literature (Radaj 2003) to model the welding torch. Although the double ellipsoid model (Goldak & Akhlaghi 2005) is the most desirable model for the modeling of arc welding process, its calibration requires considerable data in terms of registered welding temperature history. In this stage of study, a simple

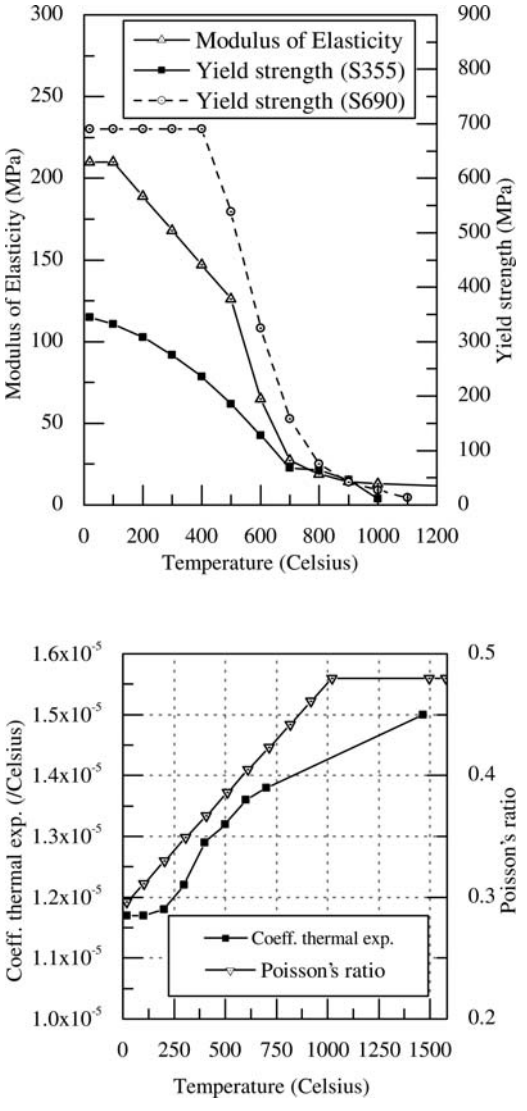

Figure 3. (Top) Change of E and σ_y with temperature for S355 and S690 steels (Michaleris 2011, EN1993 2005b); (Bottom) Temperature dependent ν and α for the same steel grades (Michaleris 2011).

model, as recommended in MORFEO (2011), was employed. The weld torch specifications are presented in Table 2. The selected volumetric heat source shape was a cylinder with a linear heat input intensity distribution in the longitudinal direction of cylinder. The base radius and height of the cylinder for the single-pass weld model were selected as 15 mm. The volume dimensions were calibrated according to the size of fusion zone. The cylindrical heat sources for the three passes of the multi-pass simulation were scaled down to fit into their corresponding weld beads whose shapes can be seen in Figure 5c.

The sequence for the welding of the two braces is shown in Figure 4. The welding for each brace

Table 2. Arc welding parameters used in modeling of heat source.

Parameter	Value
Number of welding passes	7
Welding torch speed [mm/s]	5.5
Welding current [A]	270
Voltage [V]	30
Arc welding efficiency [%]	0.732
Heat power input per pass [kW]	5.93
Total heat power input [kW]	41.5

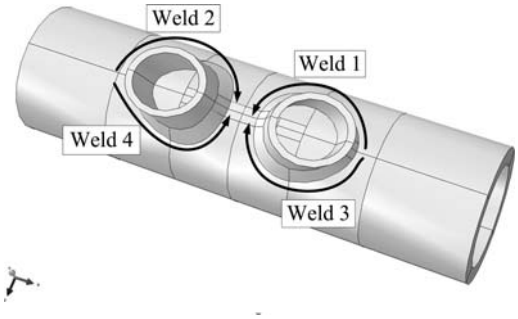

Figure 4. Welding sequence for the four weld parts of the K-joint connection.

started at the crown heel and finished at the crown toe on each side of the connection. Once one pass of all 4 weld parts were done, the next pass would start and so forth. The welding start and stop positions were selected according to the welding procedure used at the time of fabrication of the fatigue-tested specimens made of steel grade S355J2H. Although having the weld stop position at the crown toe can potentially accelerate the fatigue crack propagation, the fatigue tests did not show any significant deviation from the CIDECT fatigue strength curves (Acevedo & Nussbaumer 2012), likely because of the high quality of welding workmanship. It is worth mentioning that the fabricator has recently revised its welding procedure to relocate the weld stops outside the crown toe region.

The seven weld passes were simplified in the analyses into either a lumped single pass or a lumped three-pass weld. The total heat input was kept as the same value shown in Table 2 for all analyses, according to Radaj (2003). For the three-pass welding simulation, the heat power input for each of the three passes was one-third of the total heat power input given in Table 2. The heat loss through convection and radiation was modeled by using a combination film coefficient in the model. Table 3 depicts the detailed time steps for the simulation of an equivalent single pass weld. for the three-pass weld, the same timing (i.e. 25 seconds for welding, followed by a 120 seconds cooling period, with a long cooling time step at the end of welding) was selected. A preheating temperature of 100°C was assumed for the three-pass welding simulation.

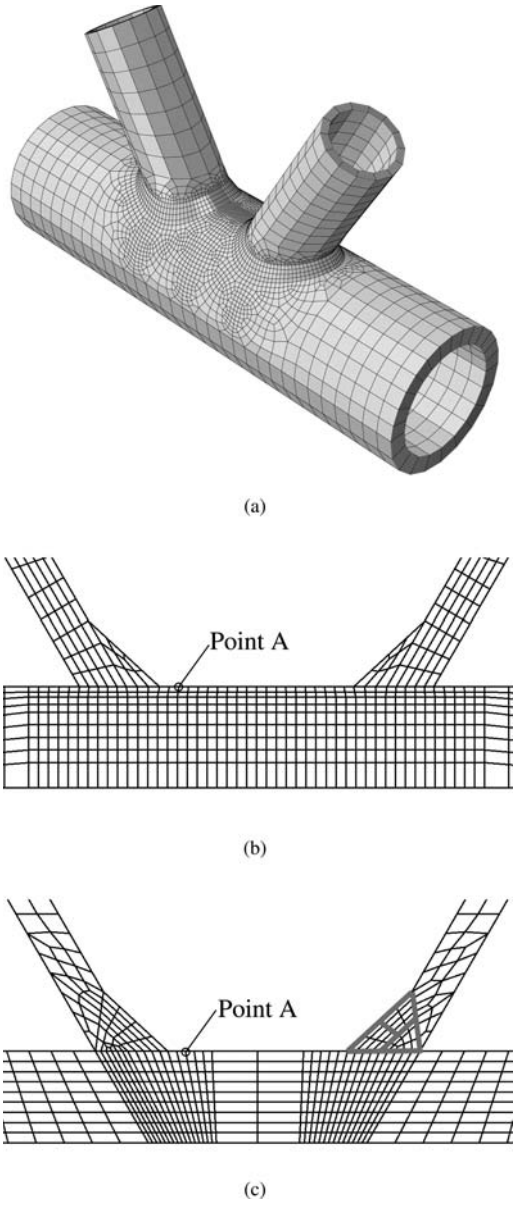

Figure 5. Finite element meshes used in analyses; (a) Overview; (b) Detail of the mesh at the gap region for the single-pass weld models; (c) Detail of the mesh and partitioning of the weld bead at the gap region for the multi-pass weld model. Point A is the point where the temperature history is evaluated.

The deformation of the model was not restrained. to maintain the equilibrium, only the three translational displacement components were fixed at one end of the chord (right side).

2.3 *FE analysis details*

The analysis was carried out in MORFEO/Welding (2011) manufacturing simulation program. The model was created using 8-node linear isoparametric solid elements (Fig. 5a). It is known from the fatigue tests of the two full-scale specimens that the fatigue cracking first occurs at the hot spot located on the chord at the crown weld toe (the gap region between the two braces). Therefore, for the estimation of residual stress field, the mesh is refined in that location, with an element dimension of 1 mm to 2.2 mm (Fig. 5b and c).

In order to simulate the weld metal deposition for the multi-pass welding, the element activation option of the MORFEO/Welding program is utilized. Of the two available methods, namely activation by analysis time and activation by temperature, the former is chosen. In the temperature activation method, the elements are activated once the temperature reaches a threshold value (melting point). The method can result in some isolated elements which produce convergence problems during analysis. In the time-based element activation, a moving box passes along the weld trajectory with a user-defined speed. Once an element is within the box, the element will be activated. The effect of material deposition on the thermal solution is negligible, but it has significant impact on the mechanical solution. Therefore, the element activation was only used for the mechanical part of the problem.

Table 3. Welding sequence for equivalent single-pass weld simulation. Weld part numbering is as shown in Figure 4.

Step name	Start time seconds	End time seconds
Waiting	0	24
Welding, part 1	25	50
Cooling	51	174
Welding, part 2	175	200
Cooling	201	324
Welding, part 3	325	350
Cooling	351	474
Welding, part 4	475	500
Cooling	501	9000

3 RESULTS

3.1 *Thermal solution*

The temperature history at a node located on the chord surface in the gap region at 4 mm from the weld toe is reported on Figure 6 for the two types of the models (the node location is shown in Figure 5b,c as Point A). It is recalled that the thermal analysis part was identical for the two steel types. As can be seen in the figure, the analysis was continued through the final cooling time until the temperature dropped below 50°C. The two larger peaks observed for the single-path model correspond to the passage of the weld parts number 2 and 4 (see Figure 4) at the vicinity of the considered point. The calculated maximum temperature for the single-pass model is 23% higher than the peak temperature from the three-pass weld model. The reason being that the heat input in the latter model is more

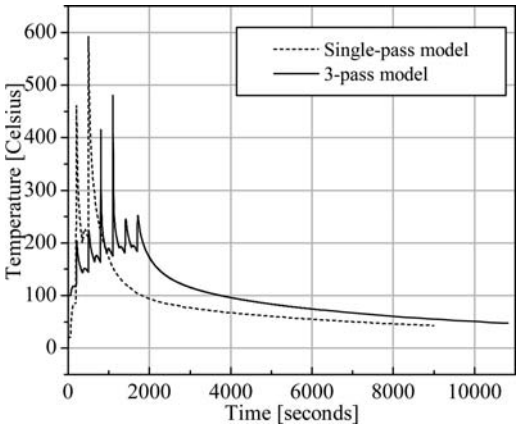

Figure 6. Calculated temperature time history for the single-pass and multi-pass simulations.

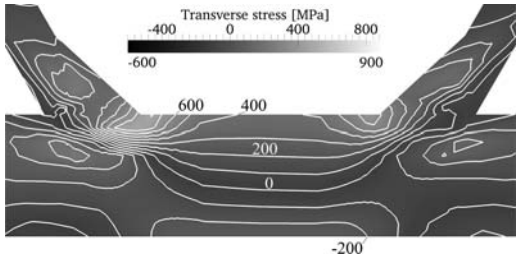

Figure 7. Distribution of the transverse stress component in the chord at gap region for steel S690QH (multi-pass weld simulation).

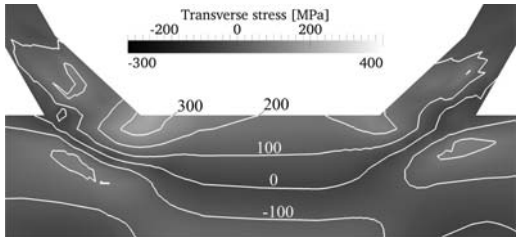

Figure 8. Distribution of the transverse stress component in the chord at gap region for steel S355J2H (multi-pass weld simulation).

gradual which allows some cooling down between the welding operations.

3.2 *Mechanical solution*

As mentioned before, ongoing and previous fatigue experiments at ICOM have shown that the critical location for the fatigue cracking is at the crown toe location in the gap region. Cracking initiates at the HAZ but quickly goes into base metal and propagates there (Acevedo & Nussbaumer 2012). The distributions of residual stresses in the gap region for the two studied steel grades are shown in Figures 7 and 8 for

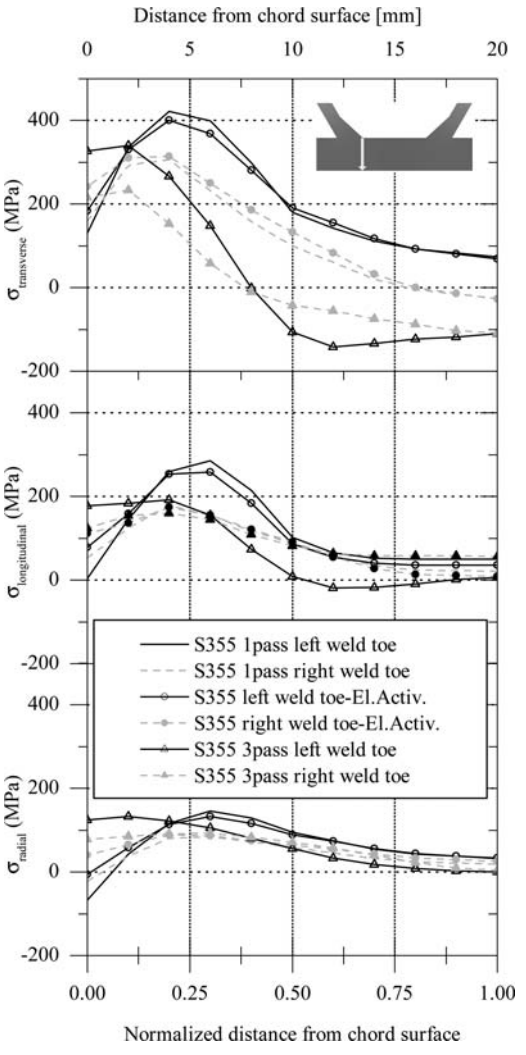

Figure 9. Through-thickness residual stress profiles at the weld toes (crown toe hot spot) for S355J2H.

the case of the three-pass weld model. The transverse stress component is shown in Figures 7 and 8, which is the component perpendicular to the weld line. The figures show the presence of high tensile residual stresses in the gap region for both steel grades. The single-pass model with element activation showed a similar trend but with higher residual stresses at the middle of the gap region. This can be described by the higher calculated thermal strains due to the higher temperatures which was explained in the previous section.

Both models for S355J2H and S690QH predict low compressive transverse residual stresses at the location of weld roots (slightly dark regions in the locations of weld roots). This is in agreement with the observation of no root cracking in the aforementioned fatigue tests which were conducted with $R = 0.1$ (thus likely diminishing the effect of stress range).

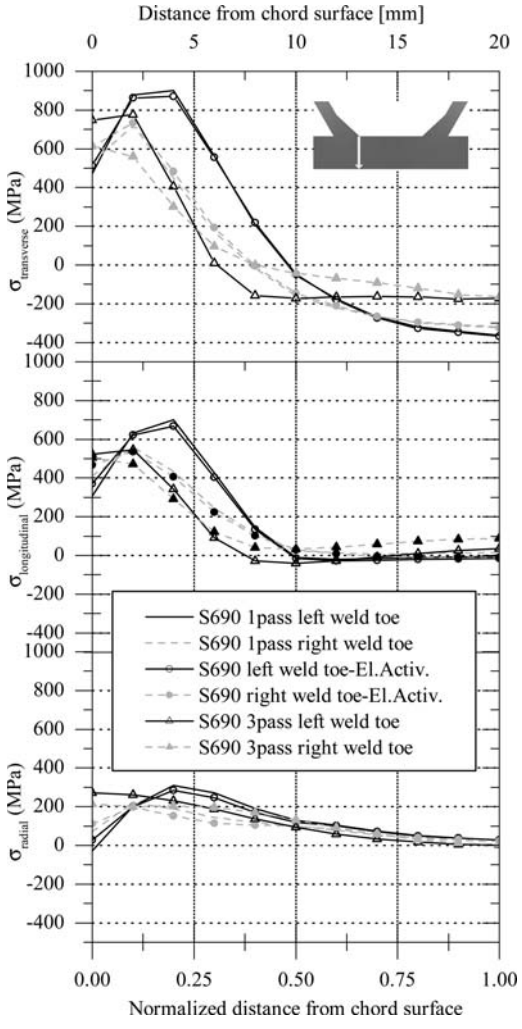

Figure 10. Through-thickness residual stress profiles at the weld toes (crown toe hot spot) for S690QH.

The through thickness profiles of three residual stress components at the left (dark lines) and right (gray lines) crown toes for the two steel grades S355J2H and S690QH are presented in Figures 9 and 10. Comparing these profiles, a similar trend for the distribution of residual stresses between the two steel grades can be observed. However, this would not be the case when other modeling parameters such as volumetric changes due to phase transformations are taken into consideration.

As can be seen, the longitudinal component (i.e. the component tangent to the weld line) is less than the transverse component for all models. Considering the transversal component, all models indicate high residual stresses up to and even higher than the yield stress. The impact of the modeling method (single-pass versus multi-pass) is considerable for both steel grades, for which both peak value and peak locations are different between the two modeling methods. The difference is higher for the case of S355J2H compared to the S690QH despite the fact that the two steel grades underwent identical temperature histories. The difference between models becomes less significant for the case of longitudinal and radial components of residual stresses. The radial stress profiles at the weld toe show that the radial stress component is not zero at the chord surface. Although the equilibrium of stresses implies that there should not be any radial residual stresses at the surface of the chord, but this does not hold for the weld toe corner, where the resultant of residual stresses is not necessarily parallel to the chord surface. The evaluated tensile radial component at the surface from the multi-pass model is higher than the single-pass model. This shows that a triaxial residual stress state exists at the weld toe near the chord surface, with the largest component being the transversal component and the smallest component being the radial stress.

For both of the studied steel grades, the single-pass models predict a higher maximum value for the longitudinal residual stress component, compared to the three-pass models. However, the maximum value for the three-pass models occur in the chord surface, while the single-pass models report the maximum longitudinal stress to be at the depth of around 0.2T. Due to this difference in prediction of residual stresses, the prediction of fatigue life (and crack path) will be different in the subsequent crack propagation analyses, specially for the case that the joint undergoes compressive fatigue loading.

The asymmetry of the stress field can be observed by comparing the stress profiles at the right and left weld toes. However, the difference between the stress profiles at the two weld toes is reduced in the case of multi-pass welding simulation.

4 CONCLUSION

Thermo-mechanical welding analysis was utilized to evaluate welding residual stresses in a planar K-shaped tubular joint for two grades of structural steel. The element activation analysis technique made no considerable difference for the equivalent single pass welding simulation; however, the results from multi-pass welding analysis showed considerable change in the distribution of residual stress field, specially for the case of transversal residual stresses.

For both of the steel grades studied, the transversal stress component in the gap region was the largest stress component, with the values at f_y. Also, the distribution of residual stresses calculated from multi-pass weld simulations show a similar trend. This conclusion should be taken with caution as volumetric changes due to phase transformation were not considered. Transformation plasticity will be implemented in future work.

ACKNOWLEDGMENTS

This research is part of the project P816 “Optimal use of hollow sections and cast nodes in bridge

structures made of S355 and S690 steel", supervised by the Versuchsanstalt für Stahl, Holz und Steine at the Technische Universität Karlsruhe, which is supported financially and with academic advice by the Forschungsvereinigung Stahlanwendung e. V. (FOSTA), Düsseldorf, within the scope of the Stiftung Stahlanwendungsforschung, Essen.

REFERENCES

Acevedo, C. & Nussbaumer, A. 2012. Effect of Tensile Residual Stresses on Fatigue Crack Growth and S–N Curves in Tubular Joints Loaded in Compression. *International Journal of Fatigue* 36 (1): 171–180.

Costa Borges, L.A. 2008. Size Effects in the Fatigue Behaviour of Tubular Bridge Joints (Thesis No. 4142). Lausanne: EPFL.

EN:10210-1. 2006. Hot Finished Structural Hollow Sections of Non-alloy and Fine Grain Steels. Technical Delivery Requirements. *European Standard.*

EN1993. 2005a. *Eurocode 3: Design of steel structures – Part 1–2:General rules – Structural fire design.* Brussels: European Committee for Standardization.

EN1993. 2005b. *Eurocode 3: Design of steel structures – Part 1–9: Fatigue.* Brussels: European Committee for Standardization.

EN1993. 2007. *Eurocode 3: Design of steel structures – Part 1–12:General – High strength steels.* Brussels: European Committee for Standardization.

Goldak, J.A. & Akhlaghi, M. 2005. *Computational Welding Mechanics.* Springer Verlag.

Hobbacher, A. 2003. *Recommendations for Fatigue Design of Welded Joints and Components.* IIW Document XIII-1965-03/XV-1127-03, Paris.

Michaleris, P. 2011. Courses at Pennsylvania State University.

MORFEO. 2011. *V1.5.2 User's Manual.* Brussels: Cenaero.

Nussbaumer, A. & Herion, S. & Veselcic, M. & Dietrich, M. 2010. New S-N Curves for Details in Bridges with Steel Truss Tubular Superstructure. In ISTS 13, Hong Kong.

Radaj, D. 2003. *Welding Residual Stresses and Distortion.* DVS – Verlag.

Schumacher, A. & Nussbaumer A. 2006. Experimental Study on the Fatigue Behaviour of Welded Tubular K-joints for Bridges. *Engineering Structures* 28 (5): 745–755.

Withers, P. J. 2007. Residual stress and its role in failure. *Reports on Progress in Physics* 70 (12) : 2211–2264.

Zhao, X.L. & Herion, S. & Packer, J.A. & Puthli, R.S. & Sedlacek, G. & Wardenier, J. & Weynard, K. & van Wingerde, A.M. & Yeomans N.F. 2000. *Design guide for circular and rectangular hollow section joints under fatigue loading.* CIDECT, Comité International pour le Développement et l'Etude de la Construction Tubulaire. Construction with Hollow Steel Sections 8. Köln, Germany: TÜV-Verlag

Tubular Structures XIV – Gardner (Ed.)
© 2012 Taylor & Francis Group, London, ISBN 978-0-415-62137-3

Analysis of the load transfer in composite columns with concrete filled hollow sections – bolts as load transfer devices

R.H. Fakury, R.B. Caldas & P.H.F. Almeida
Federal University of Minas Gerais, Brazil

A.H.M. Araújo
Vallourec & Mannesmann Tubes, V&M, Brazil

ABSTRACT: Natural bond is sometimes not enough to allow load transfer between a tubular steel profile and the concrete core in composite columns with Concrete Filled hollow Steel sections (CFS). European Standard EN 1994-1-1:2004 and Brazilian Standard ABNT NBR 8800:2008 for composite structures recommend the use of mechanical connectors if the interface shear stress in a CFS column exceeds a limiting value between 0.40 MPa and 0.55 MPa. This paper presents a numerical analysis of a load transfer device, which uses bolts as connectors in concrete filled columns. A nonlinear numerical model was developed using the commercial finite element program ABAQUS. Solid elements were used for the steel and concrete, and also the contact between these two materials was considered. Comparisons with experimental results were conducted to validate the numerical model. Finally, the numerical model was used to perform a parametric study in order to verify the validity of an analytical model presented by the new Brazilian Draft Standard for design of tubular steel and composite structures (TB-NBT:2011).

1 INTRODUCTION

Composite columns with concrete filled hollow steel sections (CFS) have many advantages over steel or concrete columns. The interaction between the tubular steel profile and the concrete core increases the structural properties of the materials. Confinement provided by the steel tube increases the bearing capacity of the concrete due to the multi-axial stress state. Also, the concrete core prevents deformation of the tube toward the inside, increasing the resistance to local buckling. Additionally, the tube also eliminates the need for concrete formwork, reducing costs and construction time.

The loads are transferred between steel tube and concrete core by shear strength at the contact surface (adhesion and friction) or by mechanical means. European Standard EN 1994-1-1:2004 and Brazilian Standard ABNT NBR 8800:2008 specify a design shear strength equal to 0.40 MPa and 0.55 MPa for rectangular and circular sections, respectively. Shear connectors should be provided, based on distribution of the design value of longitudinal shear, where this exceeds the design shear strength.

The development and use of shear connectors was the subject of several works: Viest (1960), Chapman (1964), Leonhardt et al. (1987), Jacobs & Hajjar (2010), Starossek et al. (2008a, b; 2009), Chien & Ritchie (1984); Ghavami (1998), Zellner (1987) and Veríssimo (2007), among others.

Recently, the Brazilian Draft Standard for design of tubular steel and composite structures, TB-NBT:2011, provided an analytical model for the design of bolts as a shear transfer device in CFS columns.

This paper presents a numerical analysis used to verify the validity of the analytical model presented by the TB-NBT:2011.

2 NUMERICAL MODEL

Numerical methods, with emphasis on the finite element method (FEM), have become a powerful tool for analyzing structures. Although experiments are important in research on composite structures, they are expensive and time-consuming, and often made in small amounts. Thus, analysis via FEM provides complementary information to experimental analyses.

In this work, first, numerical analysis was performed using the commercial finite element program ABAQUS (Simulia, 2010) with the aim of reproducing the experimental and numerical results obtained by Starossek et al. (2008a, b; 2009). The models have a tubular profile with 168.3 mm diameter, 5 mm thickness and 750 mm length. A gap of 25 mm between the top of steel tube and the top of concrete core was left, as shown in Figure 1.

For models identified with the label "Sc", the load was applied only at the top of the steel profile (Figure 1) and for models labeled with the initials

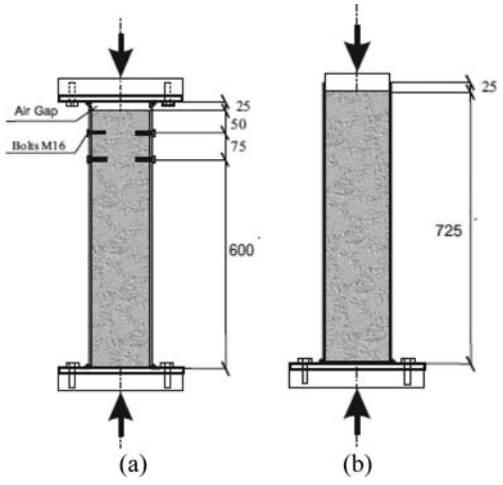

Figure 1. Load applied only to steel, model "Sc" (a) and model "SP" with load applied only to concrete (b) (Starossek et al., 2008a).

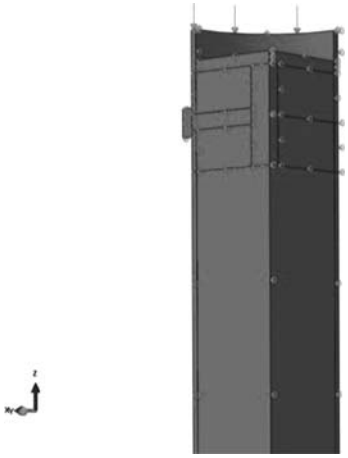

Figure 2. Boundary conditions for the model UD-C1-Sc-2B.

"SP", the load was applied only to the concrete. Additionally, the models with the label "UD" indicate that the inner surface of the tubes was polished and greased before casting the concrete, in order to eliminate friction and adhesion between steel and concrete.

Due to symmetry and the finite element type used, only one quarter of the models analyzed by Starossek et al. (2008a, b; 2009) were modeled, according to Figure 2. This procedure allowed the minimization of computational time.

The nodes on the lower surface of the steel profile were fixed in all directions, while the nodes on the upper surface were released only in the direction of the length of the model. At the bottom surface of the concrete, nodes were fixed only in the direction of the length of the model.

The bolts used by Starossek et al. (2008a, b; 2009) were type M16 threaded throughout their length.

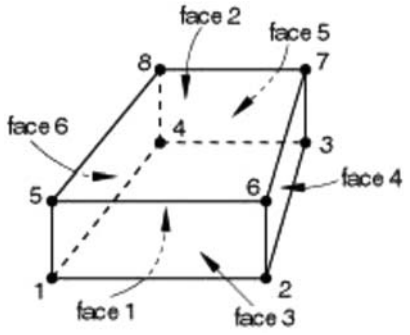

Figure 3. Solid finite element C3D8 (Simulia, 2010).

In this paper, the bolt diameter was reduced to simulate the thread. According to the ABNT NBR 8800:2008, the nominal bearing capacity of bolts when the shear plane passes through the threads is given by:

$$F_{v,Rn} = (0.67 A_b)(0.6 f_{ub}) \quad (1)$$

where A_b is the nominal bolt cross-sectional area and f_{ub} is the steel bolt specified ultimate tensile strength. This equation shows the coefficients related to the effective area of the threads and shear failure of the steel, equal to 0.67 and 0.6 respectively. Thus, the following value for the effective diameter (d_{eff}) of the bolt was used:

$$d_{eff} = d_n \sqrt{0.67} \quad (2)$$

where d_n is the nominal bolt diameter.

The element type C3D8 was used (linear hexahedral solid), which has eight nodes and three degrees of freedom per node. This element can be used for complex non-linear analysis involving contact, plasticity and large deformations. Figure 3 shows the ordering of the nodes and the numbering of the faces of the element.

Interactions at the contact surface between the steel and concrete may occur in the tangential and normal directions of the models. For models C1-UD-4B-Sc (with load applied to the steel profile indicated by the label Sc, greased surface, label UD, and four bolts, label 4B) and C1-UD-2B-Sc (with two bolts), it was considered that slip between the concrete and tube occurs freely in the tangential direction thus simulating no friction. In the normal direction, the interaction model considers the compressive stress between the components and allows separation between them. In the model C1-SP2 (with load applied to the concrete core, indicated by label SP), a coefficient of friction at the interface between the steel tube and concrete core was used.

In models with bolts, a high coefficient of friction between these bolts and concrete was considered to simulate the effect of the threads. At the interface between each bolt and the tube, the model assumes that adjacent nodes have the same displacement.

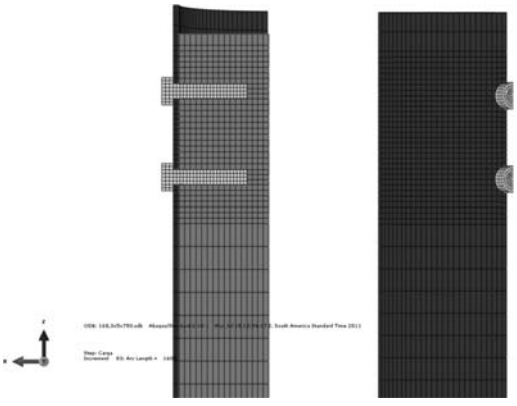

Figure 4. Mesh refinement.

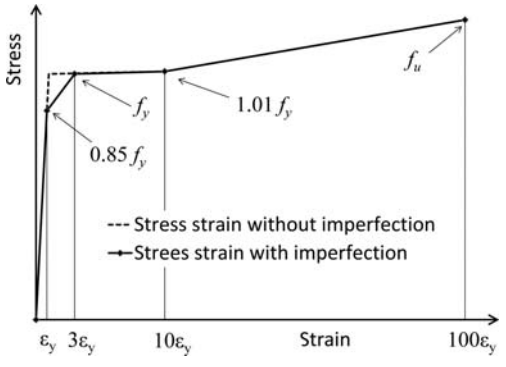

Figure 5. Stress-strain diagram of steel.

In a region around the bolts (40 mm above and below), a mesh with elements of maximum size equal to 5 mm (in all directions) was used for both the steel tube and for the concrete core. In the other regions elements were used with a maximum size equal to 5 mm in the transverse direction and 20 mm in the longitudinal direction of the model. Bolts were meshed with a maximum dimension of 3 mm, as shown in Figure 4.

The stress-strain diagram of steel adopted in the numerical models is shown in Figure 5, with modulus of elasticity of 210168 MPa, yield strength of 487 MPa and a tensile strength of 594 MPa, with bilinearity beginning at 85% of yield strength. This imperfection, which considers various effects that influence the numerical results, was defined from initial analysis with values of 90%, 85%, 80%, 75% and 70%. It was observed that 85% was appropriate in comparison to experimental results obtained by Starossek et al. (2008a). The deformations corresponding to the end of each branch of the diagram shown in Figure 5 were set based on the stress-strain diagram presented by Salmon & Johnson (1990).

The steel bolt was modeled with the stress-strain diagram without imperfection (Figure 5) and with a yield strength of 300 MPa, tensile strength of 500 MPa and modulus of elasticity of 210000 MPa.

Table 1. Comparison of the maximum load.

Model	FEM, present paper (A)	Starossek et al. (2008a) (B)	A/B
C1-UD-4B-Sc	1273	*1310	0.97
C1-UD-2B-Sc	1272	*1339	0.95
C1-SP2	2031	2203	0.92

*Graphical results obtained for a relative displacement between 6 to 12 mm.

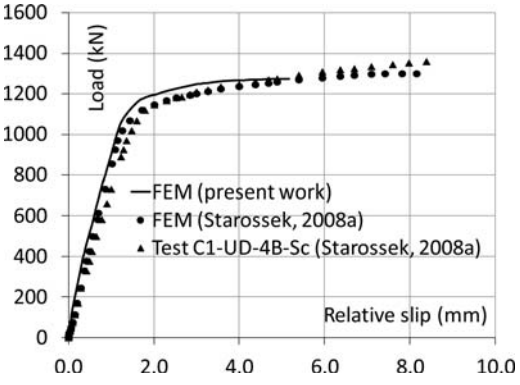

Figure 6. Comparison between results, model C1-UD-4B-Sc.

The nonlinear inelastic behavior of steel was simulated considering the isotropic hardening von Mises model. For the concrete, the stress-strain relationship presented by EN 1992-1-1:2004 was adopted, with parameters to consider the confinement and tensile cracking. Softening of the concrete was not considered and the tensile strength was taken as 10% of the compressive strength. The nonlinear inelastic behavior of concrete was simulated considering the concrete damaged plasticity model in the program ABAQUS. The model uses the concept of isotropic damaged elasticity in combination with isotropic tensile and compressive plasticity to represent the inelastic behavior of concrete.

The values found for the maximum load were compared, as shown in Table 1, with experimental and numerical results obtained by Starossek et al. (2008a).

In Figures 6 to 8 the numerical results of this paper are compared with experimental and numerical values taken from Starossek et al. (2008a, b, 2009).

The numerical model was considered adequate. The maximum difference between the ultimate load obtained by it and the experimental results was 8% (Table 1). Additionally, it was noted that the numerical model simulated, with good accuracy, the initial stiffness of the test specimen and the variation of stiffness during loading.

3 CODE PREDICTION

A standard for design of steel and composite structures with hollow sections (TB-NBT:2011) is in final phase

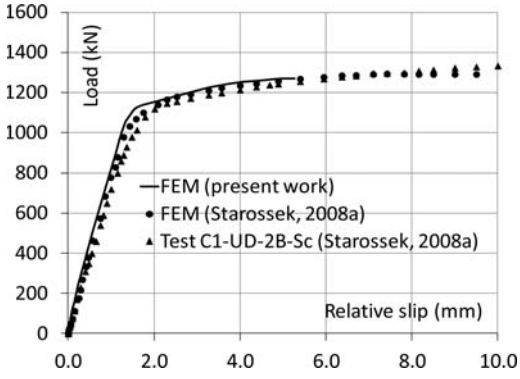

Figure 7. Comparison between results, model C1-UD-2B-Sc.

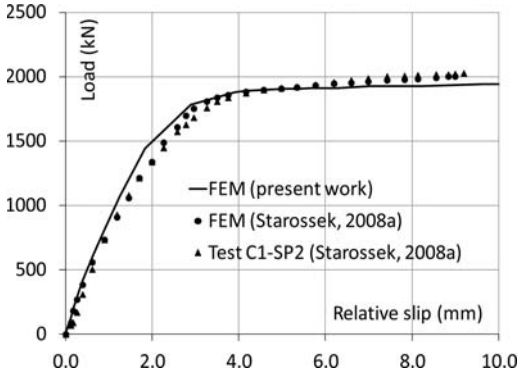

Figure 8. Comparison between results, model C1-SP2.

of development in Brazil. In this standard, the load transfer mechanism with bolts ("common" or high-strength) shown in Figure 9 is presented. The bolts are designed based on their shear strength and crushing of the concrete, as well as checks on the crushing and tearing of the tube.

According to the TB-NBT:2011, the bolt spacing in any direction cannot be less than six diameters. The nominal strength of each bolt is given by the lowest value from:

$$V_{Rn} = l_b\, d_b\, \sigma_{c,Rn} \le 5 d_b^{\,2}\, \sigma_{c,Rn} \tag{3}$$

$$V_{Rn} = 0.4\pi \frac{d_b^{\,2}}{4} f_{ub} \le 2.4 d_b\, t\ f_u \tag{4}$$

where l_b and d_b are the length and diameter of the bolts, respectively, t is the thickness tube, f_u and f_{ub} are the tensile strength of steel tube and bolt, respectively, and $\sigma_{c,Rn}$ is the nominal bearing stress on concrete, taken equal to the concrete characteristic compressive strength multiplied by a factor of 1.4.

4 RESULTS OF NUMERICAL STUDY

Numerical analysis using the program ABAQUS was performed to simulate the behavior of high-strength

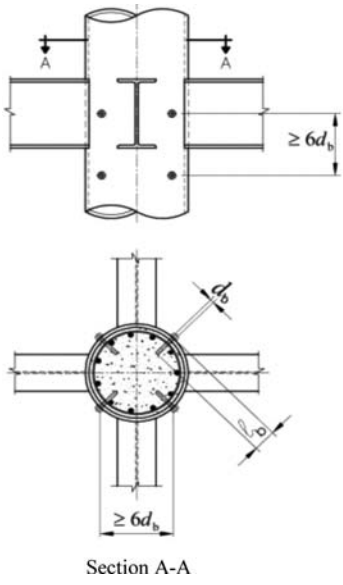

Figure 9. Load transfer mechanism using bolts (TB-NBT:2011).

bolts as force transfer devices in composite columns with concrete filled tubes.

A study was conducted consisting of 44 numerical models with 1000 mm length and bolts at mid-height. The parameters varied were: the thickness and diameter of the tubes; quantity, length and diameter of bolts; and, concrete compressive strength.

For steel tubular profiles, the modulus of elasticity was taken equal to 205000 MPa, yield strength equal to 350 MPa and tensile strength equal to 485 MPa.

For high strength steel bolts, a similar stress-strain diagram to that shown in Figure 5 was used, but with a strain at tensile strength of $25\varepsilon_y$. The yield and tensile strengths were taken as 635 MPa and 825 MPa, respectively. The modulus of elasticity was 200000 MPa. The length of the bolts was 89 mm.

The load was applied at the top of the steel profile and only the base of the concrete core was supported. At the contact surface between the concrete core and steel tube, the coefficient of friction was considered to be zero in the tangential direction. In the normal direction, separation was permitted.

Figure 10 shows the numerical result for the model 219x8.2-4x12.7-30. The label means diameter by thickness of tubes, in millimeters, quantity by diameter of bolts, in millimeters, and concrete compressive strength in MPa. The code-predicted strength from TB-NBT:2011 is also shown in Figure 10, indicating conservative prediction.

Figures 11 to 13 present the stress distribution at the ultimate load. In Figure 11 the von Mises stress above 485 MPa is grey, showing the parts of the model with von Mises stress above the tensile strength of the steel tube. This analysis demonstrates that much of the thickness of the tube in contact with the bolt is completely loaded.

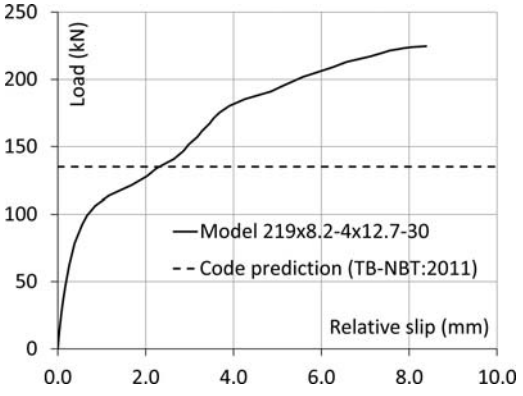

Figure 10. Load-displacement curve for model 219x8,2-4x12,7-30.

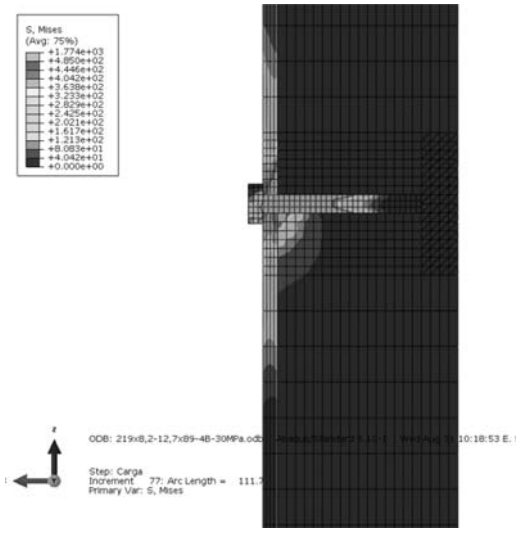

Figure 11. Von Mises stress limited to 485 MPa (tensile strength of steel tube).

In Figure 12 the von Mises stress above 825 MPa is grey, showing the parts of the model with stress above the tensile strength of the steel bolt, indicating that much of the length of the bolt is completely loaded.

In Figure 13 the compressive longitudinal stress (negative) above 30 MPa is dark grey, showing the parts of the model with stress above the concrete strength, indicating a highly loaded area under the bolt.

Table 2 presents the numerical results obtained by finite element model and code-predicted results obtained using the expressions (3) and (4).

Three models (355x9.5-4x19-30, 355x9.5-4x25.4-30 and 355x9.5-4x12.7-40) had convergence difficulties and were neglected.

The average relationship between the code-predicted result (lowest among the last four columns of Table 2 – the cell of this value is shaded) and the numerical result is equal to 0.725, with a minimum value of 0.51 and a maximum of 0.94. The standard

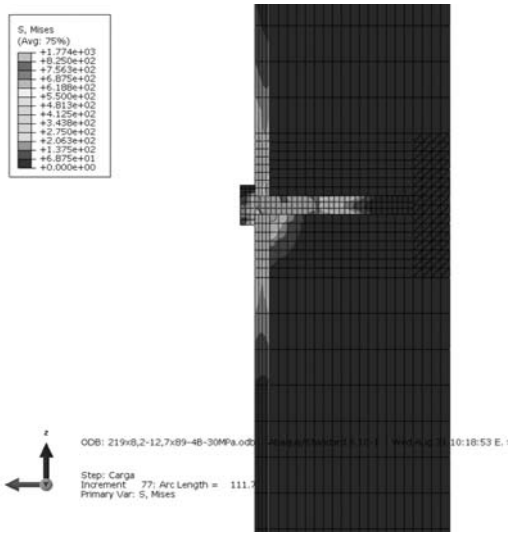

Figure 12. Von Mises stress limited to 825 MPa (tensile strength of steel bolt).

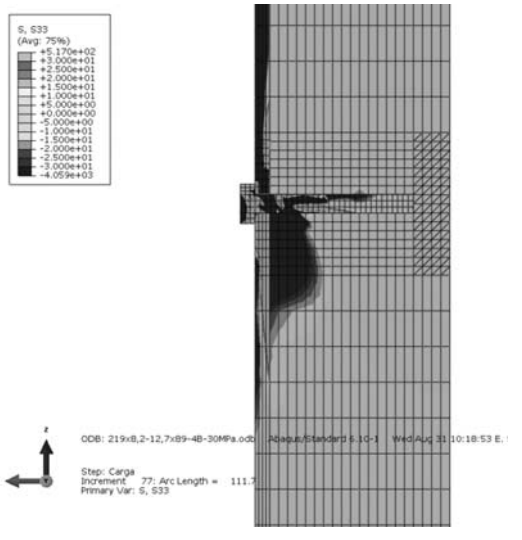

Figure 13. Longitudinal stress limited to 30 MPa (concrete strength).

deviation is equal to 0.12. The code-predicted capacities are always conservative compared to the numerical results.

5 CONCLUSIONS

This work presents a numerical study of a load transfer device, which uses bolts as connectors in composite columns with concrete filled hollow steel sections. A nonlinear numerical model was developed using the program ABAQUS. Solid finite elements were used for the steel and concrete, and also to consider the contact

Table 2. Comparison between code and numerical results.

Model	FEM (kN)	Expression (3) (kN)		Expression (4) (kN)	
		$l_b d_b \sigma_{c,Rn}$	$5 d_b^2 \sigma_{c,Rn}$	$0.4\pi d_b^2 f_{ub}/4$	$2.4 d_b t f_u$
219x8.2-4x12.7-30	225	190	135	167	485
219x8.2-8x12.7-30	430	380	271	334	970
219x8.2-4x19-30	311	284	304	374	725
219x8.2-8x19-30	784	568	607	749	1451
219x8.2-4x25.4-30	512	380	543	669	970
219x8.2-8x25.4-30	1042	760	1085	1338	1940
219x8.2-4x12.7-40	231	254	180	167	485
219x8.2-8x12.7-40	453	507	362	334	970
219x8.2-4x19-40	403	379	405	403	1290
219x8.2-8x19-40	807	759	809	807	1290
219x8.2-4x25.4-40	564	507	723	669	970
219x8.2-8x25.4-40	1138	1013	1446	1338	1940
219x15.1-4x12.7-30	224	190	135	167	893
219x15.1-8x12.7-30	474	380	271	334	1786
219x15.1-4x19-30	468	284	304	374	1336
219x15.1-8x19-30	902	568	607	749	2672
219x15.1-4x12.7-40	242	254	180	242	1120
219x15.1-8x12.7-40	494	507	362	494	1120
219x15.1-4x19-40	462	379	405	374	1336
219x15.1-8x19-40	926	759	809	749	2672
355x9.5-4x12.7-30	213	190	135	167	562
355x9.5-8x12.7-30	427	380	271	334	1124
355x9.5-8x19-30	831	568	607	749	1681
355x9.5-8x25.4-30	1215	760	1085	1338	2247
355x9.5-8x12.7-40	454	507	362	334	1124
355x9.5-4x19-40	408	379	405	374	840
355x9.5-8x19-40	819	759	809	749	1681
355x9.5-4x25.4-40	593	507	723	669	1124
355x9.5-8x25.4-40	1215	1013	1446	1338	2247
355x15.1-4x12.7-30	237	190	135	167	893
355x15.1-8x12.7-30	486	380	271	334	1786
355x15.1-4x19-30	459	284	304	374	1339
355x15.1-8x19-30	926	568	607	749	2672
355x15.1-4x25.4-30	749	380	542	749	2486
355x15.1-8x25.4-30	1480	760	1085	1480	2486
355x15.1-4x12.7-40	180	254	180	167	893
355x15.1-8x12.7-40	534	507	362	334	1786
355x15.1-4x19-40	464	379	405	374	1336
355x15.1-8x19-40	874	759	809	749	2672
355x15.1-4x25.4-40	746	507	723	669	1786
355x15.1-8x25.4-40	1505	1013	1446	1337	3572

between the elements. Comparisons with experimental results were conducted to validate the numerical model. A parametric study was conducted in order to verify the validation of the model presented in the Brazilian Draft Standard for design of tubular steel and composite structures, TB-NBT:2011.

The study showed that the code-predicted results are always conservative compared to numerical results.

REFERENCES

ABNT NBR 8800:2008. Design of steel and composite structures for buildings. *Brazilian Association of Technical Standards.*

Chapman, J.C. 1964. Composite construction in steel and concrete – The Behaviour of composites beams. The Structural Engineer, 42 (4), 115–125.

Chien, E.Y.L. & Ritchie, J.K. 1984. Design and construction of composite floor systems. Canadian Institute of Steel Construction.

EN 1992-1-1:2004. Eurocode 2: Design of Concrete Structures, Part 1.1: General Rules and Rules for Buildings. European Committee for Standardization.

EN 1994-1-1:2004. Eurocode 4: Design of Composite Steel and Concrete Structures, Part 1.1: General Rules and Rules for Buildings. European Committee for Standardization.

Ghavami, K. 1998. Ultimate load behaviour of flexible and rigid connectors in composite beams. Journal Construction Steel Research, 46, 208–210.

Jacobs, W.P. & Hajjar, J.F. 2010. Load transfer in composite construction; Structures Congress 2010, ASCE/SEI, 1229–1240.

Leonhardt, F., Andrä, W., Andrä, H.P. & Harre, W. 1987. Neues vorteilhaftes verbundmittel für stahlverbundtragwerk mit höher dauerfestigkeit (New Improved Shear Connector With High Fatigue Strength for Composite Structures). Beton und Stahlbetonbau, 12, 325–331.

Salmon, C.G. & Johnson, J.E. 1990. Steel Structures: Design and Behavior. Emphasizing Load and Resistance Factor Design. HarperCollins College Publishers, 4th edition.

Simulia 2010. Software ABAQUS 6.10. Dassault Systèmes, USA.

Starossek, U. & Falah, N. 2009. The interaction of steel tube and concrete core in concrete-filled steel tube columns. 12th International Symposium on Tubular Structures, 84, 75–84.

Starossek, U., Falah, N. & Löhning, T. 2008a. Numerical Analyses of the Force Transfer in Concrete-Filled Steel Tube Columns. 4th International Conference on Advances in Structural Engineering and Mechanics (ASEM'08).

Starossek, U. & Falah, N. 2008b. Force transfer in concrete-filled steel tube columns. 5th European Conference on Steel and Composite Structures, Eurosteel 2008.

TB-NBT:2011. Brazilian draft standard for design of steel and composite tubular structures.

Veríssimo, G.S. 2007. Development of an indented rib shear connector for steel-concrete composite structures and an investigation of its structural behaviour. Ph.D. Thesis (in Portuguese), Federal University of Minas Gerais, Brazil.

Viest, I.M. 1960. Review of research on composite steel-concrete beams. Journal of the Structural Division, ASCE, 86(ST6), 2496, 1–21.

Zellner, W. 1987. Recent designs of composite bridges and a new type of shear connectors. Proceedings of the IABSE/ASCE Engineering Foundation Conference on Composite Construction, Henniker, 240–252.

Tubular Structures XIV – Gardner (Ed.)
© 2012 Taylor & Francis Group, London, ISBN 978-0-415-62137-3

Proposed corrections for EN 1993-1-8, Part "Hollow Section Joints"

J. Wardenier
Delft University of Technology, Delft, The Netherlands
National University of Singapore, Singapore

R.S. Puthli
Research Centre for Steel, Timber and Masonry, Karlsruhe Institute of Technology, Karlsruhe, Germany

G.J. van der Vegte
Van der Vegte Consultancy, The Netherlands

ABSTRACT: The current EN 1993-1-8 (2005) recommendations are based on the IIW recommendations of 1989 (IIW 1989) and the CIDECT Design Guides 1 and 3 (Wardenier et al. 1991, Packer et al. 1992). Recently, in 2008 and 2009, IIW and CIDECT revised their recommendations (Zhao et al. 2008, ISO 2009, Wardenier et al. 2008, Packer et al. 2009). The recommendations of both organisations are consistent with each other and have also been accepted as Draft ISO recommendations (ISO 14346 2009). In principle, it has been agreed to include these new recommendations also in the next revision (amendment) of EN 1993-1-8. The proposed corrections dealt with in this paper should be included as soon as possible to cover errors, parts which are not clear, corrections related to the extension of the recommendations to S460 and corrections resulting from research of the last 10 years which showed that otherwise the safety level would be lower than expected.

1 INTRODUCTION

The current EN 1993-1-8 (2005) recommendations are based on the IIW recommendations of 1989 (IIW 1989) and the CIDECT Design Guides 1 and 3 (Wardenier et al. 1991, Packer et al. 1992). These EN 1993-1-8 recommendations have already been corrected with Corrigenda up to the end of 2010.

Recently, IIW and CIDECT revised their recommendations in 2009 and 2008/2009, respectively (Zhao et al. 2008, IIW 2009, Wardenier et al. 2008, Packer et al. 2009). The recommendations of both organisations are consistent with each other and have also been accepted as Draft ISO recommendations (ISO 14346 2009).

In principle, it has been agreed to include these new recommendations of IIW (2009), or similarly the Draft ISO 14346 (which were adopted by CIDECT in their Design Guides), in the next revision (amendment) of EN 1993-1-8.

The proposed corrections dealt with in this paper cover errors, parts which are not clear, corrections related to the extension of the recommendations to S460 and corrections resulting from research of the last 10 years which showed that the safety level of the current recommendations would be lower than expected, in some instances.

Editorial errors, and parts which are corrected to make the text clearer, are generally not discussed here. This paper therefore does not give a complete overview but a detailed survey of all proposed corrections is given in Wardenier & Puthli (2011). In this paper, comma's are used as decimal points to follow the Eurocode practice.

2 CONFUSING ITEMS

2.1 *Welding in cold-formed zones*

The text and note in EN 1993-1-8, Clause 4.14 should be corrected to make clear that, for the conditions specified, welding in the cold-formed corners and the adjacent zones is permitted.

Hence, the text should read:

Welding may be carried out in the corners and the adjacent cold formed zones, provided that one of the following conditions is fulfilled:

- the cold-formed zones are heat-treated appropriately after cold-forming but before welding;
- the inside corner-to-thickness ratio r/t satisfies the relevant value of Table 4.2 of EN 1993-1-8.

Further, the note should be presented more clearly:

Welding in the corners and within a distance of 5t from the corners is also permitted for those cold-formed hollow sections according to EN 10219 (2006), which do not satisfy the limits given in Table 4.2, provided that the hollow sections satisfy the following additional requirements:

- the thickness $\leq$12,5 mm
- the steel is Al-killed

– the quality is J2H, K2H, MH, MLH, NH or NLH
– the chemical analysis meets the following limits: $C \leq 0{,}18\%$, $P \leq 0{,}020\%$ and $S \leq 0{,}012\%$.

In other cases, welding in this area is only allowed if it can be shown by tests that welding can be permitted for that particular application.

Note: At present EN 1993-1-10 (2005) is also being extended to cover the material selection for cold-formed hollow sections. As soon as this is included, the provisions in EN 1993-1-8 can be deleted and reference made to EN 1993-1-10.

2.2 *Minimum wall thickness*

The joint strength is only determined by the geometrical parameters and not by the nominal wall thickness, provided that the welds are properly made and proper material is used. The quality of welds is covered by EN 1090-2, that is why, deviating from the IIW and CIDECT recommendations, a lower limit for the wall thickness is proposed.

To allow smaller wall thicknesses for light structures such as production greenhouses, the text in EN 1993-1-8, Clause 7.1.1 (5) should read:

The nominal wall thickness of hollow sections should not be less than 2,5 mm unless welding qualification tests show that the welds can be properly executed. In such cases, the minimum nominal wall thickness should be 1,5 mm.

2.3 *Validity ranges*

In several tables, the validity ranges have to be better specified, including all relevant parameters. Further, typing errors have to be corrected, for example in EN 1993-1-8, Table 7.8 in the third box below "gap or overlap", the typing error for overlap joints $b_i/b_j \leq 0{,}75$ should be corrected to $b_i/b_j \geq 0{,}75$. In addition, in the same box the following validity range should be added: "for CHS braces: $d_i/d_j \geq 0{,}75$".

2.4 *Chord stress*

EN 1993-1-8 defines a chord compression load as positive whereas all other recommendations and codes in the world (ISO, IIW, AISC, CIDECT) designate tension as positive. It would have been better to also designate tension as positive in EN 1993-1-8, but that is not feasible anymore. To avoid confusion with all other recommendations and codes, it is proposed to put the chord stress parameters n_p and n between absolute signs, i.e. $|n_p|$ and $|n|$.

In Clause 7.2.1(3) it should be indicated that for the chord stress functions the chord stress at the chord connecting face should be taken.

2.5 *Chord stress effect*

EN 1993-1-8 stipulates that for CHS joints the effect of the chord stress on the joint capacity should be incorporated by a prestress parameter n_p, based on the chord preload, see Figure 1 (i.e. the chord load excluding the reaction forces for the brace load components).

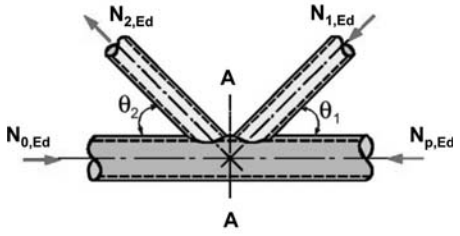

$$N_{0,Ed} = \Sigma N_{1,2,Ed} \cos\theta_{1,2} + N_{p,Ed}$$

$$n_p = \frac{N_{p,Ed}}{A_0 f_{y0}} = \frac{\sigma_{p,Ed}}{f_{y0}} \quad \text{for CHS joints}$$

$$n = \frac{N_{0,Ed}}{A_0 f_{y0}} = \frac{\sigma_{0,Ed}}{f_{y0}} \quad \text{for RHS joints}$$

Figure 1. Definition of n_p and n.

For RHS joints, the chord stress effect is based on the parameter n which considers the maximum chord load. This gives rise to confusion, however, this is due to the compromise in the previous IIW recommendations (IIW 1989) which formed the basis for these Eurocode 3 recommendations.

In the new recommendations of IIW 2009 and CIDECT (Wardenier et al. 2008, Packer et al. 2009) this inconsistency has been solved by considering the chord stress function using the maximum chord stress at the connecting face, both for CHS and RHS joints. This could not be introduced anymore in the corrections for EN 1993-1-8 since all CHS joint strength functions would then have to be modified, which was not feasible for this edition of EC3.

2.6 *Chord shear check for cross joints*

If the angle θ between the braces and the chord becomes very small, i.e. $\cos\theta > \beta$ in the case of CHS X joints or $\cos\theta > h_1/h_0$ in case of X joints with an RHS or I section chord, shear in the chord cross section between the braces can occur, see Figure 2 (Choo et al. 2004). This has to be checked similar to a member check for shear and axial load. In EN 1993-1-8, this check, which is already included in the current AISC specification, should be included.

2.7 *Plate-to-RHS joints*

For the transverse plate-to-RHS joint in Table 7.13 of EN 1993-1-8, the brace failure criterion has been erroneously deleted in the previous corrigenda and should be included again.

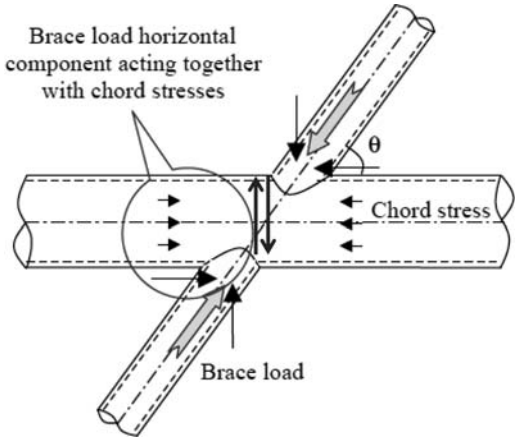

Figure 2. Shear failure of an X joint with a small angle θ.

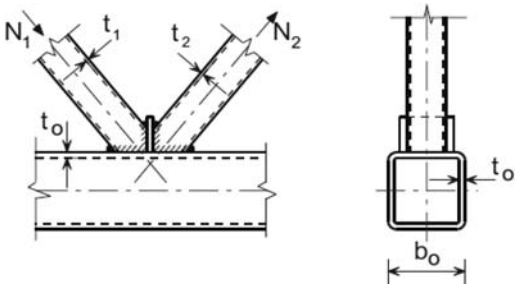

Figure 3. Stiffened joint.

2.8 *Joints stiffened by plates*

In Table 7.18 of EN 1993-1-8, the current titles and text for joints stiffened by plates are contradictory, and hence, a proposal is made for clarification, see Wardenier & Puthli (2011).

Further, the use of only a division plate in between the braces, as shown in Figure 3, does only provide a real increase in strength if the chord wall is relatively stocky or β is high and therefore this provision is proposed to be deleted or more restrictions should be given.

Also, it is not permitted to infringe the validity range of 25% overlap, thus the text "…because of insufficient overlap" is misleading.

The text for the other stiffened joints should also be corrected (see Wardenier & Puthli (2011)) because sometimes it is either contradictory or not clear.

2.9 *Multiplanar joints*

For CHS multiplanar joints a reduction factor of 0,9 is given for KK joints. Research by Liu & Wardenier (2001, 2003) showed that the reduction is caused by a larger chord load in a KK joint if compared to the chord load in a uniplanar K joint. This effect is not included in the chord prestress function k_p since in EN 1993-1-8, for CHS joints, n_p is still based on the preload.

In Tables 7.7 and 7.19 of EN 1993-1-8, it should be indicated that the reduction factor μ only applies for chord plastification (CHS) or chord face failure (RHS).

In Table 7.19, for RHS joints, the validity has to be changed from $60° \le \varphi \le 90°$ to $\varphi = 90° \pm 5°$ because no evidence exists for angles $\varphi < 90°$. To avoid misinterpretation, for KK joints with $h_0 = b_0$ the interaction equation in the gap should be replaced by:

$$\left(\frac{N_{0,Ed}}{N_{pl,0,Rd}}\right)^2 + \left(\frac{V_{0,Ed}\sin(\varphi/2)}{V_{pl,0,Rd}}\right)^2 \le 1{,}0$$

where

$$N_{pl,0,Rd} = \frac{f_{y0}\,A_0}{\gamma_{M0}}$$

$$V_{pl,0,Rd} = \frac{\left(f_{y0}/\sqrt{3}\right)A_{V.0}}{\gamma_{M0}} = \frac{f_{y0}}{\sqrt{3}}\left(0{,}5A_0\right)\frac{1}{\gamma_{M0}}$$

3 ITEMS RELATED TO THE EXTENSION OF THE RECOMMENDATIONS TO S460

In the previous ENV version of Eurocode 3, the validity of the design rules for Hollow Section Joints was limited to steel S355. Since only limited experimental evidence was available from CHS joint tests in Japan, Germany and the Netherlands, an evaluation of the data and an additional numerical study for RHS K joints was carried out by Liu & Wardenier (2004). It was found that due to the relatively increased deformations when using a deformation limit of 3% d_0 or 3% b_0 (Lu et al. 1994), for the chord face failure criterion, a correction factor of 0,9 should be used for the strength. Also, considering the lower ductility of S460, it was decided by commission IIW-XV-E to use this factor in general for all criteria. This factor is already incorporated in EN 1993-1-8 through the Corrigenda. Recently, this factor 0,9 has been confirmed from research by Puthli et al. (2009).

However not yet included is chord side wall buckling due to out-of-plane bending moments on the brace; here the same buckling coefficient should be applied as that for brace axial load. For brace in-plane-bending moments, no experimental data exists for chord side wall buckling for S460. Therefore, for X joints under brace in-plane bending, it is proposed to adopt the same buckling stress as that for axial loading and bending out-of-plane. Since for T joints, based on tests in Karlsruhe (Mang et al. 1983), no buckling coefficient was applied for steels up to S355, the authors of the IIW (2009) recommendations assumed that the limitation of class 2 sections with a 14% lower h_0/t_0 limit for S460 than for S355, in combination with the

reduction factor 0,9 covered the higher buckling sensitivity for S460. As a result, no correction is proposed for T joints loaded by in-plane-bending moments.

In summary: to cover the validity extension to S460 and to be consistent with Table 7.11 of EN 1993-1-8, the equations for in-plane bending applied to RHS joints, given in Table 7.14, should read:

$$M_{ip,1,Rd} = 0,5 k_n f_b t_0 (h_1 + 5t_0)^2 / \gamma_{M5}$$

$f_b = f_{y0}$ for T joints
$f_b = 0,8 \chi f_{y0}$ for X joints

For out-of-plane bending moments, they should read:

$$M_{op,1,Rd} = k_n f_b t_0 (b_0 - t_0)(h_1 + 5t_0) / \gamma_{M5}$$

$f_b = \chi f_{y0}$ for T joints
$f_b = 0,8 \chi f_{y0}$ for X joints

The above proposed corrections are in agreement with the new recommendations of IIW (2009) and CIDECT (2008, 2009).

4 CHORD STRESS FUNCTIONS FOR CHORD IN TENSION

In the current EN 1993-1-8 and in the previous recommendations of IIW (1989) and CIDECT (1991, 1992), the chord stress functions for tension k_p and k_n are 1,0. For CHS joints, this function was based on the results of experiments by Togo (1967) and further analyses by Kurobane (1981) on K joints using the "preload" concept. For RHS joints, the chord stress function for tension was based on the analysis by Wardenier (1982). For RHS K joints, the effect of high chord loads was also verified by girder tests (de Koning & Wardenier 1979).

However, at that time, no chord deformation criterion was used to limit the ultimate joint strength as later adopted by IIW (Lu et al. 1994). Re-evaluating the experimental tests using this deformation criterion also shows that, depending on the geometrical parameters, joints with high chord tensile loads may have a reduced strength.

In CIDECT programme 5BK for CHS joints (Van der Vegte et al. 2001a, b, 2003), it was analytically and numerically investigated whether the chord prestress or the chord maximum stress was governing for the joint behaviour. These investigations showed that the maximum chord stress is the governing parameter, which resulted in a complete reanalysis of the CHS joint strength equations which are now incorporated in the new recommendations of IIW (2009), Draft ISO 14346 (2009) and CIDECT (2008, 2009).

Also, detailed numerical studies on RHS joints (Wardenier et al. 2007a, b) showed that large chord tension loading may have a negative effect on the joint strength of RHS joints.

Based on these research programmes, new simplified chord stress functions have been developed for the recommendations of IIW (2009) and Draft ISO, which were also adopted in the CIDECT (2008, 2009) design guides. All are now based on the maximum chord stress, thus solving the inconsistencies between the previous functions, where either the chord prestress parameter n_p was used for CHS joints or the maximum chord stress parameter n for RHS joints.

Since the modifications for EN 1993-1-8 did not permit the change of all equations, only those which are really necessary are changed. Thus, for compression loading, no changes are proposed in the chord stress functions in EN 1993-1-8, although using different parameters n_p and n for CHS and RHS joints is still unsatisfactory and confusing.

However, for tension loading, modification of the chord stress function is really necessary, which is also independently concluded for CHS joints by Choo et al. (2003, 2004, 2006), Voth & Packer (2010) and Pecknold et al. (2000, 2001), as now included in the offshore API rules (API, 2007).

Tables 1a and 1b show the chord stress functions of EN 1993-1-8 and those of the new recommendations of IIW (2009), Draft ISO (2009) and CIDECT (2008, 2009).

The function $k_n = (1 - |n|)^{0,10}$ for RHS joints is, in general, a lower bound for the test results for RHS K joints. For CHS joints, the exponent is 0,20. A more refined and less conservative approach, depending on the joint parameters β and γ and the type of joint, is possible but this will result in more complicated functions or separate functions for the various types of joints. For example, Figure 4 shows a less conservative lower bound for RHS K gap joints only.

Due to the more sensitive nature of T and X joints for chord loading, a more conservative function has

Table 1a. Current chord stress functions in EN 1993-1-8.

	Compression	Tension
CHS joints	$k_p = 1 - 0,3\|n_p\| - 0,3n_p^2$	$k_p = 1,0$
RHS joints	$k_n = 1,3 - \frac{0,4}{\beta}\|n\| \le 1,0$	$k_n = 1,0$

Table 1b. Chord stress functions in IIW (2009) and CIDECT (2008, 2009).

	Compression	Tension
CHS joints	$k_n = (1 - \|n\|^{C_1})$	$k_n = (1 - \|n\|)^{0,2}$
RHS joints	$k_n = (1 - \|n\|^{C_1})$	$k_n = (1 - \|n\|)^{0,1}$
	$C_1 = f(\beta)$ is not specified here	

Note: for comparison, here, absolute values are used for n and n_p because a compression stress is taken as negative in the recommendations of IIW (2009), Draft ISO (2009) and CIDECT (2008, 2009) and positive in EN 1993-1-8. In this table, the EN 1993-1-8 symbols are used.

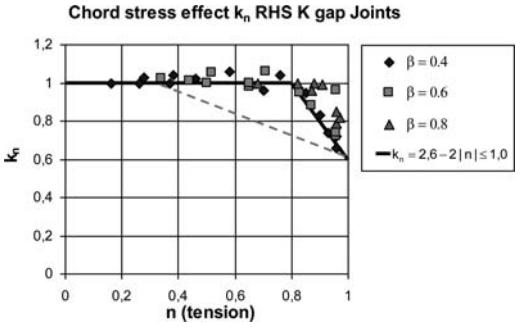

Figure 4. Comparison of numerical data vs. equations k_n for RHS K gap joints with chord tension (dotted, straight line is the approximation for the CHS X joint data in Figure 5 which is proposed also to be adopted for RHS X joints).

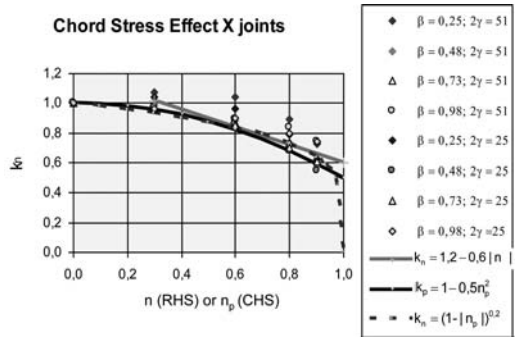

Figure 5. Comparison of numerical data vs. IIW (2009) (dotted line) and proposed equations $k_p = 1 - 0,5n_p^2$ for CHS X joints and $k_n = 1,2 - 0,6|n|$ for RHS X joints, all with chord tension.

to be adopted for these joints. Since limited relevant data is available (Yu, 1997), for RHS T and X joints a similar reduction is proposed as for CHS X joints (see Fig. 5) but expressed as a linear function, consistent with the chord stress function used in EN 1993-1-8 for RHS joints subjected to chord compression.

In the new IIW/CIDECT (2009) recommendations, the chord stress factor, accounting for the effect of chord tension in RHS joints with a longitudinal plate (k_m in EN 1993-1-8), is taken equal to the chord stress factor for RHS chord joints with CHS or RHS braces (k_n in EN 1993-1-8). This can also be adopted in Table 7.13 of EN 1993-1-8, i.e.: $k_m = k_n$ for T and X joints, but for compression $k_n \ge 1{,}3(1 - |n|)$.

As shown in Figure 5, the quadratic and linear approximations for X joints proposed for EN 1993-1-8 are well in line with the equation adopted in IIW (2009) and CIDECT (2008).

For CHS K joints, the effect of the brace load components in the chord is already included in the joint strength function, thus the determination of k_p for chord tension loading should be based on n_p. Evidence for this analysis can be found in Van der Vegte et al. (2003), Choo et al. (2003, 2006) and Pecknold et al. (2000, 2001).

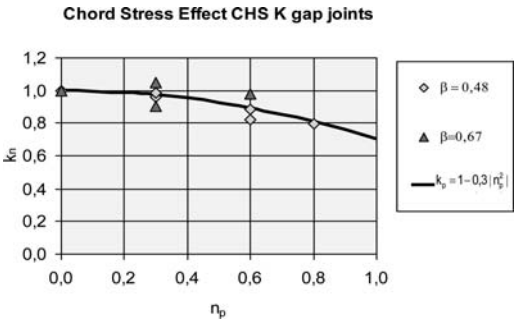

Figure 6. Comparison numerical data vs. proposed equations k_p for CHS K gap joints with chord tension at both sides.

Table 2. Proposed chord tension (pre)stress functions for EN 1993-1-8.

		Proposed chord tension (pre)stress function
CHS joints	T and X joints	$k_p = 1 - 0,5n_p^2$
	K joints	$k_p = 1 - 0,3n_p^2$
RHS joints	T and X joints	$k_n = 1,2 - 0,6\|n\| \le 1,0$
	K joints	$k_n = 2,6 - 2\|n\| \le 1,0$

However, Choo et al. (2003, 2006) used an energy criterion for limiting the chord deformation which is slightly more conservative (smaller deformations) than the 3% d_0 limit adopted by IIW, whereas Pecknold et al. (2000, 2001) used Yura's deformation criterion which allows considerably larger deformations. Further, in the models used, the end conditions of the chord also deviate. This is why the numerical data of Van der Vegte et al. (2003) for K gap joints with tension at both sides of the joint and based on the 3% d_0 deformation limit are used here to determine the parameter k_p for chord tension, see Figure 6.

Cases with chord compression at one side and chord tension at the other side of the joint are slightly more favourable and not shown in Figure 6, but for those cases, the k_p factor varies from 0,7 to 1,0. For consistency with the k_p functions for chord compression, for CHS joints simplified quadratic chord stress functions for chord tension are proposed to be incorporated as a correction in EN 1993-1-8.

Table 2 summarizes the corrections for the chord stress functions for chord tension proposed for EN 1993-1-8.

4.1 *Discussion*

Although all numerical investigations of the last ten years show an effect for chord tension loading of hollow section joints, the chord tensile stress reduction has not yet been advocated by CIDECT for incorporation in EN 1993-1-8.

In addition to the directly related CIDECT investigations, also independent numerical investigations by

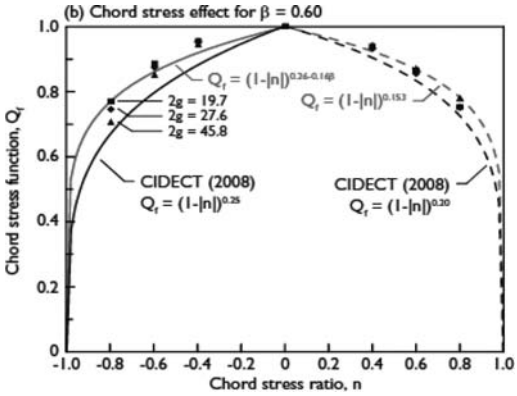

Figure 7. Comparison of the numerical data of Voth & Packer (2010) for plate-to-CHS joints under chord tension with the chord stress equation recommended by IIW (2009) and CIDECT Design Guide No. 1 (2008).

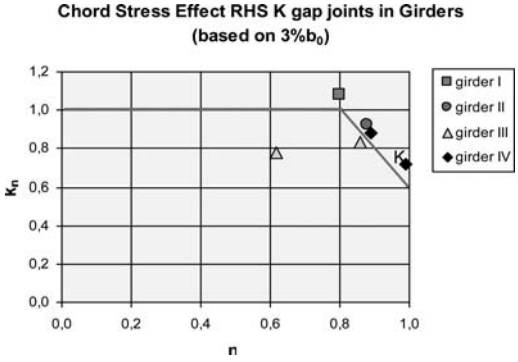

Figure 8. Comparison of the experimental data vs. proposed chord stress equation for RHS K gap joints with chord tension at both sides (joints in Girder III of CIDECT programme Qg – Report 5Qg-79/5).

Pecknold et al. (2000, 2001) on CHS joints, Choo et al. (2003, 2006) on CHS joints, and Voth & Packer (2010) on plate-to-CHS joints (see Figure 7) came to similar reductions for the joints investigated.

Besides the numerical investigations, the girder tests of CIDECT programme 5Qg by de Koning & Wardenier (1977) were re-evaluated.

Figure 8 shows the experimental results of four girder tests (K joints) of CIDECT program 5Qg, re-analysed based on the 3% b_0 deformation limit. There is one deviating low point of Joint J3 of girder III which requires a more detailed analysis with a numerical simulation; all other results fully agree with the proposed influence function in Figure 4 based on the numerical data, thus confirming the proposed reduction for chord tensile loading.

At present, CIDECT has proposed to postpone introducing the chord tension functions in EN 1993-1-8 (until the next amendment of the Eurocode), because they have funded a research programme to provide more experimental data to refine the above- mentioned chord tensile stress effect.

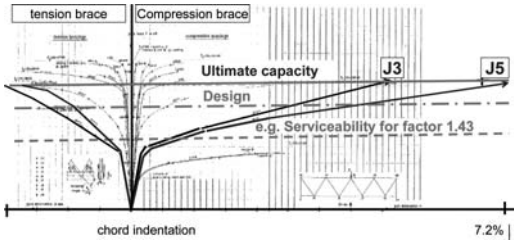

Figure 9. Load deformation diagrams of the joints in Girder III of CIDECT programme 5Qg (Report 5Qg-79/5).

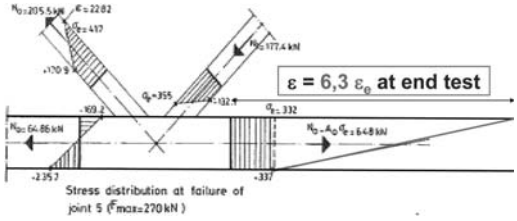

Figure 10. Stress distribution at failure in Joint J5 of Girder III of CIDECT programme 5Qg.

4.2 *Effects and consequences of ignoring chord tensile stress functions*

Figure 9 shows the original load deformation diagrams for Girder III of CIDECT program 5Qg where, for the two K gap joints J3 and J5 subjected to chord tension, the curves have been highlighted.

It shows that for Joint J5, at failure, the chord indentation was 7,2%b_0. In the figure, the design strength is also shown as 0,82 times the mean ultimate strength as well as a possible serviceability strength with an average load factor of 1,43 (load factor varies between 1,35 and 1,5).

It is clearly shown that if the chord tensile effect is not included, even at serviceability, the joint is in the non-linear range.

Figure 10 shows, for Joint J5 of girder III, the stresses in the members at failure. Due to the redistribution of the secondary bending moments, the chord face starts to yield at an early stage and at the time of reaching the full yield load in the chord, the strain in the chord face increases to 6,3 ε_e, which is very high.

In summary:

Large deformations in the joints may have a detrimental effect on the deformation of girders with a possible effect of ponding, permanent deformation under service load, and on second-order effects of built-up columns (stability).

The large strains, and potentially being in the plastic region at serviceability load could have a detrimental effect on (unexpected) low cycle fatigue effects and on (unexpected) seismic loading.

Further, the large strains in combination with strain concentrations may especially be detrimental in case of high strength steels.

5 OVERLAP JOINTS

Through the corrigenda of EN 1993-1-8, a note is given in the various clauses (although not yet included in all relevant tables) that for overlaps exceeding $\lambda_{ov,lim}$ the connection between braces and chord has to be checked for shear.

Detailed information with all equations for all types of overlap joints can be found in IIW (2009), Wardenier (2007c), Qian et al. (2007), Wardenier et al. (2008), Packer et al. (2009), Wardenier et al. (2010a, b) and Puthli et al. (2011).

ACKNOWLEDGEMENT

A version of this paper has been published with a more detailed proposal of the corrections in the German Journal "Der Stahlbau" (Wardenier & Puthli, 2011). Appreciation is extended to the Editors of "Der Stahlbau" to allow the publication of this article in a more condensed form for ISTS 14.

SYMBOLS

CHS	circular hollow section
RHS	rectangular hollow section
C_1	coefficient used in the chord stress function
$M_{ip,1,Rd}$	design resistance of a joint expressed in terms of in-plane moment in brace 1
$M_{op,1,Rd}$	design resistance of a joint expressed in terms of out-of-plane moment in brace 1
N_0	design axial chord load
$N_{i,Ed}$	design force in brace i for the ultimate limit state
$N_{i,Rd}$	design resistance of a joint expressed in terms of axial load in brace i
N_i	axial load in member i (i = 0, 1, or 2)
Ov	overlap
$V_{0,Ed}$	resulting design shear force in the gap
b_0	external RHS chord width
b_i	external RHS brace width (i = 1 or 2)
d_i	external CHS brace diameter (i = 1 or 2)
f_b	buckling strength of the chord side wall
f_{yi}	yield strength of member i (i = 0, 1 or 2)
h_0	external chord depth
h_i	external RHS brace depth (i = 1 or 2)
k_n	chord stress function (RHS joints)
k_p	chord prestress function (CHS joints)
n	non-dimensional chord stress ratio based on maximum chord load
n_p	non-dimensional chord prestress ratio based on chord preload
r	inside corner radius of an RHS section
t	wall thickness of an RHS section
β	width ratio between braces and chord
γ	half width- or diameter-to-thickness ratio of the chord, $\gamma = b_0/2t_0$ or $\gamma = d_0/2t_0$
ε_e	strain at yield
η	ratio of the brace member depth to the chord diameter of width, $\eta = h_1/d_0$ or $\eta = h_1/b_0$
θ_i	angle between brace member *i* and the chord
λ_{ov}	overlap
$\lambda_{ov,lim}$	overlap for which shear between braces and chord connecting face has to be checked
μ	reduction factor for chord plastification in multiplanar joints
ϕ	out-of-plane angle between braces in multiplanar joints
χ	buckling coefficient according Eurocode 3

REFERENCES

API. 2007. Recommended practice for planning, designing and constructing fixed offshore platforms – Working stress design. API RP 2A, 21st Edition, Suppl 3, American Petroleum Institute, Washington, DC, USA.

Choo, Y.S., Qian, X.D., Liew, J.Y.R. & Wardenier, J. 2003. Static strength of thick-walled CHS X-joints – Part II: Effect of chord stresses. *Journal of Constructional Steel Research*, 59(10), pp.1229–50.

Choo, Y.S., Qian, X.D. & Foo, K.S. 2004. Static strength variation of thick-walled CHS X-joints with different included angles and chord stress levels. *Marine Structures*, 17, pp. 311–324.

Choo, Y.S., Qian, X.D. & Wardenier, J. 2006. Effects of boundary conditions and chord stresses on static strength of thick-walled CHS K-joints, *Journal of Constructional Steel Research*, 62, pp. 316–328.

EN 1090. 2008. Execution of steel structures and aluminium structures. Technical requirements for the execution of steel structures. Execution of steel structures and aluminium structures. Technical requirements for the execution of steel structures

EN 1993-1-8. 2005. Eurocode 3: Design of steel structures – Part 1-8: Design of joints. European Committee for Standardization, Brussels, Belgium.

EN 1993-1-10. 2005. Eurocode 3: Design of steel structures – Part 1-10: Material toughness and through-thickness properties. European Committee for Standardization, Brussels, Belgium.

EN 10219. 2006. Cold formed welded structural hollow sections of non-alloy and fine grain steels. European Committee for Standardization, Brussels, Belgium.

IIW 1989. Design recommendations for hollow section joints – Predominantly statically loaded. 2nd Edition, Intern. Institute of Welding, Sub-commission XV-E, Annual Assembly, Helsinki, Finland, *IIW Doc. XV-701-89*.

IIW. 2009. Static design procedure for welded hollow section joints – Recommendations. 3rd Edition, Intern. Institute of Welding, Sub-commission XV-E, Annual Assembly, Singapore, *IIW Doc. XV-1329-09.*

ISO. 14346. 2009. Static design procedure for welded hollow section joints – Recommendations. Draft prepared for ISO by ISO TC/SC 15/WG 15. Intern. Standard Organization, Geneva, Switzerland.

Koning, C.H.M. de & Wardenier, J. 1979. Tests on welded joints in complete girders made of square hollow sections. *CIDECT Report 5Q/79/5 and 5Qg-79/5*, Delft University of Technology, Delft, The Netherlands.

Kurobane, Y. 1981. New developments and practices in tubular joint design (+ Addendum). Intern. Institute of Welding, Annual Assembly, Oporto, Portugal, *IIW Doc. XV-488-81.*

Liu, D.K. & Wardenier, J. 2001. Multiplanar influence on the strength of RHS multiplanar gap KK-joints. *Proc. 9th Intern. Symp. on Tubular Structures*, Düsseldorf, Germany, Tubular Structures IX, Swets & Zeitlinger, Lisse, The Netherlands, pp. 203–212.

Liu, D.K. & Wardenier, J. 2003. The strength of multiplanar KK-joints of square hollow sections. *Proc. 10th Intern. Symp. on Tubular Structures*, Madrid, Spain, Tubular Structures X, Swets & Zeitlinger, Lisse, The Netherlands, pp. 197–205.

Liu, D.K. & Wardenier, J. 2004. Effect of the yield strength on the static strength of uniplanar K-joints in RHS (steel grades S460, S355 and S235). *IIW Doc. XV-E-04-293*, Delft University of Technology, Delft, The Netherlands.

Lu, L.H., Winkel, G.D. de, Yu, Y. & Wardenier, J. 1994. Deformation limit for the ultimate strength of hollow section joints. *Proc. 6th Intern. Symp. on Tubular Structures*, Melbourne, Australia, Tubular Structures VI, Balkema, Rotterdam, The Netherlands, pp. 341–347.

Mang, F., Bucak, Ö., & Wolfmuller, F. 1983. The development of recommendations for the design of welded joints between steel structural hollow sections (T- and X-type joints). *Final Report on ECSC Agreement 7210 SA/I 09.*

Packer, J.A., Wardenier, J., Kurobane, Y., Dutta, D. & Yeomans, N. 1992. *Design guide for rectangular hollow section (RHS) joints under predominantly static loading.* 1st Edition, CIDECT series "Construction with hollow steel sections" No. 3, Verlag TÜV Rheinland, Köln, Germany.

Packer, J.A., Wardenier, J., Zhao, X.-L., Vegte, G.J. van der & Kurobane, Y. 2009. *Design guide for rectangular hollow section (RHS) joints under predominantly static loading.* 2nd Edition, CIDECT series "Construction with hollow steel sections" No. 3, CIDECT, Geneva, Switzerland.

Pecknold, D.A., Ha, C.C. & Mohr, W.C. 2000. Ultimate strength of DT tubular joints with chord preloads *Proc. 19th Intern Conf. on Offshore Mechanics and Arctic Engineering*, New Orleans, U.S.A

Pecknold, D.A., Park, J.B. & Koppenhoefer, K.C. 2001. Ultimate strength of gap K tubular joints with chord preloads. *Proc. 20th Intern. Conf. on Offshore Mechanics and Arctic Engineering*, Rio de Janeiro, Brazil.

Puthli, R.S., Herion, S. & Fleischer, O. 2009. Adaption and extension of the valid design formulae for joints made of high-strength steels up to S690 for cold-formed and hot-rolled sections. *CIDECT Interim Report 5BT-4/09.*

Puthli, R.S., Ummenhofer, T., Wardenier, J. & Pertermann, I. 2011. Anschlusse mit Hohlprofile nach DIN EN 1993-1-8: 2005; Hintergrund, Kommentare, Beispiele *Stahlbau-Kalender*, pp. 394–459

Qian, X.D., Wardenier, J. & Choo, Y.S. 2007. A uniform approach for the design of CHS 100% overlap joints. *Proc. 5th Intern. Conf. on Advances in Steel Structures* Singapore, Vol. II, pp. 172–182

Togo, T. 1967. Experimental study on mechanical behaviour of tubular joints. *Dissertation* (in Japanese), Osaka University, Osaka, Japan.

Vegte, G.J. van der, Makino, Y., Choo, Y.S. & Wardenier, J. 2001a. The influence of chord stress on the ultimate strength of axially loaded uniplanar X-joints. *Proc. 9th Intern. Symp. on Tubular Structures*, Düsseldorf, Germany, Tubular Structures IX, Swets & Zeitlinger, Lisse, The Netherlands, pp. 165–174.

Vegte, G.J. van der & Makino, Y. 2001b. The effect of chord stresses on the static strength of CHS X-joints. *Memoirs of the Faculty of Engineering, Kumamoto University* 46(1), pp. 1–24.

Vegte, G.J. van der, Liu, D.K., Makino, Y. & Wardenier, J. 2003. New chord load functions for circular hollow section joints. *CIDECT Final Report (revised) 5BK-4/03*.

Voth, A.P. & Packer, J.A. 2010. Branch plate-to-circular hollow structural section connections. *CIDECT Final Report (revised) 5BS-3/10.*

Wardenier, J. 1982. *Hollow section joints*. Delft University Press, The Netherlands, ISBN 90-6275-084-2.

Wardenier, J., Kurobane, Y., Packer, J.A., Dutta, D. & Yeomans, N. 1991. *Design guide for circular hollow section (CHS) joints under predominantly static loading.* 1st Edition, CIDECT Series "Construction with hollow steel sections" No. 1, Verlag TÜV Rheinland, Köln, Germany.

Wardenier, J, Vegte, G.J van der & Liu D.K. 2007a Effect of chord loads on the strength of RHS uniplanar gap K joints. *CIDECT Final Report 5BU-7/07.*

Wardenier, J., Vegte, G.J. van der & Liu, D.K. 2007b. Chord stress functions for K gap joints of rectangular hollow sections. *Intern. Journal of Offshore and Polar Engineering*, ISOPE, 17(3), pp. 225–232.

Wardenier, J. 2007c A uniform effective width approach for the design of CHS overlap joints. *Proc 5th Intern. Conf on Advances in Steel Structures*, Singapore, Vol. II, pp. 155–165

Wardenier, J., Kurobane, Y., Packer, J.A., Vegte, G.J. van der & Zhao, X.-L. 2008. *Design guide for circular hollow section (CHS) joints under predominantly static loading.* 2nd Edition, CIDECT Series "Construction with hollow steel sections" No. 1, CIDECT, Geneva, Switzerland.

Wardenier, J., Packer, J.A., Zhao, X.-L. & Vegte, G.J. van der 2010a. *Hollow section joints in structural applications.* CIDECT, Bouwen met Staal, Zoetermeer, The Netherlands, ISBN 978-90-72830-86-9.

Wardenier, J., Packer, J.A., Zhao, X.-L. & Vegte, G.J. van der 2010b. Background of the new RHS joint strength equations in the IIW (2009) recommendations. *Proc. 13th Intern. Symp. on Tubular Structures*, Hong Kong, China, Tubular Structures XIII, Taylor & Francis, London, UK, pp. 403–412.

Wardenier, J. & Puthli, R.S. 2011. Korrekturvorschläge für die DIN EN 1993-1-8 zum Thema Hohlprofilanschlüsse. *Stahlbau* 80, Heft 7. Germany, pp. 393–459.

Yu, Y. 1997. The static strength of uniplanar and multiplanar connections in rectangular hollow sections. *Dissertation*, Delft University of Technology, The Netherlands, Delft University Press.

Zhao, X.-L., Wardenier, J., Packer, J.A. & Vegte, G.J. van der 2008. New IIW (2008) static design recommendations for hollow section joints. *Proc. 12th Intern. Symp. on Tubular Structures*, Shanghai, China, Tubular Structures XII, Taylor & Francis, London, UK, pp. 261–269.

Tubular Structures XIV – Gardner (Ed.)
© 2012 Taylor & Francis Group, London, ISBN 978-0-415-62137-3

Nonlinear formulation for tubular X-joints in frame analysis

Xudong Qian, Yang Zhang & Yoo Sang Choo
Department of Civil and Environmental Engineering, National University of Singapore, Singapore

ABSTRACT: This paper presents a set of new joint formulations to describe the load-deformation characteristics for Circular Hollow Section (CHS) X-joints under monotonic brace axial compression. The proposed formulation couples the ultimate joint strength with the nonlinear deformation to determine the resistance of the joint at varying levels of the applied displacement. The ultimate joint capacity used in the current formulation follows the mean strength equations in the latest IIW recommendations, while the geometric-dependent parameters derive from regression analyses of a calibrated finite element investigation covering a practical range of joint parameters. This proposed formulation for CHS X-joints also includes the redevelopment of the joint strength at the contact of two opposing brace members under compression. The experimental results from the large-scale 2-D and 3-D frame tests validate the accuracy of the proposed formulation, which is implemented in a nonlinear pushover analysis as user-defined joint-spring elements.

1 INTRODUCTION

Numerous installed offshore platforms especially of jacket types have reached their twenty years design life. For obvious economic reasons, operators decide to proceed with these structures' exploitation (API 2000). Thus, the reassessment of these older platform structures requires advanced nonlinear frame analyses, which should include an accurate description of the local joint response under overloading conditions.

Conventional analytical models assume that tubular members are rigidly connected to each other at the intersection. However, joints may show considerable flexibility in the elastic as well as the elastic-plastic range, which may cause excessive deflections and different internal force distributions in the structure (Bouwkamp 1981). A precise analytical joint model requires the capability not only to simulate the linear flexibility of the joints, but also to incorporate the joint nonlinearity and joint capacity into the overall nonlinear behavior of the offshore platform.

The phenomenological representation of the critical joint behavior through the user-defined nonlinear joint springs, as schematically represented in Figure 1, allows incorporation of the nonlinear joint behavior in the global frame analysis. Previous researchers develop their joint formulations either by a perfect elastic-plastic spring (Ueda *et al.* 1986) or by a piecewise linear load-deformation curve (Choo *et al.* 2005). The joint industry-university project, led by a UK company, developed a joint formulation, namely the MSL formulation (Dier & Hellan 2002), which encompasses the interaction of the chord and brace loads in the joint response. Many researchers have also derived

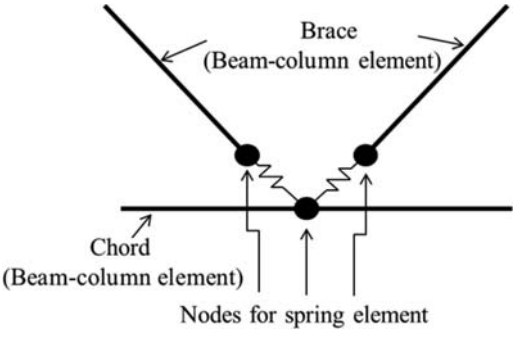

Figure 1. Joint spring representation in the global frame analysis.

the flexibility parametric formula for various types of joints based on either experimental tests (Fellser *et al.* 1986) or the finite element (FE) analysis (Efthymiou 1985, Hellan 1995, Chen *et al.* 2001).

This study develops a complete representation of the nonlinear joint behavior, which predicts closely the load-deformation responses for CHS X-joints based on their geometry and material properties using a continuous and smooth curve. The proposed joint formulation predicates on results from calibrated finite element analyses. The nonlinear pushover analysis, performed in the numerical tool USFOS (an acronym for Ultimate Strength for Frame Offshore Structure) proves the validity of the proposed formulation by using a nonlinear joint spring in the pushover analysis for 2-D and 3-D space frames (USFOS 2001), as shown in Figure 1.

Table 1. Geometric parameters of the X-joint specimens in the reported test.

Joint	d_0(mm)	β	γ	α	τ	θ
X-joint	408	0.6	20	12	1	–

2 JOINT FORMULATION

2.1 *Verification of nonlinear FE analyses*

Calibrated numerical analyses provide an economical alternative to develop the extensive database needed for the load-deformation formulation of the X-joint. This section verifies the accuracy of the elastic-plastic load deformation finite element analysis based on the experimental results for CHS X-joints, reported by van der Vegte (1995). Table 1 lists the geometric dimension for the joint specimen, where the β ratio indicates the ratio of the brace diameter over the chord diameter. The γ value stands for the chord radius to the chord wall thickness ratio. The parameter α refers to the chord length to the chord radius ratio and τ denotes the ratio of the brace wall thickness over the chord wall thickness.

The elastic-plastic, large-deformation analysis utilizes the general-purpose finite element package, ABAQUS (2010). The finite element models employ the twenty-node solid elements with reduced integration (C3D20R from ABAQUS element library). The adoption of solid element allows more accurate representation of the weld profile which follows the specifications in AWS (2010).

Figure 2a shows the X-joint reported by van der Vegte (1995), which fails by extensive plastic deformation in the chord wall around the brace-to-chord intersection under brace axial compression. The finite element mesh, shown in Figure 2b, is generated from an automatic procedure developed in the Patran Command Language (Qian, *et al*. 2002). The chord member employs four layers of 20-node quadratic brick elements over the thickness. Figure 2c plots the uniaxial true stress versus the true strain relationship measured during the experiment (Van der Vegte, 1995). The welds assume the same material properties as the incoming brace member. The numerical procedure applies a displacement-controlled loading at the end of the brace to facilitate numerical convergence near the peak of the joint resistance.

Figure 3 demonstrates the close agreement between the experimental load-deformation response of the CHS X-joint and that from the FE analysis. The deformation plotted in Figure 3 refers to the displacement measured at the end of the brace member.

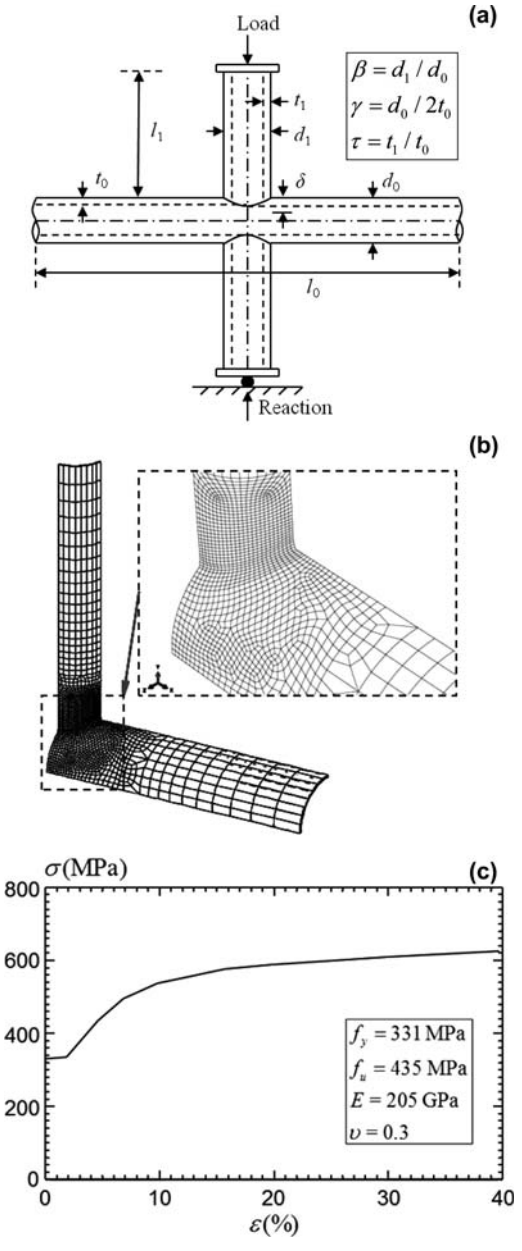

Figure 2. (a) Configuration of a CHS X-joint; (b) finite element mesh; and (c) uniaxial stress-strain curves for the steel.

2.2 *X-joint behavior*

The current study includes extensive finite element analyses of the X-joint under brace axial loading, following the same procedure discussed above. The non-dimensional joint parameters considered in the parametric study covers a β ratio from 0.3 to 1.0 and a γ ratio from 7 to 25. The numerical analyses form the database to develop the nonlinear joint formulation. The understanding on the typical X-joint behavior under brace axial compression provides the key information needed for the joint formulation, especially the evolution of the joint resistance near and after the ultimate joint capacity.

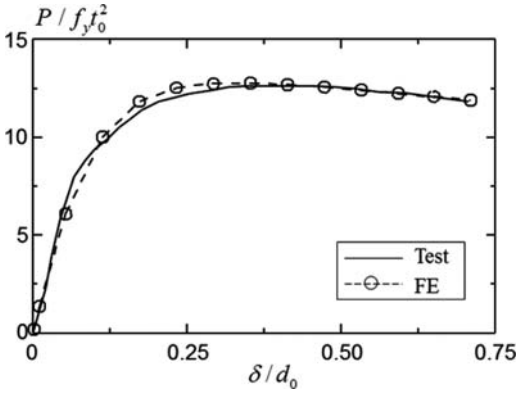

Figure 3. Comparison of the load-deformation response of the X-joint computed from the FE analysis and that recorded in the test.

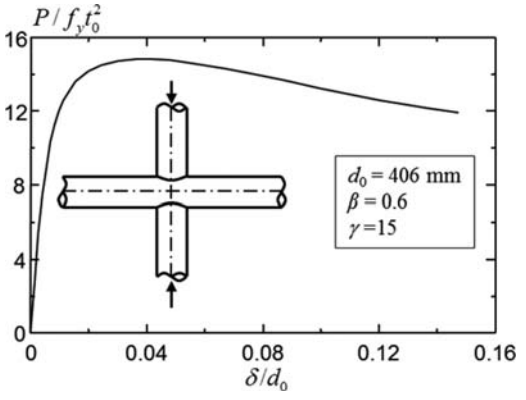

Figure 4. Typical load-deformation curves for an X-joint under axial brace compression.

Figure 4 shows the typical load-deformation curve for an X-joint under the brace axial compression. Except for very thick-walled chords (Choo *et al.* 2003), the X-joint under brace axial compression often exhibits a peak load as the deformation increases. The joint resistance decreases gradually after the peak load as the plastic deformation propagates in the chord wall.

The load-deformation characteristics of the X-joint depend significantly on the geometric parameters, measured by the non-dimensional parameters β and γ, which affect significantly the amount of membrane, shear and bending actions generated in the wall of the chord member. Based on the plastic hinge model proposed by Togo (1967), plastic hinges form at the saddle point and the middle point of the chord cross section when X-joint achieves the peak load. The load transfer mechanism changes as the β ratio decreases from 1.0. For a joint with a small β ratio, the chord wall around the brace-to-chord intersection area undergoes membrane, bending and shearing actions. As the β ratio increases, the two braces become closer in locations and the load transfer thus depends more on the membrane action in the chord wall between the two braces.

The transverse shear action becomes negligible over the wall thickness of the chord for thin-wall joints with a large γ value. The joint strength depends, therefore, mainly on the interaction of bending and axial stresses. For thick-wall joints with a small γ value, the transverse shear also contributes to the joint strength. The load transfer in the joint does not depend solely on the bending and axial stresses in the chord wall. Consequently, the load decreases after the plastic hinges form is not as quick as that for thin wall joints with a large γ ratio.

2.3 *Proposed joint formulation*

The proposed joint formulation aims to cover three important stages of the X-joint behavior, the initial response represented by the stiffness of the joint, the ultimate resistance of the joint and the post-peak response of the joint. The proposed load deformation assumes,

$$\overline{P} = f(\overline{P_u})g(\overline{\delta}) \tag{1}$$

where $\overline{P}$ refers to the non-dimensional load, or,

$$\overline{P} = \frac{P \sin\theta}{f_y t_0^2} \tag{2}$$

and $\overline{P_u}$ indicates the non-dimensional ultimate load with $P = P_u$ in Equation 2. The parameter f_y in Equation 2 denotes the yield strength of the chord material, t refers to the thickness of the chord member, and θ measures the intersection angle between the brace and the chord, the $\overline{\delta}$ in Equation 1 represents the non-dimensional deformation of joint,

$$\overline{\delta} = \frac{\delta}{d_0} \tag{3}$$

where d_0 indicates the outer diameter of the chord. By expressing $f(\overline{P_u})$ as a linear function of the non-dimensional load and $g(\overline{\delta})$ as a logarithmic function of the non-dimensional displacement, the final joint formulation follows,

$$\overline{P} = \overline{P_u}(1 - A[\ln(1 + B\overline{\delta}) - 1/\sqrt{A}]^2) \tag{4}$$

The values of A and B demonstrate strong dependence on the geometric parameter of the joint.

The current approach utilizes the mean strength equations in the latest IIW (2009) recommendations for $\overline{P_u}$,

$$\overline{P_u} = 3.16\left(\frac{1+\beta}{1-0.7\beta}\right)\gamma^{0.15} \tag{5}$$

Equation 5 defines the non-dimensional ultimate strength for X-joints under axial brace loading. The

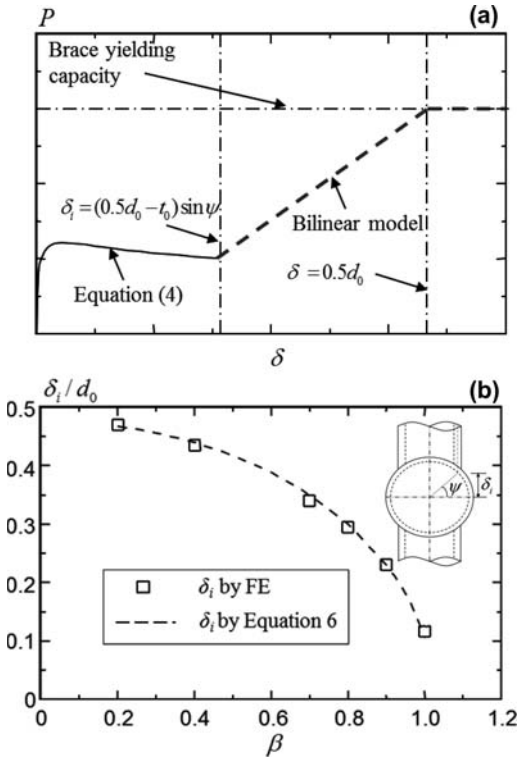

Figure 5. (a) Representation of the strength redevelopment in X-joint; and (b) comparison of the deformation level corresponding to the strength redevelopment between FE analysis and Equation 6.

effect of the chord axial force could also be reflected in $\overline{P_u}$ by the incorporation of $f(n')$, where n' denotes the chord force level.

For X-joints under axial compression loading, BOMEL 2D and 3D frame tests (Bolt *et al.* 1994, Bolt & Billington 2000) demonstrate that a re-development of the joint strength occurs at a large deformation level due to the direct contact of the compression braces, as shown in Figure5a. The re-gained strength level equals the brace yield strength, which corresponds to the brace deformation $\delta = 0.5d_0$. The initialization of the strength re-development depends on the β ratio. The displacement level, δ_i, at which the initial contact of the two braces occurs, becomes,

$$\delta_i = (0.5d_0 - t_0)\sin\psi \tag{6}$$

where δ_i measures the vertical distance of the chord inner surface near the saddle point, along the mid-thickness of the brace wall. The angle ψ equals,

$$\psi = \cos^{-1}\left(\frac{0.5d_1 - 0.5t_1}{0.5d_0 - t_0}\right) \tag{7}$$

The angle ψ defines an angle formed by the radius of the chord, passing through the intersection between the chord inner diameter and the mid-thickness of the brace, against the horizontal, as shown in Figure 5b.

Table 2. Coefficient in the proposed formulation for X-joints.

Coefficient	Formula	Proposed/FE Mean	Standard Deviation	No. of data
A	$0.27\beta^{5.2}\gamma^{(2.5\beta^2-7.5\beta+4.3)}$	1.00	0.08	30
B	$(233\gamma^{3.24\beta} - 40\gamma + 820)\beta^{0.6}$	1.01	0.09	30
C	1.00	1.00	0.02	30

Figure 5b compares Equation 6 and the δ_i computed from a half-symmetric FE model, which includes the contact between the opposite inner surfaces of the chord. The contact algorithm implemented in ABAQUS (2010) does not allow self-penetration between the inner surfaces of the chord. The discrete symbols in Figure 5b corresponds to the displacement level, at which the joint resistance starts to increase again after the gradual decrease caused by extensive plastic deformations observed in the chord material.

2.4 *Regression analysis*

The proposed formulation in Section 2.3 includes two parameters, A and B to be determined from a regression analysis. The regression analysis used to determine the values of A and B utilizes the numerical load-deformation data prior to the contact of the two compression braces, since the joint formulation (the bilinear model shown in Figure 5a) after the contact of the two braces is independent of the joint formulation in Equation 4.

Table 2 shows the geometric-dependent formulations of A and B determined from a nonlinear regression procedure (Greenwood & Nikulin, 1996). The finite element results used in the regression analysis consist of 30 elastic-plastic, large-deformation analyses on CHS X-joint. The current parametric study includes six β ratios: 0.3, 0.6, 0.9, 0.93, 0.96, and 1.0; as well as five γ ratios: 7, 10, 15, 20 and 25. The corresponding formulation for A and B demonstrates a close agreement with the discrete values obtained using the FE results, as shown by the small standard-deviation values. Figure 6 illustrates the good comparison between the load-deformation curves predicted by the proposed joint formulation and those computed from the large deformation, elastic-plastic FE analysis for four typical CHS X-joints. Qian *et al*. (2011) demonstrate that both the initial stiffness and the deformation level corresponding to the ultimate limit state derived from the proposed formulation (Equation 4) agree closely with the results reported by previous researchers (Choo *et al*. 2005, Lu *et al*. 1994).

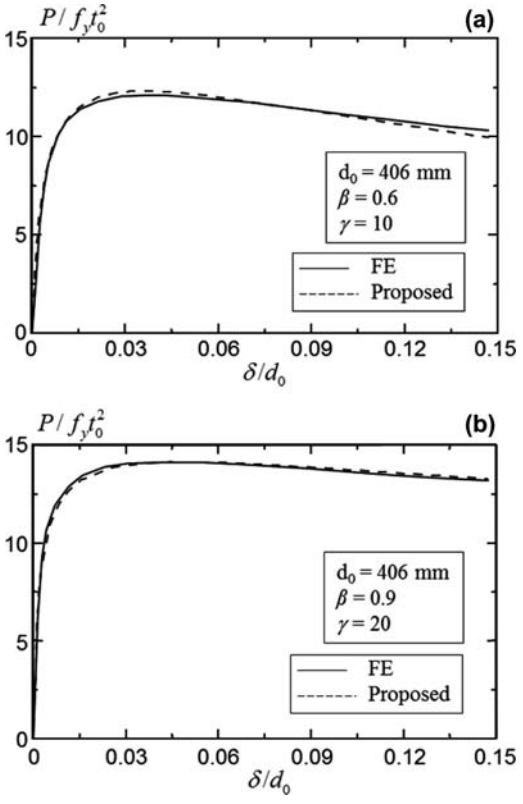

Figure 6. Typical comparison of the proposed load-deformation formulation with the FE results for CHS X-joints with: (a) $\beta = 0.6$, $\gamma = 10$; and (b) $\beta = 0.9$, $\gamma = 20$.

3 VALIDATION OF THE PROPOSED FORMULAITON IN FRAME ANALYSIS

This section proves the robustness of the proposed joint formulation through the nonlinear pushover analysis performed on 2-D and 3-D frames designed with weak joints. The pushover analysis employs USFOS to incorporate the nonlinear joint behavior as user-defined nonlinear spring elements between the brace member and the chord member. USFOS represents each individual member in the structure based on the exact solution of the beam-column governing equation subjected to end-forces. This allows accurate representations of each physical member with a single element. The element formulation utilizes the large-deformation theory and includes the plastic hinge and material nonlinearities (USFOS 2001). The current study benchmarks the proposed joint formulation against the large scale 2D and 3D frame tests reported in the joint industry project (Bolt *et al*. 1994, Bolt & Billington 2000).

3.1 *BOMEL 2D frame*

Bolt *et al.* (1994) conducted an experimental study of two series of 2D large-scale frames under static loading. This study focuses on three out of the six X-joint frame tests reported by Bolt *et al*. (1994). Figure 7 sketches the detail configuration of the X-braced frames Frame I and II. Frame III has a similar configuration as Frame I, except that the mid-horizontal member in Frame I is absent in Frame III.

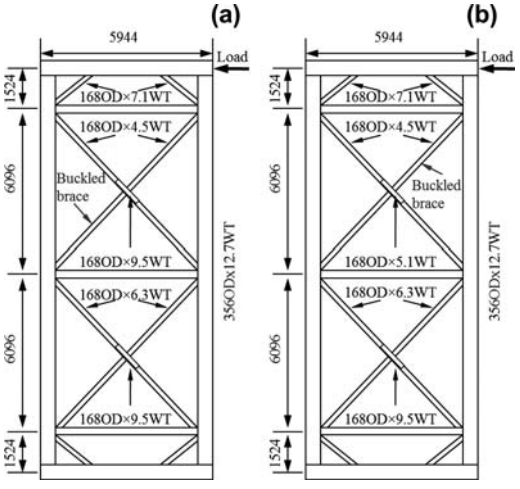

Figure 7. Configuration of BOMEL 2D frames: (a) Frame I; and (b) Frame II.

The design of X-frames follows essentially the same configuration representative of offshore jacket structures. The study tests the frames in plane, pin connected at the base to the triangulated test rig and supported by six primary leg joints representing the restraint of out-of-plane bracing. The test arrangement applies a horizontal load incrementally at the top of the frame.

The calibration process contains three types of joint formulation for each frame analysis: 1) the rigid joint analysis, 2) MSL joint formulation available in USFOS (2001), and 3) the proposed joint formation. The rigid joint analysis is often the default assumption adopted by practicing engineers in the design procedure. The MSL formulation (Dier & Hellan 2002) represents an advanced joint formulation recently developed by the research project led by MSL. All the modeled frames employ different joint assumptions for critical joints, with the default rigid joint assumption for the other joints.

3.1.1 *Frame I*

Frame I is designed with strong high yield joint cans at both top and bottom bays and a mid-height horizontal member. Figure 8a compares the numerical analysis and the test results for Frame I, where top bay compressive member buckling dominates the frame strength. The different analyses do not show noticeable differences in the failure mechanism. The proposed formulation gives a slightly better agreement with the test result.

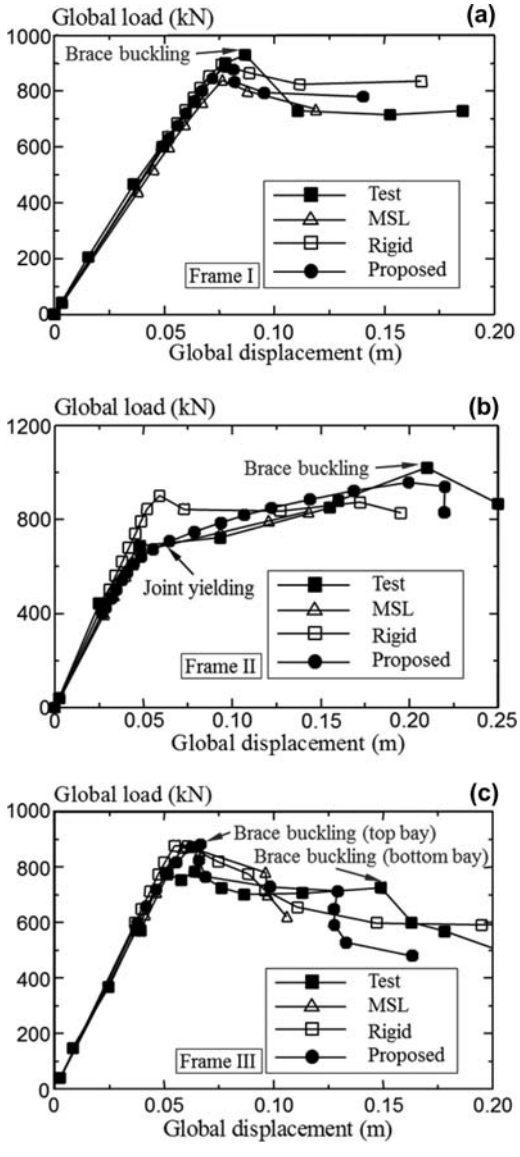

Figure 8. Comparison of the global load-deformation response between numerical analysis and experimental records for: (a) Frame I; (b) Frame II; and (c) Frame III.

3.1.2 *Frame II*

Frame II employs a weak joint can at the top bay to investigate the load shedding and redistribution. Figure 8b compares the global response for Frame II, where the top bay X-joint is the critical component. The compression X-joint gradually softens until the peak capacity is achieved. The X-joint re-gains strength due to the contact of the two braces under a large deformation level. The global load sustained by the frame continues to increase until the buckling of the top bay compression brace followed by the buckling the lower bay compression brace.

The rigid joint assumption leads to an incorrect prediction of the joint response. The MSL formulation shows the softening of the X-joint in accordance with the test results. However, a deformation limit for the joint in the MSL formulation limits the maximum deformation a joint can sustain. Therefore, the MSL formulation does not capture the top bay brace buckling in the Frame II test. The proposed joint formulation predicts both the softening of the CHS joint due to plastic deformations in the chord wall and the re-strengthening of the X-joint at a large deformation level. The predicted frame response using the proposed joint formulation thus reflects correctly the buckling failure of the test frame, at a slightly more conservative load level compared to the test result.

3.1.3 *Frame III*

Without the horizontal member, Frame III shows a similar ultimate strength level as compared to Frame I, as shown in Figure 8c. The absence of the horizontal member generates more significant load redistribution and the load from the top bay passes directly to the bottom bay compression brace. This causes an earlier buckling of the bottom bay member after the buckling of the top bay brace. The frame analysis based on the proposed joint formulation provides a better prediction on the global frame response than the analysis using the MSL formulation and that based on the rigid joint assumption.

3.2 *BOMEL 3D Frame*

Bolt & Billington (2000) report a series of large-scale 3D frame tests. Figure 9 shows the configuration of the 3-D frame. The test specimen is a double-bay frame, consisting of six vertical legs. As shown in Figure 9a, the six leg test structure is rotated onto its side to enable loads to be applied from and reacted to the ground.

The test program includes three load cases on the frame. The current paper focuses on the comparison of Load Case II, in which the X-frame panel (Panel E) forms the primary load path in the structure, as illustrated in Figure 9b.

In Load Case II, the rear X-braced panel along Panel E experiences a vertical load. The softening of the X-joint in Panel E leads to a ductile frame response. Similar to Frame II in the 2D frame, the contact of the two compression braces under large deformation leads to the redevelopment of the joint strength and causes the buckling the compression brace. The rigid joint assumption over-predicts the frame resistance as the X-joint softens, but under-predicts the frame capacity at the bucking of the compression brace. The rigid joint formulation provides a relatively smaller frame capacity as the compression brace buckles at a very small global deformation level. Both the MSL joint formulation and the proposed joint formulation capture the response of the weak joint, as shown in Figure 10. For the MSL joint formulation, the limitation in the deformation capacity terminates the global analysis at a small deformation level insufficient to generate

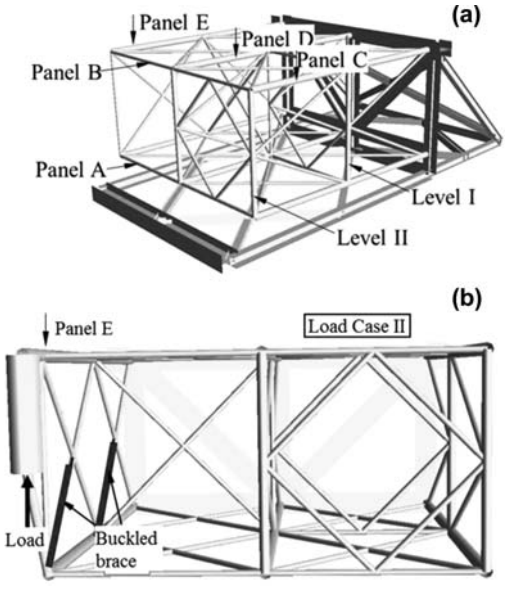

Figure 9. Configuration of BOMEL 3D frame test: (a) test model; and (b) Load Case II.

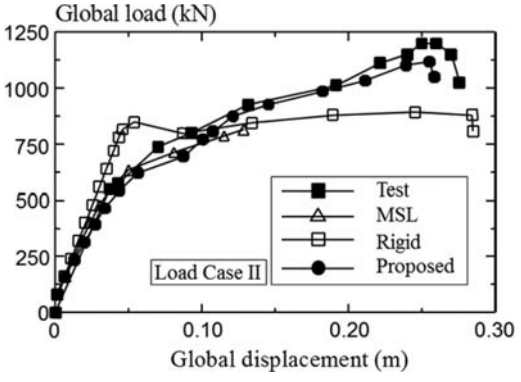

Figure 10. Comparison of the global load-deformation response between numerical analysis and experimental records for BOMEL 3D test Load Case II.

buckling of the compression brace. In contrast, the proposed joint formulation shows a good agreement as compared with the test result.

4 SUMMARY AND CONCLUSION

The proposed joint formulation provides a convenient approach to incorporate the nonlinear load-deformation relationship for CHS X-joints in the global pushover analysis. The parametric formulation based on the joint geometry and loading conditions eliminates the need for the elastic-plastic, large-deformation finite element analyses. The verification using the reported experimental study proves the accuracy of the proposed formulation.

The comparison of the frame analyses using different joint formulation with the experimental frame data demonstrates the significance of the nonlinear load-deformation joint behavior in the frame response, especially for simple 2-D frames with low redundancy. The rigid joint assumption leads to completely different failure modes in a frame with weak joints. The proposed joint formulation, implemented as joint-spring elements in the frame analysis, provides a close prediction on both the failure modes and the ultimate frame capacity for 2-D and 3-D tested frames.

REFERENCES

ABAQUS. 2010. ABAQUS/Standard User's Manual Version 6.10-EF. Rising Sun Mills(USA): Hibbitt Karlsson and Sorensen Inc.

American Petroleum Institute (API). 2000. Recommended practice for planning, designing and constructing fixed offshore platforms, API RP2A-WSD, 21st ed.

American Welding Society (AWS). 2010. Structural Welding Code – Steel. AWS D1.1/D1.1M:2010.22nd edition.

Bolt, H.M., Billington, C.J. & Ward, J.K. 1994. Result from Large Scale Ultimate Load Tests on Tubular Jacket Frame Structures. *Proc. 24th Offshore Tech. Conf.* 7451-MS, Houston, Texas, USA, May 2–5, 1994.

Bolt, H.M., Billington, C.J. & BOMEL Ltd. 2000. Results from ultimate load tests on 3D jacket-type structures. *Proc. 31st Offshore Tech. Conf.* 11941-MS, Houson, Texas, USA, May 1–4, 2000

Bouwkamp, J.G., Hollings, J.P., Maison, B.F. & Row, D.G. 1980. Effects of joint flexibility on the response of offshore towers. *Proc.11th Offshore Tech. Conf.* 3901-MS, Houston, Texas, USA. May 5–8, 1980.

Chen, B., Hu, Y.& Tan, M. 1990. Local joint flexibility of tubular joints of offshore structures. *Marine Structures*, 3(3):177–197.

Choo, Y.S., Qian, X.D. & Foo, K.S. 2005. Nonlinear analysis of tubular space frame incorporating joint stiffness and strength. *Proc. 10th Int. Jack-up Platform Conf. Design, Construction and Operation*, City University, London, UK,

Choo, Y.S., Qian, X.D., Liew, J.Y.R. & Wardenier J. 2003. Static strength of thick-walled CHS X-joints – Part I. new approach in strength definition. *J. Constr. Steel Res*. 59:1201–28

Choo, Y.S., Qian, X.D. & Wardenier, J. 2006. Effects of boundary conditions and chord stresses on static strength of thick-walled CHS K-joints. *J Constr. Steel Res.* 62:316–28.

Dier, A.F. & Hellan, O. 2002. A non-linear tubular joint response model for pushover analysis.*Proc. 21st Int. Conf. Offshore Mech. Arctic Eng.* Oslo, Norway.

Efthymiou, M. 1985. Local rotational stiffness of unstiffened tubular joints. ReportPKER.85.199. KSEPL, Shell, The Netherlands.

Fessler H, Webster JJ. & Mockford PB. 1986. Parametric equations for the flexibility matrices of single brace tubular joints in offshore structures. *Proc. Institution Civil Eng*. (81)4:659–73.

Hellan, O. 1995. Nonlinear pushover and cyclic analysis in ultimate limite state design and reassessment of tubular steel offshore structures. Doctor dissertation. The Norwegian Institute of Technology. 1995.

International Institute of Welding (IIW) 2009. Static design procedure for welded hollow section joints – Recommendations, 3rd Edition, International Institute of Welding. Commission XV, IIW Doc. XV-1329-09 and IIW Doc. XV-E-09-400

Lu, L.H., Winkel, G.D. de, Yu, Y. & Wardenier, J. 1994. Deformation limit for the ultimate strength of hollow section joints. *Proc. 6th. Int. Symp. Tubular Structures*, Tubular Structures VI, 341–347.

Romeijn, A., Puthli, R.S. & Wardenier, J. 1991. Flexibility of uniplanar and multiplanar joints made of circular hollow sections. *Proc. 1st Int. Offshore Polar Eng. Conf.* Edinburgh, UK. Aug. 11–16, 1991.

Qian, X., Romeijn, A., Wardenier, J. & Choo, Y.S. 2002. An automatic FE mesh generator for CHS tubular joints. *Proc. 12th Int. Offshore Polar Eng. Conf.*, Kitakyushu, Japan, May 26–31, 2002.

Qian, X., Zhang, Y. & Choo, Y.S. 2011. A load-deformation formulation for CHS X- and K-joints in push-over analyses. Manuscript submitted to: *J. Constr. Steel. Res.*

Togo, T. 1967. Experimental study on mechanical behavior of tubular joints. Doctor dissertation. Japan: Osaka University. 1967.

Ueda, Y., Rashed, S.M.H. & Nakacho, K. 1986. Flexibility and yield strength of joints in analysis of tubular offshore structures. *Proc. 5th Int. Conf. Offshore Mech. Arctic Eng*. Tokyo, Japan.1986.

USOFS. 2001. USFOS course manual. Marintek SINTEF group.

Van der Vegte, G.J. 1995. The static strength of uniplanar and multiplanar tubular T- and X-joints. Doctor dissertation. Delft University of Technology, The Netherlands.

Tubular Structures XIV – Gardner (Ed.)
© 2012 Taylor & Francis Group, London, ISBN 978-0-415-62137-3

Numerical and analytical investigation of geometrical imperfections on adhesive bonded cast steel – steel joints

M. Albiez, F. Götz, R.S. Puthli & T. Ummenhofer
Karlsruhe Institute of Technology, Research Center for Steel, Timber and Masonry, Karlsruhe, Germany

ABSTRACT: Hollow and tubular sections are used as structural members in buildings and bridges as well as in crane and wind energy plant constructions. Tubulars have until now been mainly connected by welding. When subjected to fatigue loading, fatigue cracks often initiate at the internal – in many cases inaccessible – root areas of weld seams. Adhesive bonded joints between cast steel nodes and steel hollow sections can be a solution for such problems. Adhesive bonding of two cylindrical components such as a steel tube and a cast steel node can be realized by building an overlap joint. Inserting the two parts of different diameter into one another results in a tubular gap between external and internal members. This resulting adhesive gap size depends on dimensional tolerances of the components. Additionally, the influence of geometrical imperfections such as out of roundness, centerline eccentricity and canting on the bearing behavior is investigated.

1 INTRODUCTION

Due to aesthetic and structural advantages, hollow section steel frameworks open new possibilities of application. The main applications of hollow section steel frameworks are in bridge, crane and offshore structures, as well as long-span roof structures such as exhibition halls and stadiums.

A key factor contributing to the durability of hollow section frameworks under fatigue loadings is the design of the joints, including the details of the welds. Under fatigue loading, cracks in welded hollow section frameworks mainly occur in the joint area. In contrast to the static framework model with ideal hinges, the joints between the members are in reality rigidly connected, resulting in secondary bending stresses. Moreover, stress concentrations from the notch geometry appear. As a result, secondary bending stresses and stress concentrations superimpose to the nominal stresses. For this reason, framed joints are analyzed semi-empirically, by considering stress concentrations (hotspot-strain/-stress).

Based on important developments in new cast steel materials, hollow section joints can be constructed using cast steel parts, see Figure 1. There is no assembly method that offers a comparable variety of material choices regarding strength, toughness, corrosion resistance and wear resistance. The predominant advantage of cast steel parts is the almost arbitrary geometrical design of the components. This allows a smoother tension flow and a reduction of stress peaks resulting from notch effects of sharp corners, edges, abrupt variations of wall thicknesses and other construction details.

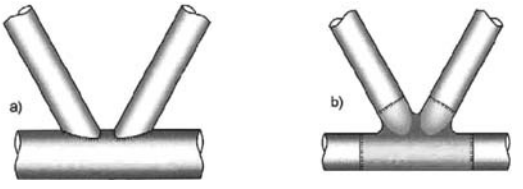

Figure 1. Alternative joint design: a) direct welding of tubes b) cast joint.

Furthermore, the possibility of arbitrary geometries allows an optimized joint design that follows the stress flow ideally and leads to more uniform stress distributions.

In the past years, several bridge structures and building constructions were realized using cast steel components.

An important and innovative one, the central railway station in Berlin, with the adjoining railway bridges over the Humboldthafen, was inaugurated in 2006. At the time, investigations concerning the cast-steel steel joint were carried out at the research center for steel, timber and masonry at Karlsruhe Institute of Technology (KIT). These bridges were one of the biggest construction projects where the supporting elements were completely composed of cast steel.

Cast steel joints are also used in mechanical engineering, in the automotive industry in medical engineering to name just a few. Examples in the area of mechanical engineering are the connection parts of rotating tower cranes.

2 STATE OF THE ART

2.1 *Structural steel engineering*

The first fundamental research in the design of hollow section joints started in the middle of the 1960s in Europe. The basis for the preparation of the DIN 18808 [3] in 1984 in Germany was the research of Mang and Bucak at the research center for steel timber and masonry. Within the scope of the development of EN 1993-1-8 [5] and EN 1993-1-9 [6] results of international investigations were summarized and considered.

In the context of the European offshore research program, at the end of the 1970s and the beginning of the 1980s, different long-term investigations of structures subjected to fatigue loadings were performed. Those investigations resulted in the further development of design methods for structures subjected to fatigue (stress concentration factor (SCF) and strain concentration factor (SNCF)). The state of the art in this field of application is listed in the Design Guides 8 [1] and 9 [2] of CIDECT (world association of hollow section producers).

Within the FOSTA research project "P591 – hollow section road and railroad bridges", investigations on single-side welded butt joints between cast components and hollow sections [7] were performed at the Research Center for Steel, Timber and Masonry at KIT. The main focus was the investigation and optimization of lattice girder joints subjected to fatigue loading, with dimensions specific to bridge constructions.

During the research project, it was observed that the fatigue cracks of specimens subjected to tensile stress always started from the weld root. As cracks become visible only at an advanced state of the crack development, they are detected far too late during planned inspections. This implies that visible cracks appear only once the crack has penetrated through the whole wall thickness and has affected large areas of the cross section of the tube. More than others this failure mechanism is particularly insidious because it can be detected only at a very advanced state. Thus, higher safety measures are required during the design process such as a classification in low FAT classes.

2.2 *Automotive industry*

In the building industry, structural adhesive bonding is rarely carried out, because of a lack of suitable design methodology. In contrast, structural adhesive bonding is frequently used in the safety relevant areas of car bodies for many years. The adhesive bonds are proven to be reliable and fully functional [12] throughout the lifetime of an automobile. In the automotive industry, structural adhesive bonding with cylindrical joint geometries predominantly occurs in the design of a shaft to collar connection. The optimal design of bonded shaft to collar connections is discussed in numerous publications [13, 15].

Generally, in the area of shaft to collar connections, high-strength structural epoxy resin adhesives and anaerobic hardening adhesive systems are applied using joint gap thicknesses of about 0.1 mm. Therefore the knowledge gained here cannot be transferred directly to cast steel-steel bonded joints in the building industry where tolerances are significantly greater.

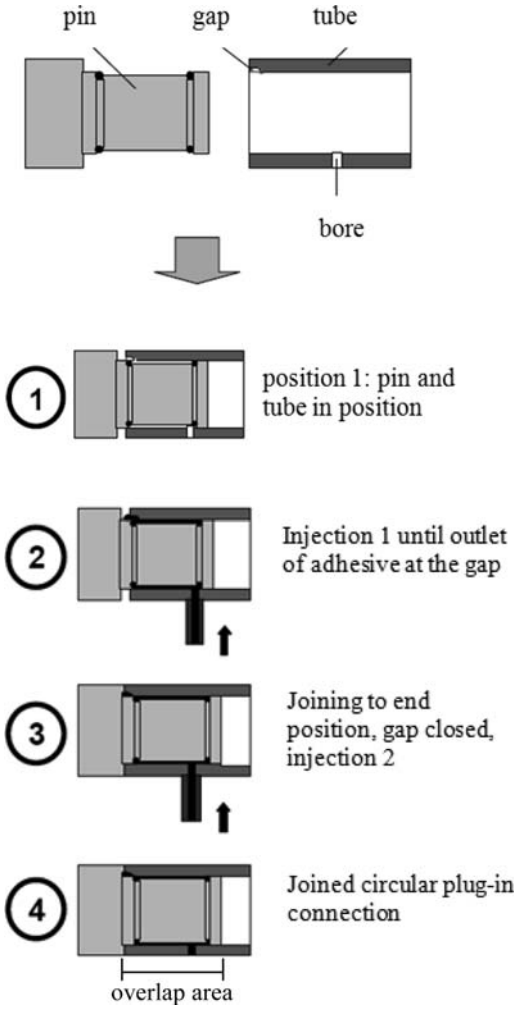

Figure 2. Schematic design of an adhesive injection according to Schlimmer [15]; descriptions translated by authors.

2.3 *Manufacturing technology*

In the project "Process-reliable bonding of cylindrical connectors made of metallic materials under harsh manufacturing conditions (AIF 13455N)", Schlimmer [15] already developed concepts to join elements made of stainless steel in structural applications, see Figure 2.

During this research project, initially unsatisfactory results with the adhesive application on the lateral faces of the members in the overlap area led to the development of a new method for adhesive application, including a new injection unit.

Using a specimen the basic suitability of the adhesive injection has been shown. The dimensions of the parts investigated by Schlimmer were about 0.2 mm gap size and 50 mm tube diameter.

In Figure 2 the injection method according to Schlimmer is shown as a combination of injection and longitudinal joining. Inserting the two parts of different diameter into one another results in a tubular gap between external and internal members. Then, a fluid two-component adhesive is injected from outside with low pressure through an inlet bore filling the adhesive gap. Limitations such as sealing washers prevent the adhesive from leaking out of the adhesive gap region. The fill level of the adhesive gap can be determined using an outlet bore. Hardening of the two-component adhesive takes place at ambient temperature.

In order to determine the mechanical properties, quasi-static tension and torsion tests were performed on the adhesive joints manufactured using the above-mentioned injection method. The results were compared to values for common joint specimens, showing high joint strength.

2.4 *Pipeline construction*

Concepts in the area of pipeline construction pick up the injection method described in [12] as a combination of injection and classical longitudinal joining. Within the research project Join-Tec, two steel tubes with a diameter of about 17 cm are bonded with the injection method as a component of pipeline construction [8]. A pipe collar serves as an auxiliary joining component.

For the arrangement of the tubes, a hydraulic inner centering is applied. Thick film bonding is performed using a two-component polyurethane adhesive. In tests, the structural strength of the adhesive bond is verified for load cases common in installation and operation of the pipeline.

3 DIMENSIONAL TOLERANCES

3.1 *Imperfections arising from production*

As described in chapter 2, adhesive joints are normally designed with an adhesive layer of thickness less than one mm. In these dimensions, adhesive tests result in high strengths and small elongations at fracture. However, such adhesive layer thicknesses are not feasible for adhesive bonding of tubes in civil engineering. This is due to dimensional deviations resulting from the production process of hollow sections and associated manufacturing imperfections. In order to be able to make a statement about the expected thickness of the adhesive layer, it is necessary to know the dimensional tolerances of the adherents used. Therefore, standards such as DIN EN 10210-2 [7] for hollow sections and DIN EN ISO 8062-3 [9] for cast components set the maximum allowable deviations from the perfect shape.

Circular hollow sections are produced indicating nominal diameter, wall thickness, steel grade and length. This results in possible differences between the ideal and real values of a circular hollow section as presented in Figure 3 for the cross-section. Combinations of the three variants are the usual case.

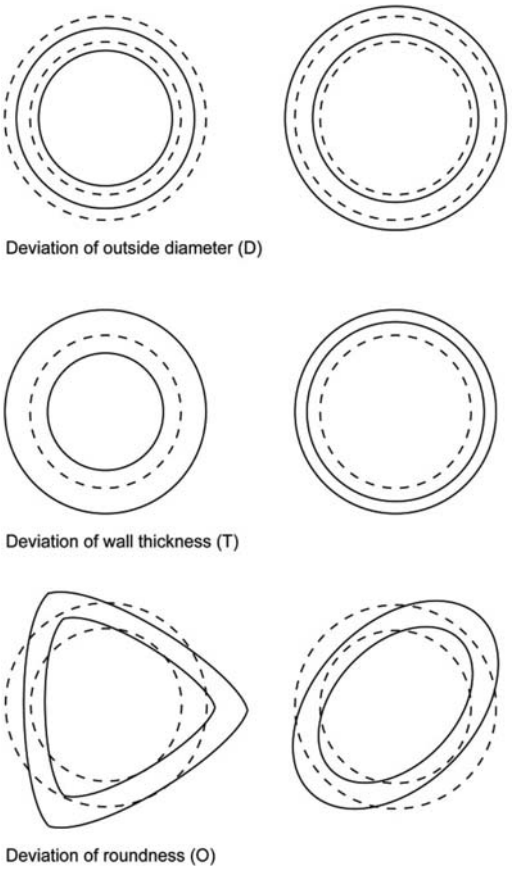

Figure 3. Possible geometric imperfections of hollow sections.

3.2 *Tolerances of cold finished, welded tubes*

Cold finished, welded tubes can be produced in two different ways. The first method is based on bending steel plates to a hollow section in order to subsequently weld their edges in longitudinal direction. The second method is winding the plates helically and welding them to a closed body at the edges.

The domain of application of longitudinally welded tubes is the steel industry since they can be welded more easily with other components. Table 1 provides the limiting deviations of manufacturer's data set by [7].

3.3 *Tolerances of hot finished tubes*

In the following Table 2 the allowable dimensional tolerances for hot finished tubes according to DIN EN 10210-2 [8] are given:

Comparing Table 1 and Table 2 shows that the limiting values only vary for the wall thickness T. This

Table 1. Extract from DIN EN 10219-2 [7].

Feature	Hollow section with circular cross-section
Outside dimensions (D, B und H)	±1%, with a minimum of ±0,5 mm and a maximum of ±10 mm
Thickness (T)	For D ≤ 406,4 mm: T ≤ 5 mm: ±10% T > 5 mm: ±0,5% For D > 406,4 mm: ±10%, with a maximum of ±2 mm
Out-of-roundness (O)	2 % for hollow sections having a diameter to thickness ≤100[a]
Straightness (e)	0,20 % of total length and 3 mm over any 1 m length
Mass (M)	±6% on individual delivered length

[a]Where the diameter to thickness ratio exceeds 100, the tolerance on out-of-roundness shall be agreed.

Table 2. Extract from DIN EN 10210-2 [8].

Feature	Hollow sections with circular cross-section
Outside dimensions (D, B und H)	±1%, with a minimum of ±0,5 mm and a maximum of ±10 mm
Thickness (T)	−10%[a,b]
Out-of-roundness (O)	2 % for hollow sections with a ratio of diameter to wall thickness ≤100[c]
Straightness (e)	0,20 % over the total length and 3 mm per 1 m of length
Mass (M)	±6% for the individual length supplied [d]

[a]The positive deviation is limited by the tolerance on mass.
[b]For seamless sections thicknesses of less than 10% but not less than 12,5% of the nominal thickness may occur in smooth transition areas over not more than 25% of the circumference.
[c]Where the diameter to thickness ratio exceeds 100, the tolerance on out-of-roundness shall be agreed.
[d]The positive tolerance on the mass of seamless hollow sections is 8 %.

is based on the fact that steel plates with a defined thickness are the base material of cold finished tubes. Deviations of thickness can be easily ascertained prior to the manufacturing process. However, for seamless manufactured tubes, the mandrel forming the hollow space could be out of center (Figure 4) or even have an out of roundness.

For hot finished tubes, the limiting upper value of the wall thickness is given by the allowance of the total mass.

3.4 *Bonding gap thickness considering the dimensional tolerances*

For the determination of the bonding gap, the dimensional tolerances are of high importance. Likewise, the

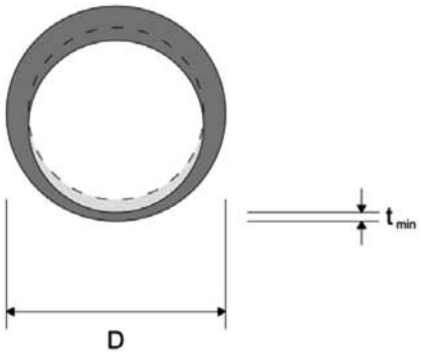

Figure 4. Deviating wall thickness.

definition of the adhesive layer thickness is of fundamental significance for the further investigation of the adhesive bonded tubular joint. The joint between steel tube and cast joint can be fabricated by two methods. The first method is to slide the circular hollow section on to and around the cast component, while the second is to slide the hollow section inside the cast joint. The choice of the method has a considerable influence on the resulting deviations of the proposed bonding gap thickness. Comparing Tables 1 and 2, there is no difference in the allowable deviation of diameter between cold and hot finished hollow sections. Further, the essential difference is for the deviation of the wall thickness for the latter. Thus, using hot finished hollow sections, the method inserting the hollow section into the cast joint turns out to be the more practical. Using cold formed hollow sections both manufacturing methods are possible.

In order to determine the actual bonding gap thickness, imperfections of the cast component must also be considered. For this purpose, EN ISO 8062-4 [9] provides limiting values. However, these values exceed the acceptable tolerances for the realization of a bonded connection. For this reason, allowable geometrical deviations linked with the deviations for the hollow sections are also necessary for the cast component. According to statements from steel foundries, this dimensional accuracy can be achieved without any problems either by foundry technology or by mechanical post-processing.

The required tolerances are:
0.0 mm < D ≤ 101.6 mm → 0.5 mm
101.6 mm < D ≤ 273.0 mm → 1.0 mm
273.0 mm < D ≤ 406.4 mm → 1.5 mm
406.4 mm < D ≤ 508.0 mm → 2.0 mm

The deviation of the ideal adhesive gap is the sum of two parameters:

D1 – Dimensional deviation of the hollow section
D2 – Dimensional deviation of the cast component

For a joint with a tube inserted into the cast node, maximum values of deviations from the aspired bonding layer thickness are typically presented in Table 3 for three tubular hollow sections.

Table 3. Deviation of adhesive layer thickness.

Tube diameter D [mm]	Cast steel component max. deviation acc. to steel foundry [mm]	Tube max. deviation acc. to DIN EN 10210 and DIN EN 10219 [mm]	Deviation of adhesive layer thickness [mm]
42.4	0.50	0.25	0.75
244.5	1.00	1.22	2.22
508.0	2.00	2.54	4.54

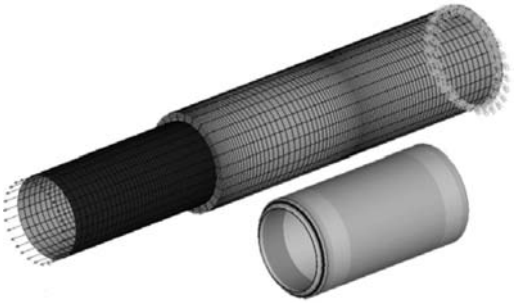

Figure 5. FE-Model of the shear stress in the adhesive layer.

Producing a joint with a planned adhesive layer thickness of 5 mm in, for example, a tube with D = 244.5 mm can lead to a maximum thickness of 7.22 mm and a minimum thickness of 2.78 mm.

Therefore, to sum up, the thin adhesive layers produced in the automotive industry cannot be achieved for steel structures. Imperfections arising from the production have a significant influence on the design of the adhesive layer.

4 NUMERICAL ANALYSIS

4.1 *Numerical model*

The finite element model used in the analyses is shown in Figure 5. The numerical work was performed using the Program ANSYS 13.0. The thickness of the adhesive layer is divided into ten elements. The perimeter is divided into 150 elements.

For the adhesive layer, volume elements ("Solid185") were used.

The numerical analysis is performed using a linear elastic material law. Of course, this is a simplification. In reality, adhesives exhibit a more complex material behavior.

Nevertheless, to evaluate the qualitative changes in the stress distribution due to geometric imperfections, a linear elastic material law is adequate. This approach is applied in several applications [11, 15].

In the numerical model, the steel tube is inserted into the cast steel component. Therefore, the influence of the wall thickness (T) of the steel tube described in chapter 3 does not affect the adhesive layer.

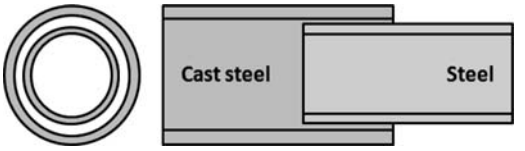

Figure 6. Joint without geometrical imperfections.

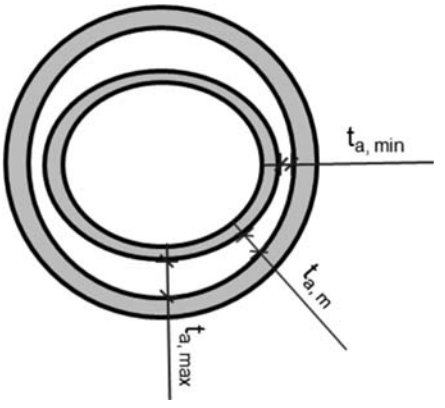

Figure 7. Imperfection: Out of roundness.

4.2 *Possible geometric imperfections*

When inserting a tube into the cast steel node, several geometric imperfections may influence the structural behavior of the adhesive bonded cast-steel steel joint. Figure 6 shows an ideal joint without geometrical imperfections.

The following geometric imperfections have been considered in the analyses:

4.2.1 *Out of roundness*

In chapter 3, it was discussed that the outer diameter may differ from the ideal value by 1% at most. As Figure 7 shows, these deviations can occur at many different positions. Therefore, the diameter of the ellipse shown in Figure 7 was set to a minimum and a maximum value. This results in a geometry in which both limiting cases occur at the same time.

4.2.2 *Centerline eccentricity*

The imperfection "centerline eccentricity" describes the eccentric joint shown in Figure 8. This type of imperfection can result from incorrect installation or during hardening of the adhesive.

4.2.3 *Canting*

Figure 9 shows a possible canting of the tubes. As for the centerline eccentricity, this imperfection can result from an incorrect assembly. In addition, disregarded imperfections such as centerline eccentricity

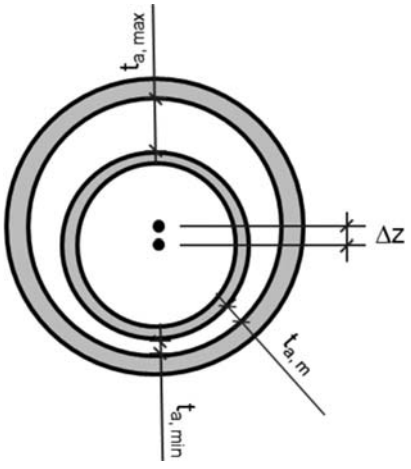

Figure 8. Imperfection: Centerline eccentricity.

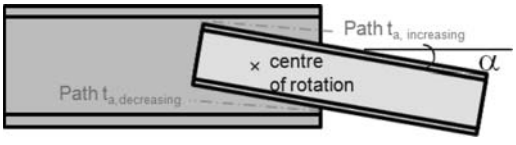

Figure 9. Imperfection: Canting.

Table 4. Mechanical characteristics of the numerical model.

	Steel tube	Adhesive
Young's modulus	210 000 MPa	2 000 MPa
Poisson's ratio	0.3	0.41
Shear modulus	80 769 MPa	709 MPa
Yield strength steel	355 MPa	–
Tensile shear strength adhesive	–	12.5 MPa

can cause bending moments in the overlap area. Bending moments cause deformations of the flexible adhesive layer resulting in a distortion of the tube. For the finite element modeling, the center of rotation of the hollow section is positioned at the center of the overlap area.

4.3 *Analysis of the shear stress distributions*

In Table 4 mechanical parameters of the numerically modeled connection are summarized. The mechanical parameters for the adhesive correspond to the values of an epoxy resin.

The geometrical dimensions of the model are listed in the following:

- Diameter/wall thickness inner tube: 244.5/10.0 mm
- Diameter/wall thickness outer tube: 274.1/9.8 mm
- Thickness of adhesive layer in the numerical model: 5.0 mm

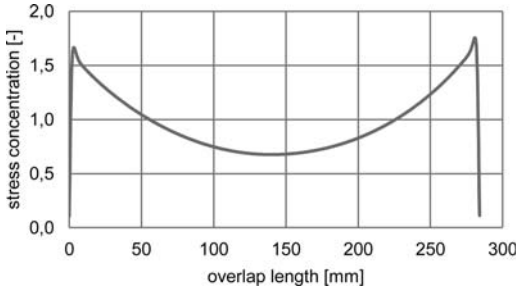

Figure 10. Shear stress distribution in the adhesive layer of the ideal geometry.

The adhesive layer thickness is based on the dimensional tolerances and considers the manufacturing of the joint using the adhesive injection method.

The overlapping length was calculated with the simplified approach of a constant stress distribution across the overlapping length.

$$l_o = \frac{f_y \cdot s}{\tau_{Rd}} = \frac{355 \cdot 10}{12{,}5} = 284mm \quad (1)$$

where l_0 = overlap length; f_y = yield strength; s = wall thickness tube; τ_{Rd} = shear strength.

The shear stress concentration in the middle of the adhesive layer for the ideal geometry is shown in Figure 10. The shear stress concentration is calculated as the ratio of the local element stresses and the nominal stress in the overlap area.

4.3.1 *Out of roundness*

At first, the influence of the out of roundness imperfection on the shear stress distribution is investigated. According to [7] and [8], a maximum deviation of the diameter of ±1% is allowed. This results in an adhesive layer thickness of $t_{a,min} = 5.00 - 1.22 = 3.78$ mm and $t_{a,max} = 5.00 + 1.22 = 6.22$ mm.

An evaluation of the shear stress distribution in the center of the adhesive layer for the thin and thick area results in the diagram shown in Figure 11. The distribution of the perfect connection is presented as t_a.

The maximum stress difference to the perfect tube occurs in the area of the stress peaks and differs for $t_{a,max}$ and for $t_{a,min}$ by about 20%.

4.3.2 *Centerline eccentricity*

In this case, the possible maximum displacement of the neutral axis of the steel tube is 5.0 mm. For this eccentricity, the steel tube would be in direct contact with the cast component. The successive stress distributions for the eccentricities of 1.0 mm, 2.0 mm, 3.0 mm and 4.00 mm results in increasing stress as shown in Table 5. Here, $t_{a,max}$ is increased by the magnitude of the eccentricity and $t_{a,min}$ is reduced.

With a reduction of the adhesive layer thickness by 1.00 mm, the maximum stress increases by 10% in the thin area. While the shear stress with an adhesive layer becoming thicker changes less, the stress in the area becoming thinner increases exponentially.

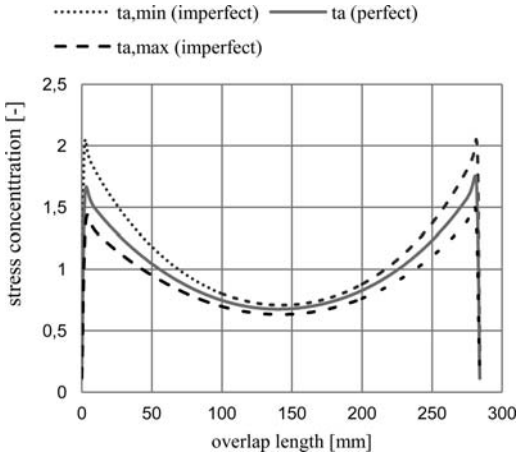

Figure 11. Shear stress distribution in the center of the adhesive layer for $t_{a,max}/t_a/t_{a,min}$ (Out of roundness).

Table 5. Change in state of stress due to center eccentricity.

	$t_{a,max}$		$t_{a,min}$	
Eccentricity in mm	τ_{max} [MPa]	Reduction to previous (original) value [%]	τ_{max} [MPa]	Increase to previous (original) value [%]
0	21.7		21.7	
1.00 (20 %)	20.0	8,00 (8.00)	24.0	10,6 (10.6)
2.00 (40 %)	18.7	6,52 (14.0)	28.0	16,6 (28.9)
3.00 (60 %)	17.6	5,70 (18.9)	34.7	24,0 (60.0)
4.00 (80 %)	16.8	5,08 (23.0)	49.8	43,5 (129.5)

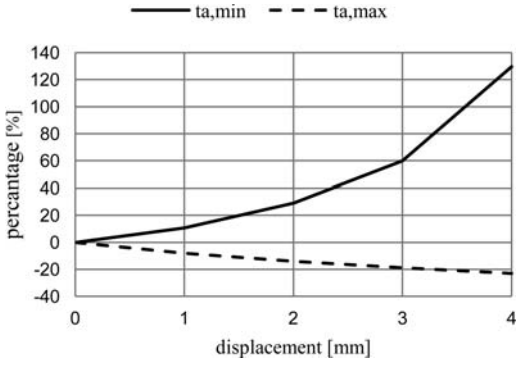

Figure 12. Increase of the stress maximum related to the ideal situation (centerline eccentricity) (see Figure 8).

4.3.3 *Canting*

Compared to out of roundness and centerline eccentricity, canting induces a change in the adhesive layer thickness in both longitudinal and transverse directions. A varying adhesive layer thickness in longitudinal direction affects the stress distribution in the bond in a very unfavorable way.

The rotation of the steel tube is indicated as a percentage of the maximum angle. At 100 % the hollow section would touch the cast component. Table 6 provides an overview of the modeled cantings and the corresponding change of the adhesive layer thickness.

For the varying layer thickness in longitudinal direction, two cases occur: on one side of the connection the layer becomes thinner ($t_{a,max} \rightarrow t_{a,min}$) and on the opposite side it becomes thicker ($t_{a,min} \rightarrow t_{a,max}$) (see Figure 9). The change of the adhesive layer thickness is quasi asymmetric.

Figure 13 shows the shear stress distributions in the center of the adhesive layer for the path in the adhesive layer becoming thicker (see Figure 9). As already found for centerline eccentricity, the numerical analysis shows that with an increase of the adhesive layer thickness the corresponding maximum stress reaches asymptotically a value. By reducing the adhesive layer thickness, the shear stress grows exponentially.

Table 6. Adhesive layer thickness due to canting.

Canting in %	$t_{a,max}$ in mm	$t_{a,min}$ in mm
0.0	5.0	5.0
22.5	6.1	3.9
45.0	7.3	2.8
67.5	8.4	1.6
90.0	9.5	0.5

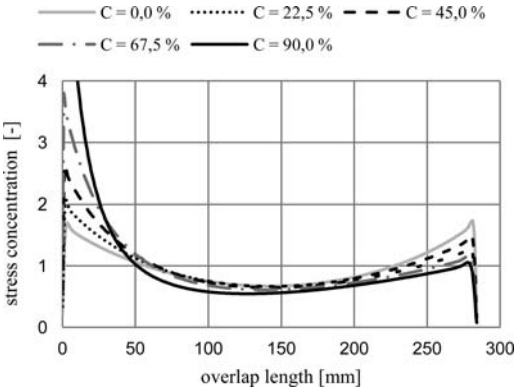

Figure 13. Shear stress distribution in the center of the adhesive layer for different inclinations ($t_{a,min} \rightarrow t_{a,max}$).

5 SUMMARY AND OUTLOOK

Adhesive bonding in the field of steel structures is a challenge due to their specific characteristics. In this paper, the results of a first investigation concerning

dimensional tolerances and geometrical imperfections of tubulars inserted into cast steel joints are presented. As a consequence of dimensional tolerances adhesive bonding using thin adhesive layers cannot be realized. The discussed imperfections (out of roundness, centerline eccentricity and canting) are shown to influence the shear stress distribution in the overlap joint. Out of roundness based upon the permitted tolerances in [7] and [8] lead to stress variations of about 20%. The imperfections due to centerline eccentricity and canting can lead to a significant increase of the stress peaks and have to be limited.

Within the scope of an ongoing research project, further investigations will show whether adhesive connections could represent a real alternative solution to welded nodes. This comparison will consider the following criteria: fabrication, structural safety, durability and operational safety of supporting structures of steel constructions under operational loading. Focuses of this ongoing research are pretreatment of the surfaces in the overlap area, production process and experimental and numerical investigations concerning the load bearing capacity of the adhesive bonded joints. Experimental studies of ageing and temperature behavior of the glued joints are also important aspects in this project.

Results gained from future research will be presented in forthcoming ISTS conferences.

The research in this project is carried out by the following research centers:

- Karlsruhe Institute of Technology (KIT), Research Center for Steel, Timber and Masonry
- Munich University of Applied Sciences, Laboratory for Steel and Lightweight Structures
- Fraunhofer Institute for Manufacturing Technology and Advanced Materials (IFAM), Bremen

The work presented is carried out as a part of the joint FOSTA research project P 884 “Adhesive bonded tubular cast steel – steel joints in framework structures” and funded by the Federal Ministry of Economics and Technology.

REFERENCES

[1] CIDECT Design Guide 8: For CHS and RHS welded joints under fatigue loading 2001. Köln: TÜV Verlag.
[2] CIDECT Design Guide 9: For structural hollow section column connections 2005. Köln: TÜV Verlag.
[3] DIN 18808, “Steel structures consisting of hollow sections predominantly static loaded“ 1984. Berlin: Beuth-Verlag.
[4] EN 1993-1-1, Design of steel structures – Part 1–1, General rules and rules for buildings 2005.
[5] EN 1993-1-8, Design of steel structures – Part 1–8, Design of joints 2010.
[6] EN 1993-1-9, Design of steel structures – Part 1–9, Fatigue 2010.
[7] DIN EN 10210-2, Warmgefertigte Hohlprofile für den Stahlbau aus unlegierten Baustählen und aus Feinkornbaustählen – Teil 2: Grenzabmaße, Maße und statische Werte 2006.
[8] DIN EN 10219-2, Kaltgefertigte geschweißte Hohlprofile für den Stahlbau aus unlegierten Baustählen und aus Feinkornbaustählen – Teil 2: Grenzabmaße, Maße und statische Werte 2006.
[9] DIN EN ISO 8062-3, Geometrische Produktspezifikationen (GPS) – Maß-, Form- und Lagetoleranzen für Formteile – Teil 3: Allgemeine Maß-, Form- und Lagetoleranzen und Bearbeitungszugaben für Gussstücke 2008.
[10] Puthli, R. 2010. Wirtschaftliches Bauen von Straßen- und Eisenbahnbrücken aus Stahlhohlprofilen, Abschlussbericht Forschung für die Praxis P 591, Verlag und Vertriebsgesellschaft mbH, Düsseldorf.
[11] Hahn, O. et al. 2010. Konzeptentwicklung und Machbarkeitsstudien an Stahlrohren, Klebtechnisches Fügen von Pipelines, Adhäsion Kleben&Dichten, 4/2010, Vieweg+Teubner Verlag.
[12] D. Symietz & A. Lutz 2007. Structural Bonding in Automotive Manufacturing, Verlag Moderne Industrie.
[13] R. Adams 1977. Stress analysis in adhesive-bonded tubular lap joints, J. Adhesion 9.
[14] G. Romanos 1997. Beanspruchungsgerechte Gestaltung geklebter Welle-Nabe-Verbindungen, Informationskreis Verbindungstechnik Hochfeste Welle/Nabe-Verbindungen.
[15] IGF-Projekt Nr. 13.455 N (2003-2005): Prozesssicheres Kleben von Rundsteckverbindungen aus metallischen Werkstoffen unter rauen Fertigungsbedingungen, IFW Kassel.

Tubular Structures XIV – Gardner (Ed.)
© 2012 Taylor & Francis Group, London, ISBN 978-0-415-62137-3

Axially loaded Elliptical Hollow Section X joints, Part I: Experiments and numerical calibration

W. Shen & Y.S. Choo
National University of Singapore, Singapore

J. Wardenier
National University of Singapore, Singapore,
Delft University of Technology, Delft, The Netherlands

G.J. van der Vegte
Van der Vegte Consultancy, The Netherlands

J.A. Packer
University of Toronto, Canada

ABSTRACT: Elliptical Hollow Sections (EHS) are especially attractive for architectural applications. Since limited evidence exists for the design of directly welded joints between EHS, a new research programme has been initiated. The first phase of this programme aims at providing information for developing design rules for axially loaded T and X joints between EHS. This paper covers the programme, numerical calibrations with experiments and initial numerical investigations on axially loaded X joints with the braces connected to the wide sides of the EHS chord.

1 INTRODUCTION

Elliptical Hollow Sections (EHS) are especially attractive for architectural applications. Due to their major-to-minor outside dimensions of 2:1, with the narrow sides facing the viewer, they give the impression of very small dimensions.

In recent years more and more architects have specified designs using EHS, see Packer et al. (2009b). Section property tables and column resistance tables for EHS have also recently been produced for both the American and Canadian Institutes of Steel Construction (AISC, CISC). Although at present only a limited number of manufacturers (Condesa and Tata) are producing EHS it may be expected that, after growing the market, this number will increase. Further, available design information will also increase the market.

Since nearly no evidence exists regarding EHS joint design, a research programme was initiated to investigate the joint behaviour more in detail.

This programme is sponsored by the participating universities, the authors and CIDECT, and is designated as programme 5BW. This first phase aims at providing information for developing design rules for axially loaded T and X joints between EHS. This paper and a companion paper (Shen et al., 2012) cover the investigations on axially loaded X joints with the braces connected to the wide sides of the EHS chord.

2 DIMENSIONS, SECTIONAL AND MECHANICAL PROPERTIES

At present EHS are available with major-to-minor outside dimensions of H:B = 2:1. The hot finished EHS are covered in EN 10210 (2006a, b) with section properties for EHS ranging from $120 \times 60 \times 3.2$ mm to $500 \times 250 \times 16.0$ mm. They are commonly available with up to 16 mm wall thickness in the grade S355J2H with minimum yield strength of 355 MPa and a Charpy impact resistance of 27 Joules at $-20°$C.

3 DESIGNATION

In publications and standards, various designations are used for the outside dimensions of the elliptical sections, for example 2a, 2A or H for the larger dimension and 2b, 2B or B for the smaller dimension.

In this paper the following designation (shown in Figure 1) is used when *members* are considered:

When these sections are used in joints, the usual designations for Rectangular Hollow Section (RHS) joints b_0, h_0, b_1 and h_1 apply for chord and braces.

For the types of joints the designation proposed by Choo et al. (2003) is used, see Figure 2.

As shown in Figure 2, various orientations are possible, but it is expected that, because of the slender

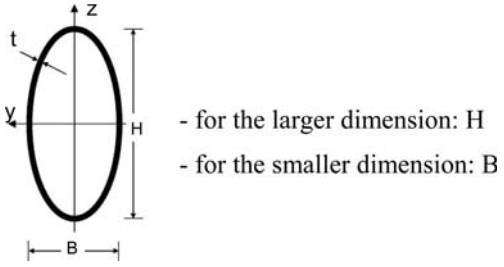

Figure 1. Elliptical Hollow Section designation.

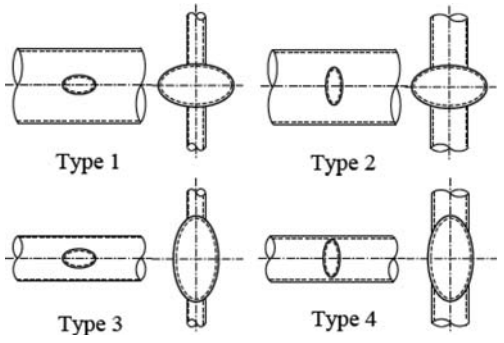

Figure 2. EHS joint types.

appearance, Type 2, dealt with in this paper, may be the type most commonly used in architectural designs.

4 LITERATURE STUDY

Up-to-date detailed reviews, including references, are given by Packer et al. (2009b) and Chan et al. (2010b).

4.1 *Member classification*

Chan et al. (2006, 2010a, b), and Gardner & Chan (2006, 2008), have classified EHS into Classes by treating the EHS as a Circular Hollow Section (CHS) with an equivalent diameter $D_{e,CHS}$, Two definitions of $D_{e,CHS}$ have evolved in the literature, which are herein termed $D_{e,old}$ and $D_{e,new}$.

Zhao & Packer (2008) classified EHS into Classes by treating the EHS as an equivalent RHS with a width equal to the EHS width and a depth $h_{0,eq}$, which is determined by maintaining the same cross-sectional area as the EHS. It was shown that the "equivalent RHS" approach was a good estimator for member classification when compared with available tests and it was shown to be better than either of the "equivalent CHS" approaches. Packer et al. (2009b), Zhao et al. (2010) and Haque et al. (2012) confirmed this also for bending.

The proposed member classifications for EHS based on (H/t – 3) and related to RHS sections according to Eurocode 3, are given in Table 1.

Both the CHS and RHS equivalent member approaches have been checked to see whether these could be used to relate the capacity of EHS joints to that for CHS or RHS joints. However, these did not result in acceptable correlations, see Packer et al. (2012).

Table 1. Proposed (H/t – 3) limits for EHS.

	$\varepsilon = \sqrt{235/f_y}$) and f_y in N/mm^2		
EHS	Class 1	Class 2	Class 3
(H/t – 3) limit	33ε	38ε	42ε

Table 2. EHS X Joint Types 1 and 2 tested at the University of Toronto (UT).

	X-Type		
Type	compression	tension	2γ-β-τ
1	90°–45°	90°	37-0.5-1.0
2	90°–45°	90°	37-1.0-1.0

Toronto tests with EHS 220 × 110 × 6 for chord and braces.

4.2 *EHS joints*

Most investigations on EHS joints relate to gusset-plate joints or through-plate joints and slotted-plate joints, both investigated at the University of Toronto, which are not the subject of this investigation (see Martinez-Saucedo et al. 2008).

Bortolotti et al. (2003) and Pietrapertosa & Jaspart (2003) performed some tests and FE work on N and K joints with EHS braces welded to the wide side of the EHS chord, however, the tests were not loaded up to failure.

Choo et al. (2003) carried out numerical studies on EHS X joints with both braces welded at 90°, either to the wide or the narrow sides of the chord. They compared the capacities of the joint configurations in Figure 2 with those of corresponding CHS joints and concluded that for joints loaded in compression, the capacity of an axially loaded X joint of CHS sections is between that of EHS X joints Types 2 and 4 defined in Figure 2. Further, it was found that the capacity increases from Type 1, 2, 3 to Type 4.

5 EXPERIMENTAL PROGRAMME

5.1 *Programme*

The testing programmes for the X joint Types 1 and 2 tests carried out at the University of Toronto and at the National University of Singapore (NUS) are given in Tables 2 and 3.

5.2 *Test specimens*

The test specimens were made from steel EN 10210 S355J2H. The brace member lengths of the specimens

Table 3. EHS X Joints Types 1 and 2 tested at the National University of Singapore (NUS).

	X-Type		
Type	compression	tension	2γ-β-τ
1	90°	90°	31-0.25-0.6
2	90°–45°	90°–45°	31-0.5-0.6

NUS tests with EHS 250 × 125 × 8 and 120 × 60 × 5.

were 5 times the largest dimension and the chord member length was (for the NUS tests) 6 times the largest dimension of the chord whereas it varied for the tests at the University of Toronto.

At the nearly flat parts at the crown and saddles, fillet welds with a nominal throat thickness of $a = 1.1t_1$ were used but for the larger β ratios at the saddles partial (for $\beta < 1.0$) or full penetration ($\beta \leq 1.0$) welds were used. Since the actual dimensions of the welds were sometimes larger, these were measured and recorded.

6 EXPERIMENTAL RESULTS

The test results are presented in load-displacement diagrams where, for the displacement, the chord indentation perpendicular to the chord face at the connection is used. The governing joint capacity is the peak load in the load-displacement diagram if this occurs before a chord indentation of 3% b_0, or the load at 3% b_0 indentation if the peak load occurs after the 3% indentation.

All test results are recorded with the actual dimensions and mechanical properties, the actual geometrical parameters, the joint configuration, the load-displacement diagram and the failure mode.

7 INITIAL ANALYSIS OF EXPERIMENTS

In a preliminary analysis of the EHS experimental results the members are converted to CHS or RHS sections as proposed for member classification by Chan et al. (2010b) for CHS and by Zhao & Packer (2008) for RHS.

7.1 *Equivalent CHS member method*

Using the equations of Table 4.1 from CIDECT Design Guide 1 (Wardenier et al. 2008) for chord plastification and chord punching shear, and by converting the EHS chord into an equivalent CHS, joint capacity predictions were made and compared with the test results. The chord punching shear capacity (not critical) is here also based on the equivalent CHS brace section.

Considering the large scatter and deviating results, this EHS to CHS conversion method, originating from local buckling studies of EHS members under normal stress, seems not to be a promising method for EHS joint design.

As a second method, the CHS chord plastification equations were used with d_0 being the width b_0 of the EHS chord and d_1 being the width b_1 of the braces. Chord punching shear is not critical but should, with this second method, be based on the EHS brace perimeter. Also here the variation in results is very large.

7.2 *Equivalent RHS member method*

Using the equations of Table 4.1 from CIDECT Design Guide 3 (Packer et al. 2009a) and by converting the chord into an equivalent RHS, joint capacity predictions were made.

In order to calculate the chord side-wall failure limit state, the limiting stress of the material has an effect in the f_k term. For tension, $f_k = f_{y0}$, but for compression, a reduction factor χ for column buckling, becomes relevant. For the normalized slenderness the reduction factor χ for column buckling can, for example, be obtained from EN 1993-1-1.

This conversion procedure produces a good prediction of the failure mode and a better prediction of the joint capacity than the CHS conversion method. To address the chord side wall failure better, analyses were also carried out with the EHS chord converted into an RHS where the EHS depth h_0 was used, thus not diminished. This method does not keep the A_{EHS} constant, but H, B and t (i.e. h_0, b_0 and t_0) are all unaltered. By maintaining h_0, χ decreases and results in lower capacity predictions for $\beta = 1.0$ joints in compression. However, this method does not produce any improvements.

In additional analyses, both chord and braces were converted to equivalent RHS sections with b_0, $h_{0,eq}$, and b_1 with $h_{1,eq}$, but this method also shows considerable variations in results.

7.3 *Method comparison*

This initial analysis showed that using a simple conversion method for EHS members to CHS or RHS and relating the strength to the CHS or RHS joint strength equations does not always give a good estimate of the capacity. As an example Figure 3 shows the results based on an equivalent RHS method. The number of tests is too small to give detailed conclusions for a strength analysis because of the many variables, but the tests are useful for calibration of the numerical models and the observation of the failure modes.

8 NUMERICAL CALIBRATION AND PARAMETER STUDY

The main characteristics of the FE analyses for the EHS tubular joints, including determination of material properties, guidelines for the choice of the finite element type and meshing, boundary conditions and loading conditions plus the solver procedures, are here

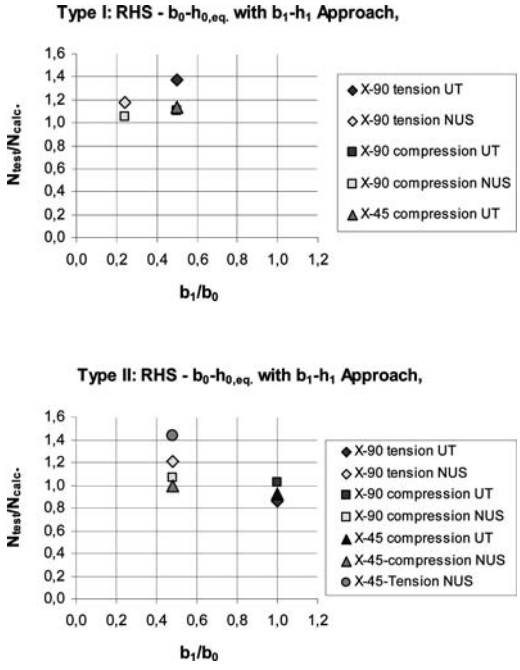

Figure 3. Comparison between EHS X joint Types 1 (top) & 2 (bottom) test data and the equivalent RHS approach with $b_0 - h_{0,eq.}$ for the chord and $b_1 - h_1$ for the braces.

briefly presented, and given more in detail by Shen et al. (2013). Furthermore, the influence of the weld geometry is discussed.

8.1 *Main characteristics of FE analyses for EHS joints*

For the numerical analyses, the commercial FE software package ABAQUS/Standard v.6.7 (SIMULIA 2007) has been employed. The dimensions of the tubular members assumed in the FE analyses are in accordance with the measured dimensions of the test specimens. Based on the appropriate symmetry in geometry, loading, and boundary conditions, a particular EHS joint may be modelled by either a half, a quarter or an eighth of a full joint.

8.1.1 *Material properties*

Since the numerical simulations are performed up to failure of the tubular joints, material nonlinearity and geometrical nonlinearity are incorporated in the analyses by using the NLGEOM option in ABAQUS (SIMULIA 2007). The consideration of large deformations requires a complete material true stress-true strain curve ($\sigma_T - \varepsilon_T$) (Van der Vegte 1995). Furthermore, in all numerical analyses, the Von Mises yield criterion and isotropic hardening are used.

8.1.2 *Finite Element selection*

In the current study, 20-noded solid elements with reduced integration (ABAQUS element type C3D20R) are employed to model the uniplanar EHS tubular X joints.

8.1.3 *Mesh density*

The EHS joints are modelled with the measured dimensions of chord and brace as recorded in the experiments without imperfections. In member thickness, three layers of elements are used for both chord and brace. A denser mesh is used close to the intersection region of brace and chord, and is gradually changed to a coarser mesh in less stressed regions.

The weld geometry is included in the FE model using the geometrical dimensions of the leg length as measured. The geometry of the weld for joints with $\beta = 1$ is different from that with $\beta < 1$. Such details are captured in the FE model.

8.1.4 *Boundary conditions and loading*

In order to reduce the size of the FE models, symmetry in geometry and loading is used and, as a result, boundary conditions are required in the planes of symmetry. Boundary conditions are applied so as to simulate the real behaviour of a full joint. In this study, the displacement control method is employed.

8.1.5 *Iteration procedure and convergence criteria*

In the present research, geometrical and material nonlinearities are taken into account. The (displacement-controlled) brace load is applied in a number of increments, employing full Newton-Raphson iterations, which ABAQUS performs by default. This method is characterized by its quadratic convergence, based on the assembly and decomposition of the stiffness matrix in each iteration. Convergence is checked by the default value of 0.5% for the iteration procedure for both forces and moments. If the residual forces or moments are less than the default value, ABAQUS accepts the solution and proceeds to the next increment.

8.2 *Effects of modelling of weld geometry*

For the fillet welds, various ways of modelling were investigated. It was found that the difference due to different weld modelling, either modelled as a butt-fillet weld (fully connected between brace and chord) or as a fillet weld, is small and can be ignored. Also the effect of coarse and dense-mesh-butt-fillet weld modelling was investigated and the difference in terms of load-displacement is small, indicating that the meshing strategy used for CHS joints can also be employed for EHS joints. This also applies for small deviations in the weld leg lengths at brace or chord. Some results are shown in Figure 4.

For joints with $\beta = 1$ it was found that the weld modelling is extremely important and that the measured weld convexity had to be taken into account for a good correlation with the test result (Shen et al. 2013). This case showed that the weld convexity at the saddle may affect the result significantly (by more than 10% for the peak load).

8.3 *Numerical simulation of the experiments*

The numerically simulated joints with the experimental results (load-displacement diagrams and governing

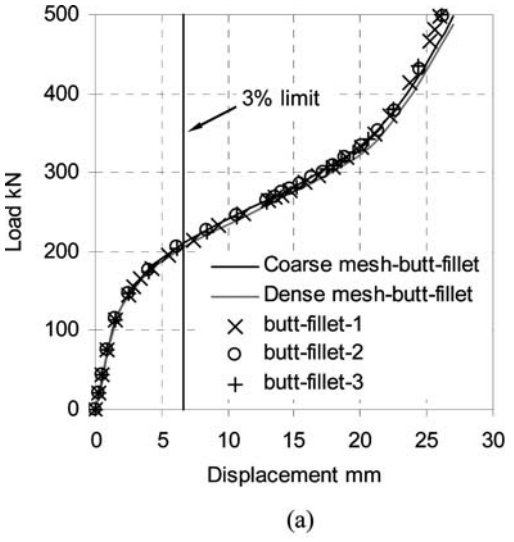

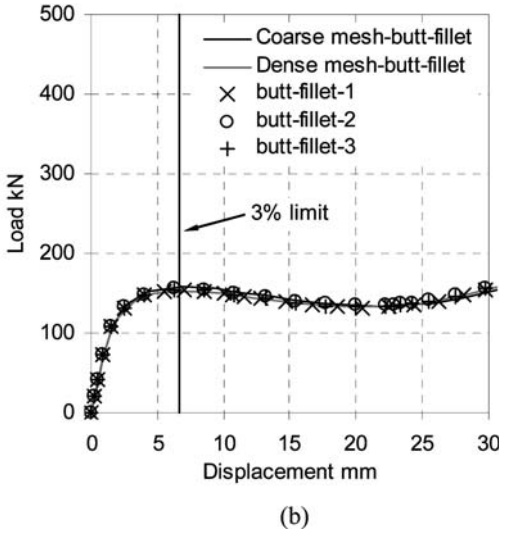

Figure 4. Comparison of FE results with different mesh configuration and density for butt-fillet weld modelling: (a) X90-1T-UT (tension) and (b) X90-1C-UT (compression) with $\beta < 1$.

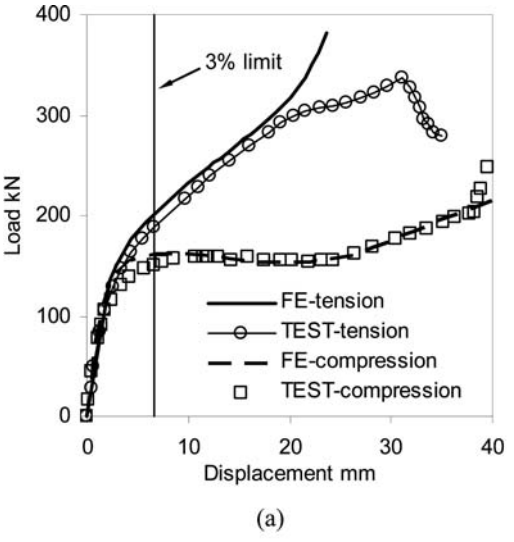

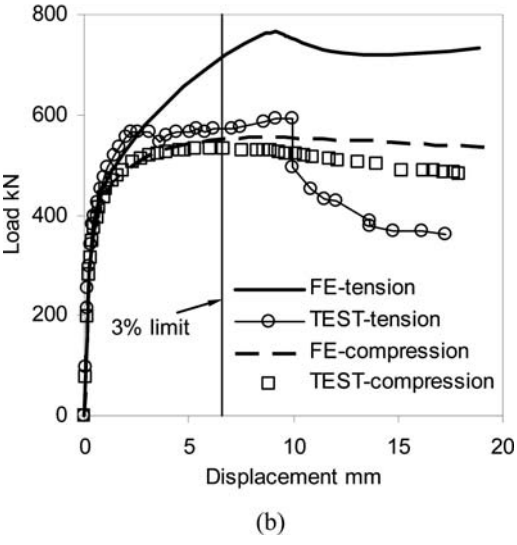

Figure 5. Comparison of the behaviour under brace tension and compression loading for the same configuration of joints: (a) X90-1T-UT and X90-1C-UT; (2) X90-2T-UT and X90-2C-UT.

loads) gave satisfactory agreement for most cases, except for cases with fracture by cracks under tension loading and failures by overall buckling or chord instability in the case of compression loading because the eccentricities were not modelled (see Figure 5).

If in the design recommendations the static strength is not differentiated for tension and compression brace loads, like the current practice for CHS joints, the compression case can be used for the parametric study.

From this calibration study the following conclusions can be drawn:

– The mesh scheme for modelling of fillet welds, whether modelled as butt-fillet weld or as fillet weld, does not affect the static strength of the EHS X joints.
– For $\beta = 1$, when modelling the geometry of the butt weld at the saddle, both the dimensions and the convexity affect the static strength significantly.
– The current FE approach, using 20-noded solid elements with reduced integration and 3 layers of elements for chord and brace, is demonstrated to be suitable for EHS joints. The FE results are generally in satisfactory agreement with the test results.

8.4 *Numerical parameter study*

A summary of the 93 numerical analyses for the parameter study is shown in Table 4. The basic series covers β ratios of 0.24, 0.4, 0.6, 0.8 and 1.0 in combination with 2γ ratios of 16, 20, 31 and 42. In general an

Table 4. Summary of numerical analyses of X joint Types 1 and 2 (see figure 2).

Analyses	Initial	Basic parameters	Brace angle	Chord stress	Total
Type 1		7	3	18	28
Type 2	8	16	5	36	65

angle of $\theta_1 = 90°$ is used but also analyses with an angle of $\theta_1 = 45°$ were investigated. Further, the chord stress effect was investigated for 3 chord compression and 3 chord tensile load ratios n. The chord has, in all analyses, dimensions of $250 \times 125 \times t_0$.

9 INITIAL NUMERICAL STUDIES

Before the full numerical parametric study, an initial numerical study was carried out to investigate more in detail the effects of weld type (fillet and butt weld), chord end boundary conditions and chord length. These investigations are discussed in detail in Shen et al. (2013). Here only the conclusions are given.

9.1 *Influence of the geometry of welds*

Two types of welds are investigated more in detail, i.e. fillet welds with a throat thickness equal to the brace thickness and butt welds according to AWS (2010) with two weld foot print lengths of $1.25\ t_1$ and $1.5t_1$ at the chord sides.

The joints with fillet welds show a somewhat larger strength than those with butt welds; the butt welds with the minimum AWS weld foot print length $1.25t_1$ only show a marginal (2%) lower strength than those with a foot print length of $1.5t_1$. Since the welds are modelled proportional to the thickness of the brace wall and the τ ratio is kept constant at 0.5 in this study, the effective β ratio is (especially for fillet welds) larger for larger brace thicknesses leading to an increase in strength. Further, the effect is more significant for joints loaded in compression.

Since a foot print length of $1.5\ t_1$ was used for the FE studies for CHS joints (Van der Vegte 1995), it was decided to perform the parametric study for EHS joints also with butt welds according to AWS with a foot print length of $1.5\ t_1$.

For the cases studied and also in the experiments, the compression load capacity based on the first peak load or the 3% b_0 deformation load, is lower than that for tension, therefore the compression load capacity will be taken to represent the brace axial load capacity of EHS X joints. (Note: In the actual tests it was shown that crack initiation for the tension tests occurred at loads higher than the governing load for the companion test with brace compression, see Figure 5(b).

9.2 *Influence of chord end boundary conditions*

In addition to the weld geometry, it was investigated whether the chord end boundary condition had an effect on the joint capacity. Three restraint conditions as well as a free end were tested for fillet-welded joint types with a chord length of $6b_0$.

The analyses showed no effect of the chord end restraint condition and it was decided to perform further numerical tests with a chord free end.

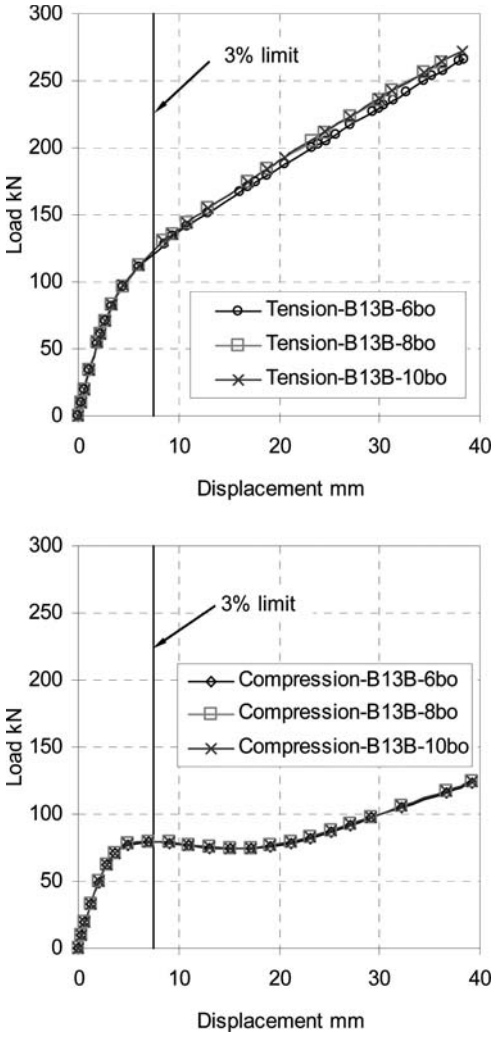

Figure 6. Load-displacement curves for joints B13 ($\beta = 0.4$ and $2\gamma = 42$) with different chord length: tension (top); compression (bottom).

9.3 *Effect of chord length*

For joints with two β ratios (0.4 and 0.6) and 2γ ratios of 20 and 42, joints with chord lengths $6b_0$, $8b_0$ and $10b_0$ were studied.

Each joint configuration was numerically analysed with brace tension and compression loading. In total 24 numerical analyses were conducted. All analyses showed (see Figure 6) no effect of the chord length and $6b_0$ was hence taken for the parametric study.

10 CONCLUSIONS

For the numerical cases studied and also in the experiments, the compression load capacity based on the first peak load or the 3% b_0 deformation load, is lower than the governing capacities for tension, therefore the brace compression load capacity is taken to represent the brace axial load capacity of EHS X joints.

An initial analysis of the experiments showed that using a simple conversion method for EHS members to CHS or RHS and relating the strength to the CHS or RHS joint strength equations does not always give a good estimate of the capacity.

The numerically simulated joints and the experimental results (load-displacement diagrams and governing loads) gave satisfactory agreement for most cases, except for cases with fracture by cracks under tension loading and failures by overall buckling or chord instability in case of compression loading, because the eccentricities were not modelled.

The analyses showed no effect of the chord end restraint condition and it was decided to perform further numerical analyses with a chord free end.

All tests showed no effect of the chord length so a length of $6b_0$ was hence taken for the parametric study.

Based on a comparison of the experimental results and the numerical calibration it can be concluded that:

- The mesh scheme for modelling of fillet welds, whether modelled as butt-fillet welds or as fillet welds, does not affect the static strength of the EHS X joints:
- For $\beta = 1$, the modelling of the geometry of the groove weld at the saddle, both the dimensions and the convexity affect the static strength significantly.

ACKNOWLEDGEMENTS

Appreciation is extended to Tata Tubes for delivering the EHS sections, and to the University of Toronto (plus SSEF and NSERC), Canada, the National University of Singapore, Singapore and Delft University of Technology, The Netherlands for their financial and/or in-kind contributions.

Further appreciation is extended to the Comité International pour le Développement et l'Etude de la Construction Tubulaire (CIDECT) for sponsoring this programme and for the discussions in their Project Working Group.

The experimental results presented in this paper are extracted from the MASc report of Ms. T. Haque (University of Toronto) and the research report of Ms. Y. Fang (National University of Singapore).

SYMBOLS

A	cross sectional area
A_{EHS}	cross sectional area EHS
B	smaller dimension of EHS member
c_x	spreading coefficient for brace dimension h_1
c_y	spreading coefficient for weld leg length
$D_{e,new}$	equivalent diameter (new definition)
$D_{e,old}$	equivalent diameter (old definition)
$D_{e,CHS}$	equivalent diameter (= new definition by Chan & Gardner 2008b)
H	larger dimension of EHS member
Q_f	chord stress function
a	throat thickness of weld
b_1	external width of RHS brace 1 (perpendicular to the plane of the joint), also used for an EHS brace
b_0	external width of a RHS or EHS chord
f_k	critical local buckling stress of the chord side wall
f_y	yield stress
h_0	external depth of a RHS or EHS chord
h_1	external depth of a RHS brace 1 (in the plane of the joint), also used for an EHS brace
$h_{0,eq}$	equivalent external depth of an EHS chord converted to a RHS member
n	chord stress ratio
t_i	thickness of hollow section member i ($i = 0, 1$)
β	width (or diameter) ratio between brace and the chord
$\beta*$	average width ratio for EHS X joints ($\beta* = (b_1 + h_1)/2b_0$)
γ	half width-to-thickness ratio of the chord ($\gamma = b_0/2t_0$) or half diameter-to-thickness ratio of the chord ($\gamma = d_0/2t_0$)
γ_M	partial (safety) factor
θ_1	included angle between brace member 1 and the chord
τ	thickness ratio between brace and chord
χ	buckling coefficient

Subscripts

i subscript used to denote the member of a hollow section joint. Subscript $i = 0$ designates the chord; $i = 1$ refers in general to the brace for T, Y and X joints

Abbreviations

CHS	circular hollow section
EHS	elliptical hollow section
RHS	rectangular or square hollow section
SHS	square hollow section

REFERENCES

This paper also contains the reference and symbols for the second paper: Shen et al. 2012. Axially loaded elliptical hollow section X joints, Part II – Results and analysis, being published at this conference

AISC, 2010: Specification for structural steel buildings. ANSI/AISC 360-10, American Institute of Steel Construction, Chicago, USA.

AWS D1.1 2010. Structural Welding Code – Steel. American Welding Society, Miami, USA.

Bortolotti, E., Jaspart, J.P., Pietrapertosa, C., Nicaud, G., Petitjean, P.D., Grimmault, J.P. & Michard, L. 2003. Testing and modelling of welded joints between elliptical hollow sections. Proceedings 10th International Symposium on Tubular Structures, Madrid, Spain, pp. 259–264.

Chan, T.M. & Gardner, L. 2006. Experimental and numerical studies of Elliptical Hollow Sections under axial compression. Proceedings 11th International Symposium on Tubular Structures, Québec City, Canada, pp. 163–170.

Chan, T.M., Abela, J.M. & Gardner, L. 2010a. Biaxial bending and compression of elliptical hollow sections. Proceedings 13th International Symposium on Tubular Structures, Hong Kong, China, Tubular Structures XIII, Taylor & Francis Group, London, UK. pp.303–312.

Chan, T.M., Gardner, L. & Law, K.H. 2010b. Structural design of elliptical hollow sections; a review. Proceedings of the Institution of Civil Engineers, Structures and Buildings 163(SB6): 391–402.

Choo, Y.S., Liang, J.X. & Lim, L.V. 2003. Static strength of elliptical hollow section X-joint under brace compression. Proceedings 10th International Symposium on Tubular Structures, Madrid, Spain, pp. 253–258.

EN 1993-1-1 2005. Eurocode 3: Design of steel structures – Part 1-1: General rules and rules for buildings. European Committee for Standardization, Brussels, Belgium.

EN 10210-1 2006a. Hot finished structural hollow sections of non-alloy and fine grain steels – Part 1: Technical delivery conditions. European Committee for Standardization, Brussels, Belgium.

EN 10210-2 2006b. Hot finished structural hollow sections of non-alloy and fine grain steels – Part 2: Tolerances, dimensions and sectional properties. European Committee for Standardization, Brussels, Belgium.

Fang, Y. 2011. Static strength of Elliptical Hollow Section joints. MEng Report for PhD qualifying examination. National University of Singapore.

Gardner, L. & Chan, T.M. 2006. Cross-section classification of elliptical hollow sections. Proceedings 11th International Symposium on Tubular Structures, Québec City, Canada, pp. 171–177.

Haque, T.O. 2011. Elliptical hollow section T and X connections. MASc thesis, University of Toronto.

Haque, T., Packer, J. A. & Zhao, X. L. 2012. Equivalent RHS approach for the design of EHS in axial compression or bending. Advances in Structural Engineering, Vol. 15, No. 1, pp. 107–120.

Martinez-Saucedo, G., Packer, J.A. & Zhao, X.L. 2008. Static design of elliptical hollow section end connections. Proceedings of the Institution of Civil Engineers, Structures and Buildings 161 (SB 2):103–113.

Packer, J.A., Wardenier, J., Zhao, X.L., Vegte, G.J. van der, & Kurobane, Y. 2009a. Design guide for Rectangular Hollow Section (RHS) joints under predominantly static loading. 2nd edition, CIDECT, Geneva, Switzerland.

Packer, J.A., Wardenier, J., Choo, Y.S. & Chiew, S.P. 2009b. Elliptical steel tubes. Steel News and Notes, Singapore Structural Steel Society, SN&N 25th Anniversary Issue, pp. 86–90.

Packer, J.A., Choo, Y.S., Shen, W., Wardenier, J. & Vegte, G.J. van der 2012. Axially loaded T and X joints of Elliptical Hollow Sections. CIDECT final report 5BW. To be published.

Pietrapertosa, C. & Jaspart, J.-P. 2003. Study of the behaviour of welded joints composed of elliptical hollow sections. Proceedings 10th International Symposium on Tubular Structures, Madrid, Spain, pp. 601–608.

Shen, W., Wardenier, J., Packer, J.A., Choo, Y.S. & Vegte, G.J. van der 2012. Axially loaded elliptical hollow section X joints, Part II – Results and analysis. Proceedings 14th International Symposium on Tubular Structures, London, UK.

Shen, W., Choo, Y.S., Wardenier, J., Packer, J.A. & Vegte, G.J. van der 2013. Static strength of axially loaded elliptical hollow section X joints with braces welded to the wide sides of the chord. Part I: Numerical investigations. To be published.

SIMULIA 2007. Abaqus 6.7-1. Analysis manual.

Vegte, G.J. van der 1995. The static strength of uniplanar and multiplanar tubular T and X joints. Ph.D. Thesis, Delft University of Technology, Delft, The Netherlands.

Vegte, G.J. van der, Wardenier, J., Zhao, X.-L., & Packer, J.A., 2008: Evaluation of new CHS strength formulae to design strengths. Proceedings 12th International Symposium on Tubular Structures, Shanghai, China, Tubular Structures XII, Taylor & Francis Group, London, UK, pp. 313–32

Wardenier, J., Kurobane, Y., Packer, J.A., Vegte, G.J. van der, & Zhao, X.L. 2008. Design guide for Circular Hollow Section (CHS) joints under predominantly static loading. 2nd edition, CIDECT, Geneva, Switzerland.

Zhao, X.L. & Packer, J.A. 2008. Tests and design of concrete-filled elliptical hollow section stub columns. Thin-Walled Structures, Vol. 47, Nos. 6/7, pp. 617–628.

Zhao, X.L., Kernot, A., Packer, J.A. & Haque, T. 2010. Slenderness limits for EHS and OHS subject to bending using the RHS approach. Proceedings 13th International Symposium on Tubular Structures, Hong Kong, China, Tubular Structures XIII, Taylor & Francis Group, London, UK. pp. 293–302.

Tubular Structures XIV – Gardner (Ed.)
© 2012 Taylor & Francis Group, London, ISBN 978-0-415-62137-3

Axially loaded Elliptical Hollow Section X joints, Part II: Results and analysis

W. Shen
National University of Singapore, Singapore

J. Wardenier
National University of Singapore, Singapore
Delft University of Technology, Delft, The Netherlands

J.A. Packer
University of Toronto, Canada

Y.S. Choo
National University of Singapore, Singapore

G.J. van der Vegte
Van der Vegte Consultancy, The Netherlands

ABSTRACT: Elliptical Hollow Sections (EHS) are especially attractive for architectural applications. Since limited evidence exists for the design of directly welded joints between EHS, a new research programme has been initiated. The first phase of this programme aims at providing information for developing design rules for axially loaded T and X joints between EHS. This second paper on this subject deals with the analysis of the numerical and experimental results of axially loaded X joints with the braces connected to the wide sides of the EHS chord.

1 INTRODUCTION

This paper, as well as a companion paper (Shen et al. 2012), deals with investigations on axially loaded X joints of Elliptical Hollow Sections (EHS) with the braces connected to the wide sides of the chord, designated as Types 1 and 2 in Figure 1.

The first paper by Shen et al. (2012) covers the special aspects of EHS, the available evidence for EHS joints, the experimental and numerical programme, the calibration and validation of the numerical model and the initial numerical investigations regarding effect of weld type and chord length.

This second paper deals with the numerical and experimental results and the analysis thereof.

This programme is sponsored by the participating universities, the authors and CIDECT, and is designated as programme 5BW. This first phase aims at providing information for developing design rules for axially loaded T and X joints between Elliptical Hollow Sections.

2 DESIGNATION

For the EHS used in joints, the usual designations for Rectangular Hollow Section (RHS) joints, i.e.: chord width b_0, chord depth h_0, brace width b_1 and brace depth h_1, are adopted. For the types of joints the designation proposed by Choo et al. (2003) is used, see Figure 1.

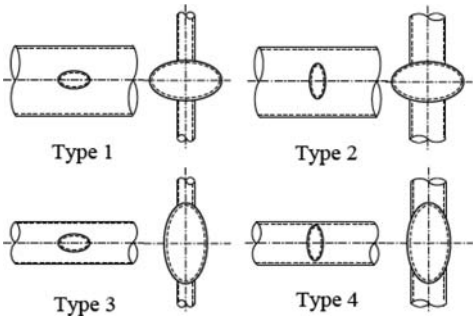

Figure 1. EHS joint types.

3 NUMERICAL RESULTS

The numerical analyses are summarized in Table 1.

The basic series covers β ratios of 0.24, 0.4, 0.6, 0.8 and 1.0 in combination with 2γ ratios of 16,

20, 31 and 42. In general, an angle of $\theta_1 = 90°$ is used but also analyses with an angle of $\theta_1 = 45°$ were investigated.

Further, the chord stress effect was investigated for 3 chord compression and 3 chord tensile load ratios, n. The chord has, in all analyses, dimensions of $250 \times 125 \times t_0$.

Table 1. Summary of numerical X joint, Types 1 and 2 analyses.

Analyses	Initial	Basic parameters	Brace angle	Chord stress	Total
Type 1		7	3	18	28
Type 2	8	16	5	36	65

3.1 *X joints, Type 1*

Typical load-displacement diagrams are given in Figure 2 for $\beta = 0.4$ showing the effect of 2γ in Figure 2(a), the angle θ_1 in Figure 2(b) and the effect of chord stress in Figures 2(c) and (d).

The governing capacities are recorded in Figure 3 for the influence of the parameters β and 2γ. Similarly as for CHS and RHS joints, the capacity increases with β and decreases with 2γ. Figure 4 shows that the effect of the angle θ_1 is somewhat stronger than $1/\sin\theta_1$. As shown in Figure 5 the chord stress effect function Q_f (ratio of capacities with chord stress to that without chord stress) for $\beta = 0.4$ is nearly independent of 2γ and for chord compression stronger than for chord tension.

For comparison, Figures 3 and 4 also show the experimental data and it can be concluded that the numerical and experimental data agree well.

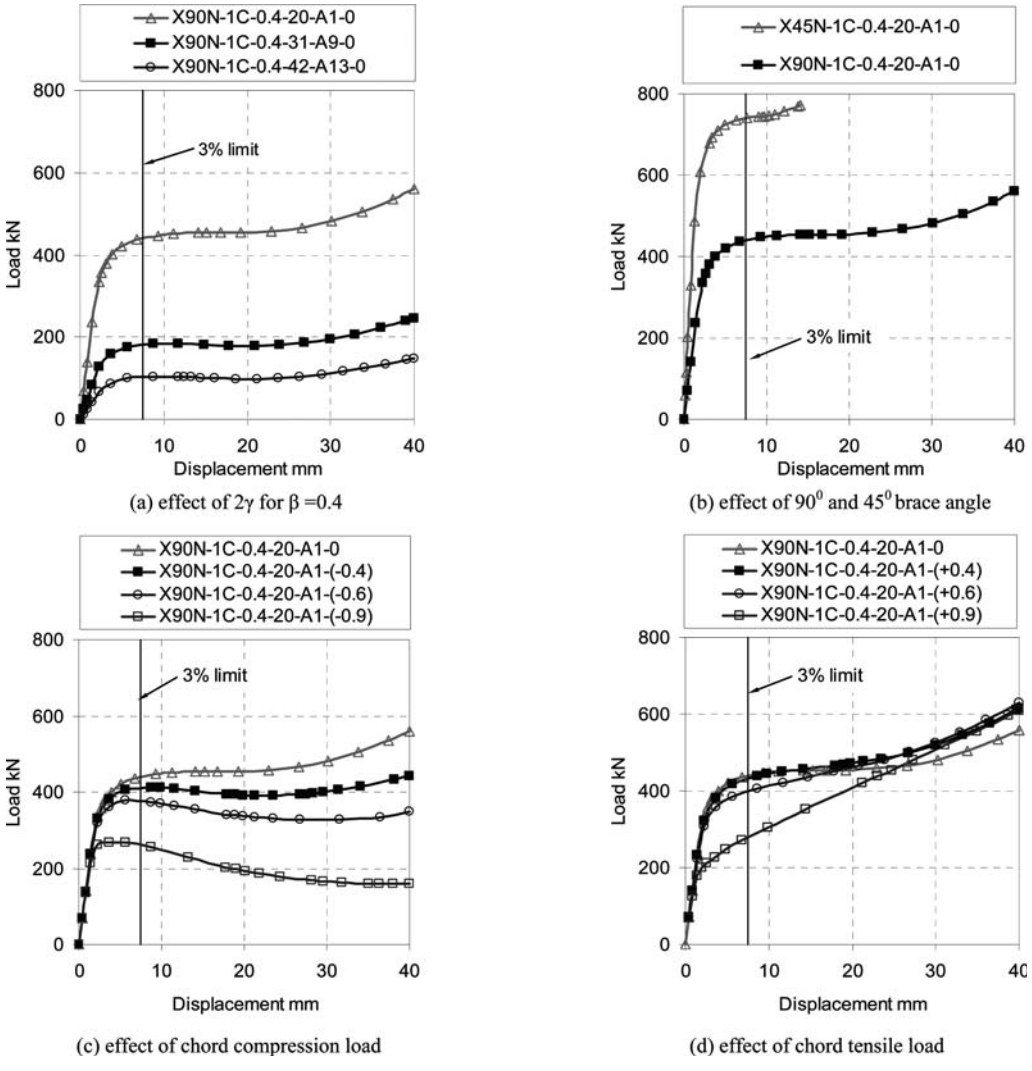

Figure 2. Typical load-displacement curves for X joint, Type 1.

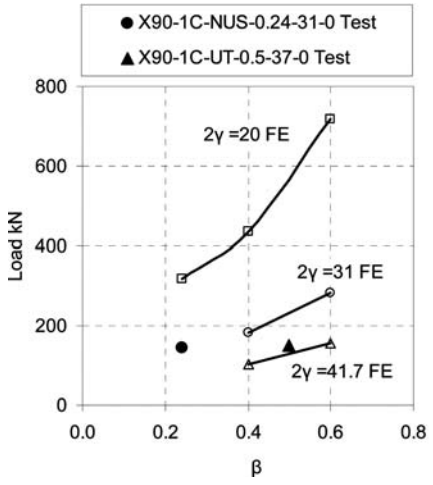

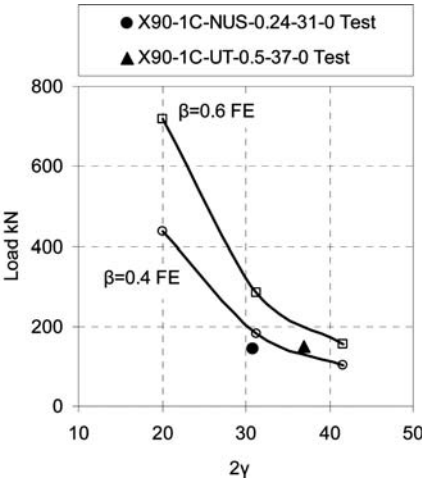

Figure 3. FE and test results for EHS X joints Type 1 with 90° brace angle subjected to brace compression without chord load: effect of β and 2γ.

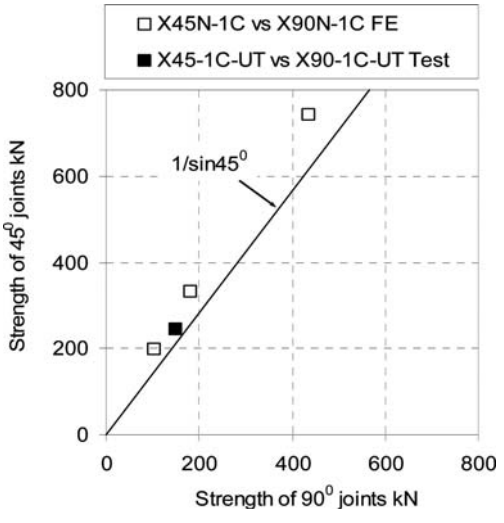

Figure 4. Effect of brace angle θ_1 for EHS X joints Type 1.

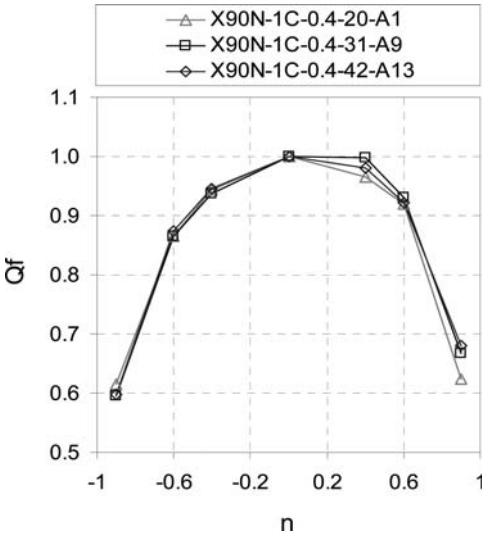

Figure 5. Effect of chord stress n; EHS X joints Type 1.

3.2 *X joints, Type 2*

Typical load-displacement diagrams are given in Figure 6 for $\beta = 0.4$ and 2γ showing the effect of 2γ in Figure 6(a), the angle θ_1 in Figure 6(b) and the effect of chord stress in Figures 6(c) and (d).

The governing capacities are recorded in Figure 7 for the influence of the parameters β and 2γ. Similarly as for CHS and RHS joints, the capacity increases with β and decreases with 2γ.

Figure 8 shows that the effect of the angle θ_1 is somewhat smaller than $1/\sin\theta_1$. Figure 9 shows that the chord stress effect is somewhat dependent on β and 2γ and for chord compression stronger than for chord tension.

As shown, the numerical and experimental data agree well.

4 ANALYSIS

4.1 *X Joints, Types 1 and 2*

Since the Type 1 and Type 2 joints have the same orientation of the chord it is expected that they would show a comparable behaviour for the basic failure mode of chord plastification, similar to chord face failure for RHS joints. That is the reason why these joints have been analysed together.

4.1.1 *Chord plastification*

4.1.1.1 Influence of β and 2γ

The basic numerical data for X joints Types 1 and 2 with 90° have been analysed as a function of β and $N_{1,u}\ \sin\theta_1/f_{y0}t_0^2$. As shown in Figure 10(a), for Type 1,

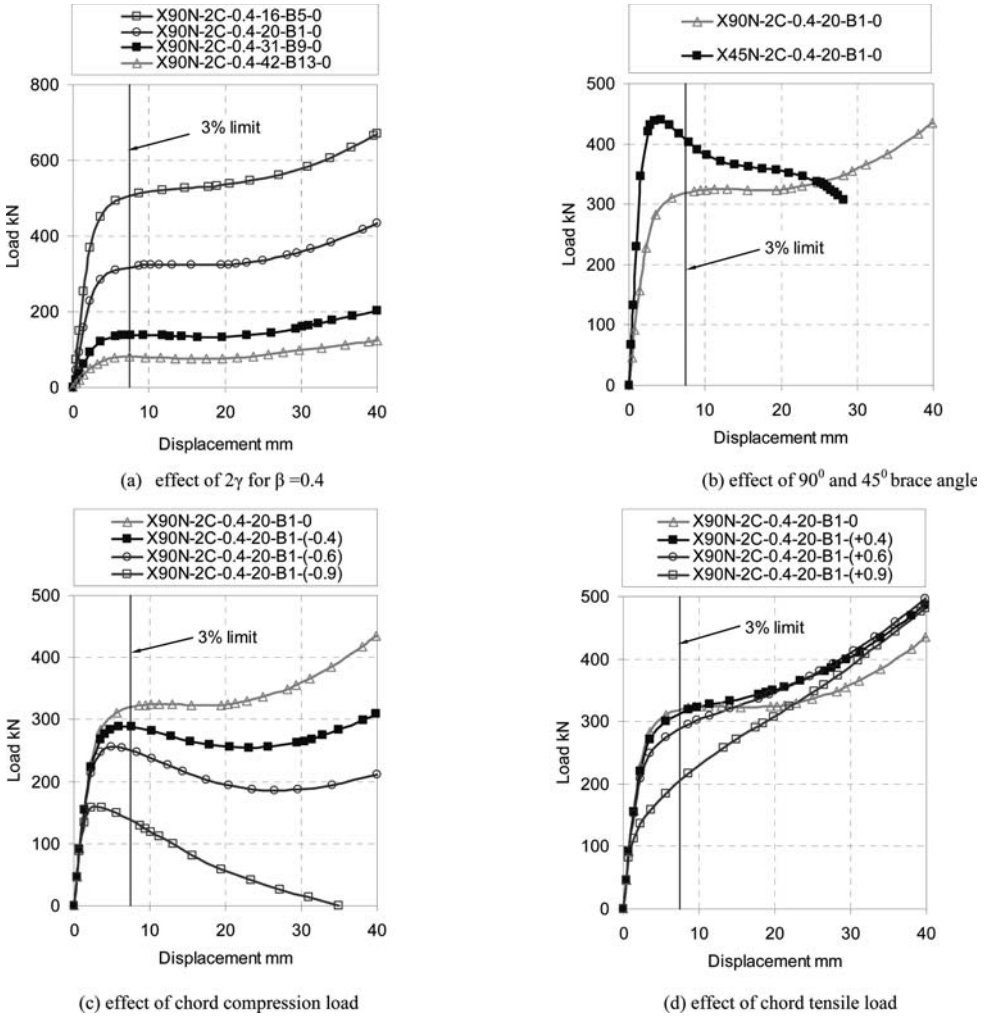

Figure 6. Typical load-displacement curves for X joint, Type 2.

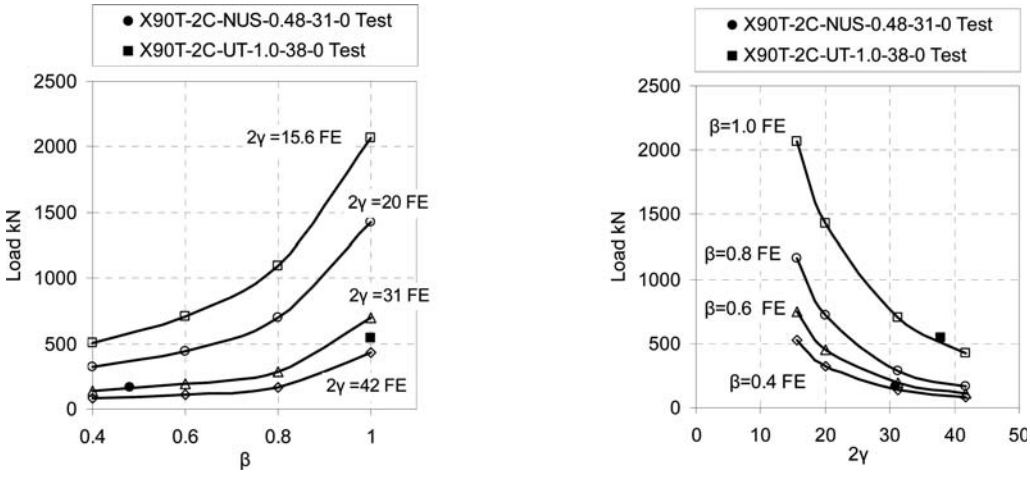

Figure 7. FE and test results for EHS X joints Type 2 with 90° brace angle subjected to brace compression, without chord load: Effect of β and 2γ.

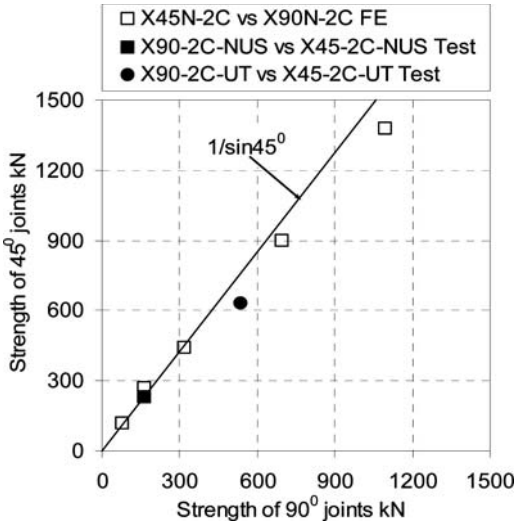

Figure 8. Effect of brace angle θ_1 for EHS X joints, Type 2.

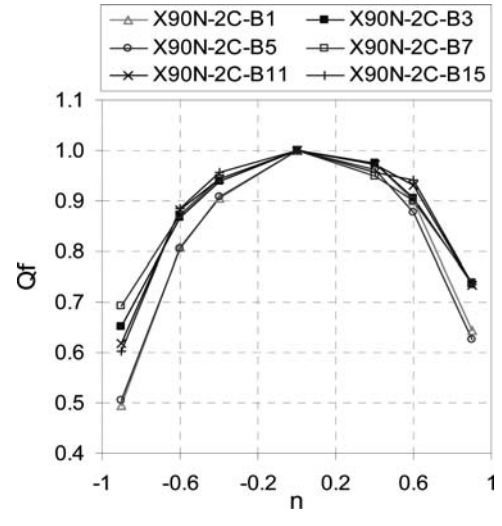

Figure 9. Effect of chord stress n; EHS X joints, Type 2.

up to $\beta \leq 0.6$ there is almost no influence of 2γ and the same applies for Type 2 up to about $\beta \leq 0.8$.

For practical applications, the β ratio of Type 1 will not exceed 0.5, because then the brace and chord will have the same larger outer dimension and it is not logical that the brace would be larger than the chord (although in this investigation the maximum β ratio was taken as 0.6).

For comparison with the Type 2 data, the mean line for the Type 1 data is indicated with a dotted line in Figure 10(b). For the same β ratio, the data of Type 1 are higher if related to β because of the 4 times larger h_1.

In Figure 11(a) the Type 2 data and the mean for the Type 1 data are related to $\beta^* = (b_1 + h_1)/2b_0$ although this is not realistic for the Type 2 joints with $\beta = 1.0$ which fail by chord side wall failure.

After further analysis of the basic data, it was found that a simple transition rule can be used for Type 1 to use the strength equation for Type 2. For chord plastification the strength is not only governed by b_1 but to a somewhat lower extent also by h_1.

Using the average parameter β^* for Type 1 and β for Type 2 takes this effect into account because, for a particular β^* for Type 1 equal to a β for Type 2, the perimeter of a brace in a Type 1 joint will be somewhat larger than that for a Type 2 joint.

With this transition, Figure 11(b) shows that the data for Type 1 joints with $\beta^* \leq 0.75$ (practical range $\beta \leq 0.5$) are in excellent agreement with the Type 2 data for $\beta \leq 0.8$.

4.1.1.2 Influence of angle θ_1

As shown in Figure 12(a) for the Type 1 joints with $\beta = 0.4$ the effect of the angle $\theta_1 = 45°$ was larger than $1/\sin\theta_1$, being about 25% larger which nearly agrees with the increase of the CHS connection perimeter $k_a = 1.21$. However, as shown in Figure 12(b), for the Type 2 joints with $\beta = 0.4$ and 0.8 the angle effect was smaller than $1/\sin\theta_1$. This could be caused by the effect of an in-plane chord rotation because the chord ends were not supported. Therefore a few additional analyses have been carried out (see Figure 13).

Figure 13 shows that if the chord ends would have been fixed to avoid rotation in-plane, the strength would have been additionally increased by 13% for

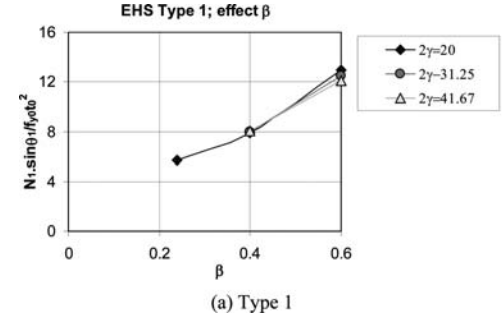

Figure 10. Influence of β and 2γ for Types 1 and 2.

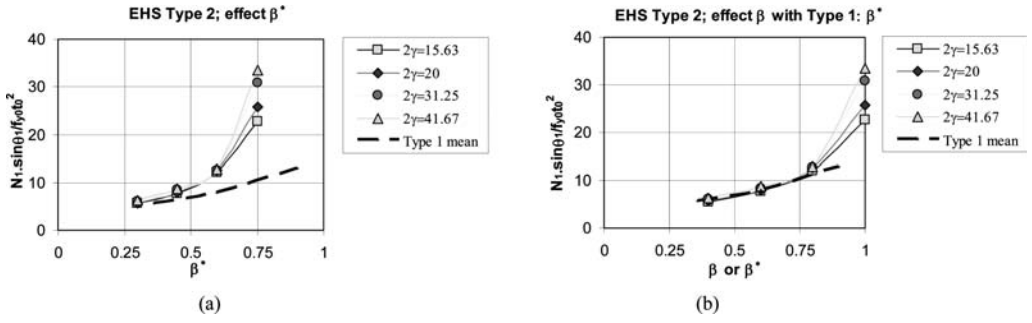

Figure 11. Influence of β* or β and 2γ: (a) β*for Types 1 and 2; (b) β for Type 2 and β* for Types 1.

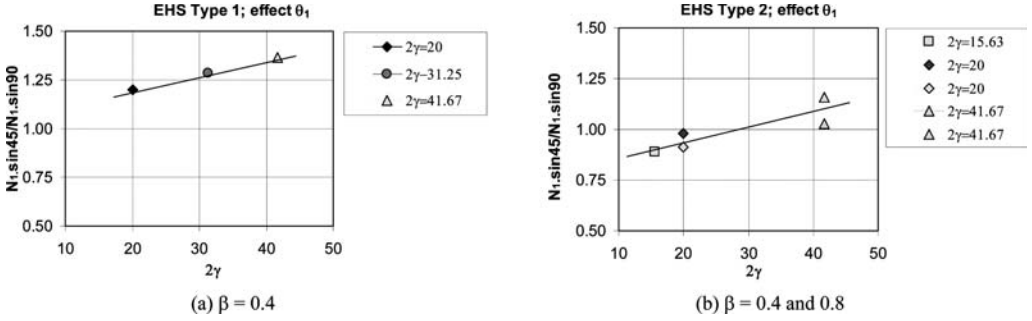

Figure 12. Effect of angle θ for chord plastification.

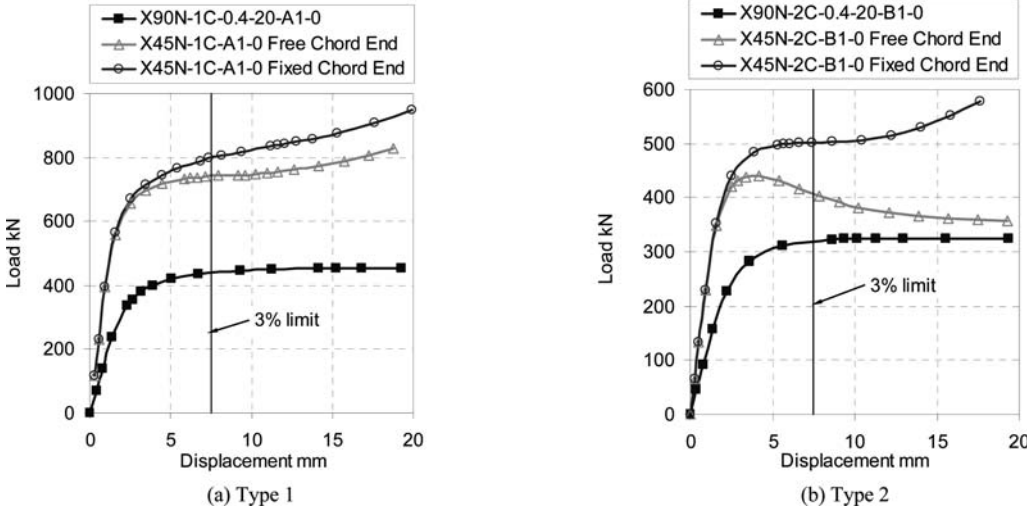

Figure 13. Effect of chord end fixation (additional analyses).

X joints Type 1 and 20% for X joints Type 2. Including the fixation effect gives, for both Types of X joints, an influence of the angle larger than $1/\sin\theta_1$. The latter is proposed as a simple rule.

4.1.1.3 Influence of chord stress parameter n

The chord stress effect is shown in Figure 14 for Type 2 joints with $\beta = 0.4$. For simplicity, a similar basic function is chosen as used for CHS and RHS joints. Due to the low scatter in data, the exponents in the chord stress functions for compression and tension (0.2 and 0.15) are somewhat smaller than for CHS and RHS joints. The chord stress effect for $0.24 \leq \beta \leq 0.8$ is the same for both types of joints.

4.1.2 *Chord side wall failure*

4.1.2.1 Basic influencing parameters

For chord side wall failure, it is logical that the strength equation should have a similarity with that for RHS

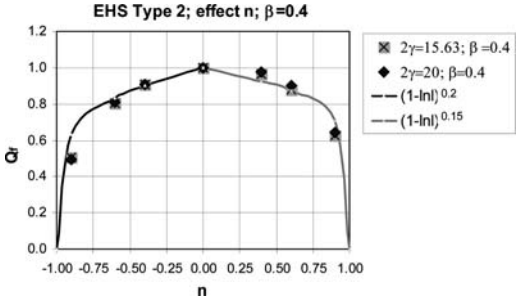

Figure 14. Chord stress effect for Type 2 joints with $\beta = 0.4$.

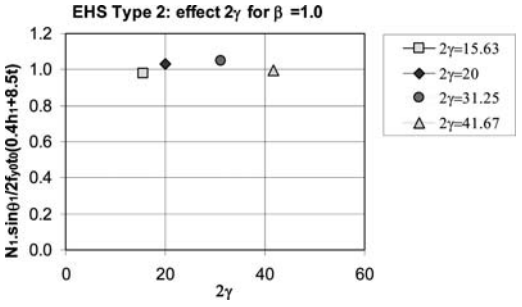

Figure 15. X joints Type 2 data for $\beta = 1.0$ with various 2γ for brace in compression.

joints with $\beta = 1.0$, thus:

$$N_{1,u} = 2f_k t_0 (c_x h_1 + c_y t_1 + 5t_0) \frac{Q_f}{\sin\theta_1} \qquad (1)$$

where c_x an c_y are coefficients to take into account the effect of the spreading by the brace dimension h_1 and the weld leg length which is a function of t_1. Figure 15 shows a comparison of the numerical data with the best fit of Eq. 1 with $c_x = 0.4$ and $(c_y t_1 + 5t_0) = 8.5t_0$ (which is physically too large). After the evaluation to design strengths these values may be reduced somewhat.

4.1.2.2 Influence of angle θ_1 for chord side wall failure

Initially no analyses were planned for $\theta_1 = 45°$ with $\beta = 1.0$, but to check the influence of the angle additional analyses have been carried out for $2\gamma = 20$. The analyses for $\theta_1 = 45°$ with $\tau = 0.5$ only showed a small increase due to local buckling of the brace. Increasing the τ to 0.8 showed, for $\theta_1 = 45°$ and fixed chord ends, an increase of 35%, thus close to $1/\sin\theta_1$ which is adopted.

4.1.2.3 Influence of chord stress parameter n

To check the chord stress effect for $\beta = 1.0$, additional analyses, shown in Figure 17, were carried out, which show that the chord stress functions for chord plastification are conservative for chord side wall failure.

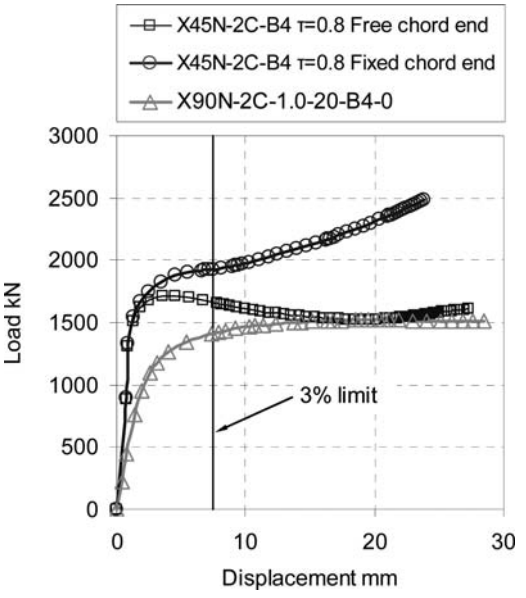

Figure 16. Effect of angle $\theta = 45°$ for Type 2 with $\beta = 1.0$, $2\gamma = 20$ and $\tau = 0.8$ (additional analyses).

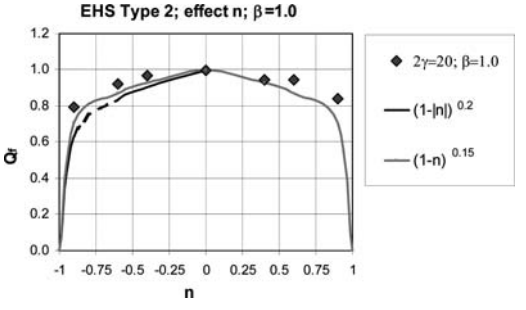

Figure 17. Effect of chord stress parameter n for $\beta = 1.0$ and $2\gamma = 20$ (additional analyses).

The best fit is given by $Q_f = (1 - |n|)^{0.1}$ which agrees with that for RHS joints with $\beta = 1.0$ (see Packer et al. 2009a).

5 PROPOSED BEST-FIT EQUATIONS

Based on the previous analyses, the following basic joint strength equations for Type 1 and Type 2 X joints are proposed for further evaluation to design strengths:

– For Type 2 X joints the best-fit equation for chord plastification for $\beta \le 0.8$ is given by:

$$N_{1,u} = (3.5 + 13.5\beta^2) \frac{f_{y0} t_0^2}{\sin\theta_1} Q_f \qquad (2)$$

with, for $\theta_1 = 90°$, a mean of 1.01 and a CoV = 5.6%.

– For Type 1 X joints Equation (2) for chord plastification applies if β^* is used instead of β.

Table 2. Proposed exponent c_1 for chord stress function.

	Chord plastification		Chord side wall
	Chord Compression $c_1 = 0.20$	Chord Tension $c_1 = 0.15$	Chord tension or compression $c_1 = 0.10$
Mean	1.0	1.03	1.01
CoV	7.2%	4.8%	2.1%

– For chord side wall failure for $\beta = 1.0$ (only Type 2) the best-fit equation is given by:

$$N_{1,u} = 2f_k t_0 (c_x h_1 + 8.5t_0) \frac{Q_f}{\sin\theta_1} \text{ with } f_k = f_{y0} \qquad (3)$$

with, for $\theta_1 = 90°$, a mean of 1.01 and a CoV = 3.2%.

– For the chord stress function $Q_f = (1 - |n|)^{c_1}$ and exponents, the variables in Table 2 are obtained.

Equations (2) and (3) still have to be evaluated to limit state equations for design by taking account of the scatter in data, tolerances in dimensions, variation in mechanical properties and the partial factors γ_M to be adopted, see Van der Vegte et al., (2008). However, this will be done together with the data for T joints and also considering a possible more direct relationship with CHS or RHS T or X joints.

6 CONCLUSIONS

Based on analyses of the results of a FE parametric study, the best – fit equations for predicting the static strength of EHS X joints Types 1 and 2, are proposed together with functions to account for the chord stress effect. Best-fit equations for Type 2 X joints are given for chord plastification (for $\beta \leq 0.8$) and chord side wall failure (for $\beta = 1.0$). For Type 1 X joints the chord plastification Equation (2) for Type 2 can be used, however, by replacing β with β*. When checked against available evidence, the proposed equations give satisfactory accuracy.

Further study will be carried out for the interaction of the two limit states, for joints with a β ratio between 0.8 and unity.

ACKNOWLEDGEMENTS

Appreciation is extended to Tata Tubes for delivering the EHS sections, and to the University of Toronto (plus SSEF and NSERC), Canada, the National University of Singapore, Singapore and Delft University of Technology, The Netherlands for their financial and/or in-kind contributions.

Further appreciation is extended to the Comité International pour le Développement et l'Etude de la Construction Tubulaire (CIDECT) for sponsoring this programme and for the discussions in their Project Working Group.

The experimental results presented in this paper are extracted from the MASc report of Ms. T. Haque (University of Toronto) and the research report of Ms. Y. Fang (National University of Singapore).

REFERENCES AND SYMBOLS

References and symbols are given in the companion paper:

Shen, W., Choo, Y.S., Wardenier, J., Vegte, G.J. van der & Packer, J.A. 2012. Axially loaded elliptical hollow section X joints, Part I – Experiments and numerical calibration. Proceedings 14th International Symposium on Tubular Structures, London, UK.

Elliptical hollow sections

Tubular Structures XIV – Gardner (Ed.)
© 2012 Taylor & Francis Group, London, ISBN 978-0-415-62137-3

Numerical modeling and design of cold-formed steel oval hollow section compression members

J.H. Zhu
Shenzhen Key Lab on Durability of Civil Engineering, College of Civil Engineering, Shenzhen University, Shenzhen, China

B. Young
Department of Civil Engineering, The University of Hong Kong, Hong Kong, China

ABSTRACT: The numerical analysis and design of cold-formed steel compression members of oval hollow sections have been investigated. A finite element model was developed to simulate the existing tests on fixed-ended columns of oval hollow sections. The failure modes observed from the tests included material yielding, local buckling and flexural buckling as well as interaction of local and flexural buckling. The finite element model was developed using ABAQUS. The material non-linearities obtained from tensile coupon tests as well as the initial local and overall geometric imperfections were incorporated in the model. Convergence study was performed to obtain the optimized mesh density. A parametric study included 100 columns was conducted using the verified numerical model. The experimental column strengths and numerical results predicted by the parametric study were compared with the design strengths calculated using the current North American, Australian/New Zealand and European specifications for cold-formed steel structures. In addition, the direct strength method, which was developed for cold-formed carbon steel members for certain qualified cross sections, was also used to predict the design strengths for the oval hollow sections.

1 INTRODUCTION

Oval hollow section (OHS) is one of the new sections used in steel structure constructions. Typical steel sections such as I-section, channel section, circular hollow section and rectangular hollow section are used in various structures. However, new sections are being developed with the requirements on both the efficiency and aesthetics. The geometry of the OHS combined with its aesthetic appearance makes it an exciting choice for architects. Besides, it has the advantage of different major and minor axes properties. Gardner & Ministro (2005) reported some applications of oval hollow sections in structural engineering projects.

In the previous research, different definition of oval hollow section has been used. The elliptical geometry, which is commonly referred as oval hollow section, has been investigated by a number of researchers. Bortolotti et al. (2003) investigated welded joints of elliptical hollow sections. Gardner & Chan (2007) proposed slenderness parameters and cross-section classification limits for elliptical hollow sections. The flexural buckling behaviour was also investigated by Chan & Gardner (2008, 2009). Theofanous et al. (2009) investigated stainless steel elliptical section compression members. Silvestre (2008) investigated the buckling behaviour of elliptical cylindrical shells and tubes under compression. It should be noted that the aforementioned oval hollow sections were focused on elliptical hollow sections, which is different to the oval hollow sections presented in this study.

A series of fixed-ended column tests on cold-formed steel oval hollow sections has been conducted and presented by Zhu & Young (2011). The oval hollow section investigated in this study is composed of two flat web plates and two semi-circle flanges, as shown in Figure 1. The oval hollow sections were cold-rolled at room temperature and then the electric resistance welding was used to close the hollow sections. The test program included 28 columns compressed between fixed ends. The observed failure modes included material yielding, flexural buckling and local buckling in the flat web plates as well as interaction between local and flexural buckling. Local buckling of the curved flanges of semi-circle was not observed since the cross-sections were relatively compact in the test program. Following the experimental investigation, a numerical investigation using FEA is performed and presented in this paper with particular emphasis on slender sections, where local buckling was observed in the curved flanges. It should be noted that the semi-circle element with W/t ratio less than 40 should be considered as fully effective according to the Australian/New Zealand Standard for cold-formed

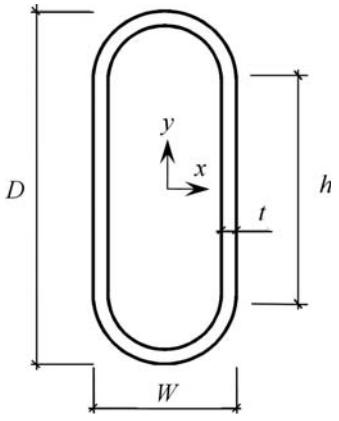

Figure 1. Definition of symbols.

steel structures (AS/NZS 2005). Therefore, the expressions of compact and slender sections were used to identify the oval hollow section in this study. The objective of this study is firstly to develop an advanced non-linear FEM for the investigation on the strengths and behaviour of cold-formed steel oval hollow section columns; secondly, to compare the test strengths with the design strengths predicted using the current North American (NAS 2007a, 2007b), Australian/New Zealand (AS/NZS 2005) and European (EC3 2005, 2006a, 2006b) specifications for cold-formed steel structures with certain assumptions on the calculation of effective width. The direct strength method, which has been adopted by the North American Specification for cold-formed steel structures as an alternative procedure, was also used in this study; and lastly, to examine the reliability of these design rules using reliability analysis. Finite element program ABAQUS (2009) was used to perform the numerical analysis. Initial geometric imperfections and material non-linearity were included in the model. The finite element model was verified against the column test results conducted by Zhu & Young (2011).

2 SUMMARY OF TEST PROGRAM

The test program presented by Zhu & Young (2011) provided experimental ultimate loads and failure modes of cold-formed steel oval hollow sections compressed between fixed ends. The experimental program consisted of 28 specimens of four test series with different cross-section sizes and steel grades, as shown in Table 1 using the symbols illustrated in Fig. 1. The measured cross-section dimensions and material properties of each specimen are detailed in Zhu & Young (2011). The specimens were tested between fixed ends at various column lengths ranged from 90 to 3000 mm, and the nominal maximum slenderness ratio (λ_{max}) for each test series ranged from 75.5 to 131.6. The longest specimen lengths produced l_{ey}/r_y ratios of 75.5, 94.5, 97.5 and 131.6 for Series A, B, C and D, respectively,

Table 1. Oval section column test series.

Test series	Dimension, $D \times W \times t$ (mm)	λ_{max}
A	$120 \times 48 \times 2.0$	75.5
B	$115 \times 38 \times 2.0$	94.5
C	$42 \times 21 \times 2.8$	97.5
D	$30 \times 15 \times 1.6$	131.6

Table 2. Comparison of test strengths with FEA strengths of different mesh densities for Series A.

	Comparison		
Specimen	P_{Exp}/P_{FEA1}	P_{Exp}/P_{FEA2}	P_{Exp}/P_{FEA3}
A360	1.00	1.00	1.00
A360#	1.03	1.03	1.03
A600	1.07	1.06	1.07
A1200	1.05	1.05	1.05
A1200#	1.04	1.06	1.06
A1800	1.04	1.04	1.05
A2400	1.04	1.05	1.04
A3000	1.08	1.08	1.08
Mean, P_m	1.04	1.04	1.04
COV, V_P	0.023	0.024	0.025

where l_{ey} is the effective length for buckling about the minor y-axis and r_y is the radius of gyration of full unreduced cross-section about the y-axis.

The test specimens were labeled such that the test series and specimen length could be easily identified, as shown in Table 2. For example, the label "A360#" defines the following specimen: the first letter indicates the specimen dimension and test series, where "A" refers to an OHS with nominal cross-section dimension of $120 \times 48 \times 2.0$ mm for overall depth (D), overall width (W) and thickness (t) of the section, respectively. The cross-section dimensions for other sections are shown in Table 1. The following digits in the label indicate the nominal specimen length in millimeters (360 mm); and if a test was repeated, then the symbol "#" indicates the repeated test. Measured initial overall geometric imperfections, experimental ultimate loads (P_{Exp}) and failure modes observed at ultimate loads are also detailed in Zhu & Young (2011).

3 DEVELOPMENT OF FINITE ELEMENT MODEL

The finite element program ABAQUS (2009) version 6.9 was used in the analysis for the simulation of cold-formed steel OHS columns tested by Zhu & Young (2011). The measured geometry, initial geometric imperfections, and material non-linearity of the test specimens were included in the finite element model. The model was based on the centerline dimensions of the cross-sections. The simulation consisted of two

steps. The first step is the Eigenvalue analysis to determine the buckling modes, whereas the second step is the load-displacement nonlinear analysis. The finite element model described in this section followed the same approach as detailed in Yan & Young (2004) for cold-formed steel columns.

Shell element is one of the most appropriate types of element for modeling thin-walled metal structures. The 4-noded doubly curved shell elements with reduced integration S4R were used in the model. The S4R element has six degrees of freedom per node and shown to provide accurate results from previous research as described in Yan & Young (2004). The finite element mesh dimension is important on the calculation efficiency and simulation accuracy. Hence, a convergence study was performed on Series A test specimens with three different mesh dimensions of FEA1 (3.6 × 3.6 mm, length by width), FEA2 (5 × 5 mm) and FEA3 (8 × 8 mm), as shown in Table 2. The three mesh dimensions separated the cross-section into 80, 56 and 36 elements, respectively. It can be seen from Table 2 that the experimental-to-FEA ultimate load ratios P_{Exp}/P_{FEA1}, P_{Exp}/P_{FEA2} and P_{Exp}/P_{FEA3} are very close for each specimen, with the same mean value of 1.04, and the corresponding coefficient of variation (COV) of 0.023, 0.024 and 0.025, respectively. By considering calculation efficiency, the FEA2 (5 × 5 mm) is a better choice for Series A. The finite element mesh dimensions of Series B, C and D are detailed in Zhu & Young (2012).

The fixed-ended boundary condition was simulated by restraining all the degrees of freedom of the nodes at both ends, except for the translational degree of freedom in the axial direction at one end of the column. The nodes other than the two ends were free to translate and rotate in any directions. The displacement control loading method, which is identical to that used in the column tests, was used in the finite element model. Compressive axial load was applied to the column by specifying an axial displacement to the nodes at one end of the column.

The material properties obtained from the flat tensile coupon tests were used in the numerical modeling of the respective test series. Both initial local and overall geometric imperfections were incorporated in the model. The modeling is detailed in Zhu & Young (2012).

4 TEST VERIFICATION

The developed finite element model was verified against the experimental results. The ultimate loads and failure modes predicted by the FEA are compared with the experimental results as shown in Zhu & Young (2012). It is shown that the ultimate loads (P_{FEA}) obtained from the FEA are in good agreement with the experimental ultimate loads (P_{Exp}).

The failure modes at ultimate load obtained from the tests and FEA for each specimen are also shown in Zhu & Young (2012). The failure modes included material yielding, local buckling and flexural buckling

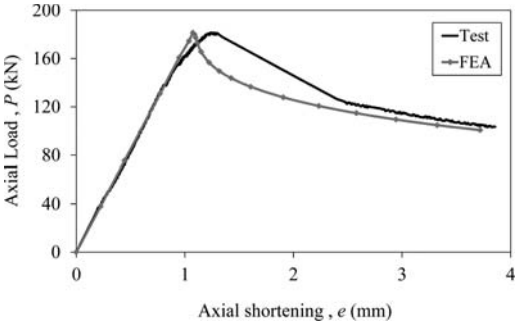

Figure 2. Axial load versus shortening of specimen A360.

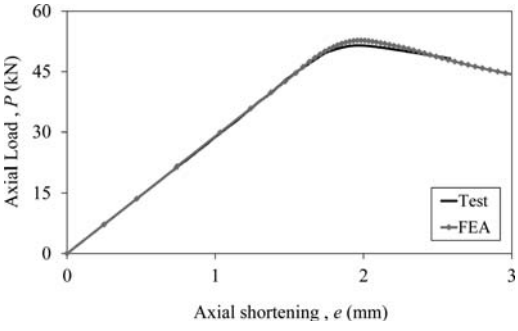

Figure 3. Axial load versus shortening of specimen C1500.

as well as interaction of local and flexural buckling. The failure modes predicted by the FEA are generally in good agreement with those observed in the tests, except for a few specimens, as detailed in Zhu & Young (2012). Figs 2 and 3 show the comparison of the load-shortening curves obtained from the tests and predicted by the FEA for the specimens A360 and C1500, respectively. It is shown that the FEA curves followed the experimental curves closely. Fig. 4(a) shows the photograph of test specimen B1200 immediately after the ultimate load has reached. The specimen failed in interaction of local and flexural buckling. Fig. 4(b) shows the deformed shape of the specimen predicted by the FEA right after the ultimate load. The resemblance of Figs. 4(a) and 4(b) demonstrates the reliability of the FEA predictions.

5 PARAMETRIC STUDY

The FEM closely predicted the experimental ultimate loads and failure modes of the cold-formed steel OHS columns conducted by Zhu & Young (2011). Hence, the model was used for an extensive parametric study. The parametric study included 100 specimens that consisted of 20 series, as shown in Table 3. Each series contained 5 specimens with column lengths of 500, 1200, 2000, 2700 and 3500 mm.

The material properties of the specimens in the parametric study are identical to the material properties of

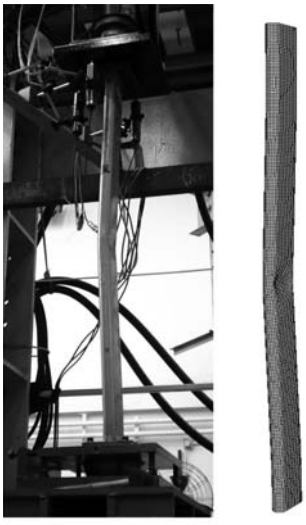

(a) Test (b) FEA

Figure 4. Comparison of experimental and FEA deformed shapes for specimen B1200.

Table 3. Cross-section dimensions of each series for parametric study.

Series	Depth D (mm)	Width W (mm)	Thickness t (mm)	h/t	W/t
W60T2	300	60	2	120.0	30.0
W60T2.4	300	60	2.4	100.0	25.0
W60T3	300	60	3	80.0	20.0
W60T4	300	60	4	60.0	15.0
W60T10	300	60	10	24.0	6.0
W75T1.9	300	75	1.9	118.4	39.5
W75T2.2	300	75	2.2	102.3	34.1
W75T2.8	300	75	2.8	80.4	26.8
W75T3.8	300	75	3.8	59.2	19.7
W75T10	300	75	10	22.5	7.5
W100T1.7	300	100	1.7	117.6	58.8
W100T2	300	100	2	100.0	50.0
W100T2.5	300	100	2.5	80.0	40.0
W100T3.3	300	100	3.3	60.6	30.3
W100T10	300	100	10	20.0	10.0
W150T1.3	300	150	1.3	115.4	115.4
W150T1.5	300	150	1.5	100.0	100.0
W150T1.8	300	150	1.8	83.3	83.3
W150T2.5	300	150	2.5	60.0	60.0
W150T10	300	150	10	15.0	15.0

Series B in the experimental program. The local imperfection magnitude was 10% of the section thickness and the overall imperfection magnitude was 1/1500 of the column length. The size of the finite element mesh was 10×10 mm (length by width) since the specimen cross-section dimensions are much larger than the specimens in the experimental program. The column strengths (P_{FEA}) obtained from the parametric study are shown in Zhu & Young (2012).

6 DESIGN APPROACHES

6.1 *Current design rules*

The current North American Specification (NAS 2007a, 2007b), Australian/New Zealand Standard (AS/NZS 2005) and European Codes (EC3 2005, 2006a, 2006b) provide design rules for cold-formed steel structures. However, these specifications do not cover design rules of the oval hollow sections investigated in this study. Therefore, certain assumptions on the calculation of effective width have been made in the calculation of the column strengths in this study, as described in Zhu & Young (2011). The OHS investigated in this study was considered as two flat web plates and two semi-circle flanges. The flat plates are supported by the two semi-circle flanges and assumed to be stiffened elements. Hence, the plate buckling coefficient k of the flat plates is taken as 4.0. The NAS, AS/NZS and EC3 specifications do not have design rules for effective width of curved plate, except for cylindrical tubular member. However, the local buckling resistance of a curved plate, such as semi-circle, is greater than a flat plat. Local buckling was not observed in the curved portions of the OHS for all the test specimens. In this study, the semi-circle flanges are considered as fully effective. The calculation procedure of NAS, AS/NZS and EC3 specifications are detailed in Zhu & Young (2011).

It should be noted that the Automotive Steel Design Manual (AISI 2002) published by the American Iron and Steel Institute, although it was not developed for structural members, includes design rules for local instability of sections with curved and straight elements. However, it has been demonstrated that the design strengths predicted using the specification are generally unconservative for the cold-formed steel OHS columns, as concluded by Zhu & Young (2011). Therefore, the Automotive Steel Design Manual was not used in this study.

6.2 *Direct strength method*

The direct strength method, which was developed for cold-formed steel members, is based on the same underlying empirical assumption as the effective width method: ultimate strength is a function of elastic buckling and yielding of the material (Schafer 2002a). The direct strength method has been proposed by Schafer & Peköz (1998) for laterally braced flexural members undergoing local and distortional buckling. Subsequently, the method has been developed for concentrically loaded pin-ended cold-formed steel columns undergoing local, distortional and overall buckling (Schafer 2000, 2002b). In this study, distortional buckling is not considered since the oval hollow section is a closed section. As summarized in the North American Specification (NAS) for cold-formed steel structures, the column design rules of the direct strength method that considered the local and overall flexural buckling are shown in Eqs (1)–(3). The values of 0.15 and 0.4 are the coefficient and exponent of the direct strength

equation, respectively, that were calibrated against test data of concentrically loaded pin-ended cold-formed steel columns for certain cross-sections and geometric limits. It should be noted that the direct strength method does not cover OHS.

$$P_{DSM} = \min\left(P_{ne}, P_{nl}\right) \tag{1}$$

$$P_{ne} = \begin{cases} \left(0.658^{\lambda_c^2}\right) P_y & \text{for } \lambda_c \le 1.5 \\ \left(\frac{0.877}{\lambda_c^2}\right) P_y & \text{for } \lambda_c > 1.5 \end{cases} \tag{2}$$

$$P_{nl} = \begin{cases} P_{ne} & \text{for } \lambda_l \le 0.776 \\ \left[1 - 0.15\left(\frac{P_{crl}}{P_{ne}}\right)^{0.4}\right]\left(\frac{P_{crl}}{P_{ne}}\right)^{0.4} P_{ne} & \text{for } \lambda_l > 0.776 \end{cases} \tag{3}$$

where $P_y = f_y A$; $\lambda_c = \sqrt{P_y / P_{cre}}$; $\lambda_l = \sqrt{P_{ne} / P_{crl}}$.
A = Gross cross-section area;
f_y = Material yield strength which is the static 0.2% proof stress ($\sigma_{0.2}$);
$P_{cre} = \pi^2 EA/(l_e/r_y)^2$, critical elastic buckling load in flexural buckling for OHS columns;
P_{crl} = Critical elastic local buckling load;
E = Young's modulus;
l_e = Column effective length;
r_y = Radius of gyration of gross cross-section about the minor y-axis of buckling.

The nominal axial strengths (P_{DSM}) are calculated for the two cases, as shown in Eqs (2) and (3), respectively, where P_{ne} refers to the nominal axial strength for flexural buckling, and P_{nl} refers to the nominal axial strength for local buckling as well as interaction of local and overall buckling. The nominal axial strength, P_{DSM}, is the minimum of P_{ne} and P_{nl}, as shown in Eqn. (1). In calculating the axial strengths, the critical elastic local buckling load (P_{crl}) of the cross-section was obtained from a rational elastic finite strip buckling analysis (Papangelis & Hancock, 1995). Fig. 5 shows the comparison of FEA and experimental results against the direct strength curve plotted from Equations (2) and (3). The unfactored design strengths P_{DSM} calculated using the direct strength method are compared with the numerical and test results, as detailed in Zhu & Young (2012).

7 COMPARISON OF NUMERICAL AND EXPERIMENTAL RESULTS WITH DESIGN PREDICTIONS

The nominal column strengths (unfactored design strengths) predicted by the NAS Specification (P_{NAS}), AS/NZS Standard ($P_{AS/NZS}$), European Code (P_{EC3}) and the direct strength method (P_{DSM}) are compared with the column strengths obtained from the parametric study (P_{FEA}) and experimental investigation (P_{Exp}), as detailed in Zhu & Young (2012). The experimental and FEA results are also compared with the

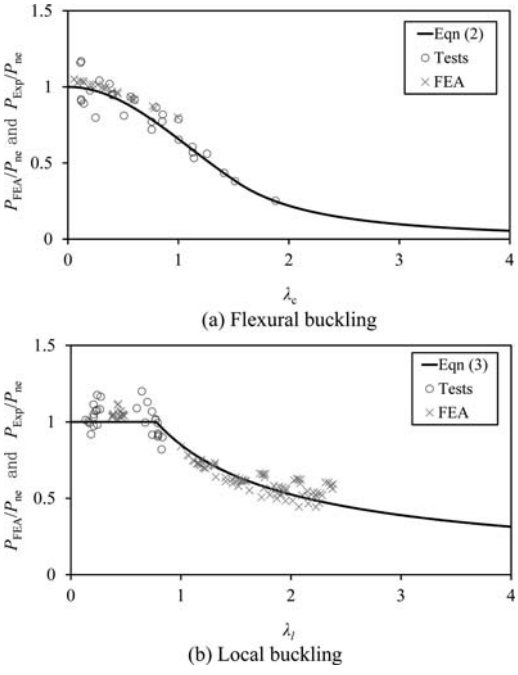

Figure 5. Comparison of FEA and experimental data with design rules (PDSM) for columns: (a) flexural buckling and (b) local buckling.

column design curves obtained from the design rules, as shown in Fig 6 for Series W150T2.5. The design strengths of specimens from the experimental program were calculated using the material properties for each series of specimens, as presented in Zhu & Young (2011), and the 0.2% proof stress ($\sigma_{0.2}$) was used as the corresponding yield stress. The design strengths of specimens from the parametric study were calculated using the material properties of Series B which have been also used in the finite element modeling. The fixed-ended column specimens were designed as concentrically loaded compression members, and the effective length (l_e) was taken as one-half of the column length (L), as recommended by Young and Rasmussen (1998).

It is shown that the design strengths predicted by the NAS, AS/NZS and EC3 specifications are generally unconservative for the numerical results and generally conservative for the experimental results. It is also shown that the DSM design strengths are generally conservative for both numerical and experimental results. This is due to the fact that the oval hollow sections are compact in the experimental investigation. The design strengths predicted by the NAS and AS/NZS specifications are identical. The EC3 design strengths are more conservative compared to the NAS and AS/NZS predictions, as detailed in Zhu & Young (2012).

It should be noted that local buckling in the semicircle flanges of the oval hollow sections was not

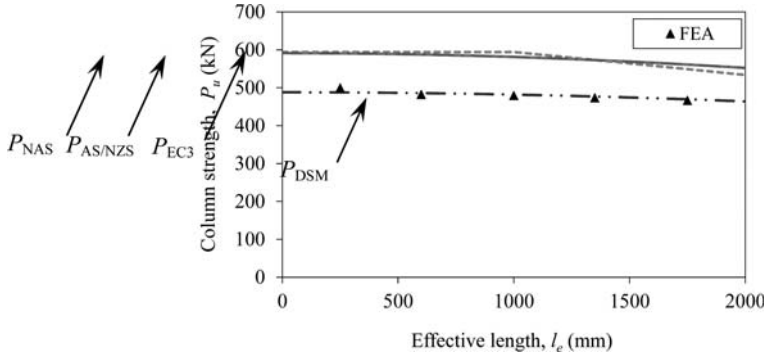

Figure 6. Fixed-ended column curves for Series W150T2.5.

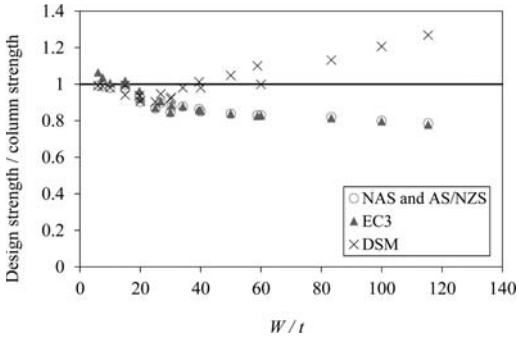

Figure 7. Average ratios of design strengths obtained from different specifications over numerical column strengths against W/t.

observed for the columns in the experimental investigation, whereas this is not the case for the slender sections in the parametric study and local buckling was observed in the semi-circle flanges. Fig. 7 shows the average ratios of design strengths obtained from different specifications over numerical column strengths against W/t for each series of specimens as shown in Table 3. It is demonstrated that the design rules of the current NAS, AS/NZS and EC3 specification for cold-formed steel structures can be used for the design of compact oval hollow sections by adopting the two assumptions that firstly the flat plates are supported by the two semi-circle flanges as stiffened elements with the plate buckling coefficient k equal to 4.0; and secondly, the semi-circle flanges are fully effective, as described in Zhu & Young (2011). The reliability of these design rules was evaluated using reliability analysis. It is also demonstrated that the direct strength method is reliable and can be used for the design of both compact and slender oval hollow section columns, as detailed in Zhu & Young (2012).

8 CONCLUSIONS

The paper presents the numerical analysis and design of cold-formed steel oval hollow section columns. A parametric study of cold-formed steel oval hollow section columns using finite element analysis was performed. An accurate finite element model was developed. The column strengths obtained from the tests and numerical investigation were compared with the design strengths predicted using the current North American, Australian/New Zealand and European specifications for cold-formed steel structures. Direct strength method was also used to predict the column strengths. It is shown that the column design rules in the current North American, Australian/New Zealand and European specifications for cold-formed steel structures can be used for compact oval hollow sections. It is also shown that the direct strength method is conservative for both compact and slender cold-formed steel oval hollow section columns.

ACKNOWLEDGMENTS

The research work described in this paper was supported by the Chinese National Natural Science Foundation (Project No. 50808126, 51078237) and a grant from The University of Hong Kong under the seed funding program for basic research.

REFERENCES

ABAQUS 2009. ABAQUS analysis user's manual, Version 6.9.

AISI 2002. Automotive Steel Design Manual – Revision 6.1. Automotive Applications Committee, American Iron and Steel Institute, Southfield, MI.

AS/NZS 2005. Cold-formed steel structures. AS/NZS No. 4600:2005, Standards Australia, Sydney, Australia.

Bortolotti, E., Jaspart, J.P., Pietrapertosa, C., Nicaud, G., Petitjean, P.D. & Grimault, J.P. 2003. Testing and modelling of welded joints between elliptical hollow sections. *Proceedings of the 10th International Symposium on Tubular Structures, Madrid: 259–266.*

Chan, T.M. & Gardner, L. 2008. Bending strength of hot-rolled elliptical hollow sections. *Journal of Constructional Steel Research 64(9): 971–986.*

Chan, T.M. & Gardner, L. 2009. Flexural Buckling of Elliptical Hollow Section Columns. *Journal of Structural Engineering – ASCE 135(5): 546–557.*

EC3 2005. Design of steel structures – Part 1.1: General rules and rules for buildings. European Committee for Standardization, ENV 1993-1-1, CEN, Brussels.

EC3 2006a. Design of steel structures – Part 1.4: General rules – Supplementary rules for stainless steels. European Committee for Standardization, ENV 1993-1-4, CEN, Brussels.

EC3 2006b. Design of steel structures – Part 1.5: Plated structural elements. European Committee for Standardization, ENV 1993-1-5, CEN, Brussels.

Gardner, L. & Chan, T.M. 2007. Cross-section classification of elliptical hollow sections. *Steel and Composite Structures 7(3): 185–200.*

Gardner, L. & Ministro, A. 2005. *Structural Steel Oval Hollow Sections*. *The Structural Engineer 83(21): 32–36.*

NAS 2007a. Commentary on North American Specification for the Design of Cold-Formed Steel Structural Members. American Iron and Steel Institute: Washington, D.C.

NAS 2007b. North American Specification for the Design of Cold-Formed Steel Structural Members. American Iron and Steel Institute: Washington, D.C.

Papangelis, J.P. & Hancock, G.J. 1995. Computer analysis of thin walled structural members. *Comput. Struct 56(1): 157–176.*

Schafer, B.W. 2002a. Progress on the direct strength method. *Proceeding of 16th International specialty conference on cold-formed steel structures, Orlando, Florida: 647–662.*

Schafer, B.W. & Peköz, T. 1998. Direct strength prediction of cold-formed steel members using numerical elastic buckling solutions. *Proceedings of the 14th Int. specialty conference on cold-formed steel structures. University of Missouri-Rolla, Rolla, Mo: 69–76.*

Schafer, B.W. 2000. Distortional buckling of cold-formed steel columns. *Washington, DC: August Final Report to the American Iron and Steel Institute*.

Schafer, B.W. 2002b. Local, distortional, and Euler buckling of thin-walled columns. *Journal of Structural Engineering – ASCE 128(3): 289–299.*

Silvestre, N. 2008. Buckling behaviour of elliptical cylindrical shells and tubes under compression. *International Journal of Solids and Structures 45(16): 4427–4447.*

Theofanous, M., Chan, T.M., & Gardner, L. 2009. Structural response of stainless steel oval hollow section compression members. *Engineering Structures 31(4): 922–934.*

Yan, J. & Young, B. 2004. Numerical investigation of channel columns with complex stiffeners-part I: tests verification. *Thin-walled structures 42(6): 883–893.*

Young, B. & Rasmussen, K.J.R. 1998. Design of lipped channel columns. *Journal of Structural Engineering – ASCE 124(2): 140–148.*

Zhu, J.H. & Young, B. 2011. Cold-formed Steel Oval Hollow Sections under Axial Compression. *Journal of Structural Engineering – ASCE 137(7): 719–727.*

Zhu, J.H. & Young, B. 2012. Design of cold-formed steel oval hollow section columns. *Journal of Constructional Steel Research 71:26–37.*

Tubular Structures XIV – Gardner (Ed.)
© 2012 Taylor & Francis Group, London, ISBN 978-0-415-62137-3

Interaction relations for members of hot rolled elliptical hollow sections

F. Nowzartash & M. Mohareb
University of Ottawa, Ontario, Canada

ABSTRACT: This paper combines the findings of two recent studies to propose interaction relations for the design of elliptical sections: 1) A lower bound interaction relation recently developed for elliptical hollow sections (EHS) under axial force, biaxial bending, twisting moments, and capturing plasticity effects but not addressing member stability behaviour, residuals stresses, nor initial imperfection effect; and 2) Another numeric study generating column curves for EHS including stability effects, residual stresses and initial out-of-straightness, but limited to pure compressive forces. In this paper, both studies are linked by proposing an interaction relation for EHS members which incorporates member stability effects, residual stresses and initial out-of-straightness effects. A Practical design example is then solved using the proposed interaction equation and shown to compare well against nonlinear FEA. The example also illustrates the superiority of the proposed interaction equation compared to that based in current codes.

1 INTRODUCTION AND SCOPE

The advancement of the structural steel manufacturing industry has led to the recent emergence of steel members with Elliptical Hollow Sections (EHS). A lower bound interaction relation for EHS subject to combination of axial force, bi-axial bending moments and torsion was developed by Nowzartash and Mohareb (2009). The interaction relations are based on the cross-sectional plastic capacity resistance and do not include member stability effects. Column curves for EHS members including residual stresses and initial imperfection effects were also developed by Nowzartash & Mohareb (2011a). Column curves developed are applicable for EHS members subject to axial compression.

Within this context, this paper is intended to utilize the cross-sectional interaction relations and column curves to develop interaction relations for EHS members including plasticity, slenderness effects, residual stresses, and geometric initial imperfections.

2 LITERATURE REVIEW

Steel Elliptical Hollow Sections emerged as a structural section only recently. Thus, a limited number relevant studies has been published on EHS to date. This includes the work of Grigorenko and Rozhok (2002) who investigated the effects of variation of load eccentricity and thickness on the stress fields of cylinders with elliptical hollow sections. A series of compression and bending tests were conducted on elliptical hollow sections members (Gardner & Ministro 2004; Gardner 2005). The study was followed by numerical analysis which has suggested the validity of finite element models in predicting the buckling behaviour of EHS under such loading. A finite element study aimed at investigating the local buckling behaviour of EHS was conducted by Zhu and Wilkinson (Zhu & Wilkinson 2007). Gardner and Chan developed analytical expressions for the yield compressive strength and plastic bending resistances of hot-rolled EHS and verified them against experimental results (Chan & Gardner 2008a; b). The local elastic buckling of EHS including shear deformation effects was investigated by Ruiz-Teran & Gardner (2008). Silvestre (2008) formulated a buckling solution for EHS and studied the buckling failure modes of EHS under axial compression in a thorough parametric finite element analysis. Nowzartash & Mohareb (2009) developed a lower bound interaction relation for EHS under combined action of axial force, bi-axial bending moments and twisting moments based on statistically admissible stress field. They also extended their formulation to Semi-Elliptical Hollow sections (Nowzartash & Mohareb 2010).

Nowzartash & Mohareb (2011b) developed a methodology to predict the residual stress in EHS. members and verified it against available experimental results.

Then starting with the residual stresses predicted (Fig. 1) and out-of-straightness (OOS) from codes and industry standards, they (Nowzartash & Mohareb 2011a) conducted a series of nonlinear load deformation FEA including material and geometric nonlinearity to generate points on the column curves

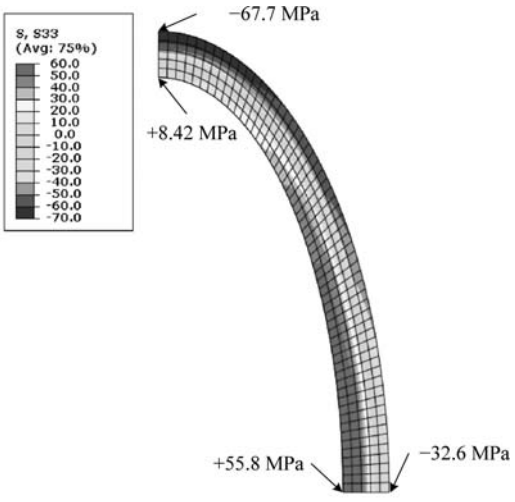

Figure 1. Longitudinal residual stresses in EHS-200 × 100 × 10.

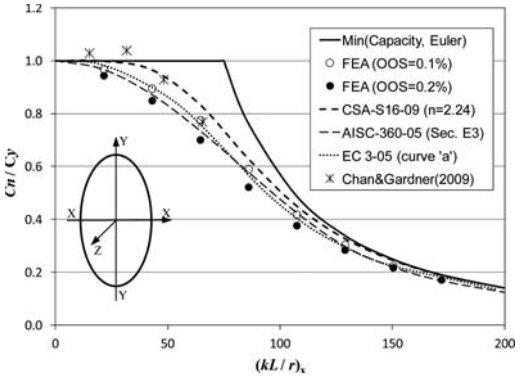

Figure 2. Column curves for EHS major axis buckling.

(i.e., FEA curves on Fig. 2 and Fig.). These figures present Euler/Capacity of the EHS columns, finite element results based on 0.1% and 0.2% OOS and one available experimental results (Chan & Gardner 2009). The appropriate design relationship based on Canadian Standard (CAN/CSA-S16 2009), American Specifications (AISC-360 2005) and European Code (EN 1993-1-1 2005) have been superimposed for comparison.

Nowzartash & Mohareb also proposed two column curves for members of EHS for the buckling about major and minor axes (Fig.) in a format analogous to that presently used in CAN/CSA-S16 (2009). These interactions are

$$C_n = C_r / \phi = AF_y \left(1 + \lambda^{2n}\right)^{-1/n}$$
$$\lambda = \frac{KL}{\pi r}\sqrt{\frac{F_y}{E}} \qquad (1)$$

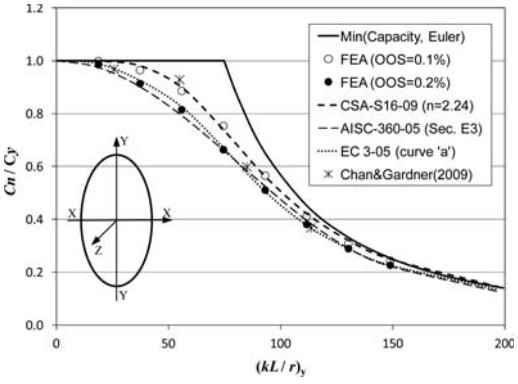

Figure 3. Column curves for EHS minor axis buckling.

where C_n = section nominal capacity, C_r = section resistance capacity, ϕ = resistance factor (i.e., 0.9 for structural steel), A = cross sectional area, F_y = yield stress, E =modulus of elasticity, L = member length, K = Effective length factor. In Eq. 1, the study proposed $n = 1.32$ and $n = 1.57$ for major and minor axis buckling, respectively. On this figure, also the two appropriate curves based on Euro-code (EN 1993-1-1 2005) have been superimposed.

3 CROSS-SECTIONAL INTERACTION EQUATIONS

The interaction equation for EHS of common geometry subject to axial tensile load N, bending moment about major axis M_x, bending moment about minor axis M_y and torsion T as given in Nowzartash & Mohareb (2009) is

$$\left[\frac{M_x/M_{xp}}{\sqrt{1-\left(T/T_P\right)^2}}\right]^{2.0} + \left[\frac{M_y/M_{yp}}{\sqrt{1-\left(T/T_P\right)^2}}\right]^{1.7} + 2\left[\frac{N/N_P}{\sqrt{1-\left(T/T_P\right)^2}}\right]^{1.75} - \left[\frac{N/N_P}{\sqrt{1-\left(T/T_P\right)^2}}\right]^{3.5} = 1 \qquad (2)$$

where M_{xp} is the major axis bending moment plastic capacity, M_{yp} is the minor axis bending moment plastic capacity, T_p is the torsional plastic capacity and N_p is the tensile capacity, all in the absence of any other internal forces. Equation delineates an envelope of the admissible internal force combinations (C, M_x, M_y, T). A safe load combination would lie inside the interaction surface defined by Eq. 2, i.e., the left hand side of Eq. 2 will be smaller than unity while an unsafe load combination will correspond to a left hand side greater than unity.

4 PROPOSED MODIFICATION TO CROSS-SECTIONAL INTERACTION EQUATION

When a member is subject to axial compressive load instead of tension, two modifications are proposed in Eq. 2. The validity of these propositions will later on be validated through a numeric example.

1. The tensile capacity of the section N_p needs to be replaced by the member nominal compressive capacity C_n including residual stress and inelastic buckling effects
2. The applied bending moments, M_x and M_y need to be replaced by the corresponding second order bending moments $M_{x\delta}$ and $M_{y\delta}$ which incorporate the $p-\delta$ effects.

In general, a given internal force combination (C, $M_{x\delta}$, $M_{y\delta}$, T) will not lie on the interaction surface, i.e., the left hand side of Eq. 2 will generally differ from unity. We thus introduce a load proportionality scaling factor α to the internal force combination, so that the new load combination α (C, $M_{x\delta}$, $M_{y\delta}$, T) lies on the interaction surface. By applying the above modifications, one obtains the modified interaction equation

$$\left[\frac{\alpha M_{x\delta}/M_{xp}}{\sqrt{1-(\alpha T/T_P)^2}}\right]^{2.0}+\left[\frac{\alpha M_{y\delta}/M_{yp}}{\sqrt{1-(\alpha T/T_P)^2}}\right]^{1.7} +2\left[\frac{\alpha C/C_n}{\sqrt{1-(\alpha T/T_P)^2}}\right]^{1.75}-\left[\frac{\alpha C/C_n}{\sqrt{1-(\alpha T/T_P)^2}}\right]^{3.5}=1 \quad (3)$$

For a given section and a load combination, the only unknown in Eq. 3, is the load proportionality factor α. Equation 3 is to be solved for α. A value of unity indicates that the load combination (C, $M_{x\delta}$, $M_{y\delta}$, T) lies on the interaction surface. A value larger than unity indicates that the original load combination was inside the interaction surface (i.e., safe) and thus had to be magnified to lie on the interaction surface, while a value lower than unity indicates that the original load combination was outside the interaction surface (i.e., unsafe), and thus need to be scaled down to lie on the interaction surface.

The value of C_n is to be determined from column curves (Eq. 1 or Fig. 2–4). The values of modified bending moments need to be determined using either (a) a finite element analysis including geometric and material nonlinear effects or (b) an approximate code approach. Code approaches (e.g., AISC-360 2005; CAN/CSA-S16 2009) are generally based on increasing the applied bending moments by a magnification factor or reducing the plastic capacity of the section by a reduction factor (e.g., EN 1993-1-1 2005). In the FEA approach, the second order bending moments at the section of interest are calculated using the internal stresses and the deformed configuration of the member.

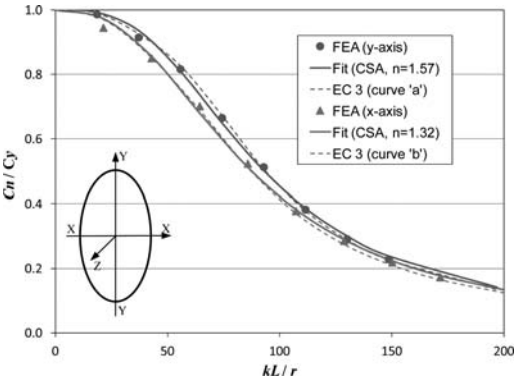

Figure 4. Best representative column curves.

4.1 *Design example*

The problem described in the Nowzartash & Mohareb (2009) is solved again here. It is recalled that the forces applied to the design section (i.e., middle portion of the member) are $C=1000\,kN$, $M_x=50\,kNm$, $M_y=15\,kNm$ and $T=20\,kNm$. Member length is 3.0 m and is simply supported with respect to bending moments. It is required to determine the percentage of the applied loads the member is able to withstand.

4.2 *Solution proposed in present study*

In contrast with the solution presented in Nowzartash & Mohareb (2009), geometric nonlinearities were evoked in the present solution to capture buckling effects induced by the compressive force. This enabled the Abaqus model to capture second order resistance reduction caused by the $p-\delta$ effect. The sectional properties of EHS-250 × 125 × 8 as extracted from Corus tubes (2005) are radii of gyration $r_x=77.8\,mm$, $r_y=44.9\,mm$, the plastic section modulii $Z_x=307\times10^3\,mm^3$, $Z_y=186\times10^3\,mm^3$ and cross sectional area $A=4510\,mm^2$.

Using Eq. 1 and considering that the section buckles about weak axis one has

$$\lambda_y=\frac{1.0\times3000}{\pi\times44.9}\sqrt{\frac{350}{200000}}=0.89$$
$$C_n=C_{ny}=AF_y\left(1+\lambda_y^{2\times1.57}\right)^{-1/1.57} \quad (4)$$
$$=4510\times350\times\left(1+0.89^{3.14}\right)^{-0.64}=1126kN$$

The section flexural and torsional capacities are

$$M_{xp}=Z_xF_y=307\times10^3\times350=107.4\,kNm$$
$$M_{yp}=Z_yF_y=186\times10^3\times350=65.1\,kNm$$
$$T_p=2\pi abtF_y/\sqrt{3}= \quad (5)$$
$$2\times\pi\times121\times58.5\times8\times350/\sqrt{3}=71.8kNm$$

From the FEA model, the maximum bending moments including second order effects at the middle

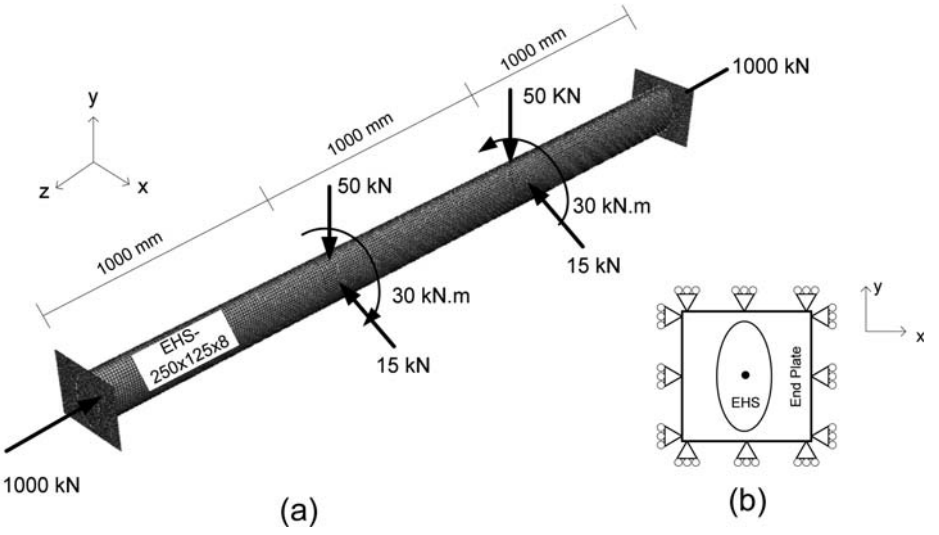

Figure 5. (a) FEA model, (b) End plates and boundary conditions.

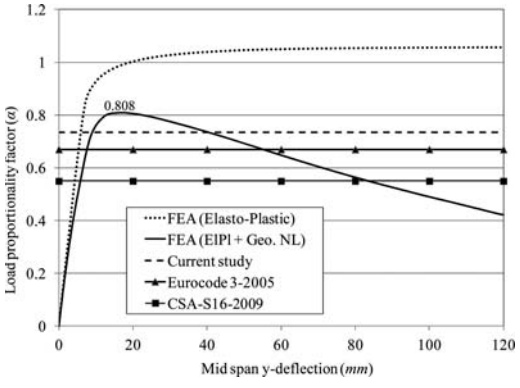

Figure 6. Load vs. Deflection curve for the design example.

section of the member were found as $M_{x\delta} = 56.5\ kNm$ and $M_{y\delta} = 26.5\ kNm$. These values were calculated by adding the longitudinal forces (z direction) induced by the externally applied axial force by the displacements in the x and y axes (in the deformed configuration), respectively.

By substituting the second order moment values into Eq. 3 and using the Newton-Raphson method, a load proportionality factor $\alpha = 0.785$ was obtained. This value compares to 0.808 as predicted from a geometrically and materially nonlinear FEA as depicted in the load versus midspan deflection on Fig. 6 for comparison. Also, shown on the figure is a plot for the moment versus midspan deflection when geometrically nonlinear effects are suppressed.

4.3 *Canadian Standard Solution*

Using CAN/CSA-S16 (2009) and targeting nominal resistances setting the resistance factor ϕ to unity, one obtains the nominal compressive resistance

$$C_n = C_{ny} = AF_y\left(1+\lambda_y^{2\times 2.24}\right)^{-1/2.24} = 1282kN \tag{6}$$

Also, the Euler buckling loads are

$$\begin{aligned} C_{ey} &= \frac{\pi^2 E}{\left(L/r_y\right)^2}A = \frac{\pi^2\times 200000}{\left(3000/44.9\right)^2}\times 4510 = 1994kN \\ C_{ex} &= \frac{\pi^2 E}{\left(L/r_x\right)^2}A = \frac{\pi^2\times 200000}{\left(3000/77.8\right)^2}\times 4510 = 5987kN \end{aligned} \tag{7}$$

For a laterally loaded member, the moment gradient factor is taken as $\omega_1 = 1.0$, and the corresponding coefficients U_{1x}, U_{1y} which account for the combined effects of P-δ and moment gradient effects are taken as

$$\begin{aligned} U_{1y} &= \frac{\omega_1}{1-C_f/C_{ey}} = \frac{1.0}{1-1000/1994} = 2.00 \\ U_{1x} &= \frac{\omega_1}{1-C_f/C_{ex}} = \frac{1.0}{1-1000/5987} = 1.20 \end{aligned} \tag{8}$$

By using the interaction equation provided in Clause 13.8.3, one has

$$\begin{aligned} &\frac{C_f}{C_n} + \frac{U_{1x}M_{fx}}{M_{xp}} + \frac{U_{1y}M_{fy}}{M_{yp}} = \\ &\frac{1000}{1282} + \frac{1.20\times 50}{107.4} + \frac{2.00\times 15}{65.1} = 1.80 \end{aligned} \tag{9}$$

The corresponding proportionality scaling factor α is $1/1.80 = 0.55$ which is superimposed on Fig. 6.

4.4 *Eurocode 3 Solution*

According to Eurocode 3 (EN 1993-1-1 2005) members subjected to combined bending and axial compression should satisfy the interaction relations

$$\frac{N_{Ed}}{\frac{\chi_y N_{Rk}}{\gamma_{M1}}} + k_{yy}\frac{M_{y,Ed}+\Delta M_{y,Ed}}{\chi_{LT}\frac{M_{y,Rk}}{\gamma_{M1}}} + k_{yz}\frac{M_{z,Ed}+\Delta M_{z,Ed}}{\chi_{LT}\frac{M_{z,Rk}}{\gamma_{M1}}} \le 1$$
$$\frac{N_{Ed}}{\frac{\chi_z N_{Rk}}{\gamma_{M1}}} + k_{zy}\frac{M_{y,Ed}+\Delta M_{y,Ed}}{\chi_{LT}\frac{M_{y,Rk}}{\gamma_{M1}}} + k_{zz}\frac{M_{z,Ed}+\Delta M_{z,Ed}}{\chi_{LT}\frac{M_{z,Rk}}{\gamma_{M1}}} \le 1 \quad (10)$$

where N_{Ed} is the compression force design value, $M_{y,Ed}$ and $M_{z,Ed}$ are the bi-axial bending moments design values. N_{Rk} is the section resistance to normal forces, $M_{y,Rk}$ and $M_{z,Rk}$ are the section resistance to bi-axial bending moments. $\Delta M_{y,Ed}$ and $\Delta M_{z,Ed}$ are moments due to shift of centroid for class 4 sections. χ_{LT} is the reduction factor due to lateral torsional buckling. χ_z and χ_y are reduction factors due to flexural buckling, γ_{M1} is unity for steel in the buildings, and k_{yy}, k_{yz}, k_{zy} and k_{zz} are interaction factors.

The EHS used in this example is Class 2, (Nowzartash & Mohareb 2009) (i.e., $\Delta M_{y,Ed}$ and $\Delta M_{y,Ed}$ vanish, and section reaches its plastic bending resistances) and is not susceptible to torsional buckling (i.e., $\chi_{LT} = 1$). Under these conditions, the interaction relations simplify to

$$\frac{N_{Ed}}{\chi_y A f_y} + k_{yy}\frac{M_{y,Ed}}{W_{pl,y} f_y} + k_{yz}\frac{M_{z,Ed}}{W_{pl,z} f_y} \le 1$$
$$\frac{N_{Ed}}{\chi_z A f_y} + k_{zy}\frac{M_{y,Ed}}{W_{pl,y} f_y} + k_{zz}\frac{M_{z,Ed}}{W_{pl,z} f_y} \le 1 \quad (11)$$

where f_y is the yield stress, A is the cross section area, $W_{pl,y}$ and $W_{pl,z}$ are the plastic section modulii.

From Eurocode 3 section 6.3.1, non-dimensional slenderness ratio about strong axis is

$$\bar{\lambda}_z = \frac{L}{r_z \pi}\sqrt{\frac{f_y}{E}} = \frac{3000}{77.8\pi}\sqrt{\frac{350}{200000}} = 0.51 \quad (12)$$

and the reduction factor due to flexural buckling about strong axis is

$$\Phi_z = 0.5\left[1+\alpha\left(\bar{\lambda}_z - 0.2\right)+\bar{\lambda}_z{}^2\right]$$
$$= 0.5\left[1+0.21\left(0.51-0.2\right)+0.51^2\right] = 0.66 \quad (13)$$
$$\chi_z = \frac{1}{\Phi_z + \sqrt{\Phi_z{}^2 - \bar{\lambda}_z{}^2}} = 0.93$$

In a similar manner,

$$\bar{\lambda}_y = 0.89\ ;\ \Phi_y = 0.97\ ;\ \chi_y = 0.74 \quad (14)$$

From Annex B, table B.3 one gets $C_{my} = C_{mz} = 0.9$. Also, from Table B1 of Annex B, one obtains

$$k_{yy} = C_{my}\left(1+\left(\bar{\lambda}_y - 0.2\right)\frac{N_{Ed}}{\chi_y N_{Rk}}\right)$$
$$= 0.9\left(1+\left(0.89-0.2\right)\frac{1000\times10^3}{0.74\times4510\times350}\right) = 1.43$$
$$k_{zz} = C_{mz}\left(1+\left(\bar{\lambda}_z - 0.2\right)\frac{N_{Ed}}{\chi_z N_{Rk}}\right) \quad (15)$$
$$= 0.9\left(1+\left(0.51-0.2\right)\frac{1000\times10^3}{0.93\times4510\times350}\right) = 1.09$$
$$k_{yz} = 0.6k_{zz} = 0.65$$
$$k_{zy} = 0.6k_{yy} = 0.86$$

By substituting into Eq. 11 one can calculate the interaction coefficients.

$$\frac{1000}{0.74\times1578.5} + 1.43\frac{15}{65.1} + 0.65\frac{50}{107.4} = 1.49$$
$$\frac{1000}{0.93\times1578.5} + 0.86\frac{15}{65.1} + 1.09\frac{50}{107.4} = 1.39 \quad (16)$$

The corresponding load proportionality factor α is $1/1.49 = 0.67$. This value is superimposed on Fig. 6.

As can be seen in this example, the interaction relation proposed in the present study predicts a compressive resistance of the member that is 97% of that predicted by the FEA. This is an improvement compared to the current Canadian code which predicts a compressive resistance of 68% of the FEA solution and the Eurocode which predicts a compressive resistance of 83% of the FEA solution.

5 CONCLUSION

The efficiently design members of elliptical hollow sections necessitates the use of interaction relations which account for residual stress effects, initial out-of straightness, local and global buckling effects and plasticity effects. Towards, this goal a methodology has been proposed in this paper to generate such interaction equations for the case of biaxial bending, torsion, and axial force. A comparison with non-linear finite element results suggests the validity of the approach proposed and its less conservative nature when compared to existing interaction relations in the Canadian and Eurocode.

REFERENCES

AISC-360. (2005). *Specification for Structural Steel Buildings*, Chicago.

CAN/CSA-S16. (2009). *Limit States Design of Steel Structures.*, Rexdale, ON.

Chan, T. M., and Gardner, L. (2008a). "Bending Strength of Hot-Rolled Elliptical Hollow Sections." *J. of Construc. Steel Res.*, 64(9), 971–986.

Chan, T. M., and Gardner, L. (2008b). "Compressive Resistance of Hot-Rolled Elliptical Hollow Sections." *Engineering Structures*, 30(2), 522–532.

Chan, T. M., and Gardner, L. (2009). "Flexural Buckling of Elliptical Hollow Section Columns." *J. of Structural Eng.-ASCE*, 135(5), 546–557.

Corus. (2005). "Celsius® Structural Hollow Sections." Structural and Conveyance Business, Corus Tubes.

EN 1993-1-1. (2005). *Eurocode 3: Design of Steel Structures-Part 1-1: General Rules and Rules for Buildings*, CEN.

Gardner, L. (2005). "Structural Behaviour of Oval Hollow Sections." 4th Int. Conf. on Advances in Steel Structures, Shanghai, China, 517–522.

Gardner, L., and Ministro, A. (2004). "Testing and Numerical Modelling of Structural Steel Oval Hollow Sections," Imperial College, UK, London.

Grigorenko, Y. M., and Rozhok, L. S. (2002). "Stress Analysis of Hollow Elliptic Cylinders with Variable Eccentricity and Thickness." *Inter. Appl. Mech.*, 38(8), 954–966.

Nowzartash, F., and Mohareb, M. (2009). "Plastic Interaction Relations for Elliptical Hollow Sections." *Thin-Walled Structures*, 47(6–7), 681–691.

Nowzartash, F., and Mohareb, M. (2010). "Plastic Interaction Relations for Semi-Elliptical Hollow Sections." *Thin-Walled Structures*, 48, 42–54.

Nowzartash, F., and Mohareb, M. (2011a). "Column Curves for Elliptical Hollow Section Members." *J. of Construct. Steel Res.*, 67(10), 1525–1536.

Nowzartash, F., and Mohareb, M. (2011b). "Effect of Residual Stresses on Members of Wide Flange Sections." CSCE Annual Conference Ottawa, ON, Canada.

Ruiz-Teran, A. M., and Gardner, L. (2008). "Elastic Buckling of Elliptical Tubes." *Thin-Walled Structures*, 46(11), 1304–1318.

Yang, H., Lam, D., and Gardner, L. (2008). "Testing and Analysis of Concrete-Filled Elliptical Hollow Sections." *Engineering Structures*, 30(12), 3771–3781.

Zhu, Y., and Wilkinson, T. (2007). "Finite Element Analysis of Structural Steel Elliptical Hollow Sections in Compression," U of Sydney.

Tubular Structures XIV – Gardner (Ed.)
© 2012 Taylor & Francis Group, London, ISBN 978-0-415-62137-3

Finite Element modelling of beam to concrete filled elliptical steel column connections

D. Lam & X.H. Dai
School of Engineering, Design and Technology, University of Bradford, UK

ABSTRACT: Composite concrete filled steel tube columns are increasingly used for high-rises building structures, owing to their excellent structural performance which arises from the combination of the two different materials in the structure. Composite structures exploit the characteristics of steel and concrete: steel with its high tensile strength and ductility and concrete with its high compressive strength and stiffness. Hot finished Elliptical Hollow Section (EHS) is a new range of cross-sections recently available to the building industry; this new shape has an aesthetically pleasing appearance and improved structural efficiency due to its different major and minor axis. Numerous experimental and numerical studies have been carried out on beam to column connections of concrete filled steel tubular columns with circular, square and rectangular sections; however the behaviour of beam to concrete filled elliptical steel column connection remains unexplored to date. This paper presents the behaviour of beam to column connections with concrete filled elliptical steel columns. Finite Element (FE) models were developed using ABAQUS to investigate various types of beam to column connections for elliptical concrete filled steel columns. Based on the analysis and comparison, effect of some of the important parameters to the behaviour of the elliptical concrete-filled steel tube columns was highlighted.

1 INTRODUCTION

Composite concrete filled steel tube columns are increasingly used for high-rises building structures, owing to their excellent structural performance such as superior load-bearing capacity, high ductility, good energy dissipation which arises from the combination of two different materials. Hot finished elliptical hollow section (EHS) represents a new range of cross-sections recently available to the construction market. This new shape has an aesthetically pleasing appearance and improved structural efficiency due to its different major and minor axis. In general, concrete filled composite columns with circular hollow sections (CHS) have the advantages over columns with other section shapes due to the circular cross sections provide an uniform confinement to the concrete core. The concrete filled columns with square hollow section (SHS) and rectangular hollow section (RHS) have many common virtues to the concrete filled columns with circular hollow sections, high ductility and large energy-absorption capacity. However, the disadvantage of the square and rectangular sections lies with the stress concentration at the corners of the steel sections which may result in cracking when the member is subjected to axial compression.Experiments and numerical modelling carried out by Willibald *et al* (2006a, b) and Martinez-Saucedo *et al* (2008) for elliptical steel tube hollow section joints provided some design recommendations and guidance. This paper presents numerical research on elliptical concrete filled steel tubular column to beam connections currently being carried out at the University of Bradford.

The main objective of the research presented in this paper is to investigate the structural behaviour of elliptical concrete filled steel tube column to beam connections subjected to bending. It focuses on the following aspects: (1) develop a nonlinear finite element model through ABAQUS solver to investigate the structural behaviour of concrete filled steel tubular column and the moment and rotationalcapacity of column to beam connections; (2) identify the failure modes of typical beam to elliptical concrete filled steel tube column joints; (3) providesdesign guidance for designers.

2 ELLIPTICAL CONCRETE FILLED STEEL TUBE COLUMN TO I-BEAM JOINT ASSEMBLY

Beam-column connection is an important component in any steel framed buildings. All the loads are transferred from beam to columns through the joints; therefore how joint components behave in a framed structure has critical influence to the building integrity and behaviour. Despite extensive researches being carried out on steel-framed structures in the past and has resulted in development of design methods that are now being adopted in routine structural steel design, large gap remains in understanding the structural behaviour of concrete filled steel tube column to

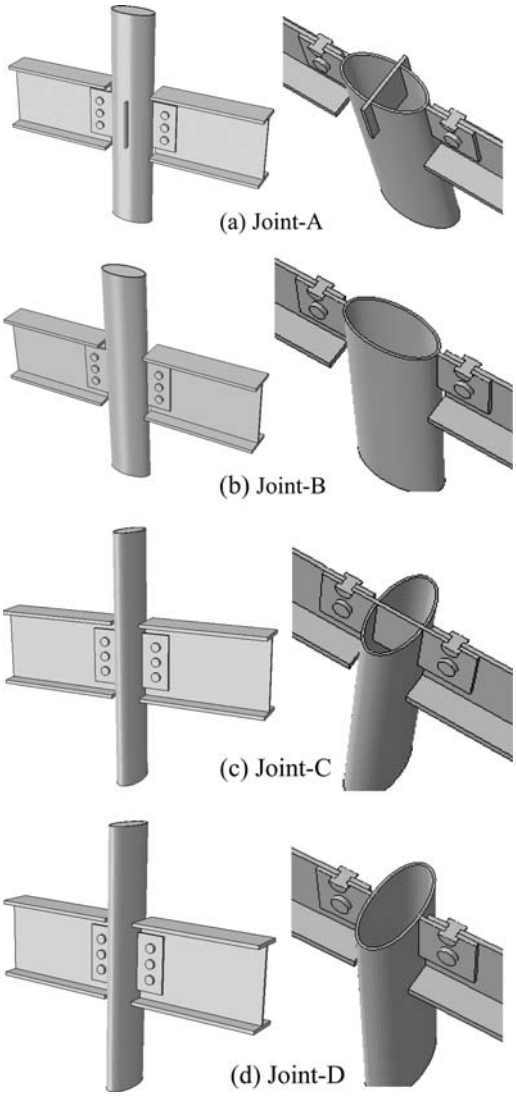

Figure 1. Joint assemblies.

beam connections; especially for columns with elliptical section shape. With the increasing use of circular hollow sections, gusset plates or welded fin plates have been the main connection components for steel hollow section to other structural members. (Willibald *et al* (2006a, b), Martinez-Saucedo *et al* (2008)) However, very few research publications could be found for elliptical concrete-filled steel tube column to beam connections.

To understand the behaviour of elliptical concrete filled tubular column to beam connections, 4 joint assemblies A, B, C and D as shown in Figure 1 are adopted to investigate the basic behaviour and failure modes. For all the assemblies, beams are connected to the column by fin plates using 3 No. M20 Gr. 8.8 bolts. All the fin plates are welded to the column. For Joint A, through plate is welded in the minor axis to represent the connection in the other direction. For the minor axis, through plate connection is tested at Joint C. For all the joint assemblies, elliptical hollow sections of $200 \times 100 \times 5$mm with length of 1000mm were used together with beam sections of $305 \times 127 \times 48$ UB; length 500 mm.

The 4 joint assemblies are:

Joint-A: two fin plates of $220 \times 110 \times 8$ mm in the major axis direction; one stiffener plate: $220 \times 140 \times 8$ mm in the minor direction.
Joint-B: two fin plates of $220 \times 110 \times 8$ mm in the major axis direction; no stiffener plate.
Joint-C: combined fin and stiffener plate of $220 \times 320 \times 8$ mm in the minor axis direction.
Joint-D: two fin plates of $220 \times 110 \times 8$ mm in the minor axis direction; no stiffener plate.

3 FINITE ELEMENT (FE) NUMERICAL MODELLING

3.1 *FE model*

It is undoubtedly that full-scale testing provides the most effective method in understanding the behaviour of a structural member, however experimental studies are costly and time consuming. This leads to the development and application of numerical method in engineering researches. Numerical modelling has been successfully utilized in prediction the axial compressive behaviour of concrete-filled steel tubular columns (Dai and Lam (2010a, b)). This section briefly describes the numerical finite element (FE) method adopted in this research.

3.2 *Member material properties*

All the joint assemblies shown in Figure 1 with unfilled and concrete filled EHS columns will be tested under multiple loading conditions at the University of Bradford, however before the measured material properties of all joint assembly member are available, stress-strain relationship of steel shown in Figure 2(a) was adopted for the FE models. Key parameters of material properties of steel for EHS columns, beams, fin plates and stiffener plates are taken as follow: elastic modulus 205 GPa, yield strength 350 MPa and corresponding strain of 0.002, ultimate strength 500 MPa with corresponding strain of 0.15. The material properties of the bolts are: elastic modulus 210 GPa, yield strength 640 MPa with corresponding strain of 0.002, ultimate strength 800MPa with corresponding strain 0.15. The elastic modulus of concrete is 26.7 GPa, maximum compressive strength of 31.9 MPa with the corresponding strain of 0.0026. The concrete stress-strain relation given in Figure 2(b) has taken the confinement effect by the EHS column into consideration.

3.3 *Loads and boundary conditions*

A typical joint assembly of the composite framed structures is shown in Figure 3(a), the top flange of the

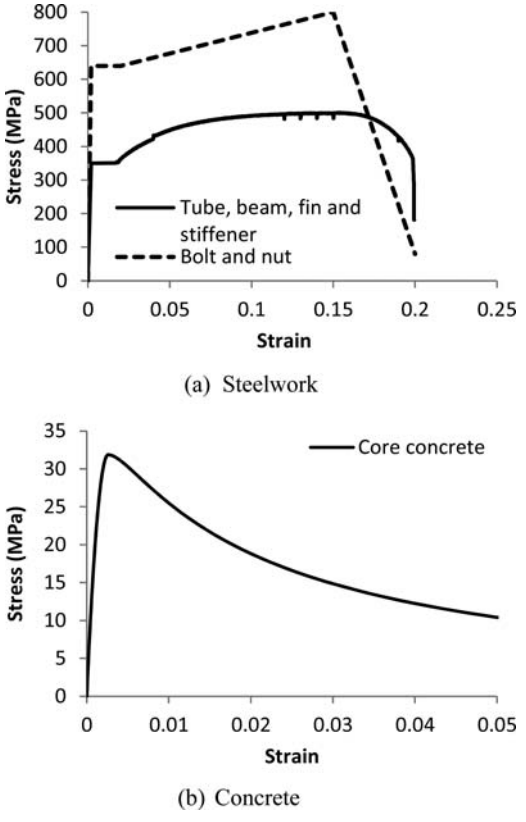

Figure 2. Material properties of joint members.

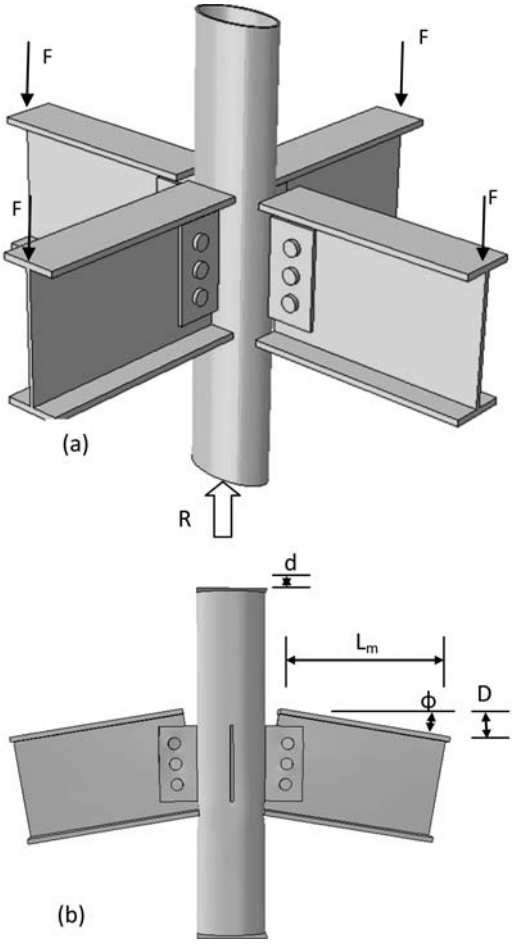

Figure 3. Loading arrangement and deformation.

beams are restrained by concrete slabs. The load is transmitted to the columns through the connection components in the forms of shear and bending. In this paper, the distribution load from slabs is simply replaced by a concentrated load applied at the beam ends.

Under the aforementioned loading conditions, the joint assembly will experience the following deformation as shown in Figure 3(b): column axial shortening, d at the top; beam rotation, ϕ through the joint. The possible failure modes expected might be column local buckling or crush yielding under compressive loads, connection components failure (shear, tensile or bearing failureof the bolts), beam web buckling, etc. In this research, lateral restraints are provided to the beams against lateral torsional buckling to occur. Figure 3 shows the loading arrangement of the joint assembly.

3.4 *Finite element mesh*

The nonlinear finite element analysis software package ABAQUS is adopted to develop a nonlinear finite element (FE) model to capture the structural behaviour of beam to EHS column connections. Three-dimensional 8-node solid element (C3D8) is adopted in the FE model. In both ends, the rigid plate is tied to the tube and core end surfaces. Contact pairs are defined as surface-to-surface contact to account for the interaction between steel tube and concrete core, boltsto fin plate and the beam web, stiffener plate to concrete core, etc. "Hard contact" was assumed for the normal contact behaviour and re-open is allowed. In tangential direction, the general bond action was simulated only through the contact friction and friction coefficient of 0.3 is adopted in this study. No imperfection is introduced into the numerical models in this study.

3.5 *Stress – strain model of the confined concrete*

For concrete-filled steel tubular column members, the confinement effect by the steel hollow section to the concrete core has been recognized, which enhanced the compressive strength of the infill concrete. The research presented in this paper adopts the stress-strain model developed by Han *et al* (2005, 2007) for concrete filled in circular sectionsand extends its application to elliptical steel hollow sections.

Details to stress-strain modelofconfined concrete in circular steel hollow sections are introduced in

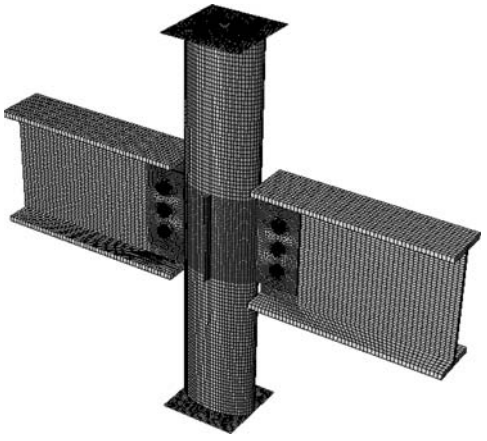

Figure 4. Typical finite element mesh.

publications (Han *et al* 2005, 2007). In whichthe basic form is described as following:

$$y = \begin{cases} 2x - x^2, & (x \le 1), \\ \dfrac{x}{\beta_0 (x-1)^2 + x}, & (x > 1), \end{cases} \tag{1}$$

where,

$x = \varepsilon / \varepsilon_0$,

$y = \sigma / \sigma_0$,

$\sigma_0 = f_{ck}$ (N/mm^2),

$\varepsilon_0 = \varepsilon_c + 800\xi^{0.2} \times 10^{-6}$,

$\varepsilon_c = (1300 + 12.5 f_{ck}) \times 10^{-6}$,

$\beta_0 = (2.36 \times 10^{-5})^{[0.25 + (\xi - 0.5)^7]} (f_{ck})^{0.5} \times 0.5 \ge 0.12$

In the above formulae, f_{ck} is the cylinder compressive strength of the concrete and ξ is the confinement factor whose expression is described as following:

$$\xi = \frac{A_s f_y}{A_c f_{ck}} \tag{2}$$

where A_s and A_c are the cross-sectional areas of the steel and concrete. f_y is the yield strength of steel and f_{ck} is the cylinder strength of the unconfined concrete. The Young's modulus of the confined concrete followed the empirical formulation provided in ACI (1999) and may be described as $E_c = 4700\sqrt{f_{ck}}$ MPa. The Poisson ratio of the confined concrete is taken as 0.2.

4 COMPARISON OF RESULTS

4.1 *Joint-A: Major axis connection with stiffener*

Figure 5 shows the comparisons of Joint-A with unfilled and concrete filled EHS columns. As expected with the unfilled EHS column, the tube wall is subjected to direct tension at the upper portion of the connection, but experienced direct compression near the bottom of the connection. Local inwards buckling occurs near the bottom of the connection. The deformed shapes of the joint are shown in Figure 5(b). Although the through plate for the minor axis connection is acting as a stiffener for the EHS, deformation of the tube wall could not be completely eliminated. For the joint assembly with concrete filled column, local inwards buckling of the column wall due to the direct compression at the bottom flange of the beam is restrained by the concrete infill, therefore higher moment capacity were obtained as shown in Figure 5(a). The deformed shapes of Joint A with concrete filled EHS column is shown in Figure 5(c).

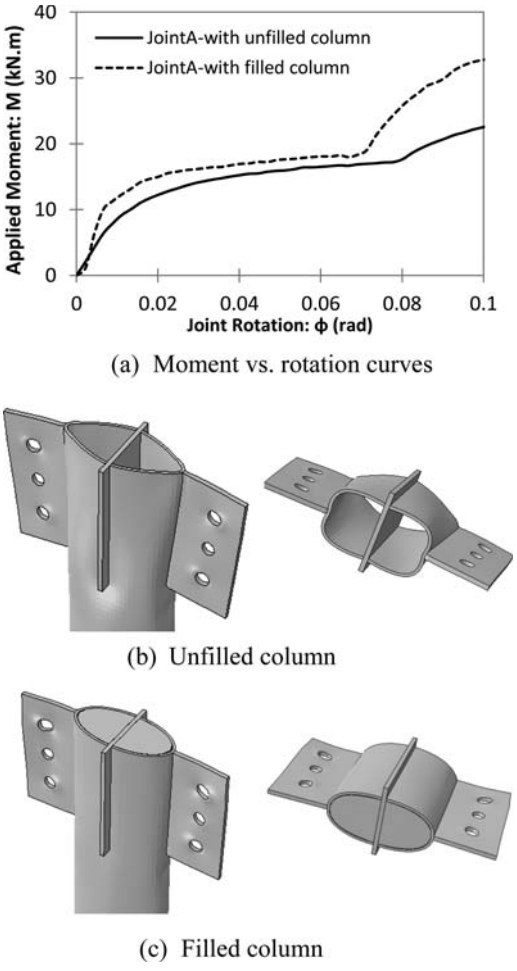

Figure 5. Joint-A: M – ϕ characteristics and deformed shapes.

4.2 *Joint-B: Major axis connection without stiffener*

Figure 6 shows the comparison of Joint-B with concrete filled or unfilled column. Similar to Joint-A, the joint assembly with unfilled EHS column experienced

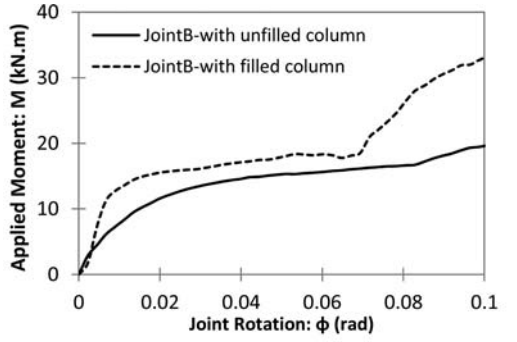

(a) Moment vs. rotation curves

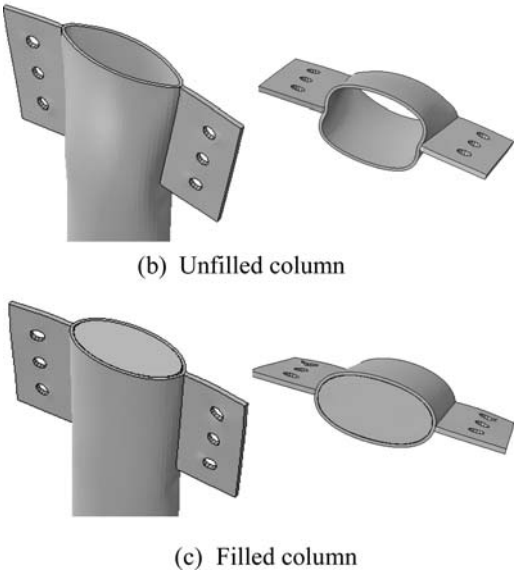

(b) Unfilled column

(c) Filled column

Figure 6. Joint-B: M – ϕ characteristics and deformed shapes.

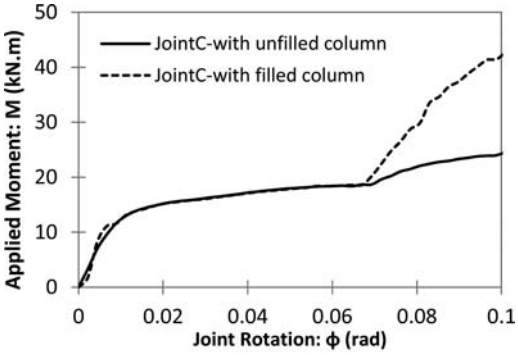

(a) Moment vs. rotation curves

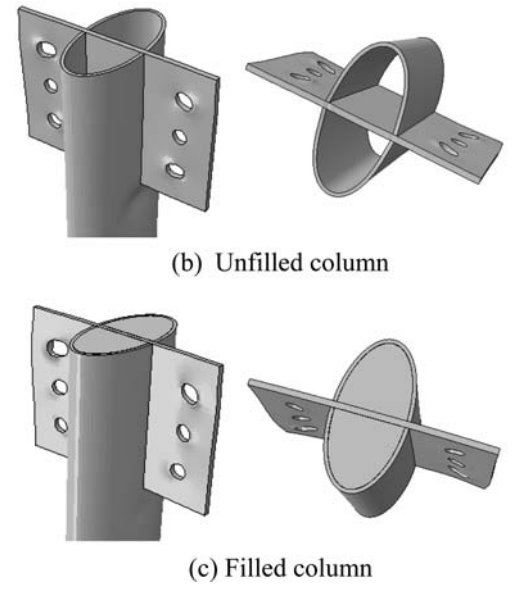

(b) Unfilled column

(c) Filled column

Figure 7. Joint-C: M – ϕ characteristics and deformed shapes.

extensive deformation at the location near the upper portion of the connection but inwards buckling near the bottom of the connection, In contrast, a relative less deformation is observed for the filled EHS column, therefore the moment capacity and connection stiffness for the joint assembly with concrete filled EHS column is significantly higher than that of joint assembly with unfilled column as shown in Figure 6(a). The deformed shapes of Joint B with unfilled and concrete filled EHS columns are shown in Figure 6(b) and (c).

4.3 *Joint-C: Minor axis through plate connection*

A through plate connection is used for Joint-C which combined the function of a fin plate and stiffener plate. Figure 7(a) shows the comparison of the moment rotation responses of the Joint-C with concrete filled or unfilled EHS columns. The shear force and bending moment were initially transferred via the combined fin and stiffener plate, therefore the moment rotation curves for both the concrete filled and unfilled columns are nearly the same up to 70 mRad. However, with further joint rotation and contact of the bottom flange of the beam, the concrete infill were able to restrained the deformation of the column wall from inward buckling, therefore leading to a significance increases in moment capacity for the joint assembly with concrete filled EHS column. The deformed shapes of both joint with unfilled and filled EHS columns are shown in Figure 7(b) and (c).

4.4 *Joint-D: Minor axis connection without stiffener*

Figure 8(a) shows the comparison of the results for the minor axis connection of Joint-D with concrete filled and unfilled EHS columns. As expected, the infill concrete restrained the inward deformation of the tube wall and led to increases in moment capacity. Although inward buckling is eliminated due to

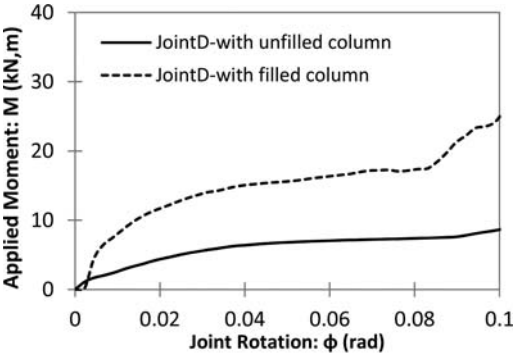

(a) Moment vs. rotation curves

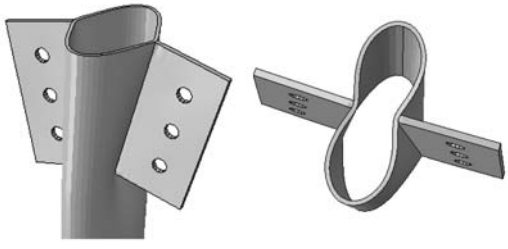

(b) Unfilled column

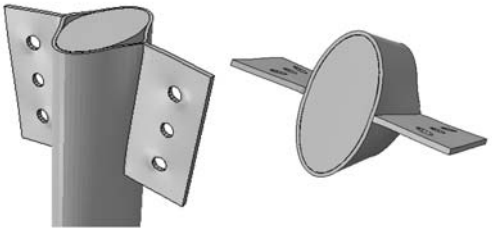

(c) Filled column

Figure 8. Joint-D: M – ϕ characteristics and deformed shapes.

the concrete infill, outward deformation near the top of the connection cannot be eliminated, some separation is observed in the deformed shape shown in Figure 8(c). For the unfilled EHS column, because the low initial stiffness and direct compression from the applied load, the moment capacity of this connection with unfilled EHS column is significantly reduced due to the inability to restrain the inward buckling of the unfilled tube wall. The deformed shapes of the minor axis connection with unfilled EHS column are shown in Figure 8(b).

4.5 *Comparison of joints with empty hollow section columns*

Figure 9 shows a comparison of joint assemblies with major axis connections and unfilled EHS columns. As expected, the moment capacity of Joint-A is slightly

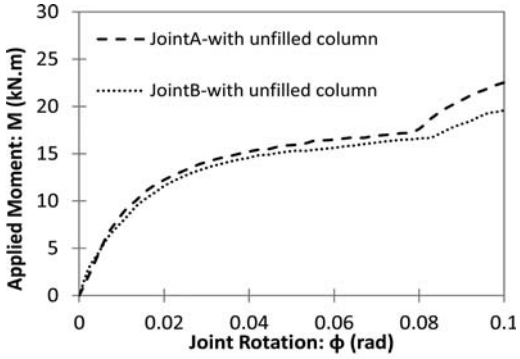

Moment vs. rotation curves

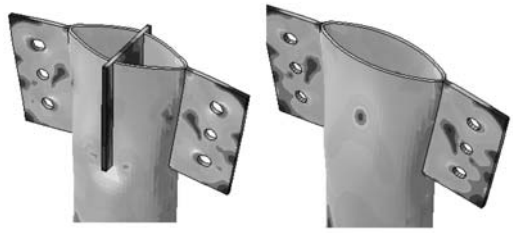

Figure 9. Comparison of joints with unfilled columns and major axis connections.

higher than that of Joint-B due to the minor axis stiffener plate. However, the effect is not evident in restraining the cross section deformation. Figure 10 shows a comparison of joint assemblies with minor axis connections and unfilled EHS columns. Obviously the moment capacity of Joint-C is much higher than that of Joint-D due to the shear force and bending moment were initially transferred via the combined fin plate and stiffener.

Figures 9 and 10 show the deformed shapesand stress distribution in the joint that indicated the higher stress location and possible failure mode: fin plates and fin to column welds.

4.6 *Comparison of joints with concrete filled columns*

Figure 11 shows a comparison of joint assemblies with major axis connection and concrete filled EHS columns. Different to the joints with unfilled EHS columns, their moment capacities are almost identical. The EHS column was restrained by the concreteinfill. Figure 12 shows a comparison of joint assemblies with minor axis connection and concrete filled EHS columns. Although the inward deformation was restrained by the concrete core in Joint-D, the separation of the core and steel section is clearly visible close to the upper portion of the fin plates. The moment capacity of Joint-D is lower than that of Joint-C. Figure 12 shown the stress distribution near the joint and possible failure modes.

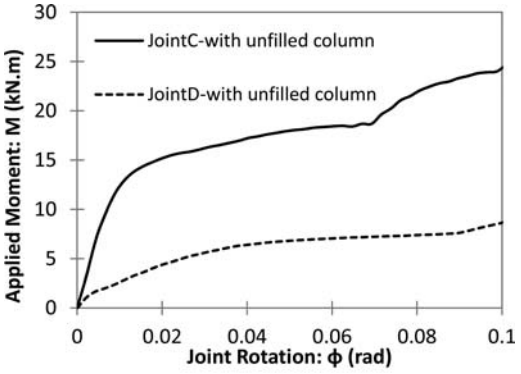

Moment vs. rotation curves

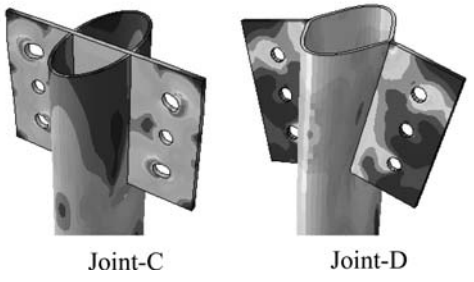

Figure 10. Comparison of joints with unfilled columns and minor axis connections.

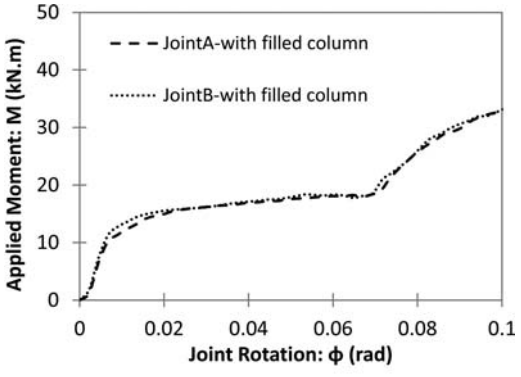

Moment vs. rotation curves

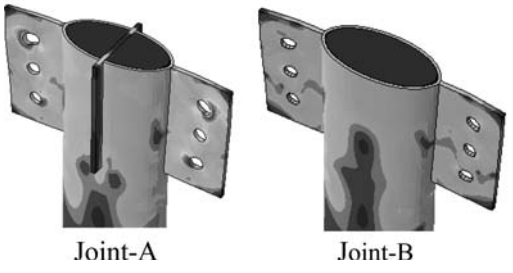

Figure 11. Comparison of joints with filled columns and major axis connections.

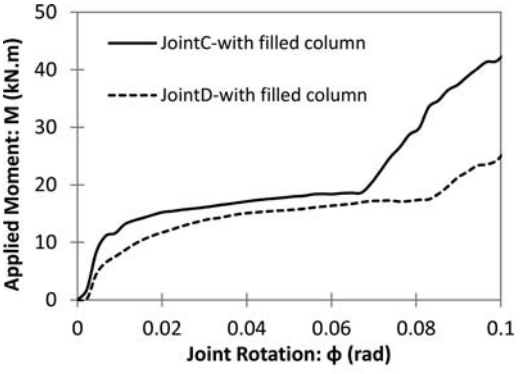

Moment vs. rotation curves

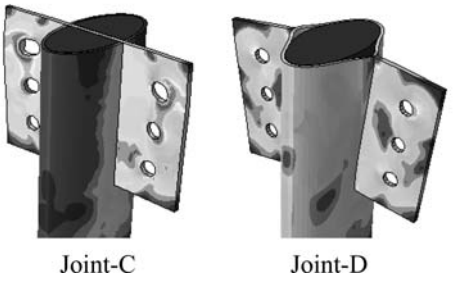

Figure 12. Comparison of joints with filled columns and minor axis connections.

5 CONCLUSIONS

This paper presents moment rotation behaviour and failuremodes of joint assemblies with concrete filled and unfilled EHS columns. Based on the comparison and analysis, the effects of connection component arrangement and effect of the concrete infill to the structural behaviour of joint assembly are highlighted. The results showed that concrete filled columns provided significant increases in moment capacity and initial stiffness to the connections. Through plate connection is recommended for minor axis beam to EHS column joints.

ACKNOWLEDGEMENT

The research reported in this paper is partly funded by the research grant from the Engineering and Physical Science Research Council (EP/G002126/1) in the UK who are gratefully acknowledged.

REFERENCES

ACI (1999). *Building code requirements for structural concrete and commentary*. Detroit (USA). American Concrete Institute, ACI 318-95, 1999.

Dai, X. & Lam, D. (2010a). Numerical Modelling of the Axial Compressive Behaviour of Short Concrete-Filled

Elliptical Steel Columns. *Journal of Constructional Steel Research* 66:931–42.

Dai, X. & Lam, D. (2010b). Axial Compressive Behaviour of Stub Concrete-filled Columns with Elliptical Stainless Steel Hollow Sections. *Steel and Composite Structures* 10:517–39.

Han, L.H., Yao, G.H. & Tao, Z. (2007) Performance of concrete-filled thin-walled steel tubes under pure torsion. *Thin-Walled Structures* 45:24–36.

Han, L.H., Yao, G.H. & Zhao, X.L. (2005). Tests and calculations of hollow structural steel (HSS) stub columns filled with self-consolidating concrete (SCC). *Journal of Constructional Steel Research* 61:1241–69.

Martinez-Saucedo, G., Packer, J.A. & Zhao, X.L. (2008). Static design of elliptical hollow section end-connections. *Proceedings of the Institution of Civil Engineers*, Structures & Buildings 161 April 2008 Issue SB2, 103–113.

Willibald, S., Packer, J.A. & Martinez-Saucedo, G. (2006a) Behaviour of gusset plate connections to ends of round and elliptical hollow structural section members. *Can. J. Civ. Eng.* **33**: 373–383.

Willibald, S., Packer, J.A., Voth, A.P. & Zhao, X. (2006b). Through-plate joints to elliptical and circular hollow sections. *Tubular Structures XI. Packer and Willibard (eds),* Taylor and Francis Group, London, ISBN 0-415-40280-8.

Tubular Structures XIV – Gardner (Ed.)
© 2012 Taylor & Francis Group, London, ISBN 978-0-415-62137-3

Elastic buckling of elliptical hollow sections under linearly varying in-plane stress distributions

J.M. Abela & L. Gardner
Department of Civil and Environmental Engineering, Imperial College London, London, UK

ABSTRACT: The structural behaviour of elliptical hollow sections has been examined in previous studies under several loading conditions, including pure compression, pure bending and combined uniaxial bending and compression. This paper examines the elastic buckling response of elliptical hollow sections under any linearly varying in-plane loading conditions, including the most general case of combined compression and biaxial bending. An analytical method to predict the elastic buckling stress has been derived and validated against finite element results. The predictive model first identifies the location of the initiation of local buckling based on the applied stress distribution and the section geometry. The critical radius of curvature corresponding to this point is then introduced into the classical formula for predicting the elastic local buckling stress of a circular shell. Comparisons reveal that the analytical predictions of elastic buckling stresses are consistently below the finite element results but within 2.5% for thin shells and 7.5% for thick shells.

1 INTRODUCTION

Research activity in the area of elliptical sections has increased in recent years due to their emergence as hot-rolled structural products. Elliptical hollow sections (EHS) combine the elegance of circular hollow sections (CHS) with the improved structural efficiency in bending associated with sections of differing flexural rigidities about the two principal axes. This behaviour has been exploited in a number of recent projects that have adopted EHS as structural elements, such as the Honda Central Sculpture in Goodwood, UK, the Society Bridge in Braemar, UK (Corus 2006) and the airport at Barajas in Madrid, Spain (Viñuela-Rueda and Martinez-Salcedo 2006). EHS were also included in the new edition of the European product standard EN 10210 (CEN 2006), which provides a standard range of dimensions of sections with an aspect ratio of 2 (i.e. $a/b = 2$, where a and b are the major and minor axis dimensions, respectively).

2 LITERATURE REVIEW

2.1 *Compression*

Marguerre (1951) made the first attempt at representing the buckling behaviour of cylindrical shells of variable curvature under compression. The work was later continued by Kempner (1962) and Hutchinson (1968). Kempner's (1962) work concluded that the elastic buckling stress of an oval hollow section (OHS) could be accurately predicted as the buckling stress of a circular hollow section (CHS) with a radius equal to the maximum radius of curvature of the OHS. This solution was shown to be a lower bound. Hutchinson (1968) found that this approach could also be applied to elliptical hollow sections (EHS), provided that the shell is sufficiently thin. The proposals were later confirmed by experiments carried out by Tennyson et al. (1971).

Further investigations have been carried out by Zhu and Wilkinson (2006), Chan and Gardner (2008a), Ruiz-Terán and Gardner (2008) and Silvestre (2008). These studies confirmed that Kempner's (1962) approach of basing the elastic buckling load of an EHS on that of a CHS with a radius equal to the maximum radius of curvature of the ellipse is acceptable but with increasing errors for higher aspect ratios and thicker sections. Analyses of the elastic buckling response of EHS using generalised beam theory (GBT) was undertaken by Silvestre (2008). Both Ruiz-Terán and Gardner (2008) and, using GBT, Silvestre (2008) proposed modifications to the Kempner equation to achieve more accurate predictions of the elastic buckling stress of EHS of various aspect ratios.

2.2 *Bending*

Investigations on elliptical cylinders subjected to major axis bending were carried out by Heck (1937) and Gerard and Becker (1957) where it was observed that although the maximum compressive stress occurs at the stiffest part of the cross-section (which is most resistant to buckling), the critical radius of curvature occurs at a point between the maximum and minimum radii of curvature. Gerard and Becker (1957) derived the critical radius for major axis bending

to be $r_{cr,b,ma} = 0.649a^2/b$ by optimising the function composed of the varying curvature expression and the elastic bending stress distribution. For minor axis bending, the location of initiation of buckling was found to be at the same location as for an EHS under compression (i.e. $r_{cr,b,mi} = a^2/b$). Once the critical radius of curvature (i.e. the location of the initiation of buckling) has been determined, the elastic buckling stress of the EHS can again be calculated by means of the elastic buckling expression for a CHS.

2.3 *Combined actions*

The performance of EHS under combined compression and uniaxial bending was investigated in Gardner et al. (2011), based on the results of the pure compression and bending results proposed in Chan and Gardner (2008a, 2008b). The critical radius of curvature for an EHS under compression and minor axis bending was found to be similar to the pure compression and pure minor axis bending cases, where $r_{cr,mi}$ is expressed as a^2/b. Under combined compression and major axis bending, the critical radius will shift towards the centroidal axis as the compressive part of the loading increases, and an expression in terms of ψ, the ratio of the end stresses, was proposed. A simplification of this expression for $a/b = 2$, considering a conservative linear transition between the pure compressive and pure major axis bending critical radii, is:

$$r_{cr,ma} = r_{cr,b,ma} + (r_{cr,c} - r_{cr,b,ma})\left(\frac{\psi+1}{2}\right) \quad (1)$$

where $r_{cr,b,ma}$ and $r_{cr,c}$ are the critical radii of curvature for pure major axis bending and pure compression respectively and ψ is the ratio of the end stresses and is in the range of $-1 \leq \psi \leq 1$.

3 ANALYTICAL STUDY OF ELASTIC BUCKLING OF EHS UNDER COMBINED ACTIONS

The elastic buckling stress σ_{cr} of an EHS may be found from the classical buckling stress (Gerard and Becker 1957, Kempner 1962) expression:

$$\sigma_{cr} = \frac{Et}{r_{cr}\sqrt{3(1-\nu^2)}} \quad (2)$$

where r_{cr} corresponds to the point of initiation of local buckling in the cross-section, which depends on the applied stress distribution, E is Young's modulus, t is shell thickness and ν is Poisson's ratio.

This section of the paper will focus on finding the exact location of the critical radius of curvature (i.e. the location of the initiation of local buckling) when an EHS is subjected to linearly varying stress distributions, with particular reference to the case of combined compression and biaxial bending. This load case can

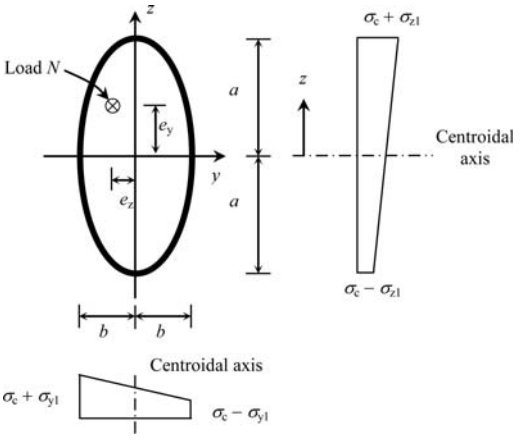

Figure 1. EHS under combined compression and biaxial bending, and stress distributions along centroidal axes.

be achieved by applying a compressive force (N) at eccentricities (e_z and e_y) to the centroid of the section, producing the stress distributions illustrated in Figure 1.

The location of the critical radius r_{cr} in this case may be found by optimising the product of the stress function σr (i.e. the product of the elastic bending stress distribution and the radius of curvature); i.e. finding the location at which the stress causing local buckling is minimum. This method was originally used by Gerard and Becker (1957) to find the critical radius for the pure major axis bending case. It is therefore necessary to define equations for stress and the radius of curvature in order to assemble the stress function. An EHS subjected to a combination of a compressive load and moments about both axes would have an elastic stress distribution defined, at any location, by:

$$\sigma = \sigma_c + \sigma_{z1}\frac{z}{a} + \sigma_{y1}\frac{y}{b} \quad (3)$$

where $\sigma_c = N/A$ is the uniform compressive stress, in which N is the applied compressive load and A is the cross-sectional area, $\sigma_{z1}(z/a)$ is the linearly varying stress associated with the major axis, $\sigma_{y1}(y/b)$ is the linearly varying stress associated with the minor axis, $\sigma_{z1} = Ne_y a/I_y$ at $z = a$, where I_y is the second moment of area about the major axis, and $\sigma_{y1} = Ne_z b/I_z$ at $y = b$, where I_z is the second moment of area about the minor axis.

The general expression for the radius of curvature of an EHS is:

$$r = \frac{a^2}{b}\left\{1 - \left[1 - \left(\frac{b}{a}\right)^2\right]\left(\frac{z}{a}\right)^2\right\}^{\frac{3}{2}} \quad (4)$$

The mathematical optimisation of the stress function σr may be performed by using the method

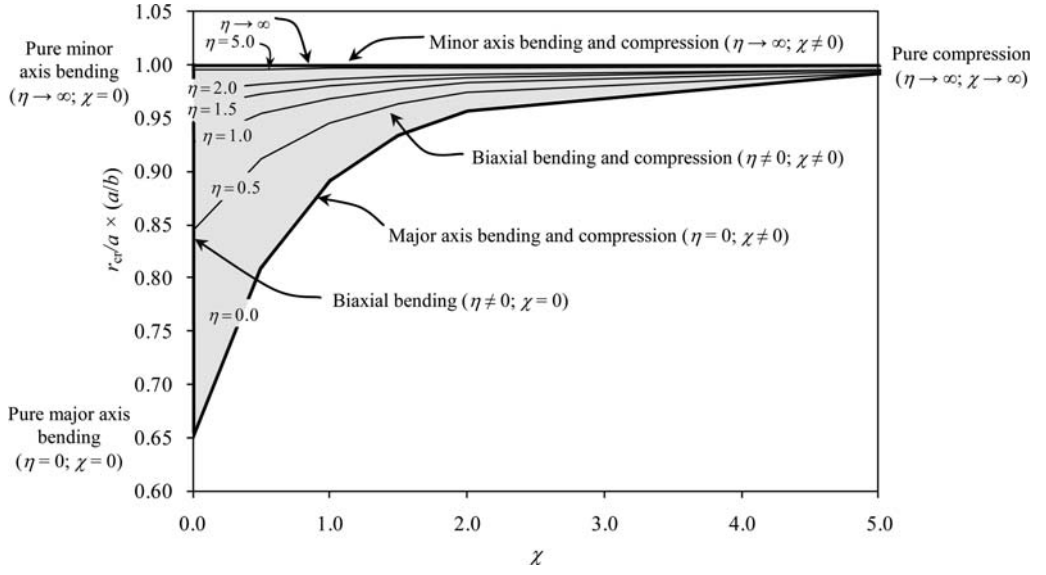

Figure 2. Critical radius r_{cr} envelope for a generalised linearly varying in-plane stress distribution for an EHS with varying stress ratio χ and a/b = 2.

of Lagrange multipliers. The expressions for the Lagrange function L and multiplier λ are found to be:

$$\mathcal{L} = \left(\frac{N}{A} + \sigma_{z1}\frac{z}{a} + \sigma_{y1}\frac{y}{b}\right)\frac{a^2}{b} \left\{1 - \left[1 - \left(\frac{b}{a}\right)^2\right]\left(\frac{z}{a}\right)^2\right\}^{\frac{3}{2}} + \lambda\left(\frac{z^2}{a^2} + \frac{y^2}{b^2} - 1\right) \tag{5}$$

$$\lambda = -\frac{\sigma_{y1}}{b}\frac{a^2 b}{2y}(1-\zeta z^2)^{\frac{3}{2}} \tag{6}$$

$$\text{where } \zeta = \frac{(a^2 - b^2)}{a^4} \tag{7}$$

By substituting, optimising and setting the partial derivatives of L to zero, an expression for z_{cr} (i.e. the distance from the centroid in the major axis direction at which local buckling initiates) may be numerically defined by Eq. (8).

$$\left(1 - \left(\frac{a^2 - b^2}{a^4}\right){z_{cr}}^2\right)\left[\sqrt{a^2 - {z_{cr}}^2} + \eta z_{cr}\right] = 3\left(\frac{a^2 - b^2}{a^4}\right) z_{cr}\sqrt{a^2 - {z_{cr}}^2}\left[a\chi + z_{cr} + \eta\sqrt{a^2 - {z_{cr}}^2}\right] \tag{8}$$

in which η and χ are:

$$\eta = \frac{\sigma_{y1}}{\sigma_{z1}} \tag{9}$$

$$\chi = \frac{\sigma_c}{\sigma_{z1}} \tag{10}$$

where η is the ratio of the extreme fibre bending stresses about the minor and major axes and χ is the ratio of the pure compressive stress to the extreme fibre major axis bending stress.

The solution for z_{cr} from Eq. (8) may then be substituted into Eq. (4) to obtain the value of the critical radius r_{cr}, which may, in turn, be substituted into Eq. (2) to determine the elastic buckling stress σ_{cr}.

4 ANALYSIS OF RESULTS AND COMPARISON WITH KEY EXISTING SOLUTIONS

Analysis of the critical radii of curvature of EHS under individual loading conditions from pure compression to pure bending has been carried out by Chan and Gardner (2008a, 2008b) and Ruiz-Terán and Gardner (2008). More recently the effect of combined compression and uniaxial bending has been studied by Gardner et al. (2011).

This section aims to validate the generalised analytical solution for the elastic buckling stress presented above by comparing it to the existing analytical solutions for EHS under the pure and combined load cases.

Figure 2 is a graphical representation of all the possible locations of initiation of buckling of an EHS under any linearly varying in-plane stress distribution for varying χ; a similar figure could be produced for varying η on the horizontal axis. Special cases of

pure compression and pure bending, and the combined cases are illustrated, showing that the result of the generalised elastic stress expression defined by substituting Eq. (8) in Eq. (4) gives the same results as the existing analytical formulations for all the key cases. Eq. (8) is solved numerically here for $a/b = 2$, where the ratio r_{cr}/a is plotted against χ for values of $\eta = 0.0$ to 5.0.

Figure 2 shows that as η increases (maintaining $\chi = 0$) the applied load changes from pure major axis bending to pure minor axis bending as $\eta \to \infty$. The variation in χ traces the position of the EHS's critical radius from pure bending (when $\chi = 0$) to pure compression (as $\chi \to \infty$). Hence ($\eta = 0$, $\chi = 0$) represents a pure major axis bending case, ($\eta \to \infty$, $\chi = 0$) represents pure minor axis bending and ($\eta \to \infty$, $\chi \to \infty$) represents pure compression.

5 NUMERICAL MODELLING

A numerical investigation was carried out to verify the results of the analytical study and to assess the effects of relative thickness $t/2a$ on the elastic buckling stress of elliptical hollow sections with a range of cross-sectional aspect ratios (a/b) subjected to various proportions of biaxial bending and compression. These analyses were carried out using the commercial nonlinear FE package ABAQUS (ABAQUS, 2010).

5.1 *Model description*

The FE models were developed with fixed major axis dimensions measuring $2a = 400$ mm and varying minor axis dimensions measuring $2b = 266.66$ mm, 200 mm and 133.33 mm representing ellipses with aspect ratios of $a/b = 1.5$, $a/b = 2$ and $a/b = 3$ respectively. These major and minor axes dimensions relate to the centre-line (mid-thickness) of the sections. The length of all models was taken as 800 mm (i.e. $L/2a = 2$).The first part of the analysis focussed on the use of thin shells to verify the analytical results. A constant cross-sectional thickness of 0.1 mm was used in this part of the analysis dealing with the effect of varying the aspect ratio on the elastic buckling stress. The relative thickness $t/2a$ used was therefore 0.00025 (or 1/4000). Thicker sections were then analysed in the second part of the study in order to investigate the influence of shear deformations. The aspect ratio was kept constant in this part of the study ($a/b = 2$; $2a = 400$ mm and $2b = 200$ mm) while the cross-sectional thicknesses used were 16, 12.5, 8, and 2 mm, corresponding to relative thicknesses $t/2a$ equal to 0.04, 0.03125, 0.02 and 0.005 (i.e. ranging from 1/25 to 1/200).

The element type employed was a quadrilateral, stress/displacement shell element S4R, with reduced integration, a large-strain formulation and six degrees of freedom per node (ABAQUS, 2010). These elements allow transverse shear deformation and use thick shell theory when the shell thickness is large, but become discrete Kirchhoff thin shell elements as the thickness decreases.

The elastic material properties of structural steel ($E = 210000$ N/mm^2 and $\nu = 0.3$) were employed for all models. Rigid end plates were affixed to the EHS members, and boundary conditions were specified to achieve pinned end conditions. Load was applied at various eccentricities to achieve a range of in-plane stress distributions. The eccentricities at which the load was applied were all combinations of 0, 10, 25, 50, 100, 200 and 1500 mm in both the major and minor axes directions.

Table 1. Comparison of the numerical and analytical values of elastic buckling stress obtained from the proposed general expression for various cases.

Loading condition	a/b	σ_A (N/mm^2)	σ_{FE} (N/mm^2)	σ_A/σ_{FE}
Pure compression	1.5	42.36	42.82	0.989
	2	31.77	32.16	0.988
	3	21.18	21.48	0.986
Pure minor axis bending	1.5	42.36	42.94	0.987
	2	31.77	32.24	0.985
	3	21.18	21.53	0.984
Pure major axis bending	1.5	65.22	66.48	0.981
	2	48.66	49.81	0.977
	3	31.50	32.33	0.974
Combined compression and minor axis bending (at $e_z = 200$ mm, $e_y = 0$ mm)	1.5	42.37	42.91	0.987
	2	31.77	32.22	0.986
	3	21.18	21.52	0.984
Combined compression and major axis bending (at $e_z = 0$ mm, $e_y = 200$ mm)	1.5	52.91	53.75	0.984
	2	40.25	41.00	0.982
	3	25.83	26.36	0.980
Combined compression and biaxial bending (at $e_z = 200$ mm, $e_y = 200$ mm)	1.5	44.19	44.79	0.987
	2	32.76	33.25	0.985
	3	21.60	21.95	0.984

5.2 *Verification of analytical model for thin shells*

All the elastic buckling loads reported in this investigation correspond to the lowest local buckling mode obtained from the numerical analyses. The results from the numerical models were used to verify the proposed general elastic buckling stress equation for all thin shells ($t = 0.1$ mm) of aspect ratios $a/b = 1.5$, 2 and 3. Table 1 and Figure 3 (results plotted against ψ for both major and minor axes) illustrate the variation in the ratio of analytical to numerical stresses (σ_A/σ_{FE}) with the ratio of end stresses in the minor and the major axes. For all cases, the ratio of stresses σ_A/σ_{FE} is close to unity, indicating good correlation between the numerical and analytical results. For the geometries considered, the maximum disparity between the analytical and numerical results is less than 2.5% (Table 1).

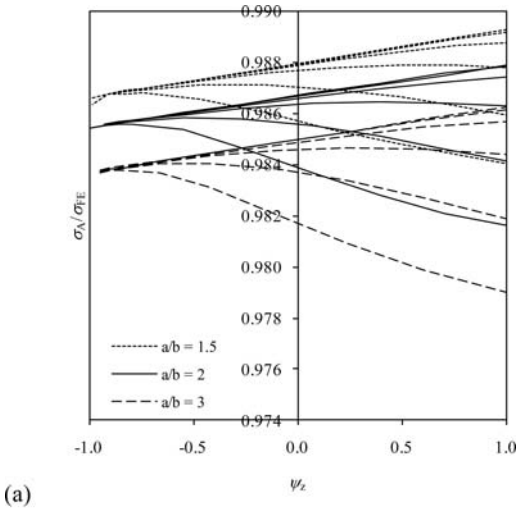

(a)

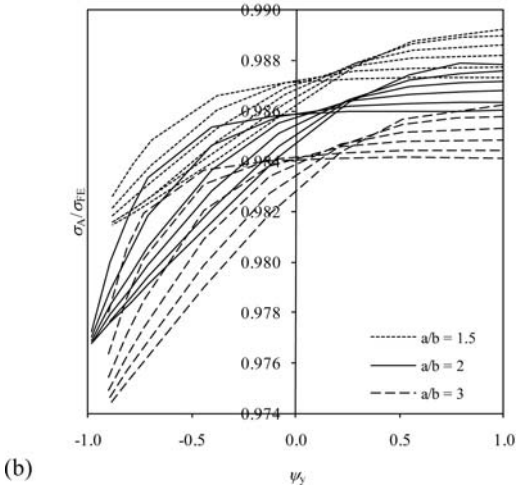

(b)

Figure 3. Variation of the ratio of analytical to numerical stresses with ψ_z (minor axis) and ψ_y (major axis) for all aspect ratios considered and a range of values of η.

5.3 *Assessment of analytical model for thick shells*

After validating the proposed generalised analytical model with the existing solutions and numerical results for thin shells, the effect of increasing shell thickness was investigated using EHS with $a/b = 2$ and additional thicknesses of 2, 8, 12.5 and 16 mm (i.e. $t/2a = 1/200$, 1/50, 1/32 and 1/25). All numerical analyses were also performed using a section length of $L/2a = 2$.

Figures 4 (a), (b) and (c) show a comparison between numerical and analytical results for combined compression and uniaxial or biaxial bending for EHS with $a/b = 2$ and a range of relative shell thicknesses.

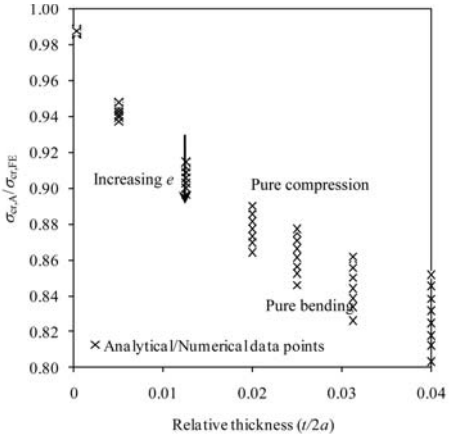

(a)

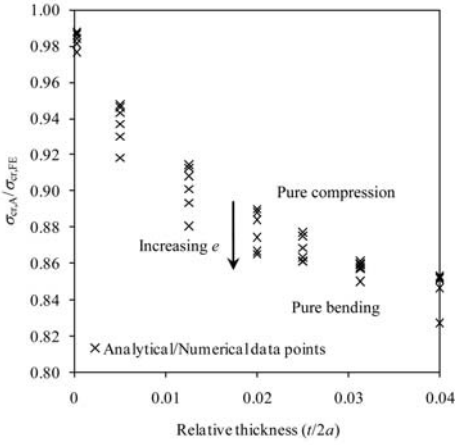

(b)

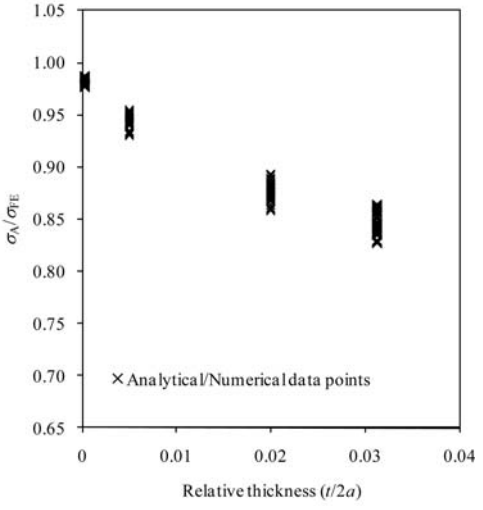

(c)

Figure 4. Comparison between numerical and analytical results for (a) combined minor axis bending and compression, (b) combined major axis bending and compression and (c) combined compression and biaxial bending with χ and η vary from 0 to infinity for EHS with $a/b = 2$ and a range of relative shell thicknesses.

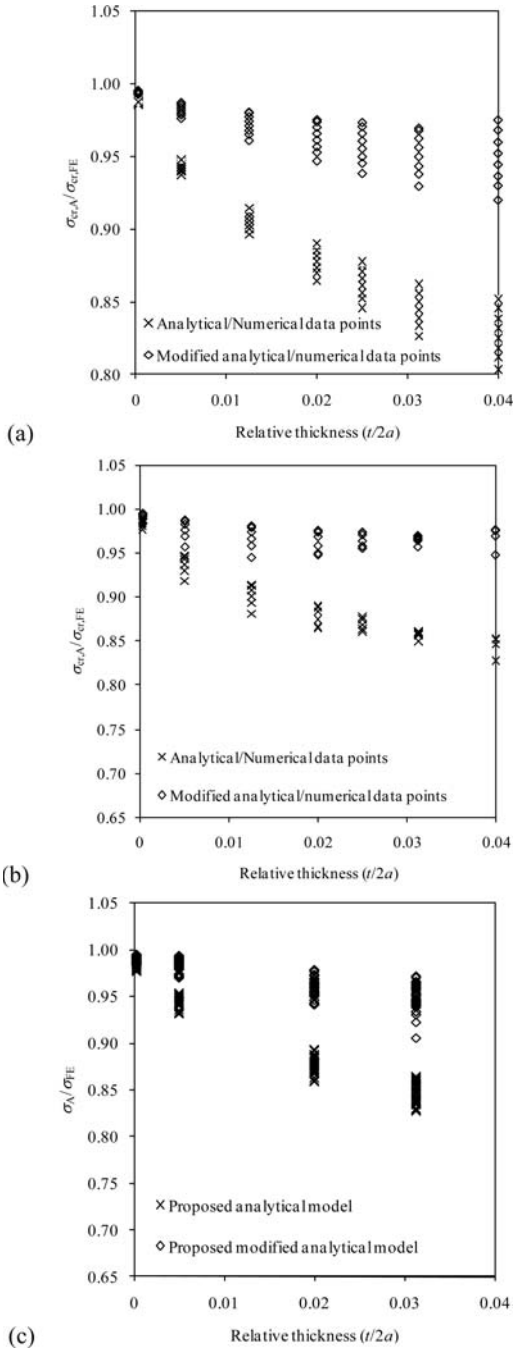

Figure 5. Comparison between numerical and modified analytical results for (a) combined minor axis bending and compression, (b) combined major axis bending and compression and (c) combined biaxial bending and compression for EHS with $a/b = 2$ and a range of relative shell thicknesses.

The comparisons show that while the analytical solutions are very accurate for thin shells, as the relative thickness increases, the analytical solutions become less accurate and diverge from $\sigma_A/\sigma_{FE} = 1$. However, for the thickest shells considered with $t/2a = 0.04$, the deviation still remains below 20%.

To address the deviation of the analytical model from the numerical results with increasing shell thickness, a modification factor g is introduced hence:

$$r_{cr,new} = \frac{r_{cr}}{g} \tag{11}$$

$$\text{where } g = 1 + \left(\frac{t}{2a}\right)^{0.6} \tag{12}$$

Figures 5 (a), (b) and (c) show the effect of the g factor on the data presented in Figures 4 (a), (b) and (c). The results for thin shells may be seen to be largely unaffected by the modification while those for thicker shells are shifted closer to the numerical results. For the cases considered, the maximum discrepancy is now less than 7.5%.

6 CONCLUSIONS

The elastic buckling of elliptical hollow sections (EHS) under combined axial compression and biaxial bending has been examined in this study. An analytical model has been derived for the calculation of elastic buckling stress for a generalised loading case. This model first identifies the location of the initiation of local buckling based on the applied stress distribution and the section geometry. The critical radius of curvature corresponding to this point is then introduced into the classical formula for predicting the elastic local buckling stress of a circular shell. The results obtained from the analytical model have been compared to existing solutions and validated against finite element results. The results showed very good correlation between the two solutions for thin shells with a disparity of less than 2.5%. For thicker shells, greater deviation was observed. Hence, the analytical solution was modified by introducing a factor g, to account for the effect of increasing shell thickness. The maximum error for thick shells under combined compression and biaxial bending was now reduced to less than 7.5%.

ACKNOWLEDGEMENTS

The authors would like to thank Evgeni Grishev Pirianov for his contribution to the paper.

REFERENCES

ABAQUS. 2010. ABAQUS, Version 6.10-1, Hibbitt, Karlsson and Sorensen, Inc. Pawtucket, USA.

Chan, T. M. and Gardner, L. 2008a. Compressive resistance of hot-rolled elliptical hollow sections. *Engineering Structures,* 30(2): 522–532.

Chan, T. M. and Gardner, L. 2008b. Bending strength of hot-rolled elliptical hollow sections. *Journal of Constructional Steel Research*, 64(9): 971–986.

Corus 2006. Celsius® 355 Ovals. Corus Tubes – Structural and Conveyance Business.

European Committee for Standardization (CEN) 2005. Eurocode 3: Design of steel structures – Part 1-1: General rules and rules for buildings, EN 1993-1-1.

Gardner, L., Chan, T.M. and Abela, J.M. 2011. Structural behaviour of elliptical hollow sections under combined compression and uniaxial bending. *Advanced Steel Construction*, 7(1): 86–113.

Gerard G. and Becker H. 1957. Handbook of structural stability: Part III – Buckling of curved plates and shells, *NACA Technical Note 3783*.

Heck, O.S. 1937. The stability of orthotropic elliptic cylinders in pure bending. *NACA Technical Memorandum*. 834.

Hutchinson, J. W. 1968. Buckling and initial postbuckling behaviour of oval cylindrical shells under axial compression. *Journal of Applied Mechanics*, 35(1): 66–72.

Kempner, J. 1962. Some results on buckling and postbuckling of cylindrical shells. *Collected Papers on Instability of Shell Structures, NASA TND–1510:*173–186.

Marguerre, K. 1951. Stability of cylindrical shells of variable curvature. *NACA Technical Memorandum 1302*.

Ruiz-Terán, A. M. and Gardner, L. 2008. Elastic buckling of elliptical tubes. *Thin-Walled Structures*, 46(11): 1304–1318.

Silvestre, N. 2008. Buckling behaviour of elliptical cylindrical shells and tubes under compression. *International Journal of Solids and Structures,* 45(16): 4427–4447.

Silvestre, N. and Gardner, L. 2011. Elastic local post-buckling of elliptical tubes, *Journal of Constructional Steel Research*. 67(3): 281–292.

Tennyson, R.C., Booton, M. and Caswell, R.D. 1971. Buckling of imperfect elliptical cylindrical shells under axial compression. *AIAA Journal*. 9(2):250–5.

Viñuela-Rueda, L. and Martinez-Salcedo, J. 2006. Steel structure and prestressed façade of the new terminal building. *Hormigon Acero*, 239(1): 71–84.

Zhu, Y. and Wilkinson, T. 2006. Finite element analysis of structural steel elliptical hollow sections in pure compression. *Proceedings of the 11th International Symposium on Tubular Structures, Québec City, Canada*: 179–186.

Tubular Structures XIV – Gardner (Ed.)
© 2012 Taylor & Francis Group, London, ISBN 978-0-415-62137-3

Elliptical hollow section beam-columns

K.H. Law
The University of Hong Kong, Hong Kong, China

L. Gardner
Imperial College London, UK

ABSTRACT: The structural behaviour of Elliptical Hollow Section (EHS) beam-columns is studied in this paper. Results of previous research on beam-columns at the cross-sectional level are summarised, while for the investigation of global instability, new experimental and numerical data are presented and analysed. Thirty three EHS beam-columns, with a constant cross-sectional aspect ratio of two, were tested and numerical models were validated based on the test results. Further parametric studies considering a range of aspect ratios and slenderness ratios were also performed. Design rules covering instabilities in elliptical hollow section beam-columns have been assessed based on the experimental and numerical findings. It was found that existing design expressions for hot-finished hollow section beam-columns are also applicable to EHS members.

1 INTRODUCTION

Elliptical hollow sections (EHS) have been recently added to the tubular product standard EN 10210 (2006) and to the industry design guidance produced by SCI and BCSA (2009), which has increased their adoption as load-bearing members in construction. Despite extensive research on EHS cross-sections and members in compression (Gardner & Chan 2007, Chan & Gardner 2008a, b, 2009, Gardner et al. 2008 & 2010, Insausti & Gardner 2010, Zhao & Packer 2009), there is limited knowledge on the member instability of EHS beam-columns; hence, this is the focus of the present study.

Research into the behaviour of hot-finished EHS at the cross-sectional level has been conducted by Gardner et al. (2011), in which the response of EHS under combined compression plus uniaxial bending was examined. A total of 4 stub columns tests under pure compression and 8 under eccentric compression with various load eccentricities (4 about the minor axis and 4 about the major axis) were performed, in parallel with numerical analyses. On the basis of the experimental and numerical findings, equivalent diameters for EHS under compression and uniaxial bending and the corresponding cross-sectional slenderness limits were derived. It was found that the fully plastic interaction formulae developed by Nowzartash & Mohareb (2009) for Class 1 and 2 cross-sections and an elastic interaction formula for Class 3 cross-sections give conservative predictions and can be safely applied to EHS for design purposes.

The beam-column problem is complex since it involves the features of column buckling, uniaxial or biaxial beam bending and beam buckling. Since the late nineteenth century, substantial research on elastic and inelastic beam-column behaviour has been carried out; the development of the theory of beam-columns has been summarised by Massonnet (1976) and Chen & Atsuta (1976, 1977). Since previous beam-column research mainly focused on I-sections, the purpose of this study is to generate experimental and numerical results and to access the applicability and reliability of existing design formulae to EHS beam-columns.

2 EXPERIMENTAL STUDIES

A full-scale experimental investigation into EHS member instability under combined compression and bending has been carried out in the Structures Laboratory at Imperial College London. The test programme comprised 10 material tensile coupon tests and 33 beam-column tests – 6 pure compression tests; 3 buckling about the major axis and 3 about the minor axis; 18 eccentric compression tests, 9 inducing bending about the major axis and 9 about the minor axis; and a further 9 tests induced compression and bending about both axes. The sections were all hot-finished from grade S355 steel and produced by Tata Steel Tubes. The tested EHS had an aspect ratio of two, overall outer cross-sectional dimensions of 150 × 75 mm and thickness of 5 mm, which is the thinnest non-slender section of the range for a yield strength of 355 N/mm^2. The primary aim of the member tests was to investigate the beam-column behaviour of EHS members with

Table 1. Key results from tensile coupon tests.

Specimen	E N/mm^2	f_y N/mm^2	f_u N/mm^2	ε_{f1} %	ε_{f2} %
BC-TC1	212900	350	481	40	64
BC-TC2	218200	343	472	36	68
BC-TC3	217000	360	485	38	64
BC-TC4	214600	344	470	39	65
BC-TC5	222400	388	510	42	65
BC-TC6	219500	326	452	39	68
BC-TC7	220200	341	473	35	65
BC-TC8	221100	358	468	37	64
BC-TC9	219200	373	489	40	66
BC-TC10	212100	377	491	40	63

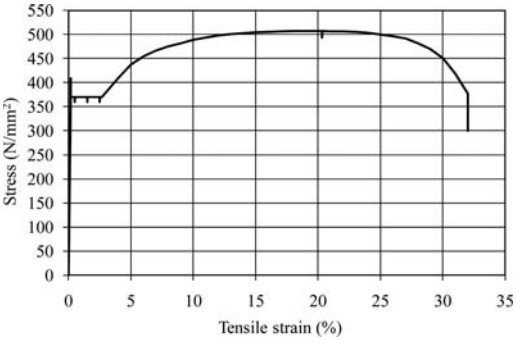

Figure 1. Stress-strain curve of BC-TC5.

pinned end conditions and under eccentric compression (generating uniform moment along the member length).

2.1 *Tensile coupon tests*

Material tensile coupon tests were conducted in accordance with EN 10002-1 (2001) to determine the basic engineering stress-strain response of the material of the tested sections. The specimens originated from 10 lengths of material and one coupon was taken from each length for material testing.

Full details of the tensile coupon tests have been described in Law & Gardner (in press), while the key results from the ten tensile coupon tests are reported in Table 1. The reported material parameters are the Young's Modulus E, static yield stress f_y, static ultimate tensile stress f_u and the plastic strain at fracture based on elongation over the standard gauge length ε_{f1} and the reduction of cross-sectional area ε_{f2} of the coupons. A typical stress-strain curve is depicted in Figure 1.

2.2 *Compression and uniaxial bending*

For the 6 pure compression tests and 18 eccentric compression tests performed, three different column lengths of 1 m, 2 m and 3 m were tested to provide a range of member slendernesses $\bar{\lambda}$ ranging from 0.28 to 0.84 for pin-ended beam-columns eccentrically loaded

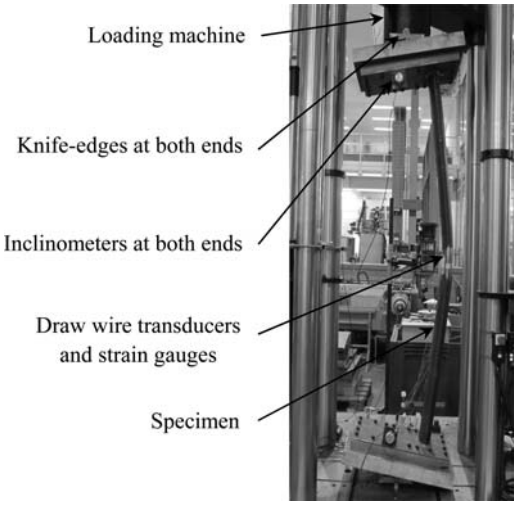

Figure 2. Eccentric compression test configuration – deformed specimen of BC-2-$e_z = 150$.

about the major axis and 0.49 to 1.46 about the minor axis. For the pure compression test specimens (BC-1-$e_y = 0$ and BC-1-$e_z = 0$), where the measured global imperfection was less than $L/1000$, an eccentricity of loading was applied such that the combined imperfection plus eccentricity was equal to $L/1000$. For other columns, the load was applied concentrically since the measured imperfections were greater than $L/1000$. For the eccentric compression tests, the load eccentricity was varied so that a range of proportions of axial load to bending could be achieved.

2.2.1 *Test set-up*

The general configuration of the set-up is depicted in Figure 2. The specimens were loaded by a 2000 kN Instron hydraulic machine through hardened steel knife-edges and welded end plates at both ends to provide pinned end conditions about the axis of buckling and fixed conditions in the orthogonal direction.

Two draw wire transducers were located at the mid-height of the specimens to measure the lateral deflections in both principal directions. Inclinometers were positioned at each end of the members to measure the end rotations about the axis of buckling. Four linear electrical resistance strain gauges were affixed to the extreme tensile and compressive fibres of the sections. Displacement control was employed to drive the hydraulic machine at a constant rate of 0.25 mm/min, 0.50 mm/min and 1.0 mm/min for 1 m, 2 m and 3 m specimens respectively. Load, strain, lateral and vertical displacements, end rotations and input voltage were all recorded using the data acquisition equipment DATASCAN and logged using the DSLOG computer package. All data were recorded at one second intervals.

The geometry of an elliptical hollow section is depicted in Figure 3, where $2a$ is the larger outer diameter, $2b$ is the smaller outer diameter, t is the thickness

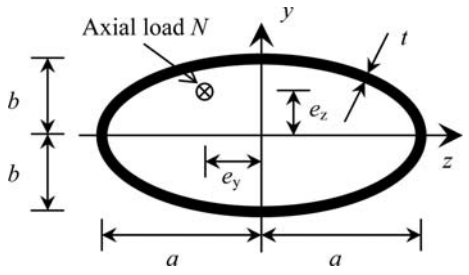

Figure 3. Geometry of an elliptical hollow section.

Table 2. Mean measured specimen dimensions and global imperfections.

Specimen	L m	$2a$ mm	$2b$ mm	t mm	ω_g mm
BC-1-$e_y = 0$	1.01	150.35	75.74	4.93	1.00
BC-1-$e_y = 25$	1.00	150.42	75.33	5.01	0.25
BC-1-$e_y = 50$	1.00	150.50	75.58	5.02	0.20
BC-1-$e_y = 150$	1.00	150.33	75.87	4.98	0.53
BC-1-$e_z = 0$	1.01	150.46	75.56	4.97	1.00
BC-1-$e_z = 15$	1.00	150.27	75.80	4.97	0.26
BC-1-$e_z = 25$	1.00	150.36	75.81	5.08	0.52
BC-1-$e_z = 100$	1.00	150.20	75.70	4.98	0.50
BC-2-$e_y = 0$	2.01	150.32	75.70	4.98	2.50
BC-2-$e_y = 25$	2.00	150.00	75.88	4.93	1.03
BC-2-$e_y = 50$	2.00	150.28	75.73	4.95	2.48
BC-2-$e_y = 150$	2.00	150.36	75.33	4.99	2.00
BC-2-$e_z = 0$	2.01	150.33	75.41	4.98	3.00
BC-2-$e_z = 25$	2.00	150.03	75.84	5.06	3.05
BC-2-$e_z = 50$	2.00	150.00	75.57	5.03	3.01
BC-2-$e_z = 150$	2.00	150.16	75.86	4.98	2.51
BC-3-$e_y = 0$	3.01	150.16	75.64	4.84	3.02
BC-3-$e_y = 25$	3.00	150.16	75.50	4.92	2.47
BC-3-$e_y = 50$	3.00	150.03	75.95	4.90	1.52
BC-3-$e_y = 150$	3.00	150.13	75.62	4.96	2.03
BC-3-$e_z = 0$	3.01	150.18	75.68	4.82	5.05
BC-3-$e_z = 50$	3.00	150.17	75.40	4.93	5.00
BC-3-$e_z = 100$	3.00	150.30	75.52	4.95	2.96
BC-3-$e_z = 200$	2.99	149.95	75.54	4.96	3.46

and e_y and e_z are the load eccentricities to the major and minor axes, respectively. Measurements of the cross-sectional geometry and maximum global geometric imperfections ω_g (determined by means of a laser beam directed along the member length) were taken prior to testing and are reported in Table 2. Residual stresses were not measured in this study, though as discussed in Law & Gardner (in press), the level of residual stresses in hot-finished EHS was found to be very low. Local geometric imperfections were not measured in this study since the proportions of the cross-sections examined are relatively stocky and insensitive to local buckling. The geometric properties for the EHS specimens were calculated using the exact formulae adopted in previous studies of EHS (Chan & Gardner 2008a, b).

Table 3. Summary of uniaxial eccentric compression test results.

Specimen	Tensile coupon	Eccentricity e_y mm	Eccentricity e_z mm	N_u kN	M_u kNm
BC-1-$e_y = 0$	BC-TC8	0	0	645.4	0.7
BC-1-$e_y = 25$	BC-TC4	25	0	390.8	9.9
BC-1-$e_y = 50$	BC-TC3	50	0	323.4	16.2
BC-1-$e_y = 150$	BC-TC5	150	0	142.4	21.4
BC-1-$e_z = 0$	BC-TC8	0	0	636.7	0.6
BC-1-$e_z = 15$	BC-TC6	0	15	350.5	5.3
BC-1-$e_z = 25$	BC-TC6	0	25	271.5	6.9
BC-1-$e_z = 100$	BC-TC6	0	100	112.3	11.3
BC-2-$e_y = 0$	BC-TC10	0	0	594.9	1.5
BC-2-$e_y = 25$	BC-TC4	25	0	339.8	8.8
BC-2-$e_y = 50$	BC-TC5	50	0	245.7	12.9
BC-2-$e_y = 150$	BC-TC9	150	0	123.5	18.8
BC-2-$e_z = 0$	BC-TC10	0	0	430.3	1.3
BC-2-$e_z = 25$	BC-TC4	0	25	211.7	5.9
BC-2-$e_z = 50$	BC-TC4	0	50	146.2	7.7
BC-2-$e_z = 150$	BC-TC9	0	150	73.3	11.2
BC-3-$e_y = 0$	BC-TC6	0	0	475.4	1.4
BC-3-$e_y = 25$	BC-TC7	25	0	281.8	7.7
BC-3-$e_y = 50$	BC-TC7	50	0	212.5	10.9
BC-3-$e_y = 150$	BC-TC7	150	0	113.5	17.2
BC-3-$e_z = 0$	BC-TC5	0	0	226.0	1.1
BC-3-$e_z = 50$	BC-TC6	0	50	109.4	6.0
BC-3-$e_z = 100$	BC-TC8	0	100	80.2	8.3
BC-3-$e_z = 200$	BC-TC8	0	200	51.6	10.5

2.2.2 *Test results*

The load eccentricities and key test results are summarised in Table 3, in which N_u is the ultimate applied load and M_u is the first-order elastic moment given by Equation 1.

$$M_{1st} = N_u \times (e + \omega_g) \tag{1}$$

All the beam-columns failed by flexural buckling and in-plane bending with no sign of lateral torsional buckling, as shown by Figure 2. For the beam-columns loaded eccentrically about the minor axis, all specimens failed in the minor axis direction only. For the beam-columns loaded eccentrically about the major axis, all specimens failed in the major axis direction only since the knife edges provided fixed end conditions about the minor axis and the buckling length in this direction was therefore halved, making major axis buckling critical. Overall, a general reduction in ultimate test load was observed with increasing eccentricities due to the higher bending effects.

2.3 *Compression and biaxial bending*

9 beam-columns of three different column lengths of 1 m, 2 m and 3 m were loaded biaxially. The tested member slendernesses of the pin-ended beam-columns ranged from 0.28 to 0.83 and 0.49 to 1.44

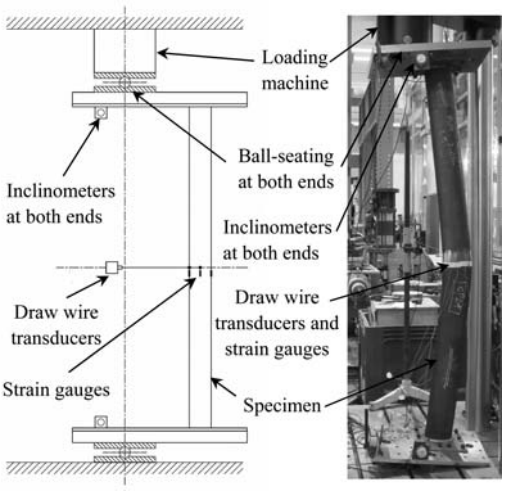

Figure 4. Biaxial compression test configuration – deformed specimen of BC-2-$e_y = 180$-$e_z = 30$.

about the major and the minor axes respectively. The load eccentricities were varied to achieve a range of load combinations.

2.3.1 *Test set-up*

The general configuration of the test set-up is depicted in Figure 4. The specimens were loaded by a 2000 kN Instron hydraulic machine through a ball-seating configuration at both ends to provide pinned end conditions about both principal axes. End plates were welded onto the specimens, as described previously.

The instrumentation employed herein was similar to that adopted in the uniaxial eccentric compression tests. In addition, two extra inclinometers were employed, one at each end of the specimens so that the end rotations about both two principal axes were measured. Four additional linear electrical resistance strain gauges were employed to monitor the strain distribution across the section. Displacement control and data logging were as previously described.

Measurements of the cross-sectional geometry and maximum global geometric imperfections in the major $\omega_{g,y}$ and minor axes $\omega_{g,z}$ were taken prior to testing and are reported in Tables 4 & 5.

2.3.2 *Test results*

The load eccentricities and key test results are summarised in Table 6, in which $M_{u,y}$ and $M_{u,z}$ are the bending moments about the major and minor axes respectively obtained at the ultimate load N_u. All the beam-columns failed by flexural buckling and bending about the two principal axes. Generally, the biaxially loaded beam-columns exhibit similar structural behaviour to the uniaxially loaded ones as described in Section 2.2. These test results, together with those from the uniaxial beam-column tests reported in Section 2.2, are further examined, replicated numerically and used for the validation of interaction formulae in the following sections.

Table 4. Mean measured specimen dimensions.

Specimen	L m	$2a$ mm	$2b$ mm	t mm
BC-1-$e_y = 40$-$e_z = 80$	1.00	150.12	75.42	4.96
BC-1-$e_y = 100$-$e_z = 60$	1.00	150.19	75.69	4.97
BC-1-$e_y = 140$-$e_z = 30$	1.00	150.16	75.52	4.99
BC-2-$e_y = 40$-$e_z = 90$	2.00	150.24	75.89	5.02
BC-2-$e_y = 120$-$e_z = 70$	2.00	150.55	75.58	5.01
BC-2-$e_y = 180$-$e_z = 30$	2.00	150.33	75.94	4.98
BC-3-$e_y = 80$-$e_z = 160$	2.96	150.17	75.57	4.96
BC-3-$e_y = 210$-$e_z = 120$	2.96	150.18	75.75	4.94
BC-3-$e_y = 310$-$e_z = 60$	2.96	150.20	75.82	4.98

Table 5. Mean measured global imperfections.

Specimen	Tensile coupon	$\omega_{g,y}$ mm	$\omega_{g,z}$ mm
BC-1-$e_y = 40$-$e_z = 80$	BC-TC7	0.25	0.25
BC-1-$e_y = 100$-$e_z = 60$	BC-TC7	0.15	0.10
BC-1-$e_y = 140$-$e_z = 30$	BC-TC6	0.13	0.25
BC-2-$e_y = 40$-$e_z = 90$	BC-TC10	1.03	2.08
BC-2-$e_y = 120$-$e_z = 70$	BC-TC10	−0.78*	0.25
BC-2-$e_y = 180$-$e_z = 30$	BC-TC9	1.00	1.50
BC-3-$e_y = 80$-$e_z = 160$	BC-TC4	3.10	2.50
BC-3-$e_y = 210$-$e_z = 120$	BC-TC2	3.00	3.00
BC-3-$e_y = 310$-$e_z = 60$	BC-TC1	2.00	1.50

* Negative value indicates that the initial imperfection is opposite to the direction of buckling.

Table 6. Summary of biaxial compression test results.

Specimen	Eccentricity e_y mm	Eccentricity e_z mm	N_u kN	$M_{u,y}$ kNm	$M_{u,z}$ kNm
BC-1-$e_y = 40$-$e_z = 80$	40	80	133.9	5.4	10.7
BC-1-$e_y = 100$-$e_z = 60$	100	60	144.3	14.5	8.7
BC-1-$e_y = 140$-$e_z = 30$	140	30	139.7	19.6	4.2
BC-2-$e_y = 40$-$e_z = 90$	40	90	107.5	4.4	9.9
BC-2-$e_y = 120$-$e_z = 70$	120	70	121.2	14.5	8.5
BC-2-$e_y = 180$-$e_z = 30$	180	30	108.7	19.7	3.4
BC-3-$e_y = 80$-$e_z = 160$	80	160	56.8	4.7	9.2
BC-3-$e_y = 210$-$e_z = 120$	210	120	56.2	12.0	6.9
BC-3-$e_y = 310$-$e_z = 60$	310	60	62.1	19.4	3.8

3 NUMERICAL SIMULATIONS

The behaviour of the tested beam-columns was initially replicated by finite element analysis using the measured dimensions of the test specimens and measured material stress-strain data. The finite element (FE) package ABAQUS (2006) was used throughout the study. The basic assumptions employed in the numerical models are similar to those employed for

the lateral torsional buckling specimens reported in Law & Gardner (in press).

Initial global geometric imperfections were incorporated by applying a lateral point load to the specimens at mid-height. The true material stress-strain relationship was generated by converting a multi-linear stress-strain curve derived from the static engineering stress-strain curves obtained from the tensile coupon tests. Boundary conditions were modelled to simulate pinned conditions at the ends of the beam-columns. The modified Riks method (ABAQUS 2006), which enables the post-ultimate behaviour to be traced, was employed to solve the geometrically and materially nonlinear numerical models.

Replication of the test results was found to be satisfactory with a mean ratio of test to FE ultimate load of 1.05. Typical load versus deflection curves are depicted in Figure 5. The numerical models were able to successfully capture the initial stiffness, ultimate capacity, general load-deformation response and failure patterns observed in the tests. It should be noted that the ultimate loads obtained from the tests were generally higher than the FE results; this is attributed to the use of static material properties in the FE models.

Upon verification of the general ability of the FE models to replicate the beam-column behaviour of EHS members with a cross-sectional aspect ratio of two, a series of parametric studies were conducted, aiming to investigate the influence of different aspect ratios and member slendernesses on the beam-column behaviour. The obtained results are used to develop design guidance for EHS beam-columns. A piecewise linear material stress-strain model developed from an average of the stress-strain curves obtained from the tensile coupon tests was employed in the parametric studies. Initial geometric imperfections with an amplitude ω_g of $L/500$, which is the tolerance stated in EN 10210-2 (2006), were included in the nonlinear parametric analyses by applying a lateral point load to the specimen at mid-height. The outer height and thickness of the cross-section considered in the parametric studies were fixed to 150 mm and 5 mm respectively. A range of cross-sectional aspect ratios from 2 to 4 and member slenderness $\overline{\lambda}_z$ of 0.5, 1.0 and 1.5 was considered. The results are utilised for the validation of proposed beam-column interaction formulae for elliptical hollow sections, as discussed in the following section.

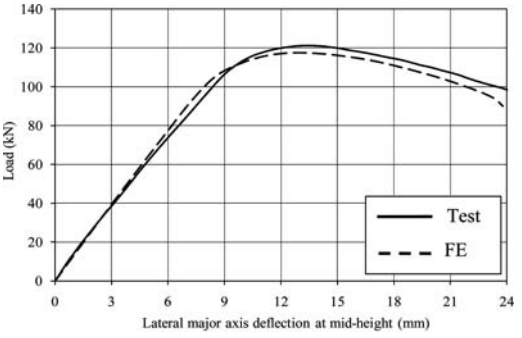

(a) Load versus major axis deflection at mid-height

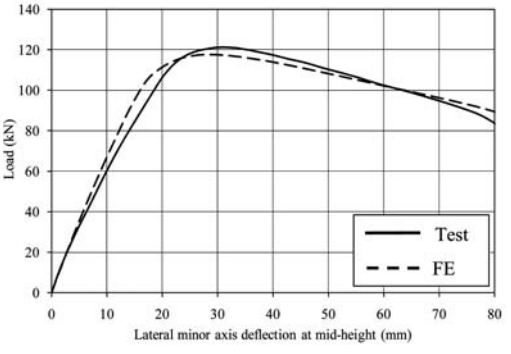

(b) Load versus minor axis deflection at mid-height

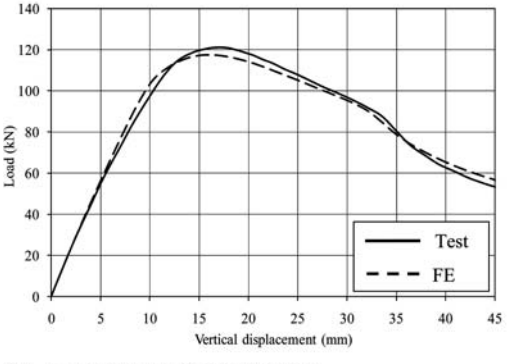

(c) Load versus vertical displacement

Figure 5. Comparison between test and FE results for BC-2-$e_y = 120$-$e_z = 70$.

4 DEVELOPMENT OF DESIGN RECOMMENDATIONS

In the design of an eccentrically loaded beam-column, either the strength of the cross-section or the stability of the member will govern the load carrying capacity, depending on the length of the beam-column. In Eurocode 3, two sets of design formulae for assessing the member stability of beam-columns, named Method 1 and Method 2 in EN 1993-1-1 (2005), were developed by the Technical Committee 8 – Structural Stability of the European Convention for Constructional Steelwork (Boissonnade et al. 2006). Method 1 was derived based on second-order in-plane elastic theory and further extended to spatial and elastic-plastic behaviour by a French-Belgian team (Boissonnade et al. 2004). Method 2 was developed on the basis of a semi-empirical approach utilising curve-fitting techniques to mainly numerical results by an Austrian-German team (Greiner & Lindner 2006).

4.1 *Existing buckling resistance check*

The design approach for treating member instability under combined compression and bending in

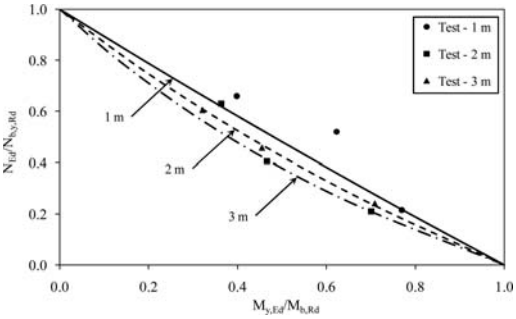

Figure 6. Interaction of axial load and major axis moment – tests and design curves in EN 1993-1-1 (2005).

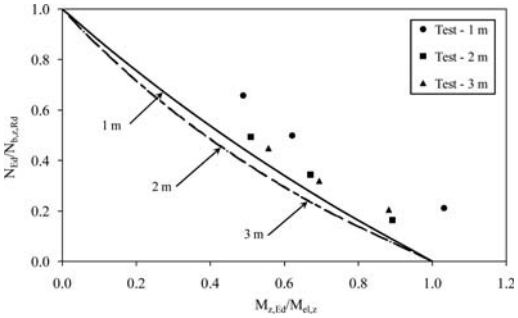

Figure 7. Interaction of axial load and minor axis moment – tests and design curves in EN 1993-1-1 (2005).

EN 1993-1-1 (2005) is based on the use of interaction formulae. In general, both Equations 6.61 and 6.62 in EN 1993-1-1 (2005) must be satisfied. Interaction factors can be found by either Method 1 or 2, which are described in Annex A and B of EN 1993-1-1 (2005) respectively. Applicability of the EN 1993-1-1 (2005) interaction formulae to EHS members is assessed in the following section on the basis of the experimental and numerical results generated in this study; the assessment and development is focussed on Method 2, since this is more practical for designers. Three principal cases: compression with major axis moment, compression with minor axis moment and compression with biaxial moments, are considered herein and design recommendations for EHS beam-columns are proposed. For the practical range of EHS column slendernesses considered ($\overline{\lambda}_z \leq 1.5$), the non-dimensional slenderness for lateral torsional buckling $\overline{\lambda}_{LT}$ is always less than 0.4 (0.4 being the slenderness below which LTB can be neglected). It is therefore assumed that lateral torsional buckling need not be considered in this study for practical EHS beam-columns.

4.1.1 *In-plane buckling under $N + M_y$*

For the EHS beam-columns loaded at an eccentricity to the major axis, all the tested specimen are classified as either Class 1 or 2 sections according to the classification guidance proposed by Gardner et al. (2011). For the stability interaction, Equation 6.61 in EN 1993-1-1 (2005) is always critical and the design buckling formula simplifies to:

$$\frac{N_{Ed}}{N_{b,y,Rd}} + k_{yy}\frac{M_{y,Ed}}{M_{b,Rd}} \leq 1 \qquad (2)$$

where N_{Ed} and $M_{y,Ed}$ are the compression force and the maximum moment about the major axis along the member length respectively, k_{yy} is an interaction factor, $N_{b,y,Rd}$ is the design buckling resistance of the member under pure compression about the major axis and $M_{b,Rd}$ is the design LTB resistance.

Figure 6 shows the test results with their corresponding interaction curves. Note that ultimate test loads and the corresponding first-order moments, as reported in Table 3, have been plotted and that $M_{b,Rd} = M_{pl,y,Rd}$. The test results generally follow the trend of the interaction curves, whereby failure occurs earlier for more slender columns due to more significant secondary effects; two data points (BC-2-$e_y = 50$ and BC-2-$e_y = 150$) lie marginally below their respective design curves.

In order to assess the effects of member slenderness $\overline{\lambda}_y$ and cross-sectional aspect ratio γ on the in-plane buckling behaviour of EHS beam-column members under axial compression and major axis bending, numerical results from the parametric studies described in Section 3 have also been compared with their corresponding design curves. Generally, the design curves provide satisfactory prediction of the actual behaviour of the EHS beam-column members with various member slendernesses and cross-sectional aspect ratios. It can be concluded that the design formulae for the in-plane buckling under axial compression and major axis bending (Equation 2) are also applicable to EHS members.

4.1.2 *In-plane buckling under $N + M_z$*

For the EHS beam-columns loaded at an eccentricity to the minor axis, all the tested specimen are classified as Class 3 sections according to the classification guidance proposed by Gardner et al. (2011). For the stability interaction, Equation 6.62 in EN 1993-1-1 (2005) is always critical and the design buckling formula simplifies to:

$$\frac{N_{Ed}}{N_{b,z,Rd}} + k_{zz}\frac{M_{z,Ed}}{M_{el,z}} \leq 1 \qquad (3)$$

where $M_{z,Ed}$ is the maximum moment about the minor axis along the member length, k_{zz} is an interaction factor, $N_{b,z,Rd}$ is the design buckling resistance of the member under pure compression about the minor axis, and $M_{el,z}$ is the elastic minor axis bending resistance.

Figure 7 shows the test results with their corresponding interaction curves. Note that ultimate test loads and the corresponding first order moments, as reported in Table 3, have been plotted.

The test results generally follow the trend of the interaction curves, whereby failure occurs earlier for the more slender members due to more significant

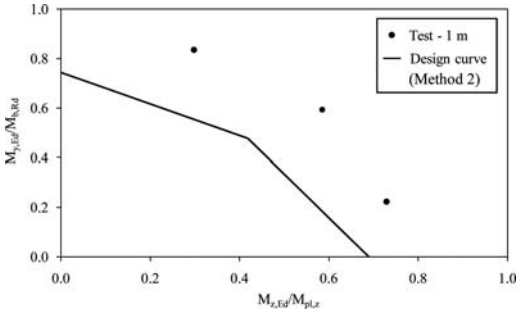

Figure 8. Interaction of axial compression and major and minor axis moments – tests and design curve from EN 1993-1-1 (2005) for 1 m beam-columns.

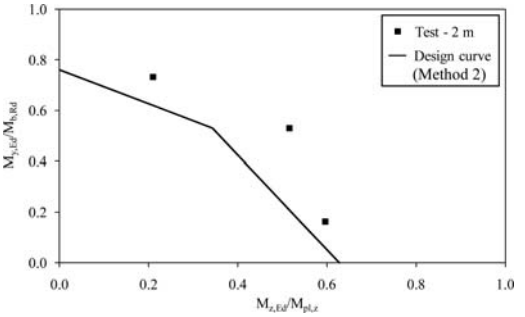

Figure 9. Interaction of axial compression and major and minor axis moments – tests and design curve from EN 1993-1-1 (2005) for 2 m beam-columns.

secondary effects. It should be noted that the non-dimensional slenderness of the 2 m and 3 m beam-columns are equal to or larger than 1.0, for which the same interaction curve applies; the response of the 2 m and 3 m test specimens are also similar, as shown in Figure 7. Satisfactory agreement between the numerical results from the parametric studies and the corresponding design curves was also achieved.

The beam-column behaviour under axial compression and minor axis bending was found to be generally similar to that under axial compression and major axis bending and it can be concluded that the existing design formulae for the in-plane buckling under axial compression and minor axis bending (Equation 3) are also applicable to EHS members.

4.1.3 *Buckling under $N + M_y + M_z$*

There is currently no guidance on the classification of EHS under combined compression plus biaxial bending. However, with reference to the classification proposal for compression plus uniaxial bending (Gardner et al. 2011), if the classification is performed considering the maximum stress from minor axis bending as uniform compression, which is clearly a conservative assumption, all the tested specimens are either Class 1 or 2 sections, or very marginally beyond Class 2 limits. Therefore, given the conservative assumption in the classification, all sections will be treated as Class 1–2, and compared with the corresponding interaction curves. For the biaxially loaded EHS beam-columns considered in this study, Equations 6.61 and 6.62 in EN 1993-1-1 (2005) simplify to:

$$\frac{N_{\mathrm{Ed}}}{N_{\mathrm{b,y,Rd}}} + k_{\mathrm{yy}} \frac{M_{\mathrm{y,Ed}}}{M_{\mathrm{b,Rd}}} + 0.6 k_{zz} \frac{M_{\mathrm{z,Ed}}}{M_{\mathrm{pl,z}}} \leq 1 \qquad (4)$$

$$\frac{N_{\mathrm{Ed}}}{N_{\mathrm{b,z,Rd}}} + 0.6 k_{\mathrm{yy}} \frac{M_{\mathrm{y,Ed}}}{M_{\mathrm{b,Rd}}} + k_{zz} \frac{M_{\mathrm{z,Ed}}}{M_{\mathrm{pl,z}}} \leq 1 \qquad (5)$$

The test results with their corresponding interaction curves are depicted in Figures 8 to 10. Note that ultimate test loads and the corresponding first order moments, as reported in Table 6, have been plotted.

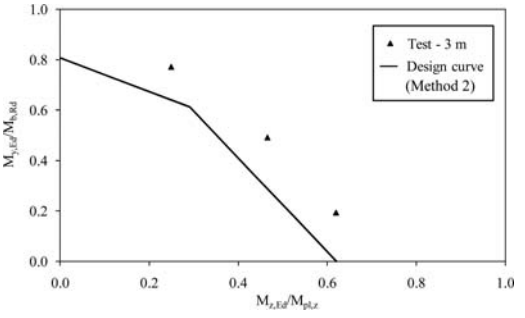

Figure 10. Interaction of axial compression and major and minor axis moments – tests and design curve from EN 1993-1-1 (2005) for 3 m beam-columns.

The test results generally follow the trend of the interaction curves, which become more conservative for the shorter beam-columns. Similar to the above sections, numerical results from the parametric studies (Section 3) on members with various slendernesses, cross-sectional aspect ratios and axial load levels have also been compared with the corresponding design curves to illustrate their effects on biaxially loaded EHS beam-columns.

Generally, the above comparisons have shown that the design curves currently given in Annex B of EN 1993-1-1 (2005) for RHS provide conservative predictions of the behaviour of the EHS beam-columns with various member slendernesses and cross-sectional aspect ratios and can be safely applied to EHS members. Similar to the beam-columns eccentrically loaded about one principal axis, the biaxially loaded members behave similarly for different aspect ratios.

5 CONCLUSIONS

Member instability in hot-finished EHS beam-columns has been investigated in this study. An experimental programme comprising 10 tensile coupon tests and 33 beam-column tests was carried out. The beam-column tests included 6 pure compression tests, 3 buckling about the major axis and 3 about the minor

axis, 18 eccentric compression tests, 9 inducing bending about the major axis and 9 about the minor axis, and a further 9 tests that induced compression and bending about both axes. All tested elliptical hollow sections had a constant cross-sectional aspect ratio of two and the non-dimensional column slenderness ranged from 0.28 to 0.84 in the major axis bending beam-column tests and from 0.49 to 1.44 in the minor axis bending and biaxially loaded beam-column tests. The key material properties, geometric measurements and test results have been reported.

A series of parametric studies based on the validated numerical models were then performed to investigate the influence of cross-sectional aspect ratios ranging from 2 to 4 and member slendernesses ranging from 0.5 to 1.5. On the basis of the experimental and numerical findings, existing design rules covering instability of hot-finished hollow section beam-columns have been assessed and were found to be applicable to EHS members.

REFERENCES

ABAQUS 2006. *ABAQUS/Standard User's Manual Volumnes I-III and ABAQUS CAE Manual. Version 6.6.* Pawtucket, USA, Hibbitt, Karlsson & Sorensen, Inc.

Boissonnade, N., Jaspart, J.P., Muzeau, J.P. & Vilette, M. 2004). New interatcion formulae for beam-columns in Eurocode 3: The French-Belgian approach. *J Constr Steel Res* 60(3–5): 421–431.

Boissonnade, N., Greiner, R., Jaspart, J.P & Lindner, J. 2006. Rules for member stability in EN 1993-1-1 Background documentation and design guidelines, *ECCS TC8, Report No. 119.*

Chan, T.M. & Gardner, L. 2008a. Compressive resistance of hot-rolled elliptical hollow sections. *Eng Struct* 30(2), 522–532.

Chan, T.M. & Gardner, L. 2008b. Bending strength of hot-rolled elliptical hollow sections. *J Constr Steel Res* 64(9): 971–986.

Chan, T.M. & Gardner, L. 2009. Flexural buckling of elliptical hollow section columns. *J Struct Eng-ASCE* 135(5): 546–557.

Chen, W.F. & Atsuta, T. 1976. Theory of beam-columns, Vol. 1 In-plane behaviour and design. McGraw-Hill, New York.

Chen, W.F. & Atsuta, T. 1977. Theory of beam-columns, Vol. 2 Space behaviour and design. McGraw-Hill, New York.

EN 10002-1 2001. *Metallic materials – Tensile testing – Part 1: Method of test at ambient temperature*, CEN.

EN 10210-2 2006. *Hot finished structural hollow sections of non-alloy and fine grain steels – Part 2: Tolerances, dimensions and sectional properties*. CEN.

EN 1993-1-1 2005. *Eurocode 3: Design of steel structures – Part 1-1: General rules and rules for buildings*, CEN.

Gardner, L., Chan, T.M. & Abela, J.M. 2011. Structural behaviour of elliptical hollow sections under combined compression and uniaxial bending. *Adv Steel Constr* 7(1): 86–113.

Gardner, L. & Chan, T.M. 2007. Cross-section classification of elliptical hollow sections. *Steel Compos Struct* 7(3): 185–200.

Gardner, L., Chan, T.M. & Wadee, M.A. 2008. Shear response of elliptical hollow sections. *P I Civil Eng – Str B* 161(6): 301–309.

Greiner, R. & Lindner, J. 2006. Interaction formulae for members subjected to bending and axial compression in Eurocode 3 – the Method 2 approach. *J Constr Steel Res* 62(8): 757–770.

Insausti, A. and Gardner, L. (2011). Analytical modelling of plastic collapse in compressed elliptical hollow sections. *J Constr Steel Res* 67(4), 678–689.

Law, K.H. and Gardner, L. (2012). Lateral instability of elliptical hollow section beams. *Eng Struct* 37: 152–166.

Massonnet, C. 1976. Forty years of research on beam-columns in steel. *Solid Mech Arch* 1:1.

Nowzartash, F. & Mohareb, M. 2009. Plastic interaction relations for elliptical hollow sections. *Thin-Walled Structures* 47(6–7): 681–691.

SCI/BSCA 2009. *Steel Building Design: Design Data in accordance with Eurocodes and the UK National Annexes*. The Steel Construction Institute and British Constructional Steelwork Association, SCI Pub. No. P363.

Zhao, X.L., Packer, J.A. (2009). Tests and design of concrete-filled elliptical hollow section stub columns. *Thin-Walled Structures* 47(6–7):617–628.

Tubular Structures XIV – Gardner (Ed.)
© 2012 Taylor & Francis Group, London, ISBN 978-0-415-62137-3

Buckling and classification of high-strength steel CHS tubular members under axial compression and bending

Patricia Pappa & Spyros A. Karamanos
Department of Mechanical Engineering, University of Thessaly, Volos, Greece

ABSTRACT: EN 1993-1-1 provisions classify high-strength steel CHS members with relatively low values of D/t ratio as Class 3 or 4, so that their strength is based on elastic behavior only, neglecting their capability of sustaining inelastic deformation before a maximum resistance is reached. To investigate the applicability of the above classification, a special-purpose numerical technique is employed to examine the resistance against local buckling of high-strength steel seamless tubular members with significant thickness, that exhibit local buckling in the plastic regime under axial compression and bending. The numerical technique employs large inelastic strains, accounts for the presence of initial imperfections/residual stresses, and is capable of describing deformation and buckling of tubular cross-sections well beyond yielding of the steel material. Imperfections and residual stresses from real measurements are used. Numerical results are presented in terms of both the ultimate load and the deformation capacity of typical cross-sections, and are compared with available experimental data. The results aim at evaluating the applicability of EN 1993-1-1 for cross-sectional classification of high-strength steel CHS seamless tubular members.

1 INTRODUCTION

High-strength steel CHS tubes are becoming popular in a variety of structural engineering applications, such as tubular columns of building systems or members of tubular lattice structures. The principal characteristic of these steel products, with respect to CHS tubes of normal steel grades, is the elevated yield stress value, which implies increased ultimate capacity, resulting in a good relationship between weight and strength. They can also be efficient in cases where space occupancy becomes a critical design criterion.

According to current design practice, the ultimate capacity of steel sections under axial and bending loads depends primarily on whether the section is classified as "compact" or "non-compact", i.e. on the ability of the cross-section to sustain significant inelastic deformation before failure in the form of local buckling. In particular, the provisions of EN 1993-1-1 standard specify four (4) cross-sectional classes, where Class 4 corresponds to thin-walled sections, which are able to sustain axial/bending load only in the elastic range, Class 1 includes thick-walled sections that are able to deform well into the plastic regime, without exhibiting local buckling, and Classes 2 and 3 refer to intermediate type of structural behavior. For the case of CHS tubular members, classification in EN 1993-1-1 is based on the value of the diameter-to-thickness ratio, as well as on the value of the material yield stress, as shown in the second column of Table 1. The same classification is also adopted by the CIDECT guidelines (Rondal *et al*., 1996) for hollow section stability, whereas similar provisions for cross-sectional classification on CHS members can be found in other specifications (e.g. AISC, API RP2A – LRFD).

Table 1. Classification in EN 1993-1-1, based on the value of the diameter-to-thickness ratio.

Class	Class limits	Class limits in terms of shell slenderness λ
1	$D/t \le 50\varepsilon^2$	$\lambda \le \lambda_1 = 0.278$
2	$50\varepsilon^2 \le D/t \le 70\varepsilon^2$	$\lambda_1 = 0.278 < \lambda \le \lambda_2 = 0.329$
3	$70\varepsilon^2 \le D/t \le 90\varepsilon^2$	$\lambda_2 = 0.329 < \lambda \le \lambda_3 = 0.373$
4	$D/t \ge 90\varepsilon^2$	$\lambda > \lambda_3 = 0.373$

The above classification provisions have not been initially developed for the case of high-strength steel CHS tubular members with $\sigma_Y > 460$ MPa. In the EN 1993 steel design framework, a new standard has been issued (EN 1993-1-12) to specify the applicability of the other EN 1993-1-xx standards in high-strength steel applications. According to EN 1993-1-12, the EN 1993-1-1 classification provisions, shown in Table 1, may be applied for high-strength steel members as well. However, the existing classification for CHS tubular members appears to be rather conservative for high-strength steel tubular members; one can readily obtain from Table 1 that CHS sections with $D/t = 35$ and $\sigma_Y = 690$ MPa, are classified as Class 4 sections, which implies a low ultimate capacity, within the elastic range.

The key issue in the above classification of CHS members is their cross-sectional strength, mainly in terms of local buckling, which constitutes a shell-buckling problem in the inelastic range. Inelastic buckling of relatively thick-walled steel cylinders under compressive loads has been the issue of significant research. Experimental observations (Lee 1962; Batterman, 1965) have been shown that under pure axial compression, thick-walled cylinders – in contrast with thin-walled ones – do not fail abruptly, but one can observed significant wall wrinkling before an ultimate load occurs. Analytically, a main challenge for solving this problem has been the combination of structural stability principles with inelastic multi-axial material behavior. In particular, it has been shown that buckling predictions depend on the choice of plasticity theory (Gelin 1979; Tvergaard 1983). For a detailed presentation of metal cylinder buckling behavior under uniform axial compression, the reader is referred to the recent papers by Bardi & Kyriakides (2006) and Bardi *et al*. (2006).

In addition to uniform axial compression, bending buckling of tubular members has also received significant attention, motivated mainly by their use in pipeline applications. Experimental works indicated that failure of thick-walled tubes under bending is associated with tube wall wrinkling, has several similarities with the case of uniform axial compression, but is characterized by a nonlinear prebuckling state – due to cross-sectional ovalization – and a more localized buckling pattern on the compression side of the cylinder. The reader is also referred to the papers by Ju & Kyriakides (1992) and Karamanos & Tassoulas (1996), where analytical/numerical tools have been developed for simulating the formation of local buckling due to bending.

The present research aims at a examining the cross-sectional classification of high-strength steel CHS seamless tubular members, and is part of an extensive European research on the structural behavior of high-strength steel tubular members. The same high-strength steel tubes have also been considered by Pournara *et al*. (2012) in terms of their structural beam-column behavior, and the need for a more accurate classification of high-strength steel CHS sections has been addressed.

The investigation described in the present paper is numerical, based on a special-purpose finite element formulation, presented elsewhere (Karamanos & Tassoulas 1996), and focuses on the buckling analysis of high-strength steel cylindrical shells under axial compression and bending loading. The analysis steps are aimed at determining the maximum load at which failure occurs, either because of bifurcation to a wavy pattern or due to localization of deformation.

The seamless tubes under consideration have yield stress equal or higher than 590 MPa, and diameter-to-thickness ratios ranging between 20 and 60, which are typical for structural applications. Initial imperfections and residual stresses from real measurements are taken into account in the present analysis. The numerical results are presented in the form of diagrams, showing the cylinder strength and deformation capacity (axial and bending) in terms of cylinder slenderness, and are aimed towards a evaluating applicability of existing classification rules for high-strength steel CHS tubes.

2 NUMERICAL TECHNIQUE

2.1 *Formulation and finite element discretization*

The nonlinear formulation adopted in the present work was introduced in its general form by Needleman (1982) and has been employed for the nonlinear analysis of relatively thick steel tubular members (Karamanos & Tassoulas 1996). The cylindrical shell is considered as a continuum, described through a Lagrangian approach with convected coordinates. The hypoelastic constitutive equations relate the convected rate of Kirchhoff stress to the rate-of-deformation tensor, where plasticity effects are taken into account through a large-strain J_2 flow plasticity model with isotropic hardening. Following classical shell theory, the traction component normal to any shell lamina is imposed to be zero and tube thickness is assumed constant.

Discretization of the continuum is considered through the use of the three-node "tube element", introduced in Karamanos & Tassoulas (1996). It couples longitudinal (beam-type) with cross-sectional deformation (ovalization and warping). Convected coordinates (θ, ζ, ρ) are in the hoop, axial and radial direction in the undeformed configuration. Nodes are located along the cylinder axis, which lies on the plane of bending, and each node possesses three degrees of freedom (two translational and one rotational). A reference line is chosen within the cross-section at node (k) and a local Cartesian coordinate system is defined, so that the $\bar{x}, \bar{y}$ axes define the cross-sectional plane. The orientation of node (k) is defined by the position of three orthonormal vectors $\mathbf{e}_x^{(k)}$, $\mathbf{e}_y^{(k)}$ and $\mathbf{e}_z^{(k)}$. For in-plane (ovalization) deformation, fibers initially normal to the reference line remain normal to the reference line. Furthermore, those fibers may rotate in the out-of-plane direction by angle $\gamma(\theta)$. Using quadratic interpolation polynomials $N^{(k)}(\zeta)$ in the longitudinal direction, the position vector $\mathbf{x}(\theta, \zeta, \rho)$ of an arbitrary point at the deformed configuration is:

$$\mathbf{x} = \sum_{k=1}^{3} \left[\mathbf{x}^{(k)} + \mathbf{r}^{(k)}(\theta) + \rho \mathbf{n}^{(k)}(\theta) + \rho\gamma(\theta)\mathbf{e}_z^{(k)} \right] N^{(k)}(\zeta) \quad (1)$$

where $x^{(k)}$ is the position vector of node (k), $r^{(k)}(\theta)$ is the position of the reference line of cross-section corresponding to node (k), and $n^{(k)}(\theta)$ is the "in-plane" outward normal of the reference line at the deformed configuration. Using nonlinear ring theory, $r^{(k)}(\theta)$ and $n^{(k)}(\theta)$ can be expressed in terms of the radial, tangential and out-of-plane displacements of the reference line, denoted as $w(\theta)v(\theta)$ and $u(\theta)$ respectively.

Functions $w(\theta)v(\theta)$, $u(\theta)$ and $\gamma(\theta)$ are discretized as follows:

$$w(\theta) = a_0 + a_1 \sin\theta + \sum_{n=2,4,\ldots} a_n \cos n\theta + \sum_{n=3,5,\ldots} a_n \sin n\theta \quad (2)$$

$$v(\theta) = -a_1 \cos\theta + \sum_{n=2,4,6,\ldots} b_n \sin n\theta + \sum_{n=3,5,7,\ldots} b_n \cos n\theta \quad (3)$$

$$u(\theta) = \sum_{n=2,4,6,\ldots} c_n \cos n\theta + \sum_{n=3,5,7,\ldots} c_n \sin n\theta \quad (4)$$

$$\gamma(\theta) = \sum_{n=0,2,4,6,\ldots} \gamma_n \cos n\theta + \sum_{n=1,3,5,7,\ldots} \gamma_n \sin n\theta \quad (5)$$

Coefficients a_n, b_n refer to in-plane cross-sectional (ovalization) deformation, whereas c_n, γ_n refer to out-of-plane (warping) cross-sectional deformation.

The nonlinear governing equations are solved through an incremental Newton-Raphson iterative numerical procedure, enhanced to enable the tracing of postbuckling "snap-back" equilibrium paths through an arc-length algorithm (Crisfield 1983).

2.2 *Bifurcation in the inelastic range*

Bifurcation instability in axially or bending loaded shells in the inelastic range is checked o, through the evaluation of Hill's "comparison solid" functional, as described in Hutchinson (1974). Loss of positive definiteness of this functional determines the buckling load. Positive definiteness is evaluated through an eigenvalue analysis on the pre-buckling solution, and the corresponding eigenfunction is the buckling shape (mode) of the cylinder.

2.3 *Material moduli for buckling calculations*

Early attempts to predict the buckling load of relatively-thick metal shells (Lee 1962; Batterman, 1965) indicated that analytical predictions are in closer agreement with test results when J_2 deformation-plasticity theory moduli are employed, instead of the classical J_2 flow-plasticity moduli. This has been verified in more recent works (e.g. Bardi *et al*. 2006), and is attributed to the "softer" moduli of the deformation theory, simulating a "vertex" or "corner" (i.e. a high-curvature region on the yield surface at the point of loading), reported in experimental observations, whereas flow theory assumes always a smooth yield surface, resulting in "stiffer" material moduli for case of abrupt change of direction in the stress space (e.g. when buckling occurs). To account for this discrepancy, the J_2-flow theory is used to trace the load-displacement equilibrium path, as described in section 2.1, whereas the J_2-deformation moduli are employed to detect bifurcation in the eigenvalue analysis of the "comparison solid" functional, as described in section 2.2.

2.4 *Initial imperfections and residual stresses*

The finite element model is capable of including the effects of initial imperfections, by prescribing a desired configuration of the shell in the initial (reference) stage. In the present analysis, the initial imperfection is assumed in a wavy form, similar to the buckling shape obtained from the bifurcation analysis on the pre-buckling equilibrium path. In addition to initial imperfections, the finite element model accounts for the presence of residual stresses, which have a significant effect on the buckling load. The amplitudes of initial imperfections and residual stresses are obtained from the corresponding measurements described in the next section.

3 IMPERFECTION MEASUREMENTS

3.1 *Imperfection measurements*

Initial wrinkling measurements have been obtained using an ultrasonic device. The tube wall wrinkling was measured every 10 mm along 8 equally-spaced generators, for a pipe length of equal to about two tube diameters, as shown in Figure 1a, for three typical generators.

These measurements along generators have been processed to estimate initial wrinkling as well as cross-sectional distortions; i.e. out-of-roundness imperfections when a specific cross section is considered.

It is assumed that the deviation of every cross-section from the perfect round shape is the superposition of an "extensional" component of uniform value around the cross-section, which can axisymmetric initial imperfection, and non-uniform part which corresponds to cross-sectional out-of-roundness in Figure 1b. In Figures 2 and 3, $\tilde{\omega}_0$ and $\tilde{\omega}_n$ represent the measured amplitudes of the axisymmetric and the non-uniform imperfection components respectively with

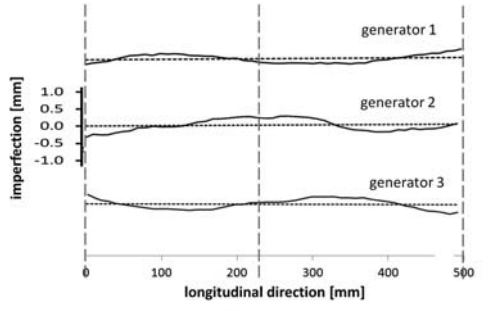

(a)

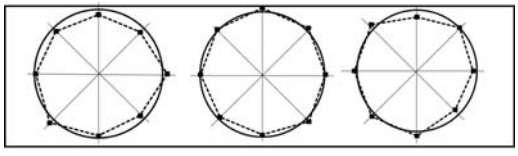

(b)

Figure 1. Typical data from (a) measurement of generator geometry (b) out-of-roundness of three cross-sections.

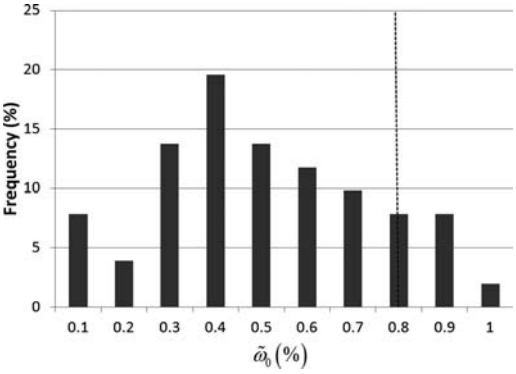

Figure 2. Statistical evaluation of $\tilde{\omega}_0$, the measured absolute-value amplitude of the axisymmetric imperfection.

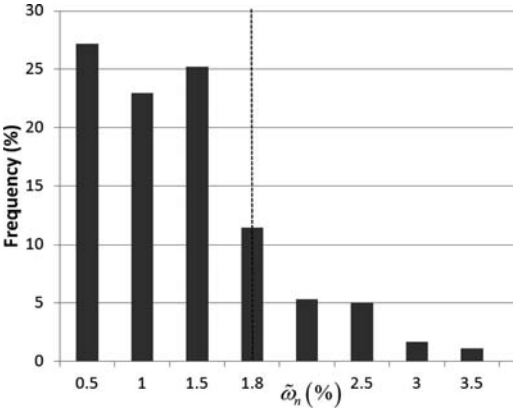

Figure 3. Statistical evaluation of $\tilde{\omega}_n$, the measured absolute-value amplitude of the non-axisymmetric imperfection.

respect to tube thickness. A statistical evaluation of $\tilde{\omega}_0$ and $\tilde{\omega}_n$ is offered in those Figures; the values of $\tilde{\omega}_0 = 0.8\%$ and $\tilde{\omega}_n = 1.8\%$ correspond to an 80% upper limit of the measurements, and are considered as representative initial imperfection values to be used the parametric study described in the next section.

3.2 *Residual stresses*

Residual stress measurements have also been performed in both the axial and the circumferential direction (Pournara *et al*. 2012). The measurements in the hoop direction are obtained through the "splitting ring" method, as specified in ASTM E1928-99, and resulted in an opening deformation (gap) of 17 mm, corresponding to a maximum hoop stress of 122 MPa (about 16% of the yield stress). Furthermore, to estimate the residual stresses in the axial direction, longitudinal strips have been obtained from the tubes, and their curvature has been measured, corresponding to a maximum stress of 26 MPa, which is only 4% of the yield stress. These values are very low and are attributed to the fact that the tubes under examination are seamless.

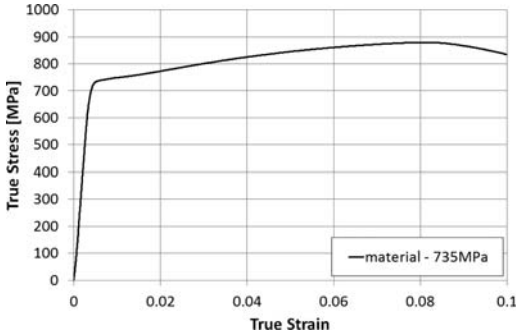

Figure 4. Nominal stress – engineering strain curve of the high-strength steel material.

4 NUMERICAL RESULTS

Results are obtained for 355.6-mm-diameter high-strength-steel tubes with thickness ranging between 6.4 mm and 16 mm covering a wide range of structural CHS sections. Two materials with yield stress equal to 590 MPa and 735 MPa are used, with nearly constant hardening modulus equal to $E/40$ (Pournara *et al*. 2012) as shown in the nominal stress – engineering strain curve of the high-strength steel material ($\sigma_Y = 735$ MPa) in Figure 4.

4.1 *Methodology for axial loading*

Infinitely long cylindrical shells with axisymmetric and non-axisymmetric initial imperfections are analyzed. Non-axisymmetric modes and bifurcations along the equilibrium path are identified by the implementation of the "tube-element". Experimental observations as well as numerical results have shown that first wrinkling in the plastic range is axisymmetric. The corresponding bifurcation load and wavelength can be calculated analytically using equations 6 and 7.

$$\sigma_{cr} = \left[\frac{C_{11}C_{22} - C_{12}^2}{3}\right]^{1/2}\left(\frac{t}{R}\right) \tag{6}$$

$$L_{hw} = \left[\frac{C_{11}^2}{12\ C_{11}C_{22} - C_{12}^2}\right]^{1/4} Rt^{\,1/2} \tag{7}$$

where R and t are the radius and wall thickness of the tube and $C_{a\beta}$ are the instantaneous material moduli according to J_2 deformation plasticity theory, at the bifurcation stage (Kyriakides & Corona 2007).

The present analysis follows the steps described by Bardi *et al*. (2006). Assuming a half-wave length from equation (7), axisymmetric wrinkling on the pre-buckling state for the uniformly-compressed cylinder is determined. Then, considering a tube segment of length equal to twice the value of half-wavelength ($L = 2L_{hw}$), and an axisymmetric initial imperfection, secondary bifurcation to a non-axisymmetric mode is

calculated. In this analysis, the axisymmetric imperfection amplitude ω_0 is 0.8%, as indicated by the measurements (section 3).

Subsequently, two possible limit states are examined. First, localization of the axisymmetric wrinkling pattern is examined, using a tube segment of length equal to several half-wavelengths. Considering a small bias in the amplitude of one wrinkle, the analysis leads to a maximum load N_1 due to wrinkle localization denoted as limit state (a). In addition, a tube segment of length equal to two half-wavelenghts with a combination of axisymmetric and non-axisymmetric imperfections is analyzed, with relative amplitudes ω_0 and ω_n equal to 0.8% and 1.8% respectively, so that a maximum load N_n is obtained. The smallest value of N_1 and N_n determines the ultimate axial load (strength) of the cross-section N_u.

4.2 *Methodology for bending loading*

The second part of this study concerns the prediction of ultimate capacity under bending loading, following the analysis steps described by Ju & Kyriakides (1992). The analysis is similar to the one in axial loading described above. At first, wrinkling on the ovalization bending prebuckling state is determined, and the corresponding half-wavelength is computed (L_{hw}). Then, using an initial imperfection on a tube segment of length equal to $2L_{hw}$, secondary bifurcation is calculated.

Subsequently, two possible limit states are examined, following a methodology similar to the one described for axial loading; (a) localization of wrinkling pattern and (b) analysis under a combination of imperfection corresponding to initial and secondary buckling modes. The minimum value from the corresponding maximum moments M_1 and M_n determines the ultimate moment of the cross-section, denoted as M_u.

4.3 *Parametric study*

The above advanced numerical tools are used to examine buckling of cylindrical high-strength steel shells under pure axial compressive load and pure bending. The cylindrical shells are thick-walled with properties shown in Table 2.

The behavior is summarized schematically in the axial load-displacement response of the thin-walled Tube 1 in Figure 5, whereas the behavior of Tube 4 is shown in Figure 6. The load is normalized with the value $N_Y = \sigma_Y A$, where A and σ_Y are the cross sectional area and the yield stress, respectively. The reported displacement is normalized by the tube length. At some displacement level indicated by the first "↓" on the response, first axisymmetric wrinkling is calculated. Secondary bifurcation to a non-axisymmetric mode on the primary path is calculated indicated by the second "↓". The paths corresponding to the two possible limit states are examined, as described in section 4.1. The ultimate axial load (strength) of the cross-section

Table 2. Geometric and mechanical properties of tubes.

Tube	t (mm)	D/t*	σ_y (MPa)	λ	Class**
1	6.4	55.56	735	0.517	4
2	8.0	44.45	735	0.463	4
3	10.0	35.56	735	0.414	4
4	12.5	28.45	735	0.370	3
5	14.2	25.05	735	0.347	3
6	16	22.22	735	0.327	2
7	14.2	25.05	590	0.311	2
8	16	22.22	590	0.293	2

** D is equal to 355.6 mm for all tubes*
*** According to EN-1993-1-1*

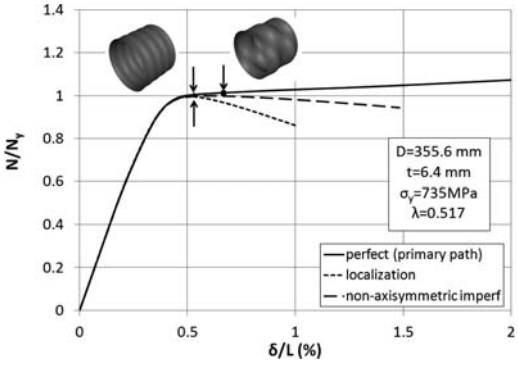

Figure 5. Axial load – displacement diagram of Tube 1.

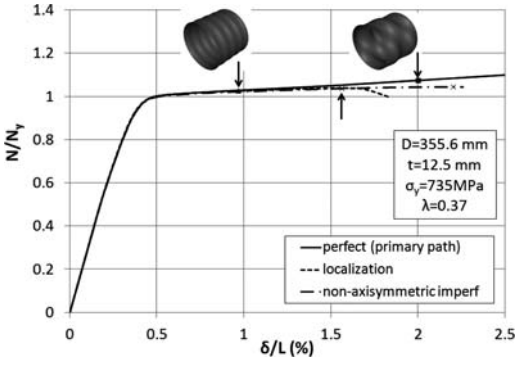

Figure 6. Axial load – displacement diagram of Tube 4.

N_u, is equal to N_1, for the localization analysis and is indicated by the arrow "↑" in the two graphs.

The bending behavior is shown in the moment-curvature response of Tube 1 in Figure 7 and of Tube 4 in Figure 8. The moment is normalized by the fully-plastic moment ($M_p = \sigma_Y t D^2$) and the curvature is normalized by the value of characteristic value $k_i = t/D^2$.

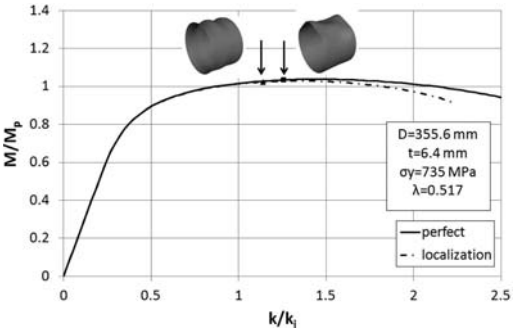

Figure 7. Moment-curvature diagram of thin-walled Tube 1.

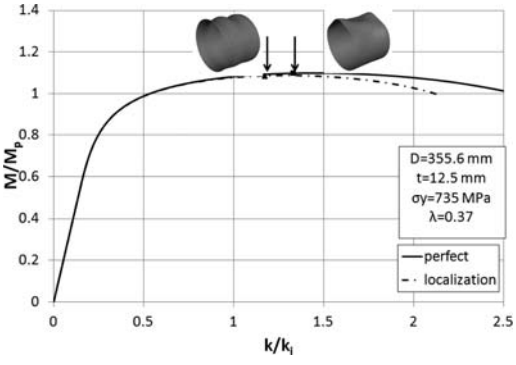

Figure 8. Moment-curvature diagram of Tube 4.

5 EXPERIMENTAL RESULTS

Some limited experimental results on the high-strength steel CHS seamless tubes under consideration are also reported, for verification purposes. The tests have been conducted by CSM, and comprise three (3) tests with uniform axial compression, and two (2) tests on bending. The tubes have cross-sections denoted as A, B and C (see Table 3), and a steel material with yield stress equal to 735 MPa. The slenderness values for sections A, B and C are equal to 0.370, 0.395 and 0.305. The axial load tests failed because of buckle development in the form of bulging near the welds, a typical failure mode for this type of loading. All three tests showed that they are capable of sustaining an axial load higher than the full plastic thrust of the section (see Table 3). The two bending experiments on sections A and B, because of test set-up limitations, did not reach the local buckling stage. Nevertheless, it has been possible to bend the two tubes at curvature levels corresponding to bending moments higher than the fully plastic moment (see Table 3).

Table 3. Experimental results on the high-strength steel tubes.

Section	D (mm)	t (mm)	Yield stress [MPa]	Ultimate thrust, N_u [kN] (N_u/N_Y)	Ultimate moment, M_u [kNm] (M_u/M_Y)
A	355.6	12.5	735	10254 (1.033)	1168.6 (1.402)
B	323.9	10	735	7961 (1.082)	805.93 (1.438)
C	193.7	10	735	4414 (1.102)	

6 CLASSIFICATION OF HSS CHS MEMBERS

6.1 *Current design practice*

Table 1 shows the classification of CHS tubular members according the EN 1993-1-1. For consistency with the present analysis, the slenderness limits have been also given in terms of the so-called "shell slenderness", defined as:

$$\lambda = \sqrt{\sigma_Y / \sigma_e} \tag{8}$$

where

$$\sigma_e = 0.605 E C_x t / R \tag{9}$$

is the elastic buckling stress, and the value of C_x is taken equal to 0.6, representing an infinitely long cylinder, free of boundary condition effects.

For Class 1, 2 and 3 CHS sections ($\lambda \leq 0.372$), the ultimate axial compressive capacity N_u is equal to the fully-plastic axial load $N_Y = \sigma_Y A$, where A is the cross-sectional area. If the value of λ exceeds 0.372, then the cross-section is classified as Class 4, implying that buckling occurs in the elastic range, and its ultimate axial compressive capacity is calculated from the EN 1993-1-6 rules for buckling of cylindrical shells, as follows:

$$N_u = \sigma_{x,Rk} A \tag{10}$$

where the buckling strength $\sigma_{x,Rk}$ can be written:

$$\sigma_{x,Rk} = \chi(\lambda)\sigma_Y \tag{11}$$

The reduction function χ depends on shell slenderness as follows:

$$\chi(\lambda) = \begin{cases} 1 & \lambda \leq 0.2 \\ 1 - 0.6\left(\dfrac{\lambda - 0.2}{\lambda_p - 0.2}\right) & 0.2 < \lambda \leq \lambda_p \\ \alpha/\lambda^2 & \lambda > \lambda_p \end{cases} \tag{12}$$

where, assuming excellent manufacturing quality

$$\alpha = \frac{0.62}{1 + 1.91\left(\Delta w_\kappa / t\right)^{1.44}} \tag{13}$$

$$\Delta w_\kappa / t = (1/40)\sqrt{R/t} \tag{14}$$

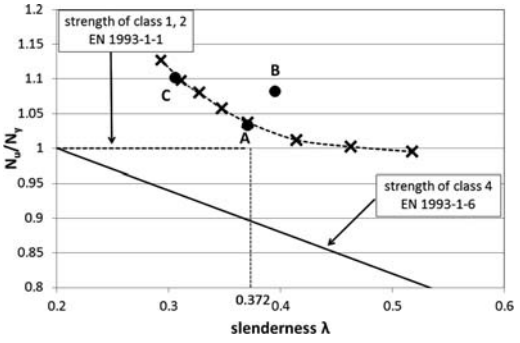

Figure 9. Stability curve in EN1993 compared with numerical results and experimental data.

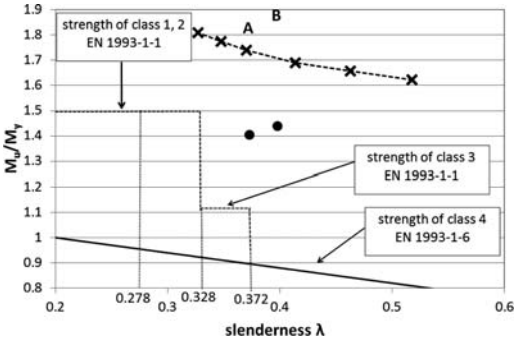

Figure 10. Stability curve in EN1993 compared with numerical results and experimental data.

$$\lambda_p = 1.581\sqrt{\alpha} \tag{15}$$

For the case of bending loading, Class 1 and 2 cross-sections have an ultimate moment capacity M_u equal to the plastic bending moment $M_P = \sigma_Y W_{pl}$, where W_{pl} is the plastic bending modulus of the cross-section. For Class 3 sections, M_u is equal to the elastic bending moment $M_Y = \sigma_Y W_{el}$, where W_{el} is the elastic bending modulus. Finally, for Class 4 CHS sections, M_u is equal to $\sigma_{x,Rk} W_{el}$, where $\sigma_{x,Rk}$ is calculated from equations (11)–(15) above.

6.2 *Comparison with numerical results and test data*

The above predictions of ultimate capacity are plotted against the finite element results and the test data, in Figures 9 and 10 for the axial compression and bending respectively, with respect to the slenderness parameter λ. The ultimate axial load and bending moment values are normalized by N_Y and M_Y respectively. The comparison between numerical results, test data and design provisions indicates that the EN 1993 standard provides a rather conservative ultimate capacity in terms of both axial and bending moment for the value of initial imperfections assumed in the present study.

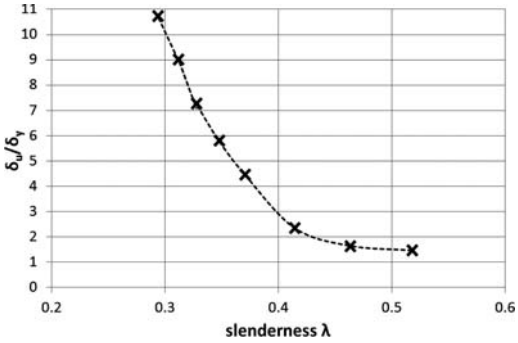

Figure 11. Deformation capacity of the cross-section under axial load conditions.

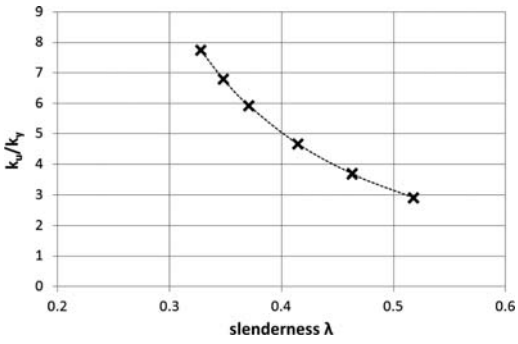

Figure 12. Deformation capacity of the cross-section under bending moment.

In addition, Figures 11 and 12 show the numerical results for the deformation capacity of the cross-section for axial (δ_u) and bending (k_u) respectively, normalized by the corresponding values at yielding stage (δ_Y and k_Y), with respect to the value of λ. The values of δ_u and k_u correspond to N_u and M_u respectively. The values of δ_u/δ_Y and k_u/k_Y indicate significant deformation capacity of the tubes under consideration, well beyond first yielding.

7 CONCLUSIONS

Using a special-purpose numerical technique, wrinkling and post-wrinkling behavior of thick-walled high-strength CHS seamless tubular subjected to both bending and axial loading have been investigated, in order to determine their ability to sustain load above the first yield level. The results have been compared with limited test data, and with the EN 1993 classification provisions.

Considering imperfections and residual stresses obtained from real measurements on high-strength steel seamless tubes, the finite element results indicated significantly higher ultimate capacity with respect to the design rules of the above specification rules, as well as a substantial deformation capacity.

ACKNOWLEDGEMENT

Financial support for this work has been provided from the Research Fund for Coal and Steel of the European Commission, within ATTEL project: "Performance-Based Approaches for High Strength Steel Tubular Columns and Connections under Earthquake and Fire Loadings", Grant No RFSR-CT-2008-00037. The authors wish to thank Centro Sviluppo Materiali S.p.A, Rome, Italy, for providing the test results, as well as measurements of initial imperfections, and material data.

REFERENCES

American Institute of Steel Construction, 2005, "Steel Construction Manual" – Thirteenth Edition, AISC 325-05.

Bardi, F.C., Kyriakides, S., 2006. "Plastic buckling of circular tubes under axial compression-part I: Experiments" *International Journal of Mechanical Sciences*, 48, 830–841.

Bardi, F.C., Kyriakides, S., Yun, H.D., 2006. "Plastic buckling of circular tubes under axial compression-part II: Analysis" *International Journal of Mechanical Sciences*, 48, 842–854.

Batterman, S. C., 1965. *Plastic buckling of axially compressed cylindrical shells*, AIAA Journal, 3, 316–325.

CEN EN 1993-1-1, 2005, "Eurocode 3: Design of steel structures. Part 1-1: General rules and rules for buildings." European Committee for Standardization.

CEN EN 1993-1-6, 2007, "Eurocode 3: Design of steel structures. Part 1-6: Strength and Stability of Shell Structures." European Committee for Standardization.

CEN EN 1993-1-12, 2007, "Eurocode 3: Design of steel structures. Part 1.12: Additional rules for the extension of EN 1993 up to steel grades S 700." European Committee for Standardization.

Crisfield, M.A., 1991. Non-*linear finite element analysis of solids and structures*, vol. 1, John Wiley and Sons.

Gellin, S., 1979. Effect of an axisymmetric imperfection on the plastic buckling of an axially compressed cylindrical shell, *ASME J. Appl. Mech*. 46, 125–131.

Hutchinson, J.W., 1974. *Plastic buckling*, Advances n Applied Mechanics, 14, 67–144.

Ju, G. T., Kyriakides, S., 1992. "Bifurcation and localization instabilities in cylindrical Shells under bending II: Predictions", *International Journal of Solids and Structures*, 29, 1143–1171.

Karamanos, S.A., Tassoulas, J.L., 1996. "Tubular members I: stability analysis and preliminary results", *Journal of Engineering Mechanics*, ASCE, **122**, 1, 64–71.

Kyriakides, S., Corona, E., 2007, Mechanics of Offshore Pipelines, Vol. I Buckling and Collapse, Elsevier.

Lee, L. N. H., 1962. *Inelastic buckling of initially imperfect cylindrical shells subjected to axial compression*, Journal of Aerospace Science 29 87–95.

Needleman, A., 1982. "Finite elements for finite strain plasticity problems", *Plasticity of Metals at Finite Strain: Theory, Experiment and Computation*, edited by E.H. Lee and R.L. Mallet, Rensselaer Polytechnic Institute, Troy, New York, 387–436.

Pournara, A. E.., Karamanos, S. A., Ferino, J., Lucci, A., 2012. Strength and stability of high-strength steel tubular beam-columns under compressive loading. *14th International Symposium On Tubular Structures*, Paper No. 103, London, UK.

Rondal, J., Würker K.G., Dutta D. Wardenier J., Yeomans N., 1996, "Structural stability of hollow sections", CIDECT (Ed.) and Verlad TÜV Rheinland.

Tvergaard, V., 1983. Plastic buckling of axially compressed circular cylindrical shells, *Int. J. Thin-Walled Struct*. 1, 139–163.

Fatigue and fracture

Tubular Structures XIV – Gardner (Ed.)
© 2012 Taylor & Francis Group, London, ISBN 978-0-415-62137-3

Assessment of brittle fracture for cast steel connections in braced frames

T. Iwashita
Ariake National College of Technology, Fukuoka, Japan

J.A. Packer
University of Toronto, Toronto, Canada

J. Carlos de Oliveira
Cast Connex Corporation, Toronto, Canada

ABSTRACT: This paper describes defect tolerances for cast steel connections in braced frames and explores the possibility of brittle fracture from assumed defects in typical cast steel connectors. A parametric study, which investigates the sensitivity of brittle fracture to defect size, defect location and material mis-match effects, is described through cast steel connector models. A toughness scaling model is used for evaluating the occurrence of brittle fracture from assumed defects in the models.

1 INTRODUCTION

During the past decade, various steel casting products for steel building structures have been developed, such as connectors between brace members and gusset plates in braced frames. A good contemporary overview is given by Herion et al. (2010). Researchers and engineers are often concerned about fatigue issues with casting products or cast steel connections (Haldimann-Sturm & Nussbaumer 2008; Veselcic et al. 2006) because casting products have been used in bridge structures, such as nodes in tubular truss bridges, for example, which sustain fatigue loadings. Castings have a clear benefit in fatigue-critical applications because steel can be placed where needed and shaped appropriately to dramatically reduce stress concentration factors. Thus, attention is then mainly focused on the casting-to-member welding detail (Puthli et al. 2009).

Some casting products are welded to steel sections, such as hollow structural section (HSS) members and I-section members in building structures where these members are expected to develop their capacity during a large-scale earthquake. Such casting products thus play a very critical role in seismic structures. It is possible that the welded region between the casting and the member, and even the casting itself, may exhibit plastic behavior during an earthquake. This suggests that brittle fracture may occur in cast steel connections if weld defects exist in the welded region. In addition, the casting itself sometimes has defects or voids and those may also induce brittle fracture. A study of defect tolerance for cast steel connections is hence very important in order to prevent brittle fracture from weld defects and casting defects.

This paper describes defect tolerances for cast steel connections in braced frames, which have become increasingly common in North America as the main earthquake lateral load resistance mechanism, and explores the possibility of brittle fracture from assumed defects in typical cast steel connectors. A parametric study, which investigates the sensitivity of brittle fracture to defect size, defect location and material mis-match effects, is performed through cast steel connector models. A toughness scaling model (Iwashita et al. 2008; Iwashita & Azuma 2011) is used for evaluating the occurrence of brittle fracture from assumed defects in the models.

2 CAST STEEL CONNECTOR

Modern castings used in recent tubular structures have been presented by Herion et al. (2010). One of the castings, a cast steel brace connector (de Oliveira et al. 2008), is studied in this paper and is shown in Figure 1. This connector is now standardized and mass-produced for use in concentrically braced frames, which are amongst the most popular lateral force resisting systems for medium- to low-rise steel structures in North America. Fell et al. (2009) suggested that I-sections and round HSS or pipe braces provide a more desirable response than rectangular HSS braces in concentrically braced frames under extreme seismic loading. In this context, this type of cast steel connector in Figure 1 is becoming popular, not only for aesthetic reasons but also for simplifying erection, reliability of connection design and its performance. Circular hollow section (CHS) members are welded to the connectors with complete joint penetration (CJP)

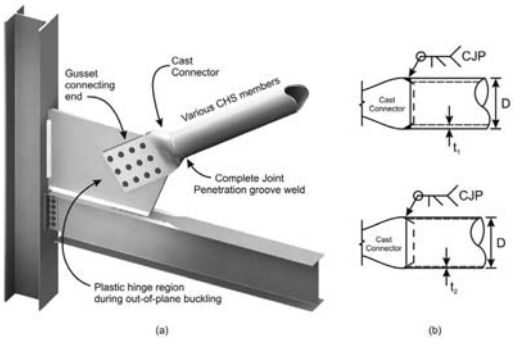

Figure 1. Standardized cast steel brace connector. (a) Brace-connector assembly in frame, (b) Beveled nose detail that accommodates CJP welding to CHS of any wall thickness.

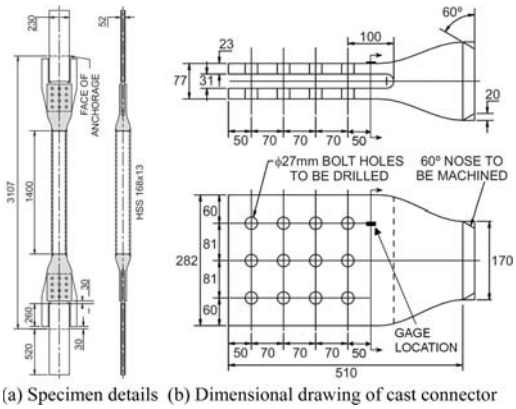

Figure 2. Specimen ST-1 (de Oliveira et al. 2008).

welding at the ends of any CHS brace of given outer diameter. At their other end, the connectors accommodate a double shear bolted connection to the gusset plate, and then offer simplified erection through the elimination of field welding.

In this paper, the authors have studied a particular high strength connector which is designed to fit tubes of 168 mm (or 6 5/8 in) outer diameter, and is moreover welded to a HSS 168 × 13 member. Such a connection corresponds to specimen ST-1 in prior research by de Oliveira et al. (2008). HSS 168 is one of the most common diagonal brace sizes in North America. This particular test specimen is especially suitable for a brittle fracture study because it sustained a higher load during testing than other test specimens with lesser wall thickness. In addition, a greater tube wall thickness induces higher plastic constraint, which may in turn induce brittle fracture, if there are defects in the connection. Specimen details and a dimensional drawing of the cast connector under study are shown in Figure 2. It is worth noting that none of the brace-connector assemblies tested by de Oliveira et al. (2008) in fact exhibited brittle fracture in the region of the cast end connectors.

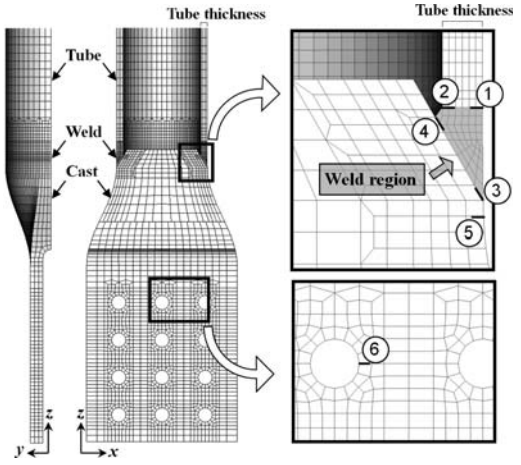

Figure 3. Finite element analysis model and defect locations.

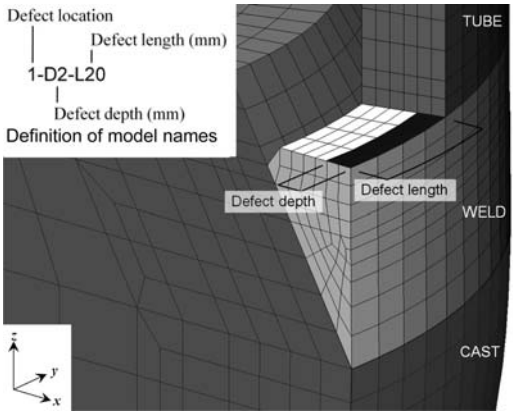

Figure 4. Example of defect depth and length, and model name.

3 ASSUMED DEFECTS

Two types of potential defects are considered in this paper:

(i) Weld defects: at locations 1 to 4 in Figure 3;
(ii) Defects in the casting itself (casting defects): at locations 5 and 6 in Figure 3.

Four patterns of defects were assumed as possible weld defects in the casting-to-tube joint and two defects were assumed as possible casting defects in the casting itself. The casting defects were located in a region which is subjected to high stresses in the casting, under brace axial loading, according to preliminary finite element analysis results in this research. Figure 4 displays defect depth and length, and also shows model names. There are some welding defects which are typical, such as lack of fusion, slag inclusion, undercut and overlap. The maximum acceptable depth of undercut is 1 mm and the maximum acceptable height and width of slag inclusions is 3 mm in BS

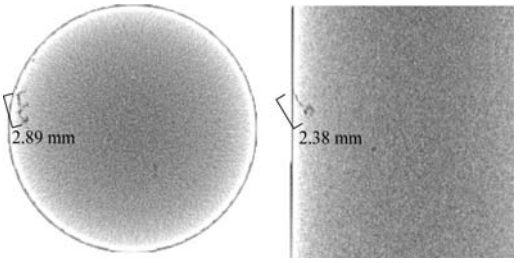

Figure 5. X-ray image of cast steel material indicating a 2.89 × 2.38 mm void.

7910 (BSI 2005). The authors, however, have adopted a relatively large size for defects (5 mm in depth and up to 40 mm in length as a maximum) in this paper according to the approach of Bai & Bai (2005) and Nakagomi & Tatsumi (2006). Only the defect at location 6 (see Figs. 2, 3) has a length of 23 mm because the thickness at location 6 is 23 mm. This, in effect, means the defect is a through crack. The above defect sizes adopted for the numerical study are likely to exceed those in practice, even for casting defects. To gauge the severity of the latter, X-rays were taken of cylinders machined from a steel casting at the University of Toronto, using a high-resolution X-ray inspection machine. The largest void detected was 2.89 mm in length and 2.38 mm in height, as indicated in Figure 5.

4 FINITE ELEMENT ANALYSIS

4.1 *Modeling methodology*

The research in this paper uses a non-linear finite element (FE) analysis to obtain data, such as J-integrals and crack tip stress states, for specimens containing assumed defects. The data are then interpreted with regard to the possibility of brittle fracture from the assumed defects.

FE analyses were performed using MSC Marc on models constructed from 8-noded 3D solid elements. This element was nonconforming and isoparametric and employs the reduced integration technique with hourglass control. The plasticity of materials was defined by the von Mises yield criteria. The material stress-strain data used for FE analyses was determined by standard tensile coupon tests of the materials. Isotropic hardening was assumed. The minimum element dimension was 0.03 mm in the defect tip region and a mesh sensitivity study was performed. Figure 3 shows a typical mesh used for modeling Specimen ST-1.

4.2 *FE analysis results*

Strains and deformations measured during laboratory testing were compared to the results of FE analysis for the purpose of validating the numerical models. The FE analysis results were comparable to the test results.

The results of finite element analyses of models with assumed defects showed that all of the defects do not significantly affect the overall load-displacement curves and load-strain curves. The maximum static load decreased less than 1.0% with a defect of 4.0 mm in depth and 40.0 mm in length in the welded joint, compared with a sound model which had no defect. This means that this kind of cross-sectional area loss does not significantly affect the axial force and deformation capacities. However, it may affect the occurrence of brittle fracture which is discussed later.

5 EFFECT OF DEFECTS

5.1 *Assumed fracture toughness*

The J-integral can be used as a fracture parameter for ductile materials and characterizes the crack tip stresses and strains. The critical J-integral value, J_c, which is a fracture toughness measure, is normally obtained from fracture toughness tests (e.g. BSI 1991), and values such as K_{Ic}, J_c, and δ_c have all been used for assessing the occurrence of brittle fracture from defects in structures (BSI 2005). The authors have herein considered brittle fracture using the J-integral. BSI (2005) shows that the use of the results of Charpy V-notch impact tests to indicate fracture toughness levels is possible, although direct measurement of fracture toughness is preferable. Since it is not common to carry out fracture toughness tests for materials in general steel structures, such as concentrically braced frames for example, the use of the results of Charpy tests could be a realistic approach to evaluate the occurrence of brittle fracture from defects. According to Folch & Burdekin (1999), there is a correlation between temperature corresponding to about 27 or 28 J Charpy energy absorption in the Charpy test and fracture toughness values (K_{Ic}) of 100 MPa $m^{1/2}$. A Charpy V-notch impact test value requirement of 27 J, at least at 0°C, is normally specified for the materials of the brace, the connector and the weld joint between those. Values of J_c are converted to equivalent K_{Ic} values by the relationship:

$$K_{Ic} = \sqrt{\frac{EJ_c}{(1-\nu^2)}} \quad (1)$$

This means that J_c is approximately 45 N/mm at 27 J Charpy energy absorption. The correlation (Folch & Burdekin 1999) is well known in the fracture mechanics field. Thus, the authors have defined the critical fracture toughness as $J_c = 45$ N/mm in this paper although this value is conservative, compared with some fracture toughness results (e.g. Iwashita et al. 2008).

5.2 *Effect of defects on J-integral and plastic constraint*

Table 1 shows the J-integral values of each model for FE analyses at the final displacement of the test specimen, 80 mm, which is almost the same value as when fracture occurred at the brace's mid-length,

Table 1. J values of each model at the final test specimen displacement (80 mm).

Defect depth and length	J (N/mm) Defect locations 1	2	3	4	5	6
D4-L40	196	70	7	19	8	14*
D4-L20	122	34	–	–	–	–
D2-L40	104	–	–	–	–	–
D2-L20	85	–	–	–	–	–

* No.6 has only a defect of 23.0 mm in length because the thickness at location 6 is 23.0 mm.
– brittle fracture not induced.

during tension loading (specimen ST-1 in de Oliveira et al., 2008). The defects at locations 3 to 6 and at location 2 (D4-L20) exhibited a very small J-integral value that does not induce brittle fracture, although the models had relatively large size defects (up to 4 mm in depth and 40 mm in length). This result is reasonable because the cast connector was designed to remain elastic up to the tensile capacity of the brace member. The J-integral at location 1 has the largest value for FE models with the same depth and length of defects (see "D4-L40" line in Table 1) and all the FE models with the defects at location 1 show higher values than J_c (= 45 N/mm). The possibility of brittle fracture is discussed later using a toughness scaling model (TSM) considering the effects of plastic constraint on brittle fracture. Clearly, if the size of the defects becomes smaller, the J-integral value also becomes lower. Although there is almost no difference in cross-sectional area loss due to defects between 1-D4-L20 and 1-D2-L40, there is a difference in J-integral value because a larger defect depth influences crack tip stresses and strains, and induces a higher J-integral value.

Figure 6 shows stress triaxiality vs. J-integral curves. The result of a SENB (Single Edge Notched Bend) model, which is used in fracture toughness tests to represent a high level of plastic constraint at the crack tip, is also added in Figure 6 (b). Stress triaxiality can be related to plastic constraint, which is also a very important factor for inducing brittle fracture. The stress triaxiality, T_s, is calculated as follows:

$$T_s = \frac{\sigma_h}{\sigma_{eq}} \tag{2}$$

where σ_h is the hydrostatic stress and σ_{eq} is the von Mises equivalent stress. Stresses were calculated from elements forming the defect tip, being approximately 0.3 mm away from the defect tip in this study. The relationship between the stress triaxiality and the J-integral influences brittle facture initiation in combination (Iwashita et al. 2003; Iwashita & Azuma 2011). The model with the defect at location 1 (1-D4-L40) is subjected to not only a large J-integral but also high stress triaxiality, compared with the other models

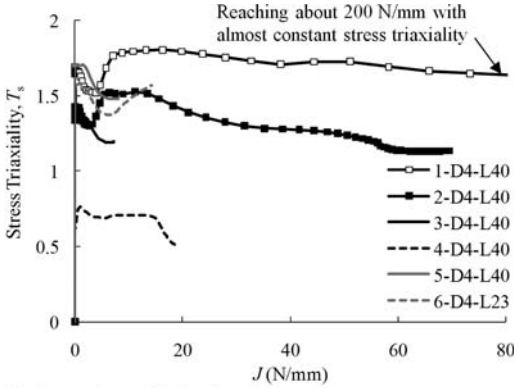

(a) Comparison of defect locations

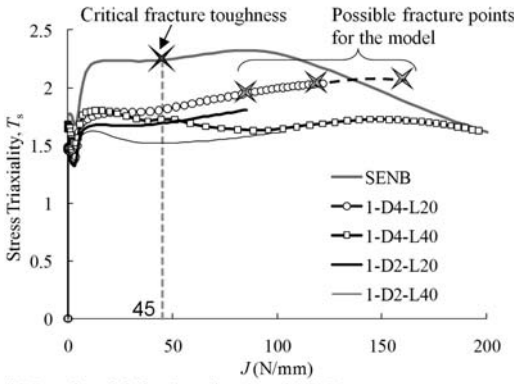

(b) Results of defect location 1 and SENB

Figure 6. Stress triaxiality vs. J-integral curves around the defect tips.

shown in Figure 6 (a). Brittle fracture may occur at a lower value of J-integral when specimens are subjected to a high level of plastic constraint at defect tips. Models 2 to 6 are subjected to a lower level of stress triaxiality, especially models 3 and 4 which are also subjected to a small J-integral value. This means that the possibility of brittle fracture from defects at locations 3 and 4 is extremely low.

Since 1-D4-L40 was the most critical case from Figure 6 (a), the models with the defects at location 1 are considered in Figure 6 (b). All the models with the defects at location 1 exhibited higher J-integral values than J_c (= 45 N/mm), as previously described, but stress triaxiality for the models is lower than that for the SENB. This means that the possibility of brittle fracture for these models is less than that for the SENB at the same J-integral. An interesting point is that 1-D4-L40 exhibits a lower value of stress triaxiality than 1-D4-L20, although 1-D4-L40 has the longer defect length. According to the FE analyses, a larger defect length induced extended yielding in the region around defect tips, and a larger increase of σ_{eq} as compared with σ_h, so stress triaxiality decreases in this case. The relationship between 1-D2-L20 and 1-D2-L40 also shows the same tendency. It is possible to

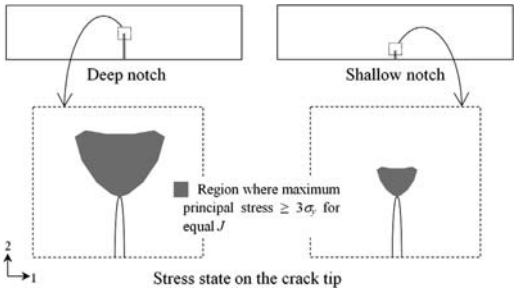

Figure 7. SENB specimens with a different notch depth.

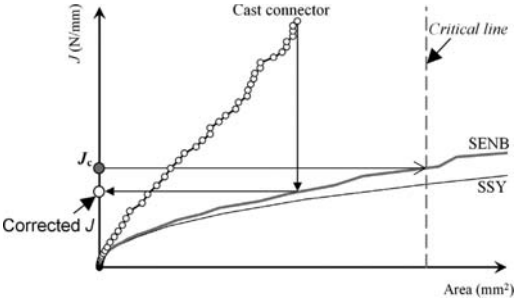

Figure 8. Evaluation procedure of corrected J using TSM.

know the extent of plastic constraint and the amount of the J-integral as described above. It is, however, difficult to predict the probable fracture point from only the relationship between stress triaxiality and J-integral as shown in Figure 6 (b). The possibility of brittle fracture is discussed in the next section.

6 POSSIBILITY OF BRITTLE FRACTURE WITH TOUGHNESS SCALING MODEL

6.1 *Toughness Scaling Model (TSM)*

Under small scale yielding (SSY) conditions, a single parameter J, calculated from the J-integral, characterizes fracture toughness at a crack tip and is a geometry-independent fracture criterion. However, single-parameter fracture mechanics does not hold when plasticity is high and fracture toughness is thus dependent on the size and geometry of the test specimen (Anderson 1994). From numerical analyses, Anderson & Dodds (1991) found that the apparent toughness of a material is highly dependent on the plastic constraint conditions at the crack tip of the test specimen. In particular, they examined the effects of crack depth in SENB specimens.

Figure 7 presents two SENB specimens with different notch depths. Moreover, this figure shows the stress state at the crack tips in both specimens under the same J value. For the stress states a plane section of the material volume surrounded by a contour at a maximum principal stress, σ_{max}, is displayed. The volume of the specimen with a shallow notch is smaller than that of the specimen with a deep notch, although the same J value is applied to each specimen. This example shows the dependency of fracture toughness on the size and geometry of the test specimens. Anderson & Dodds (1991) proposed that the probability of brittle fracture is equal for the two specimens when the volumes are equal. When the critical J value, J_c, is obtained through SENB testing of a shallow notched specimen, the value of J_c can be corrected by determining the J value at which the crack tip volume of the deep notched specimen equals that of the shallow notched specimen at fracture. Iwashita & Azuma (2011) found that the volume could be replaced with the area, which is the planar area (1–2 plane in Figure 7) at the crack tip surrounded by a contour of a certain value of σ_{max} and this approach could give more accurate predictions. The corrected J is obtained through the procedure indicated in Figure 8. The maximum principal stress is taken to be $\sigma_{max} = 3\sigma_y$, as deemed typical by Knott (1973), Anderson & Dodds (1991) and others. In addition, it was found that the ratio of corrected J to J satisfying SSY was nearly constant, between $2.8\sigma_y$ and $3.2\sigma_y$, from FE analyses by Iwashita et al. (2003).

Table 2. Corrected J value of each model at the final displacement (80 mm).

	Corrected J (N/mm)					
Defect depth and length	Defect locations 1	2	3	4	5	6
D4-L40	29.1	5.9	0.0	0.0	5.2	6.2*

*No.6 has a defect of 23.0 mm in length.

6.2 *Possibility of brittle fracture for cast connector specimen ST-1*

Table 2 shows corrected J values of each model which has the large defect size (4 mm in depth and 40 mm in length). All of the models exhibited corrected J values less than J_c (= 45 N/mm). This means that the possibility of brittle fracture for these models is low in the range of 80 mm applied specimen displacement which is almost the same as the ultimate displacement of ST-1, even if the models had the worst conditions (a low level of fracture toughness was assumed according to the lower limit Charpy absorbed energy value; large assumed defects were adopted). Consequently, the specimen (ST-1) naturally did not exhibit brittle fracture in the connection test (de Oliveira et al. 2008).

These models, except the model with the defect at location 1, had small corrected J values (see Table 2). In addition, the models with defects at locations 3 and 4 even exhibited zero corrected J since regions around the defect tips in the models were not subjected to a maximum principal stress of $3\sigma_y$ or greater. Figure 6 (a) also shows low stress triaxiality and J-integral values for the models.

Table 3. Material properties.

Material	σ_y (MPa)	σ_u (MPa)	E (GPa)
Casting[a]	565	695	206
Tube[a]	475	525	199
Casting-L_s	345	550	200
Casting-U_s	570*	700*	200
Tube-L_s	350	450	200
Tube-U_s	525	620	200

[a]: de Oliveira et al. 2008; L_s: lower limit (specification); U_s: upper limit (specification); *: not specified.
Tube per CAN/CSA-G40.20/G40.21 grade 350W (CSA 2004). Casting per ASTM A958 Grade SC8620 Class 80/50 (ASTM 2000).

7 PARAMETRIC STUDY

FE analyses were carried out to perform a parametric study in order to determine the influence of the following parameters on sensitivity of brittle fracture: material property, loading type and defect location. It should be noted that the FE analyses did not consider cyclic loading effects in this paper. The cast connectors in braced steel frames are actually subjected to reverse cyclic loading during a severe seismic event. Buckling, however, occurs in the brace members during the compression loading phase before the connectors are subjected to a large compression load, so the connectors and welded regions do not sustain plastic behavior in compression. Thus, the effect of cyclic loading on the occurrence of brittle fracture is very small in the cast connectors and could be ignored in this research.

7.1 *Material properties according to specifications*

The yield strength, σ_y, and ultimate strength, σ_u, of both the casting and tube materials of test specimen ST-1 were much higher than the minimum specified values for the casting and tube material, as shown in Table 3. Upper limits on strength for the casting are not specified by the standard (ASTM 2000) so it was assumed in FE analyses to have material properties close to that of the casting material (de Oliveira et al. 2008) which had higher material strengths. FE analyses were performed with the different material properties in Table 3 in various combinations. For example, if there are defects assumed between the tube and weld (defect locations 1 and 2), the combination of "Casting-U_s" and "Tube-L_s" is the most critical combination with regard to occurrence of brittle fracture. On the other hand, if there are defects assumed in the casting itself (defect locations 5 and 6), the combination of "Casting-L_s" and "Tube-U_s" is the most critical combination.

7.2 *Effect of loading rate*

It is well known that dynamic loading deteriorates fracture toughness: a ductile-to-brittle transition temperature shifts to a higher temperature at higher strain rates because dynamic loading is associated with inducing increased yield strength and ultimate strength. Then, fracture toughness decreases, apparently due to an increase in the higher stresses around the crack tips (Minami et al. 2000). It is therefore important to consider increased yield strength and ultimate strength in FE analyses to evaluate the corrected J for prediction of brittle fracture. The yield strength at a strain rate of about 0.4/s is approximately 10% greater than at a strain rate of about 0.004/s, and the ultimate strength increases by approximately 5% over the same differential in strain rate (JWES 1997). According to those phenomena, the corrected J, considering the effect of dynamic loading on brittle fracture, in this paper is evaluated through FE analyses with higher yield and ultimate strengths, whereby the static values are multiplied by 1.1 and 1.05 respectively, in all elements of models as a simplified way of considering the effect of loading rate.

7.3 *Sensitivity of brittle fracture*

FE analyses were performed for all the models with different combinations of the material properties in Table 3. In these FE analyses, only the model with the defect at location 1 displayed a corrected J value higher than J_c (= 45 N/mm) and all corrected J values for other models with the defects at locations 2, 3, 4 and 5 were less than 10 N/mm. This means that the possibility of brittle fracture from defects at these other locations is extremely low. On the basis of these results, the authors focused on location 1 and present mainly results of the models with the defect at location 1 in this paper. Table 4 shows corrected J values for the 1-D4-L40 model with some combinations in material property and loading type, and for 6-D4-L23 for reference, which had a casting defect at the most critical location in the cast connector. Only "Tube-L_s" was used for the tube material in the 1-D4-L40 model because it is definitely the critical case for the defect at location 1. The applied J of the model in Table 4 is the value of the J-integral at the applied displacement (80 mm in this research, which is almost the same as the ultimate displacement of ST-1 and also corresponds to about 8% story drift in a typical braced frame building). The value of applied J is corrected by determining the J value at which the crack tip area of a SENB specimen with a deep notch equals that (critical area) of the model at the final applied displacement, as shown in Figure 8 and as described previously.

All of the models except one, condition number 7 (Table 4), exhibited a corrected J value lower than J_c (= 45 N/mm), although the applied J of all the models exceeded J_c (= 45 N/mm). This illustrates that considering the effects of plastic constraint on brittle fracture is very important in order to predict the occurrence of brittle fracture. As described previously, it is known that dynamic loading increases the corrected J, which is also illustrated by comparing conditions 1 and 5 for 1-D4-L40 (Table 4). It is therefore also important to consider the dynamic loading effects.

Table 4. Results of corrected J for 1-D4-L40 and 6-D4-L23 models.

Model	Condition No.	Cast	Weld	Tube	Loading type	Applied J (N/mm)	Corrected J (N/mm)	Ratio of J to corrected J
1-D4-L40	1	Cast-L_s	Tube-L_s	Tube-L_s	Static	316	27.4	12
	2	Cast-L_s	Cast-L_s	Tube-L_s	Static	333	31.9	10
	3	Cast-U_s	Tube-L_s	Tube-L_s	Static	313	27.3	11
	4	Cast-U_s	Cast-U_s	Tube-L_s	Static	260	42.2	6.2
	5	Cast-L_s	Cast-L_s	Tube-L_s	Dynamic	340	38.4	8.9
	6	Cast-U_s	Tube-L_s	Tube-L_s	Dynamic	326	37.9	8.6
	7	Cast-U_s	Cast-U_s	Tube-L_s	Dynamic	270	58.0	4.7
6-D4-L23	1	Cast-L_s	Tube-U_s	Tube-U_s	Static	91.9	26.4	3.5
	2	Cast-L_s	Tube-U_s	Tube-U_s	Dynamic	80.1	33.7	2.4

The 1-D4-L40 model with condition 4 exhibited a higher corrected J than that with condition 3. The defect was located between the tube and weld, and the weld material for condition 4 had "Cast-U_s", which had much higher yield and ultimate strengths compared with the tube material with "Tube-L_s". This mis-match between tube and weld induced higher plastic constraint around the defect tips and this then affected the corrected J value. This is known as the mis-match effect (Ohata et al. 1996) which worked as an over-match effect in this case. The model with condition 2 also exhibited a higher corrected J value than that with condition 1 because of the mis-match effect, but the difference in corrected J values between "Tube-L_s" and "Cast-L_s" was smaller compared with the case of conditions 3 and 4 because the difference in the material strengths was also small. The ratio of applied J to corrected J in Table 4 indicates the relative extent of plastic constraint and a ratio value of "1.0" means that plastic constraint is equivalent to the SENB model with a deep notch. The difference in the ratio value between conditions 3 and 4 in Table 4 confirms that the mis-match effect increases the plastic constraint. Thus, the use of a welding consumable equivalent to the tube material strength is effective for reducing the possibility of brittle fracture due to defects.

The defect at location 6 was subjected to higher plastic constraint, illustrated by the lower value of the ratio in Table 4, because the defect in the 6-D4-L23 model was a through crack, which is the most critical crack shape. The corrected J value of this model, however, was less than J_c (= 45 N/mm) because elastic behavior of the casting connector was maintained (de Oliveira et al. 2008) and then the applied J value was also small. This kind of design could free structural engineers from concern over brittle fracture due to casting defects, even if the casting had a low material toughness like 27 J at 0°C and some defects in critical locations.

7.4 *Defect tolerance*

Table 5 shows a matrix of corrected J values at each defect depth and length at location 1 (which is the most critical location in the cast steel connection in braced frames) derived by performing FE analyses with the most critical condition which is condition 7 in Table 4. The shaded regions in Table 5 illustrate that the corrected J value is higher than J_c (= 45 N/mm). Defect depth and length naturally influence each other. If defect depth is less than 3 mm, 40 mm of defect length is allowable. In addition, if the defect is less than 10 mm in length, even 5mm of defect depth is allowable as it produces a very small corrected J value. As described previously, it is also known that defect depth is more critical to the occurrence of brittle fracture than defect length, and this is supported by comparison of D2-L40 and D4-L20, or D3-L40 and D4-L30, in Table 5, which have almost the same cross-sectional area loss, respectively.

Table 5. Matrix showing corrected J (N/mm) at each defect depth and length at location 1.

	Defect length			
Defect depth	10 mm	20 mm	30 mm	40 mm
2 mm	13	26	19	22
3 mm	15	38	35	40
4 mm	17	42	56	58
5 mm	16	51	70	7

8 CONCLUSIONS

This paper has examined the potential for brittle fracture in a cast steel connector which is now used in concentrically braced frames subjected to severe seismic loading. A particular circular hollow section-to-casting brace assembly has been used as a reference test specimen. Assumed defects of various size have then been added to this casting and welded joint. A parametric study was then performed which investigated the sensitivity of brittle fracture to defect tolerances for such cast steel connections in braced frames. The following conclusions, which are limited

to the particular configuration studied, can be drawn from this work:

1. A weld defect at the outside of the tube, and between the tube and the weld (location 1 in Figure 3), is the most critical defect location and only a defect at this location showed any possibility of brittle fracture in the parametric study. Weld defects at this location can be identified using conventional non-destructive examination methods for welds with comparative ease. The weld defects at other locations were subjected to low levels of plastic constraint. A casting defect at the edge of the bolt hole, which was subjected to the highest stress in the casting (location 6 in Figure 3), exhibited a high level of plastic constraint, but the corrected J value was less than the critical fracture toughness because of the elastic behavior of the cast connector.
2. Mis-match effects increase plastic constraint which induces brittle fracture. The use of weld consumables equivalent to the tube material strength decreases the possibility of brittle fracture.
3. Defect depth has more influence on the occurrence of brittle fracture compared to defect length.
4. The parametric study confirms allowable weld defect sizes of 5 mm in depth for 10 mm in length, or 40 mm in length for 3 mm in depth, at the most critical location between the tube and the weld (location 1 in Figure 3).

REFERENCES

Anderson, T.L. (1994). *Fracture Mechanics: Fundamentals and Applications, Second Edition.* CRC Press, Chapter 3 and 5, Boca Raton, Fl, USA.

Anderson, T.L. & Dodds, R.H. Jr. 1991. Specimen size requirements for fracture toughness testing in the ductile-brittle transition region. *Journal of Testing and Evaluation* 19(2): 123–134.

ASTM 2000. Standard Specification for Steel Castings, Carbon, and Alloy, with Tensile Requirements, Chemical Requirements Similar to Standard Wrought Grades. *ASTM-A958-00*, West Conshohocken, Pa, USA.

Bai, Y. & Bai, Q. 2005. *Subsea Pipelines and Risers*. Elsevier, Chapter 32, Amsterdam, The Netherlands.

British Standards Institution (BSI) 1991. Fracture mechanics toughness tests – Part 1: Method for determination of KIc, critical CTOD and critical J values of metallic materials. *BS 7448-1*, London, UK.

British Standards Institution (BSI) 2005. Guidance on methods for assessing the acceptability of flaws in metallic structures. *BS 7910*, London, UK.

CSA 2004. General requirements for rolled or welded structural quality steel/structural quality steel. *CAN/CSA-G40.20-04/G40.21-04*, Toronto, Canada.

de Oliveira, J.C., Packer, J.A. & Christopoulos, C. 2008. Cast steel connectors for circular hollow section braces under inelastic cyclic loading. *ASCE Journal of Structural Engineering* 134(3): 374–383.

Fell, B.V., Kanvinde, A.M., Deierlein, G.G. & Myers, A.T. 2009. Experimental investigation of inelastic cyclic buckling and fracture of steel braces. *ASCE Journal of Structural Engineering* 135(1): 19–32.

Folch, L.C.A. & Burdekin, F.M. 1999. Application of coupled brittle–ductile model to study correlation between Charpy energy and fracture toughness values. *Engineering Fracture Mechanics* 63(1): 57–80.

Haldimann-Sturm, S.C. & Nussbaumer, A. 2008. Fatigue design of cast steel nodes in tubular bridge structures. *International Journal of Fatigue* 30: 528–537.

Herion, S., de Oliveira, J.C., Packer, J.A., Christopoulos, C. & Gray, M.G. 2010. Castings in tubular structures – the state of the art. *Proceedings of the Institution of Civil Engineers: Structures and Buildings* 163 Issue SB6: 403–415.

Iwashita, T., Kurobane, Y., Azuma, K. & Makino, Y. 2003. Prediction of brittle fracture initiating at ends of CJP groove welded joints with defects: study into applicability of failure assessment diagram approach. *Engineering Structures* 25(14): 1815–1826.

Iwashita, T., Kurobane, Y. & Azuma, K. 2008. Simplified micromechanics model to assess constraint effect on brittle fracture at weld defects. *Proceedings of the 12th International Symposium in Tubular Structures*, Shanghai, China: 127–134.

Iwashita, T. & Azuma, K. 2011. Effect of plastic constraint on brittle fracture in steel: Evaluation using toughness scaling model. *Journal of Structural Engineering*: 10.1061/(ASCE)ST. 1943-541X.0000507 (Sept. 26, 2011).

JWES 1997. *Seminar for earthquake damage and steel in steel structures*. The Japan Welding Engineering Society, Chapter 4.2, Tokyo, Japan. (in Japanese)

Knott, J.F. 1973. *Fundamentals of Fracture Mechanics*. Butterworths, Chapter 3, London, UK.

Minami, F., Ochiai, T., Hashida, T., Arimochi, K. & Konda, N. 2000. Local Approach to Dynamic Fracture Toughness Evaluation. *Fatigue and Fracture Mechanics* 31, ASTM STP 1389: 271–304.

Nakagomi, T. & Tatsumi, Y. 2006. Study on brittle fracture of welded joint with weld defects based on local fracture approach. *Journal of Structural and Construction Engineering* 74(610): 169–176. (in Japanese)

Ohata, M., Minami, F., & Toyoda, M. 1996. Local approach to mis-match effect on cleavage fracture of notched material. *Journal of Physics* IV 6: C6/269–C6/278.

Puthli, R., Herion, S. & Veselcic, M. 2009. Fatigue of end-to-end CHS connections. *CIDECT Final Report 7W-9/08*, University of Karlsruhe, Karlsruhe, Germany.

Veselcic, M., Herion, S. & Puthli, R. 2006. Selection of butt-welded connections for joints between tubulars and cast steel nodes under fatigue loading. *Proceedings of 11th International Symposium and IIW International Conference on Tubular Structures*, Québec City, Canada: 585–592.

Tubular Structures XIV – Gardner (Ed.)
© 2012 Taylor & Francis Group, London, ISBN 978-0-415-62137-3

Plastic collapse loads P_c and CTODs of a cracked Circular Hollow Section (CHS) T-joint

T. Li
Maritime Research Centre, Nanyang Technological University, Singapore

S.T. Lie
School of Civil & Environmental Engineering, Nanyang Technological University, Singapore

Y.B. Shao
School of Civil Engineering, Yantai University, Yantai, Shandong, China

ABSTRACT: The Failure Assessment Diagram (FAD) is an accepted approach in assessing the structural safety and integrity of any cracked tubular joint. In order to extend its application to a more complex geometry of any cracked Circular Hollow Section (CHS) tubular T-joint, there are three major challenges needed to be overcome; firstly there is a need to validate the existing FAD curves based on a fixed crack size for the prediction of instability crack growth, secondly it is important to check the accuracy of the available 3D stress intensity factor solutions and the crack driving force J_{ep} or CTOD, and thirdly it is necessary to estimate the fully plastic collapse load P_c solutions for the cracked CHS joints of interest. This paper focus on the plastic collapse load P_c and the CTOD for a cracked CHS T-joint subjected to brace end axial loads, and both P_c and CTOD are estimated using the experimental test and non-linear Finite Element (FE) method.

1 INTRODUCTION

Circular hollow section (CHS) joints are widely used in offshore and onshore structures. In practice, fatigue crack is frequently found at the hot spot stress location of the CHS joint that is subjected to cyclic loadings during the service time. As a result, the ultimate strength of the joint is reduced, and for some extreme cases they are going to be reduced significantly. It is, therefore, very important to assess the effect of cracks on the safety and integrity of cracked CHS joints.

The most widely accepted approach for assessing the safety and integrity of a cracked CHS joint uses an FAD method. It enables the safety and integrity of the cracked CHS joint to be assessed through two separate calculations based on two extremes of fracture behavior, namely, linear elastic and fully plastic behavior. In the procedure of constructing FAD curves for the assessment of the cracked CHS joints, there are three major challenges needed to be overcome; firstly there is a need to validate the existing FAD curves based on a fixed crack size for the prediction of instability crack growth, secondly it is important to check the accuracy of the available 3D stress intensity factor solutions and the crack driving force J_{ep} or CTOD, and thirdly it is necessary to estimate the fully plastic collapse load P_c solutions for the cracked CHS joints of interest.

The plastic collapse load plays a critical role in the procedure of assessing the safety and integrity of any cracked CHS joint using an FAD approach. For the past decades, several research programs had been carried out to study the ultimate strength of cracked CHS joints (Gibstein 1986, Burdekin & Frodin 1987, Cheaitani 1994, Burdekin & Yang 1997), however, most of them were conducted by experimental tests while few of them were investigated using FE method since the mesh models of the cracked CHS joints are too complex to construct. In the current study, an automatic mesh generator is developed to construct the mesh models of a cracked CHS T-joint containing a single semi-elliptical surface crack, and the crack can be located at anywhere along the actual weld toe with arbitrary length. The completed FE models are analyzed using the ABAQUS (2009) software, and the plastic collapse loads are predicted using twice-elastic compliance criterion and Lu's (1994) deformation limit formulae.

The crack mouth opening displacements (CMODs) of the experimental test and the FE model results at the deepest crack tip are compared and then extended to calculate the CTODs of the cracked CHS T-joint using the FE model presented in the present study.

2 EXPERIMENTAL TESTS

In order to validate the performance and convergence of the FE model presented in the present study, a

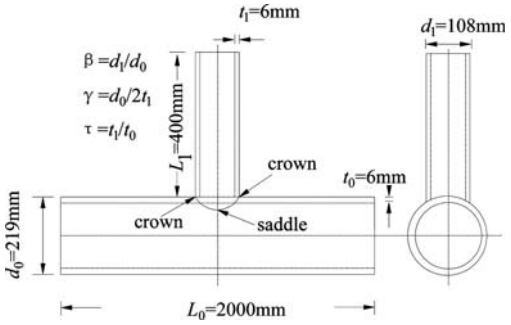

Figure 1. Dimensions of the specimen.

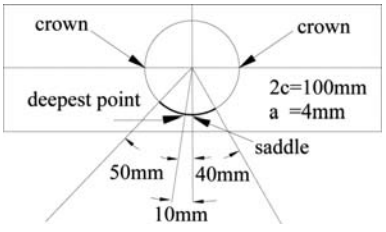

Figure 2. Crack details of the specimen.

cracked CHS T-joint was tested to failure in the laboratory of Yantai University, China. The cracked specimen was obtained from a previously completed fatigue test. The basic dimensions and typical cross-section of the cracked CHS T-joint specimen are shown in Fig. 1, while the position and the length of the crack along the actual weld toe are illustrated in Fig. 2. It must be mentioned here that the deepest point of the semi-elliptical crack front is located 10 mm beside the saddle position. A portable alternating current potential drop (ACPD) crack scan was used to measure the initial crack shape before the test, and also it was used during the test to measure the crack shapes while the specimen was subjected to different level of loads. The length of the initial crack is $2c = 100$ mm, and the depth of the deepest point is $a = 4$ mm.

The cracked CHS T-joint was subjected to brace end axial tensile load and the test rig is shown in Fig. 3. It can be seen that both the ends of the chord were pinned and a LVDT was placed to measure the deformation of the joint. During the test, the testing machine record the applied loads and the corresponding displacements of the brace end automatically, and they are shown on the display of a computer screen connected to the testing machine. When the applied load reaches a certain value set before the test, the experiment was stopped for a while in order to manually measure the corresponding crack shape and CMOD at the deepest point. The crack propagation process of the specimen is shown in Fig. 4, which provides the detailed information of the crack shape. It can be found that the crack shape resembles a semi-ellipse, and therefore, it is rational to adopt a semi-elliptical surface crack assumption in the FE models. The close view of the typical fracture surface of the specimen is illustrated in Fig. 5. It can be seen

Figure 3. Test rig.

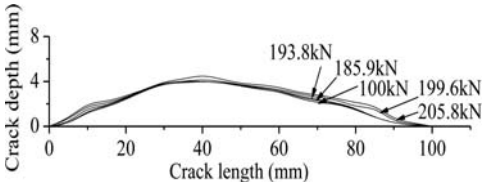

Figure 4. Crack shape development records.

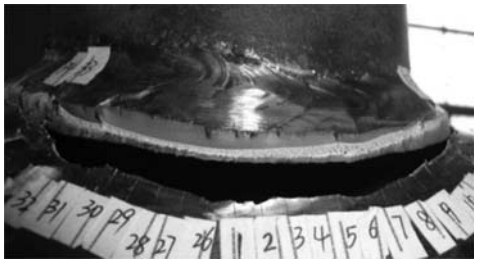

Figure 5. Close view of the fracture surface.

that ductile tearing had taken place within a certain area and the crack shape resembles a semi-ellipse that is consistent with the crack shape records.

3 FINITE ELEMENT MODEL

Because of geometrical complexity of the cracked CHS T-joint, it is very difficult to construct the mesh model of the semi-elliptical surface crack manually. Lie & Shao et al. (2005) developed an automatic mesh generator to construct the mesh model of the semi-elliptical surface crack automatically, and the crack can be located at anywhere along the actual weld toe with arbitrary length. Based on the previous research works, a new mesh generator is being developed in the present study, and a new refined mesh design of the crack block is used for elastic-plastic analysis. In the new mesh design of the crack block, only one type element, i.e. hexahedral element with 20 nodes, is adopted.

The entire mesh of the cracked CHS T-joint is shown in Fig. 6, while the close view of the mesh of the crack

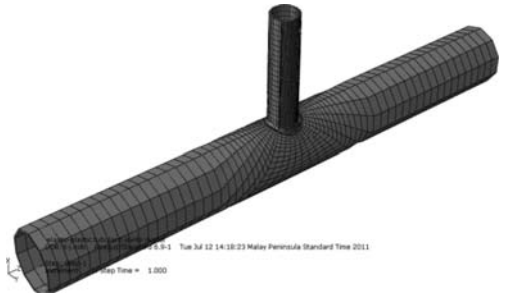

Figure 6. The mesh of the cracked CHS T-joint.

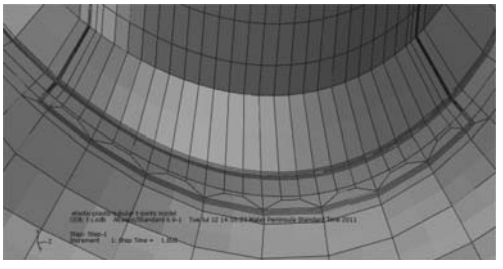

Figure 7. Local mesh of the crack block.

block is illustrated in Fig. 7. It can be seen that the mesh density is increased around the intersecting curve area to capture the high stress gradient existing at this region.

As a general rule, the appropriate level of mesh refinement of the crack tip depends on the purpose of the analysis. For investigating the residual strength of a cracked tubular joint, a relatively coarse mesh is adopted by Burdekin & Yang (1996), while for investigating the CTOD and the J_{ep}, a very refined mesh is required as suggested by Anderson (2005). The mesh design of the crack tip is shown in Figs. 8 and 9.

According to published works of Yang & Cao (1998), at least three rings of element enclosing the crack tips should be used so that the J-integral values can be calculated from sufficient contours to check the path independence of the results. The radii of the rings should be small, especially for the first ring. A model with more rings near the crack tip is also necessary to obtain accurate values of CTOD. It is suggested that the radius of the first ring should be less than 0.1 times the chord thickness. In the new mesh generator, the number of rings of element is kept as a variable and can be set as an arbitrary value theoretically. For the mesh of the specimen, crack tip models with three and six rings of elements are investigated respectively, and the radius of the first ring of the two models are all less than 0.1 times the chord thickness. The mesh design of the crack tip with three rings of element is shown in Fig. 8, while the refined mesh design of the crack tip with six rings is shown in Fig. 9. In the new mesh design, 16 elements around a ring are used.

In addition, a blunted crack tip is adopted in the elastic-plastic analysis as suggested by Anderson

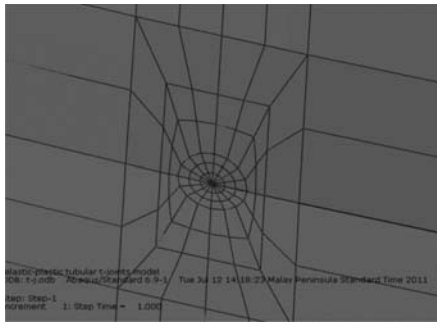

Figure 8. Mesh of the crack tip with three rings.

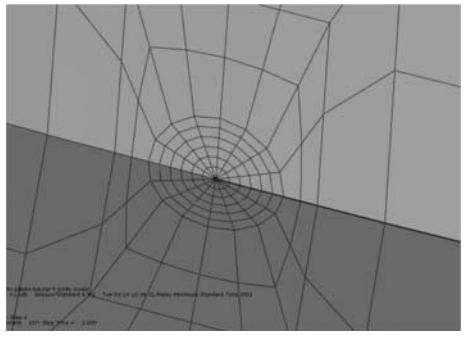

Figure 9. Mesh of the crack tip with six rings.

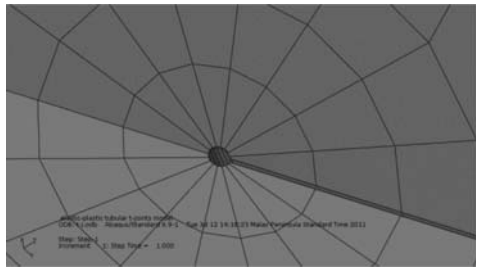

Figure 10. The small keyhole.

(2005). In order to construct the blunted crack tip, a keyhole with small radius illustrated in Fig. 10 is used. The small keyhole can be helpful when there is a large deformation, which is deemed to happen when the FE model is subjected to a very high level of loads, and to avoid the elements near the crack tip from collapsing which may give invalid J_{ep} results and less accurate CTOD values. The effect iveness of the keyhole radius on the crack driving force J_{ep} and CTOD will be addressed in another paper.

In elastic analysis, the mid-side node of the crack front element is moved to the 1/4 points in order to produce a $1/r^{1/2}$ strain singularity, while in elastic-plastic analysis, the location of the mid-side nodes is unchanged in order to produce 1/r strain singularity, which corresponds to the actual crack tip strain field for fully plastic material.

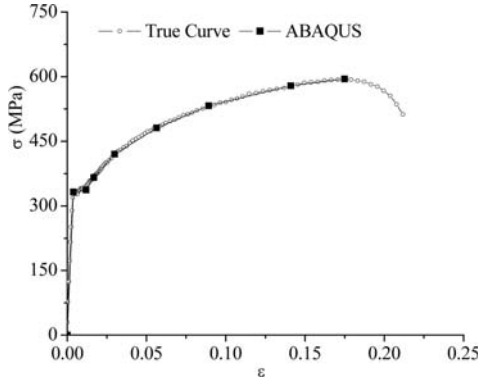

Figure 11. True stress-strain curve used in elastic-plastic analyses.

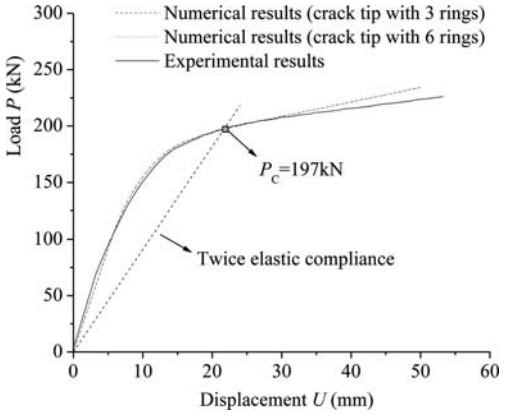

Figure 12. Load-displacement curves.

4 RESULTS AND DISCUSSION

In order to obtain the property of the steel, a set of coupon tests consisting 3 specimens were carried out, and then the engineering stress-strain curves were obtained. The true stress-strain curve shown in Fig. 11, which is derived from the engineering stress-strain curve, is used by the ABAQUS (2006) software to carry out the elastic-plastic analyses.

Fig. 12 shows the comparison between the numerical and experimental load-displacement curves. The displacement is defined as the displacement of the brace end. According to the experiment data, the crack started to propagate at the deepest point after the brace end displacement exceeded 20 mm. When the brace end displacement reached 40 mm, the crack had propagated by 1 mm at the deepest point. Since the FE model can't simulate the growth of the crack, the discrepancy between the numerical and experimental results becomes more apparent after the crack began to propagate. However, it can be seen that the two numerical curves almost converge completely. Therefore, it can be concluded that the rings of element has a small effect on the ultimate strength of the cracked CHS T-joint, which is consistent with the conclusion obtained by Yang (1996).

The load-displacement curve obtained from the finite element analysis shows a continuous trend with no maximum value to define the ultimate strength. Hence, it is necessary to find a method to define the ultimate strength of a cracked joint from the results of an FE analysis. A deformation limit is widely accepted to define the ultimate strength of a joint, but so far there is no common agreement on the choice of the deformation limit. The twice elastic compliance criterion is suggested by Burdekin & Yang (1996) to predict the plastic collapse load P_c of a cracked CHS joint, and it is based on the load-deformation response of a structure in the elastic-plastic analysis. The plastic collapse load is the load corresponding to the intersection of the load-deformation curve and a straight line known as collapse limit line, emanating from the origin of the load-deformation curve with half the slope of the initial elastic response. Yang & Lie (2011) analyzed cracked rectangular hollow section T-, Y-, and K-joints using the twice elastic compliance and obtained a good prediction. As shown in Fig. 12, the plastic collapse load of the cracked T-joint is about 197 kN, which is slightly higher than the initial tearing load of 193.8 kN.

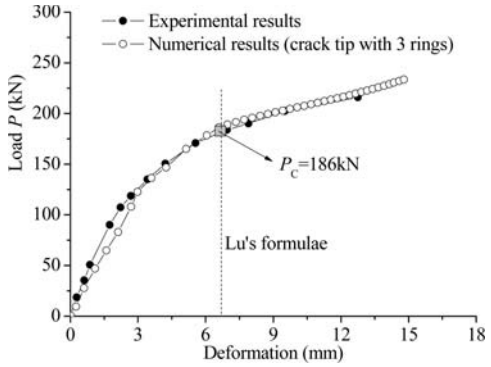

Figure 13. Load-deformation curves.

Another compliance used for predicting the plastic collapse load of a CHS T-joint was proposed by Lu (1994). According to Lu's formulae, 3% chord diameter is defined as the deformation limit. In the present study, Lu's deformation limit is also adopted to predict the plastic collapse load. The deformation is defined as the relative displacement of the top and the bottom point at the middle cross section of the chord member. Fig. 13 shows the load-deformation curves of the experimental test and the numerical analysis. The plastic collapse load is about 186 kN predicted by Lu's deformation limit, which is slightly lower than the initial tearing load.

Fig. 14 shows the comparison of CMOD-load curves at the deepest point between experimental test and numerical analyses. It can be seen that the two numerical curves are close to the experimental one before the load reaches 180 kN. After the load exceeds 180 kN, the discrepancy between the experimental test

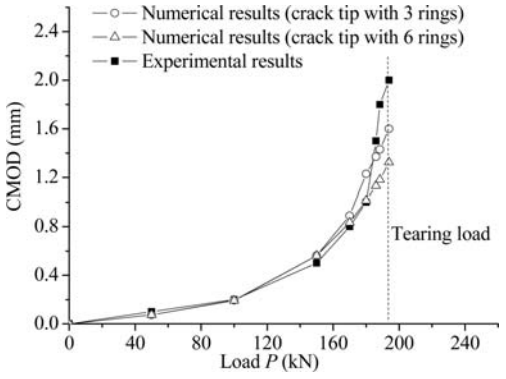

Figure 14. Comparison of CMOD results.

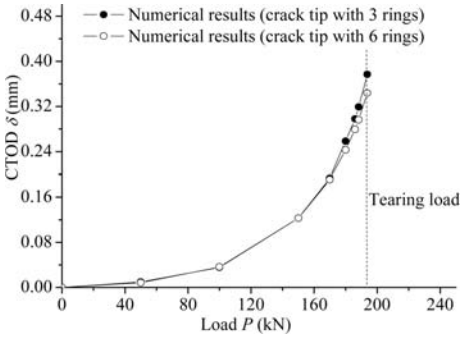

Figure 15. Comparison of CTOD results.

and the numerical results become larger and unacceptable. One of the possible explanations is that when the load reached 180kN, a large plastic zone has occurred, and then the value of CMOD increased rapidly because of the instability growth of the crack while the applied load kept relatively constant. Therefore, it is very difficult to get an accurate CMOD measurement by hand during this phase of the experimental test.

Fig. 15 shows the comparison of the CTOD curves. Only numerical results are compared because there are no available experimental results. It is found that FE models with three rings of element enclosing the crack tip can produce a good prediction of CTOD.

5 CONCLUSIONS

In order to validate the performance and convergence of the FE models presented in this study, a cracked CHS T-joint subjected to brace end axial loads was tested to failure. It was found that the tested specimen has a notable plastic deformation and ductile tearing had taken place at a certain area near the crack tips. Before a large plastic zone of the joint has occurred, the load-displacement and CMOD-load curves of the numerical results fit well with the experimental test results. Therefore, the FE model presented in this study is suitable to be used for predicting the plastic collapse load P_c and the CTOD of a cracked CHS T-joint.

The number of rings of element enclosing the crack tip has a small effect on the ultimate strength of a cracked CHS T-joint, and generally three rings are sufficient to get a good prediction of the plastic collapse load P_c and the CTODs.

Both the twice elastic compliance and Lu's deformation limit can be used to predict the plastic collapse loads of the cracked CHS T-joints.

REFERENCES

ABAQUS, 2006. Standard User's Manual, Version 6.5. Hibbett, Karlsson & Sorensen, Inc. Providence, Rhode Island, USA.

Anderson, T.L. 2005. Fracture mechanics: Fundamentals and Applications. 3st Edition. Taylor & Francis Group, USA.

Burdekin, F.M. & Frodin, J.G. 1987. Ultimate failure of tubular connections, Final Report Project DA709, Department of Civil and structural Engineering, UMIST, UK.

Burdekin, F.M. & Yang, G.J. 1997. Failure assessment diagrams for mixed mode loading and cracked tubular joints. *Advances in Fracture Research*, *Proceedings of the 9th International Conference on Fracture (ICF9)*, Sydney, Australia, I: 27–37.

Cao, J.J., Yang, G.J., Packer, J.A. & Burdekin, F.M. 1998. Crack modeling in FE analysis of circular tubular joints. *Engineering Fracture Mechanics*. Vol. 61, No. 5–6, 537–553.

Cheaitani, M.J. & Burdekin, F.M. 1994. Ultimate strength of cracked tubular joints. *Proc 6th Int Symp Tubular Struct*, Tubular Structures VI, Melbourne, Australia, 607–618.

Gibstein, M.B., & Moe, E.T. 1986. Brittle fracture risks in tubular joints, *Proc. Fifth International OMAE Conference* , Vol. II, 144–152, ASME.

Lie, S.T., Lee, C.K., Chiew, S.P. & Shao, Y.B. 2005. Mesh modeling and analysis of cracked Uni-planar Tubular K-joints. *Journal of Constructional Steel Research*, Vol. 61, No. 2, 235–264.

Lie, S.T. & Yang, Z.M. 2011. Plastic collapse load of cracked square hollow section T-, Y-, and K-joints. *Journal of offshore mechanics and arctic engineering*. Vol. 133, No. 2, 021601, 1–10.

Lu, L.H., de Winkel, G.D., Yu, Y. & Wardenier, J. 1994. Deformation limit of ultimate strength of tubular joints. *Proc 6th Int Symp Tubular Struct*, Tubular Structures VI, Melbourne, Australia, 341–347.

Yang, G.J. 1996. Effect of mixed fracture on ultimate strength of cracked tubular joints. PhD thesis. University of Manchester Institute of Science & Technology, UMIST, UK.

Tubular Structures XIV – Gardner (Ed.)
© 2012 Taylor & Francis Group, London, ISBN 978-0-415-62137-3

Root cracking in tubular joints with enhanced partial joint penetration welds

P.W. Marshall
MHP Systems Engineering, Houston, Texas, US
Department of Civil and Environmental Engineering, National University of Singapore, Singapore

X. Qian & Y. Petchdemaneegam
Department of Civil and Environmental Engineering, National University of Singapore, Singapore

C.T. Thang
Civil Engineering Department, Duy Tan University, Vietnam

ABSTRACT: This paper presents the experimental and numerical investigation on the fatigue cracking at the root of the enhanced partial joint penetration (PJP+) welds in the circular hollow section X-joint specimens subjected to constant-amplitude brace in-plane bending actions. The PJP+ welds, which include a portion of the brace wall as the inherent "back-plate", reduce the workmanship requirement on the welding procedure and improve the quality control of the welded joint. This study compares the fatigue crack developments observed at both the weld toe and the weld root in two large-scale X-joint specimens with different post-weld surface treatments. Root cracking is hardly observed in as-welded tubular X-joint specimens without post-weld surface treatment, in which the fatigue life depends on the toe failure. In specimens with post-weld grinding treatments to enhance fatigue resistance of the material near the weld toe, however, the finite-length root face triggers the initiation and propagation of fatigue cracks, but with an applied number of cycles more than that required to initiate a toe crack in the identical as-welded tubular X-joint.

1 INTRODUCTION

The geometric constraints for tubular T-, Y- and K-joints often only allows welding, *e.g*., the complete joint penetration (CJP) welds protocol (AWS, 2010), from the outside of the brace-to-chord intersections.Without a back weld or a back plate inside the tubular brace member, exceptional welder skills (6GR qualification) are required to deliver the satisfactory welds. This leads to potential weld defects and built-in discontinuity at the root, over which both the offshore companies and offshore fabricators have learned theirlessons in a hard way (Marshall *et al*., 2010). The structural design of tubular joints requires much more beyond the specification of the CJP welds, *e.g*., considerations of other failure modes including the punching shear failure (Marshall & Toprac, 1974). The American Welding Society (AWS) D 1.1 structural code (2010) recognizes that the root of the single-sided tubular welds will not always be perfect based on the findings from the small-scale fatigue test data (Marshall, 1984a). Previous attempts (MSL, 1999) to examine the effect of the root discontinuity on the fatigue performance of tubular joints fabricated by CJP welds have confirmed that the stresses near the root remain less critical than that near the toe, with the maximum stress-concentration factor (SCF) near the root equal to about 80% of the SCF value at the weld toe.

The complete joint penetration welds impose a stringent requirement on the workmanship of the welders to produce high-quality welds with satisfactory limit load and fatigue performances. Widely practiced in offshore jackets and onshore bridges, the designers and fabricators follow detailed protocols in cutting, fitting, welding and inspection to achieve satisfactory CJP welds (Marshall, 1984b, 1992, 2006). An alternative approach, practiced widely in Europe to deliver high-quality CJP welds in bridge structures, inserts a smaller tube in the brace member as a backing strip for the welding deposits. This approach elevates the fabrication cost to satisfy the strength and fatigue requirement anticipated for CJP welds in design codes (Schumacher *et al*., 2001), while leaving built-in discontinuity at the weld root.

Inspired by the backing plate approach and the partial joint penetration welds, Qian *et al*. (2009) propose the enhanced partial joint penetration (PJP+) welds for tubular connections. The enhanced partial joint penetration welds aim to reduce the workmanship requirement on the welding procedure, by introducing small and tractable root discontinuities in the welds.The PJP+ welds profile a built-in backing strip for the welding deposits. Figure 1 compares a typical

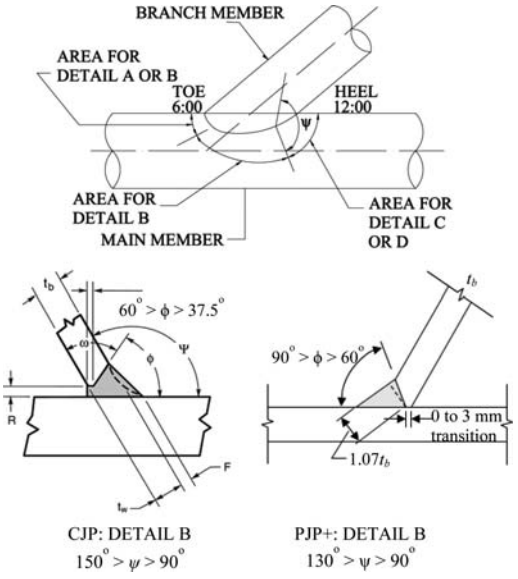

Figure 1. Comparison of the CJP welds and the enhanced partial joint penetration welds.

welding detail in the CJP prescribed in AWS (2010) and a corresponding detail with a similar range of the local dihedral angle in PJP+ welds (Qian *et al*., 2009). The PJP+ welds provide a more generous groove angle (φ in Figure 1), which facilitates end preparation and welding of the connected member, but leaves a finite-widthroot face. The root face depends on the wall thickness of the brace member (Qian *et al*., 2009). Tubular joints fabricated with the PJP+ welds anticipate equivalent ultimate and fatigue performances compared to those using the CJP welds.

This study reports the experimental findings from a joint-industry project, which examines the fatigue performance of the enhanced partial joint penetration welds on the large-scale CHS X-joints with different post-weld treatments subjected to constant-amplitude brace in-plane bending. The entire experimental program consists of five specimens, with three as-welded joints and two to-be-tested joints with the chord member infilled with ultra-high strength concrete. This paper focuses on the first two as-welded specimens.

2 EXPERIMENTAL PROGRAM

2.1 *Specimens*

Fabrication of the specimens tested in the experimental program follows a modified beveling procedure in an offshore fabrication yard. Figure 2 illustrates the configuration of the two tubular joint specimens reported herein. Both joint specimens share the same dimensions and boundary conditions. The brace-to-chord diameter ratio (β) equals 0.54, while the chord diameter over the wall thickness ratio (γ) is 15 and the brace wall thickness over the chord wall thickness

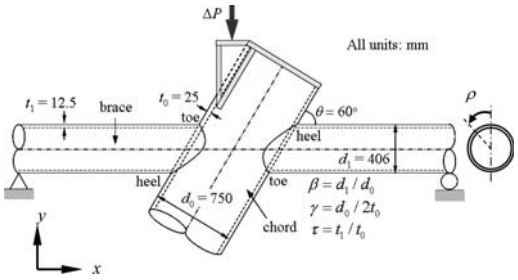

Figure 2. Geometric configuration of the tubular X-joint subjected to constant-amplitude brace in-plane bending.

ratio (τ) takes a value of 0.5, representative of typical values for new designs. The chord member has a length of 1750 mm to fit into the available space in a 200-ton cyclic testing rig in the Structural Engineering Laboratory, National University of Singapore. The anticlockwise angle ρ in Figure 2 denotes the position along the brace-to-chord intersection, with $\rho = 0$ referring to the top crown point, $\rho = 90°$ representing the saddle point facing the observer, and $\rho = 270°$ designating the saddle point at the back of the specimen.

2.2 *Experimental set-up and loading procedure*

The experimental set-up supports one end of the brace with a pin and the other end with a roller, as shown in Figure 2. The cyclic load applies on the top end of the chord member via a detachable loading fixture.

The test procedure applies a constant-amplitude load to the specimen until a fatigue crack initiates and grows to 80% of the wall thickness near the bottom of the brace-to-chord intersection. The experimental procedure then flips the specimen by 180° in the $x - y$ plane shown in Figure 2, and applies the second series of constant-amplitude brace-in-plane bending actions to the joint. The second fatigue test relocates the fatigue cracks generated in the first test to the upper side of the brace-to-chord intersection, which experiences compressive stresses in the second test. The second test terminates as the fatigue crack initiates and propagates to about 80% of the wall thickness at the bottom of the brace-to-chord intersection.

The constant amplitude loading has a minimum load level of 25 kN and a maximum load level of 235 kN with a frequency of 0.5 Hz applied through a 200-ton loading rig.

Prior to the cyclic tests, the instrumentation utilizes the five-component strip-type strain gauges to measure the strain values perpendicular to the weld line (Marshall *et al*., 2010) in the extrapolation zone, which spans across a distance between $0.4t$ and $0.4t + 10$ mm from the weld toe. During the cyclic tests, the experimental procedure measures the weld-toe crack propagation through an alternating current potential drop (ACPD) approach. The post-sectioning divides the brace-to-chord intersection region into 20–30 pieces

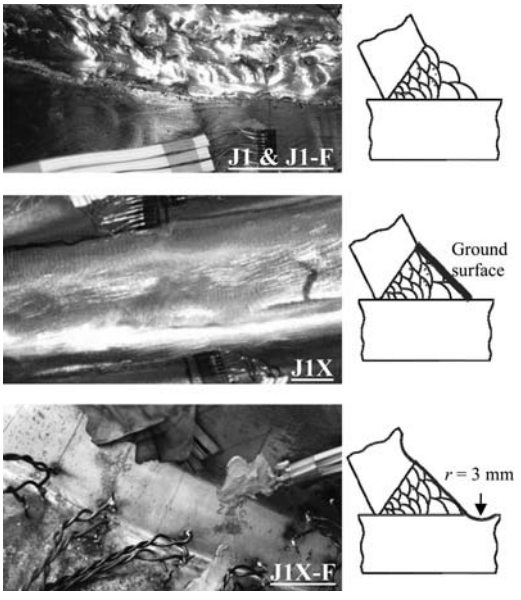

Figure 3. Different post-weld grinding treatment on different specimens.

and examines the occurrence of the root cracking in both joint specimens through etching.

The materials of the specimens utilize the typical S355 steels with a measured Young's modulus of around 200 GPa and a Poisson's ratio of 0.3. The measured material yield strength, from standard coupons, equals 345 MPa for the brace material and 360 MPa for the chord steel.

2.3 *Post-weld treatment*

The two specimens differ in the post-weld grinding treatments, as illustrated in Figure 3. The first specimen, namely J1, and its flipped configuration, J1-F, do not undergo any post-weld grinding treatment. The fabrication procedure, performed in an offshore fabrication yard, applies a surface grinding treatment to the weld surface for the second specimen J1X. Before the second test commences, the weld toe of the flipped configuration, J1X-F, experiences burr-grinding with a radius of 3 mm.

3 FATIGUE LIFE ASSESSMENTS

3.1 *Hot-spot stresses*

The experimental hot-spot strains derive from a linear extrapolation of the five measured strain components by the strip gauge to the weld toe.The SCF values calculates from the hot-spot strains (ε_{hs}) using,

$$SCF = 1.15\frac{E\varepsilon_{hs}}{\sigma_{nom}} \quad (1)$$

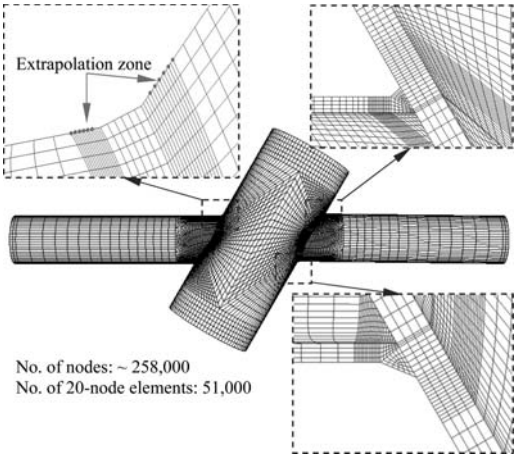

Figure 4. Typical FE meshes used in computing the linear-elastic SCF values.

where E denotes the Young's modulus of the steel material (ARSEM, 1987). Correspondingly, the current study performs a linear-elastic analysis to compute the SCF values along the brace-to-chord intersection. Figure 4 illustrates a typical, half-symmetric FE model used in computing the SCF values.

The extrapolation zone (0.4t to 1.4t away from the weld toe) in the FE model has an element size of 0.2t, where t refers to the thickness of the corresponding member. The numerical SCF values extrapolate linearly from the linear-elastic nodal stresses computed over the extrapolation zone. Figure 5 compares the measured SCF values with the numerical SCFs along the brace-to-chord intersection on the left brace resting on the pin support (see Figure 2) and on the left side of the chord.

The FE model with a 3 mm un-fused root face simulates two un-connected surfaces at the weld root in the FE model. The presence of the un-fused root face would allow opening of the root under remote tensile stresses, except that it is typically held shut by compressive residual stresses due to weld shrinkage (Barsoum & Barsoum, 2009). This forces the stresses to "flow" through the connected interface between the weld and the chord in the FE model. In contrast, the FE model without a root face simulates a continuous root in the model. The presence of the un-fused root face does not create strong variations in the SCF values at the weld toe, as shown in Figure 5.

The SCF values for the grinded specimens J1X and J1X-F do not indicate significant reductions compared to the as-welded specimens without post-weld grinding. The grinding treatment impose more effects on the localized notch stresses than on the hot-spot stresses.

3.2 *Fatigue toe cracks*

The experimental procedure utilizes a few techniques to detect the initiation of the fatigue cracks including

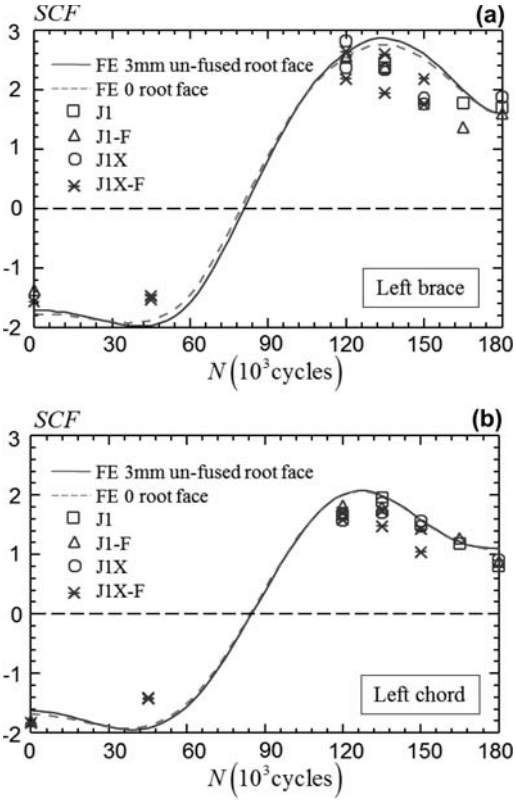

Figure 5. Comparison of the experimentally measured SCF values with the numerical computations along the weld toe for: (a) the left brace; and (b) the left side of the chord.

Table 1. Number of cycles at the first crack initiation and the location of the initiated cracks.

Specimen	Location of crack	No. of cycles
J1	$\rho \approx 245°$ on left chord	70,000
J1-F	$\rho \approx 235°$ on left chord	26,000
J1X	$\rho \approx 225°$ on left chord	175,000
J1X-F	$\rho \approx 225°$ on right chord	295,000

the eye inspection, dye penetrant, and strain monitoring near the potential hot-spot locations (Marshall *et al*., 2010; Sasaki, 1995). For all cyclic tests, the fatigue cracks initiate at the weld toe on the chord member near the maximum hot-spot stress locations. Table 1 compares the number of cycles at the initiation of the first fatigue crack in different specimens and the corresponding locations of these cracks.

The weld surface grinding performed on specimen J1X enhances the fatigue life at the crack initiation by a factor of about 2.5 compared to the crack initiation in the specimen J1. The weld-toe burr grinding in J1X-F reduces the local notch effect and removes the microscopic flaws generated in previous cyclic loads, thus postponing further the initiation of the fatigue crack.

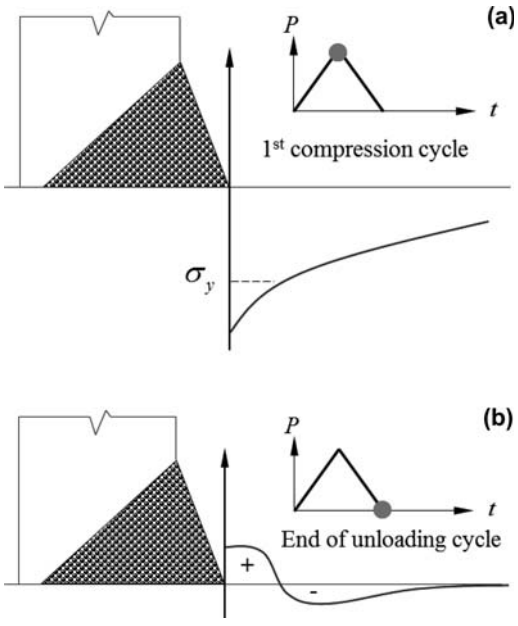

Figure 6. Schematic stress distribution in the chord material near the welds at: a) the end of the 1st compression load cycle; and (b) the end of the unloading cycle.

The initiation of the fatigue crack in the flipped specimen J1-F, however, occurs much earlier than that in the specimen J1. The fatigue crack locations near the bottom of the brace-to-chord intersection in the specimen J1-F have experienced previously compressive cyclic stresses in the first fatigue test on J1. Both the maximum measured notch stress andthe maximum numerical notch stress in the immediate vicinity of the weld toe exceed slightly the measured material yield strength. This implies local plastic deformation occurs in base materials near the weld toes. This cyclic compressive stresses, however, create a tensile residual stress field in the material, as illustrated schematically in Figure 6.

Figure 6a shows the stress distribution near the weld toe at the end of the first compression loading cycle, where the remote load reaches the maximum load level. A small volume of material at the weld toe undergoes plastic deformation since the local stress exceeds the material yield stress. As the remote load decreases to zero at the end of the unloading cycle, the plastically compressed material near the weld toe does not recover the permanent plastic deformation. Elastic recovery to its un-deformed configuration "pulls" the permanently shortened material to introduce a tensile residual stress in the immediate vicinity of the weld toe, as shown in Figure 6b.

The localized fatigue tensile residual region generated in the first fatigue test in J1, acting together with the tensile cyclic stresses in the cyclic test on the flipped specimen J1-F, reduces the number of cycles needed to initiate the first fatigue crack. Subsequent crack propagation does not seem to be affected.

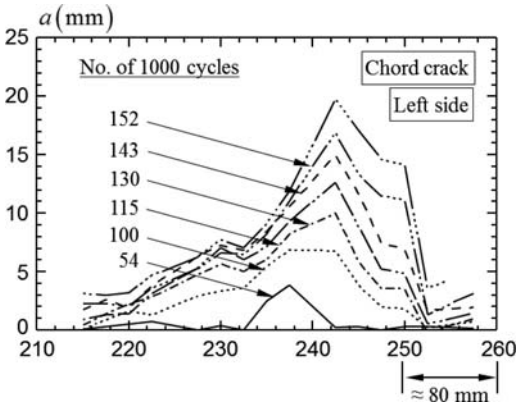

Figure 7. Fatigue crack propagation recorded during the experiment through ACPD.

Upon the initiation of the first fatigue crack, the cyclic actions often evolve multiple fatigue crack initiations at the other hot-spot locations.The fatigue tests stop as the maximum crack depth reaches about 80% of the wall thickness. Figure 7 shows the typical propagation of the fatigue crack in the chord member recorded during the test for J1-F. The crack-front profiles follows a similar shape as the crack propagates. The crack growth exhibits an initial spread in the notch region, a slower period than the near-threshold acceleration.

3.3 *Fatigue life assessments*

The fatigue life assessment for the toe fatigue cracks compares the number of cycles recorded in the current experimental investigation with three types of S-N curves in design codes, namely, the nominal stress S-N curve in AWS (2010), the hot-spot stress S-N curve in API RP 2A (2002), and the notch stress S-N curve in IIW (Hobbacher, 2007).

Figure 8 compares the S-N curves and the fatigue life at a crack depth equal to 80% of the wall thickness for all four fatigue tests. The nominal stress (σ_{nom}) shown in Figure 8 calculates from the maximum beam bending stresses in the brace member at the chord face.

The hot-spot stress (σ_{hs}) and notch stresses (σ_{notch}) in Figure 8 correspond to linear-elastic values computed from FE models.

Despite the significant differences in the fatigue life at crack initiation between the specimen J1 and J1-F, the final fatigue lives corresponding to a deep crack ($a = 0.8t$) for the specimens J1 and J1-Fagree within 25%. The difference between the fatigues lives for specimens J1X and J1X-F at a deep fatigue crack ($a = 0.8t$) remains within 20%.

The fatigue lives of the specimens J1 and J1-F exceed the estimation by the nominal stress S-N curve (AWS DT curve in Figure 8a) by more than 7 times, and surpasses the prediction based on the hot-spot stress S-N curve (API X in Figure 8a) by more than 10 times. The notch stress S-N curve (FAT225 in Figure 8a) is

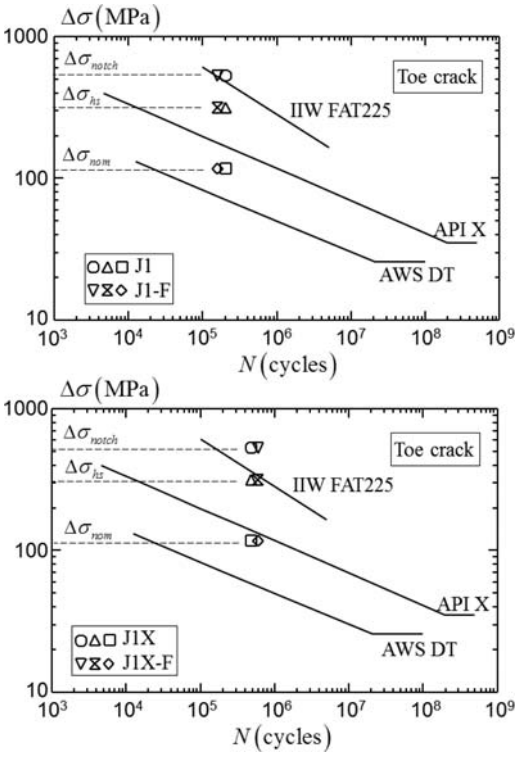

Figure 8. Comparison of the S-N curves with the fatigue test data for: (a) the un-grinded specimens J1 and J1-F; and (b) the grinded specimens J1X and J1X-F.

less conservative because the FEM mesh (Fig. 4) is coarser than the IIW 1-mm keyhole protocol.

The weld surface grinding enhances the fatigue life of J1X at $a = 0.8t$ by more than twice, while the burr-grinding at the weld toe further improves the fatigue resistance of the J1X-F specimen. The prolonged cyclic actions in the specimens with weld-surface grinding and weld-toe burr grinding exert additional fatigue loading on the weld root, for which all available post-weld mechanical treatment techniques become impractical. Post-weld heat treatment removes the favorable compressive residual stresses at the root, and is detrimental (Barsoum&Barsoum, 2009).

4 ROOT FAILURE AND ASSESSMENT

4.1 *Post-test examination*

Post-test sectioning cuts the material near the brace-to-chord intersection into 20 to 30 pieces, as shown in Figure 9a to examine the occurrence of the root cracks in all specimens. An etching process applied to the sectioned pieces allows detailed measurement of the root crack size and orientations.

For the J1 specimen without any post-weld surface treatment, root cracking does not initiate in any of

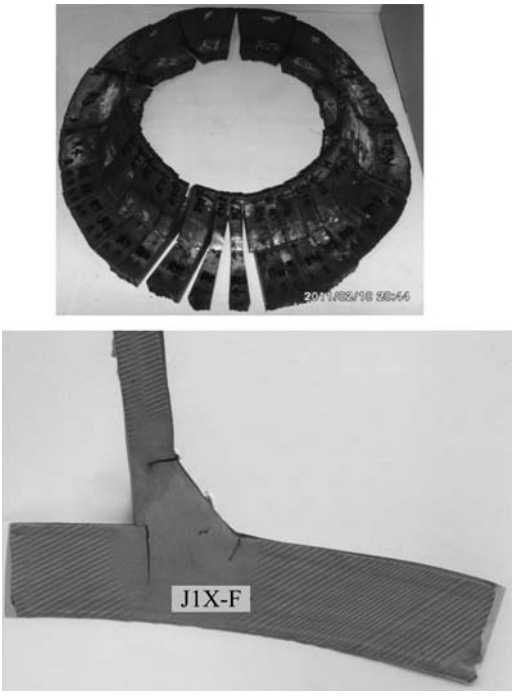

Figure 9. (a) Post-test sectioning of the brace-to-chord intersection region; and (b) root cracking in the specimen J1X-F.

the sectioned piece. The sectioning on J1-F reveals an uncritical, tiny root crack less than 2 mm in a single sectioned piece, located at $\rho = 237°$ near the deepest crack front at the weld toe in the chord.

The specimen J1X experiences weld surface grinding, which enhances significantly the toe resistance to the fatigue failure. However, the post-test sectioning does not reveal any root crack in J1X.

With the further enhancement on the toe fatigue resistance by burr grinding, two major root cracks initiate and propagate near the bottom of the brace-to-chord section on the left side of the chord member, as exemplified in Figure 9b. The two root cracks spread over $110° < \rho < 180°$ and $220° < \rho < 270°$. The maximum depth of the root crack occurs at $\rho \approx 240°$, with the crack depth equal to 15 mm. All observed root cracks penetrate into the chord wall in a direction almost parallel to the radial direction of the chord, responding by mode I to the shell bending stresses.

4.2 *Root SCF*

The direction of the root crack propagation indicates that the stresses driving the initiation and growth of the root crack remain perpendicular to the weld line, similar to the stresses driving the fatigue crack propagation of the toe cracks. The current study, therefore, computes the stress concentration factors at the weld root, using the stresses perpendicular to the weld line in the

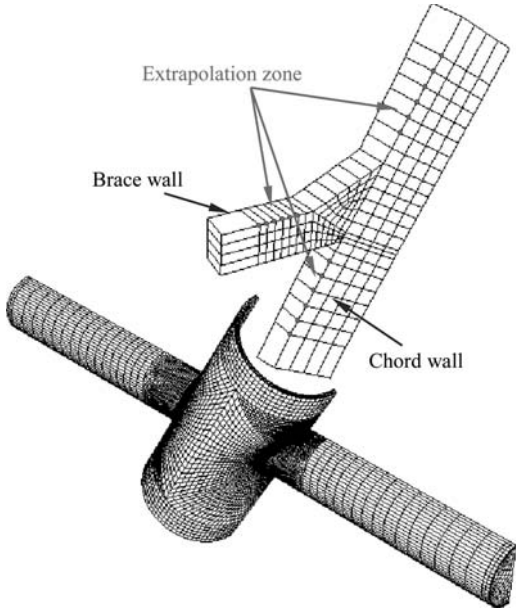

Figure 10. Extrapolation zone of the root SCF in the X-joint models.

extrapolation zone shown in Figure 10. The extrapolation zone, which contains five 20-node brick elements, extends from $0.4t_0$ to $1.4t_0$ away from the tip of the unfused root face, where t_0 denotes the wall thickness of the chord member.

Figure 11a shows the linear extrapolation of the root SCF value at a selected location $\rho = 135°$. Figure 11b compares the root SCF and toe SCF for the specimen J1X-F along the brace-to-chord intersection. The calculation of the toe SCF excludes the effect of local geometry introduced by burr grinding. The maximum root SCF remains about 10% lower than the maximum toe SCF value.

4.3 *Root crack propagation*

Instrumenting the root crack initiation and propagation has remained as a challenging task in today's engineering laboratory. This current study attempts to estimate the initiation of the root crack through an alternative, post-test numerical approach, coupling the linear-elastic stress-intensity factors with the Paris fatigue crack propagation law. The numerical approach utilizes multiple FE models each with a detailed crack-front mesh and a different crack depth to compute the variation of the effective stress-intensity factor range with respect to the crack depth. The Paris law allows the calculation of the fatigue crack propagation life based on,

$$\frac{da}{dN} = C\left(\Delta K_{eff}\right)^m \tag{2}$$

where C and m are material constants derived from the fatigue test of the compact tension, C(T) specimens

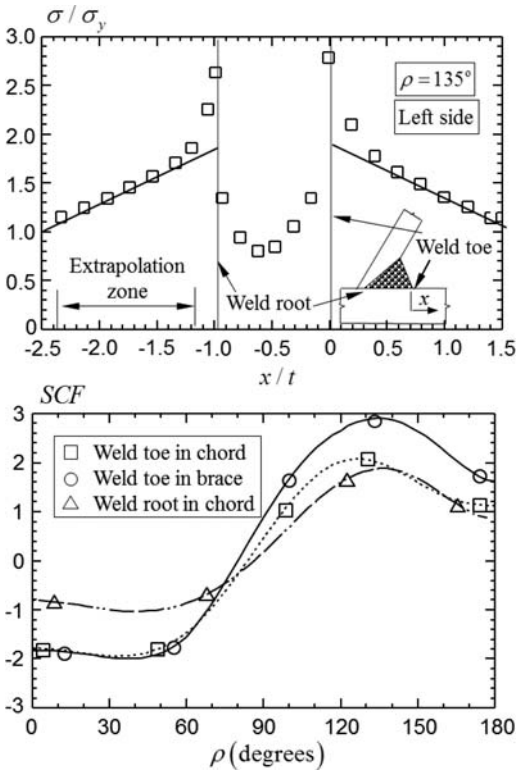

Figure 11. (a) Linear extrapolation of the root SCF values; and (b) comparison of the root SCF and toe SCF along the brace-to-chord intersection for the J1X-F specimen.

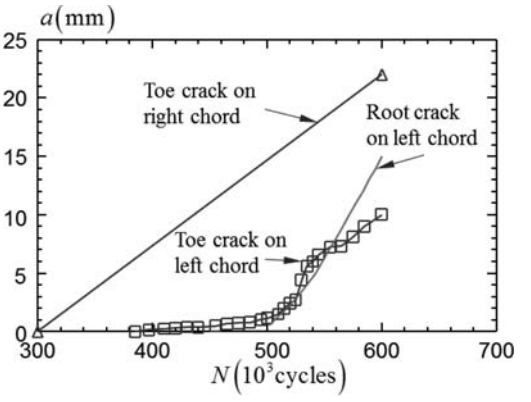

Figure 12. Comparison of the toe crack propagation and the root crack propagation.

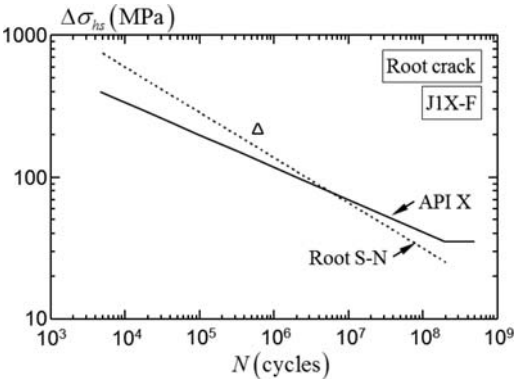

Figure 13. Comparison of the root S-N curve and the experimental data for J1X-F.

(Qian *et al*., 2011). This approach shows close agreement in estimating the toe crack propagation history for the weld-toe cracks in the PJP+ welded X-joint specimens (Qian *et al*., 2011). The effective stress-intensity factor includes the mixed-mode contributions of the crack driving forces. The current study assumes an initial crack size of 0.5 mm in calculating the fatigue crack propagation life.

Figure 12 compares the propagation of the toe cracks measured in the experiment and the root crack propagation calculated from Eq. (2). The propagation history of the toe crack on the right side of the chord is not instrumented. Figure 12 indicates that the initiation of the toe crack occurs much earlier than that of the root crack, despite the post-weld surface grinding on the weld surface and burr grinding on the weld toe. Figure 12 demonstrates that the root cracking remains less critical compared to the deepest toe crack observed in the same joint.

4.4 *Assessment of root failure*

Existing design guidelines have not yet provided any S-N approach to assess the potential root failure in tubular joints. The current study, therefore, utilizes the S-N curve proposed by Hong (2010) for root fatigue failure in plate specimens fabricated using fillet welds. Figure 13 compares the S-N curve developed by Hong (2010) and the most critical root crack in J1X-F revealed by the post-test sectioning. The S-N curve shown in Figure 13 corresponds to the mean minus twice the standard deviation curve reported by Hong (2010). Compared to the hot-spot S-N curve for weld toe fatigue failures (API X in Figure 8), the S-N curve in Figure 13 allows a longer fatigue life for the root fatigue failure if $\Delta\sigma_{hs} > 80$ MPa, while showing a steeper slope than the API X S-N curve.

5 CONCLUSIONS

The experimental investigation on the PJP+ welded X-joint specimens subjected to constant amplitude brace in-plane bending actions indicates that toe failure dominates the fatigue life of the specimens tested up to date. Both the fatigue crack initiation and final crack size for the weld-toe cracks demonstrate to be more critical than those of the root cracks.

Root cracking hardly occurs in X-joint specimens without post-weld treatment to enhance the fatigue

resistance of the weld toes. However, root failure becomes an important consideration when the post-weld treatment enhances significantly the fatigue resistance of the weld toes.

The fatigue lives of the tested specimens exceed the fatigue life estimations by the three types of S-N curves in the current design codes for toe failures. The proposed S-N curve for root failures in fillet welds accommodates a high allowable stress range, which combines with lower stresses at the root, explaining why root cracking is seldom a problem in simple as-welded tubular connections.

ACKNOWLEDGEMENT

The authors would like to express their sincere gratitude to the financial support provided by McDermott International Inc., Nippon Steel Engineering Co. and American Bureau of Shipping. The authors would also like to extend their thanks to HGG Group for the in-kind contributions on beveling protocols.

REFERENCES

American Petroleum Institute. 2000. Recommended practice for planning, designing and constructing fixed offshore platforms – working stress design. API RP 1A – WSD 21st edition.

American Welding Society. 2010. Structural Welding Code – Steel. AWS D1.1/D1.1M:2010. 22nd edition.

Association de Recherchesur les Structures Métalliques Marines (ARSEM). 1987. Design guides for offshore structures – welded tubular joints, ÉditionsTechnip, Paris.

Barsoum, Z. &Barsoum, I. 2009. Residual stress effects on fatigue life of welded structures using LEFM. *Eng. Failure Analysis*, 16, 449–467.

Hobbacher, A. Editor. 2007. *Recommendations for fatigue design of welded joints and components*. IIW Doc XIII-2151r1-07/XV-1254r1-07.International Institute of Welding.

Hong, J.K. 2010.Evaluation of weld root failure using battelle structural stress method. *Proc. ASME 29th Int. Conf. Ocean Offshore Arc.Engng.*, Shanghai, China, 6–11 June 2010.

Marshall, P.W. 1984a. Experience-based, fitness-for-purpose ultrasonic reject criteria for tubular structures. *Proc. 2nd Int. Conf. Welding Tubular Structures*, Boston, USA. 16–17, July 1984.

Marshall, P.W. 1984b. Connections for welded tubular structures.Houdremont Lecture, *Proc. 2nd Int. Conf. Welding Tubular Structures*, Boston, USA. 16–17, July 1984.

Marshall, P.W. 1992. *Design of Welded Tubular Connections – Basis and Use of AWS Code Provisions*, Elsvier.

Marshall, P.W. 2006. Material selection and fracture control for offshore structures. *Proc. 16th Int. Offshore Polar Engng. Conf.*, San Francisco, California, 28 May – 2 June 2006.

Marshall, P.W., Qian, X. &Petchdemaneegam, Y. (2010). Fatigue performance of enhanced partial joint penetration welds for tubular joints. *Proc. 13th Int. Symp. Tubular Structures*, *Tubular Structure XIII*, Hong Kong, 15–17 Dec, 2010.

Marshall, P.W. &Toprac, A.A. 1974.Basis for tubular joint design, *Welding Journal*, 1974(05), 192–203.

MSL Engineering Ltd. Fatigue life implications for design and inspection for single sided welds at tubular joints.Offshore Technology Report, OTO 1999 022, Health and Safety Executive, 1999.

Qian, X., Marshall, P.W., Cheong, W.K.D., Petchdemaneegam, Y. & Chen, Z. 2009. Partial joint penetration plus welds for tubular joints: fabrication and SCFs. *Proc. 62 Annual Assembly and Inter. Conf. Int. Institute Welding*. Singapore, 12–19 July, 2009.

Qian, X., Nguyen, C.T., Petchdemaneengam, Y., Ou,Z., Swaddiwudhipong, S. & Marshall, P.W. 2011. Fatigue performance of tubular X-joints with PJP+ welds: II – numerical investigation. Manuscript submitted to: *J. Constr. Steel Res.*.

Sasaki T. 1995. A basic study of the fatigue crack monitoring using strain gages. Research reports of the national institute of industrial safety, NIIS-RR-94. (In Japanese).

Schumacher, A., Nussbaumer, A & Hirt, M. A. (2001).Fatigue behavior of welded circular hollow section (CHS) joints in bridges. *Proc. 9th Int. Symp. Tubular Structures*, *Tubular Structures IX*, Dusseldorf, Germany, 3–5 Apr, 2001.

Tubular Structures XIV – Gardner (Ed.)
© 2012 Taylor & Francis Group, London, ISBN 978-0-415-62137-3

Fatigue behaviour of CFRP-strengthened thin-walled RHS-to-SHS cross-beam connections

Zhi-Gang Xiao
School of Applied Sciences and Engineering, Monash University, Churchill, VIC, Australia

Xiao-Ling Zhao & Daniel Borrie
Department of Civil Engineering, Monash University, Clayton, VIC, Australia

ABSTRACT: Cross-beam connections are widely used in welded thin-walled structures made of rectangular or square hollow sections mainly due to the connection's requiring less welding and no member cutting. Re-welding or bolted splicing are not suitable for repairing or strengthening fatigue cracked cross-beam connections. In this research, a new method using Carbon Fibre Reinforced Polymer composites (CFRPs) is proposed. Repair/strengthening are conducted for thin-walled RHS cross-beam connections at different levels of fatigue damage before constant amplitude fatigue experiments are conducted again on the specimens. Fatigue test results of unstrengthened intact connections are also presented for the purpose of comparison. The results show that the proposed retrofitting method is effective in repairing/strengthening fatigue-damaged thin-walled cross-beam connections when the connections are not severely cracked.

1 INTRODUCTION

Thin-walled steel rectangular hollow sections (RHS) or square hollow sections (SHS) are widely used in the road transportation industry and agriculture industry in manufacturing chassis boxes, roof frames or base frames of vehicles or equipment (Mashiri and Zhao 2005a). In many of these applications, welded cross-beam connections are often used mainly because they require less welding and no RHS or SHS member cutting. As with other weld connections, fatigue failure is a major concern to the cross-beam weld connections in tubular structures subjected to repeated or cyclic loading. Re-welding is not suitable for repairing or strengthening fatigue cracked cross-beam connections in tubular structures, which is mainly due to the concerns about the quality of field weld and further fatigue crack development from the welds. The conventional method of strengthening or repairing fatigue cracked welded details using bolted splicing plates is not applicable either due to the small thickness of hollow sections and the usual corner (mostly re-entrant corner) locations of fatigue cracks in these structures.

In this research, a method of repairing fatigue cracked thin-walled cross-beam welded connections by using carbon fibre reinforced polymer composites (CFRPs) is investigated. CFRP composite materials have advantages over traditional construction materials such as high strength, ease and speed of application, corrosion resistance, and ability to conform to irregular surfaces (Nadauld and Pantelides, 2007) and have been successfully used in concrete and masonry structures and are being increasingly used in steel structures (Zhao and Zhang 2007). Jiao and Zhao (2004), Haedir et al. (2009), Fawzia et al. (2007) and Seica and Packer (2007) strengthened circular hollow sections with CFRP sheets, while Fam et al. (2006), Nadauld and Pantelides (2007), and Pantelides et al. (2003) repaired aluminium overhead sign structures using CFRP or glass fibre reinforced polymer (GFRP) sheets. Research has been conducted on CFRP strengthening of cracked steel plates under fatigue loading (e.g. Tavakkolizadeh and Saadatmanesh 2003, Liu et al. 2009), limited research has been carried out on strengthening welded connections to extend their fatigue life (e.g. Nakamura et al. 2009).

As an extension of the research on the fatigue behaviour of welded connections of thin-walled hollow sections conducted at Monash University, this research was initiated to find a practical way of repairing fatigue-cracked RHS-to-RHS cross-beam connections with externally bonded CFRP sheets. This paper describes the surface preparation of the cross-beam connections, and the architecture and application sequence of the CFRP composite and additional strengthening plates to retrofit the connection. Repair/strengthening are conducted for thin-walled (3 mm thickness) RHS/SHS cross-beam connections at different levels of fatigue damage, i.e., uncracked (zero damage), lightly, intermediately and heavily cracked connections before constant amplitude fatigue experiments are conducted on the specimens again. Experimental results of fatigue tests on unstrengthened intact connections are also presented for the

purpose of comparison. The results show that the proposed retrofitting method is effective in repairing/strengthening fatigue-damaged thin-walled RHS cross-beam connections when the connections are not severely cracked.

2 TEST SPECIMENS AND FATIGUE TESTS

As shown in Figure 1, the cross beam specimens used in this research are made of a RHS (75 × 50 × 3 mm) and a SHS (50 × 50 × 3 mm). The specimens are of the same dimensions and configuration as S1R1R1A in Mashiri and Zhao (2005b). The RHS and SHS in the specimen are also referred to as the top and bottom members as well in this paper for convenience. The specified minimum strength grades for SHS and RHS sections are of C350LO and C450LO, respectively. The minimum yield strengths are therefore 350 MPa and 450 MPa, respectively (Standards Association Australia, 1991). The actual strength values obtained from coupon tests are greater than the specified minimum values. Refer to Mashiri and Zhao (2005b) for details of material properties. Fillet welds made with gas metal arc welding are used to join the RHS and SHS members (Mashiri and Zhao, 2005b).

A constant amplitude fatigue load with the stress ratio of R = 0.1 is applied at the free end of the bottom member to simulate the stress status of the weld under cyclic loading, Figure 1. Under the cyclic load, fatigue cracks initiate along the toe of the fillet weld on the tensile face of the bottom member around the corners before coalesce and break the whole tensile face of the bottom member. In the meantime, the other end of the cracks deviates from the weld toe on the side faces of the bottom member and propagated into the parent metal, as shown in Figure 1. In Mashiri and Zhao (2005a), fatigue failure is defined as the status when the whole crack length has reached a size equal to the width of the bottom member, 50 mm, plus twice the size of weld leg length, and the number of loading cycles at this time is taken as the final fatigue life. These definitions of fatigue failure and fatigue life are in agreement with those specified for T- and X-joints made of SHS by van Wingerde (1992). In this study, in order to investigate the effect of CFRP strengthening at different stages of fatigue damage, strain gauges are attached on the side surfaces of the bottom member and connected into the control circuit of the fatigue testing machine to stop the test once the cracks have cut the gauges, as shown in Figure 1.In each specimen, two strain gauges are set up symmetrically on two side surfaces at the location of 1/4, 1/3 or 1/2 of the depth of the bottom specimen (50 mm) to define the low, medium or high damage level. Two specimens are tested in each case and subsequently repaired with CFRP sheets and steel plates as described in Section 3.It is worth noting that the damage levels such defined may represent the stiffness loss of the specimen qualitatively, but not its fatigue damage strictly. All these cases satisfy the previous fatigue failure definition since the cracks

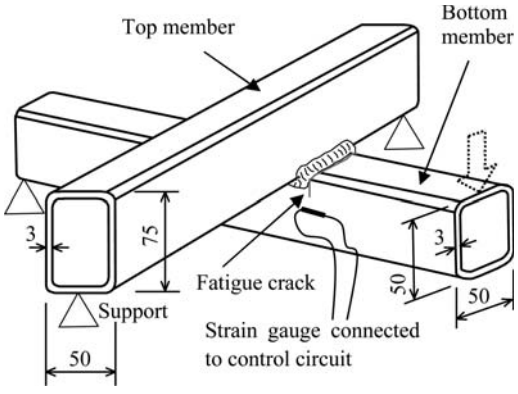

Figure 1. Schematic of test specimen (dimensions are in mm).

Table 1. Fatigue test results of cross-beam specimens.

Specimen	Damage level	Nominal stress range at fillet weld (MPa)	N (kilo - cycles)
L1	Low	147.6	411
L2	Low	147.6	1,994*
M1	Medium	184.5	343
M2	Medium	184.5	397
H1	High	147.6	1,226
H2	High	147.6	980

*Specimen L2 was tested with Rig 5, whole loading arm was found with severe angle misalignment after the test.

have propagated far beyond the corner in each case. Since the fatigue cracks propagates very fast beyond the corner of the specimen, the difference in fatigue life caused by further crack propagation among the above cases is negligible. Another point to note is that, since fatigue cracks do not initiate at two corners simultaneously in most cases and may not propagate at the same rate, either, the fatigue test was terminated by a crack reaching the strain gauge on one side surface of the specimen in all cases.

The fatigue test results are listed in Table 1. The nominal stress ranges listed are calculated with the bending moment values at the fillet weld location.

3 REPAIR AND STRENGTHENING

3.1 *Materials and surface preparation*

Both high and normal modulus CFRP sheets are used for the strengthening. The high modulus CFRP sheets are used as main strengthening sheets and low modulus ones are used as secondary sheets to anchor the main strengthening sheets. Both the high and normal modulus CFRP sheets are of MBrace family, with the properties as shown in Table 2. The adhesive used to join the CFRP sheets is a two-part epoxy adhesive, Araldite 420, which has a lap shear strength of 37 MPa (Fawzia et al. 2007).

Table 2. Properties of MBrace CF530 and CF130 specified by the manufacturer.

CFRP	High modulus CF530	Normal modulus CF130
Fibre modulus (GPa)	640	240
Tensile strength (MPa)	2650	3800
Tensile elongation, ultimate	0.4%	1.55%
Thickness (mm)	0.19	0.176

The surface of the member is sandblasted and cleaned with acetone over the bonding area before applying CFRP. Such preparation creates a lightly abraded surface which gives a better key to adhesives than the original galvanized surface does.

Figure 2. Stop hole drilled at the end of fatigue crack.

3.2 *Stop holes*

In the tested cross-beam connections, fatigue cracks initiating at the corner of the bottom member along the weld toe on the tensile surface of the member coalesce and break the tensile face of the bottom member, while the other ends of the coalesced cracks deviate from the weld toe and propagate in the side surfaces of the bottom member (Figure 1). To deter or arrest the crack propagation, stop holes of 5 mm or so in diameter were drilled at the ends of the crack after surface preparation. Though big stop holes will help decrease the stress concentration, a drill of 5 mm in diameter was used to minimize the reduction of cross section. The photo of a stop hole drilled at the end of the crack in a low damage specimen is shown in Figure 2.

3.3 *CFRP application*

The application of CFRP is undertaken in the following steps.

- Step 1: Six layers of CF530 CFRP sheets are applied over the tensile face of the bottom member across the fatigue crack and over the top member. The part on the bottom member is 100 mm at each end (Figure3a). Some details of the bonding procedures are as follows. Following sandblasting and surface cleaning, adhesive is applied uniformly on both the specimen and CFRP sheet before attaching the sheet to the specimen. A roller is then used to squeeze out excess adhesives and maintain uniform thickness of adhesive over the bond area. Special care is taken to make the CFRP sheet closely bonded around the weld toe in the corner region. For the application of subsequent layers of CFRP sheets, adhesive is applied on both the outside face of the attached sheet and the inside face of the following layer of sheet before attaching and rolling. The procedure is repeated until the last layer of sheet is attached.
- Step 2: After 3 days' curing of the CFRP sheets applied in Step1, six layers of CF530 sheets are wrapped over the other three surfaces of the bottom member along the same length as covered by CFRP sheets in Step1 to strengthen the webs of the bottom member (Figure 3b). Six layers of CF530 are also applied over the surface of the top member adjacent to the crack (Figure 3b). The length of the sheets on this surface is 250 mm which ensures that the sheets extend over the bottom member surfaces 100 mm at each end. In combination with the CFRP sheets to be applied in the next step, the function of the sheets on the top member is to restrain the CFRP applied in Step 1 and prevent early debonding from happening on the surface of the top member.
- Step 3: After 3-day curing of Step 2 CFRP, a CF130 sheet of 100 mm wide is wrapped around the top member for 4 rounds at each side of the bottom member to restrain the CFRP sheets applied over the top member in Step 2 (Figure 3c). Care is taken to make the wrapping sheet as close to the bottom member as possible.
- Step 4: To restrain the CFRP sheets applied in Steps 1 and 2 and increase the stiffness of the repaired specimen, an L-shaped steel plate is attached in this step (Figure3d). The thickness of the plate is 3 mm and the width is 40 mm. The L-plate is cold formed from a flat plate with a round corner of 10 mm (inner radius) to conform to the geometry of the corner of the specimen. A covering plate is also used to hold the short leg of the L-plate onto the CFRP-applied surface of the top member. As with the surface treatment of previous specimens, the surfaces of the strengthening steel plates are sandblasted and cleaned with acetone before being attached to CFRP sheets or to each other.
- Step 5: After 3-day's curing, two CF130 sheets of 100 mm wide are wrapped around the bottom member for 4 rounds to restrain the L-shaped plate and the CFRP applied in Steps 1 and 2. Care is taken to make the CFRP sheets as close to the surface of the top member as possible (Figure 3e). Two CF130 sheets of 100 mm wide are also wrapped around the top member for 4 rounds to restrain the covering plate (Figure 3e).

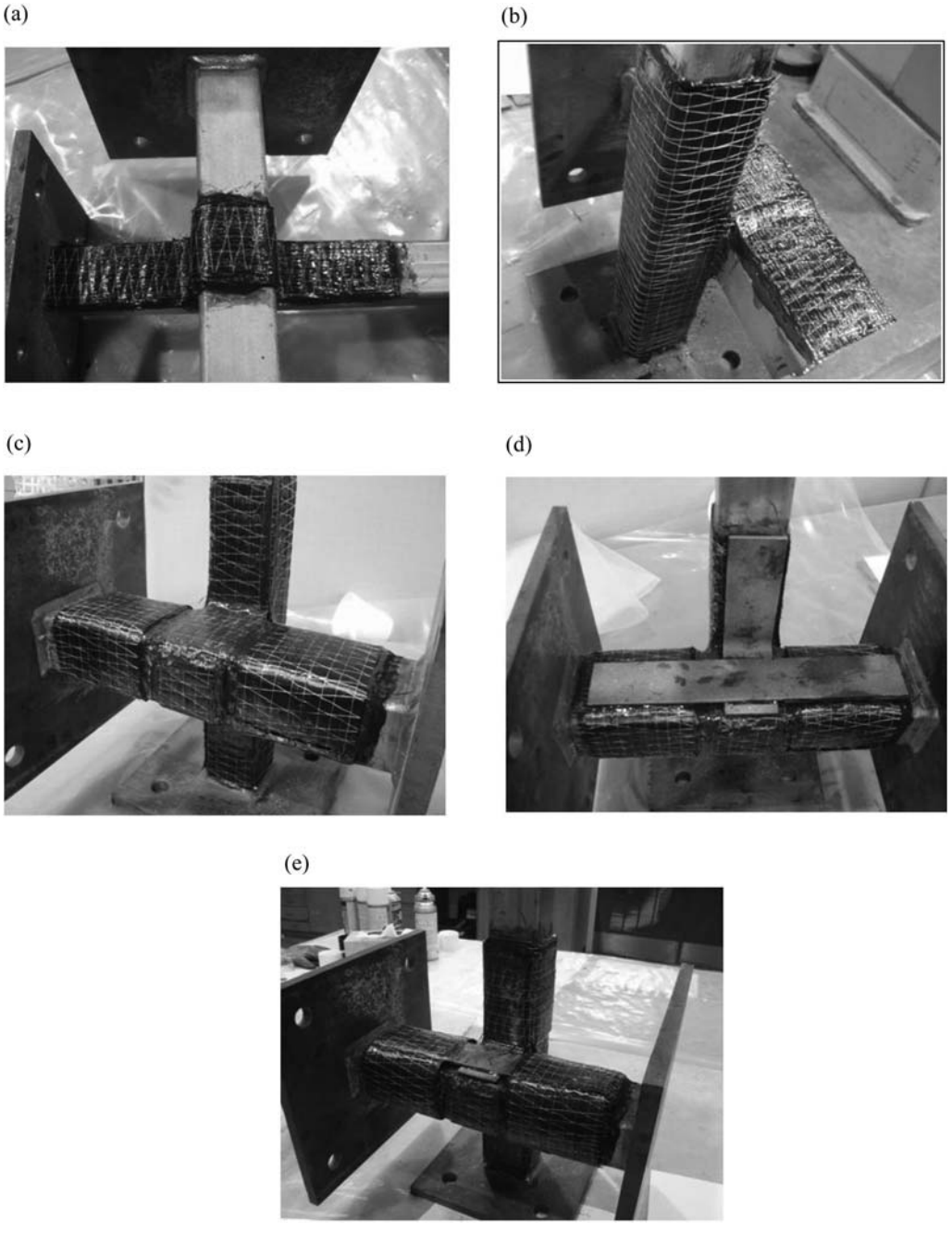

Figure 3. Repair and strengthening steps.

4 FATIGUE TESTS ON STRENGTHENED SPECIMENS

4.1 *Setup of fatigue tests*

The repaired specimens are tested with the same constant amplitude fatigue loads as in the original tests. Some of them are tested with the same test rigs as in the original tests, as shown in Figure 4a. The bottom member is mounted vertically in the rig with one end connected to the loading arm and the other bolted to the testing rig. The top member is also bolted to the rig at both ends. Pressured air is used to apply cyclic load to the free end of the bottom member, and the maximum and minimum loads are monitored by a load cell

(a)

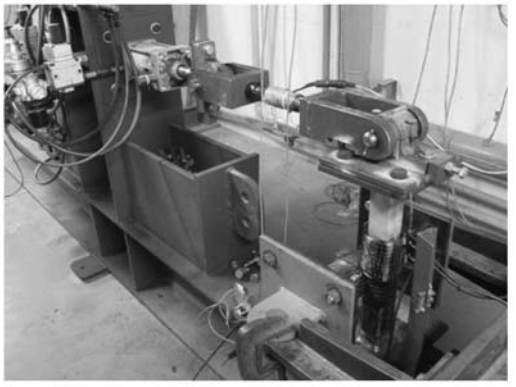

(b)

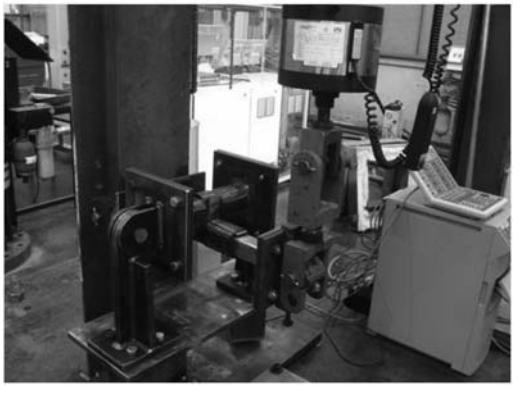

Figure 4. Testing setup. a) pneumatic testing rig; b) hydraulic testing rig.

exciter and can be controlled by adjusting the maximum and minimum air pressure valves, respectively. A break detector is set in the control circuit to stop the fatigue test automatically when the displacement at the loading end of the bottom member (in vertical position on the rig) reaches a preset limit. The displacement at the loading end of the bottom member is measured each time the experiment is inspected and the number of loading cycles is recorded. However, after connecting the strain gauges shown in Figure 1 into the machine control circuit for setting up the crack length, the test is always terminated by the cutting of the strain gauges.

In the later stage of the tests, a new test rig powered by a hydraulic actuator (Figure 4b) is set up to increase the loading frequency to 5 Hz. Both the maximum and minimum loads and corresponding displacements at the loading point are monitored during the test, and test is set to stop once the maximum displacement exceeds the 10% of the normal value.

A point to note is that, due to the mass of the loading arm in the new test rig, the stress ratio applied to the test specimen may be slightly different from the intended $R = 0.1$, which is different from the previous pneumatic rig in which the loading arm has no influence on the applied loads. However, due to the existence of high tensile residual stresses in the critical weld toe region where fatigue cracks develop, the actual stress ratio in the crack region is much higher (close to 1). In comparison, the influence of the rig mass is negligible.

Table 3. Fatigue test results of strengthened specimens.

Specimen	Damage level	Nominal stress range at fillet weld (MPa)	N (kilo - cycles)
L1	Low	147.6	5,042*
L1	Low	147.6	2,520*
M1	Medium	184.5	906
M2	Medium	184.5	1,543
H1	High	147.6	134
H2	High	147.6	114
N1	Zero	147.6	4,000*

Note:*Fatigue tests were terminated after a large number of cycles without failure

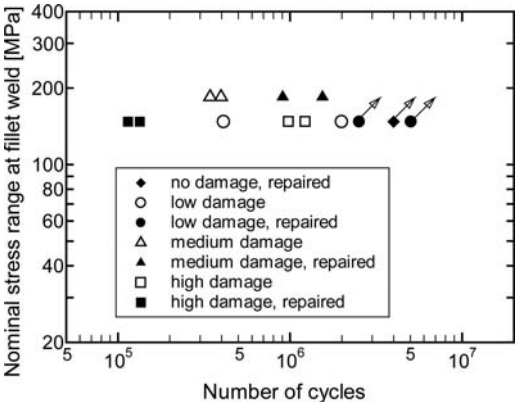

Figure 5. Fatigue test results.

4.2 *Test results*

The results of completed tests are listed in Table 2, and plotted in Figure 5 along with those before strengthening. An intact (zero-damage) specimen, designated as N1 in Table 2, is also strengthened in the same way as the other fatigue damaged specimens, and is subsequently fatigue tested with the same fatigue load as low and high damage specimens. This specimen was manually stopped after 4 million cycles without signs of failure or stiffness loss. The two low damage specimens strengthened with CFRP and steel plates were tested for 2.5 and 5 5 million cycles, respectively, without showing any sign of bonding failure or stiffness loss. The testing was also manually terminated in both cases. The rest results were plotted with arrows in Figure 5. The extended fatigue lives of the

two strengthened medium damage specimens (M1 and M2) were significantly greater than their original lives as well (2.6 and 3.9 times greater). In comparison, the extended lives of two repaired high damage specimens (H1 and H2) are very short. Based on these limited test results, it can be said a significant extension of fatigue life can be expected if the repair or strengthening is undertaken when the specimens are still not severely cracked.

5 CONCLUSIONS

A repair/strengthening method using CFRP and steel plates is proposed for cross-beam weld connections of thin-walled hollow sections, and repair/strengthening is conducted for connection specimens fatigue cracked at different damage levels. Available fatigue test results on strengthened specimens indicate that the proposed repair/strengthening method is effective in extending the fatigue life of the connection when the fatigue damage is not severe.

REFERENCES

Fam, A., Witt, S. and Rizkalla, S. 2006. Repair of damaged aluminium truss joints of highway overhead sign structures using FRP, *Construction and Building Materials* 20(10): 948–956.

Fawzia, S., Al-Mahaidi, R., Zhao, X.L. and Rizkalla, S. 2007.Strengthening of circular hollow steel tubular sections using high modulus CFRP sheets, *Construction and Building Materials* 21(4): 839–845.

Grove, A.T. 1980. Geomorphic evolution of the Sahara and the Nile. In M.A.J. Williams & H. Faure (eds), *The Sahara and the Nile*: 21–35. Rotterdam: Balkema.

Haedir, J., Bambach, M.R., Zhao, X.L. and Grzebieta, R.H. 2009. Strength of circular hollow sections (CHS) tubular beams externally reinforced by carbon FRP sheets in pure bending, *Thin-Walled Structures* 47 (10): 1136–1147.

Jiao, H.& Zhao, X.L. 2004.CFRP strengthened butt-welded very high strength (VHS) circular steel tubes, *Thin-Walled Structures* 42(7): 963–978.

Liu, H.B., Al-Mahaidi, R. and Zhao, X.L. 2009. Experimental study of fatigue crack growth behaviour in adhesively reinforced steel structures, *Composite Structures* 90(1): 12–20.

Mashiri, F.R.& Zhao, X.L. 2005a.Fatigue behaviour of welded thin-walled RHS-to-angle cross-beams under bending. In M.G.Stewart & B. Dockrill (eds), *Structural Engineering-Preserving and Building into the Future, Australian Structural Engineering Conference (ASEC2005)*, 11–14 September 2005, Newcastle, Australia.

Mashiri, F.R. & Zhao, X.L. 2005b.Fatigue Behaviour of Dura-Gal Cross-Beam Welded Connections, One Steel Market Mills Project, Interim Report No. 04/05, Department of Civil Engineering, Monash University, Clayton, Australia.

Nadauld, J.D. & Pantelides, C.P. 2007. Rehabilitation of cracked aluminum connections with GFRP composites for fatigue stresses, *Journal of Composites for Construction* 11(3): 328–335.

Nakamura, H., Jiang, W., Suzuki, H., Maeda, K. and Irube, T. 2009. Experimental study on repair of fatigue cracks at welded web gusset joint using CFRP strips, *Thin-Walled Structures* 47(10): 1059–1068.

Pantelides, C.P., Nadauld, J. and Cercone, L. 2003. Repair of cracked aluminum overhead sign structures with glass fiber reinforced polymer composites, *Journal of Composites for Construction* 7(2): 118–126.

Seica, M.V. & Packer, J.A. 2007. FRP materials for the rehabilitation of tubular steel structures, for underwater applications, *Composite Structures* 80(3): 440–450.

Standards Association of Australia. 1991.*Structural steel hollow sections, Australian Standard AS1163-1991*. Standards Association of Australia, Sydney, Australia.

Tavakkolizadeh M. & Saadatmanesh, H. 2003. Fatigue strength of steel girders strengthened with carbon fibre reinforced polymer patch, *Journal of Structural Engineering* 129(2): 186–196.

vanWingerde, A.M. 1992. The fatigue behaviour of T- and X-joints made of SHS, *Heron* 37(2): 1–180.

Zhao, X.L.& Zhang, L. 2007.State-of-the-art review on FRP strengthened steel structures, *Engineering Structures* 29(8): 1808–1823.

Tubular Structures XIV – Gardner (Ed.)
© 2012 Taylor & Francis Group, London, ISBN 978-0-415-62137-3

Further experimental study on assessment of safety of beam-column connections with weld defects from brittle fracture

K. Azuma
Sojo University, Kumamoto, Japan

T. Iwashita
Ariake National College of Technology, Fukuoka, Japan

ABSTRACT: This paper concerns further experimental studies on the assessment of safety for brittle fracture initiating from weld defects existing at the weld terminations. Welded plate bend models, which were designed to represent a connection of an I-section beam to an RHS column member with through diaphragms, were tested under cyclic loads. Through cracks or surface cracks, which were created by inserting aluminium plates into the grooves before welding, were installed on both sides of weld terminations. The sizes of through cracks were decided so that the brittle fracture would and would not occur, while the dimensions of the surface cracks were decided so that the cross-sectional area of the surface crack agreed with that of the through crack. Test results supported prediction; brittle fracture occurred from tips of defects. It was attempted to predict the fracture moment. The predicted moments using J values which was taken into account plastic constraint of crack tips roughly coincide with the test results.

1 INTRODUCTION

During the Kobe earthquake, brittle fractures occurred frequently caused by cracks growing from the corner of cope holes or weld tab regions in the beam bottom flange groove welds. Post-earthquake inspections showed that many of these fractures occurred at or around beam flange groove welds starting from various weld defects and from tips of ductile cracks that grew from geometrical discontinuities. One of the post-earthquake proposals is to use improved profiles of cope holes (AIJ, 1996). These new details, however, revealed other weld defects. Therefore it is important that the influences of the weld defects on the integrity of welded joints are assessed to determine a tolerable flaw size in quantitative terms. This study place emphasis on the assessment of susceptibility to brittle fracture from weld defects.

Fracture toughness properties of numerically modelled connections were evaluated by using modified failure assessment diagram (FAD) approach, considering the effect of enhanced apparent toughness of material due to the loss of crack tip constraint (Iwashita et al. 2003). Previous testing of welded plate bend models, which were designed to represent a connection of an I-section beam to an RHS column member with through diaphragms, showed that the proposed approach predict the brittle fracture precisely (Azuma et al. 2008).

This paper concerns further experimental studies on the assessment of safety for brittle fracture initiating from weld defects existing at the weld terminations. Welded plate bend models were tested under cyclic loads in order to investigate the influence of position and configuration of weld defects. The specimens were fixed to a strong reaction frame with high strength bolts through the diaphragm plate. The load was applied to the end of the cantilever by a hydraulic ram statically.

Complete joint penetration groove welds were used or the connection between the beam flange and the diaphragm. Specimens had those discontinuities at the roots of welds to the beam bottom flanges, which were created by inserting aluminium plates into the grooves before welding. Through cracks or surface cracks were installed on both sides of weld terminations. For the specimens with through cracks, the plastic constraint at the crack tips of the specimen was close to that of the double edge notched tension (DENT) specimens.

The prediction of brittle fracture with a variety of defect sizes by using the FE analysis was conducted. The sizes of through cracks were decided so that the brittle fracture would and would not occur, while the dimensions of the surface cracks were decided so that the cross-sectional area of the surface crack agreed with the area of the through crack. Test results supported prediction; brittle fracture occurred from tips of defects.

2 NOMENCLATURE

b	material constant
E	Young's modulus
$E.L.$	elongation
J	J-integral obtained by elastic-plastic analysis
J_c	critical J-integral of material obtained by SENB testing
$_{app}J_c$	apparent J_c
J_e	J-integral obtained by elastic analysis
J_{ef}	J-integral at the fracture point obtained by elastic analysis
L	length between loading point and the edge of the diaphragm
M	bending moment at the edge of the diaphragm
M_{max}	maximum moment of the cantilever
M_p	full plastic moment of the cantilever
T_s	stress triaxiality
u_1, u_2, u_3	horizontal displacement
$_vE(0)$	Charpy absorbed energy at 0 (°C)
$_vE_{shelf}$	shelf energy obtained from Charpy tests
$_vTE$	energy transition temperature
η	cumulative deformation factor
η_s	cumulative total plastic rotation factor
θ	rotation of cantilever segment between loading point and the edge of the diaphragm
θ_p	beam rotation at M_p obtained from elastic stiffness
σ_h	hydrostatic stress
σ_{eq}	von Mises's equivalent stress
σ_u	tensile strength obtained from coupon tests
σ_y	yield stress of unstressed steel
$\sigma_{1\text{-}3}$	principal stress

3 CYCLIC TESTING OF WELDED PLATE BEND MODELS

3.1 *Specimens and loading procedures*

Welded plate bend models, which were designed to represent a connection of an I-section beam to an RHS column member with through diaphragms, were tested under cyclic loads. The specimens consisted of 25 mm thick flange plate, 32 mm thick diaphragm and 16 mm thick rib plates. All plates were grade SN490B. Complete joint penetration (CJP) groove welds were used for the connection between the beam flange and the diaphragm. Weld metal was produced by electrodes designated as YGW-18. Stringer passes were used for all welding and heat inputs during welding were approximately 30 kJ/cm for each layer. The configuration of the specimen is shown in Figure 1. Specimens had those discontinuities at the roots of welds to the beam bottom flanges, which were created by inserting aluminium plates into the grooves before welding. Five specimens, two with through cracks installed on both sides of weld terminations, designated as FTC

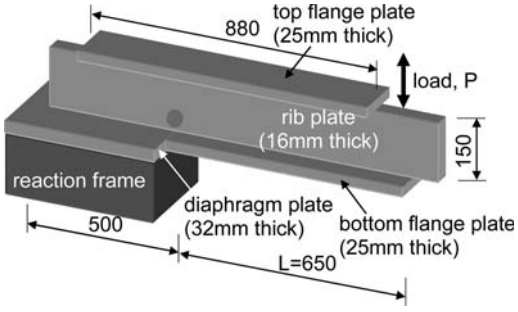

Figure 1. Specimen configuration.

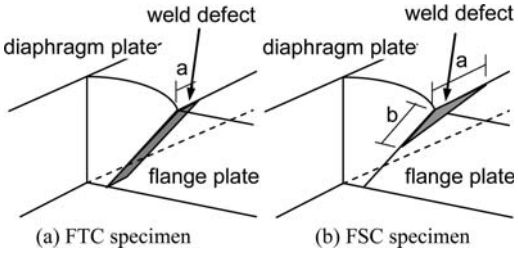

Figure 2. Locations of the defects.

specimens, and three with surface cracks installed on the corner of both sides of weld terminations, designated as FSC specimens. For the FTC specimens, the plastic constraint at the crack tips of the specimen was close to that of the DENT specimens. The locations of each defect are shown in Figure 2 and inserting condition of aluminum plates are shown in Figure 3. The defect sizes for FTC specimens were decided so that the crack depths were 4 mm and 8 mm, while the defect sizes for FSC specimens were decided as same sectional area of defects for FTC specimens. The defects sizes of FSC-7 specimen were half size of FSC-14 specimen. The defect sizes are summarized in Table 1.

Cyclic loads in the horizontal direction were applied to the end of the cantilever by a hydraulic ram statically, while the specimens were fixed to a strong reaction frame with high strength bolts through the diaphragm plate. Figure 4 shows the position of load application and the displacement measurements. The bending moment M and the rotation angle θ of the cantilever were calculated by the following equations, respectively:

$$M = P \cdot L \tag{1}$$

$$\theta = \frac{u_1 - u_3}{L} - \frac{u_2}{700} \tag{2}$$

Cyclic loading consisted of a few cycles in the elastic range and then cantilever rotations of θ_p, $2\theta_p$, $3\theta_p$, . . . with positive (tension) and negative (compression) displacement at each amplitude, until failure. The full plastic moment M_p was calculated using measured yield strengths of materials. The rotations at full plastic moment θ_p, namely M_p divided by the elastic stiffness

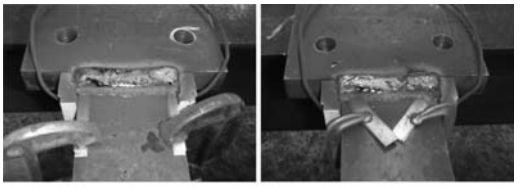

(a) FTC specimen (b) FSC specimen

Figure 3. Inserting condition of aluminium plates.

Table 1. Defect seizes (See Figure 2).

	a mm	b mm
FTC-4	4	–
FTC-8	8	–
FSC-7	7	7
FSC-14	14	14
FSC-21	21	21

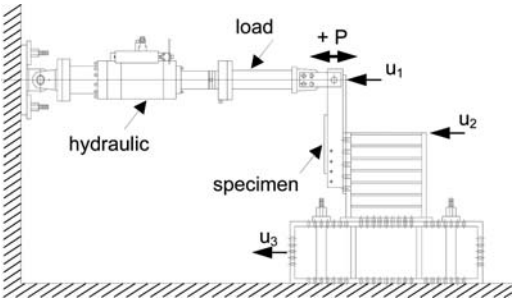

Figure 4. Positions of load application and displacement measurements.

Table 2. Results of tensile coupon tests.

Location	σ_y MPa	σ_u MPa	E.L. %	E GPa
Top flange	368.6	558.1	31.9	221.3
Bottom flange	336.3	549.3	31.8	215.8
Diaphragm	338.6	577.2	28.7	213.4
Rib plate	406.2	571.1	36.1	216.1

of the cantilever, were calculated. The elastic stiffness was determined by using slopes at unloading portions of hysteresis loops.

3.2 *Material properties*

The material properties, in terms of engineering stress-strain, were obtained by tensile coupon tests for the flanges, diaphragms andrib plates, which are summarized in Table 2.

The fracture toughness was obtained by Charpy impact tests. Test pieces were taken from plates welded

Table 3. Results of Charpy impact test.

	${}_vE(0)$ J	${}_vE_{shelf}$ J	${}_vT_{re}$ °C
Top flange	81	195	6
Bottom flange	161	177	−33
Diaphragm	170	237	−20
HAZ	136	198	−15
DEPO	114	171	−12

Figure 5. Fracture surface of FSC-7 specimen.

Table 4. Strength magnification, deformation capacity and depth of ductile cracks.

Specimen	M_{max} kNm	θ_{max} 10^{-2} rad.	M_{max}/M_p	η^+	η_s^+	d mm
FTC-4	252.8	6.34	1.45	8.54	3.61	1.0
FTC-8	192.3	2.61	1.15	1.15	0.75	0.8
FSC-7	233.6	4.94	1.30	8.90	3.04	3.0
FSC-14	243.5	5.20	1.40	9.07	3.42	3.7
FSC-21	203.4	2.91	1.24	2.95	1.60	2.0

under the same welding conditions as those for the specimens. The positions of notch roots were base metal of flange plate, diaphragm plate, HAZ (heat affected zone) and DEPO (deposited weld metal). Test pieces were cooled to temperatures between −80°C and 60°C by using dry ice and alcohol or hot water. Three test pieces were tested at each temperature. The results of Charpy impact test are shown in Table 3. The energy transition curve was obtained by fitting test results into the follow equation:

$$vE(T) = \frac{{}_vE_{shelf}}{e^{-b(T-vTE)}+1} \tag{3}$$

3.3 *Deformation capacity and failure modes*

All specimens sustained brittle fracture from the tips of the ductile cracks. The specimen after failure is shown in Figure 5. Ductile cracks initiated at tips of defects

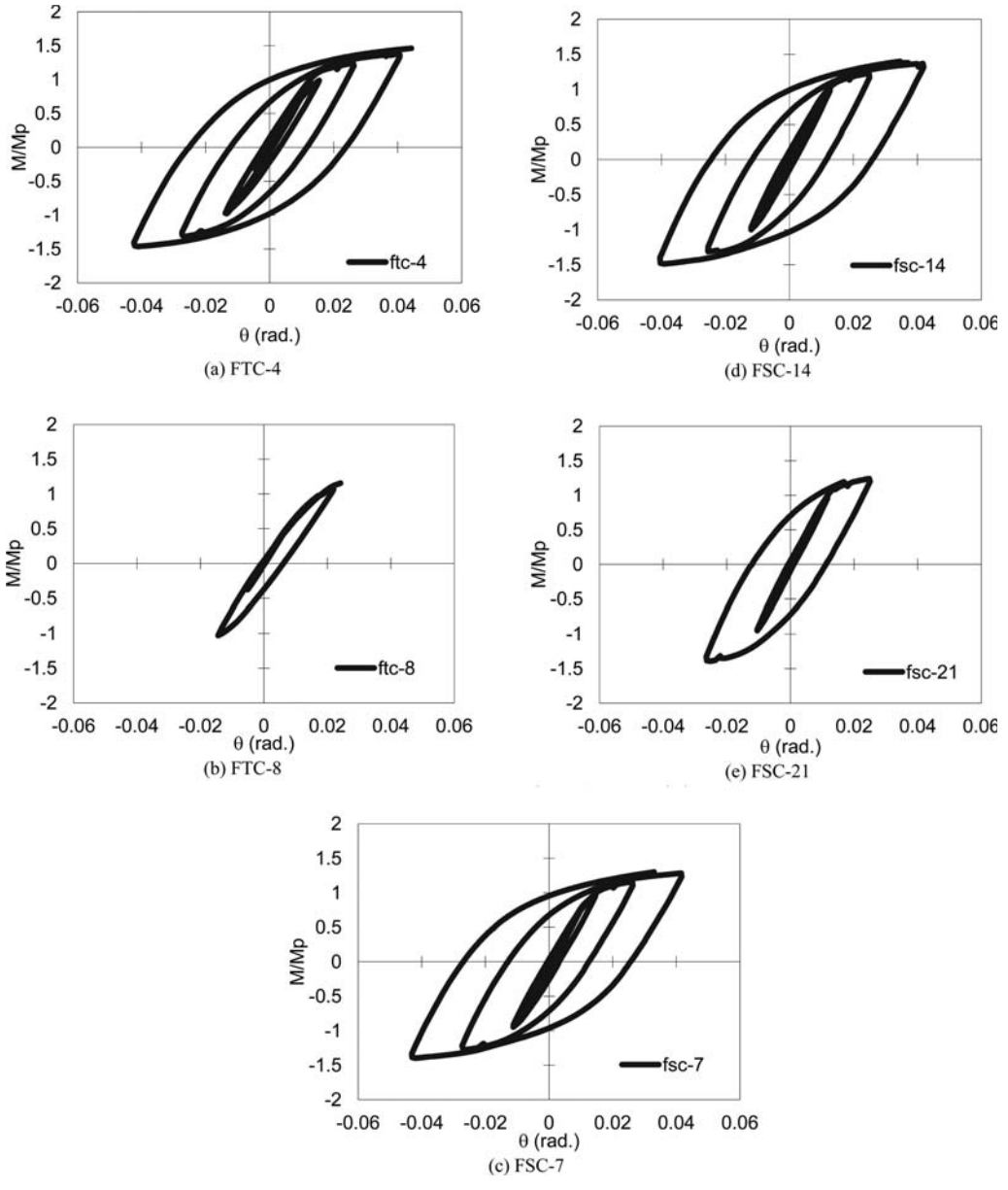

Figure 6. Hysteresis loops.

and extended stably. Table 4 summarized the maximum moments with the corresponding rotations, strength magnification,the cumulative plastic rotation factors η_s and depth of ductile cracks of each specimen. η_s was obtained from the skeleton curves for each specimen (See Appendix A).

Figure 6 shows hysteresis loops for all specimens. The moment is that at the edge of the diaphragm and is non-dimensionalized by dividing it by the full-plastic moment of the cantilever. The moment is herein defined as the positive moment when the flange plate is in tension.

Figure 7 shows moment vs. rotation skeleton curves for all specimens. Deformation capacities of FTC-8 and FSC-21 were much lower than that of other specimens. FSC-7 and FSC-14 showed almost same capacities, although the defect size for FSC-14 was twice the size of FSC-7.

3.4 *FE analysis*

A finite element analysis of the specimens was carried out using the ABAQUS (2011) general-purpose finite element package. The models were constructed

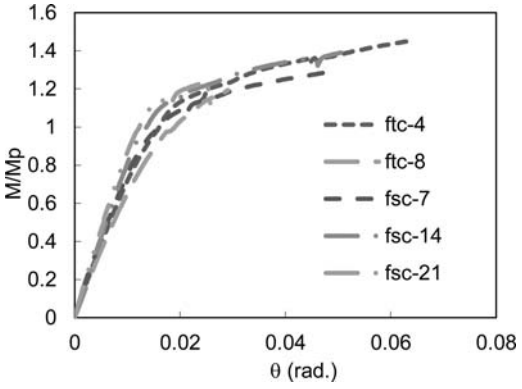

Figure 7. Moment vs. rotation skeleton curves.

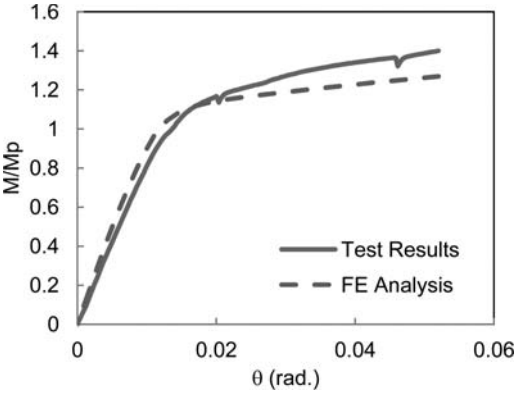

Figure 8. Moment vs. rotation skeleton curves obtained from FE analysis (FST-14).

from 8-noded linear 3D elements. This element is nonconforming and isoparametric and employs the reduced integration technique with hourglass control. The plasticity of the material was defined by the von Mises yield criterion. The isoparametric hardening law was used for this analysis. The ABAQUS program requires the stress-strain data to be input in the form of true stress and logarithmic strain, and the stress-strain curves were transformed accordingly. The material data in the analysis were calculated from tensile coupon test results. Mesh models were generated for a half of the specimens because of symmetry in configuration.

The incomplete penetration of defects was generated by the nodes in the discontinuities area on the contact surfaces between the flange and the weld metal. These surfaces were separated in each element as double nodes. A monotonic load was applied to the end of cantilever. The moment-rotation curves are compared with the skeleton curves that were obtained from experimental results for each specimen. The analysis results coincide well with the test results as seen in Figure 8.

Figure 9 shows the contour plot of equivalent stress around the defect when the deformation reached the final failure stage in FSC specimen. The greatest stress concentration was found at the tips of the defect.

Figure 10 shows the stress triaxiality, T_s, vs. J-integral curve. The stress triaxiality, which is related to plastic constraint, was defined using the following equations:

$$T_s = \frac{\sigma_h}{\sigma_{eq}} \tag{4}$$

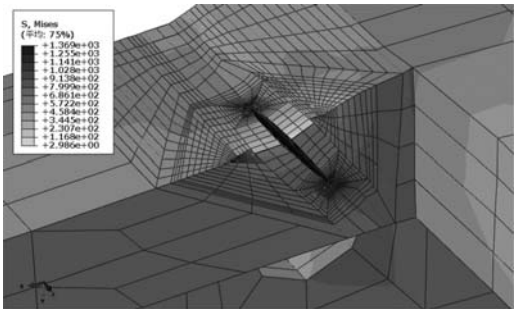

Figure 9. Contour plot of von Mises equivalent stress around the defects.

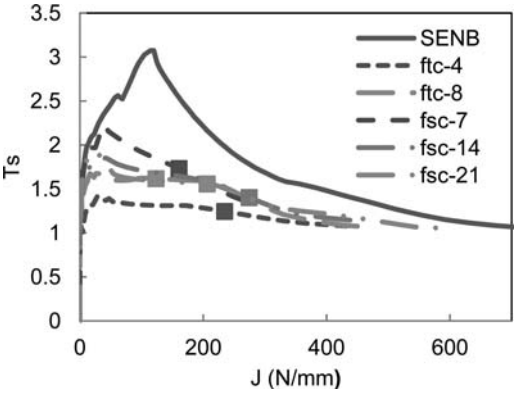

Figure 10. Stress triaxiality vs. J-integral curve.

T_s was taken as a peak value found below the blunted crack tips in FE analysis models. Plotted marks on each curve represent the fracture point. FE analysis results for SENB (single edge notched bend) models are also plotted in this figure for reference. The fracture points show a tendency for J at fracture to be large, while the stress tiaxiality is low, which is in contrast to with SENBmodels. For all specimen, the brittle fracture occurred at final stage of the test. The development of the J-integral is large as shown in Figure 10, so that ductile cracks extended before fracture. Crack growth increases the chance of sampling hard particles and may lead to brittle fracture even if the stress triaxiality is low. It is therefore necessary to consider crack growth to predict stress triaxiality and J-integral more adequately.

4 ASSESSMENT OF WELD DEFECTS

4.1 *Assessment procedure*

Fracture toughness properties of the simplified beam-to-column connections specimens, which sustained brittle fractures, were assessed by using a modified FAD approach (Iwashita et al. 2003), which plastic constraint is taken into account. The same approach was applied to the numerically modeled defects to evaluate the fracture toughness properties of tested specimens.

BS 7910 gives guidance on fracture mechanics based method for assessing the acceptability of defects in structures. Assessment is generally made by means of a FAD based on the principles of fracture mechanics. The defect is assessed by evaluating the fracture and plastic collapse parameters and plotting the corresponding point on the FAD. The vertical axis of the FAD is a ratio of the applied fracture toughness to the required fracture toughness. The horizontal axis is the ratio of the applied load to that required to cause plastic collapse. An assessment lines is plotted on the diagram. Calculations for a flaw provide the co-ordinates of an assessment point. The location of the point is compared with the assessment line to determine the acceptability of the flaw.

The assessment procedures are given as follows:

1. Determination of assessment curve
2. Calculation of plastic collapse parameters (L_r) using the ratio of moment
3. Calculation of fracture parameters (K_r) taking into account the effect of plastic constraint

4.2 *Prediction of brittle fracture*

The assessment curve of Level 3C in the BS 7910 is applied to the FAD. L_r for the assessment curve is calculated from the following equation:

$$L_r = \frac{M}{M_p} \qquad (L_r \le L_{r,\max}) \tag{5}$$

$L_{r,\max}$ is determined using the following equation:

$$L_{r,\max} = \frac{\sigma_y + \sigma_u}{2\sigma_y} \tag{6}$$

K_r is calculated from the following equation:

$$K_r = \sqrt{\frac{J_e}{J}} \tag{7}$$

where J and J_e are the values at same applied load and obtain from FE analysis.

K_r and L_r at the fracture point of each specimen were determined by using the following equations:

$$L_r = \frac{M_{\max}}{M_p} \tag{8}$$

$$K_r = \sqrt{\frac{J_{ef}}{J_e}} \tag{9}$$

4.3 *Plastic constraint effects*

The fracture toughness of a material is frequently measured by a three points bending test using SENB specimens. SENB specimens may be subjected to much greater plastic constraint at the crack tips as compared with tips of surface cracks in wide plate specimens. Therefore, critical fracture toughness for a wide plate under tensile loads is possibly under-estimated.

The stress state at crack tips resembles that of a notched bar with a volume of material surrounded by a contour of a certain value of the maximum principal stress, σ_1. The volume for the specimen with shallow notch is smaller than that for the specimen with deep notch, even if the same J value is applied to each specimen. This is an example of the fracture toughness depending on the size and geometry of the specimens. Anderson and Dodds (1991) proposed that the probability of brittle fracture may be equal for two specimens when the volumes are equal. The volume could be replaced with the area. The area in this case

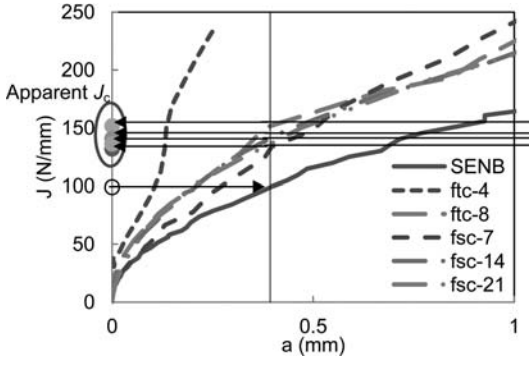

Figure 11. J-integral vs. area curves for all models.

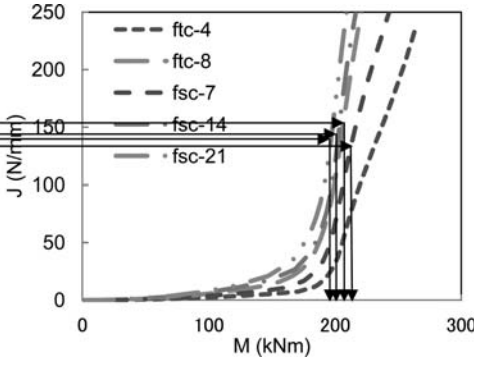

Figure 12. J-integral vs. moment curves for all models.

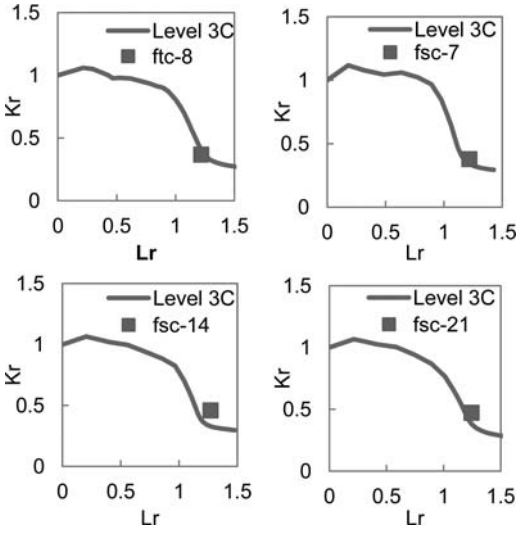

Figure 13. Failure assessment diagram.

is the plane area at the crack tip surrounded by the contour of a certain value of σ_1. The maximum principal stress is assumed as $\sigma_1 = 3\sigma_y$.

Figure 11 shows J-integral vs. area curves for all models. The vertical axis is the applied J-integral while the horizontal axis is the area surrounded by a contour of a certain value of σ_1 at the crack tip. When the critical J value, J_c, is obtained from SENB testing of a deeply notched specimen, the value of J_c can be corrected by determining the J value at which the crack tip area of the shallowly notched specimen equals that of the deeply notched specimen at J_c. The corrected J_c is called the apparent $J_{c,app}J_c$. Notch toughness J_c of base metal of specimens was99 N/mm, which was obtained from SENB testing. ${}_{app}J_c$ of each specimens were summarized in Table 5.

4.4 *Assessment*

Following the procedures discussed in previous sections, the assessment of susceptibility to brittle fracture was made for numerically modelled joints with defects. Figure 13 shows the modified FAD plotting the failure point that is obtained by using the ${}_{app}J_c$ in the calculation of K_r.

Plastic constraint at tips of defects of FTC specimens was lower than that of FSC specimen, and was much lower than SENB model. For the FTC-4 specimen, ${}_{app}J_c$ could not be obtained because the area at crack tips surrounded by the contour of maximum principal stress did not reached that of the SENB model, as shown in Figure 11. Therefore, it was unlikely to have a brittle fracture starting from the tips of defects, while test result showed the specimen sustained brittle fracture.

For the rest specimens which ${}_{app}J_c$ could be obtained, the failure point of each specimen, except for FSC-14 specimen, was plotted on the assessment curve. These results show that the modified FAD using ${}_{app}J_c$ could predict the risk of brittle fractures precisely. For the FSC-14 specimen, the failure point was plotted outside of assessment curve. This result shows that brittle fractures would occur from the tips of the ductile cracks when the ductile cracks grew more. The test result supported the prediction; ductile cracks grew from the tips of defects under cyclic loading and the specimen showed much larger deformation capacity.

Table 5. Apparent Jc and maximum moment.

Specimen	${}_{app}J_c$ N/mm	M_{max} kNm	M_{pre} kNm	M_{max}/M_{pre}
FTC-4	–	252.8	–	–
FTC-8	151	192.3	206.3	0.93
FSC-7	132	233.6	212.2	1.10
FSC-14	141	243.5	202.4	1.20
FSC-21	136	203.4	196.6	1.03

4.5 *Prediction of fracture moment*

It was attempted to predict the fracture moment using the apparent J_c. Figure 12 shows J-integral vs. moment curves and Table 5 summarized M_{max}, M_{pre} and the ratio of M_{max} and M_{pre}. The predicted Moments roughly coincide with test results, except for FSC-14 specimen.

5 CONCLUSIONS

A modified fracture mechanics approach was examined on five welded plate bend models using apparent J_c obtained by FE analyses. Deflection measurements as well as FE analysis results showed that stress sustained at the tips of the defects before cracks extended significantly were about equal in magnitude irrespectively of the defect size. Plastic constraint, crack growth and failure behaviour also same in each series of specimen, varied slightly with the location of defects. Note that ductile crack growth is ignored in the calculations. Some difficulties found in the proposed approach lies in how to evaluate the effect of ductile crack growth. To appraise this approach, the ductile tearing analysis had to be included into FAD approach.

APPENDIX A

The skeleton curve constructed from moment versus rotation hysteresis loops is defined here. To simplify the following description hysteresis loops are assumed to increase their rotation range incrementally with the cycle as shown in Figure A1. When the load during the 2nd cycle exceeds the peak load on the 1st cycle, the exceeding portion of the loop during the 2nd cycle is connected to the point at the peak load on the 1st

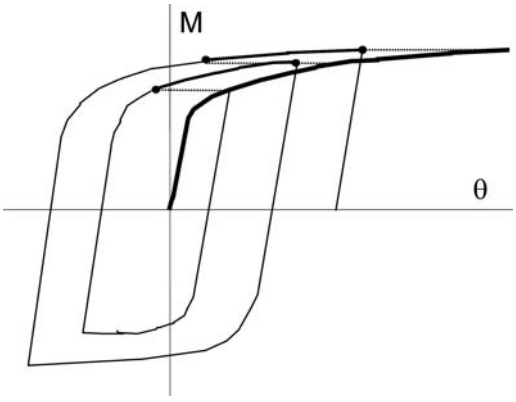

Figure A1. Definition of skeleton curve.

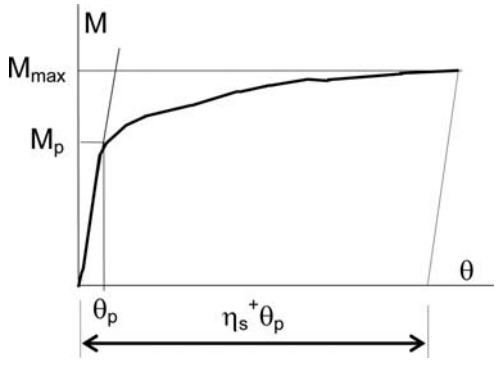

Figure A2. Definition of cumulative plastic rotation factor.

cycle. The same process is repeated until the highest moment is reached. The piece-wise continuous curve thus constructed from hysteresis loops is called the skeleton curve. The skeleton curves are drawn on both positive and negative rotation sides.

The plastic component of rotation at the maximum moment, non-dimensionalized by dividing it by θ_p, is called the cumulative plastic rotation factor and is denoted by η_s^+ (See Figure A2). The skeleton curve can be constructed also from stress versus strain hysteresis loops.

The skeleton curve for the elastic-plastic material or structure roughly coincides with the monotonic stress-strain or load-deflection curve.

ACKNOWLEDGMENT

This work was partly supported by the Japanese Society for the Promotion of Science Grant-in-Aid for Scientific Research under the number 22560579. The authors would like to thank the Japan Iron and Steel Federation for providing steel material for this test. Thanks are extended also to B.Sc. students for hard work in laboratories.

REFERENCES

ABAQUS 2011. ABAQUS v6.6 Manuals (User's Manuals I, II and III), Dassault Systemes Simulia Corp.

AIJ Kinki. 1997. Full-scale test on plastic rotation capacity of steel wide-flange beams connected with square tube steel columns. Committee on Steel Building Structures, Kinki Branch of Architectural Institute of Japan, Osaka, Japan. (in Japanese)

AIJ. 1996. Technical recommendations for steel construction for buildings. Part 1 guide to steel-rib fabrications. Architectural Institute of Japan, Tokyo, Japan. (in Japanese)

Anderson, T.L. and Dodds, R.H., Jr. 1991.Specimen size requirements for fracture toughness testing in the ductile-brittle transition region. Journal of Testing and Evaluation. Vol. 19(2), pp. 123–134

Azuma, K., Kurobane, Y. and Makino, Y. 2000. Cyclic testing of beam-to-column connections with weld defects and assessment of safety of numerically modeled connections from brittle fracture. Engineering Structures, Vol. 22, No. 12, Elsevier Science Ltd., pp. 1596–1608

Azuma, K., Kurobane, Y. and Makino, Y. 2003. Full-scale testing of beam-to-column connections with partial joint penetration groove welded joints. Proceedings ofthe 10th International Symposium on Tubular Structures, pp. 419–427

Azuma, K., Kurobane, Y. Iwashita, T. and Dale, K. 2006. Applicability of Partial Joint Penetration Groove Welded Joints to Beam-to-RHS Column Connections and Assessment of Safety from Brittle Fracture. Proceedings of the 11th International Symposium on Tubular Structures, pp. 611–619

Azuma, K., Kurobane, Y. Iwashita, T. and Dale, K. 2006.Assessment of safety from brittle fracture initiating at tips of PJP groove welded joints. Proceedings of the 4th International Symposium on Steel Structures, Vol.1, pp. 186–197

BSI. 1997. Guidance on methods for assessing the acceptability of flaws in metallic structures. BS 7910

Iwashita, T., Kurobane, Y., Azuma, K., and Makino, Y. 2003. Prediction of brittle fracture initiating at ends of CJP groove welded joints with defects: study into applicability of failure assessment diagram approach. Engineering Structures, Vol. 25, Issue 14, Elsevier Science Ltd., pp. 1815–1826

Tubular Structures XIV – Gardner (Ed.)
© 2012 Taylor & Francis Group, London, ISBN 978-0-415-62137-3

Stress concentration factors for fatigue design of CHS-SHS T-joints

L.W. Tong & H.Z. Zheng
College of Civil Engineering, Tongji University, Shanghai, China

F.R. Mashiri
School of Engineering, University of Western Sydney, Penrith South DC, NSW, Australia

X.L. Zhao
Department of Civil Engineering, Monash University, Melbourne, Australia

ABSTRACT: Alternative type of nodal joints consisting of Circular Hollow Section (CHS) braces and Square Hollow Section (SHS) chords (CHS-SHS joints)have increasingly been studied to understand strain distribution and therefore Stress Concentration Factors (SCFs) at weld toes on the braces and chords for fatigue design in structural systems subjected to cyclic loading. Experimental Strain Concentration Factors (SNCFs) for eight CHS-SHS T-joints with unique non-dimensional parameters were determined in this research resulting in the evaluation of SCFs for fatigue design. Using the ANSYS software, a three-dimensional Finite Element Model (FEM) was then developed to simulate the stress distribution at the brace-chord welded interface under axial force and in-plane bending in the brace. A parametric study was carried out to determine the SCFs for numerous models with unique non-dimensional parameters. Graphs are drawn which can be used for the estimation of SCFs in these joints.

1 INTRODUCTION

Tubular T- joints made up of circular hollow section braces (CHS) and square hollow section (SHS) chords (CHS-SHS T-joints) have the advantage that they require less complex end preparation compared to nodal T-joints made up of circular hollow section (CHS) braces and circular hollow section (CHS) chords (CHS-CHS T-joints). Since profiling of the brace is not required in CHS-SHS T-joints, this means that the cost of fabrication and hence construction of these joints is relatively lower. When compared to nodal T-joints made up of square hollow section braces (SHS) and square hollow section (SHS) chords (SHS-SHS T-joints), CHS-SHS T-joints have been found to have reduced stress concentrations at the brace-chord welded interface (Bian and Kim 2003, Mashiri et al 2004, Tong et al 2006). This is mainly because of the change of the brace from a square hollow section in SHS-SHS T-joints to a circular hollow section in CHS-SHS T-joints results in a reduction in stress concentration factors at the brace weld toes as well as the chord weld toes.

Previous research by Bian and Kim (2003) and Mashiri et al (2004) did not carry out any comprehensive parametric studies for the determination of SCFs that are required for fatigue design.

In this investigation, eight CHS-SHS T-joints with unique non-dimensional parameters were strain gauged for the determination of strain concentration factors (SNCFs) and therefore SCFs. A three-dimensional finite element model was then developed using the ANSYS software to simulate the stress distribution at the brace-chord welded interface under axial force and in-plane bending in the brace. Validation of the model was carried out by comparing the SNCFs determined from the experiment and those determined from the finite element model. A parametric study was carried out to determine the SCFs for numerous models with unique non-dimensional parameters, β ($=d_1/b_0$); 2γ ($=b_0/t_0$) and τ ($=t_1/t_0$). Graphs are drawn which can be used for the estimation of SCFs in these joints.

2 SPECIMENS AND MATERIAL PROPERTIES

Figure 1 shows the schematic diagram of a CHS-SHS T-joint. The joints are made up of a CHS brace and SHS chord. The CHS-SHS T-joints were tested under two types of loading respectively: (1) Axial force in the brace and (2) In-Plane Bending (IPB) in the brace.

Eight CHS-RHS T-joints were manufactured for testing. The joints were manufactured using steel of grade Q345B which complies with the Chinese Standards. Grade Q345B steel has a minimum specified yield stress of 345 MPa and a minimum specified ultimate tensile strength of 470 MPa. The joints were welded using prequalified welding methods from the AWS Code (2008). Full penetration welds were used

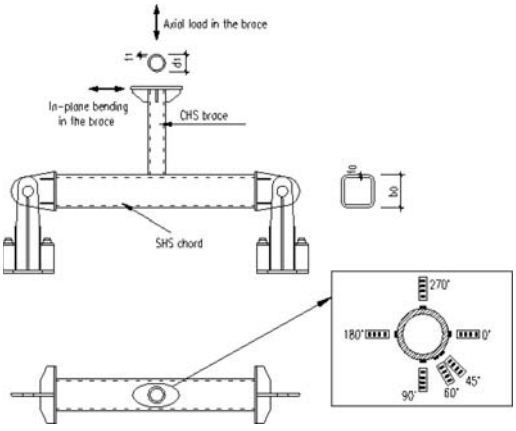

Figure 1. Schematic diagram of CHS-SHS T-joint and location of strain gauges.

Table 1. Test Specimens.

	SHS Chord		CHS Brace		Non-Dimensional Parameters		
Joint	b_0 *mm*	t_0 *mm*	d_1 *mm*	t_1 *mm*	β	γ	τ
T1	250	12	133	6	0.53	10.42	0.50
T2	250	12	133	4	0.53	10.42	0.33
T3	250	12	133	10	0.53	10.42	0.83
T4	250	10	133	5	0.53	12.50	0.50
T5	250	8	133	4	0.53	15.63	0.50
T6	200	10	133	5	0.67	10.00	0.50
T7	300	12	133	6	0.44	12.50	0.50
T8	200	12	180	8	0.90	8.33	0.67

in the manufacture of the welded CHS-SHS T-joint specimens.

The eight specimens that were investigated are characterized by the following non-dimensional parameter ranges for β ($=d_1/b_0$), 2γ ($=b_0/t_0$) and τ ($=t_1/t_0$):

$$0.44 < \beta < 0.90$$

$$16.67 < 2\gamma < 31.25$$

$$0.33 < \tau < 0.83$$

It can be seen from Table 1 that there are 3 different connections series. In the first series, the non-dimensional parameters β and γ are kept constant while τ is changing, see T1, T2 and T3 in Table 1. In the second series, the non-dimensional parameters β and τ are kept constant while γ is changing, see T1, T4 and T5 in Table 1. For the third series, the non-dimensional parameters γ and τ are kept constant while β is changing, see T4, T6 and T7 in Table 1, where the γ of T6 was chosen close to γ of T4 and T7 because no SHS chord with exactly the same γ and τ simultaneously as T4 and T7 could be found in the market. A specimen was also chosen to investigate the influence of a particular large value of β, see T8 in Table 1.

3 STRAIN CONCENTRATION FACTORS (SNCFS) – AXIAL FORCE IN THE BRACE

Strain measurements in the CHS-SHS T-joints were measured at the locations shown in Figure 1. Strip strain gauges with four strain sensitive gauges were used to measure the strain distributions close to the weld toes. In both the brace and the chord, the strip gauges were located at 0, 45, 60 and 90 degrees, the locations indicated in Figure 1. The location of the first strain gauge from the toes of the weld was based on the current recommendations in CIDECT Design Guide No. 8 (Zhao et al 2000) for the measurement of strains used in the extrapolation for hot spot strains in SHS joints. The first strain gauge should be located at a distance 0.4t but not less than 4 mm from the toe of the weld.

The determination of SNCF was based on both linear and quadratic extrapolation. The linear and quadratic extrapolation methods were both used in determining SNCF in order to determine the degree of non-linearity along the different lines of measurement along which SNCF was measured. The degree of non-linearity can be seen through the magnitude of the ratio of the SNCF determined through quadratic extrapolation ($SNCF_{quad}$) to the SNCF determined through linear extrapolation ($SNCF_{lin}$). The strain distribution close to the weld toes, at the lines of measurements in the brace can be considered to be significantly non-linear compared to the strain distribution at weld toes in the main chord for the load "axial force in the brace". The average ratio of the $SNCF_{quad}$ to $SNCF_{lin}$ ranges from 104% to 165% in the brace. For the chord, a relatively smaller average ratio of 101% to 116% was found between $SNCF_{quad}$ and $SNCF_{lin}$. The current fatigue design guidelines such as CIDECT Design Guide No. 8 (Zhao et al 2000) recommend the use of the linear extrapolation method for CHS tubular joints and the quadratic extrapolation for RHS tubular joints. It is therefore important that new research on joints made up of a combination of CHS and RHS investigates the suitable methods for extrapolation in these joints. Based on the observations from this investigation, it is recommended that for CHS-SHS T-joints, the quadratic extrapolation should be adopted for the determination of hot spot strain.

4 STRAIN CONCENTRATION FACTORS (SNCFS)– IN PLANE BENDING IN THE BRACE

For the load type "in-plane bending in the brace", strain measurements were also obtained in the CHS-SHS T-joints at the locations shown in Figure 1. In both the brace and the chord, the strip gauges were therefore located at 0, 45, 60 and 90 degrees, as shown in Figure 1.

The SNCFs in the brace and the chord were also based on both linear and quadratic extrapolation to

determine the degree of non-linearity along the different lines of measurement along which SNCFs were measured. The strain distribution close to the weld toes, at the lines of measurements in the brace can also be considered to be significantly non-linear compared to the strain distribution at weld toes in the main chord for the load "in-plane bending in the brace". The average ratio of the $SNCF_{quad}$ to $SNCF_{lin}$ ranges from 112% to 151% in the brace. For the chord, a relatively smaller average ratio of 102% to 127% was found between $SNCF_{quad}$ and $SNCF_{lin}$. The stress distribution under in-plane bending therefore also shows that quadratic extrapolation should be adopted for the accurate determination of hot spot strain.

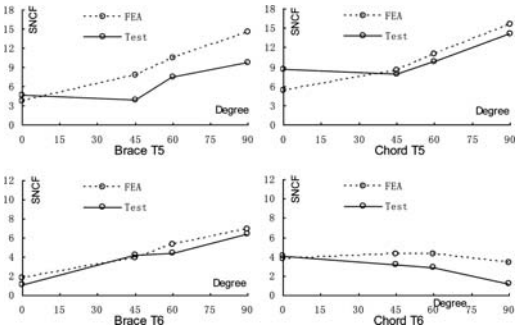

Figure 2. Comparison of typical SNCF in CHS-SHS T-joints under axial force in the brace between FEA and tests.

5 MAXIMUM SNCF – AXIAL AND IN PLANE BENDING IN THE BRACE

The typical results of the SNCFs for the load "Axial force in the brace" are shown in Figure 2. It can be concluded that maximum SNCFs are located at 90 degrees in the brace and at 0 and 90 degrees in the chord for all the tested specimens. Carrying out measurements at these two locations should therefore be sufficient to capture the maximum SNCF in CHS-SHS T-joints under axial force in the brace.

Figure 3, on the other hand, shows the typical results for the SNCFs for the load "In-plane bending in the brace". The results in Figure 3 shows that the maximum SNCF in the brace occurs at 2 locations, 0 and 60 degrees for all the tested specimens. The maximum SNCF in the chord occurs at either 0 or 45 degrees. It can however be observed that when the maximum SNCF occurs at 45 degrees, it is of comparable magnitude to the maximum SNCF measured at either location 0 or 60 degrees. When the maximum SNCF occurs at 45 degrees, the average ratio of the maximum SNCF at 45 degrees to the maximum SNCF at either 0 or 60 degrees is 1.085 showing that the magnitude of these SNCF is comparable. For design purposes, it is therefore recommended that the maximum SNCF in the chord should be reasonably determined by measuring SNCF at 0 and 60 degrees. This therefore enables the measurements in both the brace and the chord to be measured at both 0 and 60 degrees in order to determine the maximum SNCF. It is an important feature that 0 degree is not always the location where the maximum SNCF occur for the load "In-plane bending in the brace". The SNCF at 60 degree may also become maximum so that the location must be paid attention to.

Using the above observations for the locations of maximum SNCF in the brace and chord under both axial force and in-plane bending in the brace, it can be concluded that for CHS-SHS T-joints, strain measurements should be carried out at locations 0, 60 and 90 degrees in order to reasonably determine the maximum SNCF in these joints.

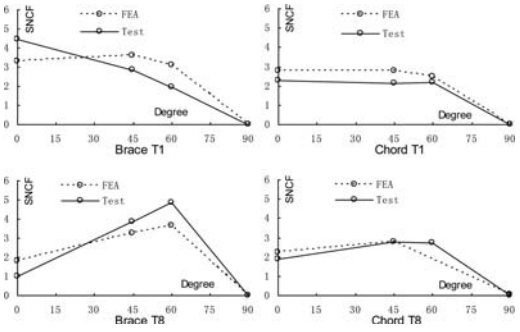

Figure 3. Comparison of typical SNCF in CHS-SHS T-joints under in-plane bending in the brace between FEA and tests.

6 FINITE ELEMENT ANALYSIS OF CHS-SHS T-JOINTS

Finite element analysis was used to model the CHS-RHS T-joints in order to carry out a parametric study of the effects of non-dimensional parameters on SCFs. Eight joints with unique non-dimensional parameters were modeled and analyzed under two types of loads, axial force in the brace and in-plane bending in the brace. The ANSYS Software was used (ANSYS 2010). The Solid 92 element was chosen for meshing. The Solid 92 element is a 3D, 10 node tetrahedral structural solid element. Its advantage is that it enables quadratic displacement behavior (ANSYS 2010). It also enables flexibility in modeling that is suitable for simulating behavior in irregular shaped objects. For the CHS-SHS joints, this flexibility is important in modeling the brace, chord and weld interface. Elements were chosen to have a size of 0.4t (t = thickness of brace or chord) around the welded joint, in order to capture the stress distribution within the recommended extrapolation region. The size of the mesh was gradually increased to as large as 1.5t away from the welded interface. A modulus of elasticity of 2.05×10^5 MPa and a Poisson's ratio of 0.3 was used for the steel tubes and weld metal. The length of the brace and chord used in the model was the same as that in the welded specimens. The length of the chord was $6b_0$ and the length of

the brace was $5d_1$. Only half of the specimen was modeled because of symmetry when considering in-plane bending in the brace. The weld size used in the modeling of the specimens was an average of the weld size in the tested specimens. A detail of the brace to chord welded interface is shown in Figure 4(a). Extrapolation for the determination of hot spot stresses was carried out at the seven locations from 0 to 90 degrees with an interval of 15 degrees, see Figure 4(b) which also covered the hot spot stresses at the locations determined experimentally.

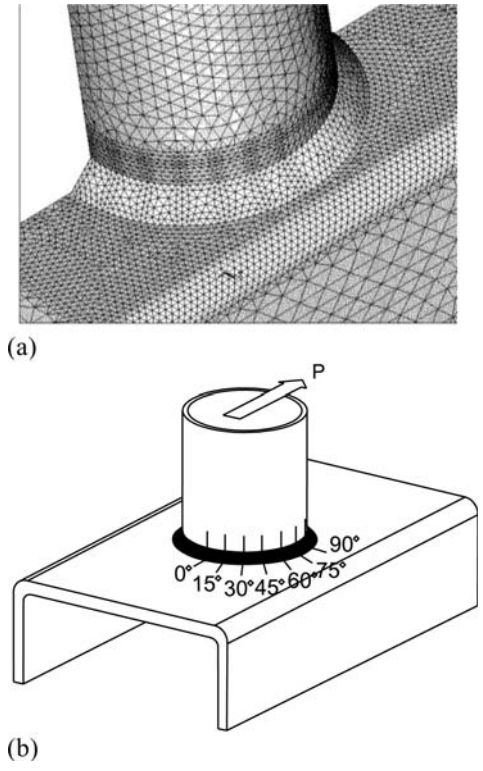

Figure 4. Finite element analysis: (a) Mesh of brace-chord welded interface, (b) Locations of extrapolation for hot spot stresses.

Figure 2 shows a comparison of the SNCF determined experimentally and those determined from the finite element models for the load "axial force in the brace". The comparison in Figure 2 shows that the finite element models are able to capture not only similar magnitudes in SNCFs but also similar trends in SNCF at the different locations around the brace-chord welded interface. The models adopted can therefore be considered to be suitable for determining stress concentration factors in CHS-SHS T-joints under axial force in the brace.

Figure 3, on the other hand, shows a comparison of the SNCF determined experimentally and those determined from the finite element models for the load "in-plane bending in the brace". The comparison in Figure 4 also shows that the finite element models are also able to capture not only similar magnitudes in SNCFs but also similar trends in SNCF at the different locations around the brace-chord welded interface. The models adopted can therefore also be considered to be suitable for determining stress concentration factors in CHS-SHS T-joints under in-plane bending in the brace.

In the determination of a finite element suitable for representing joints under fatigue loading, it is also important that the finite element model should be able to capture the maximum SCF in the joint. The maximum SCF in the joint is used in determining the fatigue life of the joint. Figure 5 (a) and (b) show the comparison of the SNCF in the brace and chord respectively when the CHS-SHS T-joint is under axial load in the brace. Figure 5(a) and (b) show that there is a good correlation between the SNCF determined experimentally and those determined by the finite element models. More importantly, Figure 5(c) shows a comparison of the maximum SNCF in the joints for SNCFs determined experimentally and through finite element analysis for the load "axial force in the brace". Figure 5(c) shows that the finite element models are able to effectively capture the maximum SNCF in the joints.

Figure 6(a) to (c) on the other hand shows the comparison of SNCFs when the CHS-RHS T-joints are subjected to in-plane bending in the brace. Figure 6(a) and (b) show that there is a good correlation between

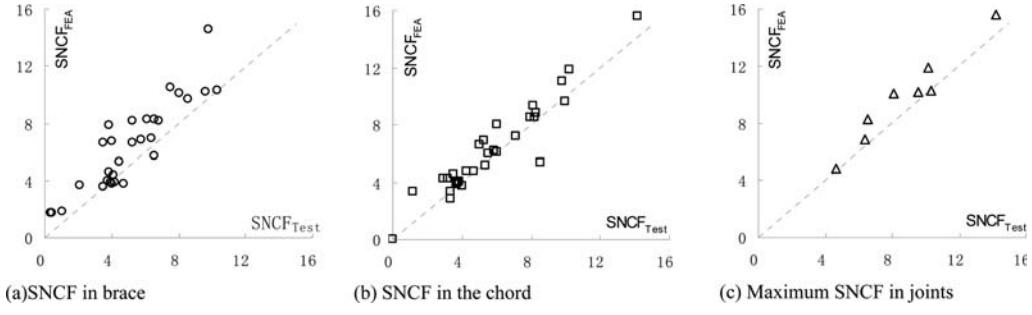

Figure 5. Comparison of SNCFs determined experimentally and those from FEA for CHS-SHS T-joints under axial force in the brace.

the SNCF determined by the finite element models and those determined experimentally for the load "in-plane bending in the brace". Figure 6(c) also shows that the finite element models are able to capture the maximum SNCF in the CHS-SHS T-joints for the determination of fatigue life. Figure 6(c) shows that there is a good correlation between maximum SNCFs in the joints determined experimentally and those determined from finite element analysis.

7 PARAMETRIC ANALYSIS

Since the finite element models are able to capture the SNCFs around the welded brace to chord interface in CHS-SHS T-joints under both axial force and in-plane bending in the brace, the models can therefore be used in parametric studies to determine the influence of non-dimensional parameters on SNCFs and therefore SCFs.

Finite element models were analyzed to determine the influence of the non-dimensional parameters, β ($=d_1/b_0$); $2\gamma(=b_0/t_0)$ and $\tau(=t_1/t_0)$. These are the non-dimensional parameters that have been also been found to greatly influence the SCFs at the weld interface of tubular joints (van Wingerde 1992). For the CHS-SHS T-joints under axial force in the brace, 101 finite element models were analyzed to determine the influence of the non-dimensional parameters β, 2γ and τ. The influence of β on SCFs in the brace and the chord when 2γ and τ are kept constant is shown in Figure 7 when the CHS-SHS T-joints are subjected to axial force in the brace. The trends of SCFs against β are plotted for the locations 0, 60 and 90 degrees in the brace as well as in the chord. These are locations which can be used to determine the maximum SNCFs in both the brace and the chord when CHS-SHS T-joints are under axial load in the brace. Figure 7 shows that in general, under axial force in the brace:

(a) For the brace, the magnitude of SCF increases as the value of τ decreases, for a given value of β and 2γ.
(b) For the brace, the magnitude of SCF increases as the value of 2γ increases, for a given value of β and τ.

On the other hand the SCFs in the chord can also be seen to depend on the non-dimensional parameters β, 2γ and τ. The magnitude of SCF almost increases as the value of 2γ increases, for a given value of β and τ. However, the influence of the non-dimensional parameter τ on SCFs in chord is more complex for a given value of β and 2γ, with trends changing from one location to another. This shows that the trends of SCFs in CHS-SHS T-joints are complex and depended not only on the non-dimensional parameters but also on the relative location of the hot spot around the welded brace-chord interface.

For the CHS-SHS T-joints under in-plane bending in the brace, 101 finite element models were also analyzed to determine the influence of the non-dimensional parameters β, 2γ and τ. The influence of β on SCFs in the brace and the chord when 2γ and τ are kept constant is shown in Figure 8, when the CHS-SHS T-joints are subjected to in-plane bending in the brace. The trends of SCFs against β are plotted for the locations 0 and 60 degrees in the brace as well as in the chord. These are locations which can be used to determine the maximum SNCFs in both the brace and the chord when CHS-SHS T-joints are under in-plane bending in the brace. Figure 8 shows that in general, for both the brace and the chord:

(a) The magnitude of SCF is influenced by the value of τ, for a given value of β and 2γ.
(b) The magnitude of SCF increases as the value of 2γ increases, for a given value of β and τ.

Figure 8 also shows that the relationship between SCF and the non-dimensional parameters, β; 2γ and τ is also seen to be influenced by the location of the hot spot along the welded brace-chord interface.

8 CONCLUSIONS

Recent research on fatigue of welded nodal joints has focused on non-traditional joints such as CHS-SHS T-joints. A review of existing research shows that there are no graphs or parametric equations for determining SCFs for CHS-SHS T-joints. The focus of this paper is to determine graphs that can be

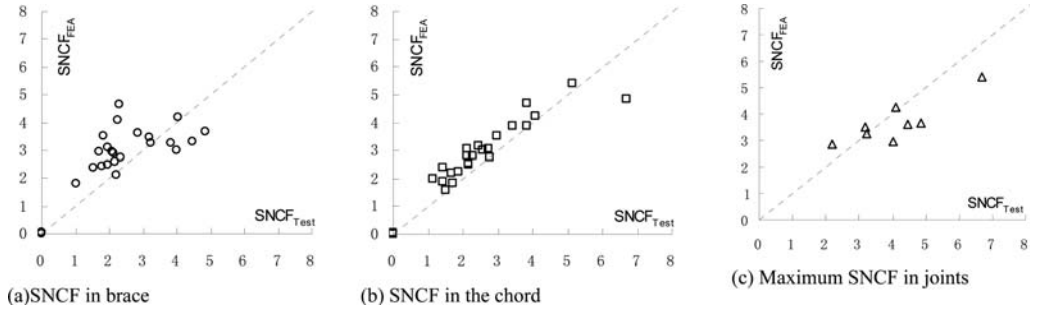

Figure 6. Comparison of SNCFs determined experimentally and those from FEA for CHS-SHS T-joints under In-Plane Bending (IPB) in the brace.

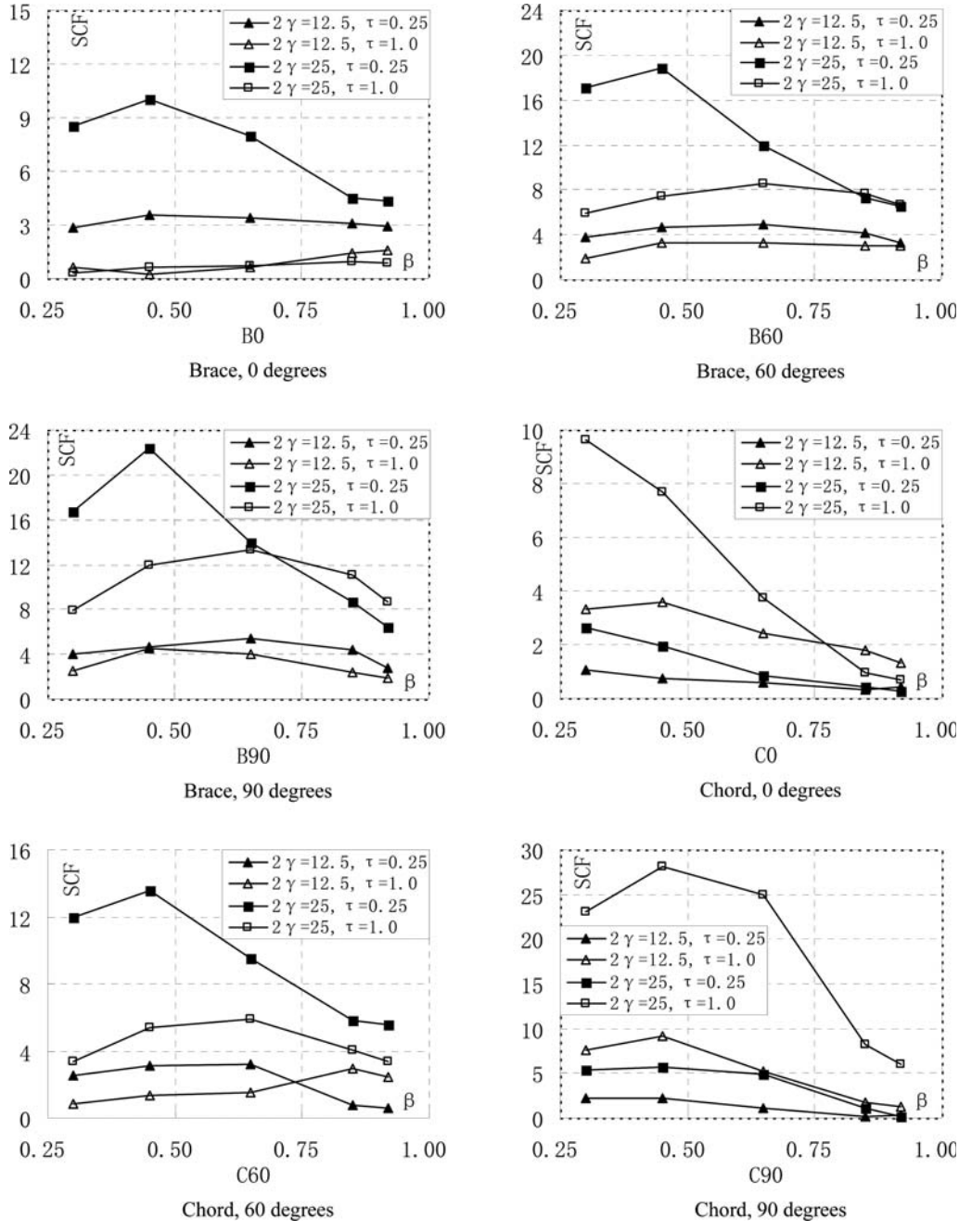

Figure 7. Influence of β on SCFs when 2γ and τ are kept constant for axial force in the brace.

used for the determination of SCFs in CHS-SHS T-joints subjected to axial and in-plane bending in the brace. In this paper, an experimental investigation was used to determine SNCFs in a series of CHS-SHS T-joints with unique non-dimensional parameters. This was followed by the development of a 3D model to simulate the stress distribution at weld toes in the CHS-SHS T-joints. Validation of the model was carried out through comparison of strain distribution at weld toes in the model to those determined experimentally. The calibrated finite element models were used in a parametric study to determine SCFs for a variety of non-dimensional parameters β, 2γ and τ values.The following conclusions were made:

(1) The strain distributions at the weld toes in the CHS-SHS T-joints were found to be non-linear in both the brace and the chord. The ratio of the

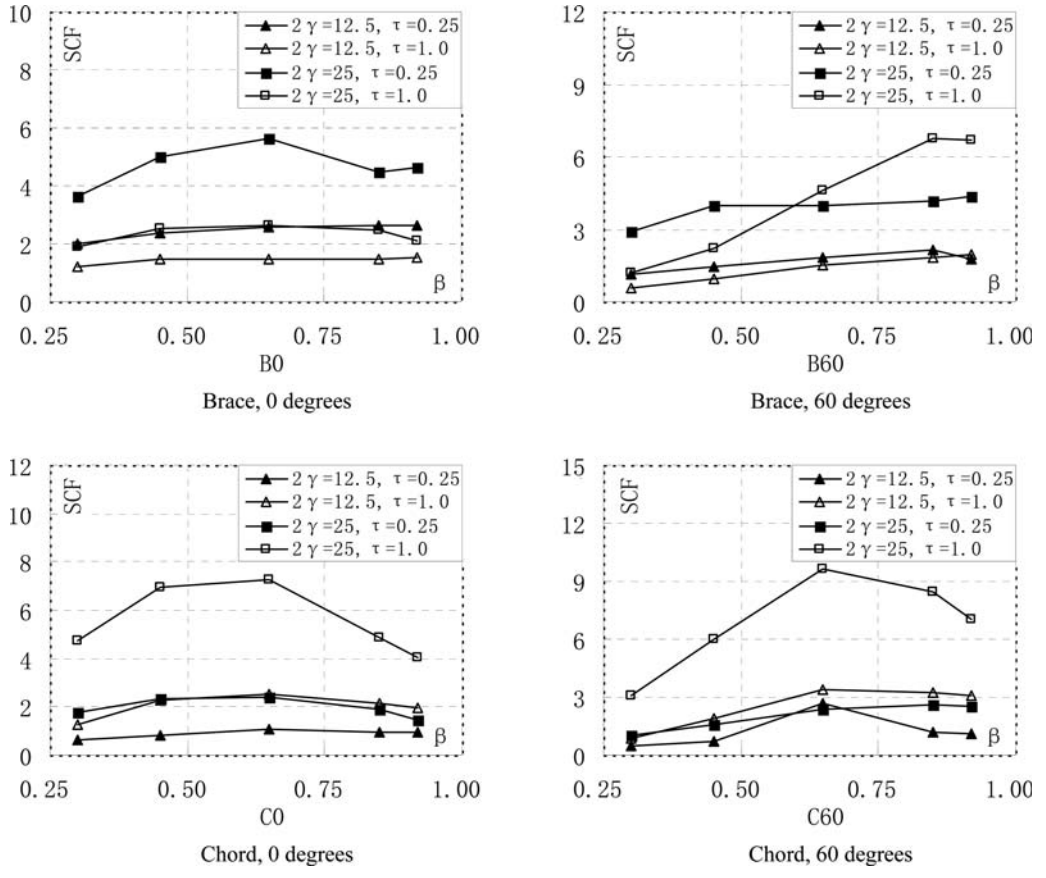

Figure 8. Influence of β on SCFs when 2γ and τ are kept constant for in-plane bending in the brace.

SNCF determined through quadratic extrapolation and that determined through linear extrapolation showed that the strain distribution at weld toes in the brace was significantly non-linear compared to the strain distribution at weld toes in the chord. Based on this observation, quadratic extrapolation can be recommended for the determination of SCFs at weld toes in CHS-SHS T-joints.

(2) Under the load axial load in the brace, maximum SNCFs were found to occur at 90 degrees in the brace and at 0 and 90 degrees in the chord for all the tested specimens.

(3) Under in-plane bending in the brace, maximum SNCFs in the brace were found to occur at either 0 or 60 degrees. The maximum SNCFs in the chord under in-plane bending in the brace were found to occur at either 0 or 45 degrees. When the maximum SNCF occurred at 45 degrees, its magnitude was found to be comparable to the SNCF at either 0 or 60 degrees. The SNCF at 90 degrees in the brace and the chord under in-plane bending were found to be negligible and could be taken as equal to zero.

(4) Three-dimensional finite element models developed using the ANSYS Software were found to be able to capture both the SNCF distribution around the welded brace-chord interface as well as predicting the maximum SNCF at the weld toes in the brace and chord.

(5) The 3D FEM were used to determine SCFs for a variety of non-dimensional parameters resulting in the development of graphs that can be used in the determination of SCFs for fatigue design of CHS-SHS T-joints subjected to axial and in-plane bending in the brace.

ACKNOWLEDGEMENTS

The authors wish to thank the Natural Science Foundation of China for financially supporting the research in the paper through the grant No. 50478108. This paper was written during the third author's GuangHua Education Foundation Fellowship at Tongji University from December 18, 2010 to March 17, 2011. The third author is grateful to Tongji University and in particular to his host Professor Lewei Tong, the Head of

Department of the Building Engineering, for his kind hospitality and support during this period.

REFERENCES

AWS (2008).Structural welding code-steel, ANSI/AWS D1.1-08. Miami, USA: American Welding Society.

Bian L.C. and Kim J.K. 2003, "Fatigue strength and stress concentration factors of CHS-to-RHS T-joints", Journal of Constructional Steel Research, Volume 59, Issue 5, May 2003, pp 627–640

Mashiri F.R., Zhao X.L. and Grundy P. 2004, "Stress Concentration Factors and Fatigue Behaviour of Welded Thin-Walled CHS-SHS T-Joints under In-Plane Bending", Engineering Structures, Vol 26, No. 13, Elsevier Science Ltd, 2004, pp. 1861–1875

Tong L., Zhao X.L., Mashiri F.R., Grundy P. and Zheng H.Z. 2006, "Fatigue Behaviour of Welded Thin-Walled Joints between Circular and Square Hollow Sections", International Journal of Steel Structures", Vol. 6, No. 1, The Korean Society of Steel Construction (KSSC), 2006-03, pp 37–44

vanWingerde A.M. 1992: The fatigue behaviour of T- and X-joints made of SHS, Heron, Vol. 37, No. 2, pp. 1–180

Zhao X.L., Herion S., Packer J.A., Puthli R., Sedlacek G., Wardenier J., Weynand K., Wingerde A., and Yeomans N. 2000, "Design Guide for Circular and Rectangular Hollow Section Joints under Fatigue Loading", Verlag TUV Rheinland, Koln, Germany.

Stainless steel

Tubular Structures XIV – Gardner (Ed.)
© 2012 Taylor & Francis Group, London, ISBN 978-0-415-62137-3

Investigation of the behavior of gusset plate welded slotted stainless steel tubular members under axial tension

G. Kiymaz
Department of Civil Engineering, Fatih University, İstanbul, Turkey

E. Seckin
Department of Civil Engineering, Istanbul Kultur University, İstanbul, Turkey

ABSTRACT: In this paper, an experimental study on the behaviour of slotted end tubular member tension connections in stainless steel is presented. The failure of slotted end tension connections is mostly governed by fracture near the slotted end where local peak stress concentrations develop due to shear lag. Within the connected region, shear lag causes the unconnected peripheral region of the hollow section to lag behind the welded region in resisting the axial tensile forces. Experiments were conducted on slotted and gusset plate welded tubular member connections in stainless steel. Both circular and box section members were considered in the test program. 20 specimens were tested under concentrically applied axial tensile forces for varying tube-to-gusset plate weld lengths. Load-deformation curves were obtained and comparisons were made in terms of strength and ductility. The results obtained from the study were then critically examined and compared with currently available design guidance for slotted gusset plate welded tubular end connections. It is noted that no specific rules exist in international specifications on structural stainless steel which cover the design of such connections. Therefore, the results of this study are compared with the existing design rules for carbon steel.

1 INTRODUCTION

The use of stainless steel in structural members of load-bearing systems has mostly been limited mainly due to cost considerations. These members have generally been preferred and used as secondary members in building structures with generally low structural capacity demand. Architectural concerns played an influential role in their preference and hence in real-life examples we have seen stainless steel members e.g. as load-carrying members of a building facade i.e. as exposed steel. On the other hand, the use of stainless steel in the main load-bearing elements of structural systems, e.g. building frames, may bring advantages in terms of issue regarding sustainability. Stainless steel with its favorable properties such as improved corrosion and fire resistance may provide possibilities for a more efficient balance between whole-life costs and in-service performance (Di Sarno *et al.* 2003). Combined with these advantages, its favorable strength and ductility properties would make stainless steel a material of choice in structural applications.

Relatively high initial cost of stainless steel is one burden for its structural use. To achieve a safe and economic design it is necessary to investigate the mechanical response of structural components, connections and the overall system, thus leading to efficient design (Di Sarno *et al.* 2003). With this respect, research studies on structural stainless steel (Aoki H., 2000, Burgan *et al.*, 2000, Johansson *et al.* 2000, Khoki *et al.*, 2000) has mostly covered issues that focus on more suitable design of structural stainless steel members and their connections.

The present paper aims to contribute to the above need for structural research for stainless steel and focuses on the specific subject of the behavior of slotted and gusset plate welded connections in stainless steel tubular members. Tubular members are among the most preferred member types used in structural stainless steel applications due to both their structural efficiency and attractive appearance. Hence using tubular members in stainless steel has been an architectural preference in many practical applications. Among the various alternatives of making a steel tubular connection, slotted and gusset plate welded connections is one way. As shown in Figure 1 the end connection is made by slotting the tube longitudinally, inserting the gusset plate and then placing longitudinal fillet welds at the tube-to-plate interface.

The research presented in this paper has studied the behaviour and design of such connections of stainless steel circular and square hollow section (CHS/SHS) members under static axial tensile loading. Experiments were conducted on slotted and gusset plate welded tubular member connections in stainless steel. Both circular and box section members were considered in the test program. 20 specimens were tested under concentrically applied axial tensile

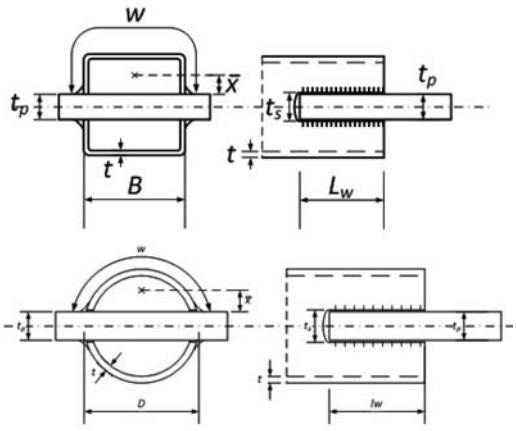

Figure 1. Schematic view for the gusset plate welded slotted end connections for box and circular section members.

forces for varying tube-to-gusset plate weld lengths. Load-deformations curves were obtained and comparisons were made in terms of strength and ductility. The results obtained from the study were then critically examined and compared with currently available design guidance for slotted gusset plate welded tubular end connections. It is noted that no specific rules exist in international specifications on structural stainless steel which cover the design of such connections. Therefore, the results of this study are compared with the existing design rules for carbon steel.

2 EXPERIMENTAL STUDY

2.1 *Description of the experiments and specimens*

The study focuses on the behavior of slotted end stainless steel tubular member connections subject to concentric axial loading. As stated earlier tests were carried out on 20 stainless steel CHS and SHS members with slotted gusset plate welded end connections. Figure 2 shows photographs of two typical test specimens. Two parameters that were considered as variables in the test program were the fillet weld length L_w and the end condition of the welded gusset plate inside the slot being welded or non-welded around the end face of the gusset plate. These end conditions are shown in Figure 3. The welded end is denoted as RW (return weld) and the non-welded end is denoted as NW (no return weld).

As shown in the photographs given in Figures 2 and 3 rigid gusset plates with 15 mm plate thickness were welded into the slots at both ends of the specimen. Tensile load was applied via these plates which were gripped inside the grip locations within the universal test machine with a total capacity of 50 tons. Loading was applied in the direction of the longitudinal axis of the member as concentric axial tensile load and specimen longitudinal elongation was monitored and recorded by using two displacement transducers attached to the sides of the specimen.

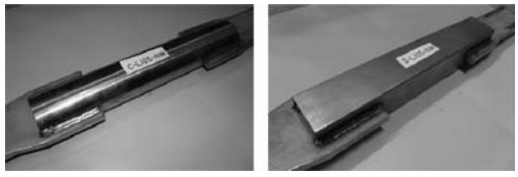

Figure 2. View of the tested specimens in CHS and SHS.

Figure 3. View of the slot end conditions.

Table 1. Dimensional properties of the test specimens.

Specimen	$w\,(mm)$	$\bar{x}\,(mm)$	$L_w/D\ldots/(w)$
C-L30-RW	104.54	24.22	0.39
C-L45-RW	104.54	24.22	0.59
C-L60-RW	104.54	24.22	0.79
C-L76-RW	104.54	24.22	1.00
C-L105-RW	104.54	24.22	1.38
C-L30-NW	104.54	24.22	0.39
C-L45-NW	104.54	24.22	0.59
C-L60-NW	104.54	24.22	0.79
C-L76-NW	104.54	24.22	1.00
C-L105-NW	104.54	24.22	1.38
S-L30-RW	122.42	26.25	0.43
S-L45-RW	122.42	26.25	0.64
S-L60-RW	122.42	26.25	0.86
S-L70-RW	122.42	26.25	1.00
S-L105-RW	122.42	26.25	1.50
S-L30-NW	122.42	26.25	0.43
S-L45-NW	122.42	26.25	0.64
S-L60-NW	122.42	26.25	0.86
S-L70-NW	122.42	26.25	1.00
S-L105-NW	122.42	26.25	1.50

Specimen dimensions are reported in Table 1. In the specimen reference, C stands for Circular and L defines the length of weld. $\bar{x}/L_w$, L_w/w and L_w/D ratios are all called weld length ratios used in the design calculations as described above. Five different weld lengths were considered starting from 30 mm up to 105 mm. For each cross-section type (CHS and SHS) 5 specimen were without a return weld (NW) and the other 5 with a return weld (RW) at the slotted end. For CHS sections a constant diameter of $D = 76.1\,mm$ and thickness of $t = 2.0\,mm$ was used for all the specimens tested whereas the SHS sections were all $70\,mm \times 70\,mm$ square sections with wall plate thickness of $t = 2.0\,mm$.

Table 1 presents the dimensional properties for the 20 specimens tested in the test program. Note that the notations are described in Figure 1. Within the

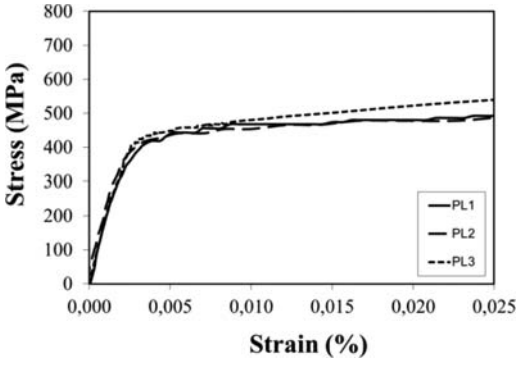

Figure 4. Stress-strain curves for the tensile test coupons.

specimen designation the C stands for Circular and S for Square. The following, e.g. L60-RW corresponds to a longitudinal weld length of 60 mm with a Return Weld at the end. A constant weld thickness of 6 mm was considered in the production of the test specimens.

2.2 *Material property tests*

Tensile tests were carried out on three tensile test coupons cut out from randomly selected tube members to determine the material property of the stainless steel used. A rounded material behavior is observed with no well-defined yield point (Figure 4). An average yield stress of 450 MPa (0.2% proof stress) and an average ultimate tensile stress level of 550 MPa was achieved which were used for the strength estimations for the tested members using the above explained design rules.

3 TEST RESULTS

Experiments were carried out as described above for the 20 different specimens with varying design strength values. The three possible failure modes that would be expected for the members with slotted end connections are yielding of the member gross cross section, block tear out of material close to the weld region and shear lag failure with fracture of the effective net cross section around the periphery of the member. Of these failure types, all the specimens in the test program failed by peripheral fracture (CF) due to shear lag. Figure 5 shows typical connection failures for a CHS and SHS section connection. A nearly perfect peripheral fracture of the whole circular/square hollow cross section occurred with crack propagating around the member periphery.

Figure 6 shows close-up views of the failed specimens around the slotted end region both for "Return Weld (RW)" and "No Return Weld (NW)" cases. In both cases fracture initiated at the slotted end region due to high stress concentrations. For the NW cases, crack initiation was relatively easier in comparison to the RW (return weld) cases where the tensile load was

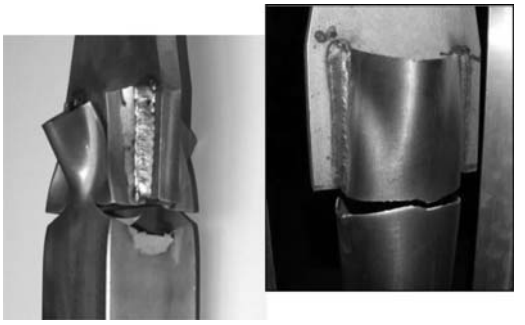

Figure 5. Typical failure mode observed in the test specimens.

Figure 6. Failure types for Return Weld (RW) and No-return Weld (NW) cases.

Figure 7. Close up view of a failed return weld region.

at some point high enough to initiate a crack with the return weld material (photo on the left).

A close-up view of a failed return weld region in the connection is shown in Figure 7. A nearly 45° shear failure plane is observed to have taken place within the weld material with associated indications of the energy spent to cause the weld failure.

Peripheral fracture due to shear lag was observed for all the specimens including the lowest and highest values of weld lengths (Figure 8). It is noted here that the welds were intentionally over-designed to suppress weld failure before the expected possible failure modes such as cross-section yielding, block shear or peripheral shear lag failure.

Figures 9 and 10 present the load displacement response curves for the NW and RW cases for both SHS and CHS sections, respectively. In general the behavior of the RW and the NW specimens are similar with close initial stiffness values and a rounded overall load-displacement response. However, for the RW

Figure 8. Shear lag failure observed in specimens with different weld lengths.

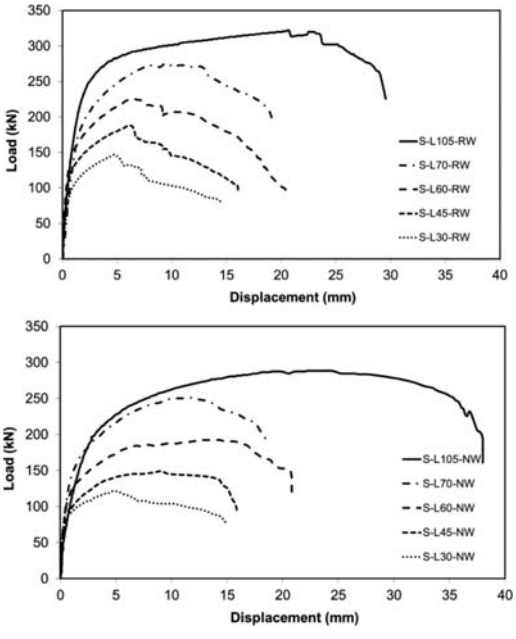

Figure 9. Load-displacement curves for the 'With Return Weld (RW) and No-return weld (NW)' specimens for Square Hollow Sections.

cases for all the 5 specimens a sudden drop in strength is observed right after the maximum load is achieved whereas for the NW specimens a smooth transition is noted. This observation is valid for both square and circular section specimens. For all the RW specimens the maximum load levels after which a sudden drop is observed correspond to load levels at which crack initiation was observed to occur during the tests within the return weld material. In other words, as soon as the return weld cracked a sudden drop in load occurred. On the other hand for the "No return weld" specimens, load was not as sensitive to the crack initiation which started directly on the CHS member material near the slotted end – gusset plate juncture where there is no return weld. With this respect, a more ductile behavior is observed for the specimens with their slotted ends un-welded to the gusset plate. In general the RW specimens reached higher ultimate loads than the NW specimens but apparently at higher elongation levels.

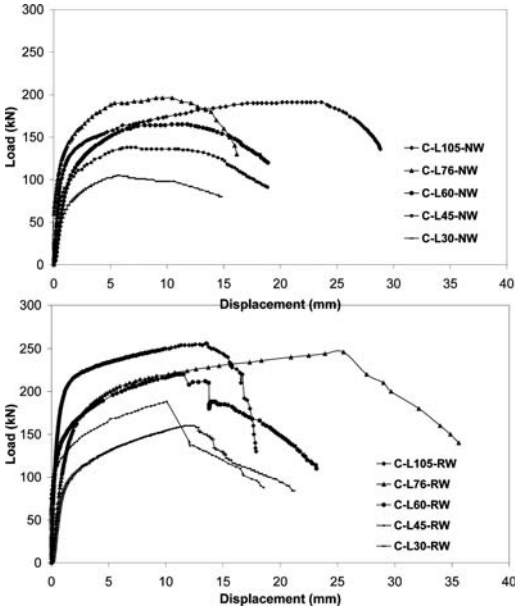

Figure 10. Load-displacement curves for the 'With Return Weld (RW) and No-return weld (NW)' specimens for Circular Hollow Sections.

4 DESIGN CONSIDERATIONS

The resistance of a steel tension member is given as the minimum of the resistance in yielding of the gross section area ($P_n = F_y \,.\, A_g$) and the resistance in fracture of an effective net section area (A_e) within the connection region ($P_n = F_u \,.\, A_e$). The effective area is used to determine the efficiency of the connection under the effects of shear lag and calculated by using a shear lag reduction coefficient, U. Design rules related to failure of slotted end tension connections with welded gusset plates can be found in three major international specifications on steel structures namely the American AISC 360 (2005), the Canadian CAN/CSA-S16 (2001) and the European EN1993-1-8 (2005). Design methods adopted in these specifications are shown in Table 1 and Table 2 for shear lag and block shear tensile fracture failures respectively. Note that in EC3 Part 1.8 there are no design provisions for shear lag effect for such connections in hollow sections. In this design guide, rules for shear lag effect is given only for bolted connections for angles connected by one leg and other unsymmetrically connected tension members. Comparing the approaches adopted in these codes it is noted that for block shear failure the three codes present similar resistance equations. Nominal resistances predicted by these codes are equal (a slightly different value predicted by EC3 in which shear yield coefficient is taken as the theoretical $1/\sqrt{3}$ value) but the design resistance values differ due to different resistance factors adopted in each code. However, it should be noted that in the block shear design equation of

Table 2. Design provisions for shear lag in hollow sections with slotted end connection with single welded concentric gusset plate.

Specification	Shear lag coefficient, U	Validity range
AISC (2005)	$U = 1 - \bar{x}/L_w$ for $1.3D > L_w \geq D$ $U = 1$ for $L_w \geq 1.3D$ (*CHS only*)	$L_w \geq D$
CSA (2001)	$U = 1$ for $L_w/w \geq 2.0$ $U = 0.5 + 0.25L_w/w$ for $2.0 > L_w/w \geq 1.0$ $U = 0.75L_w/w$ for $L_w/w < 1.0$	N.A

CSA (2001), the multiplication of two factors (0.85 and 0.90) equals 0.765 which is very close to the resistance factor used in the design equation of AISC (2005) which is 0.75. On the other hand, the resistance factor adopted in EN1993-1-8 (2005) is 1/1.25 which is again equal to a close value of 0.80. As for shear lag effect two general approaches are adopted. As presented in Table 1, shear lag coefficient, U, is calculated as a function of the ratio of the eccentricity of the connection ($\bar{x}$) to the weld length (L_w) in the American specification whereas in the Canadian specification U is a function of the ratio of the weld length (L_w) to peripheral distance between the welds (w). In both specifications the adverse effect of shear lag decreases as weld length L_w increases. In the American specification shear lag factor U is taken as unity for $L_w \geq 1.3D$ and in the Canadian specification this limiting value is given as $L_w \geq 2.0w$ or assuming $w = \pi.(D/2)$ this value becomes $L_w \geq 1.57D$. Therefore a more conservative limit is adopted in the Canadian specification. For weld lengths smaller than the smallest specified limits for shear lag i.e. $L_w < 1.0D$ in AISC (2005) and $L_w < 1.0w$ in CSA (2001) specifications , the collapse behaviour tends to be governed by a block shear type of failure. In between these upper and lower limits design equations are given for the calculation of shear lag coefficient, U.

The design of structural stainless steel members and connections are covered in Eurocode 3 – Design of steel structures – Part 1–4: General rules – Supplementary rules for stainless steels (EN 1993-1-4: 2006) and the American ASCE Specification for the Design of Cold-Formed Stainless Steel Structural Members, SEI/ASCE (2002). In both specifications, no specific rules exist which cover the design of slotted end tension connections with welded gusset plate.

In an attempt to find out how well the current design rules for such connections in carbon steel apply to stainless steel cases Table 3 was prepared. Table 3 presents code estimations for the test specimens and compares the minimum of the estimated values (N_{Design}) calculated for various failure modes and using different codes with the test maximum strength values, N_{Test}. Note that the code values are all nominal values i.e. partial safety factors were set to unity. Also note that these values were calculated using the material property values given earlier in the paper.

Table 3. Comparison of test failure strengths with code predicted nominal resistance values for carbon steel.

Specimen	$N_{design}(kN)$	$N_{test}(kN)$	$\frac{N_{test}}{N_{design}}$
***C**-L30-RW*	*55,12*	*160.00*	*2,90*
***C**-L45-RW*	*82,69*	*188.00*	*2,27*
***C**-L60-RW*	*110,25*	*220.00*	*2,00*
***C**-L76-RW*	*139,65*	*246.00*	*1,76*
***C**-L105-RW*	*192,17*	*256.00*	*1,33*
C-L30-NW	48,01	105.00	2,19
C-L45-NW	72,02	138.00	1,92
C-L60-NW	96,02	165.00	1,72
C-L76-NW	121,63	196.00	1,61
C-L105-NW	167,37	210.00	1,25
***S**-L30-RW*	*54,29*	*147.2*	*2,71*
***S**-L45-RW*	*81,44*	*188.4*	*2,31*
***S**-L60-RW*	*108,59*	*225.6*	*2,08*
***S**-L70-RW*	*126,69*	*274.7*	*2,17*
***S**-L105-RW*	*190,03*	*321.8*	*1,69*
S-L30-NW	48, 23	121.6	2,52
S-L45-NW	72,34	149.1	2,06
S-L60-NW	96,46	192.3	1,99
S-L70-NW	112,54	251.1	2,23
S-L105-NW	168,80	288.4	1,71

Among the design estimations (see Table 2), the Canadian CSA shear lag fracture strength estimations (N_{CSA}) are the most conservative. It also covers a wider range of weld lengths whereas the AISC does not cover smaller weld lengths as also explained above in Table 2. One important finding here is that these values are all for peripheral shear lag fracture and hence also well represents the failure type observed for the specimens as peripheral fracture.

It is observed that both test and design strength values increase with increasing longitudinal weld lwngth. Comparing the test maximum strengths (N_{Test}) with the above defined code minimum values (N_{Design}) it is observed that the code values are all very conservative. Maximum test strengths are the peak load levels on the load-displacement curves given above in Figures 9 and 10. In Table 3 also note that for higher weld lengths both for RW and NW cases there is a decreasing level of conservatism which seems to be more pronounced for the CHS specimens.

Using the data given in Table 3, Figures 11 and 12, present comparisons of experimental ultimate loads (N_{Test}) with minimum code strength predictions (N_{Design}) both for RW and NW cases on a "connection strength"-versus-"weld length ratio" plots. For CHS models the weld length ratio was taken as L_w/D whereas for SHS models L_w/w was used. It is easier on these plots to see that the test maximum strengths are in general higher than the design estimations.

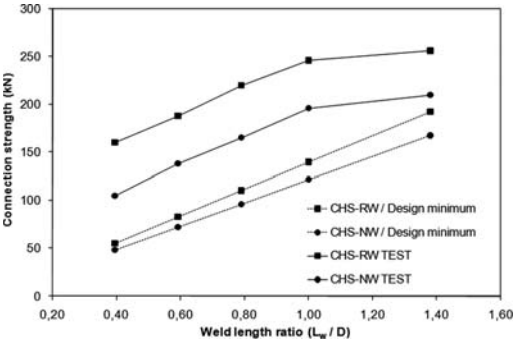

Figure 11. Comparison of experimental ultimate loads with minimum code strength predictions (CHS sections).

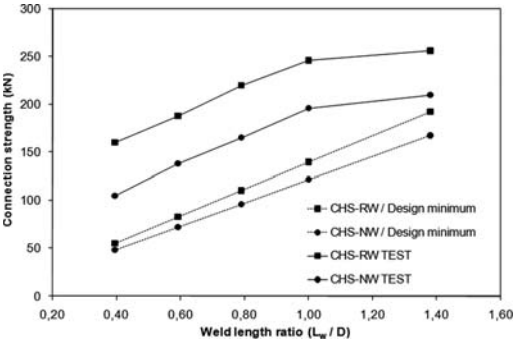

Figure 12. Comparison of experimental ultimate loads with minimum code strength predictions (SHS sections).

Figure 13. Typical excessive deformation observed at maximum load level.

4.1 *Deformation limit to prevent excessive distortion*

As evidenced by the load-displacement response curves and visual observations made on the specimens, all the slotted gusset plate connections achieved their maximum strength after high deformations which create excessive distortions in the geometry of the connection (Figure 13). In order to prevent this impractical behaviour a servicability limit should be applied in design. For example a limit on the distortion of the

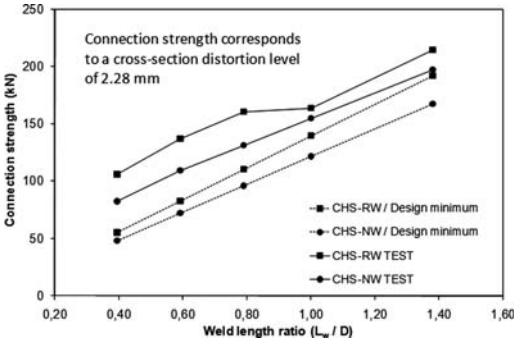

Figure 14. Comparison of experimental ultimate loads at a distortion level of %3 of diameter (D) (=*2.28 mm*) with minimum code strength predictions (CHS sections).

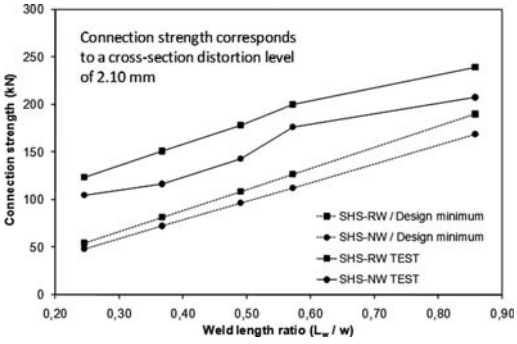

Figure 15. Comparison of experimental ultimate loads at distortion level of %3 of side B (=*2.10 mm*) with minimum code strength predictions (SHS sections)

tube cross-section could be imposed to limit the "ultimate capacity" of these connections. A limit of 3% of the CHS diameter (D) has been popularly recommended for tubular structures (Lu et al. (1994)) and now adopted by the International Institute of Welding. This limit has been adopted and applied in this study (also for SHS members as 3% of side width B) for the connection test strengths and the plots given in Figures 11 and 12 updated accordingly. Updated plots are presented below in Figures 14 and 15. It is observed that if decreased values of test strengths are assumed as described, the test connection strengths get closer to the design estimations.

However, the design estimations for all the specimens are still conservative with differences up to design estimations being half that of the test strengths.

5 CONCLUSIONS

In this paper, shear lag induced failure of slotted end tension connections is investigated for circular and square hollow section members in stainless steel. An experimental program was carried out on 20 slotted gusset plate welded stainless steel circular and square member end connections. Two parameters that were

considered as variables in the test program were the fillet weld length L_w and the end condition of the welded gusset plate inside the slot being welded or non-welded. All the specimens in the test program failed by peripheral fracture due to shear lag with fracture initiating at the slotted end region due to high stress concentrations both for slot end welded (RW) and un-welded (NW) cases. Load-displacement response curves for the specimens were plotted and comparisons were made between the RW and NW cases for varying longitudinal weld lengths. For all RW specimens a sudden drop in strength is observed right after the maximum load is achieved whereas for the NW specimens a smoother transition is noted. With this respect, a more ductile behavior is observed for the specimens with their slotted ends un-welded to the gusset plate. In general the RW specimens reached higher ultimate loads than the NW specimens but at higher elongation levels. The maximum strength results obtained from the test program were compared with currently available design guidance for slotted gusset plate welded tubular end connections. It is noted that no specific rules exist in international specifications on structural stainless steel which cover the design of such connections. Therefore, the results of this study were compared with the design rules for carbon steel. The design estimation for a typical specimen is calculated as the minimum of the strength estimations for three distinct failure modes namely, gross-section yielding, block-shear rupture and peripheral shear leg failure. For the design estimations a high level of conservatism was observed for all the specimens when compared with the test peak strength values. It is also noted that for higher weld lengths both for RW and NW cases there is a decreasing level of conservatism which seems to be more pronounced for the CHS specimens. Applying a servicability limit to prevent excessive distortion of cross-sections resulted in decrease in test strengths but although the test connection strengths get closer to the design estimations in general, the test strengths are higher than the design estimations. Therefore, this research has provided evidence for the need for possible adjustments in the current design formulations for carbon steel if they will be applied to the design of slotted gusset plate welded CHS/SHS connections in stainless steel.

REFERENCES

ANSI/AISC 360 (2005) Specification for structural steel buildings, Chicago: *American Institute of Steel Construction* (AISC)

Aoki H. (2000) Establishment of design standards and current practice for stainless steel structural design in Japan. *Journal of Constructional Steel Research* 54(1):191–210.

Burgan BA, Baddoo NR, Gilsenan KA. (2000) Structural design of stainless steel members: comparison between Eurocode 3, Part 1.4 and tests results. *Journal of Constructional Steel Research* 54(1):51–73.

CAN/CSA-S16 (2001). Limit states design of steel structures, Toronto *Canadian Standards Association* (CSA).

Cheng Roger, J.J., Kulak, G.L and Khoo, H.A. (1998). Strength of slotted tubular tension members. *Canadian Journal of Civil Engineering* 25:982–991

Di Sarno L., Elnashai A.S. and Nethercot D.A. (2003) Seismic performance assessment of stainless steel frames. *Journal of Constructional Steel Research*, 59 1289–1319

EN1993-1-8 (2005) Eurocode 3 Design of steel structures-general rules—part 1–8: Design of Joints, Brussels: *European Committee for Standardisation*.

EN1993-1-4 (2006) Eurocode 3 Design of steel structures – Part 1–4: General rules – Supplementary rules for stainless steels, Brussels: *European Committee for Standardisation*.

Johansson B, Olsson A. (2000) Current design practice and research on stainless steel structures in Sweden. *Journal of Constructional Steel Research* 54(1):3–29.

Korol RM. (1996) Shear lag in slotted HSS tension members. *Canadian Journal of Civil Engineering* 23:1350–4

Kouhi J., Talja A., Salmi P., Ala-Outinen T. (2000) Current R&D work on the use of stainless steel in construction in Finland. *Journal of Constructional Steel Research* 54(1):31–50.

Ling, T.W., Zhao, X.L., Al-Mahaidi, R. and Packer, J.A. (2007) Investigation of shear lag failure in gusset plate welded structural steel hollow section connections. *Journal of Constructional Steel Research* 63, 293–304

Martinez-Saucedo G., Packer J.A., Willibald S. (2006) Parametric finite element study of slotted end connections to circular hollow sections. *Engineering Structures*, 28, Pages 1956–1971

Martinez-Saucedo G., Packer J.A and Christopoulos, C. (2008) Gusset plate connections to circular hollow section braces under inelastic cyclic loading. *Journal of Structural Engineering*, ASCE, 134:7, 1252–1258.

Martinez-Saucedo G. and Packer J.A. (2009). Static design recommendations for slotted end HSS connections in tension. *Journal of Structural Engineering*, ASCE, 135:7, 797–805.

SEI/ASCE (2002) 8-02. Specification for the design of cold-formed stainless steel structural members. *American Society of Civil Engineers*.

Willibald S. and Martinez-Saucedo G. (2006). Behaviour of gusset plate connections to ends of round and elliptical hollow structural section members. *Canadian Journal of Civil Engineering* 33 (4), 373–383

Tubular Structures XIV – Gardner (Ed.)
© 2012 Taylor & Francis Group, London, ISBN 978-0-415-62137-3

Numerical modelling of prestressed stayed stainless steel columns

L.R.O. de Lima, P.C.G. da S. Vellasco & J.G.S. da Silva
UERJ – State University of Rio de Janeiro, Faculty of Engineering, Rio de Janeiro, Brazil

R.R. Araújo
CEFET-RJ – Federal Centre for Technological Education Celso Suckow da Fonseca, Rio de Janeiro, Brazil

ABSTRACT: Slender steel columns generally have their load bearing capacity mainly controlled by the global structural buckling ultimate limit state. These structural members can be optimized with the use of a prestressed stay system. They become very efficient structural solutions for various challenging civil engineering problems. The use of the prestressed system reduces the column buckling length to at least half of its original size and substantially improves its load bearing capacity. This motivated a series of numerical tests executed in 12 meters prestressed stayed stainless steel columns. The aim of this paper is therefore to present a numerical model developed to predict the structural response of these stainless steel stayed systems.

1 INTRODUCTION

Stainless steel have been used in various types of constructions due to its main characteristics associated to high corrosion resistance, durability, fire resistance, ease of maintenance, appearance and aesthetics (Gardner & Baddoo 2006). The development of the construction process and, the new tendencies adopted in the architecture design conception, highlighted the need for materials that can combine versatility with durability. Therefore, the stainless steel present itself as a promising material for constructions that require these characteristics, mainly related to high corrosion strength avoiding the need for short period maintenance.

Stainless steel is indicated as a structural element in construction for numerous reasons. Its high ductility allows its use in structures subjected to cyclic loadings, enabling the dissipation of the energy associated to these loads, through load redistributions before the structural collapse. The cost reduction achieved with the less need for structure maintenance, and the increase in its capacity to dissipate impact loads, also enhanced the stainless steel structure reliability.

The use of sophisticated computational models that simulate real structural behaviour enable the adoption of advanced structural design methods that can provide more accurate, trustworthy and reliable results, thus reducing the final construction costs. An example of these design trends was the Rock in Rio III main stage roof (Andrade et al. 2003a & 2003b), assembly and erection, where the complexity, number of structural members and construction time-scheduling restrictions were a constant challenge for the engineering team (Fig. 1).

Figure 1. Real structure being erected with prestressed carbon steel stayed column (Andrade et al. 2003a & 2003b).

The adopted structural solution for shoring the main stage roof with 82 meter span and 36 meter height during construction stages has reduced the column buckling length, at least, to half of its original size, increasing its load bearing resistance. This was due to the additional restriction provided by the tie forces that are transferred to the main columns by means of horizontal tubes, perpendicularly welded to the column midpoint. This ingenious and simple structural system allows the adoption of extremely slender columns by the construction industry.

The main objective of the investigation was to access and evaluate the theoretical response of these prestressed steel columns by means of full-scale laboratory tests and calibrated finite element simulations. The proposed new horizontal test layout required the development of a carefully planned load application system and associated instrumentation. This test layout was conceived aiming to minimize secondary effect

influence over test results, i.e., column self-weight and the rotation restriction provided by the supports. Another contribution of the investigations was the development of an innovative measuring device configuration used for measuring the column tie forces along the test.

2 STAYED STEEL COLUMNS BACKGROUND

Civil engineers and architects widely used stayed systems over the years in steel construction (Andrade et al. 2003a & 2003b, Voevodin 1970, Belennya 1977, Hafez et al. 1982, Wong & Temple 1979, Chan et al. 2002 and Servitova & Machacek (2011) mainly due to their lightness, malleability, resistance and for its aesthetically attractive configuration. Various stayed structural systems can be identified in footbridges, bridges, ship mast, slender columns and even structures used in space.

Steel members are widely employed as tension-resisting structures, but on the other hand when columns have ties welded to them, even quite slender steel columns could present a substantial load bearing capacity. The main objective of the ties is to reduce the column buckling length creating lighter structures with reduced cross-section. Despite these facts designers should have in mind that adequate column tie pre-stress force can increase the structural system capacity. Alternatively, excessive pre-stress forces can lead to structures not achieving its optimum load bearing capacity.

Pre-stressed steel structural systems are not new and have been studied since 1970 by Voevodin (1970), Belenya (1977), Hafez et al. (1982), Wong & Temple (1979), Chan et al. (2002) and Servitova & Machacek (2011). These studies improved such systems and were treated as the basis of the present study.

The system functionality is achieved by applying a pre-stress force on one of the tie extremities that passes by one or more braced points of the main column. These points in the investigated stayed system layout are defined by four tubular cross disposed bars, figure 1, or, in other configurations, by three steel bars disposed with a 120° angle arrangement.

Figure 2. Experimental layout – carbon steel column (Araujo et al. 2008).

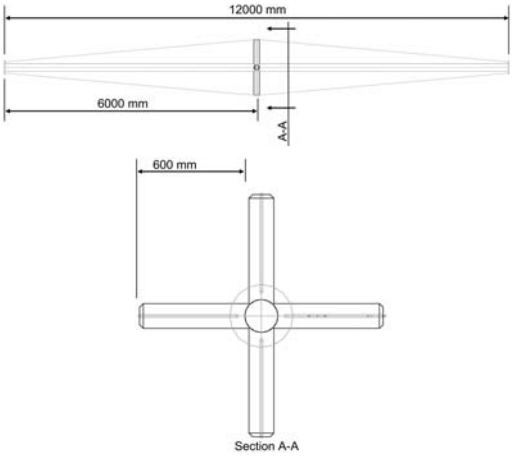

Figure 3. Stayed carbon steel columns layout and dimensions (Araujo et al. 2008).

3 EXPERIMENTAL PROGRAM

3.1 *Prestressed stayed carbon steel columns*

The first numerical model presented in this work was calibrated with experimental results from tests performed by Araujo et al. (2008) for prestressed stayed carbon steel columns.

Figures 2 and 3 illustrate the pre-stressed column, made of a twelve meter central tubular column and four 600 mm length smaller tubular cross bars. The main columns and cross bars were made of tubes with an external diameter of 89.3 mm (3.2 mm thick) and 42.6 mm (3 mm thick), respectively, while the ties used 6.35 mm diameter cables.

The steel column main tube mechanical properties were determined by four coupons tested according to the American Standard STM E8 (1993) leading to yield and rupture mean stress values equal to 403.8 MPa and 465.3 MPa with standard deviations of 29.3 MPa and 4.9 MPa.

The cables used in the ties were anchored by hooks at the column ends and were also locked by three cable clamps adopted according the supplier specifications (CIMAF 2000). After the pre-stress operation

the cables were also locked at the pre-stressed column midpoint to ensure the bracing effect.

A loading frame was conceived and designed to apply a direct load to the column. This was due to the fact that a twelve meter length vertical test created substantial difficulties in erection and positioning the measuring devices. Two equal loading frames were fabricated, for each column end, and were subsequently anchored to the lab reaction slab.

Restrictions in geometry, tested elements flexibility and the adopted test dimensions significantly complicated the test instrumentation. This phase was one of the major contributions of the investigation and still is, as far as the authors know, the first full-scale three-dimensional test made on these structural systems.

The main column and secondary cross bars strains were measured by sixteen linear strain gauges. Ten displacement transducers (LVDT's) were used along the column length and loading frames. The additional difficulty of measuring lateral displacements in circular tubes was surpassed by the use of small flat plates positioned at the LVDT's ends. The midpoint main tube lateral displacements could not be directly measured due to the presence of the secondary tubes implying that this displacement value was obtained with LVDT's positioned 200 mm apart from this particular point.

The visual monitoring and displacement control of the investigated structure was made with additional dial gauges devices. This proved to be extremely valuable due to the system non-linear response, especially near collapse, to avoid unnecessary risks to lab personnel and equipment.

The column applied load and stays force acquiring system used two adjacent load cells. The first measured the total load applied by the hydraulic jack while the stay forces were measured by an additional load cell positioned between one of the column ends and a steel plate where the cable were anchored.

Difficulties related to effects like the structure self-weight, the rotation restriction provided by the supporting points and the lack of space for positioning a second universal hinge were found during the column assembly process.

Due to the columns dimensions and the adopted horizontal test layout, the self-weight induced an excessive 115 mm deflection, at centre span, surpassing the maximum limiting values prescribed by the Brazilian Standard (NBR8800 2009) and Eurocode 3 (2005). The first strategy to compensate this effect was made by increasing the pre-stress force on the lower stays. Unfortunately, this strategy unbalanced the adopted stay forces and created and eccentricity at the load application point due to the universal hinge rotation located at the column ends. The solution to the problem consisted on using an extra steel cable anchored to a reaction frame supporting the column at its centre.

Naturally, this solution can affect some of the possible column buckling modes but, as it will be subsequently seen in the numerical simulation results comparisons with the experimental data and it did not affected the controlling buckling mode. The simulations also indicated that the use of this extra cable did not affect the global system ultimate limit state. Temporary supports were also used to shore the column until a certain minimum load was applied to the structural system. A partial rotation restriction was noticed at the column supports due to the use of these temporary "G-type" clamps.

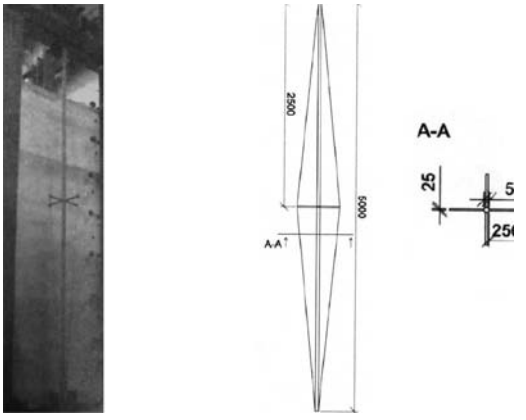

Figure 4. Stayed stainless steel columns layout and dimensions. Servitova & Machacek (2011).

3.2 *Prestressed stayed stainless steel columns*

The prestressed stainless steel stayed column was tested in Central Laboratory of CTU in Prague by Servitova & Machacek (2011) – see Figure 4. This column was made of a stainless steel 1.40301 with 5 m long tube with a 50 mm diameter and 2 mm thickness. The cross bars at the column midpoint were made with four tubes with a 0.25 m length and 1.5 mm thickness. The ties used 4 mm diameter Macalloy cables.

During the tests, the deflections were measured at seven points in two perpendicular directions by the potentiometers fixed to the experimental frame. The cables tensile forces were measured by strain gauges. The initial column shape/imperfection and its deflection during the test were measured by 3D scanning. No information about the magnitude of the experimental imperfections was provided in the reference (Servitova & Machacek, 2011).

Three tests were performed and loaded in vertical position as showed before in the Figure 4. One of the tests was loaded without cables. The other tests were prestressed before the application of the subsequent compression loading. Three levels of prestress forces were considered: 3.9 kN, 4.54 kN and 5.44 kN per cable. The column was hinge supported ensuring free rotation in all directions.

The maximum column compression load without cables reached 7.04 kN, while for prestressed columns, the maximum loads were 17.75 kN, 14.93 kN and 16.23 kN, respectively, for the three different prestress force levels described previously. During the second

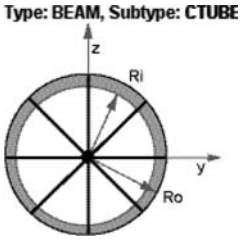

Figure 5. Finite element BEAM188 – CTUBE (Ansys 12.1 2009).

test the ultimate strength was reduced due the presence of a column inclination caused by a large initial imperfection.

4 NUMERICAL MODELLING

A finite element computational model was developed adopting the usual mesh refinement techniques present in the adopted finite element software ANSYS 12.1 (2009). The main tubular column and secondary cross bars were modelled by BEAM188 elements with subtype CTUBE while the ties were simulated with LINK180 elements (specified with a tension only option) having three degree of freedom per node: translations in the nodal x, y, and z directions. Both elements specifications can be observed in the Figure 5. Material (bi-linear) and geometrical non-linear analysis were performed to model the stayed columns experiments. In the prestressed carbon steel stayed column, an 8 mm amplitude sinusoidal initial imperfection was introduced in the numerical model to be compatible with the measured test imperfections. For the prestressed stainless steel stayed column, a number of imperfections levels were tested since the actual test value was not informed, Servitova & Machacek (2011).

Two different materials were used in the first analysis (carbon steel column). The first, used in the main column and secondary cross bars, possessed a 205000 MPa Young's modulus, a 20500 MPa tangential modulus, a 0.3 Poisson ratio and a 380 MPa specified yield stress. The second, used in the tie cables, possessed a 100000 MPa Young's modulus, a 10000 MPa tangential modulus, a 0.3 Poisson ratio and a 750 MPa specified yield stress.

For the second column (stainless steel), the real stress versus real strain relationship was used considering a 204000 MPa Young's modulus and a 290 MPa yield stress.

The prestressed steel column model was divided in three parts: the central tubular column, the secondary cross bars and the tie cables. Elements with 10 mm length were used in the central column and in the secondary cross bars, Figure 6. These arrangements resulted in a 10% slope angle for the column ties, each modelled by a single element. An extensive parametric study was performed for the prestressed stainless

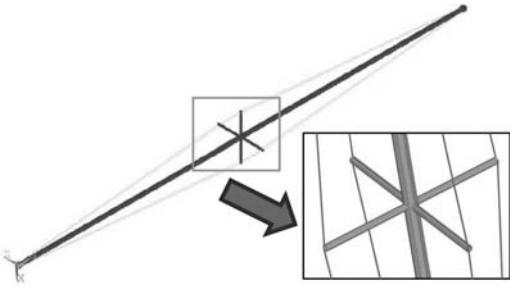

Figure 6. Stayed steel column numerical model.

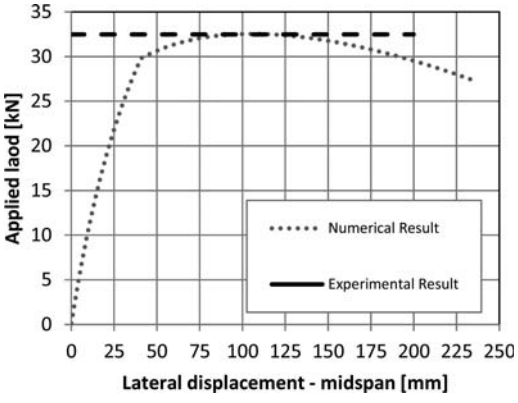

Figure 7. Load versus lateral displacement – carbon steel column.

steel stayed column, to be presented in a subsequent section of this paper.It was performed and focused on the evaluation of initial imperfection amplitude (1 mm, 10 mm, 15 mm, 20 mm, 25 mm and 30 mm) and stay prestress force level.

All the numerical analyses were made in simply supported configurations. These boundary conditions can be observed in the Figure 6.

5 NUMERICAL RESULTS

The first numerical model analysed was the prestressed carbon steel stayed column tested in laboratory by Araújo et al. (2008). In this test, for a pretension load of 3.0 kN per cable, the maximum load reached was 33.07 kN. In the numerical simulation, the maximum load was 32.53 kN showing a good agreement between the test and numerical values as can be observed in the Figure 7. This first model was used only to calibrate the numerical model since the main objective of this paper was to model the global response of prestressed stainless steel stayed columns.

The three columns tested by Servitova & Machacek (2011) were simulated. The results for the first pretension level of 3.90 kN per cable are presented in Figure 8. This figure depicts the load versus lateral displacement curves for all the investigated initial imperfection amplitudes.

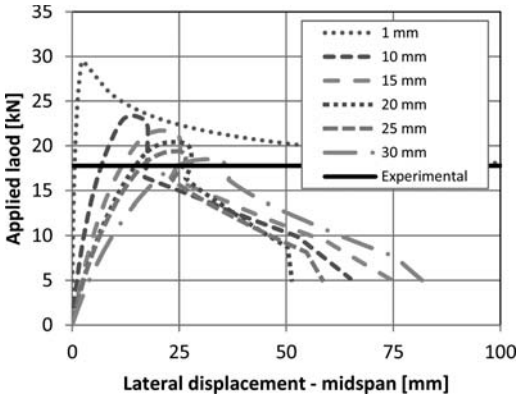

Figure 8. Load versus lateral displacement – stainless steel column – pretension load = 3.90 kN.

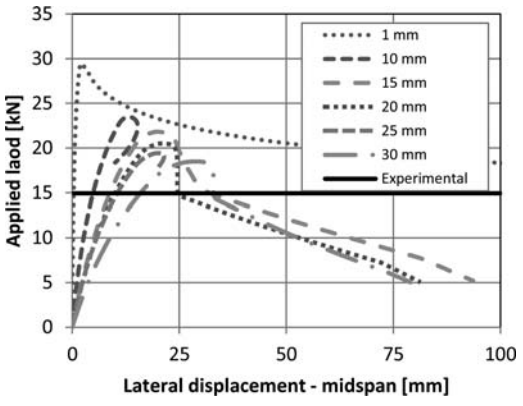

Figure 9. Load versus lateral displacement – stainless steel column – pretension load = 4.54 kN.

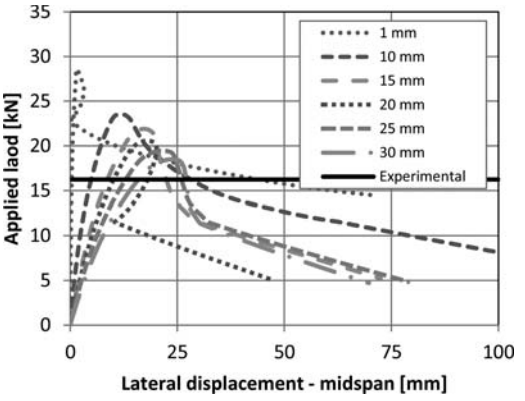

Figure 10. Load versus lateral displacement – stainless steel column – pretension load = 5.44 kN.

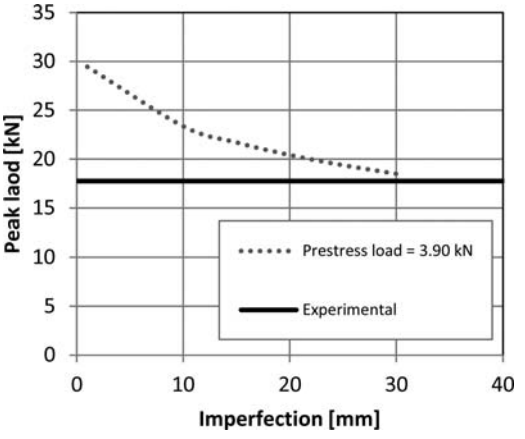

Figure 11. Load versus initial imperfection evaluation – stainless steel column – pretension load = 3.90 kN.

An inspection of Figure 8 indicates that the numerical results associated with a 30 mm initial imperfection amplitude reached the closest agreement with the experiments. This imperfection level corresponds to a value of L/167, greater than the maximum imperfection (L/500 i.e. 10 mm) value specified in the Brazilian standard (NBR8800 2009). Using this value the ultimate numerical load was equal to 23.61 kN, approximately 20% higher than the experiments ultimate load of 17.75 kN.

The second adopted prestress force was equal to 4.54 kN per cable. The results are presented in the Figure 9. At this point it is important to quote again the observations made by Servitova and Machacek (2011) regarding the fact this particular test ultimate load was lower than the others tests. This was due the presence of a column inclination caused by a larger initial imperfection magnitude. Due to this fact, only a qualitative comment will be presented. As expected, increasing the initial imperfection value in the numerical models, the maximum loads applied to the column decrease as can be observed in the Figure 9.

Figure 10 presents the numerical load versus lateral displacements curves obtained for the third test considering a prestress force magnitude of 5.44 kN. Once again, the optimum numerical model ultimate load was obtained for an initial imperfection of 30 mm. One more time using the maximum imperfection amplitude specified in the Brazilian standard (equal to 10 mm), the corresponding ultimate numerical load was 21.9, 35% higher than the experiments ultimate load of 16.23 kN.

6 FINAL REMARKS

Figure 11 illustrates the maximum load variation according to different values of initial imperfections.This was made for the column with a prestress force equal to 3.90 kN per cable in terms of its ultimate load versus adopted imperfection amplitude. For this particular prestress force magnitude, the stainless steel stayed system optimum load was reached in the experiments. As can be also observed in Figure 11, the

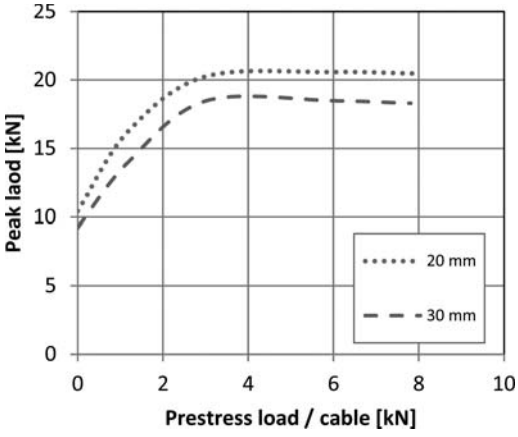

Figure 12. Load versus prestress load – stainless steel column – two imperfection values.

best performance of the numerical model was reached with a 30 mm initial imperfection amplitude.

Finally, Figure 12 presents curves showing the peak load variation according to the prestress load magnitude per cable. As can be observed in this figure, the best result was obtained considering a prestress load of approximately 4.0 kN being in agreement with the experimental results.

This paper presented a numerical investigation of the structural response of prestressed stayed stainless steel columns. Initial imperfection amplitudes and prestress force magnitudes were investigated proving to be key factors for the optimum performance of the studied structural system. The results were calibrated against experiments to validate the proposed numerical model and led to accurate and consistent findings. The present investigation will continue with the adoption of a two half sinusoidal initial imperfection model, different column lengths and other stainless steel grades like the duplex and the ferritic.

ACKNOWLEDGEMENTS

The authors would like to thank CAPES, CNPq and FAPERJ for the financial support to this research program.

REFERENCES

Andrade, S.A.L.de, Vellasco, P.C.G.daS. & Silva, J.G.S.da. 2003a. Concepção e Projecto Estrutural do Palco Principal do Rock in Rio III, Construção Magazine, 6, 4–11, Porto, (in portuguese).

Andrade, S.A.L.de, Vellasco, P.C.G.daS. & Silva J.G.S.da. 2003b. Sistema Construtivo e Montagem do Palco Principal do Rock in Rio III", Construção Magazine, 7, 30–55, Porto, (in portuguese).

ANSYS 12.1. 2009. Swanson Analysis Systems, Inc., P.O. Box 65, Johnson Road, Houston, PA, 15342-0065, Version 5.5, Basic Analysis Procedures, Second Edition.

Araujo, R.R.de, Andrade, S.A.L.de, Vellasco, P.C.G.da.S., Silva, J.G.S.da and Lima, L.R.O. de. 2008. Experimental and numerical assessment of stayed steel columns. Journal of Constructional Steel Research 64: 1020–1029.

Belenya, E. 1977. Prestressed load-bearing metal structures, English Translation, MIR Publishers Moscow.

Chan, S., Shu, G. & Lü, Z. 2002. Stability analysis and parametric study of pre-stressed stayed columns, Engineering Structures, Elsevier, 24, 115–124.

CIMAF. 2000. Cables S/A, Catalog, www.cimaf.com.br.

Eurocode 3. 2005. Design of steel structures, Part 1.1: General rules & rules for buildings, European Standard ENV1993-1-1.

Gardner, L. & Baddoo, N.R. 2006. Fire testing and design of stainless steel structures. Journal of Constructional Steel Research; 62: 532–43.

Hafez H. H., Temple M. C. & Ellis J. S. 1982. Pretensioning of single-cross-arm stayed columns, Journal of the Structural Division, ASCE, 108(7), 1623–1640.

NBR 8800. 2009. Projeto e execução de estruturas de aço em edifícios. ABNT – Associação Brasileira de Normas Técnicas.

Servitova, K. & Machacek, J. 2011. Prestressed Stainless Steel Stayed Columns. In Proceedings of 6th European Conference on Steel and Composite Structures, Budapest, Hungary, 31 August–2 September 2011.

STM E8–93. 1993. Standard Test Methods for Tension Testing of Metallic, Materials, American Association State Highway and Transportation, Officials Standard – ASHTO No.: T68.

Voevodin A.A., 1970. Ustoichivost predvaritelno-napryazhennoy shprengelnoy stoiki (Stability of a Prestressed Trussed Column), Trudy NIIR, Russia.

Wong K. C., Temple M. C. 1979. Stayed column with initial imperfection, J. Struc. Division, ASCE, 105(2), 359–375.

Tubular Structures XIV – Gardner (Ed.)
© 2012 Taylor & Francis Group, London, ISBN 978-0-415-62137-3

Experimental studies on recycled aggregate concrete filled stainless steel tube stub columns

Y.F. Yang, G.L. Ma & J. Wang
School of Civil Engineering, Dalian University of Technology, P.R. China

ABSTRACT: The concentrically compressive behaviour of Recycled Aggregate Concrete (RAC) Filled Stainless Steel Tube (RACFSST) stub columns was experimentally studied, and a total of 14 composite specimens were tested. The experiments were carried out on circular and square specimens with recycled aggregate replacement ratio of 0, 25%, 50% and 75%, and both recycled coarse aggregates and recycled fine aggregates were used in the tests. The main objectives of the tests were threefold: first, to describe a series of tests on RACFSST stub columns; second, to evaluate the effects of cross-section type and recycled aggregate replacement ratio on the behaviour of RACFSST stub columns; and finally, to predict the load versus deformation relation of RACFSST stub columns by a Finite Element Analysis (FEA) model. The test results indicated that the RACFSST stub columns subjected to concentric compression had the stable load versus deformation response, and the compressive behaviour of RACFSST stub columns were significantly affected by the recycled aggregate replacement ratio. Moreover, the predicted load versus deformation relation of RACFSST stub columns was generally agreed well with the tested results.

1 INTRODUCTION

Recycled aggregate concrete (RAC) filled stainless steel tube (RACFSST) is a new kind of composite structures, and the durability of the structures with RACFSST can be improved greatly. Similar to RAC filled carbon steel tube (Yang & Han 2006), RACFSST also makes the RAC to be in a state of protection with the outer stainless steel tube, and the composite members are less likely to be affected by the harmful environmental factors (e.g. water, temperature and winds). Furthermore, RACFSST can broaden the application field of stainless steel, and at the same time the stability of stainless steel tube can be increased by the core RAC.

To investigate the possibility of using RAC in composite structures, the studies on RAC filled carbon steel tube members have recently been carried out by several researchers (Yang 2010). In recent years, the behaviour and design method of concrete filled stainless steel tube (CFSST) have become the interests of several researchers, and the performance of CFSST columns with circular and square (with or without inner stiffness rib) sections has been theoretically and experimentally studied, as summarized and presented in Uy et al. (2011). Furthermore, Dai & Lam (2010) presented the test results of the axial compressive behaviour of stub concrete-filled columns with elliptical stainless steel, and the finite element method developed based on ABAQUS was adopted to carry out the theoretical modelling. The tests on axially loaded concrete-filled stainless steel elliptical hollow sections were carried out by Lam et al. (2010) and the simplified equations for such composite sections were also proposed. Tao et al. (2011) developed a three-dimensional nonlinear finite element (FE) model for the analysis of square CFSST stub columns under axial compression. Feng & Young (2008, 2009) experimentally investigated the behaviour of concrete filled stainless steel tubular T- and X-joints. To date, there is no information for the behaviour of RACFSST members.

The present study is an attempt to experimentally study the behaviour of RACFSST stub columns, and the test results of concentrically loaded fourteen specimens, including seven circular columns and seven square columns, are presented. Both recycled coarse aggregate and recycled fine aggregate were adopted in the tests, and the recycled aggregate replacement ratio varied from 0 to 75%. The results showed that the performance of RACFSST stub columns was mainly determined by the recycled aggregate replacement ratio. The accuracy of the predicted ultimate strength of RACFSST stub columns by using the design codes of AIJ (1997), ANSI/AISC 360-05 (2005), DB21/T1746-2009 (2009) and EC4 (2004) was evaluated. Finally, the load versus strain relation of the tested specimens was predicted using a finite element analysis (FEA) model developed based on ABAQUS software (ABAQUS 2007), and in general the predicted results agreed well with the measured results.

Table 1. Information of the tested specimens.

No.	Specimen labels	$D \times t$ (mm)	r	f_{cu} (MPa)	E_{sc} (N/mm^2)	N_{ue} (kN)
1	C0	120 × 1.77	0	63.4	40828	823.2
2	Cc1	120 × 1.77	25%	59.7	38351	813.8
3	Cc2	120 × 1.77	50%	57.3	36888	802.2
4	Cc3	120 × 1.77	75%	56.9	34867	774.3
5	Cf1	120 × 1.77	25%	58.6	37019	806.7
6	Cf2	120 × 1.77	50%	56.2	35373	768.4
7	Cf3	120 × 1.77	75%	55.3	33861	777.2
1	S0	120 × 1.77	0	63.4	34709	923.4
2	Sc1	120 × 1.77	25%	59.7	32093	871.5
3	Sc2	120 × 1.77	50%	57.3	30077	848.5
4	Sc3	120 × 1.77	75%	56.9	28446	830.0
5	Sf1	120 × 1.77	25%	58.6	31404	857.1
6	Sf2	120 × 1.77	50%	56.2	29100	826.9
7	Sf3	120 × 1.77	75%	55.3	26351	831.1

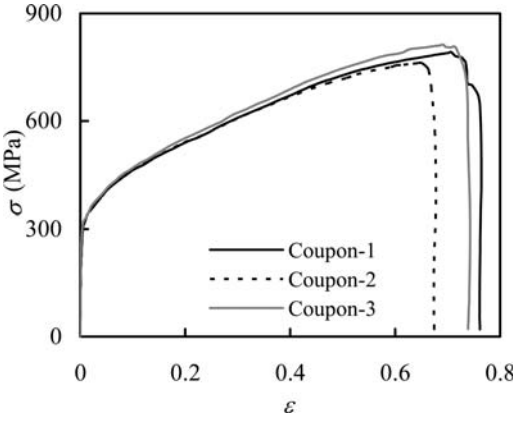

Figure 1. Stress-strain relations of stainless steel.

2 EXPERIMENTAL PROGRAMME

2.1 *Specimens*

Fourteen specimens, including twelve RACFSST stub columns and two reference normal CFSST specimens, were tested in present study. The parameters considered in the tests were: 1) steel tube section: circular and square, and 2) recycled aggregate replacement ratio r: 0 (CFSST), 25%, 50% and 75%. Both recycled coarse aggregate (RCA) and recycled fine aggregate (RFA) were adopted in the tests, and r was defined as the ratio of RCA or RFA mass to the mass of all coarse aggregate or fine aggregate, respectively. Each recycled aggregate concrete (RAC) had only one type of recycled aggregate. For all specimens, the stainless steel plate was selected to manufacture the tubes by machining and welding. The information of the tested specimens is listed in Table 1, where D is the outside diameter or width of the tube, t is the wall thickness of the tube, f_{cu} is the cube compressive strength of concrete, E_{sc} is the elastic modulus of the tested specimens, and N_{ue} is the ultimate strength of the tested specimens. The height of the specimens is 360 mm. In Table 1, the first capital letters 'C' and 'S' in specimen label denote circular and square stainless steel tube respectively, and the second lower case letters 'c' and 'f' indicate the recycled aggregates of RCA and RFA respectively. The last numbers '0', '1', '2' and '3' represent r of 0, 25%, 50% and 75%, respectively.

2.2 *Material properties*

The steel type of the specimens is the austenitic stainless steel type AISI 304. The properties of stainless steel were determined by testing three tensile coupons randomly taken from the stainless steel plate. The measured stress (σ)-strain (ε) relations of stainless steel are shown in Figure 1. From the tests, the average yield strength (0.2% proof stress), tensile strength, modulus of elasticity and Poisson's ratio of the steel were 286.7 MPa, 789.6 MPa, 1.85×10^5 N/mm^2 and 0.276 respectively. The average elongation of the stainless steel is 72.7%.

Seven types of concrete, including normal concrete with natural aggregates, RAC with 25%, 50% and 75% RCA, and RAC with 25%, 50% and 75% RFA, were prepared in the tests. The normal concrete mix was designed for mean cube compressive strength at 28 days of approximately 50 MPa. RCA and RFA were obtained by crushing waste concrete taken from failure normal concrete filled carbon steel tube specimens, and the cube compressive strength of the waste concrete was about 60 MPa. The maximum size of RCA and natural coarse aggregate was 20 mm and 25 mm, and the water absorption of RCA and natural coarse aggregate was 8.49% and 0.78% respectively. The fineness modulus of RFA and natural sand was 3.0 and 2.7, and the water absorption of RFA and natural sand was 8.3% and 1.6% respectively. To measure the compressive strength of concrete, several 150 mm cubes were cast and cured in conditions similar to the composite specimens.

The mix proportions of all concretes were same, and water reducing agent was added to improve the workability of the concrete incorporating the recycled aggregates. The test results showed that, the slump of new concrete decreased with the increase of recycled aggregate replacement ratio, and the RAC with RFA resulted in a higher slump compared to RAC with RCA. This may be caused by that RFA has a better surface feature than RCA. The cube compressive strength (f_{cu}) of all concrete at the time of the tests is presented in Table 1. It can be seen that the cube compressive strength of RAC was lower than that of normal concrete ($r = 0$), and the higher the recycled aggregate replacement ratio, the lower the compressive strength. Moreover, the cube compressive strength of RAC with RCA is higher than that of RAC with RFA under the same recycled aggregate replacement ratio.

2.3 *Failure modes and load-strain relations*

The tests were carried out on a 3000 kN capacity testing machine. Eight strain gauges were uniformly

(a) Circular section

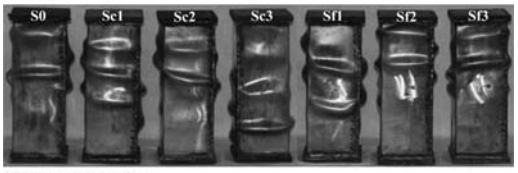

(b) Square section

Figure 2. Failure pattern of the tested specimens.

positioned at the mid-height section of the specimens to obtain the strain variation under the concentrically compressive loads, and two displacement transducers (DTs) were used to measure the axial deformations.

From the experiments, it was found that all specimens had relatively good deformation ability and post-peak load-bearing capacity. The tests were conducted in a smooth and controlled fashion, and the recycled aggregate replacement ratio (r) had little effect on the failure pattern up to and beyond the ultimate strength of the specimens. However, due to the poor confinement of square steel tube to core concrete compared with circular steel tube, the steel tube of square specimens had more buckling positions and resulted in a larger peak deformation at the buckling positions. The failure pattern of the tested specimens is demonstrated in Figure 2.

The measured axial load (N) versus strain (ε) relations of the tested specimens are shown in Figure 3, where the compressive and tensile strains are treated as positive and negative, and ε_y is the yield strain of stainless steel under axial tension. It can be seen from Figure 3 that, similar to the corresponding normal CFSST stub columns, the RACFSST specimens also have the stable load versus deformation response and the good deformation resistant ability.

It can also be seen from Figure 3 that, the strain corresponding to the ultimate strength (N_{ue}) of the circular specimens is higher than the yield strain; however, the strain corresponding to ultimate strength (N_{ue}) of the square specimens is lower than the yield stain (ε_y). This phenomenon is similar to the findings of normal concrete filled carbon steel tube (Han 2007), and is produced by the stronger confinement to core concrete of circular steel tube than square steel tube under the same parametric conditions.

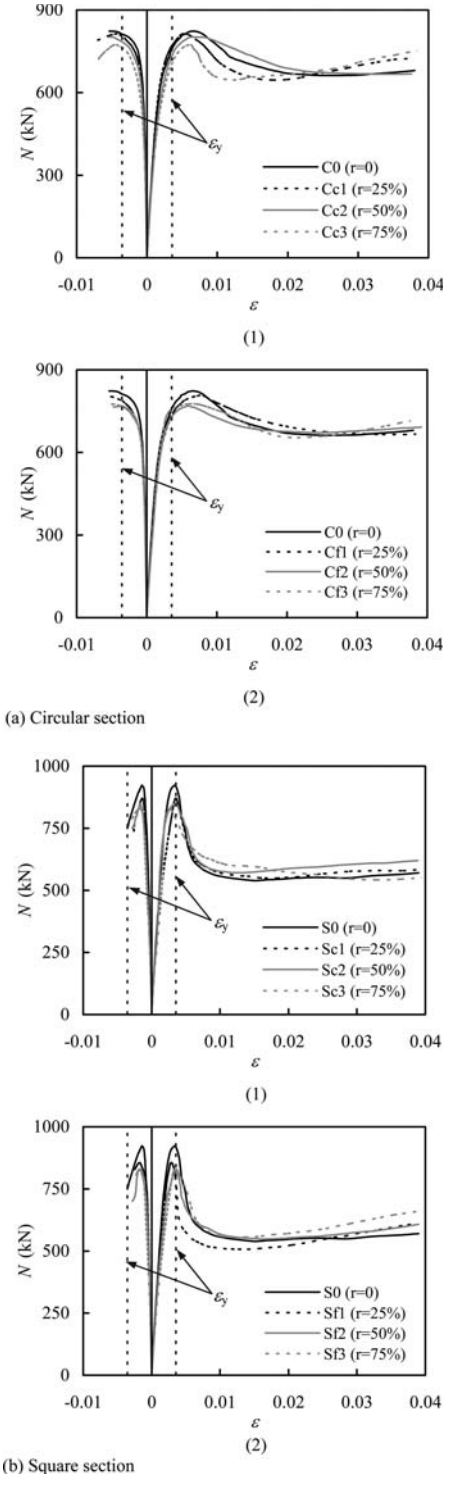

Figure 3. Axial load versus strain relations.

3 ANALYSIS OF TEST RESULTS

3.1 *Ultimate strength*

The measured ultimate strength (N_{ue}) of the RACFSST specimens is given in Table 1. Figure 4 illustrates the variation of the ultimate strength of all specimens. It can be seen that, in general, circular and square specimens have the similar variation

rules. The ultimate strength (N_{ue}) of RACFSST specimens is lower than that of the corresponding normal CFSST specimens, and the higher the recycled aggregate replacement ratio (r), the lower the ultimate strength (N_{ue}). Furthermore, under the same recycled aggregate replacement ratio (r), the specimens with RCA (Cs series) have the higher ultimate strength (N_{ue}) compared with the specimens with RFA (Cf series).

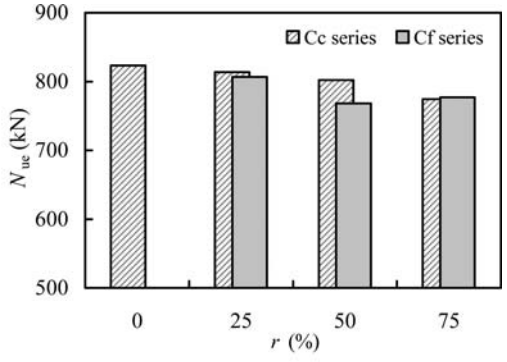

(1) Circular section

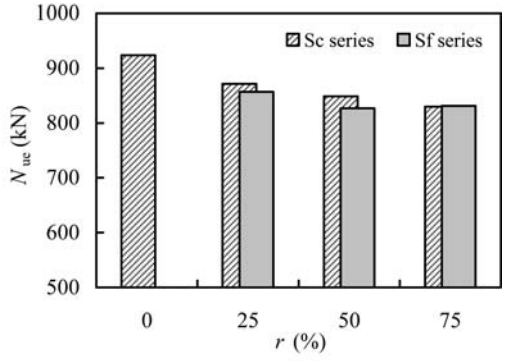

(2) Square section

Figure 4. Effects of r on ultimate strength.

Currently, there is no recommendation for the ultimate strength of RACFSST members. In this paper, the formulae in design code for normal concrete filled carbon steel tube are temporarily used for predicting the ultimate strength of RACFSST stub columns. In all design calculations, the material partial safety factors are set to unity, and the measured yield strength of stainless steel and cube compressive strength of recycled aggregate concrete (RAC) in the tests are adopted.

The ultimate strength of RACFSST stub columns calculated (N_{uc}) using the design equations in AIJ (1997), ANSI/AISC 360-05 (2005), DB21/T1746-2009 (2009) and EC4 (2004) are compared with the measured results (N_{ue}). Table 2 shows the comparison between the predicted and measured ultimate strength.

It can be found from Table 2 that, four design codes are all conservative for predicting the ultimate strength of RACFSST stub columns. On average, AIJ (1997) and ANSI/AISC 360-05 (2005) give the ultimate strength about 14% lower than the results obtained in the tests, and the predicted ultimate strength of DB21/T1746-2009 (2009) is about 10% lower than the tested results. Overall, the design equations in EC4 (2004), which give a mean value (μ_0) of 0.986 and a standard deviation (σ_0) of 0.032, are the best predictor for determining the ultimate strength of RACFSST stub columns.

3.2 *Elastic modulus*

The elastic modulus (E_{sc}) of the RACFSST stub columns obtained in the tests, which is defined as the secant modulus while axial load equal to 40% of the ultimate strength (N_{ue}), is listed in Table 1.

Table 2. Comparison between the predicted and measured ultimate strength.

No.	Specimen	N_{ue} (kN)	AIJ		ANSI/AISC 360-05		DB21/T17 46-2009		EC4	
			N_{uc} (kN)	$\frac{N_{uc}}{N_{ue}}$	N_{uc} (kN)	$\frac{N_{uc}}{N_{ue}}$	N_{uc} (kN)	$\frac{N_{uc}}{N_{ue}}$	N_{uc} (kN)	$\frac{N_{uc}}{N_{ue}}$
1	Cc1	813.8	668.8	0.822	662.9	0.815	693.2	0.852	775.7	0.953
2	Cc2	802.2	651.1	0.812	643.3	0.802	675.4	0.842	755.7	0.942
3	Cc3	774.3	648.2	0.837	640.1	0.827	672.5	0.869	752.5	0.972
4	Cf1	806.7	660.7	0.819	654.0	0.811	685.1	0.849	766.6	0.950
5	Cf2	768.4	643.0	0.837	634.4	0.826	667.3	0.868	746.6	0.972
6	Cf3	777.2	636.3	0.819	627.1	0.807	660.6	0.850	739.2	0.951
7	Sc1	871.5	786.8	0.903	782.2	0.898	817.0	0.937	883.2	1.013
8	Sc2	848.5	764.2	0.901	759.8	0.895	793.9	0.936	856.7	1.010
9	Sc3	830.0	760.5	0.916	756.2	0.911	790.1	0.952	852.3	1.027
10	Sf1	857.1	776.5	0.906	772.0	0.901	806.5	0.941	871.1	1.016
11	Sf2	826.9	753.9	0.912	749.6	0.907	783.4	0.947	844.5	1.021
12	Sf3	831.1	745.4	0.897	741.3	0.892	774.7	0.932	834.6	1.004
	μ_0		0.865		0.857		0.898		0.986	
	σ_0		0.043		0.046		0.046		0.032	

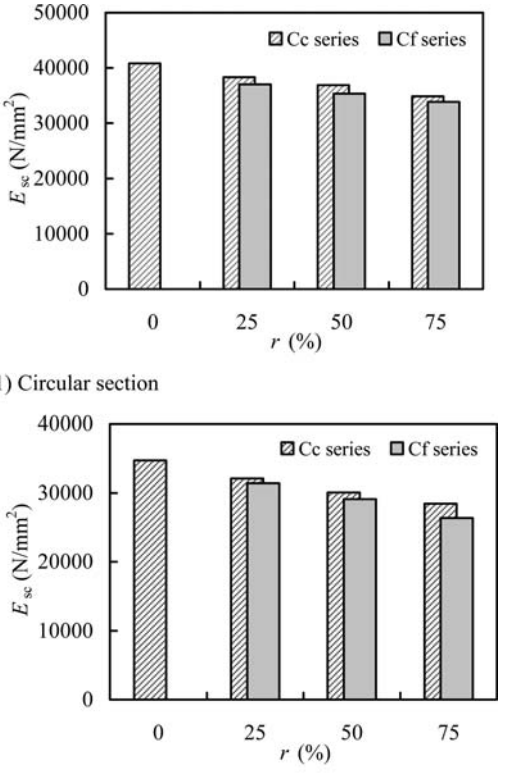

Figure 5. Variation of the elastic modulus.

The variation of the elastic modulus of all specimens is shown in Figure 5. It can be seen that, in general, the elastic modulus (E_{sc}) of RACFSST specimens is lower than that of the corresponding normal CFSST specimens, and the higher the recycled aggregate replacement ratio (r), the lower the elastic modulus. Owing to the worse confinement to core concrete of square steel tube than circular steel tube, the elastic modulus of square specimens is lower than that of circular specimens. Furthermore, under the same recycled aggregate replacement ratio (r), the specimens with RCA (Cs series) have the higher elastic modulus (E_{sc}) compared with the specimens with RFA (Cf series).

4 NUMERICAL SIMULATION

Based on ABAQUS software (ABAQUS 2007), a nonlinear finite element analysis (FEA) model for the simulation of RACFSST stub columns subjected to concentric compression is developed. The stress-strain curve with strain hardening in EC3 (2006) is adopted for stainless steel, and for core RAC the uniaxial engineering stress (σ) versus strain (ε) relation presented in Hou (2011) is used in this paper, in which the effect of recycled aggregate replacement ratio (r) is considered.

The uniaxial engineering stress (σ) versus strain (ε) relation for RAC (Hou 2011) is as follows:

$$y=\begin{cases}2x-x^2 & (x\le 1)\\ \dfrac{x}{\beta(x-1)^{\eta}+x} & (x>1)\end{cases} \tag{1}$$

where, $x=\varepsilon/\varepsilon_0$, $y=\sigma/\sigma_0$,

$$\sigma_0=f_{c,r}^{'}=\begin{cases}f_c^{'}\cdot\left(1-0.28r+0.08r^2\right) & \text{(RCA)}\\ f_c^{'}\cdot\left(1-0.36r+0.12r^2\right) & \text{(RFA)}\end{cases}$$

$$\varepsilon_0=\begin{cases}\left(\varepsilon_{cc}+800\xi_r^{0.2}\right)\cdot\left(1+r/\theta\right)\times10^{-6} & \text{(RCA)}\\ \left(\varepsilon_{cc}+800\xi_r^{0.2}\right)\cdot\left(1+2r/\theta\right)\times10^{-6} & \text{(RFA)}\end{cases}$$

$$\varepsilon_{cc}=\left(1300+12.5f_{c,r}^{'}\right)\times10^{-6}$$

$$\theta=65.715r^2-109.43r+48.989$$

$$\eta=\begin{cases}2 & \text{(Circular)}\\ 1.6+1.5x & \text{(Square)}\end{cases}$$

$$\beta=\begin{cases}0.5\cdot\left(2.36\times10^{-5}\right)^{\left[0.25+\left(\xi_r-0.5\right)^7\right]}\cdot\left(f_{c,r}^{'}\right)^2 & \text{(Circular)}\\ \left(f_{c,r}^{'}\right)^{0.1}/\left[1.2\sqrt{1+\xi_r}\right] & \text{(Square)}\end{cases}$$

in which, $f_{c,r}^{'}$ and $f_c^{'}$ are the cylinder compressive strength of RAC and the corresponding normal concrete; r is the recycled aggregate replacement ratio; $\xi_r[=f_y\cdot A_s/(f_{ck,r}\cdot A_c)=\alpha\cdot f_y/f_{ck,r}]$ is the confinement factor of RAC, where $\alpha(=A_s/A_c)$ is the steel ratio, A_s and A_c are the cross-sectional area of the steel and core concrete respectively, f_y is the yield strength of stainless steel, $f_{ck,r}$ is the characteristic strength of the RAC and equals to 0.67% of the cube compressive strength of RAC.

The material models, contact models and boundary conditions in FEA model were detailed in Hou (2011). The vertical deformations were imposed on the bottom surface of the columns in several incremental steps, and the outputs of the columns after each step are obtained from the equilibrium equations, which is solved by the Newton-Raphson iteration method (ABAQUS 2007). The comparison of axial load (N) versus longitudinal strain (ε_l) relation of RACFSST stub columns between predicted and measured results is demonstrated in Figure 6. It is shown that, generally, the predicted results agree well with the tested results, and the predicted curves have the similar changing rules as the tested ones.

Figure 7 shows the comparison between the predicted (N_{uc}) and measured ultimate strength (N_{ue}) of RACFSST stub columns.

It can be seen from Figure 7 that, generally, a good agreement is obtained between the predicted and measured results. However, for circular specimens, the predicted ultimate strength is about 10% lower than the measured results. This may be induced by the inaccuracy of the material models.

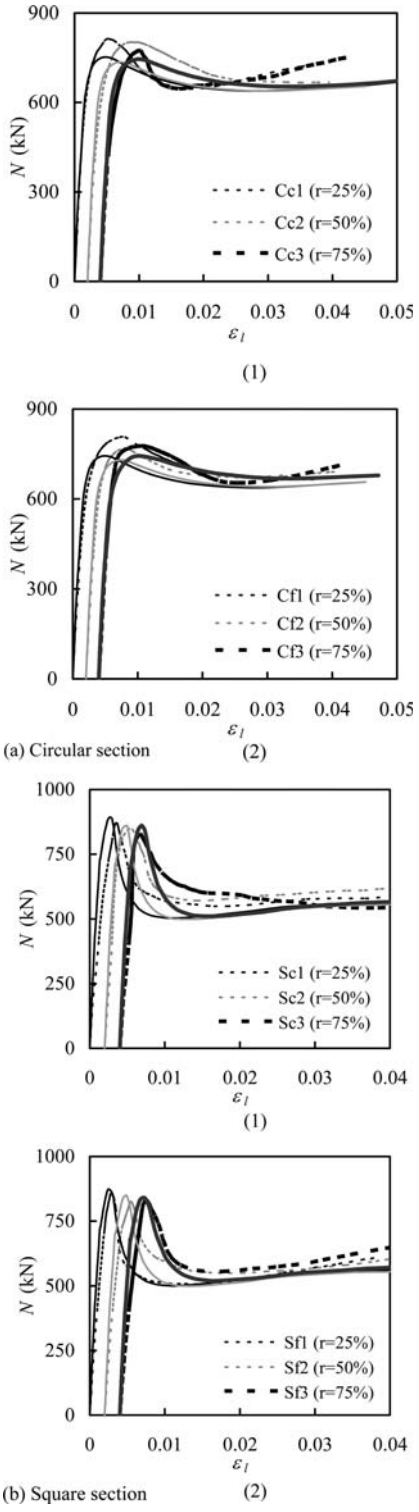

Figure 6. Comparison of axial load versus longitudinal relation between predicted and measured results.

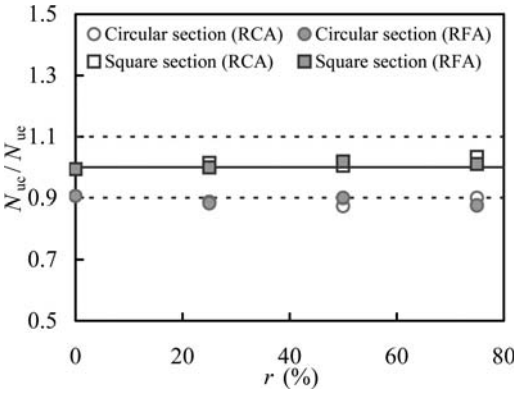

Figure 7. Comparison between the predicted and measured ultimate strength.

5 CONCLUSIONS

The behaviour of RACFSST stub columns and the corresponding normal CFSST specimens is experimentally investigated. Based on the results in present paper, the following conclusions can be drawn:

(1) Similar to the corresponding normal CFSST specimens, RACFSST stub columns under concentric compression have the stable load versus deformation response and the good deformation resistant ability.
(2) Due to the existence of recycled aggregates, the ultimate strength and elastic modulus of RACFSST stub columns are lower than those of the corresponding normal CFSST specimens.
(3) The ultimate strength of RACFSST stub columns can be conservatively predicted using formulae in AIJ, ANSI/AISC 360-05, DB21/T1746-2009 and EC4, and EC4 is the best predictor among them.
(4) The FEA model developed can be applied to simulate the performance of RACFSST stub columns with a generally good precision.

ACKNOWLEDGEMENTS

The studies in this paper are financially supported by the Independent Research Funds of the State Key Laboratory of Coastal and Offshore Engineering (SL2012-1) and the Natural Science Foundation of Liaoning Province (No. 20092154). The financial support is gratefully acknowledged.

REFERENCES

ABAQUS. 2007. ABAQUS Standard User's Manual, Version 6.7. Dassault Systèmes Corp., Providence, RI, USA.

AIJ. 1997. Recommendations for design and construction of concrete filled steel tubular structures. Architectural Institute of Japan, Tokyo, Japan.

ANSI/AISC 360-05. 2005. Specification for structural steel buildings. American Institute of Steel Construction, Inc., Chicago, USA.

DB21/T1746-2009. 2009. Technical specification for concrete-filled steel tubular structures. Liaoning, China. (in Chinese).

Dai, X. & Lam, D. 2010. Axial compressive behaviour of stub concrete-filled columns with elliptical stainless steel hollow sections. *Steel and Composite Structures*, 10(6): 517–539.

EC3. 2006. Design of steel structures-Part 1-4: General rules-Supplementary rules for stainless steels. EN 1993-1-4, Brussels, Belgium.

EC4. 2004. Design of steel and concrete structures-Part 1-1: General rules and rules for building. EN 1994-1-1, Brussels, Belgium.

Feng, R. & Young B. 2008. Tests of concrete-filled stainless steel tubular T-joints. *Journal of Constructional Steel Research*, 64(11): 1283–1293.

Feng, R. & Young B. 2009. Behaviour of concrete-filled stainless steel tubular X-joints subjected to compression. *Thin-Walled Structures*, 47(4): 365–374.

Han, L.H. 2007. Concrete-filled steel tubular structures-theory and practice (2rd Edition). Beijing: China Science Press. (in Chinese).

Hou, R. 2011. Study on compressive behavior of recycled aggregate concrete-filled steel tubes after exposed to high temperatures. Master thesis, Dalian University of Technology.

Lam, D., Gardner, L. & Burdett, M. 2010. Behaviour of axially loaded concrete filled stainless steel elliptical stub columns. *Advances in Structural Engineering*, 13(3): 493–500.

Tao, Z., Uy, B., Liao, FY. & Han, LH. Nonlinear analysis of concrete-filled square stainless steel stub columns under axial compression *Journal of Constructional Steel Research* 67(11): 1719–1732.

Uy, B., Tao, Z. & Han, L.H. 2011. Behaviour of short and slender concrete-filled stainless steel tubular columns. *Journal of Constructional Steel Research* 67(3): 360–378.

Yang, Y.F. 2010. Performance of recycled aggregate concrete-filled steel tubular members under various loadings. *Proceedings of the Second International Conference on Waste Engineering and Management (ICWEM2010)*, October 13–15, Shanghai, China, pp. 475–484.

Yang, Y.F. & Han, L.H. 2006. Experimental behaviour of recycled aggregate concrete filled steel tubular columns. *Journal of Constructional Steel Research*, 62(12): 1310–1324.

Tubular Structures XIV – Gardner (Ed.)
© 2012 Taylor & Francis Group, London, ISBN 978-0-415-62137-3

Predictive models for strength enhancements in cold-formed structural sections

B. Rossi
University of Liège, Liège, Belgium

S. Afshan & L. Gardner
Imperial College London, London, UK

ABSTRACT: Cold-formed structural sections are manufactured at ambient temperature and hence undergo plastic deformations which result in an increase in the yield stress and ultimate stress, but reduced ductility. This paper begins with a comparative study of existing predictive models to harness this strength increase. Modifications to the existing models are then made and an improved model is presented. Tensile coupon tests from the literature have been used to validate and compare the predictive models. A wide range of structural section types from both cold-rolling and press-braking fabrication processes and structural materials, including various grades of carbon steel and stainless steel, have been considered.

1 INTRODUCTION

Cold-formed structural sections are widely used in construction, offering high strength and stiffness–to–weight ratios. Structural elements in a range of section shapes – tubular sections, including the familiar square, rectangular and circular hollow sections and the recently added elliptical hollow sections, and open sections such as angles, channels and lipped channels – are commonly used in building design. Cold-formed structural sections are manufactured at ambient temperature and hence undergo plastic deformations, which occur during both the sheet rolling and cross-section forming processes, causing strain hardening of the material. Upon application of stress, the strain hardened or cold-worked material follows a new loading path with an increased yield stress and ultimate stress, but reduced ductility. In metallic materials with a distinctly defined yield point, such as carbon steels, the stress-strain behaviour becomes rounded following the cold-forming process. Non-uniformity in the material properties around cold-formed sections also exist, due to the varying level of plastic strain experienced, with the corner regions being the most influenced. Materials, such as stainless steel, with rounded stress-strain behaviour and significant strain hardening show a more pronounced response to cold-working.

With increasing emphasis being put on the sustainable use of resources, fully exploiting material properties in structural design is paramount. The performance of finite element models is also often highly sensitive to the prescribed material parameters, making an accurate representation of the material characteristics essential. Therefore, developing suitable predictive models for harnessing the increases in material strength caused by plastic deformations, experienced during the cold-forming production routes, is required. In this paper, predictive models from the literature for determining the strength enhancement observed in cold-formed metallic sections are reviewed. Two recently proposed predictive models, developed by Cruise and Gardner (2008) and Rossi (2008), have been assessed extensively. Improvements to the existing models have been made and a new predictive model is presented. Results from tensile coupon tests from existing experimental programs have been gathered and used to validate the predictions from the models. Comparisons between the presented predictive equations have been made. The collated database covers a range of structural section types – square hollow sections (SHS), rectangular hollow sections (RHS), angles, lipped channels and hollow flange channel sections from both cold-rolling and press-braking fabrication processes – and structural materials, namely carbon steel and stainless steel (EN 1.4301, 1.4306, 1.4318, 1.4016, 1.4003, 1.4512 and 1.4162).

2 PRODUCTION ROUTES

Cold-rolling and press-braking are the two methods commonly employed in the manufacture of light gauge cold-formed structural sections. In press-braking the sheet material is formed into the required shape by creating individual bends along its length. It is a semi-automated process used to produce open sections, such

as angles and channels, in limited quantities. Air press-braking, where elastic spring back is allowed by over-bending the material, is more commonly adopted than coin press-braking, where the die and the tool fit into one another. Cold-rolling is an automated continuous bending process in which the gradual deformation of the uncoiled metal sheet through a series of successive rollers produces the final cross-section profile.

In case of tubular box sections, the flat metal sheet is first rolled into a circular tube and is welded closed. It is subsequently deformed into a square or rectangle by means of dies. The tube's cross-section is initially circular whereas the cross-section at the end of the process is a square or rectangle with round corners. Finite element models with contact boundary conditions allow simulation of this continuous process, but are rather complex and time consuming and require sophisticated software.

3 PREDICTIVE MODELS

3.1 *Literature review*

Early studies of the strength enhancement in the corner regions of cold-formed carbon steel sections were carried out by Karren (1967). A power model to predict the strength increases in the corner regions of cold-formed sections, in terms of the yield stress of the unformed sheet material and the internal corner radius to thickness ratio was proposed. The model was developed based on available test data, including specimens formed by both cold-rolling and press-braking processes. The author suggested that since the corner regions typically represent 5% to 30% of the total cross-sectional area, the influence of the enhanced corner strength should be incorporated in structural calculations. Coetzee et al. (1990) performed an experimental study into strength enhancements of cold-formed stainless steel sections. Material tests on press-braked lipped channel sections of three stainless steel grades (EN 1.4301, 1.4401 and 1.4003) were conducted. Karren's expression was later modified by van den Berg and van der Merwe (1992) on the basis of Coetzee et al.'s test data and further test data on stainless steel single press-braked corner specimens in grades EN 1.4301, 1.4016, 1.4512 and 1.4003. Gardner and Nethercot (2004) studied test data from cold-rolled box sections and observed a linear relationship between the 0.2% proof strength of the corner regions and the ultimate strength of the flat faces.

Ashraf et al. (2005) analysed all stainless steel test results, from a variety of fabrication processes, to investigate the application of the predictive equations proposed by van den Berg and van der Merwe (1992). Comparisons of the predicted strength and the test results showed that modifications to the models were required. Three empirical predictive models for the evaluation of the corner yield strength were proposed. Two power models based on the properties (0.2% proof strength and the ultimate tensile strength) of the unformed sheet material were developed to predict the corner 0.2% proof strength of both cold-rolled and press-braked sections. The linear expression proposed by Gardner and Nethercot (2004), to predict the 0.2% proof strength of the corners in cold-rolled box sections was also recalibrated. Furthermore, in order to obtain a full insight into the influence of cold-work on the corner material properties, an equation to predict the ultimate strength of the corner material was developed.

Cruise and Gardner (2008) later recalibrated the Ashraf et al. (2005) expressions in light of further stainless steel experimental data and proposed two revised expressions to predict the enhanced corner strength of press-braked and cold-rolled sections. In addition, expressions for evaluating the 0.2% proof stress and the ultimate tensile stress of the flat faces of cold-rolled box sections were developed. Similarly, based on corner material test results on structural carbon steel box sections, Gardner et al. (2010) modified the predictive model given in the AISI Specification for the Design of Cold-formed Steel Structural Members (2002). Values of the coefficients in the predictive equation were proposed that enabled the model to be applied to the assessment of the enhanced corner strength of cold-rolled square and rectangular hollow sections. An alternative formula to evaluate the enhanced 0.2% proof strength in the flat faces and corner regions of cold-formed sections, using the properties of the unformed sheet material and the final cross-section geometry, was proposed by Rossi (2008). The proposed model may be applied to a range of nonlinear metallic materials.

3.2 *Cruise and Gardner (2008) predictive model*

Cruise and Gardner (2008) carried out an extensive experimental program on cold-formed stainless steel structural sections, produced from both cold-rolling and press-braking production routes. Based on the experimental results, including tensile coupon tests and hardness tests, the distributions of the 0.2% proof strength and ultimate strength around a series of cold-rolled box sections and press-braked angle sections were identified. The generated test data were combined with all other available published experimental data and used to develop models for predicting the strength enhancements around stainless steel sections due to cold-forming. The experimental observations showed that, for press-braked sections, the enhancements are confined to the corner regions, whereas cold-rolled box sections also exhibited significant strength increases in the flat faces, indicating that the flat faces in cold-rolled box sections also experience plastic deformations during forming. New models were therefore proposed to predict the strength enhancements in the flat faces of cold-rolled box sections. Expressions for the 0.2% proof stress $\sigma_{0.2,f,pred}$ and the ultimate tensile stress $\sigma_{u,f,pred}$, Eqs. (1) and (2) respectively, were provided, in which t, b and d

are the section thickness, breadth and depth respectively, and $\sigma_{0.2,mill}$ and $\sigma_{u,mill}$ are the 0.2% proof stress and ultimate tensile stress of the unformed material, as provided by the mill certificate.

$$\sigma_{0.2,f,pred} = \frac{0.85\sigma_{0.2,mill}}{-0.19+\frac{1}{12.42\left(\frac{\pi t}{2(b+d)}\right)+0.83}} \quad (1)$$

$$\sigma_{u,f,pred} = \sigma_{u,mill}\left(0.19\left(\frac{\sigma_{0.2,f,pred}}{\sigma_{0.2,mill}}\right)+0.85\right) \quad (2)$$

Existing literature models were also modified to predict the strength enhancement in the corner regions of cold-rolled and press-braked stainless steel sections. The simple power model proposed by Ashraf et al. (2005) was recalibrated based on a more comprehensive experimental database to predict the 0.2% proof stress of the corners in press-braked sections. For cold-rolled sections, the model presented in Gardner and Nethercot (2004) and later recalibrated by Ashraf et al. (2005), providing a linear relationship between the 0.2% proof stress of the formed corners and the ultimate strength of the flat faces, was again updated. The proposed expressions for the corner strength enhancement $\sigma_{0.2,c,pred}$ are given by Eqs. (3) and (4) for press-braked sections and cold-rolled sections, respectively, in which R_i is the internal corner radius. The experimental data also indicated that, the corner strength enhancement extends beyond the curved corner region for cold-rolled sections, and it is confined to the corner region for press-braked sections. It was therefore proposed that Eq. (4) should be used to predict a uniform strength enhancement for the corner region plus an extension of 2t, where t is the material thickness, beyond the corner radius into the flat faces of the section.

For press-braked section:

$$\sigma_{0.2,c,pred} = \frac{1.673\ \sigma_{0.2,mill}}{\left(\frac{R_i}{t}\right)^{0.126}} \quad (3)$$

For cold-rolled section:

$$\sigma_{0.2,c,pred} = 0.83\ \sigma_{u,f,pred} \quad (4)$$

3.3 *Rossi (2008) predictive model*

Rossi (2008) examined the through-thickness residual stress distributions and strength enhancements induced during cold-forming of sections composed of nonlinear metallic materials. The proposed model for predicting the cold-work strength enhancement is essentially based on the determination of the plastic strains caused during the fabrication process and evaluation of the corresponding stresses, through an appropriate material model. The cold-rolling fabrication process was broken down into four key steps: (A) coiling of the sheet material, (B) uncoiling of the sheet material, (C) forming into a circular section and (D) subsequent deforming into a square or rectangular section.

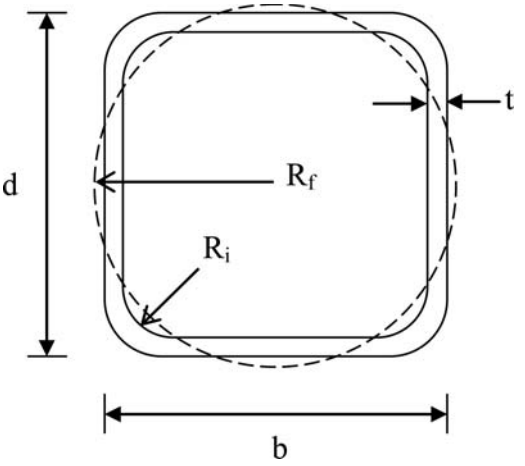

Figure 1. Definition of symbols for SHS and RHS.

The flat faces of cold-rolled hollow sections were thus assumed to undergo coiling and uncoiling in the rolling direction followed by bending and unbending in the direction perpendicular to the rolling direction. Step C was considered to have the greatest influence on strength enhancement in the flat faces of cold-rolled box sections and was used as the dominant stage for subsequent analysis. For the corner regions, in both cold-rolled and press-braked sections, the final formation of the corner was considered as the dominant stage of the process.

The induced plastic strains associated with the dominant stages of the flat face and corner forming processes were determined. Assuming pure bending, the strain experienced by the section face during the formation of the circular tube (step C) was taken as $\varepsilon_f = (t/2)/R_f$, where R_f is the radius of the circular tube and can be expressed in terms of the section geometry – see Figure 1 – leading to $\varepsilon_f = \pi t/2(b+d)$. Similarly, the strain induced during corner forming was given as $\varepsilon_c = (t/2)/R_c$, where $R_c = R_i + t/2$. Note that these are essentially the same strains considered by Cruise and Gardner (2008).

The inverted compound Ramberg-Osgood material model, proposed by Abdella (2006) was employed within the predictive model to mimic the stress-strain response of the unformed sheet material, with key points obtained from the mill certificate. The resulting predictive model (Rossi, 2008) is given by Eq. (5). The proposed formula may be used to evaluate the strength enhancement $\sigma_{0.2,forc,pred}$ in the flat faces of cold-rolled box sections and the corner regions of both cold-rolled sections and press-braked sections, based on the appropriate radius: $R_f = (b+d)/\pi$ for flat faces and $R_c = R_i + t/2$ for the corner regions.

$$\frac{\sigma_{u,mill}}{\sigma_{0.2,f\text{ or }c,\ pred} - \sigma_{0.2,mill}} = C_1\left(\frac{R}{t/2}\right) + C_2\left(\frac{R}{t/2}\right)^{\alpha} \quad (5)$$

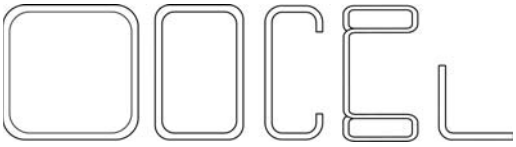

Figure 2. Variety of cold-formed cross-sections considered in this study.

where,

$$C_1 = \frac{\varepsilon_{t,0.2}}{r_2}\frac{\sigma_{u,mill}}{\sigma_{0.2,mill}} \quad (6)$$

$$C_2 = \frac{(r^* - 1)\varepsilon_{t,0.2}}{r_2(\varepsilon_u - \varepsilon_{t,0.2})^{p^*}}\frac{\sigma_{u,mill}}{\sigma_{0.2,mill}} \quad (7)$$

where, $r_2 = E_{0.2}\varepsilon_{t,0.2}/\sigma_{0.2}$, $E_{0.2} = \sigma_{0.2}E/(\sigma_{0.2} + 0.002nE)$, $r^* = E_{0.2}(\varepsilon_u - \varepsilon_{t,0.2})/(\sigma_u - \sigma_{0.2})$, $p^* = r^*(1 - r_u)/(r^* - 1)$, $r_u = E_u(\varepsilon_u - \varepsilon_{t,0.2})/(\sigma_u - \sigma_{0.2})$, $E_u = E_{0.2}/[1 + (r^* - 1)m]$, $m = 1 + 3.5\sigma_{0.2}/\sigma_u$, $\alpha = 1 - p^*$ and $\varepsilon_{t,0.2} = 0.002 + \sigma_{0.2}/E$.

4 COMPARISONS OF EXSISTING PREDICTIVE MODELS

4.1 *Experimental database*

In order to assess the wider applicability of the predictive models presented in Sections 3.2 and 3.3, tensile coupon data from a broad spectrum of existing testing programs have been gathered. The collated database covers a range of structural section types – SHS, RHS, angles, lipped channel sections (LCS) and hollow flange channel sections (HFCS) from both cold-rolling and press-braking fabrication processes, as illustrated in Figure 2, and a range of structural materials including carbon steel grades and austenitic (EN 1.4301, 1.4306, 1.4318), ferritic (EN 1.4016, 1.4003, 1.4512) and lean duplex (EN 1.4162) stainless steel grades. In order to investigate the strength enhancement due to face forming processes in cold-rolled sections, reported tensile coupon tests for this portion of the section have been used. Table 1 provides a summary of the collected database for the flat faces of the cold-rolled sections analysed herein. Based on the available published corner test data, for both cold-rolled and press-braked sections, the performance of the predictive models for corners has also been assessed. The compiled database for corner coupon tests considered in this study is summarized in Table 2.

The collected information includes the section geometric dimensions, mill certificate material properties – $\sigma_{0.2,mill}$ and $\sigma_{u,mill}$ – and the measured material properties of the formed sections – the 0.2% proof stress $\sigma_{0.2,test}$ and the ultimate tensile stress $\sigma_{u,test}$. For cold-formed sections, the mill test is carried out on sheet material prior to section forming and the results are supplied by the manufacturer. The Ramberg-Osgood material model parameters, required for the Rossi (2008) model, were sourced from Ashraf et al. (2006) and Rasmussen (2003), with the relevant material properties obtained from, EN 1993-1-1 (2005) for carbon steel sections and EN 10088-1 (2005) for stainless steel sections.

Table 1. Summary of database for coupon tests on flat material in cold-rolled sections from literature.

Reference	Material	Section
Gardner et al. (2010)	CS (S235)	SHS,RHS
Guo et al. (2007)	CS (S235)	SHS,RHS
Niemi (1990)	CS (S355)	SHS
Zhu & Wilkinson (2007)	CS*	HFCS
Ala-Outinen (2007)	SS(1.4301)	SHS
Cruise (2007)	SS (1.4301)	SHS,RHS
Gardner (2002)	SS (1.4301)	SHS,RHS
Gardner et al. (2006)	SS (1.4318)	SHS,RHS
Hyttinen (1994)	SS (1.4301)	SHS
Rasmussen & Hancock (1993)	SS (1.4306)	SHS
Talja & Salmi (1995)	SS (1.4301)	SHS
Afshan & Gardner (2012)	SS (1.4003)	SHS,RHS
Hyttinen (1994)	SS (1.4003)	SHS
Hyttinen (1994)	SS (1.4512)	SHS
Theofanous & Gardner (2010)	SS (1.4162)	SHS,RHS

*Material grade was not reported.

Table 2. Summary of database for coupon tests on corner material from literature.

Reference	Material	Section
Gardner et al. (2010)	CS (S235)	SHS,RHS
Guo et al. (2007)	CS (S235)	SHS,RHS
Niemi (1990)	CS (S355)	SHS
Zhu & Wilkinson (2007)	CS*	HFCS
Ala-Outinen (2007)	SS (1.4301)	SHS
Coetzee et al. (1990)	SS (1.4301)	LCS
Coetzee et al. (1990)	SS (1.4401)	LCS
Cruise (2007)	SS (1.4301)	SHS,RHS
Cruise (2007)	SS (1.4301)	Angle
Gardner (2002)	SS (1.4301)	SHS,RHS
Garddner et al. (2006)	SS (1.4318)	SHS,RHS
Lecce & Rasmussen (2005)	SS (1.4301)	LCS
Rasmussen &Hancock (1993)	SS (1.4306)	SHS
van den Berg & van der Merwe (1992)	SS (1.4301)	Angle
Afshan & Gardner (2012)	SS (1.4003)	SHS,RHS
Coetzee et al. (1990)	SS (1.4003)	LCS
Lecce & Rasmussen (2005)	SS (1.4016)	LCS
Lecce & Rasmussen (2005)	SS (1.4003)	LCS
van den Berg & van der Merwe (1992)	SS (1.4512)	Angle
van den Berg & van der Merwe (1992)	SS (1.4016)	Angle
van den Berg & van der Merwe (1992)	SS (1.4003)	Angle
Theofanous & Gardner (2010)	SS (1.4162)	SHS,RHS

*Material grade was not reported.

Table 3. Comparison of the predictive models for flat faces of cold-rolled sections.

Predictive model		Cruise & Gardner (2008)	Rossi (2008)
All	Mean	1.09	0.96
	COV	0.20	0.20
Carbon steel	Mean	(1.25)	0.94
	COV	(0.22)	0.16
Stainless steel	Mean	1.06	0.97
	COV	0.18	0.21

Table 4. Comparison of the predictive models for corner regions of cold-formed sections.

Predictive model		Cruise & Gardner (2008); Gardner et al. (2010)	Rossi (2008)
All	Mean	0.98	1.04
	COV	0.11	0.14
Carbon steel	Mean	0.95	0.95
	COV	0.10	0.09
Stainless steel	Mean	0.98	1.05
	COV	0.12	0.14

4.2 *Comparison of predictive models*

This section provides a broad comparison, in terms of both the accuracy of the predictions and the ease of use, of the two predictive models. Numerical comparisons, including the mean and coefficient of variation (COV), of the two predictive models with the test data, in terms of the predicted strength to the test strength ratio, are presented in Tables 3 and 4 for flat faces and corner regions, respectively. Although the proposed predictive model for flat faces of cold-rolled sections provided by Cruise and Gardner (2008) was calibrated only for stainless steel, it has also been applied herein to carbon steel test data for comparison purposes and the results are shown in Table 3 in brackets.

Analysis of the results shows that for the flat faces of cold-rolled stainless steel sections, the predictive model from Rossi (2008) is able to predict more accurate results, in terms of the mean value, than the predictive equation proposed by Cruise and Gardner (2008) but, has higher scatter. The results for the corner regions show that for stainless steel, the Cruise and Gardner (2008) model offers more accurate prediction of the test data with lower scatter. Also, Rossi (2008) and the modified AISI (Gardner et al. 2010) predictions for the corner strength enhancements of carbon steel sections are in good agreement, with the former showing a lower scatter of 0.09.

As far as the flat faces of cold-rolled sections are concerned, both models use the same measure of cold-work induced strain in their formulations, but different material models. The Rossi (2008) model employs the compound Ramberg-Osgood material model whereas, Cruise and Gardner (2008) assume a linear hardening

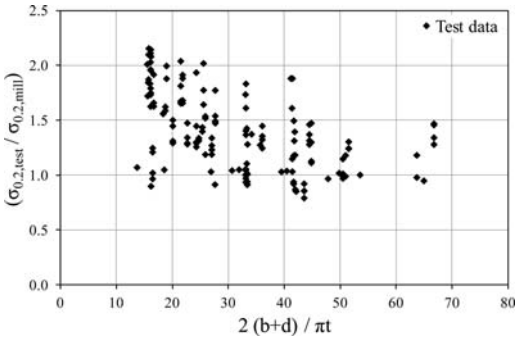

Figure 3. Normalized measured 0.2% proof stress for the flat faces of cold-rolled sections.

material behaviour for stainless steel with the material model incorporated into the model coefficients. As a result, while the Rossi (2008) predictive model may be applied to any structural section of non-linear material, the Cruise and Gardner (2008) model is specific to structural sections with the material for which the models were calibrated against, which included austenitic stainless steel grade EN 1.4301.

Due to the complicated mathematical form and the number of input parameters required to evaluate the cold-work induced strength enhancement from Rossi's (2008) predictive equation, it is lengthy to implement in design calculations. In order to overcome the shortcomings of the two predictive models, a new predictive model is developed in the next section.

5 EXTENSION OF PREDICTIVE MODELS

5.1 *Introduction*

In this section a simple and accurate method for predicting the strength enhancement in cold-formed structural sections is presented. The model development is based on the same concept as used in the Rossi (2008) predictive model, which involves the determination of the cold-work induced plastic strain followed by the evaluation of the corresponding stress from the stress-strain response of the unformed sheet material, using an appropriate material model. Given the scatter in the test data, see Figures 3 and 4 for flat faces and corner regions, respectively, and the assumptions made in simplifying the forming processes, using a simple material model, in place of the compound Ramberg-Osgood model, is deemed more appropriate. In addition, analysis of the results shows that the plastic strain from both the sheet forming and cross-section forming processes contribute to the overall strength enhancement of the flat faces of cold-rolled box sections.

5.2 *Material stress-strain models*

In order to represent the stress-strain response of the unformed sheet material, the suitability of a power law

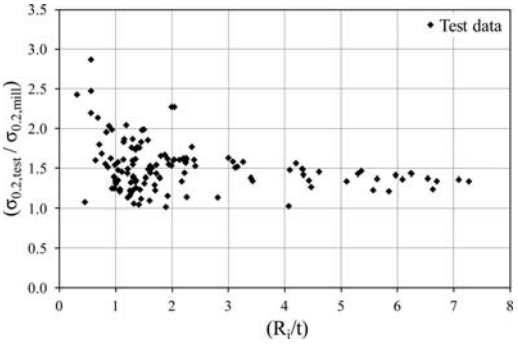

Figure 4. Normalized measured 0.2% proof stress for the corner regions of cold-formed sections.

model and a tri-linear material model with strain hardening, Eqs. 8 and 9, respectively, have been assessed. The parameters which define each model are based on the key material properties from the mill certificate.

The power law model parameters, a and b, are calibrated such that it passes through the 0.2% proof stress ($\varepsilon_{t,0.2}$, $\sigma_{0.2}$) and the ultimate stress (ε_u, σ_u) points. The model's inability to provide a good fit to the actual stress-strain response at low strains will not influence the predicted strength due to the relatively large magnitude of the plastic strains induced during cold-forming processes. The first stage of the tri-linear model has a slope E, taken as the material initial Young's modulus, up to the yield point, defined as the 0.2% proof stress and the corresponding elastic strain $\varepsilon_{0.2} = \sigma_{0.2}/E$. The strain hardening slope is determined as the slope of the line passing through the defined yield point ($\varepsilon_{0.2}$,$\sigma_{0.2}$) and a specified maximum point (ε_{max},σ_{max}) with ε_{max} taken as $0.5\varepsilon_u$, where ε_u is the ultimate tensile strain, and σ_{max} is taken as the ultimate tensile stress σ_u. A similar approach has been recommended in EN 1999-1-1 (2007) for modelling the stress-strain response of aluminium alloys. In order to prevent significant over-predictions of strength at large strains, a maximum stress limit equal to the ultimate tensile stress σ_u has been added. No strength enhancement would 0 result from strains less than the yield strain; hence the initial part of the model will not be used for strength enhancement predictions. The ultimate tensile strain ε_u is not provided in the material mill certificate and has been determined herein based on Rasmussen's (2003) recommendations. Further work for accurately predicting this parameter is currently underway.

$$\sigma = a\,\varepsilon^b \qquad \text{for} \quad 0 \le \varepsilon \le \varepsilon_u \tag{8}$$

$$\sigma = \sigma_{0.2} + \left(\frac{\sigma_u - \sigma_{0.2}}{0.5\varepsilon_u - \varepsilon_{0.2}}\right)(\varepsilon - \varepsilon_{0.2})$$
$$\text{for} \quad \varepsilon_{0.2} < \varepsilon \le 0.5\varepsilon_u \tag{9}$$
$$\sigma = \sigma_u \qquad \text{for} \quad 0.5\varepsilon_u < \varepsilon \le \varepsilon_u$$

5.3 *Cold-work induced plastic strains*

Cold-work plastic strains are induced during both coiling/uncoiling of the sheet material and cross-section forming processes. The plastic strain components from both processes contribute to the overall strength enhancement of the flat faces of cold-rolled box sections whereas for corners of cold-rolled sections and press-braked sections, the plastic strains from the formation of the corner are generally much larger in magnitude than the plastic strains induced prior to corner forming.

The through thickness strains induced during the coiling/uncoiling processes is related to the internal coil radius and the radial location of the sheet in the coil. The critical coil radius associated with the initiation of through thickness plastic strains from sheet coiling depends on the thickness and material properties of the sheet. If the coil radius is greater than this critical radius, no plastic strains are introduced; otherwise, varying degrees of thorough thickness plastic strains are produced. As it is not possible to provide an exact measure of the plastic strains associated with the coiling/uncoiling processes, due to the unknown value of the coil radius coinciding with the as-formed member, this strain may be determined on the basis of an average coil radius, as recommended in Moen et al. (2008). From Moen et al.'s (2008) research, an average coil radius $R_{coiling} = 450$ mm is used herein.

The total plastic strain experienced by the flat faces of cold-rolled box-sections is taken as the sum of the strains from the coiling, uncoiling, formation of the circle and crushing into the final cross-section geometry – referred to as steps A, B, C and D in Rossi (2008). The strain from the sheet uncoiling and formation of the final geometry are taken as equal and opposite to the strains from coiling and formation of circular tube respectively. Hence the total plastic strains assumed to be experienced by the flat faces $\varepsilon_{f,total}$ and the corner regions ε_c are given by:

$$\varepsilon_{f,total} = 2\left[(t/2) / R_{coiling}\right] + 2\left[(t/2) / R_f\right]$$
$$\varepsilon_c = \left[(t/2) / R_c\right] \tag{10}$$

where, $R_c = R_i + t/2$ and $R_f = (b+d)/\pi$.

5.4 *Analysis of results*

The experimental database presented in Section 4.1 has been used to investigate the applicability of the two simple stress-strain models and the plastic strain measures introduced in Sections 5.2 and 5.1, respectively for predicting the strength enhancement in cold-formed sections. Numerical comparisons, including the mean and coefficient of variation (COV), of the predictions from both material stress-strain models with the test data, in terms of the predicted strength to the test strength ratio, are presented in Tables 5 and 6 for flat faces and corner regions, respectively.

Table 5. Comparison of the proposed predictive models for flat faces of cold-rolled sections.

Predictive model		Power model	Linear model
All	Mean	1.06	0.96
	COV	0.19	0.18
Carbon steel	Mean	0.99	0.97
	COV	0.19	0.16
Stainless steel	Mean	1.08	0.96
	COV	0.19	0.19

Table 6. Comparison of the proposed predictive models for corner regions of cold-formed sections.

Predictive model		Power model	Linear model
All	Mean	1.05	1.04
	COV	0.15	0.15
Carbon steel	Mean	0.96	0.95
	COV	0.09	0.11
Stainless steel	Mean	1.08	1.06
	COV	0.15	0.15

Analysis of the results shows that for both the flat faces and corner regions, the linear hardening material model gives more accurate results in terms of both the mean and the COV, than the power model. The linear hardening model and the Rossi (2008) model give the same mean of 0.96 for the flat faces of cold-rolled stainless steel and carbon steel sections with the former having a lower COV of 0.18. As far as the corner regions of cold-formed sections are concerned, both Rossi (2008) and the proposed linear hardening model over-predict the test data, highlighting the possible over-estimation of the cold-work induced plastic strains in the corner regions. Overall, the proposed linear hardening material model with the new strain measure predictions are in good agreements with the test data and may be employed to predict the strength enhancement in cold-formed structural sections. The new proposed predictive model is simple to use in structural calculations and is applicable to any metallic structural sections.

6 CONCLUSIONS

A review of predictive models from the literature for harnessing the strength increase in cold-formed sections has been carried out. Two recently proposed predictive models, developed by Cruise and Gardner (2008) and Rossi (2008), were assessed extensively. Improvements to the existing models were subsequently made and a new predictive model was presented. A comprehensive database of the tensile coupon tests from existing experimental programs were used to validate the predictions from the models.

Analysis of the results showed that for the flat faces of cold-rolled stainless steel sections, the predictive model from Rossi (2008) is able to predict more accurate results, in terms of the mean value, than the predictive equation proposed by Cruise and Gardner (2008) but, has higher scatter. The results for the corner regions show that for stainless steel, the Cruise and Gardner (2008) model offers more accurate prediction of the test data with lower scatter. Also, Rossi (2008) and the modified AISI model (Gardner et al. 2010) predictions for the corner strength enhancements of carbon steel sections are in good agreement, with the former showing a lower scatter of 0.09. It was highlighted that while the Rossi (2008) predictive model may be applied to any structural section of non-linear material, Cruise and Gardner's (2008) model is specific to austenitic stainless steel structural sections. Also, Rossi's (2008) predictive equation was considered lengthy to implement in design calculations. In order to overcome the shortcomings of these models, a linear hardening material model, with new strain measures, was proposed to predict the strength enhancement in cold-formed structural sections. The new proposed predictive model predictions are in good agreement with the test data. It is simple to use in structural calculations and is applicable to any metallic structural sections.

ACKNOWLEDGEMENTS

The authors are grateful to the Outokumpu Research Foundation, the Steel Construction Institute and the University of Liège for their financial and technical contributions to the project.

REFERENCES

Abdella, K. (2006) Inversion of a full-range stress–strain relation for stainless steel alloys. *International Journal of Non-Linear Mechanics.* 41 (3), 456–463.

Afshan, S. & Gardner, L. (In press) Experimental Study of Cold-Formed Ferritic Stainless Steel Hollow Sections. *Journal of Structural Engineering (ASCE).*

Ala-Outinen, T. (2007) Members with Class 4 cross-sections in fire: Work package 3. ECSC project 'Stainless steel in fire (SSIF)'. Contract no. RFS-CR-04048. The Steel Construction Institute UK.

American Iron and Steel Institute (AISI). (1996) *Specification for the design of cold-formed steel structural members*. American Iron and Steel Institute, Washington, D.C.

Ashraf, M., Gardner, L. & Nethercot, D. A. (2005) Strength enhancement of the corner regions of stainless steel cross-sections. *Journal of Constructional Steel Research.* 61 (1), 37–52.

Ashraf, M., Gardner, L. & Nethercot, D. A. (2006) Finite element modelling of structural stainless steel cross-sections. *Thin-Walled Structures.* 44 (10), 1048–1062.

Coetzee, J. S., van den Berg, G. J. & van den Merwe, P. (1990) The effect of work hardening and residual stresses due to cold work of forming on the strength of cold-formed stainless steel lipped channel section. Proceedings

of the 10th international specialty conference on cold-formed steel structures, University of Missouri, USA. pp. 143–162.

Cruise, R.B. (2007) The influence of production routes on the behaviour of stainless steel structural members. *Ph.D. Thesis.* Department of Civil and Environmental Engineering, Imperial College London, UK.

Cruise, R. B. & Gardner, L. (2008) Strength enhancements induced during cold forming of stainless steel sections. *Journal of Constructional Steel Research.* 64 (11), 1310–1316.

European Committee for standardization (CEN). (2005). *Stainless steels – Part 1: List of stainless steels, EN 10088-1*. Brussels, Belgium.

European Committee for standardization (CEN). (2005). *Eurocode 3: Design of steel structures – Part 1-1: General rules and rules for buildings, EN 1993-1-1*, Brussels, Belgium.

European Committee for standardization (CEN). (2007). Eurocode 9: *Design of aluminium structures – Part 1-1: General structural rules, EN 1999-1-1*. Brussels, Belgium.

Gardner, L. (2002) A new approach to structural stainless steel design. *Ph.D. Thesis.* Department of Civil and Environmental Engineering. Imperial College London, UK.

Gardner, L. & Nethercot, D. A. (2004) Experiments on stainless steel hollow sections—Part 1: Material and cross-sectional behaviour. *Journal of Constructional Steel Research.* 60 (9), 1291–1318.

Gardner, L., Saari, N. & Wang, F. (2010) Comparative experimental study of hot-rolled and cold-formed rectangular hollow sections. *Thin-Walled Structures.* 48 (7), 495–507.

Gardner, L., Talja, A. & Baddoo, N. R. (2006) Structural design of high-strength austenitic stainless steel. *Thin-Walled Structures.* 44 (5), 517–528.

Guo, Y., Zhu, A., Pi, Y. & Tin-Loi, F. (2007) Experimental study on compressive strengths of thick-walled cold-formed sections. *Journal of Constructional Steel Research.* 63 (5), 718–723.

Hyttinen, V. (1994) Design of cold-formed stainless steel SHS beam-columns. Report 41: Laboratory of Structural Engineering, University of Oulu. Finland.

Karren, K.W. (1967) Corner properties of cold-formed steel shapes. *Journal of Structural Division (ASCE)*, 93 (ST1), 401–432.

Lecce, M. & Rasmussen, K.J.R. (2005) Experimental investigation of the distortional buckling of cold-formed stainless steel sections. Research Report R844. Centre for Advanced Structural Engineering. University of Sydney.

Moen, C. D., Igusa, T. & Schafer, B. W. (2008) Prediction of residual stresses and strains in cold-formed steel members. *Thin-Walled Structures.* 46 (11), 1274–1289.

Niemi, E. & Rinnevalli, J. (1990) Buckling tests on cold-formed square hollow sections of steel Fe 510. *Journal of Constructional Steel Research.* 16 (3), 221–230.

Rasmussen, K. J. R. & Hancock, G. J. (1993) Design of cold-formed stainless steel tubular members. I: Columns" *Journal of Structural Engineering, ASCE,* 119 (8), 2349–2367.

Rasmussen, K. J. R. (2003) Full-range stress–strain curves for stainless steel alloys. *Journal of Constructional Steel Research.* 59 (1), 47–61.

Rossi, B. (2008) Mechanical properties, residual stresses and structural behaviour of thin-walled stainless steel profiles. *PhD Thesis*. University of Liège, Belgium.

Talja, A. & Salmi, P. (1995) Design of stainless steel RHS beams, columns and beam-columns. Research note 1619. Finland: VTT building technology.

Theofanous, M. & Gardner, L. (2010) Experimental and numerical studies of lean duplex stainless steel beams. *Journal of Constructional Steel Research.* 66 (6), 816–825.

van den Berg, G. J. & van der Merwe, P. (1992) Prediction of corner mechanical properties for stainless steels due to cold forming. Proceedings of the 11th international specialty conference on cold-formed steel structures, University of Missouri, USA. pp. 571–586.

Tubular Structures XIV – Gardner (Ed.)
© 2012 Taylor & Francis Group, London, ISBN 978-0-415-62137-3

Behaviour of cold-formed lean duplex stainless steel sections

Y. Huang & B. Young
Department of Civil Engineering, The University of Hong Kong, Hong Kong, China

ABSTRACT: The behaviour of cold-formed lean duplex stainless steel sections is investigated. The material properties of high strength cold-formed lean duplex stainless steel square and rectangular hollow sections were examined. Tensile coupons and stub columns were tested for steel for six different sections. The Young's moduli, 0.2% proof stresses, tensile strengths, elongation at fracture and the Ramberg-Osgood parameter of lean duplex stainless steel material were measured. The initial local geometric imperfections of the six sections were measured. Residual stresses were measured using the method of sectioning. The membrane and bending residual stress distributions in the cross-section were obtained and plotted. The stub column test strengths obtained from this studyand the available data were also compared with the design strengths predicted by the American Specification, Australian/New Zealand Standard and European Code for stainless steel structures. Generally, the three specifications conservatively predicted the column strengths.

1 INTRODUCTION

Stainless steel sections have been increasingly used in architectural and structural applications, due to their aesthetic appearance, superior corrosion resistance, ease of maintenance and ease of construction. Currently, most of the stainless steel structures are made of austenitic and ferritic stainless steel. However, the lean duplex stainless steel has been developed and becoming an attractive choice for application in construction projects, due to its superior structural performance and the comparable corrosion resistance compare to austenitic type of stainless steel. In addition, the low content of the expensive alloying element Nickel in lean duplex stainless steel makes it economically advantageous over the other stainless steel grades. The lean duplex stainless steel material of type EN 1.4162 (LDX2101) investigated in this study is 1.5% Nickel composition, compared to 5.7% in duplex stainless steel of grade EN 1.4462 and 8.3% in Austenitic stainless steel of grade EN 1.4301 (ASTM 304) (Yrjola, 2008).The lean duplex stainless steel is also considered to be high strength, with nominal yield strength of 450 MPa compared to 210 MPa in grade 1.4301 (Yrjola, 2008). The lean duplex material is relatively new in civil engineering application, hence, it is not covered in the American Specification (ASCE, 2002), Australian/New Zealand Standard (AS/NZS, 2001) and European Code (EC3, 2006a).The investigation on the material behaviour of lean duplex stainless steel is limited at current stage, and thus further study is necessary to facilitate the structural application of lean duplex material.

Young & Lui (2005) investigated the behaviour of cold-formed high strength austenitic and duplex stainless steel of square hollow sections (SHS) and rectangular hollow sections (RHS). Tensile coupon tests, residual stress measurements and stub column tests were conducted to obtain the material properties of the test specimens. The initial local geometric imperfections of the specimens were also measured. It was shown that the American Specification (ASCE, 2002), Australian/New Zealand Standard (AS/NZS, 2001)and European Code (EC3, 2006a)are generally conservative for cold-formed high strength stainless steel stub columns. Theofanous & Gardner (2010) carried out material tests on lean duplex stainless steel, including tensile and compressive coupon tests at flat and corner portions of SHS and RHS. Gardner & Nethercot (2004) conducted a series of tensile and compressive coupon tests as well as stub column tests on austenitic stainless steel type EN 1.4301 cold-formed SHS, RHS and circular hollow sections (CHS). A stress-strain model predicting corner material properties base on flat material properties was proposed. It was also found that EC3 is conservative in predicting cross-section compression strength, especially for stocky columns, while the proposed method by Gardner & Nethercot (2004) provides better and less scatter predictions. Chen & Young (2006) conducted a series of coupon tests on duplex and austenitic stainless steel types EN 1.4462 and EN 1.4301 at elevated temperatures. The coupons were tested under steady state and transient state methods. A unified equation for yield strength, elastic modulus, ultimate strength and ultimate strain at elevated temperatures was proposed. Furthermore, a stress-strain model was also proposed and the stress-strain model accurately predicted the test results. Theofanous & Gardner (2009) performed a series of tests and numerical analysis on lean duplex

stainless steel columns, and the results were compared with the EC3 Code predictions and the recommended class limits as suggested by Gardner and Theofanous (2008).

The purpose of this paper is to investigate the behaviour of cold-formed lean duplex stainless steel square and rectangular hollow sections. The material properties of the test specimens were investigated by carrying out tensile coupon tests. Hence, the Young's modulus, 0.2% proof stress and tensile strength of lean duplex material for each section were obtained. The material properties of the complete cross-section in the cold-worked state were also obtained from stub column tests. The initial local geometric imperfections of the sections were also measured, and the local imperfections profile was plotted for a section. Residual stresses induced in the cold-forming process were measured using the method of sectioning. The membrane and bending residual stress distributions in the cross-section of the specimen were obtained and plotted. Furthermore, the stub column test strengths,together with the available lean duplex stub column strengths reported by Theofanous and Gardner (2009), were compared with the design strengths predicted by the American Specification (ASCE, 2002), Australian/New Zealand Standard(AS/NZS, 2001) and European Code (EC3, 2006a).

2 TEST SPECIMENS

The tests were carried out on two square hollow sections (SHS) and four rectangular hollow sections (RHS) of lean duplex stainless steel type EN 1.4162. The test specimens were cold-rolled from flat strips and the nominal 0.2% proof stress is 450 MPa with Nickel (Ni) content of 1.5% (Yrjola, 2008). One stub column was compressed between fixed ends for each section. The nominal lengths of the stub columns are 150, 150, 150, 210, 300 and 450 mm for specimens with nominal cross-section dimensions $50 \times 30 \times 2.5$, $50 \times 50 \times 1.5$, $50 \times 50 \times 2.5$, $70 \times 50 \times 2.5$, $100 \times 50 \times 2.5$ and $150 \times 50 \times 2.5$, respectively. The measured cross-section dimensions of the test specimens, which were the average measured values at both ends of each specimen, are shown in Table 1 using the nomenclature defined in Figure 1. The test specimens were supplied by the manufacturer in un-cut length of 6000 mm. Each specimen was cut to a specified length. Both ends of the specimens were milled flat and then welded to 20 mm thick steel end plates for testing.

3 GEOMETRIC IMPERFECTION MEASUREMENTS

Initial local geometric imperfections of specimens were measured for each section. The measurements were obtained at mid-length of the specimens using dial gauge with an accuracy of 0.001 mm. For each side of the cross-sections,local geometric imperfections were assumed to be zero at the corners, and the vertical distance of the flat portions relative to the corners were measured as the geometric imperfection. Readings were taken at 2 mm intervals across the cross-sections. The convex profiles are indicated by positive values and the concave profiles as negative values. The measured local geometric imperfection profile of section $100 \times 50 \times 2.5$ is shown in Figure 2. The vertical axis plotted the measured local imperfections and the horizontal axis plotted the location in cross-section of the specimens. The maximum measured initial local geometric imperfections were 0.066, 0.310, 0.101, 0.226, 0.348, and 0.679 mm for $50 \times 30 \times 2.5$, $50 \times 50 \times 1.5$, $50 \times 50 \times 2.5$, $50 \times 70 \times 2.5$, $100 \times 50 \times 2.5$, and $150 \times 50 \times 2.5$ specimens, respectively.

Table 1. Measured specimen dimensions.

Specimen	D (mm)	B (mm)	t (mm)	r_o (mm)	r_i (mm)	L (mm)
SC1L150	50.2	30.3	2.557	5.0	1.8	150.0
SC2L150	50.5	50.5	1.493	3.0	1.0	150.0
SC3L150	50.3	49.7	2.487	3.2	1.0	150.0
SC4L210	70.4	50.8	2.523	4.0	1.0	210.0
SC5L300	100.1	50.9	2.510	3.3	1.2	300.1
SC6L450	150.0	50.2	2.463	4.3	2.0	450.0

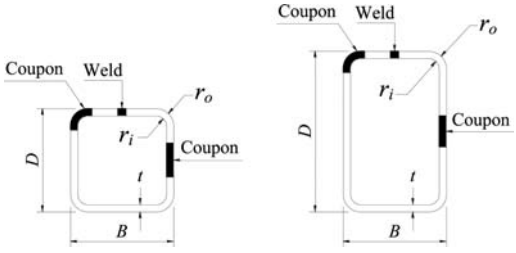

Figure 1. Definition of symbols and location of tensile coupon in cross-section.

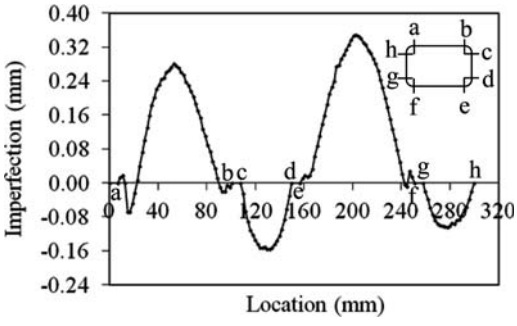

Figure 2. Measured local geometric imperfection profiles of section $100 \times 50 \times 2.5$.

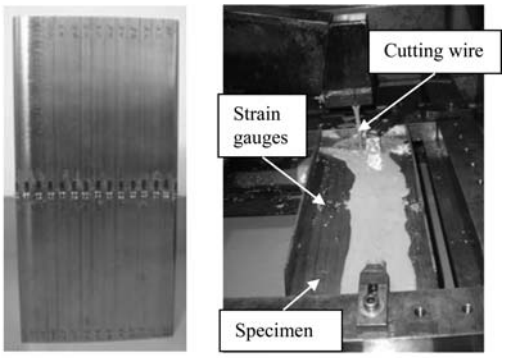

(a) Strain gauges on specimen (b) Wire-cutting under water

Figure 3. Residual stress measurements.

4 RESIDUAL STRESS MEASUREMENTS

Residual stressesare induced in the specimens during the cold-forming process.The magnitudes and distributions of the residual stresses for the cold-formed lean duplex stainless steel sections were measured. The residual stress measurements were conducted on a 150 × 50 × 2.5 specimen of 300 mm length. The longitudinal residual strains were measured by the method of sectioning, and the strains were converted to residual stresses. The flat portion of the specimen was marked into strips of 10 mm widths, and the strain gauges of 3 mm gauge lengths were attached around half of the cross-section, as shown in Figure 3a. The seamless weld was located in the middle of the flange of the section. Therefore, the residual stress distribution is assumed to be symmetric in half of the section.

The initial readings before cutting the specimen were recorded for each strip on both outer and inner surfaces. The specimen was then cut into strips using a GF Agie Charmilles wire cut machine with an accuracy of 0.005 mm. The specimen was cut by a wire-cutting method under water to eliminate any additional stresses resulting from the cutting process, as shown in Figure 3b. After cutting, the residual strains were then measured on both outer and inner surfaces of each strip. However, strain gauges cannot be attached on the inner surfaces of corners, due to the small inner corner radius. Therefore, residual stresses at the corners are not plotted in Figures 4, 5. The differences in longitudinal strains in each strip before and after cutting were converted to residual stresses by multiplying the measured Young's modulus. The membrane and bending residual stresses were calculated as the average and difference in residual stress measurements on the outer and inner surfaces, respectively. The negative value of membrane stress indicates a compressive stress in the specimen.The negative value of bending stress indicates a higher measured stress at the outer surface of the cross-section when the strips bent inward during cutting. The

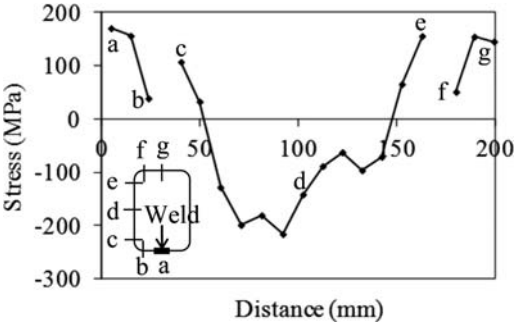

Figure 4. Measured membrane residual stress distributions in section 150 × 50 × 2.5.

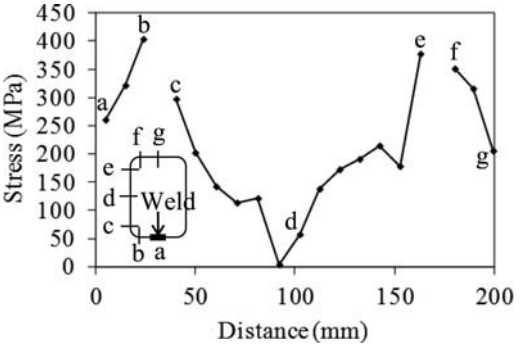

Figure 5. Measured bending residual stress distributions in section 150 × 50 × 2.5.

maximum membrane and bending residual stresses of the specimen are 32.5% and 60.8% of the measured 0.2% proof stress, respectively. Figures 4 and 5 showed the measured membrane and bending residual stresses distributions in the cross-section of the RHS 150 × 50 × 2.5 specimen, respectively.

5 TENSILE COUPON TESTS

5.1 *General*

Tensile coupon tests were conducted to determine the material properties of the test specimens. Longitudinal tensile coupons, which are extracted from the untested specimens belong to the same batch of the stub column specimens, were tested for each section. The tested coupons were taken from both flat portions and corners of the cold-formed lean duplex stainless steel specimens. The material properties of the coupons including the static 0.2% proof stress ($\sigma_{0.2}$), static ultimate tensile strength (σ_u), initial Young's modulus (E_o) and elongation at fracture (ε_f) of a gauge length of 25 mm were measured. Stress-strain curves obtained from the tensile coupon tests were plotted for each section, and the Ramberg-Osgood parameter (n) using the Ramberg-Osgood expression $n = \ln(0.01/0.2)/\ln(\sigma_{0.01}/\sigma_{0.2})$ were calculated.

Table 2. Coupon test results obtained from flat coupons.

Specimen	$\sigma_{0.2,f}$ (MPa)	$\sigma_{u,f}$ (MPa)	$E_{o,f}$ (GPa)	n	ε_f (%)
50 × 30 × 2.5	683	764	198	7	39
50 × 50 × 1.5	610	734	194	5	44
50 × 50 × 2.5	635	756	198	6	44
70 × 50 × 2.5	613	738	194	8	44
100 × 50 × 2.5	625	727	200	6	49
150 × 50 × 2.5	664	788	202	4	35

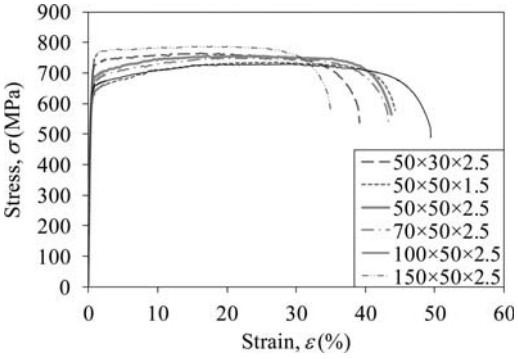

Figure 6. Static stress-strain curves obtained from tensile coupon tests at flat portions.

5.2 *Flat coupon tests*

The flat coupons were taken from the center of the face at 90° angle from the weld for all specimens. The location of the flat coupons extracted from the sections is shown in Figure 1. The flat coupons were extracted from the web of RHS. The dimension of flat coupons was conformed to the Australian Standard AS 1391 (2007) and the American Standard ASTM E 8M (1997) for the tensile testing of metals using a 6 mm wide coupon and a gauge length of 25 mm.

An MTS testing machine was used in the tests. The calibrated extensometer of 25 mm gauge length was mounted onto the specimens by a three-point contact knife edges to measure the longitudinal strain during the tests. Two linear strain gauges were attached at mid-length to the center of both faces of each coupon to determinate the initial Young's modulus. Tensile load was applied to the specimens with the loading rate of 0.04 mm/min in the elastic range and 0.8 mm/min in the plastic range of the stress-strain curves. The strain rate of the tests measured by the extensometer was conformed to the Australian Standard AS 1391 (2007) and the American Standard ASTM E 8M (1997). To eliminate the effect of loading rate during the tests, the static stress-strain curves were obtained by pausing the applied straining for 1.5 minutes near the 0.2% proof stress, the ultimate tensile strength and post-ultimate strength.

The measured material properties are summarized in Table 2. It is shown that the static 0.2% proof stress ($\sigma_{0.2,f}$) ranged from 610 to 683 MPa and the ultimate tensile strength ($\sigma_{u,f}$) ranged from 727 to 788 MPa. The Ramberg-Osgood parameter (n) is ranged from 4 to 8. The test specimens elongated by 35 to 49% of 25 mm gauge length at fracture. The static stress-strain curves for the six sections are shown in Figure 6.

5.3 *Corner coupon tests*

The cold-forming process of the cold-formed lean duplex stainless steel leads to a significant strength enhancement of the material properties at the corners compared to the flat portions in the sections. Therefore, coupons obtained from corners of each section were also tested. The corner coupons were extracted near the welds of the sections as shown in Figure 1. The tested corner coupons were 4 mm width and 25 mm gauge length. Two holes having a diameter of 7 mm were drilled at a distance of 20 mm from both ends of the coupons and the coupons were tested between two pins, so that the coupons were loaded through the centroid.

Table 3. Coupon test results obtained from corner coupons.

Specimen	$\sigma_{0.2,c}$ (MPa)	$\sigma_{u,c}$ (MPa)	$E_{o,c}$ (GPa)	n	ε_f (%)	$\frac{\sigma_{0.2,c}}{\sigma_{0.2,f}}$	$\frac{\sigma_{u,c}}{\sigma_{u,f}}$
50 × 30 × 2.5	788	975	192	4	22	1.15	1.28
50 × 50 × 1.5	824	1012	200	5	15	1.35	1.38
50 × 50 × 2.5	833	1079	207	5	19	1.31	1.43
70 × 50 × 2.5	844	995	200	5	21	1.38	1.35
100 × 50 × 2.5	882	1033	203	5	17	1.41	1.42
150 × 50 × 2.5	831	967	199	6	18	1.25	1.23

The corner coupons were tested using the same MTS testing machine as the flat coupons. The same method of testing as the flat coupon tests was adopted, except the three-point contact knife edges of the extensometer were replaced by a standard knife edge mounted onto the curved specimens. Similar to the flat coupon tests, static stress-strain curves were obtained by pausing the applied straining during testing. The measured material properties are summarized in Table 3. It is shown that the 0.2% proof stress ($\sigma_{0.2,c}$) is ranged from 788 to 882 MPa and the ultimate tensile strength ($\sigma_{u,c}$) from 967 to 1079 MPa. The Ramberg-Osgood parameter (n) is ranged from 4 to 6. The test specimens elongated by 15 to 22% of 25 mm gauge length at fracture. The static stress-strain curves for the six sections are shown in Figure 7. To investigate the strength enhancement effect due to cold-working, the static 0.2% and the ultimate tensile strength (σ_u) of the flat and corner coupons are compared in Table 3. The 0.2% proof stress ($\sigma_{0.2}$) was increased by 15 to 41%, and the ultimate tensile strength (σ_u) was increased by 23 to 43%.

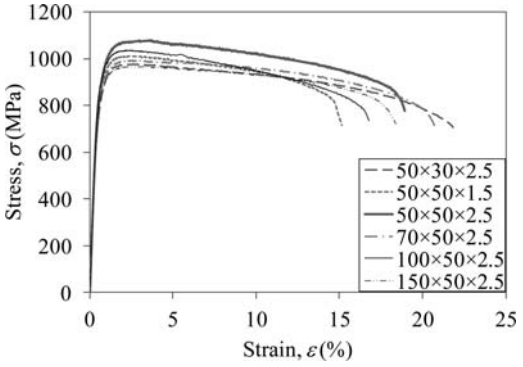

Figure 7. Static stress-strain curves obtained from tensile coupon tests atcorners.

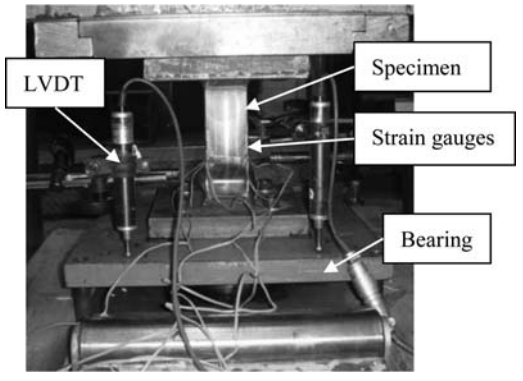

Figure 8. Test setup of stub column.

6 STUB COLUMN TESTS

Stub column tests were conducted for each cold-formed lean duplex stainless steel section to determine the material properties of the complete cross-section in the cold-worked state. A total of six stub columns were tested which consisted of specimens SC1L150, SC2L150, SC3L150, SC4L210, SC5L300 and SC6L450. The specimen lengths of the stub columns were complied with the Structural Stability Research Council Guidelines (Galambos, 1998). The measured cross-section dimensions and specimen length of the stub columns are shown in Table 1. The columns were compressed between fixed ends using a hydraulic testing machine, as shown in Figure 8. The fixed-ended bearings were restrained against the minor and major axis rotations as well as twist rotations and warping. Two steel end plates were welded to the ends of each specimen. The axial strains were obtained by longitudinal strain gauges attached at the four corners of the stub columns at the mid-length in order to avoid the effect of local buckling. In addition, three transducers were used to measure the axial shortening of the specimens.

A hydraulic testing machine was used to apply compressive axial force to the stub column specimens.

Table 4. Material properties obtained from stub column tests.

Specimen	$\sigma_{0.2}$ (MPa)	σ_u (MPa)	E_o (GPa)	n	Failure Mode
SC1L150	660	880	205	4	Y
SC2L150	N/A	515	194	4	L
SC3L150	690	791	202	3	Y
SC4L210	621	723	204	3	Y
SC5L300	545	548	207	4	L
SC6L450	430	452	202	8	L

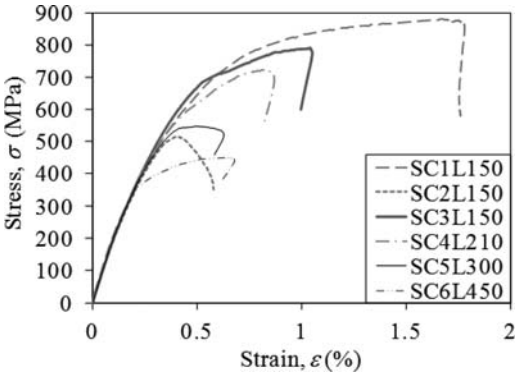

Figure 9. Static stress-strain curves obtained from stub column tests.

Displacement control was used to drive the hydraulic actuator at a constant speed of 0.5 mm/min. The static load was obtained by pausing the applied straining for 2 minutes near the 0.2% proof stress, ultimate strength and post ultimate range of the stub columns. Table 4 shows the measured material properties obtained from the stub column tests, which included the static 0.2% proof stress ($\sigma_{0.2}$), static ultimate strength (σ_u), initial Young's modulus (E_o), parameter n and failure mode, where "L" indicates local buckling and "Y" indicates material yielding. The average yield strength of the specimen is the yield stress in the flat portion multiply by the area of flat portion plus corner yield stress multiply by the area of corners. In this study, the specimen is regarded as failed by material yielding when the experimental ultimate load (P_{Exp}) is greater than the average yield strength of the specimen. The static stress-strain curves obtained from the stub column tests for each section are plotted in Figure 9.

In comparison with the tensile coupon tests, the stub column tests included the effect of residual stress and the strength enhancement due to the cold-forming process. For specimens SC2L150, SC5L300 and SC6L450, the ultimate stresses obtained from the stub column tests are much smaller than those obtained from coupon tests due to local buckling failure. It should be noted that due to local buckling, the 0.2% proof stress ($\sigma_{0.2}$) of stub column specimen SC2L150 could not be reached before the ultimate

strength. According to clause 6.3 of the ASCE Specification (ASCE, 2002), the compressive yield stresses shall be taken as either the maximum compressive strength of the section divided by the cross-section area or the stress determined by the 0.2% offset method, whichever is reached first in the test. Therefore, the ultimate stress was regarded as the compressive yield stress for specimen SC2L150. For specimen SC4L210, which is classified as slender section in EC3 Part 1-4 (EC3, 2006a), the failure was found to be material yielding. The stub column may be influenced by local buckling. Therefore, the ultimate stress of the stub column is slightly smaller than that of flat coupon, although it was failed by material yielding. For specimens SC1L150 and SC3L150, the ultimate stresses of stub columns are greater than that of flat coupons, and smaller than that of corner coupons.

7 COMPARISON OF TEST STRENGTHS WITH DESIGN STRENGTHS

The test strengths of stub columns and those of the specimens conducted by Theofanous and Gardner (2009) were compared with the unfactored design strengths (nominal strengths) calculated using the American Society of Civil Engineers (ASCE, 2002) Specification for the design of cold-formed stainless steel structural members, Australian/New Zealand Standard (AS/NZS, 2001) for cold-formed stainless steel structures and European Code (EC3, 2006a): Design of steel structure – Part 1.4: General rules – Supplementary rules for stainless steels. In calculating the design strengths, the effective lengths (l_e) were taken as half of the measured specimen lengths for fixed-ended column tests. The effective length factor (k) of fixed-ended column was taken as 0.5. The design strengths were calculated using the average measured cross-section dimensions and the measured material properties obtained from the coupon tests in flat portions for each section as detailed in Table 2. It should be noted that these specifications do not cover the material of lean duplex stainless steel.

In ASCE Specification, the column design rules are detailed in clause 3.4 of the Specification for concentrically loaded compression members. The tangent modulus (E_t) equation as a function of buckling stress is shown in Appendix B of the ASCE Specification. This design procedure involves iterative process. Firstly, a trial normal stress is assumed and then the tangent modulus is computed. Based on the calculated tangent modulus, a new normal stress is obtained until it converges. The effective area (A_e) is calculated according to clause 2.2.1 of the Specification, and the corners are assumed to be fully effective.

In AS/NZS Standard, the stub column design strengths were calculated using the alternative design method given in clause 3.4.2 of the standard. The calculation of buckling stress (f_n) requires the determination of values α, β,λ_o and λ_1 according to the type of materials. It should be noted that the values of lean duplex material are not covered by the AS/NZS Standard. Therefore, the values of S31803 (duplex) given in Table 3.4.2 of the AS/NZS Standard were used to calculate the buckling stress. The calculation of effective areas was based on clause 2.2.1.2 of the standard. Similarly, the corner areas were considered as fully effective.

Table 5. Comparison of stub column strengths obtained from tests and design predictions.

Specimen	P_{Exp} (kN)	$\frac{P_{Exp}}{P_{ASCE}}$	$\frac{P_{Exp}}{P_{AS/NZS}}$	$\frac{P_{Exp}}{P_{EC3}}$
SC1L150	316.1	1.23	1.23	1.27
SC2L150	147.1	0.95	0.95	1.12
SC3L150	362.2	1.23	1.23	1.24
SC4L210	413.2	1.19	1.19	1.29
SC5L300	394.0	1.05	1.05	1.17
SC6L450	428.1	1.06	1.06	1.20
100 × 100 × 4-SC1	1022.0	1.17	1.17	1.26
100 × 100 × 4-SC2	1037.0	1.16	1.16	1.26
80 × 80 × 4-SC1	923.0	1.19	1.19	1.18
80 × 80 × 4-SC2	915.0	1.20	1.20	1.20
60 × 60 × 3-SC1	613.0	1.19	1.19	1.19
60 × 60 × 3-SC2	616.0	1.16	1.16	1.16
80 × 40 × 4-SC1	709.0	1.21	1.21	1.27
80 × 40 × 4-SC2	710.0	1.20	1.20	1.20
	Mean	1.16	1.16	1.22
	COV	0.070	0.070	0.041

In European code, the design strengths of stub columns were calculated based on the resistance of cross-sections in compression. According to clause 5.1 of EC3 Part 1.4 (EC3, 2006a), the design strengths of stub columns were calculated based on clause 6.2.4 of the EC3 Part 1.1: General rules and rules for buildings (EC3, 2005). Section classification of the specimens according to Table 5.2 of the EC3 Part 1.4 for maximum width-to-thickness ratios for compression parts are required to calculate the design strengths. In this study, specimens SC1L150 and SC3L150 were classified as class 3 sections, whereas specimens SC2L150, SC4L210, SC5L300 and SC6L450 were classified as class 4 sections. According to clause 5.2.3 of the EC3 Part 1.4, the effective widths (b_{eff}) were calculated based on EC3 Part 1.5: Plated structural elements (EC3, 2006b), except that the reduction factor (ρ) was calculated by Equation 5.1 of the EC3 Part 1.4 for cold-formed or welded internal elements.

The stub column test strengths obtained from this study and the available data were compared with the unfactored design strengths predicted by the ASCE Specification (ASCE, 2002), AS/NZS Standard (AS/NZS, 2001) and European Code (EC3, 2006a) for the stainless steel structures, as shown in Table 5. The design strengths predicted by the ASCE, AS/NZS and EC3 Specifications are all conservative, except for the prediction to specimen SC2L150 by ASCE Specification and AS/NZS Standard. The mean values of P_{Exp}/P_{ASCE}, $P_{Exp}/P_{AS/NZS}$ and P_{Exp}/P_{EC3} ratios are 1.16, 1.16 and 1.22 with the corresponding

coefficients of variation (COV) of 0.070, 0.070 and 0.041, respectively. Generally, the European Code provides the most conservative predictions, while the American Specification and the Australian and New Zealand Standard are less conservative. The design strengths of the stub column specimens were calculated using the material properties obtained from the flat coupons. Therefore, the conservativeness of the design predictions is due to the effect of cold-working in the cold-forming process, where the corners of the sections have a relatively higher strength than the flat portions. Furthermore, the conservative predictions by the EC3 Code implied the possible inappropriateness in Classification limit and the effective width calculation for lean duplex stainless steel. Further study for the improvement of EC3 Code is recommended.

8 CONCLUSIONS

The behaviour of cold-formed lean duplex stainless steel sections has been investigated. The test specimens were cold-rolled from lean duplex stainless steel. Initial local geometric imperfections of these sections were measured. The membrane and bending residual stresses were also measured using the method of sectioning, and the residual stress distributions in the cross-section of the specimen were plotted. Tensile coupon tests were conducted in flat portion and corner of the cross-section for each section. It is shown that the material properties of 0.2% proof stress and ultimate tensile strength of the corner coupons increased up to 41% and 43% compared with the flat coupons due to cold-working process, respectively. Stub column tests were also conducted to determine the material properties of the complete cross-section in the cold-worked state. Furthermore, the stub column test strengths obtained from this study together with the available test data were compared with the design strengths predicted by the American, Australian/New Zealand Standard and European specifications for stainless steel structures. It is shown that the design strengths predicted by the three specifications are generally conservative for the cold-formed lean duplex stainless steel stub columns, of which the EC3 Code provids the most conservative prediction and the ASCE Specification provides less conservative prediction.

ACKNOWLEDGEMENTS

The authors are grateful to STALA Tube Finland for supplying the lean duplex stainless steel test specimens. The research work described in this paper was supported by a grant from The University of Hong Kong under the seed funding program for basic research.

REFERENCES

AS1391 2007. Metallic materials – Tensile testing at ambient temperature. Australian Standard, AS 1391-2007. Sydney (Australia): Standards Association of Australia.

ASCE 2002. Specification for the design of cold-formed stainless steel structural members. SEI/ASCE 8-02; Reston, VA: American Society of Civil Engineers.

AS/NZS 2001. Cold-formed stainless steel structures. Australian/New Zealand Standard, AS/NZS 4673:2001. Sydney (Australia): Standards Australia.

ASTM E 8M1997. Standard Test Methods for Tension Testing for Metallic Materials. E 8M-97. West Conshohocken, USA: American Society for Testing and Materials.

Chen, J. & Young, B. 2006. Stress-strain curves for stainless steel at elevated temperatures. *Engineering Structures 28: 229–239*.

EC3 2005. Design of steel structures – Part 1.1: General rules and rules for buildings. European Committee for Standardization, ENV 1993-1-1, CEN, Brussels.

EC3 2006a. Design of steel structures – Part 1.4: General rules – Supplementary rules for stainless steels. European Committee for Standardization, ENV 1993-1-4, CEN, Brussels.

EC3 2006b. Design of steel structures – Part 1.5: Plated structural elements. European Committee for Standardization, ENV 1993-1-5, CEN, Brussels.

Galambos, T.V. 1998. Guide to stability design criteria for metal structures. In John Wiley & Sons (eds), New York.

Gardner, L. & Nethercot, D.A. 2004. Experiments on stainless steel hollow sections—Part 1: material and cross-sectional behaviour. *Constructional Steel Research* 60: 1291–1318.

Gardner, L. & Theofanous, M. 2008. Discrete and continuous treatment of local buckling in stainless steel elements. *Constructional Steel Research* 64: 1207–1216.

Theofanous, M. & Gardner, L. 2010. Experimental and numerical studies of lean duplex stainless steel beams. *Constructional Steel Research* 66: 816–825.

Theofanous, M. & Gardner, L. 2009. Testing and numerical modelling of lean duplex stainless steel hollow section columns. *Engineering Structures* 31: 3047–3058.

Young, B. & Lui, W.M. 2005. Behavior of cold-formed high strength stainless steel sections. *Structural Engineering* 131: 1738–1745.

Yrjola, P. 2008. Stainless steel hollow sections handbook. Finnish Constructional Steelwork Association, Finland.

Tubular Structures XIV – Gardner (Ed.)
© 2012 Taylor & Francis Group, London, ISBN 978-0-415-62137-3

2D finite-element modelling of stainless steel cold-formed RHS subjected to elevated temperatures

O. Salem
Carleton University, Ottawa, Ontario, Canada

O. El-Husseiny, E. Matar & M. El-Dib
Zagazig University, Zagazig, Egypt

ABSTRACT: Over the last two decades, there has been an increasing interest in the use of stainless steels in structural applications. This interest can be attributed to different reasons; such as the aesthetic considerations, excellent corrosion resistance and low life-cycle cost of stainless steels. The metallurgical microstructure of stainless steels may be ferritic, martensite, austenitic or austenitic-ferritic. Each alloy has different properties with respect to strength, stiffness and corrosion resistance. The work described in this paper is limited to austenitic stainless steel, specifically Polarit 725 (or EN 1.4301). A two-dimensional finite-element model was developed using MATLAB software to calculate the biaxial bending moment capacity of different open and tubular cold-formed stainless steel sections subjected to elevated temperatures.

In this paper, the focus is given to Rectangular Hollow Sections (RHS), where a rectangular tubular section has been analyzed under different temperature distribution models. These models vary according to fire location and the position of structural member cross section relative to building partitions. Different linear and non-linear temperature distribution models were used in the finite-element model presented in this paper. The model was validated against published experimental work, as good agreement has been achieved between the finite-element model predictions and the experimental results. The presented finite-element model can be used as a simple design tool to predict the bending moment capacity of stainless steel tubular sections in fire.

1 INTRODUCTION

The interest in the use of stainless steel as a structural material is increasing. Although stainless steel is an expensive construction material when compared to carbon steel, it has several special structural applications. Besides the architectural appealing of stainless steel, other advantages such as corrosion resistance, ease of maintenance and low-life cycle cost are among the reasons for specifying stainless steel in certain structural applications. The metallurgical microstructure of stainless steels may be ferritic, martensite, austenitic or austenitic-ferritic. Each stainless steel alloy type has different properties with respect to strength, stiffness and corrosion resistance. Austenitic stainless steels exhibit greater strength retention than carbon steel above 550°C due to the different crystal structure of the two metals. In addition, austenitic stainless steels do not undergo a structure change at the range of elevated temperatures relevant to fire-resistance design. The study presented in this paper is limited to austenitic stainless steels, specifically Polarit 725. Over the last two decades, significant progress has been made in the research of the structural behaviour of stainless steel members, as a considerable number of researchers focussed their work into this scope, such as Rasmussen and Hancock (1993), Mirambell and Real (2000), Young and Liu (2003) and Gardner and Nethercot (2003 & 2004). However, fire resistance of stainless steels has received less attention, since a relatively small number of researchers directed their research work into this area, such as Ng and Gardner (2007) and Vila Real et al. (2008). In elevated-temperature environments, stainless steels can be efficiently used in several applications, such as for boilers and pressure vessels, as well as structural applications where good corrosion resistance and considerable fire resistance are both required.

Austenitic stainless steels exhibit different stress-strain behaviour than carbon steel, since they have different plateau of stress-strain curve. In addition, austenitic stainless steels have non-linear stress-strain relationship with no well defined yield stress. A few researchers have studied and defined the stress-strain relationship of different stainless steel alloys at elevated temperatures, such as Ala-Outinen (1996), who studied the fire resistance of two types of austenitic stainless steels, Polarit 725 and Plarit 761 (conforming

to material number EN 1.4301 or AISI 304 and EN 1.4571 or AISI 316 Ti, respectively). Tubular members are increasingly used in modern construction due to many reasons, such as their high strength to weight ratios, which make them cost effective, and the good resistance to compression, bending and torsion. For cases in which the design stresses are largely reduced by lateral buckling, tubular members are more favourable than open section members due to their good moment of inertia about the minor axis of their cross sections. Considerable research work has been done to investigate the structural behaviour of different stainless steel cross-section profiles, such as the work carried out by Ashraf et al. (2006) and Theofanous et al. (2009).

Conducting fire-resistance tests is very important to study the behaviour of stainless steel structural members that are built of different tubular cross-section profiles, such as rectangular, square, elliptical and oval. However, finite-element modelling allows for expanding the range of research and extending the study to investigate other parameters that have not been experimentally examined. A simple and easy-to-use 2D finite-element model has been developed using MATLAB software in order to calculate the biaxial bending moment capacity of different open and tubular cold-formed stainless steel sections subjected to elevated temperatures. In this paper, the focus is given to rectangular hollow sections (RHS), which have been analyzed under different temperature distribution models that varied according to fire location and cross section position relative to building possible partitions, i.e. slab and/or walls. Different linear and non-linear temperature distribution models were used in the FE model. The bending capacity of the stainless steel RHS subjected to the different temperature distribution models is expressed in terms of moment utilization factors, m_x and m_y, about both major and minor axes of the cross section, respectively. The moment utilization factor is defined here as the ratio of the cross-section bending moment resistance at elevated temperature to its bending moment capacity at normal temperature.

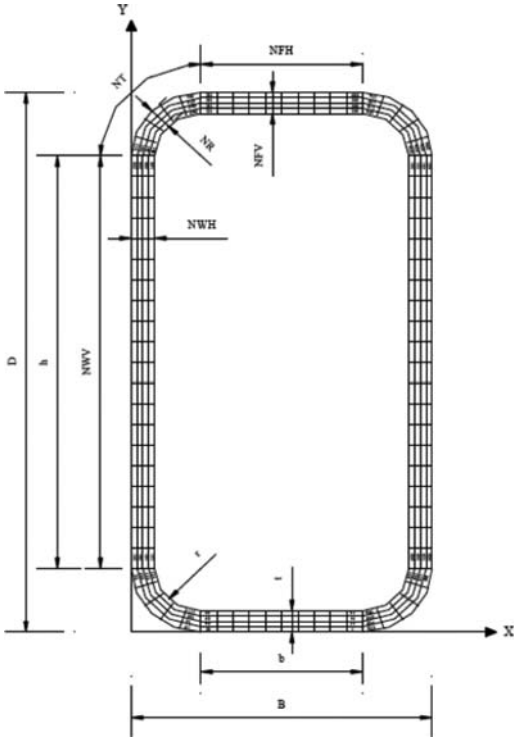

Figure 1. Discretized rectangular hollow section.

2 FE MODEL DESCRIPTION

2.1 *Discretization*

In the two-dimensional finite-element model presented in this paper, the RHS was divided into three main zones; the flange, the web and the corner zone, and then was discretized into a number of finite elements (N). For each flange with a flat width of b, its width was divided into a number of horizontal elements equal to (NFH), while its thickness t was divided into a number of vertical elements equal to (NFV). Accordingly, each finite element in the flange zone has an area equal to $[(t/\text{NFV}) \times (b/\text{NFH})]$. Similarly, each element in the web zone has an area equal to $[(t/\text{NWH}) \times (h/\text{NWV})]$, where t and h are the web thickness and depth, respectively. For the section corners, the corner curved length l_c was divided into a number of tangential elements equal to (NT), while the section thickness at the corners t was divided into a number of elements in the radial direction equal to (NR). Accordingly, each element in the corner zone has an area equal to $[(t/\text{NR}) \times (l_c/\text{NT})]$. Figure 1 shows a discretized cross section with a constant number of elements through its thickness in all zones, as NFV, NWH and NR were taken equal to 4. The FE model presented in this paper allows the input of any required number of elements for each zone of the cross section without restrictions. However, trial runs with different numbers of elements through the section thickness were conducted prior to the final run of the model in order to test the most effective number. It was found that three or four layers of elements through the thickness of the cross section is the optimum choice.

2.2 *Thermal boundary conditions*

During fire action, a typical temperature distribution for the cross section of a structural member is hard to achieve. It is common to have non-homogeneity of the temperature distribution in the cross section of a structural member. Two different types of models have been considered in this study; the linear and non-linear temperature distribution models that were developed by

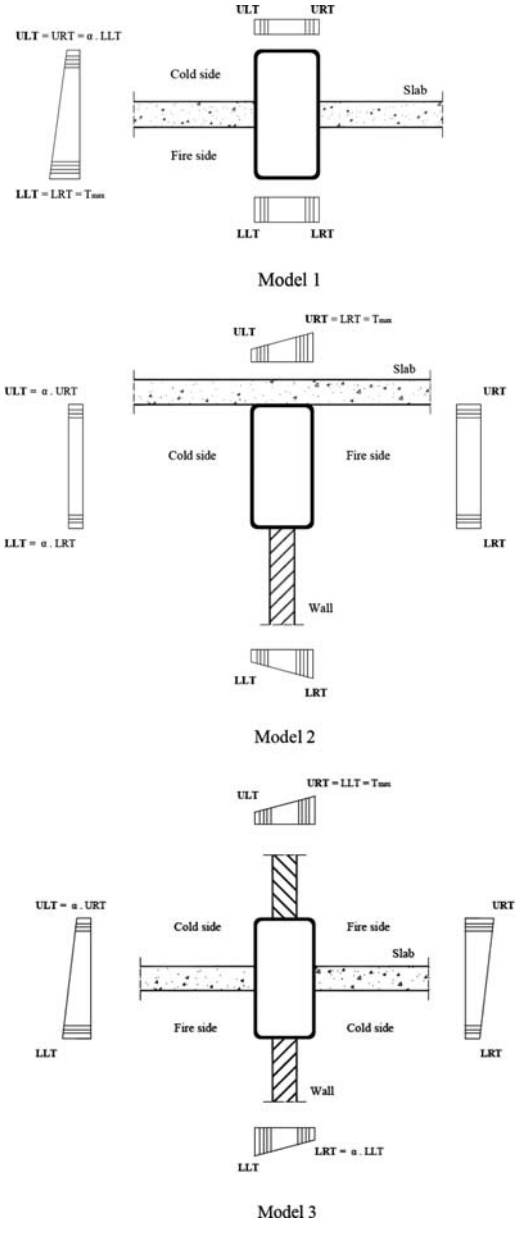

Figure 2. Linear temperature distribution models.

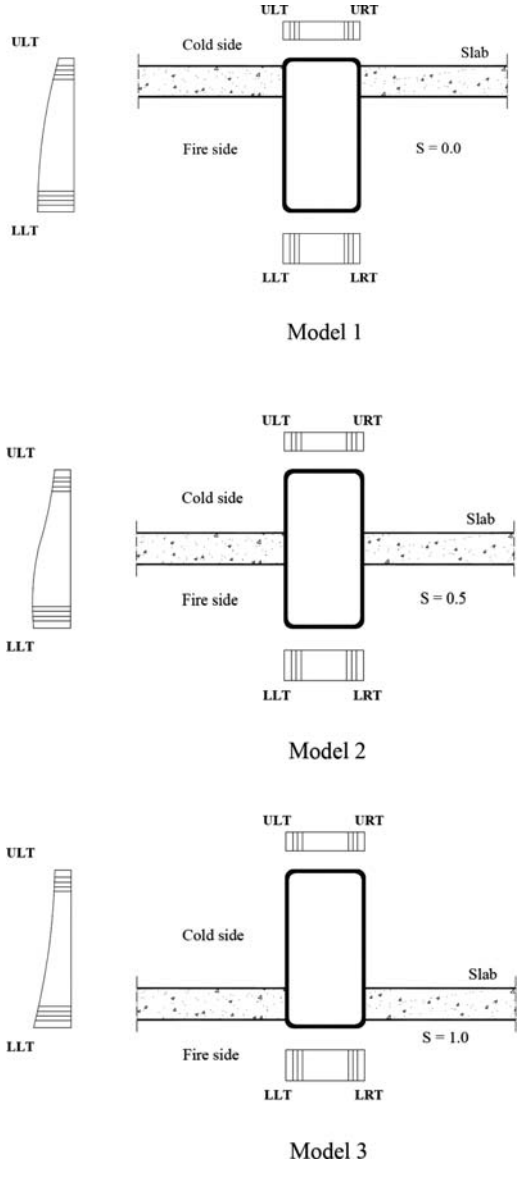

Figure 3. Non-linear temperature distribution models.

Kruppa (1975) and McLaughlin (1970), respectively. For the linear temperature distribution, three models were used in the finite-element model, Figure 2.

In these temperature distribution models, the temperature varies linearly either in one direction or in both vertical and horizontal directions according to the existing building partitions, such as slab and/or walls. The temperatures of the finite elements in the cross section vary from the maximum temperature T_{max} to the minimum temperature T_{min} with a gradient α. This gradient varied according to the degree of fire proof of the building partition, and takes the value of 0.0, 0.2 or 0.4, as suggested by Kruppa (1975).

For the non-linear temperature distribution, three other models were used in the finite-element model presented in this paper, Figure 3.

Based on the non-linear temperature distribution models developed by Mclaughlin (1970), Equations 1 and 2 were used to calculate the temperatures of the cross section lower flange T_L and upper flange T_U, respectively.

$$T_L = T_o + [1.0 - 0.07.S - 0.3.S^2](T_i - T_o) \quad (1)$$

$$T_U = T_o + [0.2575 - 0.5.S - 0.15.S^2](T_i - T_o) \quad (2)$$

where T_i = fire temperature; T_o = normal temperature; and S = exposure factor.

The section exposure factor S recognizes the portion of the cross-section web that is exposed to cold air. It is equal to zero for the face-exposed condition as in Model 1, and is equal to 0.5 for the partially-exposed condition as in Model 2, while it takes a value of 1.0 for the mostly-exposed condition as in Model 3 of the non-linear temperature distribution models shown in Figure 3. After calculating the temperatures of the cross-section lower and upper flanges, the temperature of each finite element in the cross section can be accurately estimated in both the hot and cold sides of the cross section using Equations 3 and 4, respectively.

$$T(y) = T_L\left(1 - \frac{(T_L - T_U)}{T_L}.(\frac{y}{D})^2\right) \quad (3)$$

$$T(y) = T_L\left(1 - \frac{(T_L - T_U)}{T_L}.(\frac{y}{D})\right)^{0.5} \quad (4)$$

where; y = vertical distance from the element center to x-axis; and D = cross-section total depth.

2.3 *Material properties*

After calculating the temperature of each finite element in the cross section, the reduction factors for the yield strength and modulus of elasticity of the Polarit 725 stainless steel (or EN 1.4301) that are prescribed in Eurocode 3, Part 1.2 (2005), were used in the finite-element model in order to calculate the stainless steel material properties at elevated temperatures.

3 ANALYSIS PROCESS

3.1 *General*

Different degrees of non-linearity were considered in the analysis of the finite-element model presented in this paper, such as the material non-linearity and the temperature distribution non-linearity across the tubular cross section, which appears due to the existence of building partitions. In addition, local buckling of the thin walls of the cold-formed tubular section was taken into consideration in the analysis process of the FE model.

3.2 *Element's critical stress*

The reduced yield stress for each finite element of the cross section was calculated based on the temperature distribution model in use. In addition, the critical buckling stress for the rectangular plates forming the walls of the cross section was predicted using Equation 5, which was developed by Van Den Berg (1998), in order to consider the local buckling effects in the cross section walls.

$$f_{cr} = \left(\frac{\eta k \pi^2 E}{12(1 - \nu^2)(w/t)^2}\right) \quad (5)$$

where f_{cr} = critical local buckling stress; η = plasticity reduction factor; k = buckling coefficient; E = elastic modulus; ν = Poisson's ratio; w = width of the flat part; and t = thickness of the flat part.

The buckling coefficient k depends on different parameters, such as the edge rotational restraint, the type of loading and the aspect ratio of the plate. Its value is equal to 4 for stiffened compression plates, as the case of tubular cross section walls. If local buckling of a plate occurs under compressive stress that exceeds the temperature-dependant proportional limit of stainless steel, the resulting inelastic behaviour is accounted for by the introduction of the plasticity reduction factor η.

In Equation 5, the width of the flat part w is equal to b in case of flanges and h in case of web, Figure 1. After calculating both the critical local buckling stress and the temperature-dependant yield stress for each compressed element in the cross section, the least value was considered as the governing stress for such element. For tensioned elements, the governing stress is always the temperature-dependant yield stress.

3.3 *Neutral axis position*

By determining the critical stress and the area of each finite element, the force developed in each element can be calculated. Afterwards, iterative technique based on the assumption of initial position and rotation of the neutral axis is followed in the finite-element model analysis process. The assumed initial position of the neutral axis divides the cross section into tension and compression parts. The element is considered to be in one of these parts according to the coordinates of its center with respect to the neutral axis. After summing up the forces developed in the elements on each side of the neutral axis, a balance check for total force equilibrium of the cross section is carried out. The iteration is considered to be successful if the difference between tension and compression forces is smaller than 3%, hence the assumed coordinates and orientation of the neutral axis is to be considered valid, otherwise additional iterations with new neutral axis coordinates and orientations are needed until force equilibrium is achieved.

3.4 *Cross-section bending strength*

A step-by-step numerical summation that takes into consideration the different properties of each finite

Table 1. Fire resistance of austenitic stainless steel beams, Baddoo and Burgan (1998).

Beam section	Moment resistance (kN · m)	Utilization factor	Fire resistance (min)	Critical temp. (°C)
RHS	67.3	0.41	54.0	884
I-Shaped	61.0	0.28	69.0	944

element, such as its coordinates and minimum allowable stress $\sigma_{min(i)}$, was used to calculate the cross-section bending moment resistances about x and y axes at elevated temperatures, $M_x(T)$ and $M_y(T)$, respectively.

4 MODEL VALIDATION

4.1 *Experiments*

The finite-element model predictions were validated against the experimental results obtained by Baddoo and Burgan (1998). Their test program consisted of full-scale fire-resistance tests on Polarit 725 austenitic stainless steel beams and columns. The tests included four columns of 3.4 m long and two 4.25 m beams supporting concrete slabs. One of the beam specimens had a rectangular hollow section with dimensions of 200 × 125 × 6.0 mm, which was built using two cold-formed channel sections welded at their flange tips. The other beam specimen had an I-shaped section with dimensions of 200 × 150 × 6.0 mm that was built using two cold-formed channel sections welded back to back. A concrete slab was casted along the top of each beam and was keyed to the beam top flange using five steel lugs. The concrete slabs were segmented in order to prevent composite action. The fire tests were carried out in accordance with BS 476: Part 21 (1987). The transverse loads were applied to the beams through the concrete slabs by means of a hydraulic loading rig. The applied loads were equally distributed over four points spaced at 1.0 m centers and arranged evenly over the length of the beam. The total applied load was 40.0 and 20.0 kN on the RHS and I-shaped beam, respectively. Table 1 shows the experimental results of the two beams, such as the moment resistance, utilization factor, failure time and critical temperature.

4.2 *Results comparison*

The finite-element model predictions of a RHS subjected to the first non-linear temperature distribution model, Model 1 shown in Figure 3, were compared with the experimental results of the RHS beam test carried out by Baddoo and Burgan (1998). Figure 4 demonstrates that the finite-element model predictions of the bending moment utilization factors are in good agreement with the experimental values. As shown in

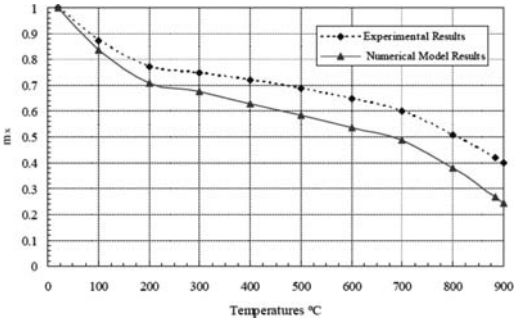

Figure 4. Comparison of the FE model predictions against the experimental results.

Figure 4, the finite-element model results are conservative, where at 500°C the finite-element model predicted a utilization factor of bending moment about x-axis equals to 0.58, while the experiment gave a value of 0.69.

However, at failure temperature, 884°C, the model predicted a utilization factor of 0.27, while the experiment gave a value of 0.41. The difference between the test results and the model predictions can be attributed to the existence of the concrete slab, which contributed to the reduction of the temperature of the cross section top flange, as the concrete slab worked as a heat sink. Accordingly, the beam cross section experienced slightly greater values of moment utilization factors than the values predicted by the finite-element model, which does not consider the concrete slab heat-sink effects.

5 MODEL RESULTS

The finite-element model was employed to calculate the utilization factors of the bending moment for a RHS with dimensions of 200 × 100 × 6.0 mm about both x and y axes, m_x and m_y, respectively. In this section, the numerical results obtained from the finite-element model using the three suggested linear temperature distribution models are presented, since part of the results of the non-linear models is discussed in the model validation section of this paper. Figure 5 illustrates a comparison of the finite-element model predictions for the utilization factors of the bending moment about x-axis for the three suggested linear temperature distribution models shown in Figure 2. The utilization factors m_x were calculated at constant value of α equal to 0.2. From Figure 5, it can be noticed that the utilization factor values of the three linear temperature distribution models declined with temperature increase in very similar trend. However, at temperatures above 700°C the first linear distribution model, Model 1, was found to give the lowest utilization factor values; where at 900°C the RHS experienced a utilization factor of about 42% compared to 53% and 51% for the second and third

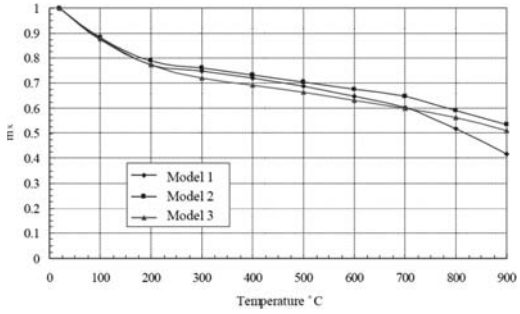

Figure 5. Comparison between the utilization factors m_x of the three linear temperature distribution models for RHS.

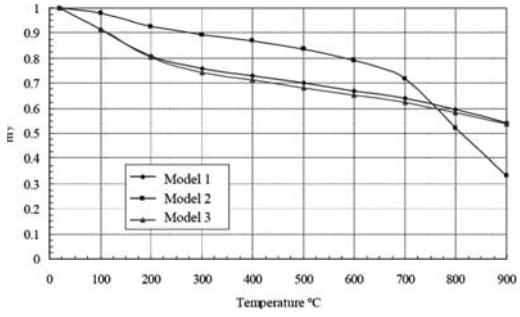

Figure 6. Comparison between the utilization factors m_y of the three linear temperature distribution models for RHS.

temperature distribution models, Models 2 and 3, respectively. This can be attributed to the fact that in Model 1 the entire bottom flange of the section was subjected to the maximum temperature in the section, unlike the case of Models 2 and 3 with only half of the bottom flange was subjected to the maximum temperature.

Figure 6 illustrates a comparison of the finite-element model predictions for the utilization factors of the bending moment about y-axis for the three suggested linear temperature distribution models shown in Figure 2.

From Figure 6, it can be noticed that the utilization factors m_y of the first and third linear temperature distribution models, Models 1 and 3, declined with temperature increase in very similar trend, while the second model, Model 2, gives considerable greater utilization factor values up to a temperature of about 750°C. However, at temperatures higher than 750°C the utilization factors from the second model, Model 2, started to decline more rapidly than the factors obtained from the first and third models; where the second model gave a utilization factor of only 33% at 900°C compared to 54% for the first and third distribution models. That is because in the second model, Model 2, one of the section webs is completely subjected to the maximum temperature, which makes the elements in that web almost not to sufficiently contribute to the section moment resistance about y-axis, especially at very high temperatures.

6 CONCLUSION

A 2D finite-element model for unprotected cold-formed RHS subjected to either linear or non-linear temperature distribution model with different building partitioning layouts was developed using MATLAB software. The finite-element model was validated against published experimental outputs of full-scale fire-resistance tests. The comparisons demonstrated that the finite-element model is capable of predicting the bending moment capacities of a tubular stainless steel section about both its major and minor axes at elevated temperatures.

The finite-element model results show that the first linear temperature distribution model, Model 1, gives the most critical utilization factors of bending moment about x-axis, while the second linear temperature distribution model, Model 2, gives the most critical utilization factors of bending moment about y-axis at elevated temperatures.

Lastly, the presented finite-element model can be used as a simple design tool to predict the bending moment capacity of stainless steel tubular sections subjected to elevated temperatures.

REFERENCES

Ala-Outinen, T. 1996. Fire resistance of austenitic stainless steels Polarit 725 (EN 1.4301) and Polarit 761 (EN 1.4571). Research notes 1760. VTT Building Technology, Finland.

Ashraf, M., Gardner, L. and Nethercot, D.A. 2006. Finite element modelling of structural stainless steel cross-sections. *Thin-Walled Structures*, 44(10): 1048–1062.

Baddoo, N.R. and Burgan, B.A. 1998. Fire resistant design of austenitic structural stainless steel. *Journal of Construction Steel Research*, 46: 458–459.

British Standards Institute. 1987. BS 476: Fire Tests on Building Materials and Structures, Part 21: Methods for Determination of the Fire Resistance of Load-Bearing Elements of Construction, London, UK.

Gardner, L. and Nethercot, D.A. 2003. Tests on stainless steel structural hollow sections. *Proceedings of the Structural Stability Research Council Annual Technical Session and Meeting*: 379–401. Baltimore, USA.

Gardner, L. and Nethercot, DA. 2004. Numerical modelling of stainless steel structural components – A consistent approach. *Journal of Structural Engineering*, ASCE, 130(10): 1586–1601.

Kruppa, J. and Arnault, P. 1975. Resistance Au Feu Des Poutres Isostatinques En Acier. Revue Construction Metalique 1: No. 1.

McLaughlin, E.R. 1970. Temperature effect on tall steel framed buildings, Part 1: Response of steel columns subjected to temperature exposure, National Engineering Conference, AISC. Pittsburgh, USA.

Mirambell, E. and Real, E. 2000. On the Calculation of deflections in structural stainless steel beams: an experimental and numerical investigation. *Journal of Constructional Steel Research*, 54: 109–133.

Ng, K.T. and Gardner, L. 2007. Buckling of stainless steel columns and beams in fire. *Engineering Structures*, 29: 717–713.

Rasmussen, K.J.R. and Hancock, G.J. 1993. Design of cold-formed stainless steel tubular members. *Journal of Structural Engineering*, ASCE, 119(8): 2349–2367.

Theofanous, M., Chan, T.M. and Gardner, L. 2009. Structural response of stainless steel oval hollow compression members. *Engineering Structures*, 31(4): 922–934.

Van Den Berg, J.G. 1998. The behaviour of cold-formed stainless steel structural members. *Journal of Constructional Steel Research*, 46: 463.

Vila Real, P.M., Lopes, N., Simoes da Silva, L. and Franssen, J.M. 2008. Lateral-torsional buckling of stainless steel I-beams in case of fire. *Journal of Constructional Steel Research*, 64: 1302–1309.

Young, B. and liu, Y. 2003. Experimental investigation of cold-formed stainless steel columns. *Journal of Structural Engineering*, ASCE 129(2): 169–176.

Tubular Structures XIV – Gardner (Ed.)
© 2012 Taylor & Francis Group, London, ISBN 978-0-415-62137-3

Web crippling of ferritic stainless steel tubular members strengthened with high modulus CFRP plate

S.M.Z. Islam & B. Young
Department of Civil Engineering, The University of Hong Kong, Hong Kong, China

ABSTRACT: This paper presents a series of tests on strengthened ferritic stainless steel tubular members using externally bonded high modulus Carbon Fibre-Reinforced Polymer (CFRP) plate. The CFRP plate strengthening is only applied to a small localize region subjected to concentrated load. The tubular members of square and rectangular hollow sections subjected to web crippling were tested. The web crippling tests were conducted under two loading conditions of End-Two-Flange (ETF) and End-One-Flange (EOF). The tests were performed on five different sizes of tubular sections. Tensile coupon tests were conducted to determine the material properties of the ferritic stainless steel specimens. Most of the strengthened specimens were failed by debonding of CFRP plate from the ferritic stainless steel tubes. Two different failure modes were observed in the tests of the strengthened specimens, namely the adhesion failure as well as the combination of adhesion and cohesion failure. The failure loads, failure modes and the load-web deformation behaviour of the ferritic stainless steel sections are also presented in this paper.

1 INTRODUCTION

The most commonly use of ferritic grade stainless steel in structural application contain approximately 11.5% chromium and 0.5% nickel. In this study, the ferritic stainless steel type EN 1.4003 was used. Stainless steel tubular structural members often experience web crippling failure due to high local intensity of concentrated loads or reactions. However, it is often difficult to provide transverse stiffeners in square and rectangular tubular members. In the absence of the stiffeners, the webs of cold-formed stainless steel members may cripple due to concentrated bearing load. The web crippling strength can be enhanced by FRP strengthening in the web of the sections in a localize region. Thin-walled steel structural members subjected to web crippling have been tested (Paker, 1984; Zhao & Hancock, 1995; Young & Hangcock, 2001 & 2004). Web crippling of stainless steel tubular members have been investigated by Zhou and Young (2006, 2007a & 2007b). However, these investigations did not consider any strengthening in the web of the sections. Little research is being reported on CFRP strengthening of stainless steel structures. Previous research on strengthening of steel structures is mainly focused on carbon steel members as summarized by Zhao & Zhang (2007). Investigation of CFRP strengthened aluminium tubular sections subjected to end bearing force and web crippling have been reported in Wu et al. (2012), and Islam & Young (2011). The use of CFRP is an efficient method to strengthen metallic structural members Wu et al. (2012). Strengthening of rectangular carbon steel tubes and light steel beams using CFRP subjected to end bearing loads have been reported by Zhao et al. (2006), Fernando et al. (2009), and Zhao & Al-Mahaidi (2009). The stress-strain behaviour of carbon steel and stainless steel is quite different.

Currently, there is little research on CFRP strengthening of stainless steel tubular sections under two loading conditions for web crippling, and the two loading conditions are End-Two-Flange (ETF) and End-One-Flange (EOF) loadings. Different failure modes for CFRP strengthened of metallic structures have been reported (Schnerch, 2005; Xia & Teng, 2005; Zhao et al., 2006; Zhao & Zhang, 2007; Fernando et al., 2009; Zhao & Al-Mahaidi, 2009; Islam & Young, 2011; & Wu et al., 2012). In this study, a series of web crippling tests of ferritic stainless steel tubular structural members strengthened with high modulus CFRP plate was conducted. The test specimens were subjected to ETF and EOF loading conditions. The tests were performed on five different square and rectangular hollow sections.

2 MATERIAL PROPERTIES

Tensile coupon tests were carried out to determine the material properties of the ferritic stainless steel tubular members. The tensile coupons were extracted from the centre of the web plate in the longitudinal direction of the untested specimens. The tensile coupon specimens were prepared and tested according to the American (ASTM, 1997) and Australian (AS, 2007) standards for the tensile testing of metals using

12.5 mm wide coupons of gauge length 50 mm. The coupons were tested in a displacement controlled testing machine using friction grips. Two strain gauges and a calibrated extensometer of 50 mm gauge length were used to measure the longitudinal strain. A data acquisition system was used to record the load and strain at regular intervals during the tests. The static load was obtained by pausing the applied straining for 1.5 minutes near the 0.2% tensile proof stress and ultimate tensile strength. This allowed stress relaxation associated with plastic straining to take place.

The chemical composition of the specimens given by the mill certificates is shown in Table 1. Table 2 shows the material properties of the ferritic stainless steel sections obtained from the tensile coupon tests that includes the static 0.2% tensile proof stress ($\sigma_{0.2}$), static tensile strength (σ_u), initial Young's modulus (E_o), exponent of Ramberg-Osgood expression (n), and elongation after fracture (ε_f) based on a gauge length of 50 mm. The measured stress–strain curves obtained from the tensile coupon tests were used to determine the parameter n according to Ramberg-Osgood expression (Ramberg and Osgood, 1943). A comparison of the measured material properties with the values given in the mill certificates for 0.2% tensile proof stress, tensile strength and elongation after fracture is shown in Table 3.

The high modulus CFRP Sika CarboDur H514 laminate plate was used for the strengthening of the ferritic stainless steel tubular sections. It was shown that the high modulus CFRP Sika CarboDur H514 laminate plate and adhesive Araldite 2015 provided the best strengthening performance for ferritic stainless steel tubular sections subjected to web crippling (Islam & Young, 2010). The high modulus CFRP laminate plate had the nominal modulus of elasticity of 300 GPa, ultimate tensile strength of 1500 MPa, tensile strain at fracture of 0.45% and thickness of 1.4 mm. This high modulus CFRP Sika CarboDur H514 laminate plate was symbolized as 'f', which is the same symbol used in Islam and Young (Islam & Young, 2010). Furthermore, adhesive Araldite 2015 was used for the strengthening of the ferritic stainless steel tubular sections in this study. The adhesive Araldite 2015 had the measured tensile strength of 19.7MPa, modulus of elasticity of 1.8 GPa and tensile strain at fracture of 3.3% based on a gauge length of 50 mm coupon test. The coupon test of the adhesive Araldite 2015 is detailed in Islam and Young (2011).

Table 1. Chemical composition of ferritic stainless steel material.

Section	C (%)	Si (%)	Mn (%)	Cr (%)	Ni (%)
F50 × 50 × 4	0.016	0.42	1.39	11.50	0.40
F60 × 40 × 3	0.011	0.32	1.12	11.27	0.55
F80 × 80 × 3	0.011	0.44	0.57	11.01	0.42
F100 × 50 × 3	0.011	0.44	0.57	11.01	0.42
F120 × 40 × 3	0.016	0.44	0.62	11.05	0.39

Table 2. Measured material properties of ferritic stainless steel obtained from tensile coupon tests.

Test specimen	$\sigma_{0.2}$ (MPa)	σ_u (MPa)	E_o (GPa)	n	ε_f (%)
F50 × 50 × 4	504	514	202.0	6.4	11.9
F60 × 40 × 3	430	446	201.1	5.3	15.1
F80 × 80 × 3	434	461	199.1	5.9	19.9
F100 × 50 × 3	472	487	204.3	4.8	10.0
F120 × 40 × 3	426	459	203.5	6.2	21.5

Table 3. Comparison of experimental results with results from mill certificates.

Specimen	Yield strength $\sigma_{0.2}/\sigma_{0.2,mill}$	Ultimate strength $\sigma_u/\sigma_{u,mill}$	Elongation $\varepsilon_f/\varepsilon_{f,mill}$
F50 × 50 × 4	1.35	1.05	0.48
F60 × 40 × 3	1.35	0.95	0.50
F80 × 80 × 3	1.10	0.87	0.83
F100 × 50 × 3	1.19	0.92	0.42
F120 × 40 × 3	1.03	0.83	0.98

3 TEST SPECIMENS AND LABELLING

A test program on strengthening of ferritic stainless steel tubular members using externally bonded CFRP was conducted. The test specimens were subjected to web crippling. A total of nineteen specimens was tested under the End-Two-Flange (ETF) and End-One-Flange (EOF) loading conditions. Both rectangular hollow sections (RHS) and square hollow sections (SHS) strengthened with high modulus CFRP plate were considered. Five different section sizes were investigated and the sizes of each test specimen are shown in Table 2. The specimens had the nominal thickness ranged from 3 to 4 mm, the nominal depth of the webs ranged from 50 to 120 mm, and the flange widths ranged from 40 to 80 mm. The measured web slenderness values (flat portion of web depth-to-thickness) of the tubular sections ranged from 8.9 to 37.7. The measured dimensions of the test specimens subjected to ETF and EOF loadings are shown in Tables 4–5 using the nomenclature defined in Figure 1.

The test specimens of ferritic stainless steel type EN 1.4003 were used. The specimen lengths were determined according to the ASCE Specification (2002) for End-Two-Flange (ETF) loading condition. The clear distance between opposed loads was generally set to 1.5 times the overall depth (d) of the web rather than 1.5 times the depth of the flat portion of the web (h), the latter being the minimum specified in the specification. The bearing length of 50 mm was used. However,

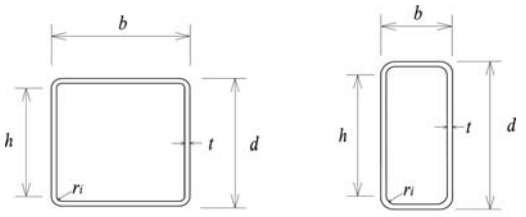

(a) Square hollow section b) Rectangular hollow section

Figure 1. Definition of symbols of ferritic stainless steel test specimen for web crippling tests.

the specimen length for EOF loading does not comply with the ASCE specification (2002). This is due to a high concentrate load applied to the middle of the specimen and failure tends to occur near the mid-length of the specimen. Therefore, reduced bearing length and specimen length were used for EOF loading to avoid failure near the mid-length of the specimen. The bearing length of 30 mm was used for EOF loading. In the EOF loading condition, the sections having stocky webs were not considered in order to avoid shear failure.

The test specimens were labelled such that the type of material, nominal dimensions of the specimen, loading condition, type and number of CFRP layer can be identified from the label as shown in Tables 4–5. For example, the label "F100 × 50 × 3-ETF-f1" defines the specimen as follows: The first letter indicates the material type of the specimen, where "F" refers to ferritic stainless steel. The following symbols are the nominal dimensions of the specimen in mm, where 100 × 50 × 3 ($d \times b \times t$) means the web depth = 100 mm, flange width = 50 mm and thickness = 3 mm. The following three letters indicate the loading condition of End-Two-Flange (ETF). The following two letters indicate the type and number of carbon fibre-reinforced polymer (CFRP) layer, where "f1" means Sika CarboDur H514 of one layer, but the reference test specimen without CFRP is represented as '0'. If a test was repeated, then the letter "R" indicates the repeated test. The CFRP strengthened width for all specimens was 50 mm which is the same length as the bearing length N, except for the EOF loading condition as shown in Table 5. The width of CFRP strengthening was 30 mm at each end of the specimen and represented by the parenthesis in the label for the EOF loading. The bearing length was also kept at 30 mm at each end of the specimen. For example, the label "F100 × 50 × 3-EOF-f1(30)" where "(30)" represent the CFRP width of 30 mm.

Initial local geometric imperfections were measured on the specimens prior to testing. The geometric imperfections along the web plate directions were measured. Five readings of equal distance were obtained along each web. The maximum measured initial local geometric imperfections occurred in the middle of the web plates. The maximum imperfections are 0.062, 0.078, 0.098, 0.131 and 0.158 mm for F50 × 50 × 4, F60 × 40 × 3, F80 × 80 × 3, F100 × 50 × 3 and F120 × 40 × 3 respectively, as shown in Table 6.

The strength of the adhesive bond is directly proportional to the quality of the surfaces to which it is mated (Fawzia et al., 2007). It was found that the most suitable surface preparation method for ferritic stainless steel is by sanding (Islam & Young, 2010). An electric sander was used for the surface treatment of the ferritic stainless steel sections. The silicon carbide 80 medium grit sand paper was used for the surface treatment. The silicon carbide sand paper comprising an average particle size of 192 μm was used in the electric sander. The outer surfaces of the stainless steel sections were

Table 4. Measured dimensions of CFRP strengthened ferritic stainless steel tubular sections subjected to ETF loading condition.

Specimen	d (mm)	b (mm)	t (mm)	r_i (mm)	L (mm)	h/t
F50 × 50 × 4-ETF-0	50.2	50.2	3.865	4.00	125.4	8.9
F50 × 50 × 4-ETF-f1	50.1	50.1	3.838	4.00	125.6	9.0
F50 × 50 × 4-ETF-f1-R	50.1	50.1	3.800	4.00	125.9	9.1
F60 × 40 × 3-ETF-0	60.0	40.2	2.773	3.00	140.6	17.5
F60 × 40 × 3-ETF-f1	60.0	40.0	2.703	3.00	140.4	18.0
F80 × 80 × 3-ETF-0	80.1	80.0	2.816	3.25	169.8	24.1
F80 × 80 × 3-ETF-f1	80.0	80.0	2.766	3.25	169.0	24.6
F100 × 50 × 3-ETF-0	100.2	50.0	2.804	2.75	201.1	31.8
F100 × 50 × 3-ETF-f1	100.1	50.1	2.761	2.75	200.0	32.3
F120 × 40 × 3-ETF-0	120.0	40.1	2.840	4.00	230.5	37.4
F120 × 40 × 3-ETF-f1	119.9	39.9	2.821	4.00	231.6	37.7

Table 5. Measured dimensions of CFRP strengthened ferritic stainless steel tubular sections subjected to EOF loading condition.

Specimen	d (mm)	b (mm)	t (mm)	r_i (mm)	L (mm)	h/t
F60 × 40 × 3-EOF-0	60.0	40.2	2.757	3.00	330	17.6
F60 × 40 × 3-EOF-f1(30)	60.0	39.9	2.720	3.00	330	17.9
F80 × 80 × 3-EOF-0	80.0	80.0	2.811	3.25	391	24.1
F80 × 80 × 3-EOF-f1(30)	80.0	80.1	2.756	3.25	390	24.7
F100 × 50 × 3-EOF-0	100.1	50.1	2.814	2.75	450	31.6
F100 × 50 × 3-EOF-f1(30)	100.1	50.0	2.806	2.75	451	31.7
F120 × 40 × 3-EOF-0	119.9	40.0	2.831	4.00	511	37.5
F120 × 40 × 3-EOF-f1(30)	120.1	39.9	2.821	4.00	510	37.7

Table 6. Maximum measured local imperfection of ferritic stainless steel tubular sections.

Specimen	Max. local imperfection (mm)
F50 × 50 × 4	0.062
F60 × 40 × 3	0.078
F80 × 80 × 3	0.098
F100 × 50 × 3	0.131
F120 × 40 × 3	0.158

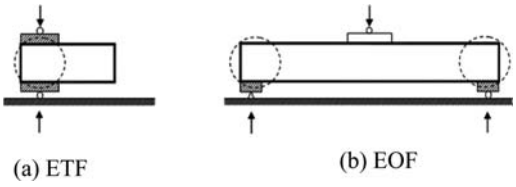

Figure 2. Loading conditions of web crippling tests.

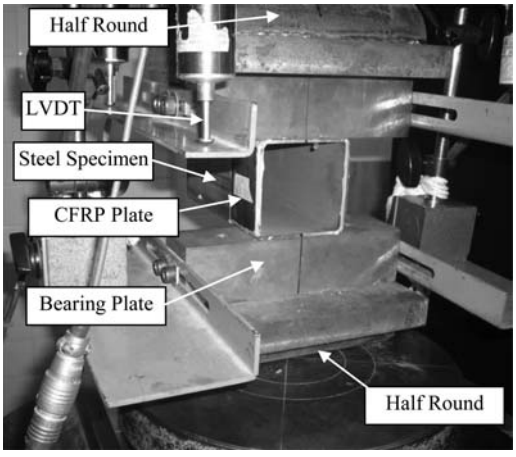

Figure 3. Test setup of End-Two-Flange loading condition.

cleaned with acetone. The adhesive was then applied uniformly on the CFRP plates and then attached onto the ferritic stainless steel surfaces. The excess adhesive and air were removed using a ribbed roller that applied on the CFRP plates with a small amount of force. The fibre direction was along the web direction. The thickness of the adhesive layer was maintained uniform. The adhesive thickness for most of the specimens was found to be approximately 1.0 mm. The test specimens were tested after 7 days of curing at room temperature.

4 WEB CRIPPLING TEST

The web crippling tests were conducted under the End-Two-Flange (ETF) and End-One-Flange (EOF) loading conditions as specified in the ASCE Specification (2002), as shown in Figure 2. Photographs of the test setup of ETF and EOF loading conditions are shown in Figures 3 and 4, respectively. A servo-controlled hydraulic testing machine was used to apply a concentrated compressive force to the test specimens. Displacement control was used to drive the hydraulic actuator at a constant speed of 0.3 mm/min for all tests. Two identical bearing plates with half round of the same width were positioned at the end of the specimen for ETF loading condition. The hinge supports were simulated by two half rounds. Four LVDT transducers were used to record the web deformations of the specimens for ETF loading condition as shown in Figure 3.

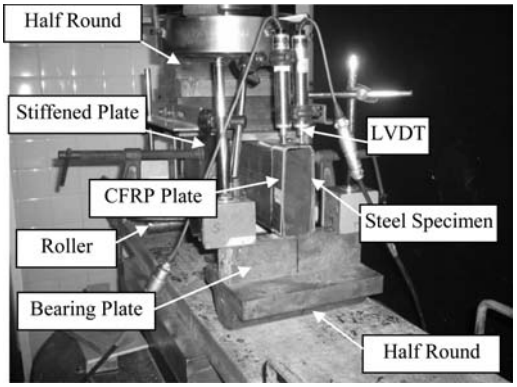

Figure 4. Test setup of End-One-Flange loading condition.

Two identical bearing plates of the same width were positioned at both ends of the specimens for EOF loading condition. Half round and round bar were used to simulate the hinge and roller supports at the ends of the specimen. The mid-length of the specimen was subjected to concentrated applied load, and stiffened plates and wooden block were used to prevent web crippling failure at mid-length of the specimen.

The wooden block was inserted into the mid-length of the ferritic stainless steel tubular sections. Four transducers were used to measure the web deformations of the specimens between the bearing plates and the top flanges of the specimens, as shown in Figure 4.

5 TEST RESULTS AND DISCUSSION

The tests without the CFRP plate strengthening were conducted as reference and the specimens failed by web crippling. The failure modes of each test specimen are listed in Tables 7–8. The webs of the specimens were buckled outward. In this study, two main failure modes were observed for the CFRP plate strengthened ferritic stainless steel tubular members. The adhesion failure and the combination of adhesion and cohesion failure subjected to ETF loading condition are shown in Figure 5. The failure mode of specimen F120 × 40 × 3 strengthened by CFRP plate is shown in Figure 6 for EOF loading condition. The adhesion failure was found at physical interface between the adhesive and the adherents, whereas the cohesion failure is fully controlled by the adhesive properties. The effects of adhesive and FRP on the failure modes of strengthened stainless steel and aluminium tubular members subjected to web crippling are detailed in Islam & Young (2010, 2011).

The contribution of the CFRP plate relies on the stress transfer mechanism of the adhesive layer for strengthening of ferritic stainless steel tubular section. Hence, the enhancement of the ultimate load of such strengthening is often governed by the failure of the adhesive layer. The CFRP plates were found to be debonded from the ferritic stainless steel tubes for all

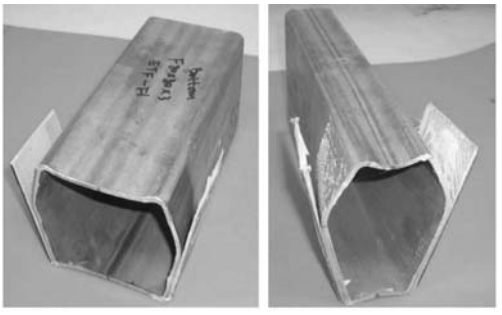

(a) Adhesion failure (b) Combination of adhesion and cohesion failure

Figure 5. Two different failure modes of CFRP strengthened ferritic stainless steel specimens subjected to ETF loading condition.

Figure 6. Failure mode of CFRP strengthened ferritic stainless steel F120 × 40 × 3-EOF-f1 section subjected to EOF loading condition.

of the specimens. The debonding was initiated from the end of the CFRP plate that experienced high interfacial stresses, and the debonding gradually propagated towards the mid-height of the webs.

Figures 7–8 show the load-web deformation plots of the specimens. It is shown that the initial cracking propagated to a certain limit and then the CFRP suddenly debonded, hence, caused the load to drop suddenly. The adhesion failure was observed for all the specimens with CFRP strengthening, except for F100 × 50 × 3-ETF-f1, F120 × 40 × 3-ETF-f1, and F100 × 50 × 3-EOF-f1(30) where combination of adhesion and cohesion failure was found for these specimens as shown in Tables 7–8.

The web crippling test strengths per web with CFRP (P_u) and without CFRP (P_{u0}) plates are shown in Tables 7–8 for ETF and EOF loading conditions. The reference tests without CFRP plate were also conducted. The web slenderness (h/t) ratio of the ferritic stainless steel tubular sections is ranged from

Table 7. Test results of CFRP strengthened ferritic stainless steel tubular sections subjected to ETF loading.

Specimen	h/t	P_u (kN)	P_u/P_{u0}	Failure mode
F50 × 50 × 4-ETF-0	8.9	39.5	1.00	W
F50 × 50 × 4-ETF-f1	9.0	43.8	1.11	A
F50 × 50 × 4-ETF-f1-R	9.1	43.3	1.10	A
F60 × 40 × 3-ETF-0	17.5	23.7	1.00	W
F60 × 40 × 3-ETF-f1	18.0	26.8	1.13	A
F80 × 80 × 3-ETF-0	24.1	23.0	1.00	W
F80 × 80 × 3-ETF-f1	24.6	26.9	1.17	A
F100 × 50v3-ETF-0	31.8	24.4	1.00	W
F100 × 50 × 3-ETF-f1	32.3	30.5	1.25	A+C
F120 × 40 × 3-ETF-0	37.4	20.7	1.00	W
F120 × 40 × 3-ETF-f1	37.7	31.2	1.51	A + C

W = Web buckling failure A = Adhesion failure and C = Cohesion failure A + C = Combination of adhesion and cohesion failure.

Table 8. Test results of CFRP strengthened ferritic stainless steel tubular sections subjected to EOF loading.

Specimen	h/t	P_u (kN)	P_u/P_{u0}	Failure mode
F60 × 40 × 3-EOF-0	17.6	26.2	1.00	W
F60 × 40 × 3-EOF-f1(30)	17.9	26.6	1.02	A
F80 × 80 × 3-EOF-0	24.1	26.1	1.00	W
F80 × 80 × 3-EOF-f1(30)	24.7	27.1	1.04	A
F100 × 50 × 3-EOF-0	31.6	29.1	1.00	W
F100 × 50 × 3-EOF-f1(30)	31.7	31.3	1.08	A + C
F120 × 40 × 3-EOF-0	37.5	25.1	1.00	W
F120 × 40 × 3-EOF-f1(30)	37.7	27.9	1.11	A

W = Web buckling failure A = Adhesion failure and C = Cohesion failure A + C = Combination of adhesion and cohesion failure.

8.9 to 37.7. It is shown that as the web slenderness (h/t) ratio increases, the web crippling load enhancement also increases for the two loading conditions. For ferritic stainless steel sections F50 × 50 × 4, F60 × 40 × 3, F80 × 80 × 3, F100 × 50 × 3 and F120 × 40 × 3 having the measured web slenderness values of 9.0, 18.0, 24.6, 32.3 and 37.7 subjected to ETF loading, the enhancement of web crippling loads per web (P_u) was found to be 11%, 13%, 17%, 25%, and 51%, respectively, as shown in Table 7.

It is shown that the web crippling strength enhancement for the ferritic stainless steel specimens with slender web increased more than those specimens with relatively compact web. The maximum enhancement of web crippling strengths per web (P_u) was found to be 2%, 4%, 8% and 11% for specimens had a 30 mm width of CFRP strengthening at each end of the specimens subjected to EOF loading condition for sections F60 × 40 × 3, F80 × 80 × 3, F100 × 50 × 3 and F120 × 40 × 3, respectively, as shown in Table 8.

The load enhancement is more pronounced for ETF loading condition. Therefore, the CFRP strengthening

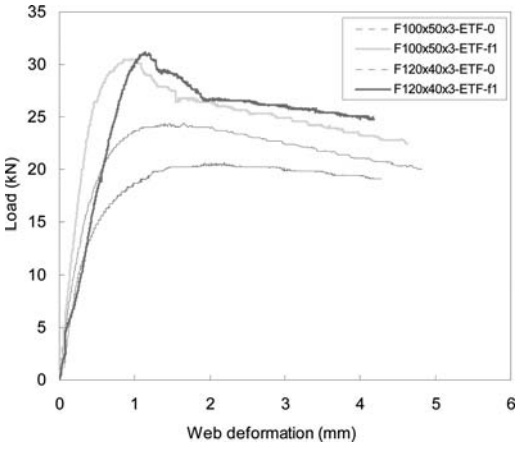

Figure 7. Load-web deformation behaviour of F100 × 50 × 3 and F120 × 40 × 3 sections subjected to ETF loading condition.

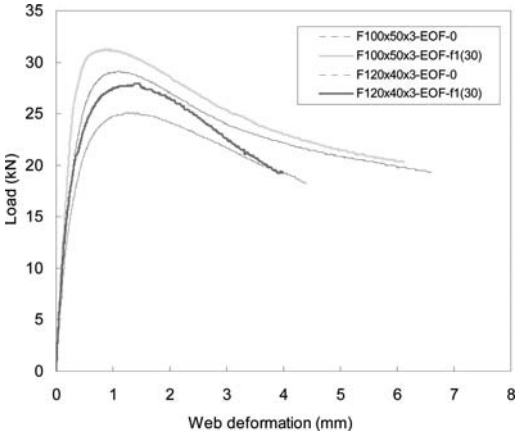

Figure 8. Load-web deformation behaviour of F100 × 50 × 3 and F120 × 40 × 3 sections subjected to EOF loading condition.

against web crippling is found to be more effective for specimens subjected to ETF loading condition. The load-web deformation behaviour of F100 × 50 × 3 and F120 × 40 × 3 specimens subjected to ETF and EOF loading conditions are plotted in Figures 7–8. It was observed that considerable increase in load carrying capacity due to CFRP strengthening for specimen F120 × 40 × 3 as shown in Figure 7.

Figure 9 depicts the web crippling load ratio (P_u/P_{u0}) against the web slenderness (h/t) for the ETF loading condition. The web crippling strengths of CFRP strengthened ferritic stainless steel tubular sections were increased up to 51% and 11% for ETF and EOF loading conditions, respectively.

6 CONCLUSIONS

The ferritic stainless steel tubular members strengthened with high modulus carbon fibre-reinforced

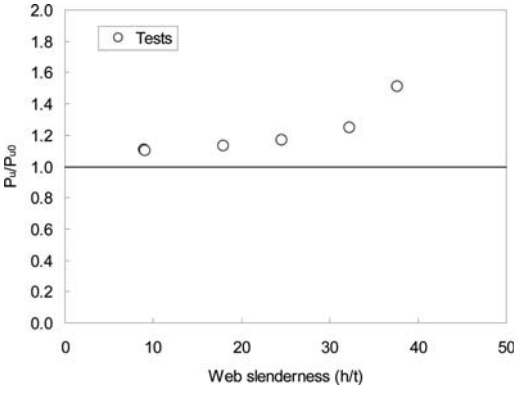

Figure 9. Load enhancement of CFRP strengthened ferritic stainless steel sections subjected to ETF loading condition.

polymer subjected to web crippling were tested. The high modulus CFRP Sika CarboDur H514 laminate plate and adhesive Araldite 2015 were used for the strengthening of the ferritic stainless steel tubular sections. The tubular sections of square and rectangular hollow sections were used in the investigation. A series of web crippling tests was conducted under End-Two-Flange (ETF) and End-One-Flange (EOF) loading conditions. It was found that the specimens strengthened with CFRP plate failed by either adhesion or combination of adhesion and cohesion failure. The failure modes, failure loads and load-web deformation behaviour of the ferritic stainless steel sections have also been presented. It is shown that the enhancement of the web crippling load increases as the web slenderness increases for both loading conditions. The web crippling strengths of CFRP strengthened ferritic stainless steel tubular sections were increased up to 51% and 11% for ETF and EOF loading conditions, respectively.

ACKNOWLEDGEMENTS

The authors gratefully acknowledge the STALA tube Finland for supplying the test specimens. The research work described in this paper was supported by a grant from The University of Hong Kong under the seed funding program for basic research. The authors are also grateful to Miss Mei-Ni Su for her assistance in the experimental program as part of her final year undergraduate research projects at The University of Hong Kong.

REFERENCES

AS 2007. Metallic materials – Tensile testing at ambient temperature", Australian Standard, AS 1391-2007. sydney, Australia: Standards Association of Australia.

ASCE 2002. Specification for the design of cold-formed stainless steel structural members. SEI/ASCE 8-02; 2002. Reston, VA: American Society of Civil Engineers.

ASTM E 8M-97. Standard test methods for tension testing of metallic materials, West Conshohocken: American Society for Testing and Materials.

Fawzia, S., Al-Mahaidi R., Zhao, X. L. and Rizkalla S. 2007. Strengthening of circular hollow steel tubular sections using high modulus CFRP sheets. *Construction and Building Materials*, 21(4):839–845.

Fernando, D., Yu T., Teng, J.G., and Zhao, X.L. 2009. CFRP strengthening of rectangular steel tubes subjected to end bearing loads: effect of adhesive properties and finite element modelling, *Thin-Walled Structures*, 47(10): 1020–1028.

Islam, S. M. Z. and Young, B. 2010. Effects of different adhesive and FRP on strengthening of stainless steel tubular structural members, *Proceedings of the 13th International Symposium on Tubular Structures*, Hong Kong, China, 273–280.

Islam, S. M. Z. and Young, B. 2011. FRP strengthened aluminium tubular sections subjected to web crippling. *Thin-Walled Structures*, 49(11):1392–1403.

Packer, J.A. 1984. Web crippling of rectangular hollow sections. *Journal of Structural Engineering*, ASCE, 110(10): 2357–2373.

Ramberg, W, Osgood, W. R.1943. Description of stress–strain curves by three parameters. Technical note No. 902, National Advisory Committee for Aeronautics.

Schnerch, D., 2005. Strengthening of steel structures with high modulus carbon fiber reinforced polymer (CFRP) materials. PhD dissertation, North Carolina State University, Raleigh (NC).

Wu, C., Zhao, X.L., Duan, W.H. and Phipat, P. 2012. Experimental and numerical study on CFRP strengthened aluminium tubular sections subjected to end bearing force. International *Journal of Structural Stability and Dynamics*, 12(1): (Article in Press).

Xia, S.H, and Teng, J.G. 2005. Behaviour of FRP-to-steel bonded joints, *Proceedings of the International Symposium on Bond Behaviour of FRP in Structures*, Hong Kong, China, 411–418.

Young, B. and Hancock, G.J. 2001. Design of cold-formed channels subjected to web crippling. *Journal of Structural Engineering*, ASCE, 127(10):1137–1144.

Young, B. and Hancock, G.J. 2004. Web crippling of cold-formed unlipped channels with flanges restrained. *Thin-Walled Structures*, 42(6):911–930.

Zhao, X.L. and Hancock, G.J. 1995. Square and rectangular hollow sections under transverse end-bearing force. *Journal of Structural Engineering*, ASCE, 121(9): 1323–1329.

Zhao, X.L. and Zhang, L., 2007. State-of-the-art review on FRP strengthened steel structures. *Engineering Structures*, 29(8):1808–1823.

Zhao, X.L., and Al-Mahaidi, R. 2009. Web buckling of lightsteel beams strengthened with CFRP subjected to end-bearing forces, *Thin-Walled Structures*, 47(10): 1029–1036

Zhao, X.L., Fernando, D. and Al-Mahaidi, R. 2006. CFRP strengthened RHS subjected to transverse end bearing force, *Engineering Structures*, 28(11):1555–1565.

Zhou, F. and Young, B. 2007a. Experimental and numerical investigations of cold-formed stainless steel tubular sections subjected to concentrated bearing load. *Journal of Constructional Steel Research*, 63(11):1452–1466.

Zhou, F. and Young, B. 2007b. Cold-formed high-strength stainless steel tubular sections subjected to web crippling. *Journal of Structural Engineering*, ASCE, 133(3): 368–377.

Zhou, F. and Young, B. 2006. Cold-formed stainless steel sections subjected to web crippling. *Journal of Structural Engineering*, ASCE, 132(1):134–44.

Tubular Structures XIV – Gardner (Ed.)
© 2012 Taylor & Francis Group, London, ISBN 978-0-415-62137-3

Ultimate capacity of stainless steel RHS subjected to combined compression and bending

M. Theofanous
Department of Civil Engineering, Aristotle University of Thessaloniki, Thessaloniki, Greece

A. Liew & L. Gardner
Department of Civil and Environmental Engineering, Imperial College London, London, UK

ABSTRACT: To maintain consistency with carbon steel design guidance, the current European design code for stainless steel structures EN 1993-1-4 employs many of the relevant design expressions from the equivalent carbon steel design code EN 1993-1-1. While this is generally satisfactory, there are a number of instances in which overly conservative designs result. Given the high initial material cost of stainless steel, the derivation of more economic design expressions in accordance with the actual material response is warranted. To this end, the Continuous Strength Method (CSM) has been developed and verified against experimental and numerical results. To date, the scope of the CSM has been restricted to stainless steel cross-sections subjected to compression or uniaxial bending. The present paper aims to extend the scope of application of the CSM to cross-sections subjected to more general loading conditions likely to occur in practice. Furthermore, a simplified version of the CSM, with a more straightforward base curve and material model, but still capturing the essential strain hardening features of stainless steel, is considered. The comparisons show that the simplifications lead to very little loss of accuracy and will be developed further in future studies.

1 INTRODUCTION

Stainless steel tubular members are gaining increasing usage in modern construction practice due to their favourable structural properties, excellent durability and aesthetic appeal. Owing to the attempt to maintain consistency with carbon steel design guidance, the current European design guidance for stainless steel structures EN 1993-1-4 (2006) employs many of the relevant design expressions from the equivalent carbon steel design code EN 1993-1-1 (2005). While this generally leads to satisfactory designs, numerous researchers (Burgan et al. 2000, Gardner & Theofanous 2008) have demonstrated that the currently codified design expressions for cross-section capacity are unduly conservative, as they do not account for the significant strain hardening exhibited by stainless steel components of low and intermediate slenderness. Given the high initial material cost of stainless steel, the derivation of more economic design expressions in accordance with the actual material response is warranted.

To this end, the Continuous Strength Method (CSM) has been developed by Gardner & Nethercot (2004a, 2004b), Ashraf et al. (2008), Gardner (2008) and Gardner
et al. (2011) and verified against experimental and numerical results. More recently, the CSM has been modified to account for the effect of element interaction on cross-section capacity (Theofanous & Gardner 2012) by utilizing the cross-section slenderness concept, similar to the Direct Strength Method (DSM), which originated from Schafer (2008) for cold-formed steel and was adapted to stainless steel by Becque et al. (2008).

To date the scope of the CSM has been restricted to stainless steel cross-sections subjected to compression or uniaxial bending, for which a significant pool of experimental data is available (Gardner & Theofanous 2008). Experimental (Talja & Salmi 1995, Burgan et al. 2000) and numerical (Greiner & Kettler 2008) research in stainless steel members subjected to more complex loading arrangements remains scarce and mainly focuses on beam-column response, whilst the cross-section response under combined compression and bending remains largely unverified. Despite the provision of interaction equations for stainless steel beam-columns in EN 1993-1-4 (2006), no specific guidelines are given for the cross-section capacity of stocky (Class 1 and 2) cross-sections under combined compression and bending; these are designed according to the respective carbon steel provisions (EN 1993-1-1 2005) that allow for nonlinear interactions for Class 1 and 2 cross-sections. Hence, the nonlinear response of stainless steel is not accounted for and a rigid plastic material model is assumed at cross-sectional level. In the present paper the results of an extensive parametric study of rectangular hollow

sections (RHS) subjected to a combination of loads are presented, which allow for the assessment of current and the suggestion of novel interaction equations for stainless steel sections under combined loads.

2 NUMERICAL MODELLING

For all numerical studies presented herein the general-purpose FE software ABAQUS (2006) has been used. A full account of the basic assumptions adopted in the current paper for the model generation is given in Theofanous & Gardner (2012). In short, a geometrically and materially nonlinear analysis has been conducted for each cross-section and loading case considered. Prior to the nonlinear analysis an eigenvalue buckling analysis was performed to obtain the lowest buckling mode shape, which was introduced as the geometric imperfection pattern with a suitable amplitude (Gardner & Nethercot 2004c, Dawson & Walker 1972) $w_0 = 0.023(f_{0.2}/f_{cr})t$, f_{cr} being the elastic critical buckling stress of the most slender plated element of the cross-section. Typical lowest elastic buckling mode shapes and corresponding failure modes for an SHS $100 \times 100 \times 5$ and an RHS $200 \times 100 \times 5$ cross-section subjected to biaxial bending and compression are depicted in Figures 1 and 2 respectively.

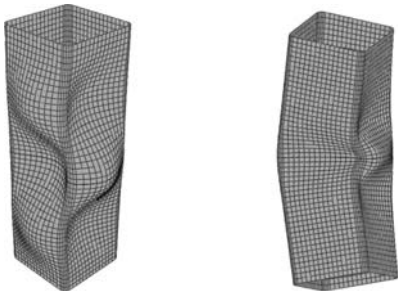

Figure 1. Lowest buckling mode shape and failure mode for a SHS subjected to combined compression and biaxial bending.

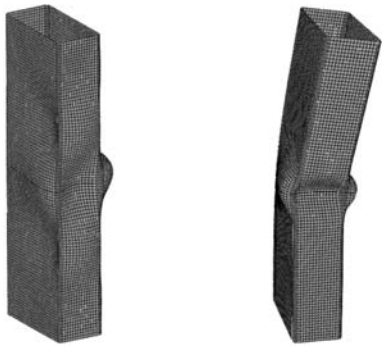

Figure 2. Lowest buckling mode shape and failure mode for a RHS subjected to combined compression and biaxial bending.

The adopted material model was a two-stage Ramberg-Osgood law (Mirambell & Real 2000, Rasmussen 2003, Gardner & Nethercot 2004a) with the material properties given in Table 1, which correspond to typical values of austenitic stainless steels (Groth & Johansson 1990), where E is the Young's modulus, $f_{0.2}$ and $f_{1.0}$ are the stresses corresponding to 0.2% and 1% plastic strain respectively and n and $n_{0.2,1.0}$ are strain-hardening exponents (Gardner & Nethercot 2004a).

The effect of incorporating residual stresses in numerical models has been studied in detail by Jandera et al. (2008). In accordance with similar studies (Gardner & Nethercot 2004c), the effect of residual stresses was not explicitly modeled. Moreover the well-documented pronounced effect of cold-forming on corner material properties, which results in significant corner strength enhancements has also been neglected, in order to simplify the analysis of the results and the derivation of novel interaction curves. Relevant literature (Cruise & Gardner 2008, Ashraf et al. 2006, Rossi et al. 2009) provides suitable methods to quantify such an effect for various material properties, cross-sections and production routes.

Two aspect ratios (SHS 100×100 and RHS 200×100) and five wall thicknesses (3, 4, 5, 6 and 8 mm) have been considered in the present study, thereby encompassing a wide range of cross-section slenderness. The mid-surface of the cross-sections was modelled with a relatively fine uniform mesh of linear reduced integration finite strain shell elements S4R (ABAQUS 2006). In order to reduce computational time, symmetry was exploited by modelling half the member length and applying suitable symmetry boundary conditions. The nodes of the end cross-section were constrained to displace and rotate as a rigid body and were restrained against in plane displacements and rotation about the member axis.

A compressive force and moments about the principal axes were applied simultaneously on the centroid of the end cross-section, which were increased proportionally until failure. In order to simulate a multitude of loading conditions likely to occur in practice, the ratio of the bending moments about either axis to the applied compression force (i.e. eccentricities of the applied compression force) was varied significantly. In particular, for a given compression force the initially applied bending moment about each axis was obtained by assuming a linear elastic stress distribution and varying the stress ratio of the webs of the cross-section from -0.75 to 1 (corresponding to pure compression) with a step of 0.25, resulting in 8 stress ratios per

Table 1. Adopted material properties.

Material	E (N/mm^2)	$f_{0.2}$ (N/mm^2)	$f_{1.0}/f_{0.2}$	n	$n_{0.2,1.0}$
Austenitic	200000	306.1	1.2	5.6	2.7

axis and hence 64 load combinations in total. An additional 11 analyses were performed for each section to simulate the special case of biaxial bending with various moment ratios, without the presence of an axial force. In total, 75 loading arrangements were considered for each cross-section thereby resulting in 750 analyses. Scripting in Python was employed to utilize the parametric capabilities of ABAQUS (2006). Based on the obtained results, current design provisions are assessed in the following sections of the paper.

3 ASSESSMENT OF CURRENT DESIGN GUIDANCE

The design provisions for stainless steel components under combined bending and axial compression codified in EN 1993-1-4 (2006) focus primarily on member instability; cross-section response under combined loads is not covered in detail. Stress redistribution within a cross-section subjected to combined compression and biaxial bending is allowed for, provided that the section is classified as Class 1 or 2, by adopting the relevant carbon steel provisions (EN 1993-1-1 2005). The codified interaction expressions of EN 1993-1-1 (2005) for a stocky (i.e. Class 1 or 2) RHS is given by Equation 1:

$$\left[\frac{M_{y,Ed}}{M_{N,y,Rd}}\right]^{\frac{1.66}{1-1.13n^2}} + \left[\frac{M_{z,Ed}}{M_{N,z,Rd}}\right]^{\frac{1.66}{1-1.13n^2}} \leq 1 \qquad (1)$$

where N_{Ed}, $M_{Ed,y}$ and $M_{Ed,z}$ are the applied loads and $M_{N,y,Rd}$ and $M_{N,z,Rd}$ are the plastic moment resistances about the relevant axis, reduced due to the axial force N_{Ed} and $n = N_{Ed}/(Af_y)$. The design expressions for $M_{N,y,Rd}$ and $M_{N,z,Rd}$ are given in EN 1993-1-1 (2005). For Class 3 and Class 4 sections, the maximum longitudinal stress due to the applied loads should be smaller than the yield stress f_y, which effectively results in a linear interaction equation.

For each simulated cross-section and each load case (i.e. eccentricities of the applied compression force) considered, a triplet of axial force N_{Ed}, bending moment about the major axis $M_{Ed,y}$ and bending moment about the minor axis $M_{Ed,z}$ was obtained, thus enabling the determination of interaction surfaces in the (N_{Ed}, $M_{Ed,y}$, $M_{Ed,z}$) space and the assessment of current interaction equations. This is done in the following sub-sections for the cases of axial compression and uniaxial bending, biaxial bending and compression and biaxial bending. In the following Figures, $W_{pl,y}$, $W_{pl,z}$ are the section plastic moduli about the respective principal axes, A_{eff} is the effective cross-section area (gross area for Classes 1-3), $\beta_w = 1$ for Class 1 or 2 cross-sections, $\beta_w = W_{el}/W_{pl}$ for Class 3 cross-sections and $\beta_w = W_{eff}/W_{pl}$ and f_y is the nominal yield stress $f_{0.2}$. Compression and uniaxial bending

The numerically obtained loads at failure for cross-sections subjected to axial compression and uniaxial bending normalized by the respective codified resistances are depicted in Figures 3–5 for SHS and RHS subjected to compression and minor axis bending and RHS subjected to compression and major axis bending respectively. The Eurocode nonlinear interaction curve applicable to cross-sections classified as Class 1 or 2 and the linear interaction applicable to Classes 3 and 4 are also included. Massive sentence.

As evidenced in Figures 3–5, the current design provisions of EN 1993-1-4 (2006) are unduly conservative for cross-sections subjected to compression and uniaxial bending. The level of conservatism

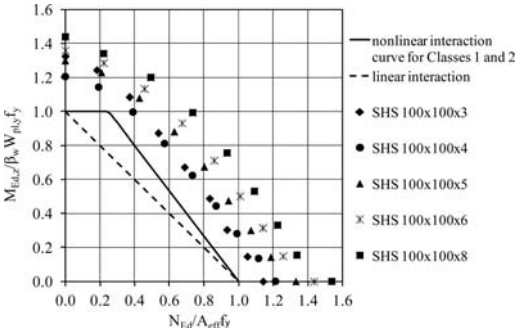

Figure 3. Interaction of axial compression and uniaxial bending ($N_{Ed} + M_{Ed,z}$, $M_{Ed,y} = 0$) for SHS.

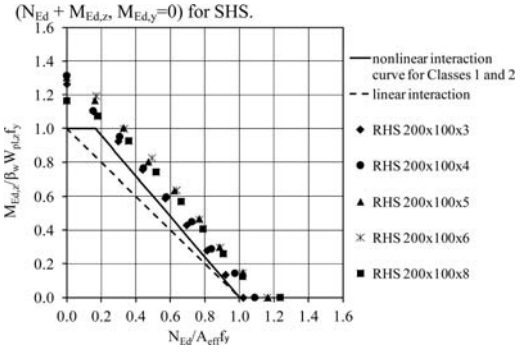

Figure 4. Interaction of axial compression and minor axis bending ($N_{Ed} + M_{Ed,z}$, $M_{Ed,y} = 0$) for RHS.

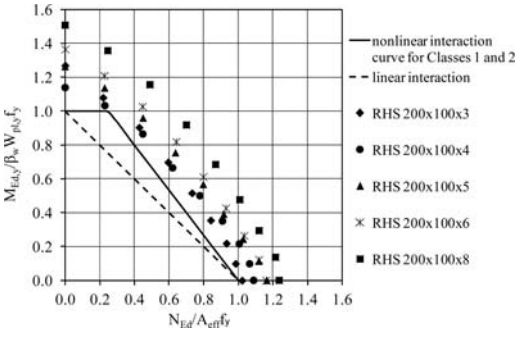

Figure 5. Interaction of axial compression and major axis bending ($N_{Ed} + M_{Ed,y}$, $M_{Ed,z} = 0$) for RHS.

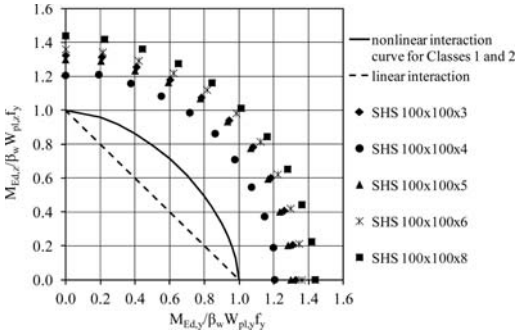

Figure 6. Interaction of major and minor axis bending ($M_{Ed,z} + M_{Ed,y}$, $N_{Ed} = 0$) for SHS.

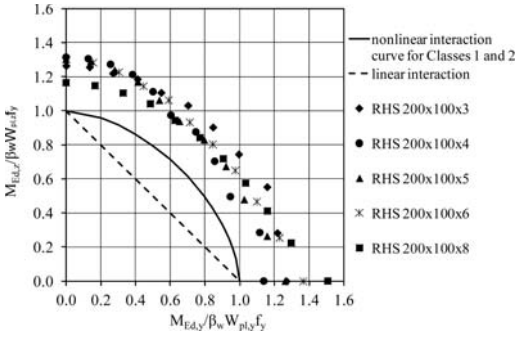

Figure 7. Interaction of major and minor axis bending ($M_{Ed,z} + M_{Ed,y}$, $N_{Ed} = 0$) for RHS.

increases with decreasing slenderness as shown in Figures 3 and 5, where an increased scatter of the results can be observed and stocky cross-sections can reach capacities well beyond their plastic moment resistances. In Figure 4 it can be observed that both the scatter of the results and the embedded conservatism for RHS subjected to axial compression and minor axis bending decrease. This is attributed to the high slenderness of the simulated cross-sections; with the exception of RHS 200 × 100 × 8, which is classified as Class 1, the remaining RHS are Class 4.

3.1 *Biaxial bending*

Figures 6 and 7 depict the major and minor axis bending resistances normalized by the respective codified resistances, together with the codified interaction curve for stocky (Class 1 and 2) cross-sections and the linear interaction curve for semi-compact and slender cross-sections (Classes 3 and 4). A high degree of conservatism and scatter in the predictions can be observed.

3.2 *Compression and biaxial bending*

For the more general case of cross-sections subjected to compression and biaxial bending, similar remarks on the conservatism and scatter of the predictions to

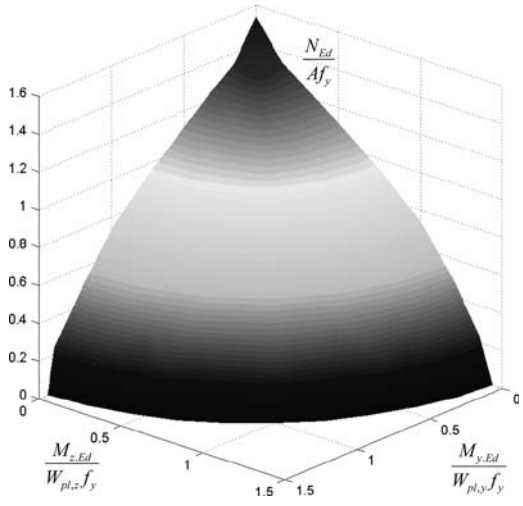

Figure 8. Interaction surface for SHS 100 × 100 × 8.

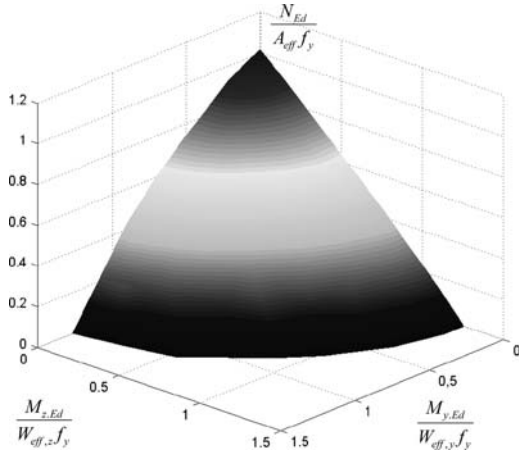

Figure 9. Interaction surface for RHS 200 × 100 × 3.

the ones made for the more simplified loading cases previously hold. Rather than interaction curves, interaction surfaces can be obtained from the numerical failure loads. Figures 8 and 9 depict the interaction surfaces of SHS 100 × 100 × 8 and RHS 200 × 100 × 3 as typical examples of a stocky and a slender cross-section subjected to combined loading. In both Figures the numerically obtained cross-section loads at failure are normalized by the relevant codified cross-section capacity, which is determined assuming that each load acts in isolation.

In Figures 8 and 9 it can be observed that the actual interaction surface is convex and that the stocky cross-section exhibits a more rounded interaction curve than the slender one, particularly at the bottom part of the surface (i.e. for small axial compression). A quantitative assessment of the accuracy of the predictions of EN 1993-1-4 (2006) is given in Table 2, where the codified utilization at failure (i.e. 1) is normalized by the actual cross-section utilization as determined from the

Table 2. Comparison of Eurocode predictions with FE data.

	Codified predictions/FE	
	Mean	COV
SHS	0.76	0.18
RHS	0.74	0.14
ALL	0.75	0.16

FE results. A high level of conservatism accompanied by a high scatter of the predictions can be observed for both SHS and RHS cross-sections. It should be noted that Equation (1) was applicable to all SHS except SHS $100 \times 100 \times 3$ and to RHS $200 \times 100 \times 8$, which were classified as Class 1 for all loading cases, whilst the remaining cross-sections were classified Class 4.

4 DESIGN RECOMMENDATIONS

The conservatism of the current design provisions highlighted in the previous section can be attributed to the inefficiency of current design provisions in determining the ultimate capacity for the fundamental loading cases acting in isolation for stocky cross-sections and the use of inappropriate interaction curves. Possible remedies are proposed herein, and include the application of the CSM in the determination of the axial and bending capacities and the modification of the codified interaction curve.

4.1 *The Continuous Strength Method (CSM)*

The CSM is a strain based design approach that employs a 'base curve' to determine the strain that a cross-section can sustain, in conjunction with a material model that allows for strain hardening, to determine section resistance. In this section, a 3 coefficient base curve and a compound Ramberg-Osgood material is used. In Section 4.3, the accuracy of a simplified version of the CSM, with a two coefficient base curve and a bilinear (elastic, linear hardening) material model, is assessed. As evidenced in Figures 3–9 and highlighted by various researchers (Burgan et al. 2000, Gardner & Nethercot 2004b, Ashraf et al. 2008), current design provisions significantly underestimate the cross-section capacity of stocky cross-sections as they fail to account for the material strain-hardening. The actual material response can be taken into account in the design process, if the cross-section capacities for the fundamental cases of uniaxial bending and axial compression are determined by the CSM. For each of the fundamental loading cases of axial compression, major axis bending and minor axis bending, the cross-section slenderness is obtained from Equation (2):

$$\bar{\lambda}_p = \sqrt{f_y / f_{cr}} \tag{2}$$

where f_{cr} is the critical buckling stress corresponding to the lowest (local) buckling mode pertaining to the loading case considered, which can be obtained by eigenvalue buckling analysis using a finite element or finite strip analysis. In this paper the software CUFSM (Li & Schafer 2010) was utilized to obtain the critical buckling stresses. Conservatively, cross-section slenderness could also be calculated on the basis of the most slender plate element in the section. The maximum strain ε_{csm} that the section can attain (as limited by local buckling) is given by Equation (3) (Theofanous & Gardner 2012):

$$\frac{\varepsilon_{csm}}{f_y / E} = \frac{1.22}{\bar{\lambda}_p^{2.71-0.69\bar{\lambda}_p}} \leq 15 \tag{3}$$

Having established the maximum strain that can be reached by the cross-section and assuming uniform strain at failure for a cross-section subjected to axial compression, the stress at failure f_{csm} is obtained from the two-stage Ramberg-Osgood law (Mirambell & Real 2000, Rasmussen 2003, Gardner & Nethercot 2004a) which is multiplied by the gross cross-sectional area to yield the axial capacity. Similarly, a linear strain distribution for cross-sections subjected to bending is assumed and the corresponding stress distribution at failure is obtained, which is integrated to give the ultimate moment resistance about the respective axis. The CSM allows for a rational exploitation of strain hardening up to strains 15 times larger than the elastic strain at f_y in accordance with codified ductility requirements (EN 1993-1-4 2006, EN 1993-1-1 2005). A further restriction pertaining to the CSM is the slenderness of the cross-sections at which it is applied. Due to the non-monotonic nature of Equation (2) and to the possible shift in neutral axis of slender cross-sections (Rusch & Lindner 2001), which is not accounted for by the method, erroneous results may be obtained for slender cross-sections. A slenderness limit of 0.748 is adopted herein, beyond which the relevant cross-section capacity may be calculated from EN 1993-1-4 (2006). Among the cross-sections considered, the CSM was not applicable to RHS $200 \times 100 \times 3$ and $200 \times 100 \times 4$ under axial compression and minor axis bending.

4.2 *New interaction equations*

Following the aforementioned procedure, the axial, minor axis bending and major axis bending capacities of all sections were determined. The numerical failure loads were normalized by the respective capacities and utilized to derive a suitable interaction curve that fits the data. Two different interaction surfaces are defined by Equations (4) and (5):

$$\left(\frac{N_{Ed}}{N_{csm}}\right)^2 + \sqrt{\left(\frac{M_{y,Ed}}{M_{csm,y}}\right)^2 + \left(\frac{M_{z,Ed}}{M_{csm,z}}\right)^2} \leq 1 \tag{4}$$

$$\frac{N_{Ed}}{N_{csm}} + \sqrt{\left(\frac{M_{y,Ed}}{M_{csm,y}}\right)^2 + \left(\frac{M_{z,Ed}}{M_{csm,z}}\right)^2} \leq 1 \tag{5}$$

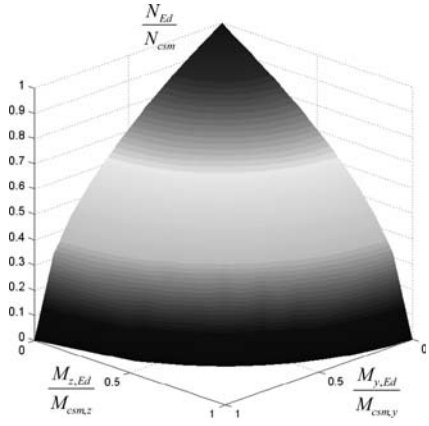

Figure 10. Interaction surface defined by Equation (4).

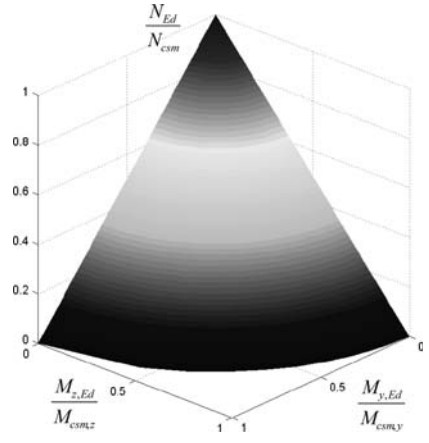

Figure 11. Interaction surface defined by Equation (5).

where N_{csm}, $M_{csm,y}$ and $M_{csm,z}$ are the axial resistance, the minor axis bending resistance and the major axis bending resistance from the CSM respectively. The proposed interaction surfaces are depicted in Figures 10 and 11.

4.2.1 *Compression and uniaxial bending*

In Figures 12–14 the proposed interaction curves are plotted together with the numerical failure loads normalized by the respective cross-section resistances determined by CSM. Overall an increased consistency of the predictions can be observed, as the normalized failure loads fall within a narrow band compared to the respective figures based on the codified resistances. Equation (4) provides an excellent fit to the numerical predictions for SHS as shown in Figure 10, whereas Equation (5) provides a more safe interaction surface for RHS. Differences between SHS and RHS can be largely attributed to the greater slenderness of the RHS which tends to produce a linear interaction between compression and bending, whilst this interaction appears more rounded for SHS.

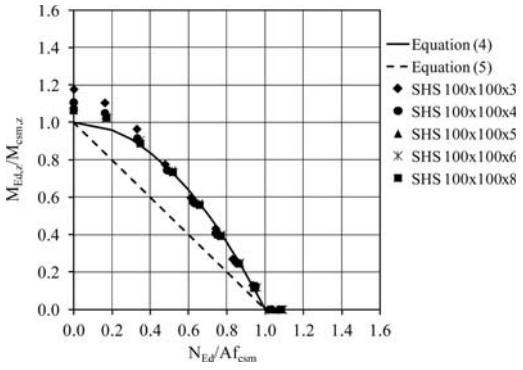

Figure 12. Interaction of axial compression and uniaxial bending ($N_{Ed} + M_{Ed,z}$, $M_{Ed,y} = 0$) for SHS.

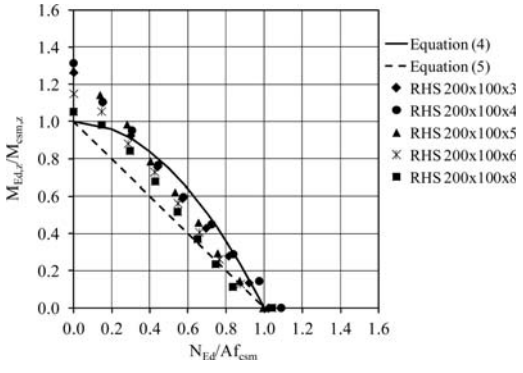

Figure 13. Interaction of axial compression and minor axis bending ($N_{Ed} + M_{Ed,z}$, $M_{Ed,y} = 0$) for RHS.

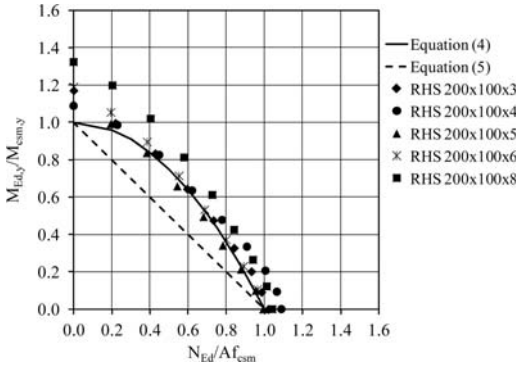

Figure 14. Interaction of axial compression and major axis bending ($N_{Ed} + M_{Ed,y}$, $M_{Ed,z} = 0$) for RHS.

4.2.2 *Biaxial bending*

In Figures 15 and 16 the interaction of major and minor axis bending is shown for SHS and RHS respectively. The proposed interaction equations coincide and closely follow the trend of the numerical data. A linear interaction is also depicted for comparison purposes.

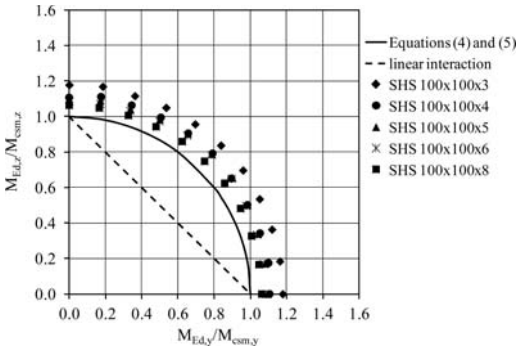

Figure 15. Interaction of major and minor axis bending ($M_{Ed,z} + M_{Ed,y}$, $N_{Ed} = 0$) for SHS.

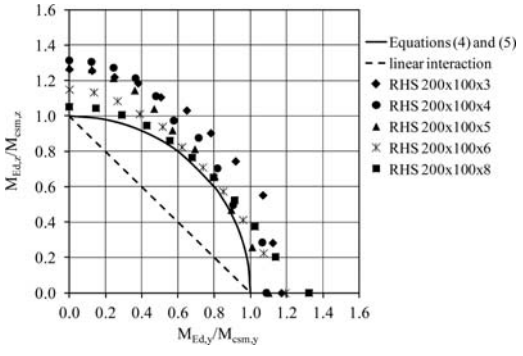

Figure 16. Interaction of major and minor axis bending ($M_{Ed,z} + M_{Ed,y}$, $N_{Ed} = 0$) for RHS.

Table 3. Assessment of proposed interaction equations (FE/predicted).

	Equation (4)		Equation (5)		Linear interaction	
	Mean	COV	Mean	COV	Mean	COV
SHS	0.91	0.07	0.80	0.07	0.75	0.12
RHS	0.99	0.09	0.85	0.05	0.77	0.08
ALL	0.95	0.09	0.83	0.07	0.76	0.11

4.2.3 *Compression and biaxial bending*

For the more general case of compression and biaxial bending, the accuracy of the proposed interaction Equations (4) and (5) is quantified in Table 3, which provides the FE/predicted utilization ratio, where the accuracy of a planar interaction surface is also included for comparison purposes.

4.3 *Simplified Continuous Strength Method*

The CSM has been shown to offer significant advantages over alternative design methods in ultimate capacity predictions, both in terms of design efficiency as well as in terms of consistency of the predictions. However its application to cross-sections in bending is cumbersome due to the fact that the employed material model, albeit accurate, does not lend itself to explicit design equations. To this end, simplifications to the CSM are proposed herein for stainless steel by adopting the simple bilinear material model (Gardner 2008) shown in Figure 17 and a simplified base curve (Gardner et al. 2010), with coefficients determined on the basis of both carbon steel and stainless steel test data.

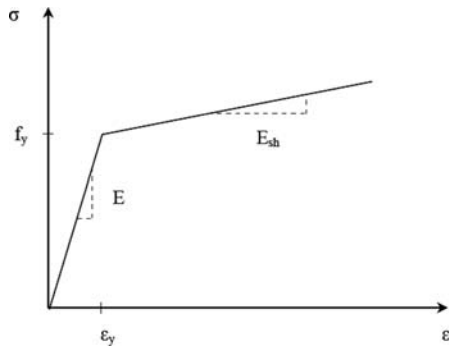

Figure 17. Bilinear elastic-strain hardening material model.

Table 4. Assessment of simplified CSM (FE/predicted).

	Equation (4)		Equation (5)		Linear interaction	
	Mean	COV	Mean	COV	Mean	COV
SHS	0.93	0.08	0.82	0.08	0.80	0.12
RHS	1.04	0.10	0.89	0.07	0.81	0.08
ALL	0.99	0.10	0.86	0.09	0.81	0.11

The strain-hardening modulus is given by Equation (6) and the maximum attainable strain ε_{csm} is given by Equation (7), with the upper strain limit corresponding to the strain at the 1% proof stress:

$$E_{sh} = \frac{f_{1.0} - f_y}{0.008 + (f_{1.0} - f_y)\frac{1}{E}} \tag{6}$$

$$\frac{\varepsilon_{csm}}{f_y/E} = \frac{0.4}{\bar{\lambda}_p^{-3.25}} \text{ but} \leq \frac{0.01 + f_{1.0}/E}{f_y/E} \tag{7}$$

With the adopted material model the ultimate moment resistance M_{csm} is given (Gardner et al. 2011) by Equation (8):

$$\frac{M_{csm}}{M_{pl}} = 1 + \frac{E_{sh}}{E}\frac{W_{el}}{W_{pl}}\left(\frac{\varepsilon_{csm}}{\varepsilon_y} - 1\right) - \left(1 - \frac{W_{el}}{W_{pl}}\right)\left(\frac{\varepsilon_{csm}}{\varepsilon_y}\right)^{-2} \tag{8}$$

The simplified CSM is assessed in Table 4, which provides the FE/predicted utilization ratio, where the interaction Equations (4) and (5) and a linear interaction are shown. Equation (4) provides and the most efficient design predictions (with a slightly higher COV). It is proposed that this equation in conjunction with the simplified CSM be adopted. Comparing the simplified CSM predictions (Table 4) with the original CSM predications (Table 3) reveals similar

results – the simplifications in fact result in a slightly improved mean prediction though a slightly higher scatter. Both the original and simplified CSM show a considerable improvement over current practice (Table 2).

5 CONCLUSIONS

An extensive parametric study on stainless steel RHS subjected to a combination of loads was summarized and the results were presented. The current design provisions of EN 1993-1-4 (2006) were assessed on the basis of the numerical failure loads and were found to be unduly conservative. The conservatism is attributed to the significant strain-hardening of the material, which is not explicitly accounted for in EN 1993-1-4 (2006). Possible remedies of the above conservatism include the determination of the cross-section capacities based on the CSM and more refined interaction curves. Moreover, a simplification to the original CSM is proposed, by adopting a bilinear material model, which allows for explicit ultimate capacity predictions, thereby eliminating the need for cumbersome numerical integration. Both the original CSM, as well as the simplified one offer improved predictions of cross-sectional capacity over the respective EN 1993-1-4 (2006) predictions both in terms of consistency and design efficiency. The adoption of interaction Equation (4) in conjunction with the simplified CSM for the design of stainless steel cross-sections under combined loading is proposed, based on the findings of the extensive numerical study reported herein; experimental validation is warranted. Moreover, the proposed interaction equations have to be verified for other cross-sectional shapes commonly adopted in practical applications.

REFERENCES

ABAQUS/Standard user's manual volumes I-III and ABAQUS CAE manual. Version 6.6. (Pawtucket, USA): Hibbitt, Karlsson & Sorensen, Inc. 2006.

Ashraf, M., Gardner, L. & Nethercot, D.A. 2006. Compression strength of stainless steel cross-sections. Journal of Constructional Steel Research 62(1–2): 105–115.

Ashraf, M., Gardner, L. & Nethercot, D.A. 2008. Structural stainless steel design: Resistance based on deformation capacity. Journal of Structural Engineering, ASCE 134(3): 402–411.

Becque, J., Lecce, M. & Rasmussen, K.J.R. 2008. The direct strength method for stainless steel compression members. Journal of Constructional Steel Research 64(11): 1231–1238.

Burgan, B.A., Baddoo, N.R. & Gilsenan, K.A. 2000. Structural design of stainless steel members–comparison between Eurocode 3, Part 1.4 and test results. Journal of Constructional Steel Research. 54(1): 51–73.

Cruise, R.B. & Gardner, L. 2008. Strength enhancements induced during cold forming of stainless steel sections. Journal of Constructional Steel Research 64(11): 1310–1316.

Dawson, R.G. & Walker, A.C. (1972). Post-buckling of geometrically imperfect plates. Journal of the Structural Division, ASCE. 98:ST1, 75–94.

EN 1993-1-1. 2005. Eurocode 3. Design of Steel Structures: Part 1-1: General rules and rules for buildings. CEN.

EN 1993-1-4. 2006. Eurocode 3: Design of steel structures: Part 1.4: General rules – Supplementary rules for stainless steel. CEN.

Gardner, L. (2008). The Continuous Strength Method. Proceedings of the Institution of Civil Engineers – Structures and Buildings. 161(3): 127–133.

Gardner, L. & Nethercot, D.A. 2004a. Experiments on stainless steel hollow sections – Part 1: Material and cross-sectional behaviour. Journal of Constructional Steel Research, 60(9): 1291–1318.

Gardner L. & Nethercot D.A. 2004b. Experiments on stainless steel hollow sections – Part 2: Member behaviour of columns and beams. Journal of Constructional Steel Research, 60(9): 1319–1332.

Gardner, L. & Nethercot D.A. 2004c. Numerical Modeling of Stainless Steel Structural Components-A Consistent Approach. Journal of Structural Engineering, ASCE 130(10): 1586–1601.

Gardner, L. & Theofanous, M. 2008. Discrete and continuous treatment of local buckling in stainless steel elements. Journal of Constructional Steel Research 64(11): 1207–1216.

Gardner, L., Wang, F. & Liew, A. (2011). Influence of strain hardening on the behavior and design of steel structures. International Journal of Structural Stability and Dynamics. 11(5), 855–875.

Greiner, R. & Kettler, M. 2008. Interaction of bending and axial compression of stainless steel members. Journal of Constructional Steel Research 64(11): 1217–1224.

Groth, H.L. & Johansson, R.E. 1990. Statistics of the mechanical strength of stainless steels. Proc. of the Nordic Symposium on Mechanical Properties of Stainless Steels SIMR, Sigtuna, Sweden October 1990: 17–31.

Jandera, M., Gardner, L., Machacek, J. 2008. Residual stresses in cold rolled stainless steel hollow sections, Journal of Constructional Steel Research 64(11): 1255–1263.

Li, Z. & Schafer, B.W. 2010. Buckling analysis of cold-formed steel members with general boundary conditions using CUFSM: conventional and constrained finite strip methods Proc. of the 20th Int. Spec. Conf. on Cold-Formed Steel Structures, St. Louis, MO. November, 2010.

Mirambell, E. & Real, E. 2000. On the calculation of deflections in structural stainless steel beams: an experimental and numerical investigation. Journal of Constructional Steel Research 54(1): 109–133.

Rasmussen, K.J.R. 2003. Full-range stress-strain curves for stainless steel alloys. Journal of Constructional Steel Research 59(1): 47–61.

Rossi, B., Degée, H. & Pascon, F. 2009. Enhanced mechanical properties after cold process fabrication of non-linear metallic profiles. Thin-Walled Structures 47(12): 1575–1589.

Rusch, A. & Lindner, J. 2001. Remarks to the Direct Strength Method. Thin-Walled Structures 39(9): 807–820.

Schafer, B.W. 2008. Review: The Direct Strength Method of cold-formed steel member design. Journal of Constructional Steel Research 64(7–8): 766–778.

Talja, A. & Salmi, P. (1995). Design of stainless steel RHS beams, columns and beam-columns. Research Note 1619, VU Building Technology, Finland.

Theofanous, M. & Gardner, L. 2012. Effect of element interaction and material nonlinearity on the ultimate capacity of stainless steel cross-sections. Steel and Composite Structures 12(1): 73–92.

Tubular Structures XIV – Gardner (Ed.)
© 2012 Taylor & Francis Group, London, ISBN 978-0-415-62137-3

Eccentric compression tests on high strength duplex stainless steel columns

W.M. Lui
Department of Civil Engineering, Hong Kong University of Science and Technology, Hong Kong, China

B. Young
Department of Civil Engineering, The University of Hong Kong, Hong Kong, China

M. Ashraf
School of Engineering and Information Technology, The University of New South Wales, Canberra, Australia

ABSTRACT: Attractive appearance, corrosion resistance and ease of maintenance are the obvious reasons for widespread use of stainless steel in a variety of structures, whilst beneficial mechanical properties such as high ductility, better fire resistance and high strength demonstrated by the duplex grades add significant value to the aesthetics of stainless steel. Reliable experimental investigations are a prerequisite to explore the full potential of stainless steel members and to evaluate the performance of the existing design rules. The current paper describes a test program on cold-formed stainless steel SHS columns subjected to eccentric compression to investigate beam-column interaction. Considered cross-sections were produced from high strength duplex stainless steel with the measured yield stress up to 700 MPa. Material properties were obtained from the tensile coupons cut from within the cross-sections, whilst initial geometric imperfections were measured at mid-height of each of the pin-ended column specimens. Two different column lengths were considered with varying eccentricity for each specimen. The strength and behaviour of the cold-formed high strength stainless steel beam-columns were investigated. The test resistances were compared with those predicted using the American and the Australian/New Zealand design specifications for cold-formed stainless steel structures. It is observed that the code predictions are mostly conservative for stainless steel beam-columns with rooms for improvement in the available design guidance.

1 INTRODUCTION

In recent times, stainless steel is being regarded as more of a construction material rather than using it for its obvious aesthetic appeal. Stainless steel is recyclable, offers extended life span for structures and requires negligible maintenance; all these special advantages are promoting widespread use of stainless steel in structures. Sluice and flood gates in Tampere Finland, spillway control system in Adelaide Australia, Stockholm Waterfront project and 'The Helix Bridge' in Singapore are only a few examples of versatile applications of stainless steel in construction. The last decade has seen the development of major design codes for cold-formed structural stainless steel. Preliminary design rules, however, were mostly based on assumed analogies with carbon steel; this process provided an easier transition for the practitioner engineers to adopt stainless steel, although it deemed to be a costly assumption for an expensive material like stainless steel. Testing schemes on stainless steel members reported by Rasmussen and Hancock (1993a, b), Talja and Salmi (1995), Gardner and Nethercot (2004a, b), Young and Hartono (2002), Young and Lui (2005), Young and Liu (2003) provided useful experimental evidence, although there is considerable lack in test data for stainless steel members to appropriately validate the currently proposed design rules. It is now evidenced that stainless steel offers pronounced strain hardening without showing any well defined yield point, which requires the currently available stainless steel design codes to be modified to include the observed discrepancies between stainless steel and carbon steel.

Tests on individual beams and columns are available in a number of reported literatures but very limited experimental evidence is available on the beam-column interaction of stainless steel members. Becque and Rasmussen (2009a, b) recently reported experimental results on beam-column interaction of lipped channel and I sections produced from Grade 304 stainless steel. The current research investigates the beam-column interaction for square hollow sections by applying eccentric loading on pin-ended columns. Four different series of SHS columns were subjected to compression with various eccentricities. Structural performance of the considered columns are compared against those predicted by the American SEI/ASCE-02

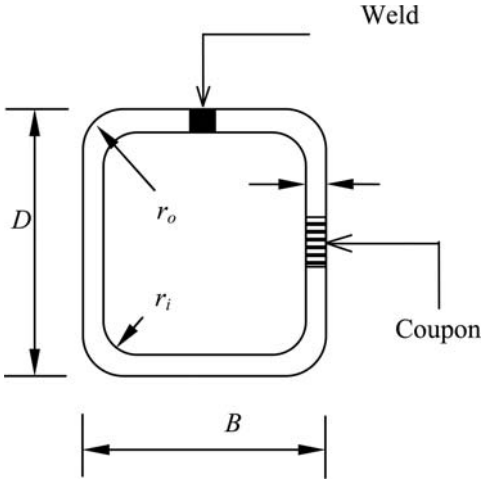

Figure 1. Definition of symbols and the location of the tensile coupon in cross-section.

(2002) and the Australia/New Zealand Standard AS/NZS 4673 (2001). Experimental interaction curves for the test specimens are also plotted against those obtained using design codes.

2 TEST SPECIMENS

Eccentric compression tests were performed on two square hollow sections, which were cold-rolled from annealed flat strips of Grade 2205 duplex stainless steel. One of the SHS specimens had nominal dimensions of 40 mm × 40 mm with a thickness of 2 mm (S1), whilst the other one was 50 mm × 50 mm with a thickness of 1.5 mm (S2). The specimens were supplied by the manufacturer in uncut lengths of 3400 mm, which were cut into two different lengths of 550 mm (L1) and 1100 mm (L2). Both ends were welded to carbon steel end plates to ensure full contact between the specimen and the end bearings. The l_e/r_y ratio, where l_e is the effective length of the column and r_y is the radius gyration about the minor y-axis, of the considered beam-column specimens were 42, 78, 32 and 60 for Series S1L1, S1L2, S2L1 and S2L2 respectively. It is worth mentioning that the effective length l_e is equal to the actual column length between knife-edges, which includes the length of the SHS specimen and the thickness of both the end plates and the bearing plates. Four considered series were tested at various eccentricities varying from 0 to 60 mm. Table 1 lists the measured cross-section dimensions of the test specimens using the nomenclature defined in Figure 1.

The test specimens were labelled such that the series and specimen eccentricity could be identified from the label. Adopted labelling technique includes cross-section size – S1 for 40 × 40 × 2 and S2 for 50 × 50 × 1.5, length of the specimen – L1 and L2 refers to 550 mm and 1100 mm respectively and eccentricity is denoted by the letter E and followed by a number showing the eccentricity in mm.

Table 1. Measured dimensions for column specimens.

Series	Specimen	Depth D (mm)	Width B (mm)	Thickness t (mm)	Length L (mm)	Eccentricity e (mm)
S1L1	S1L1E00	40.3	39.9	1.918	550	0
	S1L1E00*	40.2	39.9	1.919	550	0
	S1L1E10	40.2	39.9	1.920	549	10
	S1L1E25	40.2	39.9	1.921	550	25
	S1L1E60	40.1	40.0	1.920	549	60
S1L2	S1L2E00	40.2	40.0	1.951	1100	0
	S1L2E10	40.3	39.9	1.956	1100	10
	S1L2E25	40.3	40.2	1.949	1100	27
	S1L2E60	40.2	39.9	1.972	1100	60
	S1L2E60*	40.1	40.0	1.943	1100	60
S2L1	S2L1E00	50.2	50.1	1.537	550	0
	S2L1E10	50.3	50.0	1.536	550	10
	S2L1E10*	50.2	50.0	1.548	550	10
	S2L1E25	50.2	50.1	1.531	550	25
	S2L1E60	50.1	50.0	1.537	550	60
S2L2	S2L2E00	50.2	50.1	1.535	1100	0
	S2L2E10	50.1	50.0	1.543	1100	10
	S2L2E10*	50.2	49.9	1.535	1100	10
	S2L2E25	50.1	50.0	1.527	1099	25
	S2L2E60	50.2	50.0	1.534	1100	60

Note: * refers to 2nd test.

Table 2. Measured material properties obtained from tensile coupon tests.

Test series	$\sigma_{0.2}$ (MPa)	σ_u (MPa)	E_o (GPa)	ε_f (%)	n
S1L1 and S1L2	707	827	216	29	4
S2L1 and S2L2	622	770	200	37	5

3 MATERIAL PROPERTIES

Tensile coupon tests were conducted to obtain the material properties of the test specimens. Longitudinal tensile coupons were taken from the centre of the face, which is perpendicular to the welded face, as shown in Figure 1. The coupon dimensions conformed to the Australian Standard AS 1391 (2007) for the tensile testing of metals using 12.5 mm wide coupon with a gauge length of 50 mm. Important mechanical properties such as the static 0.2% proof stress ($\sigma_{0.2}$), static tensile strength (σ_u), initial Young's modulus (E_o) and elongation after fracture (ε_f), as obtained from the coupon tests, are summarised in Table 2. The magnitudes of Ramberg-Osgood exponent n determined from the measured stress-strain curves are also reported in Table 2.

4 INITIAL GEOMETRIC IMPERFECTIONS

Initial geometric imperfection is an inevitable feature of thin-walled members, which could significantly

Table 3. Measured overall geometric imperfections at mid-length for specimens with L = 1000 mm.

Series	δ_{oy}/L
S1L2E00	1/3331
S1L2E10	1/7874
S1L2E25	1/656
S1L2E60	1/601
S1L2E60#	1/509
S2L2E00	1/5769
S2L2E10	1/893
S2L2E10#	1/4559
S2L2E25	1/5769
S2L2E60	1/1031

affect their structural performance. The magnitude and distribution of geometric imperfections are, though, highly uncertain and hence it is important to take measurements to identify if there is any notable geometric irregularity. In the current research, initial local and overall geometric imperfections of the column specimens were measured prior to testing. Local geometric imperfections were measured using a Mitutoyo Co-ordinate Measuring Machine with an accuracy of 0.001mm, whilst a theodolite was used to measure overall imperfections at the mid-length. Measured geometric imperfections at mid-length for specimens S1L2 and S2L2 are shown in Table 3. The average overall imperfections at mid-length were 1/939 and 1/1883 of the specimen length for Series S1L2 and S2L2 respectively. The maximum initial local geometric imperfection for the S1 series was 0.113, whilst that for Series S2 was 0.164 mm.

5 COLUMN TESTING RIG AND THE ADOPTED PROCEDURE

Figure 2 shows an illustration of the testing rig used for beam-column tests. A multi-channel DARTEC testing system was used to apply compressive axial force to the specimens. Applied eccentric loads resulted in equal and opposite end moments to the specimens causing overall bending in single curvature ($\beta = -1$). The upper end support of the test rig was movable to allow tests to be conducted at different specimen lengths. The pin-ended bearing, as shown in Figure 3, was used to allow free rotation about minor axis. The bearing includes two parts – a plate containing a knife-edged wedge (wedge plate), which allows the end plates to be bolted at various eccentricities, and a plate containing a long V-shaped pit (pit plate). One of the pit plates was connected to the upper end support, whilst the other pit plate was connected to the lower spherical rocker bearing. Two end plates attached to the specimen were bolted to the wedge plates at a specified eccentricity. Later, the specimen, together with the bolted wedge plates, was placed into the machine so that the wedge fits into the pit. The ram of the actuator was slowly

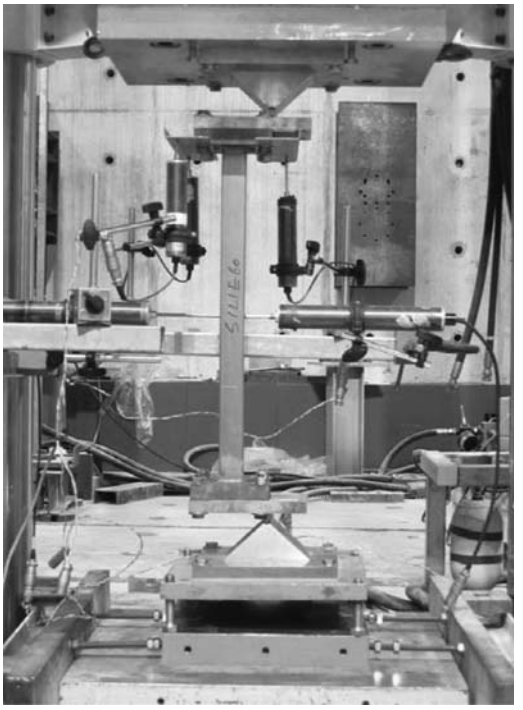

Figure 2. Test rig for beam-column tests (2500 kN capacity).

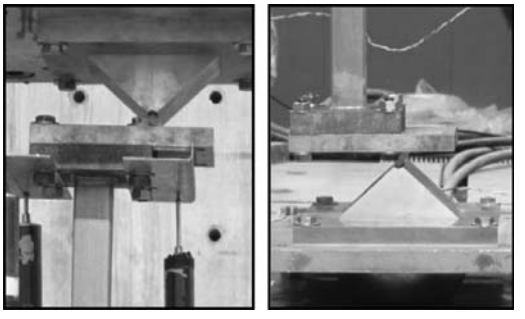

Figure 3. Pin-ended bearings at both ends.

lifted downwards until the pits could hold the specimen without any manual support. The spherical bearing was free to rotate in any directions during this initial loading stage. The position of the specimen was adjusted to ensure the edge of the pin-ended wedge was in line with the V-shaped pit. To close the gap and to ensure full contact, a compressive load of 3 kN was applied. At this point, the spherical rocker bearing was restrained from any rotation by tightening the vertical and the horizontal bolts. This arrangement confirmed the pin-ended condition allowing uniaxial bending. The applied load was released to approximately 1kN so that the test commences with a small initial load. Two steel stripes were bolted to the upper end plate,

which had two parallel lines drawn on them as shown in Figure 4. Three vertical displacement transducers were positioned and pointed to the drawn lines to measure the axial shortening of the specimen and to calculate the rotation of the specimen. Meanwhile, two horizontal displacement transducers were positioned and pointed to the middle of the column to measure the lateral deflection of the specimen. Displacement control technique was used to drive the hydraulic actuator at a constant speed of 0.5mm/min; this process allowed the test to continue to post-ultimate stage. A data acquisition system was used to record the applied load and the readings obtained from the displacement transducers at regular intervals during the test. The static load was recorded by halting the applied displacement for 1.5 minutes near the ultimate load; this allowed the stress relaxation associated with plastic straining to take place.

Figure 4. Two steel stripes bolted to the upper end plate with two parallel lines drawn.

6 TEST RESULTS

The ultimate axial load N_u, the ultimate maximum inelastic moments M_{mi} and the corresponding end moments M_{end} as obtained from the beam-column tests are summarized in Table 4. The ultimate maximum inelastic moment M_{mi} was calculated as the sum of the end moment M_{end} measured at the ultimate load N_u and the second-order moment $\delta_u N_u$, where δ_u is the maximum deflection at mid-length measured at the ultimate load.

A number of duplicate specimens were tested with eccentricities of 0, 60, 10 and 10 mm for Series S1L1, S1L2, S2L1 and S2L2 respectively. Discrepancies observed between the measured δ_u for the original specimens and those for the corresponding duplicate specimens were negligible for Series S1 but the difference was in the order of 5 to 10% for Series S2; this was largely due to the difficulty in adjusting an accurate eccentricity for the Series S2 specimens. Failure modes observed for the beam-column specimens showed overall flexural buckling (F) and combined

Table 4. Comparison of test strengths with design strengths .

	Test						Comparison	
Specimen	Failure mode	l_e (mm)	N_u (kN)	M_{end_u} (kNm)	M_{mi_u} (kNm)	M_{me_u} (kNm)	$\frac{M_{end_u}}{M_{ASCE}}$	$\frac{M_{end_u}}{M_{AS/NZS}}$
S1L1E00	F	630	160.6	0.00	0.37	0.00	1.06	1.07
S1L1E00#	F	630	161.0	0.00	0.48	0.00	1.06	1.07
S1L1E10	F	629	97.5	0.98	2.10	1.38	1.19	1.14
S1L1E25	F	630	60.6	1.52	2.52	1.86	1.16	1.08
S1L1E60	F	629	36.9	2.21	3.03	2.49	1.27	1.16
S1L2E00	F	1180	76.8	0.00	0.90	0.00	0.97	1.04
S1L2E10	F	1180	56.9	0.57	2.11	1.40	1.19	1.19
S1L2E25	F	1180	39.5	1.07	2.62	1.81	1.14	1.11
S1L2E60	F	1180	25.6	1.54	2.74	2.10	1.16	1.10
S1L2E60#	F	1180	24.9	1.49	2.58	2.02	1.12	1.06
S2L1E00	L + F	630	157.6	0.00	0.60	0.00	1.05	1.06
S2L1E10	L + F	630	99.7	1.00	1.85	1.22	1.12	1.12
S2L1E10#	L + F	630	104.8	1.05	1.80	1.30	1.18	1.18
S2L1E25	L + F	630	66.9	1.67	2.30	1.91	1.16	1.16
S2L1E60	L + F	630	40.6	2.44	2.96	2.63	1.26	1.26
S2L2E00	F	1180	81.2	0.00	1.28	0.00	0.75	0.81
S2L2E10	F	1180	70.7	0.71	2.33	1.30	1.11	1.15
S2L2E10#	F	1180	62.6	0.63	2.23	1.05	0.99	1.02
S2L2E25	F	1179	50.0	1.25	2.76	1.84	1.13	1.16
S2L2E60	L + F	1180	31.2	1.87	3.00	2.34	1.15	1.17
						Mean	1.11	1.11
					Coefficient of variation (COV)		0.103	0.083

local and overall flexural buckling (L + F). Figure 5 shows failure modes for all test specimens. Formation of plastic hinges was observed in specimens for Series S2L1 and S2L2 as the overall depth-to-thickness D/t ratios are comparatively larger than those for Series S1L1 and S1L2.

Figures 6 and 7 show the axial load versus moment curves for Series S1L2 and S2L1. Both the end moment M_{end} and the inelastic moment M_{mi} ($=M_{end} + N\delta$) are plotted against axial load N. End moment M_{end} varies linearly with axial load N, whilst inelastic moment M_{mi} increases nonlinearly with N as M_{mi} is affected by the lateral deflection δ at mid-length. Moment-rotation and load-deflection curves were recorded for all eccentrically loaded test specimens. Lateral deflection δ at mid-height is the sum of the measured initial geometric imperfection δ_o and the lateral displacement caused by bending δ_1. Figure 8 shows the obtained moment-rotation and load-deflection curves for Series S1L2.

7 DESIGN RULES FOR STAINLESS STEEL BEAM-COLUMN INTERACTION

The design strengths of the cold-formed stainless steel eccentrically loaded beam-columns were predicted using the SEI/ASCE-02 (2002) and AS/NZS 4673 (2001) specifications. It is worth noting that the design rules specified both in ASCE Specification and AS/NZ Standard adopt the same interaction equations for stainless steel beam-columns. Although, the predicted design strengths for beam-columns are not always equal due to the difference in formulations used to obtain resistances against individual actions i.e. compression resistance of the cross-section N_s, compression resistance of the member N_c and bending resistance M_b. The following interaction equations are proposed both in ASCE and AS/NZS design guidance for SHS cross-sections:

$$\frac{N_{ASCE}}{N_c} + \frac{C_m M_{ASCE}}{M_b \alpha_n} \le 1.0 \quad (1)$$

$$\frac{N_{ASCE}}{N_s} + \frac{M_{ASCE}}{M_b} \le 1.0 \quad (2)$$

$$\frac{N_{ASCE}}{N_c} + \frac{M_{ASCE}}{M_b} \le 1.0 \quad (3)$$

N_{ASCE} and M_{ASCE} are the compression force and the simultaneous bending moment that can be safely applied to a given member following ASCE guidelines. These two parameters are related using the relationship $M_{ASCE} = e.N_{ASCE}$, where e is the loading eccentricity. C_m is a coefficient for unequal end moment, whilst α_n

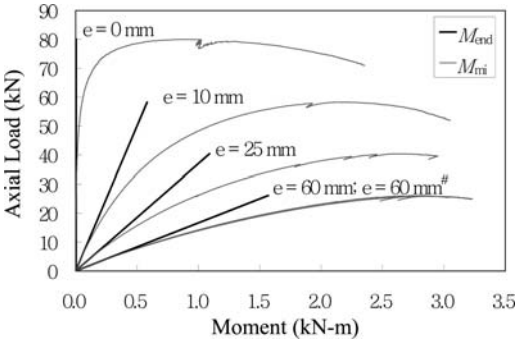

Figure 6. Axial load versus moment curves for Series S1L2.

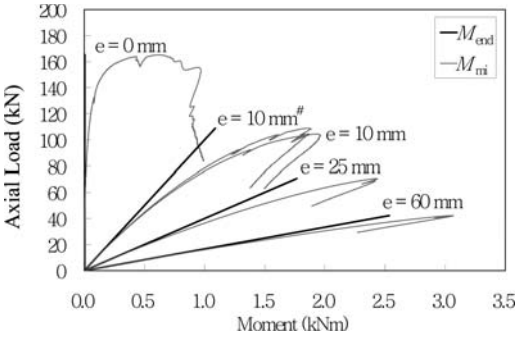

Figure 7. Axial load versus moment curves for Series S2L1.

Figure 5. Observed failure modes for the beam-column specimens.

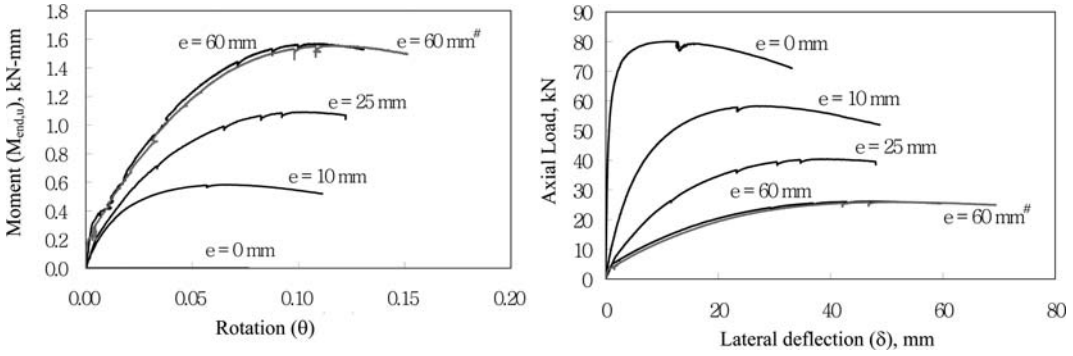

Figure 8. Moment-rotation and load-deformation curves for series S1L2.

is the moment amplification factor and N_e is the Euler's buckling load. Equations 4 and 5 show the expressions to calculate α_n and N_e, where E_o is the Young's modulus, I_b is the moment of inertia of full, unreduced cross-section about the axis of bending, l_{eb} is the effective length in the plane of bending.

$$\alpha_n = 1 - \frac{N_{ASCE}}{N_e} \tag{4}$$

$$N_e = \frac{\pi^2 E_o I_b}{l_{eb}^2} \tag{5}$$

For a given cross-section with known material and boundary conditions, N_{ASCE} can be easily obtained to satisfy the aforementioned three constraint equations. Hence the simultaneous bending moment for safe beam-column interaction can be easily determined using the knowledge of eccentricity e. In the case of AS/NZ Standard, as well, Equations 1–4 are used to determine the axial force $N_{AS/NZS}$ and the corresponding moment $M_{AS/NZS}$. The magnitudes obtained for $N_{AS/NZS}$ and $M_{AS/NZS}$ are, however, different from those of N_{ASCE} and M_{ASCE} due to the differences in calculation of N_s, N_c and M_b.

ASCE Specification adopts an iterative design procedure to determine the resistance of a member subjected to pure compression. The design rules of the AS/NZ Standard allow the option to use either the Euler column curve or the Perry curve to determine compression resistance; the second approach was used in the current research to predict beam-column interaction following AS/NZ Standard. Imperfection parameters α, β, λ_o and λ_1, as adopted in AS/NZS Standard, are determined using the equations proposed by Rasmussen and Rondal (1997). The calculated values of the parameters α, β, λ_o and λ_1 are 1.262, 0.191, 0.701 and 0.404 respectively for section S1 ($40 \times 40 \times 2$), whilst those for section S2 ($50 \times 50 \times 1.5$) are 1.066, 0.117, 0.686 and 0.488 respectively. It is worth mentioning that these parameters depend on material properties, which were obtained through tensile coupon tests in the current study.

The ASCE Specification predicts the bending resistance of a box type cross-section on the basis of initiation of yielding. The AS/NZ Standard, on the other hand, predicts the bending resistance for a compact section i.e. section S1 ($40 \times 40 \times 2$), based on plastic yielding; whilst that for a non-compact section i.e. section S2 ($50 \times 50 \times 1.5$), is determined based on initiation of yielding, which is similar to the technique adopted in ASCE Specification.

8 TEST RESISTANCE VS CODE RESISTANCE

8.1 *General*

Experimentally obtained compression resistance N_u and the simultaneous bending resistance $M_{end,u}$ for the considered beam-column specimens are compared with the unfactored design resistances predicted using the American (ASCE 2002) and the Australian/New Zealand (AS/NZS 2001) specifications for cold-formed stainless steel structures. Material properties obtained from the tensile coupon tests as shown in Table 2 are used to predict beam-column action. Table 4 compare the experimental results with those obtained using ASCE and AS/NZS specifications. It is worth mentioning that the bending resistance $M_{end,u}$ is a multiple of compression resistance N_u i.e. $M_{end,u} = e.\ N_u$. Hence, for a given eccentricity, the ratio of the compression resistance i.e. N_u/N_{ASCE} is the same as the ratio of bending resistance $M_{end,u}/M_{ASCE}$.

8.2 *Interaction curves for the beam-column specimens*

Figures 9 and 10 compare the resistances of Series S1L1 and S2L2 beam-column specimens obtained from experiments to those computed using design codes. The axial compressive loads are plotted against the second-order elastic moments. End moments determined using the code guidelines were converted to second-order elastic moments to be in line with the interaction diagrams specified in ASCE and AS/NZS

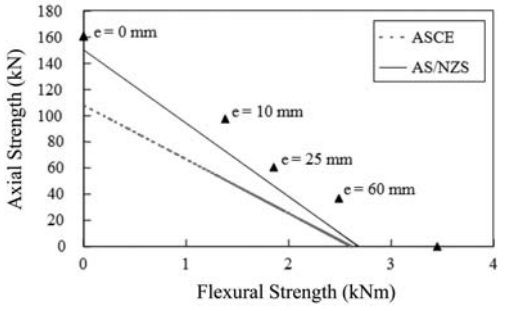

Figure 9. Interaction curves for Series S1L1.

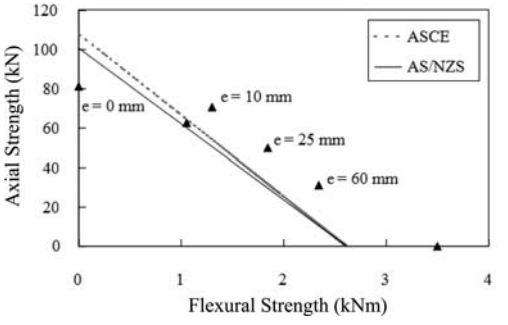

Figure 10. Interaction curves for Series S2L2.

Standards. The design second-order elastic moment M^D_{me} was calculated as the product of the design end moment M^D_{end} and the amplification factor given by Equation 6, in which N was replaced by the design axial compressive load N^D, whilst N_e is the elastic flexural buckling load as given by Equation 4.

$$\delta_b = \frac{1}{1 - N/N_e} \tag{6}$$

Experimentally obtained end moments were also converted to second-order elastic moment following a similar approach. The experimental second-order elastic moment $M_{me,u}$ was calculated as the product of the end moment at ultimate load $M_{end,u}$ and the amplification factor α_n as shown in Equation 4, in which N was replaced by the ultimate axial force N_u. The values of the experimental second-order elastic moments $M_{me,u}$ are also shown in Table 4.

8.3 *Discussion*

Most of the design resistances predicted by the ASCE and the AS/NZS specifications are observed to be conservative. Material properties obtained from the tensile coupon tests have been used in the calculation process. Code guidelines, however, produced some unsafe predictions for longer specimens, i.e. Series L2, with smaller eccentricities. For the specimen S1L2E00 the ratio of the test resistance to the ASCE prediction N_u/N_{ASCE} was 0.97, whilst that for the S1L2E00 specimen was 0.75. Table 4 shows the mean values and coefficients of variation (COV) of ratio of the test N_u to those obtained using the ASCE and the AS/NZS specifications. It is observed that the AS/NZS Standard produces slightly more consistent predictions than those obtained using the ASCE guidelines.

9 CONCLUSION

A test program on cold-formed high strength stainless steel beam-columns has been presented. The specimens were produced from duplex stainless steel. Two SHS cross-sections and two different column lengths were combined to obtain four series of beam-column specimens, which were compressed between pin ended supports at different eccentricities and interaction curves were obtained for each test series. The test strengths were compared with the design strengths predicted using the American and Australian/New Zealand specifications for cold-formed stainless steel structures. It is shown that the design strengths predicted by the two specifications using the material properties obtained from tensile coupon tests are generally conservative for the cold-formed high strength stainless steel square hollow section columns. From the values of COV of the N_u/N_{ASCE} and $N_u/N_{AS/NZS}$ ratios, it is observed that the design rules of the AS/NZ Standard are comparatively more consistent. It is obvious from the comparisons that there is room for improvement in the design rules. It is shown that the code predictions are mostly conservative for duplex stainless steel beam-columns. Performance of the European standard is currently being investigated to come up with modified formulation to accurately predict the beam-column behaviour of stainless steel sections.

REFERENCES

AS1391-2007. 2007. Metallic materials – Tensile testing at ambient temperature, Standards Australia.

AS/NZS-4673. 2001. Cold-Formed Stainless Steel Structures, Australian Standard/New Zealand Standard.

A. Talja & P. Salmi. 1995. Design of stainless steel RHS beams, columns and beam-columns, in, VTT Building Technology, Finland.

B. Young & W. Hartono. 2002. Compression Tests of Stainless Steel Tubular Members, Journal of Structural Engineering, 128: 754–761.

B. Young & W.M. Lui. 2005. Behavior of Cold-Formed High Strength Stainless Steel Sections, Journal of Structural Engineering, 131: 1738–1745.

B. Young & Y. Liu. 2003. Experimental Investigation of Cold-Formed Stainless Steel Columns, Journal of Structural Engineering, 129: 169–176.

J. Becque & K.J.R. Rasmussen. 2009a. Experimental investigation of local-overall interaction buckling of stainless steel lipped channel columns, Journal of Constructional Steel Research, 65: 1677–1684.

J. Becque & K.J.R. Rasmussen. 2009b. Experimental Investigation of the Interaction of Local and Overall Buckling of Stainless Steel I-Columns, Journal of Structural Engineering, 135: 1340–1348.

K.J.R. Rasmussen & G.J. Hancock. 1993a. Design of Cold-Formed Stainless Steel Tubular Members. I: Columns, Journal of Structural Engineering, 119: 2349–2367.

K.J.R. Rasmussen & G.J. Hancock. 1993b. Design of Cold-Formed Stainless Steel Tubular Members. II: Beams, Journal of Structural Engineering, 119: 2368–2386.

L. Gardner & D.A. Nethercot. 2004a. Experiments on stainless steel hollow sections–Part 2: Member behaviour of columns and beams, Journal of Constructional Steel Research, 60: 1319–1332.

L. Gardner & D.A. Nethercot. 2004b. Experiments on stainless steel hollow sections–Part 1: Material and cross-sectional behaviour, Journal of Constructional Steel Research, 60: 1291–1318.

Outokumpu. 2011. (Web source) Industry Offerings: Architecture, Building and Construction, in: http://www.outokumpu.com/Industry-offerings/Architecture-Building-and-Construction/.

SEI/ASCE-8-02. 2002. Specifications for the design of cold-formed stainless steel structural members, American Society of Civil Engineers.

Tubular Structures XIV – Gardner (Ed.)
© 2012 Taylor & Francis Group, London, ISBN 978-0-415-62137-3

Lean duplex stainless steel hollow stub columns of Square, L-, T-, and +−shaped cross sections under pure axial compression – a finite element study

M.L. Patton & K.D. Singh
Civil Engineering Department, Indian Institute of Technology Guwahati, India

ABSTRACT: In this paper, Finite Element (FE) studies for LDSS (Lean Duplex Stainless Steel) square, L, T, and +−shaped hollow stub columns (i.e. SHC, LHC, THC and +HC, respectively) are presented using Abaqus, to gain an understanding of the cross-sectional shape effects. The LDSS SHC is compared with its counter NRHCs (Non-rectangular hollow columns i.e. LHC, THC and +HC) having equal material cross-sectional areas (or equal material consumption) with thickness varying from 5 to 20 mm, under uniform axial compression. Columns with lengths (∼1800 mm) of about three times the outer width of square were considered for the analyses. Based on the analyses, it has been found that for all the NRHCs considered, a nearly linear variation of P_u (ultimate laod) with section thicknesses has been observed, although the increase for SHC was relatively slower in thinner sections ($t < 12.5$ mm). The increase in P_u with 400% increase in t (from 5 m to 20 mm) is of the order ∼ 1273%, 1252%, 1401% and 679%, respectively, for square, LHC, THC and +HC. Ductility at ultimate load has been observed to be ∼0.1%–0.6 % for SHC and LHC (all thicknesses), THC ($t \leq 12.5$ mm), and +HC ($t \leq 10$ mm). For thicker sections of THC ($t \geq 15.0$ mm) and +HC ($t \geq 12.5$ mm), significant deformation of ∼0.6 % and ∼1.0%, respectively are seen.

1 INTRODUCTION

Construction industry is generally dominated by carbon steel due to low cost, long experience, applicable design rules and a large variety of strength classes; however it suffers inherently from comparatively low corrosion resistance and higher material cost. But in contrast to carbon steel, various stainless steel types can provide a very wide range of mechanical properties and material characteristics to suit the demands of numerous and diverse engineering applications, along with the advantages of not needing for surface corrosion protection in moderate to highly aggressive environments. Its main advantages include high corrosion resistance, high strength, smooth and uniform surface, aesthetic appearance, high ductility, impact resistance and ease of maintenance and construction. These benefits have prompted a moderately upsurge of using stainless steel in construction industry in the recent years. Traditionally, in the constructional industry, austenitic steel grades are used prominently. However, with increasing nickel prices (nickel content of ∼8% -11% in austenitic stainless steel) there is an escalation in the demand for lean duplexes stainless steel (LDSS) with low nickel content of ∼1.5%, such as grade EN 1.4162 (Baddoo 2008, Gardner 2005, & EN 1993-1-4 2006). LDSS grade EN 1.4162 in particular, with twice the mechanical strength of conventional austenitic and ferritic stainless steel has a potential for use in constructions, and its use has seen significant growth and development over the last 20 years. The prime movers for this development have been soaring raw material costs, such as nickel, along with increasing demand for improved corrosion resistance and strength, enabling a reduction in section sizes (leading to higher strength to weight ratios). As such, several recent investigations have been attempted on both normal and high strength stainless steel hollow (tube) columns with square, rectangular, circular and elliptical sections (Dabaon et al. 2009, Young & Lui 2005, Lui & Young 2003, Gardner & Nethercot 20041, & 2, Theofanous et al. 2009, Ashraf et al. 2008, Ellobody & Young 2006).

In addition to the aforementioned conventional cross-sectional shapes of columns, it is worthwhile to mention that, in the past two decades, the construction industry has shown increasing interest in the use of Non-rectangular columns (NRCs) (e.g. L-, T-, and +−shaped cross-sections) especially for reinforced concrete columns (Xu & Wu 2009). Compared with columns with rectangular/square cross-sections, NRCs have the advantage of providing a flushed wall face, resulting in an enlarged usable indoor floor space area and also in making the interior space more regular. So, NRCs (reinforced concrete) were applied in residential high-rise buildings and were welcomed by architects. These NRCs with L- or T- sections also share unique advantages of having large stiffness and

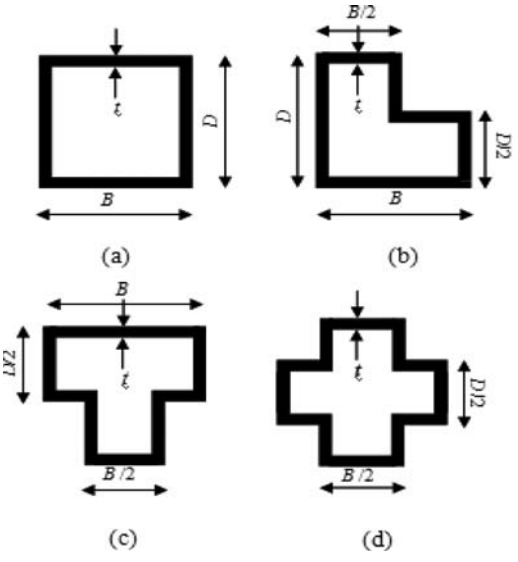

Figure 1. a) SHC; b) LHC, c) THC, and d) +HC (or NRHCs).

strength in the direction of their longer sections. Whilst several experimental and numerical studies (Wang & Lu 2005, Lu et al. 2007) on the behavior of reinforced concrete NRCs with L- or T- sections was reported, to the best of authors' knowledge, there is an apparent lack of systematic studies relating to Non-rectangular hollow columns (NRHCs), particularly for LDSS. Hence, in this paper an attempt has been made to investigate the behaviour and strength of LDSS hollow columns by employing finite element approach. The main objective of this study is to explore and compare the behaviour (e.g. ultimate load and axial deformation at ultimate load) of LDSS square hollow column (SHC) with those of Non- or NRHCs viz., L-shaped hollow column (LHS), T-shaped hollow column (THC), and +−shaped hollow column (+HC) (see Fig. 1) under pure axial compression, but noting that all these column types have equal material cross-sectional areas (or same material consumption). FE analyses on fixed-ended cold formed LDSS for square and NRHCs are presented.

2 FINITE ELEMENT MODELLING

2.1 *Introduction*

In the present work, general purpose commercial finite element software Abaqus (2009) has been used to conduct various parametric studies (e.g., effect of cross-sectional shapes and thicknesses) on load carrying capacity of LDSS SHC and NRHCs subjected to pure axial compression. In the initial part of the study, validation of the FE analysis has been performed for a SHC by comparing with an available experimental data from the literature (Theofanous & Gardner, 2009).

Figure 2. Typical FE mesh and boundary conditions of LDSS SHC.

The FE modeling details are shown in the subsequent sub-sections.

2.2 *Geometry and boundary conditions*

The present modeling approach follows those published in the literature (Theofanous & Gardner 2009, Hassanein 2010, & Ashraf et al. 2006). Figure 2 shows a typical geometry of the LDSS SHC with square cross-section. The bottom part of SHC is fixed while the top loaded part is allowed for free vertical translation (i.e. along the column length direction). The boundary conditions were accomplished using two reference points (RP-1 and RP-2) that were tied to the column ends via node-to-node tie constraints available in Abaqus (2009). The reference points restrained all degrees of freedom apart from vertical translation at the loaded end via kinematic coupling to follow the same vertical displacement. A central concentrated normal load was applied statically at the reference node (RP-2) (Figure 2) using displacement control, thus applying uniform pressure at the top edges of the column.

2.3 *Finite element types*

Shell elements were employed to discretise the models. Four-noded doubly curved shell element with reduced integration S4R (Abaqus 2009) with six degrees of freedom per node and known to provide accurate solutions to most applications (for both thin and thick shell problems) has been utilised in this study. The aspect ratio of the element is kept at ∼1.0 in all the FE models (Figure 2). The number of S4R elements used in the analyses for various models ranges from ∼2400 – 10,000. Linear eigenvalue buckling analysis was then used to check mesh convergence by monitoring the

first eigen buckling mode with mesh refinement. Typical first eigen modes for SHC and NRHCs are shown in Figure 8.

2.4 *Local geometric imperfection*

Linear elastic eigen value buckling analyses were initially performed to extract local buckling mode shapes using subspace iteration method (Abaqus 2009). The first (i.e. lowest) local buckling mode shapes were then utilised as initial geometric imperfection patterns to perturb the geometry of the columns by scaling with imperfection amplitude as adapted for stainless steels (Gardner & Nethercot 2004), given by Equation 1.

$$w_0 = 0.023 \left(\frac{\sigma_{0.2}}{\sigma_{cr}}\right) t \tag{1}$$

where $\sigma_{0.2} = 0.2\%$ proof stress; and $\sigma_{cr} =$ elastic critical buckling stress determined from the buckling analysis given by Equation 2.

$$\sigma_{cr} = E_0.\epsilon = E_0.\lambda.\left(\frac{\Delta l}{L}\right) \tag{2}$$

where $\lambda =$ eigenvalue obtained from the results of FE analysis; $E_0 =$ initial Young's modulus of elasticity; $\Delta l =$ initial displacement at the movable end input in the boundary conditions; and $L =$ length of the column.

2.5 *Material modeling*

The minimum specified material properties of LDSS Grade EN 1.4162 according to EN 10088-4 (2009) are 0.2% proof stress ($\sigma_{0.2}$) of 530 MPa and ultimate stress (σ_u) of 700–900 MPa. In the present study, the material properties given by Theofanous & Gardner (2009) (Table 1) were used in deriving the stress-strain curve of LDSS material through Gardner & Ashraf (2006) model (modified version of the original Ramberg–Osgood (1943)). Poisson's ratio was taken as 0.3.

The stress (σ) – strain (ε) curve of LDSS has been divided into two parts viz. (Figure 3), (1) up to 0.2% proof stress ($\sigma_{0.2}$), where Ramberg-Osgood model (1943) is used to define the curve, and (2) from $\sigma_{0.2}$to $\sigma_{1.0}$, where Gardner & Ashraf (2009) model was used (Equation 3), in the absence of necking phenomena in compression.

$$\epsilon = \frac{(\sigma-\sigma_{0.2})}{E_{0.2}} + \left(\epsilon_{t1.0} - \epsilon_{t0.2} - \frac{\sigma_{1.0}-\sigma_{0.2}}{E_{0.2}}\right) \times \left(\frac{\sigma-\sigma_{0.2}}{\sigma_{1.0}-\sigma_{0.2}}\right)^{n'_{0.2,1.0}} + \epsilon_{t0.2} \tag{3}$$

where $\epsilon_{t0.2}$ & $\epsilon_{t1.0} =$ total strains at $\sigma_{0.2}$and $\sigma_{1.0}$, respectively; and $n'_{0.2,1.0} =$ strain hardening exponent. Equation 3 has been found to give excellent agreement with measured stress–strain curves in both tension and compression.

Table 1. Compressive flat material properties (Theofanous & Gardner 2009).

Cross-section	E (Mpa)	$\sigma_{0.2}$ (Mpa)	$\sigma_{1.0}$ (Mpa)	Compound R-O coefficients	
				n	$n'_{0.2,1.0}$
80 × 80 × 4-SC2	197200	657	770	3.81	3.6

Table 2. Stub column dimensions (Theofanous & Gardner 2009).

Specimen	L mm	B mm	H mm	t mm	r_i mm	w_0 mm
80 × 80 × 4-SC2	332.2	80	80	3.81	3.6	Eq. (1)

*$L =$ Length, $B =$ Width, $H =$ Depth, $t =$ thickness, $r_i =$ internal corner radius, $w_0 =$ local geometric imperfection.

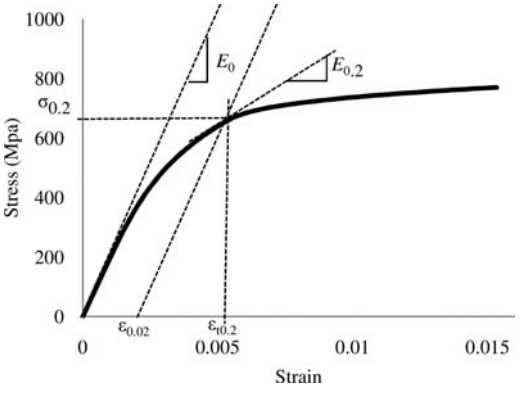

Figure 3. Experimental stress-strain curve of LDSS material Grade EN 1.4162 (Theofanous & Gardner 2009).

2.6 *Validation of FE model*

An experimental investigation on LDSS stub SHC conducted by Theofanous & Gardner (2009) was used to verify the developed FE modeling approach used in this study. Tables 1 & 2 shows the LDSS material properties and column dimensions for flat portions of the tested specimen. It may be noted that although this column has been formed using cold-form technique at the corners resulting in different properties between flat and corner portions of the column, same compressive flat material properties (Table 1) has been used for both the flat and corner portions of the column. Hence the strength enhancement in the corner regions by cold forming-process is neglected.

Figure 3 shows the stress-strain plot of the LDSS material using the material properties from Table 1 with Gardner & Ashraf (2006) model as mentioned in Section 2.5. The material model shown in Figure 3

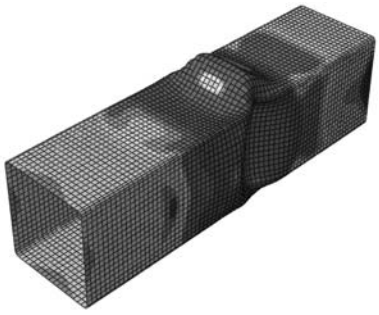

Figure 4. Typical FE deformed shape for stub column (80 × 80 × 4-SC2).

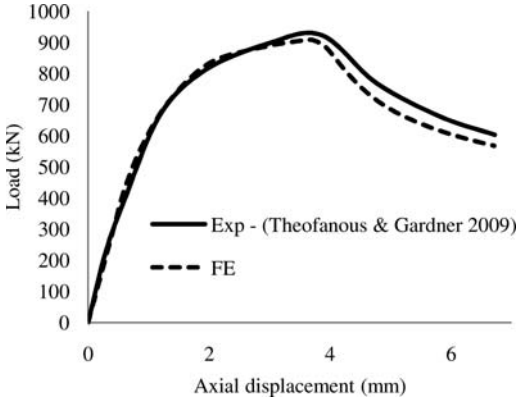

Figure 5. Variation of load with axial displacement for stub column (80 × 80 × 4-SC2).

is then used as input parameters to Abaqus (2009), by converting into true stress (σ_{true}) and true plastic strains (ϵ^{pl}_{ln}) using the following Equation 4 & 5.

$$\sigma_{true} = \sigma_{nom}\,(1+\epsilon_{nom}) \tag{4}$$

$$\epsilon^{pl}{}_{ln} = ln\,(1+\epsilon_{nom}) - \frac{\sigma_{true}}{E_0} \tag{5}$$

where σ_{nom} and ϵ_{nom} are engineering stress and strain respectively.

Imperfection magnitude is seeded in the FE model using Equation 1. Modified Riks method (Abaqus 2009), (a variation of the classical arc-length method (Riks 1972, Riks 1979, & Wempner 1971), was employed for the non-linear analyses to capture the full (i.e. both pre and post ultimate load) load-deformation response. The deformed shape of a typical FE model is shown in Figure 4.

Figure 5 shows comparision of experimental (Theofanous & Gardner 2009) and FE load-axial displacement plots of the hollow stub column (80 × 80 × 4-SC2). From Figure 5, it can be seen that good agreement has been achieved between both

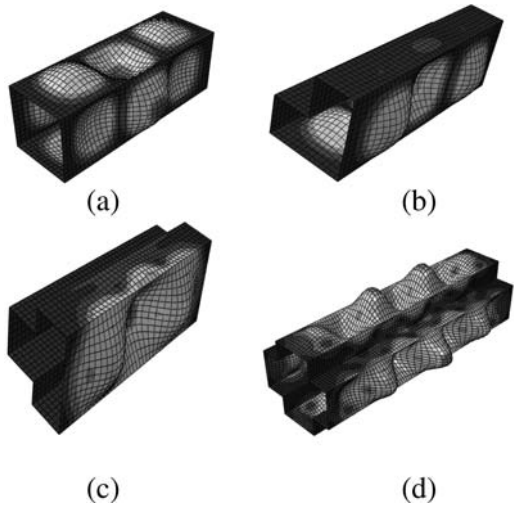

Figure 6. First eigen buckling modes for (a) SHC; b) LHC, c) THC, and d) +HC.

results, and is used in the subsequent FE analyses for the fixed-ended hollow stub columns.

2.7 *Parametric study of LDSS hollow columns*

Various SHC and NRHCs with equal material cross-sectional areas with varying thickness were considered to investigate the effects of cross-sectional shapes on the behavior of these stub columns under pure axial compression. The SHC section has a side width of 600 mm (i.e. $B = D = 600$ mm). The maximum side (distance between opposite faces) width of all the NRHCs are maintained equal to that of the square section, however the smaller side width is made equal to half the larger width i.e. 300 mm ($D/2 = B/2 = 300$ mm). Altogether, 28 FE models have been studied. The FE modelling method is similar to those discussed in the previous sections. The first eigen buckling modes (Figure 6) are then used along with local amplitudes proposed by (Gardner 2002) (Equation 1) to simulate the local geometric imperfections. The column lengths were set equal to three times the maximum outer dimension (3×600 mm $= 1800$ mm) to avoid the effects of flexural buckling and end conditions, while the thicknesses were varied from 5 mm to 20 mm to encompass a wide range of cross-sectional slenderness ratios. To simplify the modeling process and also due to lack of experimental material properties for the corner part (in case of cold work), together with the possibility of welding at the corners, corners of the square and NRHCs sections are assumed to be at right angles (i.e. corner radii as in the validation (Section 2.6) are not considered). Further, it is assumed that the material properties are same both at the flat and corner regions. Similar material properties as that found out by Theofanous and Gardner (2009) are adopted for the FE modeling (Table 1).

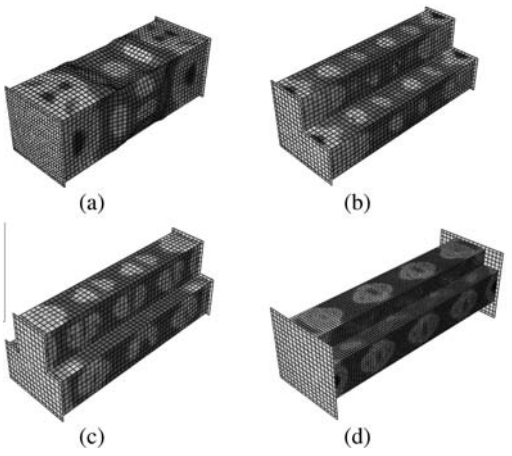

Figure 7. Von-Mises stress (superimposed on deformed shape) at ultimate load of (a) SHC, (b) LHC, (c) THC, and (d) +HC ($t = 5$ mm).

3 RESULTS AND DISCUSSIONS

3.1 *Deformed shapes at ultimate load*

Von-Mises stress (superimposed on deformed shape) at ultimate load is shown in Figure 7 for SHC and NRHCs ($t = 5$ mm).

From Figure 7, the onset of local buckling modes at ultimate load can be seen along with distribution of Von-Mises stress over the surface.

3.2 *Variation of ultimate load*

Figure 8 depicts variation of $P/A_g f_y$ (where P, A_g, and f_y are load, material cross sectional area, and yield stress respectively) versus axial displacement for SHC and NRHCs for both 5 mm and 20 mm thick columns. It may be noted that as the perimeter of the cross-sections are same for all the types of sections considered the quantity $A_g f_y$ remains constant. The term $A_g f_y$ can be considered as the global yielding load. The ratio of $P_u/A_g f_y < 1.0$ (P_u is the ultimate load) indicates that the sections are slender and can buckle prior to yield [30]. For P_u/Agfy ≥ 1.0 (i.e. stocky sections), yielding precedes buckling, and may be followed by hardening prior to buckling. It can be observed from Figure 8 that the ultimate strength of the column increases as it goes from square, L-, T-, to +−shaped sections. This can be related to the higher stiffening effects of the corner regions and the potential for stress redistribution once local buckling of the wider face plate occurs. As the numbers of corners (right angled joints) are increased the ultimate load also increases. It can readily be noticed that as it goes from square to +−Rshaped section, the sharper is the load-axial deformation behaviour (for $t = 5$ mm). This sharper load-deformation behaviour enforces the column to undergo smaller deformations at relatively higher loads. From Figure 8, it can be

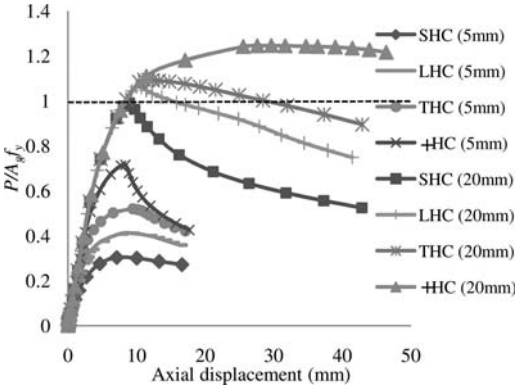

Figure 8. Variation of $P/A_g f_y$ with axial displacement for SHC and NRHCs ($t = 5$mm and 20 mm).

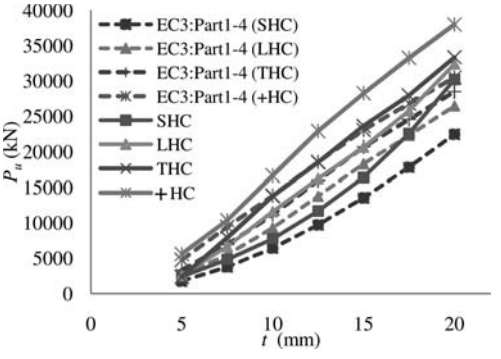

Figure 9. Variation of ultmate load (P_u) with section thicknesses.

seen that +HC has the highest ultimate load (P_u), with ($P_{u(sq)} < P_{u(L)} < P_{u(T)} < P_{u(+)}$ where subscripts sq, L, T and $+$ denotes the corresponding sections). For 5 mm thick sections an increase in sharpness of the load-displacement curve at ultimate load can also be observed as the cross-section shapes are changed from square → L → T → + (Figure 8). These kinds of behavior are found to be typical for 10 mm, 12.5 mm, 15 mm and 17.5 mm sections for SHC, LHC, and THC (not shown in Figure 8 for clarity). However, it can be seen that for 20 mm thick sections, it is quite apparent that the sections have become stocky and global yielding ($P_u/A_g f_y \geq 1.0$) takes place prior to buckling (except for SHC where $P_u/A_g f_y \sim 1.0$). Again an increase of P_u as the cross-section shapes are changed from square → L → T → + are seen. In the case of +HC, a distinct pattern can be seen in the load-deformation curve, indicative of hardening before buckling i.e. pre-ultimate load and a flatter (plateau) behavior in the post-ultimate load.

The variation of P_u with section thicknesses are shown in Figure 9 for all the cross-sections tested. It can be seen from Figure 9 that the variation of P_u with t is nearly linear ($R^2 = \sim 0.99$) for NRHCs, in

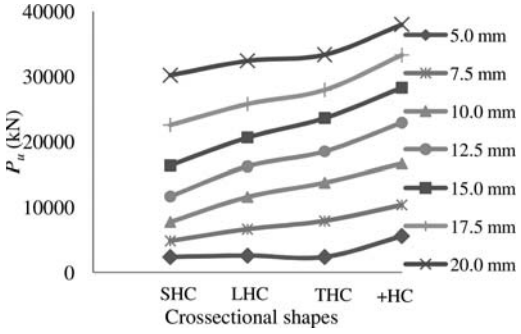

Figure 10. Variation of ultmate load (*Pu*) with cross-sectional shapes.

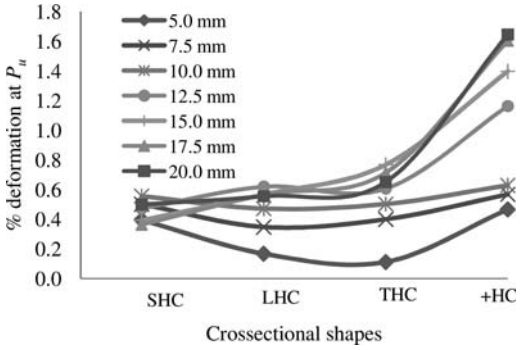

Figure 11. Variation of % deflection at P_u for different sectional shapes.

comparison to SHC where the increase in P_u is relatively slower in thinner sections ($t < 12.5$ mm). The % increase in P_u with 400% increase in t (from 5 m to 20 mm) is of the order ∼1273%, 1252%, 1401% and 679%, respectively, for SHC, LHC, THC and +HC. The variation of P_u according to the EN 1993-1-4 (2006) are also plotted for comparison. It may be noted that there are no specific guidelines provided in EN 1993-1-4 (2006) for computing axial strength for the types of cross sections considered in this study (except for square). However, the 'effective area' approach for cross-sections lying in Class 4 (Table 5.2, EN 1993-1-4 2006) are used in the computations of codal strength, by considering the effective widths (valid for Class 4 cross-sections), in order to take care of the local buckling effect. For this reason, a reduction factor (ρ) given in Clause 5.2.3 was used during the calculation of the effective area. However, for cross-sections which do not lie in Class 4, gross area was used in the calculations of the design strengths. From Figure 9, It can be seen that FE predicted increasingly higher values of P_u with increasing thickness when compared to that computed using 'effective' area concept of EN 1993-1-4 (2006). At t = 20 mm, FE predicted in increase of ∼25% more as compared to that of codal prediction. However, at lower thicknesses (e.g., 5 mm and 7.5 mm), values of P_u obtained from both FE and EN 1993-1-4 (2006) are comparable. It thus can be seen that the calculation of P_u based on EN 1993-1-4 (2006) are on the conservative side when compared to that of FE predictions.

Figure 10 shows the variation of P_u with sectional shapes (SHC→ LHC → THC → +HC) for different thicknesses. It can be observed that for all the thicknesses considered there appears to be a linear increase in P_u as the sections are changed from SHC → LHC → THC → +HC. For changes in section from square to + shape the increase in P_u are ∼136%, 114%, 110%, 96%, 72%, 48% and 26% respectively for 5 mm, 10 mm, 12.5 mm, 15 mm, 17.5 mm and 20 mm showing that the increase in P_u is more effective at thinner sections ($t < 12.5$ mm) where the increase in more than 70 %.

3.3 *Variation of axial deformation at ultimate load*

Variation of % deflection (δ/L*100%; $L = 1800$ mm and δ is the deflection) at P_u are plotted in Figure 11, to give a measure of ductility at ultimate load.

It can be observed that % deflection = ∼0.1%–0.6 % for SHC, and LHC (all thickness), THC ($t \leq 12.5$ mm), and +HC ($t \leq 10$ mm). Only for thicker sections ($t \geq 15.0$ mm) of THC and ($t \geq 12.5$ mm) of +HC, a significant % deformation is seen ≥0.6 % and ≥1.0 %, respectively. It can be seen that this behavior is related to the elongated plateau of the load-deformation plot as a result of the increasing number of corners along with t/D ratio, leading to significant increase in stiffness.

4 CONCLUSIONS

Finite element analyses of LDSS (Lean Duplex Stainless Steel) hollow stub columns with square, L, T, and +−shaped cross-sections (i.e. SHC, LHC, THC and +HC respectively) for various thicknesses are presented using Abaqus (2009) to gain an understanding of the cross-sectional shape effects on both ultimate load and ductility at ultimate load. Based on the study following conclusions are identified:

(a) For all the NRHCs (i.e., LHC, THC and +HC) considered, a nearly linear variation of P_u with section thicknesses has been observed, although the increase for SHC was relatively slower in thinner sections ($t < 12.5$ mm). The % increase in P_u with 400% increase in t (from 5 m to 20 mm) is order ∼1273%, 1252%, 1401% and 679%, respectively, for square, L, T and + shaped sections.
(b) For all the thicknesses considered, a nearly linear increase in P_u as the sections are changed from square → L → T → + has been seen. For changes in section from square to + shape, the increase in P_u are ∼136%, 114%, 110%, 96%, 72%, 48% and 26% respectively for 5 mm, 10 mm, 12.5 mm, 15 mm, 17.5 mm and 20 mm, showing that the increase in P_u is more effective at thinner

sections ($t < 12.5$ mm) where the increase in more than 70 %.

(c) Ductility at ultimate load (expressed as δ/L*100%; $L = 1800$ mm and δ is the deflection) has been observed to be = ~0.1%–0.6 % for SHC and LHC (all thickness), THC ($t \leq 12.5$ mm), and +HC ($t \leq 10$ mm). Only for thicker sections ($t \geq 15.0$ mm) of THC and ($t \geq 12.5$ mm) of +HC, a significant % deformation is seen ≥0.6 % and ≥1.0 %, respectively.

REFERENCES

Abaqus 2006. Hibbitt, Karlsson & Sorensen, Inc. Abaqus/ Standard user's manual volumes I-III and ABAQUS CAE manual. Version 6.9-EF1, Pawtucket, USA.

Ashraf M., Gardner L., Nethercot D.A. 2006. Finite element modeling of structural stainless steel cross-sections. Thin-Walled Struct; 44: 1048–1062.

Ashraf M., Gardner L.,& Nethercot D.A. 2008. Resistance of stainless steel CHS columns based on cross-section deformation capacity. J Construct Steel Res; 64: 962–970.

Baddoo N.R. 2008. Stainless steel in construction: a review of research, applications, challenges and opportunities. J Construct Steel Re; 64: 1199–1206.

Dabaon M.A., El-Boghdadi M.H., & Hassanein M.F. 2009. A comparative experimental study between stiffened and unstiffened stainless steel hollow tubular stub columns. Thin-Walled Struct; 47: 73–81.

Ellobody E. & Young B. 2006. Design and behaviour of concrete-filled cold-formed stainless steel tube columns. Eng Struct; 28: 716–728.

EN 1993-1-4. 2006. Eurocode 3: Design of steel structures-Part 1.4: General rules- Supplementary rules for stainless steel. CEN.

EN 10088-4. 2009. Stainless steels_part 4: technical delivery conditions for sheet/plate and strip of corrosion resisting steels for general purposes. CEN.

Gardner L. 2002. A new approach to structural stainless steel design. PhD. Thesis. Structures Section, Dept of Civil and Environmental Eng. Imperial College London, UK.

Gardner L. 2005. The use of stainless steel in structures. Progress in Structural Engineering and Materials; 7(2): 45–55.

Gardner L. & Ashraf M. 2006. Structural design for non-linear metallic materials. Eng Struct; 28: 925–936.

Gardner L & Nethercot D.A. 2001. Numerical modelling of cold-formed stainless steel sections. In: NSCC 2001 proceedings: NSCC 2001 ninth Nordic steel construct conference, Helsinki, Finland. 781–790.

Gardner L. & Nethercot D.A. 2004. Experiments on stainless steel hollow sections-Part 1: Material and cross-sectional behavior. J Construct Steel Res; 60: 1291–1318.

Gardner L. & Nethercot D.A. 2004. Experiments on stainless steel hollow sections-Part 2: Member behaviour of columns and beams. J Construct Steel Res; 60: 1319–1332.

Gardner L. & Nethercot D.A. 2004. Numerical modeling of stainless steel structural components-A consistent approach. J Struct Eng, ASCE; 130(10): 1586–601.

Hassanein M.F. 2010. Numerical modelling of concrete-filled lean duplex slender stainless steel tubular stub columns. J Construct Steel Res; 66: 1057–1068.

Lu X., Li X., Wang D. 2007. Modelling and experimental verification on concrete-filled steel tubular columns with L or T section. Frontiers of Architecture and Civil Eng in China; 1: 163–169.

Lui Y. & Young B. 2003. Buckling of stainless steel square hollow section compression members. J Construct Steel Res; 59: 165–177.

Ramberg W. & Osgood W.R. 1943. Description of stress_strain curves by three parameters. NACA Technical Note No. 902.

Riks E. 1972. The application of Newton's method to the problem of elastic stability. J Applied mechanics; 39: 1060–1065.

Riks E. 1979. An incremental approach to the solution of snapping problems. Inter J Solids and Struct; 15: 529–551.

Theofanous M., Chan T.M., Gardner L. 2009. Structural response of stainless steel oval hollow section compression members. Eng Struct; 31: 922–934.

Theofanous M. & Gardner L. 2009. Testing and numerical modelling of lean duplex stainless steel hollow section columns. Eng Struct; 31: 3047–3058.

Wang D. & Lu X. 2005. Experimental study on the seismic behavior of concrete filled steel tubular columns with TL section. J Building Struct; 26: 39–44.

Wempner G.A. 1971. Discrete approximation related to nonlinear theories of solids. Inter J Struct Division; 7: 1581–1599.

Xu Y. & Wu B. 2009. Fire resistance of reinforced concrete columns with L-, T-, and +-shaped cross-sections. Fire safety J; 44: 869–880.

Young B. & Lui W.M. 2005. Behavior of Cold-Formed High Strength Stainless Steel Sections. J Struct Eng, ASCE; 1738–1745.

Architecture, applications and case studies

Tubular Structures XIV – Gardner (Ed.)
© 2012 Taylor & Francis Group, London, ISBN 978-0-415-62137-3

E-conditioned Chimneys in Madrid

X. Aguiló i Aran
BOMAINPASA Engineering & Architectural Consultancy, Spain

ABSTRACT: The E-conditioned Chimneys, situated in a peripheral area in Madrid, has been designed by the Spanish architect Federico Soriano. The project defines five chimneys, 40 meters high approximately, which allow the placement of tubes that conduct the smoke and fumes from the cogeneration plant situated just underneath them. At the same time, the project creates a new public space in an area with a high level of social conflict. The Chimneys are clearly designed and conceived as light cantilever elements, which provide the structure for the support and accompaniment of the smoke ventilation ducts. They are covered with a light-permeable mesh as a covering element. The structure cap has been designed using tubular profiles and braces.

1 INTRODUCTION

1.1 *Bio*

Location: Puente Vallecas, Madrid
Architect: S&Aa,Federico Soriano
Structural Consultant: BOMAIPASA
Developer: Ayuntamiento de Madrid
Project: 2008–2009
Site Works: 2010–2011
Total area: 540 m^2

1.2 *Location*

The project is located in Puente Vallecas, a peripheral area in Madrid, with a high level of social conflicts. A development plan aims to improve the neighbourhood, demolishing houses declared in ruins, where people still live, and building new social housing, thinking of a system to provide economical energy. For this purpose, a waste central is built, associated to a central District Heating. This plant is the basement of our great plaza, which is pierced by the smoke evacuation chimneys. The project described in this paper gives technical and architectural solution to this conflict, resulting in the generation of a very interesting public space.

1.3 *General description of the architectural project*

The project defines five chimneys, 40 meters high approximately, which allow the placement of tubes that conduct the smoke and fumes from the cogeneration plant situated just underneath them. The minimum height of the towers is defined according to the buildings surrounding the site. The project of the chimneys generates a recreational space around them protected by canopies. These are generated with a tensile structure, which will be the support for the covering element.

Figure 1. Image of the five Chimneys.

1.4 *Architect*

The architect of the E-conditioned Chimneys is Federico Soriano. His study, named S&Aa after Soriano and Associates Architects is located in Madrid.

1.5 *Architectural design idea*

Given the implementation conditions of the square, that is, the existence of a central heating underneath and consequently the unquestionable presence of smoke ventilation ducts, the place is seen as a public space dominated by five slender chimneys, two of which are so close that share a canopy, and are treated as a group.

Figure 2. Image of the Chimneys by night.

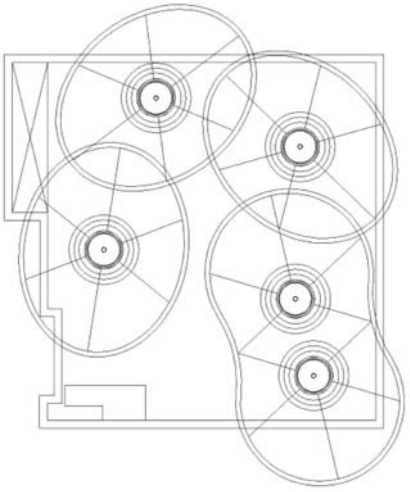

Figure 3. Organization of the Chimneys on the site plan.

They are clearly designed and conceived as light cantilever elements, which provide the structure for the support and accompaniment of the smoke ventilation ducts, up to two meters above the highest adjacent building. The chimneys are covered with a light-permeable mesh as a covering element. This mesh also supports strips of LEDs that light up at night.

Canopies are placed at the base of these towers, as entities that will provide shade and shelter, and under which concrete benches are placed.

The fact that the base of the chimney is accessible to the public, given the position of benches, requires solving the base of the chimney as a solid element in order to avoid vandalism. The rest of the mast can be lighter.

2 DESCRIPTION OF THE STRUCTURE

2.1 *Structural design idea*

The structure of the chimneys is based on a cantilever mast. The architectural project defines two types of shaft: on the lower part a massive element but with a minimum dimension, which allows the support of the stresses from wind loads on the chimneys, and avoids vandalism. It is materialized as an armed tube.

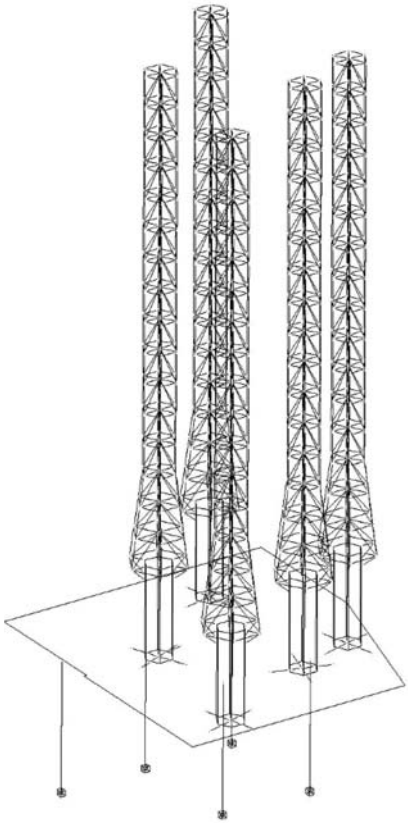

Figure 4. 3D Model used for the calculation of the model.

On the higher part the mast is much smaller, and it is stabilized through cables, creating an evolving tensile structure and achieving the needed inertia. As it can be seen in the following figures, it is materialized as a sequence of tubular structure rings, separated approximately 4.60m each. Each ring has a central and a perimetrical tube, joined by six radial tubular profiles.

The inferior evolving maximum diameter is 4.40m, while it only reaches 2.50m on the superior part.

2.2 *Structural principles*

These chimneys are mainly affected by wind loads. Dead loads and a possible use load such as maintenance are secondary compared to lateral pressures caused by wind.

A peculiarity needs being highlighted in this project, which is no less important than wind loads. It is the compression stress caused in the central mast due to the prestressing forces on the bars all along the height of the chimneys.

Given these conditions, the vertical cantilever has to be stable under these circumstances.

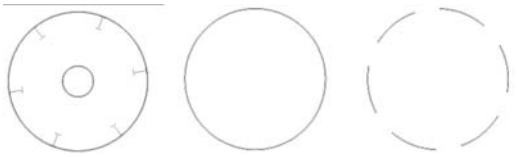

Figure 5. Lower shaft typical section: Ø2100 mm tubular and vertical IPE-200 profiles. Ø2100 mm tubular profile and its equivalent effective section.

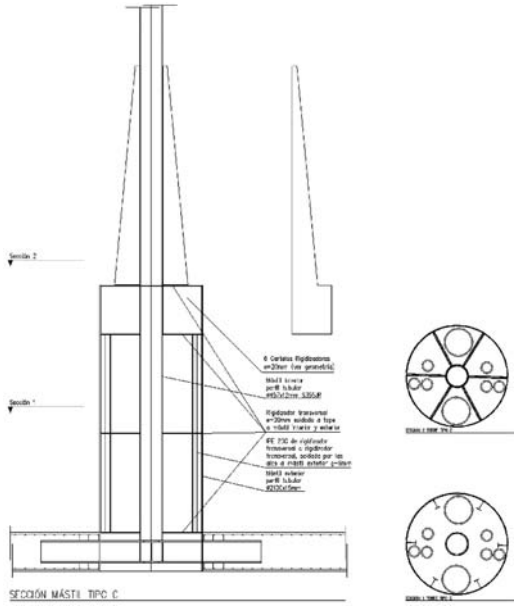

Figure 6. Elevation and cross-section of the lower shaft.

The design of the cross section of the shaft of the chimney is the key element in this project. It has already been mentioned that the base has a more solid solution, while the rest is lighter.

2.2.1 *Lower shaft*

The lower shaft is a Ø2100 mm tubular profile, 15mm thick, with vertical IPE-200 profiles acting as stiffeners on its interior perimeter.

According to the 5.3 table on the CTE SE A regulation, the profile has been classified as Class 4. Section 5.2.5 defines the characteristics of class 4 sections. The effective cross section has been sought in order to proceed with all the bar and section checkings established in the named regulation.

The lower shaft has a diaphragm mechanism, implemented by steel plates embedded in the section at different heights, which provide rigidity to the element. These plates have the necessary holes for the passing of the ducts, as well as for the placement of a vertical ladder, so that the whole structure is accessible for maintenance. The vertical stiffeners, the IPE-200, are placed from one to the next diaphragm.

A transition system has been designed in order to transmit the axial load from the central shaft to the

Figure 7. Image of the lower shaft.

Figure 8. Image of the transition system.

Figure 9. Image of the point where compressions and tensions are transmitted to the lower shaft.

Ø2100 mm tubular profile. As can be seen in figures 6 and 8, this system is made up of six L shaped plates welded to the central shaft and the perimeter tube.

These plates do not only receive the compression force, but also the tension from the braces that are fixed at this level, and derived to the transition system through the tubular profiles shown in the following picture.

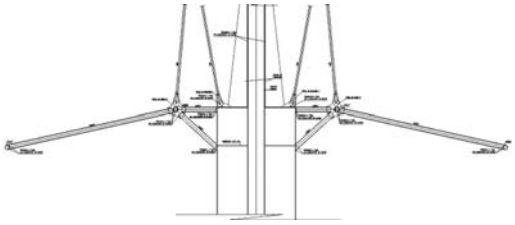

Figure 10. Detail of the point where compressions and tensions are transmitted to the lower shaft.

Figure 11. Metallic profiles designed to transmit stresses from the shaft to the concrete slab.

The base or starting diaphragm mechanism is the concrete slab on which the towers are placed, which is later described. As shown in figure 11, a device has been designed with the capability of transmitting the bending moments from the shaft base to the slab.

2.2.2 *Upper shaft*

The upper shaft has been designed as a tensile structure, consisting of a Ø457 mm central tube and a Ø125 mm perimeter tube. They are joined by six Ø125 mm or Ø100 mm profiles depending on the stresses. This group makes up a structural ring. Each of these rings is joined by VSL-Stress-bar braces, with an anticorrosive treatment, their diameters ranging from Ø20 mm to Ø56 mm, and their yield strength being 460 MPa.

The shaft is divided into three parts, defined by the construction process and the buckling effects on the mast. This process seeks for the stability during the lifting of the chimneys on the construction phase. At this stage, since the finishing mesh is not placed, the wind loads are significantly reduced.

The construction process, described below, provides for the placement of the three main braces on each of the three defined parts, allowing the positioning of the secondary braces once the entire height of the tower is built.

Figure 12. Upper shafts.

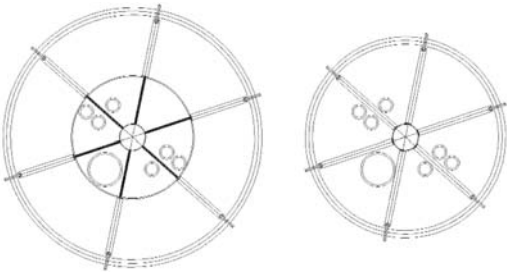

Figure 13. Cross-sections. Left: At the transition level between lower and upper shaft. Right: Typical cross section of the upper shaft.

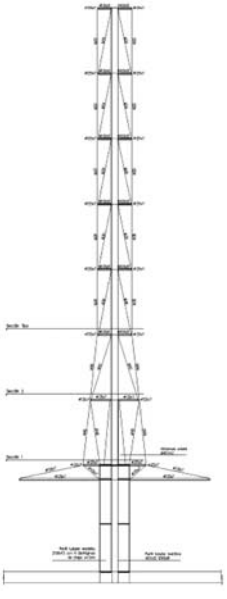

Figure 14. Elevation of a chimney.

The following image shows the metallic plates used for the fixing of the braces to the perimeter tubular profile on each of the structural rings in the upper shaft. This system enables keeping the convergence

Figure 15. Transition plate where braces are fixed.

Figure 16. Transition plate where braces are fixed.

of the axis of all the structural elements, avoiding eccentricities.

2.2.3 *Canopies*

The sinuous curves that define the boundary of the canopies are generated by a Ø200 mm tubular profile, supported, suspended and braced by a set of Ø125 mm tubular profiles, in tension.

2.2.4 *Concrete slab*

The five towers are supported on an 80cm deep concrete slab, which is the roof of the central heating plant. This slab transmits the loads to five columns, spanning 9 meters. A concrete wall is placed on the perimeter of this slab.

The position of the chimneys does not and cannot coincide with that of the inferior concrete columns that sustain the slab and everything fixed on it. The position

Figure 17. Two chimneys are joined by a canopy.

of the columns responds to the optimal position for the correct development of the cogeneration plant, while the position of the chimneys is a result of the facilities strategic decisions. The concrete slab projected and constructed has been duly studied and reinforced. The hypotheses used are those indicated in the Spanish codes.

3 CONSTRUCTION PROCESS

Chronologically, implementation phases are detailed as follows:

Phase 1. This phase starts once the concrete slab has been executed, having placed the metallic moment transmission system in its depth. Proceed to the assembly of the lower mast (inner and outer mast), in a logical sequence of assembly of both horizontal and vertical stiffeners, trying to assemble as many parts as possible in the workshop, to ease installation on site.

Phase 2. In this phase starts the placing of the upper mast. After placing the second inner mast height, proceed to the assembly of the perimeter rings with their corresponding radii. Then place main braces. To complete this phase, braces must be submitted to a predefined tensioning load of 237 kN.

Phase 3. After placing the third height of the inner mast, proceed to the assembly of the perimeter rings with their corresponding radii. Then place main braces. To complete this phase, braces must be submitted to a predefined tensioning load of 117 kN.

Phase 4. After placing the forth height of the inner mast, proceed to the assembly of the perimeter rings with their corresponding radii. Then place main braces. To complete this phase, braces must be submitted to a predefined tensioning load of 26 kN.

Phase 5. In towers A1 and D the last inner mast is placed before proceeding, as in the rest of the towers, to put the rings and radii of the top floor with their braces. Finally, the remaining braces (secondary ones) must be placed.

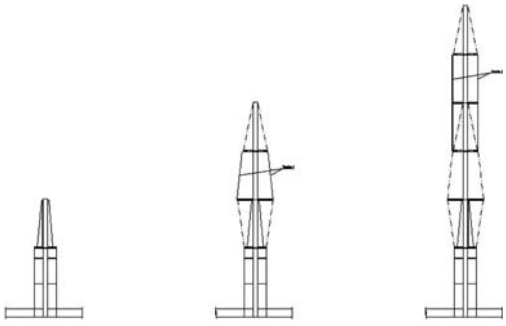

Figure 18. Graphics showing phases 1, 2 and 3.

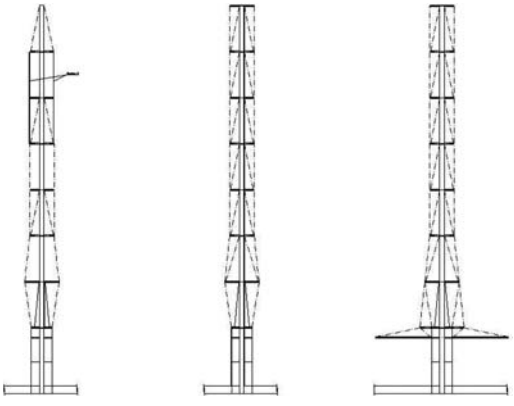

Figure 19. Graphics showing phases 4, 5 and 6.

Phase 6. To finish the construction process, the canopies are mounted on each tower.

It should be noted that the construction company did not follow this system proposed in the project, but opted for the placement of a scaffold for each of the chimneys "floors". To stabilize the whole structure tensile cables were anchored to dead weight. It resulted in a more rigid construction system than the proposed one.

4 CALCULATIONS

Regulations used as reference are the Eurocodes and their national transcriptions (CTE- Actions and Structural Design) along with internationally recognized design guides.

The main aim of the calculation of each tower is to ensure that in none of the hypotheses any braces are in compression. So consequently, each of the braces is prestressed in order not to be compressed in any of the hypotheses.

A mathematical equations system was defined in order to relate the effect that tensioning one of the bars had on the rest of the bars. Consequently, this system related loads on structure with tensions on bars. This system allowed reaching a solution in which, as said, all braces were tensed in all hypotheses.

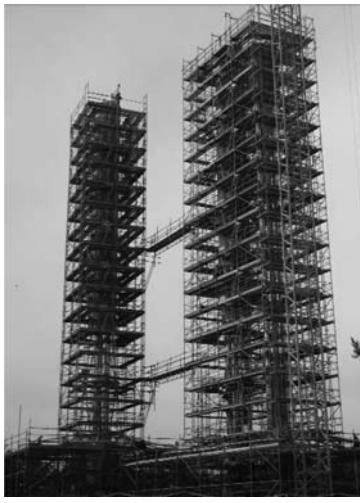

Figure 20. Scaffolding of the chimneys.

4.1 *Loads on structure*

As previously mentioned, the chimneys, which are cantilevered structures, are mainly submitted to horizontal wind loads. Both the dead weight of the structure and ducts, as well as the possible use load for maintenance are secondary loads to the tubular structure.

It has already been noted that there is a very important internal load, which is the compression generated on the inner mast due to the tension applied on the braces.

4.2 *Wind loads*

The Eurocode has been used for calculating the wind load that applies to our structure, using in particular the section dedicated to masts.

The finishing mesh that will cover the chimneys has been taken as opaque for the study of wind effects.

The effect of horizontal loads on the canopies has also been taken into account.

4.3 *Calculation. First and second stage*

On a first approach the calculation of the building's dome is made using the AGE program v3.2 [BOMAINPASA slp]: linear analysis of bar and sheet structures using the finite element method.

A linear calculation has been performed by studying the individual stresses on each bar and affecting them by buckling effects.

On a second stage, the structure has been studied using a nonlinear analysis (second-order P-Delta, which takes into account the change of bending rigidity according to axial forces, the additional perpendicular

rigidity and limitations/constraints due to deflection). The method used is the "complete Newton-Raphson" where the K rigidity matrix is updated after every subdivision and after each iteration. The computer program verifies the convergence of the calculation automatically and stops when it reaches equilibrium.

Once the calculation is done, the consequent stresses are studied in three different sections on each bar, and for each ELU scenario. That is, for each bar 6 checkings are carried out. The analysis is performed only at section level, since according to the CTE DB-SE, for a structure calculated in second order with geometric imperfections no bar analysis is needed. For each bar section, and for each scenario, the following stresses are obtained: Fx (axial force), Fy (shear force, y direction), Fz (shear force, z direction), Mx (torsion), My (bending moment, y direction) and Mz (bending moment, z direction). For bars submitted to tension stresses, only Fx applies. With these values, sections have been verified according to the following formulas:

N, Ed / Nt, Rd + My, Ed / My, c, Rd <1.00

(taken from the regulation: DB-SE steel, 6.2.8.(1)) Vz, Ed / Vz, pl, T, Rd <1.00
(taken from the regulation: DB-SE Steel, 6.2.8(4)) For those bars where at least one section does not satisfy the previous formulas (that is, their results are >1), they are replaced by a larger section tube profile Once these changes are carried out, the model is recalculated reiterating this process until all the bars meet the conditions described above.

In our case, the second order calculation did not contribute in offering any additional information to the first order one, so the calculation was followed under first order conditions.

4.4 *Buckling of the inner mast*

The inner mast is a Ø457*15 mm tubular profile, approximately 40m high. The specification of its steel is S355-JO. This is necessary because of the average minimum temperature in Madrid.

The overall stability of the inner mast has been considered within the full height of the tower, with an inertia equivalent to that used in the structural model. Considering the mast as a cantilever, that is with $\beta = 2$, the results have been satisfactory.

On the other hand, the buckling that may occur in the mast between tensed frames has been studied, considering a height of 9.20 m and $\beta = 1$. This situation corresponds to one of the phases of the construction process.

Both β values indicated above gave similar values to these taken when studying under second order conditions.

In calculating the inner mast all checkings established in the Spanish regulation CTE were made. According to the 5.3 table on the CTE SE A, the profile has been considered as being Class 2.

Figure 21. 3D model under showing horizontal movements.

Figure 22. Image of the public space created.

4.5 *Stresses in braces*

The structural system of the upper tower is based primarily on structural braces for the transmission of loads. The material of the bars has a minimum yield strength of 460 N/mm^2, which means a 30% higher than the S355 type steel. The braces have diameters between 20 and 56 mm.

After analyzing the various towers subjected to wind loads, and to the actions of the prestressing of bars, stresses on braces were compared to the strength at yield, the latter being greater. Therefore, these loads do not cause resistance problems.

4.6 *Lack of verticality*

Horizontal movements of the towers have been limited to a 1/100 of the total height. After the analysis of

Figure 23. Image of the public space created.

the structure the results were all below the value of collapse limitation noted above. The dimension of the movement was of 22.18 cm for towers 39.40 m and 40.3 0m high, and of 17.46 cm for the rest of the towers, being 37.10 m, 38.70 and 36.40 m high, also below the value of collapse limitation noted above.

5 CONCLUSIONS

The E-Conditioned Chimneys Project has been a very interesting exercise of working with cantilever structures, designed with tubular profiles and tensioned braces, in order to design a cantilevered truss where braces are in tension under all hypotheses. Working with tubular bars has resulted in a very attractive architectural object.

Working with class C4 elements has allowed the study of local buckling, effective areas in tubes (that is, the decrease of the real area) and analyzing its structural response with diaphragms and rigidity plates.

The change in the construction process proposed by the construction company was very interesting. In order to reduce operations in site, they constructed in a workshop each structural ring with the corresponding height of the inner mast, which only needed assembly in site.

Collaboration with the architects of the project has been intense and close, so that the result has been the best for the space and the chimneys, as well as the most optimal for the structure.

Pictures 1, 2, 7, 9, 12, 17, 22 and 23 have been taken by the photographers Ricardo Santoja and Alberto Cubas.

Tubular Structures XIV – Gardner (Ed.)
© 2012 Taylor & Francis Group, London, ISBN 978-0-415-62137-3

Towards a new balance between architecture and building technology

M. Eekhout
Faculty of Architecture, Delft University of Technology, Director of Octatube, Delft, The Netherlands

ABSTRACT: In spite of the current economical crisis from 2008 onwards, the subsequent architectural portfolio crisis (down to 30%) and the construction crisis to come in the next 5 years, the developments in architecture have a slower pace. A longer lasting modus of transition. In the last decade many aspects have intertwined in designing tubular structures in architecture, have changed architecture, never to return to the former content.

1 FROM TODAY'S ARCHITECTURE

The spatial environment is being shaped by landscapes, public spaces, private and public buildings, in short by buildings and spaces. The torn apart functions in spatial environment as approved in the Fifties by CIAM, seemed clear enough at first. But, while its popularity grew, thoughtless work brought about more poverty by the isolation of functions. Nowadays functions in urban environments are gradually brought together again and integrated into a higher level of the richness of life and variation. This may mean that the solely functional value will not necessarily increase, but the experience value certainly will. The city originated from crossroads, human contacts and material exchange. Buildings, as an intersection of human communication, can achieve the same complexity as a small city.

Within the great frame of Modernism subsequent architectural trends have been variants, each of which was surpassed by a following sub-trend in one or two decades. Structuralism's ambition is to accommodate life from the smallest human level to a greater cooperating whole. It has the shape of a built image of the beehive-like character of society. Next to that many sub trends busied themselves particularly with different external shapes of buildings as material appearances in which the characters of later generations always can be distinguished. A distinction to show an age difference and a difference of opinions. In a building technology sense this leads to a different choice of materials and shapes of building components. It is normally not because of technical performances that building products fall out of grace. More often the changes in functions and aesthetics, spurred on by the urge of manifestations of new generations, will lead to this.

After the age of the clarity of Modernism with its analysis and separation as a *thesis*, the integration as an *antithesis* shot forward and started to overrule the architectonical profession. Everybody has to cooperate with everybody. Everybody interferes with everything and only a few are ready to take clear responsibilities. A communal game of shifting off responsibilities is the result. Everything has to be integrated until nobody remembers cause and effect and who is responsible for what. In fact integration has often struck inward, it imploded. Instead of a large community, a great fogginess occurred. As a possible *synthesis* the introduction of individual actions will again be distinctive and clarifying. The building process is a social process and as such influenced by the spirit of the times. Both building and spatial environment are the result of a super integration, they are achieved more and more laboriously and cost fortunes in these stages of preparation. To justify interventions in public areas is a right which should be kept safely, but it often results in inactivity. Some investment is needed in the search for a better balance in this public process of integration, in order to get it manageable again. Would it not be better to gradually get rid of the outgrowth of the achievements of participation as seen in the Seventies and to go back to personal achievements and adventures?

In these days of increasing computer sciences and virtual reality, the question should be asked whether it is still logical to create a material envelopment for a society which changes so rapidly. An envelopment for which the preparation and realization take such a long time and of which the material form is so rigid that every subsequent changes will outdate any building. Should we, in the future, build like we have in the past? If so, how adaptable must these buildings be! This leads to a different answer than that of Archigram in the Sixties, where the building of the future was looked upon as a material framework which could be changed and adapted at random, by which individual spatial needs can be plugged in, zoomed out and blown up (Cook, 1999) From this image of material adaptability within a minimally conditioning framework grew the concept of the Centre Pompidou in the early Seventies.

For that matter it was the first building which materialized Archigram's idea so clearly. And even that

building hardly changes on the outside, certainly not in the way it was meant to be or in the way the building is capable of. This may be a matter of limited vision of the building management. After twenty years of intensive use the building has been painted again and once more looked like the High-Tech architecture bomb that changed architecture for ever. But many of the buildings from the Seventies and Eighties, flirting with their skeleton-like nature and flexibility of usage, prove to be unchanging buildings when it comes to their usage.

The point has not yet been reached that the use of the virtual reality of Cyberspace has changed the view on the built reality. But, minding the imperfection and the enormous energy which material building brings along, and the apparent perfection of virtual reality, the future holds a transition from the concrete to the abstract world, from material to immaterial world. This image is summoned by the apparent nonchalance with which images of a newly designed building can be generated on the computer in 3D. For that matter it is known that *not everything which is drawn, can actually be built.* First the laws of the material world, the logic of building technology and rational estimating shall have to meet their requirements. As for now, for many observers digital designs are not only a dream but also a lie as they are un-true.

The new buildings of the first decade of the new millennium stand out because, in general, they do not outshine by technical newness, but are sooner compositions of conventional components, built with established materials and by known production manners. Sometimes the material composition of a building can be eccentric in its components, in order to give the building distinction. Usually, however, *the maximum freedom granted to the architect, is the positioning of material components in space.* The different positioning of components of the building in space has everything to do with the shape of the building, the shape of building parts and the shape of components. This is highly stimulated by using the computer mainly for coordinating shape and geometry. Without the help of 3D modeling and up to date computer science for the benefit of the phases of both materializing and working drawings, architecture would never, or only with great difficulty, have been released from the orthogonal system. One single slant or bent line is just possible in conventional architecture. Scharoun and Aalto were masters of the slanted line.

But when the geometry of a building can no longer be described as mainly orthogonal, a border is crossed: the geometrical complications of predominantly slanting and bent influences in buildings can hardly be worked out by hand. However, the Eiffel tower has been produced with the help of approximately 15,000 drawings, done by hand, of mainly straight components with non-orthogonal endings. So, we no longer have our hand in it, also by the conveniences of the straight T-square and the orthogonal Modernism. In contrast with the shipbuilding industry, architecture is capable of functioning without bent and slanting lines. Is oblique and curved the fashionable trend of the moment? Working with the computer on these complex geometries goes at the cost of valuable time by many, in preparation as well as in realization: it takes a lot of energy and effort.

2 THROUGH COMPONENT DESIGN AND PRODUCT DEVELOPMENT

The traditional building techniques were mastered by both designers and builders. This brought rest and matter of course in the communication between them. Both parties had acquired sufficient knowledge and experience to have the building industry in all its elements be a known process. By the introduction of many new techniques and components which are shut out of the communal field of experience, however, the building process has become very restless. What is more, it seems there is no way back anymore. Due to the common ruling suspicion among ad hoc constitutional parties in the building team, sometimes tangled together for one single building project like a Gordian knot, the learning curve is not positive, if it exists at all.

During the transition period from '*traditional & rational building*' to the '*prefabricated & assembly building*' it is not surprising that certain knowledge and experience get lost. This happens with every succession of generations. It goes hand in hand with the introduction or the pushing through of newly developed building techniques by the new generation. The senior generation will, at first, look with unholy glee upon the lack of knowledge of the junior generation when it comes to technique, but will thereupon be amazed to have to come to the conclusion that after a period of learning the new techniques are adequately being mastered. With that, designers have the courage to make bold proposals, in manners of working, compositions and details, by which they pull forward the building technology considerably. This assumption is based on the designer's eagerness to learn about building technology. Of course, it will sink the ship if young architects only occupy themselves with purely conceptual designing and not with the preparation for the actual building.

The young generation of building technology students at TU Delft is taught, with the help of all the usual metal workshop techniques, how to design prototypes of metal façades, how to fabricate these themselves and how to test them. And after graduation these designers will demonstrate in five or ten years how they have become competent technical architects when materializing building designs, and professional consumers with respect to the building industry. They look upon architecture and building technology as one integral item which cannot be separated. Twenty years ago, this professional view on the future stimulated me to introduce the term '*product architect*': a designer of building products with architectonical ambitions (Groenendijk, 1989). He is cousin to the '*component architect*', who designs and develops the components

of the building at the office of the architect, like the *component designer* does at the design & engineer department of a special component producer and like the *product designer* does for industrial household products. These young designers know that for the development of new building techniques an inventor cum engineer is needed standing between the architect and the engineering parties, who serves as 'Jumping Jack' between concept and building, in a renewing and surprising way with a mixture of commercial, scientific and artistic aspirations. The Delft students see the world of technology differently before and after making a real material prototype. The TU Delft experience to make a metal workshop an obligatory part of the curriculum for the Master of Architecture course is an inspiration for architectural schools worldwide. After 16 years of full service the Laboratory of Prototypes changes its environment for a mobile laboratory, enabling students to work on building sites and different factory environments to experiment with quite different components.

Some industrial designers try to converse the very limited choice of mass manufactured consumer products into a broader choice for the consumer. The building industry has traditionally always been directed mainly at the wishes of the customer. A contractor usually builds exactly what his principal wants, he follows the consumer's wishes precisely. Producers in the building industry, particularly system producers, know that only the additional requirements of the consumer-architect complete the program of requirements for the product in question. With special products only a direct development between consumer and producer can precede the manufacturing. In the building industry '*customising*' or customer directedness has never been absent. Indeed, this is the cause that the industrialization of the building branch stuck fast at the level of serial prefabrication. A level of industrialization as is usual with the production of cars, will never get started up in a comparable manner in the building industry, because of the fragmentation of the order flow and the diversificationof consumer demands and (ad hoc) the changing of the production teams. Although standard products like the smallest components are actually industrialized, this level of industrialization recedes in the series '*Standard product – System product – Special product*'. But the building industry has its own charming way to work as rationally and efficiently as possible within the given parameters. Components are often manufactured from trade materials with the help of computerized manipulation machines. And when the series' size does not allow it, building components will be produced mechanically or even manually if necessary. The level of quality and costs of fully industrially manufactured products will then, of course, only remain a wish-dream to be pursued by the next generation.

Quality was, traditionally, something which was achieved at the building-site and could be checked there as well. With the introduction of more and more building components which are produced outside the building-site, both designers and builders have lost sight somewhat of the production manners. By moving the place of production, to the specialist-producers of components both architect and contractor lost sight on the daily supervision of achieving quality. The quality of the many components to be prefabricated elsewhere depends on the quality assurance processes of the involved producers. On the one hand, the lower thresholds of the building industry cause few producers to take initiatives to develop new building products and introduce them on the market, because there is only a small chance that the products will be protected and a far greater chance of being copied by competitors. On the other hand these lowered thresholds are a direct cause for the enormous level of boredom which buildings reveal. Our built environment is the literary result of spiritual poverty and lack of courage to take new initiatives. This goes for the party calling for tender, the owners, real estate developers and architects cum suis (advisers) as well as for the tendering parties: contractors and producers. And when new courses are being taken, the vision from the party calling for tender on that of the producing party is often merciless. Many sacrifices are expected for a cleverly built feat. An example is the bankruptcy of both the steel construction company and the glazing company at Nicholas Grimshaw's Waterloo Station in London, while the building itself and its architect were praised highly. The steel and glass 'whale' roof of the DG Bank in Berlin brought Frank O'Gehry further fame, but the specialist contractor Gartner almost went bankrupt and was taken over by Permasteelisa and ceased to exist as Europe's finest façade builder.

Conservative designers are of the opinion that sufficient materials and techniques are known and ready to be used in the building technology. In general the architect will be more selective and combining than being a re-inventor of the wheel. Indeed, there is an over-supply of material means to build buildings with. However, these material means regularly fall out of use. Directed interest is capable of completely brushing aside a matured technology and to direct itself at something different. After twenty years of research and developments the concrete industry knows how to make perfect parapets in washed clean concrete which will not get dirty anymore, come rain come shine. Unfortunately architects are no longer interested to propose this material for lining a façade. 'Beton brut' is also hardly used anymore. The knowledge of formwork carpenters to make timber formwork for rough concrete exposures, has almost gone lost. Tadao Ando starts a very revival. The architect's choice of materials and techniques has a lot to do with what they, abstract looking in their generation, want to express to society through the building.

In the personal workplace environment it almost seems a contradiction for the increasing immaterialisation of electronic information flows via the uncheckable usage and development of the computer to house them in their opposite: ultimate material and heavy stony buildings. In there, hope for eternity is

radiating. Sooner fine building techniques, which are developed with care and intelligence, would be considered for a contemporary expression. Large, washed concrete panels have lost it from lightweight suspended façades, build up with sandwich panels from millimetres veneer layered natural stones on a rigid aluminium honeycomb structure. Sandwich panels have an energetic accountability without an annoying warmth-accumulation. Glass panels get a growing insulation value, in combination with a highly light transparent quality and a low transmission of sun-energy. In the future glass coatings will be developed with characteristics which can adapt to seasons, as well as to the time of day, in reaction to the amount of received sunlight. This adjustment of physical characteristics is done chemically and does no longer need to be directed mechanically, like in the Institut du Monde Arabe of Jean Nouvel, or architecturally like the earlier 'brises soleil' of Le Corbusier and the beetling roofs of Frank Lloyd Wright. An irreversible transmission can be traced in the interest in building technology from civil engineering, where she leaned against for generations, to mechanical engineering, which notably in façades, interior building, climate installation services and movable components of the building, begin to predominate architectural expression more and more.

Façades and climate installations put together often make up more than half of the building budget. Reinforced concrete load-bearing structures are functionally speaking still of an essential importance, but to architects they are no longer interesting because there is no designing in them. They have given up their sculptural aspirations. Steel structures show virtually all of their muscular play of forces and are much loved for that reasons and*tubular structures take the elegant part of steel structures in this case.*

Through that the building technology has developed further, unfortunately at the cost of necessary spatial quality. Which, by the way, does not mean to say that architecture should become less sculptural. But more values get lost in the delusion of the complex geometry. Architects who have always worked conscientiously and cautiously for 'durable' and 'sustainable' architecture and who used the orientation on the sun as their starting point for an optimum spatial geography of their buildings, now watch helplessly the orientation on the North for photosensitive activities disappear as a consideration for designing in the workplace environment. The home environment, on the other hand, aims far more at logical duration and energy-economy. The individual needs more protection than the organization. The second generation of sustainable architecture only started recently its development research. It will take a decade before its technology is mature enough for popular application, although EU expects clear energy neutral results in 2020.

The growing demands which are claimed upon materials and components with which buildings are being assembled will no doubt result in the going out of use of certain materials. In general the material assembly will become more complex in order to fulfil the growing demands of different natures. With the increasing demands goes a longer duration of materials, often founded on guarantees. On the other hand it can be stated that technical performances no longer determine durations, but rather aesthetical, functional or economical considerations.

Even durably designed buildings will have to be adapted, long before their technical duration of life is reached. In a way durable materials will provide their own specific problems. How to re-use materials which still wear well, but never again will be used in the same form of elements and components because between use and re-use there is normally a generation of years and ideas? In architecture, till the end of the Middle Ages, re-use of components always occurred. Blocks of marble and purposely hatched natural stones were often re-used as precious building stones for buildings of later generations, until the days of prosperity and plenty made an end to this re-using. The San Marco in Venice and the cysterns in Istanbul are a proof of that. Today politics subsidize conscience-easing developments to use more durable materials in society. The building industry, as a branch of industry in which materials already have a relatively long duration of life, joins gladly in this way of thinking.

The growing ingenuity to answer to higher quality demands brings along an improvement of materials which are, for that reason, not so simple to re-use. Coated glass with silicon edges in double glass panels pollutes the melting bath of recycled glass so much, that a far much lower quality of glass would be the result. Therefore, this coated glass is no longer recycled. Nobody wants to re-use the heavily reflecting silver-colored and bronze-tinted glass anymore. This glass is now downgraded to beer bottles. So, valuable material which could live much longer, is being removed as non-degradable waste. The future generation of coatings therefore has to be degradable again or possible to melt down without problems. And we have not even started to incorporate nano-technology in building products!

3 VIA IDEA AND METHODOLOGY

Architects are in arrears because of their lack of knowledge of contemporary production techniques of industrial and prefabricated building products, compared to manufacturers. Manufacturers are orientated on results and interested in the medium long and long-term survival chances of their company. They lack knowledge and insight when it comes to architecture, their market. They know more of the building industry and the building process. From their point of view, architects complain that it is difficult to get data from producers. The reservedness in the attitude of manufacturers also comes from the number of times when they got no appreciation for their design inputs. The only way to get a flowing stream of information going is to achieve a direct dialogue between architects and

manufacturers, based on mutual respect and trust. An architect can, in general, 'shop' only once at a manufacturer's sales department, the next time he will lack the courage or will find the door closed.

Innovations of building processes and building products have to be well prepared. The main part of the innovation route has to take place outside the application process of the building project, in a preceding or parallel development route of the innovation system. Separation of development and application of innovations finds its cause in the great difference between thinkers and doers. The building industry knows many doers and the thinkers are being forced to canalize and temporize their thinking. Few principals will be willing to pay for innovative research with a somewhat more fundamental character than the direct applicability. Not many main-contractors will offer the opportunity for this. 'Nimop': 'not in my own project'. Leave it to the competition first. Let they take the risks first. Innovation in an ongoing building process can sometimes have the same effect as a stick between the spokes of a riding bicycle.

Headwork, preceding innovations in the conceptual design, are often stimulated by architects by means of design competitions and magazine publications. Amongst main-contractors this is done by reflections on logistics and organization. Manufacturers work with material research and developments which, next to the objectives of the company, aim at the rousing of new products or the improvement of quality and prolonging the duration of life of existing products in operation, building up or assembly and continuation of the manufacturing company.

With the increase of complexity of building tasks and buildings, there is also an increasing work division for preparing and guiding the engineering of building projects. Next to the complexity, a number of added advice and management layers became a fact. These specialists, however, are only capable in their autonomous fields and by this they burden the communication in the process. Although every specialty contains autonomy and responsibilities, in the building industry it seems to become a sport to throw responsibilities to one another, from the calling to the tendering parties, hierarchically from the first contracted parties to the last contracted ones. This excess of participants with diminished liability asks for a better order, back to a well-organized and manageable building process. Concentration of authority and responsibility would clarify the relations within the building team considerably. It is up to the architects to manifest themselves strongly enough to take charge again of the revealing weeds of the building management, and by so doing retrieve, for a great part, their earlier position in the building process.

This will only happen if the architect places himself squarely before his task and accepts again full responsibility for the growing importance of the process of, for instance, the attending and control of building components drawings, made by specialist-producers. The drawings of the architect are insufficient for engineering purposes. Legally the architect used to take no responsibility for any measurement. Also on drawings of prefabricated buildings and their components sometimes the phrase '*measurements in the work to be taken before engineering*' still appears which is may be legally correct, but in technical engineering is an incomprehensible anachronism. We will hopefully live to see that the design and engineering drawings, clustered in a real 3D model, the Building Information Model (BIM), will serve as the basis for the engineering and production drawings of all subcontractors and manufacturers involved in the project process at hand. The architect will then have to take responsibility for the correctness of his work, in the knowledge that other building team members will rely on it. There is an unique opportunity for the architect to regain his lost power in the building process with the introduction of the 3D model of the building to be realized, the BIM. He has to set up, develop and guard this overall 3D-model. The certified 3D-CAD-model architect will be introduced. In the end all quality assurances of all building team members, as set in certificates ISO 9000/9001, must correspond. None of the building team members will be able to withdraw from that, not one single manufacturer and not one architect. The formula of the building team is directed at co-operation, while the usual system of tendering and sub-tendering leads to passive or even forced co-operation, whereby too much sand causes a considerable slowing-down of the smooth running of the wheels.

The ever increasing perfection of computerized engineering, challenges a greater spatial quality which can be calculated mathematically up to an unprecedented high complexity level. As a result of this, the preparation route will win considerably in quality from complexity and refinement. If the computer processing of the engineering parties and those of the architect will be coupled, then the rapidity and accuracy of the describing of components in working-drawings will increase as well. For orthogonal buildings, that are also in the near future expected to be designed in a 3D BIM model, goes that every automation can mean profit in many respects. But particularly more complex geometries will, with decreasing surplus energy, inevitably be laid down in 3D models. The step to the actual manufacturing will be considerable and the assembly at the building-site will drop behind a good deal. The computer pulls forward the preparation process, while material production and on-site building stay behind, because these are more material and human committed activities.

As far as the author knows, there is no building component in The Netherlands yet which is placed in an automated procedure, for instance with the help of a barcode. Considerable investments will have to be made in the engineering process, in order not to lose the profit in spatial quality, as made possible by the computer in the conceptual phase. The pioneers of complex, computer stimulated geometries, like architect Frank O'Gehry, who in their design instrument also find a stimulus to get to better designs, will

initially have to take entirely in tow their building team members of the engineering team, in order to diminish the widening gap between CAD and CAD/CAB (Computer-Aided Building).

4 TOWARDS FUTURE ARCHITECTURE

The work environment becomes more and more coupled to physical and virtual information flows. Location and position with respect to pedestrians, cars and public transport play an important part, buildings are alive thanks to the infrastructure of the city. The information revolution with its unprecedented high speed of development, will ever more quickly influence the discomfort of an unchangeable building. Many facilities, like computer floors, which a decade ago testified to a foresight are being rendered out of date by the great strides of miniaturization of the computer.

Large, bright glass façades for office spaces are, because of the great and blinding power of light, no longer to be combined with working behind com-puter screens. The relevant health & safety regulations can be adapted. The current office environment gets a more and more pleasant atmosphere by the partly turned-off neon lights. The building and the façade as its visually most important part, will have to symbolize the evolving of the organization with its time. The building becomes a three-dimensional infrastructure, capable of growing with the changes of the twenty-first century. Therefore, the façade as a metaphor is interpreted by many architects in their own way and translated into a material design with their own signature.

The architecture of durable building will doubtlessly result in a neutralizing and abstracting of buildings, in order to give the entire building a longer life, functionally and aesthetically. Buildings which are over-measured in floor space and volumes will, for that matter, go along with changes of organizations and different visions on use longer and better than in economically dimensioned and tightly cut-in buildings. This requires a change in the economic way of investment thinking.

The on-going developments in hardware and software of computer technology may result in an increase of working speed, a greater efficiency and completeness of production and perfection of the built result. The critical factors remain, after the vision of the principal, creativity and imaginative faculties, the search for spatial tension and unexpected surprises in the work of the architect. Important are the knowledge, know-how and insight of the architect to choose the most appropriate materials, elements and components and to know and describe the artistic design of singular materials via various methods of manufacturing. Designers with sufficient knowledge and skills, but without insight and vision will increasingly be unmasked when the revolution in the designing information science will have spent itself. *'Architecture is still about making good and excellent buildings'.* It is the author's opinion that the architect must be completely responsible for the entire building. This can be done on a continuous basis if he watches over the entire building development route. Ad hoc project processing in which at the same time the long term is not directed at, will not lead to a consolidated 'body of knowledge'. In those cases an equal surplus energy will be necessary, which will eventually lead to loss of interest of the parties involved and to a slowly disappearing out of sight of the started search for a better quality.

Improved material assemblies, details and material performances require a higher level of building technology than the mere geometric fiddling with the computer. Engineering follows design, as an activity essential to come to a good processing of the design. From a building technical point of view, the computer designs of Bernard Tschumi are assembled from very conventional, if not to say traditional elements and components. Spatially curved roofs in his designs are build up from curved rolled open steel profiles, while the building technology was already far more developed into a higher level of refinement in the form of curved tubular steel elements. Excellent in the field of geometry, but not so in building technical assembly. The secret might be that one can only spend one's interest once, either on a complex geometry or on a complex and refined assembly or structures, but not yet on both. Architects do have the ambition to create the new spatial quality by means of new building techniques, but for the time being they must '*reculer pour mieux sauter*'. First go back to education, collect knowledge and insight before the forward jump, and only later refine this in the striving to an intelligent form, an intelligent assembly and possibly even an intelligent responsive building, the step into the future. That level of a pre-programmed responsive intelligence of buildings is surely a prospect in the near future if architectural technology will be intertwined with climate installation services and façade technology at a higher level.

In general, building technology becomes ever less massive and ever more influenced by mechanical engineering. The steel industry preceded the concrete industry in this respect. Even the concrete building industry will experience its influences. As the bearer of all finished constructions, increasingly higher demands will have to be met by the load bearing framework, in the sense of strictness and tolerances. The precision of steel structures is high. Steel structures lead the state of the art. The precision of the concrete building industry cannot remain what it is now and was it one generation ago. This requirement will influence the manufacturing manners of concrete. It will lead to new 3-D definitions and the dimensional surveying of the reinforced concrete framework after pouring or the dry assembly. It will lead to a new generation of concrete building technology.

There is an increasing need for a defining party at the building-site as an independent surveying activity, not forced by bad work, but as a necessary and demanding intermediary between the building parties.

Especially on the fracture in between rough building and finishing stage many obscurities and non-fulfillments occur. In earlier days the building contractors surveyor did this job, but it is now taken off his hands. The building parties have to be affiliated to the project-CAE, (Computer Aided Engineering) which watches over and determines geometries yet to be built, a necessary step to CAB (Computer Aided Building). In several fields, the computer shall have to simplify local building (i.e. the pouring of concrete) and the assembling of prefabricated components. A control function, instigated by a specialist surveying operator, in future mechanization, automation and robotizing of a growing number of activities at the building-site, will be a prospect for the next computer generation's use of the onsite.

The manufacturing techniques of building products and components, which came into use during the last generation of industrial architecture, the High-Tech Architecture era, are available and absorbed as common knowledge. That will provide a balance between the knowledge and know-how of the architect at a building technical level, like it was known in the traditional and rational days. The current tendency to escape into conceptual thinking because of the lack of knowledge and insight in manufacturing techniques, and stimulated by the strive for performance estimates will, after the injection of the present very mechanical engineering-like production techniques, form a new balance again. The architect has to regain his mastership of integration of all components into a building which bears his view on spatial quality. The designing of buildings has to lead to architecture with a highly functional and spatial quality and a long duration of life. But, most of all, architecture has to be exciting, surprising and give us the feeling of living in an exciting world. And tubular structures stimulate the technical quality of architecture.

5 CONCLUSION

"The younger generation has to surpass the accomplishments of the established generation of designers. Not to copy their work, but rather to stand on their shoulders, interpret the signs for the future, investigate new possibilities and develop new interpretations, make a new generation statement and look fresh into the future. Knowhow and insight may increase, it also has to be applied in ever changing situations according to the best knowledge available, yet with an ambition to surpass the current world. Stand on the shoulders of the current generation and look further!"

REFERENCES

Cook, P., 1999, Archigram, Princeton Architectural Press, New York.

Groenendijk, P. & Vollaard, 1989, Boosting in bedrijf, 010 Publishers.

Eekhout, M., 2011, Tubular Structures in Architecture, Cidect Geneva & TU Delft.

Tubular Structures XIV – Gardner (Ed.)
© 2012 Taylor & Francis Group, London, ISBN 978-0-415-62137-3

Application of concrete filled steel tubular arch bridges in China

Y.Y. Wang, X.R. Wu, Y. Geng & S.M. Zhang
School of Civil Engineering, Harbin Institute of Technology, Harbin, China

ABSTRACT: China is a mountainous developing country, in which a lot of streams and rivers rush through deep valleys. Arch bridges are economically applicable to span river valleys and deep ravines with high-gradient rocky riverbank and fast water flow. Concrete-Filled Steel Tubes (CFST) are ideal structural solution for arch bridges in China because of their high compressive strength as well as efficiency in construction. This paper conducted an extensive survey of the standing CFST arch bridges in China. The design of this kind of bridge, including the structural information of the bridge, the geometries and material properties of the arch, and the construction method of the arch are discussed. Typical CFST arch bridges were introduced in more details. Suggestions on the design of this kind of bridges were brought forward.

1 GENERAL INSTRUCTIONS

Concrete filled steel tubes (CFST) are members made of hollow steel tubes filled with concrete (also called core concrete). Concrete filled steel tubes can combine the advantages of steel and concrete material. The encased core concrete prevents the thin-walled steel tube from local buckling. In return, the steel tubes provide confinement to the core concrete improving the compressive capacity and ductility of the CFST members. During construction, the hollow steel tubes can act as permanent formwork for the pumping of the core concrete, saving time and cost for establishing and demoulding the temporary shoring systems.

Considerable research efforts have been devoted over the past decades to investigate the static and dynamic behaviour of CFST columns. General reviews of the investigations have been presented by Tomii (1991), Shams & Saadeghvaziri (1997), Shanmugam & Lakshmi (2001), Uy (2005), Goode (2006), and Zhong (2006). As a result, CFST members have gained their popularity in subway structures, towers, tall buildings and bridge applications.

In bridge construction, CFST members have been used as the piers, the falsework, pylons, main girders, and arch ribs, etc. Among all possible applications of CFST members in bridges, their use as main arch ribs is the most extensive one. These bridges are called CFST arch bridges. Using CFST members as arches can make a full use of their advantages on load bearing capacity due to the fact that arches are almost under pure compression when subjected to distributed loading. During the construction of CFST arch bridges, the hollow steel tubes are first hoisted and erected to span the river or valley. After the closure of the hollow steel arches, the concrete is pumped inside the steel tube. The light weight and strong resistance of the steel tubes make it possible for the structure to span long distances and, because of this, construction techniques such as the slipform method are not needed.

This paper presents the development of CFST arch bridges, as well as an extensive survey of the standing CFST arch bridges in China, including the structural information, the geometries and material properties, the construction method, and existing problems in CFST arch bridges etc.. Designing suggestions are provided based on the survey results.

2 DEVELOPMENT OF CFST ARCH BRIDGES

The first CFST arch bridge in the world was built in 1939 over the Icet River (Исеть) in Siberia, former Soviet Union, with a span length of 140 m (Figure 1). Compared to the steel arch bridge, this bridge is considered to be more economical by reducing 52% of the amount of steel and saving 20% of the cost (Cai 2007). The bridge is built with on-ground-type scaffolding method, with which the advantage of the CFST members in the efficiency and cost effectiveness during the construction is not utilized.

Figure 1. First CFST arch bridge in the world (Cai 2007).

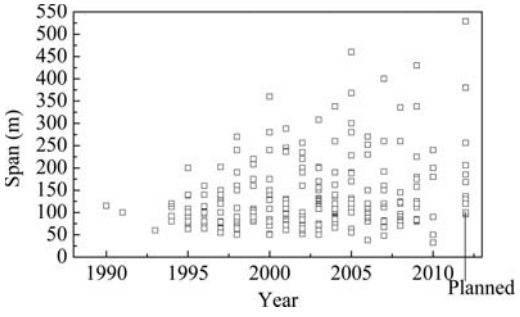

Figure 2. Development of the CFST arch bridges in China.

After this first bridge, no other CFST arch bridges were built for more than 50 years due to the limitations in the construction method. It was not until the 1990s that the CFST arch bridges started to become an attractive structural solution. Although this competitiveness is not predomingant in developed countries as the construction of this kind of bridge needs site pouring of the concrete, some applications have been constructed in Europe, Japan and America.

The real development of the CFST arch bridge has been taking place in China. China is a mountainous developing country, where concrete is still more economical than steel. Availability of more high-strength steels and concrete as well as the improved segmental hoisting and concrete pumping techniques further expanded the feasibility of CFST arch bridges. Since 1990, when the first CFST arch bridge, the Wang Cang East River Bridge, opened to traffic, more than 300 of this kind of bridges have been built in China, among which more than 85 bridges have a span longer than 150 m.

Figure 2 presents the development of CFST arch bridges in China during the past decades, in which 'Planned' depicts bridges under construction. It is clear that the span of the bridge become longer with time and the number of the bridge built every year is also increasing. According to the location of the deck to the arch, the CFST arch bridges can be categorized into three types: the deck arch bridge, with the deck completely above the arch; the through arch bridge, with the deck located at the height of the arch springing; and the half-through arch bridge, with the deck passing through the arch at the mid height. So far, the longest span among CFST deck arches in the world is the 430 m long Zhi Jing River Bridge in Hubei Province (China), opened for service in 2009. The longest CFST through arch bridge in the world is the Yong River Bridge in Guangxi province (China), opened to traffic in 2004, with a span of 338 m and a deck width of 35 m. The He River No. 1 Bridge (under construction) in the Si Chuan province of China, is the longest half-through CFST arch bridges in the world with a span length of 529 m. This bridge is also the world's longest CFST arch bridges.

Figure 3. Zhi Jing River bridge.

Figure 4. Yong River bridge.

3 REPRESENTATIVE CFST ARCH BRIDGES

3.1 *Deck arch bridge*

The longest CFST deck arches in the world (Zhi Jing River Bridge, 430 m long, China) is presented in Figure 3. The truss arch ribs are 6.5 m high at the arch crown and 13 m high at the arch springing, and have a constant width of 4 m throughout the arch length, comprising four 1.2 m diameter circular CFST arch ribs with a thickness of 24 (30, or 35) mm and webs formed by diagonal and vertical hollow steel tubes. The catenary arch rib has a rise-over-span ratio of 1/5.5. The distance between the two arch ribs is 13 m. Twenty wind braces are installed between the ribs to ensure the lateral stability of the bridge.

3.2 *Through arch bridge*

The longest CFST through arch bridge in the world (the Yong River Bridge, 338 m long, China) has the deck width of 35 m (Figure 4). The rise over span ratio is 1/4.5. There are sixteen windbraces between the arch ribs to increase the lateral stability of the structure. The parabolic arch rib is 3 m wide and 8∼13.29 m high, consisting of bottom and upper dumbbell shaped CFST chords and diagonal and vertical hollow steel tubular truss webs. The circular steel tubes of the CFST chords are 1220 mm in diameter and 16(20) mm in thickness.

Figure 5. Wu Xia Long River bridge.

Figure 6. Second Saikai bridge.

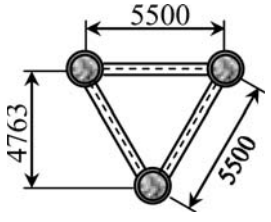

Figure 7. Cross-section of arch ribs of second Saikai bridge.

3.3 *Half-through arch bridge*

The construction of the world's longest CFST half-through arch (He River No. 1 Bridge, 529 m long, China) started in 2009 (Figure 5). Four 1320 mm diameter CFST members filled with 50 MPa concrete and hollow steel tubular webs constitute the 4 m wide and 8∼16 m high catenary truss arch rib. The rise over span ratio is 1/4.5.

3.4 *CFST arch bridges without wind braces*

In 2006, the world's longest CFST arch bridge without wind braces, i.e. the Second Saikai Bridge, was built in Japan with a span length of 230 m (Figure 6). The span to rise ratio is 4.79. The arch rib has a regular triangular truss cross-section (Figure 7) consisting of three steel tubes with an outer diameter of 812.8 mm and a maximum thickness of 50 mm. The bridge has a width equal to 20.2 m.

3.5 *Cable stayed CFST arch bridges*

The 400 m-span Xiang Jiang Si Bridge (China) opened to traffic in 2007 (Figure 8). The tower is in H-shape with a height of 90 m. The distance between the two arch ribs is 34 m, with eleven windbraces. The parabolic truss arch rib with the rise over span ratio of 1/5.19 has six 850 mm diameter circular CFSTs (three in the upper chord with the steel tube thickness of 22(24, 28) mm and the other three in the bottom chord with the steel tube thickness of 20(24, 28) mm) connected with CFST solid webs in the horizontal direction and 450 mm diameter hollow circular steel tubular truss webs in the vertical direction, except for the part at the arch springing where the cross-section is fully filled with concrete to improve their impact resistance from boats and ships. The arch is 9 m high at the arch crown and 5 m high at the arch springing, and has a width of 3.55 m.

Figure 8. Xiang Jiang Si bridge.

4 SURVEY OF CFST ARCH BRIDGES

An extensive survey of the standing CFST arch bridges was conducted with the information collected through the website, the literature review or provided by some bridge designers in China. The designing information collected from 313 CFST arch bridges is an update of the designing information reported by Chen (2007) on 202 CFST arch bridges. In this section, an overview and discussion of the design information are presented, including the structural information of the bridge, and the geometries and material properties of the arch.

4.1 *Structural information*

4.1.1 *Bridge type*

Out of the 313 CFST arch bridges, 148 are half-through arch bridges, 144 are through arch bridges, and the remaining 21 are deck bridges (Figure 9). For those bridges with a span longer than 150 m, there are 62 half-through arch bridges, 11 through arch bridges and 12 deck arch bridges.

It can be seen that the number of the deck arch bridges is limited, being only 7% of the total number of built bridges and 15% of those bridges possessing a span longer than 150 m. This is because, for this type of arch bridge, the elevation of the deck is high, making it only suitable for very deep valleys with steep walls. The use of the through arch bridges represents a competitive solution for small spans. More than 58%

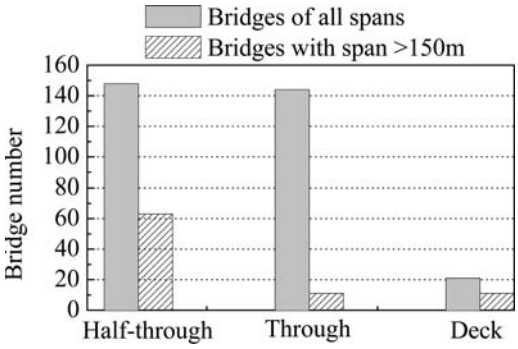

Figure 9. Different bridge types for CFST arch bridges.

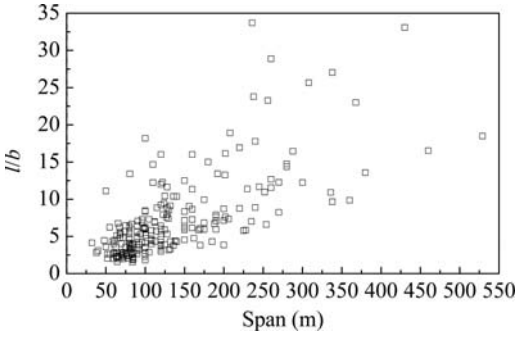

Figure 10. Ratio of span over width for bridges with different span length.

of the CFST arch bridges with a span smaller than 150 m are through arch bridges. They lose their competitiveness when moving to longer spans, because the limited clearance over the water cannot meet the navigation requirements for broad rivers. The half-through arch bridge therefore is the dominant bridge type used for long span CFST arch bridges, representing more than 71% of the total number of built bridges.

4.1.2 *Ratio of the span over width*

In the designing of CFST arch bridges, the designers normally determine the width of the bridge according to the number of traffic lanes required, leading to a great range of ratios of span length (l) over bridge width (b) (Figure 10). From Figure 10, it can be observed that the value of l/b gets larger as the span gets longer, meaning that the CFST arch bridges tend to be narrower compared to the longer spans. As a result, most of the CFST arch bridges with a span longer than 150 m will buckle in the lateral direction under ultimate loading, which may be further triggered by the increasing deformations produced by time effects.

4.2 *Geometrical information for arches*

4.2.1 *Arch profiles*

Figure 11 summarizes the number of CFST arch bridges with different arch profiles.

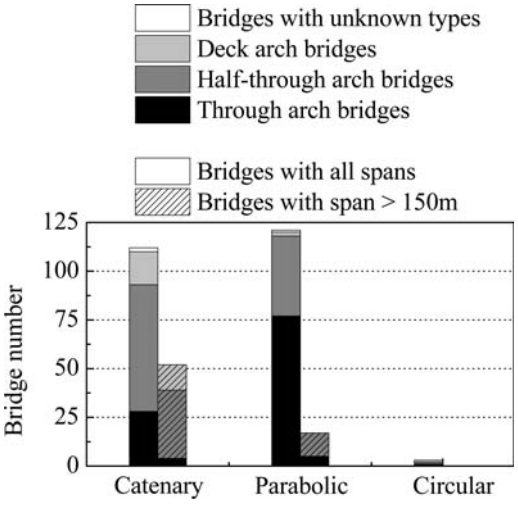

Figure 11. Different arch profiles for CFST arch bridges.

In deck arch bridges, the catenary arch curve is the most used, being used in 85% of the total number of bridges. All deck bridges with a span longer than 150 m possess catenary arches. For half-through arch bridges, the catenary arch profile is more competitive than the parabolic one: 65 out of 107 half-through arch bridges have catenary arches. Its advantages become more pronounced when the span is longer than 150 m, in which case the number of catenary arch bridges is almost three times of those with parabolic profiles. The use of the parabolic curve is more popular in through arch bridges (accounting for 72.6% of the total number) because the deck loading, distributed uniformly along the span, is more significant. Among the 311 bridges, only three bridges use circular arches, none of which has a span longer than 150 m. Though the catenary curve and parabolic curve are almost equally popular in CFST arch bridges, the former one possesses the dominant number in bridges with a span length longer than 150 m.

4.2.2 *Span-to-rise ratio*

The flatter rise of the arch leads to higher horizontal thrust, causing difficulty in the design of buttress, foundation and the ties if adopted. The bending moment inside the arch ribs increases with the increasing span-to-rise ratio. A low value of the span-to-rise ratio, on the other hand, leads to higher material costs for the arch and causes difficulties in the construction of the arch as it becomes higher, also leading to possible problems with lateral buckling. In this context, the span-to-rise ratio should always be carefully determined.

The span-to-rise ratio (l/f) for the standing CFST arch bridges covers the range 2–10 (Figure 12). It is obvious that most of the bridges, especially those bridges with a large span, have the span-to-rise ratio between 4 and 5.5 to achieve the best balance between cost and structural safety. For bridges with small spans,

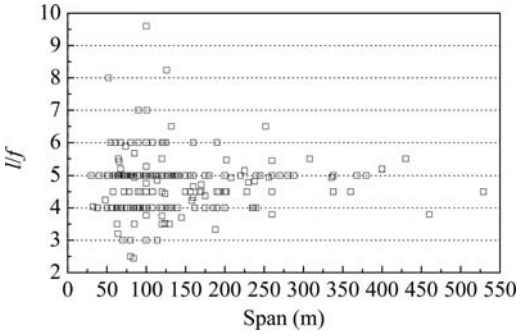

Figure 12. Span to rise ratio for bridges with different span length.

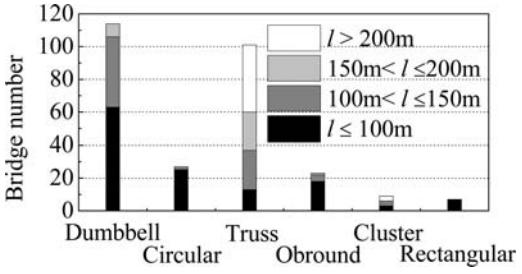

Figure 13. Different arch cross-sections for CFST arch bridges.

the ratio of span over rise tends to have a large variety to fulfill aesthetic needs.

4.2.3 *Cross sections of the arch*

A wide range of cross-sectional shapes can be used for the CFST arch member, including dumbbell shaped, trussed, circular, obround, cluster type, and rectangular. The number of bridges with different cross-sections is illustrated in Figure 13. The dumbbell shaped cross-section was adopted in the first CFST arch bridge, the Wang Cang East River Bridge. Since then, 114 CFST arches have been built using dumbbell shaped cross-sections. Despite its extensive use, this kind of cross-section is not recommended (Zhong 2000) as it commonly has a poor pouring quality of the concrete inside the web and the welding connection between the steel web and the steel tube has a high possibility of tearing up during the web concrete pumping. Besides, the dumbbell shaped CFST members attract more bending moment along the arch compared to CFST members in a truss structure. The trussed arch is another popular arch type in CFST arch bridges, with a total number of 101 bridges being built. The trussed rib is more desirable for long span arches. Among the 44 CFST arch bridges with the span longer than 200 m, 41 are built in the trussed form. Dumbbell shaped cross section and single circular shaped one only suit for bridges with a span length shorter than 200 m. The latter one has 26 applications with the maximum span of 158 m, 92% of which have a span shorter than 100 m. The obround arch cross-sections

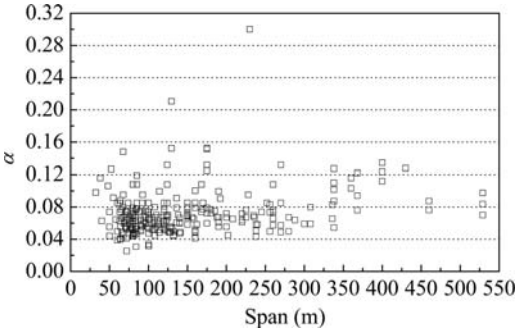

Figure 14. α value at the cross-section of CFST members for arch bridges with different span length.

are used in 23 bridges with a span length no longer than 150 m. In the 1990s, the designers tried to use the cluster type arch in CFST arch bridges but realized that it was not as effective as the trussed rib in resisting bending moments and it required complex connection detailing between the circular tubes. As a result, this kind of bridge was only used in 9 projects constructed between 1996 and 1999. After 2000, CFST arches with rectangular cross-sections appeared, with the total number of 7 bridges whose span length is limited to 100 m.

4.2.4 *Ratio of steel area over concrete area*

Figure 14 illustrates the ratio of steel area over concrete area (α) at the cross section of CFST arches for bridges with different arch spans. It can be observed that the generally used ratios of α cover a range of about 0.04 to 0.16, which is relatively low compared to CFST tall buildings with the α ratio of 0.08∼0.2. Among all the CFST arch bridges, 85% have the α ratio smaller than 0.08, some even lower than 0.04. Though the α value increases with the span length, only 3 bridges have a α ratio larger than 0.12.

4.3 *Material information*

4.3.1 *Steel*

The application of steel tubes with different yield strength (f_y) in CFST arch bridges built in China is presented in Figure 15. Steel with the yield strength of 345 MPa is the commonly specified material for the steel tubes used in CFST arches especially when the span of the bridge gets longer or the bridge is built more recently, taking 83% of the total number of bridges, 91% of bridges with spans longer than 150 m, and 92% of bridges opened to traffic after 2000. Only for one out of the 42 bridges completed after 2000 the steel has a yield strength of 235 MPa.

4.3.2 *Core concrete*

Figure 16 compares the number of CFST arch bridges using core concrete with different strengths. In this figure, the concrete strengths are graded following the Chinese Code (GB 50010-2010), with the characteristic strength being measured from concrete cubes

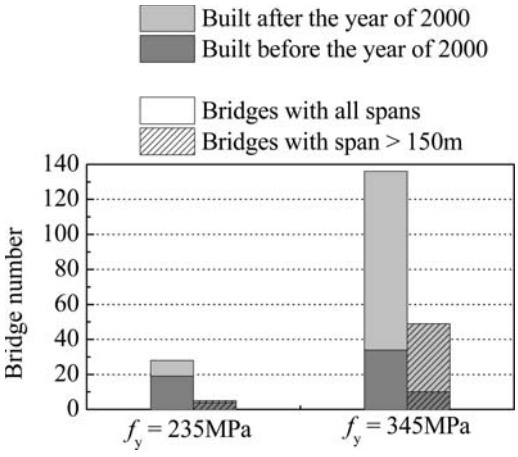

Figure 15. Different arch cross-sections for CFST arch bridges.

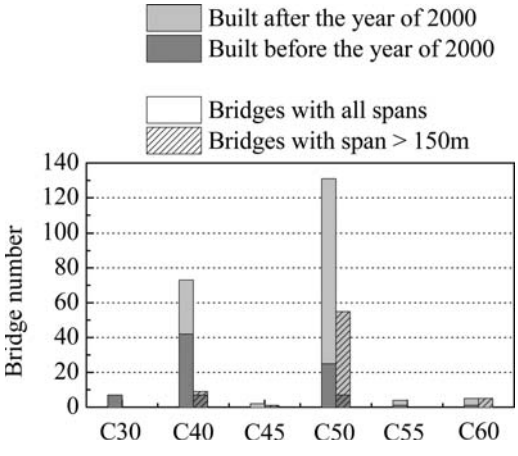

Figure 16. Application of concrete with different strengths in CFST arch bridges.

with the dimensions of 150 × 150 × 150 mm ($f_{ck\text{-}cube}$). The corresponding cylinder characteristic strengths ($f_{ck\text{-}cylinder}$) are listed in Table 1 (CEB-FIP 1993). As expected, the core concrete strength tends to increase for more recent bridges and with longer spans. C50 is the most popular concrete grade in the standing CFST arch bridges, with 59% applications in the total number and 79% within bridges with the span longer than 150 m. C40 concrete is also commonly adopted in CFST arches, especially for those bridges built before 2000, among which 55% built with C40 concrete. There are 7 bridges which used C30 concrete to fill the steel tubes and their spans remained below 125 m. After 2000, C30 concrete is no longer used for the main structural members, and CFST arches started to be filled with higher concrete compressive strength, i,e, C50∼C60.

Table 1. Characteristic strength values (MPa).

Concrete grade	C30	C40	C45	C50	C55	C60
$f_{ck\text{-}cube}$	30	40	45	50	55	60
$f_{ck\text{-}cylinder}$	24.2	32.3	36.2	40	45	50

5 ISSUES REQUIRING SPECIAL ATTENTION IN DESIGN

5.1 *Time-dependent behaviour*

The creep and shrinkage of the core concrete increase the deformation of the CFST members leading to more considerable deflection in CFST arch applications. For example, the constructional-site-monitor system installed on the Nan Pu Bridge (Zhe Jiang, China, span length 308 m, open to traffic in 2003) detected that the displacement of the arch crown was increased by 20 mm due to the time-dependent behaviour of the core concrete in arch ribs after 230 days from concrete pumping, equivalent to 20% of the total deflection caused by its self-weight (Zhang 2007). The arch of the Ya Ji Sha Bridge (Guang Dong, China, span length 360 m, open to traffic in 2000) was detected to sag by 0.12 m after one year of operation (18 months under loading from the core concrete pouring) (Xin & Xu 2003). The increased deflection of the arch caused by the time-dependent behaviour of the core concrete need to be considered in the design as it can make the arch axis deviate from the dead-load thrust line inducing incremental moments along the arch. It is also important to consider the time-dependent deflection of the arch when determining the length and jacking forces of the suspenders during the construction to ensure the flatness of the bridge deck and to prevent concrete cracking of the deck.

The time effects of the core concrete modifies the initial stress and strain patterns at the steel and concrete cross-sections, relaxing the stresses in the core concrete due to imposed strains, and increasing the stresses in the steel tubes. Measurements obtained from on-site monitoring of the Qian Island Lake Bridge (Zhe Jiang, China, span length 252 m, open to traffic in 2006) indicate that the stress in the steel tube at the arch crown increased by 45% 140 days after the core concrete pumped into arch ribs due to the time effect (Chen et al 2007). Used as the template and falsework of the core concrete pumping, the steel tubes normally have a relatively high initial stress which will be further increased by time effects of core concrete sometimes causing unexpected steel yielding during the bridge service life. An example in this sense consists of the Wanxian Yangze River Bridge (Si Chuan, China, span length of 420 m, open to traffic in 1997) (Gu et al 1999). Without the consideration of time effects of core concrete, the predicted stress states in the steel tubes of this bridge are acceptable in all the phases. After considering creep effects of the core concrete, the steel tube with the yield stress

of 345 MPa yield at the arch crown of the top flange at the end of the construction. The measured stresses are even higher (already yielded at the completion of concrete casting).

5.2 *Separation of concrete core from steel tubes*

Monitor programs carried out in construction sites have pointed out that, for CFST members, there is the tendency of the concrete to separate from the steel tubes, especially when used in bridge applications. Some of the main reasons at the basis of this separation include poor pouring and curing conditions, shrinkage of the concrete core, and daily temperature fluctuations.

Site detections were conducted for some CFST arch bridges built in the 1990s to check the bonding condition between the concrete and the steel tubes by using the Ultrasonic Flaw Detectors and by drilling small holes on the arches. The detection results indicate that for some of the bridges the concrete core severely separate from steel tubes in main CFST arches. The Fochen Bridge (Guang Dong, China, span length 112.8 m, open to traffic in 1994) was detected to have 288 separations with the area larger than 400 cm^2 and the depth bigger than 0.5 mm in main arches after 5 years in service. At the arch crown, the separation is 30∼100 mm in depth, while the outer diameter of steel tube is only 1000 mm (Zheng & Sun 2000). For the Nanhai Sanshanxi Bridge (Guang Dong, China, span length 200 m, open to traffic in 1995), after working for 13 years, separations between the steel tube and the concrete core are all along the main arch ribs with the depth ranging from 2 to 22 mm (the steel tube has a diameter of 750 mm) (Huang 2010). In some cases this behaviour may become sufficiently severe to reduce the confinement effects and to induce local buckling problems for steel tubes and hence affect the ultimate capacity of the structural system. Taking the Wujiang Second Bridge (Chongqing, China, span length 140 m, built in 1996) for example, after opened to traffic for 6 years, the separation between the concrete core and the steel tube is 20 m long at the arch crown with the depth ranging from 3 mm to 20 mm, while the steel tube has the diameter of 750 mm (Zhang 2005). Yang et al (2008) conducted experiments to investigate the reduction of the ultimate strength for members with the same separation ratio (ratio of separation area over the area of the cross-section) and found out that the ultimate strength can reduce by up to 16%.

Most of the severe separations in CFST arch bridges are induced by unreasonable arrangement of the air exit hole along the steel tubular arches, and the poor fluidity of the core concrete which needs particular attention for the designers. A possible solution to address these problems is to add expansive additive to the concrete mix. The commonly used amount of the expansive additive is 11.3%∼15.2% of the cement weight.

5.3 *Durability of CFST members*

Working out of the doors during operation, CFST members need to be carefully protected from rusting in bridge applications. Due to the poor anti-corrosion measures, some steel tubes of the CFST members in bridge practices were already found to be rusted after several years of operation. One of the examples is the CFST arches of the Fochen Bridge (Guang Dong, China, span length 112.8 m, open to traffic in 1994). Using acrylic enamel as the corrosion protection, the main arches of the Fochen Bridge have been found slightly rusted in the steel tubes of upper and bottom chords and heavily rusted in steel webs and wind braces after 5 years in service (Zheng & Sun 2000). The acrylic enamel can only effectively protect steel from rusting for 1∼5 years, and hence needs be checked and repainted frequently in bridge practices. The CFST main arches of the Wujiang Second Bridge (Chongqing, China, span length 140 m, built in 1996) also suffered severe rusty problem (Zhang 2005). This bridge adopted fiber reinforced plastics and composite material to coat steel tubes for anti-corrosion purposes. 6 years after operation, the steel tubes were found to be rusted all along the arch, though the fiber reinforced plastic or composite material coating was still in good condition. One of the effective ways to protect the steel tubes of CFST members from rusting is thermal spraying with Zinc, Aluminium or various amalgams (Chen 2007). With a service life of 20∼40 years, this technique has been widely used in steel bridges in developed countries like UK and USA.

6 CONCLUSIONS

CFST members can be a competitive structural solution for arch bridges. When the bridge is expected to span long distances, half-through CFST trussed arch bridges are recommended with the catenary arches possessing the span-to-rise ratio of 4∼5.5, which are prone to lateral buckling problems due to the high span-to-width value. Time effects have a considerable influence on the static response of CFST arch bridges as the ratios of steel area over concrete area (α) at the cross section are commonly rather low ($\leq$0.12). Currently built CFST arches normally comprise steel with yielding strength of 345 MPa and concrete with the 28-day cylinder compressive strength of 40 MPa. Based on site monitoring data from real bridges, this paper also pointed out some design issues that need designers' particular concern. These include the time effects of the core concrete, the separation of the core concrete from steel tubes and the anti-rust treatment for steel tubes.

ACKNOWLEDGEMENTS

The research reported in the paper was supported by the National Natural Science Foundation of China

(No. 51178146) and by the Project to support oversea doctors in Harbin Institute of Technology.

REFERENCES

Cai S. H. 2007. *Modern steel tube confined concrete structures.* China Communications Press, Beijing, China. (in Chinese).

CEB-FIP. 1993. *CEB-FIP Model Code 1990*, CEB bulletin d'Information, London: Thomas Telford.

Chen B. C. 2007. *Concrete filled steel tubular arch bridge*, China communication press, Bei Jing, China. (in Chinese).

Chen S. F., Yang D. W. & Yang X. S. 2007. Research on concrete creep effect of CFST arch rib concrete of Qiandao Lake Bridge. *Highway*, 52(6), 32–35. (in Chinese).

GB 50010-2010. 2010. *Code for design of concrete structures*, Ministry of Construction of the People's Republic of China, Bei Jing, China. (in Chinese).

Goode C. D. 2006. A review and analysis of over one thousand tests on concrete filled steel tube columns. *8th International concrete on steel-concrete composite and hybrid structures proceedings*. *12–15 August 2006.* Harbin, China, 17–23.

Gu A. B., Liu Z. & Zhou S. X. 1999. Analysis of time dependent effects of concrete, geometrical nonlinearities, material nonlinearities of Wanxian Yangtze River Bridge. *Journal of Chong Qing Jiao Tong Institute*, 18(4), 1–7. (in Chinese).

Huang Y. H. 2010. *Mechanism and effect of arch rib disease and suspender replacement for concrete-filled steel tube arch bridge*. Doctoral Thesis, South China University of Technology, Guang Dong, China

Shams M. & Saadeghvaziri M. A. 1997. State of the art of concrete-filled steel tubular columns. *ACI structural journal*, 94(5), 558–571.

Shanmugam N. E. & Lakshmi B. 2001. State of the art report on steel-concrete composite columns. *Journal of constructional steel research*. 57(10), 1041–1080.

Tomii M. 1991. Ductile and strong columns composed of steel tube, infilled concrete and longitudinal steel bars. *Proceedings of the 3rd International Conference on Steel-Concrete Composite Structure. 26–29 September 1991*, Fukuoka, Japan, 39–66.

Uy B. 2005. High strength steel-concrete composite columns: Applications and design. *Proceedings of the Structures Congress and Exposition*. *20–24 April 2005*. New York, United States, 1089–1100.

Xin B. & Xu S. Q. 2003. Analysis of creep of long span steel tubular concrete arch bridge. *Railway Standard Design*. 47(4), 31–32. (in Chinese).

Yang S. C., Wang F. M. & Qu P. 2008. Brief introduction to the core concrete's empty influence on the mechanical performance of concrete filled steel tube components, *Journal of Chong Qing Jiao Tong University (Natural Science)*, 27(3), 360–365. (in Chinese).

Zhang T. 2005.*Research of pathological analyses and remedial measures in long span bunched CFST arch bridge*. Master Thesis, Chongqing Jiaotong Institute, Chongqing, China

Zhang Z. C. 2007. Creep analysis of long span concrete-filled steel tubular arch bridges. *Engineering mechanics*. 24(5), 151–160. (in Chinese).

Zheng Q. & Sun G. A. 2000. Defects analysis and reinforcement of Fochen Bridge. *China Railway Science.* 21(4), 21–29. (in Chinese).

Zhong S. T. 2000. Several problems in the design of concrete filled steel tubular (CFST) arch bridges. *Journal of Harbin University of C. E. & Architecture*. 33(2), 13–17. (in Chinese).

Zhong S. T. 2006. Application and research achievement of concrete filled steel tubular (CFST) structures in China. *8th International concrete on steel-concrete composite and hybrid structures proceedings*. *12–15 August 2006.* Harbin, China, 24–29.

Tubular Structures XIV – Gardner (Ed.)
© 2012 Taylor & Francis Group, London, ISBN 978-0-415-62137-3

Blue Tree in a Red Landscape: Structure of a sculpture

R.H. Keays
Keays Engineering, Melbourne, Australia

ABSTRACT: "Blue Tree in a Red Landscape" was conceived by sculptor Konstantin Dimopoulos for the RACV Country Club in Healesville in country Victoria, and installed in March 2010. The author of the paper had the task of designing the structure to achieve the sculptor's concept. Blue Tree is about 7.5 m high and consists of 75 RHS planks with 150 connections – all different. Purpose-written programs were used to convert the sculptor's model to a finite element model for analysis and CAD models for automatic drawing preparation of each component. Corrosion protection was achieved using a high-build paint system.

1 INTRODUCTION

More than 2000 homes were lost and nearly 200 people died in Victoria's Black Saturday fires in February 2009. The Healesville Country Club was not physically affected, but the surrounding hills were covered with the blackened trunks of burnt trees. The Country Club was a major refuge for people evacuated from their homes and served as temporary headquarters for the fire fighters.

Konstantin Dimopoulos (Kon) took this vista as the inspiration to create a work that spoke of both the fragility and the strength of the human spirit. He described it as a homage to the community through a natural metaphor of energy and vitality of the tree and its renewal.

The work is coloured an intensely rich blue to signify the renewal of life from the black. The base of the sculpture is in black to reflect the black slate of the pool surrounding the sculpture, and then rises into this intense blue.

The author was engaged by Kon to design the structural form and its connections and supervise drafting of the details.

This paper starts with a review of design loads for sculptures in general, drawing on the author's experience. It then moves to the details of the design to accommodate those loads, and thence to the practical aspects of design and construction.

Figure 1. Kon Dimopoulos: Blue Tree in a Red Landscape 2010.

2 DESIGN LOADS

2.1 *Gravity loads*

Self-weight is the most obvious source of gravity loads, and is easily addressed, but Live Load could well be critical in a structure accessible to the public.

The author recalls an incident in a school playground where a bearer for a scramble net failed. When a teacher was asked how many children were on the net, the answer was "All of them!" Bearing this in mind when the author designed the structure of the sculpture of Rod Laver (Figure 2) at the Rod Laver Arena, his racket shaft was designed to sustain the weight of one person bouncing on the frame.

For Blue Tree, there was a clear need to allow for at least one person standing on the end of a branch, and perhaps a number on the structure as a whole.

2.2 *Wind loads and wind-induced vibration*

With the complex shapes associated with sculptures, assessment of wind actions on the structure is not easy

Figure 2. Rod Laver Statue with Racket.

Figure 3. Cracking in tubular discovered by lighting technician.

to do accurately. Facioni & Smith (1999) had accurate scale models which they placed in a wind tunnel, but this was not a practical option with Blue Tree.

An assessment was made of the drag of the structure as a lattice tower to give the total base moment and shear. This was then crudely distributed amongst the members in the structural model by applying a lateral acceleration to all members in the cardinal directions. The 1:500 year wind base moment corresponded to a horizontal acceleration of 2.4 g.

Wind-induced vibration is a potential problem with any unusual slender structure. Keays (2008) noted ten such problem structures including two sculptures and two phallic symbols atop of high-rise buildings. Most of these were constant cross-section cantilevers in Melbourne where afternoon sea breezes up to 20 knots occur three times a week. Those where vibration was not addressed in the original design showed signs of failure within 6 months of construction.

An unusual one was Manchester's "B of the Bang" (Figure 4), which had tapered conical sections. The texts on vortex shedding suggest that tapered sections are not likely to experience correlated vortex shedding. They also suggest that "cluttered" structures have considerable aerodynamic damping which should minimize the magnitude of vibration. Hence the early failure of "B of the Bang" might not have been predicted. Nevertheless, the author observed vibration in 10 knots of breeze in September 2006 (after ISTS11) as the probable cause of the clearly visible failures.

Kon, as a sculptor, has a different perspective on wind-induced vibration from that of a structural engineer. Figures 5 and 6 show two of his earlier works. The thin high performance composites fronds are dynamic, moving hundreds of mm in even gentle breezes.

Kon's concept for Blue Tree was for a more substantial structure than his earlier works. The tree branches were seen as Planks projecting from a central trunk. Such Planks might well suffer from wind-induced

Figure 4. B of the Bang.

vibration leading to possible failure, or a shortened fatigue life. So a decision was made to ensure the vortex shedding wind speed for individual Planks was greater than 30 knots, making it unlikely there would be sufficient time spent in wind-induced vibration to cause fatigue failures.

3 MATERIAL SELECTION

Budget requirements suggested mild steel was the only practical material for the Tree. A flat bar section was considered first, but this proved either too flexible or too heavy. This led to the use of an RHS section. The

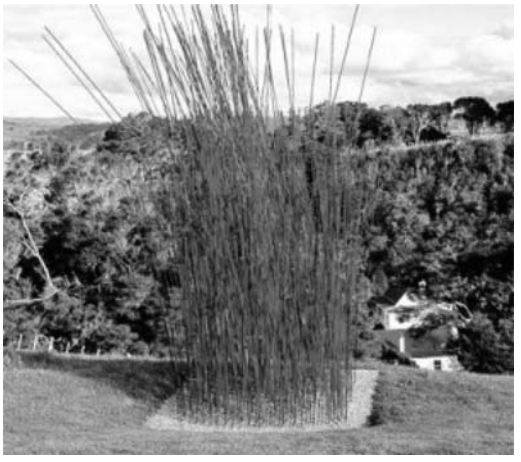

Figure 5. Kon Dimopoulus: Kete 2004.

Figure 6. Kon Dimopoulus: Firebird 2006.

standard 150 × 50 size proved acceptable artistically and structurally. 150 × 50 × 3 proved to be sufficient for all but a few Planks, with 150 × 50 × 5 for some critical members, and 150 × 100 × 6 for the four legs planted in the pond.

The calculated vortex shedding wind speed for the 150 × 50 × 3RHS was over 30 knots at 1.6m cantilever, so this was adopted as the maximum cantilever allowed in the structural form.

4 CORROSION PROTECTION

Blue Tree is planted in a 9m diameter pond. The edge of the pond is level so that water flows out round the full perimeter. The pond water is treated and recycled. This makes an aggressive environment for corrosion of steel.

Figure 7. Maquette.

The client's specification included a requirement for a 5-year minimum design life without maintenance. An expert on corrosion protection (Mark Dromgool of KTA-Tator Australia) was consulted on surface protection. He recommended a high-build epoxy paint system on Blast Class 2.5, with 375 microns DFT and coloured polyurethane top coat on the Planks, and 450 microns DFT and black epoxy on the four Legs (immersed steelwork) and the splash zone.

As part of the corrosion protection requirements, all RHS ends were capped and seal-welded, and sharp edges ground to a radius. Because the sculpture was too large to transport as a whole, it was decided that all connections would be bolted, with sleeves welded into the RHS to ensure a totally sealed internal structure.

The sculptor accepted galvanized bolts without paint as a feature of the construction. (The author welcomes an artist prepared to allow the structural form its own credibility.) All bolts were M16 Grade 8.8.

Blue Tree is an excellent example of construction design for durability without the use of exotic materials such as stainless or weathering steel.

5 MODEL CREATION

5.1 *Concepts*

The sculptor first made a maquette (rough model) at about 1/10th scale using timber slats for the Planks and bailing wire for the connections (see Figure 7).

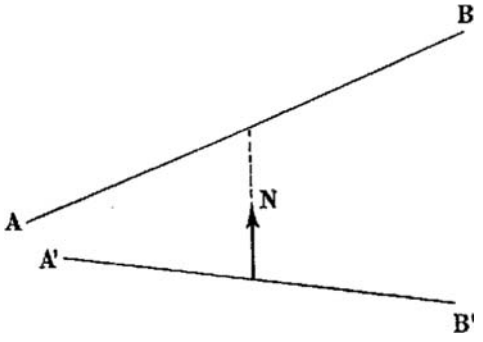

Figure 8. Vector $\mathbf{N} = (\mathbf{B} - \mathbf{A}) \times (\mathbf{B}' - \mathbf{A}')$.

The positions of the ends of all Planks on the model were measured, along with a list of all the Planks that each one connected to. A simple numbering scheme was adopted with the Planks being P01 through to P75. The connections from Plank to Plank were 4-digit numbers, so that, for example, C2659 was the connection between Plank 26 and Plank 59.

A third of the Planks had only two connections, but the four main Legs forming the trunk had up to twelve attached Planks, and the most difficult Plank connected to eight other Planks.

A program was written in QuickBasic to take the model measurements and convert these to input files for Finite Element Analysis for structural analysis and AutoCAD for graphical presentation.

The first simple three-dimensional AutoCAD model of the Planks proved extremely useful to show the sculptor and the client what the structure would look like before proceeding to detailed design.

Subsequently, further programs were written to feed an adjusted AutoCAD model back into the start of the process, and to prepare details of the connection elements.

5.2 *Finding the connection points*

Having recently read Arianrhod (2003), and Turnbull (1929), the author appreciated that determining the best point for each connection was a natural application of Vector Mechanics. Reference was made to the author's text from undergraduate mathematics (Christie, 1952) to refresh the memory on Vector Mechanics.

The direction of the vector of the shortest distance between two lines in space is the Cross Product of their vectors. The distance between those two points is the Dot Product of that vector and a vector between points on the two lines. The points at the ends of the shortest distance line are found by solving two simultaneous equations.

This simple concept formed the basis for rational development of the structural model.

Further use was made of vector mathematics to define the "twist" of each Plank, and to set out the connections (described later).

5.3 *Interfacing to AutoCAD*

The QuickBasic program prepared an AutoCAD "Script File" – normal AutoCAD command lines in a text file – to define each Plank as an extruded rectangular shape. Each Plank had its own AutoCAD layer and coordinate system. This allowed selective display of the Planks during development, and allowed the sculptor to quickly choose the colours.

It proved convenient to modify some of the Plank positions in the AutoCAD model. To retain model integrity, the AutoCAD data was fed back to the QuickBasic program via the "LIST" data extraction feature.

5.4 *Massaging the model*

The sculptor and engineer joined forces to produce the final layout by modifying the original in various ways. Fudge factors were introduced into the translation routine to stretch, squeeze, rotate and twist groups of Planks whilst maintaining the original connection relationships. Some members were added, some removed, and others pruned until the shape and details met the artistic intent.

Vector mathematics gave the distance between the centerlines of the Planks, which made it relatively easy to get a rough idea of how close members were to each other. It was hoped that some form of simple fuzzy logic could be used to automatically adjust the Planks so they did not interfere, but that hope proved fruitless.

In the end, the brute force approach of moving and rotating the Planks one at a time proved the only practical means of achieving a structure where every Plank was straight, and no Planks interfered. The AutoCAD command "Interfere" was used extensively to check clearances and adjust Plank positions and Connection layouts.

5.5 *Structural analysis*

Finite element analysis was carried out using the Strand package to determine member loads, support reactions, and tip deflections. Plank members were checked to code requirements. Connection members were checked by hand calculations.

Overall sway of the structure was significant, with a calculated 150mm sway at the top in the more flexible direction at 1:500 wind speed.

6 CONNECTION DESIGN

The size of the sculpture meant that all connections between Planks were bolted. Most were made with a loose connection piece, so that the Plank member was simply drilled and sleeved for a single bolt connection at discrete points along the length. This meant that all the complexity of the connection was contained within the connection piece. Where the design loads exceeded

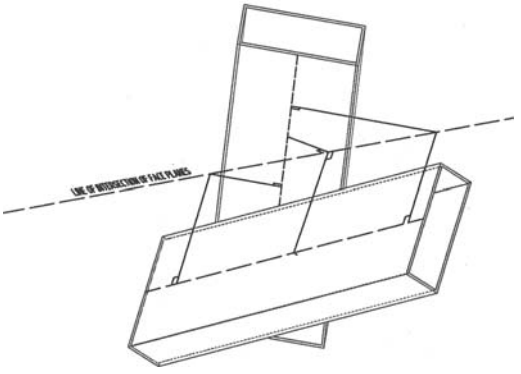

Figure 9. Intersection geometry.

Figure 10. Folded Plate Connection (note head of bolt for connection on far side).

the capacity of a single bolt connection (mainly at connections to the trunk), two bolts were used side by side across the wide face of the RHS.

Where possible a simple folded plate was adopted for the connection piece. Vector Mechanics was used to determine the fold line, which is the intersection of the planes of the wide faces of the connecting RHS.

In other cases, where the angle between the faces exceeded 45° (or so), the connection piece was made with a short length of 50 × 50 × 5 EA angle iron mitre-cut both ends and capped with a flange plate.

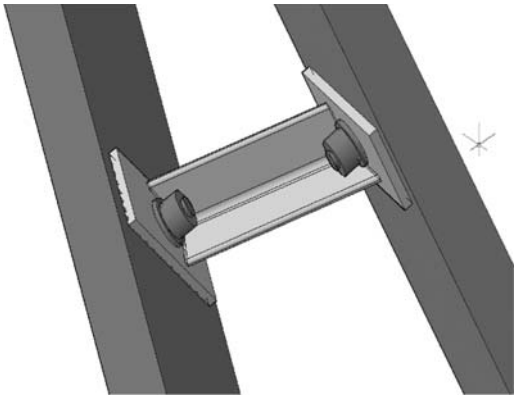

Figure 11. Angle and Flange Connection in AutoCAD model.

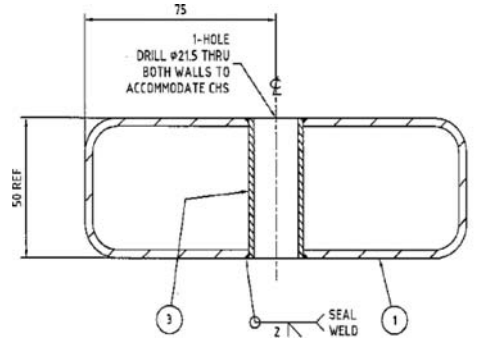

Figure 12. Bolt sleeve detail.

The flange plate and folded plate were both from 10mm plate, and extended to the shoulder of the RHS, so that moments were carried through the joint by differential action between the pre-loaded bolt and the edge of the plate bearing on the shoulder.

The bolts did not need an excessive pre-load – snug-tight proved sufficient to transfer design moments.

As noted in the discussion of corrosion protection, all bolt holes in the RHS were sleeved to the detail shown in Figure 12.

The mitre-cuts on the angles were carefully detailed to facilitate fabrication. Cuts were made with an angle grinder. The flange plates were laser-cut, and etched with the connection piece mark and the end. So C1620-16 was the flange on the Plank 16 end of the connection between Planks 16 and 20.

Prior to final detailing the fabricator's brake press was calibrated so that the holes in the folded plate could be laser-cut at the same time as the edges were profiled.

In all, this careful attention by the designer to the details of the connections resulted in a solution where the complexity of the geometry was resolved by a collection of relatively simple fabrication tasks.

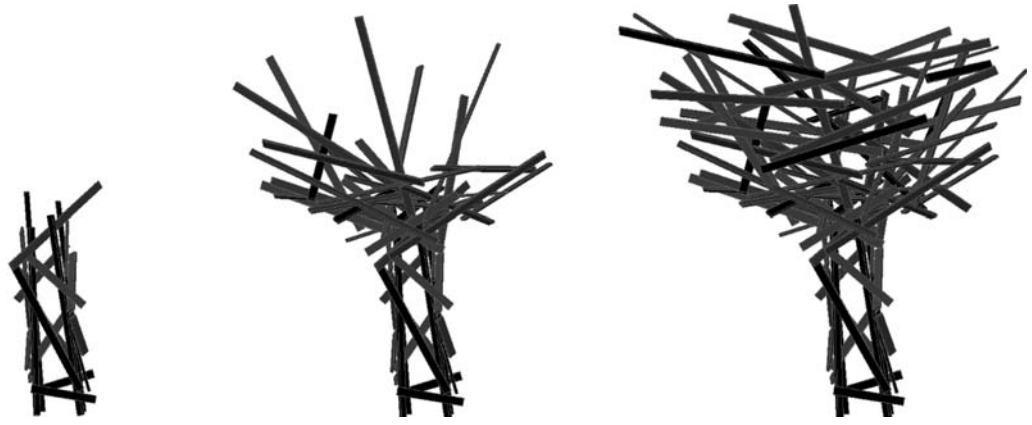

Figure 13. Three stages of construction as simulated in AutoCAD – 20 Planks, 45 Planks, Complete.

Figure 14. Trial assembly in the fabricator's works.

Figure 15. Detail of connections at top of legs.

7 FABRICATION AND CONSTRUCTION

The design allowed fabrication using simple techniques. There were no complex welds – all were simple fillet welds or seal welds at corners. The simplicity of the components allowed parts to be turned so that all welds could be completed down-hand.

The Planks were originally numbered as they were measured on the model. After the final geometry was settled, they were renumbered to the order in which they were to be installed. The four Legs of the trunk were installed first. The algorithm for subsequent numbers was quite simple – add the Plank with the lowest altitude that connects to two (or more) Planks already installed.

Construction was simulated in the AutoCAD model by simply switching on the Layers associated with successive Planks in numerical order.

The components were trial-assembled in the fabrication workshop as production progressed. There were a couple of minor errors in fabrication found during the trial assembly; these were easily fixed.

One aspect of the design was left to the fabricator. In a few places the angle-section connector was oriented such that water could pond between the angle heel and the flange plate. These places were identified during trial assembly and drain holes drilled.

After completion of trial assembly, the parts were disassembled, transported to the paint shop, painted, and transported to site.

Erection on site required a small crane and two elevating work platforms. It took just three days to complete erection and final-tightening of the bolts.

8 COSTS

Fabrication was completed within the original budget set down at tender time with only a rough guide to the scope of works and details of the structure.

Engineering and drafting took longer and more man-hours than anticipated, but was within the financial capacity of those involved. As a rough guide, the true engineering and drafting costs were roughly the same magnitude as the fabrication cost, with both at about $A1,000 per member.

9 CONCLUSIONS

Blue Tree is an iconic sculpture, paying homage to the environment and to the recent history of the Black Saturday Fires.

From a structural engineering perspective, the sculpture is a success, achieving the form required by the sculptor with a modest total cost. There have been no indications of wind-induced vibration in eighteen months of service.

The corrosion protection system has worked to expectations with no signs of deterioration to date. Blue Tree is a graphic example of how structural form of a sculpture can be achieved without the use of exotic materials.

ACKNOWLEDGEMENTS

The author designed the structure and sorted out the geometry. He was ably assisted by:

- Konstantin Dimopoulos – Sculptor.
- George Deutsch – Project Engineer and reviewer of the structural design.
- John Dickman, Andrew Higgins, and Adel Demetry – drafters.
- Mark Dromgool – corrosion protection consultant,
- Steve Sweeney – Project Manager for Agfab Engineering, fabricator.
- RACV Country Club – Client.

REFERENCES

Arianrhod, R., 2003, “Einstein’s Heroes. Imagining the world through the language of mathematics”, St Lucia, University of Queensland Press.

Christie, D.E., 1952, “Intermediate College Mechanics. A Vectorial Treatment”, New York, McGraw-Hill.

Facioni, R.J. & Smith, E.T., 1999, “Analysis, design and construction of the Olympic sculptures, AMP Tower, Sydney”, 16th Australasian Conference on Mechanics of Structures and Materials, Sydney, Balkema, 665-670.

Keays, R.H., 2008, “Structural Failures – Lessons for designers from one engineer’s experience”, Australasian Structural Engineering Conference, Engineers Australia, Melbourne.

Turnbull, H.W., 1929 “The great mathematicians”, London, Methuen.

Tubular Structures XIV – Gardner (Ed.)
© 2012 Taylor & Francis Group, London, ISBN 978-0-415-62137-3

Helicoidal footbridge over the Manzanares River

C. Castañón Jiménez, A. Serrano Corral & J. Martínez Calzón
MC2 Engineering Consultant Office, Madrid, Spain

ABSTRACT: The Arganzuela Footbridge is a helico-conical spatial truss with two bodies spanning 117 m and 96 m over the Manzanares River and the Arganzuela Park. In addition to the unusual shape and dimensions, the foundation is very complex and is greatly conditioned by the existence of underground motorway tunnels, sewers and a parking lot. The manufacture at the steel workshop and the construction process on site had to be carefully planned and taken into account during the structural design.

1 INTRODUCTION

The Arganzuela Footbridge runs over the Manzanares River in Madrid (Spain) and a new park area over the M30 motorway, the innermost ring of the city which as of 2008 runs underground at this point, leaving a green area at its previous surface location. The footbridge links both riversides and provides the city of Madrid access to the new Arganzuela Park. The architectural design of the footbridge was carried out by Dominique Perrault Architecture, and the structural design by MC2 Engineering Consultant Office. (Figs. 1 and 2)

The footbridge consists of two single span bodies: the "South Footbridge", 150 m long with a main span of 117 m over the Manzanares River; and the "North Footbridge", 128 m long, with a main span of 96 m over the Arganzuela Park. Both bodies meet at an "artificial hill", from which the pedestrians and cyclists may enter the park (Fig. 3).

The main structure of both bodies may be described as a conical spatial steel truss, of circular main section, with curved diagonals and straight longitudinal chords, all of them inscribed in a tronco-conical surface. Two thirds of the pseudo-triangles formed between diagonals and chords are covered with a non-structural set of steel ribs and a permeable skin made of a metallic mesh.

2 STRUCTURE DESCRIPTION

Both footbridges (North and South) follow the same structural concept, with a main bearing structure formed by the spatial helicoidal truss formed by longitudinal chords and diagonals, which holds the deck with two lanes, pedestrian and cyclist.

The two footbridges each have two end cantilever spans, between 12 m and 16 m long. These ends come out onto a road at the North end, and onto the sports facilities of the park at the South end, on top of an underground parking lot. The inner ends meet at an artificial hill which provides access to the park (Fig. 4).

The secondary structure that forms the deck runs inside the cone, bearing on the main structure, and

Figure 1. Lateral view of one of the footbridges.

Figure 2. Inside view: Pedestrian and cyclist lanes.

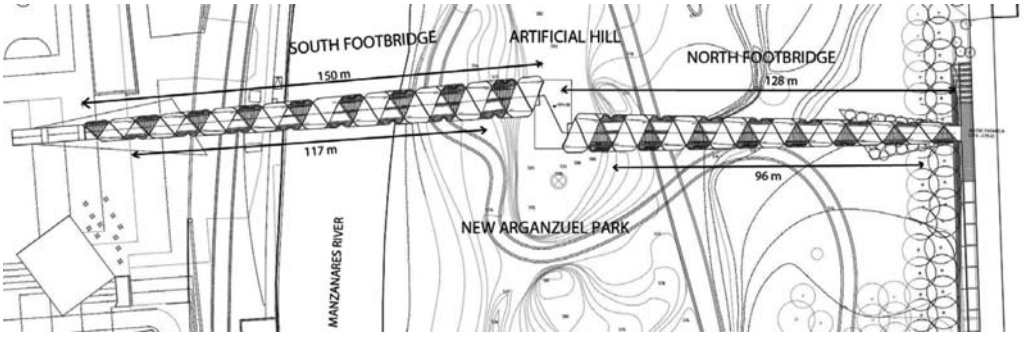

Figure 3. General plan view.

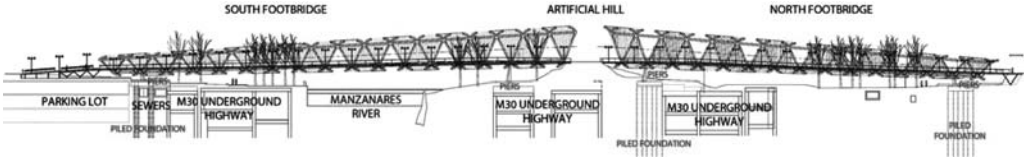

Figure 4. General cross section of the footbridge, showing the river and the complex underground distribution (underground highways, sewers and a parking lot), which greatly conditioned the design.

extends on its ends onto the road and sports facilities area with a length up to 29 m. This length requires that the secondary structure of the deck is supported on additional inclined struts, with their own, independent, foundation.

The main bearing structure of the footbridges consists of a spatial truss of circular section, of which the diagonals are curved tubes along a cone. The diagonals run along four helixes which may be grouped into two families of contrary direction. This configuration determines the structure of the footbridges which, although it has an adequate overall depth in relation to the span and being a truss a favorable typology for a longitudinal structure, it loses part of this favorable disposition due to the curving of the diagonals, which introduce undesired bending stresses in the diagonals. These stresses, which the diagonals in a conventional truss with straight elements don't have, cause shortenings and elongations several times higher than those expected in a straight truss, which gives rise to significant shear-deformations of considerable importance at the diagonals close to the piers.

The diagonal section thus required has been set as a square section 450 mm × 450 mm, the same for all the elements of the main structure: diagonals and longitudinal chords. The thickness of the tubes is small to moderate (between 8 mm and 25 mm) although in the central upper chords and in the diagonals close to the piers this thickness is greater, up to 40 mm. All the steel employed is type S355 J2 G3.

The main superstructure of each footbridge bears onto two pairs of inclined piers, one at each end, which more or less follow the direction of the main diagonals, with a spatial orientation that determines very high bending stresses, which the piers must transmit down to the foundation.

The foundation is piled, and, as it will be later explained, it is highly conditioned by the existence of the underground motorways and sewers. Each pair of piers share a common pile cap, and three out of the four pile caps are right on top or right next to the underground motorways or sewers.

The circulation area of the footbridges consists of a substructure which bears directly onto the main superstructure, and has a geometrically flexible configuration that allows housing the pedestrian and bicycle lanes, of variable and independent slopes.

The deck is composed of 145 mm × 50 mm ipe wood planks, set transversally along the footbridges. These planks are screwed against longitudinal steel joists, set every 2 m. The joists are pin-fixed onto transversal beams, which bear upon two longitudinal 180 mm × 180 mm square tubes. These tubes bear onto inclined "V" struts which rise from the bottom diagonals of the main structure.

2.1 *Main structure*

The main bearing structure of the footbridges consists of a steel tubular truss enclosed in a tronco-conical surface. Thus, the transversal cross-sections are circles of linearly-variable diameter, from 6 m diameter in the smaller ends, up to 12 m in diameter at the greater ends. On four points of each cross-section, set 90° apart, four longitudinal tubes are set, which form the longitudinal chords of the spatial truss, and have a

square cross-section of 450 mm side. These tubes are oriented so that two of the sides of the square section are enclosed in a longitudinal cone, and the other two sides are set orthogonally to these. This way, the real cross-section is a pseudo-square, with the outer and inner faces curved.

The diagonal bars are curved elements which are also contained in the tronco-conical surface, each diagonal belonging to one of the four helixes that run through the footbridges. The four longitudinal chords connect together the intersection points of these helixes, which cross each other two by two. This way, six bars meet at each node of the truss (a longitudinal chord, and two helixes), and these nodes have been carefully studied in order to guarantee an adequate structural behavior and constructability.

The configuration so described determines two pseudo Warren trusses with out-of-the-plane curved diagonals, connected together through two other sets of pseudo Warren out-of-the-plane diagonals on the top and bottom.

The diagonals are also pseudo-square sections, and as with the chords, the outer and inner faces are curved, contained in two conical surfaces, while the other two faces are set perpendicular. As the diagonals run through a helix, the section constantly turns around its axis.

The influence of the joints being fully fixed, fully pinned, or in-between, has been very carefully considered, in order to simplify the welding operations both at the steel workshop and on-site, while at the same time keeping an adequate structural behavior. A fully fixed joint reduces considerably the deformation and is very favorable against the bending stresses that the curved shape of the diagonals induce. From a thorough FEM analysis, it's been determined that a fully fixed joint isn't necessary, and that keeping the continuity of just the outer and inner (curved) sides of the diagonals by fully welding them at the connection is sufficient to guarantee an adequate behavior, while the perpendicular sides are simply welded.

The connections of the longitudinal chords are fully welded in order to guarantee an adequate transfer of the axial stresses the chords are subject to. These chords are also subject to bending stresses due to wind and secondary effects at the partially fixed joints of the diagonals. Nonetheless, the thickness of the chords is moderate, ranging from 8 mm to a maximum of 35 mm. At the joints with the piers, where the bending stresses would be very high, the bottom chords have a mechanical hinge, which allows the chord to rotate, but adequately transfers the shear and axial stresses (see section 3.2).

2.2 *Piers*

The piers are inclined steel elements (see Figs. 5 and 6), set in vertical planes oriented in continuation of the main diagonals, two at each end of the footbridges. The geometry set by the architectural design implies great bending stresses, due to the "double inclination" of the piers. In order to reduce theses bending stresses, a staged construction was devised, making the base of the piers pinned during construction, and, after the unpropping of the finished structure, fully fixed thereon. Thus, under service loads the base of the piers are fully fixed (see section 3.3).

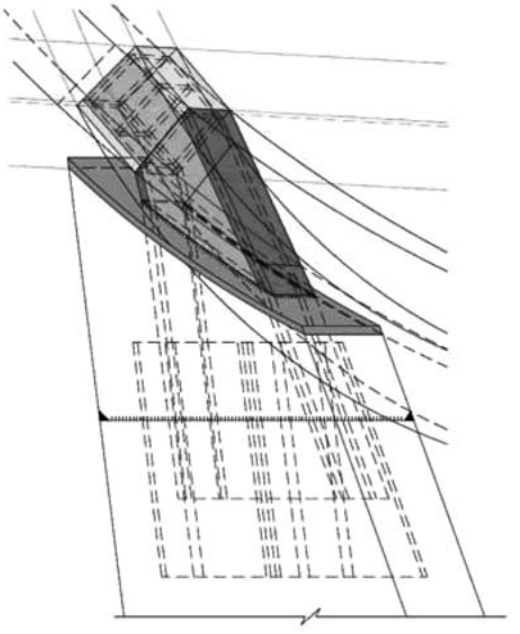

Figure 5. Pier 3D sketch. Notice the transfer element between the smaller section and the complete pier section.

The upper end of the piers are fully continuously welded against the main diagonal that transfers the vertical load from the main structure. The rest of the bars that meet at the joint (chords and diagonals) have pinned connections in order to remove secondary bending moments.

Regardless of the continuity between the pier and the main diagonal, there is a narrowing of the cross-section of the pier for architectural reasons. This *neck* has the same cross-section dimensions than the main diagonal (450 mm × 450 mm) and it enters the pier, into which it transfers all the loads to the whole greater section of the pier (Fig. 5). The space between the outer dimension of the pier and the diagonals, of just 10 cm, allows the metallic mesh skin to continue through the pier.

The use of a pinned joint at the base of the piers in the first phase, and rigidly fixed connection on the second, service phase, permits not using any sort of movable bearing, and simplifies the expansion joints at the artificial hill and outer ends.

2.3 *Foundation*

The foundation design was very much influenced by the presence of the motorway and the sewers. These underground tunnels beneath three of the four pile

Figure 6. Piers. View from beneath.

caps makes it impossible to place piles directly under the axis of the piers, so auxiliary elements to bridge these obstacles, or eccentric foundations, are necessary. Nonetheless, in order not to increase the cost of these complex foundations, the foundation makes use of the tunnels retaining walls.

The vertical loads carried to the foundations are of moderate value, but the presence of inclined piers fixed against the pile cap under service loads induces important horizontal forces into the foundation, which must in some cases be resisted exclusively by the piles. Being the upper eight meters of soil very low-resisting fills, this conditions greatly the number and size of the piles.

The main features of the foundations are:

- The geometric disposition of some of the piles makes them to be in tension in some cases
- The pile caps are sized and reinforced to transmit to the piles not only the vertical loads but also bending stress due to the fixation of the pier's base, transforming them into pairs of axial loads into the piles
- There are pinned connections between the pile caps and the retaining walls of the underground tunnels, in order to reduce any possible secondary bending stress into these walls

The retaining walls of the underground tunnels are able to withstand the horizontal and vertical loads induced by the footbridge's foundation.

2.4 *Deck*

The deck is formed by an independent conventional steel substructure with built-up open sections and laminated hollow sections, all in S275 steel. The work of this substructure is disengaged from the main structure, in order to simplify the construction, and to formally separate both systems, as the architectural project required (see Figs. 7 and 8).

This substructure is formed by four levels of structural elements, from top to bottom:

- Ipe wood planks that form the transitable platform both for pedestrian use and bicycles

Figure 7. Deck substructure: "V" inclined struts, longitudinal tubes and transversal beams.

Figure 8. Deck substructure under construction. Notice the two lanes–pedestian, bicycle- with different slopes.

- Longitudinal joists on which the wood planks rest
- Transversal beams, in some cases stepped, as the pedestrian and bicycle lanes have different variable slopes, on which the longitudinal joists rest
- Longitudinal continuous hollow section chords on which the transversal beams sit
- Inclined "V" struts, contained in vertical planes, which support the longitudinal chords to the curved diagonals of the main structure.

The longitudinal joists are built-up "T" sections with a variable span of around 4 m, simply supported on the transversal beams. The simple connection to the transversal beams is carried out through the top flange, which rests on the top flange of transversal beams, thus reducing the depth. The inter-axis between joists is set around 2 m, which is the maximum length the ipe wood planks can withstand.

The transversal beams are built-up "H" beams, of variable length and depth, with a central span and two lateral cantilevers. They are set every 4 m, and are sometimes "stepped" in order to accommodate both the pedestrian and bicycle lanes, which have independent and variable slopes all through the footbridges.

The inclined struts are formed by 140 mm square hollow sections, fixed joined against the bottom curved diagonals of the main structure, not needing any transversal bracing.

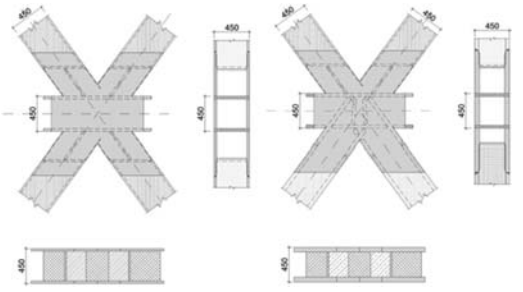

Figure 9. Elevations and cross-sections of nodes ("stars"). Left: Semi-pinned node; right: Fully continuous node.

2.5 *Artificial hill*

Both footbridges meet at an artificial hill, where an elevated platform serves as landing between both footbridges and provides an access to the park. The structure of this artificial hill, which also lies right on top of one of the underground motorway tunnels, is a conventional composite steel deck structure, on steel beams and columns, adequately braced, which rise from three concrete lintels of great depth, that span the width of the tunnel and bear upon the retaining walls, thus not introducing any vertical load into the roof of the tunnel, which it would not be able to withstand.

Both the inside and surroundings of the artificial hill, as well as other artificial hills all through the park, are covered in polysterene blocks, which makes a lighter fill over the limited capacity of the tunnels' roofs.

3 SPECIAL CONSTRUCTION CONSIDERATIONS

The complex geometry of the footbridges greatly conditioned both their structural behaviour and its constructability, which required to take several special measures in its design.

3.1 *Nodes ("stars")*

There are 139 nodes in both footbridges (74 in the South footbridge and 65 in the North one), all of them different. Special attention was paid to these elements, in order to simplify their manufacture. For one thing, six bars meet at these nodes (two longitudinal chords and four diagonals); for another, the inner and outer faces of the chords, diagonals and the nodes themselves are curved, contained in two parallel conical surfaces); and for another, the overall cross section of the cone changes linearly, as the circular section widens as we move along the axis.

Thus, the nodes were devised as individual pieces with the ends of the six bars extended waiting to receive the welded connection against the chords and diagonals. Due to their shape, these pieces were named "*stars*" (see Figs. 9 and 10).

Figure 10. "Star" under construction on site, with two diagonals and one chord waiting to be connected.

There are two types of stars: "semi-pinned" and "fully continuous". In the "semi-pinned" one (Fig. 9, left), the most common throughout the footbridges, the stresses that are carried by the diagonals are transfered through the nodes mainly by the outer and inner faces which are fully welded against the star; the lateral faces of the diagonals are simply welded. The "fully continuous" stars exist in the most solicited nodes, close to the piers (Fig. 9, right), where the outer and inner faces aren't enough to transmit all the stresses through the node, and thus require the full connection of the lateral faces as well.

3.2 *Longitudinal chords' joints*

In order to reduce the nonetheless huge stresses that enter the piers through the strangled neck connection, the longitudinal chords at these nodes are pinned at both sides (one hinge to the inside span, and one hinge to the cantilever span). These hinges, of very complex geometry due to the crooked inclination of the piers in relation to the main diagonals, are fitted inside the small dimensions of the longitudinal chord 450 mm × 450 mm cross-section.

3.3 *Piers' bases pinned-fixed joints*

As it has been previously explained, the footbridges are built in two phases; in the first phase, the base of the piers are pinned and allow the rotation of the piers when the structure is un-propped, under the self weight and dead loads. Once this rotation has taken place, the bases are fixed in the second phase, in order to act as a rigid connection against further service loads.

This pinned-fixed connection required a special element to make it possible (Figs. 11 and 12). A reception chamber for each pier was encased in the pile caps, which had a spherical steel hinge at the bottom, and connecting bars protruding from the perimeter of the base, adequately anchored to the pile cap. The connection element was then inserted through these bars

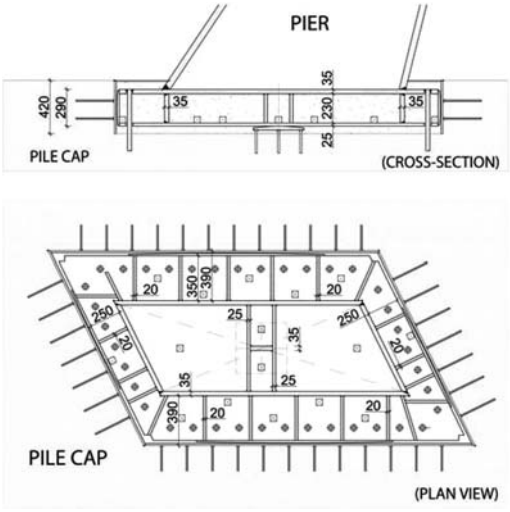

Figure 11. Cross-section and plan view of the pinned-fixed connection element at the base of the piers.

Figure 12. General view of a pile cap concreted, with the reception chambers with connecting bars, and the pinned-fixed connection elements waiting to be inserted, on top.

into the chamber; the drills in the connection element were sufficiently loose to allow slight movements of the connection element. The connection element thus placed on top of the spherical hinge and encased against the chamber through cylindrical contact plates allowed any small rotation to take place.

The piers were then welded against the connection elements, and once the rotation of the ensemble took place during the un-propping, the fixation was carried out. This fixation was done by welding all the perimeter bars to the connection element and filling the reception chamber and connection element with a high strength and low shrinkage mortar. This filling was done through four plastic tubes inserted into the piers, which from the bottom of the chamber to the top filled all the compartments, driving out the bubbles of air and adequately filling all the gaps through the multiple orifices practiced previously on the connection element.

Through this welding of the bars and filling with high-strength mortar a fully fixed connection of the base of the pier was guaranteed under service loads.

3.4 *Analysis and modeling*

The analysis and design of the structure of the footbridges was carried out through the Finite Element Method. A global bar model was analysed for each footbridge, together with local models to study specific details or substructures.

Special care was taken in the modelization of the bars and the orientation of their axis, especially in the diagonals. As these diagonals twist through the helixes they are contained in, the section constantly rotates and changes its orientation. This had to be taken into account, to accurately establish the boundary conditions and correctly assess the stresses in the cross-sections.

A staged analysis was carried out, considering the first phase (un-propping the structure with the piers pinned at the base) and second phase (under service loads, piers fixed at the base). An optimization process was carried out, considering the two stages and several load combinations, taking into account the ultimate and service limit states, together with a modal and dynamic analysis to limit both vertical and horizontal vibrations.

The analysis was also geometrically non-linear as the deformed (curved) geometry of the elements conditioned the stresses.

An automatic post-processing of the results allowed to check the resistance and deformability limits of all the elements of the footbridges, determining the optimal sizes and thicknesses of all the bars.

4 CONSTRUCTION PROCESS

As in the analysis and design stages, the construction process was complex, and had to be carefully thought and taken into account in the structural design itself.

Prior to the construction competition, a small prototype of a diagonal and star ensemble was carried out in a workshop to test the viability of the devised construction procedure, validating it and learning important points of the process.

4.1 *Modeling and workshop drawings*

The first and most critical part of the process was determining the exact geometry of each of the pieces to be manufactured. The workshop office team started from the geometrical CAD model generated and employed by the architectural and structural teams, and manipulated it in order to determine the precise geometry of each of the elements to be cut, curved and welded at the workshop and on-site.

Thus, the curved –conical- surfaces were digitally flattened and/or adapted to precisely define in

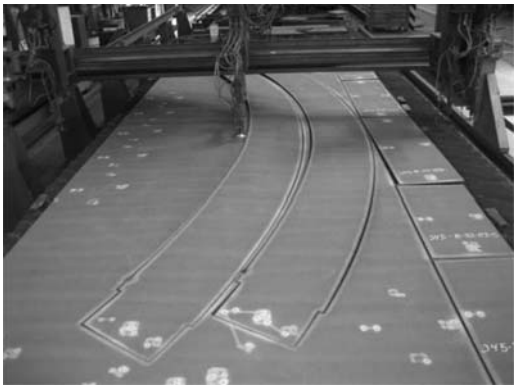

Figure 13. Oxycutting of the flattened geometry.

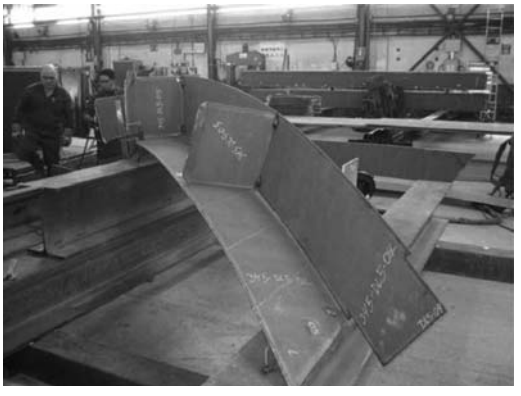

Figure 14. Assembly and welding of a diagonal

the workshop drawings the exact geometry to be manufactured.

4.2 *Steel workshop*

From there on, several steps were carried out at the workshop, starting with the cutting of the elements, curving, assembling, welding, etc.

4.2.1 *Cutting and curving*

By numerically controlled cutting machinery all the plates that would later conform the diagonals, chords and stars were flame cut, following the geometry defined in the workshop drawings (Fig. 13).

The plates were then curved, either by curving machines or by discretely bending plates into smooth almost-curved geometry, undistinguishable by plain sight. The plates to be curved were the outer and inner faces belonging to the conical surfaces, corresponding to longitudinal chords, diagonals and stars (Fig. 14).

4.2.2 *Longitudinal chords*

Being straight – although with the inner and outer faces curved- the manufacture of the longitudinal chords was the simplest and most straightforward. The curving of each of the outer and inner faces was carried

Figure 15. Cut and curved outer and inner faces of the stars.

Figure 16. Star welded against a longitudinal chord.

out through 15 small bends, very close together; these two faces were then welded to the perpendicular faces, forming the pseudo-square section chord.

4.2.3 *Nodes ("stars")*

Following the geometry defined in the workshop drawings, the outer and inner faces were cut and then curved. Although the theoretical curvature would be variable along the star, the approximation to a constant curvature – cylindrical instead of conical- meant a slight deviation of up to 1 mm, perfectly acceptable and indistinguishable from the theoretical geometry. Each star was then assembled and the inner plates were welded in a precise sequence that allowed a correct welding of all the different plates that form each star (Figs 9, 10, 15 and 16).

4.2.4 *Diagonals*

The outer and inner plates were cut following the flattened geometry of the workshop drawings, and then variably curved to fit the twisting geometry of the helix. They were then assembled and welded on auxiliary substructures that delimited the geometry (Fig. 14 and 17).

Figure 17. A diagonal finished with its ends prepared to be welded against two stars.

Figure 18. Pre-assembling of diagonals, chords and stars at the workshop.

4.2.5 *Workshop pre-assembly*

Once the corresponding longitudinal chords, diagonals and stars were manufactured, they were pre-assembled at the workshop prior to sending them to site. This pre-assembly took place on auxiliary desks which allowed controlling precisely the position of each element. Special care was taken in positioning the stars at their pre-cambered location, so that, once un-propped, the structure's geometry would be the theoretical one (Fig. 18) Slight smoothing of the ends of the diagonals was carried out to adapt to this geometrical configuration, and once every piece was fit into place it was all disassembled and taken to site, to be re-assembled and welded definitely there.

4.2.6 *Piers and connection elements*

Figs. 19 and 20 show one pier and one connecting element (pier's base) under construction at the workshop.

4.3 *On-site construction*

Once the different elements had been manufactured at the steel workshop, they were transported by truck to the site. But before assembling any part of the steel

Figure 19. Pier under construction at workshop.

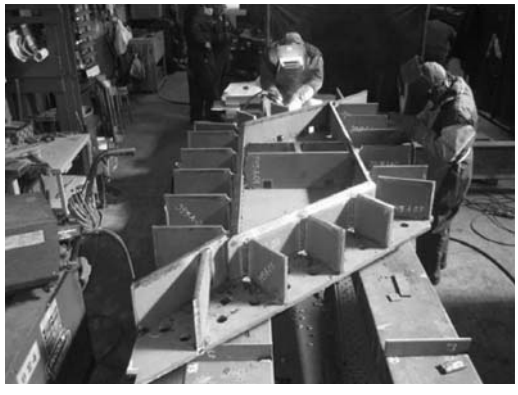

Figure 20. Connecting element at the base of piers under construction.

structure, all the foundations were carried out, boring the piles and executing the pile caps, which, as described in section 2.3, had sometimes to overcome the underground tunnel roofs to be connected to the retaining walls.

The temporary props on which the main structure would be assembled were micro-piled, as the soil on which they sat, with 8 m of artificial fills, wasn't sufficient to withstand the loads (Fig. 21). Then, the longitudinal chords with stars attached to their ends were placed on top of the temporary props, and the diagonals were placed and welded against them (Fig. 22).

Once the main structure was in place and welded, the secondary structure of the deck (inclined "V" struts, longitudinal chords, transversal beams and joists) was carried out. With the deck finished, and with the auxiliary elements of the steel ribs and metallic mesh skin in place, the un-propping of the structure took place. Once the structures were unpropped, the final step was to fix the connecting element at the base of the piers.

Figure 21. Propped footbridge over the river.

Figure 22. Welding of a diagonal to a star.

Figure 23. General view from the artificial hill.

Figure 24. General view of the footbridges and the Arganzuela park.

5 CONCLUSIONS

The design, analysis and construction of these footbridges with such a complex, although regular, geometry has required a thorough planning and overall conception. The variable curvature of the square sections forming the bars of the spatial tronco-conical helixes had to be carefully considered in the design, and special details and building procedures had to be thought and taken into account in the analysis. A precise workshop drawing preparation and steel manufacture was necessary to carry out the structure with excellent results

6 CREDITS

Architectural design: DPA Dominique Perrault Architecture; Structural Design: MC2 Engineering Consultant Office; Construction managers: joint venture formed by Dragados and Acciona; Steel workshops: “Talleres Centrales de Acciona” and “JOAMA Construcciones Metálicas”.

Aluminium

Tubular Structures XIV – Gardner (Ed.)
© 2012 Taylor & Francis Group, London, ISBN 978-0-415-62137-3

Investigation of concrete-filled aluminum circular hollow section columns

F. Zhou
Department of Building Engineering, Tongji University, Shanghai, China

B. Young
Department of Civil Engineering, The University of Hong Kong, Hong Kong, China

ABSTRACT: This paper presents finite element analysis of concrete-filled aluminum Circular Hollow Section (CHS) columns. A finite element model has been developed and verified against test results. A parametric study was carried out to study the effects of cross-section sizes on the concrete-filled aluminum CHS columns. The outer diameter-to-thickness ratio of the sections ranged from 10 to 160, and the infilled concrete cylinder strength was 40 MPa. The test and numerical results of the concrete-filled aluminum CHS columns were compared with the design strengths to evaluate the reliability of the design rules in the American and Australian/New Zealand specifications for aluminum and concrete structures. Furthermore, the composite column design equations have been proposed. The proposed design equations consider the benefits of composite action between the aluminum CHS tube and the concrete infill. It is shown that the proposed design equations accurately predicted the strengths of the concrete-filled aluminum CHS columns.

1 INTRODUCTION

Infilled concrete is one of the ways to increase the stiffness and the load carrying capacity of aluminum tubular columns. Concrete-filled aluminum tubular columns can effectively take advantages of these two materials to provide both high strength and high stiffness. These findings have been reported by Zhou and Young (2008) for concrete-filled aluminum square and rectangular hollow section (SHS and RHS) stub columns and Zhou and Young (2009) for concrete-filled aluminum circular hollow section (CHS) stub columns. Zhou and Young (2008) reported an experimental investigation of concrete-filled aluminum SHS and RHS composite columns. It was shown that the stiffness and the load carrying capacity of the composite columns improve compared with the aluminum SHS and RHS tubular columns without concrete infill. Local buckling of the aluminum SHS and RHS tubes was found for specimens with slender sections. Generally, the composite columns failed by the aluminum tubes splitting near the corner of the SHS and RHS sections. Zhou and Young (2009) reported a series of tests on concrete-filled aluminum CHS composite columns. It was also shown that the stiffness and the load carrying capacity of the composite columns improve compared with the aluminum CHS tubular columns without concrete infill. The failure modes of the aluminum tubes splitting were not observed for CHS composite columns.

In addition to experimental investigation, numerical investigation can also provide a good understanding of the structural behavior of concrete-filled aluminum CHS columns. The CHS tube could provide confinement to the concrete infill for concrete-filled aluminum CHS columns. When concrete is subjected to lateral confining pressure, the uniaxial compressive strength and the corresponding strain are much higher than those of unconfined concrete. On the other hand, the CHS tube is stiffened by the concrete infill, which can prevent the inward buckling of the tube, hence increase the strength of the column. Therefore, the interface between the aluminum CHS tube and the concrete infill in the composite column have to be considered in the numerical modeling. Numerical investigation of concrete-filled steel tubular columns has been reported by Hu et al. (2003), Ellobody and Young (2006), Ellobody et al. (2006) and many other researchers. This paper presents the numerical simulation of concrete-filled aluminum CHS columns using finite element program ABAQUS (2007). The composite action between the aluminum tube and concrete infill has been carefully considered in the finite element model (FEM). The results obtained from the finite element analysis (FEA) were verified against the test results reported by Zhou and Young (2009). A parametric study was performed to investigate the effects of cross-section sizes on the strengths of concrete-filled aluminum CHS columns. The reliability of the design rules in the American specifications (AA 2005, ACI 2008) and Australian/New Zealand standards (AS/NZS 1997, AS 2001) for aluminum and concrete structures was evaluated using reliability analysis by comparing with the

concrete-filled aluminum CHS column strengths predicted from the FEA (P_{FEA}) and column strengths obtained from the tests (P_{Exp}) reported by Zhou and Young (2009). Furthermore, design equations for concrete-filled aluminum CHS columns were proposed based on the results obtained from the numerical investigation in this study and the test results reported by Zhou and Young (2009). The proposed design equations considered the composite action between the aluminum CHS tube and the concrete infill.

2 FINITE ELEMENT MODEL

The non-linear finite element analysis program ABAQUS (2007) was used to simulate the structural behaviour of concrete-filled aluminum CHS columns. The aluminum CHS tube, concrete infill and the interface between the aluminum tube and the concrete infill have been carefully modeled.

The numerical analysis was performed over a range of diameter-to-thickness (D/t) ratio for the aluminum tubular sections that included from compact sections to slender sections. Types of elements for composite columns were chosen from element library in the ABAQUS. The element of C3D8 is a three-dimensional eight-node solid element, which is suitable for compact sections. The element of S4R is a four-node doubly curved thin or thick shell element with reduced integration, which is suitable for slender sections having complex buckling behaviour. In this study, the aluminum tubes were stiffened by the concrete infill, which prevented the inward buckling of the tubes. Hence, fine mesh of C3D8 element was used to model both of the concrete infill and the aluminum tubes for the composite columns. The finite element mesh used in the model was investigated by varying the size of the elements in order to provide both accurate results and less computational time. It is found that a mesh size of 1(length): 1(width): 1(depth), for most of the elements, achieved accurate results. The typical finite element mesh of the concrete-filled aluminum CHS columns is shown in Figure 1. The aluminum CHS stub columns without concrete infill were also simulated for reference purposes, where the element of S4R was used to model the aluminum tubes.

Following the test procedure conducted by Zhou and Young (2009), the top and bottom surfaces of the concrete-filled aluminum CHS columns were restrained against all degrees of freedom except for the displacement at the loaded end, which is the top surface, in the direction of the applied load. The loading method used in the finite element model (FEM) was identical to that used in the tests. The displacement control method was used for the analysis of the concrete-filled aluminum CHS columns. Vertical compressive uniform loads were applied to the specimen by specifying a displacement to each node of the loaded end in the top surface. Generally, a displacement of 20 mm was specified.

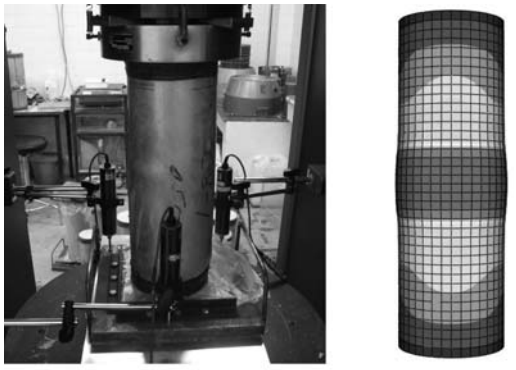

(a) Experimental (b) FEA analysis

Figure 1. Comparison of experimental and finite element analysis failure modes.

The measured stress-strain curves reported by Zhou and Young (2009) for the aluminum CHS tubes were used in the analysis. The Misses yield criterion with associated plastic flow is used in the multiaxial stress state. The aluminum alloy is assumed to have isotropic hardening behaviour. The material behaviour provided by ABAQUS (using the *PLASTIC option) allows a multi-linear stress–strain curve to be used. The first part of the multi-linear curve represents the elastic part up to the proportional limit stress with measured Young's modulus and Poisson's ratio equal to 0.33. Since the analysis involves large in-elastic strains, the nominal (engineering) static stress-strain curve was converted to a true stress and logarithmic plastic strain curve. The true stress ($\sigma_t rue$) and plastic true strain (ε^{pl}_{true}) are specified in ABAQUS (2007).

The aluminum CHS tube could provide confinement to the concrete infill for the concrete-filled aluminum CHS columns. When concrete is subjected to laterally confining pressure, the uniaxial compressive strength and the corresponding strain are much higher than those of unconfined concrete. The confinement model for concrete infill used by Ellobody et al. (2006) was adopted in this study. The concrete in the composite columns is usually subjected to triaxial compressive stress, and the failure of concrete is dominated by the compressive failure surface expanding with increasing hydrostatic pressure. Hence, a linear Drucker-Prager yield criterion was used with associate flow and isotropic hardening rule. The material angle of friction (β_{cc}) and the ratio of flow stress in triaxial tension to that in compression (K) were taken as 20° and 0.8, respectively, as recommended by Wu (2000).

The interfaces between the aluminum tube and the concrete infill were modeled using the contact pair. The "surface-to-surface contact" option was used. The concrete infill was defined as the master element, while the aluminum tube was defined as the slave element of the interface elements in the FEM. Along the normal direction to the interface; the "hard contact"

relation was used. The contact pair allows the surfaces to separate under the influence of a tensile force. However, the two contact surfaces are not allowed to penetrate each other. Along the tangential direction to the interface, "Penalty" option was used and a friction coefficient of 0.25 was also used in the analysis. The finite element model is detailed in Zhou & Young (2012).

3 VERIFICATION OF FINITE ELEMENT MODEL

3.1 *Summary of experimental investigation*

An experimental investigation of concrete-filled aluminum circular hollow section (CHS) columns performed by Zhou and Young (2009) was used to verify the developed finite element model (FEM) in this study. Ten series of CHS tubes (CHS1 – CHS10) fabricated by extrusion using 6061-T6 heat-treated aluminum alloy (high strength material) with concrete infill were tested. The nominal section sizes ($D \times$ t) of the series CHS1, CHS2, CHS3, CHS4, CHS5, CHS6, CHS7, CHS8, CHS9 and CHS10 are 38×4, 50×3, 60×2.5, 76×2, 100×2, 120×2.5, 150×2.5, 150×5, 160×4 and 180×3.5 mm, respectively, where D is the diameter and t is the thickness of the sections. The measured diameter-to-thickness (D/t) ratio of the CHS tubes ranged from 9.7 to 59.7. The column lengths (L) were chosen so that the length-to-diameter ratio (L/D) for the concrete-filled aluminum CHS stub columns generally remained at a constant value of 3 to prevent overall column buckling. The column specimens were tested using nominal concrete cylinder strengths of 40, 70 and 100 MPa. The aluminum CHS stub columns without concrete infill were also tested for reference purposes. Table 1 summarizes the measured dimensions and material properties of the tested specimens. The details of the experimental investigation are reported in Zhou and Young (2009).

Table 1. Summary of test program (Zhou & Young 2009).

Specimen	D mm	t mm	D/t	f_y MPa	f_c MPa
CHS1-C0	38.0	3.91	9.7	242.4	0
CHS1-C40	38.0	3.89	9.8	242.4	44.8
CHS1-C70	38.0	3.90	9.7	242.4	70.2
CHS1-C100	38.0	3.92	9.7	242.4	106.0
CHS2-C0	50.0	3.13	16.0	238.4	0
CHS2-C40	50.0	3.13	16.0	238.4	44.8
CHS2-C70	50.0	3.12	16.0	238.4	70.2
CHS2-C100	50.0	3.13	16.0	238.4	106.0
CHS3-C0	60.0	2.52	23.8	237.8	0
CHS3-C40	60.0	2.55	23.5	237.8	44.8
CHS3-C70	60.0	2.54	23.6	237.8	70.2
CHS3-C100	59.9	2.53	23.7	237.8	106.0
CHS4-C0	76.1	2.05	37.1	237.0	0
CHS4-C40	76.1	2.06	36.9	237.0	44.8
CHS4-C70	76.0	2.06	36.9	237.0	70.2
CHS4-C100	76.0	2.05	37.1	237.0	106.0
CHS5-C0	99.9	2.02	49.5	244.3	0
CHS5-C40	99.7	2.02	49.4	244.3	44.8
CHS5-C70	99.8	2.06	48.4	244.3	70.2
CHS5-C100	100.0	2.05	48.8	244.3	106.0
CHS6-C0	119.7	2.55	46.9	253.1	0
CHS6-C40	119.8	2.49	48.1	253.1	44.8
CHS6-C70	120.0	2.55	47.1	253.1	70.2
CHS6-C100	119.9	2.48	48.3	253.1	106.0
CHS7-C0	149.8	2.51	59.7	267.9	0
CHS7-C40	150.1	2.53	59.3	267.9	44.8
CHS7-C70	150.1	2.54	59.1	267.9	70.2
CHS7-C100	149.9	2.53	59.2	267.9	106.0
CHS8-C0	150.2	4.99	30.1	216.9	0
CHS8-C40	150.2	5.03	29.9	216.9	44.8
CHS8-C70	150.2	5.04	29.8	216.9	70.2
CHS8-C100	150.2	5.03	29.9	216.9	106.0
CHS9-C0	160.2	4.01	40.0	254.2	0
CHS9-C40	160.1	4.03	39.7	254.2	44.8
CHS9-C70	160.5	4.07	39.4	254.2	70.2
CHS9-C100	160.5	4.06	39.5	254.2	106.0
CHS10-C0	180.2	3.75	48.1	264.9	0
CHS10-C40	180.0	3.71	48.5	264.9	44.8
CHS10-C70	180.4	3.69	48.9	264.9	70.2
CHS10-C100	180.5	3.75	48.1	264.9	106.0

3.2 *Comparison of finite element analysis results with experimental results*

In the verification of the developed FEM, a total of forty concrete-filled aluminum CHS columns tested by Zhou and Young (2009) were analyzed. A comparison between the experimental results and the finite element results was carried out. The main objective of this comparison is to verify and check the accuracy of the finite element model. The comparison of the test results (P_{Exp}) with the column strengths (P_{FEA}) predicted from the FEA are shown in Table 2. It is shown that the finite element results agreed well with the test results. A maximum difference of 10% was observed between the experimental and numerical results for specimen CHS6-C40. The mean value of the P_{Exp}/P_{FEA} ratio is 0.99 with the corresponding coefficient of variation (COV) of 0.058, as shown in Table 2. The failure mode of concrete-filled aluminum CHS column was also verified against the finite element model, as shown in Figure 1. It is shown that both the ultimate loads and the failure modes reflect good agreement between the experimental and finite element results.

4 PARAMETRIC STUDY

It is shown that the developed finite element model (FEM) closely predicted the failure loads of the concrete-filled aluminum circular hollow section (CHS) columns. Hence, parametric study was carried out to study the effects of cross-section sizes on the concrete-filled aluminum CHS column strengths. A total of 96 specimens with 4 Series were analyzed in the parametric study. The parametric study was carried

Table 2. Verification of finite element model.

Specimen	D/t	Exp. P_{Exp} kN	FEA P_{FEA} kN	P_{Exp}/P_{FEA}
CHS1-C0	9.7	114.5	124.5	0.92
CHS1-C40	9.8	158.9	165.7	0.96
CHS1-C70	9.7	167.2	173.3	0.96
CHS1-C100	9.7	171.5	189.3	0.91
CHS2-C0	16.0	141.2	134.6	1.05
CHS2-C40	16.0	217.0	238.8	0.91
CHS2-C70	16.0	238.9	251.3	0.95
CHS2-C100	16.0	327.5	301.2	1.09
CHS3-C0	23.8	121.3	111.7	1.09
CHS3-C40	23.5	244.1	250.2	0.98
CHS3-C70	23.6	292.4	307.3	0.95
CHS3-C100	23.7	412.6	412.7	1.00
CHS4-C0	37.1	113.4	113.4	1.00
CHS4-C40	36.9	329.9	356.0	0.93
CHS4-C70	36.9	415.7	451.9	0.92
CHS4-C100	37.1	611.4	592.0	1.03
CHS5-C0	49.5	162.7	153.0	1.06
CHS5-C40	49.4	543.6	506.7	1.07
CHS5-C70	48.4	712.0	687.2	1.04
CHS5-C100	48.8	995.8	942.9	1.06
CHS6-C0	46.9	264.5	248.9	1.06
CHS6-C40	48.1	822.8	747.6	1.10
CHS6-C70	47.1	1010.3	1011.4	1.00
CHS6-C100	48.3	1388.7	1366.9	1.02
CHS7-C0	59.7	283.9	310.9	0.91
CHS7-C40	59.3	1111.1	1124.6	0.99
CHS7-C70	59.1	1496.4	1540.0	0.97
CHS7-C100	59.2	2057.8	2120.4	0.97
CHS8-C0	30.1	525.8	535.1	0.98
CHS8-C40	29.9	1481.9	1532.9	0.97
CHS8-C70	29.8	1740.6	1845.0	0.94
CHS8-C100	29.9	2666.1	2491.9	1.07
CHS9-C0	40.0	456.1	502.0	0.91
CHS9-C40	39.7	1494.1	1538.3	0.97
CHS9-C70	39.4	1974.4	1988.4	0.99
CHS9-C100	39.5	2797.3	2627.8	1.06
CHS10-C0	48.1	482.8	531.0	0.91
CHS10-C40	48.5	1690.2	1721.7	0.98
CHS10-C70	48.9	2274.2	2296.7	0.99
CHS10-C100	48.1	3139.2	3119.6	1.01
			Mean, P_m	0.99
			COV	0.058

Table 3. Parametric study.

Section	D mm	t mm	D/t	P_{FEA-T5} kN C0	P_{FEA-T5} kN C40	P_{FEA-T6} kN C0	P_{FEA-T6} kN C40
D80-1	80	0.5	160	18.7	242.2	21.8	253.0
D80-2	80	0.6	133	23.7	245.3	32.2	259.8
D80-3	80	0.8	100	35.7	261.4	51.3	282.9
D80-4	80	1.0	80	44.9	271.9	64.6	296.3
D80-5	80	1.4	57	63.6	288.7	91.2	325.3
D80-6	80	2.0	40	91.7	334.4	130.2	396.0
D80-7	80	4.0	20	194.0	488.9	263.6	621.6
D80-8	80	8.0	10	382.9	675.0	523.0	888.5
D200-1	200	1.3	154	121.3	1520.6	148.5	1601.1
D200-2	200	1.6	125	158.3	1584.3	224.5	1689.9
D200-3	200	2.0	100	223.4	1635.7	321.5	1774.5
D200-4	200	2.5	80	282.4	1703.0	405.2	1869.6
D200-5	200	3.3	61	373.6	1777.6	535.1	1989.3
D200-6	200	5.0	40	573.9	2086.7	813.5	2473.7
D200-7	200	10.0	20	1209.5	3041.9	1638.0	3323.8
D200-8	200	20.0	10	2385.9	4160.5	3241.4	5460.1
D300-1	300	2.0	150	310.4	3469.3	354.2	3653.8
D300-2	300	2.3	130	357.7	3524.9	478.0	3757.4
D300-3	300	3.0	100	502.2	3693.6	723.4	3964.0
D300-4	300	3.8	79	641.9	3815.4	923.1	4182.9
D300-5	300	5.0	60	853.3	3995.6	1219.5	4483.0
D300-6	300	7.5	40	1289.4	4983.8	1832.8	5857.6
D300-7	300	15.0	20	2672.5	7037.3	3661.0	8857.1
D300-8	300	20.0	15	3613.1	7977.7	4910.0	10299.7

out on aluminum CHS tubes of normal strength material (T5) and high strength material (T6) using nominal concrete strength of 40 MPa. The aluminum tubular columns without concrete infill were also analyzed for reference purposes. Hence, the 4 series analyzed in this study were T5-C0, T5-C40, T6-C0 and T6-C40. The T5 and T6 stand for the material type of aluminum CHS tubes, where T5 stands for normal strength material, and T6 stands for high strength material. The letter "C" in the series label defines the concrete strength followed by the value of the concrete cylinder strength in MPa. Each series consists of 24 different section sizes. The overall depth-to-thickness (D/t) ratio of the sections ranged from 10 to 160. The length-to-diameter ratio (L/D) for the concrete-filled aluminum CHS stub columns remained at a constant value of 3 to prevent overall column buckling. The cross-section dimensions and concrete-filled aluminum CHS column strengths (P_{FEA}) predicted from the finite element analysis (FEA) are summarized in Table 3.

The measured material properties of the aluminum CHS tubes and concrete infill were used in the parametric study. The nonlinear stress-strain curve of the normal strength non-welded aluminum CHS tube (N-C2-NW) tested by Zhu and Young (2006) having the yield stress of 185.9 MPa was used in the parametric study for normal strength (T5) aluminum tubes. The nonlinear stress-strain curve of the high strength aluminum CHS tube (series CHS7) tested by Zhou and Young (2009) having the yield stress of 267.9 MPa was used in the parametric study for high strength (T6) aluminum tubes. The measured compressive concrete cylinder strength of 44.8 reported by Zhou and Young (2009) are used in the parametric study for the concrete infill.

5 RELIABILITY ANALYSIS

The reliability of the concrete-filled aluminum column design rules was evaluated using reliability analysis. The reliability index (β) is a relative measure of the safety of the design. A target reliability index of 2.5 for aluminum structural members is recommended as a lower limit in the AA Specification (2005). The

design rules are considered to be reliable if the reliability index is greater than or equal to 2.5. The load combination of $1.2DL + 1.6LL$ as specified in the American Society of Civil Engineers Standard (ASCE 2005) was used in the reliability analysis, where DL is the dead load and LL is the live load. The statistical parameters are obtained from AA Specification for aluminum column strength, where $M_m = 1.10$, $F_m = 1.00$, $V_M = 0.06$, and $V_F = 0.05$, which are the mean values and coefficients of variation for material properties and fabrication factors. The statistical parameters P_m and V_P are the mean value and coefficient of variation of load ratio, respectively, as shown in Tables 4–11. In calculating the reliability index, the correction factor in the AA Specification was used. Reliability analysis is detailed in the AA Specification (2005).

6 COMPARISON OF EXPERIMENTAL AND NUMERICAL RESULTS WITH CURRENT DESIGN STRENGTHS

The concrete-filled aluminum CHS column strengths (P_{FEA}) predicted from the finite element analysis (FEA) were compared with the nominal design strengths (P_n) predicted using the American specifications (AA 2005, ACI 2008) and Australian/New Zealand standards (AS/NZS 1997, AS 2001) for aluminum and concrete structures. The design strengths (P_n) of concrete-filled aluminum CHS stub columns were obtained by determining the strength of the aluminum tube ($A_a F_L$) using the specifications (AA 2005, AS/NZS 1997) for aluminum structures as well as the strength of concrete infill ($0.85A_c f_c$) using the specifications (ACI 2008, AS 2001) for concrete structures, as shown in Eq. (1).

$$P_n = A_a F_L + 0.85 A_c f_c \tag{1}$$

where A_a is the full cross-section area of aluminum tube, F_L is the limit state stress calculated using Sections 3.4.7 through 3.4.10 and Sections 4.7.2 and 4.7.4 of the American (AA) Specification (AA 2005), and Sections 3.4.8 through 3.4.11 and Sections 4.7.2 and 4.7.4 of the Australian/New Zealand (AS/NZS) Standard (AS/NZS 1997), A_c is the area of concrete and f_c is the concrete cylinder strength. The design rules in the AS/NZS Standard (1997) for calculating the design strengths of aluminum columns are generally identical to those in the AA Specification (2005), except that the AS/NZS Standard reduces the yield load of the column using a coefficient k_c which is not included in the AA Specification. The American Specification (ACI 2008) and Australian Standard (AS 2001) for concrete structures generally use the same formula to calculate the strength of the concrete infill.

The comparison of concrete-filled aluminum CHS column strengths (P_{FEA}) predicted from FEA with design strengths (P_{AA} and $P_{AS/NZS}$) is shown in Tables 4–7. The composite column test strengths (P_{Exp}) reported by Zhou and Young (2009) were also compared with the design strengths (P_{AA} and $P_{AS/NZS}$) to evaluate the reliability of the current design rules, as shown in Table 7 for the high strength (T6) aluminum tubes. For the American specifications (AA 2005, ACI 2008), the mean values of the P_{FEA}/P_{AA} or (P_{Exp} and P_{FEA})$/P_{AA}$ ratio are 1.12, 1.29, 1.15 and 1.33 with the corresponding coefficients of variation (COV) of 0.044, 0.090, 0.085 and 0.070, and the reliability index (β) are 2.97, 3.59, 2.94 and 3.84 for series T5-C0, T5-C40, T6-C0 and T6-C40, respectively, as shown in Tables 4–7. For the Australian/New Zealand standards (AS/NZS 1997, AS 2001), the mean values of the P_{FEA}/P_{AA} or (P_{Exp} and P_{FEA})$/P_{AA}$ ratio are 1.17, 1.32, 1.19 and 1.37 with the corresponding COV of 0.046, 0.121, 0.052 and 0.097, and the reliability index (β) are 3.14, 3.48, 3.22 and 3.80 for series T5-C0, T5-C40, T6-C0 and T6-C40, respectively, as shown in Tables 4–7. It is shown that the American and AS/NZS specifications are generally conservative and reliable for the concrete-filled normal and high strength aluminum CHS stub columns having nominal concrete cylinder strength of 40 MPa with the D/t ratio of the CHS tubes ranging from 9 to 160.

7 PROPOSED DESIGN EQUATIONS

The aluminum CHS tube provides confinement to the concrete infill for the composite columns. On the other hand, the aluminum tube is stiffened by the concrete infill, which can prevent the inward buckling of the aluminum tube and increase the stability and strength of the column as a composite system. These enhancements of concrete-filled aluminum CHS columns due to the composite action between the constituent elements are not considered in the current American and Australian/New Zealand design rules. In this study, the ultimate strengths (P_p) of the concrete-filled aluminum CHS columns are proposed, as shown in Eqs. (2)–(4).

$$P_p = A_a f_y + 0.85 A_c f_c + \eta A_c f_y \tag{2}$$

in which,

$$\eta = 0.31 - 0.0055\frac{D}{t} \quad \text{for } 9 \le \frac{D}{t} \le 50\left(1 - 0.377\frac{f_c}{f_y}\right) \tag{3}$$

$$\eta = 0.045 - 0.0002\frac{D}{t} + 0.1\left(\frac{f_c}{f_y}\right) \quad \text{for } 50\left(1 - 0.377\frac{f_c}{f_y}\right) < \frac{D}{t} \le 160 \tag{4}$$

where P_p is the proposed column strength of concrete-filled aluminum CHS; A_a is the full cross-section area

Table 4. Comparison of numerical results with design strengths for aluminum CHS columns of series T5–C0.

Specimen	D/t	P_{FEA} kN	P_{FEA}/P_{AA}	$P_{FEA}/P_{AS/NZS}$
T5-D80-1-C0	160.0	18.7	1.14	1.14
T5-D80-2-C0	133.3	23.7	1.13	1.13
T5-D80-3-C0	100.0	35.7	1.18	1.18
T5-D80-4-C0	80.0	44.9	1.13	1.13
T5-D80-5-C0	57.1	63.6	1.08	1.11
T5-D80-6-C0	40.0	91.7	1.04	1.13
T5-D80-7-C0	20.0	194.0	1.09	1.22
T5-D80-8-C0	10.0	382.9	1.14	1.27
T5-D200-1-C0	153.8	121.3	1.12	1.12
T5-D200-2-C0	125.0	158.3	1.11	1.11
T5-D200-3-C0	100.0	223.4	1.18	1.18
T5-D200-4-C0	80.0	282.4	1.14	1.14
T5-D200-5-C0	60.6	373.6	1.09	1.10
T5-D200-6-C0	40.0	573.9	1.04	1.13
T5-D200-7-C0	20.0	1209.5	1.09	1.22
T5-D200-8-C0	10.0	2385.9	1.13	1.27
T5-D300-1-C0	150.0	310.4	1.23	1.23
T5-D300-2-C0	130.4	357.7	1.18	1.18
T5-D300-3-C0	100.0	502.2	1.18	1.18
T5-D300-4-C0	78.9	641.9	1.13	1.13
T5-D300-5-C0	60.0	853.3	1.09	1.11
T5-D300-6-C0	40.0	1289.4	1.04	1.13
T5-D300-7-C0	20.0	2672.5	1.07	1.20
T5-D300-8-C0	15.0	3613.1	1.10	1.24
		Mean, P_m	1.12	1.17
		COV, V_p	0.044	0.046
		Reliability index, β	2.97	3.14
		Resistance factor, ϕ	0.95	0.95

Table 5. Comparison of numerical results with design strengths for aluminum CHS columns of series T5–C40.

Specimen	D/t	P_{FEA} kN	P_{FEA}/P_{AA}	$P_{FEA}/P_{AS/NZS}$	P_{FEA}/P_p
T5-D80-1-C40	160.0	242.2	1.19	1.19	0.99
T5-D80-2-C40	133.3	245.3	1.19	1.19	0.97
T5-D80-3-C40	100.0	261.4	1.22	1.22	0.99
T5-D80-4-C40	80.0	271.9	1.23	1.23	0.99
T5-D80-5-C40	57.1	288.7	1.22	1.23	0.99
T5-D80-6-C40	40.0	334.4	1.28	1.32	0.98
T5-D80-7-C40	20.0	488.9	1.47	1.56	1.01
T5-D80-8-C40	10.0	675.0	1.47	1.60	1.10
T5-D200-1-C40	153.8	1520.6	1.19	1.19	0.99
T5-D200-2-C40	125.0	1584.3	1.22	1.22	0.99
T5-D200-3-C40	100.0	1635.7	1.22	1.22	0.99
T5-D200-4-C40	80.0	1703.0	1.23	1.23	0.99
T5-D200-5-C40	60.6	1777.6	1.22	1.22	0.98
T5-D200-6-C40	40.0	2086.7	1.28	1.31	0.98
T5-D200-7-C40	20.0	3041.9	1.46	1.55	1.01
T5-D200-8-C40	10.0	4160.5	1.45	1.57	1.09
T5-D300-1-C40	150.0	3469.3	1.21	1.21	1.00
T5-D300-2-C40	130.4	3524.9	1.21	1.21	0.99
T5-D300-3-C40	100.0	3693.6	1.23	1.23	0.99
T5-D300-4-C40	78.9	3815.4	1.22	1.22	0.98
T5-D300-5-C40	60.0	3995.6	1.21	1.22	0.98
T5-D300-6-C40	40.0	4983.8	1.36	1.39	1.04
T5-D300-7-C40	20.0	7037.3	1.50	1.60	
T5-D300-8-C40	15.0	7977.7	1.51	1.61	
		Mean, P_m	1.29	1.32	1.01
		COV, V_p	0.090	0.121	0.035
		Reliability index, β	3.59	3.48	2.76
		Resistance factor, ϕ	0.90	0.90	0.90

Table 6. Comparison of numerical results with design strengths for aluminum CHS columns of series T6–C0.

Specimen	D/t	P_{FEA} kN	P_{FEA}/P_{AA}	$P_{FEA}/P_{AS/NZS}$
T6-D80-1-C0	160.0	21.8	1.28	1.28
T6-D80-2-C0	133.3	32.2	1.26	1.26
T6-D80-3-C0	100.0	51.3	1.25	1.25
T6-D80-4-C0	80.0	64.6	1.19	1.19
T6-D80-5-C0	57.1	91.2	1.11	1.11
T6-D80-6-C0	40.0	130.2	1.05	1.11
T6-D80-7-C0	20.0	263.6	1.03	1.15
T6-D80-8-C0	10.0	523.0	1.08	1.21
T6-D200-1-C0	153.8	148.5	1.28	1.28
T6-D200-2-C0	125.0	224.5	1.21	1.21
T6-D200-3-C0	100.0	321.5	1.26	1.26
T6-D200-4-C0	80.0	405.2	1.19	1.19
T6-D200-5-C0	60.6	535.1	1.12	1.12
T6-D200-6-C0	40.0	813.5	1.05	1.11
T6-D200-7-C0	20.0	1638.0	1.02	1.15
T6-D200-8-C0	10.0	3241.4	1.07	1.20
T6-D300-1-C0	150.0	354.2	1.28	1.28
T6-D300-2-C0	130.4	478.0	1.26	1.26
T6-D300-3-C0	100.0	723.4	1.26	1.26
T6-D300-4-C0	78.9	923.1	1.19	1.19
T6-D300-5-C0	60.0	1219.5	1.12	1.12
T6-D300-6-C0	40.0	1832.8	1.05	1.11
T6-D300-7-C0	20.0	3661.0	1.02	1.14
T6-D300-8-C0	15.0	4910.0	1.04	1.17
		Mean, P_m	1.15	1.19
		COV, V_p	0.085	0.052
		Reliability index, β	2.94	3.22
		Resistance factor, ϕ	0.95	0.95

of aluminum tube; f_y is the aluminum yield stress (0.2% proof stress); A_c is area of concrete; f_c is the concrete cylinder strength; D is the outer diameter of CHS tube; and t is the thickness of aluminum CHS tube. The ultimate strengths of concrete-filled aluminum CHS columns are influenced not only by its constituent material properties such as the compressive cylinder strength of the concrete (f_c) and the yield stress (f_y) of the aluminum tube, but also the confining pressure on the concrete infill which depends on the overall depth-to-thickness (D/t) ratio of the aluminum CHS tube. The limitations of the Eqs (2)–(4) are $9 \leq D/t \leq 160$.

8 COMPARISON OF EXPERIMENTAL AND NUMERICAL RESULTS WITH PROPOSED DESIGN STRENGTHS

The unfactored design strengths calculated using the proposed design equations (2)-(4) were compared with the concrete-filled aluminum column strengths obtained from the tests (P_{Exp}) reported by Zhou and Young (2009) and the column strengths (P_{FEA}) predicted by the FEA obtained from this study. The proposed design strengths were calculated using the measured cross-section dimensions and measured

Table 7. Comparison of numerical results with design strengths for aluminum CHS columns of series T6–C40.

Specimen	D/t	P_{FEA} kN	P_{FEA}/P_{AA}	$P_{FEA}/P_{AS/NZS}$	P_{FEA}/P_p
CHS1C40*	9.8	158.9	1.27	1.39	0.92
CHS2C40*	16.0	217.0	1.35	1.45	0.88
CHS3C40*	23.5	244.1	1.29	1.37	0.81
CHS4C40*	36.9	329.9	1.33	1.38	0.89
CHS5C40*	49.4	543.6	1.42	1.43	1.05
CHS6C40*	48.1	822.8	1.45	1.47	1.07
CHS7C40*	59.3	1111.1	1.33	1.33	0.95
CHS8C40*	29.9	1481.9	1.45	1.53	0.94
CHS9C40*	39.7	1494.1	1.37	1.40	0.92
CHS10C40*	48.5	1690.2	1.30	1.32	0.96
T6-D80-1-C40	160.0	253.0	1.24	1.24	0.98
T6-D80-2-C40	133.3	259.8	1.23	1.23	0.96
T6-D80-3-C40	100.0	282.9	1.26	1.26	0.97
T6-D80-4-C40	80.0	296.3	1.25	1.25	0.97
T6-D80-5-C40	57.1	325.3	1.25	1.25	0.97
T6-D80-6-C40	40.0	396.0	1.34	1.37	0.96
T6-D80-7-C40	20.0	621.6	1.51	1.62	0.99
T6-D80-8-C40	10.0	888.5	1.46	1.60	1.07
T6-D200-1-C40	153.8	1601.1	1.25	1.25	0.98
T6-D200-2-C40	125.0	1689.9	1.26	1.26	0.98
T6-D200-3-C40	100.0	1774.5	1.26	1.26	0.98
T6-D200-4-C40	80.0	1869.6	1.27	1.27	0.97
T6-D200-5-C40	60.6	1989.3	1.25	1.25	0.97
T6-D200-6-C40	40.0	2473.7	1.33	1.36	0.96
T6-D200-7-C40	20.0	3323.8	1.29	1.39	0.85
T6-D200-8-C40	10.0	5460.1	1.44	1.57	1.06
T6-D300-1-C40	150.0	3653.8	1.26	1.26	0.99
T6-D300-2-C40	130.4	3757.4	1.26	1.26	0.98
T6-D300-3-C40	100.0	3964.0	1.25	1.25	0.97
T6-D300-4-C40	78.9	4182.9	1.25	1.25	0.97
T6-D300-5-C40	60.0	4483.0	1.24	1.24	0.97
T6-D300-6-C40	40.0	5857.6	1.40	1.44	1.01
T6-D300-7-C40	20.0	8857.1	1.53	1.64	1.00
T6-D300-8-C40	15.0	10299.7	1.53	1.65	1.03
		Mean, P_m	1.33	1.37	0.97
		COV, V_p	0.070	0.097	0.058
		Reliability index, β	3.84	3.80	2.53
		Resistance factor, ϕ	0.90	0.90	0.90

*Tests conducted by Zhou and Young (2009)

material properties. The resistance factor $\phi = 0.90$ for composite columns was obtained from reliability analysis, and the resistance factor $\phi = 0.95$ for aluminum columns without concrete infill was used in the reliability analysis. The load combination of 1.2DL + 1.6LL was used to determine the reliability index (β), as shown in Tables 4–7.

The proposed design strengths are generally conservative and reliable for the concrete-filled aluminum CHS columns. The mean value of the load ratio (P_{FEA}/P_p) is 1.01 with the corresponding COV of 0.035 and the value of $\beta = 2.76$ for concrete-filled normal strength aluminum columns of series T5-C40, as shown in Table 5. The mean value of the load ratio is 0.97 with the corresponding COV of 0.058 and the value of $\beta = 2.53$ for concrete-filled high strength aluminum columns of series T6-C40, as shown in Table 7. The reliability indices (β) are greater than the target value for all the specimens. It is shown that the proposed design strengths are more accurate than the current design strengths.

9 CONCLUSIONS

A numerical investigation of concrete-filled aluminum circular hollow section columns including geometric and material non-linearities has been presented. The developed finite element model was verified against test results. It is shown that the numerical model closely predicted the structural behaviour of concrete-filled aluminum CHS columns. Hence, a parametric study was carried out to study the effects of cross-section sizes of concrete-filled aluminum CHS column strengths. A total of 96 specimens were analyzed in the parametric study. The aluminum tubular columns without concrete infill were also analyzed for reference purposes. The reliability of the concrete-filled aluminum column design rules in the current American and Australian/New Zealand specifications for aluminum and concrete structures was evaluated using reliability analysis. The composite column strengths obtained from the finite element analysis and the tests were compared with the design strengths. It is shown that the American and Australian/New Zealand specifications are generally conservative and reliable for the concrete-filled normal and high strength aluminum CHS stub columns having nominal concrete cylinder strength of 40 MPa.

REFERENCES

ABAQUS. 2007.*ABAQUS Standard User's Manual*. 2007. Hibbitt, Karlsson and Sorensen, Inc. Vols. 1–3, Version 6.7, USA.

ACI. 2008. *Building code requirements for structural concrete and commentary*. ACI 318–08. Detroit (USA): American Concrete Institute.

Aluminum Association (AA) 2005. *Aluminum design manual – Part I: Specification for Aluminum Structures*. Washington, D.C.

ASCE. 2005. *Minimum design loads for buildings and other structures*, ASCE Standard 7–05. American Society of Civil Engineers Standard. New York,.

Australian/New Zealand Standard (AS/NZS) 1997. *Aluminium structures – Part 1: Limit state design*. AS/NZS 1664.1:1997, Standards Australia, Sydney, Australia.

Australian Standard (AS). 2001. *Concrete structures*. AS3600-2001. Sydney (Australia): Standards Australia.

Ellobody, E. & Young, B. 2006. Nonlinear analysis of concrete-filled steel SHS and RHS columns. *Thin-Walled Structures* 44: 910–930.

Ellobody E., Young B. & Lam D. 2006. Behaviour of normal and high strength concrete-filled compact steel tube circular stub columns. *Journal of Constructional Steel Research* 62(7):706–715.

Hu H.T, Huang C.S., Wu M.H. & Wu Y.M. 2003. Nonlinear analysis of axially loaded concrete-filled tube columns with confinement effect. *Journal of Structural Engineering* ASCE 129(10): 1322–1329.

Wu, M.H. 2000. *Numerical analysis of concrete filled steel tubes subjected to axial force*. M.S. Thesis, Department of Civil Engineering, National Cheng Kung University, Tainan, Taiwan.

Zhou, F. & Young, B. 2008. Tests of concrete-filled aluminum stub columns. *Thin-Walled Structures* 46: 573–583.

Zhou, F. & Young, B. 2009. Concrete-filled aluminum circular hollow section column tests. *Thin-Walled Structures* 47: 1272–1280.

Zhu, J.H. & Young, B. 2006. Experimental investigation of aluminum alloy circular hollow section columns. *Engineering Structures* 28(2): 207–215.

Zhou, F. & Young, B. 2012. Numerical analysis and design of concrete-filled aluminum circular hollow section columns. *Thin-Walled Structures* 50(1): 45–55.

Tubular Structures XIV – Gardner (Ed.)
© 2012 Taylor & Francis Group, London, ISBN 978-0-415-62137-3

Compression tests of aluminium alloy cross-sections

M.N. Su & B. Young
Department of Civil Engineering, The University of Hong Kong, Hong Kong, China

L. Gardner
Department of Civil and Environmental Engineering, Imperial College, London, UK

ABSTRACT: Aluminium structural members are being used increasingly widely nowadays due to a range of advantageous characteristics such as high strength to weight ratio, good corrosion resistance, ease of fabrication and aesthetic appearance. A test program on aluminium Square Hollow Sections (SHS) and Rectangular Hollow Sections (RHS) as well as SHS and RHS with internal cross stiffeners was conducted. A total of nine stub columns with a wide range of cross-section slenderness were compressed between fixed ends. Two kinds of aluminium alloy, 6063-T5 and 6061-T6, were investigated. Material properties were determined by tensile coupon tests and hardness measurements. Significant strain hardening was observed for most of the columns. The test strengths obtained from this study, together with the previous test data conducted by other researchers, were compared with the design strengths predicted by the American, Australian/New Zealand and European specifications for aluminium structures. Furthermore, the test strengths were also compared with the strengths predicted using the deformation based Continuous Strength Method (CSM). The design strengths predicted by the three specifications were generally conservative for all columns. The Continuous Strength Method provides better predictions for aluminium alloy columns with stocky sections.

1 INTRODUCTION

The first building structure made from an aluminium alloy was found in Europe in the 1950s (Mazzolani, 1994). Structural hollow sections are now widely used in a range of engineering applications such as building facades, roof systems, moving bridges and structures situated in humid environments. Therefore, a reliable evaluation of the compression capacity of non-slender aluminium alloy sections is necessary. The compression resistance of non-slender aluminium alloy non-slender sections is influenced by strain hardening, which occurs in stocky sections experiencing large plastic strains.

As for long columns and welded columns influenced by the heat-affected zone (HAZ), previous studies have reported that the current design codes generally provide conservative predictions (Bijlaard & Fisher, 1953; Mennick, 2002; Zhu & Young, 2006; Zhu & Young, 2008; Ashraf & Young, 2010; Mazzolani et al., 2011). Gardner & Ashraf (2006) explained that existing codes generally underestimated column strengths and did not adequately allow for non-linearity of the stress-strain response below the yield point and the strain hardening beyond the yield point. Additionally, Mazzolani et al. (2011) have identified some limitations of cross-section classification in Eurocode 9 (EC9, 2007), while use of the bi-linear material model and the concept of section classification ensures convenience in structural design calculations (Gardner & Ashraf, 2006). A number of studies (Mennick, 2002; Gardner & Ashraf, 2006; Ashraf & Young, 2010; Mazzolani et al., 2011) have revealed that the strain hardening has a significant effect on aluminium compression resistance and section classification that cannot be negligible. Thus, this study mainly focused on non-slender sections of aluminium alloy stub columns.

The experimental program was performed on four different extruded aluminium alloy sections: rectangular hollow sections (RHS), square hollow sections (SHS) and RHS and SHS with internal cross stiffeners. The aluminium alloys 6061-T6 and 6063-T5 were used for the test specimens. Previous test data conducted by other researchers on various classes of sections were also used in this study. The stub column test data covering a large range of b/t ratios were used to assess the section classification approach given in EC9 (2007). These test results were compared with the compression resistance predicted by the American Aluminium Design Manual (AA, 2010), the Australian/New Zealand Standard (AS/NZS, 1997), Eurocode 9 (EC9, 2007) and the Continuous Strength Method (Gardner et. al., 2011) for aluminium columns. The aim of this paper is to evaluate the existing design rules for aluminium columns using the test results obtained from this study and previous investigations.

2 EXPERIMENTAL INVESTIGATION

2.1 *Test specimens*

A series of aluminium alloy stub column tests comprising four section shapes was performed at the Structural Laboratory in the University of Hong Kong. The test specimens were manufactured by extrusion using 6061-T6 and 6063-T5 heat-treated aluminium alloys of different cross-sectional geometry, as shown in Table 1, using the symbols illustrated in Figures 1 and 2. The cross-section dimensions shown in Table 1 are the average measured values for each test specimen. The additional symbols used in Table 1 are defined as follows: L is the stub column length, $\sigma_{0.2}$ is material yield stress (taken as the 0.2% proof stress), σ_u is material ultimate stress, n is the exponent of Ramberg-Osgood expression and Hardness is the material surface hardness index. Initial local geometric imperfections were measured at mid-span on all four faces of selected columns. The imperfection measurements were conducted by mounting the specimen on a milling machine and measuring by a digital displacement transducer, as shown in Figure 3. The imperfection measurements were recorded at 2 mm intervals to obtain the profiles, as plotted in Figure 4.

2.2 *Specimen labelling*

The test specimens in this study were labelled according to the material strength and cross-section dimensions, as shown in Table 1. For example, the label "H70 × 55 × 4.2C-R" defines the following specimen. The first letter "H" refers to high strength aluminium alloy 6061-T6, while "N" refers to normal strength aluminium alloy 6063-T5; the nominal cross-section has dimensions of width (70 mm) × height (55 mm) × thickness (4.2 mm); if there is a "+" in front of the label, it means the hollow section has internal cross stiffeners; the symbol "C" following the dimensions mean a column compression test. Finally, if the test is repeated, a letter "R" will be shown in the label.

2.3 *Material properties*

The measured material properties of each specimen are summarized in Table 1. The material properties were determined by longitudinal tensile coupon tests which conformed to the Australian standard AS 1391 (AS, 2007) and the ASTM standard (ASTM, 1997). Furthermore, hardness tests were also conducted according to the Standard Test Method for Indentation Hardness of Aluminium Alloys by Means of a Webster Hardness Gage (ASTM, 2010).

The 6061-T6 and 6063-T5 tempers have different mechanical properties and behaviour. The temper T5

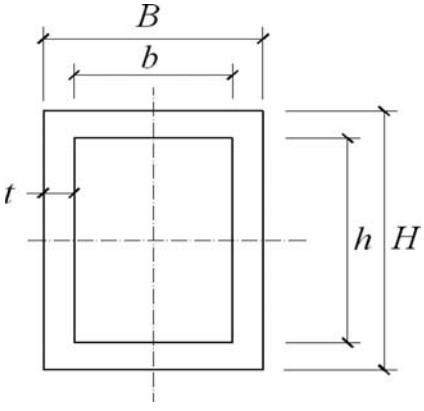

Figure 1. Definition of symbols for SHS/RHS.

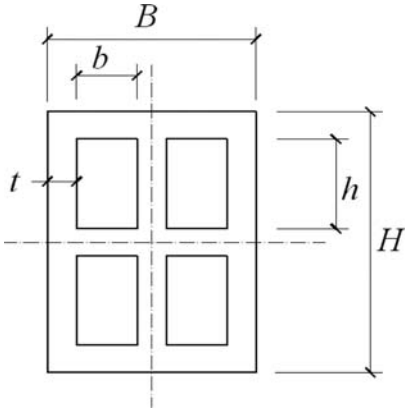

Figure 2. Definition of symbols for SHS/RHS with internal stiffeners.

Table 1. Measured stub column dimensions and material properties from tensile coupons.

Specimen	B (mm)	H (mm)	t (mm)	L (mm)	E (GPa)	$\sigma_{0.2}$ (MPa)	σ_u (MPa)	n	Hardness
H70 × 55 × 4.2C	69.9	54.9	4.08	209.8	65	193	207	22	12
H64 × 64 × 3.0C	63.9	63.9	2.81	191.1	66	234	248	12	13
H120 × 120 × 9.0C	120.0	120.0	8.91	360.2	65	225	234	13	12
N120 × 70 × 10.5C	119.9	69.8	10.45	360.9	71	139	194	9	11
N120 × 120 × 9.0C	120.0	120.0	8.92	361.3	69	181	228	9	11
H70 × 55 × 4.2C-R	69.9	54.9	4.09	209.9	65	193	207	22	12
H64 × 64 × 3.0C-R	63.9	63.9	2.85	191.5	66	234	248	12	13
+ H95 × 95 × 4.3C	95.4	95.3	4.17	284.8	67	228	240	12	12
+ H95 × 95 × 4.3C-R	95.4	95.3	4.17	284.8	67	228	240	12	12

has low yield strength, considerable strain hardening, a low hardness value and high ductility, whereas temper T6 has higher yield strength, lesser strain hardening, a higher hardness value and lower ductility, as illustrated in Figure 5.

The coupon specimens were machined from the structural sections with a 50 mm gauge length. The static curves were achieved by pausing the applied strain for 1.5 min near the 0.2% proof stress and the ultimate tensile strength. The Webster hardness tests were measured directly from the flat surfaces of the column specimens.

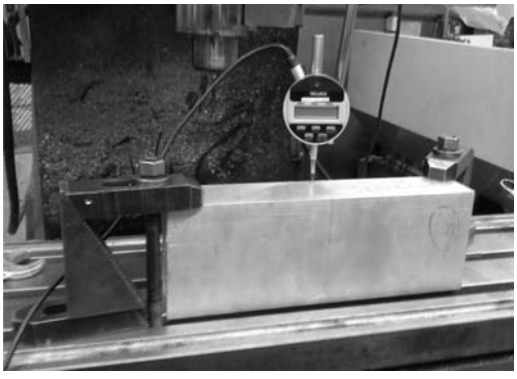

Figure 3. Measurement of initial local geometric imperfections.

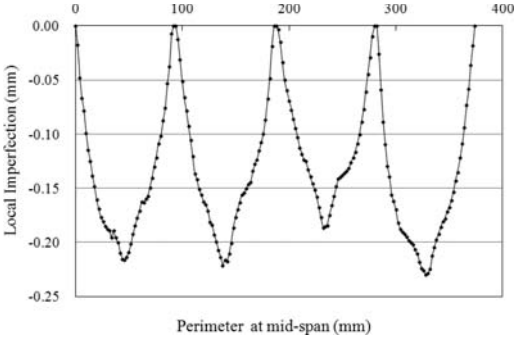

Figure 4. Initial local geometric imperfection profiles of specimen +H95 × 95 × 4.3C-R.

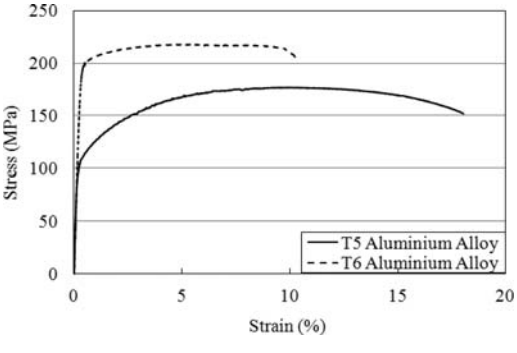

Figure 5. Static stress-strain curves for T6 (high-strength) and T5 (normal-strength) material.

2.4 *Testing procedure*

An experimental program of nine stub columns was conducted on aluminium alloy SHS and RHS as well as SHS and RHS with internal cross stiffeners to investigate load-carrying capacity and the significance of strain hardening. The nominal length of the stub columns was selected as three times of the larger cross-section dimension. After cutting the specimens, the ends of the columns were milled flat to ensure uniform load applied to the specimens. The columns were compressed between fixed ends, restrained against rotations, twisting and warping. The test configuration of specimen H70 × 55 × 4.2C is shown in Figure 6.

Three 25 mm-range LVDTs were used to measure the vertical deformation of the specimens. Strain gauges were attached at 10 mm intervals in the axial direction at mid-length of the columns to determine the axial strain and to monitor local buckling. Since all the sections are doubly symmetric, strain gauges were only adhered to one-quarter of the section perimeter.

A servo-controlled hydraulic testing machine was used to apply compressive force by displacement control at a constant speed of 0.4 mm/min for all tests. An initial load of 2 kN was applied on the specimens to ensure full contact between the specimen and upper and lower end plates. The applied load and the readings of the LVDTs and strain gauges were recorded by a data logger every second during the tests.

2.5 *Results*

The test results obtained from this study and by previous researchers are used in this investigation. The experimental ultimate loads (P_{exp}) were compared with the nominal compressive design strengths predicted by the American Aluminum Design Manual

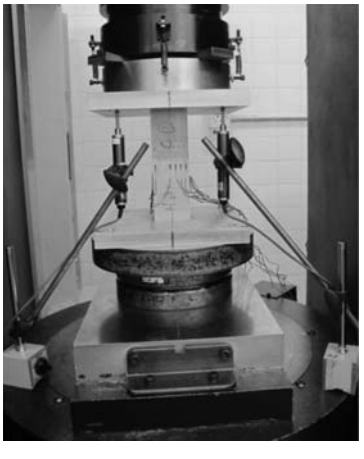

Figure 6. Test configuration for stub column H70 × 55 × 4.2C.

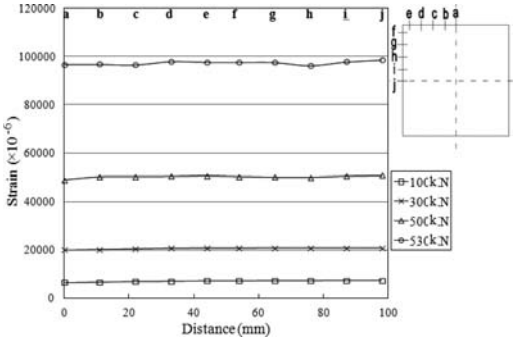

Figure 7. Strain distribution of specimen + H95 × 95 × 4.3C.

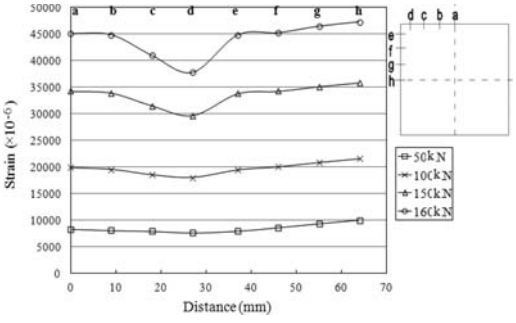

Figure 8. Strain distribution of specimen H64 × 64 × 3.0C.

(P_{AA}), AS/NZS ($P_{AS/NZS}$), EC9 (P_{EC9}) and the CSM (P_{csm}) for aluminium stub columns.

2.5.1 *Test results obtained from this study*

High deformation capacity and large plastic strains were observed in the response of the stocky sections. In the case of class 1 sections, such as + H95 × 95 × 4.3C, local buckling is only identifiable at the peak load after significant plastic deformation, as shown in Figure 7, while local buckling is far more pronounced in the class 3 specimen H64 × 64 × 3.0C, as shown in Figure 8. The majority of the columns failed by material yielding and inelastic local buckling, as shown in Figure 9, though in some specimens, evidence of local buckling prior to yielding and a degree of global buckling was observed. The test results conducted by the authors are plotted in Figure 10.

2.5.2 *Previous test data from other researchers*

Langseth & Hopperstad (1997) carried out an experimental investigation to study the local buckling behaviour of SHS of aluminium alloy 6060. In order to provide data for the development of EC9 (2007), Faella et al. (2000) conducted an extensive experimental program on aluminium hollow section columns and developed an empirical formulation to predict the column strengths. Mennink (2002) reported a series of

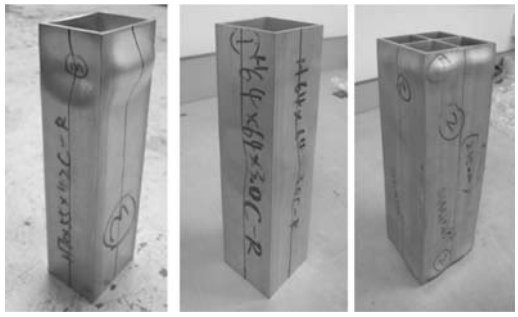

Figure 9. Stub column failure modes of specimens H70 × 55 × 4.2C-R, H64 × 64 × 3.0C-R and + H95 × 95 × 4.3C.

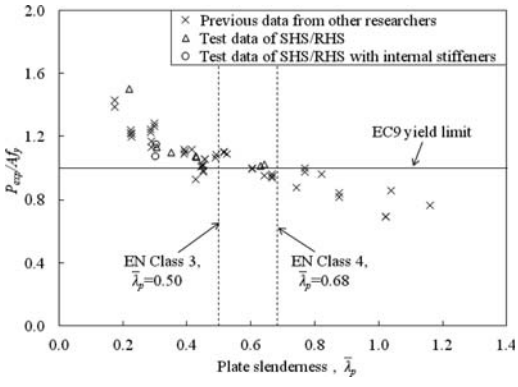

Figure 10. Comparison between tests results and EC9 yield limit with classification boundaries.

aluminium column tests and compared the test results with design strengths predicted by international codes, but only four stub columns related to this study were used. The dimensions and material properties of these specimens are shown in Table 2. The test results are also plotted in Figure 10.

3 SECTION CLASSIFICATION

Eurocode 9 (EC9, 2007) is one of the international codes providing quantitative classification criterion for aluminium alloy sections, which accounts for material properties and section dimensions. The characteristics of the different classes are as follows: class 1 and class 2 sections are able to develop their plastic moment capacity; class 3 sections are capable of reaching their yield stress before the onset of local buckling; class 4 sections fail by local buckling below the yield stress (Faella et al., 2000).

Based on this section classification, the structural behaviour can be examined. The experimental ultimate loads (P_{exp}) are generally higher than the yield limit (Af_y) for the class 1 and class 2 sections, while the class 4 slender sections have ultimate loads lower than

Table 2. Measured stub column dimensions and tensile material properties from literature (Langseth & Hopperstad, 1997; Faella et al., 2000; Mennink, 2002).

Specimen	B (mm)	H (mm)	t (mm)	L (mm)	E (GPa)	$\sigma_{0.2}$ (MPa)	σ_u (MPa)	n
SHS1-A	15.0	15.0	1.90	44.5	68	214	241	22
SHS1-B	15.0	15.0	1.90	46.0	68	214	241	22
SHS2-A	40.1	40.1	4.10	115.7	72	224	244	19
SHS2-B	40.1	40.1	4.10	120.0	72	224	244	19
SHS3-A	51.2	50.0	3.06	149.4	65	223	245	29
SHS3-B	51.2	50.0	3.06	149.4	65	223	245	29
SHS4-A	50.4	50.3	4.27	149.4	64	203	225	31
SHS4-B	50.4	50.3	4.27	149.3	64	203	225	31
SHS5-A	70.2	70.1	4.12	209.5	70	176	203	21
SHS5-B	70.2	70.1	4.12	209.5	70	176	203	21
SHS6-A	79.9	79.9	4.25	239.0	72	194	220	27
SHS6-B	79.9	79.9	4.25	239.0	72	194	220	27
SHS7-A	100.0	99.8	3.93	296.0	71	210	228	28
SHS7-B	100.0	99.8	3.93	299.0	71	210	228	28
SHS8-A	60.4	60.4	2.26	179.0	72	158	187	12
SHS8-B	60.4	60.4	2.26	179.0	72	158	187	12
SHS9-A	80.4	80.2	2.08	239.5	65	187	204	28
SHS9-B	80.4	80.2	2.08	239.0	65	187	204	28
SHS10-A	100.3	99.9	6.00	303.0	65	294	324	27
SHS10-B	100.3	99.9	6.00	303.0	65	294	324	27
SHS11-A	150.2	150.1	5.00	437.0	75	209	252	11
SHS11-B	150.2	150.1	5.00	451.0	75	209	252	11
SHS12-A	149.9	149.9	5.11	451.0	68	258	300	13
SHS12-B	149.9	149.9	5.11	452.0	68	258	300	13
RHS1-A	34.0	20.0	3.00	46.8	63	219	251	24
RHS1-B	34.0	20.0	3.00	46.8	63	219	251	24
RHS2-A	39.9	29.9	4.00	73.6	70	202	214	31
RHS2-B	39.9	29.9	4.00	120.4	70	202	214	31
RHS3-A	50.1	20.0	4.08	52.3	68	211	233	27
RHS3-B	50.1	20.0	4.08	52.3	68	211	233	27
RHS4-A	50.0	30.3	3.05	80.7	71	217	242	20
RHS5-A	50.3	40.3	2.70	104.5	70	222	244	48
RHS6-A	60.2	34.1	3.00	88.8	78	213	235	19
RHS21-A	47.0	40.0	2.90	140.0	68	251	277	33
RHS21-B	47.0	40.0	2.90	141.0	68	251	277	33
AA6060-T4-1.8	80.0	80.0	1.80	310.0	68	77	167	10
AA6060-T4-2.0	80.0	80.0	2.00	310.0	68	77	167	10
AA6060-T4-2.5	80.0	80.0	2.50	310.0	68	77	167	10
AA6060-T6-1.8	80.0	80.0	1.80	310.0	68	188	214	30
AA6060-T6-2.0	80.0	80.0	2.00	310.0	68	188	214	30
AA6060-T6-2.5	80.0	80.0	2.50	310.0	68	188	214	30
AA6060-T4*-2.5	80.0	80.0	2.50	310.0	68	115	196	15
RHS01	50.0	50.0	2.97	50.0	70	230	258	30
RHS02	50.0	50.0	2.96	100.3	69	230	258	30
RHS04	50.0	50.0	3.13	149.7	67	230	258	30
RHS05	50.0	50.0	3.13	200.0	68	199	218	28

the yield limit, as shown in Figure 10. According to the aforementioned characteristics for the four classes, there is a possibility to modify the limits of the different classes.

4 COMPARISON OF TEST STRENGTHS WITH DESIGN STRENGTHS

A total of 55 stub column test strengths (P_{exp}) are compared with the unfactored design strengths predicted using the AA (2010), AS/NZS (1997) and EC9 (2007) for aluminium structures, as shown in Figures 11–13. The comparisons were performed using the measured material properties and cross-section dimensions, with all safety factors set equal to unity.

The American Aluminum Design Manual (AA, 2010) provides design rules for aluminium alloy stub columns, in which the resistance of stocky sections is the yield stress multiplied by the gross cross-sectional area, while a reduced stress is used for slender sections. The AS/NZS (1997) provisions are the same as

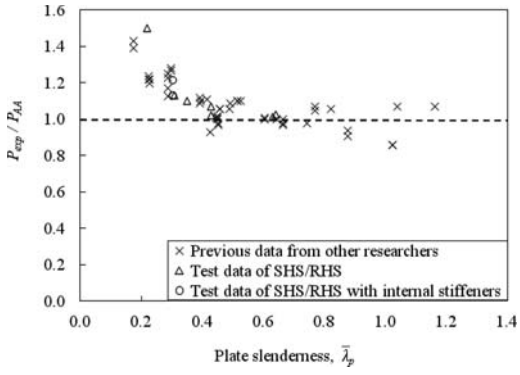

Figure 11. Comparison between test results and design strengths predicted by American Aluminum Design Manual (AA, 2010).

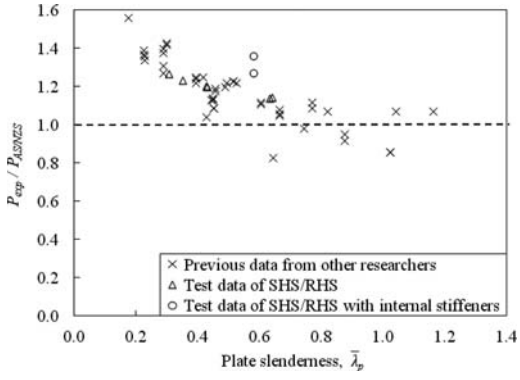

Figure 12. Comparison between test results and design strengths predicted by Australia/New Zealand Specification (AS/NZS, 1997).

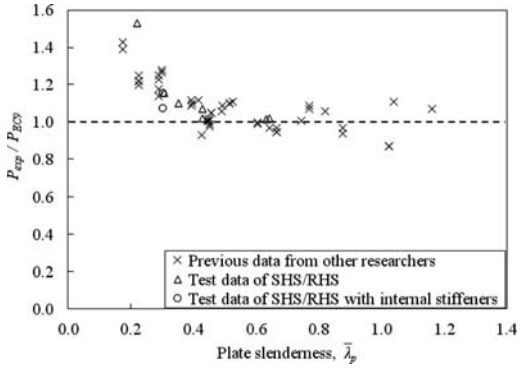

Figure 13. Comparison between test results and design strengths predicted by Eurocode 9 (EC9, 2007).

AA (2010), except with a coefficient for compression members. The ratios of experimental ultimate loads to design loads for the AA (P_{exp}/P_{AA}) and the AS/NZS ($P_{exp}/P_{AS/NZS}$) have mean values of 1.09 and 1.20, with

Table 3. Comparison summary of all stub column test results.

Specimen	$\frac{P_{exp}}{P_{AA}}$	$\frac{P_{exp}}{P_{AS/NZS}}$	$\frac{P_{exp}}{P_{EC9}}$	$\frac{P_{exp}}{P_{csm}}$
Mean	1.09	1.20	1.09	1.02
COV	0.119	0.146	0.120	0.088

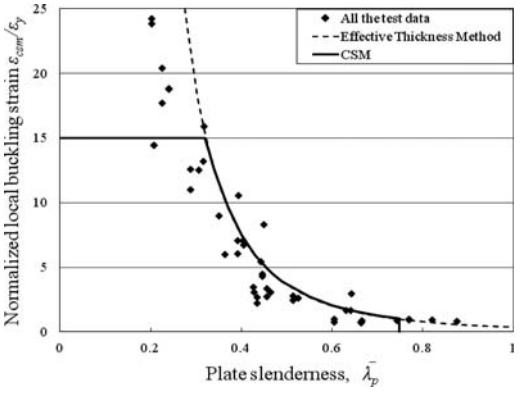

Figure 14. Comparison between test results and the CSM design base curve (Gardner et al., 2011).

the corresponding coefficients of variation (COV) of 0.119 and 0.146, respectively, as shown in Table 3. In calculating the design strengths of aluminium stub columns, EC9 (2007) employs an effective thickness approach. The comparison of test strengths and design strengths (P_{exp}/P_{EC9}) for EC9 (2007) has the mean value of 1.09 and a corresponding COV of 0.120, as shown in Table 3. It can be seen that the design strengths predicted by the AS/NZS (1997) is more conservative than EC9 (2007) and AA (2010), and predicts approximately 80% of the column test strengths. Table 3 indicates that EC9 (2007) and AA (2010) have similar performance regarding stub column capacity predictions. It is reflected in Figures 11–13 that the design strengths predicted by the three codes are more conservative for columns of class 1 and class 2 sections than columns of class 3 and class 4 sections.

A deformation-based design approach for aluminium and other nonlinear metallic material was proposed by Gardner & Ashraf (2006), and improved and broadened by Gardner et al. (2011). The Continuous Strength Method (CSM) for metallic columns is now simple to apply in that it uses a single base curve for aluminium, stainless steel and carbon steel to determine deformation capacity and an elastic, linear hardening material model to account for strain hardening. A comparison of the test results with the CSM design base curve is shown in Figure 14. The comparison indicates that the CSM base curve is applicable to aluminium. The CSM also provides a more accurate

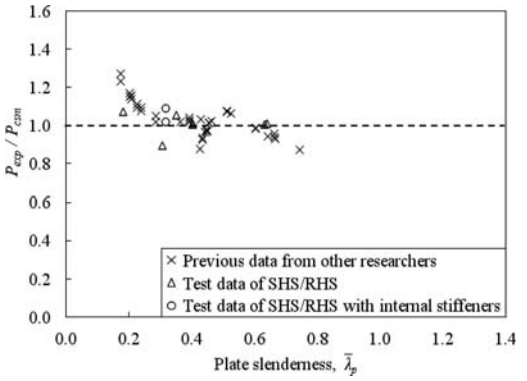

Figure 15. Comparison between test results and design strengths predicted by the CSM (Gardner et al., 2011).

prediction of capacity than other international structural aluminium design codes, with a mean value of 1.02 for the load ratio P_{exp}/P_{csm} and COV of 0.088, as shown in Table 3 and plotted in Figure 15. This is attributed to a rational exploitation of strain hardening. It should be noted that the cross-section slenderness ($\bar{\lambda}p$), as plotted in Figures 11–15, considered element interaction (Seif & Schafer, 2010) instead of considering the most slender element in the section. In this study, the strain hardening slope E_{sh} was determined from coupon test results for the tested stub columns, while the E_{sh} is assumed to be *E/100* (EC3, 2006) for the column data obtained from other researchers. To sum up, the design strengths of stub columns predicted by the AA (2010), AS/NZS (1997) and EC9 (2007) specifications are safe, but conservative, while the CSM provides accurate predictions.

5 CONCLUSIONS

A test program on fixed-ended aluminium alloy stub columns of square and rectangular hollow sections with and without internal cross stiffeners has been presented. The materials investigated in these experiments are heat-treated aluminium alloy 6063-T5 and 6061-T6, whose properties have been obtained from tensile coupon tests. Initial local geometric imperfections of the column specimens were measured. A series of aluminium alloy hollow section stub columns of different grades and sizes from previous studies by other researchers was also used in this investigation. The newly generated and existing experimental data were compared with the design strengths predicted by the American, Australian/New Zealand and European specifications and the Continuous Strength Method (CSM) for aluminium structures. Generally, the design strengths predicted by the three specifications are quite conservative, whereas the design strengths predicted by the CSM are more accurate than the current design methods. It is found that the design predications are more conservative for stocky sections due to the effect of strain hardening; the significance of this effect will be further investigated.

ACKNOWLEDGEMENTS

The research work described in this paper was supported by a grant from The University of Hong Kong under the seed funding program for basic research. The authors are also grateful to Mr. Yi-Ran Li for his assistance in the experimental program as part of his final year undergraduate research project at the University of Hong Kong.

REFERENCES

AA. (2010) *Aluminium design manual*, The Aluminium Association Washington, D.C.

ASTM. (1997) Standard Test Methods For Tension Testing of Metallic Materials. *E 8M–97*, American Society for Testing and Materials, West Conshohocken, Pa.

ASTM. (2010) Standard Test Method for Indentation Hardness of Aluminium Alloys by Means of a Webster Hardness Gage, *ASTM B647–10,* American Society for Testing Materials, West Conshohocken, Pa.

Ashraf, M. & Young, B. (2010) Compression Resistance of Aluminium Stub Columns Using Continuous Strength Method. *Proceeding of the 13th International Symposium Tubular Structures,* 257–263, Hong Kong, (December, 2010).

AS. (2007) Methods for Tensile Testing of Metals. *AS 1391–2007*, Australian Standard, Standards Association of Australia, Sydney, Australia.

AS/NZS. (1997) Aluminium Structures Part 1: Limit State Design. *AS/NZS 1664.1:1997*, Australian/New Zealand Standard, Sydney, Australia.

Bijlaard, P. P., & Fisher, G. P. (1953) Column Strength of H-Sections and Square Tubes in Post buckling Range Of Component Plates. *National Advisory Committee for Aeronautics Technical Note 2994*, Washington.

EC3. (2006) EUROCODE 3: Design of Steel Structures—Part 1–5: Plated Structural Elements. *EN 1993-1-5:2006*, European Committee for Standardization, CEN.

EC9. (2007) EUROCODE 9: Design of Aluminium Structures—Part 1–1: General Rules—General Rules and Rules for Buildings. *BS EN1999-1–1:2007+A1:2009*, European Committee for Standardization, CEN.

Faella, C., Mazzolani, F.M., Piluso, V. & Rizzano, G. (2000) Local Buckling of Aluminium Members: Testing and Classification. *Journal of Structural Engineering* 126(3):353–360.

Gardner, L. & Ashraf, M. (2006) Structural Design for Non-Linear Metallic Materials. *Engineering Structures* 28(6):926–934.

Gardner, L., Wang, F. & Liew, A. (2011) Influence of Strain Hardening on the Behaviour And Design Of Steel Structures. *International Journal of Structural Stability and Dynamics*, 11(5): 855–875.

Langseth, M. & Hopperstad, O. S. (1997) Local Buckling of Square Thin-Walled Aluminium Extrusions. *Thin-Walled Structures* 27(1):117–126.

Mazzolani, F.M. (1994) *Aluminium alloy structures 2nd.* E&FN Spon Press.

Mazzolani, F.M., Piluso, V., & Rizzano, G. (2011) Local Buckling of Aluminium Alloy Angles Under Uniform Compression. *Journal of Structural Engineering, ASCE* 137(2):173–184.

Mennink, J. (2002) *Cross-Sectional Stability of Aluminium Extrusions: Prediction of the Actual Local Buckling Behaviour.* the Netherlands.

Seif, M. & Schafer, B.W. (2010) Local Buckling of Structural Steel Shapes. *Journal of Constructional Steel Research* 66(10): 1232–1247.

Zhu, J.H. & Young, B. (2006) Tests and Design of Aluminium Alloy Compression Members. *Journal of Structural Engineering, ASCE* 132(7):1096–1107.

Zhu, J.H. & Young, B. (2008) Behaviour and Design of Aluminium Allot Structural Members. *Advanced Steel Construction* 4(2):158–172.

Tubular Structures XIV – Gardner (Ed.)
© 2012 Taylor & Francis Group, London, ISBN 978-0-415-62137-3

Bending tests of aluminium alloy cross-sections

M.N. Su & B. Young
Department of Civil Engineering, The University of Hong Kong, Hong Kong, China

L. Gardner
Department of Civil and Environmental Engineering, Imperial College, London, UK

ABSTRACT: The use of aluminium alloys in civil engineering is becoming more and more popular. An experimental investigation was performed on aluminium alloy square and rectangular hollow sections subjected to bending. The test program consisted of 11 three-point bending tests and 11 four-point bending tests. The test specimens were fabricated by extrusion using 6061-T6 heat-treated aluminium alloy, and had width-to-thickness ratio ranging from 2.8 to 20.5. The lengths of the beam specimens were 690 mm for the three-point bending tests and 990 mm for the four-point bending tests. Material properties were obtained from tensile coupon tests and hardness measurements. The available data from previous studies on aluminium simply supported beams of square and rectangular hollow sections were also considered in this study. A comparison of the test strengths with the design strengths calculated from the American, Australian/New Zealand and European specifications for aluminium structures is presented. The test results were also compared with the moment capacities obtained from deformation-based Continuous Strength Method (CSM). It is shown that the design strengths predicted by the three specifications are generally conservative, while the CSM provides a more accurate prediction. This is attributed to the occurrence of strain hardening in stocky cross-sections, which is neglected by the three specifications but allowed for in the CSM.

1 INTRODUCTION

The first aluminium structural members were produced and utilised in the 1930s (Kissell & Ferry, 2002). In recent years, the application of aluminium alloys in the civil engineering industry has become more popular. This building material satisfies the requirements of engineers with its advantageous characteristics of high strength-to-weight ratio, good corrosion resistance, ease of fabrication and the flexibility on cross-section shapes. Some aluminium alloys are relatively ductile, with fracture strains as large as 15%, and appreciable strain hardening (Mazzolani, 1994).

The available experimental data on simply supported beams of square hollow section (SHS) and rectangular hollow section (RHS) were reported by Lai & Nethercot (1992), Moen et al. (1999) and Zhu & Young (2006, 2009). The design specifications of the American Aluminum Design Manual (AA, 2010), the Australian/New Zealand Standard (AS/NZS, 1997) and Eurocode 9 (EC9, 2007) are widely used. However, only EC9 specifies aluminium alloy cross-section classification that is similar to steel codes. It is shown that the design strengths predicted by these specifications are generally conservative (Moen et al., 1999; Zhu & Young, 2006; Zhu & Young, 2009; Kim & Peköz, 2010). EC9 (2007) is the first specification allowing a complete inelastic analysis (De Matteis et al., 2001). The width-to-thickness ratio and the yield stress are recognized as the governing design parameters in the aforementioned specifications. The previous studies reflected that although the existing design specifications are widely used by structural engineers, they are not so efficient without considering strain hardening. Thus, recently attention has turned to the development of new design methods for metallic material. The Direct Strength Method (DSM) has been proposed by Schafer & Peköz (1998) for cold-formed carbon steel flexural members and later applied to aluminium alloy flexural members by Zhu & Young (2009). The Continuous Strength Method (CSM) for determinate steel structural members (Gardner, 2008) and indeterminate structural members (Gardner et al., 2011) is a deformation-based design approach, employing a continuous relationship between cross-section slenderness and cross-section deformation capacity together with a material model that allows for strain hardening in stocky sections experiencing large plastic strains.

To date, the majority of aluminium alloy bending tests were conducted on specimens of semi-compact and slender sections. The assessment of reliability and accuracy of design specifications for plastic and compact sections are relatively scarce. Bending tests on stocky SHS and RHS specimens with high rotation capacity are presented in this paper, including

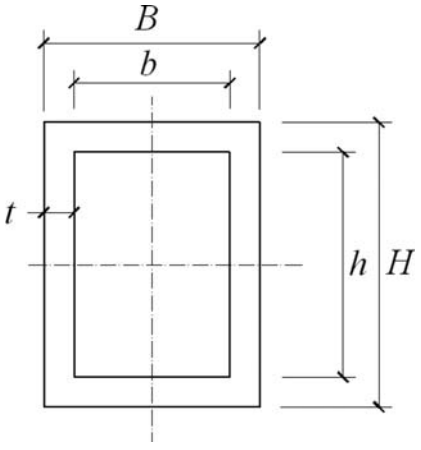

Figure 1. Definition of symbols for SHS/RHS.

experiments in the three-point and four-point configurations. The test results and previous experimental data from other researchers are compared with the design strengths predicted by the aforementioned design specifications and the CSM. In addition, the comparison between three-point and four-point bending test results is also discussed.

2 EXPERIMENTAL INVESTIGATION

2.1 *Test specimens*

The test specimens were manufactured by extrusion using 6061-T6 heat-treated aluminium alloy. There are 22 flexural specimens of different cross-sectional geometry, defined using the symbols illustrated in Figure 1. The cross-sectional dimensions shown in Tables 1 and 2 are the average measured values for each test specimen in this study.

In addition, the symbols shown in Tables 1 and 2 are defined as follows: L is the beam length, E is the Young's Modulus obtained from tensile coupon tests, $\sigma_{0.2}$ is the material yield stress (taken as the 0.2% proof stress), σ_u is the material ultimate stress, n is the exponent of Ramberg-Osgood expression and the material surface hardness is also reported.

2.2 *Specimen labelling*

The specimens were labelled according to the type of material, cross-sectional dimensions and test configurations. For example, the label "H70 × 55 × 4.2B3-R" defines the RHS specimen of high strength aluminium alloy 6061-T6, with nominal cross-sectional dimension of width (70 mm) × height(55 mm) × thickness (4.2 mm). The symbol "B3" following dimensions refers to the three-point loading configuration, whereas "B4" signifies the four-point loading configuration. If a test is repeated, a letter "R" is included in the label. The arrangement of the cross-sectional dimensions also refers to the bending axis. In this case, the specimen H70 × 55 × 4.2B3-R was bending about the minor axis.

2.3 *Material properties*

Material properties were determined by means of longitudinal tensile coupon tests and hardness measurements, as summarized in Tables 1 and 2. The typical tensile coupon tests conformed to the Australian standard AS 1391 (AS, 2007) and the ASTM standard (ASTM, 1997). Hardness measurements were conducted to determine the aluminium surface hardness which varies in different aluminium alloy tempers according to the Standard Test Method for Indentation Hardness of Aluminium Alloys by Means of a Webster Hardness Gage (ASTM, 2010).

2.4 *Testing procedure and failure modes*

The bending tests were conducted to assess moment capacity, rotation capacity and the significance of strain hardening. Stiffening steel plates of 100 mm width and 10 mm thickness as well as wooden blocks were employed at the loading points and supports to prevent web crippling due to load concentration. A steel bearing plate was placed between the specimen and loading/support point for the purpose of spreading the concentrated load. A 1000 kN capacity servo-controlled hydraulic testing machine was used to apply compressive force by displacement control at a constant speed of 0.8 mm/min for all tests. The applied loads as well as the readings of LVDTs and strain gauges were recorded by a data logger at one second intervals during the tests. Hinges and pins were simulated by half rounds and rollers, respectively.

2.4.1 *Three-point bending tests*

In the three-point bending tests, the simply supported specimens were loaded at the mid-span under the bearing plates and rollers, as shown in Figure 2. The span between the loading point and the supports was 300 mm for all tests so that the failure of beams was governed by moment capacity rather than fail by shear. One 100 mm LVDT was used to measure the vertical deflection mid-span. Two 25 mm LVDTs were placed at each end to measure the end rotation, since three-point bending specimens do not have constant moment along the beam length. Three strain gauges were adhered to the compressive flange next to the loading point, two near the flange-web junctions and one in the middle of the flange, for the relatively slender sections (H70 × 55 × 4.2B3, H55 × 70 × 4.2B3 and H64 × 64 × 3.0B3) to monitor the possible local buckling.

2.4.2 *Four-point bending tests*

In the four-point bending tests, the simply supported specimens were loaded symmetrically at two points using a spreader beam, as shown in Figure 3. One 100 mm LVDT and two 50 mm LVDTs were used

Table 1. Measured three-point bending specimen dimensions and material properties from tensile coupon tests.

Specimen	B (mm)	H (mm)	t (mm)	L (mm)	E (GPa)	$\sigma_{0.2}$ (MPa)	σ_u (MPa)	n	Hardness
H70 × 55 × 4.2B3	69.8	55.2	4.09	694.8	67	207	222	16	13
H55 × 70 × 4.2B3	54.7	69.8	4.09	693.4	67	207	222	16	13
H95 × 50 × 10.5B3	94.7	49.6	10.34	695.0	68	229	242	11	11
H50 × 95 × 10.5B3	49.5	94.6	10.34	693.0	68	229	242	11	12
H64 × 64 × 3.0B3	63.9	63.8	2.89	692.7	67	232	245	10	12
H120 × 120 × 9.0B3	120.0	119.9	8.90	691.4	65	225	234	13	12
H120 × 70 × 10.5B3	119.8	69.8	10.28	691.4	68	226	238	10	12
H70 × 120 × 10.5B3	69.8	119.8	10.26	691.8	68	226	238	10	12
H70 × 55 × 4.2B3-R	69.8	54.8	4.07	694.1	65	193	207	22	12
H50 × 95 × 10.5B3-R	49.5	94.7	10.33	692.8	68	229	242	11	11
H64 × 64 × 3.0B3-R	63.9	63.9	2.83	696.3	67	232	245	10	12
Q1-1m-1[#]	99.6	100.3	5.91	1000.0	69	316	324	—	—
Q1-1m-2[#]	99.6	100.3	5.91	1000.0	69	316	324	—	—
Q1-2m-1[#]	99.6	100.3	5.91	2000.0	69	316	324	—	—
Q1-2m-3[#]	99.6	100.3	5.91	2000.0	69	316	324	—	—
Q2-1m-1[#]	100.0	100.0	5.91	1000.0	67	177	284	—	—
Q2-1m-2[#]	100.0	100.0	5.91	1000.0	67	177	284	—	—
Q2-2m-1[#]	100.0	100.0	5.91	2000.0	67	177	284	—	—
Q2-2m-2[#]	100.0	100.0	5.91	2000.0	67	177	283	—	—
Q3-1m-1[#]	100.0	99.7	2.87	1000.0	67	120	221	—	—
Q3-1m-2[#]	100.0	99.7	2.87	1000.0	67	120	221	—	—
Q3-2m-1[#]	100.0	99.7	2.87	2000.0	67	120	221	—	—
Q3-2m-3[#]	100.0	99.7	2.87	20000	67	120	221	—	—
Q4-2m-1[#]	100.1	100.0	5.97	2000.0	67	314	333	—	—
Q4-2m-2[#]	100.1	100.0	5.97	2000.0	67	314	333	—	—
R1-1m-1[#]	60.0	119.4	2.45	1000.0	67	289	302	—	—
R1-2m-1[#]	60.0	119.4	2.45	2000.0	67	289	302	—	—
R1-2m-2[#]	60.0	119.4	2.45	2000.0	67	289	302	—	—
R1-3m-1[#]	60.0	119.4	2.45	3000.0	67	289	302	—	—
R1-3m-2[#]	60.0	119.4	2.45	3000.0	67	289	302	—	—
R2-1m-1[#]	60.1	100.0	2.93	1000.0	66	281	290	—	—
R2-1m-2[#]	60.1	100.0	2.93	1000.0	66	281	290	—	—
R2-2m-1[#]	60.1	100.0	2.93	2000.0	66	281	290	—	—
R2-2m-2[#]	60.1	100.0	2.93	2000.0	66	281	290	—	—
R2-3m-1[#]	60.1	100.0	2.93	3000.0	66	281	290	—	—
R2-3m-2[#]	60.1	100.0	2.93	3000.0	66	281	290	—	—

[#] Test results from Moen et al. (1999).

to measure the vertical deflection at mid-span and at the loading points, respectively, in order to obtain the curvature in the constant moment region. The Moment-curvature curve for H120 × 120 × 9.0B4 is shown in Figure 4. Two 25 mm LVDTs were placed at each end of the beams to measure the end rotation. Similarly, three strain gauges were used in the compressive flange at mid-span for the relatively slender sections (H70 × 55 × 4.2B4, H55 × 70 × 4.2B4 and H64 × 64 × 3.0B4) to detect the possible local buckling.

2.4.3 *Failure modes*

The specimens generally failed by spread of plasticity and inelastic local buckling, except for beams H50 × 95 × 10.5B3 and H70 × 120 × 10.5B3 which failed by tensile material fracture at mid-span. A distinct sound could be heard when the material split on the tensile flange at failure, as seen in Figure 5. It should be noted that significant visual local buckling was not observed in the tests.

2.5 *Test results and previous test data from other researchers*

The following experimental data on hollow sections collected from other researchers were used in this investigation. Moen et al. (1999) conducted 25 three-point bending tests on aluminium hollow section beams, considering plastic behaviour under a moment gradient. On the other hand, four-point bending experiments on high strength aluminium RHS beams have been reported by Lai & Nethercot (1992). Zhu & Young (2006, 2009) also conducted four-point bending tests of thin-walled aluminium RHS and SHS to achieve a constant moment region with zero shear force. The

Table 2. Measured four-point bending specimen dimensions and material properties from tensile coupon tests.

Specimen	B (mm)	H (mm)	t (mm)	L (mm)	E (GPa)	$\sigma_{0.2}$ (MPa)	σ_u (MPa)	n	Hardness
H70 × 55 × 4.2B4	69.9	54.9	4.09	990.0	67	207	222	16	14
H55 × 70 × 4.2B4	54.9	69.9	4.10	993.1	67	207	222	16	14
H95 × 50 × 10.5B4	94.7	49.6	10.35	993.8	68	229	243	11	12
H50 × 95 × 10.5B4	49.6	94.7	10.37	988.3	68	229	243	11	12
H64 × 64 × 3.0B4	63.9	63.9	2.86	991.2	67	232	245	10	12
H120 × 120 × 9.0B4	120.0	112.0	8.92	995.8	65	225	234	13	12
H120 × 70 × 10.5B4	119.8	69.8	10.40	993.6	68	226	238	10	12
H70 × 120 × 10.5B4	69.9	119.8	10.30	996.5	68	226	238	10	12
H64 × 64 × 3.0B4-R	63.8	63.9	2.87	993.4	67	232	245	10	12
H70 × 55 × 4.2B4-R	70.0	54.9	4.08	989.5	67	207	222	16	14
H55 × 70 × 4.2B4-R	54.9	70.0	4.09	989.5	67	207	222	16	14
S1-PB#	44.6	44.6	1.14	—	68	296	300	—	—
R1-PB#	100.1	44.1	1.32	—	70	260	276	—	—
R2-PB#	99.8	43.9	2.90	—	69	275	283	—	—
R2-PB##	99.8	44.0	2.91	—	69	275	283	—	—
H32 × 32 × 2*	32.0	32.0	1.94	1240.0	66	243	261	—	—
H40 × 40 × 5*	39.9	39.9	4.85	1440.0	70	226	246	—	—
H50 × 50 × 2*	50.7	50.7	1.95	1640.0	67	264	271	—	—
H50 × 50 × 3*	50.5	50.5	3.09	1640.0	64	268	273	—	—
H65 × 65 × 3*	64.1	64.1	2.99	1840.0	68	222	236	—	—
H76 × 76 × 3*	76.1	76.1	3.10	1840.0	68	246	264	—	—
H90 × 90 × 2*	88.2	88.2	1.75	2040.0	67	246	263	—	—
H100 × 100 × 2*	102.0	102.0	2.31	2240.0	68	234	258	—	—
H110 × 110 × 3*	111.6	111.6	3.13	2640.0	66	290	291	—	—
H153 × 153 × 3*	153.6	153.6	3.36	3000.0	72	244	267	—	—
N-1000-P-2^	50.9	102.2	4.50	1200.0	71	373	430	33	—
N-1000-P-3^	50.9	102.2	4.50	1200.0	71	373	430	33	—
N-2000-P-1^	50.9	102.2	4.50	2200.0	71	373	430	33	—
N-2000-P-2^	50.9	102.2	4.50	2200.0	71	373	430	33	—

Test results from Zhu & Young (2006)
*Test results from Zhu & Young (2009)
^Test results from Lai & Nethercot (1992).

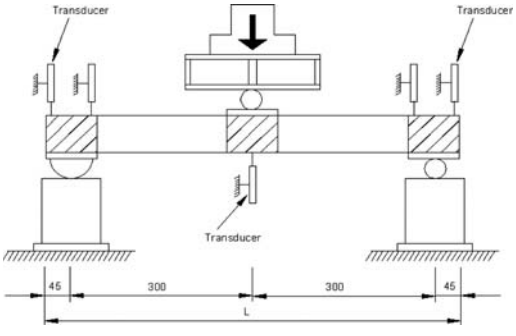

Figure 2. Test configuration for three-point bending tests (dimensions in mm).

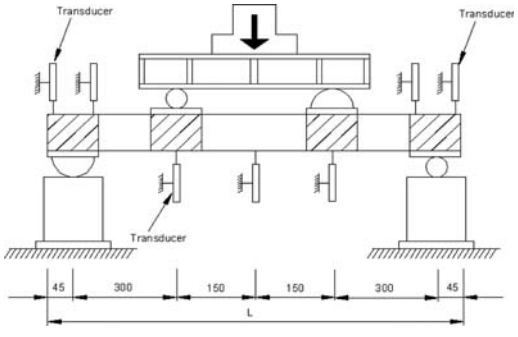

Figure 3. Test configuration for four-point bending tests (dimensions in mm).

hollow sections examined by other researchers consist of both slender and non-slender sections. The test results from the current study are given in Table 3; a comparison of the response in three-point and four-point bending is given in the following section. The combined data set from the literature and the newly generated data from this study, are presented in Tables 4–5, and are used to assess the beam design rules in the current specifications and the CSM design method.

3 COMPARISON BETWEEN THREE-POINT AND FOUR-POINT BENDING TESTS

Two bending test configurations – three-point bending and four-point bending – were employed for each section in the current study. The investigation focused on non-slender sections subjected to a moment gradient with maximum shear stress for three-point bending tests and a constant moment without shear stress

for four-point bending tests. Typical failed specimens from the three-point and four-point bending tests are shown Figures 6 and 7, respectively.

Generally, it can be seen from Table 3 that the three-point bending tests lead to 15% to 20% higher ultimate moment capacity than four-point bending tests for the same sections, which coincides with the findings of Chan & Gardner (2008). Meanwhile, the end rotations are also improved by 10% to 15% in three-point bending tests as compared to those four-point bending tests. Theofanous et al. (2009) and Chan & Gardner (2008) explained the reason as the "stabilizing effect from the stiffer material surrounding the plastic hinge, which is at a lower stress level in the three-point bending arrangement and helps to delay local buckling, whereas in four-point bending, the whole central region experiences constant moment and the point of local buckling receives less restraint". Furthermore, Theofanous et al. (2009) summarized many previous studies (Lay & Galambos, 1965; Lay & Galambos, 1967; Kuhlmann, 1989) and drew the conclusion that the moment gradient has a more pronounced effect for stocky sections.

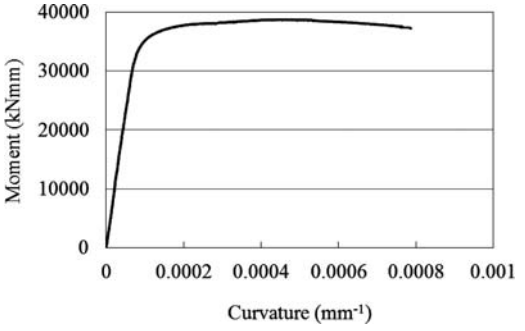

Figure 4. Moment-curvature curve for H120 × 120 × 9.0B4.

Figure 5. Material splitting on the tensile flange.

4 COMPARISON OF TEST STRENGTHS WITH DESIGN STRENGTHS

The experimental ultimate bending moments ($M_{exp,u}$) obtained from this study and previous studies are compared with the nominal flexural design strengths predicted by the American (AA, 2010), Australian/New Zealand (AS/NZS, 1997) and European (EC9, 2007) specifications for aluminium structures, as shown in Tables 4–5 and Figures 8–9. In addition, the flexural design strengths (M_{csm}) calculated from the CSM (Gardner et al., 2011) are also compared with the experimental ultimate bending moments. Overall, the experimental bending moments are 25% and 30% higher than the nominal flexural strengths ($M_{AS/NZS}$) predicted by the AS/NZS (1997) for the three-point bending and four-point bending, respectively, which are higher than the AA (2010), EC9 (2007) and the CSM predictions. The stocky sections with low b/t values were not well predicted, owing to the neglecting of the strain hardening. Moen et al. (1999) reported in their study that "EC9 is unable to account for the

Figure 6. Three-point bending test specimen H95 × 50 × 10.5B3.

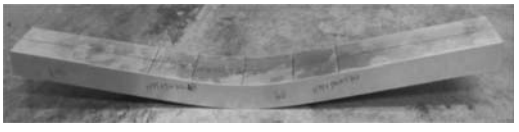

Figure 7. Four-point bending test specimen H95 × 50 × 10.5B4.

Table 3. Comparison of moment capacity between three-point and four-point bending tests.

Specimen	$M_{exp,u}$ (kNm)	Specimen	$M_{exp,u}$ (kNm)	$\frac{B3M_{exp,u}}{B4M_{exp,u}}$
H70 × 55 × 4.2B3	4.75	H70 × 55 × 4.2B4	4.72	1.01
H55 × 70 × 4.2B3	6.76	H55 × 70 × 4.2B4	6.49	1.04
H95 × 50 × 10.5B3	12.09	H95 × 50 × 10.5B4	10.35	1.17
H50 × 95 × 10.5B3	21.09	H50 × 95 × 10.5B4	18.04	1.17
H64 × 64 × 3.0B3	4.10	H64 × 64 × 3.0B4	3.59	1.14
H120 × 120 × 9.0B3	44.42	H120 × 120 × 9.0B4	38.75	1.15
H120 × 70 × 10.5B3	23.59	H120 × 70 × 10.5B4	19.66	1.20
H70 × 120 × 10.5B3	37.86	H70 × 120 × 10.5B4	33.00	1.15

Table 4. Comparison between the three-point bending test results and design capacities predicted by different methods

Specimen	b/t	$\frac{M_{exp,u}}{M_{csm}}$	$\frac{M_{exp,u}}{M_{AA}}$	$\frac{M_{exp,u}}{M_{AS/NZS}}$	$\frac{M_{exp,u}}{M_{EC9}}$
H70 × 55 × 4.2B3	11.5	1.13	1.31	1.42	1.20
H55 × 70 × 4.2B3	15.1	1.37	1.58	1.77	1.45
H95 × 50 × 10.5B3	2.8	1.18	1.52	1.61	1.24
H50 × 95 × 10.5B3	7.2	1.24	1.46	1.73	1.29
H64 × 64 × 3.0B3	20.1	1.11	1.18	1.29	1.29
H120 × 120 × 9.0B3	11.5	1.16	1.32	1.45	1.20
H120 × 70 × 10.5B3	4.8	1.17	1.42	1.52	1.22
H70 × 120 × 10.5B3	9.7	1.25	1.45	1.68	1.30
H70 × 55 × 4.2B3-R	11.5	1.14	1.33	1.44	1.21
H50 × 95 × 10.5B3-R	7.2	1.22	1.44	1.70	1.27
H64 × 64 × 3.0B3-R	20.5	1.18	1.25	1.37	1.37
Q1-1m-1[#]	15.0	0.96	1.06	1.16	1.16
Q1-1m-2[#]	15.0	0.96	1.06	1.16	1.16
Q1-2m-1[#]	15.0	0.94	1.03	1.13	1.13
Q1-2m-3[#]	15.0	0.95	1.04	1.14	1.14
Q2-1m-1[#]	14.9	1.08	1.25	1.37	1.15
Q2-1m-2[#]	14.9	1.07	1.24	1.36	1.14
Q2-2m-1[#]	14.9	1.04	1.20	1.32	1.11
Q2-2m-2[#]	14.9	1.07	1.24	1.36	1.14
Q3-1m-1[#]	32.8	0.98	1.01	1.06	1.13
Q3-1m-2[#]	32.8	0.96	0.99	1.04	1.11
Q3-2m-1[#]	32.8	0.95	0.98	1.03	1.10
Q3-2m-3[#]	32.8	1.00	1.03	1.08	1.15
Q4-2m-1[#]	14.8	0.99	1.09	1.20	1.20
Q4-2m-2[#]	14.8	0.96	1.06	1.16	1.16
R1-1m-1[#]	46.7	0.91	0.85	0.94	1.00
R1-2m-1[#]	46.7	0.91	0.85	0.94	1.00
R1-2m-2[#]	46.7	0.91	0.85	0.94	1.00
R1-3m-1[#]	46.7	0.86	0.80	0.88	0.94
R1-3m-2[#]	46.7	0.85	0.79	0.87	0.93
R2-1m-1[#]	32.1	0.97	1.02	1.11	1.15
R2-1m-2[#]	32.1	0.97	1.02	1.11	1.15
R2-2m-1[#]	32.1	0.96	1.01	1.10	1.14
R2-2m-2[#]	32.1	0.98	1.04	1.13	1.17
R2-3m-1[#]	32.1	1.01	1.07	1.16	1.20
R2-3m-2[#]	32.1	1.00	1.06	1.15	1.19
Mean		1.04	1.14	1.25	1.16
COV		0.118	0.183	0.198	0.092

[#] Test results from Moen et al. (1999)

Table 5. Comparison between the four-point bending test results and design capacities predicted by different methods.

Specimen	b/t	$\frac{M_{exp,u}}{M_{csm}}$	$\frac{M_{exp,u}}{M_{AA}}$	$\frac{M_{exp,u}}{M_{AS/NZS}}$	$\frac{M_{exp,u}}{M_{EC9}}$
H70 × 55 × 4.2B4	11.4	1.14	1.31	1.43	1.20
H55 × 70 × 4.2B4	15.1	1.31	1.51	1.69	1.39
H95 × 50 × 10.5B4	2.8	1.01	1.30	1.38	1.06
H50 × 95 × 10.5B4	7.1	1.05	1.25	1.48	1.10
H64 × 64 × 3.0B4	20.4	0.98	1.04	1.14	1.14
H120 × 120 × 9.0B4	11.5	1.01	1.15	1.26	1.04
H120 × 70 × 10.5B4	4.7	0.96	1.17	1.25	1.01
H70 × 120 × 10.5B4	9.6	1.08	1.26	1.46	1.13
H64 × 64 × 3.0B4-R	20.3	0.98	1.04	1.14	1.14
H70 × 55 × 4.2B4-R	11.4	1.16	1.35	1.46	1.23
H55 × 70 × 4.2B4-R	15.1	1.23	1.41	1.58	1.29
S1-PB[#]	37.1	1.23[+]	1.17	1.16	1.23
R1-PB[#]	31.4	1.18[+]	1.30	1.32	1.18
R2-PB[#]	13.1	0.89	1.13	1.21	1.24
R2-PB#[#]	13.1	0.87	1.11	1.18	1.22
H32 × 32 × 2*	14.5	1.02	1.16	1.27	1.07
H40 × 40 × 5*	6.2	0.99	1.21	1.34	1.06
H50 × 50 × 2*	24.0	1.04	1.00	1.07	1.11
H50 × 50 × 3*	14.3	1.00	1.10	1.20	1.01
H65 × 65 × 3*	19.4	1.04	1.12	1.22	1.23
H76 × 76 × 3*	22.5	0.99	1.00	1.09	1.09
H90 × 90 × 2*	48.4	0.98[+]	0.97	0.99	0.98
H100 × 100 × 2*	42.2	1.11[+]	1.07	1.09	1.11
H110 × 110 × 3*	33.7	1.11[+]	1.04	1.06	1.11
H153 × 153 × 3*	43.7	1.00[+]	0.95	0.97	1.00
N-1000-P-2^	20.7	1.07	1.43	1.65	1.31
N-1000-P-3^	20.7	1.09	1.46	1.68	1.34
N-2000-P-1^	20.7	0.96	1.29	1.48	1.18
N-2000-P-2^	20.7	0.98	1.32	1.52	1.21
Mean		1.04	1.19	1.30	1.15
COV		0.096	0.129	0.159	0.093

[#] Test results from Zhu & Young (2006).
* Test results from Zhu & Young (2009).
^ Test results from Lai & Nethercot (1992).
[+] Calculated by Effective Thickness Method in EC9, and not included in the mean and COV values.

increased rotational capacity resulting from increased strain hardening". De Matteis et al. (2001) demonstrated that EC9 has not considered "the hardening of the material" and "the moment gradient in the beam"; moreover, "no provision is made for the influence of plastic anisotropy that may be exhibited by aluminium alloys".

Three-point and four-point bending configurations produced different flexural moment capacities. In the case of three-point bending, the mean values of the moment ratio $M_{exp,u}/M_{AA}$ and $M_{exp,u}/M_{AS/NZS}$ are 1.14 and 1.25, with the corresponding Coefficients of Variation (COV) of 0.183 and 0.198 respectively, while $M_{exp,u}/M_{EC9}$ has the mean value of 1.16 and a corresponding COV of 0.092. In the case of four-point bending, the mean values of moment ratio $M_{exp,u}/M_{AA}$, $M_{exp,u}/M_{AS/NZS}$ and $M_{exp,u}/M_{EC9}$ are 1.19, 1.30 and 1.15, with the corresponding COVs of 0.129, 0.159 and 0.093, respectively. In both cases, EC9 (2007) provides better agreement with the test results and a smaller scatter of the predictions. The comparison of the CSM with the results of simply supported beam tests shows a mean value of 1.04 for both three-point bending and four-point bending, with COVs of 0.118 and 0.096, respectively. Clearly, the CSM provides a more accurate prediction of the bending capacity. In the calculation of M_{csm}, the cross-section slenderness $\overline{\lambda}_p$ (λ_p) was determined according to Seif & Schafer (2010) that considers element interaction. The strain hardening slope (E_{sh}) was determined from the coupon test results using the 0.2% ($\sigma_{0.2}$) and 1% ($\sigma_{1.0}$) proof stresses for the data obtained in this study, while the E_{sh} is assumed to be $E/100$ (EC3, 2006) for the data obtained from other researchers.

The predictions of all three specifications were more conservative for the stocky sections, as shown in Tables 4 and 5. The explanation is linked directly to the strain hardening characteristics of the material, which are effectively harnessed by the CSM.

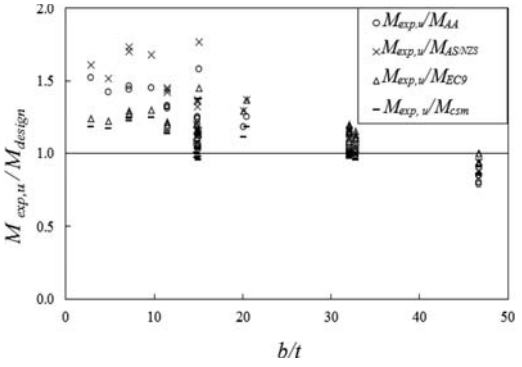

Figure 8. Comparison between the three-point bending test results and design strengths.

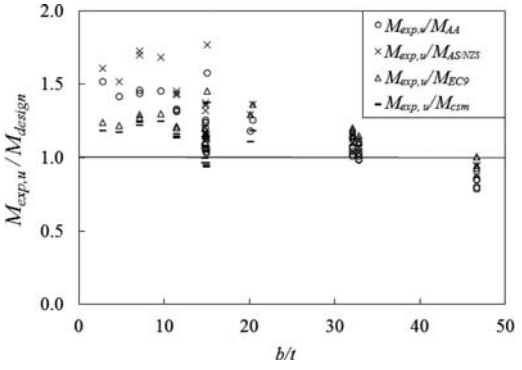

Figure 9. Comparison between the four-point bending test results and design strengths.

5 CONCLUSIONS

A series of experiments on aluminium alloy 6061-T6 hollow section beams, consisting of 22 three-point bending and four-point bending tests has been presented. The specimens were non-slender sections with mostly class 1 sections according to Eurocode 9 (EC9, 2007). This experimental program aims to assess the accuracy of the Continuous Strength Method (CSM) and three international design specifications: the American Aluminum Design Manual (AA, 2010), the Australian/New Zealand Standards (AS/NZS, 1997) and Eurocode 9 (EC9, 2007), on moment capacity prediction of simply supported beams. Furthermore, 25 three-point bending tests and 18 four-point bending tests of both slender and non-slender hollow sections conducted by other researchers were also used in this investigation. The results generally revealed that the three current design specifications have underestimated the bending moment capacity of the hollow sections, especially for stocky sections. The stocky section specimens achieved flexural moment capacities markedly beyond the design capacities. The current specifications are unable to exploit the strain hardening of aluminium alloys rationally. The CSM provides much better performance and increases the bending capacity prediction accuracy as much as 26% compared to the three specifications. Strain hardening has been observed at large plastic strains during the experiments in this study. The on-going research by the authors is to evaluate the significance of strain hardening in aluminium alloy stocky sections and to utilize it in developing new design guidelines.

ACKNOWLEDGEMENTS

The research work in this paper was supported by a grant from the University of Hong Kong under the seed funding program for basic research. The authors are also grateful to Mr. Man-Tat Lin for his assistance in the experimental program as part of his final year undergraduate research project at the University of Hong Kong.

REFERENCES

AA. (2010) *Aluminum design manual*, the Aluminum Association, Washington, D.C.

ASTM. (1997) Standard Test Methods for Tension Testing of Metallic Materials. *E8M–97*, American Society for Testing and Materials, West Conshohocken, Pa.

ASTM. (2010) Standard Test Method for Indentation Hardness of Aluminium Alloys by Means of a Webster Hardness Gage, *ASTM B647–10,* American Society for Testing and Materials, West Conshohocken, Pa.

AS. (2007) Methods for Tensile Testing of Metals. *AS 1391–2007*, Standards Association of Australia, Sydney, Australia.

AS/NZS. (1997) Aluminium Structures Part 1: Limit State Design. *AS/NZS 1664.1:1997*, Australian/New Zealand Standard, Sydney, Australia.

Chan, T.M. & Gardner, L. (2008) Bending Strength of Hot-rolled elliptical Hollow Sections. *Journal of Constructional Steel Research* 64(9):971–986.

De Matteis, G., Moen, L.A., Langseth, M., Landolfo, R., Hopperstad, O.S. & Mazzolani, F.M. (2001) Cross-Sectional Classification for Aluminium Beams—Parametric Study. *Journal Of Structural Engineering, ASCE* 127(3): 271–279.

EC3. (2006) EUROCODE 3: Design of Steel Structures—Part 1-5: Plated Structural Elements. *EN 1993-1-5:2006*, European Committee for Standardization, CEN.

EC9. (2007) EUROCODE 9: Design of Aluminium Structures—Part 1-1: General Rules—General Rules and Rules for Buildings. *BS EN 1999-1-1:2007+A1:2009.* European Committee for Standardization, CEN.

Gardner, L. (2008) The Continuous Strength Method, *Proceeding of the Institution of Civil Engineers - Structures & Buildings* 161(3):127–133.

Gardner, L., Wang, F. & Liew, A. (2011) Influence of Strain Hardening on the Behavior and Design of Steel Structures. *International Journal of Structural Stability and Dynamics*, 11(5):855–875.

Kim, Y. & Peköz, P. (2010) Ultimate Flexural Strength of Aluminium Sections. *Thin-walled structures* 48(10-11):857–865.

Kissell, J.R. & Ferry, R.L. (2002) *Aluminium Structures-A Guide to Their Specifications and Design, 2nd.* Wiley and Sons.

Kuhlmann, U. (1989) Definition of flange slenderness limits on the basis of rotation capacity values. *Journal of Constructional Steel Research* 14(1):21–40.

Lai, Y.F.W. & Nethercot, D.A. (1992) Strength of Aluminium Members Containing Local Transverse Welds. *Engineering Structures* 14(4):241–254.

Lay, M.G. & Galambos, T.V. (1965) Inelastic steel beams under uniform moment. *Journal of the Structural Division, ASCE* 91(6):67–93.

Lay, M.G. & Galambos, T.V. (1967) Inelastic beams under moment gradient. *Journal of the Structural Division*, *ASCE* 93(1):381–99.

Mazzolani, F.M. (1994) *Aluminium alloy structures 2nd*. E&FN Spon Press

Moen, L.A., Hopperstad, O.S. & Langseth M. (1999) Rotational Capacity of Aluminium Beams Under Moment Gradient. I: Experiments. *Journal of Structural Engineering, ASCE* 125(8):910–920.

Schafer, B. W. & Peköz, T. (1998) Direct Strength Prediction of Cold Formed Steel Members Using Numerical Elastic Buckling Solutions. *Proceeding of the 14th International Specialty Conference on Cold-Formed Steel Structures. Missouri, USA, (October, 2000)*

Theofanous, M., Chan, T.M. & Gardner, L. (2009) Flexural Behaviour of Stainless Steel Oval Hollow Sections. *Thin Walled Structures*, 47(6-7):776–787.

Zhu, J.H. & Young, B. (2006) Experimental Investigation of Aluminium Alloy Thin-Walled Tubular Members in Combined Compression and Bending. *Journal of Structural Engineering, ASCE* 132(12):1955–1966.

Zhu, J.H. & Young, B. (2009) Design of Aluminium Alloy Flexural Members Using Direct Strength Method. *Journal of Structural Engineering, ASCE* 135(5):558–566.

Tubular Structures XIV – Gardner (Ed.)
© 2012 Taylor & Francis Group, London, ISBN 978-0-415-62137-3

Dynamic three-point bending tests on aluminium foam filled steel tubes

G. Rathnaweera
CAST Cooperative Research Centre, IRIS, Swinburne University of Technology, Hawthorn, Australia
Faculty of Engineering and Industrial Sciences, Swinburne University of Technology, Hawthorn, Australia

D. Ruan & V. Nagaraj
Faculty of Engineering and Industrial Sciences, Swinburne University of Technology, Hawthorn, Australia

Y. Durandet
CAST Cooperative Research Centre, IRIS, Swinburne University of Technology, Hawthorn, Australia
Faculty of Engineering and Industrial Sciences, Swinburne University of Technology, Hawthorn, Australia

ABSTRACT: In the present paper, a type of hybrid tubes made of steel tubes and filled with closed-cell aluminium foam was investigated. Dynamic three-point bending tests were conducted on both hollow and hybrid steel tubes using a Drop Hammer. The effects of the length of foam insert and impact velocity (or drop height of indenter) on the deformation mode and energy absorption of hybrid tubes were investigated. Results showed that the energy absorption of the steel tubes was higher with foam inserts than without, and the overall bending of the tubes decreased. For the range of experimental conditions studied, it was found that the effect of the foam insert's length on specific energy was more significant than that of impact velocity. This was clearly related to changes in local deformation of the tube area enclosing the foam insert and in contact with the indenter.

Keywords: aluminium foam, steel tube, deformation behaviour, dynamic three point bending, energy absorption

1 INTRODUCTION

Tubular structures are popularly used in automotive, civil (building and construction), aerospace, aircraft and marine industries. Hollow tubes with square or circular cross sections have been studied comprehensively (Stronge 1993, Wierzbicki et al. 1994a, b, Kim & Reid 2001, Lu & Yu 2003, Hilditch et al. 2009). Hybrid tubes made of two or more appropriate materials can offer the distinguishing advantage of having increased high strength to weight ratio. They may replace the traditional hollow tubes to reduce weight without compromising mechanical performance.

Aluminium foam, as a novel cellular material, has been developed with the advantages of being light weight, recyclable, non-flammable, and having significant capability for energy absorption (Gibson & Ashby 1997, Ruan et al. 2002, 2007, Shen et al. 2010). The cellular structure endows it with the ability to undergo large plastic deformation at nearly constant and relatively low stress, and thus can dissipate considerable energy before collapsing to a more stable configuration or fracture. It is widely used as a core material for hybrid structures to absorb energy during impact.

One application of tubular structures in automotive industry is the intrusion beam in vehicles, which is expected to carry load and absorb impact energy in vehicle crash. In such application, the intrusion beam is subjected to a point load and bent. Hanssen et al. (2000) studied the bending of square tubes filled with aluminium foams. Santosa & Wierzbicki (1999) and Santosa et al. (2000, 2001) conducted experiments and numerical simulation to study the effect of foam insert on the bending of prismatic columns. Recently, circular hybrid tubes have also been studied. Kinoshita et al. (2010) conducted experiments and finite element simulation of hybrid circular tubes made of aluminium tubes and closed-cell aluminium foam subjected to three-point bending. They found that foam insert improved the specific energy and changed the deformation mode of tubes. Guo & Yu (2011) studied the dynamic three- point bending response of circular double aluminium tubes filled with closed-cell aluminium foam. Their structure demonstrated a steadier load carrying capacity and much efficient energy absorption.

In this paper, dynamic three-point bending tests are conducted on circular hollow and hybrid steel tubes with foam inserts using a Drop Hammer. The effects of impact velocity and length of foam insert on the energy absorption and deformation mode of hybrid tubes are investigated.

Table 1. Specimen information.

Specimen No.	Mass of hollow tube (g)	Mass of foam insert (g)	Foam length (mm)	Drop height (m)
1	664.7	0	0	1.5
2	651.0	0	0	1.5
3	697.1	24.4	50	1.5
4	677.4	24.6	50	1.5
5	695.1	33.7	75	1.5
6	707.1	33.8	75	1.5
7	723.9	47.8	100	1.5
8	717.5	48.2	100	1.5
9	654.0	0	0	2
10	667.0	0	0	2
11	693.0	24.7	50	2
12*	510.1	23.9	50	2
13	709.9	33.6	75	2
14	697.4	33.9	75	2
15	719.5	47.9	100	2
16	715.0	47.4	100	2
17	666.7	0	0	2.5
18	660.0	0	0	2.5
19	671.4	24.3	50	2.5
20	696.1	24.1	50	2.5
21	720.3	47.3	100	2.5
22	721.3	47.6	100	2.5

*The specimen has a wall thickness of 1.2 mm.

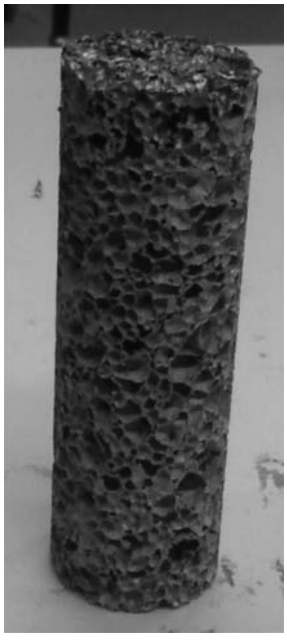

Figure 1. A photograph of a cylindrical aluminium foam insert.

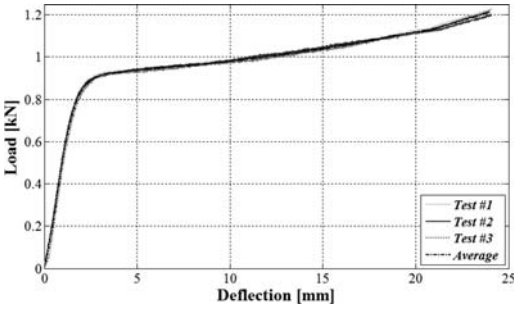

Figure 2. The measured load-deflection curves in lateral compressive tests of short steel tubes.

2 EXPERIMENTS

2.1 *Specimens*

Hollow mild steel (BST21) tubes with an outer diameter of 50 mm and length of 360 mm were used in the experiments. Most tube specimens had a wall thickness of 1.6 mm, except for one case (specimens 12 in Table 1) whose wall thickness was 1.2 mm. Hybrid tubes were filled with ALPORAS closed-cell aluminium foam. Theses foam inserts were wire-cut from a big foam block into cylinders (Fig. 1) of 36.2 mm diameter and with various lengths of 50 mm, 75 mm and 100 mm. Although the big foam block had a nominal density of 9%, the actual relative density of individual foam insert might be different. Therefore, each individual foam insert was measured and weighed. The measured mass of hollow tubes and foam inserts is listed in Table 1. The foam insert was placed into the middle part of the hollow tube without applying any adhesive.

2.2 *Material property testing*

The compressive stress-strain curves of the same batch of ALPORAS aluminium foam were comprehensively studied by Xu et al. (2010). Thus no additional compressive test on this type of foam was conducted in the current study. Results from Xu et al.(2010) were employed here. In summary, this type of foam with a nominal density of 9% has a plateau stress of 2.3 MPa and densification strain of 0.5.

Steel tubes used in the current study have an outer diameter of 50 mm. It is very difficult to cut traditional flat or slightly curved dog-bone specimens from those tubes in order to conduct standard tensile test. Thus the method proposed by Rathnaweera et al. (2011), i.e. lateral compression of tubes, was employed in the present study to estimate the mechanical properties of tubes. Three short tubes with a length of 60 mm were cut from steel tubes and compressed laterally by using MTS machine. Load-deflection curves were recorded and are shown in Figure 2. It can be seen that the results of the three repeated tests are very similar. Thus an average curve was used to inversely derive the mechanical properties of the steel which the tubes are made of. The calculated Young's modulus and yield strength of tubular material are 200 GPa and 295 MPa

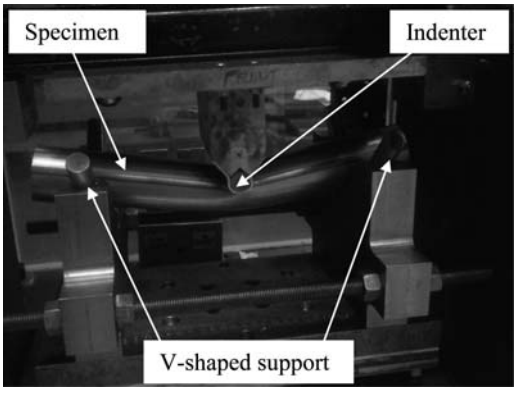

Figure 3. Experimental set-up: V-shaped supports, a specimen and the cylindrical indenter.

respectively. The work-hardening can be described by a power law, $\sigma = k\varepsilon^n$, where and are stress and strain, k and n are constants and are calculated from the above measured force-displacement curves. For the tubular material, $k = 358.7$ MPa and $n = 0.03$.

2.3 *Three-point bending testing*

A Drop Hammer was employed to conduct dynamic three-point bending tests on the above hollow and hybrid tubes. Tubes were placed on two rigid V-shaped supports (Fig. 3). The distance between these two supports was 260 mm. A cylindrical indenter with a diameter of 20 mm was attached to the upper carriage and was lifted up to various heights, 1.5 m, 2 m and 2.5vm, respectively, and then released to drop freely. The total mass of the indenter and upper carriage was 22.6 kg. A Kistler load cell (model 9801A) was placed under the supports to measure the force. An laser optical displacement measurement device (Opto NCDT 1607) was employed to measure the displacement of the indenter. Two repeated tests were conducted per condition except for one for which the drop height was 2 m and foam insert length was 50 mm (specimens 11 and 12 who had different wall thickness, 1.6 mm and 1.2 mm, respectively). Details of the various specimens and test conditions are given in Table 1.

3 RESULTS AND DISCUSSIONS

3.1 *Force-displacement curves*

Measured force-displacement curves were plotted in Figures 4(a)–(k). Each figure except Figure 4(e) shows two repeated test results per condition (the same foam insert length and drop height). Since the mass for each individual tube was different, there was some difference in force-displacement curve between two repeated tests. However, the discrepancy is acceptable.

In Figure 4(e), specimen 12 has a wall thickness of 1.2 mm, thinner than that of specimen 11. Thus the force level is much lower. However since the mass falls from the same height (i.e. total input energy is the same), the travel distance of the indenter, i.e. intender displacement, is larger.

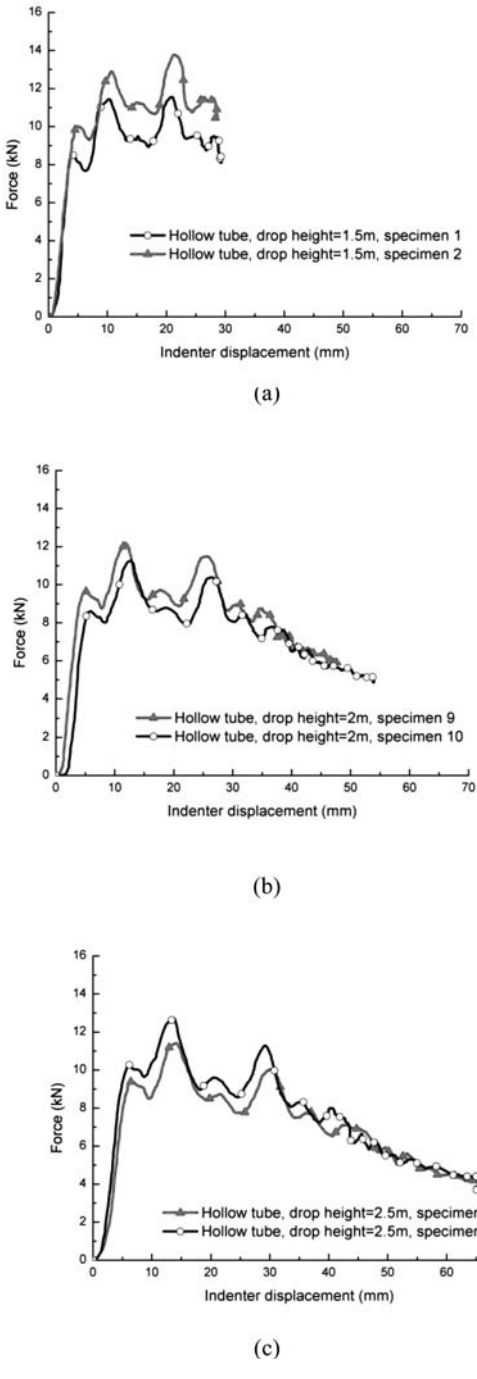

Figure 4. Three-point bending: Force-displacement curves. (Cont. on next page.)

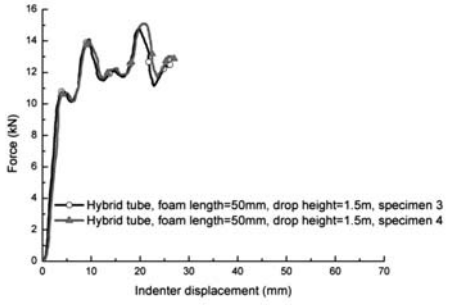

(d)

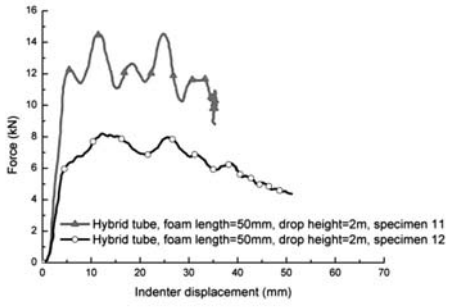

(e)

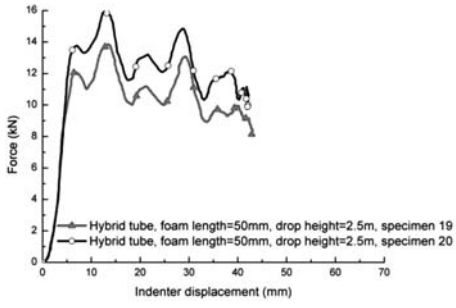

(f)

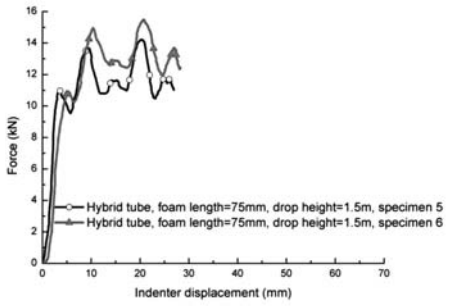

(g)

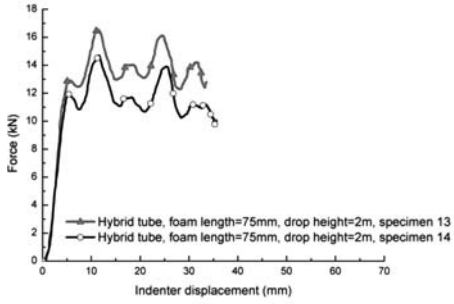

(h)

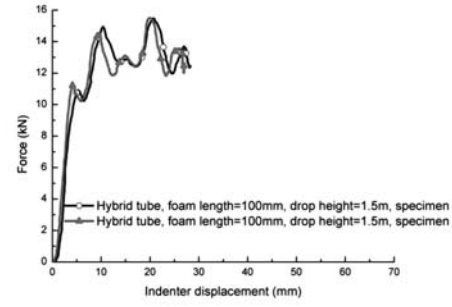

(i)

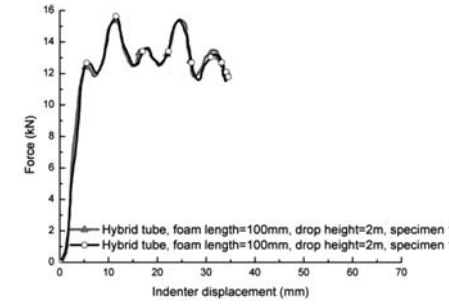

(j)

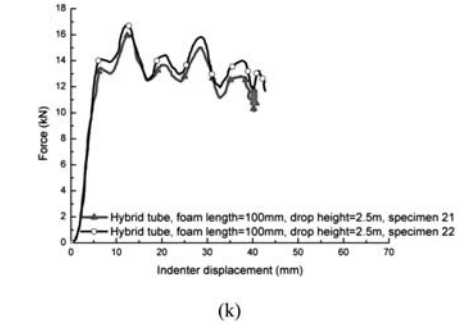

(k)

Figure 4. Continued.

Table 2. Energy absorbed by hollow and hybrid tubes.

Specimen No.	Total mass of tube and foam core (g)	Impact velocity (m/s)	Energy absorbed (J)	Specific energy (J/kg)
1	664.7	5.4	227.6	342
2	651.0	5.4	264.9	407
3	721.5	5.4	292.1	405
4	702.0	5.4	293.3	418
5	728.8	5.4	282.4	387
6	740.9	5.4	299.7	405
7	771.7	5.4	299.7	388
8	765.7	5.4	302.1	395
9	654.0	6.3	235.2	360
10	667.0	6.3	203.7	305
11	717.7	6.3	290.0	404
12*	534.0	6.3	169.2	317
13	743.5	6.3	324.2	436
14	731.3	6.3	280.9	384
15	767.4	6.3	312.4	407
16	762.4	6.3	311.6	409
17	666.7	7.0	205.2	308
18	660.0	7.0	229.5	348
19	695.7	7.0	258.6	372
20	720.2	7.0	297.9	414
21	767.6	7.0	304.8	397
22	768.9	7.0	318.0	414

When the input energy is sufficient, the force-displacement curves (Figs. 4b, c and curve for specimen 12 in 4e) are similar to those in quasi-static tests. However, when the input energy is not enough due to either low drop height (Figs. 4a, d, g and i) or tubes are strong with foam inserts (Figs. 4e for specimen 11, f, h, j and k), the indenter displacement is short due to less input energy.

3.2 *Energy absorption*

Total energy absorbed by tubes was calculated as the area under the force-displacement curve up to the indenter displacement of 26 mm, which was the minimum displacement in all tests. Specific energy was defined as the ratio of energy absorbed to the total mass of tube and foam insert. Data of energy absorbed and specific energy for each specimen are listed in Table 2.

In order to study the effects of drop height or impact velocity and the length of foam insert, the specific energy was plotted against impact velocity and length of foam insert in Figures 5(a) and (b) respectively. Impact velocity was calculated by $v = \sqrt{2gh}$, where v, g and h are impact velocity, gravity acceleration and drop height respectively.

Since the impact velocity only varied slightly, from 5.4 m/s to 7.0 m/s, in the tests conducted, the specific energy did not change with impact velocity (Fig. 5a) in this velocity range.

On the other hand, the specific energy increased slightly with the length of foam insert, as shown in Figure 5(b). In order to quantify the effect of length of foam insert, the average specific energy was calculated by taking the average of specific energy for hollow tubes or hybrid tubes with the same length of foam insert. For example, the average specific energy for hollow tubes was the average specific energy of specimens 1, 2, 9, 10, 17 and 18. In turn, the average specific energy for hybrid tubes with 50 mm long foam insert was the average specific energy of specimens 3, 4, 11, 12, 19 and 20. The average specific energy for hollow tubes, hybrid tubes with 50 mm, 75 mm and 100 mm long foam inserts are 345 J/kg, 388 J/kg, 403 J/kg and 401 J/kg, respectively. The contribution of foam insert is 13% for 50 mm long foam inserts, 17% for 75 mm and 100 mm long foam inserts respectively. For the hybrid tubes tested, foam inserts with a length of 75 mm performed the best in terms of specific energy.

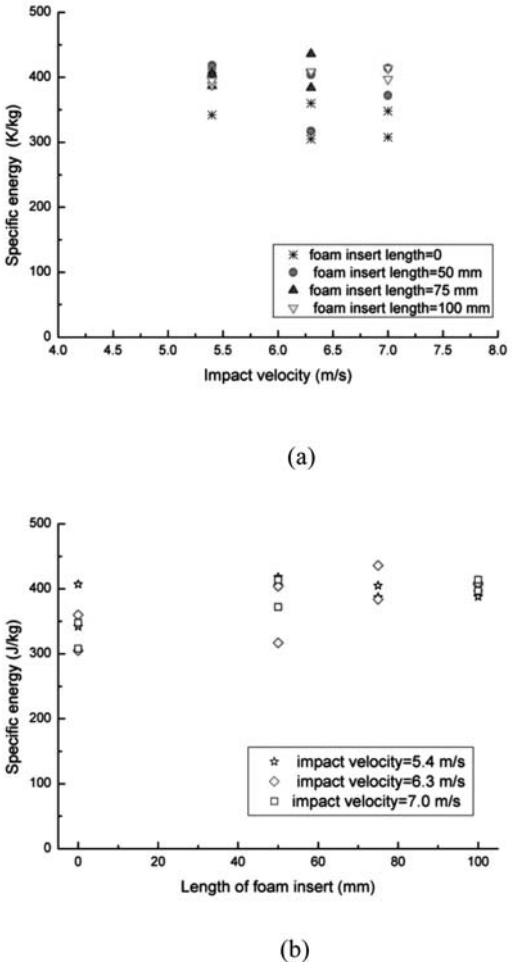

Figure 5. Specific energy *vs* : (a) impact velocity; (b) length of foam insert.

Figure 6. The deformation of tubes when the carriage dropped from 2.0 m. From the front to back: specimens 15, 13, 11 and 9 with foam insert length of 100 mm, 75 mm, 50 mm and 0 respectively.

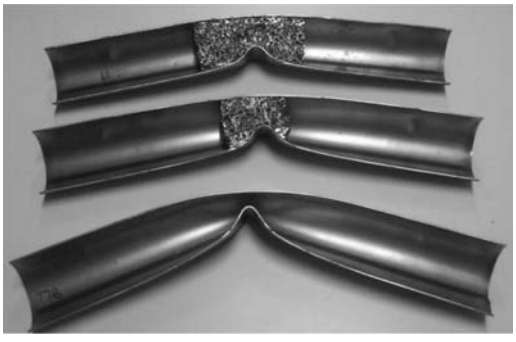

Figure 7. The interior of tubes after tests. From front to back: a hollow tube (specimen 9), hybrid tubes with 50 mm and 75 mm long foam inserts (specimens 11 and 13).

3.3 *Deformation modes*

Figure 6 shows a photograph taken after testing of a hollow tube and hybrid tubes with foam insert length of 50 mm, 75 mm and 100 mm respectively. In order to have a clear view of the deformation of both the tube and foam insert, specimens 9, 11 and 13 were cut in half and a photograph is shown in Figure 7. It can be seen that the deformation of hollow and hybrid tubes is similar with respect to the formation of a plastic hinge and tube bending behaviour. However, Figures 6 and 7 clearly show that the macro deflection or overall bending of the specimens was greatest for the hollow tubes and was significantly reduced with the addition of the foam inserts. This can be related to changes in the formation of the plastic hinge. The deformation of foam insert happens locally in the area under the indenter. The shorter the foam insert, the greater the deformation in both tube and foam insert. No apparent crack was observed in all steel tubes. In the hybrid tubes that were cut after tests, no crack was observed in foams as well. However, since not all hybrid tubes were cut, it is still unknown whether there was any crack in foam cores.

At the mid span of tubes, tubes are flattened, i.e. they are compressed in the vertical (drop height) direction while expanding in the horizontal (lateral) direction. The deformation of foam insert, i.e. the distance between the top and bottom surfaces of a tube (shown as d_1 in Fig. 8a) was measured and values are listed in Table 3 for each specimen except specimen 12

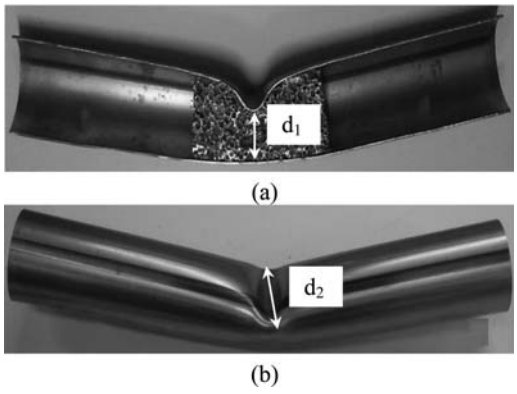

Figure 8. Deformation of a hybrid tube (specimen 11): (a) d_1; (b) d_2.

Table 3. Deformation of tubes.

Specimen No.	Foam length (mm)	Drop height (m)	d_1 (mm)	d_2 (mm)
1	0	1.5	31.3	64.6
2	0	1.5	38.5	66.5
3	50	1.5	34.9	57.8
4	50	1.5	36	58.9
5	75	1.5	36.4	58.9
6	75	1.5	35	60
7	100	1.5	38.3	57.5
8	100	1.5	37.8	57.4
9	0	2	22.7	70.5
10	0	2	19.8	72.3
11	50	2	29.8	64
12*	50	2	–	–
13	75	2	35	61.1
14	75	2	28.9	65.6
15	100	2	33.2	62.0
16	100	2	32.8	62.5
17	0	2.5	10.9	76
18	0	2.5	13.1	75.0
19	50	2.5	16.0	69.4
20	50	2.5	27.0	67.0
21	100	2.5	29.0	66.6
22	100	2.5	31.0	66.0

for which there is no record. The width of a tube at the mid-span after test, i.e. d_2 shown in Figure 8(b), was also measured and data are given in Table 3. The effects of the foam insert length and carriage drop height on d_1 and d_2 are shown in Figures 9(a) and (b) respectively. Overall, the higher the drop height and the shorter the foam insert, the smaller the d_1 and the larger the d_2.

4 CONCLUSIONS

Dynamic three-point bending tests were conducted by using a drop hammer on steel hollow and hybrid tubes filled with aluminum foam inserts. The carriage

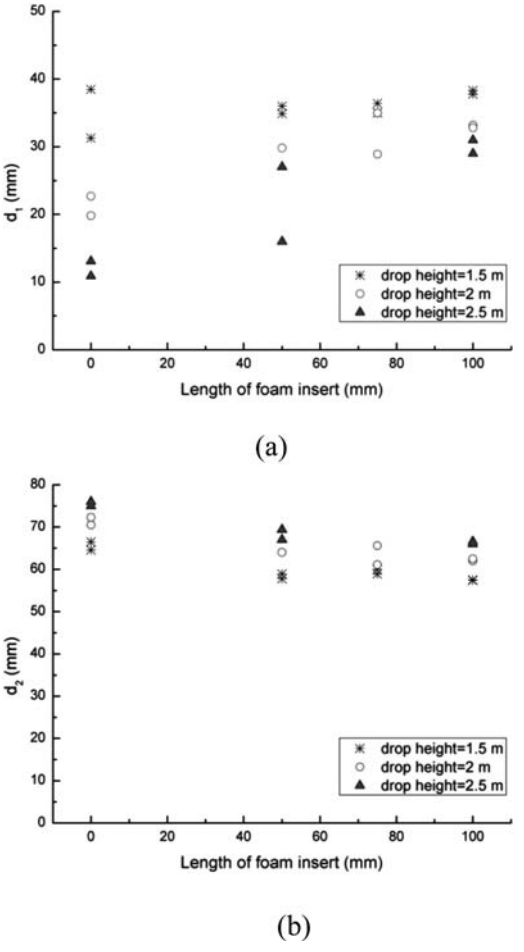

Figure 9. The measurement deformation: (a) d_1 *vs*. foam insert length; (b) d_2 *vs*. foam insert length.

dropped from 1.5 m, 2 m and 2.5 m respectively. Three different lengths of foam inserts, 50 mm, 75 mm and 100 mm were employed.

It has been found that the specific energy does not change with the drop height or impact velocity within the present range of tests conditions, saying 1.5 m (corresponding to impact velocity of 5.4 m/s) to 2.5 m (corresponding to impact velocity of 7.0 m/s).

On the other hand, hybrid tubes with foam insert length of 75 mm performed the best in terms of specific energy. Thus the optimal length of foam insert is 75 mm in this study.

The deformation of hollow and hybrid tubes was similar, while the hybrid tubes deformed less due to the contribution of foam inserts. The local compression of foam inserts in the area under the indenter aided the dissipation of energy, thereby decreasing the extent of the plastic hinge and related bending of the steel tubes. The shorter the foam insert, the greater the deformation in both tube and foam insert.

In order to obtain larger displacement in hybrid tubes, larger input energy is required. This can be achieved by increasing the drop height or the weight of the carriage, which is expected to be conducted in the near future.

ACKNOWLEDGEMENTS

The authors would like to thank CAST CRC for the financial support through a Postgraduate scholarship. The technicians in the Faculty of Engineering and Industrial Sciences, Swinburne University of Technology are also acknowledged for cutting tubes and foam inserts.

REFERENCES

Gibson, L. & Ashby, M. 1999. *Cellular solids: structure and properties.* Cambridge: Cambridge University Press.

Guo, L. & Yu, J. 2011. Dynamic bending response of double cylindrical tubes filled with aluminium foam. *International Journal of Impact Engineering* 38: 85–94.

Hanssen, A.G. & Hopperstad, O.S. & Langseth, M. 2000. Bending of square aluminium extrusions with aluminium foam filler. *Acta Mechanica* 142: 13–31.

Hilditch, T. & Atwell, D. & Easton, M & Barnett, M. 2009. Performance of wrought aluminium and magnesium alloy tubes in three-point bending. *Materials and Design* 30: 2316–2322.

Kim, T.H. & Reid, S.R. 2001. Bending collapse of thin-walled rectangular section columns. *Computers and Structures* 79: 1897–1911.

Kinoshita, S. & Lu, G. & Ruan, D. & Beynon, J. 2010. Experimental and FE analysis of quasi-static three point bending of foam-filled structures. SAE International *Journal of Materials and manufacturing* 3(1): 44–54.

Lu, G. & Yu, T.X. 2003. *Energy absorption of structures and materials.* Cambridge: Woodhead Publishing Ltd.

Rathnaweera, G. & Durandet, Y & Ruan, R and Kinoshita, S. 2011. Characterizing the material properties of a tube from a lateral compression test. *International Journal of Protective Structures* 2: 465–475.

Ruan, D. & Lu, G. & Chen, F.L. & Siores, E. 2002. Compressive behaviour of aluminium foams at low and medium strain rates. *Composite Structures* 57: 331–336.

Ruan, D & Lu, G. & Wang, B. 2007. Triaxial compression of aluminium foams. *Composites Science and Technology* 67: 1218–1234.

Santosa, S. & Wierzbicki, T. 1999. Effect of an ultra-light metal filler on the bending collapse behaviour of thin-walled prismatic columns. *International Journal of Mechanical Sciences* 41: 995–1019.

Santosa, S. & Banhart, J. & Wierzbicki, T. 2000. Bending crush resistance of partially foam-filled sections. *Advanced Engineering Materials* 2: 223–227.

Santosa, S. & Banhart, J. & Wierzbicki, T. 2001. Experimental and numerical analyses of bending of foam-filled sections. *Acta Mechanica* 148: 199–213.

Shen, J & Lu, G. & Ruan, D. 2010. Compressive behaviour of closed-cell aluminium foams at high strain rates. *Composites Part B: Engineering* 41: 678–685.

Stronge, W. J. 1993. Impact on metal tubes: indentation and perforation. In N. Jones & T. Wierzbicki (eds), *Structural Crashworthiness and Failure*. London: Elsevier Applied Science.

Wierzbicki, T. & Recke, L. & Abramowicz, W. & Gholami, T. 1994a. Stress profiles in thin-walled prismatic columns subjected to crush loading. I. Compression. *Computers and Structures* 51: 611–623.

Wierzbicki, T. & Recke, L. & Abramowicz, W. & Gholami, T. 1994b. Stress profiles in thin-walled prismatic columns subjected to crush loading. I. Bending. *Computers and Structures* 51: 625–641.

Xu, S. & Ruan, D & Beynon, J. & Lu, G. 2010. Experimental investigation of the dynamic behavior of aluminium foams. *Materials Science Forum* 654–656: 950–953.

Tubular Structures XIV – Gardner (Ed.)
© 2012 Taylor & Francis Group, London, ISBN 978-0-415-62137-3

Theoretical analysis of foam-filled aluminum tubes subjected to bending and denting

M. Elchalakani
Civil Engineering Department, Dubai Mens College, Higher Colleges of Technology, UAE

D. Ruan
Department of Mechanical Engineering, Swinburne University, Hawthorn, Australia

ABSTRACT: This paper presents a theoretical analysis for aluminum tubes filled with aluminum foam deforming in a kink collapse mode under large deformation bending and indentation. The local indentation of a tube by an indenter is a generic problem that arsis in many areas of structural mechanics and in safety considerations in applications such as vehicle safety and accident research. The classical beam on elastic foundation model was modified to predict the critical buckling stress which was compared to the classical elastic stress for the empty tube to quantify the effect of the foam. A closed form solution was obtained for the critical elastic buckling stress. During deep collapse of the tube, the fold formation process was such that the shell curvature flattened on the compression side transforming into two large flat triangles attached to each other. The collapse proceeded progressively by folding about the base and sides of these triangles. An expression for the plastic collapse load was obtained by equating the total energy absorbed in bending and flattening to the external work carried out by the indenter during deformation of the tube. A good agreement was found between the predicted load-deflection curves and those obtained from recent experiments carried out by the second author which were published elsewhere.

1 INTRODUCTION

The local indentation of a tube by an indenter is a generic problem that arsis in many areas of structural mechanics and in safety considerations in applications such as vehicle safety and accident research. Previous research was performed to theoretically derive the load-deflection response of empty tubes under bending and denting being an important loading condition for offshore structures subjected to ship collision. However, little theories were devoted to study foam-filled tubes under such loading condition.

In regards to empty hollow tubes subjected to combined denting and bending, Thomas et al (1976) studied the behaviour of aluminium and mild steel circular hollow tubes under 3-point bending with a wedge-shaped indenter with the aim of determining the residual strength of these tubes when subjected to indentation and bending. They derived an expression for the ultimate strength as a function in the distorted section dimensions. Wierzbicki and Suh (1988) predicted the collapse response of a dented CHS using the principle of virtual velocities for the case of combined bending, axial force and lateral indentation. Mamalis et al (1989) presented an expression for the mean collapse moment of a cantilevered short, thick-walled tubes. They developed a kinematic model where the section distortion was modelled using a two-hinge mechanism. In their tests, an end plug was inserted inside the tube to control the mode of collapse. Therefore, ovaling of the tube was not permitted. Reid and Goudie (1989) determined the capacity of a dented CHS under bending, which is often found in an offshore structure where there is a risk of collision. Wierzbicki and Sinmao (1997) developed a closed-form relationship for the full moment-curvature response of a circular tube using a four-hinge mechanism to model ovalisation for very large deformations. Zeinoddini et al (2000) modified the four-hinge mechanism to study dented CHS under lateral concentrated loads. Zeinoddini et al's results showed that the modified four-hinge model is more compatible with the experimental results when compared to the two-hinge model. In this paper, the models by Reid and Goudie (1989), and Wierzbicki and Suh (1988) will be modified to model the response of the foam-filled tube under indentation and bending.

In regards to foam-filled tubes subjected to axial crushing, a number of studies were devoted to predict the energy absorption for crashworthiness structures, such as: Abramowicz and Wierzbicki (1988),

Lampinen, and Jeryan (1982), Reddy and Wall (1988), Reid et al (1986a). Reid and Reddy (1986b), Thornton, and Amberger (1987), Pokharel and Mahendran (2003), Pokharel and Mahendran (2004), Zarei, H. R. and M. Kroger (2008). Sironic (2002) performed elastic analysis using beam on elastic foundation model and applied Airy Stress Functions to simulate the deformations and to predict the elastic buckling stress of a square tube filled with foam.

In regards to foam-filled tubes subjected to combined denting and bending, finite element analyses were performed by Kinoshita et al (2010) for circular tubes and Zarei and Kroger (2008) for square tubes where the predicted and measured responses are in good agreement. This paper attempts to provide closed-form solution for the full response of foam-filled tubes subjected to bending and denting. The predicted load-deflection curves were compared with those obtained from careful experiments carried out by the second author which were recently published elsewhere.

2 ELASTIC AND INELASTIC BUCKLING

In the following, the well-known beam-on-elastic foundation theory (Timoshenko and Gere 1961) will be used to derive the critical buckling stress of foam-filled circular tube under pure bending. Consider a perfectly straight elastic thin-walled foam-filled tube beam under pure bending, of length L and of constant cross section subjected to a pure bending moment (Fig. 1). At the critical buckling moment (M_{cr}), the tube will form buckling waves which can be modeled as shown in Figure 1. Small in-extensional deformations and linear elastic material response are assumed. Thus the out of plane deflections (w) of one element such as *AB* can be represented in the case of simply supported edges, by the general sinusoidal double series as

$$w = a_1\left(1 - \cos\frac{2\pi x}{l}\right) \tag{1}$$

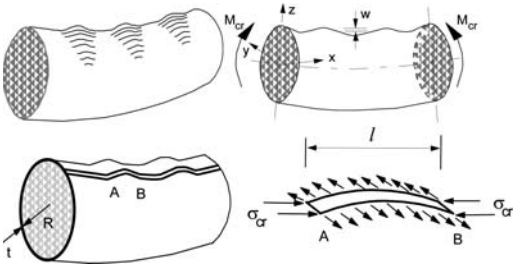

Figure 1. Foam-filled circular tube under bending.

where a_1 is the maximum amplitude of displacement, and x and y are the rectangular coordinates. The change in strain energy due to bending of one buckle is

$$\Delta U_1 = \frac{1}{2}E_1 I\int_0^l\left(\frac{d^2w}{dx^2}\right)^2 dx = \frac{1}{2}\frac{E_1}{2(1-\nu^2)}\cdot\frac{t^3}{12}\int_0^l\left(\frac{d^2w}{dx^2}\right)^2 dx \tag{2}$$

$$\Delta U_1 = \frac{1}{2}\frac{E_1 t^3}{12(1-\nu^2)}\left(\frac{4\pi^2}{l^2}\right)^2\int_0^l\left(a_1\cos\frac{2\pi x}{l}\right)^2 dx =$$

$$\frac{a_1^2}{2}\frac{E_1 t^3}{12(1-\nu^2)}\left(\frac{4\pi^2}{l^2}\right)^2\left(\frac{l}{2}\right)$$

The change in strain energy due to elastic foundation (Timoshenko and Gere 1961):

The change in strain energy due to elastic foundation is:

$$\Delta U_2 = \frac{\beta}{2}\int_0^l w^2 dx = \frac{\beta}{2}\int_0^l a_1^2\left(1-\frac{\cos 2\pi x}{l}\right)^2 dx = \frac{\beta}{2}a_1^2\left(\frac{3l}{2}\right) \tag{3}$$

The axial shortening of a typical buckle can be assumed as the difference between its original length (*l*) and its length after deformation. Integrating over one buckle, we obtain the change in the work done by the axial force P as:

$$\Delta W = \frac{1}{2}P\int_0^l\left(\frac{dw}{dx}\right)^2 dx = \frac{1}{2}Pa_1^2\frac{4\pi^2}{l^2}\int_0^l\sin^2\left(\frac{2\pi x}{l}\right)dx$$
$$= \frac{1}{2}Pa_1^2\frac{4\pi^2}{l^2}\left(\frac{l}{2}\right) \tag{4}$$

Equating the work done given in Equation 3 to the total strain energy given in Equations 2 and 3, the displacement amplitude a_1 will cancel out, and hence the critical compressive force per unit length (across the hoop) at the extreme fibbers (P) and its corresponding critical buckling stress ($\sigma_{cr} = P/t$) are:

$$P = \frac{E_1 t^3}{12(1-\nu^2)}\left(\frac{4\pi^2}{l^2}\right) + \frac{3\beta l^2}{4\pi^2} \tag{5}$$

$$\sigma_{cr} = \frac{E_1 t^2}{12(1-\nu^2)}\left(\frac{4\pi^2}{l^2}\right) + \frac{3\beta l^2}{4\pi^2 t} \tag{6}$$

The critical buckling half-wave length is given by Elchalakani (2003) as:

$$l = \pi\sqrt[4]{\frac{t^2R^2}{12(1-\nu^2)}} \tag{7}$$

After substituting Equation 7 into Equation 6 and ignoring the second term in the latter equation, the final approximate form of the elastic buckling stress can be obtained as:

$$\sigma_{cr} = \frac{2\sqrt{3}E_1 t}{R\sqrt{3(1-\nu^2)}} \tag{8}$$

In the case of inelastic buckling, the inelastic modulus $\sqrt{E_l E_h}$ is often used to replace the elastic modulus (E_l),thus the inelastic buckling stress and corresponding moment can be written as:

$$\sigma_{cr} = \frac{2\sqrt{3}\sqrt{E_l E_h}\,t}{R\sqrt{3(1-\nu^2)}} \tag{9}$$

$$M_{cr} = \frac{2\pi R t^2 \sqrt{E_l E_h}}{\sqrt{(1-\nu^2)}} \tag{10}$$

The critical buckling stress given in Equation 8 is $\sigma_{cr} = 2\sqrt{3}\sigma_b$ where σ_b is the classical buckling stress of an empty tube under pure bending (Elchalakani 2003). In the experiment on 40mmx1.6mm foam-filled tube, the buckling stresses were not measured as the buckling spot was located immediately under the load (Kinoshita etal 2010). Therefore it is difficult to compare the theoretical and measured critical stresses.

3 THE LOAD-DEFLECTION CURVE

3.1 *Elastic-plastic curve (denting and bending)*

The model adopted by Wierzbicki and Suh (1988) will be followed very closely in the following analysis except for the foam effect. For a simply supported tube (Fig 2) subjected to bending and indentation, a velocity field approach can be used to derive an expression for the rate of change in the time domain of the total internal energy consumed in (i) laterally crushing the tube, (ii) bending the generators and (iii) crushing the foam, thus the total internal energy is:

$$\dot{E}_{int} = \dot{E}_{crush} + \dot{E}_{gen} + \dot{E}_{foam} \tag{11}$$

The crushing energy is made of two-parts, the flattening of the section and bending about true hinge lines (for complete notation see Wierzbicki and Suh 1988):

$$\dot{E}_{crush} = \int_s M^{\alpha\beta}\dot{\kappa}_{\alpha\beta}\,ds + \sum_i M_o^i [\Omega]^i = \frac{8 M_0 \zeta \dot{\delta}}{R} \tag{12}$$

$$\dot{E}_{gen} = \int_0^{2\pi R}\int_0^{2\xi} |N_0 \dot{\varepsilon}_{xx}|\,dx\,ds = \frac{\pi N_0 R \delta \dot{\delta}}{4\zeta} \tag{13}$$

where $N_0 = \sigma_y t$, and $M_0 = \sigma_y t^2/4$

Where $N_0=\sigma_y t$, and $M_0=\sigma_y t^2/4$

$$\zeta = R\sqrt{\frac{\pi\delta}{8t}} \tag{14}$$

The external energy is equal to the rate of change in the external energy and equal to the product of the applied load and the rate of change in the central lateral indentation

$$\dot{E}_{foam} = \int_0^{2\pi}\int_0^{2\zeta_f} (K_f w)\dot{w}\,d\phi\,dx \tag{15}$$

Within the foam filled zone identified by ζ_f, the vertical deformation and foam stiffness take the form:

$$w_x = \delta\left(1 - \frac{x}{\zeta_f}\right)$$
$$K_{f,x} = \left(1 - \frac{x}{K_f}\right)^3 \tag{16}$$

Note, ζ is the extent of the plastic hinge as shown in Figure 2(b), whereas ζ_f is the extent of the foam along

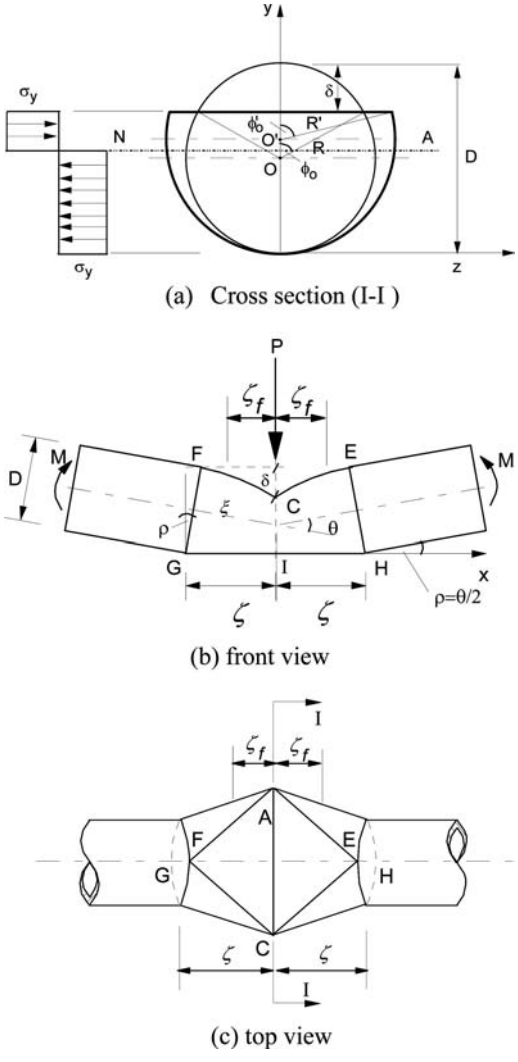

Figure 2. Plastic mechanism of the tube.

the tube (Fig 2c). This energy consumed in deforming the foam can be simplified using Equation 16 to:

$$\dot{E}_{foam} = 4K_f\delta\dot{\delta}\int_0^{\zeta_f}\int_0^{\pi}\left(1-\frac{x}{\zeta_f}\right)^5 dx.d\phi = \frac{\pi K_f\zeta_f\delta\dot{\delta}}{2} \quad (17)$$

$$K_f = \frac{E_{50,av}}{(1-\nu_f^{\,2})} \quad (18)$$

Where K_f is the reduced average stiffness of the foam obtained from the stress strain curve of the foam. The rising curve ends at $\delta = R$ where the strain in the foam at mid-span will be $\varepsilon = 50\%$. The foam stiffness is given as the plane strain elastic modulus at 50% axial strain level. From the measured stress-strain curves on the aluminum foam type "D" (Kinoshita etal 2010) a reduced average value of $E_{50,av}$ 30.77 MPa was used in the analysis. The external energy is equal to the rate of the change in the internal energy and equal to the product of the applied load and rate of change in the central lateral indentation

$$\dot{E}_{ext} = P\dot{\delta} \quad (19)$$

Equating the external energy given in Equation 19 to the internal energy given by Equation 11, the indentation rate ($\dot{\delta}$) will cancel out and an expression for the load – deflection curve could be obtained as:

$$P = \frac{8M_0\zeta}{R} + \frac{\pi N_0 R\delta}{4\zeta} + \frac{\pi\zeta_f K_f\delta}{2} \quad (20)$$

3.2 *Structural collapse curve*

It was observed during the test that at deep collapse of the tube, the fold formation process was such that the shell curvature flattened on the compression side transforming into two large flat triangles attached to each other (Fig 2c). The collapse proceeded progressively by folding about the base and sides of these triangles. The structural collapse curves can be obtained by integrating the fully plastic stress distribution shown in Figure 2 over the distorted section identified by the radius R' (Elchalakani 2003). The collapse load can be obtained as (note for simply supported beam P = 4M/L).

$$P = \frac{2\pi^2(2\sin\varphi - \sin\phi_0' + \sin\phi_0'\cos\phi_0')}{L(\pi - \phi_0' + \sin\phi_0')}(M_p' + M_{pf}) \quad (21)$$

where all the terms are defined as:

$$M_{pf} = 2\sigma_{yf}R'^3\{0.5\cos\phi_c'(\phi_c' - \phi_0' - 0.5\sin\phi_c' + 0.5\sin 2\phi_0') - (\sin\phi_c'^3 - \sin\phi_0'^3)/3\} \quad (22)$$

$$\varphi = 0.5(\pi + \phi_0' - \sin\phi_0') \quad (23)$$

$$\phi_c' = \frac{2\sin\phi_0'}{3\phi_0'} \quad (24)$$

$$R' = \frac{\pi R}{(\pi - \phi_0' - \sin\phi_0')} \quad (25)$$

$$\delta = \frac{R(2\sin\phi_0' + \pi - 2\phi_0' - \pi\cos\phi_0')}{(\pi - \phi_0' + \sin\phi_0')} \quad (26)$$

M_p' and M_{pf} are the plastic moment capacities of the tube and foam respectively located in the distorted region identified by the radius R' and subjected to the stress distribution shown in Figure 2. It is worth noting that the portion of the foam located below the neutral axis that is subjected to tensile stresses was ignored in the determination of M_{pf}. σ_y(=225 MPa) and σ_{yf} (=2.0 MPa) are the measured yield stresses of the tube and the foam respectively. For the foam σ_{yf} was assumed as the stress in the foam at 50% strain from the measured stress-strain curve (Kinoshita et al 2010). D is the average diameter of the tube and t is the thickness of the tube. A closed-form expression can be derived of if the mechanism angles ϕ_0 and ϕ_0' can be determined. Therefore, empirical equations based on extensive measurements of empty metal tubes subjected to bending (Elchalakani et al 2002a,b) will be used to obtain a simple relationship between ϕ_0' and the bending angle θ ($\phi = \sqrt{2\theta}$ and $\phi_0' = 1.65\phi_0$). For the foam-filled tubes similar expressions are used except for ($\phi_0' = 1.14\phi_0$) as the collapse of such tubes was less rapid compared to the empty ones. The tubes are subjected to the combined effect of shear and bending, therefore the reduced moment ($M_p' = M_y = \pi D^2 t$) will be used instead of the full moment M_p ($M_p = \sigma_y D^2 t$). Accurate determination of M_p' is required in the future.

4 RESULTS OF THE ANALYSIS

An example for the elastic-plastic (denting-bending) curve for empty and foam – filled tubes given by Equation 20 and the collapse curve (Equation 21) are shown in Figure 3 where the gains in strength and stiffness are clearly shown for a circular tube 40x1.6 due to foam filling. Note, in Equation 20, for empty tube the foam stiffness is $K_f = 0$. The Aluminum tube is grade AA6060T5 filled with Aluminum foam type "D" grade ALPORAS with a relative density of 8.2%. Figure 4 shows the tube during and after testing as well as a close up on the aluminum foam insert (Kinoshita etal. 2010).

The tube was partially filled with the foam with a longitudinal distance of $\zeta_f = 50$ mm (see Fig 2). The denting-bending curve is shown up to $\delta = R = 19.2$ mm and the collapse curve is shown up to the end of experiment. It is worth noting that the peak load in the test for the foam-filled tube was larger than the corresponding one for an empty tube. This could be

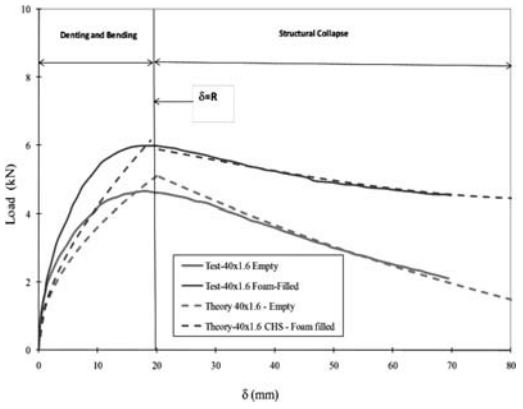

Figure 3. Load-deflection curve for empty and foam filled tubes 40×1.6 partially filled with aluminum foam ($\zeta_f = 50\,\text{mm}$).

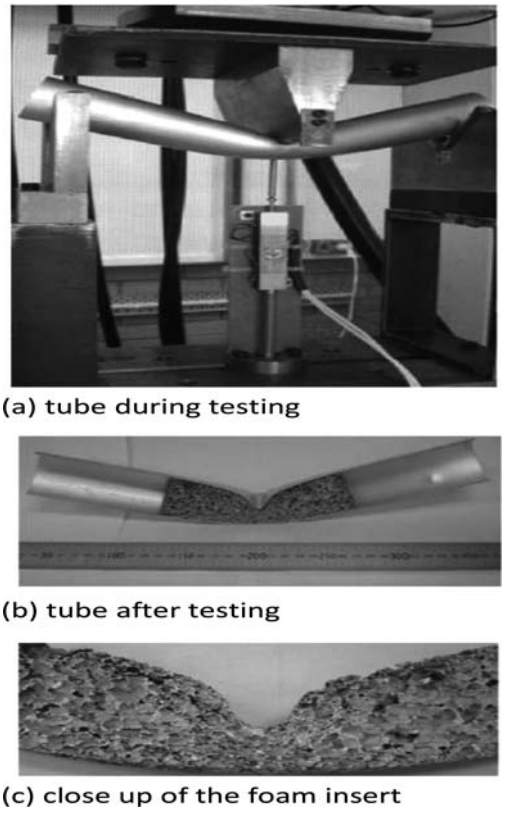

Figure 4. Testing of aluminum tubes $40\,\text{mm} \times 1.6\,\text{mm}$ partially filled with aluminum foam where $\zeta_f = 50\text{mm}$. Reprinted with permission from SAE paper 2010-01-0020 (c) 2010 SAE International.

explained by the fact that foam filling restricted buckling in the inelastic range as was discussed in Section 2 where the inelastic buckling stress of the foam-filled was found equal to times the empty tube's buckling stress.

It is seen that the slope and ordinates of the predicted collapse curves for both the empty and the foam-filled tubes are in very good agreement with the measured ones in the experiments. It is worth noting that the predicted portion of the load-deflection curves in the denting and bending phase are close to the measured curves, but the slope of such curves are not well matching. Thus, more work is needed to theoretically model the foam response in the elastic-plastic region.

5 CONCLUSIONS

This paper presents a theoretical analysis for Aluminum tubes filled with foam deforming in a kink collapse mode under large deformation bending and indentation. The classical beam on elastic foundation model was modified to predict the critical buckling stress which was compared to the classical stress for the empty tube to quantify the effect of the foam. During deep collapse of the tube, the fold formation process was such that the shell curvature flattened on the compression side transforming into two large flat triangles attached to each other.

An expression for the plastic collapse load was obtained by equating the total energy absorbed in bending and flattening to the external work carried out by the indenter during deformation of the tube. The predicted load-deflection curves were compared with those obtained from careful experiments carried out by the second author which were recently published elsewhere. It was found that the slope and ordinates of the predicted collapse curves for both the empty and the foam-filled tubes are in a good agreement with the measured ones in the experiments.

It is worth noting that the predicted load-deflection curve in the denting and bending phase is close to the measured curve, but the slope of such curves are not well matching particularly for the foam-filled tube. Thus, more work is needed to accurately model the foam response in the elastic-plastic region. More tests are currently performed at Swinburne University to further verify the present theory.

REFERENCES

Abramowicz, W. and T. Wierzbicki. "Axial crushing of foam-filled columns." International Journal of Mechanical Sciences 30(3–4): 263–271., 1988.

Elchalakani, M. "Cyclic bending behaviour of hollow and concrete filled cold-formed circular steel members." PhD thesis, Monash University, 2003.

Elchalakani, M., Zhao, X. L. and Grzebieta, R. H., Bending Tests to Determine Slenderness Limits for Cold-Formed Circular Hollow Sections, Journal of Constructional Steel Research, Vol. 58, No. 11, pp. 1407–1430, 2002a.

Elchalakani, M., Zhao, X. L. and Grzebieta, R. H., Plastic Mechanism Analysis of Circular Tubes under Pure Bending, International Journal of Mechanical Sciences, Vol. 44, No. 6, pp. 1117–1143.

Kinoshita S., Lu G., Ruan D. and Beynon J. Experimental and FE analysis of quasi-static three point bending of foam-filled structures. SAE International Journal of Materials and manufacturing, 2010; 3(1): 44–54.

Lampinen, B. E. and R. A. Jeryan, "Effectiveness of Polyurethane Foam in Energy Absorbing Structures." Society of Automotive Engineering Paper 820494: 2059–2076, 1982.

Mamalis, A.G., Manolakas, D.E., Baldoukas, A.K., and Viegelahn, G. L., Deformation Characteristics of Crashworthy Thin Walled Steel Tubes Subjected to Bending, Journal of Mechanical Science, Proceedings of Institute of Mechanical Engineers, Vol. 203, pp. 411–417, 1989.

Pokharel, N. and M. Mahendran, "Experimental investigation and design of sandwich panels subject to local buckling effects." Journal of Constructional Steel Research 59(12): 1533–1552, 2003.

Pokharel, N. and M. Mahendran. "Finite element analysis and design of sandwich panels subject to local buckling effects." Thin-Walled Structures 42(4): 589–611, 2004.

Reddy, T. Y. and R. J. Wall. "Axial Compression of Foam-Filled Thin-Walled Circular Tubes." International Journal of Impact Engineering 7(2): 151–166, 1988.

Reid, S. R. and Goudie, K., Denting and Bending of Tubular Beams under Local Loads, in Structural Failure, Wierzbicki, T. and Jones, N. (eds), John Wiley and Sons, pp. 331–364, 1989.

Reid, S. R. and T. Y. Reddy. "Axial Crushing of Foam-Filled Tapered Sheet Metal Tubes." International Journal of Mechanical Science 28(10): 643–656, 1986a.

Reid, S. R., Reddy, T. Y. and M. D. Gray. "Static and Dynamic Axial Crushing of Foam-Filled Sheet Metal Tubes." International Journal of Mechanical Science 28(5): 295–322, 1986b.

Sironic, L. (2002), The Elastic Buckling of Void-filled Thin-Walled Box Sections, PhD Thesis, Monash University.

Timoshenko, S. and Gere, J., Theory of Elastic Stability, McGraw-Hill, New York, 2nd Edn, pp. 541, 1961.

Thomas, S. G., Reid S. R. and Johnson, W., Large deformations of Thin-Walled Tubes under Transverse Loading (II), An Experimental Survey of the Bending of Simply Supported Tubes under a Central Load, International Journal of Mechanical Sciences, Vol. 18, pp. 325–333, 1976.

Thornton, P. H. and C. J. Amberger. "The Effect of Foam Filling upon the Energy Absorption of Spot Welded Sheet Metal Tubes." ASME, Journal of Engineering Material and Technology 107: 334–337, 1987.

Wierzbicki, T. and Sinmao, M. V., A simplified Model for Brazier Effect in Plastic Bending of Cylindrical Tubes, International Journal of Pressure Vessels and Piping, Vol. 71, pp. 19–28, 1997.

Wierzbicki, T. and Suh, M. S., Indentation of Tubes under Combined Loading, International Journal of Mechanical Sciences, Vol. 30, No. 3/4, pp. 229–248, 1988.

Zarei, H. R. and M. Kroger. "Bending behavior of empty and foam-filled beams: Structural optimization." International Journal of Impact Engineering 35(6): 521–529, 2008a.

Zarei, H. R. and M. Kroger. "Optimization of the foam-filled aluminum tubes for crush box application." Thin-Walled Structures 46(2): 214–221, 2008b.

Zeinoddini, H., Harding, J. E. and Parke, G. A. R., Contribution of Ring Resistance in the Behaviour of Steel Tubes subjected to a Lateral Impact loads, International Journal of Mechanical Sciences, Vol. 42, pp. 2303–2320, 2000.

Earthquake and dynamic response

Tubular Structures XIV – Gardner (Ed.)
© 2012 Taylor & Francis Group, London, ISBN 978-0-415-62137-3

Seismic response and damage limit of concrete filled steel tube frame

K. Goto
Miyakonojo National College of Technology, Miyazaki, Japan

ABSTRACT: Seismic response and damage of Concrete Filled steel Tube frame (CFT frame) under strong ground motion are calculated. The damage ratios of cracking and local buckling of CFT column and H-section beam, which are closely related to the collapse of CFT frame, are obtained in relation with the column-over-design factor and the strength ratio of CFT column. On the basis of the calculated results, the damage limits of CFT frame are investigated to prevent the local buckling and steel tube cracking of CFT column in relation with the ultimate state design conditions which are the column-over-design factor of CFT frame, the strength ratio of CFT column and the maximum velocity of input ground motion.

1 INTRODUCTION

It is well known that the concrete filled steel tube column (CFT column) is ductile and useful member as earthquake resistant element. In some case, however, CFT column fractures because of the cracking of steel tube while under strong seismic load. This fracture is brittle and predicted to be worked to collapse of CFT frame. From this reason, seismic response collapse and cracking damage of CFT frame, which is composed of CFT columns and H-section beams, have been investigated. Seismic response collapse of multi-story CFT frame is closely related to the fracture of structural members, especially to fracture of columns (Saisho & Goto 2004, Goto & Saisho 2010). Therefore, the restoring force characteristics and fracture mechanism of CFT column caused from steel tube cracking have been studied, and restoring force model and fracture condition of it were obtained (Saisho & Goto 2001).

According to the damages of recent severe earthquakes, H-section beams of multi-story steel frame have cracked. From this reason, the cracking of H-section beam that is connected with CFT column of CFT frame should not be disregarded for both the cracking of CFT column and the collapse of CFT frame. Therefore, the cracking condition and the damage ratio equation of H-section beam have been proposed on the basis of the very low-cycle fatigue failure (Goto 2010, Goto & Saisho 2010).

In this study, using these two cracking analysis (cracking of CFT column and H-section beam), seismic response and damage limit of CFT frame are investigated in relation with the ultimate state design conditions which are the column-over-design factor of frame, the strength ratio of CFT column and the maximum velocity of input ground motion to prevent the local buckling and cracking of CFT column subjected to strong seismic load.

2 SEISMIC RESPONSE ANALYSIS

2.1 *Multi-story CFT frame model*

In the dynamic collapse analysis of CFT frame, multi-story plane frame is assumed to be composed of the rigid panel zones of beam-column connection and the axially elastic members with elastic-plastic hinges at both ends as explained in Figure 1 (Saisho & Goto 2004). This assumption related to the rigid panel zone can be satisfied in most real CFT frames because the steel beam to CFT column moment connection has large shear strength. The mass of frame is concentrated in every panel zone and distributed uniformly in it. The displacement of frame can be expressed only by the rotation (θ_i, i: number of panel zone), the horizontal displacement (u_i) and the vertical displacement (w_i) of every rigid panel zone.

The viscous damping of frame is expressed by the Rayleigh Damping in which the damping factors of the first mode (h_1) and the second mode (h_2) are assumed to be $h_1 = 0.02$ and $h_2 = 0.02$.

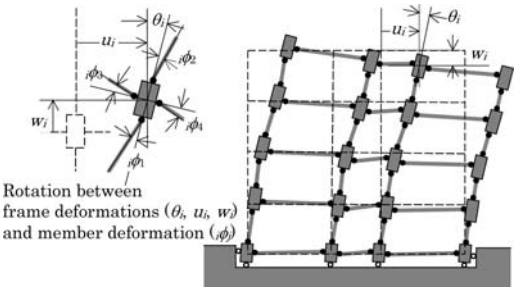

Figure 1. Multi-story CFT frame model for numerical analysis.

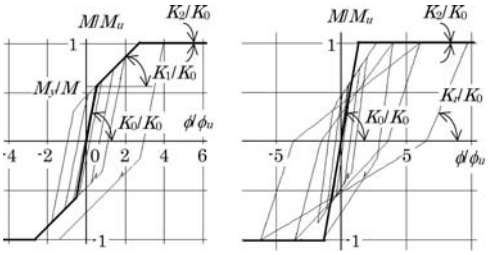

(a) Before local buckling (K_1/K_0=0.2, K_2/K_0=0.001) (b) After local buckling (K_2/K_0=0.001, K_t/K_0: unloading stiff.)

Figure 2. Restoring force models of CFT column.

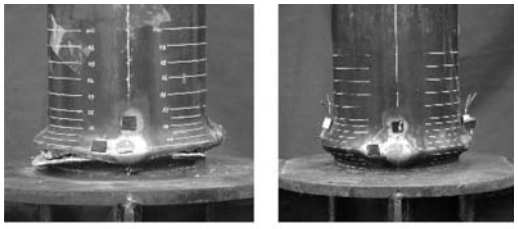

(a) Steel tube cracking (b) Local buckling

Figure 3. Cracking and local buckling of CFT column.

2.2 *Restoring force model of CFT column*

The restoring force model of elastic-plastic hinge is obtained on the basis of the dynamic loading tests of CFT column (Saisho & Goto 2001). According to the test results the non-dimensional restoring force (M/M_u) of CFT column until the local buckling of steel tube is approximated by the Tri-linear model whose skeleton curve is explained in Figure 2(a). After the local buckling of steel tube, it is expressed by the Clough model (Clough & Johnston 1966) as shown in Figure 2(b). The stiffness ratios at the plastic range in Figures 2(a)–(b) are given as $K_1/K_0 = 0.2$, $K_2/K_0 = 0.001$ which are approximated on the basis of the test results (Saisho & Goto 2001). The restoring force models mentioned above are defined by the non-dimensional restoring force (M/M_u) in which the ultimate bending strength (M_u) changes at every moment by the varying axial force of CFT column. Accordingly the restoring force model can simulate the effect of varying axial force of CFT column. M_u is obtained by the generalized superposed strength method considering the confined effect (Saisho & Goto 2001).

2.3 *Cracking and local buckling of CFT column*

From the cyclic loading tests of CFT column it is shown that the steel tube of CFT column cracks and fractures as shown in Figure 3(a) when the accumulated plastic strain of steel tube becomes to be equal to the critical value ($\alpha\varepsilon_f$). From this result the cracking condition of CFT column is expressed by Equation 1 (Saisho & Goto 2001).

$$\sum \varepsilon_{TC} + \sum \varepsilon_T = \alpha\varepsilon_f \tag{1}$$

where ε_T : the plastic tension strain of steel tube in the tension stress side, ε_{TC} : the plastic tension strain due to the local buckling deformation of steel tube in the compression stress side. α ($= -0.3\rho + 5.0$): constant expressed by the strength ratio of filled concrete to steel tube ρ ($= \sigma_c A_c / \sigma_u A_s, A_c, A_s$: sectional areas of concrete and steel tube respectively, σ_c: compression strength of filled concrete, σ_u: tensile strength of steel tube), ε_f: fracture elongation of steel tube, Σ: summation of plastic strain under cyclic load. From Equation 1, the cracking damage ratio of CFT column ($_cD_{cr}$) is expressed by Equation 2.

$$_cD_{cr} = (\sum \varepsilon_{TC} + \sum \varepsilon_T) / \alpha\varepsilon_f \tag{2}$$

As shown in Equation 1, the local buckling of steel tube (Fig. 3(b)) is closely related to the steel tube cracking. The local buckling condition is obtained on the basis of the upper bound theorem of the limit analysis (Saisho et al. 2004). The damage ratio of local buckling ($_cD_{lb}$) is decided by the use of critical deformation ($_c\delta_{lb}$) that corresponds to the CFT column deformation for the steel tube to buckle locally.

$$_cD_{lb} = (_c\delta_{PC} - _c\delta_{PT}) / _c\delta_{lb} \tag{3}$$

where ($_c\delta_{PC} - _c\delta_{PT}$) is the amplitude of plastic deformation of CFT column. By the use of Equations 2–3, the local buckling and the steel tube cracking in the restoring force of CFT column mentioned above are decided.

2.4 *Restoring force model of H-section beam*

The H-section beam of multi-story CFT frame is also expressed by the axially elastic member with the elastic-plastic hinges at both ends as shown in Figure 1. The restoring force of the elastic-plastic hinge is decided by the Tri-linear model shown in Figure 4 in which the restoring force characteristics are given by the full plastic moment (M_p) and the ultimate bending strength of H-section beam ($_bM_u$). The strain hardening behavior of H-section beam affects the seismic response and collapse of CFT frame under strong ground motion. Accordingly the strain hardening of H-section beam in the model can not be neglected. It is given by the value K_1 which is obtained by assuming H-section beam is approximated by two-flange section member.

$$\frac{K_1}{K_0} = \frac{1/y - 1}{1.5y(1-y)(1+u) - 1} \tag{4}$$

where y ($= \sigma_y/\sigma_u$) and u ($= \varepsilon_u/\varepsilon_y$) mean the yield stress ratio and the ultimate tensile strain ratio respectively.

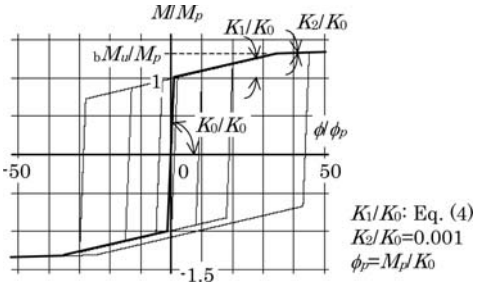

Figure 4. Restoring force model of H-section beam.

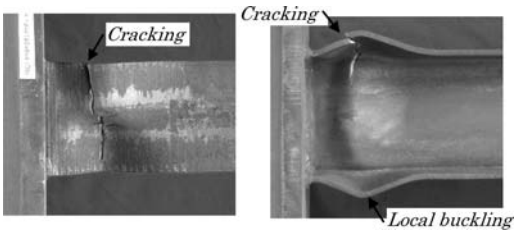

Figure 5. Cracking and local buckling of H-section beam.

2.5 *Cracking and local buckling of H-section beam*

When strong alternating repeated load is applied to the H-section cantilever beam, flange buckles locally and after that cracks (Fig. 5) even if the fracture at the welded joint is avoided. According to the dynamic loading tests of H-section cantilever beam, the cracking fracture of H-section beam is considered as the very low-cycle fatigue behavior and assumed to be approximated by the Palmgren-Miner rule (Goto 2010, Goto & Saisho 2010). From the Palmgren-Miner rule, the damage ratio is given by the accumulation of the each cycle damage (Dowling 2007). Therefore, the cracking damage ratio of H-section beam ($_bD_{cr}$) in each instant under random repeated load can be expressed by Equation 5.

$$ {}_bD_{cr} = \sum_j \frac{1}{N_{fj}} \tag{5} $$

where N_{fj} means the number of cycle to fracture under j-th cycle load and N_f is approximated by the Coffin-Manson relationship as shown in Equation 6.

$$ \varepsilon_{pa} = \varepsilon_f (2N_f)^c \tag{6} $$

where ε_{pa}: the plastic strain amplitude of H-section beam flange buckled locally (Goto & Saisho 2010), ε_f: fracture elongation, c: material modulus.

The local buckling condition of flange at the beam end is obtained on the basis of the upper bound theorem of the limit analysis (Goto 2010). The damage ratio of local buckling ($_bD_{lb}$) is decided by the use of critical deformation ($_b\delta_{lb}$).

$$ {}_bD_{lb} = ({}_b\delta_{PC} - {}_b\delta_{PT}) / {}_b\delta_{lb} \tag{9} $$

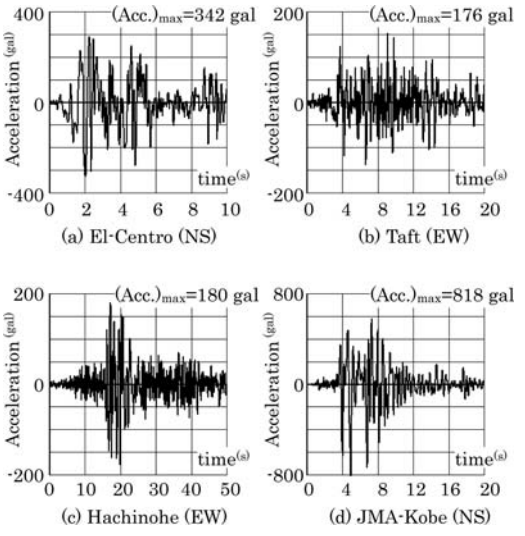

Figure 6. Time-histories of input ground motions.

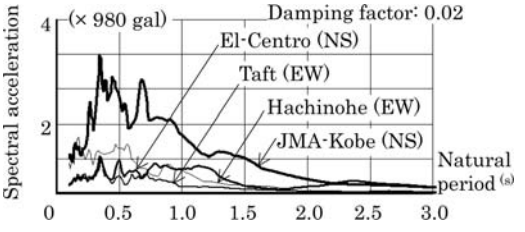

Figure 7. Response spectra of input ground motions.

where ($_b\delta_{PC} - {}_b\delta_{PT}$) is the amplitude of plastic deformation of H-section beam.

2.6 *Input ground motion*

To calculate the seismic response and damage of CFT frame, El-Centro (California 1940), Taft (California 1952), Hachinohe (Aomori, Japan 1968), JMA-Kobe (Kobe, Japan 1997) are used as input ground motion. These time histories of acceleration and acceleration response spectra are shown in Figures 6-7 respectively.

2.7 *Design of multi-story CFT frame*

CFT frames to be calculated in this study are the 15-story 3-bay frames and 7-story 3-bay frames. They are designed under the following conditions.

1. The distribution of story shear strength ratio is decided by the Japanese design code. The base shear strength coefficient C_B ($= Q_1/W$, Q_1: ultimate shear force of the first story, W: weight of frame) of 15-story frame and 7-story frame are also decided by the design code and they are $C_B = 0.25$ and $C_B = 0.40$ respectively. The frame strength is calculated by the limit analysis assuming

the collapse mechanism of frame with plastic hinges at every beam-end and the upper and lower column-ends in the top story and the first story.
2. The column-over-design factor (r_c) of every beam-to-column connection except for the highest story is the same and they are $r_c = 1.0 - 6.0$.
3. The strength ratio of filled concrete to steel tube (ρ) affects the restoring force characteristics of CFT column strongly (Saisho & Goto 2001). From this reason the strength ratios (ρ) of all CFT columns are assumed to be the same and they are $\rho = 0.5 - 16.0$ in this study.
4. Every H-section beam of multi-story frame satisfies the critical conditions of the width-to-thickness ratio of flange (b/t_f) and web (h/t_w) and the lateral buckling parameter ($L_b h/A_f$). They are b/t_f = 5, $h/t_w = 71$ and $L_b h/A_f = 375$ (b: half width of flange, h: depth of beam, t_f, t_w: thicknesses of flange and web respectively, A_f: sectional area of flange, L_b: beam length).

All CFT frames are designed under the conditions mentioned above and another condition that any dimensions of steel tube and H-section are available.

The story-height of every CFT frame is 4.0 m and the span lengths of outer span and inner span are 8.0 m and 6.0 m respectively. The weight of each story is 2000 kN. The yield stress (σ_y) and the tensile strength (σ_u) of steel tube and H-section beam are $\sigma_y = 340\ \mathrm{N/mm^2}$ and $\sigma_u = 440\ \mathrm{N/mm^2}$. The fracture elongation (ε_f) of steel tube and H-section beam is $\varepsilon_f = 0.20$. The compression strength of filled concrete (σ_c) is $\sigma_c = 30, 60, 120\ \mathrm{N/mm^2}$.

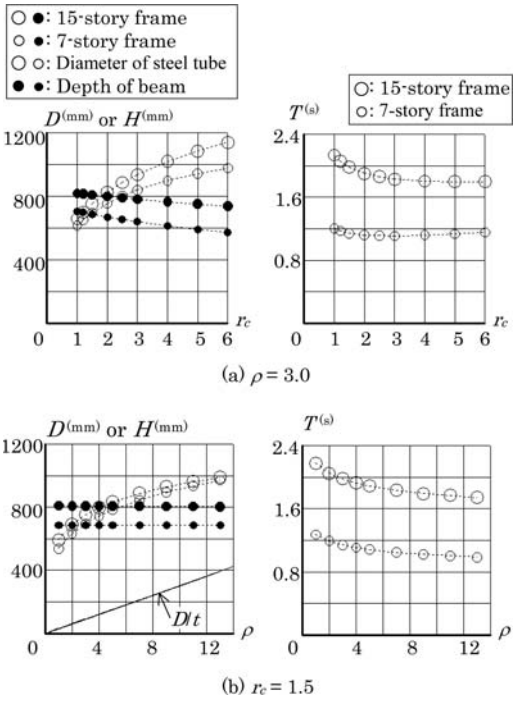

Figure 8. Dimensions of members (D, H) and natural periods (T) of designed CFT frames ($\sigma_c = 60\ \mathrm{N/mm^2}$).

Some results of designed CFT frames are shown in Figure 8(a)–(b) in which there are diameter (D) of CFT column, depth (H) of H-section beam at the first story and natural period (T) of CFT frame. The design conditions of CFT frames are quite different among them. But every diameter (D) of CFT column and depth (H) of H-section beam is practical dimension and the natural periods (T) of 15-story frames and 7-story frames are almost constant respectively. From these designed frames it is ascertained that the design method of multi-story CFT frame is useful.

3 SEISMIC RESPONSE AND DAMAGE RATIO

3.1 *Effect of column over design factor on maximum damage ratios of CFT frame*

The damage distributions of CFT frames under JMA-Kobe are shown in Figure 9(a)–(b). The damages of CFT frame are the rotation of elastic-plastic hinge (ϕ), the local buckling damage ratios of CFT column ($_cD_{lb}$) and H-section beam ($_bD_{lb}$) and the cracking damage ratios of CFT column ($_cD_{cr}$) and H-section beam ($_bD_{cr}$). These damage and damage ratios are expressed by the length of thick line perpendicular to the axis of column and beam. The numerical values in the figures explain the damage or damage ratios of CFT columns in the first story and the highest story.

To show the effect of the column-over-design factor (r_c), the calculations in these figures are carried out under the condition of $r_c = 1.0$ and $r_c = 3.0$. Although all CFT frames are designed under the same design condition on the ultimate story shear strength, the strength distribution along the story and the strength ratio of filled concrete to steel tube (ρ), we can see the remarkable differences of the damage ratio distribution among the CFT frames. In the CFT frame of $r_c = 1.0$ (Fig. 8(a)), many CFT columns buckle locally and high cracking damage ratios of CFT column appear. On the other hand, the local buckling of CFT column does not appear in the CFT frame of $r_c = 3.0$ (Fig. 8(b)). Therefore, the cracking damage ratios of CFT columns are low.

The relations between the column-over-design factor (r_c) and the maximum damage ratios of CFT frame under JMA-Kobe and Hachinohe (Hachinohe wave is amplified to the same spectrum intensity with JMA-Kobe) are explained in Figure 10(a)–(b). These figures show the maximum elastic-plastic hinge rotation (ϕ_m, the maximum local buckling damage ratios of CFT column $(_cD_{lb})_m$ and H-section beam $(_bD_{lb})_m$ and the maximum cracking damage ratios of CFT column $(_cD_{cr})_m$ and H-section beam $(_bD_{cr})_m$ while under strong ground motion.

According to Figure 10(a)–(b), the complicated differences due to the design conditions are observed but the maximum damage ratios of local buckling and steel tube cracking of CFT column increase monotonically

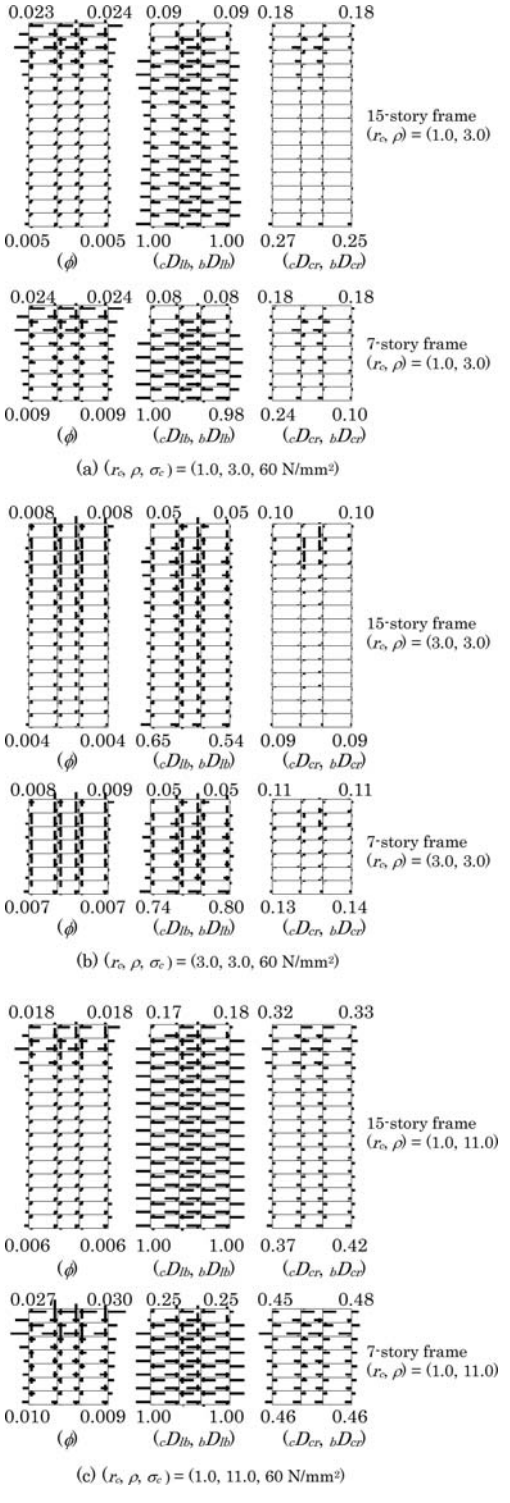

Figure 9. Damage distributions of CFT frame under strong ground motion (JMA-Kobe).

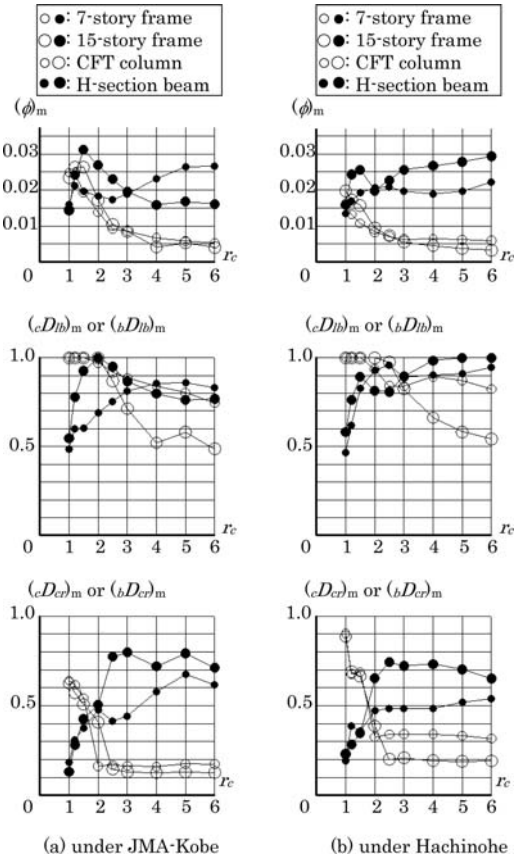

Figure 10. Effect of the column-over-design factor (r_c) on the maximum damages of CFT frame ($\rho = 3.0$, $\sigma_c = 60$ N/mm^2) under strong ground motion.

in most cases with the column-over-design factor (r_c) decreases. Especially, it is observed $(_cD_{cr})_m$-values increase remarkably when the local buckling of CFT column occurs ($(_cD_{lb})_m = 1.0$). On the other hand, the maximum cracking damage ratio of H-section beam tends to increase with the column-over-design factor (r_c), however, the H-section beam does not crack even if $r_c = 6$. From these results, it is shown that the maximum damage ratios of CFT column are clearly affected by the column-over-design factor (r_c).

3.2 *Effect of strength ratio of filled concrete to steel tube on maximum damage ratios of CFT frame*

The damage distributions of CFT frames under JMA-Kobe are shown in Figure 9(c). These calculated frames differ only in the strength ratio of filled concrete to steel tube (ρ) with CFT frames in Figure 9(a). Other design conditions which are the ultimate story shear strength, the strength distribution along the story and the column-over-design factor (r_c) and input ground motion are the same. According to these results, we can see the remarkable differences of the damage ratio distributions among the CFT frames,

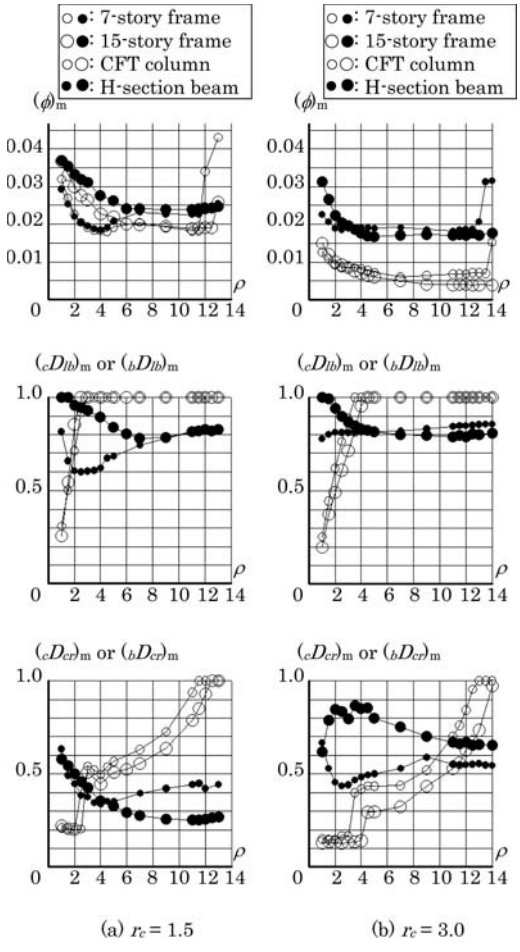

Figure 11. Effect of the strength ratio of filled concrete to steel tube (ρ) on the maximum damages of CFT frame ($\sigma_c = 60$ N/mm^2) under JMA-Kobe.

especially the damage ratios of CFT column. As comparing with CFT frames with $\rho = 3.0$ (Fig. 9(a)), many CFT columns buckle locally and high cracking damage ratios of CFT column appear in CFT frames with $\rho = 11.0$ (Fig. 9(c)).

To show the effect of the strength ratio of filled concrete to steel tube (ρ) on the maximum damage ratios of CFT frame ($(\phi)_m$, $(_cD_{lb})_m$, $(_bD_{lb})_m$, $(_cD_{cr})_m$, $(_bD_{cr})_m$), seismic response analyses of CFT frames with variable ρ-values are carried. Figure 11(a)–(b) shows the some calculated results as examples. According to Figure 11(a)–(b), the complicated differences are observed. But the maximum damage ratios of local buckling and steel tube cracking of CFT column increase monotonically with the strength ratio of filled concrete to steel tube (ρ). It is also observed that the upper bounds of ρ-value not to occur the local buckling and the steel tube cracking of CFT column exists and these bounds are strongly affected by the column-over-design factor (r_c).

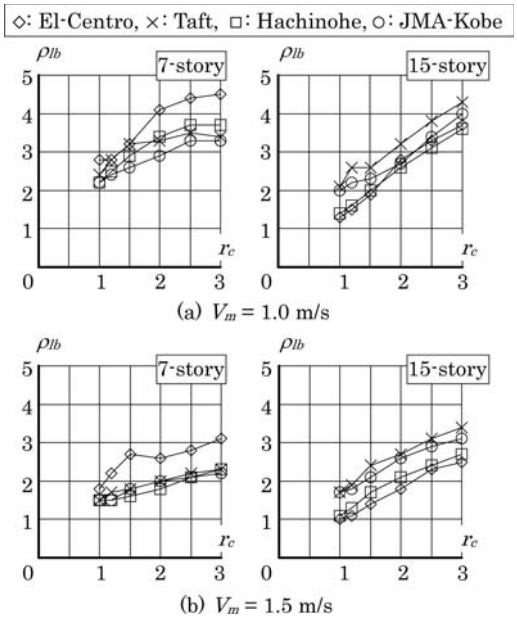

Figure 12. Lower bound of the strength ratio of filled concrete to steel tube in case the local buckling of CFT column occurs.

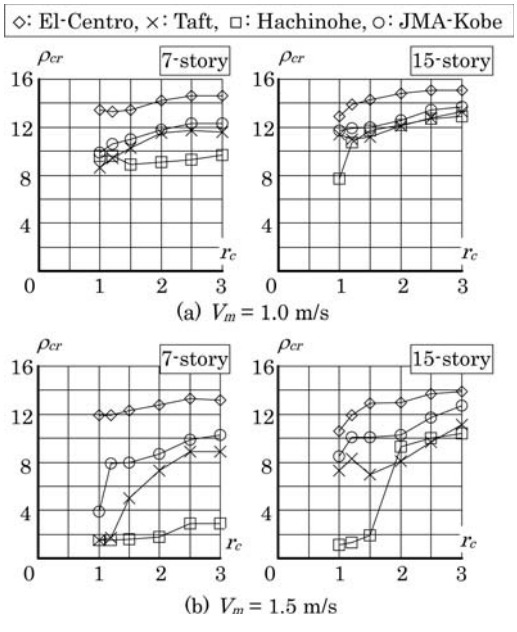

Figure 13. Lower bound of the strength ratio of filled concrete to steel tube in case the steel tube cracking of CFT column occurs.

3.3 *Limit value of the strength ratio of filled concrete to steel tube*

To avoid the local buckling and steel tube cracking of CFT column subjected to strong seismic load, the design condition limits of the strength ratio of filled

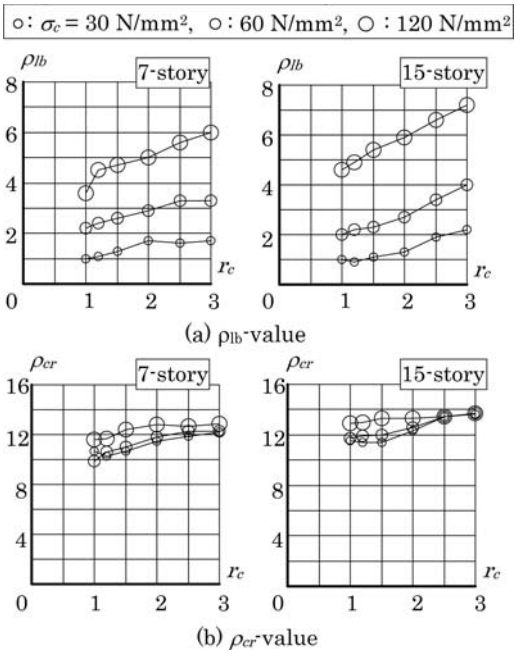

Figure 14. Effect of the compression strength of filled concrete (σ_c).

concrete to steel tube (ρ_{lb}, ρ_{cr}) are investigated. Figure 12(a)–(b) shows the lower bounds of strength ratio of filled concrete to steel tube in case the local buckling of CFT column occurs (ρ_{lb}). The input ground motions are amplified the maximum velocity (V_m) to $V_m = 1.0$ or 1.5 m/s. According to Figure 12(a)–(b), ρ_{lb}-values increase with the column-over-design factor (r_c) monotonically and linearly in each ground motion.

Figure 13(a)–(b) shows the lower bounds of the strength ratio of filled concrete to steel tube in case the steel tube cracking of CFT column occurs (ρ_{cr}). According to Figure 13(a)–(b), ρ_{cr}-value also tends to increase with the column-over-design factor (r_c).

However, ρ_{cr}-values are affected by the ground motion because of the duration of ground motion and the number of cyclic load (Hachinohe wave has long duration and many load cycles).

Figure 14 shows the effect of compression strength of filled concrete (σ_c). Input ground motion is JMA-Kobe ($V_m = 1.0$ m/s). ρ_{lb}-values are strongly affected by σ_c-value. But the diameter-to-thickness ratio are almost same value in each r_c-value because the local buckling condition of CFT column is relative to diameter-to-thickness ratio strongly (Saisho et al. 2004). On the other hand, ρ_{cr}-values are almost constant.

4 CONCLUSIONS

Seismic responses and damages of many CFT frames under strong ground motions have been analyzed and it is pointed out that not only the ultimate story shear strength and the shear strength distribution but also the column-over-design factor (r_c) and the strength ratio of filled concrete to steel tube (ρ) affect both damage ratios of the local buckling and the steel tube cracking strongly.

To prevent the local buckling and the steel tube cracking of CFT column, the lower bounds of the strength ratio of filled concrete to steel tube in case these damages occur (ρ_{lb}, ρ_{cr}) are investigated quantitatively. From these results, although both ρ_{lb}-values and ρ_{cr}-values vary according to the column-over-design factor (r_c), the input ground motion and the compression strength of filled concrete (σ_c), the strength ratio of filled concrete to steel tube should be less than 1.0 to prevent the local buckling and steel tube cracking of CFT frame under strong ground motion.

REFERENCES

Clough, R.W. & Johnston, S.B. 1966. Effect of stiffness degradation on earthquake ductility requirements. *Proceedings of Japan Earthquake Engineering Symposium*: 227–232.

Dowling, N.E. 2007. *Mechanical Behavior of Materials*. New Jersey: Person Prentice Hall.

Goto, K. 2010. Crack fracture type of H-section cantilever beam under strong cyclic load. *Proceedings of 9th Pacific Structural Steel Conference*: 1017–1023.

Goto, K. & Saisho, M. 2010. Crack damage of multi-story CFT frame under strong motion. *Proceedings of the 13th International Symposium on Tubular Structures*: 149–157

Saisho, M. & Goto, K. 2001. Restoring force model of concrete filled steel tube column under seismic load. *Proceedings of the 9th Pacific Structural Steel Conference*. Vol.1: 453–458.

Saisho, M. & Goto, K. 2004. Ultimate earthquake resistant capacity of CFT-frame. *Proceedings of the 13th World Conference on Earthquake Engineering*. Paper No.2613.

Saisho, M., Kato, M. & Gao, S. 2004. Local buckling of CFT-column under seismic load. *Proceedings of the 13th World Conference on Earthquake Engineering*. Paper No.2614.

Tubular Structures XIV – Gardner (Ed.)
© 2012 Taylor & Francis Group, London, ISBN 978-0-415-62137-3

Experimental evaluation of CHS KK-joints under out-of-plane bending for seismic applications

W. Wang & Y.Y. Chen
State Key Laboratory for Disaster Reduction in Civil Engineering, Tongji University, Shanghai, China

B.D. Zhao
Department of Building Engineering, Tongji University, Shanghai, China

ABSTRACT: This paper deals with experimental evaluation of the seismic behavior of Circular Hollow Section (CHS) KK-joints used in steel tubular structures. Cyclic Out-of-Plane Bending (OPB) loading patterns were varied in testing two full-scale specimens in order to evaluate their effect on connection behavior. Test results indicated that the strength efficiency of these joints significantly depended on the loading patterns. CHS KK-joints under Alternate Opening and Closing OPB (AOCO) load effects developed more satisfactory levels of ductility and energy dissipation than that under alternate clockwise-aligned and Anticlockwise-Aligned OPB (ACAO) load effects, although the final failure modes for both showed similar fracture initiated from the chord wall. It was found that the energy dissipation due to the ductile chord crack propagation could be utilized effectively to some extent for earthquake resistance.

1 INTRODUCTION

Single-layer reticulated shells have become a particularly popular choice for the large-span roof systems of steel structures because of their light weight, appealing architectural appearance and rapid erection. Circular hollow sections (CHS) are a common selection for primary load-carrying members of this type of onshore structures. In the practical applications, the sections are profiled and welded to form CHS unstiffened connections. The distributed load on the CHS members, especially in the event of an earthquake, may generate significant out-of-plane bending (OPB) moments on the CHS KK-joints (as highlighted in Figure 1 for a typical engineering application). Many of successful large-span tubular structural applications now exist in regions of high seismic risk, leading to the great concerns of the engineering community about the behavior of CHS connections under seismic loading.

Existing studies concerned with tubular joints focused on ultimate static capacity as their main target. Although some work has considered inelastic dynamic behavior in response to extreme wave events, it has consisted mostly of high cycle loads to investigate fatigue performance. On the other hand, limited studies on seismic behavior of tubular joints were almost restricted to the case under axial loads (Kurobane 1998, Soh et al. 2001, Wang & Chen 2007, Chen & Zhao 2007, Yin et al. 2009). Recently thick-walled CHS X-joints (Wang & Chen 2010) and CHS stiffened joints to box section girders with different details (Wang & Chen 2010) have been experimentally studies under OPB loads. However, there have been no research found on the cyclic behavior of CHS KK-joints under OPB. Due to the lack of test and analytical evidences, the strengths, the failure modes and the ductility of this joint require further investigations in order to provide a basis for a rational seismic design of such tubular structures.

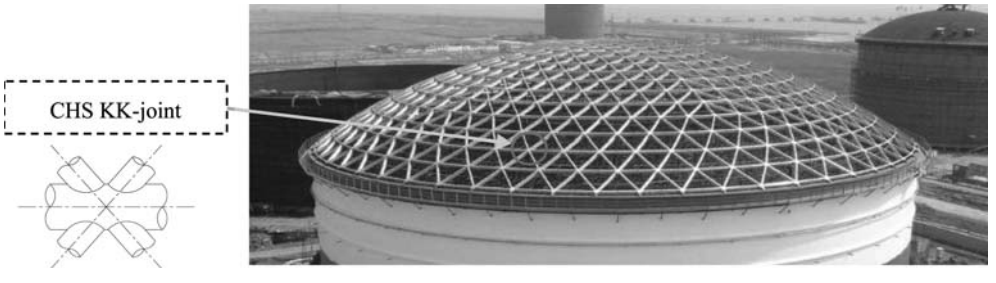

Figure 1. Engineering application of CHS KK-connections.

In this paper, the experiments of two full-scale CHS KK-joints under cyclic OPB loading are reported. Significantly different strength efficiency of KK-joints under two loading patterns were identified based on the analysis on the relationship of global responses and strain distribution. The effects of loading patterns on the ductility and energy dissipation capacity of the joints were experimentally evaluated.

2 EXPERIMENTAL PROGRAM

2.1 *Test specimen*

The cyclic tests were carried out on two full-scale CHS KK-joint specimens with different loading patterns: KKBH-1 and KKBH-2, as shown in Figure 2. They all have KK configuration and the same geometrical characteristics, as listed in Table 1. The chord length between supports was $l_c = 1240$ mm (with $\alpha = 2l_c/D = 10.1$) while the brace length was approximately 7 to 8 times the brace diameter d, preventing the effect on the joint zone caused by end constraints. The chosen geometric parameters (with $\gamma = D/(2T) = 12.3$; $\beta = d/D = 0.57$; $\tau = t/T = 0.8$) correspond to typical CHS KK-joints in large span spatial tubular structures. Table 2 summarizes the measured material properties of the chord and the braces.

2.2 *Test setup and loading procedure*

For KK-joints there are two possible cyclic OPB loading patterns: (1) Alternate opening and closing OPB (AOCO), as shown in Figure 3(a); (2) Alternate clockwise-aligned and anticlockwise-aligned OPB (ACAO), as shown in Figure 3(b). AOCO loading was adopted for KKBH-1 testing while ACAO loading was adopted for KKBH-2 testing, in order to investigate the seismic response of KK-joints under different loading patterns.

Figure 4 shows the general arrangement for the CHS KK-joint tests. The chord was placed in a horizontal position along with four braces. Spherical plain bearings were set up at the end of four braces to make sure

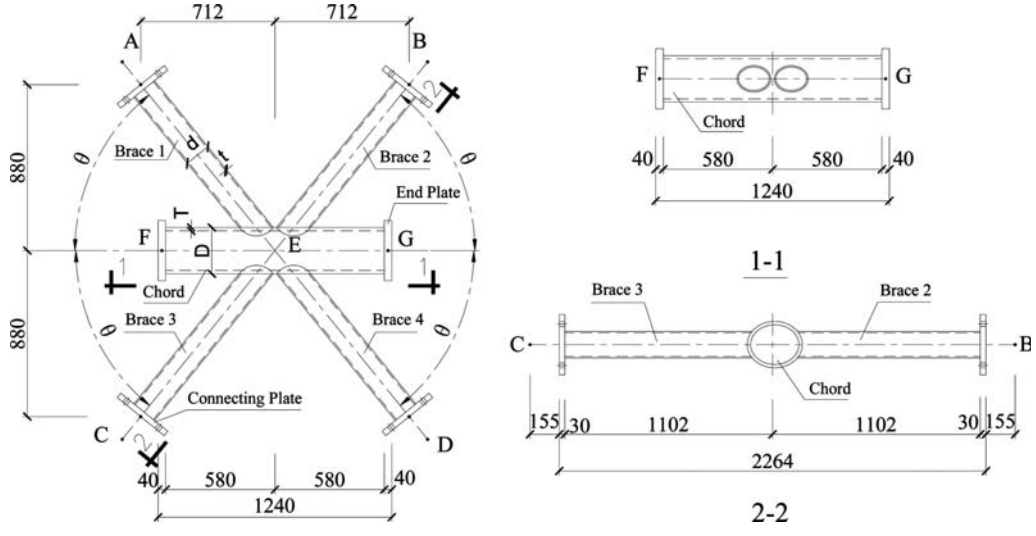

Figure 2. CHS KK-connection specimens detail.

Table 1. Overview of specimens.

Specimen	D × T	d × t	β	γ	τ	θ	Loading pattern
KKBH-1	245 × 10	140 × 8	0.57	12.3	0.8	51°	AOCO
KKBH-2	245 × 10	140 × 8	0.57	12.3	0.8	51°	ACAO

Table 2. Material properties of specimens.

Section size (mm)	Yield strength f_y (MPa)	Tensile strength fu (MPa)	Elongation δ(%)	Elastic Modulus E (MPa)
245 × 10 CHS	282	464	37.3	2.06×10^5
140 × 8 CHS	310	477	28.8	2.06×10^5

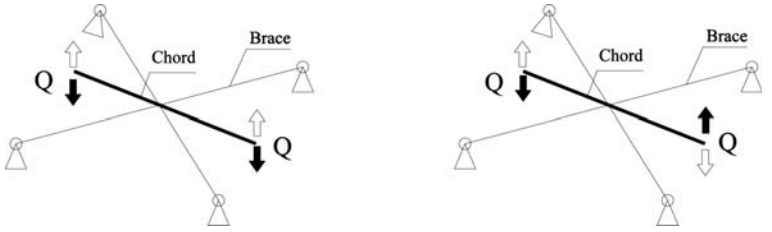

Figure 3. Two different cyclic OPB loading patterns on CHS KK-connections.

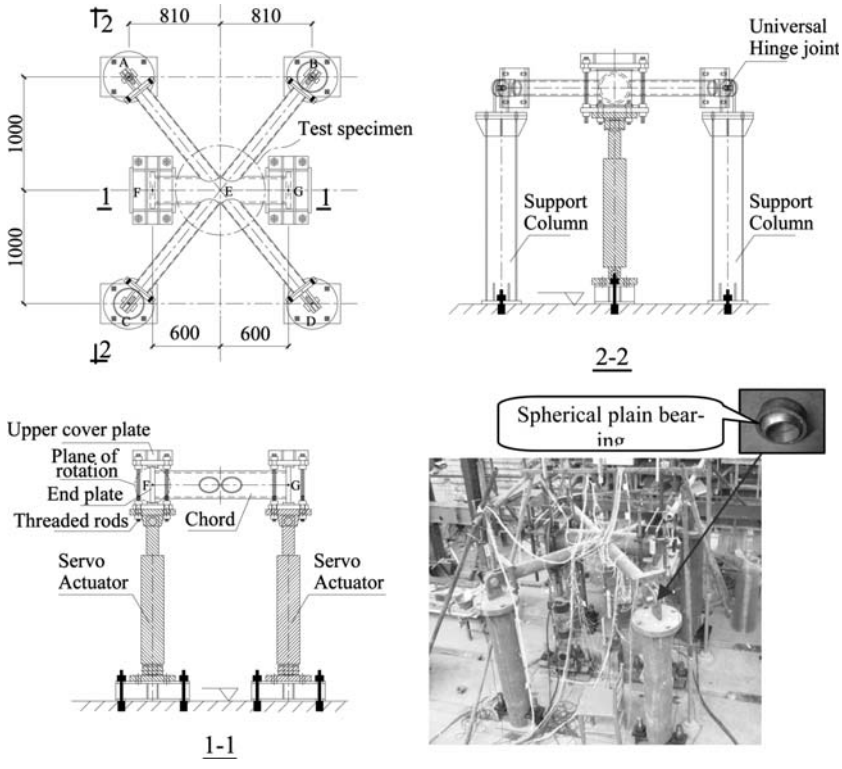

Figure 4. Test setup.

the boundary conditions were universal hinge joints. Servo hydraulic actuators were connected to each end of the chord, by clamping the chord with two cover plates through four threaded rods. The curved contacting surfaces were made between upper or bottom cover plate and the chord end, coating with lubricant oil. The basic idea behind the details is to alleviate the friction, thus allowing the end plate to rotate around its own central axis freely. As a result, pinned boundary conditions were achieved.

The loading protocol prescribed a quasi-static cyclic displacement pattern defined in terms of loading point displacement, Δ (Fig. 5). For the beginning two cycles, the specimens were tested with displacement amplitudes of $\pm 0.5\,\Delta_y$ and $\pm\Delta_y$. One cycle of displacement load was then applied at each new displacement level with 3mm increments for the subsequent loading. This process was repeated until connection failure occurred. For each specimen, the instrumentation includes strain gauges around the crown points and the saddle points to measure the strain distributions at hot spots, and transducers to measure the displacements at selected key points.

3 EXPERIMENTAL RESULTS

3.1 *Failure modes*

In the KKBH-1 test, yielding was first inspected at the chord wall near the saddle point during the third load cycle ($Q = 34$ kN). Subsequently, when the loading displacements level reached ± 42 mm, initial yielding in the brace end section was measured. Meantime, a small plastic deformation was also observed on the chord wall at intersections between the braces and the chord, convex under tension and concave under

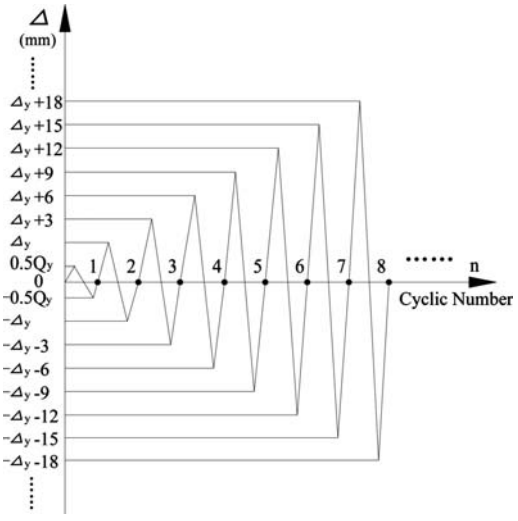

Figure 5. Loading procedure.

compression. A small crack was first observed at the welding heat affected zone (HAZ) near the saddle point between the brace 3 and the chord during the ±45 mm load cycle, followed by cracking at similar points between the other three braces and the chord. This led to the gradual strength decrease in the following load cycles. When the ±66 mm load cycle was reached, the strength decreased by around 1/3 from the peak force due to the propagation of the cracks. The specimen finally failed because of the plastic tearing of the chord wall at the intersection of the braces and the chord under AOCO load effects, as is specified in Figure 6(a).

In the KKBH-2 test, yielding was identified simultaneously at the chord wall near the saddle point and the brace end section during the third load cycle ($Q = 70$ kN). A small crack was first observed at the welding heat affected zone (HAZ) near the saddle point between the brace 2 and the chord during the ±76 mm load cycle, followed by cracking at similar points between the other three braces and the chord. This led to the gradual strength decrease in the following load cycles. When the ±100 mm load cycle was reached, the strength decreased by around 1/3 from the peak force due to the propagation of the cracks. The specimen finally failed because of the plastic tearing of the chord wall at the intersection of the braces and the chord under ACAO load effects, as is specified in Figure 6(b).

The failure modes of two specimens all demonstrated chord wall tearing near welding HAZ. However, it can be clearly seen from the observations that KKBH-1 under AOCO load effects intended to experience more considerable degree of yielding in the chord wall than KKBH-2 under ACAO load effects.

3.2 *Cyclic behavior*

The equivalent force-drift responses at brace ends of the specimens under cyclic loading are presented in Figure 7 and 8. To permit a direct comparison between

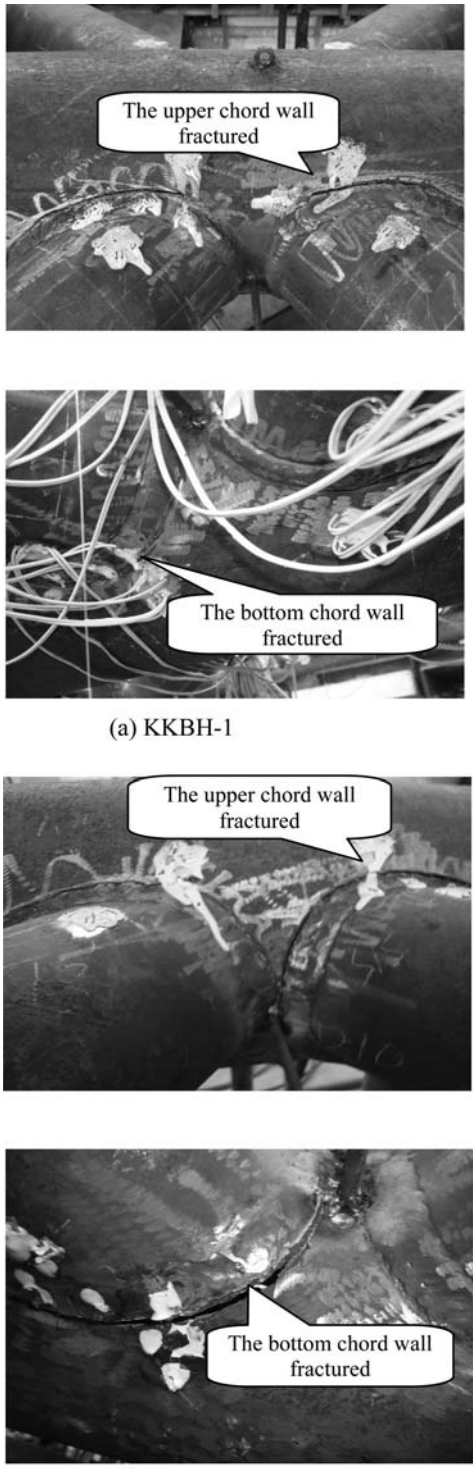

Figure 6. Failure modes after test.

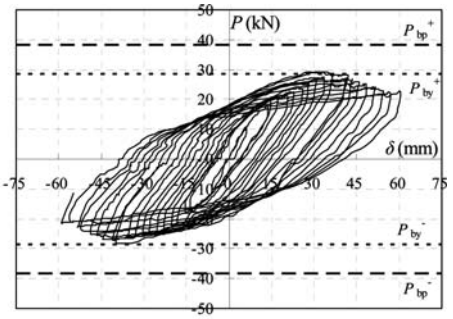

(a) Brace 1

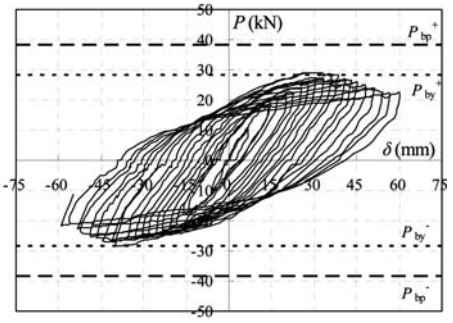

(b) Brace 2

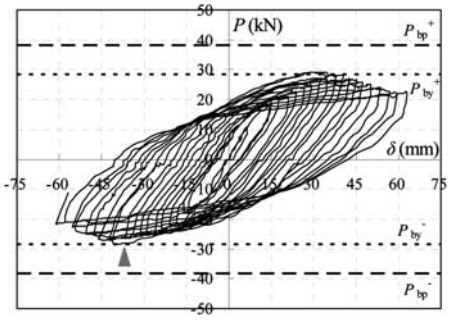

(c) Brace 3

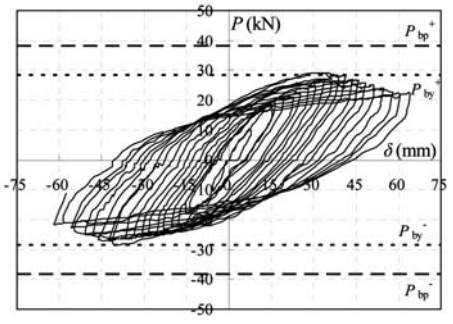

(d) Brace 4

Figure 7. Brace load versus displacement relationships of Specimen KKBH-1.

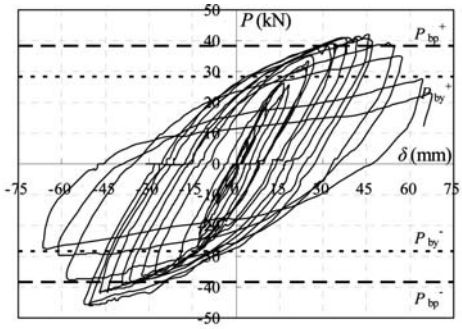

(a) Brace 1

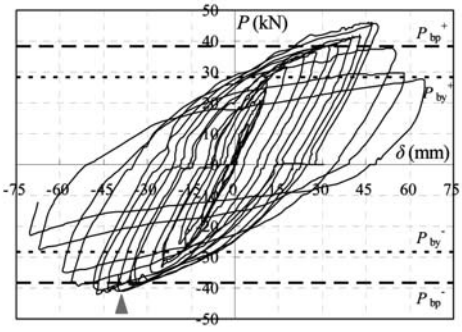

(b) Brace 2

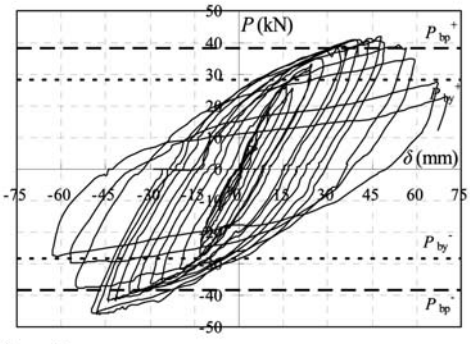

(c) Brace 3

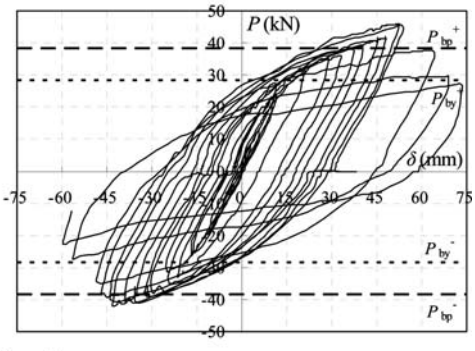

(d) Brace 4

Figure 8. Brace load versus displacement relationships of Specimen KKBH-2.

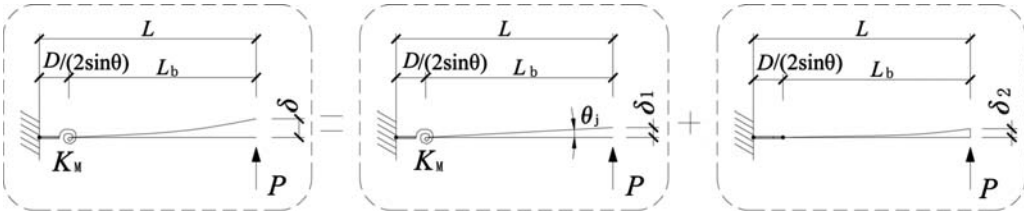

Figure 9. Components of vertical brace deflection in CHS KK-connection.

Table 3. Ductility ratio of the specimens.

Specimens		θ_{jy}^{+}	θ_{ju}^{+}	θ_{jy}^{-}	θ_{ju}^{-}	μ^{+}	μ^{-}
KKBH-1	Brace 1	0.005	0.030	0.005	0.028	5.7	5.4
	Brace 2	0.005	0.030	0.005	0.028	5.7	5.4
	Brace 3	0.006	0.031	0.005	0.029	5.4	5.4
	Brace 4	0.006	0.031	0.006	0.029	5.3	5.0
KKBH-2	Brace 1	0.006	0.021	0.005	0.024	3.7	4.5
	Brace 2	0.005	0.022	0.006	0.022	4.1	3.9
	Brace 3	0.006	0.022	0.005	0.023	3.9	4.3
	Brace 4	0.005	0.023	0.005	0.022	4.4	4.4

connection strength and adjacent member strength, the force corresponding to nominal brace yielding moment, P_{by}, and the force corresponding to nominal full plastic moment strength of the brace section, P_{bp}, are plotted in these figures. Furthermore, the first crack occurrences are marked in these figures.

For two specimens, hysteretic curves behaved stably without pinching before cracks occurred. However, it can be seen that these two specimens experienced different extent of plasticity in the chord wall. For Specimen KKBH-1 under AOCO load effects, it showed smaller connection efficiency ($P_u/P_p = 0.74$), developing remarkable chord plasticity before cracking and demonstrating very stable hysteresis loops after cracking. Only gradual drop in strength was noticeable when it underwent extremely large inelastic deformations. The connection efficiency was larger than one ($P_u/P_p = 1.1$) for Specimen KKBH-2 under ACAO load effects. In comparison with KKBH-1, KKBH-2 developed milder chord plasticity. The hysteretic curves of KKBH-2 exhibited a noticeable higher stiffness and pinching characteristics. After cracking, more significant strength decrease indicated lower energy dissipating capacity at large inelastic deformations. It is obvious that KKBH-1 developed more satisfactory levels of energy dissipation than KKBH-2, although the final failure modes for both specimens showed similar fracture initiated from the chord wall.

3.3 *Assessment of ductility*

Ductility of the joints can be assessed by calculating the ductility ratio from the moment-rotation skeleton curves of the specimens. The deflected shape of each brace in a CHS KK-connection and its dimensions and properties are shown in Figure 9. The vertical drift δ can be computed as the sum of the two deflection components shown in Figure 9, where δ_1 is vertical deflection caused by connection rotation in the intersection area, and δ_2 is vertical deflection caused by flexural deformations in the brace. The moment-rotation skeleton curves of KK-joints loaded by OPB are then obtained for determining the ductility ratio, as is listed in Table 3. The moment is taken at the chord surface at the crown position, and the joint rotation θ_j is acquired by dividing δ_1 (obtained as $\delta - \delta_2$) by the length of brace, L_b. The ductility ratio is defined as $\mu = \theta_{ju}/\theta_{jy}$, where θ_{ju} is assumed to be the rotation corresponding to ultimate connection strength and θ_{jy} is the yield rotation. It is observed that KKBH-1 demonstrated higher ductility ratio than KKBH-2, indicating AOCO load leads to better ductility of CHS KK-connections than ACAO load.

Table 4. Energy dissipation contribution before chord cracking.

Specimen	E_1/E_{total}	E_{total} (kN-mm)
KKBH-1	31%	26940
KKBH-2	47%	26745

3.4 *Analysis of energy dissipation mechanism*

Table 4 summarizes the ratios of the dissipated energy caused by chord wall and brace deformation before cracking, E_1, to the total energy dissipated during the test, E_{total}. This undoubtedly indicated different energy dissipation mechanisms. As can be seen from the table, the proportion of energy dissipation prior to the chord cracking of KKBH-1 is smaller than that after the chord cracking, with the major energy dissipation mechanism being crack propagation, along with chord plastic deformation before cracks occurred. While for KKBH-2, the proportion of energy dissipation prior to and after the chord cracking are almost the same, so its energy dissipation mechanism is different from that for KKBH-1, being contributed by the combinations of chord plastic deformation, brace plastic deformation and crack propagation.

Additionally, the initial crack propagation in the chord wall of two specimens (in particular KKBH-1) both showed ductile properties without inducing sharp decrease in the load bearing capacity. Thus the energy dissipation after the cracking can still be relied on to some extent for earthquake resistance.

4 CONCLUSIONS

Inelastic cyclic OPB loading laboratory experiments were designed and conducted on two full-scale CHS KK-connections. The strength efficiency of these connections under cyclic brace OPB moment was found to be significantly dependent on the loading patterns. Weak-brace-strong-connection behavior tended to emerge with CHS KK-joints under ACAO load effects, showing higher strength efficiency. However, AOCO load effects led to weak-connection-strong-brace behavior, thus showing lower strength efficiency.

CHS KK-joints under AOCO load effects developed more satisfactory levels of ductility and energy dissipation than that under ACAO load effects, although the final failure modes for both showed similar fracture initiated from the chord wall. This observation need to be attached importance to in seismic design of steel tubular structures.

Whatever the load pattern was, the initial crack propagation of the joints showed ductile properties without inducing sharp decrease in the load bearing capacity. Hence the energy dissipation after the cracking can still be relied on to some extent for earthquake resistance.

ACKNOWLEDGEMENTS

The presented work was supported by the Natural Science Foundation of China (NSFC) through Grant No. 51038008, Shanghai Pujiang Program through Grant No. PJ2010-00320, and the State Key Laboratory of Coastal and Offshore Engineering, Dalian University of Technology, through Grant No. LP1007.

REFERENCES

Chen YY & Zhao XZ. 2007. Experimental study on hysteretic behavior of CHS overlap K-joints and gap KK-joints. In: YS Choo, JY Richard Liew (eds). Proceedings of the 5th International Conference on Advances in Steel Structures. Singapore: Research Publishing.

Kurobane Y. 1998. Static behavior and earthquake resistant design of welded tubular structures. In: Jármai K & Farkas (eds). Mechanics and Design of Tubular Structures. Wien, Austria: Springer-Velag.

Soh CK, Fung TC, Qin F, Gho WM. 2001. Behavior of completely overlapped tubular joints under cyclic loading. Journal of Structural Engineering, ASCE 2001; 127(2): 122–128.

Wang W & Chen YY. 2007. Hysteretic behavior of tubular joints under cyclic loading. Journal of Constructional Steel Research 63: 1384–1395.

Wang W, Chen YY, Meng XD, Leon RT. 2010. Behavior of thick-walled CHS X-joints under cyclic out-of-plane bending. Journal of Constructional Steel Research 66: 826–834.

Wang W, Chen YY, Zhao BD. 2010. Cyclic test and analysis on CHS stiffened connections to box section girders with different details. In Ben Young (ed.), *Tubular Structures XIII: Proceedings of the 13th International Symposium on Tubular Structures, Hongkong, 15–17 December 2010*. Rotterdam: Balkema.

Yin Y, Han QH, Bai LJ, Yang HD, Wang SP. 2009. Experimental study on hysteretic behavior of tubular N-joints. Journal of Constructional Steel Research 65: 326–334.

Tubular Structures XIV – Gardner (Ed.)
© 2012 Taylor & Francis Group, London, ISBN 978-0-415-62137-3

A smart multi-spring assembling model for simulation of hysteretic behavior of unstiffened CHS X-Joint

B.D. Zhao
State Key Laboratory for Disaster Reduction of Civil Engineering, Tongji University, Shanghai, China
Zhejiang University of Technology, Hangzhou, Zhejiang, China

Y.Y. Chen
State Key Laboratory for Disaster Reduction of Civil Engineering, Tongji University, Shanghai, China

ABSTRACT: In single layered lattice steel tubular structures with large spans, CHS X-joint is one of common configurations for the connection of structural members. The main components of internal forces existing at the end of members surrounding the joint include axial force and bi-directional moment. The interaction of those internal forces is complicated especially when the joint zone develops large plastic deformation. In order to study the non-linearly dynamic behavior of the structure, an efficient model for numerical analysis is required.

A smart multi-spring model applicable to CHS X-joint is developed. In the model, the joint zone of CHS chord member is replaced with two assemblages of multi-springs. One assemblage is corresponding to one connection of chord member to a branch member. Each spring is assigned a non-liner load-deformation skeleton curve and restoring force rule, while the key indices about the skeleton curve and the restoring force rule can be determined by the geometry size of CHS members and the steel strength and elastic modulus. In the paper, the validation of the proposed model is demonstrated by the comparison with the results of hysteretic loading test on CHS X-type joint, and with the results of precise FEM analysis. Such a model can be used for time-history analysis of earthquake response of large scale structure, if the effect of non-linear property of joint on the behavior of whole system has to be taken into account.

1 INTRODUCTION

X-joint is one of common configurations for the connection of structural CHS members in single layered lattice steel tubular structures with large spans. The unstiffened tubular joint makes its behavior non-rigid in many cases (Wang 2005). In general, the main components of internal forces existing at the end of members surrounding the X-joint include axial force, out-of-plane and in-plane moment. Here, the curved surface formed by member axes is taken as the structural plane. Vertical vibration due to earthquake plays main role in seismic response of single layered lattice structure with large spans, especially in the structure featured in small curvature which makes the geometry form of the roof close to a plane. However, the in-plane moment is relatively small and can be neglected; hence, the main components of internal forces surrounding the X-join can be further reduced two: axial force and out-of-plane moment.

So far, the previous study focused on the hysteretic behavior of unstiffened tubular joints subjected to axial force (Kurobane 1998, Qin et al. 2001, Wang & Chen 2007), few on the out-of-plane bending hysteretic behavior (Meng 2009). Though numbers of hysteretic models have been proposed for beam-to-column connection, relatively few are available for unstiffened joint. Meng suggested a hysteretic model for unstiffened CHS X-joint under out-of-plane bending (Meng 2010). The moment–rotation (M–ϕ) skeleton curve of the model adopted Menegotto-Pinto curve (a classical kind of constitutive relations for steel), and its restoring force rule adopted kinematic hardening. The limitation of the model is that it cannot directly reflect the influence of axial forces on the moment-rotation behavior of the joints. Up to present, few models considering interaction of bending moments and axial forces for unstiffened tubular joint.

Referring to the multi-spring assembling model used in beam-to-column joints and the component method recommended by EC3 (Eurocod3 part 1.8, 2002), this paper proposes a four-spring model for unstiffened CHS-X joint. The stiffness matrix of the model is deduced and the key parameters of the model are studied. The model can consider interaction of out-of-plane bending and axial force.

2 CONSTITUTION OF THE MULTI-SPRING MODEL FOR CHS X-TYPE JOINT

2.1 *General multi-spring mechanical model*

With regard to the unstiffened CHS joints with only one branch such as T-type and Y-type joint, the

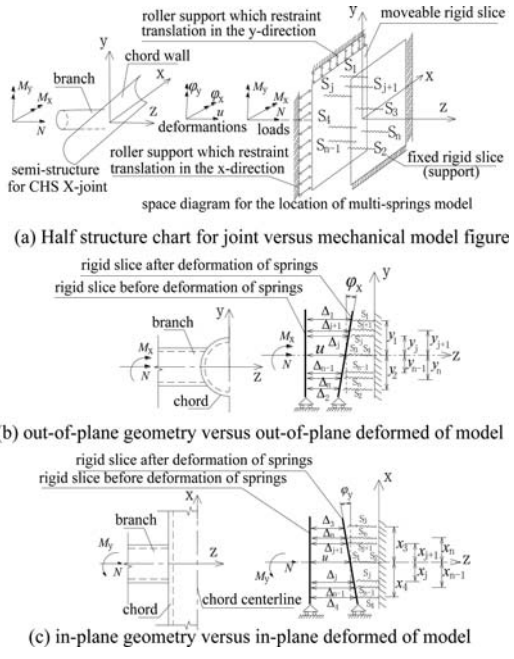

Figure 1. Generalized mechanical model for CHS joints.

generalized multi-spring model is depicted in Figure 1. For the sake of simplification, the branch connected to the joint is taken as a portion of member and the chord wall is defined as joint zone in the model. The model contains two rigid slices located in the chord central line (support slice) and the chord surface (the moveable slice restraining the shear deformation and torsion). These two rigid slices are linked by a series of parallel springs. Each of the spring is denoted as S_i and its stiffness as k_i, whilst x_i and y_i are the horizontal and vertical distances of spring i in the defined coordinates as shown in Figure 1. Among the springs, four are arranged in the x and y axis of the coordinates, in both positive and negative direction; and the others are in the different quadrants. The model is based on the following assumptions:

1) The branch section on the interface with chord keeps its shape stiff, like the plane keeping assumption in beam theory;
2) Small deflection, thus having the approximation of $\sin\phi = \phi$ and $\cos\phi = 1$, where, ϕ is rotation;
3) The impact of bi-directional shear and torsion deformation on the axial spring can be ignored.

Corresponding to the components of internal forces at the end of branch, the axial force N, out-of-plane moment M_x (or M_o) and in-plane moment M_y (or M_i), the relevant axial deformation and rotation are set as u, ϕ_x (ϕ_o) and ϕ_y (ϕ_i) respectively. Deformation of each spring in the model system can be evaluated on the basis of geometrical relationship as shown in Figures 1a, b, c. The stationary potential energy principle and small deflection assumption are used to establish

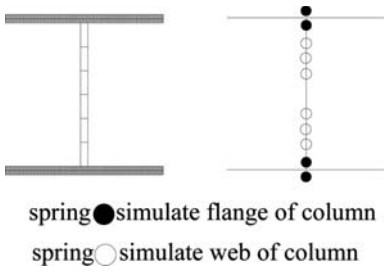

Figure 2. Multi-spring model for H-section column.

the equilibrium equations which can be illustrated as Equation 1:

$$dF = \left[K_{ij}\right]_{3x3} d\lambda \tag{1}$$

Where $dF = \{dN,\ dM_o,\ dM_i\}^T$ is the incremental load vector at the joint, dN, dM_o and dM_i are axial load increment and out-of-plane and in-plane bending moment increment respectively; $d\lambda = \{du,\ d\phi_o,\ d\phi_i\}^T$ is the increment deflections at the joint, du, $d\phi_o$ and $d\phi_i$ are increments of axial and out-of-plane and in-plane rotational deformations respectively; $[K_{ij}]_{3\times 3}$ is the model stiffness matrix with the form as Equation 2:

$$\left[K_{ij}\right]_{3x3} = \begin{pmatrix} \sum_{j=1}^{n} k_j & \sum_{j=1}^{n} k_j y_j & -\sum_{j=1}^{n} k_j x_j \\ \sum_{j=1}^{n} k_j y_j & \sum_{j=1}^{n} k_j y_j^2 & -\sum_{j=1}^{n} k_j x_j y_j \\ -\sum_{j=1}^{n} k_j x_j & -\sum_{j=1}^{n} k_j x_j y_j & \sum_{j=1}^{n} k_j x_j^2 \end{pmatrix} \tag{2}$$

It is clear that the items out of the main diagonal line of the stiffness matrix associates with the interaction between the axial and the rotational deformations.

2.2 *A simple, practicable and relative smart model with four-springs assembling for CHS X-joint*

Obviously, the generalized multi-spring model described in Section 2.1 with many variables to be determined, including the spring number, type, location and constitutive rule (namely, rigidities and strengths at each bearing phase). Generally, the more the types and numbers of springs, the more accuracy the model can be expected. But, the number of conditions used to determine the variables are limited, and it shall be very difficult to determine too many parameters. Hence, it is important issue to look for a balance between the validity, accuracy and simplicity of the model.

Figure 2 shows multi-spring model used for simulation of the hysteretic behaviors of H-section column considering local buckling (Chen 1994), and Figure 3 shows the semi-rigid connection characteristic of beam-column joint (Tschemmernegg & Humer 1988) which based on component method. In those models,

the springs and other elements are clearly corresponding to the structural components or part of the physical objectives according to the constructional details of the joint, as flange plate is one component for H-section column and bolt is one component for beam-column joint. Hence, the locations and constitutive relation of springs in those models can be determined by the component itself directly (named direct method); for example, bolt as one type of spring in the model, the location of the spring is bolt's geometric location in the beam-column joint and the constitutive relation of the spring can be obtained by tension test with bolt. By contrast with the above model, the directly physical relation of spring in CHS model to the structural component of unstiffened CHS joint is almost impossible because of its special connection feature. Hence, as for the multi-spring model of unstiffened tubular joints, the locations and constitutive relation of the springs should be determined not by direct method but by other ways. On the other hand, the assembled model must be able to accurately predict the general force-deformation relationship of unstiffened tubular joint under various kind loads. How to determine the locations and mechanical rule of every spring becomes key point for establishment of the model.

In order to solve the problem, an inverse deducing method is proposed in this paper. The key concept of this method is to set the number of springs in advance, and determine the related parameters for every spring. These related parameters are deduced by generalized force-deformation curves from unstiffened tubular joints under single load component, compressive or tensile axial force, in-plane or out-of-plane moment, respectively.

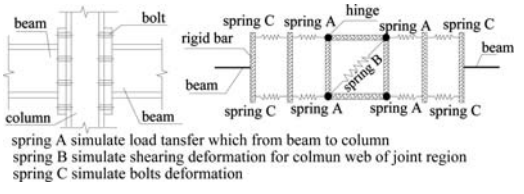

Figure 3. Multi-spring model for beam-column bolted joints.

So, the premise condition for determination of spring parameters is accurate FEA result. The generalized non-linear force-deformation curves of unstiffened X-type joints are acquired by adopting FEM software ABAQUS (2007). The smooth non-linear curves are then replaced with tri-linear lines (Fig. 4) for simplicity in succedent analysis. The first turning point of the tri-linear lines, point A, nominated as yield point, is determined according to Kurobane rule (Kurobane et al. 1984). The second turning point, point B, nominated as ultimate point, is determined by that the maximum plastic strain of chord wall near to joint region attains to about 0.1, referring to the ultimate deformation principle by Lu (Lu et al. 1994) and the ultimate rotation principle by Yura (Yura et al. 1980) under moment bending.

The main consideration and procedure to determine the details of the multi-spring model are described as followings:

(1) To preset the numbers and types of springs based on the consideration with minimum numbers and types of the springs as possible if the required accuracy of prediction can be obtained. With regard to the two main components of internal force taken into account, axial force and out-of-plane moment, for unstiffened X-type tubular joint, the necessary number of springs could be four and the constitutive relation types could be two. Among them, one pair of springs called out-of-plane spring, the function of which is mainly used to meet the balance of out-of-plane moment; cooperative with the out-of-plane spring, the second pair called in-plane spring is mainly used to meet the balance condition against axial force. Accordingly, the generalized multi-spring model mentioned in Section 2.1 is thus simplified to a four-spring assembling model (Fig. 5). Referring to Figure 5, S1 and S2 are classified as out–of-plane springs, S3 and S4 classified as in-plane springs, x and y are locations of springs.
(2) To suppose the constitutive relation for every spring is tri-linear (Fig. 6).
(3) To satisfy the equilibrium condition of joint under single load component in yielding and ultimate stage by the corresponding spring, thus, the

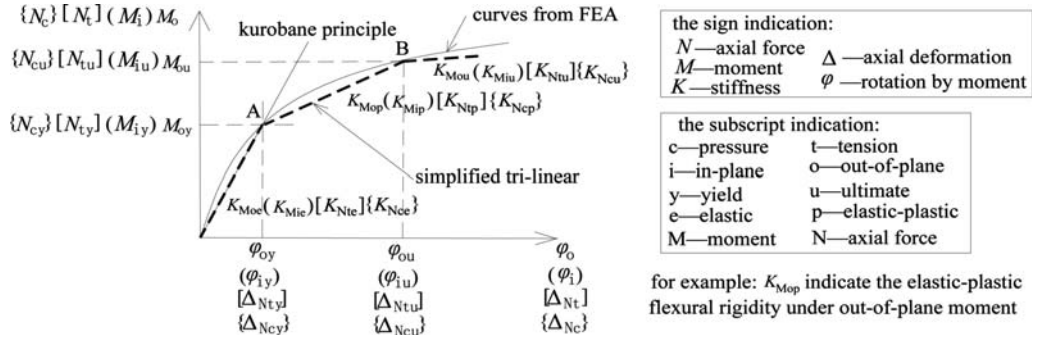

Figure 4. Load-deformation curves and its tri-linear simplification.

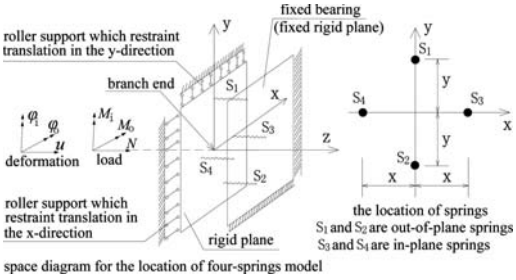

Figure 5. The four-spring model for CHS X-joints.

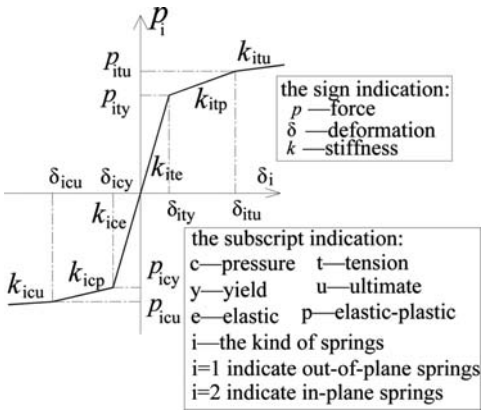

Figure 6. Constitutive relation for spring of the model.

corresponding yield and ultimate strength of the spring can be decided. For example, the out-of-plane spring at compressive side (the spring S1 in Figure 5) first enter into compressive yield when out-of-plane moment reaches yield value. Analogously, the yield and ultimate status under axial tension (or compression) for the joint are used to decided by the tension (or compression) yield and ultimate strength of in-plane springs.

(4) To set the position coordinate of each spring in accordance with the deformation compatibility condition, geometrical condition and the other supplementary condition necessary. For example, according to above item (3), next condition is necessary, $\Delta_{Ncy} = \delta_{2cy} < \delta_{1cy} = y\phi_{oy}$; here, Δ_{Ncy}, δ_{2cy}, δ_{1cy}, y and ϕ_{oy} are yield deformation of the joint under axial compression, deformation at compressive yield of in-plane springs, deformation of out-of-plane springs when they compressively yield, coordinate in y axis of out–of-plane spring, and yield rotation under out-of-plane moment for the joints, respectively. Then, a coefficient ξ (assumed greater than 1) is introduced; thus y is expressed as $y = \xi\Delta_{Ncy}/\phi_{oy}$. To obtain a proper position coordinate y, the model should avoid some invalid behavior, for example, in-plane springs arrive at ultimate strength while the out-of-plane springs still keep in elastic stage. Also is it required that the extent of yield deformation of in-plane springs should be less than that of the counterpart of out-of-plane springs. The consideration and comparison finally result in the value ξ as 1.05.

(5) To determine the stiffness of springs. As for the initial stiffness, it is assumed that elastic stiffness in tension and compression is identical, i.e., $k_{ite} = k_{ice} = k_{ie}$, referring to Figure 6, which is meant that the slight difference between tension and compression due to non-linear behavior in elastic stage is neglected here. According to the property of diagonal element in stiffness matrix referring to Equation 2, the elastic stiffness of the springs can be determined by the specific load such as axial force, in-plane moment and out-of-plane moment. For example, the elastic stiffness of out-of-plane and in-plane springs are, respectively calculated by the formula: $k_{1e} = K_{Moe}/2/^2y$ and $k_{2e} = K_{Ne}/2 - k_{1e}$.

Followed by the above procedure, the compressive and tensile yield strength p_{1cy} and p_{1ty} of out-of-plane springs (as well as p_{2cy} and p_{2ty} of in-plane springs) and the location of in-plane springs x can be calculated by follow Equations: $p_{1cy} = M_{oy}/2y$, $p_{2cy} = k_{2e}\Delta_{Ncy} = N_{cy}k_{2e}/2/(k_{1e} + k_{2e})$, $p_{1ty} = p_{1cy}N_{ty}/N_{cy}$, $p_{2ty} = k_{2e}\Delta_{Nty} = N_{ty}k_{2e}/2/(k_{1e} + k_{2e})$, $x = {}^{0.5}(K_{Moe}/2/k_{2e})$.

For determination of else parameters, such as ultimate strength and elastic-plastic stiffness for the two kinds of springs, the other conditions are established by the author, but the complex and tedious work is omitted in this paper.

The above principle and procedure are not only appropriate for one branch CHS joint, but also can be used for the one-plane or slight curved X-type CHS joint so long as the interaction of two branches on the joint zone of chord is not distinguished.

3 DETERMINATION OF THE KEY INDICES IN SKELETON CURVE AND HYSTERETIC RULE FOR NON-LINEAR SPRING

3.1 *Key indices for skeleton curve of springs*

In this section, the restoring model is discussed. Section 2.2 establishes the general relation between the indices of tri-linear constitutive rule of springs in the model and the mechanical performance of the joint. Actually, the constitutive relation will be treated as skeleton curve for restoring model. However, for practical application, the indices of the spring model should be expressed by the joint parameters both of material and geometry. The joint parameter relating material properties are the yield strength of the chord, f_y, and the steel modulus; and the non-dimensional geometrical parameters of the joint include β (diameter ratio of branch to chord), γ (ratio of chord radius to its thickness) and θ (the angle between branch and chord in the plane). The other geometrical parameters are the angles between the axes of branches and chord

members out of curved surface. Since only slight curved structure is taken into account in this paper, the influence of the out of curved surface angle can be neglected.

A great deal of non-linear FEA for the joints is carried out and a mass of data for calibration of the key indices of the skeleton curve are available. By multiple non-linear regression technique, the equations about the key indices of skeleton curves are then summarized based on the joint parameters. The expression of spring position coordinates also uses the geometry parameters of joint. The results are showed as Equation 3.

$$y = D\times\exp\{-0.589-2.798\beta+0.81\ln\gamma-4.02\beta^2 -0.085(\ln\gamma)^2-0.774\beta\ln\gamma\} \quad (3a)$$

$$x = D\times\exp\{-2.681+2.217\sqrt{\beta}+0.082/\ln\beta +0.091(\ln\gamma)^2\}\times(\sin\theta)^{0.327} \quad (3b)$$

$$k_{1e} = \exp\{(-13.21+59.775\beta-109.946\beta^2+63.106\beta^3 -6.164\ln\gamma)\div(1+2.354\beta+0.058\ln\gamma)\} \times(\sin\theta)^{(-3.478+4.7\beta+0.194\ln\gamma-1.168\beta\ln\gamma)}\times ED \quad (3c)$$

$$k_{2e} = \exp\{[-1.81+0.634\beta+1.995\beta^2-1.747\ln\gamma +0.403(\ln\gamma)^2]\div[1-0.203\beta-0.081\beta^2-0.186\ln\gamma]\} \times(\sin\theta)^{(-2.524+0.995\beta-0.261\ln\gamma+0.49\beta\ln\gamma)}\times ED \quad (3d)$$

$$p_{1cy} = \exp\{-3.92+6.085\beta-2.272\ln\gamma -4.237\beta^2-0.026(\ln\gamma)^2+1.107\beta\ln\gamma\} \times(\sin\theta)^{(-2.236+2.142\beta+0.326\ln\gamma-0.912\beta\ln\gamma)}\times f_yD^2 \quad (3e)$$

$$p_{1ty} = p_{1cy}\times\exp\{-1.293-3.397\beta\ln\beta +1.277\beta^3+0.005\gamma\ln\gamma\} \quad (3f)$$

$$p_{2cy} = \exp\{-2.212-\beta-0.468\ln\gamma+2.927\beta^2 -0.824\beta\ln\gamma-0.186(\ln\gamma)^2\} \times(\sin\theta)^{(-1.957+0.688\beta+0.227\ln\gamma-0.287\beta\ln\gamma)}\times f_yD^2 \quad (3g)$$

$$p_{2ty} = p_{2cy}\times\exp(-1.293-3.397\beta\ln\beta +1.277\beta^3+0.005\gamma\ln\gamma) \quad (3h)$$

$$k_{1cp} = k_{1e}\times\exp\{-4.26-10.33\beta\ln\beta+2.521\ln\beta +0.153\gamma/\ln\gamma\}\times(\sin\theta)^{(2.825-5.056\beta-1.282\ln\gamma+2.474\beta\ln\gamma)} \quad (3i)$$

$$k_{1tp} = k_{1e}\times\exp\{-4.967+9.879\beta-8.495\beta^2 +0.11(\ln\gamma)^2\}\times(\sin\theta)^{(3.038-5.089\beta-1.25\ln\gamma+2.119\beta\ln\gamma)} \quad (3j)$$

$$k_{2cp} = k_{2e}\times\exp\{-7.296-8.229\beta\ln\beta+3.738\beta^{1.5} -0.066\gamma+0.504\gamma/\ln\gamma\} \times(\sin\theta)^{(-2.993+7.354\beta+1.266\ln\gamma-2.66\beta\ln\gamma)} \quad (3k)$$

$$k_{2tp} = k_{2e}\times\exp\{-2.248+0.163\beta^2 +0.046(\ln\beta)/\beta^2+0.171(\ln\gamma)^2\} \times(\sin\theta)^{(-2.582+6.918\beta+1.205\ln\gamma-2.827\beta\ln\gamma)} \quad (3l)$$

$$p_{1cu} = \exp\{-2.706+4.258\beta-2.084\ln\gamma -2.424\beta^2-0.016(\ln\gamma)^2+0.677\beta\ln\gamma\} \times(\sin\theta)^{(-0.79-0.02\beta-0.1811\ln\gamma)}\times f_yD^2 \quad (3m)$$

$$p_{1tu} = \exp\{-2.745+4.23\beta-2.055\ln\gamma-2.673\beta^2 -0.021(\ln\gamma)^2+0.87\beta\ln\gamma\} \times(\sin\theta)^{(-0.626-0.3\beta-0.1971\ln\gamma)}\times f_yD^2 \quad (3n)$$

$$p_{2cu} = \exp\{-0.123+8.508\beta\ln\beta-2.149\beta^2 -0.773\sqrt{\gamma}+4.445/\sqrt{\gamma}\} \times(\sin\theta)^{(-2.892+2.795\beta+0.629\ln\gamma-0.996\beta\ln\gamma)}\times f_yD^2 \quad (3o)$$

$$p_{2tu} = \exp\{0.086+8.147\beta\ln\beta-1.992\beta^2 -0.716\sqrt{\gamma}+3.495/\sqrt{\gamma}\} \times(\sin\theta)^{(-2.627+2.554\beta+0.477\ln\gamma-0.842\beta\ln\gamma)}\times f_yD^2 \quad (3p)$$

where D is the diameter of the chord; E the elastic modulus of steel; the other parameters refer to Section 2.2.

For proper application of Equation 3, the parameter scope should be paid attention carefully, since the range of parameters adopted for FEA is limited. The valid scope of the parameter is as follows: $0.45 \le \beta \le 0.9$, $5 \le \gamma \le 25$, $0.4 \le \tau \le 1$, $45° \le \theta \le 90°$, τ is wall thickness ratio of branch to chord.

Also by the parametric analysis, the stiffness of springs in third portion of tri-line model shown in Figure 6 is determined by Equation 4.

$$\begin{cases} k_{1tu} = \lambda_1 k_{1e} \\ k_{2tu} = \lambda_1 k_{2e} \end{cases} \quad (4a)$$

$$\begin{cases} k_{1cu} = \lambda_2 k_{1e} \\ k_{2cu} = \lambda_2 k_{2e} \end{cases} \quad (4b)$$

If we take no account of the crack and post local buckling, the coefficient λ_1 can be adopted as 2%, and λ_2 as 1.5% when $\gamma \le 5$, while 0.2% when $\gamma \ge 25$, and linear interpolation between 0.2% and 1.5% when $5 < \gamma < 25$.

3.2 *The hysteretic rule for springs*

Referring to the hysteretic rule introduced by multi-spring model of H-section beam-column under the combined action of bending and compression, the curve illustrated in Figure 7 is adopted as restoring route which is applied to the springs of the four-spring model. Ramberg-Osgood function is used as the mathematical description of the restoring route. The unique technique of the model is that a 'shift coefficient', ψ, is introduced (Ohi, 1992). The hysteretic route shall change its shape with the increase of plastic deformation, thus the accumulated damage due to the plastic deformation can be reflected in the hysteretic behavior. The previous research found that when ψ was taken as 0.5, the hysteretic curve simulated test results well.

4 COMPARISON OF THE SIMULATION BY PROPOSED MODEL WITH TEST AND FEM ANALYSIS

In this chapter, the validation of the proposed model is demonstrated according to the comparison with the results of typical hysteretic loading test on CHS X-type joint, and with the results of precise FEA on the joint. The four-spring joint model is planted into a numerical analysis programming code JULIET developed by the author previously. Figure 8 graphically expresses the combination of the joint model with the beam-column element in the numerical program. Between nodes of intersection of member axes, the joint models are inserted within the center of the chord section and its wall in the direction of branch axis. For X-type joint, two joint models shall be settled in one node, in order to connect two branches. As a conceptual sketch, the shear and torsion spring separated from the four springs do not appear in the figure.

Figure 9a shows loading diagram for test (Meng, 2010). Each end of the chord was fixed on a support column extending to the laboratory base. The vertical cyclic loads (denoted as P) producing out-of-plane moment bending were applied synchronously through two actuators. Figures 9b, c illustrate the comparison between the result from finite shell element model analyzed by finite element package program ABAQUS, the proposed model and the test. It is the cases that the X-type joint were subjected to out-of-plane moment only. In the figure, the vertical axis indicates the out-of-plane moment which is equal to Pl_b referring to Figure 9a, and the horizontal axis indicates the corresponding rotation.. By the figure, the results from the proposed four-spring model are in relatively good agreement with that from the test before the occurrence of crack on weld during the test. And the proposed four-spring model obtained simulation curve almost same as that by fine shell FE model.

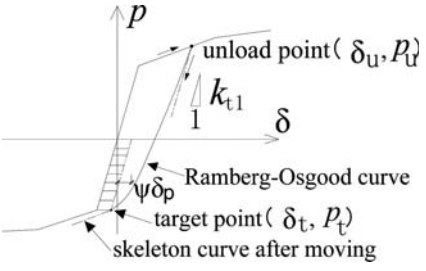

Figure 7. Skeleton curve and restoring-force model.

A series of parametrical analysis were performed. Figures 10 through 12 show two samples of them for the comparison of the simple four-spring model with FEA. The diameter of chord is set as 300 mm for all specimens. For FEA, program package ABAQUS is used with the S4R shell element to establish the fine FE model.

The loading condition of the joints which results are shown in Figure 10 is that the two branches of the joint are only subjected to identical out-of-moments. It can be observed that the hysteretic curves obtained by simple four-spring model and by precise FE model fit close, though with the increase of the rotation, there is a little difference.

Figures 11–12 show the joint response to combined loading condition of axial compression and out-of-plane moment on the branches. In the analysis, the loading path is taken the same as in the test, i.e, the axial compression is exerted at first to the given value,

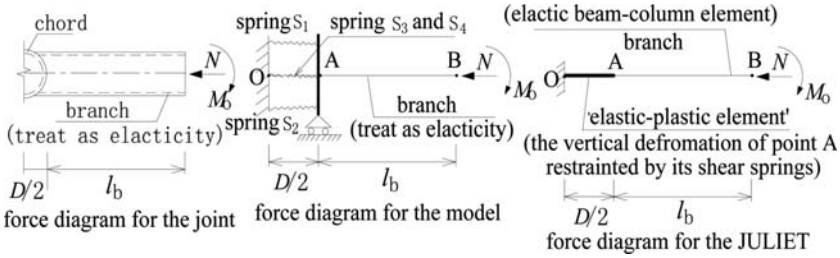

Figure 8. Hybrid model with member and CHS X-joint in JULIE.

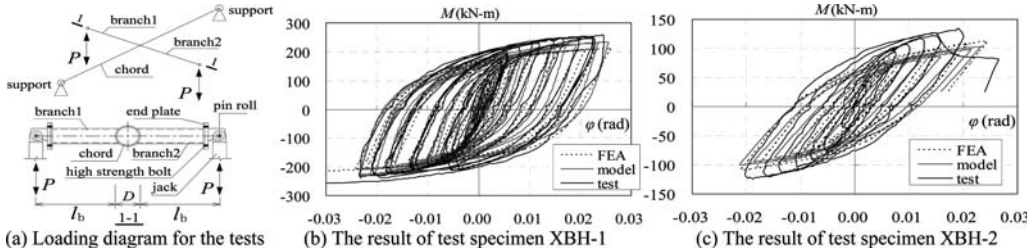

Figure 9. Test setup scheme and moment-rotation hysteretic curve comparison between test, FEA and the four-spring model.

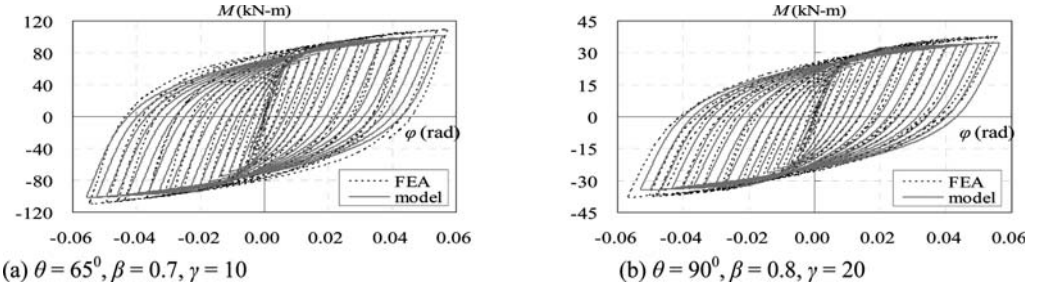

Figure 10. Moment-rotation hysteretic curve comparison between FEA and the model subjected out-of-plane bending only.

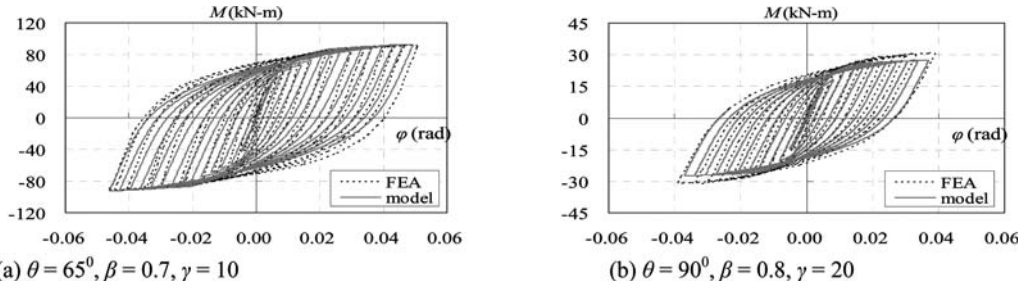

Figure 11. Moment-rotation hysteretic curve comparison between FEA and the model (axial pressure $N = 0.25N_{cu}$).

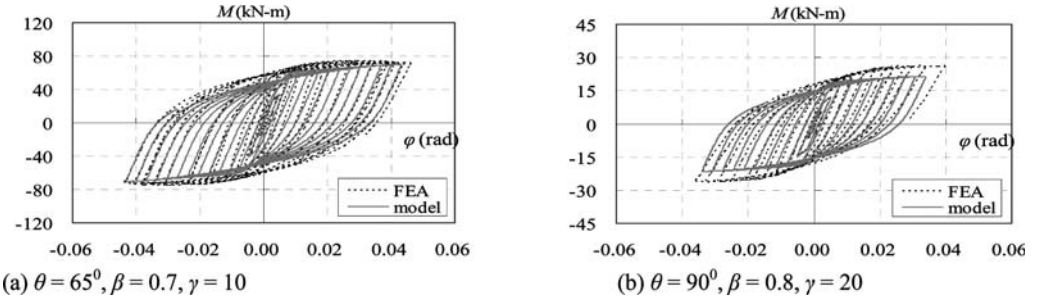

Figure 12. Moment-rotation hysteretic curve comparison between FEA and the model (axial pressure $N = 0.5N_{cu}$).

and then the moment is applied cyclically. Figure 11 is the result when the joint is subjected to branch axial compression as $0.25N_{cu}$, where N_{cu} is the design value of ultimate bearing capacity computed by Chinese steel design code (GB50017-2003, 2003) for CHS X-type joint when it is subjected to axial compression only. In computation, the design value of steel strength (f) by the code is replaced by nominal steel yield strength (f_y). The moment value in the figure is adopted that at an imagined corss-section through the crown point of interface with chord, and the second-order moment effect, i.e. the $P-\Delta$ effect is taken into account. The cases in Figure 12 are those where the branch axial compression is equal to $0.50N_{cu}$.

Figures 11, 12 and other compression reveal the following facts:

(1) The hysteretic curve predicted by simple four-spring model conforms with that by FEA quite well when axial compression is relatively small such as $0.25N_{cu}$, and the results shown in Figure 10 also support the estimation. On the other hand, with the axial compression becomes large, it can be seen that the difference exhibits a little big in the large deformation stage, as Figure 12 shown. But it can be considered accepted on the whole if we compare the results by two analysis models.

(2) By observation of Figures 11-12, it is found that the out-of-plane bending strength and rigidity are both declined to some extent with the increase of diameter-to-thickness ratio of the CHS joints. These cases also illustrate that the impact of axial pressure on the out-of-plane bending hysteretic behavior of CHS joint with thin-walled chord are more obvious than the counterpart of CHS joint with thick-walled chord.

5 CONCLUSIONS

In this paper, the main findings can be summarized as follows.

1. A general multi-spring mechanical model for simulation of hysteretic behavior of non-rigid CHS joint is established. The concept of the model is appropriate not only for the one branch CHS joints, such as T-type and Y-type joint, but also for certain multi-branch joint such as X-type joint. To overcome the difficulty that no obviously physical counterpoint of the model spring with the joint component, an inverse deducing method is proposed and applied to determine the key indices of the model springs according to the load-deformation relation of joint.
2. Apart from its simplicity, one of the advantages of the model is the ability to reflect the interaction of axial force and moments. Considering the character of unstiffened CHS X-type joint in single layered lattice structure with large spans and small curvature, the main components of internal forces at the end of branches surrounding the joint can be considered out-of-plane moment and axial force only under the action of vertical earthquake, thus the general multi-spring model can be simplified as four-spring model. Key indices for the skeleton curve of load-deformation relationship for every spring in the model are settled by the inverse deducing method based on the numerous FEA parametrical analysis and non-linear fitting regressive technique, and the hysteretic rule for the spring is also established.
3. By comparison with the test results and finite shell element model analysis, the proposed mechanical model is found to have satisfied ability to predict the hysteretic behavior of joint under combined loads of compression and out-of-plane moment, and with high efficiency. The model can be used in the non-linear dynamic analysis of tubular structures with T, Y and X-type CHS joints.

ACKNOWLEDGMENTS

The presented work was supported by the Natural Science Foundation of China with the grant No. 50578117.

REFERENCES

ABAQUS. 2007. ABAQUS analysis user's manual (version 6.6). Hibbitt, Karlsson, and Sorenson, Pawtucket, R.I

Chen, Y.Y., Shen, Z.Y., Ohi, K. et al. 1994. A numerical analysis model for steel columns subjected to cyclic varying axial load. *Journal of Tong Ji University* 22(4): 499–504

European Committee for standardization. 2002. *Eurocode 3: Design of steel structures, part 1.8–Design of joints* (PrEN 1993-1-8: 2002). London

Kurobane, Y. 1998. Static behavior and earthquake resistance design of welded tubular structures. *Mechanics and Design of Tubular Structures.* Wien, Austira: Springer-Velag: 63–116.

Kurobane, Y., Makino, Y. & Ochi, K. 1984. Ultimate Resistance of Unstiffened Tubular Joints, *Journal of structural Engineering* 110(2): 385–400.

Lu, L.H., Winkel, G.D., Yu, Y. et al. 1994. Deformation limit for the ultimate strength of hollow section joints, *Proc. Sixth International Symposium on Tubular Structures, Melbourne, Australia*: 341–7.

Meng, X.D., Wang, W., Chen, Y.Y. et al. 2009. Research on seismic behavior of unstiffened thick-walled tubular X-joints under out-of-plane bending. *Journal of Building Structures* 30(5): 126–131.

Meng, X.D. 2010. *Research on hysteretic behavior of unstiffened CHS X-joints under out-of-plane bending* (PhD thesis). Shanghai: Tong Ji University.

Ministry of Construction P.R.China. 2003. *Code for design of steel structures* (*GB50017-2003*). Beijing: China Planning Press.

Ohi, K. & Takanashi, K. 1992. *Stability and ductility of steel structures and cyclic loading* (Edited by Fukumoto, Y. & Lee, G.C), Osaka: CRC Press.

Qin, F., Fung, T.C. & Soh, C.K. 2001. Hysteretic behavior of completely overlap tubular joints. *Journal of Construction-al Steel Research* 57: 811–829.

Tschemmernegg, F. & Humer, C. 1988. The design of structureal steel frames under consideration of the non-linear behavior of joints. *Journal of Constructional Steel Research* 11:73–103.

Wang, W. 2005.*Non-rigid Behavior of Unstiffened Circular Tubular Joints and their Effects on Global Performance of Steel Tubular Structures* (PhD thesis). Shanghai: Tong Ji University.

Wang, W. & Chen, Y.Y. 2007. Hysteretic behaviour of tubular joints under cyclic loading. *Journal of Constructional Steel Research* 63: 1384–1395.

Yura, J.A., Zettlemoyer, N. & Edwards, I.F. 1980. Ultimate capacity equations for tubular joints, *Proc. Offshore Technology Conference* (Houston, Texas), Vol. 1, Paper No. 3690.

Tubular Structures XIV – Gardner (Ed.)
© 2012 Taylor & Francis Group, London, ISBN 978-0-415-62137-3

Parametric finite element analysis of the cyclic flexural behavior of hollow structural sections

M. Fadden & J. McCormick
University of Michigan, Ann Arbor, Michigan, US

ABSTRACT: Hollow Structural Sections (HSS) are highly efficient members which have been underutilized in cyclic bending application due to limited experimental testing. However, experimental testing has shown that HSS beam members can achieve desirable behavior if limiting values of the width-thickness (b/t) and depth-thickness (h/t) ratios are met. A finite element model (FEM), considering experimentally measured material properties, section geometry, and geometric imperfections, has been developed and calibrated based on experimental results. Using the calibrated FEM, a parametric study is conducted under cyclic loads with 133 different HSS beam members of sizes ranging from HSS $152.4 \times 50.8 \times 4.8$ to HSS $508 \times 304.8 \times 15.9$. The decrease of the maximum moment capacity (M_{max}) with cycling and rotational capacity at a given degradation of M_{max} are considered to provide insight into the interdependence of the b/t, h/t, and aspect ratios (h/b) on the cyclic bending behavior. Linear regression analyses of the results provide a means of predicting HSS beam member performance. From the analyses, equations for predicting the degradation of moment capacity and rotational capacity based on the b/t and h/t ratios are derived.

1 INTRODUCTION

1.1 *Background*

Steel seismic moment resisting frame (SMRF) systems are a common means of providing lateral load resistance in regions of high seismicity through the development of bending moments and shear forces in the frame members and joints (Nakashima et al. 2000). Hollow structural section (HSS) members have many desirable properties, such as favorable bending, compression and torsional resistance, which have initiated industry interest for their use in SMRF systems. This interest can be seen in the use of HSS for a variety of other structural applications including column members (hollow or concrete filled), bracing elements, truss elements, exposed structural steel, and cladding supports. In order to effectively use HSS as bending members for seismic applications, an understanding of their behavior under cyclic loading conditions must be obtained. However, most research has focused on axially loaded truss connections and connections between HSS or concrete filled tube (CFT) columns and wide flange beams, rather than HSS-to-HSS moment connections in cyclic bending (Hajjar 2000, Kurobane 2000, Packer 2000, Nishiyama & Morino 2004).

In particular, to be able to use HSS beam members in low-to-midrise HSS-to-HSS moment frame systems, it is necessary to determine whether HSS beam members can form stable plastic hinges under cyclic bending and identify limiting parameters resulting in local buckling prior to yielding. Several seismic design specifications, such as the American Institute of Steel Construction's (AISC) Seismic Design Specification (AISC 2005), require moment frames to be capable of achieving specified interstory drift levels without significant loss of capacity implying inherent ductility in the connections and members. AISC requires that moment connections in intermediate moment frame (IMF) systems and special moment frame (SMF) systems maintain at least 80% of their moment capacity under interstory drifts of 2% and 4%, respectively (AISC 2005, 2006). Previous studies have considered the use of HSS beam members under monotonically increasing loads and noted the importance of the width-thickness (b/t), depth-thickness (h/t), and aspect ratio (h/b) (Korol & Hudoba 1972, Hasan & Hancock 1988, Wilkinson & Hancock 1998). Recently, large-scale experimental testing of HSS beam members has considered their behavior under cyclic loading (Brescia et al. 2010, Fadden & McCormick 2012a). The cyclic testing results revealed similar trends as seen during monotonic testing of HSS and provided a preliminary understanding of possible limiting width-thickness ratios and depth-thickness ratios for stable hysteretic behavior.

In order to address the limitations of experimental testing, several researchers have utilized finite element models (FEM) to further understand HSS behavior. Most finite element studies of HSS in bending have considered the use of HSS in column applications. Nakashima & Liu (2005) used FEM to study HSS columns up to failure with varying axial load ratios and

found that the axial load ratio greatly affects the degradation of the hysteretic behavior. Other HSS models considered the behavior of CFT columns under cyclic loads using a fiber element model, which utilizes constitutive models for both the steel and concrete. The model also has the capacity to include effects of concrete core confinement and local buckling of the steel tube (Denavit et al. 2010). Models of HSS beam members under monotonic (Wilkinson & Hancock 2002) and cyclic (Fadden & McCormick 2012b) loads have also been developed considering experimentally measured material properties and imperfections of the section geometry. Both of these studies reiterate the importance of the b/t and h/t ratio on obtaining a stable cyclic behavior, while also demonstrating a need for further exploration of the overall hysteretic behavior and limiting values.

1.2 *Objective*

The parametric analytical study described in this paper addresses the current limited amount of experimental data on the cyclic bending behavior of HSS members by considering 133 cyclically loaded HSS beam members with a previously calibrated finite element model. The model, which was calibrated to eleven cyclically tested experimental beam sections using measured material properties and geometric imperfections, has been shown to be accurate in capturing the hysteretic behavior (Fadden & McCormick 2012b). The parametric study considers the effect of geometric properties, including the b/t, h/t, and h/b ratio, on the hysteretic behavior and the degradation of the overall maximum moment, M_{max}, with continued cycling. Plots of degradation behavior versus the h/t and b/t ratios provide insight into the interdependence of the geometric properties on the reduction in hysteretic moment capacity with continued cycling. A linear regression analysis allows for predictions of the degradation behavior and rotation capacity to be made, aiding in the selection of sections suitable for seismic design.

2 FINITE ELEMENT MODELING OF HSS

2.1 *Model setup*

The HSS members used in the parametric cyclic bending study are modeled using Abaqus FEA (Version 6.8-1) (DSS 2008). The geometry of each section, including the width, depth, and thickness is that which is reported in the AISC Manual of Steel Construction (AISC 2011). The corner radius is assumed to be twice the thickness of the specified section (Figure 1).

The boundary conditions for the model simulate a fixed-end cantilever beam. One end is completely fixed, while the opposite end is allowed to displace vertically according to the loading protocol. The loading protocol simulates the effect of a far field earthquake. The protocol begins with three small rotation levels, each consisting of six cycles, at increasing rotations ranging from 0.00375 rad. to 0.0075 rad. This

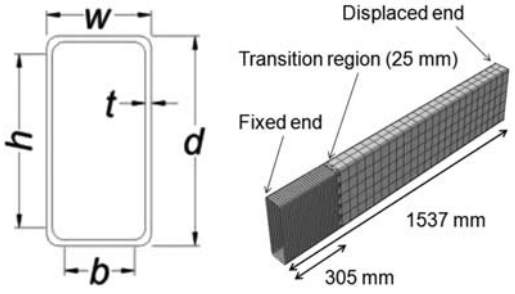

Figure 1. Typical cross-section with relevant properties labeled.

is followed by four cycles at 0.01 rad. The loading protocol finishes with a set of two cycles at eight different increasing rotation levels between 0.015 rad. and 0.08 rad.

The model mesh is divided into three sections for improved efficiency: the fixed end region, which spans from the fixed end to 304.8 mm from the fixed end; the 25.4 mm long transition region; and the displaced end region, which includes the rest of the beam. The entire beam is modeled using shell elements. The element mesh size is optimized through a convergence study. The fixed end region and displaced end region use rectangular elements of approximately 13 mm square and 50 mm square, respectively. Within these regions, S4R elements are used which are 4-node double curved thin or thick shell elements that use reduced integration, hourglass control, and consider finite member strains. The transition region utilizes S3 elements, which are 3-node general-purpose shell elements that consider finite membrane strains.

The calibrated finite element model utilizes material properties obtained from experimental tensile tests of the flats and corners of HSS members and includes a kinematic hardening law and no strain rate effects. The results of the material tests suggest that the stress-strain behavior for all sections is consistent. As a result for the finite element models, sections which are 7.9 mm or less in thickness use material properties from the HSS $203.2 \times 203.2 \times 6.4$ stress-strain behavior. The HSS $203.2 \times 203.2 \times 6.4$ has a yield stress, F_y, found using the 0.2% offset yield method, of 434 MPa and an ultimate strength, F_u, of 520 MPa for the flats and a F_y of 560 MPa and a F_u of 612 MPa for the cold worked corners. Sections that are 9.5 mm thick or greater use material properties from the HSS $203.2 \times 152.4 \times 9.5$ stress-strain behavior. The HSS $203.2 \times 152.4 \times 9.5$ has a F_y of 411 MPa and a F_u of 496 MPa for the flats and a F_y of 517 MPa and a F_u of 582 MPa for the corners (Fadden & McCormick 2012b).

2.2 *Model calibration*

In order to introduce a geometric instability into the HSS beam to better simulate local buckling and create a continuous buckling problem with no buckling

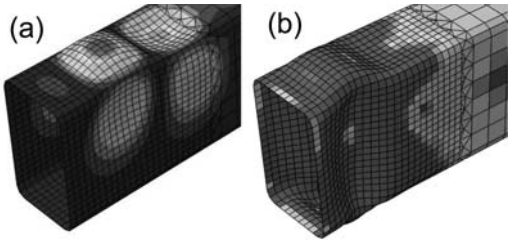

Figure 2. Typical (a) eigenvalue buckling analysis mode shape and (b) resulting buckled shape during cyclic bending loads.

bifurcation, geometric imperfections are added to perturb the mesh. The perturbations of the geometry are based on the mode shapes from an eigenvalue buckling analysis (Figure 2). The imperfections allow for buckling to initiate before the critical load is reached (DSS 2008). These perturbations cause the model to have a similar buckled shape to that observed during experimental testing of HSS in cyclic bending.

To calibrate the geometric imperfection, the magnitude of the imperfection is varied to find a value that minimizes the average difference between the experimentally recorded M_{max} (Fadden & McCormick 2012a) and the M_{max} of the finite element model for eleven sections which were previously tested experimentally. The calibration considered the effect of using no imperfection up to a maximum imperfection of 10.2 mm and found an optimal value to be 5.1 mm. However, some sections with $b/t \leq 14.2$ and $h/t \leq 19.9$ performed better when no imperfection was included because the model already under-predicted M_{max}. This can be attributed to the fact these sections had low b/t and h/t ratios and showed little buckling during experimental testing. For this reason, the calibrated model employed the following rule: when $b/t > 14.2$ and $h/t > 19.9$, a maximum imperfection of 5.1 mm is used, while all other sections with $b/t \leq 14.2$ and $h/t \leq 19.9$ used no imperfection.

Figure 3 shows a comparison of the experimental and finite element analysis hysteretic behavior for the HSS 203.2 × 152.4 × 6.4 and HSS 304.8 × 152.4 × 6.4 members. The results suggest that the finite element analyses, which include a 5.1 mm maximum imperfection, match relatively close to the experimental hysteretic behavior. The HSS 304.8 × 152.4 × 6.4 reached a maximum moment of 217.2 kN-m during experimental testing and 201.5 kN-m from the finite element analysis, showing relatively good correlation. The HSS 203.2 × 152.4 × 6.4 showed an even better correlation with the experimental results attaining a maximum moment of 115.6 kN-m during experimental testing and 117.6 kN-m from the analysis using the calibrated finite element model. Overall, these results are typical of the difference between the experimental and finite element analysis findings for all eleven specimens that were compared and used to calibrate the model.

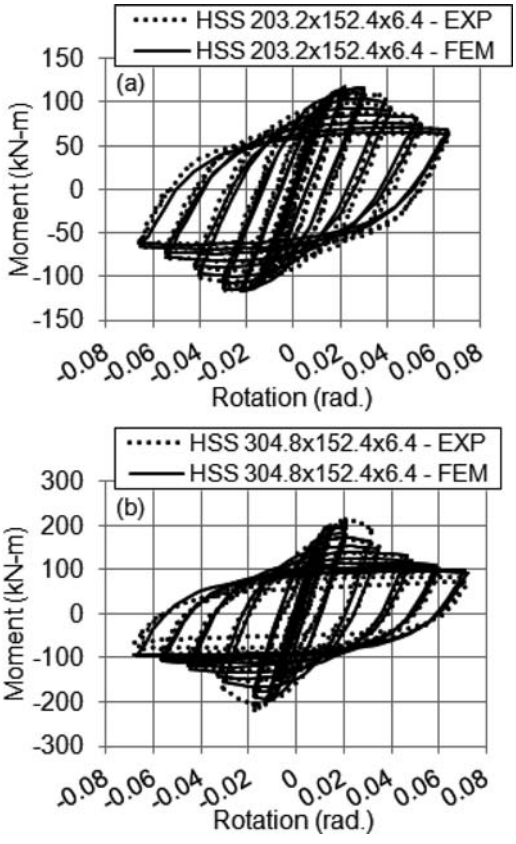

Figure 3. Comparison of the experimental and finite element analysis hysteresis for (a) HSS 203.2 × 152.4 × 6.4 and (b) HSS 304.8 × 152.4 × 6.4.

Table 1. Parameters and considered values.

Parameter	Values
w	50.8 mm–356 mm
d	129 mm–508 mm
t	4.8 mm–15.9 mm
b/t	7.0–31.5
h/t	16.4–52.0
h/b	1.0–5.23

2.3 *HSS parametric study specimens*

The parametric study considers 133 different HSS with a wide range of sizes and thicknesses (Table 1). The sections range in depth, d, from 129 mm to 508 mm; in width, w, from 50.8 mm to 356 mm; and in thickness, t, from 4.8 mm to 15.9 mm. This leads to consideration of section sizes between HSS 152.4 × 50.8 × 4.8 and HSS 508 × 304.8 × 15.9, including many sections smaller and larger than those that have been previously tested experimentally (Fadden & McCormick 2012a).

These sections have geometric properties that fall near the range of b/t and h/t ratios studied during previous experimental testing (Fadden & McCormick

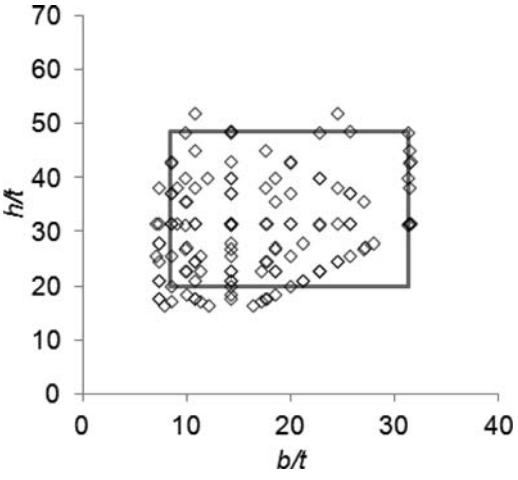

Figure 4. Dispersion of parametric study specimens with respect to their b/t and h/t ratios.

2012a), with the width-thickness ratio ranging from 7.0 to 31.5 and the depth-thickness ratio ranging from 16.4 to 52.0. Figure 4 shows the distribution of sections for the parametric study with respect to their b/t and h/t ratios. The limits for specimens which have been previously tested experimentally are given by the rectangle. This wide range of sections allows for consideration of many sections that might be suitable for use in seismic moment frames systems. This allows for a more detailed study of the limiting parameters on the formation of stable plastic hinges during cyclic bending.

3 HSS PARAMETRIC STUDY RESULTS

3.1 *Hysteretic behavior*

The moment-rotation hysteresis plots for all 133 sections are considered using the calibrated finite element model. From the parametric study, the section with the smallest M_{max} is the HSS $152.4 \times 50.8 \times 4.8$ with a value of 38.1 kN-m, while the HSS $508 \times 304.8 \times 15.9$ has the largest M_{max} of 1961.0 kN-m. Every section showed some degradation of the maximum moment with increased rotational demands. Between M_{max} and the maximum moment measured during the first cycle to 0.08 rad., the HSS $355.6 \times 254.0 \times 8.0$ ($b/t = 31.4$ and $h/t = 45.1$) had the largest decrease in maximum moment from 540.3 kN-m at 0.015 rad. to 207.4 kN-m at 0.08 rad., a reduction of 62% of the maximum moment. The HSS $304.8 \times 203.2 \times 15.9$ ($b/t = 7.33$ and $h/t = 17.7$) showed the smallest amount of degradation of M_{max} at a rotation level of 0.08 rad. with a decrease from 552.9 kN-m to 533.4 kN-m, a reduction of 9.8% of the maximum moment. The difference in the amount of degradation for each section can be attributed to the large difference in the b/t and h/t ratios for the two sections.

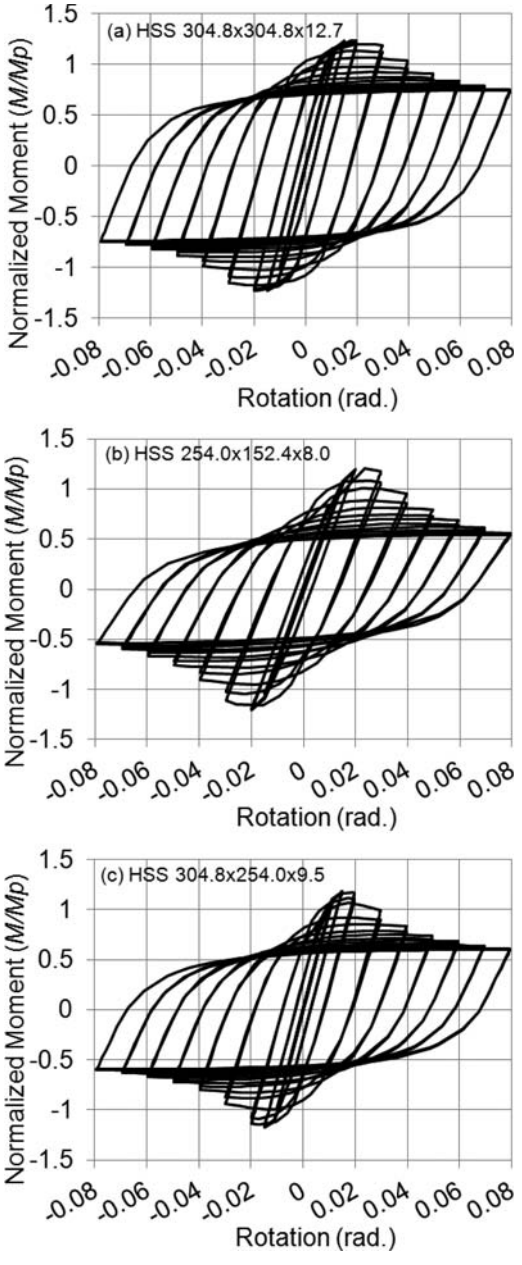

Figure 5. Moment-rotation hysteresis from the calibrated FEM for (a) HSS $304.8 \times 304.8 \times 12.7$, (b) HSS $254.0 \times 152.4 \times 8.0$, and (c) HSS $304.8 \times 254.0 \times 9.5$.

Normalized moment-rotation hysteresis plots are shown in Figure 5 for the HSS $304.8 \times 304.8 \times 12.7$, HSS $254.0 \times 152.4 \times 8.0$, and HSS $304.8 \times 254.0 \times 9.5$. The theoretical value of the plastic moment is determined using $M_p = F_y Z$, where F_y is obtained from the experimental coupon stress-strain curves used to model the material behavior of the section (Fadden and McCormick 2012b). The results from the finite element analyses clearly show that HSS

can produce stable hysteretic behavior over a range of sizes and that the degradation of the maximum moment is highly dependent on the local buckling behavior and geometric properties. Of the three sections, the HSS 304.8 × 304.8 × 12.7 reached the highest overall normalized moment of 1.24, while the HSS 304.8 × 254.0 × 9.5 had the lowest normalized maximum moment of 1.18. For all of the 133 considered sections, the normalized moment capacities are greater than 1.0 with a maximum of 1.40 and a minimum of 1.01. This indicates that all analyzed sections formed plastic hinges prior to the occurrence of local buckling. Comparing the three plotted sections, the HSS 304.8 × 304.8 × 12.7 had the highest M_{max} of 746.7 kN-m and the HSS 254.0 × 152.4 × 8.0 had the lowest M_{max} of 246.4 kN-m, well above their theoretical plastic moment capacities. This suggests that a large range of capacities are available for the use of HSS in seismic design.

Further, the three plotted sections allow for a comparison of the effect of the b/t and h/t ratios on the hysteretic behavior. A section with a moderate b/t and h/t ratio, such as the HSS 254.0 × 152.4 × 8.0 with a b/t of 17.6 and h/t of 31.4, shows consistent and stable degradation of the cyclic moment capacity throughout cycling to the maximum rotation of 0.08 rad. The HSS 304.8 × 254.0 × 9.5, with a higher b/t ratio of 25.7 and the same h/t ratio as the HSS 254.0 × 152.4 × 8.0, has a similar amount of degradation of M_{max} at 0.08 rad., but the loss of moment capacity is much faster. For example, at 0.04 rad. the HSS 245.0 × 152.4 × 8.0 loses 25.4% of M_{max}, while the HSS 304.8 × 254.0 × 9.5 loses 32.4% of M_{max}. The HSS 304.8 × 304.8 × 12.7 has only a slight increase in b/t ratio to 22.8 and a decrease in the h/t ratio to 22.8 compared to the HSS 254.0 × 152.4 × 8.0. The HSS 304.8 × 304.8 × 12.7 shows the most gradual reduction of moment capacity with cycling of the three sections shown in Figure 5. During the last cycle (0.08 rad.), the normalized moment capacity is considerably higher than the other sections shown with $M/M_p = 0.73$ compared to $M/M_p = 0.53$ for the HSS 254.0x152.4x8.0 and $M/M_p = 0.59$ for the HSS 304.8 × 254.0 × 9.5. Based on the comparison of the three example sections, it is clear that HSS beam sections can develop large stable hysteretic loops if the b/t and h/t ratios are limited. In addition, both the b/t and h/t ratios have an interrelated effect on degradation with continued cycling.

3.2 *Maximum moment and rotational capacity*

The degradation of the maximum moment capacity with cycling has been shown to be highly dependent on the b/t and h/t ratios. The effect of the geometric properties on the degradation of the maximum moment capacity can be quantified for the 133 modeled sections by considering the percent decrease of the maximum moment measured at the 0.04 rad. rotation cycle compared to the overall maximum moment for all cycles. The 0.04 rad. cycle is chosen because it will produce a rotation in the beam member greater than the 0.04 rad. interstory drift level required by seismic connection design guidelines (AISC 2005, 2006).

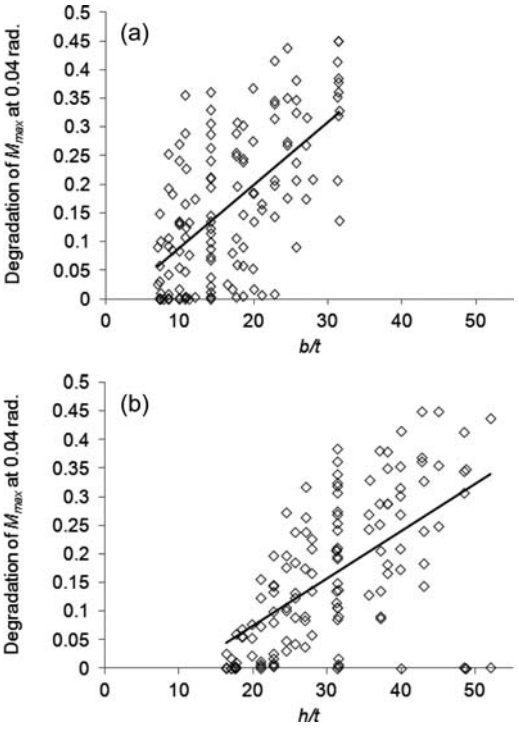

Figure 6. Degradation of M_{max} at 0.04 rad. with respect to (a) b/t and (b) h/t.

Figure 6 shows the percent degradation of M_{max} (in decimal form) for all modeled sections versus their b/t and h/t ratios. The HSS 355.6 × 254.0 × 8.0 has the largest degradation of the maximum moment at 0.04 rad., 44.9% of M_{max}. The average percent degradation of M_{max} at 0.04 rad. for all sections is 16.2%. Several sections show no degradation of M_{max} at a rotation of 0.04 rad., including the HSS 203.2 × 76.2 × 8.0, HSS 152.4 × 101.6 × 8.0, HSS 152.4 × 76.2 × 8.0, HSS 203.2 × 101.6 × 9.5, HSS 177.8 × 127.0 × 9.5, HSS 177.8 × 101.6 × 9.5, HSS 254.0 × 152.4 × 12.7, HSS 228.6 × 127.0 × 12.7, and HSS 304.8 × 152.4 × 15.9. These sections have average values of b/t and h/t of 8.7 and 18.5, respectively.

In each figure, a linear regression line is plotted which relates the b/t and h/t ratio to the percent degradation of M_{max} at 0.04 rad. (Equation 1 and 2). The linear regression shows that the degradation is affected by both the b/t and h/t ratio. Although, the b/t ratio appears to have a larger effect on degradation compared to the h/t ratio, their slopes are similar with values of 0.011 and 0.010, respectively. The linear regression analysis results suggest that a larger value of h/t causes less degradation in the moment capacity at 0.04 rad. than the same value of b/t. This implies that

the degradation of moment capacity is more dependent on the b/t ratio.

$$Deg_{0.04}(b/t)=0.011(b/t)-0.022 \quad (1)$$

$$Deg_{0.04}(h/t)=0.010(h/t)-0.155 \quad (2)$$

In addition to considering the degradation of a section at a specified rotation level, it is also useful to consider a rotation at which some percentage of M_{max} is preserved, such that stability of the plastic hinge is maintained through continued cycling up to this rotation level. In seismic design, strong column-weak beam requirements specify that a majority of the inelastic behavior occur in the beam member. For this study it is then useful to consider a rotation capacity at a reduction of 80% of M_{max}, a typical limit used to distinguish the required rotational capacity of seismic moment frame systems. This limit can then be extended to inter-story drift capacity in actual design if needed.

The rotational capacity plots shown in Figure 7 represent the rotation of the last cycle in which 80% of M_{max} is still retained. For the 133 modeled sections, the HSS 152.4 × 101.6 × 8.0, HSS 152.4 × 76.2 × 8.0, HSS 254.0 × 88.9 × 9.5, HSS 203.2 × 101.6 × 9.5, HSS 177.8 × 101.6 × 9.5, HSS 228.6 × 127.0 × 12.7, HSS 355.6 × 152.4 × 15.9, and HSS 304.8 × 152.4 × 15.9 did not degrade to 80% of their overall maximum moment capacity throughout the loading protocol. These sections had an average b/t and h/t of 8.7 and 13.6, respectively. The HSS 406.4 × 203.2 × 8.0 showed the fastest reduction in moment capacity, reaching 80% of M_{max} at the 0.022 rad. cycle. The average rotational capacity for all 133 sections is 0.045 rad. suggesting that many sections can achieve suitable behavior under large cyclic bending rotations.

Linear regression equations of the rotational capacity at 80% of M_{max} with respect to the b/t and h/t ratios are shown in Equations 3 and 4, respectively. The equations suggest an identical dependence on an increase in the b/t and h/t ratio, since the slope of each line is -0.0011. However, the b/t ratio tends to affect the rotational capacity more than the h/t ratio because a larger h/t ratio is required to cause the same amount reduction in rotational capacity.

$$\theta_{0.8M_{max}}(b/t)=-0.0011(b/t)+0.064 \quad (3)$$

$$\theta_{0.8M_{max}}(h/t)=-0.0011(h/t)+0.080 \quad (4)$$

Equations 1-4 allow for prediction of both the percent degradation of M_{max} at 0.04 rad. ($Deg_{0.04}$) and the rotational capacity at $0.8M_{max}$ ($\theta_{0.8Mmax}$). For each value, the equations for both b/t and h/t should be evaluated. When considering the percent degradation of M_{max} at 0.04 rad., the controlling value will be the maximum of Equations 1 and 2. When predicting the rotational capacity, the minimum value of Equations 3 and 4 should be chosen to find the maximum rotational capacity at which $0.8M_{max}$ is maintained.

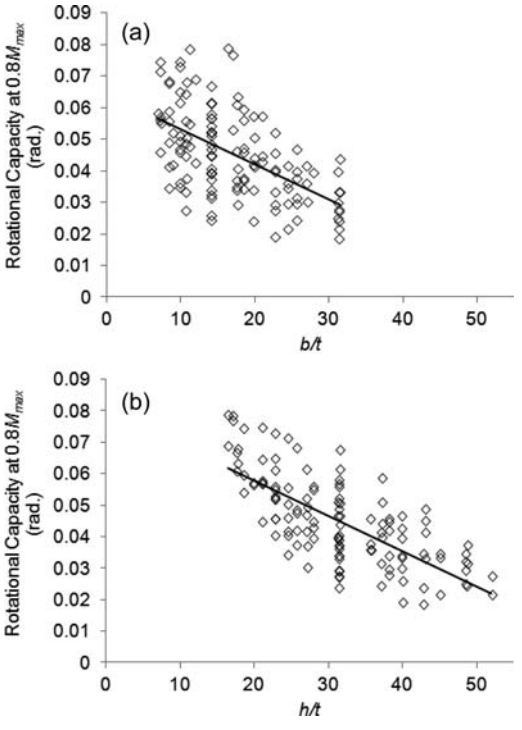

Figure 7. Rotational capacity at $0.8M_{max}$ with respect to (a) b/t and (b) h/t.

Figure 8 provides a graphical representation of Equations 1-4. The prediction of the degradation and rotational capacity is only considered for sections which fall within the bounds of the parametric study with respect to b/t and h/t (Table 1). Figure 8(a) shows that for most sections, Equation 1 will control the degradation of M_{max} at 0.04 rad. Similarly, when considering the rotational capacity at $0.8M_{max}$, Equation 3 controls for most sections producing a larger reduction in rotational capacity. In general, prediction of the degradation and rotational capacity using the b/t ratio will provide a more conservative estimate. These relationships provide a useful connection between the geometric properties and cyclic behavior. They can be utilized as a tool to predict the expected behavior of a section with continued cycling.

3.3 *Aspect ratio*

Previous studies have considered the effect of the h/b ratio on local buckling and degradation of the moment capacity (Wilkinson & Hancock 1998). Specifically, this research noted that an increase in h/b leads to higher h/t ratios and increased potential of local buckling in the web. For all 133 sections considered, the aspect ratio ranged between 1.0 for all square sections and 5.23 for the highly rectangular HSS 304.8 × 76.2 × 8.0. The aspect ratio is compared to

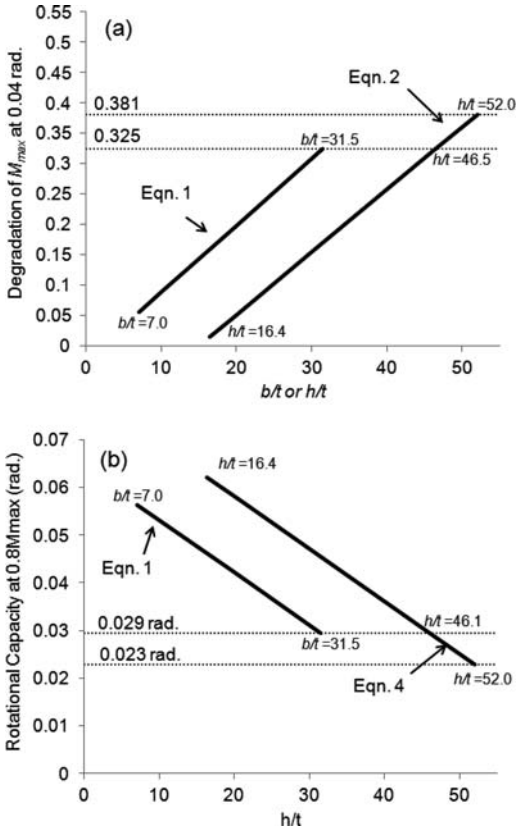

Figure 8. Prediction of the (a) degradation of the maximum moment at 0.04 rad. and (b) rotational capacity at $0.08M_{max}$.

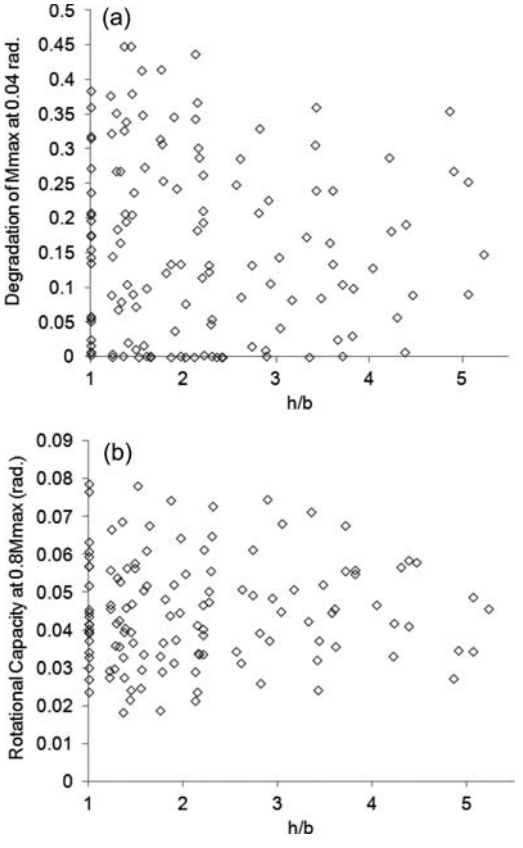

Figure 9. Effect of aspect ratio (h/b) on the (a) degradation of maximum moment and (b) the rotational capacity at $0.08M_{max}$.

the degradation of M_{max} at 0.04 rad. and the rotational capacity at $0.08M_{max}$(Figure 9) in a similar manner as the previous comparison for h/t and b/t.

Figure 9(a) displays the degradation of M_{max} at 0.04 rad. versus the h/b ratio. Based on the distribution of the data, it is clear that there is no correlation between the degradation of moment capacity and h/b. Considering Figure 9(b), data is not uniformly scattered suggesting that little correlation or trends exist between h/b and the rotation level at which the capacity decreases to $0.8M_{max}$. Based on these results, it is concluded that unlike the b/t and h/t ratio, which show a strong influence on the degradation of moment capacity, h/b does not affect the moment capacity with cycling. The results suggest that local buckling plays the most significant role in the change in moment capacity with continued cycling.

4 CONCLUSIONS

The results of a parametric finite element study of 133 different cyclically tested HSS beam members is presented. The parametric study utilizes a previously calibrated finite element model that includes geometric imperfections of the section geometry and experimentally measured material properties. All sections are cycled according to the same specified far-field type earthquake loading protocol. The effect of the b/t, h/t, and h/b ratios on the hysteretic behavior resulting from cyclic bending loads was considered with a focus on the degradation of M_{max} at the 0.04 rad. cycle and the rotational capacity at 80% of M_{max}.

The parametric study provided moment-rotation hysteresis curves for all sections. In general, all sections showed large open loops and stable, symmetric behavior. Like previous experimental testing, both the b/t and h/t affected the level of inelastic local buckling observed in the HSS beam member. The degradation of M_{max} at 0.04 rad. for the 133 sections was compared to the b/t and h/t ratios and it was found that an increase in the b/t ratio had a slightly larger effect on the degradation of M_{max} than an increase in h/t. Additionally, a smaller value of b/t than h/t causes the same amount of degradation of M_{max}. For the rotational capacity at $0.8M_{max}$, an increase in the b/t and h/t ratios was found to have the same reduction in rotational capacity. Again, it was found that a smaller b/t ratio causes the same decrease in rotational capacity as a larger h/tratio. Linear regression analyses provide equations to predict the degradation of moment

capacity and rotational capacity, which can be useful for design. Lastly, the aspect ratio (h/b) was found to have no correlation with the degradation behavior or a reduction in rotational capacity. These finding suggest that there are suitable HSS beam members that can be utilized for seismic moment frame systems.

ACKNOWLEDGEMENT

This work is supported by the BRIGE Program of the National Science Foundation under Grant No. EEC-0926858 and the American Institute of Steel Construction through the Faculty Fellowship. The views expressed herein are solely those of the authors and do not represent the views of the supporting agencies.

REFERENCES

AISC. 2005. *Seismic Provisions for Structural Steel Buildings*. Chicago: American Institute of Steel Construction.

AISC. 2006. *Seismic design manual*. Chicago: American Institute of Steel Construction.

AISC. 2011. *Manual of steel construction 14th ed.* Chicago: American Institute of Steel Construction.

Brescia, M., Landolfo, R., Mammana, O., Iannone, F., Piluso, V. & Rizzano, G. 2009. In Preliminary results of an experimental program on the cyclic response and rotation capacity of steel members. *In Proc. STESSA 2009, Philadelphia, PA*: Taylor & Francis Group.

Dassault Systemes Simulia Corp. 2008. *Abaqus FEA, Version 6.8-1, documentation collection.* Providence, RI: DSS.

Denavit, M. D., Hajjar, J. F., Perea, T. & Leon, R. T. 2010. Cyclic evolution of damage and beam-column interaction strength of concrete-filled steel tube beam-columns. *In Proc. 9th US National and 10th Canadian Conference on Earthquake Engineering, 25–59 July, 2010.* Toronto: EERI.

Fadden, M. & McCormick, J. 2012a. Cyclic quasi-static testing of hollow structural section beam members.*ASCE Journal of Structural Engineering* 138(5): in press.

Fadden, M. & McCormick, J. 2012b. *Finite element model of the cyclic flexural behavior of hollow structural sections. STESSA 2012, Santiago, Chile, 9–12 January, 2012*.

Hajjar, J.F. 2000. Concrete-filled steel tube columns under earthquake loads, *Progress in Structural Engineering and Materials* 2: 72–81.

Hasan, S. W. & Hancock, G.J. 1988. *Plastic bending tests of cold-formed rectangular hollow sections – Research report, no R586*: Sydney: School of Civil and Mining Engineering, The University of Sydney.

Korol, R. M. & Hudoba, J. 1972. Plastic behavior of hollow structural sections. *American Society of Civil Engineers Proceedings, Journal of the Structural Division* 98(ST5): 1007–1023.

Kurobane, Y. 2002. Connections in tubular structures. *Progress in Structural Engineering* 4: 35–45.

Nakashima, M. & Liu, D. 2005. Instability and complete failure of steel columns subjected to cyclic loading. *Journal of Engineering Mechanics* 131(6): 559–567.

Nishiyama, I. & Morino, S. 2004. US-Japan cooperative earthquake research program on CFT structures: achievements on the Japanese side. *Progress in Structural Engineering and Materials* 6: 39–55.

Packer, J.A. 2000. Tubular Construction. *Progress in Structural Engineering and Materials* 2: 41–49.

Wilkinson, T. & Hancock, G. J. 1998. Tests to examine compact web slenderness of cold-formed RHS. *Journal of Structural Engineering* 124(10): 1166–1174.

Wilkinson, T. & Hancock, G. J. 2002. Predicting the rotation capacity of cold-formed RHS beams using finite element analysis. *Journal of Constructional Steel Research* 58(11): 1455–1471.

Tubular Structures XIV – Gardner (Ed.)
© 2012 Taylor & Francis Group, London, ISBN 978-0-415-62137-3

Vibration analysis of tubular footbridges induced by human walking

G.L. Debona, J.G.S. da Silva, A.C.C.F. Sieira, P.C.G. da S. Vellasco & L.R.O de Lima
Civil Engineering Post-Graduate Programme, PGECIV
State University of Rio de Janeiro, UERJ, Rio de Janeiro, Brazil

ABSTRACT: The main objective of this investigation is to present the finite element modelling of the dynamic behaviour of tubular composite (steel-concrete) footbridges submitted to human walking vibrations. The investigated structural system was based on a tubular composite (steel-concrete) footbridge, spanning 82.5 m. The structural model consists of tubular steel sections and a concrete slab. This investigation is carried out based on correlations between the experimental results related to the footbridge dynamic response and those obtained with finite element modelling. The finite element model enabled a complete dynamic evaluation of the tubular footbridge in terms of human comfort and its associated vibration serviceability limit states. The peak accelerations found in the present analysis indicated that the investigated tubular footbridge presented problems related with human comfort. Hence it was detected that this type of structure can reach high vibration levels that can compromise the footbridge user's comfort.

1 INTRODUCTION

Tubular hollow sections are increasingly used in offshore structures, highway bridges, pedestrian footbridges, large-span roofs and multi-storey buildings due to their excellent properties and the associated advances in fabrication technology.

The intensive use of tubular structural elements in Brazil, such as the example depicted in Figure 1, mainly due to its associated aesthetical and structural advantages, led designers to be focused on their technologic and design issues.

Nowadays in Brazil, there is still a lack of code that deals specifically with tubular design. This fact induces designers to use other international tubular design codes. Consequently, their design methods accuracy plays a fundamental role when economical and safety points of view are considered. Additionally, recent tubular joint studies indicate that further research is needed, especially for particular geometries. This is even more significant for some failure modes where the collapse load predictions lead to unsafe or uneconomical solutions.

Figure 1. Example of a tubular steel pedestrian footbridge in Rio de Janeiro/RJ, Brazil.

Steel and composite tubular footbridges are currently subjected to dynamic actions with variable magnitudes due to the pedestrian crossing on the concrete deck. These dynamic actions can generate the initiation of fractures or even their propagation in the structure. Depending on the magnitude and intensity, these adverse effects can compromise the structural system response and the reliability which may also lead to a reduction of the expected footbridge service life.

Generally, fatigue assessment procedures are usually based on S-N curves which relate a nominal or geometric stress range S to the corresponding number N of load cycles to fatigue failure. In this situation fatigue assessment refers to the nominal stress range $\Delta\sigma$ in a tubular structural member.

The fatigue resistance is given according to a classification catalogue in the form of standardized S-N curves. Structural details classified in this catalogue, see e.g. Eurocode 3 Part 1.9 (2005), correspond specifically to a situation of stress range, direction, crack position, detail dimension and weld quality which had been characteristic for the tests on which the classification is based (Kuhlmann et al., 2003); (Leitão et al., 2011).

The use of circular hollow section members as part of the structure of pedestrian footbridges is a relatively new constructional concept. During the last couple years several steel-concrete composite footbridges had been constructed in Brazil, as illustrated in Figure 1.

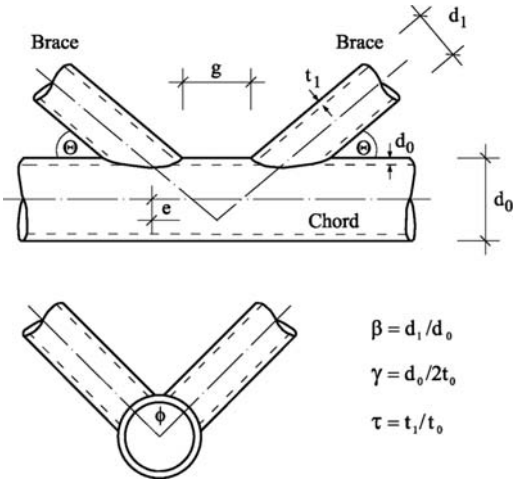

Figure 2. Typical multiplanar K-joint with notations.

The typical cross-section of this type of pedestrian footbridge generally consists of a tubular spatial truss girder carrying the concrete deck slab, as presented in Figure 1. The deck slab is connected directly to the steel structure by either shear studs, concrete dowels or in some cases where no top chord exists. At the bottom chord of the tubular space truss four brace members have to be connected to the continuous bottom chord. This type of joint is usually named K-joint, as depicted in Figure 2 (Kuhlmann et al., 2003).

Steel and composite tubular footbridges can be subjected to the material imperfections of its structural elements, such as mechanical and metallurgic discontinuities. Such defects lead to cracking in these structural elements. When these elements are subjected to dynamic actions, the fatigue phenomenon occurs and produces stress concentrations and possible fractures. These fractures are directly responsible for reducing the local or global footbridge stabilities or even its life service (Leitão et al., 2011).

On the other hand, the structural engineers experience and knowledge allied by the use newly developed materials and technologies have produced tubular steel and composite (steel-concrete) footbridges with daring structures.

This fact have generated very slender tubular steel and composite (steel-concrete) pedestrian footbridges and consequently changed the serviceability and ultimate limit states associated to their design. A direct consequence of this design trend is a considerable increase of structural vibrations (Bachmann & Ammann, 1987); (Chen, 1999); (Debona, 2011); (Figueiredo et al., 2008); (Leitão et al., 2011); (Murray et al., 2003); (Pimentel et al., 2001); (Silva et al. 2007); (Varela, 2004); (Zúñiga, 2011).

Considering all aspects mentioned before, the main objective of this investigation is to present the finite element modelling of the dynamic behaviour of tubular composite (steel-concrete) footbridges submitted to human walking vibration. Based on the results obtained in this study, a fatigue assessment will be performed, in order to evaluate the tubular footbridges service life. Further research in this area is currently being carried out.

The investigated structural model was based on a tubular composite (steel-concrete) footbridge, spanning 82.5 m. The structure is composed by three spans (32.5 m, 17.5 m and 20.0 m, respectively) and two overhangs (7.50 m and 5.0 m, respectively). The structural system consists of tubular steel sections and a concrete slab and is currently used for pedestrian crossing (Debona, 2011); (Zúñiga, 2011).

The proposed computational model adopted the usual mesh refinement techniques present in finite element method simulations, based on the ANSYS program (ANSYS, 2003).

The finite element model has been developed and validated with the experimental results. This numerical model enabled a complete dynamic evaluation of the investigated tubular footbridge especially in terms of human comfort and its associated vibration serviceability limit states (Debona, 2011); (Zúñiga, 2011).

This investigation is carried out based on correlations between the experimental results related to the footbridge dynamic response and those obtained with finite element models. The proposed computational model adopted the usual mesh refinement techniques present in finite element method simulations.

The structural system dynamic response, in terms of peak accelerations, was obtained and compared to the limiting values proposed by several authors and design standards (ISO 2631/2, 1989); (Murray et al., 2003).

The peak acceleration values found in the present investigation indicated that the analysed tubular footbridge presented problems related with human comfort. Hence it was detected that this type of structure can reach high vibration levels that can compromise the footbridge user's comfort and especially its safety.

2 HUMAN WALKING MODELLING

The present investigation was carried out based on a more realistic loading model developed to incorporate the dynamic effects induced by people walking. The loading model considered the ascent and descending movement of the human body effective mass at each step and the position of the dynamic load (human walking load) was also changed according to the individual position.

This dynamic loading model considers a space and time variation of the dynamic action over the structure that is evaluated. Additionally, also incorporates the transient effect due to the human heel impact, see Equations 1 to 4 (Varela, 2004).

The proposed mathematical model used to represent the dynamical actions produced by people walking on the floor slabs is not simply a Fourier series, due to the fact that the mentioned equations also incorporate the

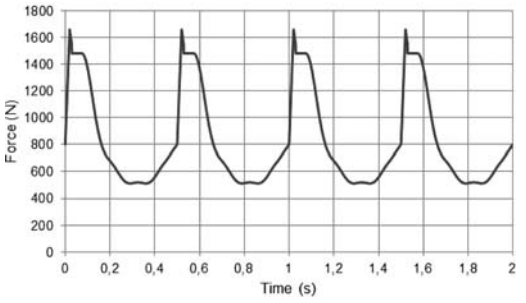

Figure 3. Dynamic load function for one person walking (f_s =2.0 Hz). Resonant harmonic of the walking load (3rd harmonic: 3 × 2.0 Hz = 6.0 Hz).

human heel impact effect (Varela, 2004); (Silva et al. 2007). The present investigation used a heel impact factor equal to 1.12 ($f_{mi} = 1.12$). However, it must be emphasized that this value can vary substantially from person-to-person (Debona, 2011); (Silva et al. 2007).

$$F(t) = \begin{cases} \left(\dfrac{f_{mi} F_m - P}{0.04 T_p}\right) t + P & if\ 0 \le t < 0.04 T_p \\ f_{mi} F_m \left[\dfrac{C_1 (t - 0.04 T_p)}{0.02 T_p} + 1\right] & if\ 0.04 T_p \le t < 0.06 T_p \\ F_m & if\ 0.06 T_p \le t < 0.15 T_p \\ P + \sum_{i=1}^{nh} P \alpha\, sen\left[2\pi i f_p (t + 0.1 T_p) + \phi_i\right] & if\ 0.15 T_p \le t < 0.90 T_p \\ 10(P - C_2)\left(\dfrac{t}{T_p} - 1\right) + P & if\ 0.90 T_p \le t < T_p \end{cases} \quad (1)$$

$$F_m = P\left(1 + \sum_{i=1}^{nh} \alpha_i\right) \quad (2)$$

$$C_1 = \left(\frac{1}{f_{mi}} - 1\right) \quad (3)$$

$$C_2 = \begin{cases} P(1 - \alpha_2) & if\ nh = 3 \\ P(1 - \alpha_2 + \alpha_4) & if\ nh = 4 \end{cases} \quad (4)$$

where F_m = maximum Fourier series value, given by Equation 2; f_{mi} = human heel impact factor; T_p = step period; f_s = step frequency; Φ = harmonic phase angle; P = person's weight; α_i = dynamic coefficient for the harmonic force; i = harmonic multiple ($i = 1, 2, 3, \ldots, n$); t = time; and C_1 and C_2 = coefficients given by Equations 3 and 4.

The pedestrian motion on the tubular footbridge was modelled based on the Equations 1 to 4 and four harmonics were used to generate the dynamic forces produced by human walking. Figure 3 illustrates the dynamic load function for an individual walking at a step frequency of 2.0 Hz ($f_s = 2.0$ Hz).

Considering the investigated tubular footbridge, the third harmonic with step frequency equal to 2.0 Hz ($f_s = 2.0$ Hz) was considered the resonant harmonic of the walking load (3 × 2.0 Hz = 6.0 Hz). In this situation, the finite element mesh has to be very refined and the contact time of application of the dynamic load over the structure depends of the step distance and step frequency, see Table 1.

Table 1. Forcing frequencies (f_s), dynamic coefficients (α_i) and phase angles ϕ_i (Bachmann, H. & Ammann, W., 1987); (Murray et al, 2003).

Harmonic i	f_s	α_i	ϕ_i
1	1.6–2.2	0.50	0
2	3.2–4.4	0.20	$\pi/2$
3	4.8–6.6	0.10	π
4	6.4–8.8	0.05	$3\pi/2$

The following strategy was adopted in this study: a step distance equal to 0.75 m corresponding to the third harmonic with a step frequency of 2.0 Hz was used, see Table 1. The step period is equal to $1/f_s = 1/2.0$ Hz = 0.50 s, corresponding to a distance of 0.75 m. This way, the adopted strategy considered three forces to model one human step and each of the dynamic loads P1, P2 and P3 were applied to the footbridge structure during 0.50/3 = 0.1667 s, corresponding to the contact time of each dynamic load.

However, the dynamic forces were not simultaneously applied. The load application begins with the first human step where the first load, P1 is applied for 0.1667 s, see Equations 1 to 4. At the end of this time period, the load P1 becomes zero while the load P2 is subsequently applied for 0.1667 s. The process continues with the application of the other load P3, based on the same procedure previously described, until the end of the first step. At this point, the load P3 from the first step is made equal to the load P1 of the second step. The process continues with subsequent step applications until all dynamic loads are applied along the entire structure length. It can be concluded that all the dynamic actions associated will be applied over the structure.

3 INVESTIGATED STRUCTURAL MODEL

The structural model consists of tubular steel sections and a 100 mm concrete slab and is currently submitted to human walking loads. The structure was based on a tubular composite (steel-concrete) footbridge, spanning 82.5 m. The structure is composed by three spans (32.5 m, 17.5 m and 20.0 m, respectively) and two overhangs (7.50 m and 5.0 m, respectively), see Figure 4.

The steel sections used were welded wide flanges (WWF) made with a 300 MPa yield stress steel grade. A 2.05×10^5 MPa Young's modulus was adopted for the tubular footbridge steel beams and columns. The concrete slab has a 20 MPa specified compression strength and a 2.13×10^4 MPa Young's Modulus.

Figure 4. Investigated structural model.

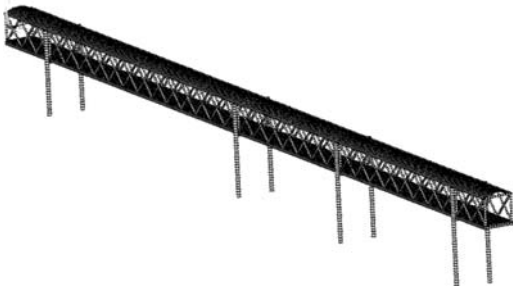

Figure 5. Tubular footbridge finite element model.

4 FINITE ELEMENT MODEL

The developed computational model adopted the usual mesh refinement techniques present in finite element method simulations, based on the ANSYS program (ANSYS, 2003). The finite element model has been developed and validated with the experimental results. This model enabled a complete dynamic evaluation of the investigated tubular footbridge especially in terms of human comfort and its associated vibration serviceability limit states (Debona, 2011), as presented in Figure 5.

In this computational model, all steel tubular sections were represented by three-dimensional beam elements (PIPE16 and BEAM44) with tension, compression, torsion and bending capabilities. These elements have six degrees of freedom at each node: translations in the nodal x, y, and z directions and rotations about x, y, and z axes.

On the other hand, the reinforced concrete slab was represented by shell finite elements (SHELL63). This finite element has both bending and membrane capabilities. Both in-plane and normal loads are permitted. The element has six degrees of freedom at each node: translations in the nodal x, y, and z directions and rotations about the nodal x, y, and z axes.

The footbridge pier bearings were represented by a non-linear rotational spring element (COMBIN39). This element is a unidirectional element with nonlinear generalized force-deflection capability that can be used in any analysis.

The finite element model presented 71540 degrees of freedom, 11938 nodes and 15280 finite elements (BEAM44: 1056; PIPE16: 5642; SHELL63: 8580 and COMBIN39: 8), see Figure 5. It was considered that both structural elements (steel tubular sections and concrete slab) have total interaction with an elastic behaviour.

5 DYNAMIC ANALYSIS

Initially, the tubular composite (steel-concrete) footbridge natural frequencies, vibration modes and peak accelerations were determined based on experimental tests (Zúñiga, 2011). The peak acceleration values were obtained considering three types of human walking: slow walking, regular walking and fast walking (Zúñiga, 2011).

Table 2. Tubular footbridge natural frequencies.

Natural frequencies (Hz)	f_{01}	f_{02}	f_{03}
Finite element modelling	1.61	2.12	5.39
Experimental results	1.56	2.34	5.08
Error (%)	3.20	9.40	6.10

Figure 6. Vibration mode associated with the 1st footbridge natural frequency ($f_{01} = 1.61$ Hz).

In a second phase, the tubular composite (steel-concrete) footbridge natural frequencies vibration modes and peak accelerations were determined with the aid of the numerical simulations, based on the finite element method using the ANSYS program (ANSYS, 2003).

It can be clearly noticed that there is a very good agreement between the structural model natural frequency values calculated using finite element simulations and the experimental results, see Table 2. Such fact validates the finite element model here presented, as well as the results and conclusions obtained throughout this investigation. The vibration modes of the tubular footbridge are depicted in Figures 6 to 8.

When the tubular footbridge freely vibrates in a particular mode, it moves up and down with a certain configuration or mode shape. Each footbridge natural frequency has an associated mode shape.

It was verified that longitudinal amplitudes were predominant in the fundamental vibration mode ($f_{01} = 1.61$ Hz), see Figure 6. In the second mode shape lateral displacements were predominant ($f_{02} = 2.12$ Hz), as presented in Figure 7. On the other

Figure 7. Vibration mode associated with the 2nd footbridge natural frequency ($f_{02} = 2.12$ Hz).

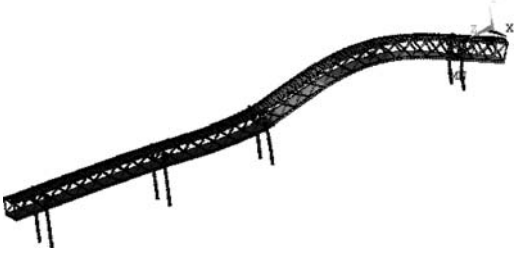

Figure 8. Vibration mode associated with the 3rd footbridge natural frequency ($f_{03} = 5.39$ Hz).

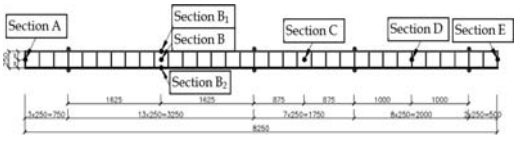

Figure 9. Tubular composite (steel-concrete) footbridge investigated sections.

hand, in the third vibration mode ($f_{03} = 5.39$ Hz), the flexural effects were predominant, as illustrated in Figure 8.

The finite element modelling follows with the evaluation of the footbridge performance in terms of vibration serviceability due to dynamic forces induced by people walking. The first step of this investigation concerned in the determination of the tubular footbridge peak accelerations, based on a linear time-domain dynamic analysis.

The dynamic loading related to one person crossing the tubular footbridge on the concrete slab centre, as presented in Figure 3, was applied over 55.0 s and an integration time step of 2×10^{-3} s ($\Delta t = 2 \times 10^{-3}$ s) was adopted in this investigation.

The peak accelerations were obtained at seven sections of the analysed structural model, as presented in Figure 9. These maximum accelerations were compared to the limits recommended by design codes (ISO 2631-2, 1989); (Murray et al., 2003).

In sequence, Figure 10 illustrates the tubular footbridge dynamic response, along the time, related to the section B (see Figure 9), when one pedestrian

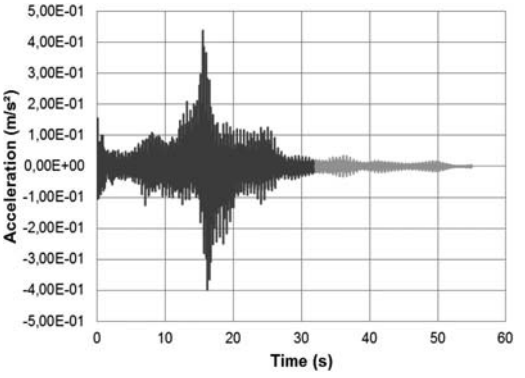

Figure 10. Tubular footbridge acceleration response at section B. One pedestrian crossing the concrete slab centre at resonance. Regular walking.

Table 3. Structural model peak accelerations corresponding to individual walking.

Tubular footbridge peak accelerations (a_p in m/s^2)
S slow walking
R regular walking
F fast walking

	A	B_1	B	B_2	C	D	E
S	1.15	0.22	0.57	0.22	0.67	0.54	0.94
R	1.00	0.16	0.44	0.16	0.38	0.33	0.78
F	**1.41**	0.18	**0.62**	0.18	**0.75**	**0.54**	**1.58**

*$a_{lim} = 1.5\%g = 0.15$ m/s^2: indoor footbridges
*$a_{lim} = 5.0\%g = 0.49$ m/s^2: outdoor footbridges

crosses the footbridge in regular walking (resonance condition).

Figure 10 presents the vertical acceleration versus time graph for the tubular footbridge at section B (see Figure 9). This figure shows that the vertical acceleration gradually increase with time. In this particular case, the third harmonic with a 2.0 Hz step frequency ($f_s = 2.0$ Hz), was the walking load resonant harmonic.

The maximum acceleration value found at section B (see Figure 9) was equal to 0.44 m/s^2. Figure 10 also indicates that from the moment that the pedestrian leaves the footbridge span (Section B, see Figure 9), when the time is approximately equal to 26 s, the structural damping minimises the dynamic structural model response, as presented in Figure 10. This assertive occurs in dynamic loading models that consider the load spatial variation.

The peak acceleration analysis was focused in three types of human walking: slow walking, regular walking and fast walking. Table 3 presents the maximum accelerations (peak accelerations: a_p in m/s^2), related to seven sections of the investigated footbridge (A, B, B_1, B_2, C, D and E), as illustrated in Figure 9.

The maximum acceleration values (peak accelerations) are respectively equal to 1.41 m/s^2 (Section A), 0.62 m/s^2 (Section B), 0.75 m/s^2 (Section C), 0.54 m/s^2 (Section D) and 1.58 m/s^2 (Section E), see Table 3.

These peak accelerations presented in Table 3 are related to a pedestrian fast walking situation. It must be emphasized that the limit acceleration value is equal to 0.49 m/s^2, when outdoor footbridges are considered in the analysis (ISO 2631-2, 1989); (Murray et al., 2003).

Based on the finite element modelling of the tubular composite (steel-concrete) footbridge dynamic behaviour, the numerical results presented in Table 3 indicated that the dynamic actions produced by human walking led to peak accelerations higher than the limiting values present in design code recommendations (Outdoor footbridges: 5%g = 0.49 m/s^2) (ISO 2631-2, 1989); (Murray et al., 2003), as depicted in Table 3.

6 CONCLUSIONS

This contribution covers the application of tubular structural elements in pedestrian footbridge design and tries to give an overview about the evaluation of tubular footbridges dynamic behaviour, objectifying to help practical structural engineers to deal with this kind of problem and to allow for a further application of tubular structural elements in pedestrian footbridge design.

The present study was carried out based on a more realistic loading model developed to incorporate the dynamic effects induced by people walking. The loading model considered the ascent and descending movement of the human body effective mass at each step and the position of the dynamic load (human walking load) was also changed according to the individual position. Additionally, also incorporates the transient effect due to the human heel impact.

The proposed analysis methodology considered the investigation of the dynamic behaviour, in terms of serviceability limit states, of a tubular composite (steel-concrete) footbridge, spanning 82.5 m. The structure is composed by three spans (32.5 m, 17.5 m and 20.0 m, respectively) and two overhangs (7.50 m and 5.0 m, respectively). The structural system consists of tubular steel sections and a concrete slab and is currently used for pedestrian crossing.

A computational model, based on the finite element method, was developed using the ANSYS program. This model enabled a complete dynamic evaluation of the investigated tubular footbridge especially in terms of human comfort and its associated vibration serviceability limit states.

The results found throughout this investigation have indicated that the dynamic actions produced by human walking could generate peak accelerations that surpass design criteria limits developed for ensuring human comfort. Hence it was detected that this type of structure can reach high vibration levels that can compromise the footbridge user's comfort and especially its safety.

The analysis methodology presented in this paper is completely general and is the author's intention to use this solution strategy on other pedestrian footbridge types and to investigate the fatigue problem. The fatigue problem is a relevant issue and certainly much more complicated and is influenced by several design parameters and footbridge types. Further research in this area is currently being carried out.

ACKNOWLEDGMENT

The authors gratefully acknowledge the financial support for this work provided by the Brazilian Science Foundations CAPES, CNPq and FAPERJ.

REFERENCES

ANSYS. Swanson Analysis Systems, Inc. 2003. P.O. Box 65, Johnson Road, Houston, PA, 15342-0065, Version 10.0, Basic analysis procedures, Second edition.

Bachmann, H. & Ammann, W. 1987. Vibrations in structures induced by man and machines, Structural Engineering Document 3e, International Association for Bridges and Structural Engineering.

Chen, Y. 1999. Finite element analysis for walking vibration problems for composite precast building floors using ADINA: modelling, simulation and comparison. Computer & Structures, 72:109–126.

Debona, G.L. 2011. Modelagem do comportamento dinâmico de passarelas tubulares em aço e mistas (aço-concreto) (Modelling of the dynamic behaviour of composite (steel-concrete) tubular footbridges), MSc Dissertation (in Portuguese), Civil Engineering Post-Graduate Programme, PGECIV, State University of Rio de Janeiro, UERJ, Rio de Janeiro, Brazil, pp. 1–152.

Eurocode 3. 2005. Design of steel structures. Part 1.9: General rule – Fatigue. European Committee for Standardisation.

Figueiredo, F.P., Silva, J.G.S. da, Vellasco, P.C.G. da S., Lima, L.R.O. de, Andrade, S.A.L. de. 2008. A parametric study of composite footbridges under pedestrian walking loads. Engineering Structures, 30: 605–615.

International Standard Organization/ISO 2631-2. 1989. Evaluation of human exposure to whole-body vibration, Part 2: Human Exposure to Continuous and Shock-Induced Vibrations in Buildings (1 to 80Hz), International Standard.

Leitão, F.N., Silva, J.G.S. da, Vellasco, P.C.G. da S., Lima, L.R.O. de, Andrade, S.A.L. de. 2011. Composite (steel-concrete) highway fatigue assessment. Journal of Constructional Steel Research, 67(1): 14–24.

Kuhlmann, U., H.-P. Günther, Saul, R., Häderle, M.-U. 2003. Welded circular hollow section (CHS) joints in bridges. ISTS 2003: Proceedings of the 10th International Symposium on Tubular Structures, Madrid, Spain.

Murray, T.M., Allen, D.E., Ungar, E.E. 2003. Floor vibrations due to human activity, Steel Design Guide Series, American Institute of Steel Construction, AISC, Chicago, USA.

Pimentel, R.L., Pavic, A., Waldron, P. 2001. Evaluation of design requirements for footbridges excited by vertical forces from walking. Canadian Journal of Civil Engineering, Vol. 28(5), 769–776.

Silva, J.G.S. da, Vellasco, P.C.G. da S., Andrade, S.A.L. de, Lima, L.R.O de, Figueiredo, F.P. 2007. Vibration analysis of footbridges due to vertical human loads. Computers & Structures, 85: 1693–1703.

Varela, W.D. 2004. Modelo teórico-experimental para análises de vibrações induzidas por pessoas caminhando sobre lajes de edifícios (Theoretical-experimental model to analyse vibrations induced by people walking on floor slabs of buildings), PhD Thesis (in Portuguese), Federal University of Rio de Janeiro, Civil Engineering Department, COPPE/UFRJ, Rio de Janeiro, Brazil, pp. 1–309.

Zúñiga, J. E. V. 2011. Análise da resposta dinâmica experimental de uma passarela tubular mista, aço-concreto, submetida ao caminhar humano (Dynamic experimental analysis of a composite (steel-concrete) tubular footbridge submitted to human walking), MSc Dissertation (in Portuguese), Civil Engineering Post-Graduate Programme, PGECIV, State University of Rio de Janeiro, UERJ, Rio de Janeiro, Brazil, pp. 1–135.

Fire

Tubular Structures XIV – Gardner (Ed.)
© 2012 Taylor & Francis Group, London, ISBN 978-0-415-62137-3

Shape effect on structural fire behaviour of axially loaded Concrete Filled Tubular (CFT) stub columns

X.H. Dai & D. Lam
School of Engineering, Design & Technology, University of Bradford, UK

ABSTRACT: Concrete Filled Tubular (CFT) columns have been extensively used in modern construction due to their excellent structural efficiency such as high load bearing capacity, ductility, large energy-absorption capacity and good structural fire behaviour. This paper presents the effect of the sectional shapes of concrete filled steel tubular stub columns on their structural fire behaviour. Four different cross sectional shapes namely Circular Hollow Section (CHS), Elliptical Hollow Section (EHS), Square Hollow Section (SHS) and Rectangular Hollow Section (RHS) are investigated. The CFT stub columns are divided into three groups by equal section strength at ambient temperature, equal steel cross-sectional area and equal concrete core cross-sectional area. The temperature distribution, critical temperature and fire exposing time of the composite columns are extracted by numerical simulations using ABAQUS. Based on FE analysis, the effect of column sectional shapes on member temperature distribution and structural fire behaviour are discussed. It shows concrete steel tubular column with circular section possesses the best structural fire behaviour, followed by columns with elliptical, square and rectangular sections. Finally, a simple formula is proposed for assessment of the ultimate axial compressive load of stub concrete filled steel tube column in fire.

1 INTRODUCTION

Steel is a highly thermal conductive material, however it loses strength and stiffness quickly when exposed to fire. Therefore, it is vitally important to consider the structural fire behaviour of steel and steel composite members to ensure that they have the appropriate fire resistance. Various fire protection methods may be adopted to promote the fire resistance ability. For example, applying intumescent coating to the steel surface is an effective approach, however it is expensive and the intumescent coating itself does not provide any structural strength to the structural elements. Concrete being a thermal inert material and has been recognized to provide an effective temperature sink which could reduce the temperature of steel during fire. Furthermore, the temperature of concrete core rises much slower than that of steel tube thus the concrete core may provide appropriate load bearing capacity even when the steel tube has reached to its critical temperature.

Researches on the structural fire behaviour of concrete filled columns under different loads have been extensively conducted. (Ding & Wang 2007, Espinos & Gardner *et al* 2011, Han *et al* 2004, Hong & Varma 2009, Huo *et al* 2009, Kodur 1998, Schaumann *et al* 2009, Tao *et al* 2011, Wang 2005 and etc.). These included experimental studies and numerical analyses for concrete filled steel tubular columns with various member geometrical features, material properties and under different loading conditions, however very few addressed the effect of the sectional shapes of concrete filled columns on the structural behaviour at elevated temperature. Different from concrete encased composite columns, the steel tube of the concrete filled steel tubular column provides confinement to the concrete core which enhances the concrete compressive strength, while the concrete core restrained steel tube against local buckling. The interaction between the steel hollow section and concrete core may be different with different sectional shapes. When the concrete filled steel tube column subjected to fire, because the thermal properties of steel and concrete are dissimilar; the interaction between the steel tube and the concrete core might change.

The structural behaviour of concrete filled steel tubular columns with typical circular, elliptical, square and rectangular section shapes at elevated temperatures has been extensive studied. The critical temperature of a structural member in fire and the ultimate load of a structural member under design temperature are important structural characteristics. For concrete filled steel tubular columns, the material properties and geometrical characteristics will dominate their fire behaviour. To understand the performance of

concrete filled steel tubular columns with various cross sectional shapes in fires. The investigation presented in this paper discusses the temperature development and critical temperature of concrete filled steel tubular stub columns with four typical sectional shapes. The critical temperature is defined as the maximum steel tube temperature above which the loaded stub column starts to experience a progressive deformation.

2 MATERIAL PROPERTIES

The mechanical and thermal properties of steel and concrete are very different. Although the strength and stiffness of both steel and concrete will reduce at elevated temperatures, comparing with steel, concrete is general taken as a thermal inert material. In this paper, all steel hollow sections are hot-finished, the aim of the research presented in this paper is focused on the effect of cross-sectional shapes to the structural fire behaviour, and therefore, identical steel material and concrete material were adopted for all selected concrete filled steel tube columns with different sectional shapes to eliminate the influence of the material properties.

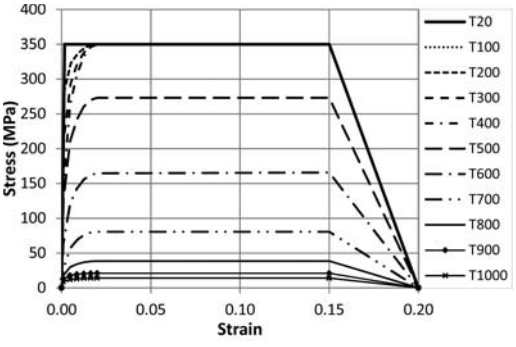

(a) Steel

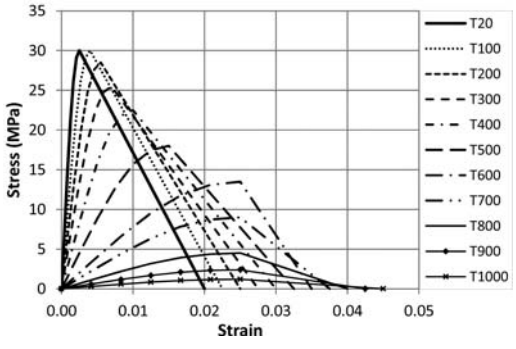

Figure 1. Stress-strain curves of steel and concrete at elevated temperatures.

The stress-strain curve of steel material at room temperature (20°C) is defined by the curve T_{20} in Figure 1(a). For all steel tubes, the yield strength, f_y is assumed to be 350 N/mm^2. The initial elastic modulus, E_s is taken as 210 GPa. The reduction factors for strength and stiffness of steel at elevated temperatures are in accordance to the BS EN 1993-1-2 for carbon steel and as shown in Figure 1(a). For concrete at room temperature, the maximum compressive strength, f_c is assumed to be 30 MPa and the corresponding strain, ε_c is taken as 0.0025. In Figure 1(b), the curve T_{20} gives the stress-strain relationship of concrete at room temperature. The reduction factors for concrete strength and stiffness at elevated temperature are in accordance to BS EN 1994-1-2 and Figure 1(b) shows the typical stress-strain curves of the normal weight concrete at different temperatures. The thermal properties of both steel and concrete are according to the thermal properties of carbon steel and normal weight concrete provided in the BS EN 1993-1-2 and BS EN 1994-1-2.

3 DESCRIPTION OF SELECTED CONCRETE FILLED STEEL TUBULAR STUB COLUMNS

To compare the effect of cross sectional shape to the structural fire behaviour of concrete filled steel tubular columns, a series of concrete filled steel tubular stub columns with four typical sectional shapes are presented. Elliptical hollow sections (EHS), circular hollow sections (CHS), square hollow sections (SHS) and rectangular hollow sections (RHS) filled with concrete are used in this paper. All selected stub columns are of 500 mm in length and with steel tube wall thickness of 5 mm. The longer diameter to shorter diameter ratio for the EHS and longer side length to shorter side length ratio for RHS are taken as 2. The selected stub columns are divided into three groups by three important aspects of the concrete filled steel tube columns: sectional strength at ambient temperature, steel cross sectional area and concrete cross sectional area. Figure 2 shows four examples of selected stub composite columns with 4 typical column sectional shapes. The basic geometrical and mechanical features of the selected composite columns are given in Table 1, 2 and 3.

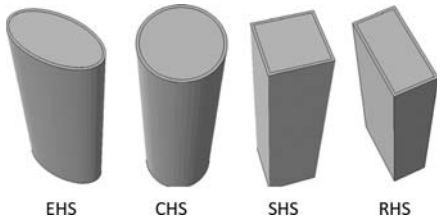

Figure 2. Typical shapes of selected concrete filled steel tubular stub columns.

Table 1. Group1 – composite columns with equal section strength.

Column ID	EHS	CHS	SHS	RHS
Section dimension (mm)	200 × 100 × 5 (2a × 2b × t)	145 × 5 (D × t)	123 × 123 × 5 (D × D × t)	169 × 84.5 × 5 (D × B × t)
l (mm)	500	500	500	500
A_s (mm^2)	2278	2199	2360	2435
A_c (mm^2)	13430	14314	12769	11845
f_y (N/mm^2)	350	350	350	350
f_c (MPa)	30	30	30	30
N_y (kN)	1200	1199	1209	1208

$*l$: composite column length; A_s: steel tube cross sectional area; A_c: concrete core cross sectional area; f_y: yield strength of steel material at room temperature; f_c: concrete compressive strength at room temperature; N_y: sectional strength of concrete filled steel tubular column at room temperature.

Table 2. Group 2 – composite columns with equal steel section area.

Column ID	EHS	CHS1	SHS1	RHS1
Section dimension (mm)	200 × 100 × 5 (2a × 2b × t)	150 × 5 (D × t)	118.9 × 118.9 × 5 (D × D × t)	158.5 × 79.3 × 5 (D × B × t)
l (mm)	500	500	500	500
A_s (mm^2)	2278	2278	2278	2278
A_c (mm^2)	13430	15394	11895	10284
f_y (N/mm^2)	350	350	350	350
f_c (MPa)	30	30	30	30
N_y (kN)	1200	1259	1154	1106

Table 3. Group 3 – composite columns with equal concrete section area.

Column ID	EHS	CHS2	SHS2	RHS2
Section dimension (mm)	200 × 100 × 5 (2a × 2b × t)	140.8 × 5 (D × t)	125.9 × 125.9 × 5 (D × D × t)	179 × 89.5 × 5 (D × B × t)
l (mm)	500	500	500	500
A_s (mm^2)	2278	2133	2418	2585
A_c (mm^2)	13430	13437	13433	13436
f_y (N/mm^2)	350	350	350	350
f_c (MPa)	30	30	30	30
N_y (kN)	1200	1150	1249	1308

4 EFFECT OF SECTIONAL SHAPES TO TEMPERATURE DEVELOPMENT

4.1 *Thermal analysis procedure and validation*

To obtain the structural fire behaviour of the composite columns under standard fire, the non-linear heat transfer analysis using commercial software ABAQUS is first carried out to determine the temperature distribution of each selected composite column. Detailed modelling procedure may be found from other literatures. In this research, it is assumed that all selected stub columns are exposed to a standard fire (ISO 834, 1975) for 60 minutes. During the fire exposure, heat is transferred to the tube surface through convection and radiation heat transfer mechanisms. The conductive coefficient of 25 W/m^{2}k recommended in BS EN 1991-1-2 is adopted. The effective surface emissivity of 0.5 and the configuration factor of 1.0 are assumed. To simplify the heat transfer analysis, the possibility of forming a gap between the steel tube and concrete core during fire is not taken into consideration and the heat flow is directly conducted from steel tube to concrete core. To validate the accuracy of the heat transfer analysis method adopted for the research, temperature developments of the concrete filled steel tubular columns under standard fire tests observed by Ding (2007) are used. Figure 3 shows the comparison of temperatures in the steel tubes (SS: at

the middle location of sides of steel hollow section, SC: at the corners of steel hollow section) and CC: at concrete core centre) from experiments and those predicted by numerical modelling, good agreement is achieved although the numerically prediction slightly underestimated the temperature development at the concrete core centres. The difference between experimental and numerical results might be resulted from the assumed concrete thermal properties not being completely identical to those of the tested specimens.

4.2 *Comparison of temperature distributions of concrete filled steel tubular columns with different sectional shapes*

After the heat transfer analysis method is verified, the method is used to extract the temperature distribution of selected concrete filled steel tubular columns. Figure 4 presents the temperature developments of steel tube and concrete core centre for all selected composite stub columns under 60 minutes standard fire exposure. "ST" refers to the maximum temperature in steel tube. "CC" refers to the temperature at the centre of the concrete core. The following behaviour of the concrete filled steel tubular columns at elevated temperature can be observed:

(1) For circular sectional shape, there is little variation in the temperature of the steel with the maximum difference of 4°C. However for columns with other sectional shapes, steel temperature at the sharp corner is much higher than that at the side, the maximum difference may reach 70°C, 55°C and 45°C for rectangular, elliptical and square sections respectively. This is due to the sharp corner having two intersected surfaces exposed to fire; therefore more heat is conducted and radiated.

(2) Figure 4 shows the temperatures of steel tube and concrete core centre changed with different column sectional shapes. It can be observed that if four columns have equal section strength (Group 1), circular section is the best in fire resistance followed by square section due to their lower temperatures developed both in the steelwork and the concrete core. The rectangular section appears to be the worst due to the shortest heat conductive distance from the exposed steel surface to the centre of the concrete core and have the least volume of concrete. For columns with equal steel cross

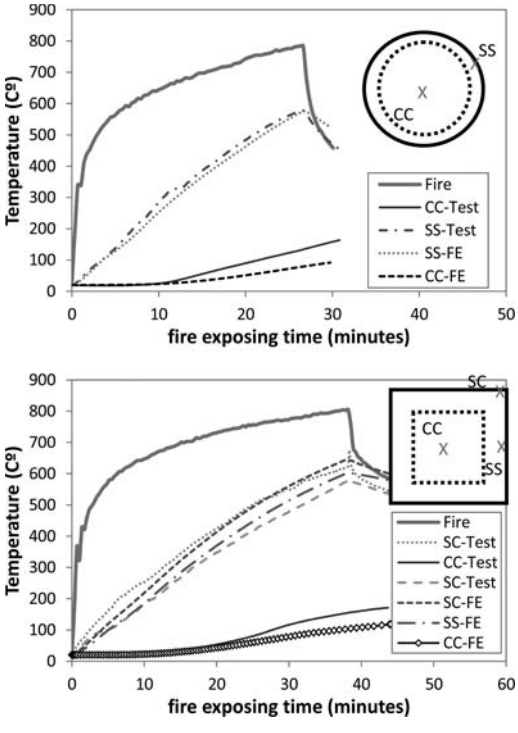

Figure 3. Comparison of numerical prediction and experimental observation.

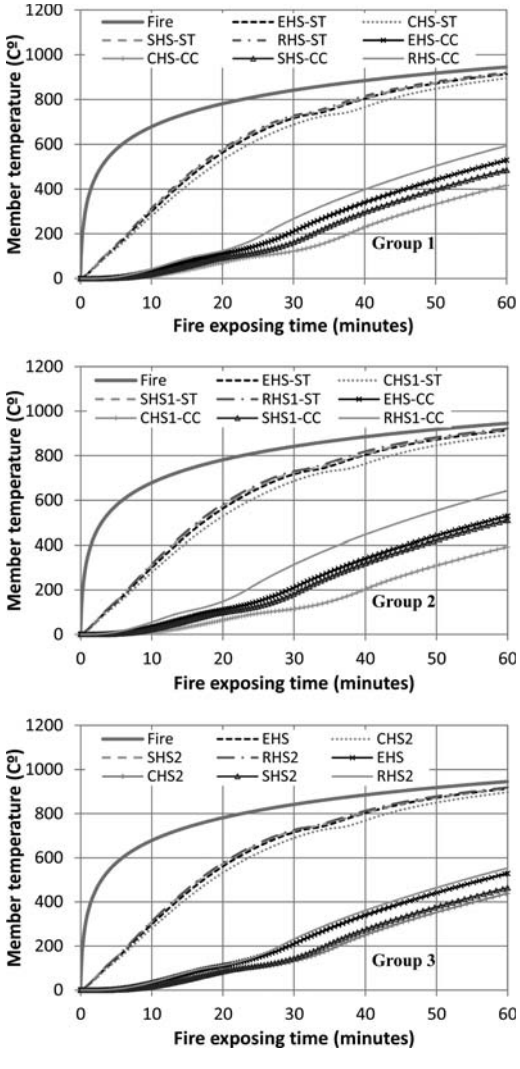

Figure 4. Temperature development of the steel tube and concrete core in 60 minutes standard fire exposing time.

sectional areas (Group 2), circular section performs much better than the rectangular section whiles the performance of the elliptical and the square sections were similar. For columns with equal concrete cross sectional areas (Group 3), it can be seen that the temperature at the centre of the concrete core for column with circular and square section were similar, which is lower than the temperatures of the concrete with elliptical and rectangular sections due to longer heat conducting distances.

5 EFFECT OF SECTIONAL SHAPES TO COMPRESSIVE BEHAVIOUR OF CONCRETE FILLED STEEL TUBULAR STUB COLUMNS AT ELEVATED TEMPERATURES

5.1 *Introduction*

After completing the heat transfer analysis of all the selected stub composite columns, the relationships of temperature to fire exposing time for selected column members are obtained, then a two steps non-linear stress analysis is subsequently conducted using ABAQUS. In the first step, the load is applied to the top end of the stub composite column through a loading plate at ambient temperature. This load is maintained during the second step. In the second step, the nodal temperatures of members are imported. In the non-linear stress analysis, the interaction between the steel tube and concrete core in normal direction is modelled as "hard" contact pair mechanism, which allows pressure to be transmitted when the surfaces are in contact. In the tangent interaction, a friction coefficient of 0.3 is introduced to accounting for composite interaction between steel tube and concrete core.

5.2 *Comparison of critical temperature of concrete filled steel tubular columns with different cross sectional shapes*

As mentioned in the previous section, the critical temperature defined in this paper is the maximum steel tube temperature just before the composite stub column experiences excessive deformation or crushing failure. Figure 5 and 6 show examples of typical relationships of the compressive displacement to fire exposing time and maximum steel tube temperature. The following points may be observed:

For columns with equal sectional strength (Group 1) and columns with equal steel cross-sectional area (Group 2), the column with circular sectional shape has the longest fire exposure time before failure. However, for columns with equal concrete core area (Group 3), the fire exposure duration of columns with square and rectangular sectional shape is longer than that of columns with circular and elliptical sectional shapes due to the latter with less steel section area.

For all selected columns in standard fires, if the axial compressive load does not exceed 600 kN, the thermal expansion dominates the stub column deformation (characterized by the negative compressive displacement at the column top) before the column failed. Regardless of the sectional shapes, generally the higher the axial compressive load applied, the lower the critical temperature.

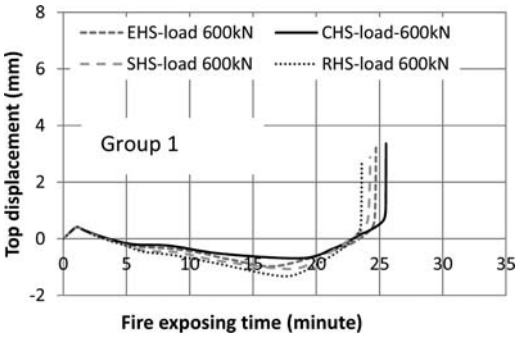

Figure 5. Compressive displacement vs. fire exposing time curves for composite columns with different sectional shapes but with equal sectional strength.

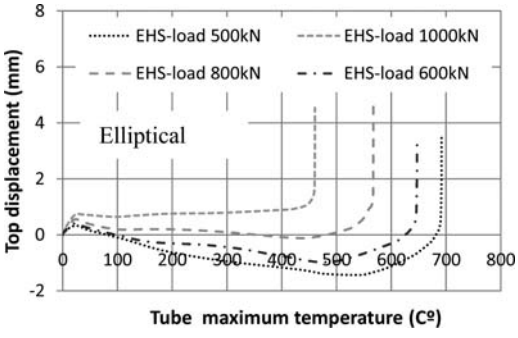

Figure 6. Compressive displacement vs. maximum tube temperature curves for identical composite columns being applied different axial compressive loads.

Figure 7 and 8 show the relationships of axial compressive load ratio vs. maximum critical temperature and fire exposure duration. It can be concluded that the critical temperature decreases with the load ratio increasing. Although for columns with different cross sectional shapes, the critical temperatures are similar. However, by comparing the fire exposure time before composite stub column experiencing progressive deformation, it appears the column with circular section has the longest fire exposure time following by column with elliptical section. The column with rectangular sectional shape has the shortest fire exposure time.

5.3 *Simplified calculation method to maximum axial compressive load of concrete filled steel tube columns in fire to Eurocodes*

When the concrete filled steel tubular column exposed to fire, the temperature develops in the steel tube and concrete core are different. The axial compressive load

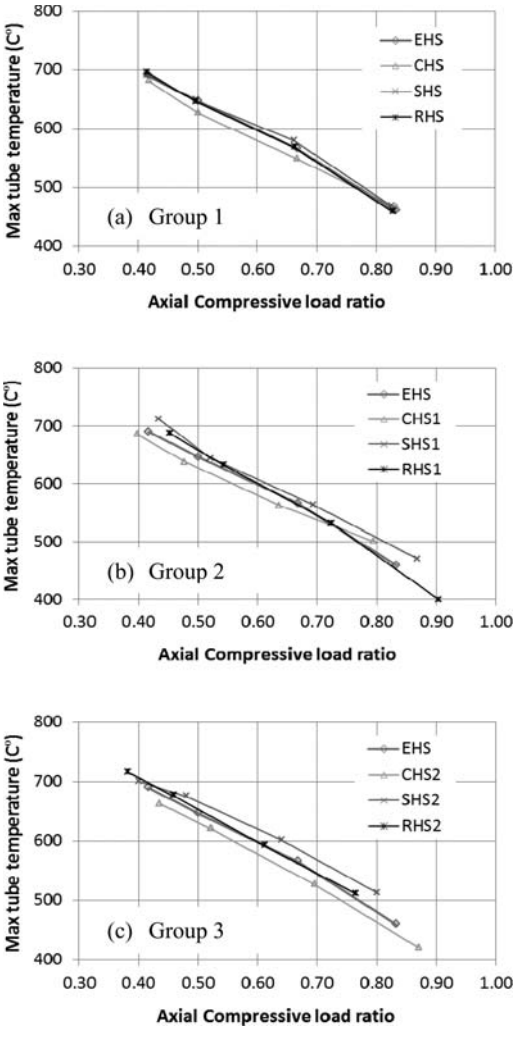

Figure 7. Relationship of axial compressive load ratio to critical temperature (steel tube).

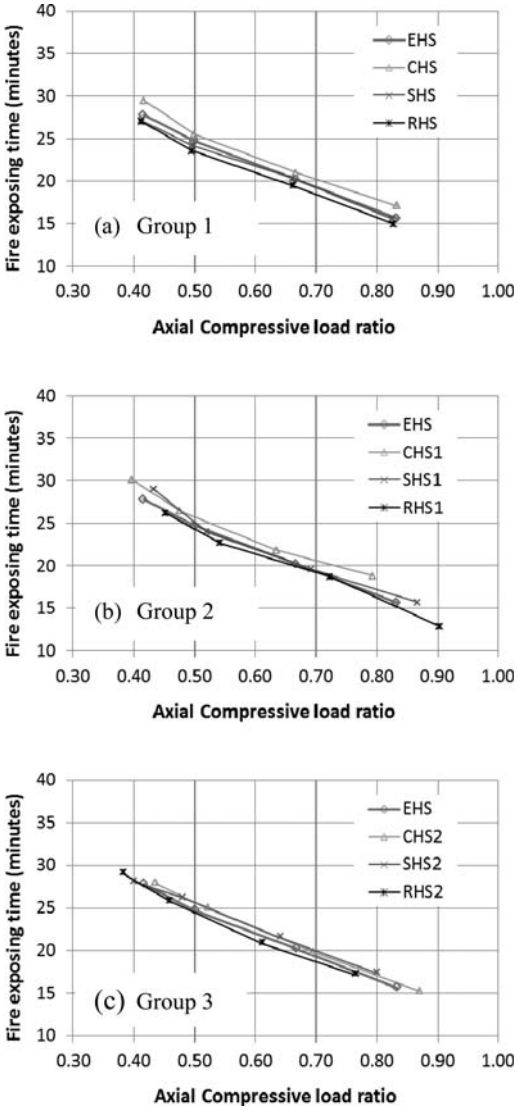

Figure 8. Relationship of axial compressive load ratio to fire exposing time.

capacity of a composite column in fire may be simply calculated by its sectional strength using equation (1):

$$N_{y,f} = A_s f_{y,\theta s} + A_c f_{c,\theta c} \quad (1)$$

Where $N_{y,f}$: sectional strength (kN) of a concrete filled steel tubular column in fire; $f_{y,\theta s}$: is the yield strength (N/mm^2) of steel material at temperature θ_s; $f_{c,\theta c}$ is the concrete compressive strength (N/mm^2) at temperature θ_c.

When using the equation (1) to assess the maximum compressive load of the concrete filled steel tube columns at elevated temperature, a problem arises in how to determine the temperatures in steel and concrete core as they are different. It is reasonable to assume that the temperature in steel is uniform and therefore the design temperature from BS EN1993-1-2 may be directly applied to equation (1) to obtain the $f_{y,\theta s}$. However, as shown in the previous section, the temperatures of the concrete at different core locations are very different and difficult to predict. Using multiple temperature values for concrete core in equation (1) to obtain the $f_{c,\theta c}$ will impair convenience and directness of the formula. Therefore, to evaluate the compressive capacity of the concrete filled steel tube columns in fire using equation (1), it is proposed to adopt a constant temperature for the whole concrete core but not to compromise the calculation accuracy. For the typical concrete filled steel tube columns selected in this research, the thermal analyses show that the average concrete core temperature is around 0.4 ~ 0.8 times of the steel tube temperature within 60 minutes standard fire exposure, the actual temperature distribution of concrete core is that the temperature in

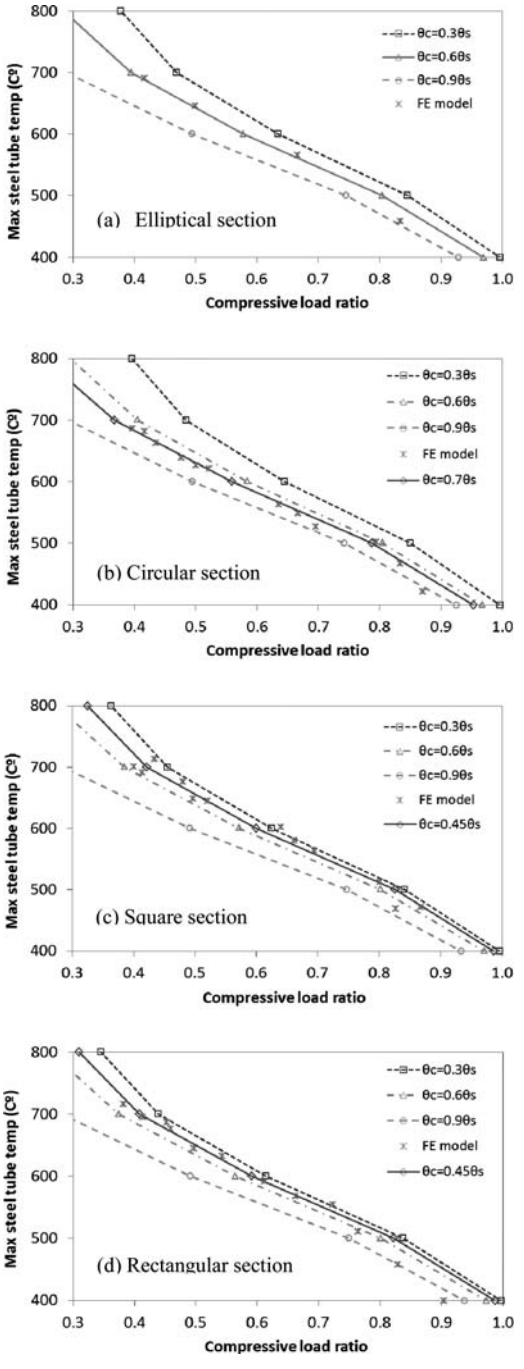

Figure 9. Comparison of FE modelling prediction and simple calculation method.

the core centre is very low, but at the surface contacting to the steel tube the concrete temperature is close to the steel temperature.

To find the most appropriate constant concrete temperature for equation (1) in design, a series of constant concrete temperatures, from $0.3 \sim 0.9$ times of the steel temperature are used to calculate the axial compressive capacity or load ratio using equation (1) for concrete filled steel tube stub columns with the aforementioned hollow section shapes. The ratio vs. steel temperature relationships are shown in Figure 9. In addition, FE models (which considered the temperature distribution in concrete core by thermal transfer analysis) are built to obtain the relations of steel tube temperature with load ratio and verify the feasibility and effectiveness of equation (1). Figure 9 shows that the proposed equation (1) can be used to assess the axial compressive capacity of stub concrete filled steel tube columns by adopting a single constant concrete temperature. The compressive load ratio is taken as the rate of applied load to the maximum load capacity of composite stub column at room temperature. When the design steel temperature is specified, the maximum load of a concrete filled steel tube column in standard fire can be obtained using the proposed equation. However for different cross sectional shapes, the rate of constant concrete core temperature to steel temperature is different. According to the research results given in this paper, the authors proposed: $\theta_c = 0.7\theta_s$ for concrete filled steel tube columns with CHS, $\theta_c = 0.6\theta_s$ for concrete filled steel tube columns with EHS and $\theta_c = 0.45\theta_s$ for concrete filled steel tube columns with SHS and RHS. It must be noted, the section dimension of selected composite columns in this research is not over 200 mm, if a larger steel hollow section size is used, with the concrete area increasing, the average concrete core temperature might be lower, and therefore using the proposed equation might be conservative.

6 CONCLUSIONS

Concrete filled steel tubular columns have been extensively used in modern construction practice owing to that they utilize the most favourable properties of both constituent materials and the composite action between the steel hollow section and concrete core. It has been recognized that concrete filled steel tubular columns provide excellent structural properties such as high load bearing capacity, ductility, large energy-absorption capacity and good structural fire behaviour. However, the structural behaviour of concrete-filled tube columns is affected by many factors, such as geometrical dimension, shapes, member material properties and load types etc. The research presented in this paper numerically investigated the important structural fire behaviour of stub concrete filled steel tubular columns with four typical column sectional shapes through analysing and comparing the temperature distribution, critical temperature, fire exposing time of a series of selected concrete filled steel tubular stub columns. The stub columns are divided into three groups by equal section strength at ambient temperature, equal steel cross sectional area and equal concrete core cross sectional area. Based on the comparison and

analysis carried out in the present study, the following conclusions and comments could be drawn:

(1) For columns with different cross sectional shapes, their temperature distributions in the steel tubes are different. Only the temperatures of CHS are evenly distributed. For concrete filled steel tubular columns with RHS and SHS, the steel temperature at the sharp corner is higher than that at flat sides. Obviously, this is a weakness for square and rectangular concrete filled steel tubular columns due to possible stress concentration might present at sharp corners. However, if the maximum steel temperature is taken as the critical temperature in the design, the design is conservative.

(2) When compare the maximum temperatures at steel tubes or the minimum temperatures at concrete cores of concrete filled steel tubular columns with equal section strength but different sectional shapes, it appears the column with circular shape come out top as both temperatures in steelwork and concrete have the lowest temperatures than those of columns with the other three sectional shapes. The temperature in column with rectangular section is the highest due to the column has the shortest heat conductive distance from steel surface to the concrete core centre and the least volume of concrete.

(3) For columns with equal section strength at ambient temperature (Group 1) and columns with equal steel sectional areas (Group 2), the columns with circular sectional shape have the longest fire exposing time before failure, followed by the columns with elliptical sectional shape. Columns with rectangular sectional shape are the worst in fire resistant duration. This shows the advantage of circular and elliptical sectional shapes. However for columns with equal concrete core sectional area (Group 3), the fire exposing durations of columns with square and rectangular sectional shapes are longer than those of columns with circular and elliptical sectional shapes due to the increases in steel sectional areas. This indicates the importance of steel sections to the concrete filled composite columns in fire.

(4) Regardless of the sectional shapes, the higher the axial compressive load applied, the lower the critical temperature and shorter the fire exposing duration. As expected, the critical temperature decreases with the load ratio increasing.

(5) A simplified equation for evaluation the cross section compressive capacity of a concrete filled steel tubular column at elevated temperature is proposed. The temperature of concrete core may be constant and simply taken as 0.7 times the steel temperature for circular CFT columns, 0.6 times the steel temperature for elliptical CFT columns and 0.45 times of steel temperature for square and rectangular CFT columns.

(6) The actual concrete temperatures at some locations may be higher than the proposed average temperature, therefore using the proposed constant temperature to replace the actually distributed concrete temperature might be overestimated the rigidity of the cross-section. However, this effect can be ignored when considering for the capacity of the axial loaded stub columns but must be taken into consideration for the analysis of the slender member.

REFERENCES

BS EN 1991-1-2, 2002. Eurocode 1: Actions on structures, Part 1-2: General actions-Actions on structures exposed to fire. British Standards Institution, London.

BS EN 1993-1-2, 2005, *Eurocode 3: design of steel structures, Part 1.2: General rules- structural fire design*. British Standards Institution, London.

BS EN 1994-1-2, 2005. *Eurocode 4: Design of composite steel and concrete structures, Part 1-2: General rules-Structural fire design.* British Standards Institution, London.

Ding, J. 2007. *Behaviour of restrained concrete filled tubular (CFT) columns and their joints in fire*. PhD thesis, School of MACE, University of Manchester.

Ding, J. & Wang, Y. 2007. Experimental study of structural fire behaviour of steel beam to concrete filled tubular column assemblies with different types of joints. *Engineering Structures* 12(29): 3485–3502.

Espinos, A., Gardner, L., Romero, M.L. & Hospitaler, A. 2011. Fire behaviour of concrete filled elliptical steel columns. *Thin-Walled Structures* 49(2):239–255.

Han, L.H. & Lin, X.K. 2004. Tests on Cyclic Behavior of Concrete-Filled Hollow Structural Steel Columns after Exposure to the ISO-834 Standard Fire. *ASCE Journal of Structural Engineering* 130(11):1807–1819.

Hong, S. & Varma, A.H. 2009. Analytical modelling of the standard fire behaviour of loaded CFT columns. *Journal of Constructional Steel Research* 65(1):54–69.

Huo, J., Huang, G. & Xiao, Y. 2009. Effects of sustained axial load and cooling phase on post-fire behaviour of concrete-filled steel tubular stub columns. *Journal of Constructional Steel Research* 65(8-9):1664–1676.

ISO 834, 1975. *Fire Resistance Tests, Elements of Building Construction*. International Organization for Standardization. Geneva.

Kodur, V.K.R. 1998. Performance of high strength concrete-filled steel columns exposed to fire. *Can. J. Civ. Eng*. 25: 975–981.

Schaumann, P., Kodur, V. & Bahr. O. 2009. Fire behaviour of hollow structural section steel columns filled with high strength concrete. *Journal of Constructional Steel Research* 65(8–9):1794–1802.

Tao, Z., Han, L.H., Uy, B. & Chen, X. 2011. Post-fire bond between the steel tube and concrete in concrete-filled steel tubular columns. *Journal of Constructional Steel Research* 67(3):484–496.

Wang, Y.C. 2005. Performance of steel-concrete composite structures in fire. *Progress in Structural Engineering and Materials* 7(2):86–102.

Tubular Structures XIV – Gardner (Ed.)
© 2012 Taylor & Francis Group, London, ISBN 978-0-415-62137-3

An experimental study of the fire behaviour of slender concrete filled circular hollow section columns

A. Espinos, M.L. Romero, A. Hospitaler, C. Ibañez & A. Pascual
Instituto de Ciencia y Tecnología del Hormigón, Universitat Politècnica de València, Valencia, Spain

V. Moliner
Centro Técnico del Fuego, AIDICO, Valencia, Spain

ABSTRACT: This paper presents the results of a series of fire tests carried out on slender concrete filled circular hollow section columns subjected to both concentric and eccentric loads. The columns tested had a relative slenderness value at room temperature higher than 0.5 in most of the cases. A first series of 14 columns were tested under concentric load and, on a second stage, another series of 24 columns were tested under eccentric load. Eccentricities of 20 and 50 mm were used. The influence of parameters such as the concrete grade (C30 and C90), load level (20% and 40%) and type of concrete filling (plain, bar reinforced and steel fiber reinforced concrete) was investigated. Special attention was paid on the influence of using high strength concrete under elevated temperatures and the effect of the addition of reinforcing bars or steel fibres. Through the results of this series of fire tests, the accuracy of the current simple calculation model from Eurocode 4 was studied and discussed.

1 INTRODUCTION

Concrete filled tubular (CFT) columns combine the action of steel and concrete when carrying compressive loads and moments showing an ideal structural performance. While the steel tube confines the concrete core enhancing its compressive strength, the concrete core prevents the steel section from local buckling. In addition, CFT columns can reach high fire resistance times without the need of external protection (Twilt et al. 1996, Wang & Kodur 2000).

The use of high strength concrete (HSC) as infilling in CFT columns has increased in recent years, becoming a good alternative to normal strength concrete (NSC) in room temperature design. At ambient temperature, high strength CFT columns show higher load-bearing capacity than those columns filled with traditional NSC. Results from Portolés et al. (2011a,b) show the utility of the concrete contribution ratio for different values of slenderness, concrete strength or confinement index.

At elevated temperatures, although it is known that HSC behaves differently from NSC (Schaumann et al. 2009), its performance is not yet completely defined. When high strength concrete is subjected to elevated temperatures, it is likely that spalling appears, affecting its behaviour as it leads to a explosive deterioration of the material due to the development of high internal pore pressures (Ali et al. 2010). The possibility of this phenomenon to appear during a fire makes it necessary to evaluate the convenience of using HSC as infilling in hollow steel columns as it can affect their fire resistance.

Whereas the fire behaviour of normal strength CFT columns has been deeply investigated for years (Lie 1994, Zha 2003, Renaud et al. 2003, Yin et al. 2006, Ding & Wang 2008, Hong & Varma 2009, Espinos et al. 2010) and numerous test programs have been carried out worldwide for both slender and non-slender columns (Lie & Chabot 1992, Chabot and Lie 1992, Kordina & Klingsch 1983 and Park et al. 2007, 2008), extensive experimental programs specifically designed for slender high strength CFT columns are required, attending to the reduced number of results found in the literature. Lu et al. (2009) studied the effect of filling CFT stub columns with HSC, but did not study its effect in slender columns. Only Hass et al. (2000), Han et al. (2003) and Kodur & Latour (2005) have performed some tests combing HSC and slender CFT columns. Nevertheless, results from these authors are not enough to evaluate the influence of the main factors affecting the fire behaviour of high strength CFT columns.

In this paper, results from an extensive experimental program on slender axially loaded CFT columns exposed to fire are presented. The influence of parameters such as the concrete grade (C30 and C90), load level (20% and 40%; 60% in some cases), type of concrete filling (plain, bar reinforced and steel fibre reinforced concrete, hereafter referred to as C, RC, FC respectively) and load eccentricity was investigated.

2 EXPERIMENTAL PROGRAM

In this experimental program, 14 fire tests were carried out on normal and high strength concrete-filled tubular columns under concentric axial load and another 24 columns were tested under eccentric loads, with eccentricities of 20 and 50 mm. The tests were carried out in the fire laboratory of AIDICO (Instituto Tecnológico de la Construcción) in Valencia, Spain. The aim of the experimental program was to investigate the effects of four parameters on the fire behaviour of CFT columns: concrete strength (f_c), type of concrete infilling (plain, reinforced and steel fibre reinforced concrete), load level (μ) and load eccentricity (e). According to the regular practice in construction, test values of these parameters were selected. All the columns were 3180 mm long and had a diameter of 159 mm and steel tube wall thickness of 6 mm. The columns were pinned at their top end and fixed at their bottom end, and for the eccentrically loaded columns, the eccentricity was only applied to the upper end. The specimens were filled with concrete mixes of 30 MPa (NSC) and 90 MPa (HSC). For all tests, the applied load was calculated as a percentage of the corresponding ultimate load at room temperature, which was obtained by means of a validated numerical model. According to the more common load levels found in practice, values of 20% and 40% were used, although in some cases a 60% was also employed. The tested specimens with their material data, test load and fire resistance ratings (FRR) are listed in Table 1 for concentric loads and Table 2 for eccentric loads. The ultimate loads at ambient temperature can be derived for each case as the test load divided by the applied load level.

The tested specimens can be identified as follows:

NXXX-T-L-FF-EE-MM (e.g. C159-6-3-30-00-20), where N stands for type of concrete (C = plain concrete, RC = reinforced concrete and FC = fibre reinforced concrete), XXX is the steel tube outer diameter in mm, T the steel tube wall thickness in mm, L the nominal length of the column in meters, FF the nominal concrete strength in MPa, EE is the load eccentricity in millimetres and MM is the load level in % of the maximum capacity at room temperature.

Table 1. Test properties and results, concentric load.

Test	Name	f_c (MPa)	f_y (MPa)	Load (kN)	FRR (min)
1	C159-6-3-30-00-20	35.75	337.8	198	42
2	C159-6-3-30-00-40	28.55	337.8	396	25
3	C159-6-3-30-00-60	34.05	337.8	594	14
4	C159-6-3-90-00-20	70.6	341.45	335	38
5	C159-6-3-90-00-40	68.7	341.45	670	11
6	RC159-6-3-30-00-20	23.9	337.8	229	43
7	RC159-6-3-30-00-40	30	337.8	458	30
8	RC159-6-3-30-00-60	33.7	337.8	687	13
9	RC159-6-3-90-00-20	68.7	337.8	343	65
10	RC159-6-3-90-00-40	77	337.8	720	19
11	FC159-6-3-30-00-20	28.3	337.8	198	37
12	FC159-6-3-30-00-40	26.7	334.4	396	22
13	FC159-6-3-90-00-20	93.1	337.8	335	36
14	FC159-6-3-90-00-40	89.9	334.4	670	16

The tests were carried out in a 5×3 m furnace equipped with a hydraulic jack of 1000 kN maximum capacity. The columns were placed vertically inside the furnace, fixed at the bottom end and pinned at the top end. Once the load was applied, it was kept constant and the gas burners were then activated, following the standard ISO-834 fire curve with unrestrained column elongation.

The axial elongation of the columns was measured by means of a LVDT located outside the furnace. A general view of the furnace can be seen in Figure 1.

Figure 2 shows one of the tested columns after failure, where the deformed shape of the column after its global buckling can be observed, together with a detail of a local buckling that typically occurred close to the mid-height of the column and the cracks in the concrete areas under tension.

More details on the experimental program carried out by the authors can be found in Romero et al. (2011).

2.1 *Steel*

The cold formed circular steel hollow section columns used in the experimental program were supplied by a manufacturer. The steel grade was S275JR,

Table 2. Test properties and results, eccentric load.

Test	Name	f_c (MPa)	f_y (MPa)	Load (kN)	FRR (min)
15	C159-6-3-30-20-20	35.83	—	169	32
16	C159-6-3-30-20-40	42.17	332.031	337	16
17	C159-6-3-90-20-20	73.70	332.031	272	34
18	C159-6-3-90-20-40	74.64	343.628	544	11
19	C159-6-3-30-50-20	30.50	—	126	30
20	C159-6-3-30-50-40	38.25	365.651	253	23
21	C159-6-3-90-50-20	79.13	365.651	194	30
22	C159-6-3-90-50-40	98.32	365.651	388	16
23	RC159-6-3-30-20-20	39	357.221	180	48
24	RC159-6-3-30-20-40	40.38	357.221	360	24
25	RC159-6-3-90-20-20	93.67	357.221	264	48
26	RC159-6-3-90-20-40	96	386.376	528	23
27	RC159-6-3-30-50-20	31	386.376	140	39
28	RC159-6-3-30-50-40	39.50	386.376	280	20
29	RC159-6-3-90-50-20	92.97	315.221	204	40
30	RC159-6-3-90-50-40	91.87	315.221	407	16
31	FC159-6-3-30-20-20	34.67	315.221	169	31
32	FC159-6-3-30-20-40	31.50	337.767	337	17
33	FC159-6-3-90-20-20	87.12	337.767	272	23
34	FC159-6-3-90-20-40	83.04	337.767	544	13
35	FC159-6-3-30-50-20	33.00	318.638	126	30
36	FC159-6-3-30-50-40	37.65	318.638	253	19
37	FC159-6-3-90-50-20	96.99	318.638	194	29
38	FC159-6-3-90-50-40	92.78	326.394	388	15

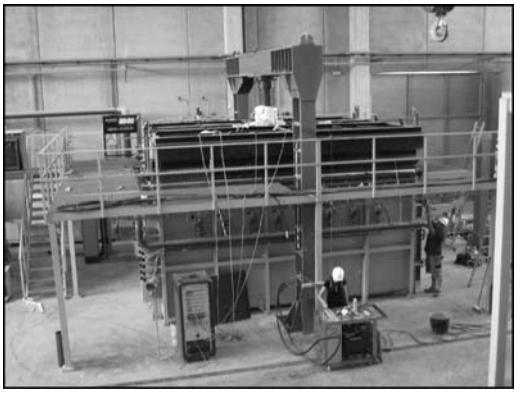

Figure 1. General view of the furnace.

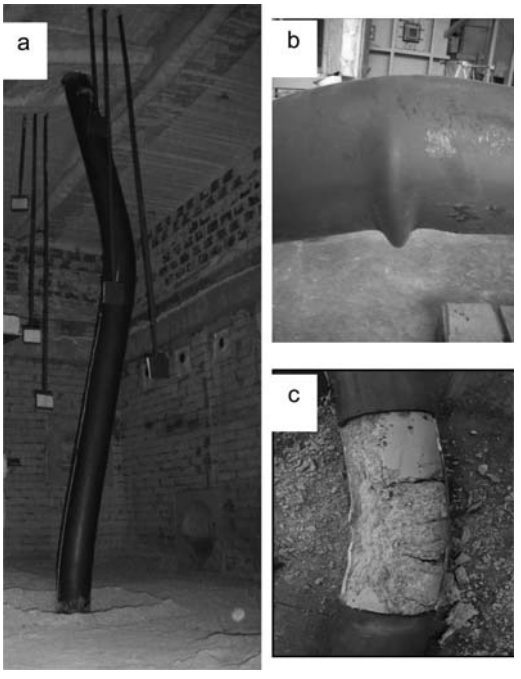

Figure 2. Column after failure: a) Overall buckling of the column, b) Local buckling at mid-height, c) Concrete cracking.

nevertheless the real strength (f_y) of the empty tubes was obtained by performing the corresponding coupon tests, and is summarized in Table 1 and Table 2. The mean value of the steel modulus of elasticity was 210 GPa according to the European standards.

2.2 *Concrete*

As mentioned above, the experimental program made use of concrete mixtures of normal (30 MPa) and high strength concrete (90 MPa).

In order to determine the compressive strength of concrete, sets of concrete cylinders were prepared and cured in standard conditions during 28 days. All cylinder samples were tested on the same day as the column fire test. In Table 1 and Table 2 the cylinder compressive strength of all the tested specimens can be found.

2.3 *Specimens*

The column specimens were 3180 mm long, having all of them a relative slenderness at room temperature higher than 0.5. All columns had an outer diameter of 159 mm and steel tube wall thickness of 6 mm. For each column, two ventilation holes of diameter 15 mm were drilled in the wall of the steel hollow sections and located at 100 mm from each column end. Steel end plates of dimensions 300 × 300 × 15 mm were welded to the column ends.

In order to register the temperature evolution within the cross-section during the fire test, a set of five thermocouples were located in the mid-length section of the columns.

The reinforced concrete (RC) specimens had an arrangement of four longitudinal reinforcing bars of 12 mm diameter and 6 mm stirrups with 30 cm spacing. The geometrical reinforcement ratio was close to a 2.5%.

The steel fiber reinforced (FC) specimens had a proportion of 40 Kg/m^3 high strength Dramix 40/60 steel fibers.

3 TEST RESULTS

3.1 *Concentrically loaded columns*

Figure 3 shows the evolution of the axial elongation versus the time of the test, for all the columns subjected to concentric axial load.

As expected, for both normal and high strength concrete, and for all type of reinforcements, the higher the axial load level applied, the lower the fire resistance rating (FRR) resulted.

From Figure 3a all the column specimens filled with plain concrete can be compared. It can be observed that for a certain load level, the fire resistance was lower for the HSC filled specimens, although it is important to clarify that for the same load level, the HSC cases were subjected to a higher axial load. It can be observed in Figure 3a that the specimen with a $\mu = 0.4$ and filled with HSC (C159-6-3-90-00-40) had a different behaviour, where the part of the curve corresponding to the contribution of the concrete core was not found (see Espinos et al. 2010 for a complete description of the typical failure mode of CFT columns under fire). This fact was also observed in the RC and FC specimens (Figures 3b and 3c) with the same load level and concrete strength combination. In all these cases the failure occurred before the load could be transferred to the concrete core, since its great magnitude made the column fail when the steel tube was still sustaining the whole applied load.

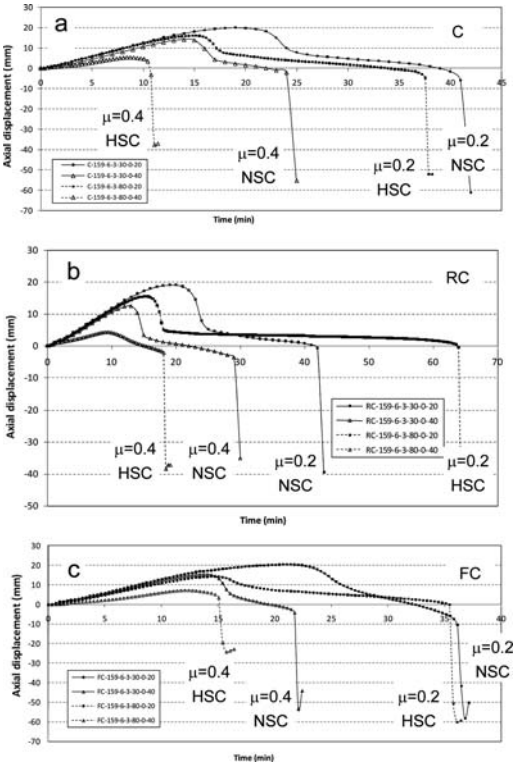

Figure 3. Axial displacement versus time curves for concentrically loaded columns: a) C, b) RC, c) FC.

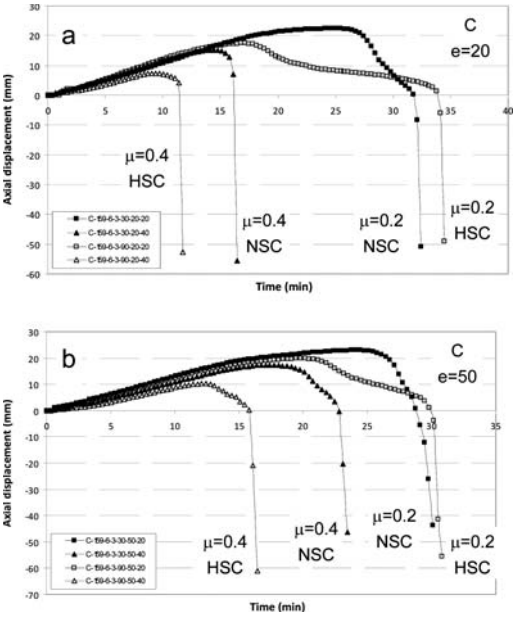

Figure 4. Axial displacement versus time curves for eccentrically loaded columns filled with plain concrete (C): a) e = 20 mm, b) e = 50 mm.

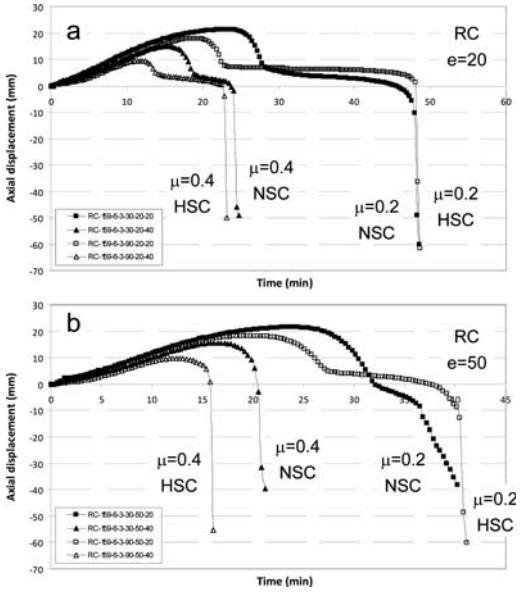

Figure 5. Axial displacement versus time curves for eccentrically loaded columns filled with bar reinforced concrete (RC): a) e = 20 mm, b) e = 50 mm.

In general, for the cases which used reinforcing bars (RC), plotted in Figure 3b, the FRR was higher compared to those filled with plain concrete, resulting specially improved for the RC159-6-3-90-00-20 (65 min). It is worth noting that all bar reinforced specimens were tested under a higher axial load (for the same load level) than their plain concrete counterparts, since their maximum capacity at room temperature was also higher.

However, filling the columns with steel fibre reinforced concrete did not improve their fire resistance, as can be seen in Figure 3c. In fact, while the axial load applied to these columns was the same than that of their plain concrete counterparts, a lower fire resistance was obtained in some of the cases. An explanation can be found in the temperature curves obtained from the thermocouples (not shown in this paper for simplicity), where a higher temperature was registered in the concrete for the FC specimens, which can be due to the lower moisture content in the fibre reinforced concrete which affects directly to the heating up of the column during the early stages of the fire tests.

Only for the column specimen with a higher axial load level and high strength concrete (FC159-6-3-90-00-40) a small increment was observed.

3.2 *Eccentrically loaded columns*

For those columns subjected to eccentric loads, the results are plotted in Figures 4 to 6 in terms of the evolution of the axial displacement of the top end of the column along the fire exposure time.

Obviously, for a certain type of concrete filling, as the load eccentricity was increased, the fire resistance

time decreased, except in those cases where the moisture content or the concrete strength was found higher in the specimen with the higher eccentricity, producing the opposite effect (see tests 5-18-22).

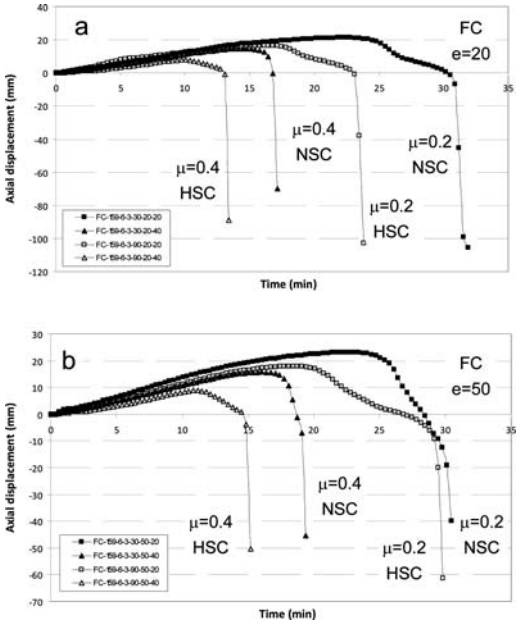

Figure 6. Axial displacement versus time curves for eccentrically loaded columns filled with fiber-reinforced concrete (FC): a) e = 20 mm, b) e = 50 mm.

The fire resistance of the HSC specimens was found lower than that of the NSC specimens for the higher load levels (40%), where in most cases the failure occurred before the load was transferred to the concrete core, thus not taking advantage of its contribution to sustain the applied load. Nevertheless, for a 20% load level, the difference was not so clear, the HSC specimens producing the same or higher fire resistance times with a higher axial load applied (except for tests 31 and 33).

From Figures 4 and 5, it can be inferred that the addition of reinforcing bars produced a benefit in the fire resistance, helping in some cases to avoid a premature failure of the column (see tests 24-26 versus 16-18), since the reinforcing bars improved the resistance of the concrete areas into tension, allowing the concrete to sustain the load for a certain time.

From Figure 6 it becomes clear that no special benefit was obtained though the addition of steel fibres, which leads to the same conclusion that was obtained for the concentrically loaded specimens.

Therefore, it can be concluded that for slender CFT columns no special benefit in the fire resistance is found through the addition of steel fibers, while the use of reinforcing bars can improve the fire performance of these columns under both concentric and eccentric loads, in some cases modifying their failure mode and allowing the contribution of the concrete core to sustain the load.

Regarding the use of high strength concrete, no particularities were encountered in the corresponding fire tests, without finding any evidences of the phenomenon of spalling, since in this type of columns the concrete core is protected from a direct exposure to the fire by means of the steel tube.

Table 3. Comparison of the buckling resistance at the time of failure between EC4 and tests, concentric load.

	Axial load (kN)				
Column specimen	TEST	EC4	TEST/EC4	EC4(H)	TEST/EC4(H)
Normal Strength Concrete					
C159-6-3-30-0-20	198	257.58	0.77	241.54	0.82
C159-6-3-30-0-40	396	490.40	0.81	507.36	0.78
C159-6-3-30-0-60	594	706.38	0.84	705.94	0.84
RC159-6-3-30-0-20	229	352.83	0.65	283.74	0.81
RC159-6-3-30-0-40	458	391.31	1.17	353.42	1.30
RC159-6-3-30-0-60	687	1146.18	0.60	1030.35	0.67
FC159-6-3-30-0-20	198	267.94	0.74	293.99	0.67
FC159-6-3-30-0-40	396	360.74	1.10	418.47	0.95
		Mean	**0.83**		**0.85**
		Std. dev.	**0.20**		**0.20**
High Strength Concrete					
C159-6-3-90-0-20	335	355.13	0.94	382.93	0.87
C159-6-3-90-0-40	670	1122.35	0.60	1128.86	0.59
RC159-6-3-90-0-20	343	328.45	1.04	234.35	1.46
RC159-6-3-90-0-40	720	727.01	0.99	736.38	0.98
FC159-6-3-90-0-20	335	443.12	0.76	541.05	0.62
FC159-6-3-90-0-40	670	1155.09	0.58	1263.36	0.53
		Mean	**0.82**		**0.84**
		Std. dev.	**0.20**		**0.35**

4 COMPARISON WITH EUROCODE 4

4.1 *Concentrically loaded columns*

In this section, the test results will be employed to study and discuss the current provisions of EN1994-1-2 (CEN 2005). This standard provides a method for calculating the fire resistance of CFT columns subjected to concentric and eccentric axial loads in its Annex H. The field of application of the method is C20/25-C40/50, so only columns with concrete cubic strength under 50 MPa can be calculated, nevertheless the application of the method for HSC specimens will be intended here in order to check its validity in this range of concrete strengths.

There is also a general simple calculation model for composite columns present in EN1994-1-2 (Clause 4.3.5.1), nevertheless the values of the reduction coefficients depending on the effect of the thermal stresses are not specified in the code for CFT columns. In the absence of predefined values, a common approach in practice is to take them as equal to unity (Lennon et al. 2007). Both methods will be studied here, where EC4 stands for the general method in Clause 4.3.5.1 and EC4(H) refers to the Annex H.

The elevated temperature strength reduction factors for steel and concrete employed for this comparison were those in Table 3.2 and Table 3.3 of EN1994-1-2 (CEN 2005), respectively.

All the tested specimens were compared with the predictions of the two approaches from EN1994-1-2 (CEN 2005). The buckling resistance of the columns at the time of test failure was obtained, and summarized in Table 3 for concentric load. The errors were computed as the test value divided by the prediction. It was found that the two simplified models (general method and Annex H) produced unsafe results, for both normal and high strength concrete with a mean value of the error under 0.85 and high dispersion of results, which demonstrates that the code does not produce accurate results for slender columns loaded in axial compression.

This result confirms the findings of previous investigations carried out by Aribert et al. (2008) and Espinos et al. (2010, 2011), who found that EN1994-1-2 simple calculation model leads to buckling load values which result unsafe for high column slenderness under concentric loads.

4.2 *Eccentrically loaded columns*

With regard to the eccentrically loaded columns, a comparison between the test results and the application

Table 4. Comparison of the buckling resistance at the time of failure between EC4 and tests, eccentric load.

	Axial load (kN)				
Column specimen	TEST	EC4	TEST/EC4	EC4(H)	TEST/EC4(H)
Normal Strength Concrete					
C159-6-3-30-20-20	169	103.91	1.63	124.47	1.36
C159-6-3-30-20-40	337	161.62	2.09	179.99	1.87
C159-6-3-30-50-20	126	57.45	2.19	57.81	2.18
C159-6-3-30-50-40	253	90.45	2.80	100.67	2.51
RC159-6-3-30-20-20	180	203.10	0.89	157.18	1.15
RC159-6-3-30-20-40	360	312.35	1.15	366.61	0.98
RC159-6-3-30-50-20	140	162.25	0.86	156.01	0.90
RC159-6-3-30-50-40	280	320.25	0.87	347.41	0.81
FC159-6-3-30-20-20	169	73.67	2.29	68.91	2.45
FC159-6-3-30-20-40	337	146.52	2.30	153.51	2.20
FC159-6-3-30-50-20	126	55.95	2.25	55.75	2.26
FC159-6-3-30-50-40	253	113.02	2.24	120.11	2.11
		Mean	**1.80**		**1.73**
		Std. dev.	**0.68**		**0.65**
High Strength Concrete					
C159-6-3-90-20-20	272	131.45	2.07	178.78	1.52
C159-6-3-90-20-40	544	334.41	1.63	343.14	1.59
C159-6-3-90-50-20	194	99.16	1.96	125.74	1.54
C159-6-3-90-50-40	388	205.16	1.89	258.54	1.50
RC159-6-3-90-20-20	264	262.63	1.01	236.70	1.12
RC159-6-3-90-20-40	528	416.67	1.27	440.69	1.20
RC159-6-3-90-50-20	204	226.92	0.90	240.05	0.85
RC159-6-3-90-50-40	407	491.24	0.83	556.02	0.73
FC159-6-3-90-20-20	272	159.84	1.70	214.41	1.27
FC159-6-3-90-20-40	544	283.98	1.92	338.43	1.61
FC159-6-3-90-50-20	194	108.21	1.79	140.52	1.38
FC159-6-3-90-50-40	388	218.53	1.78	259.01	1.50
		Mean	**1.56**		**1.32**
		Std. dev.	**0.44**		**0.29**

of the simple calculation model can be found in Table 4. For eccentric loads, a method is given in Section H.4 from Annex H of EN1994-1-2 (CEN 2005), where the buckling resistance is calculated as for columns without eccentricity, and afterwards two correction coefficients are used, as a function of the percentage of reinforcement (φ_s) and the load eccentricity (φ_δ), which are given by Figures H.1 and H.2 from the referred Annex.

For all the eccentric columns analysed in this paper, their buckling resistance at the time of failure were obtained under the two approaches explained above (Clause 4.3.5.1 and Annex H) as if they were subjected to concentric axial loads, and afterwards these loads were corrected by means of the two coefficients (φ_s and φ_δ) in order to obtain the corresponding buckling resistance under eccentric loads.

As can be seen in Table 4, for eccentrically loaded columns the two methods from EN1994-1-2 produced safe results (average value over 1 for both approaches), but with high errors and elevated dispersion of results. Similar results were obtained under the two approaches (EC4 and EC4(H)), although with a lower average error and dispersion for the high strength concrete filled specimens.

All the exposed above suggests that the current simple calculation model from EN1994-1-2 (CEN 2005) should be revised for both concentric and eccentric loads, and its applicability extended to higher concrete grades.

5 CONCLUSIONS

Through the results of the fire testing program presented here, a series of conclusions on the fire behaviour of slender CFT columns can be drawn.

Firstly, it can be concluded that in slender HSC filled columns spalling does not occur, probably due to the reduced duration of the fire tests and the reduced size of the section, which does not allow the development of high enough pore pressures inside the concrete.

The use of steel fibres did not show an increase in the fire resistance of normal or high strength concrete filled columns, probably because the failure in most of the tests was mainly due to the hollow steel column premature buckling, the concrete filling only helping to delay the heating of the column but not contributing to sustain the load. Nevertheless, an improvement was found when adding reinforcing bars, under both concentric and eccentric loads.

The current provisions of EN1994-1-2 (CEN 2005) were compared with the results of this series of fire tests, revealing that the method results unsafe for concentric loads when the slenderness of the columns is elevated (over 0.5 in all the cases studied), whereas under eccentric loads it turns to the safe side, but producing elevated errors and dispersion of results. Therefore, it is suggested here that the current simple calculation model should be improved in the future by means of test results and realistic numerical models.

ACKNOWLEDGEMENTS

The authors wish to express their sincere gratitude to the Spanish Ministry of Science and Innovation for help provided through project BIA 2009_09411, and to the European Community for the FEDER funds.

REFERENCES

Ali F, Nadjai A, Choi S. 2010. Numerical and experimental investigation of the behavior of high strength concrete columns in fire. *Engineering Structures*; 32(5):1236–1243.

Aribert JM, Renaud C, Zhao B. 2008. Simplified fire design for composite hollow-section columns. *Structures & Buildings*; 161:325–336.

CEN. 2005. *EN 1994-1-2, Eurocode 4: Design of composite steel and concrete structures. Part 1-2: General rules – Structural fire design*. Brussels, Belgium: Comité Européen de Normalisation.

Chabot M, Lie TT. 1992. *Experimental studies on the fire resistance of hollow steel columns filled with bar-reinforced concrete*. Internal report No. 628. Ottawa, Canada: Institute for Research in Construction, National Research Council of Canada (NRCC).

Ding J, Wang YC. 2008. Realistic modelling of thermal and structural behaviour of unprotected concrete filled tubular columns in fire. *Journal of Constructional Steel Research*; 64:1086–1102.

Espinos A, Romero M, Hospitaler A. 2010. Advanced model for predicting the fire response of concrete filled tubular columns. *Journal of Constructional Steel Research*; 66(8-9):1030–1046.

Espinos A, Gardner L, Romero M, Hospitaler A. 2011. Fire behaviour of concrete filled elliptical steel columns. *Thin-Walled Structures*; 49(2):239–255.

Han L, Zhao X, Yang Y, Feng J. 2003. Experimental study and calculation of fire resistance of concrete-filled hollow steel columns. *Journal of Structural Engineering*; 129(3):346–356.

Hass R, Ameler J, Zies H. 2000. *Fire Resistance of Hollow Section Composite Columns with High Strength Concrete Filling*. CIDECT Research Project 15P-12/00, Brunswick, Germany: Comité International pour le Développement et l'Etude de la Construction Tubulaire.

Hong S, Varma AH. 2009. Analytical modeling of the standard fire behavior of loaded CFT columns. *Journal of Constructional Steel Research*; 65:54–69.

Kodur VKR, Latour JC. 2005. *Experimental studies on the fire resistance of hollow steel columns filled with high-strength concrete*. Institute for Research in Construction, National Research Council of Canada (NRCC), Ottawa, Canada.

Kordina K, Klingsch W. 1983. *Fire resistance of composite columns of concrete filled hollow sections*. CIDECT Research Project 15C1/C2–83/27. Cologne, Germany: Comité International pour le Développement et l'Etude de la Construction Tubulaire.

Lennon T, Moore DB, Wang YC, Bailey CG. 2007. *Designers' guide to EN 1991-1-2, EN 1992-1-2, EN 1993-1-2 and EN 1994-1-2*. Thomas Telford Limited.

Lie TT, Chabot M. 1992. *Experimental studies on the fire resistance of hollow steel columns filled with plain concrete*. Internal report No. 611. Ottawa, Canada: Institute for Research in Construction, National Research Council of Canada (NRCC).

Lie TT. 1994. Fire resistance of circular steel columns filled with bar-reinforced concrete. *Journal of Structural Engineering-ASCE*; 120(5):1489–1509.

Lu H, Zhao X, Han L. 2009. Fire behaviour of high strength self-consolidating concrete filled steel tubular stub columns. *Journal of Constructional Steel Research*; 65(10-11):1995–2010.

Park S, Chung K, Choi S. 2007. A study on failure prediction and design equation of concrete filled square steel tube columns under fire condition. *International Journal of Steel Structures;* 7(3):183–191.

Park S, Choi S, Chung K. 2008. A study on the fire-resistance of concrete-filled steel square tube columns without fire protection under constant central axial loads. *Steel and Composite Structures*; 8(6):491–510.

Portolés JM., Romero ML, Bonet JL and Filippou FC. 2011. Experimental study of high strength concrete-filled circular tubular columns under eccentric loading. *Journal of Constructional Steel Research*; 67:623–633.

Portolés JM, Romero ML, Filippou FC, Bonet JL. 2011. Simulation and design recommendations of eccentrically loaded slender concrete-filled tubular columns. *Engineering Structures*; 33(5):1576–1593.

Renaud C, Aribert JM, Zhao B. 2003. Advanced numerical model for the fire behaviour of composite columns with hollow steel section. *Steel and Composite Structures*; 3(2):75–95.

Romero ML, Moliner V, Espinos A, Ibañez C, Hospitaler A. 2011. Fire behavior of axially loaded slender high strength concrete-filled tubular columns.*Journal of Constructional Steel Research*; 67(12):1953–1965.

Schaumann P, Kodur V, Bahr O. 2009. Fire behaviour of hollow structural section steel columns filled with high strength concrete. *Journal of Constructional Steel Research*; 65(8-9):1794–1802.

Twilt L, Hass R, Klingsch W, Edwards M, Dutta D. 1996. *Design guide for structural hollow section columns exposed to fire*. Cologne, Germany: Comité International pour le Développement et l'Etude de la Construction Tubulaire (CIDECT).

Wang Y, Kodur V. 2000. Research toward use of unprotected steel structures. *Journal of Structural Engineering;* 126(12):1442–1450.

Yin J, Zha XX, Li LY. 2006. Fire resistance of axially loaded concrete filled steel tube columns. *Journal of Constructional Steel Research*; 62(7):723–729.

Zha XX. 2003. FE analysis of fire resistance of concrete filled CHS columns. *Journal of Constructional Steel Research*; 59:769–779.

Tubular Structures XIV – Gardner (Ed.)
© 2012 Taylor & Francis Group, London, ISBN 978-0-415-62137-3

Nonlinear finite element modelling of flexible I-beam to square hollow section column connections subjected to earthquake and subsequent fire

Qian-Yi Song, Amin Heidarpour & Xiao-Ling Zhao
Department of Civil Engineering, Monash University, Melbourne, VIC, Australia

Lin-Hai Han
Department of Civil Engineering, Tsinghua University, Beijing, China

ABSTRACT: Steel beam-to-column connections are often damaged after an extreme loading. While steel I-beam to square hollow section column connections are widely used in steel frame structures, hitherto the behaviour of these connections subjected to the combined actions of earthquake and subsequent fire has not been investigated. This paper addresses a robust nonlinear 3D Finite Element Modelling (FEM) which is able to incorporate the behaviour of flexible I-beam to square hollow section column connections subjected to post-earthquake fire. The nonlinear analysis is conducted in two steps, including cyclic load and thermal load, to simulate the similar events which occur in real earthquakes. A numerical study is performed in which the effects of different parameters such as the thermal profile and thermal gradients, and degree of damage due to seismic loading are investigated. The developed finite element model will provide benchmark data for further experimental investigations and numerical models and has a potential to be used in evaluating of existing steel beam-to-column connection subjected to post-earthquake fire events.

1 INSTRUCTIONS

Earthquakes are one of the powerful nature hazards and usually lead to various types of structure damages. Moreover, it has been often followed by significant conflagrations which resulted in extensive damage. Records from historical earthquakes show that sometimes the damage caused by the subsequent fire can be much severe than the damage caused by the ground motion itself (Borden 1997). Due to the damages induced by the earthquake including damage to the structure, damage to fire protection of structural members and damage to the non-structural fire protection system (Chen et al. 2004), structures were vulnerable in the subsequent induced fire after the earthquake. Therefore, it is obvious that the safety of structures under fire after an earthquake should be evaluated.

The behaviour of the connections subjected to either seismic load or fire has been investigated in many of previous research. Recent years, although some researchers have investigated performances of structures subject to post-earthquake fire, the data is not enough to understand the behaviour of various structural components under post–earthquake fire. The results from investigation on steel frames under fire after earthquake showed a significant influence of earthquake on their fire resistance. Della Corte et al. (2003) investigated the post-earthquake fire resistance of steel frames. Modelling of frame structures was carried out in which the geometrical and mechanical damage effects by the earthquake were considered. In the other research work, Della Corte et al. (2005) investigated the behaviour of steel moment-resisting frames with numerical analysis. Two building structural systems with multiple levels of earthquake intensities and earthquake induced damage were considered. Yassin et al. (2008) presented an analytical study of two-dimensional steel frames under the effects of seismic lateral loads and subsequent fire. The study revealed that the post-earthquake fire performance of steel frames was affected by the lateral deformation caused by the seismic ground motion. Zaharia & Pintea (2009a) presented the evaluation of the fire resistance time for unprotected steel moment resisting frames damaged by the earthquake, in which both standard and natural fire scenarios were considered. Moderate and severe seismic actions were used for designing the steel structures. The methodology to evaluate the fire resistance time of the structures which were damaged by the earthquake was presented by Zaharia & Pintea (2009b).

Moreover, Collier (2005) reported the quantification of the reduction in the fire resistance of a series of plasterboard lined lightweight timber and steel-framed walls after being subjected to simulated earthquake. Mostafaei & Kabeyasawa (2010) reported results of a 3D performance simulation of a six-story reinforced concrete structure exposed to a fire after the shaking

table test for the Kobe earthquake 1995. Braxtan & Pessiki (2011) described damage patterns in sprayed fire resistive material on steel moment frame beam-column assemblages following a strong seismic event, and the thermal consequences of this damage when exposed to post-earthquake fire.

Although both geometrical and mechanical damage will be caused by the earthquake it is usually believed that only very large values of the peak ground acceleration can influence the steel strength and stiffness significantly. Then geometrical damage mostly referring to the residual plastic deformation is taken as the main damage of the structure components induced by earthquake, while the steel strength and stiffness degradation can be negligible when the earthquake is not so severe (Della Corte et al. 2003; Yassin et al. 2008). The investigations on steel frames mentioned above usually only consider the connection rotation as the damage induced by earthquake. As the connections are so important to the steel frames, it is necessary for us to understand the behaviour of various connections and evaluate their safety under the condition of post-earthquake fire, but so far the related data is very limited. Bursi et al. (2008a,b) and Alderighi et al. (2008) developed the experimental and thermal numerical models for undamaged and pre-damaged welded steel-concrete composite beam-to-column joints with concrete-filled tubes. Results showed the designed full-strength composite joints possessed enough resisting capacity under post-earthquake fire. Pucinotti et al. (2011a,b) presented and discussed an experimental program whilst the results were obtained from seismic tests, pre-damaged tests and fire tests on beam-to-column joints. The pre-damaged was induced by imposing monotonic loads equivalent to damage levels induced by seismic loading.

Steel I-beam to square hollow section column connections are widely used in steel frame structures. Hitherto, the behaviour of these connections subjected to the combined actions of earthquake and subsequent fire has not been investigated, although a post-earthquake fire is possible. This paper aims to investigate the behaviour of unprotected flexible steel I-beam to square hollow section column connections subjected to the post-earthquake fire using a numerical method.

2 FINITE ELEMENT MODELLING AND VERIFICATION

The FE modelling of connections under fire has been presented by many researchers Lee et al. (2011), Daryan & Yahyai (2009) and Al-Jabri et al. (2006). In the previous work by Gerami et al. (2011), Kumar & Rao (2006) and Pachoumis et al. (2009), the FE modelling of connections under cyclic loading also has been described. But the literature on the cyclic loading and the subsequent fire is limited. The FE modelling of the beam-to-column connections under post-earthquake fire is carried out in this paper using the finite element package ABAQUS as briefly described in the following sections.

2.1 *Material properties*

The FE analysis in this paper mainly focuses on the coupling of cyclic loading and the subsequent fire, in which heat transfer analysis and stress-strain analysis were combined to get the damage induced by earthquake and subsequent fire. The heat transfer analysis was used to get the temperature distribution of the connection under fire. As the thermal properties would not be affected by cyclic loading, those for an independent fire condition can be adopted in the post-earthquake fire condition. It is assumed that the convection heat transfer coefficient is 25 W/m^2K, and the radiation heat transfer coefficient is 0.5 W/m^2K (ECCS 1988). The specific heat (c_s) and conductivity coefficient (κ_s) are taken from ASCE manual (Lie 1992) so that

$$\rho_s c_s = \begin{cases} (0.004T + 3.3)\times 10^6 & 0°C \le T \le 650°C \\ (0.068T - 38.3)\times 10^6 & 650°C < T \le 725°C \\ (-0.086T + 73.35)\times 10^6 & 725°C < T \le 800°C \\ 4.55\times 10^6 & T > 800°C \end{cases} \quad (1)$$

and

$$\kappa_s = \begin{cases} -0.022T + 48 & 0°C \le T \le 900°C \\ 28.2 & T > 900°C \end{cases} \quad (2)$$

in which ρ_s is steel density taken as 7850 kg/m^3.

A bilinear strain-stress curve was used for the cyclic loading procedure under ambient temperature. Steel strength and stiffness usually decreases at high temperature environment. The thermal and mechanical properties for modelling the fire responds of steel connections vary with temperature. There were several temperature-stress-strain curves proposed by EC 3, ASCE manual (Lie 1992) and Poh (2001) while the comparison was listed by Kodur et al. (2010) using published experimental results. The EC3 curve was adopted by Al-Jabri et al. (2006), Mao et al. (2009), Daryan & Yahyai (2009), Franssen (2004) and Qian et al. (2009) for the material modelling, while the ASCE manual curve was used by Rahman et al. (2004) and Heidarpour & Bradford (2009, 2010) in which the ASCE manual curve (version 2) was adopted as the description of steel stress-strain relationship indicated such that

$$\sigma = \begin{cases} E_{s,T}\varepsilon_e & \varepsilon_e \le \varepsilon_p \\ (c_1\varepsilon_e + c_2)\sigma_{y,T} - c3\sigma_{y,T}^2 / E_{s,T} & \varepsilon_e > \varepsilon_p \end{cases} \quad (3)$$

where,

$$\varepsilon_p = \frac{c_2\sigma_{y,T} - c_3\sigma_{y,T}^2 / E_{s,T}}{E_{s,T} - c_1\sigma_{y,T}},\ c_1=12.5,\ c_2=0.975,$$

$c_3 = 12.5$. The variation of yield stress and elastic modulus of steel with temperature were taken from AS4100 so that

$$\frac{f_y(T)}{f_y(20)} = \begin{cases} 1.0 & 0℃ < T \le 215℃ \\ \dfrac{905 - T}{690} & 215℃ < T \le 905℃ \end{cases} \quad (4)$$

and

$$\frac{E(T)}{E(20)} = \begin{cases} 1.0 + \left[\dfrac{T}{2000\left[\ln\left(\dfrac{T}{1100}\right)\right]}\right] & 0℃ < T \le 600℃ \\ \dfrac{690\left(1 - \dfrac{T}{1000}\right)}{T - 53.5} & 600℃ < T \le 1000℃ \end{cases} \quad (5)$$

where, T = temperature of the steel, $f_y(T)$ = yield stress of steel at T°C; $f_y(0)$ = yield stress of steel at ambient temperature; $E(T)$ = modulus of elasticity of steel at T°C; $E(0)$ = modulus of elasticity of steel at ambient temperature.

The elastic modulus and Poisson's ratio at ambient temperature are assumed to be 2.06×10^5 MPa and 0.3, respectively. Steel thermal expansion coefficient under elevating temperature was taken as temperature-dependent data which is represented by (Lie 1992).

$$\alpha_s = \begin{cases} (0.004T + 12) \times 10^{-6} \text{ m/(m℃)} & T < 1000℃ \\ 16 \times 10^{-6} \text{ m/(m℃)} & T \ge 1000℃ \end{cases} \quad (6)$$

Pre-tension was not applied to the bolts during the analytical study. The combined hardening criterion was used to describe the kinematic hardening behaviour of steel under cyclic loading and isotropic hardening under the following fire. In the analysis, a subroutine named as USDFLD was used to transfer the material properties from bilinear stress-strain curve at ambient temperature to the temperature dependent strain-stress curves at elevated temperature once the cyclic loading procedure is finished.

2.2 *Element and contact relationship*

A 3D solid element was used for all steel components in the FE model. A reduced integration element with suitable mesh leads to the good results and saved calculation time. The C3D8R hexahedral element was used. Meshing Analysis was carried out to make sure the analysis is converged.

A surface-based interaction, with contact pressure model in the normal direction and a coulomb friction modelling in the tangential direction between the surfaces of the angle, beam and bolts was used. Friction coefficient of 0.3 was used by Rahman et al. (2004), 0.25 by Sarraj et al. (2007), 0.1 by Al-Jabri et al. (2006), 0.25 by Daryan & Yahyai (2009). Temperature dependent friction coefficients were adopted by Lee et al. (2011). In this paper, a coefficient of 0.25 was adopted for the contacting pairs. Edges of the angle were "tied" to the column face in ABAQUS to simulate the welding.

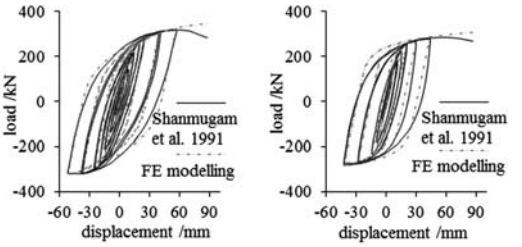

Figure 1. Comparison between test data (Shanmugam et al. 1991) and the FE modelling under cyclic loading: (a) connection CT1; (b) connection CT2.

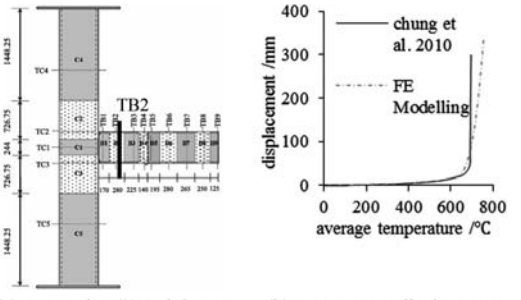

Figure 2. Fire loading comparison: (a) connection #1 and the section TB2 (Chung et al. 2010); (b) temperature-displacement relationship of TB2.

2.3 *Verification*

As the connection test under post-earthquake fire is limited and the modelling method showed above can be taken as two independent procedures under specific parameters and definition, results from cyclic loading and fire loading were used for the verification independently. Two connections named as CT1 and CT2 tested by Shanmugam et al. (1991) were used to verify the cyclic modelling depicted in Figure 1. It can be seen that the results obtained from FE modeling developed in this paper is in a good agreement with those reported test data. Consequently, the cyclic loading modelling can be used to generate reliable residual deformations for the subsequent fire procedure.

The verification under fire was carried out using the connection #1 tested by Chuang et al. (2010), and temperature-displacement relationship of TB2 is shown in Figure 2. Although the exact connection components and heated areas have not been described in detail, the difference between the numerical model and the connection test is not significant so that, overall,

the FEM result agrees well with the test data and can be used to generate reliable deformation relationship under fire procedure.

3 POST-EARTHQUAKE FIRE ANALYSIS

3.1 *Geometry and parameters*

The geometry and parameters of the connection designed to be investigated under post-earthquake fire are listed in Table 1. The details are showed in Figure 3.

The steel Grade C350 was used for the column, angle and column end plates, and the steel Grade 300PLUS was used for the beam and stiffeners. The yield stress of C350 steel was 360 MPa, and that of 300PLUS steel was 320 MPa (HRSSP 2003). Grade 8.8 of M10 bolts was adopted in this paper where the nominal yield stress of G8.8 was assumed to be 640 MPa.

3.2 *Boundary condition and loading protocol*

The beam-column connections investigated in this paper were subjected to cyclic load followed by fire . The cyclic load and the constant load in the fire were applied on the top of the beam end. One end of the column was assumed to be fully fixed in the furnace while another one was fixed in all degrees of freedom expect in axial direction. The boundary condition and the area of the beam which is subjected to fire are shown in the Figure 4a. It is assumed that the beam is subjected to fire from one side or both sides. The fire follows the ISO834 standard elevated temperature curve. The loading protocol recommended by AISC (2005) was used in this paper for the cyclic loading as shown in Figure 4b. The finite element model is depicted in Figure 5 whilst the total amount of elements was 39603.

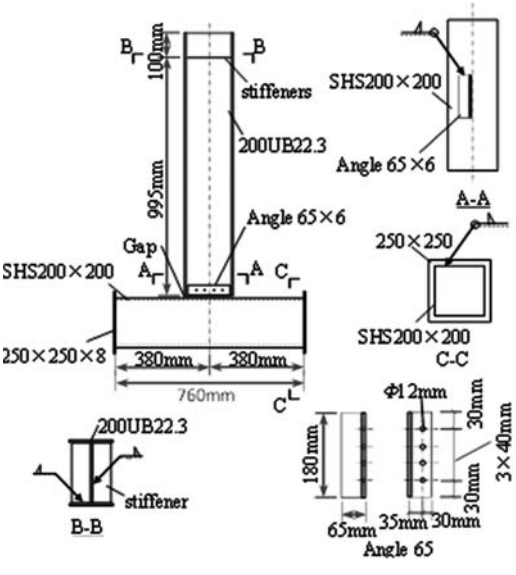

Figure 3. Geometrical details of the connection for FE model.

3.3 *Behaviour at ambient temperature and the post-earthquake damage*

As depicted in Figure 6a the static behaviour of the simple connection includes two stages. In the first stage, the beam flanges are free to rotate due to the gap between them and the column face. Bolts and the angle contribute the resistance of the connection against moment. If the bolt and angle are strong enough, when the bottom flange contacts the column face the second stage starts and the column face would help to resist loading until failure occurs.

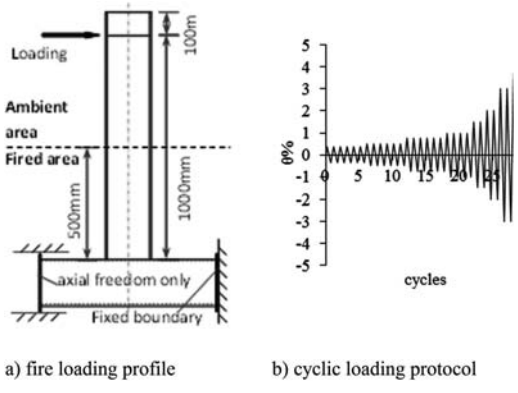

Figure 4. Loading status: (a) fire loading profile; (b) cyclic loading protocol.

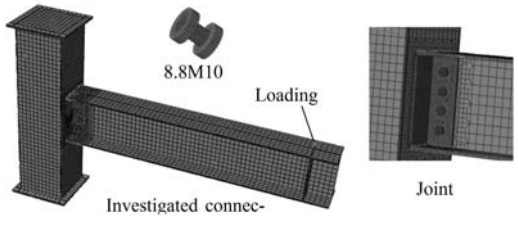

Figure 5. Finite element model of the simple connection.

Table 1. The geometry and properties of the connection components

Column		Beam		Angle	
Section (mm)	Grade	Section (mm)	Grade	Section (mm)	Bolt
200 × 5	C350	200UB22.3	300PLUS	65 × 6	8.8M10

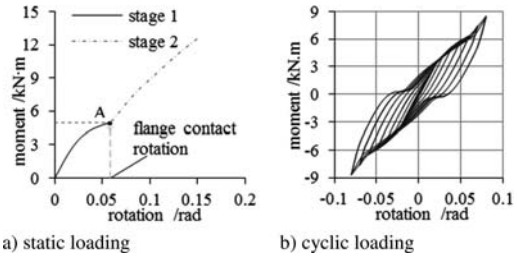

Figure 6. Moment-rotation relationships of the connection subjected to static and cyclic loadings.

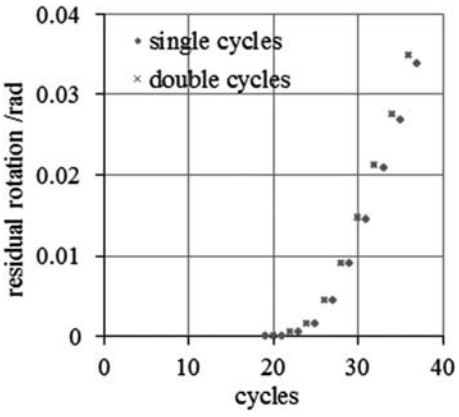

Figure 7. Positive residual rotation after cyclic loading.

The moment-rotation relationship of the connection subjected to the cyclic loading is shown in Figure 6b. Residual drift rotation exists after several cycles corresponding to zero loading force, which is taken as the main factor affecting post-earthquake behaviour of the connection. The residual rotations related to different loading cycles following AISC standard, which are assumed to be positive in clockwise direction, are shown in Figure 7. As the same amplitude is applied to two cycles after the 22nd loading cycle, the adjacent two cycles have the similar residual rotation. The residual rotation increases with the increasing of cycle numbers and the amplitude. The different residual rotation can be taken as the pre-damage characteristic which depends on the earthquake intensity.

3.4 *Heat transfer analysis*

Considering the same heat transfer procedure under fire and post-earthquake fire condition, the temperature distribution of the connection under ISO834 fire is depicted in Figures 8 and 9. Due to the density distribution of the components and the fact that whether the connection is subjected to fire at both sides of the beam section, the magnitude of the temperature varies at different parts of the connection. It is seen that the temperature distribution is symmetric when the connection is subjected to fire at both sides of the beam,

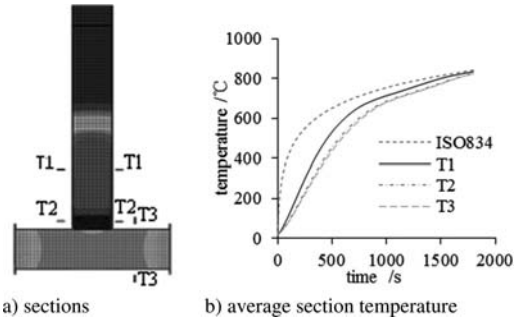

Figure 8. Temperature distribution when the connection is subjected to fire at both sides of the beam: (a) steel connection; (b) average section temperature.

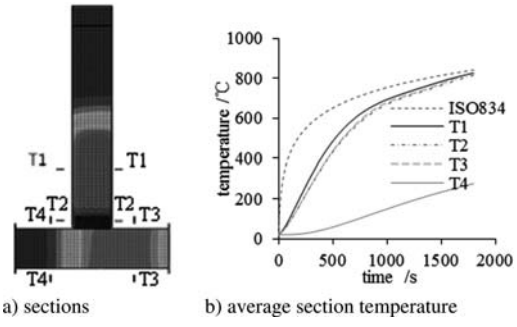

Figure 9. Temperature distribution when the connection is subjected to fire at one side of the beam: (a) steel connection; (b) average section temperature.

but in the single-side fire the temperature of the fired side is much higher than another side. As shown in Figures 8b and 9b, the average temperature of the beam section is elevated faster than other parts, and the connection temperature under single-side fire is elevated lower than that under when both sides of the beam are subjected to fire. The connection temperature was lower than the ambient ISO temperature at the beginning of the fire loading, but tended to be the same at the time of 1800s.

3.5 *Post-earthquake analysis*

In the post-earthquake fire and independent fire analyses, 1/4 of the static load (point A in Fig.6a) in which the bottom flange contacts the column face is taken as the constant static load applied to the beam end. During the post-earthquake analysis a series of the cycle numbers 20, 25, 30 and 35 are selected to simulate different earthquake intensity.

The connection rotation or deformation of beam end was usually used as the damage criterion. The column face deformation is also used as damage criterion for T connections (Zhao 2000). In this paper, the ISO terminating status is taken as damage criterion which defined as the deflection ratio on the beam end

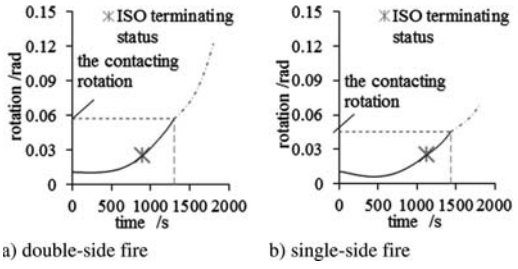

Figure 10. Time-rotation relationship of the original connection under fire without beam axial restraint: (a) double-side fire; (b) single-side fire.

exceeds $L^2/900$ h (mm/min) or the maximum deflection achieves $L^2/800$ h or L/30 (mm), in which L is the effective span of the beam and h is the height of beam section.

3.5.1 *Independent fire loading*

The time-rotation relationship of the connection without beam axial restraint under fire is depicted in Figure 10. The deformation of the connection under single-side fire decreases apparently at the beginning of the fire, due to the single side expansion. The ISO834 terminating status was taken as the criterion to determine the surviving time under fire.

3.5.2 *Post-earthquake fire loading*

Figure 11 shows the variation of the rotation of the connection with respect to time when it is subjected to post-earthquake fire on one side or both sides of the beam element.

The surviving time of the connections without beam axial restraint is shown in Figure 12 for different earthquake intensity. It is evident that when the earthquake intensity increases the residual deformation increases. Thus, taking considering the deformation limitation, the connection is damaged soon after earthquake. Since the cyclic amplitude is not too large and the cycle number $N < 25$ is not large enough, therefore the residual deformation is small and therefore does not have significant effect on the surviving time under fire. When the number of cycles N is larger than 25, the residual deformation will be larger so that the fire resistance time of the connection under post-earthquake fire is shorter than the undamaged connection when it is subjected to fire only. As shown in Figure 12, the surviving time of the connection after 30 loading cycles when it is subjected to fire at both sides of the beam is only half of the corresponding value for the undamaged connection which is subjected to fire only. For the condition that fire is on one side of the beam after 30 loading cycles, the surviving time is about 3/4 of the corresponding undamaged connection when it is subjected to elevated temperatures. Furthermore, it can be seen from Figure 11 that when the connection is subjected to severe earthquake ($35 \leq N$) it gets fully damaged such that post-earthquake fire is not meaningful.

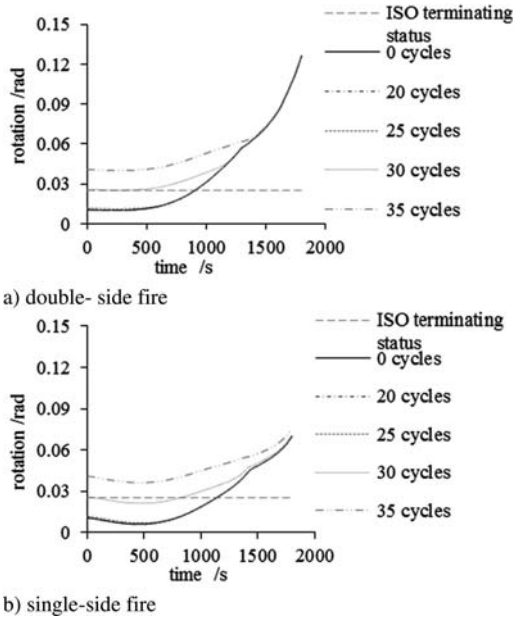

Figure 11. Results of post-earthquake fire loading: (a) double-side fire; (b) single-side fire.

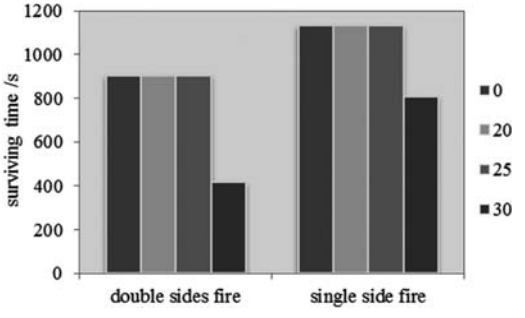

Figure 12. Comparison of the surviving time under fire.

3.5.3 *Effect of beam axial restraint*

The axial restraint effect was also investigated using the undamaged connections. In a steel frame, the steel beam is continuous and is connected to the columns so that at elevated temperature axial force exists in the beam due to expansion and the axial restraint provided by the columns. When an axial restraint is applied to the beam end, the restraint force of the beam affects the stress/strain status of the connection area and leads to different connection performance.

The temperature related time-rotation curves of undamaged connection with beam axial restraint are depicted in Figure13a. Figure 13b shows the variation of axial restraint force under ISO834 fire. It can be seen that due to the compression force induced by the axial restraint, which causes the buckling of the column face at about 1800s, the surviving time of the

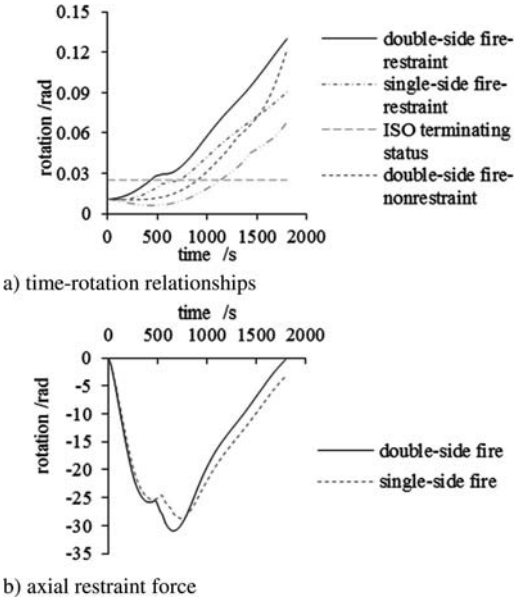

Figure 13. Temperature related curves of the undamaged connection under fire with beam axial restraint: (a) time-rotation relationships; (b) axial restraint force.

connection with axial restraint is significantly shorter than the connection without axial restraint.

For the connections damaged in the earthquake, beam axial force due to the restraints will also have significant influence on the behavior under fire loading as it was shown for the undamaged connections. The detail of the effect of axial restraint on the behavior of damaged connections will be shown in the further work.

4 CONCLUSION

This paper addressed a finite element model to investigate the behaviour of I-beam to box-column connections under post-earthquake fire where the connection deformation was taken as the main damage caused by earthquake. Based on the selected AISC cyclic loading procedure, the residual deformation after different earthquake intensity was calculated. Prior to post-earthquake fire analysis, static loading and heat transfer analysis were carried out to get the static behavior and temperature distribution. The damaged and undamaged connections were then analyzed using the proposed FEM method under fire and compared with each other.

The influence of earthquake intensity on the connections under fire was investigated. It was found that the surviving time of the connection subjected to severe earthquake will be significantly shorter than the undamaged or moderate-damaged connections. Furthermore, the effect of beam axial restraint on undamged connection was also investigated. It was shown that the restraint force has significant effect on the behaviour of the connection. Due to the limited test data available in the literature, tests will be carried out in future to investigate the behaviour I-beam to box-column connections under post-earthquake fire.

5 SYMBOLS

$E(0)$ the elastic modulus of steel at ambient temperature
$E(\mathrm{T})$ the elastic modulus of steel at T°
$E_{s,T}$ the elastic modulus of steel at T°
$f_y(\mathrm{T})$ yield stress of steel at T°
$f_y(0)$ yield stress of steel at ambient temperature
T the temperature
α_s Steel thermal expansion coefficient
ε_e the strain of steel
ε_p the strain corresponding to σ_y
σ the stress of steel
$\sigma_{\mathrm{y,T}}$ the yield stress of steel at T°

ACKNOWLEDGEMENT

The work presented in this paper was supported through a Discovery Project awarded to the second author by Australian Research Council.

REFERENCES

AISC. 2005. *Seismic Provisions for Structural Steel Buildings*. AISC 341-05, Chicago, American Institute of Steel Construction.

Al-Jabri, K.S., Seibi, A. & Karrech, A. 2006. Modelling of unstiffened flush end-plate bolted connections in fire. *Journal of Constructional Steel Research* 62(1-2): 151–159.

Alderighi, E., Bursi, O., Franssen, J.M., Lennon, T., Mallardo, R. & Pucinotti, R. 2008. Fire Performance of undamaged and pre-damaged welded steel-concrete composite beam-to-column joints with concrete filled tubes. *The 14th World Conference on Earthquake Engineering*, Beijing, China, October.

AS4100. 1998. Australian Standard *AS 4100-1998: Steel Structures*. Sydney, Australia: Standards Association of Australia.

Borden, F.W. 1997. The 1994 Northridge earthquake and the fires that followed, *Thirteenth Meeting of the UJNR Panel on Fire Research and Safety*, NISTIR 6030, March, 1996, (2): 303–312

Braxtan, N.L. & Pessiki, S.P. 2011. Postearthquake Fire Performance of Sprayed Fire-Resistive Material on Steel Moment Frames. *Journal of Structural Engineering-Asce* 137(9): 946–953.

Bursi, O.S., Cajot L.G., Ferrario, F., Gracia, J., Plumier, A., & Salvatore, W. 2008a. Seismic performance of welded steel-concrete composite beam-to-column joints with concrete filled tubes. *The 14th World Conference on Earthquake Engineering*, Beijing, China, October.

Bursi, O.S., Ferrario, F., Pucinotti, R. & Zandonini, R. 2008b. Seismic Induced Fire Analysis of Steel Concrete Composite Beam to Column Joints: Bolted Solutions. *Proceedings*

of the 2008 Composite Construction in Steel and Concrete Conference VI, Copper Mountain, July.

Chen, S., Lee G.C. & Shinozuka, M. 2004. Hazard mitigation for earthquake and subsequent fire. *ANCER Annual Meeting,Networking of Young Earthquake Engineering Researchers and Professionals*, *Honolulu, Hawaii, USA*: 29–30.

Chung, H.Y., Lee, C.H., Su, W.J. & Lin, R.Z. 2010. Application of fire-resistant steel to beam-to-column moment connections at elevated temperatures. *Journal of Constructional Steel Research* 66(2): 289–303.

Collier, P.C.R. 2005. *Post-earthquake performance of passive fire protection systems*: Building Research Association of New Zealand.

EC 3. 2005.*Design of Steel Structures Part 1–2: General Rules–Structural Fire Design*. EN 1993-1-2: 2005, Brussels: European Communities of Standardization.

ECCS. 1988. *Technical note-Calculation of the fire resistance of centrally loaded composite steel-concrete columns exposed to the standard fire*. Technical Committee 3, Fire safety of steel structures. No. 55, Brussels, Belgium: ECCS.

Daryan, A.S. & Yahyai, M. 2009. Modeling of bolted angle connections in fire. *Fire Safety Journal* 44(7): 976–988.

Della Corte, G., Faggiano, B. & Mazzolani, F.M. 2005. On the structural effects of fire following earthquake. *Proceedings of the Final Conference of COST Action C12*, *Innsbruck, Austria*, Taylor & Francis: 359–367.

Della Corte, G., Landolfo, R. & Mazzolani, F.M. 2003. Post-earthquake fire resistance of moment resisting steel frames. *Fire Safety Journal* 38(7): 593–612.

Franssen, J.M. 2004. Numerical determination of 3D temperature fields in steel joints. *Fire and Materials* 28(2-4): 63–82.

Gerami, M., Saberi, H., Saberi, V. & Aaryan, A.S. 2011. Cyclic behavior of bolted connections with different arrangement of bolts. *Journal of Constructional Steel Research* 67(4): 690–705.

Heidarpour, A., Bradford, M.A. 2009. Generic nonlinear modelling of restrained steel beams at elevated temperatures. *Engineering Structures* 31: 2787–2796.

Heidarpour, A., Bradford, M.A. 2010. Non-discretisation formualtion for the non-linear analysis of semi-rigid steel frames at elevated temperatures. *Computers and Structures* 88: 207–222.

HRSSP. 2003. *Hot rolled and structural steel products*, *the 3rd edition.* Onsteel.

ISO 834. 1975. ISO 834: *Fire resistancetests—elements of building construction*. Geneva, Switzerland: International Organization for Standardization.

Kodur, V., Dwaikat, M. & Fike, R. 2010. High-Temperature Properties of Steel for Fire Resistance Modeling of Structures. *Journal of Materials in Civil Engineering* 22(5): 423–434.

Kumar, S.R.S. & Rao, D.V.P. 2006. RHS beam-to-column connection with web opening – experimental study and finite element modelling. *Journal of Constructional Steel Research* 62(8): 739–746.

Lee, C.H., Chiou, Y.J., Chung, H.Y. & Chen, C.J. 2011. Numerical modeling of the fire-structure behavior of steel beam-to-column connections. *Journal of Constructional Steel Research* 67(9): 1386–1400.

Lie, T.T. 1992. *strucutral fire protection*. New York: American society of civil engineers.

Mao, C.J., Chiou, Y.J., Hsiao, P.A. & Ho, M.C. 2009. Fire response of steel semi-rigid beam-column moment connections. *Journal of Constructional Steel Research* 65(6): 1290–1303.

Mostafaei, H. & T. Kabeyasawa. 2010. Performance of a six-story reinforced concrete structure in post-earthquake fire. *The 9th US National and 10th Canadian Conference on Earthquake Engineering*, *Toronto, Ontario*, pp. 1–10.

Pachoumis, D.T., Galoussis, E.G., Kalfas, C.N. & Christitsas, A.D. 2009. Reduced beam section moment connections subjected to cyclic loading: Experimental analysis and FEM simulation. *Engineering Structures* 31(1): 216-223.

Poh, K. W. 2001. Stress-strain-temperature relationship for structural steel. *Journal of Materials in Civil Engineering* 13(9): 371–379.

Pucinotti, R., Bursi, O.S. & Demonceau, J.F. 2011a. Post-earthquake fire and seismic performance of welded steel-concrete composite beam-to-column joints. *Journal of Constructional Steel Research* 67(9): 1358–1375.

Pucinotti, R., Bursi, O.S., Franssen, J.M. & Lennon, T. 2011b. Seismic-induced fire resistance of composite welded beam-to-column joints with concrete-filled tubes. *Fire Safety Journal* 46(6): 335–347.

Qian, Z.H., Tan, K.H. & Burgess, I.W. 2009. Numerical and analytical investigations of steel beam-to-column joints at elevated temperatures. *Journal of Constructional Steel Research* 65(5): 1043–1054.

Rahman, A., Hawileh, R. & Mahamid, M. 2004. The effect of fire loading on a steel frame and connection. *High performance structures and materials II*. W. W. Brebbia CA, WIT Press: 307–316.

Sarraj, M., Burgess, I.W., Davison, J. & Plank, R.J. 2007. Finite element modelling of steel fin plate connections in fire. *Fire Safety Journal* 42(6–7): 408–415.

Shanmugam, N.E., Ting, L.C. & Lee, S.L. 1991. Behavior of I-Beam to Box-Column Connections Stiffened Externally and Subjected to Fluctuating Loads. *Journal of Constructional Steel Research* 20(2): 129–148.

Yassin, H., Iqbal, F., Bagchi, A. & Kodur, V.K.R. 2008. Assessment of post-earthquake fire performance of steel-frame buildings. *The 14th World Conference on Earthquake Engineering*. Beijing, China, October.

Zaharia, R. & Pintea, D. 2009a. Fire after Earthquake Analysis of Steel Moment Resisting Frames. *International Journal of Steel Structures* 9(4): 275–284.

Zaharia, R. & Pintea, D. 2009b. Advanced method for fire analysis of structures after earthquake. *Proceedings of the 11th WSEAS International Conference on Sustainability in Science Engineering*: 375–380.

Zhao, X. L. 2000. Deformation limit and ultimate strength of welded T-joints in cold-formed RHS sections. *Journal of Constructional Steel Research* 53(2): 149–165.

Tubular Structures XIV – Gardner (Ed.)
© 2012 Taylor & Francis Group, London, ISBN 978-0-415-62137-3

Performance of CHS T-joints in a standard fire test

M.P. Nguyen, K.H. Tan & T.C. Fung
School of Civil and Environmental Engineering, Nanyang Technological University, Singapore

ABSTRACT: This paper presents the performance of Circular Hollow Section (CHS) T-joints in a standard fire test. Both the experimental and numerical investigations were conducted. In the experimental programme, four T-joints, with two different brace-to-chord diameter ratios, were tested under two types of external loadings i.e. brace axial compression and in-plane bending. The fire was simulated using an electrical heating furnace with temperature following a standard ISO-834 fire curve. Thermal restraints were provided on the two ends of the chords. Temperature distributions, axial deformation, limiting temperature of steel and fire endurance of the CHS T-joints were measured. In the numerical study, finite element models of the joints were developed. Good agreement between results obtained from the experimental programme and numerical analysis shows the accuracy and validity of the FE models. The verified FE models were then used to compare fire resistance of other six T-joints which had difference β values.

1 INTRODUCTION

The behaviour of tubular joints always requires greater attention because of their complexity in stress distribution as a result of geometric discontinuity. Based on their structural geometries and load paths, tubular joints are classified in many categories from simple joints such as T-, X- and K-joints to complex multi-planar joints. For the most basic and frequently used tubular joints, such as T-joints, there have been extensive studies on their structural behaviour and joint strength from the first few tests of Toprac (1961) to massive investigation in 80s and 90s (Kurobane et al. 1984; Togo 1967; Van der Vegte and Wardenier 1995). A huge database, summarized by Packer (1985) and then updated by Makino *et al.* (1996), is now a backbone for many design codes such as EC3:P1.8 (1993), CIDECT (2010) and IIW (2009).

More recently, the investigation on behaviour of CHS T-joints are focusing on four main streams: thick-walled joints (Choo and Qian 2005), joints with initial cracks (Zerbst et al. 2002), effects of chord stresses (Van der Vegte and Makino 2006; Van der Vegte et al. 2010), and the reinforced joints (Fung et al. 2002).

However, very limited information is available on performance of the joints under fire conditions. After many fire catastrophes involving offshore structures, fire performance of tubular structures is concerned. Recently, isolated members gained more research attention (Lin and Tao 2007; Lin and Han 2005; Yang and Han 2005; Zhao et al. 2005). For T-joints, the available information is limited. Two studies have been carried out by Yu *at al.* (Yu et al. 2011) who presented an experimental study on mechanical behaviour of an impacted joint; and Jin *et al.* (Jin et al. 2011) who introduced a planar tubular truss under fire. However, the failure mechanism and performance of individual CHS T-joints at elevated temperature when the joint is subjected to a static load has not been investigated.

This paper presents the first research attempt to investigate the fire resistance of T-joints subjected to static loads. The study includes two parts: (1) standard fire tests conducted on four full-scale T-joints under two separate loading conditions and (2) finite element (FE) models to predict the behaviour of the joints. The tests provide first hand information on the performance of the joints. They also serve as calibration for FE analyses. In the test, the fire resistance of T-joints with difference brace-to-chord diameter ratios was experimentally determined to vary from 10–14 minutes with critical temperatures were 650–700°C for the 4 tested joints. By comparing the test results with the numerical analyses, a good agreement was found showing the accuracy and validity of the FE models. The FE models were also used to obtain the fire resistance of six other T-joints with different brace-to-chord diameter ratio ($\beta = d/D$) values. The verified models then were used to performed parametric analysis which will be reported in the future.

2 TEST PROGRAMME

The tests presented in this paper are part of a research project that consists of 70 T-joints both experimentally and numerically. The project focused on the structural behaviour and fire resistance of T-joints with different β and subjected to (a) brace axial compression or (b) in-plane bending. This paper presents four full-scale test results and other eight numerical analyses of

Table 1. CHS T-joint configurations subjected to the standard fire ISO 834.

Chord length, L (mm)	2200 ($\alpha = 18$)				
Brace/Chord thickness, t/T	6.3/6.3 ($\tau = 1$)				
Chord diameter, D (mm)	244.5				
Brace diameter, d (mm)	193.7	177.8	168.3	139.7	114.3
β (d/D)	0.79	0.73	0.69	0.57	0.47
Brace axial compression	BC.T.079.ISO	BC.T.073.ISO	BC.T.069.ISO	BC.T.057.ISO	BC.T.047.ISO
In-plane bending	IB.T.079.ISO	IB.T.073.ISO	IB.T.069.ISO	IB.T.057.ISO	IB.T.047.ISO

CHS T-joints subjected to the two separated loading conditions.

The specimen notations and joint configuration are shown on Table 1. For all joints in the research project, the chord diameter (D) was kept at 244.5 mm, and the brace-to-chord diameter ratios β ranged from 0.79 to 0.47. For the four tested joints considered in the current paper, the values of β were 0.47 and 0.69. Chord length-to-radius ratio ($\alpha = 2L/D$) was 18 to avoid short chord effects (van der Valk 1988) and the brace-to-chord thickness ratio ($\tau = t/T$) was 1.0 with the chord thickness as 6.3 mm. The specimens were named based on their loading condition (BC for axial compression, IB for in-plane bending) followed by the type of joint (T), and the value of β. They were all tested under the ISO standard fire condition.

2.1 *Test set-up*

The tests were conducted at the Construction Annex Laboratory of Nanyang Technological University. Figure 1 shows the test frame and the electric heating furnace. The specimen set up is presented in a 3D sketch with transparent furnace side walls for (a) brace axial compression and (b) in-plane bending. The CHS T-joint specimens were erected to the middle of the furnace. Both sides of the chord extended outside the furnace and the two ends were fixed to the upright column flanges of the two A-frames with sixteen 30 mm-diameter bolts. These frames acted as fixed supports and provided thermal restrained to the T-joint. For brace axial compression, external load was applied to the joint through a hydraulic jack placed at the center of the reaction frame. It should be noted that the jack could only generate compression forces through a manual- pump. For brace axial compression cases, the load was transferred directly to the brace as shown in Figure 1a. For in-plane bending cases, the load was transferred to the top of the brace via a pin-pin rod which provided load stability throughout the test as shown in Figure 1b. The dimensions of the opening on the furnace top were large enough to allow for bending of the brace.

The development of fire was simulated in an one-cubic-meter internal volume electric heating furnace of which the temperature-time relationship could be controlled precisely. The T-joints could be subjected to a fire conformed to EN:1363 .(1999), which states that specified specimens should be stressed to the

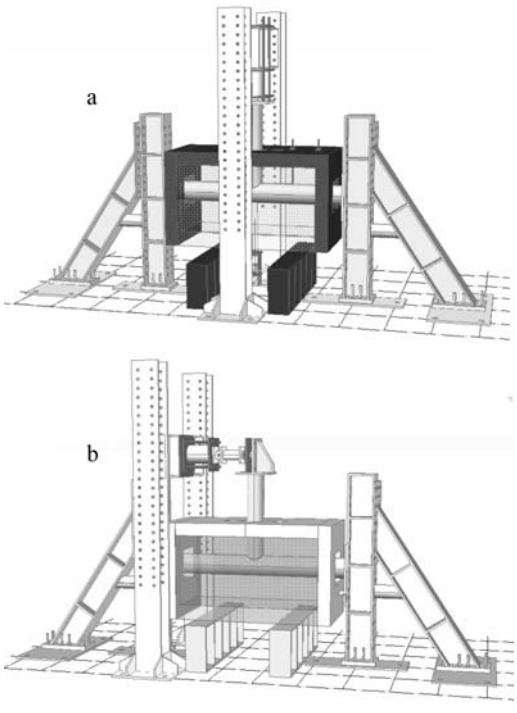

Figure 1. Overall test setup of the CHS T-joints in the standard fire test: a) Brace axial compression and b) In-plane bending.

required load level before they are heated up following a standard fire curve given

$$T = 345 \log_{10}(8t + 1) + 20 \ (^{o}\mathrm{C}) \quad (1)$$

where T is the surrounding temperature at time t in degree Celsius, and t is fire exposure time in minutes. The simulation of the standard fire test was confirmed by trial tests. Figure 2 shows the comparison of the standard fire curve with the heating generated by the furnace. At the early stage the furnace temperature was lower than the specified curve by 5 to 10°C which was within the tolerance limit of 15% stated in EN 1636-1 (1999). Therefore, it was concluded that the standard fire could be simulated by the electric heating furnace. In addition, the temperature uniformity within the furnace was also confirmed by the test, in which 18 thermocouples were installed around the furnace.

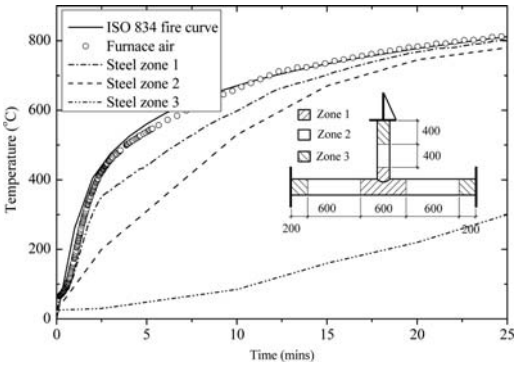

Figure 2. Temperature distribution on joint IB.T.069.ISO subjected to the standard fire.

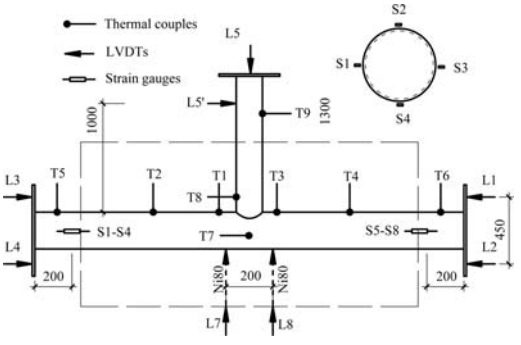

Figure 3. Instrumentation locations on specimens.

2.2 *Measurement*

Since the joints were tested within a well-insulated furnace, the joint behaviour should be captured using a high temperature heat resistance instrument. The layout of instrumentation is illustrated in Figure 3. Strains at two sections near the chord support locations were obtained through high-temperature heat-resistant strain gauges (S1 to S8). These gauges could provide high accuracy readings up to a temperature of 1100°C. It should be noted that at elevated temperature, the strain-gauge readings included thermal-expansion strain of steel material. Therefore, free-thermal-expansion strain was subtracted from the total measured strains. Based on the actual strains, the restrained forces on both sides of the chord ends can be calculated.

Nine type K mineral insulated thermocouple wires were used to measure the temperatures on the specimens as well as in the furnace interior. The thermocouples were arranged across the section of the specimens such that the temperature at the joint region could be captured.

For joints under axial compression loading, the relative deformations were obtained through reading of L5, L7 and L8. It is noted that the value of L5 is an average value of four LVDTs on the brace top. For joints under in-plane bending, the rotation of brace was obtained through reading of L5′. Rotations of the

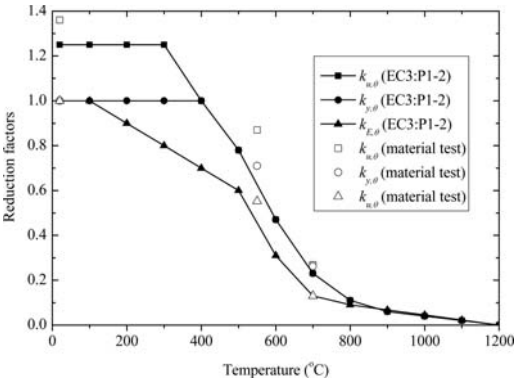

Figure 4. Chord material properties at elevated temperatures.

brace acted as a cantilever were subtracted from the measurement of L5′. On both loading cases, movements of the side supports were captured (L1 to L4) to evaluate the restraint effects.

Besides, on the top cover of the furnace, two special glass windows, which could resist high temperature, allowed for test observation. The observation was captured by using two digital cameras placed in front the glass windows.

2.3 *Material properties*

For all joints, the grade of steel was EN 10210 S355J2H. Tensile fracture tests were conducted to determine strength of the chords material. The yield strength was 380.3 MPa and ultimate strength was 519.1 MPa. The tensile fracture test was carried out at three different levels of temperatures, viz. at 28, 550 and 700°C. The temperature levels were chosen due to their effects on deterioration rates of steel elastic modulus, yield strength and ultimate strength.

Comparisons between the reduction factors from elastic modulus, yield strength and ultimate strength obtained for the tests and calculated from EC3:P1-2 (1995) are presented in Figure 4. A close relationship can be seen between the measured and calculated reduction factors for elastic modulus, yield strength and ultimate strength of the steel material used in the test programme. The continuous deterioration of steel properties with increase of temperature has to be modelled for numerical analysis. Although material tests were only done at the two elevated temperature levels, from this agreement with EC3, it is assumed that the steel deteriorations due to fire were mobilized using factors in EC3:P1-2, table C.1.

2.4 *Test procedure*

The test consisted of two phases starting with loading phase and then followed by heating phase. In the first phase, the specimens were loaded up to 60% of their ultimate strength at a loading rate in a range of 5–50 kN/minute. The ultimate strength of each joint was

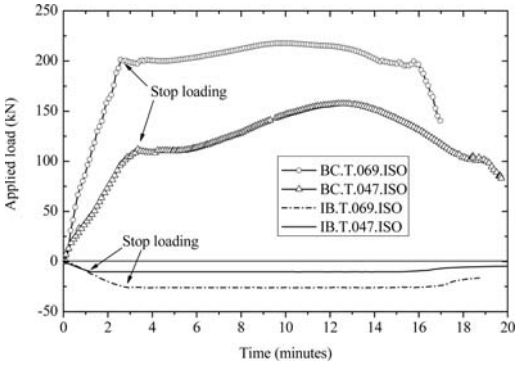

Figure 5. Load application on specimens.

determined based on tests presented in Nguyen (2010). Loading was maintained constant to the end of the test. Figure 5 presents the load-time relationship for the four tests.

Although the applied load is a compression force, in Figure 5, the values of loads for IB cases were set negative value for clearer illustration purpose. As can be seen on the figure the loads were applied continuously up to the loading levels. After the specimens were loaded to the desired loading, the second phase started. The standard fire condition was generated by the furnace according to a rate described in equation (1). During this phase, as the heating increased, the specimens started losing its strength. The test focused on the duration in which the specimens could sustain the applied load. The temperatures of the gas and the specimen were recorded when the joint failures occurred. For in-plane bending, during phase 1 and 2, it was observed that the applied loads were well maintained throughout. However, for brace compression case, the applied load fluctuated in phase 2 although it meant to be constant. During the interval between the 5th and the 12th minute, the loads on two joint BC.T.069 and BC.T.047 increased. The corresponding temperature at maximum load was 700°C, which caused additional force to the chord since these restrained on top of the braces. After the 12th minute, due to high temperature yielding that started to occur beneath the brace and steel, Young's modulus was reduced, and the applied loads reduced gradually. In an ideal test, the applied load on top of the braces should be released in accordance with the thermal expansion of the brace to keep loading unchanged. However, due to the limits of the test frame, the hydraulic jack can only provide additional pressure but not release pressure precisely.

2.5 *Failure criteria*

Although the joints were only loaded to 60% of the corresponding ultimate strength, due to the excessive deformation of the joint, the test was halted. Hence, the brace deformation was used as a major to determine the fire performance of the joints. The tests were stopped when the brace deformation reached a failure criterion specified by the deformation limit (Yura, 1981) $\delta = 24.79$ mm for axial compression and $\phi = 80 f_y / E = 0.135$ rad (24.3°) for in-plane bending. Failure ccould also be defined according to EN 1636-1 (1999) as deformation rates in which the rate for axial compression was 22 mm/min and in-plane bending was 3.3 mm/min.

3 TEST RESULTS

3.1 *Temperature development on the joints*

The development of temperature in the joint is shown in Figure 2 for Specimen IB.T.069. When the joint subjected to the ISO 834 fire curve generated by the electrical heating furnace, temperature distribution on the joint is divided into three zones based on the reading of nine thermocouples directly attached to the specimens. Zone 1 was the center part of the specimen where the brace met the chord, and the specimen temperatures were uniformly distributed. Zone 2 was defined along the length of the chord such that it was 300 mm away from the center and 200 mm from the chord ends. A linear variation of temperature was assumed and average temperature value was used to represent the temperature in this zone. As shown in Figure 2, the difference between the first two zones was not significant (100°C in first 8 minutes and 50°C after). Zone 3 was part of the joint extension beyond the furnace, where the temperature in the specimen developed much slower since these areas were surrounded by air. It could only received heat transferred from its steel body inside the furnace rather than direct expose to fire.

The same temperature developement was found for all other three tested T-joints. This was because all tested joints had identical mass distribution. Based on the temperature profiles of the four tested joints, the temperature distribution in three zones was used as input in numerical heat transfer analysis.

3.2 *Failure modes*

When subjected to ISO 834 fire curve, failures on the chords were observed for all T-joints. As the temperature increased, the steel material started to deteriorate. This caused local bending and shearing around the center welds. Plastic deformations were observed in this area and spread out on the chord wall.

Specimen failure in the case of brace axial compression is shown in Figure 6. It could be seen that the failure of the joint was a combination of overall bending and local plastification around the center welds. When exceeding the steel deteriorated yield strength, the compression stress caused by downward movement of the brace caused concentrated plastifications right beneath the saddle point. In addition, compression membrane forces due to chord overall bending caused the plastic hinge formation near the chord crown position. The plastic hinges were identified due to theirs excessive deformations, as shown

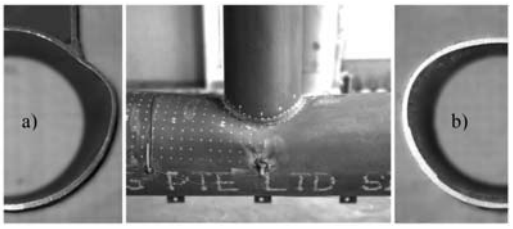

Figure 6. Failure mode of the joint BC.T.069.ISO a) cross-section at center and b) 200 mm from crow.

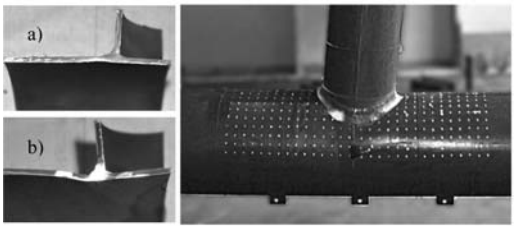

Figure 7. Failure mode of a joint IB.T.069.ISO a) tension part and b) compression part.

in Figure 6a. In addition to the local plastification process, overall bending of the chord caused significant changes to its cross section profile along the length - a process known as ovalisation (Brazier 1927; Elchalakani et al. 2002). The overall bending plastic deformations caused the circular hollow section to flatten at the top as illustrated in Figure 6b.

The specimen failure in the case of in-plane bending is show in Figure 7. The plastic deformations were a combination of tension and bending or compression and bending on two sides of the crowns. As the brace rotated, plastic hinges began to form around the weld toe at crown points, and significant deformations (downward on compression side and upward on tension side) were observed. Consequently, membrane actions occurred on the chord surface near the two crown points. The tensile membrane actions are the development of tensile stress on the whole cross section of the chord wall. It was observed using validated FE models. Figure 7a shows the plastic deformation caused by hogging moment and membrane forces on the tension side. Figure 7b, plastic deformation by sagging moment is showed. The chord material inside the brace section was observed to have little deformation.

3.3 *Fire resistance of the joint*

Responses of the CHS T-joints subjected to ISO 834 standard fire curve were shown in Figure 8 and 9 in terms of relationships between brace deformations and time. For clearer illustration purpose, deformation of joint T.047 was set to negative values. For all joints, it can be seen that the response of a joint is in accordance with the testing procedure which contains two phases. The first is loading phase, the join deformed linearly with applied load of 60% of its ultimate strength. On

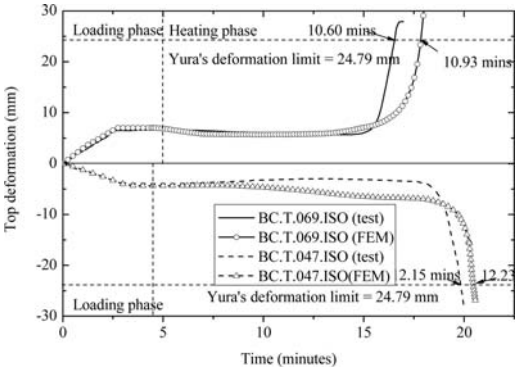

Figure 8. Fire resistance of joints subjected to brace axial compression.

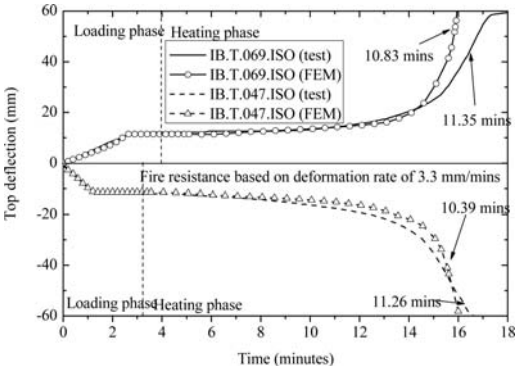

Figure 9. Fire resistance of joint subjected to in-plane bending.

the deformation-time curve (Figure 8 and 9), there is a plateau after load was applied which indicated the whole test frame is set stable under external loading, for all cases, the duration of this phase is in range of 3–5 minutes. The second phase started when the furnace operated. Subjected to a consistent load, the joint started to deform as the furnace inner gas temperature increase. It should be noted that the joint did not deform consistently but with an increasing rate. Once any of failure criteria was reached, the joint was considered to fail. Fire resistance of the joint is the duration from starting of stage two to the time when joint reached its deformation limit or deformation rate. For tubular structures, the deformation limit by Yura (1981) is well recognized. However, for in-plane bending cases, Yura's rotation limit for the joints was 0.135 rad which resulted in large deformation at loading point of 148.5 mm. Therefore, the deform rate limit by EN 1636-1 (1999) was adopted in parallel with Yura's deformation limit. Comparison of fire resistance determined by the two failure criteria was presented in Figure 10. It could be seen that for brace axial compression, the fire resistance determined based on two criteria were almost identical. For in-plane bending, good agreement was found on the fire resistant (time) but not for brace deformation.

There was significant difference on brace deformation as compared Yura's limit (148.5 mm) to deformation rate limit (58.2 mm). Considering the objective of test was the fire resistance, this study using Yura's deformation limit for brace axial compression cases and deformation rate for in-plane bending cases.

Fire resistance, gas temperature and joint temperature of all tested joints are reported in Table 2. In Figure 8, behaviour of Joint BC.T.069 and BC.T.047 subjected was shown. With a same loading ratio of 0.6, the Joint BC.T.069 had fire resistance of 10.6 minutes, which is shorter than Joint BC.T.047 which fire resistance was 12.15 minutes. In other words, at high temperature, joints with greater β would lose their strength faster than joints with smaller β. A possible reason may be the reduction on strength of the joint at high temperature is governed not only by the deterioration of yield strength but also by elastic modulus. Since the fire resistance is based on deformation limit, the reduction of Young's modulus plays a major role. Based on observation of test results and FE analysis, Nguyen (2010) concluded that the reduction of steel modulus led to faster reduction of the overall strength should the brace is smaller. The same trend was found in the in-plane bending cases. Figure 9 shows the response of the Joint IB.T.069 and IB.T.047 subjected to in-plane bending. The fire resistance of joint T.069 is 11.35 minutes while fire resistance of Joint IB.T.047 is 12.26 minutes. The critical air temperatures for all joints were listed on Table 2. They were in agreement with critical temperature of steel frame structure subjected to standard fire test obtained from EC3:P1-2(1995) which was range from 650°C to 710°C.

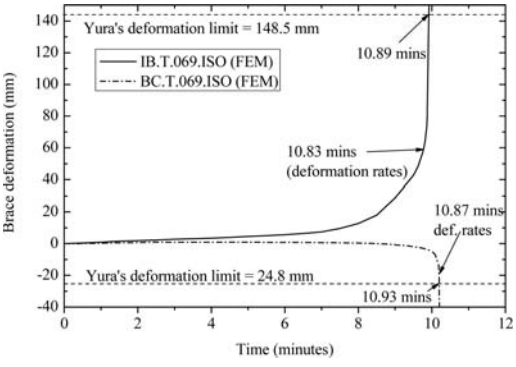

Figure 10. Comparision of the two failure criteria.

4 FINITE ELEMENT MODELS

A finite element (FE) analysis package, ABAQUS, was used to simulate the nonlinear behaviour of the CHS T-joints in standard fire test. The analysis procedure consisted of two steps. The first step was a stress analysis to obtain the deformation and stress/strain conditions of specimens subjected to preload of 60% their ultimate strength. The second step was a deformation analysis in which the deformation of the joint was monitored when the temperature of joint is prescribed to increase with time. The input of steel material with Young's modulus, yield strength and expansion as temperature dependent parameters followed coupon test measurements as presented in Section 2.4. The second step used the first step as the initial condition. It should be noted that the time step in analysis procedure was matched with the time in structural test for ease of model validations.

For the purpose of ultimate strength analysis, tubular joint are most commonly modeled by shell elements that represent the mid-surface of the joint member walls. This is generally agreed to be sufficiently accurate for simulating the joint behaviour. In this study, the FE models of the joins followed the modeling scheme of axially loaded CHS T-joints under elevated temperatures (Nguyen 2010). The models used eight-node doubly curved thick shell elements (S8R). Five layers of Gaussian integration points were generated across the chord and brace thicknesses. Temperature was assumed to be identical throughout the shell thickness and varied base on three zones mention in test results. A typical joint models subjected to brace compression was illustrated in Figure 11.

Table 2. Fire resistance of CHS T-joints.

		Fire resistance (mins)			Joint steel temp. (°C)			
	Load ratio	Test	FEM	FEM/Test	Gas temp.	Test	FEM	FEM/Test
IB.T.079.ISO	0.60		13.13				556.1	
IB.T.073.ISO	0.60		11.63				512.4	
IB.T.069.ISO	0.63	11.35	10.83	0.95	671.2	477.8	490.0	1.026
IB.T.057.ISO	0.60		10.55				483.2	
IB.T.047.ISO	0.59	11.26	10.39	0.92	663.0	476.9	454.6	0.953
BC.T.079.ISO	0.60		14.21				605.2	
BC.T.073.ISO	0.60		12.50				567.3	
BC.T.069.ISO	0.59	10.60	10.93	1.03	655.5	481.9	462.4	0.960
BC.T.057.ISO	0.60		10.42				451.3	
BC.T.047.ISO	0.59	12.15	12.23	1.00	707.6	552.1	523.2	0.948

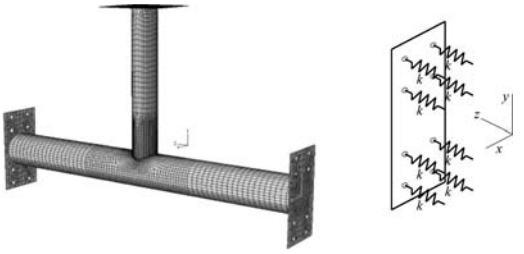

Figure 11. A typical joint models.

4.1 *Boundary condition*

In the test, chord ends were mounted to two A-frames by sixteen 30 mm-diameter-bolts. These frames and connections were designed as fix supports. However, during the tests, subjected to thermal expansion of the chords, the frames had moved outward in z direction. The chord longitudinal displacements were captured together with the chord axial compressions. In the FE modeling, the in-plane movements of bolt holes were set to zero ($u_x, u_y = 0$). In the z direction, to simulate the chord axial deformation, nonlinear springs were used. The spring stiffness k was determined base on recorded load-deformation relationship measured in the tests.

4.2 *Material models*

Material properties required in the analysis generally include elastic and inelastic mechanical properties and thermal expansion coefficient. To specified elastic mechanical properties of steel in ABAQUS, elastic modulus and poissons' ratio is required. For inelastic behaviour properties, a uni-axial stress-strain relationship, a yield function and a plastic flow rule were required to describe behaviour of steel under multi-axial stress state. It should be noted that in ABAQUS, under large deformation, true stress-strain relation is required for the uni-axial relationship rather than an engineering stress-strain one. In this study, a classic metal material model is chosen for steel. This model follows von Misses' yield function and associated plastic flow rule. Steel elastic modulus and true-stress strain relationship determined in the uni-tensile test were used, the temperature dependant rule of the steel follows EC3:P1-2. The thermal expansion coefficient of steel used in this analysis follows factor a proposed by the EC3:P1-2 (1995).

4.3 *Validations against test results*

Figures 8 and 9 present the numerical and experimental deformation-time curves for 4 tested specimens. The comparisons were made between deformation-time curves and failure modes of test results and FE predictions. From the comparisons, it can be seen that the numerical and experimental results match well. A small deviation is observed in the brace compression loading case. It might due to the fact that the applied load profile was modelled in accordance to Figure 5 (BC cases) instead of the thermal restraint at top of braces. From the comparisons, it can be conclude that the proposed FEA model was able to predict well the structural behaviour of the CHS T-joints subjected to ISO 834 fire curve.

The validated FE models then was used to estimated fire resistance of other T-joints indicated in Table 1. The results are summarized in Table 2.

5 CONCLUSION

In this paper, the findings of an experimental programme designed to investigate the performance of CHS T-joints in standard ISO 834 fire curve are presented. Failure mode and resistance of the joint in two loading condition were discussed. It was shows that fire resistance of the joints with different brace-to-chord ratios is varied from 10–14 minutes with critical air temperature were ranged from 650 to 700°C.

By comparing the results obtained from the tests and numerical analysis, a good agreement is found showing the accuracy and feasibility of the FE models. The verified models then were used to estimate fire resistance of other joint to illustrate the effect of β. Besides the models will be use for parametric analysis in future study.

ACKNOWLEDGEMENT

The research is funded by ARC 2/07 project entitled "Failures modes and ultimate strength of tubular joints under elevated temperatures" from the Ministry of Education, Singapore.

REFERENCES

ABAQUS (2009) "User Manual", Hibbit, Karlsson and Sorensen Inc. Providence, RI, Version 6.9–1.

Brazier, L. G. (1927). "On the flexure of thin cylindrical shells and other thin sections." *Proc. R. Soc*, 116, 104–114.

Choo, Y. S., and Qian, X. D. "Recent research on tubular joints with very thick-walled chords." *15th International Offrshore and Polar Engineering Conference, ISOPE-2005, June 19, 2005 - June 24, 2005*, Seoul, Korea, Republic of, 272–278.

EC3. (1993). "Eurocode 3: Design of Steel Structures, Part 1.8: General – Design of joints." EC3:P1–8.

EC3. (1995). *Eurocode 3: Design of Steel Structures, Part 1.2: General Rules – Structural Fire Design*, Brussels, Belgium.

EuroCode 1636 (1999). "BS EN 1363: Fire resistance tests – Part 1: General requirements." EN 1363:P1.

Elchalakani, M., Zhao, X. L., and Grzebieta, R. H. (2002). "Plastic mechanism analysis of circular tubes under pure bending." *International Journal of Mechanical Sciences*, 44(6), 1117–1143.

Fung, T. C., Soh, C. K., Chan, T. K., and Erni. (2002). "Stress concentration factors of doubler plate reinforced tubular T joints." *Journal of Structural Engineering*, 128(Compendex), 1399–1412.

ISO 834 (1999). "Fire-resistance tests-Elements of building construction – Part 1: General"

Jin, M., Zhao, J., Liu, M., and Chang, J. (2011). "Parametric analysis of mechanical behavior of steel planar tubular truss under fire." *Journal of Constructional Steel Research*, 67(1), 75–83.

Kurobane, Y., Wardenier, J., and de Back, J. (1984). "Ultimate Resistance of Unstiffened Tubular Joints." *ASCE Journal of Structural Engineering*, 110(2), 385–400.

Lin, X.-K., and Tao, Z. (2007). "Analysis of axially loaded concrete filled CHS stub columns after exposure to fire." *Harbin Gongye Daxue Xuebao/Journal of Harbin Institute of Technology*, 39(Compendex), 514–518.

Lin, X., and Han, L. (2005). "Load-displacement hysteretic behavior of concrete filled CHS columns after exposure to ISO-834 standard fire." *Jianzhu Jiegou Xuebao/Journal of Building Structures*, 26(Compendex), 19–29.

Makino, Y., Kurobane, Y. and K. Ochi, Van der Vegte, G.J., Wilmshurst, S.T. "Introduction to unstiffened CHS tubular joint database." *Tubular Structure* 157–164.

Nguyen, M. P., Tan K. H., Fung T. C. (2010). "Numerical models and parametric study on ultimate strength of CHS T-joints subjected to brace axial compression under fire condition." *International Symposium on Tubular Structures (ISTS 13)*, B. Young, ed., Hong Kong, 733–740.

Packer, J. A. K. J. S. M. (1985). "Database for axially loaded tubular T, Y and K-connections." *Department of Civil Engineering*, University of Toronto, Canada.

Togo, T. (1967). "Experimental Study on Mechanical Behaviour of Tubular Joints.," Osaka University, Osaka, Japan (in Japanese).

Toprac, A. A. (1961). "Investigation of corner connections loaded in tension." *Welding Journal*, 40(11), 521–528.

Van der Vegte, G. J., and Makino, Y. (2006). "Ultimate strength formulation for axially loaded CHS uniplanar T-joint." *International Journal of Offshore and Polar Engineering*, 16(4), 305–312.

Van der Vegte, G. J., and Wardenier, J. (1995). "Static behaviour of multiplanar tubular steel TT-joints excluding the effects of chord bending." *International Journal of Offshore and Polar Engineering*, 5(4), 308–316.

Van der Vegte, G. J., Wardenier, J., Qian, X. D., and Choo, Y. S. (2010). "Re-evaluation of the moment capacity of CHS joints." *Proceedings of the Institution of Civil Engineers: Structures and Buildings*, 163(Compendex), 439–449.

Yang, Y.-F., and Han, L.-H. (2005). "Fire behavior of concrete-filled double skin (CHS inner and CHS outer) steel tubular columns." *Harbin Gongye Daxue Xuebao/Journal of Harbin Institute of Technology*, 37(Compendex), 400–403.

Yu, W., Zhao, J., Luo, H., Shi, J., and Zhang, D. (2011). "Experimental study on mechanical behavior of an impacted steel tubular T-joint in fire." *Journal of Constructional Steel Research*, 67(Compendex), 1376–1385.

Zerbst, U., Heerens, J., and Schwalbe, K.-H. (2002). "The fracture behaviour of a welded tubular joint—-an ESIS TC1.3 round robin on failure assessment methods: Part I: experimental data base and brief summary of the results." *Engineering Fracture Mechanics*, 69(10), 1093–1110.

Zhao, X.-L., Hancock, G., and Wilkinson, T. (2005). *Cold-Formed Tubular Members and Connections*, Elsevier.

Tubular Structures XIV – Gardner (Ed.)
© 2012 Taylor & Francis Group, London, ISBN 978-0-415-62137-3

Structural behavior of CHS T-joints subjected to brace in-plane bending at elevated temperatures

M.P. Nguyen, T.C. Fung & K.H. Tan
School of Civil and Environmental Engineering, Nanyang Technological University, Singapore

ABSTRACT: Fire resistance of steel joints is one of the major concerns when designing structures against extreme hazards. However, little information is available for Circular Hollow Section (CHS) joints in fire condition, especially for T-joints. In order to gain greater insight into the static behaviour of CHS connections, this paper presents an experimental study of CHS T-joints subjected to in-plane bending with variation of brace-to-chord diameter ratios (β) under elevated temperatures. The tests were conducted with five specimens in isothermal heating condition where the joints were heated to the desired temperatures and then subjected to static load until failure occurred. The failure modes and ultimate strengths of such joints under various isothermal temperatures were investigated and compared with the corresponding joints at the ambient condition. Within the range of investigated parameters, at 700°C, the joint strength was only 8.40 kNm while at ambient temperature, it was 43.25 kNm. Furthermore, at high temperature, there was a change in the failure modes of the joints. Cracks formed around the weld toes before the joints reach excessive deformation. These cracks affected post-yield strength in moment-rotation curves of the joints. In order to understand the development of cracks around the welded region, material tests were performed to determine the fracture strains of chord material beneath the center weld at high temperatures. To the authors' best knowledge, these structural tests were among the first reported experimental investigations on the ultimate strength and failure mechanisms of tubular joints at elevated temperature.

1 INTRODUCTION

Steel tubular members have been widely used in steel design. As an important part of structures, tubular joints require greater attention than other components because of theirs geometric discontinuity and complexity in stress distribution at the connections. For T-joints in ambient temperature there has been extensive reported literature on the joint strength. The first few tests were conducted by Toprac (1961). Following, T-joint has been extensively studied by Van der Vegte (1995), Togo (1967) and Kurobane *et al.* (1984) in 80s and 90s. Database on the joint behaviour was first introduced by Packer (1985). In 1996, Makino (1996) updated the database which contained of 127 test and 89 numerical investigations. The database provides an excellent background for many design codes such as EuroCode3, CIDECT (2010) and IIW (2009). Up till now, the database and design codes have been continually developed by many researchers who focus on four main themes: thick-walled joints (Choo and Qian 2005), joints with initial cracks (Zerbst et al. 2002), effects of chord stresses (Van der Vegte and Makino 2006), and reinforced joints (Fung *et al.* 2002).

Besides the normal service loads, fire is always a major concern in the design of tubular steel structures, particularly the steel joints. However, it is noted that most research works of steel structures at elevated temperatures mainly concentrate on behaviour of isolated members (Lin and Tao 2007; Lin and Han 2005; Yang and Han 2005; Zhao et al. 2005) while very few publications were on steel tubular T-joints. Yu *at al.* (2011) presented an experimental study on mechanical behaviour of an impacted steel tubular T-joint in fire. Jin *et al.* (2011) conducted a parametric study on the mechanical behaviour of steel planar tubular truss under fire to investigate the failure modes, temperature distribution and load bearing capacities. However, the failure mechanism and ultimate strength of separated CHS T-joint at elevated temperature subjected to a static load have not been investigated before.

In this paper, experimental study was carried out to investigate the structural behaviour of CHS T-joints subjected to in-plane bending in fire condition. The study focused on the failure mechanisms and static strength of the joints. Therefore, isothermal heating test procedure was selected for this study and axial restraint due to thermal expansion was released. The test results provided valuable test data so as to shed light on the behaviour of CHS T-joints at elevated temperatures.

2 TEST PROGRAMME

Figure 1 shows the configuration of a typical CHS T-joint and also three geometrical ratios tubular steel joints. In this study, the chord diameter of all joints was taken as 244.5 mm, with the brace-to-chord diameter ratio ($\beta = d/D$) varying from 0.2 to 0.8. Chord length-to-radius ratio ($\alpha = 2L/D$) was 18 to avoid short chord effects (van der Valk 1988) and the brace-to-chord thickness ratio ($\tau = t/T$) is 1.0 with the chord thickness (T) as 6.3 mm. The grade of steel was EN 10210 S355J2H.

The test results shed light on the T-joint behaviour at high temperature and provide database for numerical validations. The tested specimens were a combination of three levels of temperature (i.e. 20, 550 and 700°C) and three levels of β (i.e. 0.47, 0.69, 0.79). The value of β chosen was within the practical design range. The selection of these temperatures was based on significant changes of steel properties specified in EC3:Part1-2. More specifically, at 20°C, steel properties do not change; at 550°C there are significant reductions in both the yield strength and stiffness; lastly, at 700°C steel almost entirely loses its yield strength. The nomenclature of each specimen is presented in Table 1. The nomenclature is based on the type of loading (IB for in-plane bending), followed by the type of joint (T), value of β, and the temperature at which the joint was tested.

2.1 *Test setup*

The isothermal heating test is a procedure whereby a specimen is heated to a specified temperature and then tested at that constant temperature. This testing process was performed within a 1m^3-internal-volume electric heating furnace. The maximum interior temperature could reach 1100°C and maintain at that temperature for three hours. The temperature uniformity within the furnace was first confirmed by a trial test, in which 18 thermocouples were installed around the furnace. Thermocouple readings showed that the interior gas temperature was rather uniform with a maximum variation of ±20°C at the maximum temperature of 1100°C.

The test setup is shown in Figure 2 where CHS T-joints were placed in the middle of the furnace. Each side of the specimen was bolted to an external A-frame. The chord was extended outside the furnace and its two ends were fixed to the upright column flanges of the A-frames by sixteen 30 mm-diameter bolts. To release thermal restraint during the heating process, one end of the chord was laid on a roller support. When the temperature at the joint center had reached a stable state, this roller support was tightened to the A-frame to simulate a fixed end condition.

In-plane bending was applied to the joint through a system as shown on Figure 2. Lateral force was generated by a 100-Ton hydraulic jack horizontally placed at the center of the reaction frame. The load was transferred to the top of the brace via a pin-pin rod which provided load stability throughout the test. The dimensions of the furnace opening at the top were large enough to allow for lateral deflection of the brace under bending.

To minimize heat losses and to provide a safe testing environment, all the extensions of the joint beyond the furnace were wrapped in an insulating blanket. The furnace openings after erection of specimens were filled with glass-fibre insulation as well.

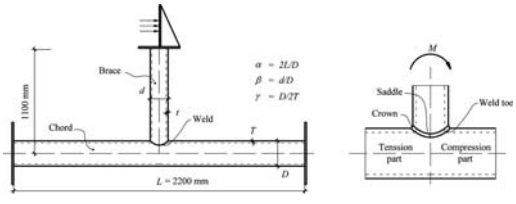

Figure 1. A general layout of a structural CHS T-joint.

Table 1. Geometrical information of the tested joints.

Name	Diameter (mm)			
	Chord (D)	Brace (d)	β (d/D)	L (mm)
IB.T.069.20	244.5	168.3	0.688	2200
IB.T.069.550	244.5	168.3	0.688	2183.5
IB.T.069.700	244.5	168.3	0.688	2177.9
IB.T.079.550	244.5	193.7	0.792	2183.5
IB.T.047.550	244.5	114.3	0.467	2183.5

*Thickness of the chord (T) and brace (t) is 6.3 mm.

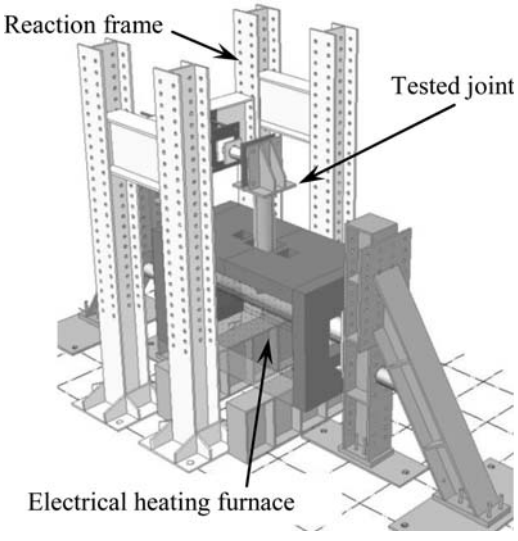

Figure 2. Overall test setup of the CHS T-joints at elevated temperature.

2.2 *Instrumentation*

The T-joints were tested within a well-insulated furnace. Therefore, it was much more challenging to place instrumentation around the joint. All available instrumentation was designed to maximize the joint behavior measurements.

Two special glass windows which could resist high temperature (1100°C) on the top furnace cover provide test observation. Two digital cameras were placed on top of the observation window. Besides, deformations of the center joint within the furnace were measured through Nicrothal wires (Ni80). To ensure the accuracy in measurements, the expansion coefficient due to temperature effect on the wire was determined through an experiment. A thermal test was carried out to measure the free expansion of the wire and this reading was subtracted from the total measurements to obtain actual vertical deflections. The Ni80 wires (expansion coefficient of 1.7×10^{-5}) were connected directly to the bottom point (L7 and L8) of the chord and transferred the chord deformations to LVDTs outside of the furnace.

Readings from these two points provided global rotations of the joint which can be calculated via:

$$\Delta_{support1} = \frac{L1+L2}{2} \text{ and } \Delta_{support2} = \frac{L3+L4}{2} (\text{mm})$$

where θ_g is the global rotation of the structural joint. For those parts of the joint outside the furnace, deflections were captured using LVDTs at six positions as shown in Figure 3 (L1 to L6). The support movements on two sides of the chord were measured by four LVDTs i.e. L1 to L4. Support rotations were calculated based on

$$\theta_{b1} = \frac{L5}{1000} \text{ and } \theta_{b2} = \frac{L6}{800} (\text{rad})$$

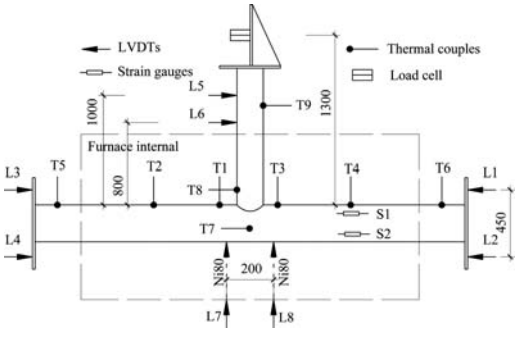

Figure 3. Instrumentation locations on specimens

The support movements were

$$\theta = \frac{(\theta_{b1}+\theta_{b2})}{2} - \theta_g (\text{rad})$$

During the test, it was observed that the two supports moved within 0.12 mm and rotated 0.002 rad (0.36°) on each end. Therefore it can be concluded that the boundary condition of the two chord ends were fully fixed. The purpose of L5 and L6 is to measure the rotation of braces

$$M = 1.3P \text{ (kNm)}$$

where θ_{b1} and θ_{b2} are the rotation of the brace corresponding to location of LVDT L5 and L6, respectively. The two rotations are used to calculate the rigid rotation of brace by comparing θ_{b1} and θ_{b2} with regard to the elastic rotation of the brace as a cantilever (θ_g). It was concluded that the brace acted rigidly, with the rotation of the joint based on

$$\theta_g = \frac{L7-L8}{200} \text{ (rad)}$$

where θ is the rotation of the joint in moment-rotation curves.

Measurements of the applied load were taken through a load cell placed on the top of the brace. The capacity of the load cell was 100 kN. Moment applied to the center joint was calculated based on

$$\theta_{support1} = \frac{L1-L2}{450} \text{ and } \theta_{support2} = \frac{L3-L4}{450} (\text{rad})$$

where P is measured by the load cell in kN.

Nine type K mineral insulated thermocouple wires were used to measure the temperatures on the specimen as well as the furnace interior. Thermocouples were arranged across the section of the specimen in such a manner so that the temperature at the joint region could be captured.

2.3 *Material properties*

Material tests were conducted to determine material strength of the chord at three different temperatures levels (20°C, 550°C and 700°C) as in the structural tests. The material tensile test results are summarized in Table 2.

In the structural tests at 550 and 700°C, steel fractures occurred along the center weld toes and penetrated through the chord thickness. Hence, additional

Table 2. Material tensile test on S355 steel material.

Coupon	Test temperature (°C)	Yield strength (MPa)	Elastic modulus (GPa)	Ultimate strength (MPa)	$k_{y,T}$
01–03	27.4	380.3	201.2	519.1	1.00
04–06	526.7	270.0	111.2	331.3	0.71
07–09	680.3	99.5	26.2	102.2	0.26

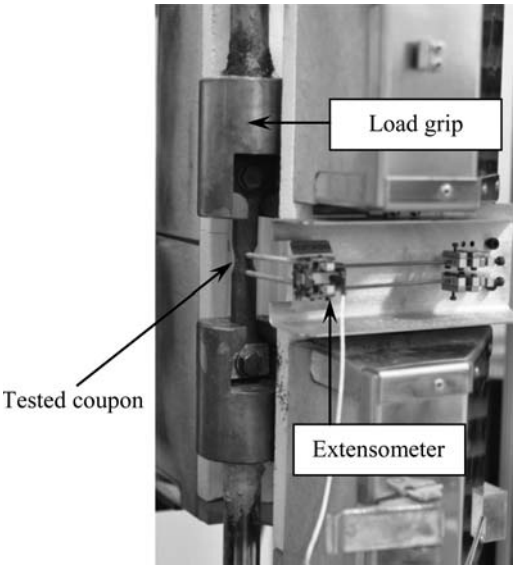

Figure 4. Fracture test of heat affected material.

material test were conducted to determine the fracture strains of the material in this heat affected (HA) zone.

The tensile coupon test was designed to have the same effect on the parent material from a welding process. As shown in Figure 4, the coupon was covered with the same volume-per-unit-length of weld material in order to generate the same heat amount as in the structural joint. The coupons were then air cooled. In order to control the fracture of the coupon in the interested zone, the welds were ground off and two notches were made at the center.

The tensile fracture test was performed at three levels of temperature 20, 550 and 700°C. Stress- strain relationships were obtained through a load cell and an extensometer as shown on Figure 4. In Figure 5, load deformation of the tested coupon is shown. The material at heat affected zone had higher strength compare to normal steel at 20°C however it possessed lesser ductility. At high temperature, it can be seen that the HA material had no strain-hardening performance and lesser ductility.

3 TEST PROCEDURE AND OBSERVATIONS

3.1 *Test procedure*

The test consisted of two phases: (1) heating phase and (2) loading phase. In the first phase, the furnace was heated up at a heating rate of 100–110°C/min up to the specified temperature. The heating rate was similar to that of a natural fire in its first five minutes. After the furnace air had attained the test temperature, it was maintained to the end of the test. During the first phase, thermal expansion was observed on the chord. However, the expansion did not cause any stress in the joint since one end of the chord was rested on a

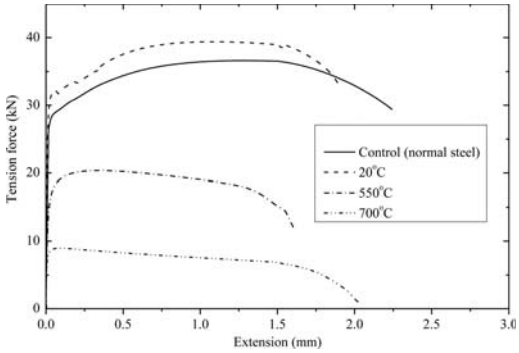

Figure 5. Load deformation of the heat affected material.

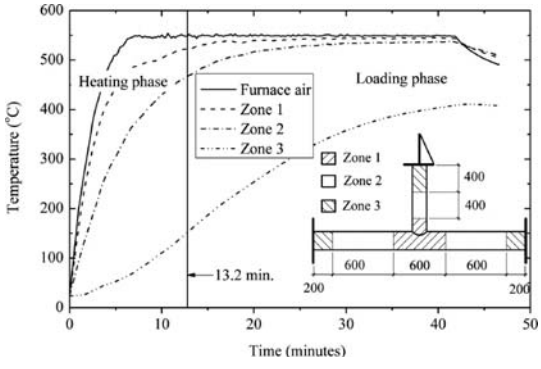

Figure 6. Temperature distribution of joint IB.T.069.550.

roller. When the center of the joint reached the preset temperature, the joint entered into second phase. Gaps on the chord ends were shim-packed with steel plates and eight bolts on the end-plate were tightened to the A-frame on each chord end (Figure 2). A small load was applied to check the adequacy of the test setup, instrumentation and loading system. In this phase, load was applied until the maximum stroke of the hydraulic jack was reached. In the fire test, there were cracking sounds when the joint reached a certain load. After the cracking sounds, the applied load started to decrease.

3.2 *Temperature distribution*

A typical development of temperature on the chord is illustrated in Figure 6 for Specimen IB.T.069.550. The joint temperature distribution is divided into three zones based on the readings of nine thermocouples.

It was observed that the center zone took 13.2 minutes to reach the specified temperature after the air temperature had stabilized. This duration was allowed for before starting the loading phase. It can also be observed that, during the loading phase, the temperature difference in each zone is within 3 to 8%. The same variation was found for all tested T-joints. However, the joint could only attain 526.3°C since there were parts of the joints extending outside of the furnace. That is also the reason why in Zone 3 (Figure 3) the temperature increased the slowest compared to that in the

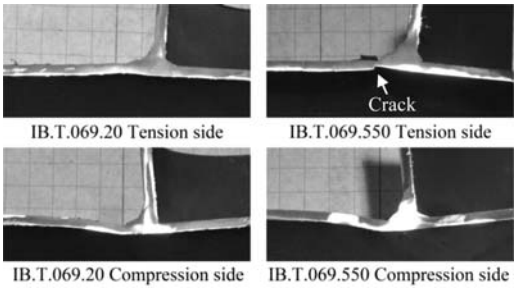

Figure 7. Failure mode of a joint IB.T.069 at 20°C and 550°C.

other two zones. Based on the measured temperatures of the four tested joints, the temperature distribution in the three zones can be used as temperature input in the analytical and numerical analyses.

3.3 *Failure modes*

Failure of CHS T-joints subjected to in-plane bending occurred on the chords in all the five joint tests. As the brace rotated, local bending and shearing occurred on the chord near the crown points. Areas with large plastic deformation were observed around the chord wall near the crown positions. However, the chord material inside the brace section was observed to have not much deformation. After the test, the center section was mechanically cut out from the joint for more detailed observation.

Failure modes of the joints at ambient and elevated temperatures are shown in Figure 7. On the compression sides of all connections, a similar failure mechanism was observed. Large plastic deformations were formed beneath the weld toe, indicating local concentration of stresses. However, on the tension sides of connections, for all joints at elevated temperatures, there were cracks along the weld toe while no cracks were found in the ambient test. In each joint at elevated temperatures, a single crack started from the crow point and developed towards the saddle points and penetrated through the chord thickness (Figure 7-IB.T.069.550 Tension side). The cracks caused the significant difference in failure modes between high temperature and ambient temperature cases. In the high temperature cases, the joint strength did not increase after the cracks were formed.

3.4 *Moment-rotation curves*

Figures 9a and 9b show the moment-rotation curve of all five CHS T-joints. They are classified into two categories for comparison purpose. Figure 9a shows the behaviour of joint IB.T.069 at three levels of temperature, i.e. 20, 550 and 700°C in order to observe the effect of temperature on the same joint. The moment-rotation curve of joint IB.T.069.20, tested at ambient temperature, is similar to a typical joint behavior

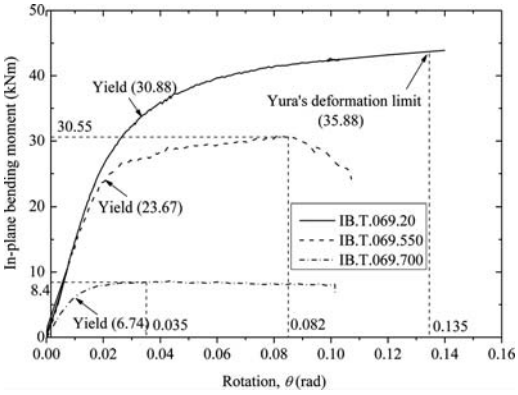

Figure 9a. Behaviour of joint IB.T.069 at different temperatures.

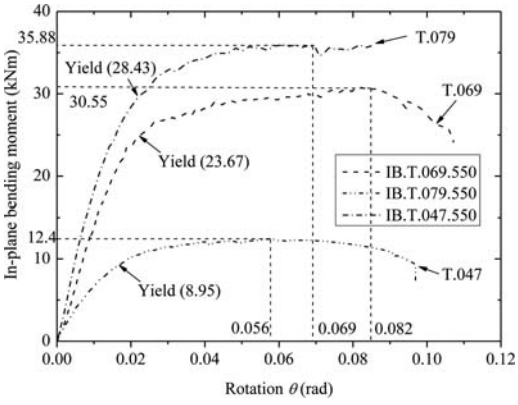

Figure 9b. Behaviour of three T-joints with different β at 550°C

reported by previous researchers (Togo 1967; Van der Vegte 1995).

As the load increased, the joint deformed linearly up to the yield value (30.88 kNm) and the strength started to increase continuously until the test was stopped. There was no failure on the joint. In this case, Yura's deformation limit ($80\sigma_y/E = 0.135$ rad) was adopted to find the ultimate joint strength. However, when the temperature was increased to 550 and 700°C, the joint started to yield earlier, i.e. 23.67 kNm at 550°C and 6.74 kNm at 700°C. When deformations reached 0.082 rad and 0.035 rad respectively, the joints could not take any more loads. Hence the highest load was considered as the ultimate strength of joints at high temperature. It was also noted that there were cracking sounds at the moment when the joints reached their maximum loads. In these cases, Yura's deformation limit was not applicable because the maximum load capacity was reached prior to Yura's deformation limit. It can be seen that the capacity of the joint is governed by strength at elevated temperatures instead of deformation control at ambient temperature.

The test results are presented in Table 3. Compared to the ambient temperature case (IB.T.069.20),

Table 3. Test results.

	Test temp. (°C)	Yield strength (kNm)	Ultimate strength (kNm)	Initial stiffness (kNm/rad)	Prediction (kNm)*	Test/ Prediction
IB.T.069.20	27.6	30.88	43.25	1420	39.625	1.09
IB.T.069.550	517.3	23.67	30.55	1376	27.532	1.11
IB.T.069.700	678.3	6.74	8.4	670.3	8.56	0.98
IB.T.047.550	532.4	28.43	12.4	1609	10.849	1.14
IB.T.079.550	536.2	8.95	35.88	588.7	31.148	1.15

*Ultimate strength prediction following CIDECT (2010), for high temperature, yield stress f_{y0} was changed accordingly to yield stress at high temperature.

the strength of joint was reduced to 77.2% at 550°C and 22.1% at 700°C. Due to the deterioration of steel, the initial stiffness has changed as well. However, at 550°C, initial stiffness of the joint was only reduced by 3% in contrast to 53% at 700°C.

In Figure 9b, the behaviour of joints with two different β values is illustrated at 550°C. The initiation of softening behaviour occurred together with fracture in the heat affected zone. This softening behaviour varied for different joints. For the joint with large β (IB.T.079.550) the softening rate was greater compared to those with smaller β (IB.T.069.550 and IB.T.047.550). The rate of joint softening indicates greater crack development. For smallest β (IB.T.047.550), this process happened slowly from rotation of 0.056 to 0.097 rad. This is due to different load levels of the three joints. Joint IB.T.047.550 was subjected to 12.4 kNm moment when cracks initiated. At this load level, the slow propagation of cracks was observed. Meanwhile, joint IB.T.079.550 sustained a greater moment of 35.88 kNm at fracture, with cracks quickly propagating to the saddle due to negligible harderning properties of steel at high temperature. The responses agreed well with crack length variations among these joints.

The ultimate strength of tested T-joints with different β values was compared with calculations based on design code. CIDECT (Wardenier *et al.* 2010) was adopted because of its popularity in practical tubular design. Although the design criteria for CIDECT are for joints in ambient condition, the design formula is based on f_{y0}, the characteristic yield strength. Hence it may be applicable for high temperature by simply modifying the yield strength f_{y0} to $f_{yT} = k_{yT} \times f_{y0}$, where k_{yT} is the reduction factor of yield strength due to elevated temperature. Values of k_{yT} are obtained from Table 3.

$$N_{1,Rd} = 4.3 \frac{f_{y0} T^2 D}{\sin 90^0} \beta \gamma^{0.5} Q_f$$

where f_{y0} is the characteristic yield strength at ambient condition, T is the chord thickness, D is the outer diameter of the brace, β and γ are respectively brace-to-chord diameter ratio and chord diameter-to-thickness ratio. For T-joint, 90° is the angle of the brace to the chord. Q_f takes into account the effect of preloads in the chord. In this case, since there are no preloads, $Q_f = 1$.

The comparison between test results and CIDECT predictions is presented in Table 4. In terms of ultimate strength prediction, the comparison shows good agreement at ambient condition. At 550°C, the formula was conservative in predicting the strength. However, at 700°C, it gave a slightly unconservative prediction. At ambient, the failure criteria for the CIDECT formulae is based on excessive deformation limit. However, at high temperature, as the failure mode changed, the joint ultimate strength is determined based on strength of material as explained on section 3.4. Therefore, the application of CIDECT formulae may cause an unconservative prediction of joint strength at high temperature as joint IB.T.069.700 (Table 3). The assessment of joint strength at elevated temperatures will be presented in other study.

4 DISCUSSIONS

Joint failure occurred on the chords beneath the brace and center welds for all five tests. Plastic deformations were mostly located on two crown points. However, as a result of in-plane bending, one side of the joint was under compression and the other side under tension.

The failure mechanism could be divided into three stages. Initially, the whole joint behaved in the elastic range where stresses were highly concentrated in two crown points and spread slowly toward the saddle points. As shown in Figure 10a, at this stage, the major actions in the area were shear and bending moments.

As the brace rotated, the joint entered into the second stage. Plastic hinges began to form around the weld toe at the crown points, and significant deformations (downward on compression side and upward on tension side) were observed. Consequently, tensile membrane actions were developed on the chord surface near the two crown points. The tensile membrane actions are the development of tensile stress on the whole cross section of the chord wall. In the FE models, illustrated in Figure 10, the black arrows is the tensile strains develop on the surface of the chord showing there was existence of tensile forces on the chord wall near the crow. These tensile forces combined with deformations on two sides of the center joint generated a resistance moment. Since tensile

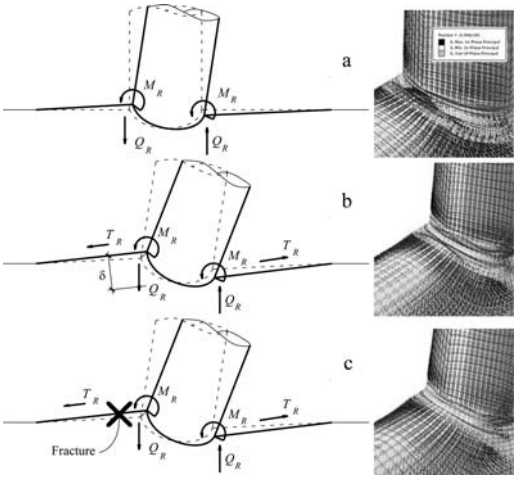

Figure 10. Failure mechanism of T-joint under in-plane bending.

membrane actions can spread on the chord surface, the resistance moment became larger as the joint further deformed. This is the main reason that the softening phase could not be observed for specimens tested in ambient temperature. The joints only reached the ultimate strength when there were actions that inhibited the development of tensile membrane action. For the joint at ambient temperature, IB.T.069.20, no ultimate strength occurred. Failure criteria based on serviceability control (Yura 1981) was applied to determined the ultimate strength.

However, when the joints were subjected to fire, tensile membrane was inhibite due to the evolvement of cracks along the weld toes. At this moment, the joints entered into stage three, the final stage. When the cracks formed, the load path was broken and moment resistance started to reduce. In Figure 10c, the stress distribution of joint IB.T.069.550 at its ultimate stage is shown. The stress concentration was released to zero near the cracks indicating the diminution of tensile membrane action. The test results also confirmed this fracture phenomenon. Based on the observation of inclined cracks from the cut-out specimen, fracture was caused by a combination of both moments and tensile forces. The formation of cracks can be explained based on the changes of steel materials at high temperature. As illustrated in Table 3, at ambient temperature, the final fracture strain of heat-affected steel material was larger. Therefore, joints tested under this condition can sustain larger deformation with the development of tensile membrane action. However, at high temperature, fracture in the material occurred earlier and caused a reduction in strength.

4.1 *Joint strength*

As mentioned in Section 3.4, the joint strength could be classified into two groups to observe the influence of two factors, viz. temperature and brace size.

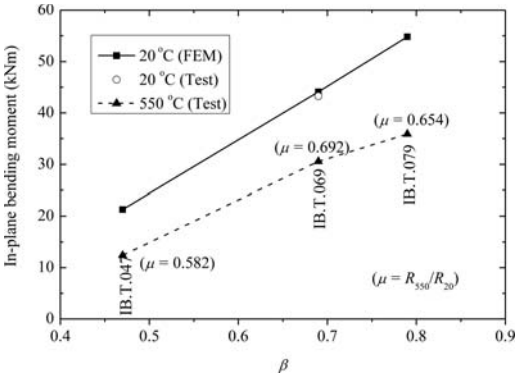

Figure 11. Normalized ultimate strength of joint at 550°C to 20°C.

4.1.1 *Influence of temperature*

Temperature has great effect on the behaviour of a joint (IB.T.069). As shown in Figure 8a, at ambient temperature the post-yield hardening response of joint IB.T.069 was continuously increasing until excessive deformation was reached. However, at 550°C the post-yield strength increase stopped at a rotation of 0.082 rad. At 700°C, at a rotation of 0.035 rad, the joint strength reached its peak of 8.4 kNm, and post-yield strength increase occurred in a shorter range. The reason was the absence of steel material strain-harderning at high temperature. Consequently, the yielded part of the joint had practically no rigidity and material softening occurred at an earlier stage. As the fracture of steel occurred earlier at high temperature, the development of tensile membrane action was stopped very soon. Therefore, the strength increase process was much shorter at 700°C compared to 550°C case. With regard to the strength loss of material at high temperature, the ultimate strength of joint was also controlled by fracture strain. In terms of yield strength, the joints at higher temperatures yielded earlier. The reason is that the non-linearity of stress-strain relationship at elevated temperature causes the joints to attain plastic deformation at an earlier strain.

4.1.2 *Influence of brace size at high temperature*

The effect of brace-to-chord diameter ratio (β) at one elevated temperature (550°C) is also shown in Figure 11. Since for all three joints the chord has the same diameter D, the smaller value of the β, the smaller was the brace. The reduction in joint strength is normalized with its strength at ambient condition. These results at ambient condition are based on the validated FE models of the joints. It is observed that, the variation (μ) in joint strength at high temperature (550°C) is less than that at the ambient temperature condition. In case of smaller brace (T.047), the yielded area beneath the joint is smaller. Hence, it is not much resistance that can be mobilized compared to a larger brace (T.079).

5 CONCLUSIONS

In this paper, the findings of an experimental programme to investigate the behaviour of CHS T-joints subjected to in-plane bending under fire condition are presented. It was observed that at high temperature, the joint failure criterion was changed from serviceability to strength due to cracks occurring on the weld toes at high temperatures. It was also found that temperature has a great effect on joint strength reduction. Besides, among five investigated joints, the smaller the diameter of the brace the greater was the effect of temperature on the joint bahviour.

ACKNOWLEDGEMENT

The research is funded by ARC 2/07 project entitled "Failures modes and ultimate strength of tubular joints under elevated temperatures" from the Ministry of Education, Singapore.

REFERENCES

Choo, Y. S., and Qian, X. D. (2005) "Recent research on tubular joints with very thick-walled chords." *15th International Offrshore and Polar Engineering Conference, ISOPE-2005,* Seoul, Korea, Republic of, 272–278.

Fung, T. C., Soh, C. K., Chan, T. K., and Erni. (2002). "Stress concentration factors of doubler plate reinforced tubular T joints." *Journal of Structural Engineering*, 128, 1399–1412.

Jin, M., Zhao, J., Liu, M., and Chang, J. (2011). "Parametric analysis of mechanical behavior of steel planar tubular truss under fire." *Journal of Constructional Steel Research*, 67(1), 75–83.

Kurobane, Y., Wardenier, J., and de Back, J. (1984). "Ultimate Resistance of Unstiffened Tubular Joints." *ASCE Journal of Structural Engineering*, 110(2), 385–400.

Lin, X.-K., and Tao, Z. (2007). "Analysis of axially loaded concrete filled CHS stub columns after exposure to fire." *Harbin Gongye Daxue Xuebao/Journal of Harbin Institute of Technology*, 39, 514–518.

Lin, X., and Han, L. (2005). "Load-displacement hysteretic behavior of concrete filled CHS columns after exposure to ISO-834 standard fire." *Jianzhu Jiegou Xuebao/Journal of Building Structures*, 26, 19–29.

Makino, Y., Kurobane, Y. and K. Ochi, Van der Vegte, G.J., Wilmshurst, S.T. (1996) "Introduction to unstiffened CHS tubular joint database." *Tubular Structure* 157–164.

Packer, J. A. K. J. S. M. (1985). "Database for axially loaded tubular T, Y and K-connections." *Department of Civil Engineering*, University of Toronto, Canada.

Togo, T. (1967). "Experimental Study on Mechanical Behaviour of Tubular Joints.," Osaka University, Osaka, Japan (in Japanese).

Toprac, A. A. (1961). "Investigation of corner connections loaded in tension." *Welding Journal*, 40(11), 521–528.

van der Valk, C. A. C. "Factors controlling the static strength of tubular t-joints." Trondheim, Norw, 1177.

Van der Vegte, G. J. (1995). "The static strength of uniplanar and multiplanar tubular T- and X-joint," PhD thesis Delf University of Technology.

Van der Vegte, G. J., and Makino, Y. (2006). "The ultimate strength of axially loaded CHS uniplanar T-joints subjected to axial chord load." *Welding in the World*, 50(SPEC ISS), 104–111.

Yang, Y.-F., and Han, L.-H. (2005). "Fire behavior of concrete-filled double skin (CHS inner and CHS outer) steel tubular columns." *Harbin Gongye Daxue Xuebao/Journal of Harbin Institute of Technology*, 37, 400–403.

Yu, W., Zhao, J., Luo, H., Shi, J., and Zhang, D. (2011). "Experimental study on mechanical behavior of an impacted steel tubular T-joint in fire." *Journal of Constructional Steel Research*, 67, 1376–1385.

Zerbst, U., Heerens, J., and Schwalbe, K.-H. (2002). "The fracture behaviour of a welded tubular joint—-an ESIS TC1.3 round robin on failure assessment methods: Part I: experimental data base and brief summary of the results." *Engineering Fracture Mechanics*, 69(10), 1093–1110.

Zhao, X.-L., Hancock, G., and Wilkinson, T. (2005). *Cold-Formed Tubular Members and Connections*, Elsevier.

Tubular Structures XIV – Gardner (Ed.)
© 2012 Taylor & Francis Group, London, ISBN 978-0-415-62137-3

FE modelling of bolted steel end-plate moment connections subjected to a standard fire

O. Salem, G. Hadjisophocleous & E. Zalok
Carleton University, Ottawa, Ontario, Canada

ABSTRACT: In fire conditions, the prediction of the behaviour of bolted steel connections becomes complicated since different parameters, such as temperature increase, beam thrust and large deformations, influence their structural behaviour. Finite-element modelling can help to better understand the three-dimensional deformations and the failure mechanisms of bolted connections at elevated temperatures. In this paper, a 3D finite-element modelling study of bolted end-plate moment connections subjected to elevated temperatures is presented. The modelled connections can be used to connect either tubular or I-shaped steel beams to tubular steel columns. The different components of the beam-to-column connection include the beam, column, beam end plate, column connecting plate, bolts and welds. The connection components were modelled using eight-node continuum hexahedral brick elements (C3D8R in ABAQUS/Standard V6.92 terminology), which have the capability of representing large deformations and the non-linearity of both geometry and material at elevated temperatures. Contact between the connection components was modelled using the surface-to-surface interaction command with a small sliding option. The model was validated using the experimental results of two full-scale fire-resistance tests. Good agreement between the model predictions and the experimental results was achieved for different measurements; such as the connection deformations, connection hogging moment, beam thrust and beam deflection.

1 INTRODUCTION

There are many types of beam-to-column connections that vary from simple shear connections, which provide no moment resistance, to rigid connections with considerable moment resistance, such as the extended end-plate moment connection. In the former type, the moment resistance allows the connection to substantially reduce the beam bending moment at the mid span at elevated temperatures affecting the beam limiting temperature. Fire-resistance testing is a direct method to investigate the behaviour of steel connections at elevated temperatures. However, conducting fire-resistance experiments is time consuming, expensive, and associated with difficulties. In addition, beam-to-column connections could be subjected to a combination of shear force, bending moment, and axial force at elevated temperatures, which makes it very complicated to study the structural behaviour of such connections. It is preferable to use experimental results to validate computer models, and then use the validated models to simulate the behaviour of beam-to-column connections in fire. Such an approach allows for the study of parameters that are not investigated experimentally. In this paper, a three dimensional finite-element model developed to simulate the structural behaviour of restrained tubular steel beams and their end connections in fire is presented. The model was developed using the commercial software package ABAQUS/Standard V6.92 (2009), and was validated against the results of full-scale fire-resistance experiments conducted at Carleton University's Fire Research Laboratories. The modelled connections can be used to connect either tubular or I-shaped steel beams to tubular steel columns.

Steel members made of Hollow Structural Sections (HSS) are increasingly used in modern steel framework due to their many advantages. In addition to the attractive appearance of HSS steel members, they posses high strength to weight ratios, which makes them cost effective. For cases in which the design stresses are largely reduced by lateral buckling, HSS steel members are more favourable than I-shaped members due to their great moment of inertia about the minor axis of their cross section. Considerable research work has been done to investigate the structural fire behaviour of beam-to-column connections joining I-shaped steel members, such as the work carried out by Liu et al. (2002), Spyros et al. (2004) and Qian et al. (2008). In contrast, very little research was conducted on HSS beam-to-column connections, such as the work done by Ding and Wang (2007) on connections joining I-shaped beams to HSS columns at elevated temperature. However, most of the research carried out on HSS steel members was to investigate the structural behaviour of concrete-filled HSS columns. A number of fire-resistance experiments of

concrete-filled HSS steel members were conducted by researchers such as Kodur (1999), Han et al. (2003), Wong and Wang (2010) and Lu and Zhao (2010).

2 FINITE-ELEMENT MODEL DESCRIPTION

The development process of the finite-element model started with the creation of individual connection components (parts in ABAQUS terminology), such as the beam, column, beam end plate, column connecting plate, bolt and fillet weld. Subsequently, the components were assembled together to form the modeled beam-to-column connection configuration. Owing to full symmetry, only one quarter of the beam-column assembly was modelled. Figure 1 shows the meshed model of the HSS-to-HSS connection. All components were modelled using the reduced integration eight-node continuum hexahedral elements (C3D8R). These brick elements have the capability of representing large deformations and geometrical and material non-linearity. They also, if controlled, can provide reliable results with no numerical problems such as shear locking or hourglassing.

2.1 *Discretization*

The mesh size of the connection different components significantly affects the finite-element model calculation time and accuracy. For example, the number of elements through the thickness of the connection plates significantly affects the accuracy of the simulation of the plate bending and the formation of yield lines. Trial models with different number of elements through the plate thickness were developed prior to the development of the final model to test the most effective number, and found that three or four layers of elements through the plate thickness is the optimum choice. For the connection thinner plates of 12.7 mm, three layers of elements through the plate thickness were used, while for the thicker plates of 19.0 mm, four layers were used.

The connecting bolts were A325 high strength bolts of 19.0 mm (3/4 in) diameter, and were also modeled using the C3D8R elements. Three different meshes for the bolts were tested before choosing the most efficient one; the three meshes were of coarse, medium and fine construction, as shown in Figure 2. It was found that the bolt with fine mesh density behaved more efficiently and did not experience contact problems, such as penetration problems between the bolt and the connection plates. As in the experiments that were used in validating the finite-element model, no pre-tension to the bolts was considered in the model.

The beam and column were made from square hollow sections (SHS) with nominal dimensions of $152 \times 152 \times 6.4$ mm ($6.0 \times 6.0 \times 1/4$ in). They were also modeled using the C3D8R elements. A relatively fine density mesh was used for the beam section in the region under the loading plate to avoid any convergence problem that might occur during the non-linear analysis and to accurately capture the deformations of the beam walls in the loading zone, Figure 3.

The top and bottom parts of the column where the supports exist were also discretized using fine meshes. Two layers of elements were used through the 6.4 mm (1/4 in) wall thickness of the beam and column sections in the finite-element model.

The fillet welds of 6.0 mm leg length joining the end plate to the beam and the vertical welds joining the column to the connecting plate were modelled using the C3D8R elements. Tie constraints were used between all welded surfaces.

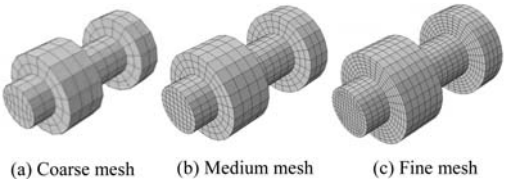

Figure 2. Different mesh densities of the connection bolts.

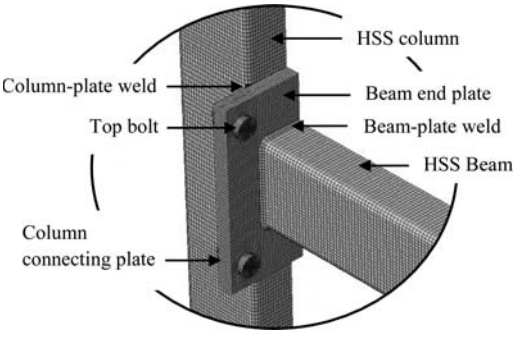

Figure 1. Meshed components of the 3D finite-element model of extended end-plate HSS-to-HSS connection.

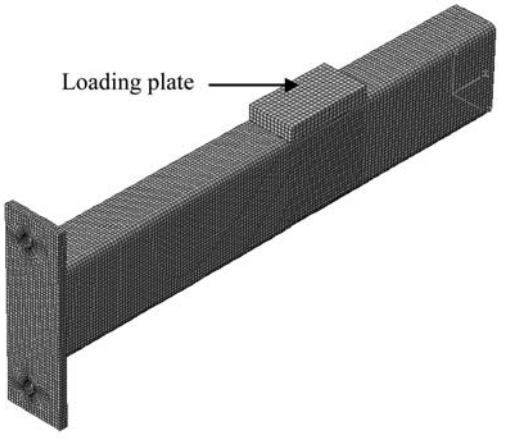

Figure 3. The HSS beam with end plate and loading plate.

2.2 *Material properties*

Reduction factors for the yield strength, proportional limit and modulus of elasticity of carbon steel that are prescribed in Eurocode 3, Part 1.2 (2005), were used in the finite-element model in order to calculate the steel material properties at elevated temperatures. For structural steel thermal properties, such as thermal elongation and conductivity, Eurocode 3, Part 1.2 (2005) correlations were employed. Since the steel material at the corners of the cross section of the HSS beams and columns was subjected to strain hardening due to the forming process during the manufacturing of these sections, the steel material in the corners is of higher strength than the material in the flat parts. In order to properly define the material strength of the corners and the flat parts in the finite-element model, tension coupons were cut from both the corner and flat regions of two samples of the HSS tubes used in fabricating the test assemblies of the tests used to validate the finite-element model. Average material properties for the corner and flat parts were used as normal-temperature steel material properties in the model.

The material used for the welds in the model was assumed to have the same yield strength of 350 MPa as the beam, columns and connection steel plates that were made of 350W steel material as specified by CSA G40.20-04/G40.21-04 Standards (2004). Bolts were assumed to have the material properties of A325 bolts as specified by ASTM A 325M-07 (2007) at normal temperatures. The elevated-temperature material properties of both welds and bolts were calculated in the finite-element model using the reduction factors specified by Eurocode 3, Part 1.2 (2005) for welds and bolts, respectively.

2.3 *Contact interaction*

The finite-element model contains several surfaces that were involved in contact interaction, such as the contact between the bolt and the connection plates and the contact between the beam end plate and the column connecting plate. Contact between the bolt and the connection plates was carefully modeled; as the contact action involved several contact pairs, such as the contact between the underside of the bolt head and the beam end plate, the nut and the column connecting plate and the contact between the bolt shank and the bolt holes in the connection plates. The contact interaction was modeled with "rough" interface to prevent slipping between the contact surfaces except for the last contact pair of the bolt shank and the bolt holes, which was modeled with frictionless interface in order to prevent penetration of the bolt into the connection plates at high connection rotations. The contact between the beam end plate and the column connecting plate was also modeled, and defined as surface-to-surface contact with a finite sliding option and node-to-surface discretization method. In the normal direction of the contact interaction between the connection plates, a hard contact was used, while in the tangential direction a friction coefficient of 0.3 was defined. In all contact pairs, the surfaces with less expected deformations were set as master surfaces and had coarser meshes than the corresponding slave surfaces, which had denser meshes.

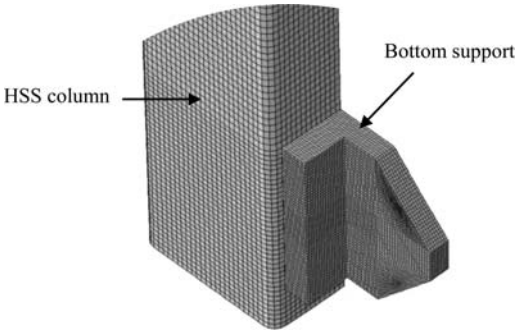

Figure 4. The HSS column with its bottom support.

2.4 *Restraints and loading*

Displacement and symmetry boundary conditions were carefully applied to ensure that the modeled assemblies were subjected to the same actions as in the corresponding tests. Also, the column top and bottom pin supports were modeled to simulate the supporting action of the real supports used in the tests, Figure 4.

Similar to the fire tests, the load was applied in the finite-element model to a loading plate placed over the beam top flange in order to avoid any instability in the non-linear analysis due to the direct loading of the relatively thin beam top flange, Figures 3. The pressure on the loading plate was calculated and provided in the finite-element model to simulate a total load representing a beam load ratio of 0.5 as applied in the tests. A tie constraint was defined between the loading plate and the beam top flange in order to ensure constant loading during the analysis. The load was applied in the finite-element model with several increments, each not exceeding 5% of the total load, in order to avoid convergence problem in the non-linear analysis.

2.5 *Analysis process*

Different degrees of non-linearity were considered in the analysis of the finite-element model presented in this paper, such as the material non-linearity and the geometric non-linearity that appear clearly in restrained steel beams subjected to fire due to the large deflections. The non-linear analysis of the model was conducted through three steps; the contact step, the load step and the fire step. In the first step, all the contact interactions were established and analyzed in the different contact pairs of the modeled beam-to-column connection. In the second step, the load was applied in increments each increment not exceeding 5% of the total applied load in order to characterize the actual load history. Lastly, the third step was

employed to apply the fire effects on the already loaded beam-to-column connection; as the increased temperatures were defined with prescribed rates obtained from the corresponding fire tests in order to simulate the thermal effects of the surrounding temperature inside the furnace. The non-linear analysis in the fire step was conducted through multiple iterations with time increments each not exceeding 30 seconds.

Both structural and heat transfer analyses were conducted in the finite-element model. For the heat transfer analysis, two heat transfer processes were involved in the model; the heat transferred from the fire environment inside the furnace to the boundary surfaces of the steel-frame assembly and the heat transferred within the steel assembly. The heat transferred from the fire to the steel assembly is due to the convected and radiated heat flux. The convected heat transferred from the fire is governed by defining the furnace gas temperature, while the radiated heat transferred from both the furnace gas and flames is governed by defining the effective radiation temperature, which may differ from the furnace gas temperature. For simplicity, a thermal measuring instrument called plate thermometer, which was developed by Wickstrom (1994), was used in the tests used to validate the finite-element model in order to provide equivalent temperature measurements that can represent both the furnace gas temperature and the effective radiation temperature. The temperature measurements of the two plate thermometers that were installed near one of the test connections of each assembly in the tests were used in the first heat transfer process. In the second heat transfer process, which represents the heat transferred within the steel assembly, the temperature of each finite element of the modeled steel–frame assembly was calculated by the model according to the outputs of the first heat transfer process and the heat conduction governing relationships prescribed in ABAQUS/Standard V6.92 (2009).

3 FIRE EXPERIMENTS

3.1 *General*

The results of two full-scale fire-resistance tests were used to validate the 3D finite-element model presented in this paper. The two fire tests were part of a research project that aimed to investigate the structural fire performance of steel-frame assemblies made of HSS steel beams and columns, with focus on the behaviour of extended end-plate beam-to-column connections. The test program consisted of 10 steel-frame assemblies with two different extended end-plate connection configurations and different study parameters, such as the end-plate thickness, degree of beam axial restraint and level of fire protection.

A large-scale furnace with internal clear dimensions of 2.7 m × 2.7 m × 2.2 m high was designed and constructed to accommodate the assemblies of this research project. The furnace temperature was controlled manually to follow the CAN/ULC-S101-07 standards (2007) time-temperature curve. In order to control the furnace temperature, six K-type insulated thermocouples each placed inside a 19.0 mm metal pipe were installed around the test assembly inside the furnace. In addition, two Inconel plate thermometers were installed near one connection of the test assembly to provide equivalent temperature measurements that can represent both the furnace gas temperature and the effective radiation temperature. The temperature measurements of the two plate thermometers were used in the heat transfer analysis in the finite-element model. The furnace is surrounded by a heavy loading steel structure that is used to apply the desired transverse loads and to support the test assemblies.

3.2 *Test assembly description*

The two test assemblies described in this paper were made of HSS steel elements with hollow square section of 152 mm × 152 mm × 6.4 mm (6.0 in × 6.0 in × 0.25 in). The steel material that was used for the assemblies including the end plates was of grade 350W as specified by CSA G40.20-04/G40.21-04 standards (2004). Each test assembly consisted of an HSS beam of about 2000 mm long connected at its ends to two HSS columns by extended end-plate moment connections. Two different end plate thicknesses were tested, 12.7 mm (1/2 in) and 19.0 mm (3/4 in), in Tests 1 and 2, respectively. The beam end plate was bolted to the column connecting plate in each beam-to-column connection using four A325 high strength bolts of 19.0 mm (3/4 in) diameter, Figure 5. The test assemblies were fire unprotected except their beams top flange, which was protected using a ceramic fibre blanket in order to simulate the effect of a concrete slab, which would exist on top of the beam in a realistic construction.

3.3 *Test setup and procedure*

After installing the test columns inside the furnace, they were connected to the loading structure and then were restrained at their ends against both in-plane and out-of-plane horizontal movement. However, the columns were rotationally unrestrained at their ends to avoid unnecessary moments that may be developed in the loading structure. To attain all these supporting conditions, four specially-designed sets of pin supports were used. Two of these supports were equipped with load measuring devices (or pin load cells) to measure the horizontal reactions of one column. The beam of each test assembly was subjected to a constant four-point flexure bending during the fire test. A total vertical transverse load of 11.2 ton (110 kN) representing a beam load ratio of 0.5 was distributed on two points over the test beam, as illustrated in Figure 6. The beam load ratio is defined as the ratio of the applied load in fire conditions to the plastic load-carrying capacity as a simply supported beam at normal temperature.

As shown in Figure 6, a number of ceramic rods were installed inside the furnace and were attached

from outside to a corresponding number of linear variable differential transformers (LVDTs) in order to measure the in-plane displacements of the test assembly at different locations. The displacements included the beam vertical deflections and the column lateral displacement at connection locations. In order to measure the surface temperatures of the test assembly, a total of 22 high-temperature resistant ceramic-fibre insulated K-type thermocouples were welded to each test assembly at different locations.

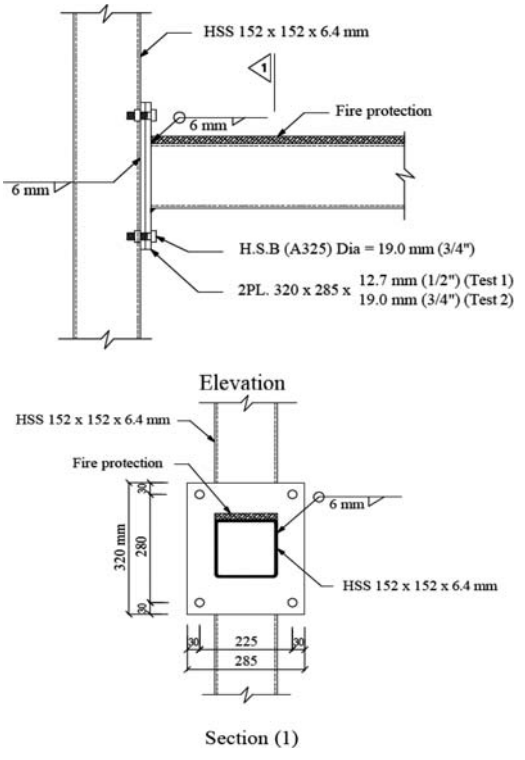

Figure 5. Details of the HSS beam-to-column connections.

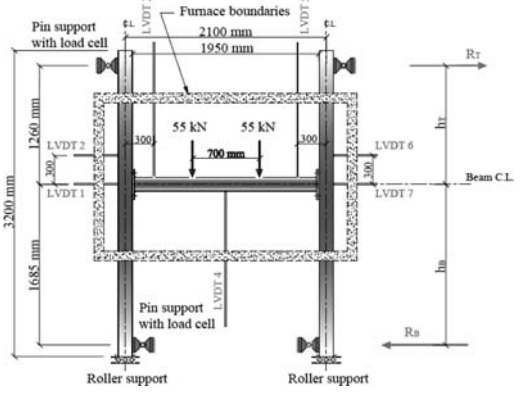

Figure 6. Layout of a general test assembly inside the furnace.

To conform with CAN/ULC-S101-07 standard (2007), the vertical transverse load was gradually applied in four increments each of 25% until reaching the full load that was applied at least 30 min before the start of the fire-resistance test. Later on, the test assembly was subjected to increasing temperatures that followed the CAN/ULC-S101-07 standard (2007) time-temperature curve.

4 MODEL VALIDATION

The predictions of the 3D finite-element model presented in this paper were validated against the outputs of two fire experiments; where good agreements have been achieved in different aspects, such as the connection deformations, connection hogging moment, beam deflection and beam thrust at elevated temperatures.

4.1 *Connection deformations*

Figures 7 and 8 illustrate comparisons between the predictions of the finite-element model and the

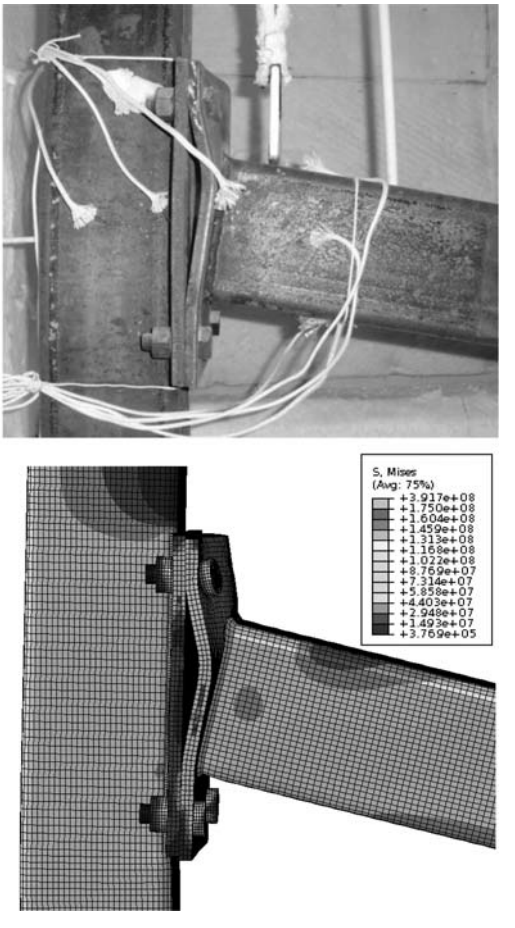

Figure 7. Comparison of the FE model predictions and the experimental results of the connection deformations of Test 1.

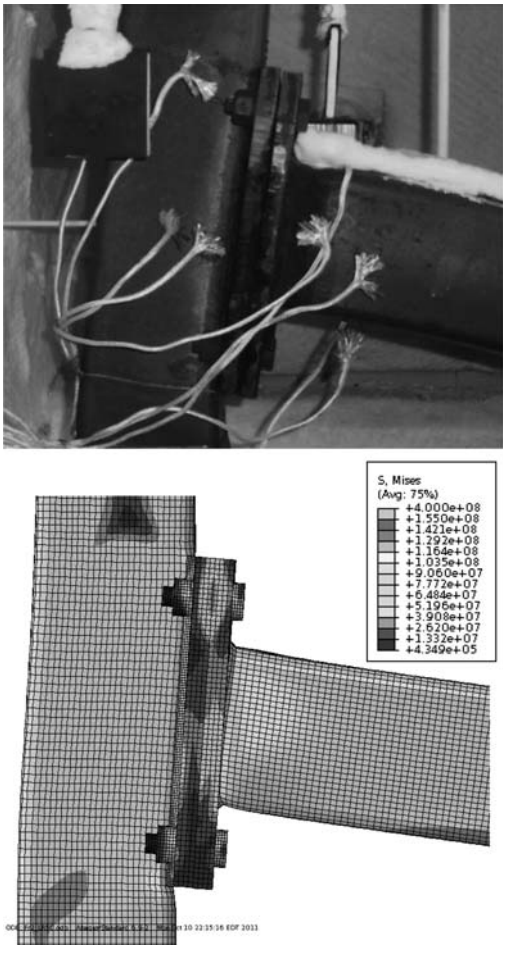

Figure 8. Comparison of the FE model predictions and the experimental results of the connection deformations of Test 2.

experimental results of the connection deformations of Tests 1 and 2 with end plates of 12.7 mm and 19.0 mm thickness, respectively.

4.2 *Connection hogging moment*

The results obtained from the finite-element model for the connection hogging moment were compared to the results of the connection of Test 1 with a thinner end plate, Figure 9. From the figure, it can be concluded that the simulation and the test results are in good agreement; where the finite-element model predicted a maximum connection hogging moment value of about 36.3 kN.m at a beam bottom flange temperature of about 538°C (at about 12.8 min), while the experiment gave a maximum hogging moment value of about 40.3 kN.m at a beam bottom flange temperature of about 460°C (at about 11.0 min). The reason for the slight discrepancy observed in Figure 9 is probably due to the uncertainty in the material properties of carbon steel at elevated temperatures below 300°C. Figure 10 shows a comparison between the finite-element model

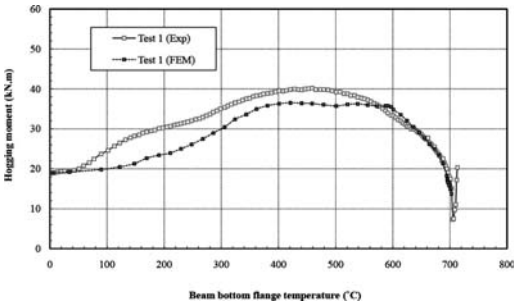

Figure 9. FE model predictions for the connection hogging moment compared to the test results of the connection of Test 1.

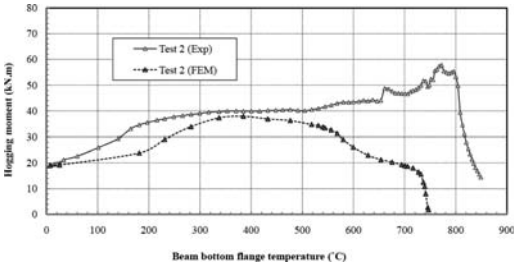

Figure 10. FE model predictions for the connection hogging moment compared to the test results of the connection of Test 2.

predictions for the connection hogging moment and the experimental outputs of the connection of Test 2 with thicker end plate. From the figure, it can be concluded that the simulation and the test results are in good agreement for elevated temperatures below 500°C; where the finite-element model predicted a maximum connection hogging moment value of about 37.0 kN.m at a beam bottom flange temperature of about 480°C (at about 4.8 min), while the experiments gave a hogging moment value of about 40.0 kN·m at the same beam bottom flange temperature of 480°C and the same time of 4.8 min.

4.3 *Beam deflection*

The beam mid-span deflection was the main failure criterion of the test assemblies; where the beam limiting deflection was span/20, which is about 100 mm for the test beams described in this paper, according to the recommendation in BS476: Part 21 (1987). Figure 11 illustrates a comparison of the beam mid-span deflection between the finite-element model predictions and the test results of the connection of Test 1. In Figure 11, the finite-element model gave slightly smaller values of the beam mid-span deflection up to a beam bottom flange temperature of about 685°C, when the model predicted a beam deflection of 23.0 mm, while the test gave a deflection of 33.0 mm. Afterwards, the deflection ran away according to the finite-element model predictions and the beam achieved a limiting mid-span deflection of span/20 at a beam bottom flange

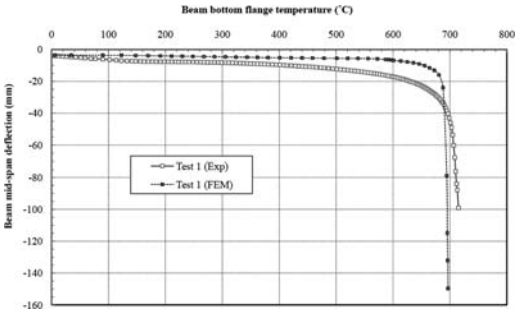

Figure 11. Comparison of the beam mid-span deflections between the FE model predictions and the results of Test 1.

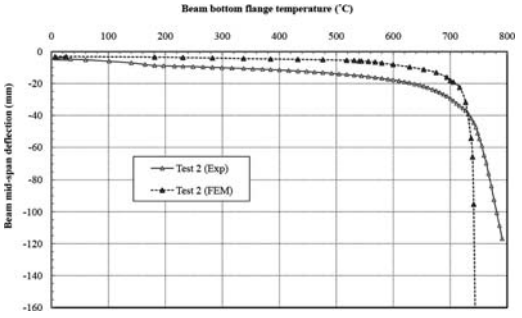

Figure 12. Comparison of the beam mid-span deflections between the FE model predictions and the results of Test 2.

temperature of about 695°C, while the limiting beam mid-span deflection was achieved at a beam bottom flange temperature of about 715°C in the fire test.

In Figure 12 a comparison of the beam mid-span deflection between the finite-element model predictions and the test results of the connection of Test 2 is presented. From the figure, it can be noticed that the model gave slightly smaller values of the beam mid-span deflection up to a beam bottom flange temperature of about 730°C. The model predicted a beam deflection of 32.0 mm, while the test gave a deflection of 37.0 mm. Afterwards, the deflection ran away according to the finite-element model predictions and the beam achieved its limiting deflection at a beam bottom flange temperature of about 745°C, while the beam limiting mid-span deflection was achieved at a beam bottom flange temperature of about 780°C in the test.

4.4 *Beam thrust*

Good agreement between the predictions of the finite-element model and the test results for the beam thrust in Test 1 can be seen in Figure 13. The finite-element model was conservative and predicted a maximum beam compressive force of 39.8 kN at a beam bottom flange temperature of about 540°C, while the test gave a maximum beam compressive force of 34.2 kN at a beam bottom flange temperature of about 646°C.

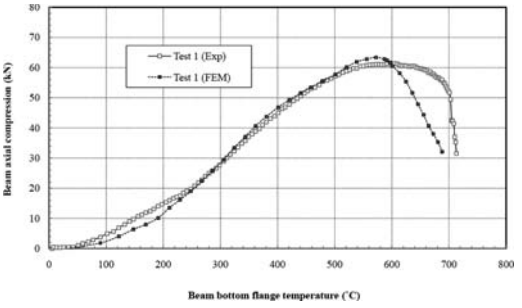

Figure 13. Comparison of the beam thrust between the FE model predictions and the results of Test 1.

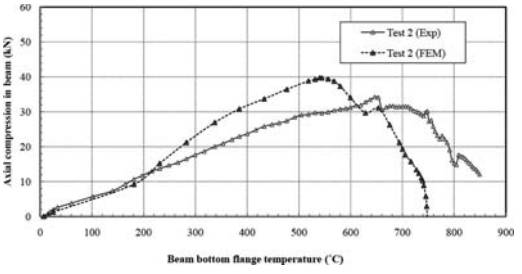

Figure 14. Comparison of the beam thrust between the FE model predictions and the results of Test 2.

Figure 14 shows a comparison between the predictions of the finite-element model and the test results for the beam thrust in Test 2; where the model was conservative and predicted a maximum beam compressive force of 39.8 kN at a beam bottom flange temperature of about 540°C, while the test gave a maximum beam compressive force of 34.2 kN at a beam bottom flange temperature of about 646°C.

5 CONCLUSIONS

A 3D finite-element model of an unprotected axially-restrained HSS steel beam connected to two HSS columns by means of extended end-plate moment connections has been developed using ABAQUS/Standard V6.92 (2009). The finite-element model was validated against the experimental outputs of two large-scale fire-resistance tests that were conducted as part of a doctoral research project at Carleton University, Ottawa, Canada. The comparisons demonstrated that the finite-element model simulated the experimental behaviour of the axially-restrained steel beams and their end connections at elevated temperature very well.

From both the experimental and the finite-element model results, it can be concluded that increasing the connection plate thickness from 12.7 mm to 19.0 mm has increased the limiting temperature of the connected steel beam at which failure occurred by about 65°C. It was also noticed that the connection of Test 1 with a thinner end plate failed due to excessive

deformations in the beam end plate. In contrast, very minimal deformations occurred in the thicker beam end plate of the connection of Test 2. However, most of the deformation in the connection of Test 2 was concentrated in the column walls as a plastic hinge was formed just below the connection plates. This raises the need for stiffening the supporting columns either by increasing their wall thickness or by the possibility of pouring concrete inside the columns' voids.

REFERENCES

ASTM A 325M-07. 2007. Standard Specification for High-Strength Steel Bolts, Classes 10.9 and 10.9.3, for Structural Steel Joints (Metric). West Conshohocken, PA.

British Standards Institute. 1987. BS 476: Fire Tests on Building Materials and Structures, Part 21: Methods for Determination of the Fire Resistance of Load-Bearing Elements of Construction, London, UK.

CAN/ULC-S101-07. 2007. Standard Methods of Fire Endurance Tests of Building Construction and Materials. Underwriters' Laboratories of Canada: Scarborough, Canada.

CSA G40.20-04/G40.21-04. 2004. General Requirements for Rolled or Welded Structural Quality Steel. Canadian Standards Association: Ontario, Canada.

Ding, J. & Wang. Y.C. 2007. Experimental Study of Structural Fire Behaviour of Steel Beam to Concrete-Filled Tubular Column Assemblies with Different Types of Joints. *Engineering Structures* 29: 3485-3502.

European Committee for Standardization, ENV 1993-1-2, Eurocode 3, Part 1.2. 2005. Design of Steel Structures: Structural Fire Design. Brussels, Belgium.

Han, L.H., Yang, Y.F. & Xu, L. 2003. An Experimental Study and Calculation on the Fire Resistance of Concrete-Filled SHS and RHS Columns. *Journal of Constructional Steel Research* 59: 427-452.

Hibbitt, Karlsson & Sorensen Inc. 2009. ABAQUS/Standard Version 6.92 User's manual, Pawtucket, Rhode Island, USA.

Kodur, V.K.R. 1999. Performance-Based Fire Resistance Design of Concrete-Filled Steel Columns. *Journal of Constructional Steel Research* 51: 21–26.

Liu, T.C.H., Fahad, M.K. & Davies, J.M. 2002. Experimental Investigation of Behaviour of Axially Restrained Steel Beams in Fire. *Journal of Constructional Steel Research* 58: 1211–1230.

Lu, H. & Zhao, X.L. 2010. Fire Resistance Design of Concrete-Filled Double Skin Tubular (CFDST) Column. *Proceedings of the 13th International Symposium on Tubular Structures*: 691–698, Hong Kong, China.

Qian, Z.H., Tan, K.H. & Burgess, I.W. 2008. Behaviour of Steel Beam-to-Column Joints at Elevated Temperature: Experimental Investigation. *Journal of Structural Engineering*, ASCE, 134: 713–726.

Spyros, S., Davison, B., Burgess, I. & Plank, R. 2004. Experimental and Analytical Studies of Steel Components at Elevated Temperatures. *Fire and Material* 28: 83–94.

Wickstrom, U. 1994. The Plate Thermometer – A Simple Instrument for Reaching Harmonized Fire-Resistance Tests. *Fire Technology* 30(2): 195–208.

Wong, M.B. & Wang, J.D. 2010. Experimental Evaluation of Steel Dual Tube Column System for Fire Protection. *Proceedings of the 13th International Symposium on Tubular Structures*: 677–682, Hong Kong, China.

Tubular Structures XIV – Gardner (Ed.)
© 2012 Taylor & Francis Group, London, ISBN 978-0-415-62137-3

Experimental behaviour of reverse channel connection component under bolt tension at elevated temperatures

M. Jafarian & Y.C. Wang
School of Mechanical, Aerospace and Civil Engineering, University of Manchester, UK

ABSTRACT: This paper reports the results of a series of experiments to quantify the load-deflection behaviour of the reverse channel component, used in reverse channel connection between steel beam to tubular column, under bolt tension at elevated temperatures. A total of 9 tests were performed to investigate the effects of different reverse channel widths (150 and 230 mm), thicknesses (5.5 and 7.5 mm), the number of bolts (one and two rows) and temperature levels (20, 550, 750°C) on the failure modes and load-deflection relationships. The results indicate that failure modes can change at elevated temperatures due to different rates of reduction in strength of the different connection components. Three failure modes were observed, including formation of yield lines around individual bolt rows, formation of yield lines along the reverse channel web length and bolt fracture. There was also some development of membrane action. The yield line results can be used to give a safe estimate of the load carrying capacity of the component.

1 INTRODUCTION

Usage of steel hollow tubes has become increased these days because of their advantages such as, aesthetically appealing, inherent high fire resistance and fast construction speed. However, one of the main obstacles holding back more widespread use of steel tube and Concrete Filled Tube (CFT) columns in construction is the difficulty of making connections with desirable properties. Among existing types, a fin plate connection lacks rotational rigidity, is weak and possesses very limited ductility (Ding & Wang (2007), Yu et al. (2009)); using blind bolting to make endplate connection is restricted to square or rectangular tubes and the technology is best used when the bolt diameter is small.

Reverse channel connection is a new type that can be used with steel tubular columns of any shape, with or without concrete infill. The behaviour of this type of connection is now being extensively researched at the University of Manchester. To make this connection, a channel is welded to a steel tube through its flanges and the beam is attached to the web of the channel via an endplate. Since the channel has a limited depth, access inside the channel is easy. Research conducted at the University of Manchester so far (Ding & Wang (2007), Jones (2008)) and at Imperial College, London (Malaga-Chuquitaype & Elghazouli (2010)) suggest that this type of connection is easy to fabricate, has good rotational stiffness and bending moment capacity that enable this type of connection to be treated as semi-rigid and partial-strength connection, and very good rotation capacity to survive severe accidental loading.

However, to design and use the component based modeling for this connection, it is necessary to have detailed results of each component. This paper deals with the reverse channel component with bolts in tension, at ambient and different elevated temperatures.

2 TEST SET UP

Figure 1 shows the test rig arrangement. The reverse channel test specimen was welded to one thick steel plate on the legs and bolted to another thick plate on the web. Tension load, through a hydraulic jack, was applied to the test specimen within a self-reacting support frame.

2.1 *Selection of the test specimens*

A total of 9 tests were performed. Details of the test specimens are presented in Table 1.

These nine tests are in three groups to investigate the effects of channel sizes and number of bolts: RCT1-RCT3 used UKPFC 150 × 75 × 18 with one row of bolts; RCT4-RCT6 used UKPFC 150 × 75 × 18 with 2 rows of bolts; RCT7-RCT9 used UKPFC 230 × 90 × 32 with one row of bolts. For the narrower channels, the bolt spacing was 75 mm and for the wider channels, the bolt spacing was 90mm. For each bolt group, three tests were performed at three temperature levels (20°C, 550°C, 750°C).

In the tests with more than one row of bolts, RCT4-RCT6, the pitch was 90 mm.

Figure 2 shows an example of the fabrication details.

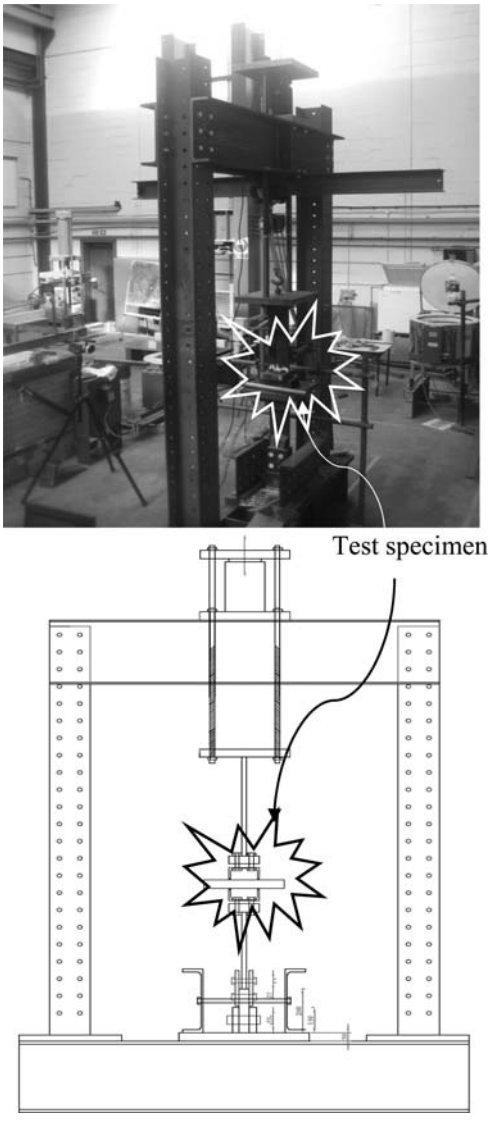

Figure 1. Test rig arrangement.

2.2 *Displacement measurement*

For ambient temperature tests, perpendicular displacements to the channel web were measured by two displacement transducers (Fig. 3) placed on top of the thick steel plate due to impossibility of directly attaching the transducers to the web.

The above transducer arrangement could not be employed for the elevated tests because the specimen, including the thick plate, was placed inside an electrical kiln (A thermal insulated oven which produces controlled temperature). Instead, small brackets were tag-welded to the thick plate. Thin guitar wires were attached to these brackets and then extended to outside the kiln and attached to displacement transducers via two pulleys. Figure 4 shows the arrangement.

2.3 *Material properties*

To determine the strength of the various segments of the channels, a series of coupon tests have been

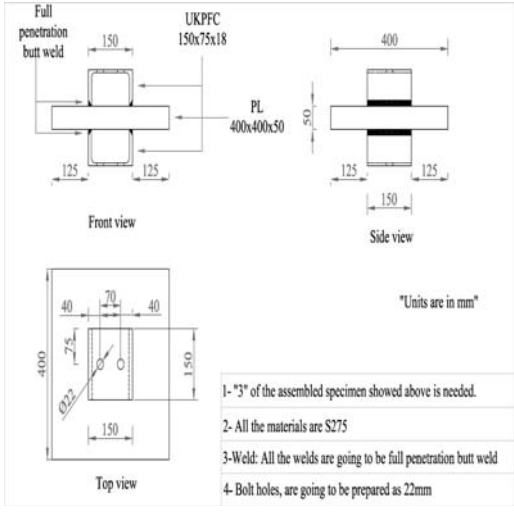

Figure 2. Typical fabrication details.

Table 1. Test specimen details.

UKPFC	Test No.	t_w	t_f	D	B	No. Bolt-row	L	T (°C)
150 × 75 × 18	RCT1	5.5	10	150	75	1	150	20
150 × 75 × 18	RCT2	5.5	10	150	75	1	150	550
150 × 75 × 18	RCT3	5.5	10	150	75	1	150	750
150 × 75 × 18	RCT4	5.5	10	150	75	2	230	20
150 × 75 × 18	RCT5	5.5	10	150	75	2	230	550
150 × 75 × 18	RCT6	5.5	10	150	75	2	230	750
230 × 90 × 32	RCT7	7.5	14	230	90	1	150	20
230 × 90 × 32	RCT8	7.5	14	230	90	1	150	550
230 × 90 × 32	RCT9	7.5	14	230	90	1	150	750

Where t_w is the channel's web thickness (mm); t_f is the channel's flange thickness (mm); D is the channel's width (mm); B is the channel's Depth (mm); L is the specimen length (mm).

performed at ambient temperature. Table 2 summarises the tensile coupon test results.

3 TEST RESULTS

The elevated tests were done under steady state. The specimen was heated to the target temperature first. Load was then applied while maintaining the specimen temperature. In all cases, the test was terminated when the specimen experienced fracture and the applied load could not be increased any further.

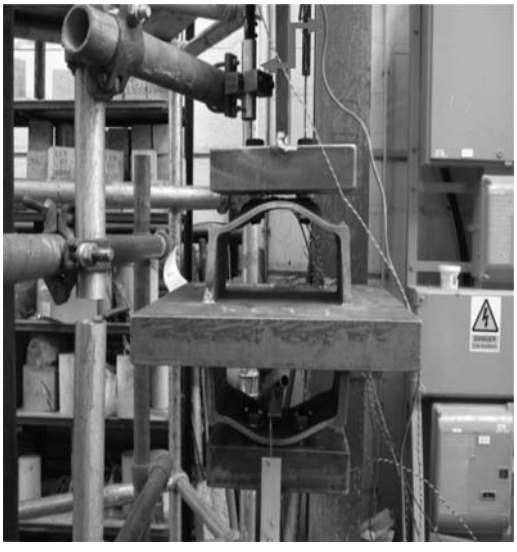

Figure 3. Transducer positions at ambient temperature.

Figure 4. Wires used to measure the displacement for elevated temperature tests.

3.1 *Deformation pattern and failure modes*

Figure 5 shows the three failure modes observed from the tests and Table 3 lists the failure mode of each test.

A. Formation of yield lines around individual bolt rows.
B. Formation of yield lines along length.
C. Bolt failure.

It seems that the bolt pitch (bolt spacing along the reverse channel length) in tests RCT4-RCT6 was too large so the yield lines still formed around individual bolt rows as in the case of using one bolt row in tests RCT1-RCT3. Because of this, the ultimate loads in RCT4-RCT6 using two rows of bolts simply doubled those in RCT1-RCT3 which used one row of bolts. For tests RCT7-RCT9, more rapid reduction in bolt strength at elevated temperatures forced a change of failure mode from yield line mechanism along the reverse channel length at ambient temperature to bolt fracture at elevated temperatures.

3.2 *Load-deflection curves*

Figure 6 compares the recorded load-deflection curves at different temperatures for RCT1-RCT3, all used the smaller channel UKPFC 150 × 75 × 18 and one row of bolts.

RCT1 was conducted at ambient temperature and its load-deflection curve experienced a sudden drop in load, which was due to cracking of the reverse channel web around the bolt position, Figure 7.

Figure 8 presents results for RCT4-RCT6. Since the failure mode in these tests was the same as in RCT1-RCT3, the recorded load-deflection curves for these tests were similar to those of RCT1-RCT3.

Using the principle of virtual work, the yield line solution for yield lines around bolt rows (Fig. 9, Pattern 1) is as follows:

$$P = 2M_p\left((2a_t)/R\right) + 2\pi - (d/R)) \quad (1)$$

where, P is the load on per row of two bolts. In deriving equation 1, the effect of bolt hole (d) should be included.

Using equation (1), the ultimate bending resistance for RCT1-RCT3 as 126.83 kN, 79.27, and 21.56 respectively and RCT4-RCT6 can be calculated as 253.67, 158.54, and 43.12 respectively, based on using the steel strength reduction factors from CEN (2005). The results for the ambient temperature cases are much

Table 2. Tensile coupon test results.

Coupon position	Thickness	Elongation	E (N/mm^2)	f_y (N/mm^2)	f_u (N/mm^2)
150 × 75 × 18 Flange	10	11.73	198322	325.08	593.59
Web	5.5	14.06	193256	326.58	626.22
230 × 90 × 32 Web	7.5	12.43	190190.4	442.11	669.48
Flange	14	13.05	186669.9	416.21	643.142

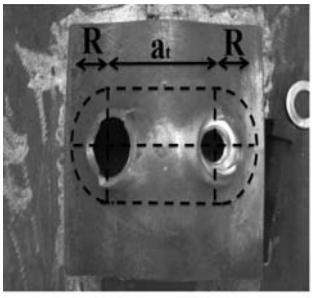

(a) Failure mode A

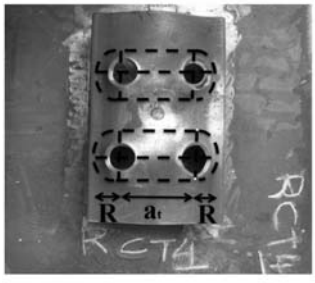

(b) Failure mode A

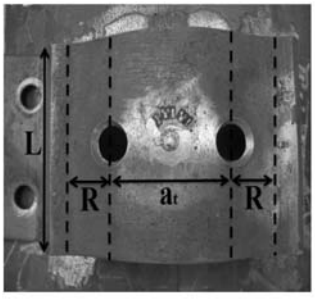

(c) Failure mode B

(d) Failure mode C

Figure 5. Observed failure modes.

Table 3. Failure loads of the tests.

UKPFC	Test no.	No. Bolt-row	Temp. (°C)	Failure load (kN)	Failure mode
150 × 75 × 18	RCT1	1	20	190.26	A
150 × 75 × 18	RCT2	1	550	86.90	A
150 × 75 × 18	RCT3	1	750	25.86	A
150 × 75 × 18	RCT4	2	20	384.7	A
150 × 75 × 18	RCT5	2	550	162.9	A
150 × 75 × 18	RCT6	2	750	46.36	A
230 × 90 × 32	RCT7	1	20	275.10	B
230 × 90 × 32	RCT8	1	550	100.3	C
230 × 90 × 32	RCT9	1	750	38.56	C

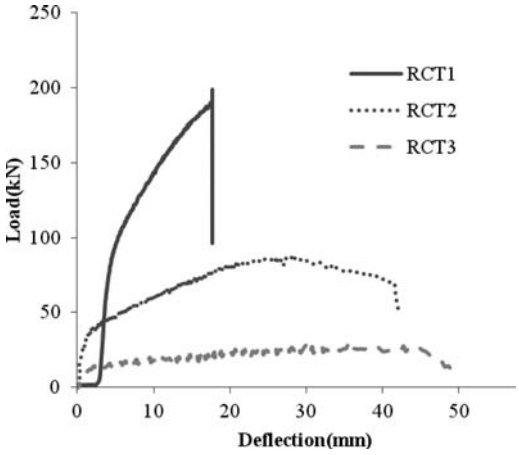

Figure 6. RCT1-RCT3 load-deflection curves.

Figure 7. RCT1, Web cracking.

lower than the test results (given in Table 3) because the calculation results were based on using the yield strength of steel but the steel has considerable strain hardening at ambient temperature. However, at high temperatures (over 500) the strain hardening effect diminishes. The calculated resistance is in good agreement with the test results. This means that the yield line solution is a safe estimate of the ultimate load of the tests.

Figure 10 compares the results of these two series of tests (RCT1-RCT3, RCT4-RCT6), with the loads for RCT4-RCT6 being divided by 2 so that the loads in Figure 10 represents that in one row of bolts. Since the channel dimensions are the same and the failure mode is formation of yield lines around individual bolt

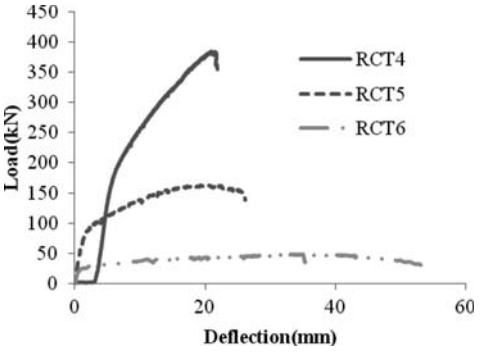

Figure 8. RCT4-RCT6 Load-Deflection.

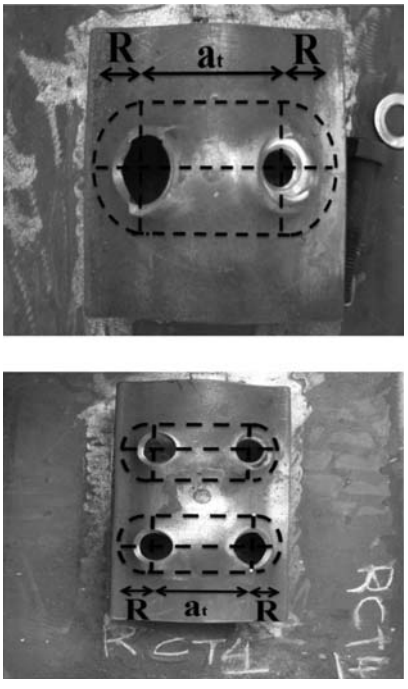

Figure 9. RC1 and RCT4 Yield patterns (Pattern 1).

row, the load-deflection behaviour per bolt row is very similar between these two series of tests.

Figure 11 presents the test results for RCT7-RCT9, which were conducted on the wider channel UKPFC 230 × 90 × 32 with one row of bolts.

This series of tests experienced two different failure modes: formation of yield lines along the entire length of the reverse channel web (RCT7, at 20°C) and fracture of the bolts (RCT8 and RCT9, at 550°C and 750°C respectively). From the load-deflection curve of RCT7, it is clear that there was considerable development of membrane action, which is illustrated by the increasing stiffness of the structure before failure. For this case, the tangent stiffness of the structure is almost constant during the initial stage of loading, then

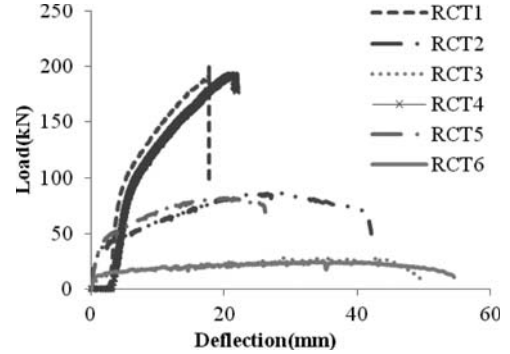

Figure 10. Comparison of all test results.

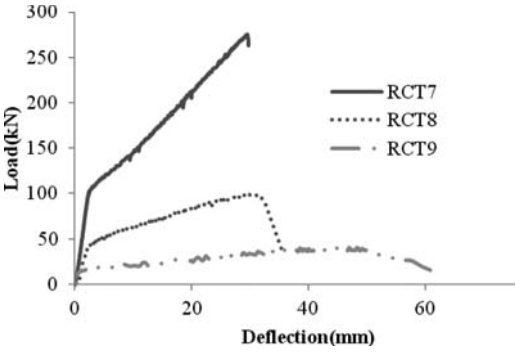

Figure 11. RCT7-RCT9 Load-Deflection curves.

gradually decreasing when the plate is under elastic-plastic bending, and starts increasing when the plate is under membrane action. The onset of membrane action may be taken when the second derivative of load with respect to deflection (the first derivative of tangent stiffness with respect to deflection) is zero. This is shown in Figure 12, corresponding to a deflection of 15 mm and a load of 177.4 kN.

Under the yield line pattern along the entire reverse channel length (Pattern 2), the strength (total load in two bolts) of a specimen may be calculated using the following equation:

$$P = \frac{4M_p L}{R} \tag{2}$$

The individual bolt fracture strength can be calculated as:

$$P_t = p_t * A_t \tag{3}$$

where A_t is the tensile stress area (M20 = 245 mm^2) and p_t is the ultimate tensile stress of the bolt.

For per row of two bolts, equation 3 gives values of 169.56, 105.98, and 28.83 at 20°C, 550°C and 750°C; equation 3 gives 392 kN, 150.92 kN and 31.36 kN respectively. In these calculations, the bolt

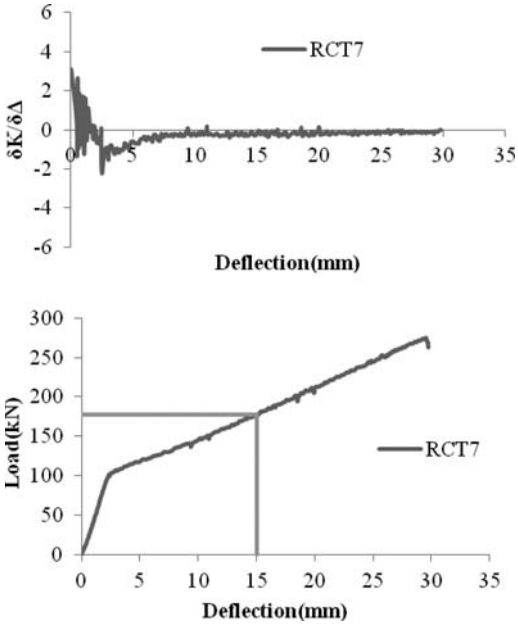

Figure 12. Corresponding load to zero stiffness variation.

strength reduction factors at elevated temperatures are taken from CEN (2005), being 0.385 at 550°C and 0.08 at 750°C respectively.

According to the above calculations, the failure mode for all three specimens should be formation of yield lines along the reverse channel length. For RCT7, this is as observed in the test. For RCT9, the bolt fracture load is slightly higher than the yield line solution. However, both modes give similar results that are close to the test values. For RCT8, the observed failure mode was bolt fracture yet the calculated value for bolt fracture is much higher than the test result. Since the equation for calculation of bolt tensile capacity (equation 3) is accurate and there was no prying action in the specimen, it appears that the only source of inaccuracy is the bolt strength reduction factor in EN 1993-1-2.

Furthermore, the calculated failure load for RCT7, based on yield line formation, is lower than the measured value. This may be attributed to the development of some membrane action in the reverse channel web that is not included in the yield line calculation. If using the previously determined load (177.4 kN) before onset of membrane action, as determined based on Figure 13, the calculated yield line solution of 169.56 kN is very close.

For comparison, the failure loads based on yield line mechanism around bolt row can be calculated as 245.56 kN, 158.54 kN and 43.12 kN for tests RCT7, RCT8 and RCT9 respectively. These values are much higher than those for the other two failure modes, eliminating this failure mode.

For further comparison, the strengths of RCT1-RCT6 have been calculated for the two failure modes observed in tests RCT7-RCT9 and the results are provided in Table 4. The governing failure mode is the formation of yield lines around bolt row, as observed in the tests.

Table 4. Comparison between different patterns.

Section	Failure pattern 1 (kN)	Failure pattern 2 (kN)	Bolt fracture (kN)
RCT1	126.83	164.65	392
RCT2	79.27	102.91	150.92
RCT3	21.56	27.99	31.36
RCT4	253.67	252.47	784
RCT5	158.54	157.79	301.84
RCT6	43.12	42.92	62.72
RCT7	245.56	169.56	392
RCT8	158.54	105.98	150.92
RCT9	43.12	28.83	31.36

Table 4 shows the comparison between test and calculation results for the two observed failure modes for all tests.

4 CONCLUSIONS

This paper has presented the experimental results of a total number of 9 tests conducted to investigate the behaviour of Reverse Channel connection to concrete filled steel tubes. The bending strengths of these tests were calculated based on the observed failure modes which included yield line formation around bolt row, yield line formation along reverse channel length and bolt fracture. The following conclusions may be drawn:

- The observed failure modes agree with the modes that give the minimum calculated strengths for all specimens except test RCT8. For RCT8, it appears that the bolt strength reduction factor at 550°C in EN 1993-1-2 is much higher than for the bolts used in the test.
- It is possible for the failure mode to change from reverse channel web failure to bolt fracture because of the faster reduction in strength of bolts at elevated temperature compared to that of steel plate.
- At ambient temperature, the effect of strain hardening is considerable. For these cases, the yield line solution gives a safe lower estimate of the load carrying capacity of the structure. The effect of strain hardening diminishes at high temperatures.
- If yield line formation is along the entire length of the reverse channel web, there is potential for considerable development of membrane action.

ACKNOWLEDGEMENT

The research reported in this paper is part of the COMPFIRE project, funded by the European Union, through grant RFCS (RFSR-CT-2009-00021).

REFERENCES

CEN 2005. EN1993-1-8: 2005 Design of steel structures. Part 1-2 General rules Structural fire design. London: British Standards Institution.

Ding, J. & Wang, Y. C. 2007. Experimental study of structural fire behaviour of steel beam to concrete filled tubular column assemblies with different types of joints. Engineering Structures, 29, 3485–3502.

Jones, M. H. 2008. Tensile And Shear Behaviour Of Fin-Plate Connections To Hollow And Concrete-Filled Steel Tubular Columns At Ambient And Elevated Temperatures. PhD, Manchester.

Malaga-Chuquitaype, C. & Elghazouli, A. Y. 2010. Behaviour of combined channel/angle connections to tubular columns under monotonic and cyclic loading. Engineering Structures, 32, 1600–1616.

Yu, H. X., Burgess, I. W., Davison, J. B. & Plank, R. J. 2009. Experimental investigation of the behaviour of fin plate connections in fire. Journal of Constructional Steel Research, 65, 723–736.

Tubular Structures XIV – Gardner (Ed.)
© 2012 Taylor & Francis Group, London, ISBN 978-0-415-62137-3

Behaviour of steel beams connected to CFT column in fire during cooling stage

S. Elsawaf, Y.C. Wang & P. Mandal
School of Mechanical, Aerospace and Civil Engineering, University of Manchester, UK

ABSTRACT: This paper focuses on steel framed structures using Concrete Filled Tubular (CFT) columns and the objective of this paper is to find means of reducing the risk of structural failure during cooling. It reports the results of a study using the general finite element software ABAQUS to numerically model the behaviour of restrained structural subassemblies of steel beam to CFT columns and their joints in fire, emphasizing on the cooling stage. Validation of the finite element model was achieved by comparing the simulation and test results for the two fire tests investigating cooling behaviour using reverse channel and fin plate connections, recently conducted at the University of Manchester. The finite element models give very good agreement with the experimental results and observations. Remarkable differences in tensile forces in the connected beams were observed during the tests depending on the beam temperature at which cooling started. This leads to the suggestion that in order to avoid connection fracture during cooling, it may be possible to reduce the limiting temperature of the connected beam by a small value ($<50°C$) from the limiting temperature calculated without considering any axial restraints in the beam.

1 INTRODUCTION

Collapse of the World Trade Center buildings (FEMA 2002) and results of the Cardington full-scale eight-storey steel framed building fire tests in the UK (Newman 2004) have demonstrated that steel joints are vulnerable during both the heating and cooling phases of fire. Joint behaviour in fire is currently one of the most important topics of research on structural fire resistance; however, most of the present research studies have focused on the heating phase.

During the cooling stage of a fire, when the beam temperature decreases, if thermal shortening of the beam is restrained, large tensile forces may be induced in the beam (Wang 2002; Wang 2005). In the meantime, because of the larger thermal mass of the connection region compared to the beam, the connection temperature may still be rising, so reduction in the connection strength continues. This coupling of connection strength reduction and beam tensile force increase may result in fracture of some connection components, leading to possible structural failure. Although this has caused concern, the authors are not aware that any systematic research has been undertaken to find ways of preventing connection failure during cooling.

This research extends the experimental study of Ding & Wang (2007) and will conduct extensive numerical simulations to explore different methods of enabling reverse channel connections to survive the entire fire exposure, particularly during the cooling phase. This study has the following two specific objectives;

- To develop and validate a three-dimensional (3-D) FE model using ABAQUS software for modelling the behaviour of restrained structural subassemblies of steel beam to Concrete Filled Tubular (CFT) columns using reverse channel connections during cooling.
- To conduct parametric studies to find means of connection design to reduce the risk of structural failure during cooling.

2 VALIDATION OF THE NUMERICAL SIMULATION MODEL AGAINST THE TEST RESULTS OF DING & WANG (2007)

2.1 *Description of the finite element model*

Figure 1 shows the experimental set up and details of the fire tests as provided in Ding & Wang (2007). As in the authors' recent research studies (Elsawaf et al. 2011; Elsawaf & Wang 2012), three-dimensional solid elements (C3D8I) were used to model the main structural members. The tested structure was symmetrical in geometry. Therefore, to save computational time, it was decided to include only half of the test assembly in the finite element model. Furthermore, to reduce the number of elements and nodes in the FE model, the column was divided into three parts and only the central part connected by the joint and

exposed in fire in the furnace was actually modelled using the solid elements. The other two parts away from the joint zone were modelled using general beam elements with "box" cross section for the steel tube and "rectangular" cross section for the concrete infill. The ABAQUS "Coupling" function was used to join the three column parts. A series of ABAQUS models were built and run to assess sensitivity of the simulation results to FE mesh. Figure 2 shows the FE mesh for fin plate and reverse channel connections. The reduction factors for strength and elastic modulus of carbon steel at elevated temperatures provided in EN 1993-1-2 were used. In the test structures, many contact pairs existed in the joints. The ABAQUS contact function was used to simulate the interaction between the contact pairs. In order to reduce the computational cost, a contact was defined as surface to surface contact with a small sliding option. "Hard contact" was assumed for the normal contact behaviour and a friction coefficient of 0.3 was used in the tangential direction of the contact pairs. The boundary conditions of the FE model were according to those in the test: the bottom of the columns was pinned in all three directions and the top of the columns was pinned in two directions but movement along the column longitudinal axis was allowed. Since only half of the beam was included in the FE model due to geometrical and loading symmetry as discussed earlier, the beam mid-section was fixed in the axial direction at all nodes, which effectively prevented rotation about any axis in the beam cross-section, but allowed the beam to twist about its longitudinal axis.

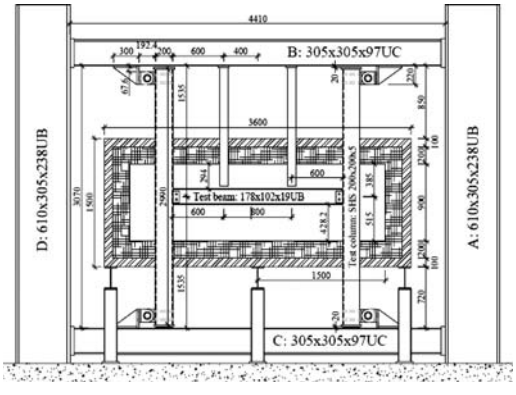

Figure 1. Elevation view of schematic arrangement of test.

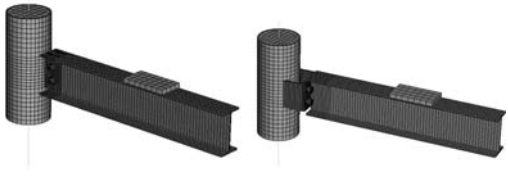

(a) Fin plate joint (b) Reverse channel joint

Figure 2. FE mesh.

The test beam had no lateral restraint and could move sideways. But in the test, in order to ensure that the loading jacks remained attached to the beam, each loading jack was inserted into a steel bracket which was then clamped on the top flange of the beam. Therefore, in the numerical model the four corners of the loading plate were laterally restrained. As in the test, the FE modelling applied the loads in two steps: (i) two point loads were applied to the beam at ambient temperature; (ii) while maintaining the structural loads, the structural temperatures were exposed to fire attack until the end of the fire test. In the FE model, six different temperature curves based on test measurements were adopted for different parts of the structure: a total of three temperature curves for the bottom flange, web and top flange of the beam; one temperature curve for the joint zone which included all the bolts, nuts and connection components as well as 100 mm length of the beam in the joint zone; one temperature curve for the steel tubular column in the joint region; one temperature curve for concrete fill in the joint region. The temperature of the column away from the joint zone was set at ambient temperature.

2.2 *Finite element results*

In order to evaluate reliability of the 3D finite element model, test results of two different fire tests recently conducted at the University of Manchester, one using reverse channel connection and the other using fin plate connection, are used for direct comparison. The test results included deformation patterns, beam mid-span deflections and beam axial forces. As detailed in the following sections, this comparison demonstrates that the 3-D finite element model is able to successfully simulate the fire tests during both the heating and cooling stages.

2.2.1 *Test 9 of Ding & Wang: fin plate connection*

Test 9 of Ding & Wang (20047) used CHS 193.7 × 5 mm tubes and fin plate connection. Figure 3 shows details of the connection. There was no fire protection on the joints. During the test, the furnace fire exposure was stopped and fan-assisted cooling started just when the beam was about to change its behaviour from bending to catenary action. Figure 4 presents the input temperature-time relationships for the beam web

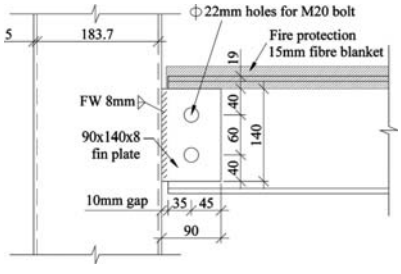

Figure 3. Geometrical details of fin plate connection in test 9.

and flanges, the steel tube, the connection zone and the concrete fill.

Figure 5 compares the modelling and experimental results for deformation modes of the beam and the joint. It can be seen that the observed deformations of the joint components and the beam were closely followed by the numerical model. As shown in Figure 5(a), there was no fracture and failure of the sub-frame. Due to expansion and bending of the steel beam, the bottom flange of the beam was bearing against the CFT columns during the heating stage, as shown in Figure 5(a) & (b). Apart from these, there was no noticeable deflection in the steel tubes. Due to large twist in the beam, the fin plates were also twisted to one side as shown in Figure 5(b). Figure 6 compares the measured and simulated beam axial force and beam mid-span deflection as functions of the beam lower flange temperature at mid-span. The test structure experienced high compression but small lateral deflection during the thermal expansion stage. Because cooling started just after the beam reached its limiting temperature for bending, the beam also developed high tension forces during the cooling stage. The simulation results have accurately captured the entire cycle of beam behaviour.

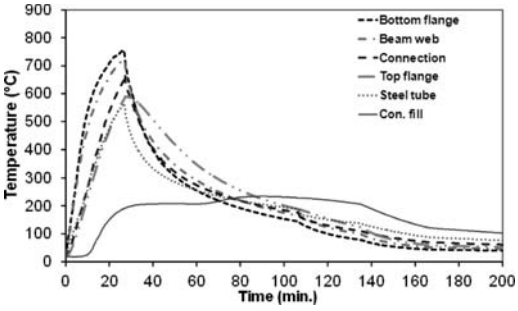

Figure 4. Time-temperature relationships used for Test 9.

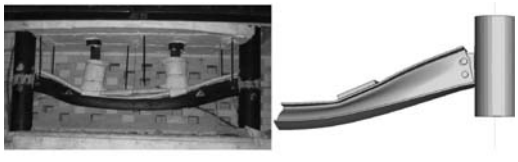

(a) Overall deformed shape

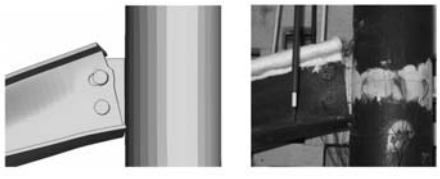

(b) Deformed fin plate

Figure 5. Behaviour of test 9 of Ding and Wang (2007).

2.2.2 *Test 10 of Ding & Wang: reverse channel connection*

Test 10 of Ding & Wang (20047) used CHS 193.7 × 5 mm tubes and reverse channel connection. Figure 7 shows details of the connection. There was no fire protection on the joints. Figure 8 presents the input temperature-time relationships for the beam web and flanges, the steel tube, the connection zone and the concrete fill.

Figure 9 compares the modelling and experimental results for deformation modes of the beam and the joint. It can be seen that the deformation patterns obtained by the simulation and from the test are very close. No failure was observed in both the test

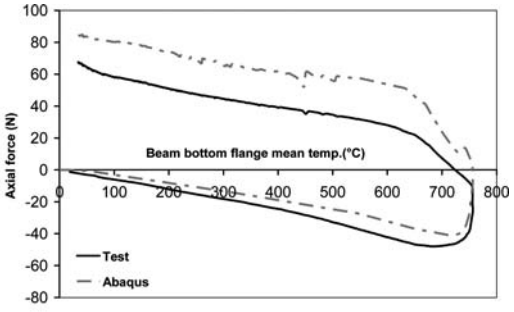

(a) Beam axial force – temperature relationships

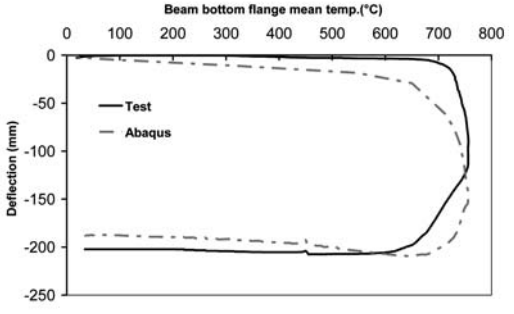

(b) Beam mid-span deflection – temperature relationships

Figure 6. Comparison between modeling and experimental results for mid-span deflection and axial force in the beam with fin plate connections (Test 9 of Ding and Wang 2007).

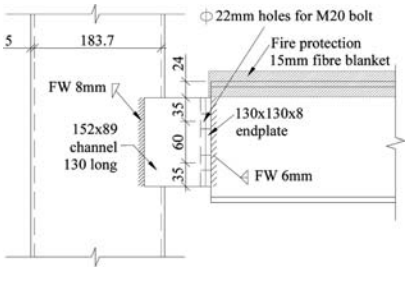

Figure 7. Geometrical details of reverse channel connection in Test 10 of Ding and Wang (2007).

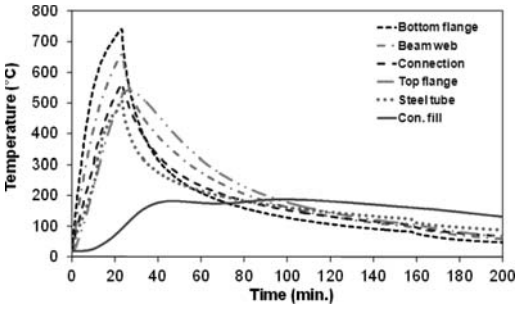

Figure 8. Time-temperature relationships used for Test 10 (reverse channel connection) of Ding and Wang (2007).

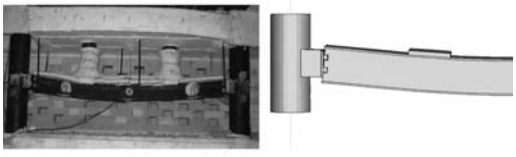

(a)Overall deformed shape

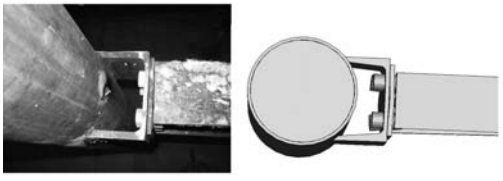

(b) Deformed reverse channel

Figure 9. Behaviour of test 10 of Ding and Wang (2007).

specimen and numerical model. The beam was bent slightly, as shown in Figure 9(a). There was no visible deformation in the steel tube and the connection region, as shown in Figure 9(b). Figure 10 shows that both the numerical and measured beam axial force and beam mid-span deflections match well. The test structure experienced large compression during the thermal expansion stage. However, unlike Test 9, because in this test cooling started just before the beam reached its limiting temperature in bending, the beam was still in substantial compression when cooling started. As a result, the residual tensile force in the beam was quite small when compared with Test 9 of Ding & Wang (2007). This is closely predicted by the FE model.

The above comparisons demonstrate that the authors' ABAQUS model is valid.

3 BEHAVIOUR OF RESTRAINED STRUCTURAL SUBASSEMBLIES OF STEEL BEAM TO CFT COLUMN IN FIRE DURING COOLING STAGE

The validated numerical model is used to conduct extensive numerical simulations in order to investigate

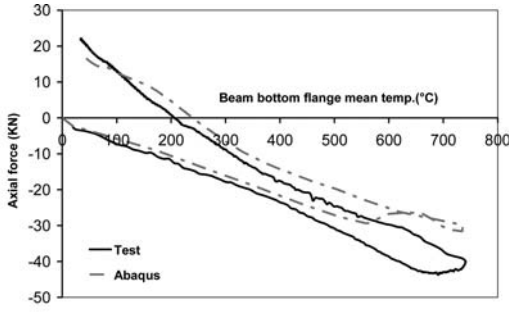

(a) Beam axial force – temperature relationships

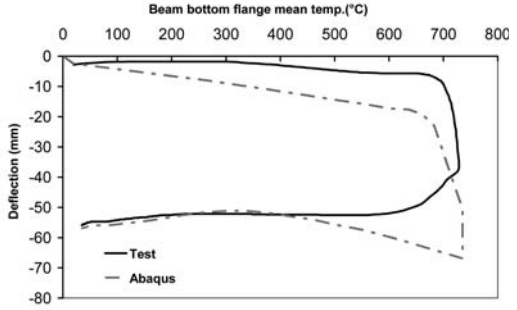

(b) Beam mid-span deflection – temperature relationships

Figure 10. Comparison between modeling and experimental results for mid-span deflection and axial force in the beam with reverse channel connections (Test 10 of Ding and Wang 2007).

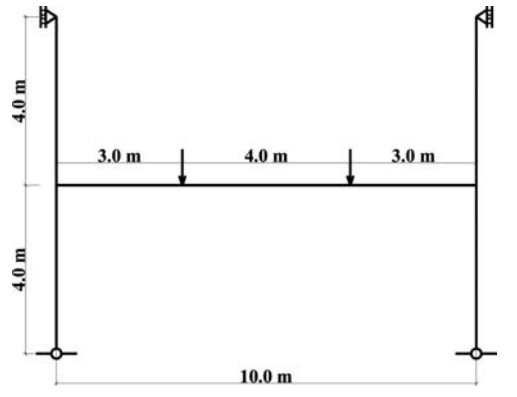

Figure 11. Dimensions and boundary condition of structure assembly.

the behaviour of reverse channel connections between steel beams and CFT columns under cooling. The aim of this investigation is to find means of reducing the risk of joint failure during the cooling stage. Compared to flush and extended endplate connections, a flexible end plate connection is more likely to fail during cooling. Therefore, this research focuses on reverse channel connection using a flexible endplate. Figure 11 show details of the connection. Figure 12 shows the

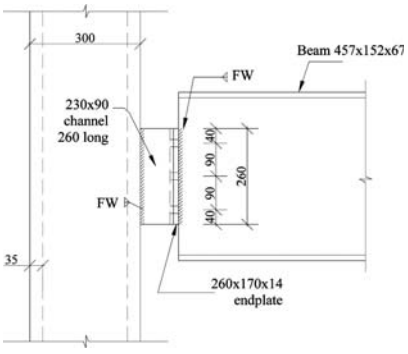

Figure 12. Basic geometrical details of flexible end plate connection to reverse channel.

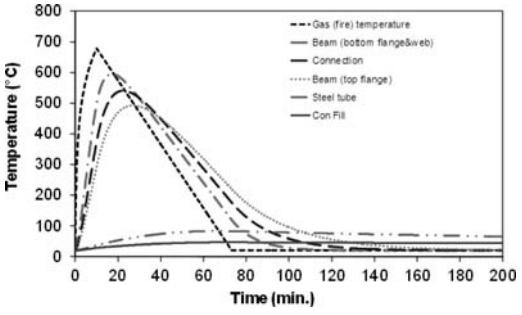

Figure 13. Input time-temperature curves for different parts of the simulation structure.

structure arrangement to be simulated in this research. It represents a steel beam connected to two Concrete Filled Tubular (CFT) columns. The top and bottom of the columns are rotationally unrestrained but are horizontally restrained to simulate the lateral stability system in a real structure. The beam was assumed to be fully restrained in the lateral direction to represent the effect of the concrete slab. Initial applied load ratio in the beam = 0.7. Here the load ratio is defined as the ratio of the maximum bending moment in the simply supported beam to the plastic moment capacity of the beam at ambient temperature. This structural arrangement is the same as used in the fire tests of Ding and Wang (2007) but the dimensions are more realistic. The temperature profiles for different parts of the structure are shown in Figure 13.

3.1 *Simulation Results for the basic case*

Figure 15a shows axial force developments in the beam with continuous heating only and with heating up to the beam's limiting temperature followed by cooling. At the beginning of fire exposure, due to restrained thermal expansion, an axial compression force is present in the beam and the compression force increases with increasing temperature until reaching the maximum value (113 kN) at 437°C. Afterwards, the beam mid-span deflection (Figure 15b) starts to increase more rapidly until reaching 658 mm (more than span/20) at

Figure 14. Failure modes of connection

the maximum beam temperature of 585°C (the beam's limiting temperature), as shown in Figure 14b. For the beam with continuous heating, failure occurs at 618°C after some catenary action has developed in the beam. For the beam in cooling, the beam deflection changes within a narrow range because the beam deflection is mainly plastic. However, due to restrained cooling, the beam develops tension force at decreasing temperature. Eventually, the connection fails at near ambient temperature (22°C) when the beam tension force reaches about 168 kN, as a result of excessive plastic strains (larger than 20% strain, see Figure 15c) in the connection. As shown in Figure 14, failure is caused by fracture of the reverse channel web around the bolt holes and fracture at the reverse channel web/flange junctions.

Figure 16 may be used to explain the variation of plastic strain during the cooling phase as shown in Figure 15(c). Assume a point in the structure is at temperature T1 (585°C, cooling start temperature), and its stress-strain state is at point A on the stress-strain curve at T1. On cooling, due to the change of the beam axial force from compression to tension, the stress decreases to point B and then starts to increase elastically. During this stage, although the stress within the steel increases as a result of the increasing tensile force in the connection due to restrained thermal contraction, the total strain is lower owing to increased stiffness at lower temperatures. Therefore, for a considerable period of time, the plastic strain is unchanged. Near ambient temperature (T2), the stress-strain relationships at different temperatures are almost identical. Therefore, further increase in tensile force in the connection can only be accommodated by further strain increase shown as point C in the figure. Once the strain exceeds 15% (point D), the stress-strain curve enters the descending branch and accelerated straining is necessary to maintain structural equilibrium. Connection failure occurs at 20% strain (point E).

4 PARAMETRIC STUDIES

The above simulation results for the basic case suggest that there is a risk of connection fracture during the cooling stage. A parametric study has been conducted to investigate the effects of different design parameters and how they may be changed to prevent joint failure during the cooling stage. Table 1 lists all the simulations carried out in the parametric study, which covered two main parameters identified in the

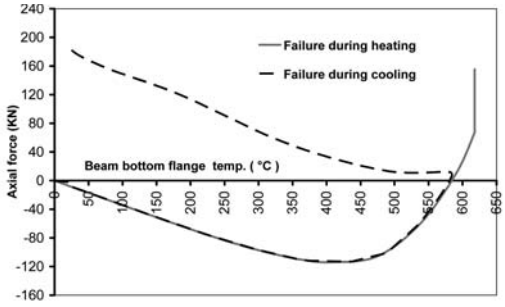

(a) Beam axial force – temperature relationships

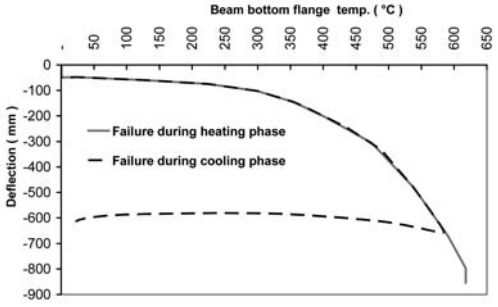

(b) Beam mid-span deflection – temperature relationships

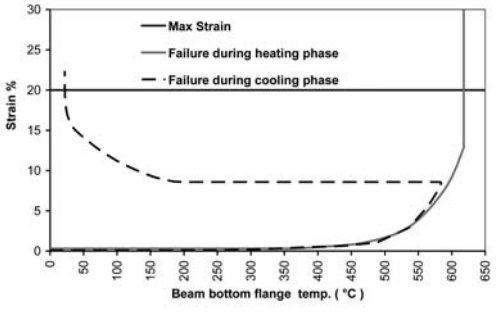

(c) Maximum plastic strain in reverse channel – temperature

Figure 15. Beam mid-span deflection – temperature, beam axial force – temperature and Maximum plastic strain – temperature relationships.

previous section: difference between the beam's limiting temperature and the temperature (before reaching its limiting temperature) at which cooling starts and the beam's axial restraint level. Table 1 also indicates whether the connection has failed or not.

4.1 *Effect of the beam maximum temperatures (simulations 1–5)*

Results of the basic parametric studies indicate that connection may fail during the cooling stage. Therefore, there is a need to find means of reducing the

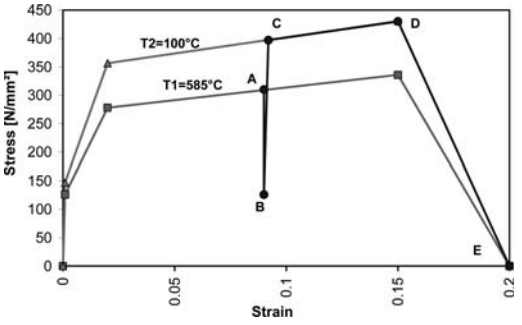

Figure 16. Movement of critical strain between two different temperatures.

Table 1. Summary of parametric study results.

Simulation ID	Ultimate strain %	Applied load ratio	Limiting temperature(°c)	Reduction in temperature (°)	The beam's axial restraint level	Results
1	20%	0.7	585	0	7.5%	F
2	20%	0.7	585	10	7.5%	F
3	20%	0.7	585	25	7.5%	NF
4	20%	0.8	545	25	7.5%	F
5	20%	0.8	545	50	7.5%	NF
6	20%	0.7	570	0	15%	F
7	20%	0.7	565	0	25%	F
8	20%	0.7	561	0	50%	F
9	20%	0.7	570	50	15%	NF
10	20%	0.7	565	50	25%	F
11	20%	0.7	561	50	50%	F
12	20%	0.7	565	75	25%	NF
13	20%	0.7	561	125	50%	NF

F = Failure, NF = No Failure.

risk of structural failure during cooling. One possibility is to reduce the maximum temperature at which cooling starts. Without considering the effects of axial restraint, this temperature at which cooling starts is the beam's limiting temperature based on bending. In an axially restrained beam, the axial force in the beam is compression at temperature lower than the limiting temperature and tension at temperature higher than the limiting temperature. If the maximum beam temperature before cooling is lower than the limiting temperature in bending, then when the beam is starting to cool down, it is still in compression and this compression can be used to reduce the tensile force in the connection when the beam cools.

Figure 17 compares the beam's axial force – temperature and vertical deflection – temperature relationships between three cases: the beam's maximum temperature is equal to the beam's limiting temperature (case 1), the beam's maximum temperature is 10°C less than the beam's limiting temperature (case 2) and the beam's maximum temperature is 25°C less

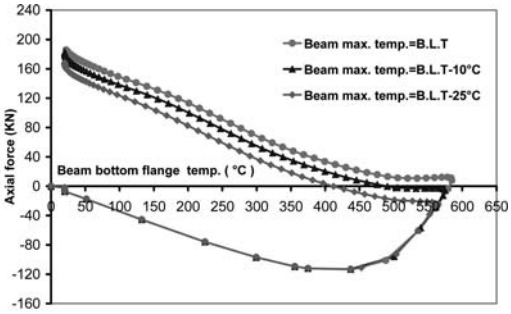

(a) Beam axial force – temperature relationships

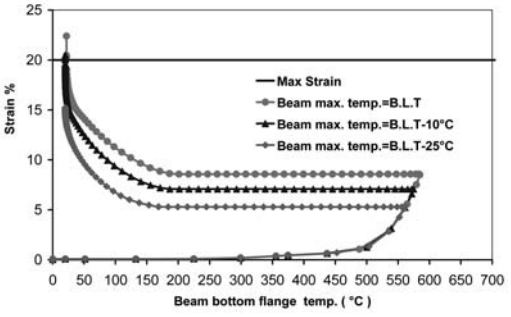

(b) Maximum plastic strain– temperature relationships

Figure 17. Effects of the beam's maximum temperature on connection failure.

than the beam's limiting temperature (case 3). From Figure 17a, it can be seen that a very large tension force (183kN) was generated in the beam, causing failure of the connection before it had cooled down to room temperature, as shown in Figure 17b with the maximum connection strain exceeding the strain limit of steel. Starting cooling at 10°C below the beam's limiting temperature prolonged the connection's survival time during cooling but the connection still failed before cooling down to ambient temperature. In contrast, because the beam in case 3 was still experiencing high compression when cooling started, maximum connection tension strain was lower than the strain limit of steel throughout the cooling phase. Therefore, there was no connection failure in case 3.

The reduction from the beam's limiting temperature to the beam's maximum temperature before cooling starts increases as the load in the beam increases because of the existing higher connection tensile strain at a higher load ratio. For example, in the case of a high load ratio (0.8), the reduction in temperature approaches 50°C, as shown in Figure 18.

4.2 *Effect of different levels of axial restraint (simulations 6–13)*

The level of axial restraint is obviously an important parameter affecting beam and connection behaviour

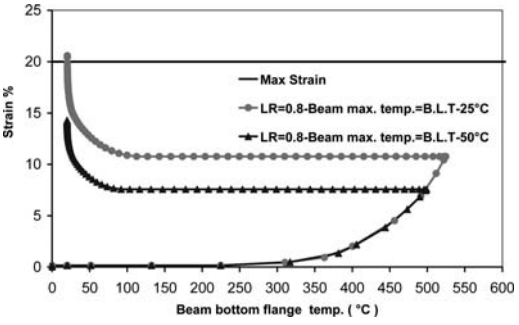

Figure 18. Effects of load ratio on the beam's maximum safe temperature during cooling-Maximum plastic strain – temperature relationships.

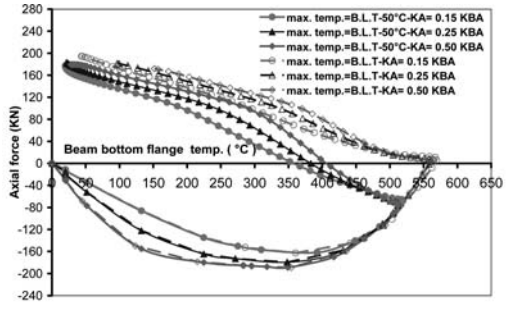

(a) Beam axial force – temperature relationships

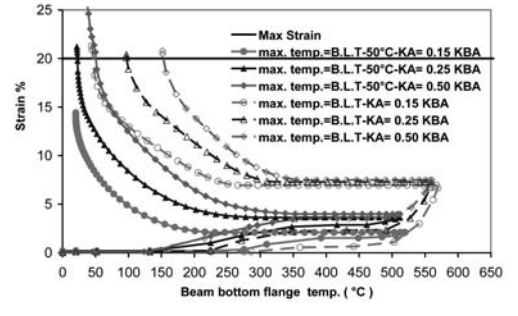

(b) Maximum plastic strain – beam temperature relationships

Figure 19. Effects of axial restraint level.

during cooling. All other conditions being the same, the tension force in the connection and the beam increases as the axial restraint stiffness increases and therefore the risk of connection failure during cooling increases. For example, Figure 19b compares the maximum connection strain at three levels of axial restraint stiffness (15%, 25% and 50% of beam axial stiffness KBA). The maximum beam temperature when cooling starts is the same, being 50°C lower than the beam's limiting temperature. The results in Figure 19 show that the connection in all the three cases failed when the

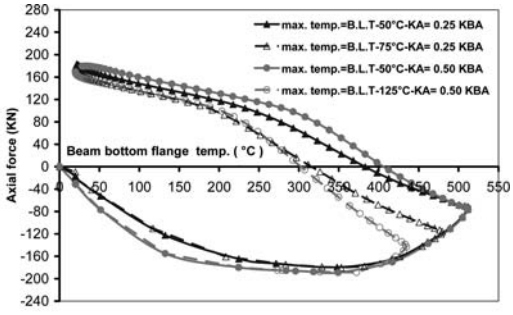

(a) Beam axial force – temperature relationships

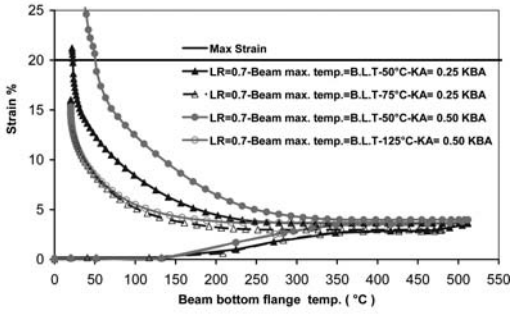

(b) Maximum plastic strain – temperature relationships

Figure 20. Effects of cooling temperature at different levels of axial restraint.

beam starts to cool at the beam's limiting temperature but failure occurred at different temperatures. When the beam starts to cool at 50°C lower than the beam's limiting temperature in case of KA = 0.15 KBA there is no failure during cooling. But connection failure occurs if the axial restraint stiffness is higher. It should be pointed out that the axial restraint stiffnesses used are high compared to that in realistic design. To enable the beam with higher axial restraint stiffnesses to survive the cooling phase without a connection failure, further reductions from the beam's limiting temperature to the maximum temperature at which cooling starts should be considered. For example, Figure 20 shows that a reduction of 75°C is necessary for the case of 25% axial restraint stiffness and 125°C for the case of 50% restraint stiffness.

5 CONCLUSIONS

Based on the results of the reported numerical results, the main conclusions are:

– For beams with realistic levels of axial restraint stiffness (connection tensile stiffness <=15% of beam axial stiffness), an effective and simple method is to reduce the temperature at which cooling starts from the beam's limiting temperature. Reducing the beam's limiting temperature by 50°C has been demonstrated to be safe to enable the beam to survive the entire cooling phase without a connection failure.

ACKNOWLEDGEMENTS

The first author of this paper would like to thank the Egyptian Ministry of Higher Education and Al-Azhar University in Cairo, Egypt for providing scholarship to enable him to pursue PhD study at the University of Manchester.

REFERENCES

Ding J., Wang Y. C.: Experimental study of structural fire behaviour of steel beam to concrete filled tubular column assemblies with different types of joints. Engineering Structures (2007); 29: 3485–3502.

Elsawaf S., Wang Y. C., Mandal P.: Numerical modelling of restrained structural subassemblies of steel beam and CFT columns connected using reverse channels in fire. Engineering Structures (2011); 33: 1217–1231.

Elsawaf S. & Wang Y. C.: Methods of improving the survival temperature in fire of steel beam connected to CFT column using reverse channel connection. Engineering Structures (2012); 34: 132–146

EN 1993-1-2, Eurocode 3: Design of steel structures, part 1.2: general rules-structural fire design. London, British Standards Institution: (2005).

Federal Emergency Management Agency (FEMA 2002), World Trade Center building performance study. FEMA, USA.

Newman G.M. Robinson J.T. Bailey C.G. Fire Safety Design: A New Approach to Multi-Storey Steel-Framed Buildings, the Steel Construction Institute, (2004).

Wang, Y.C. (2002), Steel and composite structures, behaviour and design for fire safety, Spon Press

Wang, Y. C. (2005), Performance of steel-concrete composite structures in fire, Progress in Structural Engineering and Materials, 7(2): 86–102

Tubular Structures XIV – Gardner (Ed.)
© 2012 Taylor & Francis Group, London, ISBN 978-0-415-62137-3

Fire resistance for square tubular joints with and without chord reinforcement

J. Yang, Y.B. Shao & C. Cheng
Yantai University, Yantai, PR China

S.P. Chiew & S.T. Lie
Nanyang Technological University, Singapore

ABSTRACT: The chord surface around the brace/chord weld toe for a square welded tubular joint is the critical position because failure occurs frequently at this location due to the weak stiffness in the transverse direction of the chord which is generally a thin-walled tube. To improve the load carrying capacity, the chord of a square tubular joint can be strengthened locally near the joint connection. Through Finite Element (FE) analysis, the fire resistance of both un-reinforced and chord reinforced tubular T-joints is investigated. The chord reinforcing measure for the T-joints is increasing the chord thickness around the brace/chord intersection locally. In the FE analysis, the duration of fire resistance, the reaction force in restrained chord ends and the deforming process of two typical tubular T-joints under axial compression are analyzed and discussed. The effect of brace axial loading ratio on the fire resistance is also considered. Based on the FE analysis, it is found that a tubular joint with chord reinforcement has a much longer duration of fire resistance compared to an un-reinforced joint. In addition, the failure mode of a chord reinforced tubular joint model can be changed to tube yielding if a suitable reinforcing scheme is used while joint failure is always the dominant mode for an un-reinforced tubular joint.

1 INTRODUCTION

Welded tubular structures are widely used in practical engineering such as stadium, bridge, tower and offshore engineering. For these structures, one or several smaller steel tubes (called brace member) are welded directly onto the outer surface of a bigger steel tube (called chord member) to form a connection namely tubular joint. Tubular joint is a very critical position in a welded tubular structure due to two principal reasons: (1) discontinuous stiffness at the weld toe causes high stress concentration in this region; (2) welding process produces residual stresses around the weld toe. Additionally, a tubular joint is mainly subjected to brace axial loading and thus the chord always sustains external loading in its transverse direction. As the square steel tubes used in welded tubular structures have large width/thickness ratio, especially for the chord (the ratio is generally bigger than 20), they are much closer to behave as thin-walled structures. It is well known that the transverse stiffness of a thin-walled tube is much smaller than its axial stiffness, and hence the chord surface around the weld toe becomes the failure region in most cases when a tubular joint is subjected to brace axial loading. Therefore, it is effective to improve the load carrying capacity of a tubular joint by reinforcing the chord locally near the weld toe.

In the literature, there are many reported reinforcing methods for welded tubular joints. However, most research work is focused on circular tubular joints, such as stiffened internal ring reinforcement, doubler- or collar-plate reinforcement, increasing local chord thickness reinforcement and inner plate reinforcement etc. All of the above reinforcing methods have been proved to be effective in improving the static strength or hysteresis of tubular joints if the reinforcement is positioned appropriately. Relatively scarce studies on static or hysteretic behaviour of square tubular joints have been reported. Li et al (2011) studied the hysteretic behaviour of chord reinforced square tubular T-joints and found such reinforcement can improve the energy dissipation greatly. Although tubular joints with chord reinforcement have higher load carrying capacity, this conclusion is based on the analysis for tubular joints in ambient temperature. In recent years, many reports regarding the collapse of stadiums or bridges after fire are found, and considering severe consequences of large stadium or bridge in fire, it is important to do some research work in this field to investigate the failure process of welded tubular joints in fire, and then to find some feasible measures to increase their fire resistance.

Although it is well known that steel is heat sensitive material, previous studies were focused on components or connections in building structures such as beams, columns, slabs or beam-column connects etc. Very scarce research work on fire resistance of welded tubular joints has been conducted in the past decade,

and a few research studies are focused only on circular tubular joints. Among these studies, Liu et al (2010) carried out an experimental test on a welded tubular truss under fire condition, and they found the final failure is local buckling of brace members under compression. Yu et al (2011) studied the fire resistance of a tubular T-joint after impact and found the failure is due to local buckling of the chord. Nguyen et al (2010) conducted both experimental and numerical analyses on the static strength of several tubular T-joint models in different elevated temperatures. However, they did not consider the accumulated deformation effect on the load carrying capacity in heating time under fire condition. To develop a further study on the mechanism analysis of fire resistance, it is necessary to carry out some work to investigate the behaviour of square tubular joints in fire.

2 FUNDAMENTALS OF HEAT TRANSFER ANALYSIS

2.1 *Geometry of a tubular T-joint without or with chord reinforcement*

For a square welded tubular joint without any reinforcement, one or several brace members are welded directly onto the outer surface of a chord member. A typical square tubular T-joint is shown in Fig. 1. As mentioned previously, it is effective to increase the load bearing capacity by reinforcing the chord in local position near the brace/chord intersection. Fig. 2 shows the typical reinforcing measure, i.e. chord thickness reinforcement. For this reinforcing method, the chord comprises two types of tubes which have different thicknesses. The two tubes have same outer width and they are connected together by butt weld. The tube at the brace/chord intersection region has a bigger thickness to increase its transverse stiffness.

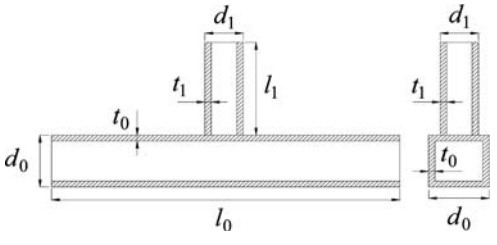

Figure 1. An un-reinforced square tubular T-joint.

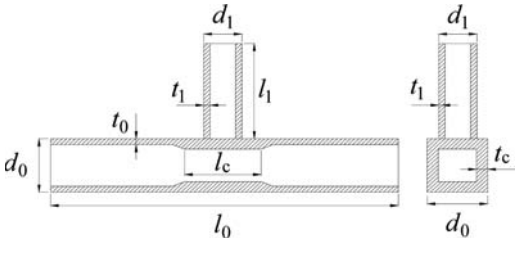

Figure 2. A chord reinforced square tubular T-joint.

2.2 *Heat transfer theory*

The fire resistance analysis can be attributed to a problem of heat transfer analysis. For a tubular joint in a fire environment, it is essential to know the exact temperature elevating process. Such a process can be evaluated from a temperature – time relationship curve. The most commonly used heating curve in fire condition is ISO 834 curve, in which the temperatures at different time are specified in the following equation

$$T_t = 345\log_{10}(8t+1)+20 \tag{1}$$

In Eq. (1), T is the environmental temperature with a unit of centigrade, and t is the heating time with a unit of second. Fig. 3 shows the temperature-time curve in accordance with Eq. (1).

Although Eq. (1) specifies the relationship between environmental temperature and heating time, it is necessary to obtain the temperature distribution on the tubular joint so as to analyze its fire resistance. In a fire condition, heat will tansfer between the environment and the tubular joint from conduction, convection or radiation. In the calculation of such heat transfer, some fundamental parameters of the environment must be known. The principal parameters include film coefficient and emissivity coefficient. The exact values of the two parameters are difficult to obtain accurately in theory. The feasible method is to study such values by using finite element investigation based on evaluation from experimental results. The temperatures at different positions are then deduced and expressed as the following equation.

$$k\frac{T_i - T_s}{l} = h(T_s - T_\infty) + \varphi\varepsilon\sigma(T_s^4 - T_{sur}^4) \tag{2}$$

where k is the coefficient of thermal conductivity, T_i is the temperature on the inner surface of the tubular joint; T_s is the temperature on the outer surface of the tubular joint; T_∞ is the surrounding atmosphere temperature; T_{sur} is the temperature of body emitting radiation; h is the coefficient of heat convection; φ is the shape influence coefficient; ε is the absorption

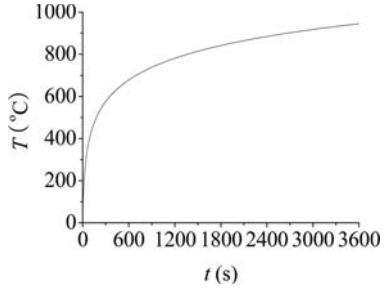

Figure 3. ISO834 heating curve.

rate; σ is Stefan-Boltzmann's constant; and l is the wall thickness of the tube.

Eq. (2) is concluded based on energy conservation criterion. The left part of the equation is heat-flow density of conduction in steel from the outer surface of tube wall to the inner surface. The right parts are convection heat-flow density and radiation heat transfer rate. The energy transferring into tube wall from the surrounding environment should be equal to the energy transferring in the tube wall.

In Eq. (2), the emissivity is assumed to be equal to the absorption rate, and the heat transferring in tube wall is one-dimensional and linear along the radial direction. The value of k is a constant value which can be obtained from material property. The value of l is determined from the chord length once the geometry of the tubular joint is determined. The values of the coefficients h and ε are $25\,h/W \cdot m^{-2} \cdot K^{-1}$ and 0.5 respectively in the finite element analysis.

2.3 *Material properties*

The material properties of steel are quite sensitive to high temperature. In general, the elastic modulus and the yield stress both reduce in an elevated temperature. The commonly used material Q235, in which Q means yielding stress and 235 means its value is 235 N/mm^2 at ambient temperature, is taken as an example. The elastic modulus for steel Q235 is 206×10^3 N/mm^2 at ambient temperature. Considering an elastic – perfect plastic material model, the stress-strain relationship at elevated temperature for steel Q235 without hardening stage can be obtained from the specification in Eurocode 3 (2005), and such a relationship is illustrated in Fig. 4. The values of the elastic modulus and the yield stress at different elevated temperatures are obtained by multiplying a reduction factor to the values of the two parameters in ambient temperature. For other material parameters, such as density, Poisson's ratio and thermal expansivity, the values can be also obtained from the specification in Eurocode 3 (2005).

Another consideration is about creep in elevated temperature. It is advised by Tan et al (2002) that transient analysis should be carried out to consider the creep effect when the temperature in the steel is beyond 450°C, which usually occurs in building fires. Taking creep into consideration is complicated and difficult

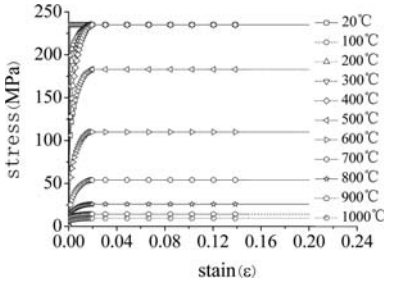

Figure 4. Stress-strain relationship at elevated temperatures.

in the analysis. However, Jiang et al (1999) presented some constitutive relations of steel material which take the creep into account. Another method to take creep into consideration is using fully coupled thermal-stress analysis. For sequentially coupled thermal-stress analysis, creep is not included. The stress-strain relationship specified in Eurocode 3 (2005) also does not take creep into account, and this study follows the method specified in Eurocode 3. Whether this assumption is suitable is needed to be assessed. The possible method to evaluate the effect of ignoring the creep effect in fire resistance analysis can compare the theoretical or numerical results with experimental results to check if the different results agree well. In this study, the feasibility of not considering the effect of creep is assessed by comparing finite element results with corresponding reported experimental measurements.

3 FINITE ELEMENT ANALYSIS FOR FIRE RESISTANCE OF TUBULAR JOINTS

Finite element (FE) method is still a widely used technique in solving many engineering problems due to its low cost, fast calculation and reasonable accuracy although experimental test is absolutely the most challenging method. Especially for fire analysis, it is quite time-consuming and expensive conducting a fire test. It is hence critical to build a correct and accurate finite element model in analyzing fire resistance of welded tubular joints. As fire resistance is a heat transfer problem, the stress/displacement solution depends on the temperature field. In the commonly used finite element software ABAQUS, a sequentially coupled thermal-stress analysis can be conducted to solve heat transfer problem. For this method, the fire resistance of a tubular joint can be classified into two stages: (1) heat transfer stage, and (2) stress/displacement analysis. In the first stage, external loading is not applied to the tubular joint, and the tubular joint is only experiencing the heating process. The temperature distributions at different time can be calculated. Then such temperatures are taken as known quantity to analyze the stress/displacement in the second stage.

3.1 *FE mesh*

During the process of pure heat transfer, element DC3D8, which is an 8-node linear heat transfer brick element, is used in the analysis. C3D8I is chosen as the element type during the analysis of stress/displacement. 'I' denotes incompatible elements which are first-order elements enhanced by incompatible modes to improve their bending behaviour. The primary effect of these modes is to eliminate the parasitic shear stresses that cause the response of the regular first-order displacement elements to be too stiffened in bending.

Convergence is another significant problem in FE analysis, and more elements should be used in the region with high stress gradient to ensure the numerical results converge to the actual solution. In a welded

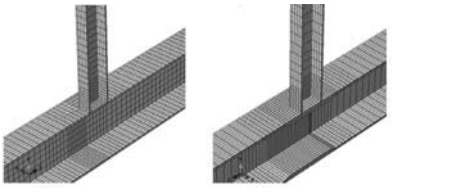

Figure 5. Finite element mesh.

tubular joint, the region around the brace/chord intersection on the chord surface is definitely important position as failure occurs mostly in this location. Therefore, more elements with smaller size are generated in this critical region. In the zones far away from the intersection, coarse mesh can be used for saving computing time. Using this mesh generation scheme, the FE meshes of tubular T-joints both without and with chord reinforcement are shown in Figs. 5(a)–5(b).

3.2 *FE results*

In the finite element analysis, two typical T-joint models in Table 1 are studied. The two T-joint models have different brace/chord diameter ratios. b_0, t_0 and l_0 are the width, the thickness and the length of the chord member respectively. Accordingly, b_1, t_1 and l_1 are the width, the thickness and the length of the brace member respectively. For the chord reinforced T-joint models, l_c and t_c are used to denote the corresponding length and thickness of the locally reinforced chord. For model T1, l_c and t_c are 80 mm and 6.4 mm respectively. For model T2, l_c and t_c are 448 mm and 14 mm respectively.

In the fire resistance analysis, the T-joint models are assumed to be subjected to brace axial compression loading with a fixed magnitude. Then the environmental temperature is elevated in accordance with the ISO 834 heating curve. During the heating process, the chord deformation at the brace/chord intersection together with the corresponding elevated temperature is analyzed to assess the fire resistance. The chord deformation is defined as the displacement difference between the top surface and the bottom surface of the chord member. In addition, both ends of the chord are fixed in the FE analysis to capture the maximum restrained reaction force at the boundary due to heat transfer and expansion. Such restrained reaction force is also significant in evaluating the fire resistance of the tubular joints because it causes compression or tension in the cross section of the chord in its axial direction. Such compression or tension may bring beneficial or harmful effect on the loading bearing capacity of a tubular joint in fire.

Before the fire resistance, the static strengths of the two un-reinforced T-joint models T1 and T2 in Table 1 at ambient temperature, F_{cr}, are calculated by using FE analysis. For each model, four loading cases, namely 20% F_{cr}, 40% F_{cr}, 60% F_{cr} and 80% F_{cr}, are applied to the brace end to investigate the influence of loading

Table 1. Dimensions of two T-joint models.

Model	b_0 (mm)	b_1 (mm)	t_0 (mm)	t_1 (mm)	l_0 (mm)	l_1 (mm)
T1	100	40	4	2.8	750	300
T2	280	224	7	4.9	2996	750

Table 2. Loading cases.

Model	F_{cr} (kN)	20% F_{cr} (kN)	40% F_{cr} (kN)	60% F_{cr} (kN)	80% F_{cr} (kN)
T1	28	5.6	11.2	16.8	22.4
T2	234	46.8	93.6	140.4	187.2

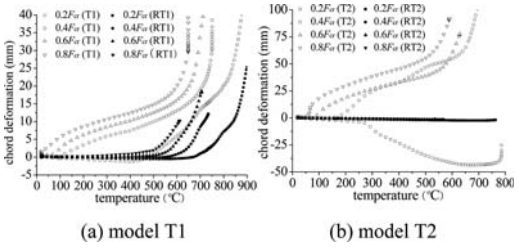

Figure 6. Relationship between chord deformation and temperature.

level on the fire resistance. The detailed values of the four loading cases are provided in Table 2.

The failure process can be evaluated reasonably from the variation of the chord deformation as the applied load is fixed at a constant value which is less than the static strength at ambient temperature. The chord deformation in a fire accumulates with elevated temperature, and Figs. 6(a) and 6(b) show the relationship between chord deformation and temperature for both un-reinforced and chord thickness reinforced T-joint models. In Figs. 6(a) and 6(b), RT1 and RT2 denote the first and the second chord reinforced T-joint models respectively. For the first T-joint model, as seen from Fig. 6(a), the deformed process of the reinforced models is different from that process of the un-reinforced one. The chord deformation of the reinforced model is smaller than that of the corresponding un-reinforced model, and the chord deformation is quite small even at 600°C. The applied loading ratio has critical effect on the deformation of the T-joint models in fire, and it deteriorates the chord stiffness in the radial direction. The chord deformation experiences a negative increase firstly, and then it increases gradually to become positive. As the chord deformation is defined as the difference of the displacement between the top and the bottom surfaces, as shown in Fig. 7(a)–7(b), a positive value means the distance between the top and the bottom surfaces becomes

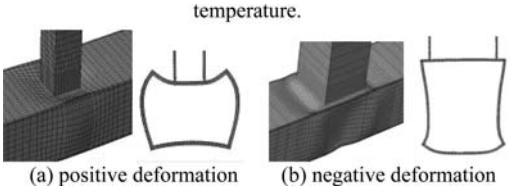

Figure 7. Definition on chord deformation.

smaller while a negative one means such distance becomes bigger. The negative value of the chord deformation in the initial stage is caused by the restrained heat expansion with fixed boundaries at the chord ends. When temperature increases, the Young's modulus and the yield stress of the steel material decrease, and the deflection of the chord becomes bigger, which reduces the restrained heat expansion. For the second T-joint model, similar conclusions can be obtained. Additionally, some differences are listed as follows: (1) chord thickness reinforcement seems to be more effective in resisting the chord deformation for the second model, and chord deformation is quite small; (2) the chord deformation is always negative when the loading ratio is 20% for the un-reinforced T-joint model. This means the displacement on the top surface is always smaller than the displacement on the bottom surface. This shows heat expansion is dominant when this model is subjected to a lower load. Heat expansion produces compression stress on the cross section of the chord, and thus causes the bottom surface to buckle locally, which can be seen from Fig. 6(b). The second T-joint model has a large β value and the top surface of the chord does not buckle easily due to the constraint of the brace.

In the failure definition of a tubular joint at ambient temperature, 3% deformation of the chord width around the weld toe is generally used when there is no apparent loading drop in the load-deformation curve of this model. To study the reinforcing efficiency in resisting fire, such definition is also used to investigate the critical temperature T_{cr} and the corresponding required heating time t. Table 3 provides a detailed comparison for the un-reinforced models and the corresponding chord reinforced models. The fire resistance of tubular joint models is evaluated from the above two indices T_{cr} and t. Obviously, T_{cr} of the reinforced models is much higher than the critical temperature of the corresponding un-reinforced models, which means the reinforced models do not fail in fire at a temperature while the un-reinforced models fail exactly at this temperature. In addition, the heating time to the critical temperature for the reinforced models is also much longer than that for the un-reinforced ones, and this also proves the reinforced models have better fire resistance. Especially for the second model, the joint will not fail in fire before the brace failure when the local chord thickness is increase to be $2T$ (T is original chord thickness).

The reaction forces at chord ends in fire for the analyzed models are shown in Figs. 8(a) and 8(b).

Table 3. Comparsion of T_{cr} and t for the un-reinforced and the corresponding chord reinforced models.

Model	F/F_{cr}	$T_{cr}(^{\circ}C)$	$t(s)$
RT1	0.2	543.1/747.4	620/1476
	0.4	185.2/651.6	190/950
	0.6	108.8/583.0	116/804
	0.8	50.2/522.9	54/684
RT2	0.2	293/BF	435/BF
	0.4	216.6/BF	324/BF
	0.6	118.4/BF	185/BF
	0.8	66.1/BF	105/BF

Note: BF stands for brace failure.

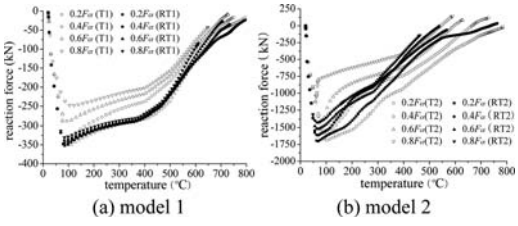

Figure 8. Relationship between reaction force at chord ends and temperature.

Generally, compression forces initiate at chord ends due to the heat expansion in elevated temperature and chord boundary constraints. As the chord ends are fixed, such expansion is restrained and compression stresses on the cross section increase with the increasing temperatures. In the initial stage, the compression forces increase quickly in an approximately linear way. The reaction forces for all models reach peak value at a critical temperature less than 100°C, and then their values begin to decrease after the critical temperature. Some differences exist for the un-reinforced models when they are subjected to different loading ratios. For example, the maximum reaction force of the un-reinforced model with a bigger loading ratio (i.e., 80% P_{cr}) is much lower while the peak value for the un-reinforced model with a lower loading ratio (i.e. 20% P_{cr}) is almost the same as that of the reaction force for the corresponding reinforced models. The above results can be explained in different mechanisms. In case of reinforcement or low loading ratio, the chord behaves mainly as an axially loaded member because its deflection is very small. In this condition, the expansion of the chord in fire is limited in a longer time. However, for the un-reinforced model with bigger loading ratio, the deflection of the chord is also bigger, which makes the chord behaves more like a flexural beam. In case of large deflection, cantenary effect initiates and tensile stresses exist on the cross section to reduce the compression due to the expansion restrictions

The peak value of the reaction force can also be used to assess the stress situation on the cross section of the chord ends. As the steel material is assumed

to be elastic-perfect plastic, the maximum stress on the cross section of the chord ends is the yield stress. Based on this condition, the maximum reaction force at chord ends, R_{max}, is calculated from the following equation

$$R_{\max} = A \cdot f_y \tag{3}$$

where A is the area of the cross section of the chord, f_y is the yield stress of the steel material.

According to Eq. (3), the maximum reaction forces for the two T-joint models are essentially the yield loads which are calculated to be 361 kN and 1796 kN respectively. From Figs. 8(a) and 8(b), the FE results of the R_{max} for the two models are 352 kN and 1705 kN respectively, which are very close to the predicted results from Eq. (3). Hence, it can be concluded that the maximum reaction force can reach yield loading value when a T-joint is fixed at both ends or subjected to a low loading scale in fire. However, the reaction force can not reach yielding load when a high scale loading is applied to the brace end. In theory, flexural action becomes dominant when the T-joint is subjected to a higher brace load, and the compression due to heat expansion and boundary constraints at chord ends will be released due to tensile action caused by bending moment when large deflection of the chord occurs. This is why the maximum reaction force of the T-joint model under higher loading scale can not reach yield load.

4 CONCLUSION

Based on finite element analyses, the fire resistance of square tubular T-joints with and without chord reinforcement is studied. From the finite element investigation, the following two conclusions can be made:

(1) The chord reinforcing methods can increase the fire duration time and the critical temperature before final failure efficiently, and thus to improve the fire resistance of welded tubular joints.

(2) The reaction force at the chord ends in a fixed condition can not be ignored when a tubular joint is subjected to fire because heat expansion can cause much bigger compression in the chord member once its ends are restrained. Generally, the magnitude of such reaction force for the reinforced models is almost the same as that of the un-reinforced models when they are subjected to small ratio loading. For brevity, the maximum reaction force can be estimated from the chord yielding load which can be calculated from the product of the yield stress of the steel material and the area of the chord cross section.

ACKNOWLEDGEMENT

This research work is supported by the Natural Science Foundation of Shandong Province of China (No. ZR2009FM014), and such support is greatly appreciated by the authors.

REFERENCES

Choo, Y.S., van der Vegte, G.J., Zettlemover, N., Li, B.H., Liew, J.Y.R. 2005. Static strength of T-joints reinforced with doubler or collar plates, I: Experimental investigations. *Journal of Structural Engineering, ASCE*, 131(1): 119–128.

Fung, T.C., Chan, T.K., Soh, C.K. 1999. Ultimate capacity of doubler plate-reinforced tubular joints. *Journal of Structural Engineering, ASCE*, 125(8): 891–899.

Jiang, S.C., Li, G.Q. 1999. Material properties of structural steel at elevated temperatures. *Steel Construction*. 32: 49–61.

Lee, M.M.K., Llewelyn-Parry, A. 2004. Offshore tubular T-joints reinforced with internal plain annular stiffeners. *Journal of Structural Engineering, ASCE*, 130(6): 942–951.

Li, T., Shao, Y.B. 2011. Study on hysteretic behavior of square tubular T-joints with increased chord thickness. *Journal of Building Structures*, 32(4): 142–150.

Liu, M.L., Zhao, J.C., Jin, M. 2010. An experimental study of the mechanical behaviour of steel planar tubular trusses in a fire. *Journal of Constructional Steel Research*, 66: 505–511.

Nguyen M.P., Fung T.C., Tan K.H. 2010. An experimental study of structural behaviours of CHS T-joints subjected to brace axial compression in fire condition. *Tubular Structures*, Hong Kong, 725–732.

Nguyen M.P., Tan K.H., Fung T.C. 2010. Numerical models and parametric study on ultimate strength of CHS T-joints subjected to brace axial compression under fire conditions. *Proceedings of the 13th International Symposium on Tubular Structures*, Hong Kong, China, 733–740.

Shao, Y.B., Zhang, J.C., Qiu, Z.H., Shang, J.J. 2009. Strength analysis of large-scale multiplanar tubular joints with inner-plate reinforcement. *International Journal of Space Structures*, 24(3): 161–177.

Tan, K.H., Ting, S.K., Huang, Z.F.2002. Visco-elasto-plastic analysis of steel frames in fire. *Structural Engineering, ASCE*. 128: 105–114.

Yu, W.J.,Zhao, J.C., Luo, H.X., Shi, J.Y., Zhang, D.X. 2011. Experimental study on mechanical behavior of an impacted steel tubular T-joint in fire. *Journal of Constructional Steel Research*. 67: 1376–1385.

Tubular Structures XIV – Gardner (Ed.)
© 2012 Taylor & Francis Group, London, ISBN 978-0-415-62137-3

Behaviour of the reverse channel joint component at elevated temperature

F.C. Lopes, A. Santiago & L. Simões da Silva
University of Coimbra, Coimbra, Portugal

T. Heistermann & M. Veljkovic
Luleå University of Technology, Luleå, Sweden

J.G.S. da Silva
State University of Rio de Janeiro, Brazil

ABSTRACT: The reverse channel connection appears to have the best combination of desirable feature under fire loading: moderate construction cost, ability to develop catenary action and extremely high ductility through deformation of the web channel (Ding & Wang 2007). This paper presents the results of the experimental investigation on a reverse channel component carried out at the University of Coimbra into the European RFCS COMPFIRE Project, which the main focus is to characterize the behaviour of steel joints between steel beams to concrete filled tubular columns under natural fire loading. A series of tension and compression tests at ambient and elevated temperatures were tested. The aim of those experimental tests was to identify the strength, stiffness and ductility of this joint component, establishing a relationship between force, displacement and temperature.

1 INTRODUCTION

1.1 *State of the art*

The composite columns are often assumed to possess inherently high fire resistance and have been used to achieve cost reduction of the steel construction without compromising safety. Although there have been extensive research studies of the joint behaviour at ambient temperature (Weynand et al. 1995, Simões da Silva et al. 2002), as well as member and frame structural behaviour under fire conditions (Wang 2005), there is a paucity of research on joint behaviour in fire. Indeed, past research studies have largely neglected how steel and composite (steel-concrete) joints actually behave in fire. Mainly, the ENV version of Eurocode 3 Part 1.2 (ENV 1993-1-2 1995) did not require evaluation of steel joint behaviour under fire loading. The main reason for that had been justified by the argument of the increased massivity of joint region and thereby slowing down temperature rises in the joint region in fire compared with the connected beams and columns. However, observations from real fires show that, on some occasions, joints fail from their tensile components (Bailey et al. 1999, Wald et al. 2006). Owing to accumulative effects of a number of factors that occur in fire conditions, including hogging bending moments, tension field action in shear and high cooling strain or pulling in effect at large deflection of the connected beam, the tensile components of the joints fracture (Santiago et al. 2008). The great danger of joint fracture is the potential for progressive collapse of the structure. Recently, in the experimental study on structural fire behaviour of different types of steel beam to concrete filled tubular column assemblies, the reverse channel connection appears to have the best combination of desirable feature: moderate construction cost, ability to develop catenary action and extremely high ductility through deformation of the web channel (Ding & Wang 2007).

1.2 *Objectives of the investigation*

The study presented in this paper is part of the European project COMPFIRE (Simões da Silva et al. 2011), which the principal aim is to provide an integrated approach for the practical application of performance-based fire engineering design of composite (steel-concrete) structures, including joint performance under natural fire conditions. Within this project, an experimental programme was performed at the University of Coimbra to evaluate the behaviour of the channel sections loaded transversely through their web at ambient and elevated temperatures. The experimental programme consisted of 13 tensile and 8 compressive tests where the aim was to evaluate the overall behaviour of the component, establishing a relationship between force, displacement and temperature and to study the influence of the parameters considered most relevant: dimensions of the loaded area and its slenderness.

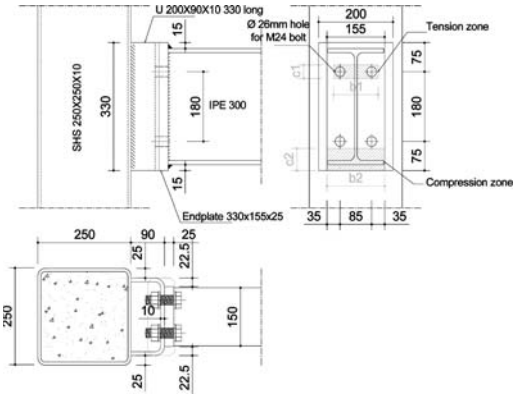

Figure 1. Reverse channel joint (dimensions given in mm).

2 CASE OF STUDY

2.1 *Typology of connection*

The reverse channel connections are created through a bolted endplate to web of a channel section and its flanges are welded to the column face (Figure 1). The columns are concrete filled tubes, being studied two cross sections typologies: square (250 mm side) and circular (244.5 mm diameter). The wall thickness is 10 mm in both profiles. An IPE300 is used for the beam. The structural steel profiles are grade S355; the end plate is 25 mm thick and grade S275 and the bolts are M24 grade 10.9.

2.2 *Analytical approach for component design*

The joint between beam and channel was assumed as an I-beam to RHS (Rectangular Hollow Section) column bolted connection using a flush endplate, which shows similar behaviour of the weak-axis joints. Because of the lack of a central stiffening web, the loaded chord of the column must support the tensile and compressive forces arising from the beam flanges in bending like a plate supported on its vertical sides (Silva et al. 2003). The bending resistance and initial stiffness of this joint typology is obtained at ambient temperature with the application of the CIDECT Report 5BP-4/05 (Jaspart et al. 2005), which identifies the following components: i) beam flange in compression; ii) bolts in tension; iii) end-plate in bending; iv) beam web in tension; v) RHS in transverse tension: chord face failure; vi) RHS in transverse compression: chord face failure; vii) RHS in transverse tension: punching shear failure; and viii) RHS in transverse compression: punching shear failure. The first four components are enshrined into the Eurocode 3 Part 1.8 (EN-1993-1-8, 2005). The analytical approach for chord face failure and punching shear of the RHS column is based on the yielding mechanism in a bolted connection (Jaspart, 1997). The deformation of the loaded face often governs the resistance of the connection. In this analytical approach two different mechanisms can lead to the failure of the loaded face: local and global failure mechanisms (Figure 2a and 2b).

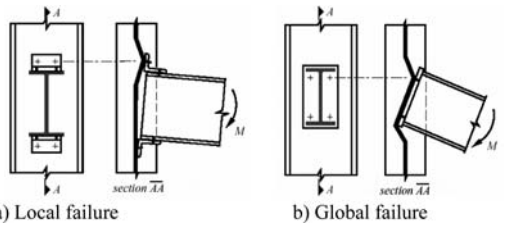

Figure 2. Failure mechanism of the chord face.

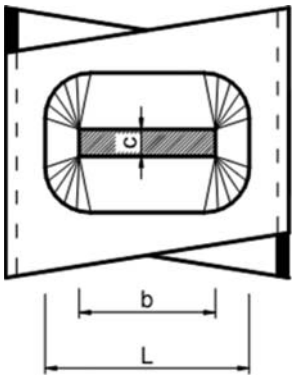

Figure 3. Yield area.

The relevant resistance of the proposed component ($F_{pl,Rd}$) is the minimum of the two failure mechanism:

$$F_{pl,Rd} = \min(F_{pl,loc}; F_{pl,glob}) \quad (1)$$

where $F_{pl,loc}$ is the local failure load and $F_{pl.glob}$ is the global failure load.

The design of the proposed joint to be studied (Figure 1) showed in general web failure by local mechanism. The experimental programme focused the evaluation of the tension and compression zones of the reverse channel connection separately, considering the local failure mechanism. The main relevant geometric characteristics which influence the resistance of the component are: i) width of the yield area L (Figure 3) of the loaded face; ii) width b_i and height c_i of the loaded area to transmit the tension and compression loads. The mean diameter of the bolt head and the distance between bolts define the rigid area $b_i \times c_i$ at the tension zone; while when the compression zone is considered, the dimensions b_i and c_i are obtained with the assumption of the dispersion at 45° through the end plate by compression forces arising from the beam flanges (Figure 1).

3 EXPERIMENTAL PROGRAMME

3.1 *Overview of the tests*

The experimental programme consisted of 21 constant-temperature tests, distributed to encompass different types of channel sections subjected to tensile

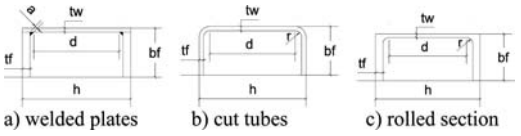

Figure 4. Reverse channel sections.

and compressive load applied transversally at the web channel. The tests were performed under constant temperatures: ambient and elevated (550°C and 750°C). The dimensions of the sections "U" were defined based on the dimensions of the structural elements (beam and column) of the joint defined in section 2.1 (Figure 1); moreover, a qualitative numerical analysis was previously carried out to evaluate the parametric variations of the dimensions of the different types of reverse channel sections, such as the length, the thicknesses of the web and flanges, and the distance between the bolts. The aim of this numerical study was to guarantee the experimental observation of: i) development of the membrane stiffness effect; ii) deformations concentrated in the loaded web and iii) no bolt failure during tests (Lopes et al. 2011). Three types of channel sections were tested: i) welded plates, ii) steel hollow section cut lengthwise, and iii) hot rolled steel channel section, as shown in Figure 4.

The welded plate section was considered to allow a variation in thickness of the web with the same width and thickness of the flanges. Channel sections cut from square tubes have the same thickness in web and flanges. The profile UPN 200 was chosen for tests with hot rolled section because it is commonly used in Portugal, allowing a comparison between the behaviour of different types of channel section and a commercially available channel section.

The welded plate sections and UPN 200 were made in the steel grade 275 while the square hollow sections for cutting lengthwise were S355. The fillet weld throat thickness was 9 mm in all welded sections. The Table 1 presents the experimental programme and dimensions of the channel sections. The first letter of identification (ID column) denotes the type of the channel sections: W for welded plates, T for cut tubes, and R for hot rolled section UPN200. The second letter, represents the applied load (T: tension and C: compression), followed by the temperature during tests. The last numbers indicate the web thickness.

3.2 *Testing procedure and setup*

The component tests were performed at the same reaction structure under ambient and elevated temperatures (Figure 5). The monotonic tensile or compressive loads were applied to the web of the specimens by a hydraulic actuator (maximum test load 1000 kN, maximum piston stroke ±150 mm). The tests were carried out under displacement control up to collapse of the specimens. In the elevated temperature tests, the specimens were heated by an electric resistance furnace until the required temperature ie reached; during this heating phase, thermal expansion of the specimens was

Table 1. Experimental programme.

Test N.	ID	h (mm)	b_f (mm)	t_w (mm)	t_f (mm)
1.	W-T20-7	202	90	7	15
2.	W-T20-10	202	90	10	15
3.	W-T20-12	202	90	12	15
4.	W-C20-7	202	90	7	15
5.	W-C20-10	202	90	10	15
6.	W-C20-12	202	90	12	15
7.	W-T550-10	202	90	10	15
8.	W-T550-12	202	90	12	15
9.	W-C550-10	202	90	10	15
10.	W-C550-12	202	90	12	15
11.	W-T750-10	202	90	10	15
12.	W-T750-12	202	90	12	15
13.	W-C750-10	202	90	10	15
14.	W-C750-12	202	90	12	15
15.	T-T20-8	200	90	8	8
16.	T-T20-10	200	90	10	10
17.	T-T20-12	200	90	12	12
18.	R-T20-8.5	200	90	8.5	11.5
19.	R-T750-8.5	200	75	8.5	11.5
20.	R-T750-8.5	200	75	8.5	11.5
21.	R-C550-8.5	200	75	8.5	11.5

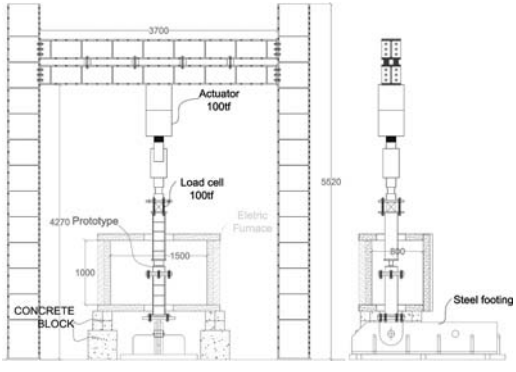

Figure 5. Schematic layout of the tests.

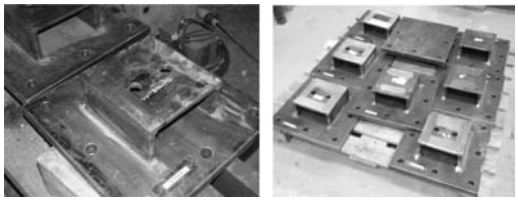

Figure 6. Example of prototypes to be tested.

allowed. After that, the monotonic loading was applied at constant temperature.

Each tested prototype was defined of a channel section welded by its flange to a steel plate with 400 mm × 400 mm × 30 mm, steel grade S355, which is bolted at the top of the support column (Figure 6).

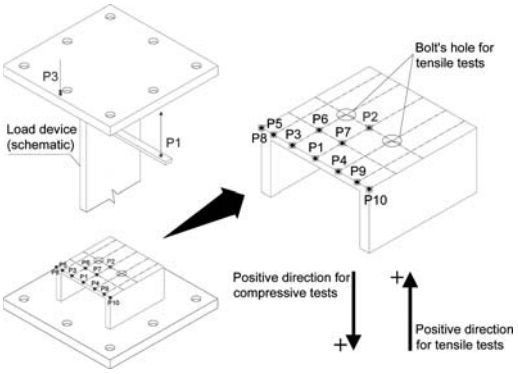

Figure 7. Measurement point: vertical displacements are measured by transducers in P1 and P3, and by photogrammetry in P2 (inside web of channel sections).

3.3 *Instrumentation*

The measurements taken from the tests should be used to describe the deformation of the specimens and the gradually increasing of applied load. Thus, the measuring instruments were placed on the test set-up to give the relevant displacement of the web channel, the temperature evolution during high temperature tests, and the load applied through the actuator. The various measurements were recorded with intervals of 5 seconds by an automatic, scanning data logger TML-TDS-530, with 30 channels. The displacements were measured by means of different types of TML displacement transducers. In some tests, vertical displacements of several points distributed on the web channel were measured with the aid of photogrammetry and image processing techniques (Figure 7). A series of thermocouples monitored the temperature evolution in the specimen at elevated temperature tests.

4 RESULTS OF THE TESTS

4.1 *Overview of the results at ambient and elevated temperatures*

Table 2 compares the experimental results with the plastic load $F_{pl,an}$, obtained from the analytical approach mentioned in section 2.2, considering the measured material and geometrical properties. Moreover, the reduction factors proposed by Eurocode 3 Part 1.2 (EN-1993-1-2, 2005) for the stress-strain relationship for steel at elevated temperatures were used at the elevated temperature calculations (550°C and 750°C).

The initial stiffness of the tensile tests was obtained from force-deformation curves with the vertical displacement measured in the centre point of the web channel by photogrametry (P2 in Figure 7). However, because during the compressive tests, P2 was not visible, the initial stiffness was calculated considering the displacement measured in the load device (P3). The plastic load (F_{pl}) was found by a bilinear approximation of the force-deformation curve (Figure 8) based on the slope of initial and post-limit stiffnesses (K_e, K_p), as proposed by Jaspart (Jaspart 1991).

The maximum applied load ($F_{max,test}$) achieved during tests is in general higher than the analytical strength ($F_{pl,an}$). It is noted that the analytical approach only considers the elastic regime and the maximum forces of the tests were measured until failure of the test specimens. However, the experimental plastic loads were lower than analytical strength in all tensile tests; on the other hand, the compressive tests at ambient temperature presented plastic load greater than analytical results, despite the geometric characteristics of the loaded area in compression does not meet the limit of validity of the analytical approach.

Table 2. Results of the tests.

Test N.	$F_{pl,an}$ (kN)	$F^1_{pl,test}$ (kN)	$F^1_{max,test}$ (kN)	$K^2_{e,test}$ (kN/mm)	Δ^3_{pl} (mm)	Δ^3_{Fmax} (mm
1.	111.5	79.2	270.1	175.6	0.5	25.6
2.	193.5	136.8	347.8	204.6	0.7	22.9
3.	270.3	236.8	502.9	276.8	0.9	27.2
4.	247.5	375.6	473.8	213.0	1.7	6.1
5.	361.6	449.7	545.9	243.0	1.9	6.1
6.	488.3	594.4	737.3	414.0	1.4	6.9
7.	117.9	64.4	155.6	19.4	3.3	43.8
8.	169.4	123.8	193.5	43.3	2.9	34.6
9.	232.8	270.0	279.1	40.1	6.7	9.9
10.	298.2	246.2	394.9	75.0	3.3	36.3
11.	31.4	21.9	40.2	9.7	2.3	42.7
12.	46.0	35.2	45.4	28.2	1.3	24.3
13.	66.0	66.9	88.8	39.8	1.7	21.5
14.	81.4	71.8	96.1	45.8	1.6	37.5
15.	159.4	122.1	279.1	181.4	0.7	30.3
16.	367.2	234.4	476.1	190.7	1.2	27.5
17.	578.8	303.2	589.1	288.7	1.1	29.5
18.	214.9	157.1	400.4	161.6	1,0	30.8
19.	137.2	113.6	134.7	32.8	3.5	12.6
20.	37.3	22.0	41.6	30.9	0.7	46.9
21.	261.9	257.2	258.5	39.4	6.5	17.0

[1] $F_{pl,test}$ and $F_{max,test}$: experimental plastic and maximum loads.
[2] $K_{e,test}$: experimental initial stiffness.
[3] Δ_{pl} and Δ_{Fmax}: vertical displacement in the $F_{pl,test}$ and $F_{max,test}$.

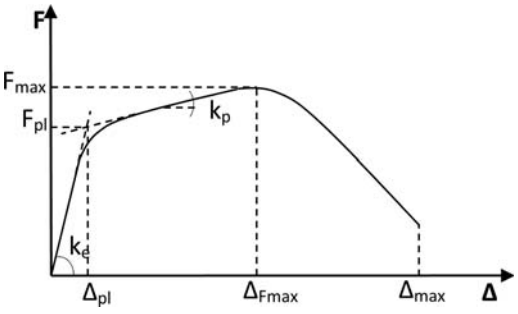

Figure 8. Force-deformation relationship.

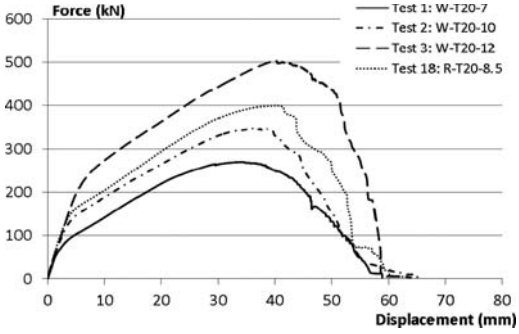

Figure 9. Tensile tests at ambient temperature: welded plates and hot rolled sections (displacement from P1, Figure 7).

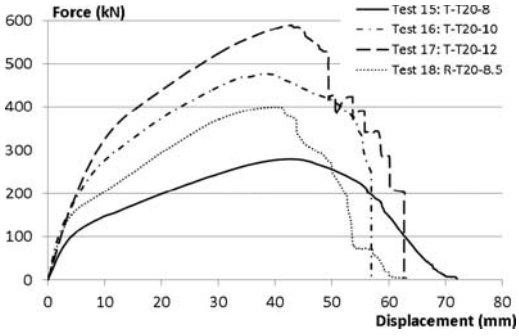

Figure 10. Tensile tests at ambient temperature: cut tube lengthwise and hot rolled sections (displacement from P1, Figure 7).

4.2 *Force-displacement curves at ambient temperature*

The reverse channel sections presented similar behaviour in the tensile tests at ambient temperature: the strength of the component increased with the increase in web thickness (Figures 9 and 10); nevertheless the hot rolled section UPN 200 showed strength higher than tests 2 (W-T20-10) and 15 (T-T20-8), even though the last one is grade S355. Both welded and cut tube sections showed similar initial stiffness increasing with the web thickness.

The thickest web thickness enhances the resistance without compromising the deformability of the sections. The welded sections presented the lowest deformation up to failure.

The ductility was quite similar in all tensile tests; the maximum vertical displacement after failure was $\Delta_{max} \approx 60$ mm in almost all tests; the exception was the test 15 (T-T20-8) which presented a maximum vertical displacement of 72 mm. The channel sections cut from square tubes showed the initial and post-limit stiffnesses and maximum applied load higher than welded and hot rolled channel sections without compromising their ductility, which was in general bigger than other sections.

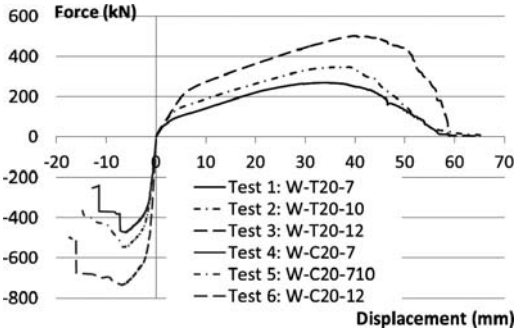

Figure 11. Tensile and compressive tests at ambient temperature: welded plate sections (displacement from P1 and P3, Figure 7).

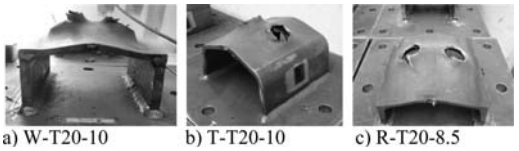

Figure 12. Deformed shape of the prototypes after tensile tests at ambient temperature.

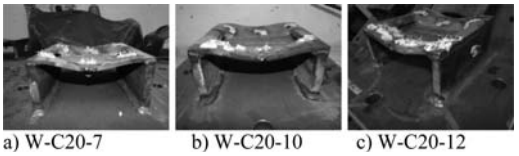

Figure 13. Deformed shape of the prototypes after compressive tests at ambient temperature.

Only the welded sections were tested in compression with different web thicknesses, varying between 7 and 12 mm. Figure 11 shows the comparison between the force-displacement response of the welded sections in tension and compression, respectively placed in the right-hand (positive) and left-hand (negative) sides of the graph.

The channel sections presented strength and initial stiffness in compression much higher than in tension; however, the maximum deformation of the prototypes in tension was approximately 300% greater than in compression.

Figures 12 and 13 present the deformed shape of some prototypes after tests. The failure modes were similar in each kind of tests: i) excessive yielding around the bolt' holes in tensile tests, but there was no failure of the bolts; ii) pushing shear on the web next to the flanges, coinciding with the end of the compressive load device in compressive tests.

4.3 *Force-displacement curves at elevated temperatures*

Figures 14 and 15 compare the tensile test results of the welded sections ($t_w = 10$ mm) and the hot rolled section UPN 200 in different test temperatures. It is noted

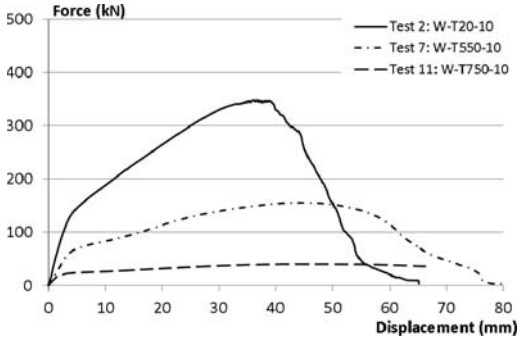

Figure 14. Comparison between the tensile tests: welded plate sections with 10 mm web thickness.

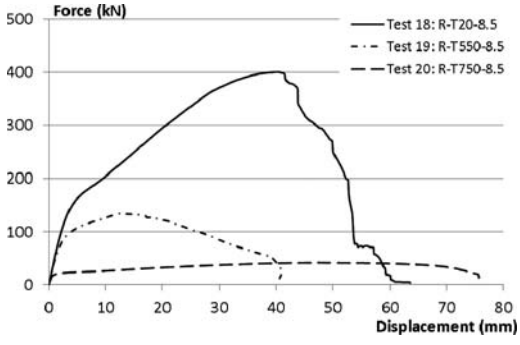

Figure 15. Comparison between the tensile tests: hot rolled sections with 8.5 mm web thickness.

that: i) the degradation of the material properties at elevated temperatures affected the strength capacity of the sections substantially; the maximum applied load at 750°C approximately corresponds to 10% of the maximum load at ambient temperature tests; ii) the reduction in the initial stiffness was about 85% at 550°C and 90% at 750°C of the initial stiffness at ambient temperature; iii) the increase of temperature enhances the deformability of the sections, however the hot rolled section showed lowest maximum deformation after failure at 550°C, $\Delta_{max} \approx 40$ mm, while the maximum displacement achieved by welded sections was bigger than 60 mm.

The results of the compressive tests of the welded sections with web thickness of 10 and 12 mm are compared in Figures 16 and 17.

The resistance of the sections drastically reduced with the increase of temperature, as previously observed in tensile tests; the maximum applied load at 750°C corresponds to about 15% of the maximum strength at ambient temperature. Moreover, a yielding plateau was developed during tensile and compressive tests at elevated temperatures which did not occur at ambient temperature tests.

The failure modes of the tests at elevated temperatures were similar to those observed at ambient temperature tests. In the tensile tests excessive yielding occurred around the holes of the bolts (Figure 18),

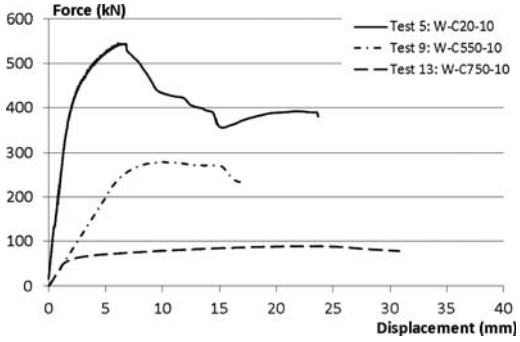

Figure 16. Comparison between the compressive tests: welded plate sections with 10 mm web thickness.

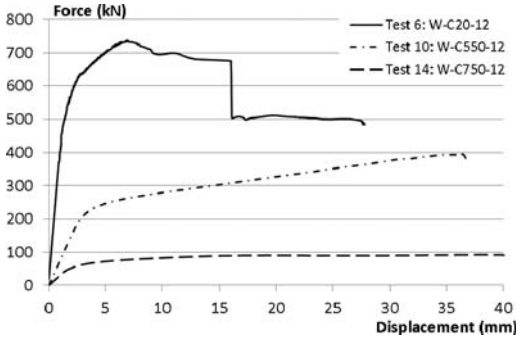

Figure 17. Comparison between the compressive tests: welded plate sections with 12 mm web thickness.

Figure 18. Deformed shape of the prototypes after tensile tests at elevated temperatures.

Figure 19. Deformed shape of the prototypes after compressive tests at elevated temperatures.

while in compressive tests the web of channel fracture by pushing shear next to the flanges (Figure 19).

5 CONCLUSIONS

This paper presented the results of a series of tensile and compressive tests on different types of reverse channel sections. The tests were performed at constant

ambient and high temperatures to evaluate the overall behaviour of the component, establishing a relationship between force, displacement and temperature and to study the influence of the parameters considered most relevant: dimensions of the loaded area and its slenderness. The results of the tests showed that:

i) the maximum applied load in the compressive tests was much higher than in tensile tests, however, the maximum deformation of the prototypes in tension was approximately 300% greater than in compression;
ii) the plastic load obtained from force-deformation curves in the elastic limit was lower than the analytical strength in all tensile tests, while the compressive tests at ambient temperature showed the experimental plastic load greater than the analytical strength;
iii) the resistance and initial stiffness of the channel sections reduced significantly with the increase of temperature caused by the degradation in the material properties;
iv) the failure of the channel sections in all tensile tests was controlled by an excessive yielding around the hole of the bolts; there was no failure of the bolts during all tests;
v) the channel sections subjected to compression load presented failure by pushing shear on the web next to the flanges, coinciding with the end of the load device;
vi) the channel sections cut from square tubes showed the initial and post-limit stiffnesses and maximum applied load higher than welded and hot rolled channel sections without compromising their ductility, which was in general bigger than other sections at ambient temperature;
vii) although the resistance capacity of the channel sections was significantly reduced with the increase of temperature, they provided good ductility at elevated temperature.

Finally, it should be pointed out that these experimental results, as part of the framework of the European RFCS COMPFIRE project, will be used to calibrate and validate numerical and analytical models for characterization of the component in fire condition.

ACKNOWLEDGMENT

The research leading to these results has received funding from the European Community's Research Fund for Coal and Steel (RFCS) under *grant agreement* n° RFSR-CT-2009-00021.

REFERENCES

Bailey, C.G., Lennon, T. & Moore, D.B. 1999. The behaviour of full-scale steel framed building subjected to compartment fires. *The Structural Engineer* 77(8): 15–21.

Ding, J. & Wang, Y.C. 2007. Experimental study of structural fire behaviour of steel beam to concrete filled tubular column assemblies with different types of joints. *Engineering Structures* 12(29): 3485–3502.

European Committee for Standardization CEN. EN 1993-1-2: 2005. Eurocode 3: Design of steel structures, Part 1.2: Structural Fire Design. Brussels.

European Committee for Standardization CEN. EN 1993-1-8: 2005. Eurocode 3: Design of steel structures, Part 1.8: Design of joints. Brussels.

European Committee for Standardization CEN. ENV 1993-1-2: 1995. Eurocode 3: Design of steel structures, Part 1.2: Structural Fire Design. Brussels.

Jaspart, J-P. 1991. Etude de la semi-rigidité des noeuds poutre-colonne et son influence sur la resistance des ossatures en acier (in French). PhD thesis, Department MSM, University of Liége, Belgium.

Jaspart, J-P. 1997. Recent advances in the field of the steel joints – Column bases and further configurations for beam-to-column joints and beam splices. Professorship thesis, Department MSM, University of Liége, Belgium.

Jaspart, J-P., Pietrapertosa, C., Weynand, K., Busse, E., and Klinkhammer, R. 2005. Development of a full consistent design approach for bolted and welded joints in building frames and trusses between steel members made of hollow and/or open sections. Application of the component method. CIDECT Research Project 5BP, Draft final report – Volume 1: Practical design guide.

Lopes, F.R.C., Rei, D.M.M., de Sousa, D.A.B., Simões, A.B.S., Santiago, A.M.C., Simões da Silva, L.A., Jordão, S.F.S., Simões, R.A.D. & da Silva, J.G.S. 2011. Avaliação do comportamento da componente de uma ligação com "U" invertido a temperaturas elevadas (in Portuguese). *VIII Congresso de Construção Metálica e Mista*, Guimarães, 24–25 November 2011.

Santiago, A., Simões da Silva, L., Vaz, G., Vila Real, P., Lopes, A.G. 2008. Experimental investigation of the behaviour of a steel sub-frame under natural fire. *Steel and Composite Structures* 8(3): 243–264.

Silva, L.A.P, Neves, L.F.N. & Gomes, F.C.T. 2003. Rotational stiffness of rectangular hollow sections composite joints. *Journal of Structural Engineering* 129(4): 487–494.

Simões da Silva, L., Santiago, A., Lopes, F., Veljkovic, M., Heistermann, T., Igbal, N., Wald, F., Jána, T., Davison, B., Burgess, I., Huang, S-S., Dong, G., Wang, Y., Mandal, P., Hu, Y., Jafarian, M., Koutlas, G. 2011. COMPFIRE: Design of composite joints for improved fire robustness, Mid-term Technical Implementation Report No. 2, Research Fund for Coal and Steel, Grant agreement n° RFSR-CT-2009-00021, European Commission, Brussels.

Simões da Silva, L., Santiago, A., Vila Real, P. 2002. Post-limit stiffness and ductility of the end-plate beam-to-column steel joints. *Computers and Structures* 80: 515–531.

Wald, F., Simões da Silva, L., Moore, D., Lennon, T., Chladná, M., Santiago, A., Beneš, M. & Borges, L. 2006. Experimental behaviour of steel strucuture under natural fire. *Fire Safety Journal* 41(7): 509-522.

Wang, Y.C. 2005. Performance of steel-concrete composite structures in fire. *Progress in Structural Engineering and Material* 7: 86–102.

Weynand, K., Jaspart, J-P., Steenhuis, M. 1995. The stiffness model of revised annex J of Eurocode 3. In R. Bjorhovde, A. Colson, R. Zandonini (eds), *Connections in steel structures III. Proceedings of the 3rd International workshop on connections*: 441–452.

Trusses and arches

Tubular Structures XIV – Gardner (Ed.)
© 2012 Taylor & Francis Group, London, ISBN 978-0-415-62137-3

Buckling analysis of steel trusses with thin-walled RHS members using Generalised Beam Theory (GBT)

C. Basaglia & D. Camotim
Department of Civil Engineering and Architecture, ICIST, Instituto Superior Técnico, Rovisco Pais, Lisboa, Portugal

ABSTRACT: This paper reports the results of an ongoing investigation on the use of Generalised Beam Theory (GBT) to assess the local and global buckling behaviour of thin-walled trusses with cold-formed steel Rectangular Hollow Section (RHS) members. After a brief overview of the main concepts and procedures involved in performing a GBT buckling analysis, the formulation and implementation of a GBT-based beam finite element are presented. Next, the constraint conditions adopted to simulate the local displacement compatibility at truss pinned-joints connecting non-aligned RHS and plain channel members are addressed. In order to illustrate the application, provide validation and show the capabilities of the proposed approach, numerical results concerning the local and global buckling behaviour of trusses formed by a combination of RHS and plain channel members with bolted joints are presented and discussed. These results are compared with values obtained from shell finite element analyses carried out in the code Ansys.

1 INTRODUCTION

The extensive use of cold-formed steel Rectangular Hollow Section (RHS) profiles in thin-walled steel trusses has been growing steadily and at a fast rising pace. However, since these trusses normally consist of several slender structural members, joined together through bolted connections, which are highly susceptible to local and global buckling phenomena, the assessment of their structural response constitutes a fairly complex task (*e.g.*, Wilkinson 1999). Indeed, in the context of numerical structural analysis, this task can only be rigorously carried out by resorting to complex shell finite element analysis, a computer-intensive approach that is both (i) very time-consuming (including data input and result interpretation) and (ii) prohibitive for routine applications at present (*e.g.*, Moazed *et al.* 2009).

In order to make the accurate analysis of cold-formed steel trusses with RHS members computationally simpler and more accessible to designers, it is necessary to develop easy-to-use numerical tools based on *beam* finite element formulations that (i) include local buckling effects and (ii) are able to handle the wall bending compatibility at the truss joints connecting non-aligned members. A very promising approach is Generalised Beam Theory (GBT), a thin-walled prismatic bar theory that incorporates genuine plate theory concepts, *i.e.*, accounts for the member cross-section in-plane and out-of-plane deformations (Camotim *et al.* 2010a,b). Moreover, its unique *modal* nature makes it possible to obtain very elegant and illuminating solutions for a wealth of structural problems. In particular, the authors have recently developed and numerically implemented GBT-based beam finite element models capable of analysing the local, distortional and global buckling behaviour of slender steel trusses built from thin-walled members exhibiting *open cross-sections* (Basaglia and Camotim 2011). Moreover, it is worth noting that GBT has already been successfully applied to assess the local and global buckling behaviour of RHS isolated members and simple frames with welded joints (Gonçalves *et al.* 2009, Basaglia and Camotim 2010) – however, no structural system with pinned joints was ever addressed.

The objective of this work is to report the current state of an ongoing investigation aimed at extending the scope of the above GBT-based approach, making it possible to analyse also the local and global buckling behaviour of cold-formed steel pinned-joint trusses with RHS members. Particular attention is paid to the determination of the finite element and overall (truss) stiffness matrices, incorporating the influence of the pinned joints. In addition, the *constraint conditions* simulating the heel plates and bolts, which appear in joints connecting plain channel and RHS members, are addressed in detail. The numerical results presented and discussed concern the local and global buckling behaviour of simple plane trusses formed by a combination of RHS (diagonals) and open cross-section (channel chords) members connected by bolted joints. For validation purposes, most GBT-based results are compared with values yielded by rigorous shell finite

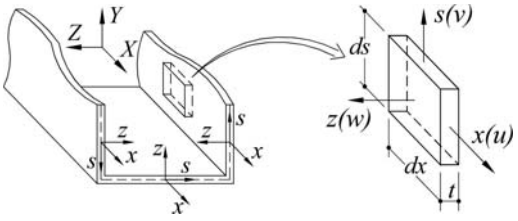

Figure 1. Arbitrary thin-walled open cross-section, coordinate axes and displacements.

element analyses performed in the code ANSYS (SAS 2009).

2 GBT BUCKLING ANALYSIS FOR TRUSSES

In a GBT formulation, the cross-section displacement field is expressed as a combination of deformation modes, leading to a very convenient and most unique form of writing the member equilibrium equations – this is achieved by performing a *cross-section analysis* (Gonçalves *et al.* 2010 and Silva *et al.* 2008), which allows for a much more in-depth understanding of the member structural behaviour.

Fig. 1 depicts a prismatic member with an arbitrary cross-section, together with the corresponding global (X, Y, Z) and local (x, s, z) coordinate systems – u, v, w are the displacement components related to the latter. In order to obtain a displacement field representation that is compatible with the classical beam theories, one must express the components $u(x,s)$, $v(x,s)$ and $w(x,s)$ as

$$\begin{aligned} u(x,s) &= u_k(s)\phi_{k,x}(x) \\ v(x,s) &= v_k(s)\phi_k(x) \\ w(x,s) &= w_k(s)\phi_k(x) \end{aligned} \quad (1)$$

where (i) subscript k follows the summation convention, (ii) a comma indicates a derivative, (iii) $u_k(s)$, $v_k(s)$ and $w_k(s)$ are "cross-section deformation mode components" and (iv) functions $\phi_k(x)$ provide the longitudinal variation of the corresponding modal amplitudes.

Fig. 2 provides the dimensions and shows the GBT discretisations of the RHS and plain channel cross-sections dealt within this work – all truss members have elastic constants *E=205 GPa* (Young's modulus) and $\upsilon = 0.3$ (Poisson's ratio). For these discretisations, the cross-section analyses lead to (i) 16 conventional (3 global, 1 distortional and 12 local) and (ii) 1 cell shear flow (torsion), for RHS, and to (i) 12 conventional (4 global and 8 local) modes, for the plain channel. Note that the torsion mode is not "conventional" in closed-cell cross-sections, since it does not comply with Vlasov's assumption $(u_{,s} + v_{,x} \neq 0)$ – Bredt's membrane shear strains are handled separately. Figs 3 and 4 depict the main features of the deformation modes that are more relevant for the analyses carried out throughout the paper.

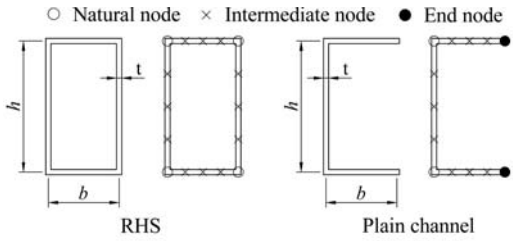

Designation	h (*mm*)	b (*mm*)	t (*mm*)
RHS-80×45×3.0	80	45	3.0
RHS-80×45×1.5	80	45	1.5
RHS-45×35×1.5	45	35	1.5
U-100×50×4.5	100	50	4.5

Figure 2. Plain channel and RHS dimensions and GBT discretisations.

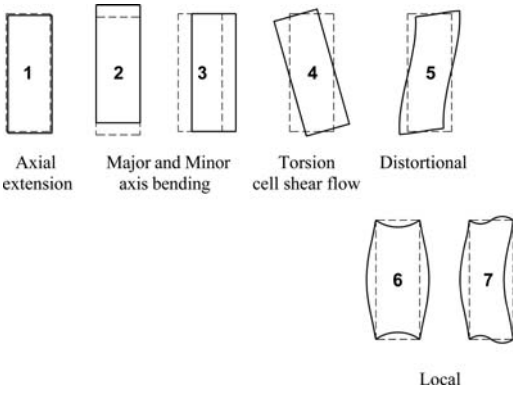

Figure 3. Main features of the most relevant RHS deformation modes.

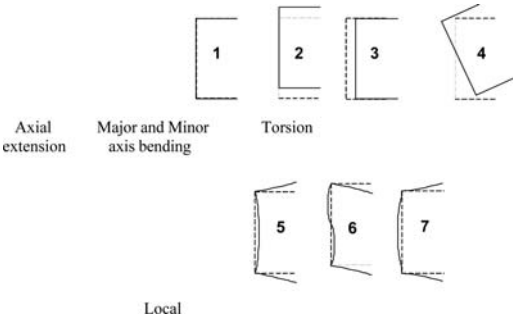

Figure 4. Main features of the most relevant plain channel deformation modes.

After knowing the deformation modes, one readily establishes the member buckling eigenvalue problem, defined by the equilibrium equation system

$$\begin{aligned} &C_{ik}\phi_{k,xxxx} - D_{ik}\phi_{k,xx} + B_{ik}\phi_k - \\ &-\lambda\left[X^{\sigma}_{jik}\left(W^0_j\phi_{k,x}\right)_{,x} - X^{\tau}_{jki}\left(W^0_{j,x}\phi_k\right)_{,x} + W^0_{j,x}X^{\tau}_{jik}\phi_{k,x}\right] = 0 \end{aligned} \quad (2)$$

where (i) λ is the load parameter, (ii) C_{ik} (warping displacement), D_{ik} (torsional rotations) and B_{ik} (local deformations – wall bending) are cross-section modal mechanical properties and (iii) X^{σ}_{jik} and X^{τ}_{jik} stand for geometric stiffness components associated with normal stress resultants W^{0}_{j} and pre-buckling shear stresses due to the non-uniform applied bending and torsion moment diagrams – all are defined in Bebiano *et al.* (2007).

2.1 *GBT-based beam finite element formulation*

In arbitrarily loaded isolated members, the solution of (2) may be obtained by means of the beam finite element formulation developed/implemented by Bebiano *et al.* (2007): 2-node elements (i) with $2n$ degrees of freedom (d.o.f.) per node (n is the number of deformation modes included in the analysis) and (ii) adopting Hermite cubic polynomials $\psi_i(x)$ to approximate the mode amplitude functions $\phi_k(x)$ – one then has

$$\phi_k(x)=\psi_1(\xi)Q_{k1}+\psi_2(\xi)Q_{k2}+ +\psi_3(\xi)Q_{k3}+\psi_4(\xi)Q_{k4} \tag{3}$$

where $Q_{k1}=\phi_{k,x}(0)$, $Q_{k2}=\phi_k(0)$, $Q_{k3}=\phi_{k,x}(L_e)$, $Q_{k4}=\phi_k(L_e)$, $\xi=x/L_e$ (L_e is the element length) and

$$\begin{aligned}\psi_1(\xi)&=L_e(\xi^3-2\xi^2+\xi)\\ \psi_2(\xi)&=2\xi^3-3\xi^2+1\\ \psi_3(\xi)&=L_e(\xi^3-\xi^2)\\ \psi_4(\xi)&=3\xi^2-2\xi^3\end{aligned} \tag{4}$$

The overall linear and geometric stiffness matrices of a truss (structural system) are obtained by assembling their finite element counterparts, a trivial procedure in isolated members (all nodes are shared by two equally oriented elements), but whose extension to trusses (or frames) poses several difficulties. Because the finite elements (members) connected at a truss joint exhibit (i) different orientations and (ii) modal d.o.f. referred to distinct coordinate systems (see Fig. 5(a)), it becomes necessary to account for all the aspects associated with ensuring the compatibility between the connected end section d.o.f. (*e.g.*, nodes a_{r+1} and b_r in Fig. 5(b)). In order to perform this task, one must (i) "transform" these modal d.o.f. into *nodal* ones (generalised displacements referred to axes $\tilde{X}-\tilde{Y}-\tilde{Z}$), at the point where the joint is deemed materialised (*e.g.*, the connecting bolt in Fig. 5(c)). This is achieved through a *joint element* concept (Basaglia *et al.* 2008) and by imposing *joint compatibility conditions*, which enforce compatibility on the transverse bending displacements of the connected end section walls (see fig. 5(c)).

To guarantee displacement compatibility at the "joint element", one uses the truss transformation matrix $[T]$, which provides the relation between the

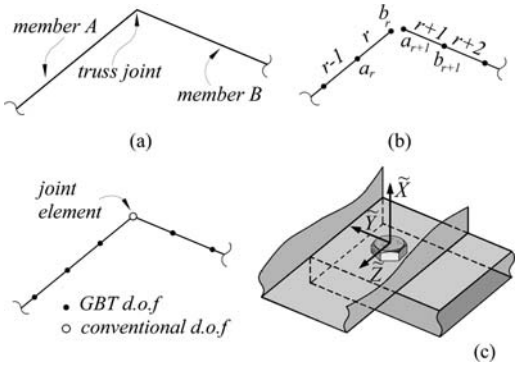

Figure 5. (a) joint element" concept, (b) longitudinal discretisation of the connected members and (c) truss joint view.

GBT (member) and nodal (joint) degrees of freedom and is defined by the expression

$$\{\tilde{\xi}\}=[T]\{d\}\Leftrightarrow\begin{Bmatrix}\{\tilde{\xi}_G\}\\ \{\tilde{\xi}_D\}\\ \{\tilde{\xi}_L\}\end{Bmatrix}=\begin{bmatrix}[R][L]_{6x6} & \\ & [I]_{qxq}\end{bmatrix}\begin{Bmatrix}\{d_G\}\\ \{d_D\}\\ \{d_L\}\end{Bmatrix} \tag{5}$$

where (i) the components of sub-vectors $\{\tilde{\xi}_G\}$, $\{\tilde{\xi}_D\}$and $\{\tilde{\xi}_L\}$ concern the global, distortional and local (nodal) generalised displacements, (ii) sub-vectors $\{d_G\}$, $\{d_D\}$ and $\{d_L\}$ contain the GBT degrees of freedom, (iii) $[R]$ corresponds to a set of rotation matrices relating the element/member end node and joint element coordinate systems, (iv) $[L]$ is a translation matrix referring the connected element/member end section generalised displacements to parallel reference axes passing through of a point where the joint is deemed "materialised", and (v) $[I]$ is the identity matrix associated with the wall flexural and membrane transverse displacements, due to the local and distortional modes – its dimension never exceeds $q=2n+1$, where n is the total number of local and distortional modes included in the analysis (the matrix [R] and [L] components are provided explicitly in the work of Basaglia *et al.* 2008).

Using the transformation matrix given in (5) entails the definition, at each joint member end section, of (i) 7 global mode degrees of freedom and (ii) $q-1$ degrees of freedom associated with the remaining modes – they must satisfy the conditions

$$\{\tilde{\xi}\}_{b_r}=\begin{bmatrix}[J]_{7\times7} & \\ & \Pi\end{bmatrix}\{\tilde{\xi}\}_{a_{r+1}} \tag{6}$$

where (i) subscripts b and a identify the end sections of the connected members r and $r+1$ (see fig. 5(b)), (ii) $[J]$ is a diagonal matrix whose components J_{ii} relate the generalised global displacements and rotations of each end section and (iii) Π are *constraint conditions* ensuring compatibility between the transverse (flexural and/or membrane) displacements, associated with the local and distortional deformation modes.

The *constraint conditions* Π (i) are dependent on the member cross-section shape and joint configuration, and (ii) involve i natural/intermediate nodes belonging to the connected member end sections – the corresponding conditions read

$$\Pi_i = \{\Delta\}^T \{\phi_k\} = 0 \tag{7}$$

where the components of vector $\{\Delta\}$ are wall flexural functions $w_k(s)$. The specific constraint conditions considered in this work are addressed in the next section.

Once all the member support and joint compatibility conditions are enforced, the truss linear ($[\widetilde{K}]$) and geometric ($[\widetilde{G}]$) stiffness matrices are readily expressed in terms of "*mixed*" (GBT modal and "conventional" nodal) degrees of freedom. The joint compatibility is incorporated into the stiffness matrix through

$$\left([\widetilde{K}] + \lambda [\widetilde{G}]\right) = [\Omega]^T \left([K] + \lambda [G]\right) [\Omega] \tag{8}$$

where (i) λ is the truss *load parameter*, (ii) the tilde (~) identifies the stiffness matrices already including the joint compatibility conditions and (iii) the compatibility matrix [Ω], given by

$$\{d\} = [\Omega] \{\widetilde{d}\} \tag{9}$$

contains the joint modal displacement values (*i.e.*, $u_k(s)$, $v_k(s)$ or $w_k(s)$) – $\{\widetilde{d}\}$ is a "mixed" vector).

Once the truss total stiffness matrix ($[\widetilde{K}] + \lambda[\widetilde{G}]$) is known, one (i) solves the buckling eigenvalue problem and (ii) transforms the nodal d.o.f. back into GBT ones, through the operation defined in (9). Then, a *fully modal* representation of the truss buckling modes is obtained, making it possible to identify and quantify the individual member deformation mode participations – this feature provides a decisive contribution towards a more in-depth understanding of the mechanics of truss buckling.

At this stage, it is worth noting that the well-known *Lagrange multiplier* technique (*e.g.*, Zienkiewicz and Taylor 2000) provides an elegant and efficient alternative to incorporate the aforementioned constraint conditions into the truss buckling analysis (Basaglia and Camotim 2011) – one is then led to the eigenvalue problem

$$\begin{bmatrix} [K+\lambda G] & \{\Delta\}_1 & \cdots & \{\Delta\}_i \\ \hline \{\Delta\}_1^T & & & \\ \vdots & & 0 & \\ \{\Delta\}_i^T & & & \end{bmatrix} \begin{Bmatrix} \{d\} \\ \hline \gamma_1 \\ \vdots \\ \gamma_i \end{Bmatrix} = \begin{Bmatrix} 0 \\ \hline \Pi_1 \\ \vdots \\ \Pi_i \end{Bmatrix} \tag{10}$$

where γ_i is the Lagrange multiplier associated with the constraint condition i.

2.2 *Constraint conditions for bolted joints that connects RHS and plain channel members*

Consider the truss joint depicted in Fig. 6(a), connecting an RHS member to a plain channel member by means of one bolt located at the flange points P and P' (see Fig. 6(b)). To ensure displacement compatibility in this joint configuration, (i) a "joint element" is placed at the bolt mid-height and (ii) constraints Π_P and $\Pi_{P'}$ are enforced – they concern the equality between the transverse bending displacements at the bolted region, involve the mid-surface points P_A, P_B, P'_A, P'_B and read

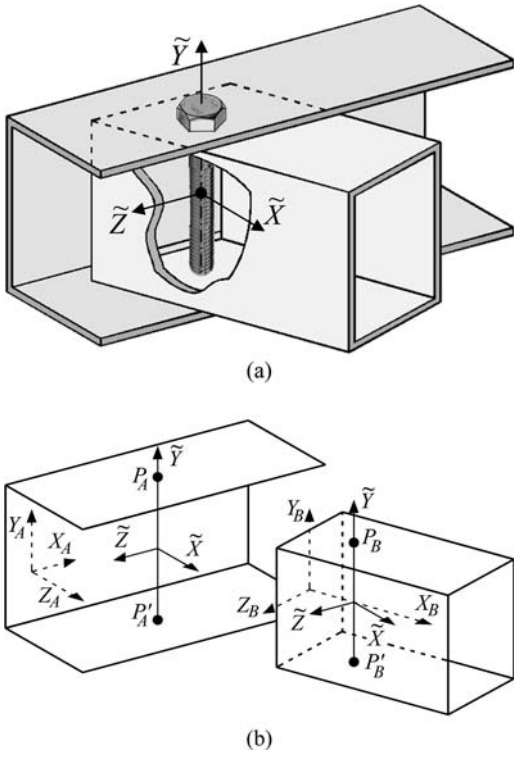

Figure 6. (a) Truss bolted joint connecting RHS and plain channel members and (b) nodes where the joint is deemed materialised.

$$\Pi_P = \sum_{k=5}^{n} w_k(p_A)\phi_k(x_{P_A}) - \sum_{k=5}^{n} w_k(p_B)\phi_k(x_{P_B}) = 0$$

$$\Pi_{P'} = \sum_{k=5}^{n} w_k(p'_A)\phi_k(x_{P'_A}) - \sum_{k=5}^{n} w_k(p'_B)\phi_k(x_{P'_B}) = 0 \tag{11}$$

It is worth noting one limitation of this approach: the developed constraint conditions do not take into account the effects stemming from the surface contact between the connected flanges.

3 ILLUSTRATIVE EXAMPLES

To illustrate the application and capabilities of the proposed GBT-based beam finite element approach, numerical results concerning the local and global buckling behaviour of plane trusses with the geometry and the dimensions depicted in Fig. 7 are presented

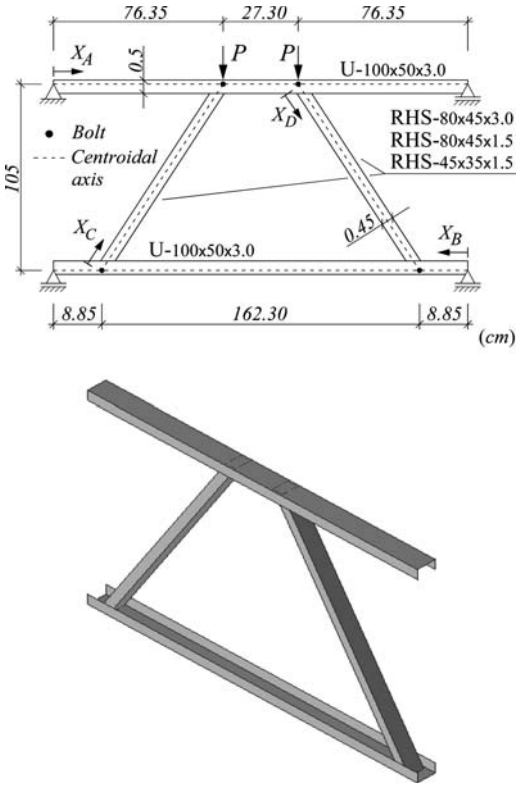

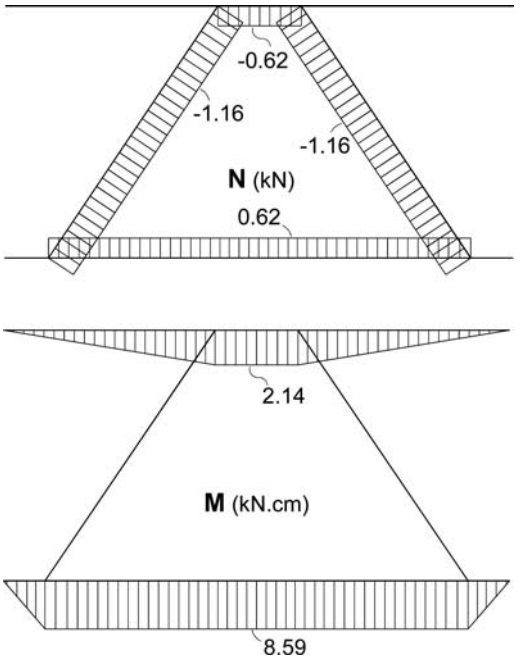

Figure 8. Axial force and minor-axis bending moment diagrams acting on the trusses.

Figure 7. Plane truss geometry and loading (not on scale), and three-dimensional view.

and discussed next. The trusses are (i) formed by two plain channel chords and two RHS diagonals and (ii) acted by two equal vertical loads P applied at the upper chord-diagonal joints. In these joints, the diagonals are connected to the chords through bolts, located at their end section centroids, which are then able to rotate freely about the common bolt axis – see Fig. 6(a). The chords exhibit locally and globally pinned end supports and the end section are free to warp. While the truss chords have U-100×50×4.5 cross-sections, three distinct RHS diagonal dimensions are considered: RHS-80×45×3.0 (truss A), RHS-80×45×1.5 (truss B) and RHS-45×35×1.5 (truss C) – dimensions given in Fig. 2. These member dimensions were selected to enable showing that the GBT analysis is able to capture accurately both local and global buckling phenomena. Except the diagonal RHS-45×35×1.5, all the other members experience in-plane minor-axis bending.

For validation purposes, most GBT-based results are compared with values yielded by ANSYS shell finite element analyses. The truss members are discretised into fine SHELL181 element meshes (ANSYS nomenclature) and the pinned bolted joints are modelled by coupling the flange node translational degrees of freedom that are associated with the bolt axis.

Fig. 8 shows the axial force and minor-axis bending moment diagrams acting on the plane trusses for loads equal to $P = 1.0$ kN. They were obtained by means of GBT first-order analyses and are incorporated into the equilibrium equation system (2), whose solution provides the truss buckling behaviour. Note that the maximum compressive axial force and minor-axis bending moment occur in the diagonals and in the lower chord, respectively.

Figs. 9 to 11 show two representations of the critical buckling modes of trusses A (with diagonals RHS-80×45×3.0), B (with diagonals RHS-80×45×1.5) and C (with diagonals RHS-45×35×1.5), namely (i) 3D views yielded by ANSYS shell finite element analysis and (ii) GBT-based modal amplitude functions $\phi(x)$ concerning the member triggering the truss critical instability (*i.e.*, the "most buckled" ones). It is worth mentioning that the GBT analyses (i) include 10 deformation modes (the in-plane shapes of 7 of them are depicted in Figs. 3 and 4) and (ii) are based on truss longitudinal discretisations into 88 finite elements (10 in the upper chord, 26 in the lower chord and 26 in each diagonal), which amounts to a total of 1800 degrees of freedom. On the other hand, the ANSYS shell finite element model involves more than 59000 degrees of freedom. Although no special effort was made to minimise the ANSYS d.o.f numbers, they are once more orders of magnitude apart from those required to perform the similarly accurate GBT analyses – which, in addition, provide very clear in-depth insight on the truss buckling mechanics. The careful observation of the critical buckling loads and mode shapes provided by the GBT and ANSYS analyses, as well as

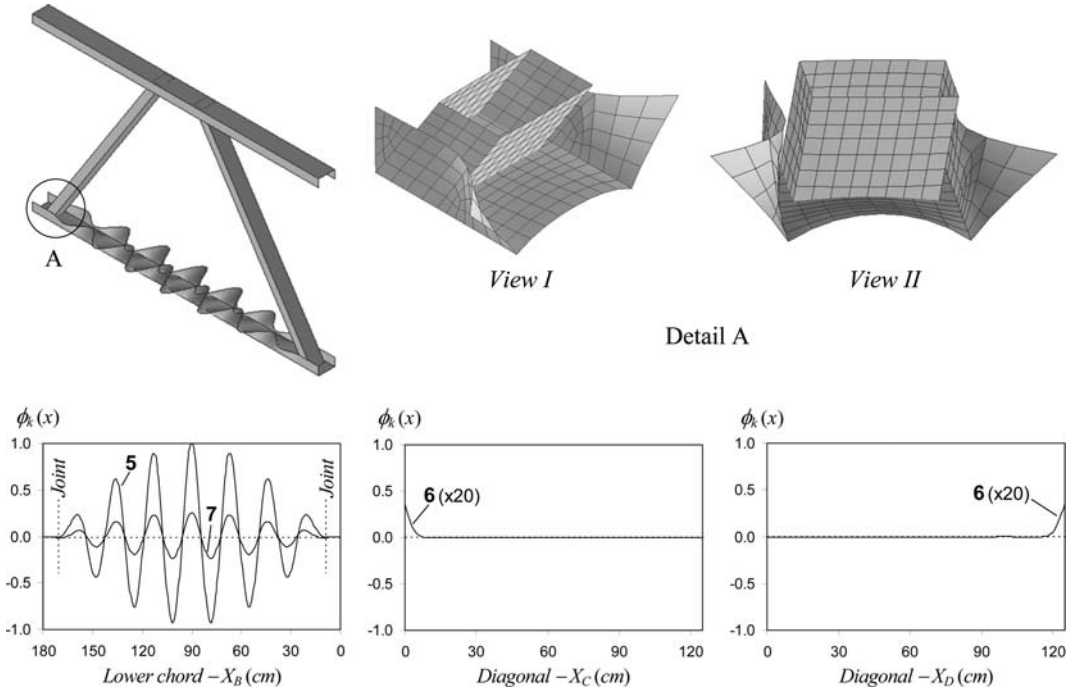

Figure 9. Truss A: GBT and ANSYS critical buckling mode representations.

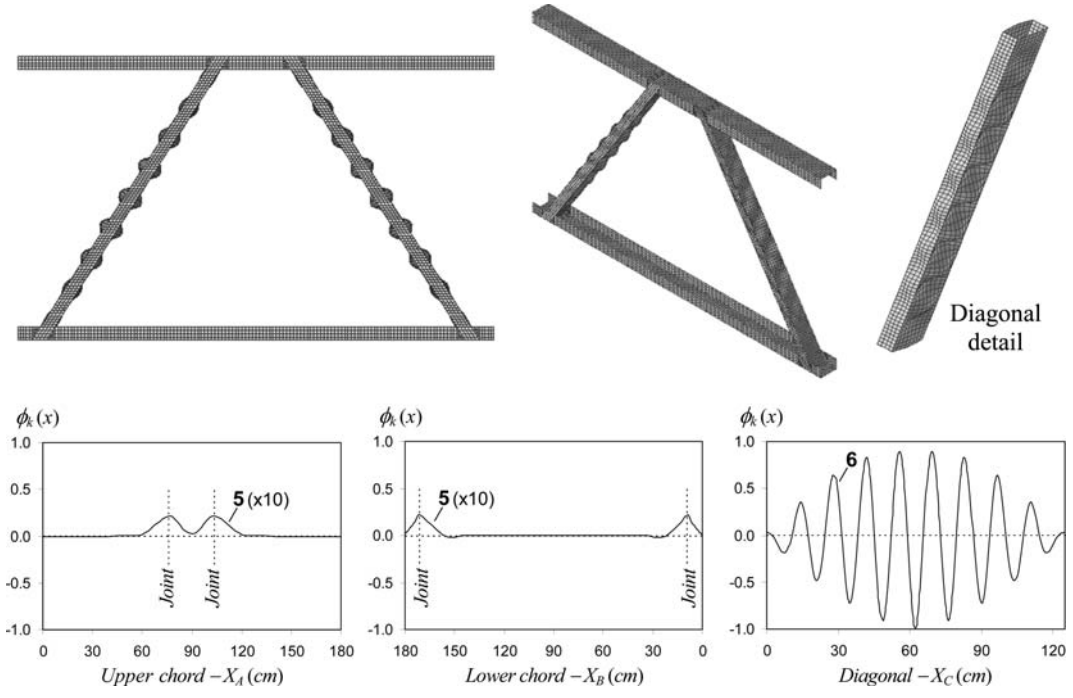

Figure 10. Truss B: GBT and ANSYS critical buckling mode representations.

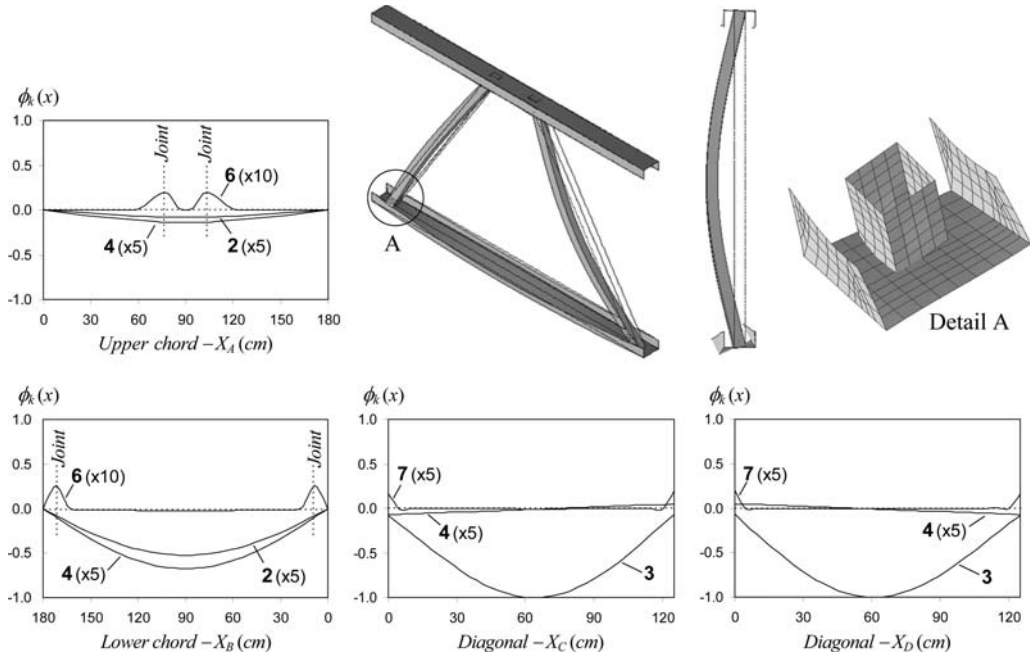

Figure 11. Truss C: GBT and ANSYS critical buckling mode representations.

the comparison between them, prompts the following remarks:

(i) First, there is an excellent agreement between the three critical load value pairs. Indeed, one has (i_1) $P_{cr.GBT} = 80.53$ *kN* and $P_{cr.ANSYS} = 77.70$ *kN* (*3.6%* difference), for truss A, (i_2) $P_{cr.GBT} = 158.36$ *kN* and $P_{cr.ANSYS} = 155.44$ *kN* (*1.9 %* difference), for truss B, and (i_3) $P_{cr.GBT} = 115.32$ *kN* and $P_{cr.ANSYS} = 112.54$ *kN* (*2.5%* difference), for truss C.

(ii) There is also a rather close agreement between the ANSYS buckling mode shapes and the GBT modal amplitude functions. Note, however, that the latter representations provide more in-depth insight on the truss buckling mechanics – for instance, the amount and nature of the local deformation involved in the buckled joint region can be readily assessed by just glancing at the GBT modal amplitude functions.

(iii) While only symmetric local deformation modes (**5** and **7**in the plain channel chairs and **6** in the RHS diagonals) have visible contributions to the buckling mode of trusses A and B, the buckling mode of truss C involves both global (major-axis flexure and torsion – **2** and **4**) and anti-symmetric local (**6** and **7** in the plain channel chords and RHS diagonals, respectively) deformation modes.

(iv) In truss A, which has RHS diagonals with thicker walls, instability is triggered by the local buckling of the lower chord span comprised between the two diagonals, which is under high sagging moments. Because only the flange tips are under compression, buckling involves mainly the flanges and barely occurs in the web. This fact is clearly reflected by the various GBT modal amplitude functions, as the contributions from the symmetric modes **5** and **7** to the buckling mode (iv_1) oppose each other in the web and (iv_1) reinforce each other in the flanges – see Figs. 4 and 9.

(v) In truss B, which has RHS diagonals with thinner walls, instability is triggered by the local buckling (mode **6**) of the two compressed diagonals, each exhibiting 17 half-waves. Moreover, the chords play virtually no role in the buckling mechanics – indeed, their deformed buckled configurations are restricted to the close vicinity of the joints.

(vi) The critical buckling of truss C occurs in a mode that combines predominant contribution from minor-axis bending (mode **3**) in the diagonals and from major-axis flexure and torsion (modes **2** and **4**) in the chords. There are also small contributions from the local modes in the vicinity of the joints.

4 CONCLUSION

This work reported the available results of an ongoing investigation on the use GBT to assess the local and global buckling behaviour of thin-walled steel pinned-joint trusses with RHS members. After briefly outlining the key concepts and main procedures involved in the performance of a GBT buckling analysis, the paper (i) addressed the formulation and implementation of

a GBT-based beam finite element intended for truss buckling analysis and (ii) devoted particular attention to establishing the constraint conditions that simulate the displacement compatibility at bolted joints connecting plain channel and RHS members (those were the only ones considered up to now). Finally, to illustrate the application and capabilities of the proposed GBT-based approach, numerical results were presented and discussed in detail. They concerned simple plane trusses formed by two pairs of plain channel chords and RHS diagonals with bolted joints, whose dimensions were carefully selected to ensure instabilities triggered by both member local and global buckling. For validation purposes, the GBT-based critical buckling loads and mode shapes were compared with values obtained from shell finite element analyses carried out in ANSYS – a virtually perfect agreement was found in all cases.

Future developments of this work include extending the proposed GBT-based approach, so that it is capable of handling a wider variety of trusses. In particular, it is intended to cover (i) truss members having only tubular sections and (ii) other joint configurations, namely those connecting more than two members, and (iii) more complex trusses, such as plane trusses formed by larger numbers of members or space trusses.

ACKNOWLEDGEMENTS

The financial support provided by *Fundação para a Ciência e Tecnologia* (FCT – Portugal), through project PTDC/ECM/108146/2008 ("Generalised Beam Theory (GBT) – Development, Application and Dissemination"), is gratefully acknowledged. The first author also thanks FCT for the financial support through the postdoctoral scholarship SFRH/BPD/62904/2009.

REFERENCES

Bebiano C., Silvestre N., Camotim D. 20007. GBT Formulation to Analyze the Buckling Behavior of Thin-Walled Members Subjected to Non-Uniform Bending, *International Journal Structural Stability and Dynamics*, 7(1): 23–54.

Basaglia C. 2010. *Non-Linear Analysis of Thin-Walled Steel Members and Frames Using Generalised Beam Theory*, Ph.D. Thesis in Civil Engineering, Technical University of Lisbon. (Portuguese)

Basaglia C., Camotim D. 2010. Buckling analysis of cold-formed RHS frames using generalised beam theory, *Proceeding of 13th International Symposium on Tubular Structures* (ISTS-13) B. Young (ed.), Hong Kong: 187–195.

Basaglia C., Camotim D. 2011. GBT-based buckling analysis of cold-formed steel trusses, *Proceeding of 6th International Conference on Thin-Walled Structures* (ICTWS 2011) D. Dubina and V. Ungureanu (eds.), Timisoara: 149-156.

Basaglia C., Camotim D., Silvestre N. 2008. Global buckling analysis of plane and space thin-walled frames in the context of GBT, *Thin-Walled Structures* 46(1): 79–101.

Camotim D., Basaglia C., Bebiano R., Gonçalves R., Silvestre N., 2010a. Latest developments in the GBT analysis of thin-walled steel structures, *Proceedings of International Colloquium on Stability and Ductility of Steel Structures* (SDSS'Rio 2010), E. Batista, P. Vellasco, L. Lima (eds.), Rio de Janeiro: 33–58.

Camotim D., Basaglia C., Silva N.F., Silvestre N., 2010b. Numerical analysis of thin-walled structures using generalised beam theory (GBT): recent and future developments, *Computational Technology Reviews*, B.H.V. Topping *et al.* (eds.), Saxe-Coburg Publications, Stirlingshire: Vol. 1, 315–354.

Gonçalves R., Dinis P.B., Camotim D. 2009. GBT formulation to analyse the first-order and buckling behaviour of thin-walled members with arbitrary cross-section, *Thin-Walled Structures* 47(5): 583–600.

Gonçalves R., Ritto-Corrêa M., Camotim D. 2010. A new approach to the calculation of cross-section deformation modes in the framework of generalized beam theory, *Computational Mechanics*, 46(5): 759–781

Moazed R., Szyszkowski W., Fotouhi R. 2009. The in-plane behaviour and FE modeling of a T-joint connection of thin-walled square tubes, *Thin-Walled Structures*, 47(6–7): 816–825.

Silva N.F., Camotim D., Silvestre N. 2008. GBT cross-section analysis of thin-walled members with arbitrary cross-sections: a novel approach, *Proceeding of 5th International Conference on Thin-Walled Structures*, M. Mahendran (ed.), Brisbane: 1161–71.

Swanson Analysis Systems (SAS) 2009. *AnsysReference Manual* (version 12).

Wilkinson T. 1999. *The Plastic Behaviour of Cold-Formed Steel Rectangular Hollow Sections*, Ph.D. Thesis, School of Civil Engineering, The University of Sydney, Australia.

Zienkiewicz O.C., Taylor R.L. 2000. *The Finite Element Method* (5th edition). Oxford: Butterworth-Heinemann.

Tubular Structures XIV – Gardner (Ed.)
© 2012 Taylor & Francis Group, London, ISBN 978-0-415-62137-3

Analytical modelling of mode jumping in the buckling of prestressed stayed columns

M. Ahmer Wadee, T. A. Hunt & L. Gardner
Department of Civil & Environmental Engineering, Imperial College London, London, UK

ABSTRACT: Prestressed stayed columns, typically comprising tubular cross-sections, offer an innovative solution where designs demand long and slender elements under compression. The cross-arms and pretensioned cables provide additional and significant lateral support to the columns that results in a marked increase of the buckling capacity. Recent finite element analysis has indicated that these structural components are likely to exhibit interactive buckling phenomena, particularly if the critical buckling mode is antisymmetric, leading to highly unstable responses. A simplified model, comprising discrete rigid-links and springs, is presented that is designed to mimic the post-buckling response of a prestressed stayed column. The results from the present model reveal similar behaviour to that observed in the earlier finite element study when certain combinations of spring stiffnesses are used. A sequence of bifurcations are found that switch the post-buckling response from one mode to another via a path of mixed modes and the effects of the sudden slackening of the cable stays is discussed.

1 INTRODUCTION

Prestressed stayed columns, as represented in Figure 1, are structural components that comprise a main column element, which is usually of tubular cross-section, a cross-arm system of elements and pre-tensioned cable stays that provide significant extra compressive strength without a commensurate increase in self-weight (Belenya, 1977; Hafez *et al.*, 1979; De Araujo *et al.*, 2008; Saito & Wadee, 2008). They are increasingly being used in the construction sector because of that advantage and because they have an aesthetic quality that is architecturally attractive (Figure 2). However, precisely because these components are structurally efficient they have also been

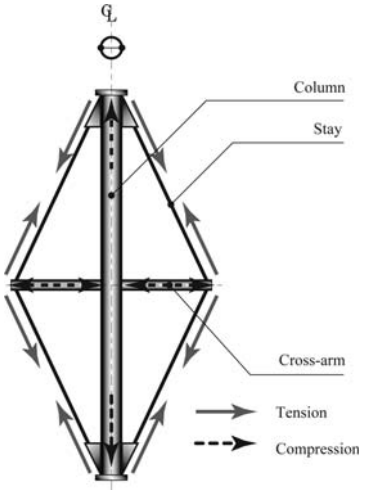

Figure 1. Prestressed stayed column.

Figure 2. Prestressed stayed tubular column in the Chiswick Park development in West London, UK.

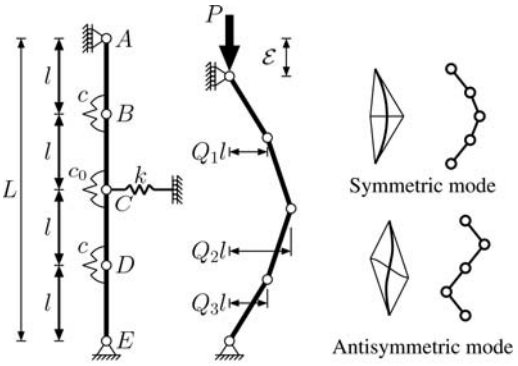

Figure 3. (a) Model with rigid links and springs; (b) continuous and discrete eigenmodes.

shown to be sensitive to initial imperfections in their geometry (Saito & Wadee, 2009a). In particular, this sensitivity has been demonstrated in a recent finite element study, which used different initial imperfection profiles of equivalent magnitudes to determine the weakest equilibrium response (Saito & Wadee, 2009b). However, by its very nature, the previous study could not reveal the bifurcational structure of the equilibrium response. The aim of the current work is to present the results from a simplified model comprising rigid links and springs, see Figure 3(a), which mimics the response and reveals the governing physical parameters that drive the behaviour. It is found, as in Saito & Wadee (2009b), that interactive buckling, which is triggered at a secondary bifurcation, is not an issue until the antisymmetric mode of buckling, see Figure 3(b), becomes the eigenmode with the lowest critical load when the strut is restrained at midspan by a translational spring of sufficient stiffness.

2 MODEL DEVELOPMENT

The prestressed stayed column has distinctive features. In its most common form it has a main column element of length L, a single cross-arm of length a and cable stays that link the top and the bottom of the main column to the ends of the cross-arm, as shown in Figure 1. The cable stays, when pre-tensioned, provide the resisting horizontal components of force that restrain the potential buckling displacement at midspan. Since the cross-arm is rigidly connected to the column, the local bending stiffness is increased somewhat. These features of restraints and identifiable increases in stiffness lend themselves to a model comprising rigid links and linear elastic springs for the strut, as shown in Figure 3(a). The advantage of this being that the total potential energy for the system V can be written in an exact form and power series approximations allow numerical solutions of the equilibrium equations. These solutions can be obtained by AUTO (Doedel & Oldeman, 2009), a powerful numerical continuation package which can compute locations of bifurcation points and separate solution branches. A three degree-of-freedom model is formulated comprising 4 rigid links each of length l, rotational springs at pins B and D of stiffness c with a further rotational spring at pin C of stiffness c_0 alongside a translational spring of stiffness k. The stiffnesses c_0 and k originate from the cross-arm and effects of the pre-tensioned cable stays respectively. The external axial load is P and the total potential energy is hence given by:

$$V = \frac{1}{2}kl^2Q_2^2 + \frac{1}{2}c\left(\theta_B^2 + \theta_D^2\right) + \frac{1}{2}c_0\theta_C^2 - P\mathcal{E}, \quad (1)$$

where $\mathcal{E}$ is the end-shortening and the angles θ_B, θ_C and θ_D are the rotations of the pins at B, C and D respectively:

$$\mathcal{E} = l\left[4 - \sqrt{1-Q_1^2} - \sqrt{1-(Q_2-Q_1)^2} - \sqrt{1-(Q_2-Q_3)^2} - \sqrt{1-Q_3^2}\right] \quad (2)$$

$$\theta_B = \arcsin(Q_1) + \arcsin(Q_2 - Q_1), \quad (3)$$

$$\theta_C = \arcsin(Q_2 - Q_1) - \arcsin(Q_2 - Q_3), \quad (4)$$

$$\theta_D = \arcsin(Q_3) - \arcsin(Q_2 - Q_3). \quad (5)$$

The total potential energy can be nondimensionalized by dividing through by c:

$$\tilde{V} = \frac{1}{2}KQ_2^2 + \frac{1}{2}\left(\theta_B^2 + \theta_D^2\right) + \frac{1}{2}R\theta_C^2 - p\tilde{\mathcal{E}} \quad (6)$$

with normalized quantities: $\tilde{V} = V/c$, $K = kl^2/c$, $R = c_0/c$, $p = Pl/c$ and $\tilde{\mathcal{E}} = \mathcal{E}/l$. It can also be diagonalized and the linear eigenvalue problem can be solved to obtain the following non-dimensional critical loads p_i^{C} for the case where $i = 1, 2, 3$ and $R = 1$ (assumed throughout the current work, *i.e.* the case when all the rotational springs are of identical stiffnesses):

$$p_1^{\mathrm{C}} = \frac{K^3 - K^2(X-2) + 2K(X-8) + 16(3-X)}{2X(X-2)},$$

$$p_2^{\mathrm{C}} = 2,$$

$$p_3^{\mathrm{C}} = \frac{K^3 + K^2(X+2) - 2K(X+8) + 16(3+X)}{2X(X+2)}.$$

Note that the non-dimensional quantity $X = \sqrt{8 - 4K + K^2}$. The linear eigenmodes are given in Figure 4 and the variation of the critical loads with the non-dimensional stiffness of the translational spring K is shown in Figure 5.

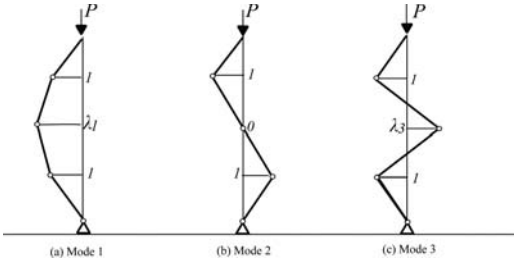

Figure 4. Linear eigenmodes. The quantities of λ_1 and λ_3 depend on the magnitude of the translational spring stiffness k. When $k=0$, $\lambda_1 = -\lambda_3 = \sqrt{2}$. As $k \to \infty$, $\lambda_1 = \lambda_3 \to 0$.

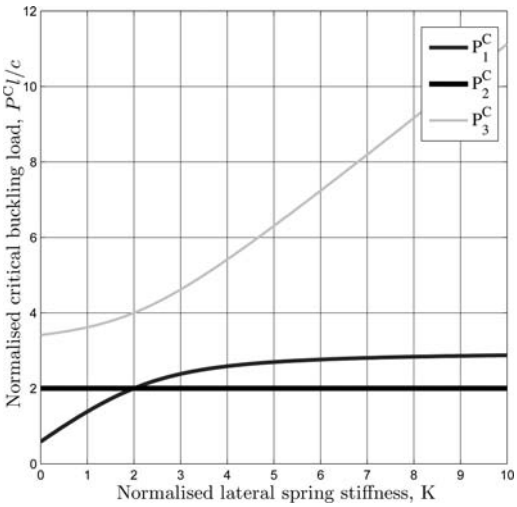

Figure 5. Distribution of critical loads with the non-dimensional stiffness of the translational spring K; note that $R=1$. When $K > 2$, Mode 2 has the lowest critical load.

2.1 *Inclusion of stay slackening*

In a prestressed stayed column the stays are in tension when the component is deployed. Under axial compression, this prestress is relieved somewhat but in most cases not totally. However, if buckling occurs, the lateral displacements for whatever eigenmode, as shown in Figure 4, can cause a rapid reduction of the cable tension due to the geometric profile; the concave sides of the buckling deformation being vulnerable to this effect. Of course if the stay tension is relieved altogether, its stiffness drops effectively to zero and the load-carrying capacity of the entire component would reduce substantially. It is therefore necessary to include this geometric effect of potential stay slackening within the current model. The numbering of the stays being defined in Figure 6; Figure 7 shows the geometry of the link model and how that relates to the stay lengths for arbitrary values of the generalized coordinates Q_i.

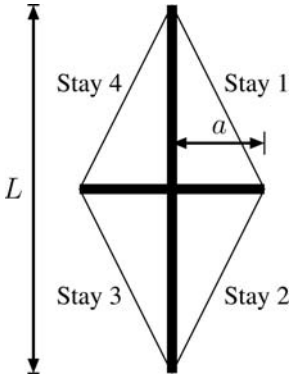

Figure 6. Number definition of cable stays.

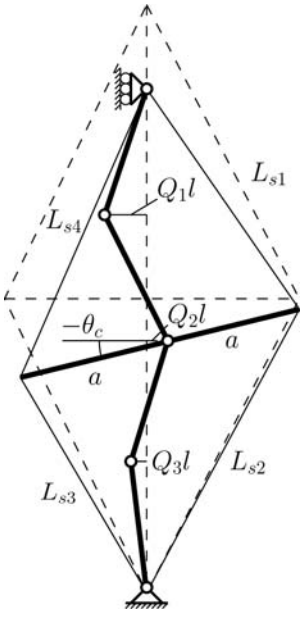

Figure 7. Asymmetric buckling mode used to define cable stay lengths under loading.

Geometrically, the vertical component of the lengths of the top two stays (1 and 4) is:

$$L_{v1} = l\left[\sqrt{1-(Q_2-Q_1)^2} + \sqrt{1-Q_1^2}\right], \qquad (7)$$

and the bottom two stays (2 and 3) is:

$$L_{v2} = l\left[\sqrt{1-(Q_2-Q_3)^2} + \sqrt{1-Q_3^2}\right]. \qquad (8)$$

Incorporating the rotation of the cross-arm θ_c, which is given by:

$$\theta_c = \left[\arcsin(Q_2-Q_1) - \arcsin(Q_2-Q_1)\right]/2, \qquad (9)$$

and assuming that any bending in the cross-arm is negligible, gives the squares of the lengths of the stays thus:

$$L_{s1}^2 = \left[(a\cos\theta_c + |Q_2|l)^2 + (L_{v1} + a\sin\theta_c)\right], \quad (10)$$

$$L_{s2}^2 = \left[(a\cos\theta_c + |Q_2|l)^2 + (L_{v2} - a\sin\theta_c)\right], \quad (11)$$

$$L_{s3}^2 = \left[(a\cos\theta_c - |Q_2|l)^2 + (L_{v2} + a\sin\theta_c)\right], \quad (12)$$

$$L_{s4}^2 = \left[(a\cos\theta_c - |Q_2|l)^2 + (L_{v1} - a\sin\theta_c)\right]. \quad (13)$$

Cable slackening is defined to occur when:

$$L_{si}^2 \leqslant \left(a^2 + 4l^2\right)\left[1 + \frac{T}{E_s A_s}\right]^{-2}, \quad (14)$$

where a is the cross-arm length, E_s and A_s are the Young's modulus and the cross-sectional area of the cable stays and T is the prestressing tensile force in the stays prior to loading. The expression in equation (14) is given by using Pythagoras's Theorem for the cable stays once the link model exhibits buckling displacements.

3 RESULTS AND DISCUSSION

The potential energy is expressed in the exact form and the respective equilibrium equations are given by the following relation:

$$\frac{\partial V}{\partial Q_i} = 0 \quad (15)$$

where $i = 1, 2, 3$, which leads to three nonlinear algebraic equations that are solved numerically in AUTO.

3.1 *Perfect post-buckling response*

For the unrestrained uniform strut case, where $R = 1$ and $K = 0$, there are three distinct critical loads p_i^C and the post-buckling response is weakly stable for the lowest (symmetric) mode, as would be expected from knowledge of the elastica. When the translational spring is introduced into the model, the critical loads for Modes 1 and 3 increase with K, but the critical load for Mode 2 remains constant owing to the pin at C remaining static. Figure 8 shows a series of solutions for the equilibrium equations where Mode 1 is critical. The post-buckling path of the symmetric mode becomes less stable and in fact the response becomes subcritical when $K \approx 0.3$. However, even when the post-buckling becomes unstable, there is no nonlinear interaction with higher modes, which implies that it is only sensitive to imperfections that are affine to the eigenmode of Mode 1. Note that, similar to the linear eigenvalue solution, the path for Mode 2 remains invariant and stable.

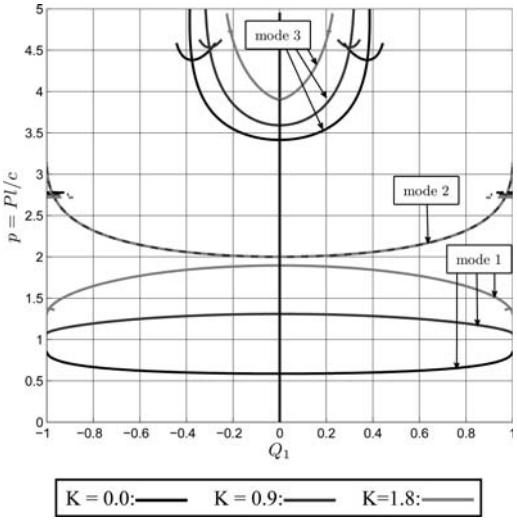

Figure 8. Post-buckling paths for $K = 0$, 0.9 and 1.8 where Mode 1 is critical. Note that the critical load associated with the first encountered eigenmode increases but that its unstable nature becomes more severe.

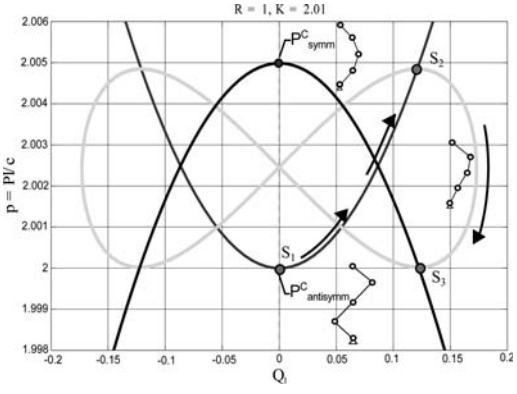

Figure 9. Post-buckling response p versus Q_1 for the discrete strut model when $K = 2.01$. Point S_1 is the critical bifurcation point, whereas points S_2 and S_3 are secondary bifurcation points on the post-buckling paths of the antisymmetric and symmetric modes respectively. The path connecting these two bifurcations contain equilibrium configurations where the geometric symmetry of the strut model is broken.

When $K = 2$ the critical loads for Modes 1 and 2 coincide, and for larger values of K Mode 2 becomes critical. However, as seen in Figures 9 and 10 where $K = 2.01$, the post-buckling path of the Mode 2 is destabilized at a secondary bifurcation point S_2 where the response transfers to a path where the modes interact, the antisymmetry is broken and eventually passes back to the subcritical symmetric mode through a further bifurcation point S_3. This entire process has been termed *mode jumping* in the literature (Hunt & Everall, 1999). Examining Figure 10, an elliptical *interaction*

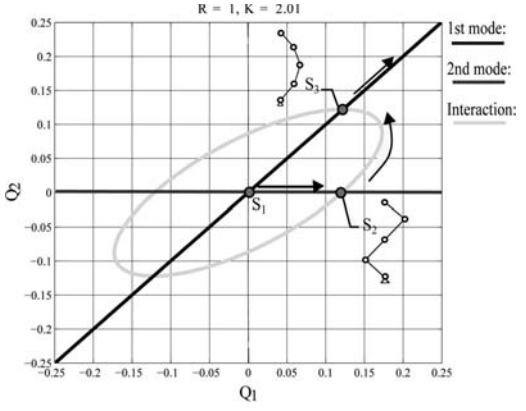

Figure 10. Post-buckling response Q_2 versus Q_1 for the discrete strut model when $K = 2.01$. The elliptical interaction loop is shown clearly. Points S_1, S_2 and S_3 are the same as in Figure 9.

loop is observed between the modal amplitudes of Q_1 and Q_2 on which the secondary bifurcations are found. This interaction loop defines combinations of the relevant amplitudes where the symmetry of the linear eigenmodes is broken at subsequent secondary instabilities and a pathway is found where one eigenmode can in fact be transformed into another.

Increasing K further causes the interaction loop to increase in size, hence the secondary instabilities become remote from the primary ones and interaction is seen less readily. Once the amplitudes of Q_i reach nearer unity (its physical limit), the loop begins to distort significantly as seen in Figure 11, which shows the solutions for two further examples of K being 2.1 and 2.6 respectively. Of course if the loop breaks, as seen in Figure 11(b), once the mode jumps to the interactive asymmetric mode, the structure would remain in that configuration. This finding resonates with a previous finite element study by Saito & Wadee (2009b), where post-buckling in Mode 2 was found to "prefer" to deform in the asymmetric mode, rather than the linear eigenmode. Recently conducted physical experiments also concur with this finding (Osofero *et al.*, 2011) where columns designed to trigger Mode 2 showed interactive post-buckling behaviour, whereas those designed to trigger Mode 1 showed deformation in the linear eigenmode.

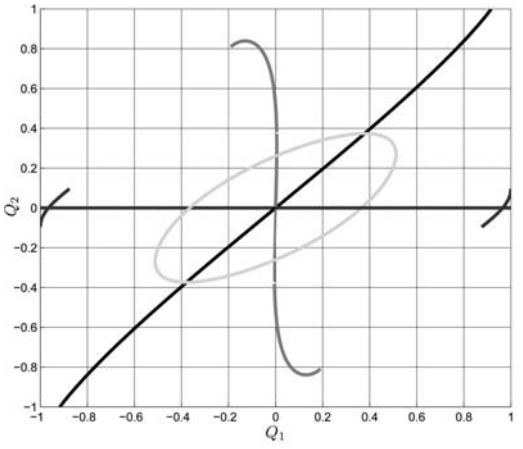

(a) Q_2 versus Q_1 for $K = 2.1$.

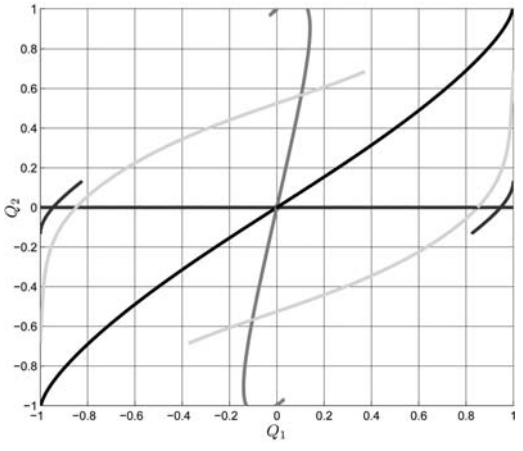

(b) Q_2 versus Q_1 for $K = 2.6$.

Figure 11. Interaction loops for higher K values. Note the significant distortion in (b) due to Q_1 and Q_2 reaching their physical limits.

3.2 *Effects of stay slackening*

The effects of stay slackening require certain properties to be assumed. The length of the main column element L is assumed to be 4 m, hence $l = 1$ m. The cross-arm length a is assumed to be equal to l, which would usually cause Mode 2 to be the lowest eigenmode. The level of the prestressing force $T = 200$ kN with the cable stay having $A_s = 730$ mm^2 and $E_s = 210$ kN/mm^2. It is also assumed that the contribution to the stiffness of each stay is equal; hence each stay going slack reduces the total stiffness of the combined initial stay stiffnesses, which contribute to K, by 25%. Pure eigenmodes cause slacking in stay pairs (an immediate 50% reduction of K), whereas interactive buckling causes slackening in individual stays (an immediate 25% reduction of K).

Figure 12 shows the post-buckling paths for Modes 1–3 for three cases where $K < 2$. Obviously, the case where $K = 0$ is unchanged, but the other cases show an immediate loss in the load-carrying capacity after the initial instability. However, as before, no mode interaction is shown for these cases. Figures 13 and 14 show the post-buckling paths for the case where $K = 2.01$ and show a far more severe response compared to Figures 9 and 10, with the secondary instabilities being triggered at much smaller values of Q_1. The response, as before first triggers Mode 2 at point S_1, then an interactive mode at point S_2 and finally triggering Mode 1 at point S_3. Figures 15 and 16 show results for $K = 4.10$ and show a similar pattern to the case for $K = 2.01$, although the interaction loop is severely

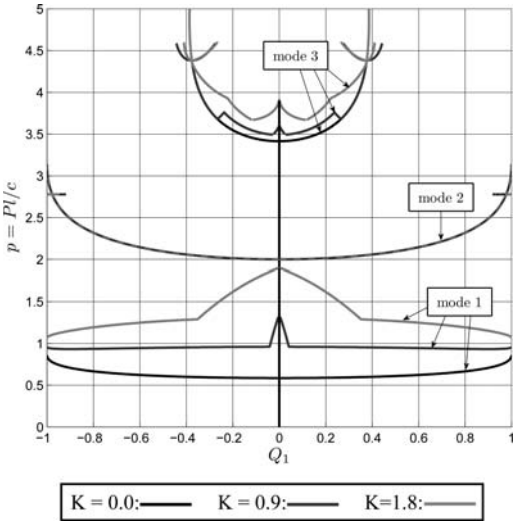

Figure 12. Post-buckling paths for cases where $K < 2$. Note the sudden drop in the load-carrying capacity beyond the lowest bifurcation point and the lack of subsequent mode interaction.

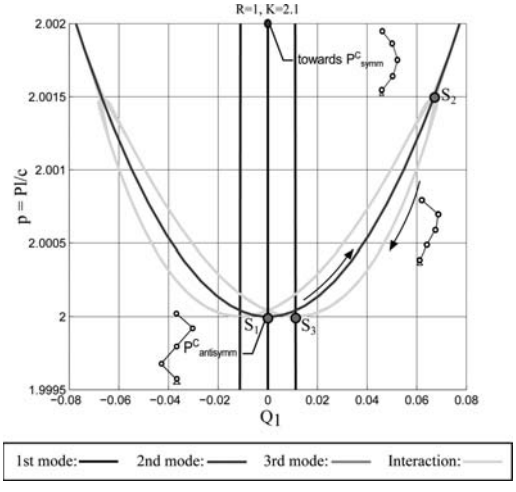

Figure 13. Normalized load p versus Q_1 for $K = 2.01$. Note that the stay slackening causes the secondary instabilities to be relatively closer to the primary one.

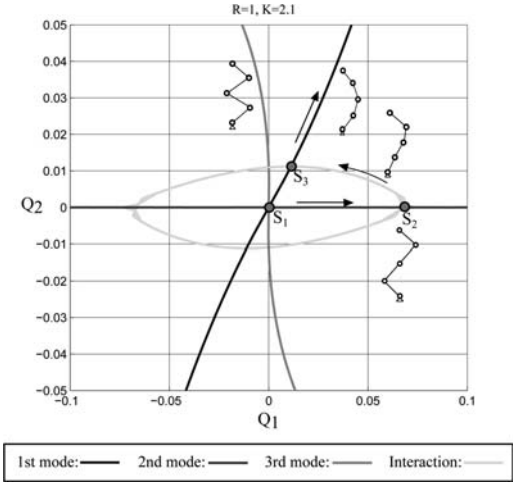

Figure 14. Plot of Q_2 versus Q_1 for $K = 2.01$. Note that the stay slackening causes the interaction loop to be slightly distorted from the elliptical shape.

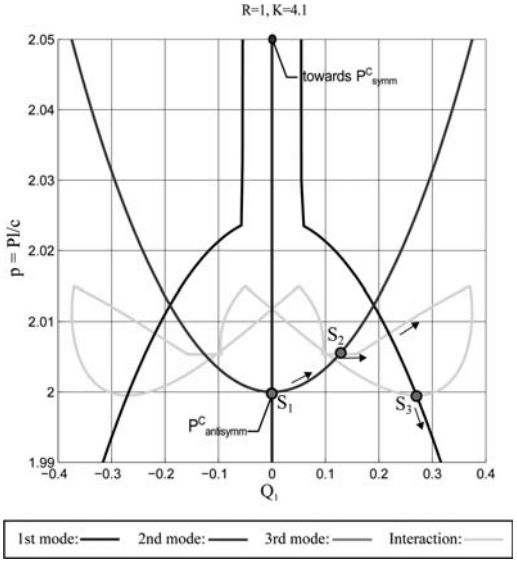

Figure 15. Normalized load p versus Q_1 for $K = 4.10$. Note that the stay slackening causes the interaction loop to be severely distorted.

distorted. Finally, Figures 17 and 18 show results for $K = 4.82$ and initially show a similar pattern to the cases for $K = 2.01$ and $K = 4.10$, although the interaction loop is broken and the response remains in the interactive mode. This finding is similar to that shown in Figure 11(b) but at much smaller combinations of the amplitudes of Q_1 and Q_2. This implies that the effects of cable slackening, even though it has been modelled with certain simplifying assumptions, is shown to be significant and drives the response. This has been shown in all the recent nonlinear modelling work on prestressed stayed tubular columns using the finite element method (Saito & Wadee, 2009b) and from recently conducted experiments (Osofero *et al.*, 2011).

4 CONCLUDING REMARKS

A simplified theoretical model, comprising rigid links and springs formulated using potential energy

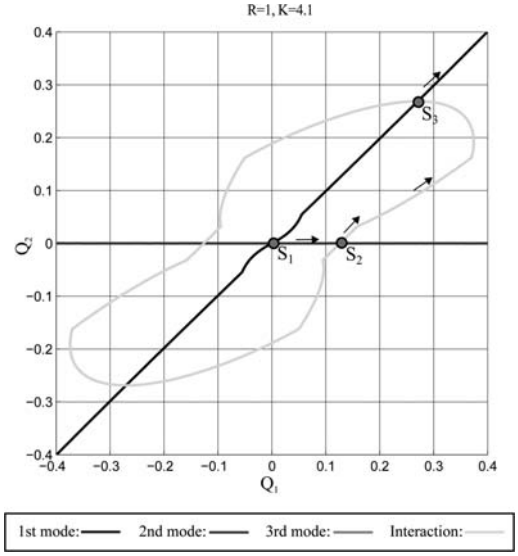

Figure 16. Plot of Q_2 versus Q_1 for $K = 4.10$. Note that the stay slackening causes the interaction loop to be severely distorted.

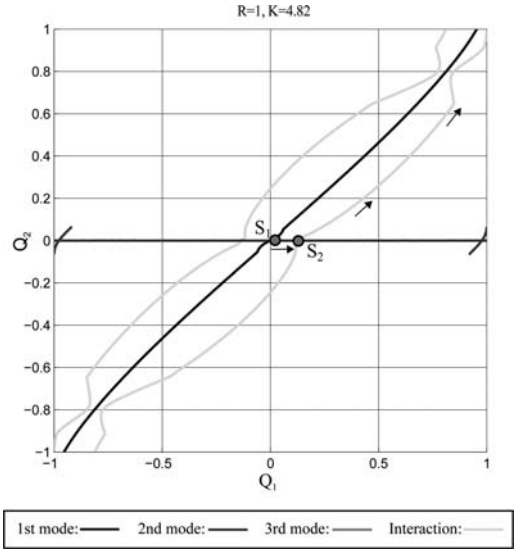

Figure 18. Plot of Q_2 versus Q_1 for $K = 4.82$. Note that the level of the stiffness and the stay slackening causes the interaction loop to be broken and the structure to remain in the interactive mode.

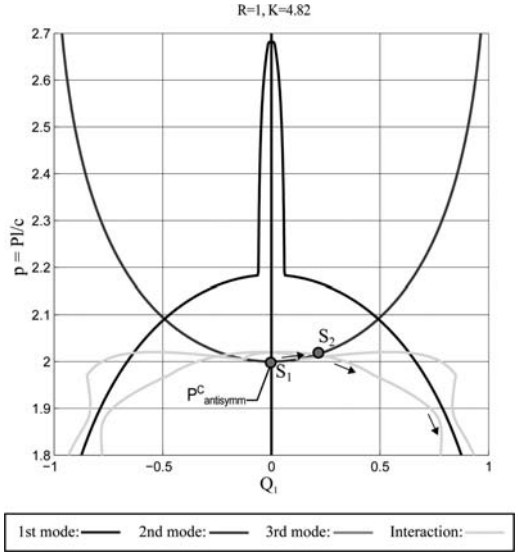

Figure 17. Normalized load p versus Q_1 for $K = 4.82$. Note that the level of the stiffness and the stay slackening causes a rapid reduction in the load-carrying capacity.

principles, has been presented to simulate the practically observed interactive buckling phenomena in prestressed stayed columns. Moreover, the destabilizing effect of the slackening of cable stays has been included from a geometric criterion. It is found that, in exactly the same way as it has been observed in practice, the link model only exhibits interactive buckling if the initial instability triggers the antisymmetric eigenmode. Moreover, it is found that if cable stay slackening is included then the secondary instability leading to mode interaction occurs at significantly smaller values of the generalized coordinates than if slackening is neglected.

This type of model has the potential for being extended to multi-bay prestressed stayed columns, which have more than one cross-arm, an example of which is shown in Figure 2. In those cases, as far as the authors are aware, no relevant nonlinear studies exist and so it is currently unclear which modes may interact. Given that the current study has been shown to replicate the behaviour for the single cross-arm case, it is suggested that a similar result may be forthcoming for more complex arrangements of this efficient load carrying structural member.

REFERENCES

Belenya, E. 1977. *Prestressed load-bearing metal structures.* Moscow: Mir Publishers.

De Araujo, R. R., De Andrade, S. A. L., Vellasco, P. C. G. da. S., & Da Silva, J. G. S. and De Lima, L. R. O. 2008. Experimental and numerical assessment of stayed steel columns. *J. Construct. Steel Res.*, **64**(9), 1020–1029.

Doedel, E. J., & Oldeman, B. E. 2009. AUTO-*07p: Continuation and bifurcation software for ordinary differential equations.* Tech. rept. Department of Computer Science, Concordia University, Montreal, Canada. Available from http://indy.cs.concordia.ca/auto/.

Hafez, H. H., Temple, M. C., & Ellis, J. S. 1979. Pretensioning of single-crossarm stayed columns. *J. Struct. Div.—ASCE*, **105**(ST 2), 359–375.

Hunt, G. W., & Everall, P. R. 1999. Arnol'd tongues and mode jumping in the supercritical post-buckling of an archetypal elastic structure. *Proc. R. Soc. A*, **455**(1981), 125–140.

Osofero, A. I., Wadee, M. A., & Gardner, L. 2011. Experimental study of critical and post-buckling behaviour of prestressed steel stayed columns. *J. Construct. Steel Res.* Accepted subject to revision.

Saito, D., & Wadee, M. A. 2008. Post-buckling behaviour of prestressed steel stayed columns. Eng. Struct., 30(5), 1224–1239.

Saito, D., & Wadee, M. A. 2009a. Buckling behaviour of prestressed steel stayed columns with imperfections and stress limitation. *Eng. Struct.*, **31**(1), 1–15.

Saito, D., & Wadee, M. A. 2009b. Numerical studies of interactive buckling in prestressed steel stayed columns. *Eng. Struct.*, **31**(2), 432–443.

Tubular Structures XIV – Gardner (Ed.)
© 2012 Taylor & Francis Group, London, ISBN 978-0-415-62137-3

Nonlinear creep analysis and buckling of shallow Concrete-Filled Steel Tubular arches

Y.-L. Pi & M.A. Bradford
Centre for Infrastructure Engineering and Safety, School of Civil & Environmental Engineering, The University of New South Wales, Sydney, Australia

ABSTRACT: Many arches of the completed Concrete-Filled Steel Tubular (CFST) arch bridges have rise-to-span ratios of 1/6 -1/5 and should be considered as shallow arches. When a CFST arch is subjected to a sustained load, the visco-elastic effects of creep and shrinkage of the concrete core produce significant time-dependent increases in the deformations and bending moments in the arch and subsequently lead to a time-dependent change of the equilibrium configuration of the arch. Accordingly, the behaviour of the CFST arch becomes more nonlinear as the time increases and the nonlinear bifurcation point and limit point of the time-dependent equilibrium path and the corresponding buckling loads of CFST arches also change with time. When the changing time-dependent bifurcation or limit point buckling load of a CFST arch becomes equal to the sustained load, the arch may buckle in a bifurcation mode or in a limit point mode under the sustained load when the time is sufficiently long. This paper investigates the long-term nonlinear bifurcation and limit point creep buckling of pin-ended shallow circular CFST arches that are subjected to a sustained uniform radial load. The algebraically tractable age-adjusted effective modulus method is used to model the time-dependent behaviour of the concrete core, based on which solutions for the nonlinear prebuckling structural life time corresponding to nonlinear bifurcation and limit point creeping buckling are derived.

1 INTRODUCTION

Under a sustained load, due to creep of the concrete core of an arch with a concrete-filled steel tubular (CFST) cross-section (Figure 1), the deformations of the arch continue to increase with time (Bradford et al 2011, Pi et al. 2011). The long-term deformations of a CFST member caused by creep and shrinkage of the concrete core are frequently larger than the initial deformations produced when the external load is first applied. In practice, many CFST arch bridges have a rise-to-span ratios in the range from 1/10 to 1/4 (Pi et al. 2012), which indicates that these CFST arches are shallow arches. It has been shown that the structural behaviour of shallow arches under transverse loading is quite non-linear and deformations and bending moment are considerable, even when the loading is not high (Pi et al. 2002). Hence, in the analysis of the long term elastic in-plane behaviour and buckling of a shallow CFST arch, recourses to non-linear analysis and buckling theory are needed.

The visco-elastic effects of creep and shrinkage of the concrete core lead to time-dependent changes of non-linear equilibrium configurations of CFST arches. As a result, both the bifurcation and limit points of the time-dependent non-linear equilibrium paths also change with time due to creep and shrinkage of the concrete core. Therefore, although the sustained load is lower than the bifurcation and limit point buckling loads of a CFST arch in the short-term, the CFST arch may buckle in long-term when the value of its time-dependent bifurcation or limit point buckling load is equal to the sustained load as result of creep buckling. Although there is no exact model available for concrete shrinkage and creep (Bradford 2005, Bradford et al 2011, Gilbert 1988, Pi et al. 2011), the age-adjusted effective modulus method has been shown (Bradford 2005, Bradford et al 2011, Gilbert 1988, Pi et al. 2011) to be efficient and accurate in predicting the long-term structural behaviour of concrete structures, and it is convenient and effective in being incorporated into the

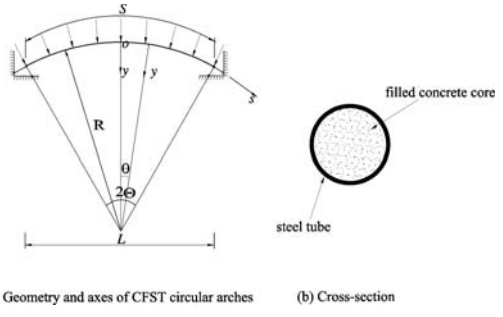

Figure 1. Concrete-filled steel-tubular arch and uniform loading.

structural analysis. This method uses algebraic formulae to model the creep and shrinkage of concrete and is recommended by ACI Committee-209 (1982) and Australian design code for concrete structures AS3800 (2001). The corresponding model is therefore used in this investigation. Experimental investigations of the shrinkage and creep strains of CFST columns have been reported by some researchers (Han et al. 2004, Uy 2001). Because the moisture in the core concrete of CFST columns is prevented from dissipating by the steel tube, the final shrinkage strain and creep coefficient of the core concrete of CFST columns were derived from experiments and were found to be lower than those of plain concrete (Uy 2001). The derived data will be used in this investigation.

The purpose of this paper is to investigate the long-term non-linear elastic in-plane behaviour and buckling of pin-ended shallow CFST circular arches due to shrinkage and creep of the concrete core that are subjected to a sustained radial uniformly distributed load around the arch axis (Figure 1).

2 DIFFERENTIAL EQUATIONS OF EQUILIBRIUM

The differential equations of equilibrium for the creep analysis of shallow CFST arches under a sustained radial uniform load q can be derived from the principle of virtual work which can be stated as

$$\int_{-\Theta}^{\Theta} \{[-NR(\delta\tilde{w}' - \delta\tilde{v} + \tilde{v}'\delta\tilde{v}') - M\delta\tilde{v}''] - qR^2\delta\tilde{v}\}\mathrm{d}\theta = 0, \quad (1)$$

where $\tilde{w} = w/R$, $\tilde{v} = v/R$, w and v are the axial and radial displacements respectively, R is the radius of the arch, $\delta(\ )$ denotes the Lagrange operator of simultaneous variations, and N and M are the axial compressive force and bending moment respectively and they are given by

$$N = -(A_s E_s + A_c E_{ec})(\tilde{w}' - \tilde{v} + \tilde{v}'^2/2) - A_c E_{ec}\varepsilon_{sh} \quad (2)$$

and

$$M = -\frac{\tilde{v}''(E_s I_s + E_{ec} I_c)}{R}, \quad (3)$$

in which A_c and A_s are the area of the concrete core and steel tube; $\varepsilon_{sh} = t\varepsilon^*/(t+35)$ is the shrinkage strain of the concrete and is a function of time, ε^* is the final shrinkage strain.

Integrating Equation 1 by parts leads to the differential equations of equilibrium as

$$\frac{\tilde{v}^{iv}}{\mu_e} + \tilde{v}'' = P \quad \text{and} \quad N' = 0 \quad (4)$$

in the radial and axial directions, respectively, where P is a dimensionless load defined by

$$P = \frac{qR}{N} - 1; \quad (5)$$

and μ_e is a time-dependent dimensionless axial force parameter defined by

$$\mu_e = \sqrt{\frac{NR^2}{E_s I_s + E_{ec} I_c}}; \quad (6)$$

in which I_s and I_c are the second moment of area of the steel tube and concrete core, E_s is the Young's modulus for steel, and E_{ec} is the age-adjusted effective modulus of concrete given by

$$E_{ec} = \frac{E_c}{1 + \chi(t,t_0)\phi(t,t_0)} \quad (7)$$

with E_c being the Young's modulus of the concrete core, $\phi(t,t_0)$ being the creep coefficient, $\chi(t,t_0)$ being the aging coefficient, and they are given by

$$\phi(t,t_0) = \frac{(t-t_0)^{0.6}\phi_u}{10 + (t-t_0)^{0.6}}$$

and (8)

$$\chi(t,t_0) = 1 - \frac{(1-\chi^*)(t-t_0)}{20 + (t-t_0)}$$

where ϕ_u is the final creep coefficient and given by $\phi_u = 1.25t_0^{-0.118}\phi_{\infty,7}$ with $\phi_{\infty,7}$ being the creep coefficient at time infinity when the first loading time is $t = 7$ days after the concrete casting, and χ^* is given by

$$\chi^* = \frac{k_1 t_0}{k_2 + t_0}, \; k_1 = 0.78 + 0.4e^{-1.3\phi_{\infty,7}}, \; k_2 = 0.16 + 0.6e^{-1.3\phi_{\infty,7}}. \quad (9)$$

Solving Equation 4 and considering the static boundary conditions $\tilde{v}'' = 0$ and the kinematic boundary condition $\tilde{v} = 0$ at $\theta = \pm\Theta$ leads to the solution

$$\tilde{v} = \frac{P}{\mu_e^2}\left\{\frac{\cos\mu_e\theta}{\cos\mu_e\Theta} - 1 + \frac{1}{2}\left[(\mu_e\theta)^2 - (\mu_e\Theta)^2\right]\right\}. \quad (10)$$

It can be seen from Equation 10 that the radial displacement is a nonlinear function of the time-dependent dimensionless axial force parameter μ_e.

3 CREEP EQUILIBRIUM EQUATIONS BETWEEN INTERNAL FORCE AND EXTERNAL LOAD

From the second equation of Equation 4, the axial compressive force N is a constant along the arch length. The non-linear equation of equilibrium between the dimensionless time-dependent axial force parameter μ_e and the dimensionless load P can be obtained by considering that the constant axial force N should be

equal to the average value of N over the entire arch calculated from Equation 2 as

$$N = \frac{1}{2\Theta}\int_{-\Theta}^{\Theta} -\left\{\begin{array}{l}\left(A_s E_s + A_c E_{ec}\right)\left(\tilde{w}' - \tilde{v} + \frac{1}{2}\tilde{v}'^2\right) \\ - A_c E_{ec}\varepsilon_{sh}\end{array}\right\} \mathrm{d}\theta \,. \quad (11)$$

Substituting Equation 10 into Equation11 and considering the boundary condition $\tilde{w} = 0$ at $\theta = \pm\,\Theta$ leads to a nonlinear equation of equilibrium between the internal force parameter μ_e and the dimensionless load P as

$$A_1 P^2 + A_2 P + A_3 = 0 \quad (12)$$

where

$$A_1 = \frac{1}{4\mu_e^2\Theta^2}\left(5 - 5\frac{\tan\mu_e\Theta}{\mu_e\Theta} + \tan^2\mu_e\Theta\right) + \frac{1}{6}, \quad (13)$$

$$A_2 = \frac{1}{(\mu_e\Theta)^2}\left(1 - \frac{\tan\mu_e\Theta}{\mu_e\Theta}\right) + \frac{1}{3}, \quad (14)$$

and

$$A_3 = \left(\frac{\mu_e\Theta}{\lambda_e}\right)^2 + \frac{A_c E_{ec}\varepsilon_{sh}}{\Theta^2\left(A_s E_s + A_c E_{ec}\right)} \quad (15)$$

with $\lambda_e = \dfrac{R\Theta^2}{r_e}$.

From Equations 10 and 12, the radial displacement and the axial compressive force of a CFST arch are non-linear functions of the dimensionless load P. For a given CFST arch under a given sustained load q at a given time t, solving Equation 12 produces the long term dimensionless axial force parameter μ_e and then substituting the obtained μ_e into Equation 6 produces the axial compressive force Nunder the sustained load q at time t. Subsequently, substituting the obtained μ_e and P into Equation 10 results in the corresponding radial displacement $\tilde{v}$ at time t.

The typical long-term nonlinear responses of pin-ended shallow CFST arches under a sustained uniform radial load are compared with their linear counterparts (Pi et al. 2011) in Figure 2 as the variations of the dimensionless central radial displacements $v_c/v_{c,15}$ with time t, where $v_{c,15}$is the central radial displacement at time $t = 15$ days.

It can be seen from Figure 2 that as time t increases, creep and shrinkage of the concrete core produce significant increase of the radial displacements of CFST arches under the sustained load. It can also be seen that the increases of the creep radial displacements of shallow CFST arches predicted by the nonlinear analysis are much greater than those predicted by the linear analysis. This indicates that the linear analysis may underestimate the long-term increases of the creep radial displacements of shallow CFST arches.

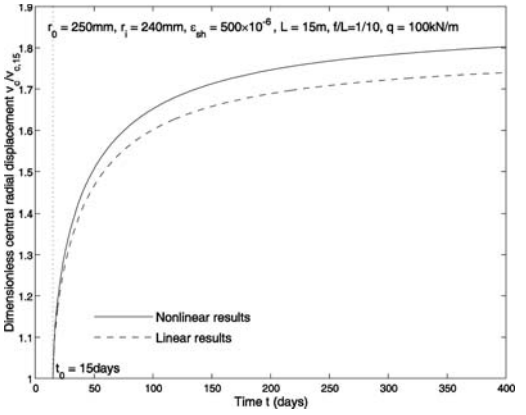

Figure 2. Nonlinear long-term radial displacements.

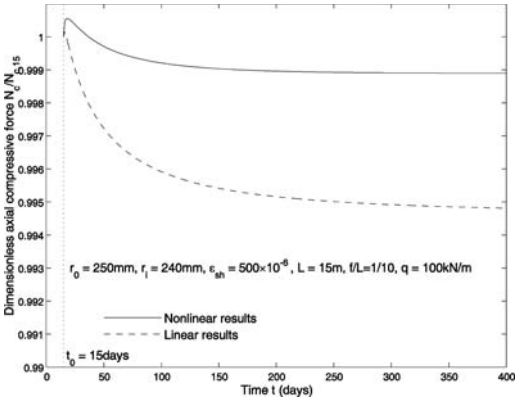

Figure 3. Nonlinear creep axial compressive force.

Variations of the dimensionless axial compressive force N/N_{15} with time t for the same arches are compared with their linear counterparts in Figure 3, where N_{15} is the axial compressive force at time $t = 15$ days. It can be seen that the nonlinear analysis predicts that creep and shrinkage of the concrete core produce increases of the long-term axial compressive forces N of the CFST arch under a sustained load while the linear analysis predicts very small decreases of the long-term axial compressive forces N.

4 CREEP LIMIT POINT BUCKLING

The limit point buckling loads of a CFST arch at a given time t can be derived by using calculus, from which the load q can be expressed as an implicit function of the time-dependent axial force parameter μ_e as $F(q, \mu_e) = 0$, and so the nonlinear equation of equilibrium between the internal force parameter μ_e and the dimensionless load P at the limit points can be obtained by setting

$$\frac{\mathrm{d}q}{\mathrm{d}\mu_e} = -\frac{\partial F(q,\mu_e)/\partial\mu_e}{\partial F(q,\mu_e)/\partial q} = 0, \quad (16)$$

which leads to the equilibrium equation at the limit points as

$$B_1P^2 + B_2P + B_3 = 0 \tag{17}$$

where

$$B_1 = 2A_1 + B_4, \quad B_2 = 4A_1, \quad B_3 = A_2 - A_3, \tag{18}$$

and

$$B_4 = \frac{7\tan^2\beta_e}{8\beta_e^2} + \frac{15}{8\beta_e^2}\left(1 - \frac{\tan\beta_e}{\beta_e}\right) - \frac{\tan\beta_e}{4\beta_e\cos^2\beta_e}. \tag{19}$$

The solutions for the limit point buckling loads and the corresponding axial force parameters for a given CFST arch at a specified time t can be obtained by solving Equations 12 and 17 simultaneously. The corresponding radial displacement can be obtained by substituting the obtained load and axial force into Equations 10. The typical nonlinear behaviour of pin-ended CFST arches is shown in Figure 4 as the variations of the dimensionless central radial displacement v_c/f with the dimensionless radial load qR/N_{cr}, and in Figure 5 as the variations of the dimensionless axial compressive force N/N_{cr} with the dimensionless radial load qR/N_{cr}, where f is the rise of the arch and the rise-to-span ratio is f/L= 1/24. In Figures 4 and 5, the fine solid line denotes the short-term equilibrium path up to a sustained load $q_{sus} = 0{:}374N_{cr}$, while the coarse solid line represents the long-term equilibrium path under the sustained load. The "equilibrium path" described by Equations 10 and 12 (the broken line) at time $t = 15$, 30, and 100 days, and the corresponding limit points obtained by Equations 10, 12 and 17 are also shown in Figures 4 and 5 for reference.

It can be seen from Figures 4 and 5 that at time $t = 15$ days, the relationship between the dimensionless displacement v_c/f and external load qR/N_{cr} and that between the axial compressive force N/N_{cr} and external load qR/N_{cr} are almost linear until the sustained load $q_{sus}R/N_{cr}$ is reached. However, the sustained load $q_{sus}R/N_{cr}$ is lower than the limit buckling load of the arch and the arch is in a stable equilibrium state and cannot buckle. As time increases, due to creep and shrinkage of the concrete core, nonlinearities of the relationships between v_c/f and $q_{sus}R/N_{cr}$ and between N/N_{cr} and $q_{sus}R/N_{cr}$ increase rapidly and the equilibrium configuration of the arch also changes. At time $t = 30$ days, the limit point buckling load of the arch is lower than that at time $t = 15$ days, but it is still higher than the sustained load $q_{sus}R/N_{cr}$. Hence, the arch is still in a stable equilibrium state.

However, the limit point equilibrium configuration is attained at the sustained load $q_{sus}R/N_{cr}$ at time $t = 100$ days. In this case, the limit point buckling load of the arch is equal to the sustained load q_{sus} and the arch may fail in a creep limit point buckling mode. It is worth pointing out that in practice, the sustained load remains constant after the creep limit point buckling, the CFST arch cannot follow the equilibrium path

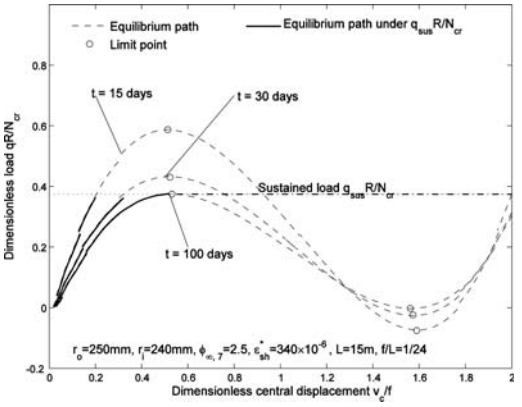

Figure 4. Central radial displacement for creep limit point buckling.

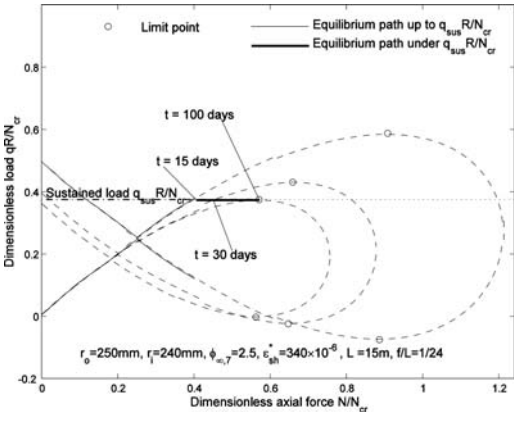

Figure 5. Axial compressive force for limit point creep buckling.

shown by the broken lines and the lower limit point cannot be reached, but the equilibrium configuration of the arch will suddenly jump from the limit point to a remote equilibrium point as shown by the horizontal dotted-dashed line in Figures 4 and 5. The horizontal path, however, is not an equilibrium path. The movement of the arch after buckling is associated with a build up of kinetic energy, which leads to the familiar sudden and noisy snap-through phenomenon.

The prebuckling structural life for the creep limit point buckling of CFST arches can be determined by using Equations 12 and 17. The typical variations of the structural life t of CFST arches prior to their creep limit point buckling with the dimensionless sustained load $q_{sus}R/N_{cr}$ are shown in Figure 6. It can be seen that the prebuckling structural life increases as the sustained load decreases. For a sufficiently low sustained load, the creep limit point buckling of the CFST arch cannot develop, while for a high sustained load, the prebuckling structural life of the CFST arch is quite short. It can also be seen in the first 130 days of prebuckling structural life, the decrease of the corresponding sustained load is quite rapid, but becomes slow in the

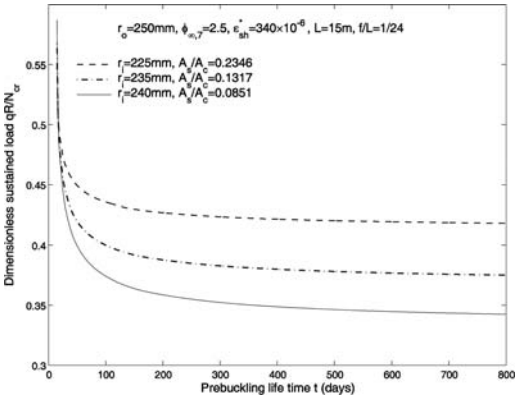

Figure 6. Prebuckling life time for creep limit point buckling.

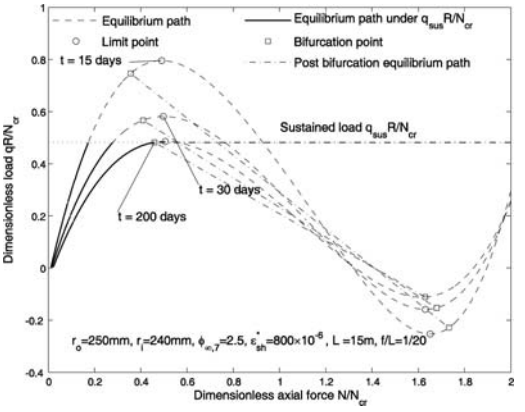

Figure 7. Central radial displacement for creep bifurcation buckling.

following days, and that under the same sustained load, the prebuckling structural life of arches decreases with a decrease of the area ratio of the steel tube to the concrete core.

5 CREEP BIFURCATION BUCKLING

In an addition to creep limit point buckling, the equilibrium configuration of a CFST arch may attain a bifurcation point in the long-term, and the arch may bifurcate from a symmetric primary equilibrium state to an antisymmetric equilibrium state, and buckle in a creep bifurcation mode. A perturbation method can be used to derive the differential equations for the creep bifurcation buckling equilibrium of a shallow CFST arch at a specified time as

$$\frac{\tilde{v}_b^{iv}}{\mu_e^2}+\tilde{v}_b''=\frac{q_bR}{N} \quad \text{and} \quad N_b'=0. \tag{20}$$

The general solution of Equation 20 is

$$\tilde{v}_b=C_1+C_e\theta+C_3\frac{\sin\mu_e\theta}{\mu_e^2}+C_4\frac{\cos\mu_e\theta}{\mu_e^2}+\frac{q_bR}{2N}\theta^2. \tag{21}$$

Because for antisymmetric buckling, $\tilde{v}_b$ is odd in θ and so the even terms on the solution of Equation 16 vanish, it follows that

$$E_1=E_4=0 \quad \text{and} \quad q_b=0, \tag{22}$$

which indicates that the external load q during bifurcation buckling is constant.

Considering Equation 22 and substituting the antisymmetric solution given of Equation 21 into the boundary conditions leads to two homogeneous algebraic equations for the coefficients C_2 and C_3 as

$$C_2\Theta+C_3\frac{\sin\mu_e\Theta}{\mu_e^2}=0 \quad \text{and} \quad C_3\sin\mu_e\Theta=0 \tag{23}$$

from which, the condition for the existence of a nontrivial solution $\tilde{v}_b$ requires that the equation

$$\sin\mu_e\Theta=0, \tag{24}$$

whose lowest solution is

$$\mu_e\Theta=\pi. \tag{25}$$

Substituting this solution into Equation 12 leads to the equation for the creep antisymmetric bifurcation buckling load P_b as

$$\left(2\pi^2+15\right)P_b^2+\left(4\pi^2+12\right)P_b+\frac{12\pi^4}{\lambda_e^2}+\frac{12A_cE_{ec}\varepsilon_{sh}}{\Theta^2\left(A_sE_s+A_cE_{ec}\right)}=0. \tag{26}$$

The typical non-linear creep bifurcation buckling behaviour for a pin-ended CFST arch ($f/L=1/20$) is shown as the variations of the dimensionless central vertical displacement v_c/f with the dimensionless external load qR/N_{cr} in Figure 7, and as the variations of the dimensionless axial compressive force N/N_{cr} with the dimensionless external load qR/N_{cr} in Figure 8, where the fine solid line represents the short-term equilibrium path up to a sustained load $q_{sus}R/N_{cr}$ while the coarse solid line denotes the long-term equilibrium path of these CFST arches due to creep and shrinkage of the concrete core. The value of the sustained radial load is $q_{sus}R=0.485N_{cr}$. The "equilibrium path" given by Equations 10. and 12 (the broken line) at time $t=15$, 30, and 200 days, the corresponding limit points obtained from Equations 10, 12 and 17, and the bifurcation points given by Equations. 10 and 26 are also shown in Figures 7 and 8 for reference.

It can be seen from Figures 7 and 8 that the relationships of the dimensionless displacement v_c/f and of the dimensionless axial compressive force N/N_{cr} with the dimensionless radial load qR/N_{cr} change with time. The bifurcation buckling load of the arch decreases

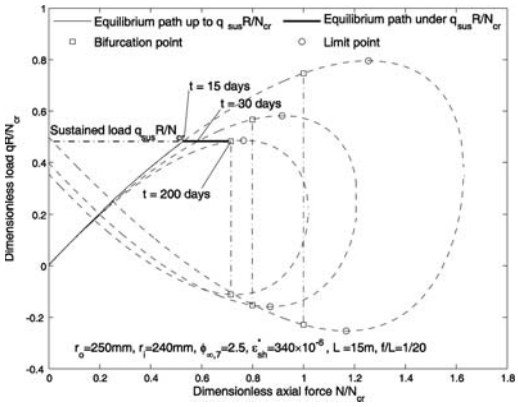

Figure 8. Axial compression force for creep bifurcation buckling.

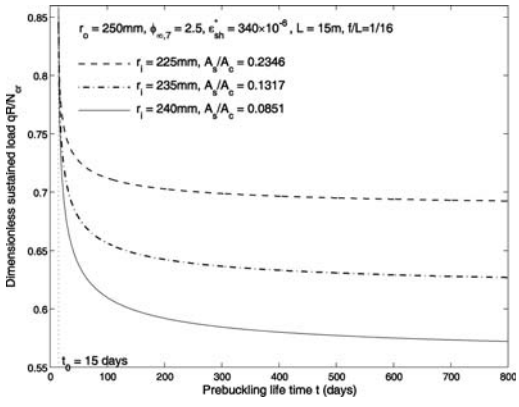

Figure 9. Structural life time for creep bifurcation buckling.

with an increase of time. At time $t = 15$ days, the relationships up to the sustained load $q_{sus}R/N_{cr}$ are almost linear and the sustained load is lower than the bifurcation and limit point buckling loads and the arches are in a stable equilibrium state. The relationships become quite non-linear at time $t = 30$ days, but the sustained load $q_{sus}R/N_{cr}$ is still lower than the bifurcation and limit point buckling loads of the arch. Hence, the arches are still in a stable equilibrium state at time t =30 days. At time $t = 200$ days for the pin-ended arch, the bifurcation buckling equilibrium configuration of the arch is attained and the sustained load is equal to the upper bifurcation buckling load and the arch may fail in a creep bifurcation buckling mode. Because the upper limit point buckling load is higher than the upper bifurcation buckling load, the creep limit point buckling will not occur. Similar to the case of limit point buckling, because the sustained load remains constant after bifurcation buckling, the CFST arch cannot follow the secondary equilibrium path shown by the fine dotted-dashed lines and the lower bifurcation point cannot be reached, but the equilibrium of the arch will jump from the bifurcation point to a remote stable equilibrium point as shown by the coarse horizontal dotted-dashed line, which, however, is not an equilibrium path. Again, the movement of the arch after buckling is associated with a build up of kinetic energy, which leads to a sudden and noisy snap-through phenomenon.

The structural life of a CFST arch prior to creep bifurcation buckling under a sustained load $q$can be determined from Equation 26. The typical variations of the dimensionless sustained load qR/N_{cr} with the structural life prior to creep bifurcation buckling are shown in Figure 9, where the rise-to-span ratio of the arch is $f/L = 1/16$. It can be seen that similar to the case of creep limit point buckling, the structural life prior to creep bifurcation buckling increases with a decrease of the sustained load. In other words, the creep bifurcation buckling load decreases as the time increases.

This indicates that the creep of the concrete core significantly reduces the bifurcation buckling resistance of CFST arches. It can also be seen that in the first 100 days, the corresponding sustained load decreases rapidly, but the decrease becomes slow in the following days, and that the ratio of the steel tube area to the core concrete area influences the creep buckling loads significantly.

6 CONCLUSIONS

This paper has studied the long-term elastic in-plane structural and buckling behaviour of pin-ended shallow CFST circular arches that are subjected to a radial load uniformly distributed around the arch axis. It has been found that creep and shrinkage of the concrete core have significant effects on the non-linear deformations and buckling behaviour of shallow CFST arches. It has been demonstrated that the time-dependent response of a shallow CFST arch is affected by the geometric non-linearity of the arch under a sustained load. The increases of the creep radial and axial displacements of a shallow CFST arch predicted by non-linear analysis have been found to be much greater than those predicted by linear analysis, which indicates that the linear analysis may underestimate the long-term increases of the radial and axial displacements of shallow CFST arches. Because the visco-elastic effects of creep and shrinkage of the concrete core produce significant long-term increases of deformations and bending moments and subsequently lead to a time dependent change of the equilibrium configuration, it was also found that a stable equilibrium state of a shallow CFST arch under a sustained load that is lower than the limit point and bifurcation buckling loads of the shallow CFST arch in short-term may develop to a critical equilibrium state at a bifurcation point or at a limit point in the long-term, and the arch may buckle in a bifurcation or limit point mode. The solutions for the possible structural life time of a shallow CFST arch prior to bifurcation or limit point buckling have been derived, which are useful for assessing quantitatively

the influence of various parameters on the long-term non-linear responses and buckling of shallow CFST arches.

ACKNOWLEDGEMENTS

This work has been supported by the Australian Research Council through an Australian Laureate Fellowship (FL100100063) awarded to the second author and through Australian Discovery Projects (DP1097096 and DP1096454) awarded to the authors.

REFERENCES

ACI Committee 209. 1982. *Prediction of Creep, Shrinkage and Temperature Effects in Concrete Structures*. Detroit: American Concrete Institute (ACI).

AS3600. 2001. *Australian Standard: Concrete Structures*. Sydney: Standard Association of Australia.

Bradford, M.A. 2005. Shrinkage and creep response of slender reinforced concrete columns under moment gradient: theory and test results. *Magazine of Concrete Research* 57(4): 235–249.

Bradford, M.A., Pi, Y.-L., & Qu, W.L. 2011. Time-dependent in-plane behaviour and buckling of concrete-filled steel tubular arches. Engineering Structures 2011; 33:1781-1795.

Gilbert, R.I. 1988. *Time Effects in Concrete Structures*. Amsterdam: Elsevier Applied Science.

Han, L.H, Y.F. Yang, Y.F., & Liu, W. 2004. The behavior of concrete-filled steel tubular columns with rectangular section under long-term loading. *Journal of Civil Engineering* 37(3): 12–18.

Pi, Y.-L., Bradford, M.A. & Uy, B. 2002. In-plane stability of arches. International *Journal of Solids and Structures* 39: 105–125.

Pi, Y.-L., Bradford, M.A. & Qu, W.L. 2011. Long-term non-linear behaviour and buckling of shallow concrete-filled steel tubular arches. *International Journal of Non-Linear Mechanics* 46: 1155–1166.

Pi, Y.-L., Liu C., Bradford M.A., & Zhang S. 2012. In-plane strength of concrete-filled steel tubular circular arches. *Journal of Constructional Steel Research* 69:77-94.

Uy, B. 2001. Static long-term effects in short concrete-filled steel box columns under sustained loading. ACI Structural Journal 98(1): 96–104.

Tubular Structures XIV – Gardner (Ed.)
© 2012 Taylor & Francis Group, London, ISBN 978-0-415-62137-3

Design and construction of a space truss for a heavy maintenance hangar in Barcelona Airport

A. Insausti, I. Ascaso, F. Hernández, X. Balda & J.I. Trueba
Asteca Estructuras, Donostia, Spain

ABSTRACT: Space trusses made of bolted joints are being increasingly used in challenging projects due to their optimized cost, assembling easiness and fast lifting. This structural solution is especially suitable to provide relatively light structures when long spans and a high loading capacity are required. Moreover, space trusses allow an accurate prediction of the deformed shape. The present paper describes the design and construction of the main structure of a 13,146-square-meter heavy maintenance hangar with a clear span of 155 meters. This structure was based on a continuous space truss using circular tubes. Due to the highly demanding technical requirements of the facility, several design geometries were assessed and new bolted joints were developed. The bolted joints were validated by means of experimental work. The assembly of the structure and the lifting process, which was specifically designed for this project, are also presented in the paper.

1 PROJECT DESCRIPTION

1.1 *Introduction*

Asteca Estructuras is an engineering company with more than 35 years experience in the design, development and construction of steel structures. Asteca's activity during the last 20 years has been mainly based on tubular space trusses. This structural solution is suitable to create pillar-free spaces combined with relatively high loads. Furthermore, modern space trusses can be tailored to create any desired shape, since they provide a three-dimensional continuous structure. Consequently, space trusses give structural solution in projects with diverse features; for instance, sports centres, industrial bays, railway stations and exhibition centres [Martínez Calzón & Ladrón de Guevara 2003, Del Campo et al. 2003].

Space trusses built by Asteca Estructuras are based on a 3-dimensional bolted joint called Nuclos, which is shown in Figure 1. The Nuclos system was developed by Asteca in the early 80s and consists of a solid sphere with thread holes that allow connecting structural tubes in any spatial direction. This system was designed in order to create an easy, fast and reliable way of assembling structural tubes.

In the last years, tubular space trusses are being increasingly used for airport facilities where specialized and versatile buildings are demanded. These facilities include maintenance hangars [Kaya et al. 2003], heliports, airport terminals and fingers, which usually need light structures capable to cover long spans combined with a good aesthetic appearance. These requirements make space trusses particularly suitable for airport facilities.

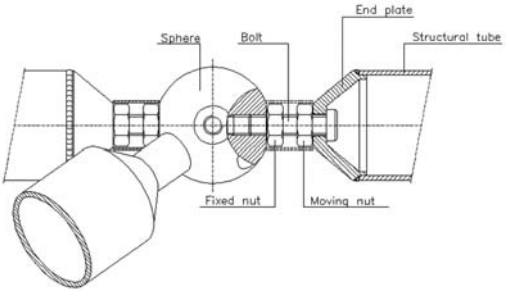

Figure 1. Nuclos joint developed by Asteca Estructuras for hollow tubes.

Among airport facilities, heavy maintenance hangars must fulfil extremely demanding aeronautic standards and provide enough versatility to allow a maximum number of maintenance configurations within a unique building. In fact, maintenance hangar must be understood as an investment rather than as a necessity, since a clever layout gives the chance to perform maintenance on a wide range of aircrafts. This versatility lets owners hire out the facility and get an important profit out of their investment.

Maintenance hangars are designed regarding the potential use of the building during its life and the different situations that could happen inside. In order to obtain an appropriate layout, the main structure of these buildings must provide big open spaces and allow the hangars to be enlarged in the future if needed. These requirements can be easily obtained with structures based on bolted space trusses.

Moreover, aircraft maintenance requires heavy overhead cranes that usually hang from the roof structure. As a consequence, hangar's structure is a key element to obtain the desired features, and should be able to provide free spaces together with an accurate deformation.

Structures that cover long spans must have high second moment of inertia due to the high bending moment values they have to transmit. This condition can be achieved increasing the overall height of the structure. Nevertheless, the height of the buildings within airports is usually limited for flight safety and, as a consequence, bending moments have to be transmitted with a limited height of the structures. This issue can only be fulfilled using tubes and joints able to support extremely high loads; however, joints based on standard bolts do not provide enough strength to transmit the loads involved in this type of structures. In order to handle this problem, Asteca Estructuras developed enhanced 3D bolted joints able to support loads values higher than usual. This development involved testing the whole joint in order to check the strength of the new elements.

Additionally, the assembly and lifting process of this type of structures is of paramount importance because of its influence in the final cost of the project. Due to their light weight, space trusses are also considered fast and easy to erect. Besides, structural elements can be manufactured in the workshop while other parts of the structure are being assembled on site.

This paper presents the design of the main structure of a maintenance hangar in Barcelona Airport for Iberia, which required the development of extremely high strength Nuclos joints. The experimental work done during this development is presented here. Moreover, the assembly and lifting process of the structure is described.

1.2 *Heavy maintenance hangar in Barcelona Airport*

Iberia's Maintenance Hangar in Barcelona is the largest hangar built in Spain during the last 20 years. This hangar was planned to perform heavy maintenance and overhaul inspections on aircrafts, and its design was thought to carry out operations on two A340 or four A320 aircrafts simultaneously. Moreover, one A380 aircraft can be accommodated inside. The surface of the building is 13,146 m2. Figure 2 presents the described hangar and shows the inner side of the building through the hangar's main door.

The inner space of the hangar is completely free of columns and the main door is 155 meters wide. These features provide a great flexibility to schedule maintenance operations. The required headroom inside the hangar was 25 meters and the allowed maximum building height due to airport limits was 40 meters. Thus, the available space for the main structure was 15 meter, which required an optimized structure. The main dimensions of the facility are shown in Figure 3.

Figure 2. Heavy maintenance hangar in Barcelona Airport.

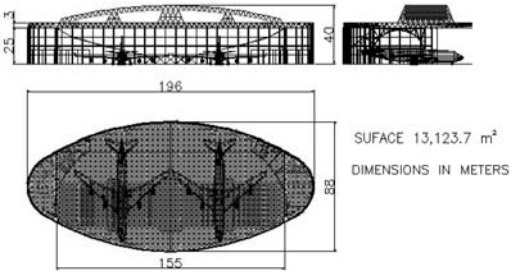

Figure 3. Main drawing of the maintenance hangar.

Among the facilities of the hangar, the cover structure supports four over-head cranes of 40,000 kg, being each over-head crane able to handle up to 20,000 kg. Therefore, the space frame is loaded with 240,000 kg hanging from the structure in different positions. The mentioned features can be observed in Figure 4, where the space truss can be seen under the roof.

The final design of the structure was carried out by means of 2,400 load combinations that took into account all the potential positions of the equipment included in the building together with dead loads, imposed loads –wind and snow- and temperature effects.

These requirements were achieved using the space truss as structural solution. This type of structure, being a continuous element along the whole roof, is able to present small and smooth deformations that can be accurately predicted. Moreover, the space truss avoids on site welding, except for the supports, and warranties a high quality product manufactured at the workshops. Besides, since the space truss is a hyperstatic structure, it is possible to remove a single element or a group of elements under controlled load conditions without affecting the behaviour of the entire structure. Comparing to other structures, this feature allows several advantages when any local change or replacement has to be done. In addition, it provides a big flexibility when lifting and assembling the structure, optimizing time and cost.

The structural design comprised a space truss covering the whole facility and two steel trusses made of welded elements that support the space truss in both ends. The cover structure included an arch on the top of the main door. This arch, which remained within

Table 1. Different size bolt properties.

Bolt reference	Outer diameter (mm)	Effective area (mm^2)	Nominal tension strength (kN)
M68	68	2905	2615
M80	80	4021	3619
M90	90	5089	4580
M100	100	6283	5655

the height limits established by the airport authorities, counteracted the lack of supports in the door side. The shape of the described arch can be seen in Figure 2 and is also represented in Figure 3.

2 DEVELOPMENT OF LARGE NUCLOS JOINTS

2.1 *Manufacturing process*

Due to the design requirements involving this project it was necessary to develop Nuclos joints able to transmit higher loads. This development demands bolts with ultimate load values higher than the strength obtained in standard bolts. The commercial range of structural bolts covers from 14 mm to 68 mm outer-diameter bolts, and the strongest material grade used for them is usually 10.9 – yield stress 900 MPa. Thus, the strongest commercial bolts available should be designed for load values up to 2,615 kN, which is not enough for this project. The challenge in this project consisted in manufacturing extremely high strength bolts and adapting the whole Nuclos system to them. This procedure had to be done together with the necessary experimental work that validates the new elements.

Table 1 shows the main properties of the largest commercial bolt, the M68, together with the desirable properties for bolts with higher strength–M80, M90 and M100-. All bolts used in this work follow the ISO metric screw threads standard, which is equivalent to the BS 3643. The pitch related to each diameter has been chosen by means of this standard [Pareto 1991]. Bolt's strength in tension is obtained from the effective area, which is also given in the ISO standard, and material properties. Table 1 shows the outer diameter, the effective area and the strength in tension of the bolt's used here. Note that the effective area to nominal area is usually close to 0.8.

When developing stronger Nuclos, the main criteria was to produce spheres and tube's end plates clearly stronger than bolts; hence, the strength of the whole joint would be based on the strength of the bolts, which is the best controlled element of the joint. It must be clarified that, taking into account the whole space truss, the structural tubes are always the weakest element; that is, design is always performed based on the yield stress of the tubes and the Nuclos joint is selected ensuring that its strength is higher than this value.

Hence, if the design load is exceeded, the tubes undergo plastic range and the behaviour of the whole structure is ductile.

Rather than using higher strength, it was decided to achieve high loads by means of enlarging bolt's area. This decision was made in order to avoid brittle behaviour that would decrease the ability of the joint to deform before collapse. Since bolts are the key element in the whole Nuclos connection, it is highly compulsory to avoid materials with high mechanical properties that do not offer enough ductility. Hence, grade 12 materials or higher have been disregarded in this work. Moreover, if bolts grade had been increased, materials in all elements connected to them –nuts and spheres- would have required stronger materials as well.

Once it was decided to maintain grade 10.9 material, different manufacturing processes were checked. Big dimension standard bolts are produced by hot forging and threads are subsequently cut by machining. Usually, bolt's forging is performed at a high temperature in order to avoid residual stresses created by cold form processes. However, when very thick elements are used, the core of the member cannot be heated up properly; thus, it is not possible to apply forging without introducing any residual stress. As a consequence, large bolts could not be produced avoiding residual stresses completely, which led to brittle material when the strength was increased. This problem was solved by means of a subsequent heat treatment. Precisely, since the aim of the process was to get high strength bolts and ensure their ductility, tempering process was applied.

2.2 *Experimental work on Nuclos joint*

The experimental work comprised 11 full-scale tests over the new Nuclos joints developed by Asteca Estructuras using high strength bolts. Two Nuclos joints with 80 mm bolts, three Nuclos joints with 90 mm bolts and six Nuclos joints with 100 mm bolts were tested. Table 2 presents all the samples and shows the bolt and sphere sizes used in each test. Figure 5 presents the drawing of the M100-A sample.

The experimental work was carried out in a MTS universal testing machine with a maximum load of 15,000 kN in tension. All tests were conducted under displacement control using a constant velocity of 2 mm/min. End connections were also especially designed for these tests so that the Nuclos joints worked in the same way as in the actual structure. Figure 6 shows the experimental set-up for the M80-A sample.

The aim of the experimental program was to check the strength of the newly developed joints; hence, joints were tested in tension up to ultimate failure. Applied load and displacement were recorded during the tests and, once each test was finished, the load at the end of the elastic behaviour and the maximum

Figure 4. Inside view of the hangar at Barcelona Airport.

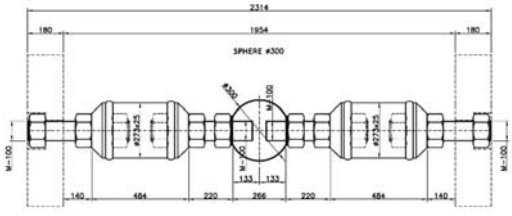

Figure 5. Drawing of the M100-A sample tested.

load of the sample were recorded. Finally, the type of failure was also analyzed in order to ensure that bolts remained as the weakest part of the joint, as it is desired in the Nuclos system. Figures 7 and 8 present the M80-A sample after being tested. The figures show that failure was presented in the bolt that deformed within the plastic range before breakage.

Table 2 shows the results obtained in tests. The failure mode observed in each test is also included in the table.

As it was intended, failures were always developed in bolts. Since the bolt is the weakest part of the joint, its strength can be used as a reference load value for design and it becomes straightforward to check that the strength of the Nuclos joint is higher than that of the structural tube. Hence, the global design of the space truss lays on the mechanical properties of structural tubes, which offer enough ductility.

Figure 9 shows load-displacement curve recorded during the M100-A test. The behaviour showed by all the tested samples was similar to that presented in Figure 9. The load-displacement curves show an initial elastic range followed by a horizontal plastic range. This initial elastic range ensures that, within these load values, all the elements remain in their elastic behaviour. Furthermore, the plastic deformation

Figure 6. Experimental set-up for the M80-A Nuclos joint.

showed by the tested Nuclos joints is large enough to accept their use in actual structures.

As a summary, it can be said that the new Nuclos joints are able to bear higher loads than the previous version based on commercial bolts. On average, the

Figure 7. M80-A Nuclos after being tested.

M80 Nuclos can transmit up to 3,550 kN remaining in the elastic range, which is the 135% of the maximum load in a M68 bolt. Besides, the M90 Nuclos can transmit up to 4,500 kN and the M100 Nuclos can transmit up to 5,233 kN remaining in the elastic range, being the 172% and the 200% of the maximum load in a M68 bolt respectively. However, the yield stress obtained in tests is lower than 900 MPa, the expected yield stress for 10.9 grade bolts. It can be concluded that, even if the manufacturing process provided stronger bolts than the commercial range, the obtained mechanical properties are not as high as 10.9 grade.

Finally the actual design of the structure was done using the following maximum load values; 3,100 kN for the M80 Nuclos, 4,000 kN for the M90 Nuclos and 5,000 kN for the M100 Nuclos. These values are

Figure 8. Bolt M80-A Nuclos after being tested.

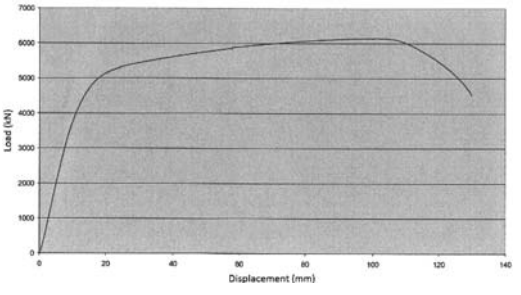

Figure 9. Load-displacement curve of the M100-A test.

equivalent to using 750 MPa as yield stress, which is a save simplification of the strength observed in the experimental work.

3 ASSEMBLY AND LIFTING OF THE STRUCTURE

The designed space truss comprised 12,362 tubes and 3,062 spheres that had to be connected by means of Nuclos joints. Additionally, a secondary structure, used to support the external cladding, had to be assembled. The structural tubes were up to 10 meters long with an outer diameter between 50 and 273 mm and a weight up to 1500 kg. The diameters of the spheres were ranged between 100 and 450 mm with a weight ranging between 4 and 375 kg each.

The assembly and lifting of the space truss was planned to be performed in 6 months but finally it was achieved in 5 months. The construction work was successfully finished on time thanks to the ease offered by bolted joints that require on-site welding only in supports.

The weight of the whole structure – 1,000,000 kg– laid on several steel columns, two arch shape steel welded trusses and two concrete walls. The concrete

Table 2. Experimental results of Nuclos joints.

Sample	Bolt size (m)	Sphere diameter (mm)	Elastic range load (kN)	Maximum load (kN)	Failure mode
M80-A	80	200	3500	4763	Breakage in bolt's threads.
M80-B	80	200	3600	4787	Breakage in bolt's threads.
M90-A	90	240	4500	6156	Breakage in bolt's stud.
M90-B	90	240	4700	6264	Breakage in bolt's stud.
M90-C	90	360	4300	5517	Breakage in bolt's stud.
M100-A	100	300	4700	6145	Breakage in bolt's stud.
M100-B	100	300	5400	6989	Breakage in bolt's stud.
M100-C	100	300	5400	6906	Breakage in bolt's stud.
M100-D	100	360	5000	6427	Breakage in bolt's stud.
M100-E	100	360	5400	7341	Breakage in bolt's stud.
M100-F	100	360	5500	7301	Breakage in bolt's stud.

walls, located at both ends of the 155 meters span door, sized 9 meters long, 1.1 meters wide and 25 meters high. The welded trusses were located by the concrete walls and consisted in two 36 meters long arches. Both concrete walls and welded trusses were used to brace the whole building. Due to the huge horizontal loads transmitted to the concrete walls, special sliding supports were designed. Figure 10 shows these sliding supports.

On ground assembly was initiated from the central part of the front arch, adding previously assembled pyramidal groups to reach the final height. Then, the space truss under the future arch was assembled. Once the central part of the arch was finished, the rest of the arch was added by means of cranes (Figure 11).

Usually space trusses are lifted in several parts using cranes; however, due to the complexity of this hangar, it was decided to lift the whole space truss between the concrete walls in one operation using hydraulic jacks. Two hydraulic jacks able to move 200,000 kg each were placed on top of the concrete walls, another two jacks with the same capacity were located on the

Figure 10. Sliding supports used on the top of the supporting structure.

Figure 11. Central part of the arch assembled on ground.

Figure 12. Main hydraulic jacks used for the elevation.

welded trusses and twelve additional hydraulic jacks of 100,000 kg each were used on the top of several steel columns. Some of the jacks were used to lift the main space truss to its final position, while the rest were employed to keep the balance of the structure during

Figure 13. General view of the structure during lifting.

the lifting process. Figure 12 shows two of the main hydraulic jacks used for lifting the structure.

The main structure was lifted in two stages. First, the space truss was lifted only 50 cm from the ground and was kept in that position during 24 hours. This manoeuvre was performed in order to check the deformations of the structure assuring that it was working correctly. After measuring the deformed shape, the space truss was steadily lifted to its final position in 8 hours. Figure 13 shows the supporting structure and the main space truss during the elevation process.

Several check-stops were carried out during the elevation. Once the main space truss was in its final position, the supports were assembled and the hydraulic jacks were removed. Then, the remaining parts of the space truss were lifted by cranes and added to the main part.

4 CONCLUSIONS

A heavy maintenance hangar was designed by Asteca Estructuras using the space truss as structural solution. The structure was designed with 155 meters span and able to support four overhead cranes of 60,000 kg each. This paper presents the main design features and the assembly and lifting carried out in this project.

New Nuclos bolted joints were developed able to transmit up to 5,233 kN. However, the experimental results indicated that the manufacturing process can be improved and the strength of this joint type could be further increased.

Asteca Estructuras is currently working in the improvement of the Nuclos system, which includes increasing the strength further and enhancing the dynamic behaviour of this bolted connection.

REFERENCES

Del Campo, F. Ausin, J. Castañeda, N. Vela, F. Gómez, J. & Bujan, I. 2003. Steel structure in Bilbao Exhibition Centre. *Proceedings of the 10th International Symposium on Tubular Structures, September 2003, Madrid (Spain).*

Kaya, T. Özyar, H. & Akman, M. 2010. A380 aircraft hangar with a clear span of 96 m and the new Amiry terminal in Kuwait Airport. *International Symposium "Steel Structures: Culture and Sustainability". September 2010, Istambul (Turkey).*

Martínez Calzón, J. & Ladrón de Guevara, G. 2003. Main roof structures in the extensión and remodelling of the Valencia Exhibition Centre (Spain). *Proceedings of the 10th International Symposium on Tubular Structures, September 2003, Madrid (Spain).*

Pareto, L. 1991. Formulario de mecánica. Barcelona. Ediciones Ceac. ISBN 84-329-3403-8.

Tubular Structures XIV – Gardner (Ed.)
© 2012 Taylor & Francis Group, London, ISBN 978-0-415-62137-3

Design and construction of long-span post-tensioned tubular steel structures

M.E. Ellen
Warren Centre for Advanced Engineering, University of Sydney, Australia

J. Gosaye, L. Gardner & M. Ahmer Wadee
Department of Civil & Environmental Engineering, Imperial College London, UK

ABSTRACT: The design of long-span post-tensioned tubular steel structures in which steel cables are housed within the hollow profiles is outlined from fundamental principles. Treatment of the structural form as a planar catenary is discussed and then extended to three dimensional shell structures. The effect of post-tensioning on the behaviour of individual members is examined through numerical and analytical modelling. The influence of the bonding material between the post-tensioned cable and tubular casing is discussed, since this is crucial to the performance of these structures. The construction methodology is outlined and examples of implemented structures spanning up to 120 m are presented.

1 INTRODUCTION

The current drive towards sustainable development now places a high level of importance on the reduction of embodied energy within the construction industry. The World Steel Association (WSA) has identified that steel production accounts for 3–4% of the World's greenhouse gas emissions and that 1.8 tonnes of CO_2 are emitted for every tonne of steel produced (WSA, 2011). Post-tensioned tubular steel structures, which have the ability to store energy under increasing preload can achieve reduced material consumption and hence a greatly reduced carbon footprint. The development of such structural solutions is outlined in the current paper.

This paper builds upon the fundamental principles of the equilibrium of arches and shows how these principles may be applied to post-tensioned steel structures. Post-tensioning of cables and cable net structures that are integrated into the structural form generates a preload condition that controls deflection. Controlling deflection in this manner substantially reduces the amount of material required in the construction of long-spanning structures. Tubular elements are fundamental to this form of construction since the post-tensioning cables are housed within the structural profiles.

The design solution of two dimensional post-tensioned arches is firstly investigated, followed by the application of post-tensioning technology to three dimensional shell structures.

2 FUNDAMENTAL PRINCIPLES

One of the main factors that determines the maximum load carrying capacity of an arch is its shape (O'Dwyer, 1999). Robert Hooke was the first philosopher to identify that the most efficient shape of an arch can be derived from the loads acting upon it. In 1675, he presented his solution to the Royal Society in the form of an anagram, 'As hangs a flexible line, so inverted will stand the rigid arch' (Huerta, 2006). Antonio Gaudi, some 200 years later became perhaps the best known exponent of this philosophy by creating hanging chains with lead shot masses contained in bags to simulate the weight of masonry (Huerta, 2006). The shape created by the chain could then be inverted to generate the line of thrust along which compressive forces are transmitted to the ground. Ingeniously, he placed a mirror under the hanging chain model to construct the arches of the Colonia Gueli Church (Huerta, 2006).

Various methods of obtaining the thrust line have been proposed, but one of the most commonly adopted methods is the graphical method of the funicular polygon (Heyman, 1982). The solution is obtained by constructing a force polygon of all the forces acting on the structure. Figure 1(a) shows the structure under consideration. Figure 1(b) shows the force polygon diagram, with the position of the centre O representing the unknown horizontal reaction. The lines radiating from this centre indicate the inclinations of the weightless chain at various sections, as illustrated in

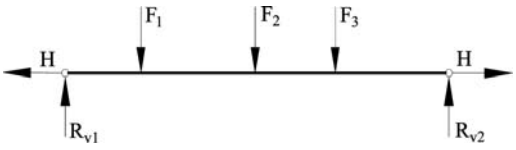

Figure 1a. Vertical forces acting on flexible chain model.

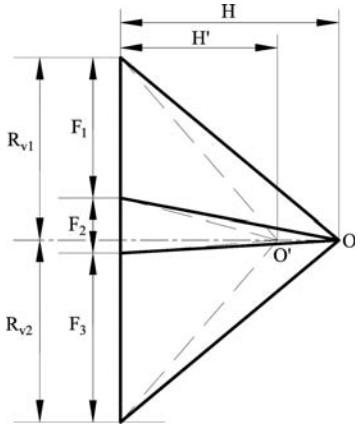

Figure 1b. Funicular force polygon constructed by assuming a value for the horizontal thrust H.

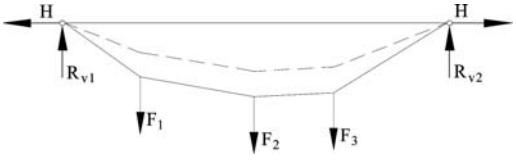

Figure 1c. Hanging chain model obtained using force polygon model.

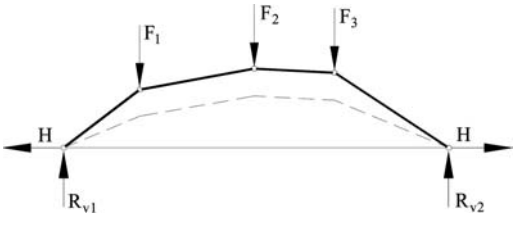

Figure 1d. Resultant thrust line when the chain model is inverted.

Figure 1(c). Finally, using Hooke's analogy, the hanging chain is inverted to give the thrust line shown in Figure 1(d). Since the horizontal reaction force can take any value, an infinite number of thrust lines can be generated for the applied loading (Heyman, 1982); the larger the horizontal reaction, the shallower the arch.

Since an arch provides support to the applied loads through compression, masonry and concrete were the original materials of choice for the construction of arches. However, owing to the relative ease and reduced construction time associated with steel structures, growing interest is now placed on the use of steel in the construction of arches (Nazir, 2003).

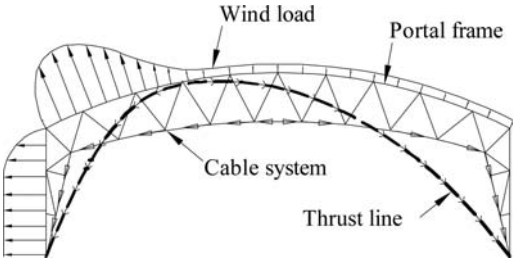

Figure 2. Application of thrust line analysis to the design of a portal frame.

Thrust line analysis is a powerful tool that can be used to design a wide range of long-spanning steel structures. Figure 2 illustrates how thrust line analysis may be applied to the design of a portal frame for an aircraft hangar.

The distributed uplift wind load in Figure 2 is applied to a weightless chain of a chosen length; using the funicular polygon method discussed earlier, the shape and tension within the chain is determined. The length of the chain is typically chosen in order to ensure that the bottom chord of the frame is always under tension during wind uplift. Inverting the resultant hanging chain gives the thrust line. It should be noted that consideration of other load cases would result in the formation of different thrust lines, from which an average thrust line can be chosen for design.

If the structure were to be built along the thrust line, it would not be subjected to bending and thus a minimum amount of material would be required to support the design loads. However, structures designed in this way, while minimising the required material, may not provide the desired space. Instead, structures, such as the hangar in Figure 2, are built to satisfy the spatial requirements by designing against the bending moments that would arise due to the lever arm between the structure and the thrust line.

3 POST-TENSIONING

Application of the post-tensioning technique to the construction of trusses is described in this section. The post-tensioned cables are located within the bottom chord of the tubular trusses and apply a compressive force to the chord members, which is opposite in nature to the resultant forces arising from the externally applied gravity loads. The capacity of the truss is maximized since the tensile strength of the lower chord is only utilized after the compressive force induced by the post-tensioned cables has been exceeded.

3.1 *Construction methodology*

As with all construction, it is imperative that the load cases which arise during assembly are given

Figure 3a. Step 1 – Construction of tubular truss components.

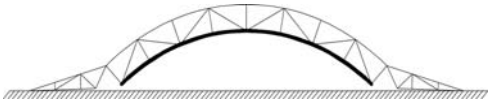

Figure 3b. Step 2 – Post-tensioning of cables encased in the bottom tubular steel chord, altering the shape of the centre span.

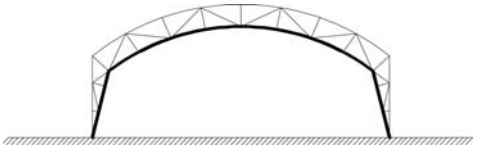

Figure 3c. Step 3 – Connection and posttensioning of the column structure to required level.

due consideration; this is especially important in this type of structure since a significant amount of force is applied to the elements through post-tensioning of the cables. Furthermore, from practical experience, designing the buildability of a structure into the architecture is vital for achieving a successful outcome. With this in mind, the following procedure has been carefully devised for the construction of post-tensioned steel frames (Ellen, 1987).

1. Construct the tubular trussed main span and connecting columns at ground level.
2. Post-tension the cables encased within the bottom chord of the centre span to obtain the required shape. The segmental length of the lower chord (i.e. the distance between the vertical/diagonal members) determines the curvature of the upper and lower chords; therefore the segmental length may be varied at the design stage to obtain the desired shape.
3. Assemble the remaining column structure to form the complete frame, connecting the bottom chord cables of the centre span to those of the column structure and post-tensioning them further. The void space between the cables and the tube is then grouted with cementitious material such as Portland cement with chemical additives.

The ability to control deflections is at the heart of a successful solution to long-spanning steel structures. Figure 4 illustrates the pre-load condition generated due to the introduction of post-tensioned cables in the bottom chord. The resultant pre-load condition, shown by the inward pointing arrows, provides resistance against deflection as well as wind uplift. An 84 m span example of such a structure is shown in Figure 5, while a smaller 25 m span temporary structure is shown in Figure 6.

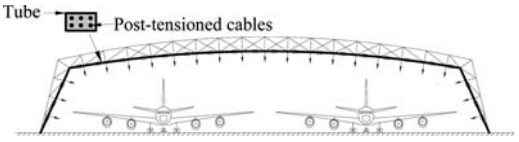

Figure 4. Post-tensioning of cables contained within the bottom chord result in pre-load condition to control deflection.

Table 1. Properties of elements of the numerical model.

Property	
Length L_o	1000 mm
Cross-sectional area of cable A_c	120 mm^2
Cross-sectional area of tube A_t	750 mm^2
Young's modulus of cable and tube E	210 000 N/mm^2
Yield strength of tube f_{ty}	250 N/mm^2
Yiled strength of cable f_{cy}	2100 N/mm^2

Figure 5. Aircraft hangar, with an 84 m clear span, constructed through the implementation of the post-tensioning technique.

3.2 *Behaviour of post-tensioned elements*

A study has been conducted to investigate the behaviour of individual post-tensioned tubular members. The aim was to establish the effect of the bonding material and pre-load on the stiffness and axial load carrying capacity. Figure 7 shows a numerical simulation of a segment of a post-tensioned chord. The chord, which is a Grade 250 circular hollow section, is bonded to the post-tensioned cables using high strength grout. The properties of the tube and cable are given in Table 1.

Figure 8 shows the numerical results when tensile strain is applied to a chord member with varying levels of post-tension forces within the embedded cables. As the graph demonstrates, the axial load carrying capacity is substantially increased when post-tension is applied to the cables. This can be attributed to the fact that the compressive force imposed by the post-tensioning of the cables must first be overcome before the chord member begins to utilize its tensile strength.

Figure 8 shows that the magnitude of the post-tension affects not only the ultimate axial load carrying capacity but also initial axial stiffness prior to yielding.

Figure 6. A temporary enclosure with a 25 m clear span.

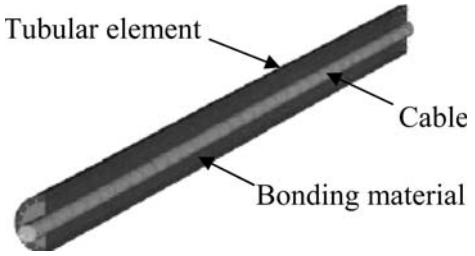

Figure 7. Post-tensioned tubular element.

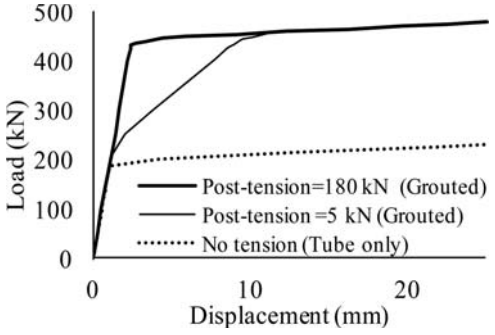

Figure 8. Numerical results for axial load carrying capacity of a post-tensioned chord member.

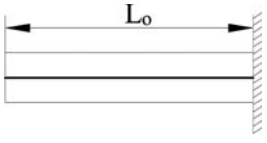

Figure 9. Dimensions of chord before post-tensioning.

Experimental studies are planned to investigate this behaviour and to assess the influence of the grouting material.

An analytical model was also devised to represent the behaviour of post-tensioned elements by considering the different stages of the post-tensioning and subsequent load application processes. The following points describe how an expression for the relationship between axial load and displacement is obtained for the case where the tube yields first.

Post-tensioning:

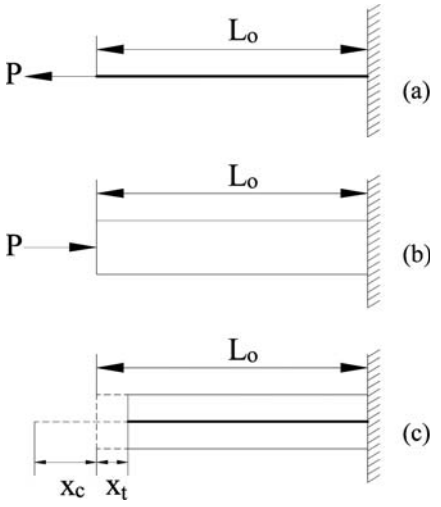

Figure 10. Post-tensioned cable (b) Compressed tube. (c) Dimensions of tube and cable after post-tensioning.

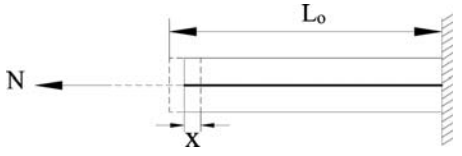

Figure 11. Tensile loading prior to initial precompression in tube being overcome.

Stage 1: Initial position

Initially, the length of the tube L_t and the cable L_c are equal, as illustrated on Figure 9, hence:

$$L_t = L_c = L_o \tag{1}$$

Stage 2: After post-tensioning

After post-tensioning, the cable is in tension and tube is in compression, with the system self-equilibrating under internal forces P.

From Figure 10(c), the lengths of the tube and cable after post-tensioning are given by Eqs (2) and (3) respectively, in which x_t is the displacement of the compressed tube and x_c is the extension of the tensioned cable.

$$L_t = L_o - x_t = L_o - \frac{PL_o}{A_t E} \tag{2}$$

$$L_c = L_o + x_c = L_o + \frac{PL_o}{A_c E} \tag{3}$$

Tensile load application:

Stage 1: $L_t \leq L_o$

As Figure 11 illustrates, in this region of axial strain, the compressed tube unloads to its original length whilst the cable is being stretched further.

Assuming that the tube is not compressed beyond its yield load, the axial displacement x_1 and axial force N_1

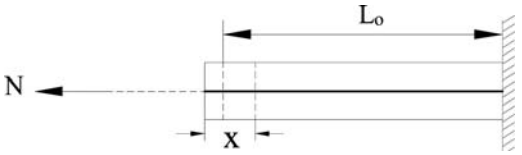

Figure 12. Tensile loading after cable fully unloads initial compression.

when the tube fully unloads ($L_t = L_o$) can be expressed by Eqs (4) and (5) respectively.

$$x_1 = x_t = \frac{PL_o}{A_t E} \tag{4}$$

$$N_1 = K_c\left(x_c + x_t\right)$$

$$\text{where } K_c = \frac{A_c E}{L_o} \tag{5}$$

Stage 2: $L_o \le L_t \le L_{ty}$

For this range of axial displacements, shown in Figure 12, both the cable and tube are in tension.

When the tube yields in tension the axial displacement x_2 and axial force N_2 are given by Eqs (6) and (7) respectively.

$$x_2 = x_1 + x_{ty} = x_1 + \frac{f_{ty}L_o}{E} \tag{6}$$

$$N_2 = N_1 + (K_c + K_t)\frac{f_{ty}L_o}{E} \tag{7}$$

where $K_t = \frac{A_t E}{L_o}$

Stage 3: $L_{ty} \le L_t \le L_{cy}$

In this region of axial displacement the tube is strain hardening whilst the cable utilises its elastic axial stiffness to resist tensile loading. When the cable yields in tension the axial displacement x_3 and axial force N_3 are given by Eqs (8) and (9) respectively.

$$x_3 = x_{cy} - x_c = \frac{f_{cy}L_o}{E} - \frac{PL_o}{A_c E} \tag{8}$$

$$N_3 = A_c f_{cy} + A_t f_{ty} + K_{c,st}\left(x_3 - x_2\right) \tag{9}$$

where $K_{c,st}$ is the strain hardening stiffness of cable.

Stage 4: $L_t \ge L_{cy}$

Both the cable and the tube will be strain hardening for axial displacements x in this range; the corresponding axial force N_4 is given by Eq (10).

$$N_4(x) = K_{st}\left(x - x_3\right) + N_3 \tag{10}$$

where K_{st} is the strain hardening stiffness of cable and tube.

The obtained analytical results, using the properties of Table 1, are compared in Figure 13 with the numerical results of Figure 8 showing a close match. It should be noted that a drop in stiffness due to the yielding of the tube is usually greater than the case when the cable yields first since axial stiffness is directly proportional to the cross-sectional area and the cross-sectional area of the tube is typically larger than the cross-sectional area of the cables.

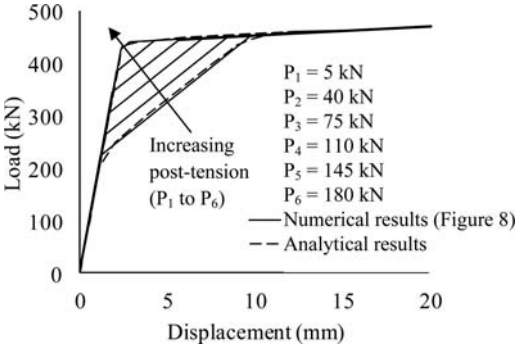

Figure 13. Comparison between analytical and numerical results for the axial response of a post-tensioned chord member.

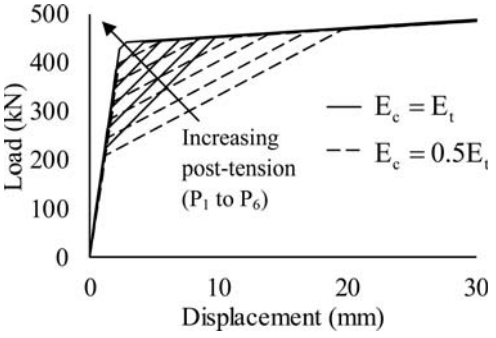

Figure 14. Analytical results showing influence of varying ratio of Young's modulus of the cable to that of the tube.

To gain further insight into to the behaviour of post-tensioned chord members, the parameters that define the axial stiffness of the cable and the tube were altered. The material properties given in Table 1 and post-tensioning values as shown in Figure 13 were used as a control for this investigation. The results shown in Figure 14 are for the case in which the Young's modulus of the cable is halved from the value given in Table 1. In Figure 15, the cross-sectional areas of the tube and the cable were chosen such that the ultimate yield load, defined herein as the load at which both the tube and the cable yield, is kept constant while the ratio of cable to tube cross-sectional area is altered.

Figure 14 shows that when the Young's modulus of the cable is reduced the tube yields at a lower load and that the stiffness drop after the tube yields is more significant.

Figure 15 shows that the tube yields at a lower load and a higher displacement when the ratio of the cross-sectional area of the tube and cable decreases; both observations can be attributed to the fact that the

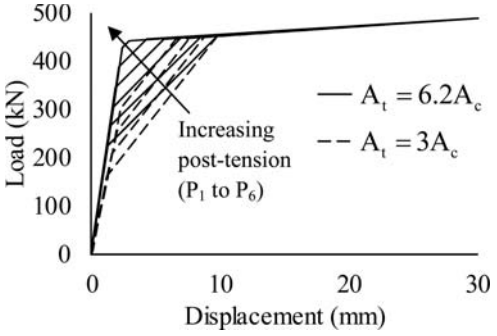

Figure 15. Analytical results showing the influence of the variation of the relative areas of tube and cable.

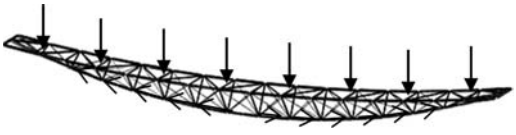

Figure 16. Component of the roof structure of the Sydney Olympic Stadium.

overall cross-sectional area was reduced to ensure that the ultimate yield load was kept constant. Figure 15 also shows a stiffer response of the structure after the yielding of the cable which is due to the increase in the cross-sectional area of cable. Note in Figure 15 that, for the lower cross-sectional area of the tube ($A_t = 3A_c$) the post-tension levels P_5 and P_6 were found to be beyond the compressive yield load of the tube which would introduce inelastic deformation; post-tension levels P_5 and $P_6$are therefore excluded from the graph.

3.3 *Reverse loading*

For structures where the dominant loads are downward, the chain model can again be inverted to find the optimal curvature to resist vertical loading through tensile action. Figure 16, which is part of the roof structure of the Sydney Olympic Stadium, illustrates how the vertical force may be transmitted to the supports through tensile action. Application of post-tensioned cables within the tubular bottom chord can again further enhance the structural system.

3.4 *Application to shells and other structures*

Through the extension of the inverted chain philosophy, solutions to three dimensional shell structures can also be achieved. Figure 17 illustrates, just as in the hanging chain, how a hanging net adopts a shape when subjected to its self-weight and perhaps some wind loading. Following Hooke's principle, the net could then be inverted to give the shape of the shell which can efficiently support the applied load. However, unlike the flexible chain, the hanging flexible net has multiple thrust paths which enable it to carry a wider range of load without changing its shape (Heyman, 1977). And thus the inverted shape can support significant amount

Figure 17. Hanging net forms the thrust surface for a shell when inverted, in similar manner to Hooke's inverted chain.

Figure 18. Aircraft hangar with a shell type roofing constructed using intersecting tubular arches.

of loading without incurring significant bending in any part.

The thrust line analysis of structures becomes complicated when three dimensional forces are involved such as in the case of shell structures (O'Dwyer, 1999). Several attempts have been made to determine the stability of masonry shells which require the thrust surface to be contained within the thickness of the shell since the material used in masonry construction such as stones and concrete have negligible tensile strength. One of the simplest, but also safe, approaches that can be used in the analysis of shell structures is a slicing technique. The analysis checks the overall stability of the masonry shell by dividing it into discrete sections and checking their equilibrium (Heyman, 1977). A more complex analysis of masonry shells which is attracting increasing interest is the force network model. Just as in the funicular polygon method for the analysis of arches, this model discretizes the loads. However, for shells an optimization procedure is required to determine the thrust surface and the collapse load factor. (O'Dwyer, 1999)

Reducing force equilibrium to a two dimensional problem, as in the slicing technique described earlier, the first author has designed and constructed several shell structures. Figure 18 shows an aircraft facility with shell type roofing that was constructed using intersecting truss arches which were designed using the post-tensioning technology described earlier.

3.5 *Comparison with conventional methods*

Owing to the relatively large structural members associated with long-spanning steel structures, the ease

Figure 19. Award winning post-tensioned aviation hangar with a 78 m clear span erected with minimal assembly time.

Figure 20. Erecting a shell structure made using post-tensioned LSB members without cranes.

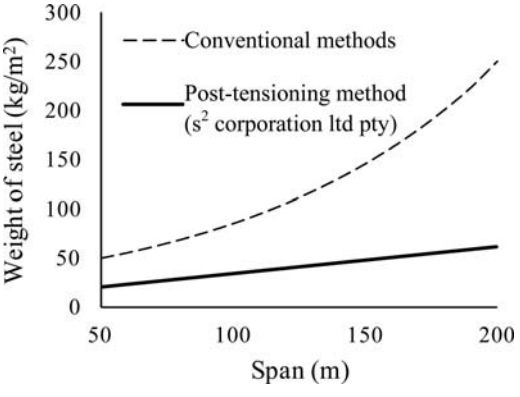

Figure 21. Illustrative comparison between conventional construction methods and the new post-tensioning technology.

of transportation of structural components during the assembly of the structure is important. The post-tensioning technique reduces the total weight of the structure considerably, thereby minimising the time and cost spent on erecting the structure using cranes. Figure 19 shows a 78 m span post-tensioned portal frame being erected using just two cranes. The innovative solution led to an award, from the Australian Steel Institute.

Post-tensioning has also been employed in conjunction with LiteSteel Beams (LSB), which are cold-formed channel sections with tubular flanges, to form shell structures (Keerthan and Mahendran, 2010). The post-tensioning cables are fitted inside the hollow flanges of the LSB member. Steel sheeting or other roofing fabrics can be installed at ground level. Shell structures with areas up to $35\,m \times 35\,m$ can be erected using lifting tripods, as shown in Figure 20, in less than 2 hours, without the need for cranes.

The first author has constructed over 30 structures with a wide range of configurations and spans using the post-tensioning technology discussed. Figure 21 provides an approximate graphical comparison of the weight of steel as a function of span of the structure for construction using conventional methods and the new design solution. Clearly there is significant potential benefit to be gained through application of the post-tensioning technology.

4 CONCLUSIONS

The addition of post-tensioned cables housed within the tubular chords of steel trusses has been shown herein to offer effective and efficient structural solutions. Application of thrust line analysis to the design of planar frames and three dimensional shell structures is discussed. The funicular force polygon diagram method was found to be a suitable means of obtaining the thrust line of tubular trussed arches. By designing shell structures with intersecting vaults, the three dimensional problem can be simplified using the slicing technique.

Post-tensioned cables induce compressive forces in tubular chord members which are opposite in nature to the forces caused by the imposed loading; the preload must first be overcome before the tensile capacity of the tubular chord members is utilised, enabling lighter sections to be used. This behaviour was demonstrated by means of numerical and analytical models.

A series of examples for a range of structures from around the world have been presented to demonstrate successful application of the post-tensioning technology.

REFERENCES

Ellen, P.E. 1987. *Post-tensioned steel structure*. US 4,676,045 (Patent)

Heyman J. 1977. Equilibrium of shell structures, Oxford, Oxford University Press

Heyman, J. 1982. *The masonry Arch.* West Sussex, England, Ellis Horwood Limited

Huerta, S. 2006. Structural Design in the Work of Gaudi. *Architectural Science Review*, 494 (4), 324–339

Keerthan P., Mahendran M. 2010. Experimental studies on the shear behaviour and strength of LiteSteel beams. *Engineering Structures*, 32(10), 3235–3247

Nazir, C.P., 2003. Prestressed Arch Bridge., *Institute of Engineers (India) Journal*, 84, 72–76

O'Dwyer, D., 1999. Funicular analysis of masonry vaults. *Computer and Structures*, 73 (1–5), 187–197

Troitsky, M.S., 1990. *Prestressed Steel Bridges Theory and Design*. New York (USA), Van Nostrand Reinhold

World Steel Association (WSA). 2011. *World steel in s 2011*. Available from: http://www.worldsteel.org [Accessed online 24/10/2011]

Structural behaviour

Tubular Structures XIV – Gardner (Ed.)
© 2012 Taylor & Francis Group, London, ISBN 978-0-415-62137-3

Effect of cross sectional configurations on the bending strength of Hollow Flange Beams

A. Ibrahim, A. Shaat, A. Matloub & A. Dessouki
Ain Shams University, Cairo, Egypt

ABSTRACT: In the past decade, the use of Hollow Flange Beams (HFB) has found many applications in the building industry because of their advantages compared to the common C and Z cold-formed sections. Failure of HFBs is governed mainly by Lateral Distortional Buckling (LDB) prior to achieving their full bending strength. The current study aims at optimizing the cross sectional configurations of HFBs for performance improvement. Therefore, a finite element model has been developed to investigate the effect of different geometrical configurations on the bending strength of HFBs. Values for the hollow flange aspect ratio ranging from 0.67 to 0.80 are recommended for better cross sectional utilization. Finally, a modification to the HFB slenderness equation, presented in the AS/NZS-4600 (2005) standards, is proposed to accurately predict the bending strength of HFBs.

1 INTRODUCTION

Different types of hollow flange beams have been developed over the past two decades. These types include either triangular or rectangular hollow flanges, as shown in Figure 1.

Both HFB sections are manufactured from a single sheet strip using a combined process of cold-forming and dual electrical resistance welding. This unique profile avoids many of the problems commonly associated with other cold-formed sections such as flange local buckling, while maintaining a high level of structural efficiency.

For laterally unsupported HFBs, the weakness of the slender web compared to the torsional rigidity of the hollow flange promotes the failure by lateral distortional buckling prior to achieving the beam's lateral torsional buckling strength.

Triangular hollow flange beams were first introduced during the 90s and researchers investigated their behavior (PI & Trahair (1997)). Design rules have also been developed to predict their bending capacity (AS/NZS-4600 (2005)).

In the last decade the production of triangular hollow flange beams has stopped and the rectangular hollow flange beams were introduced.

The rectangular HFB sections, as shown in Figure 2, are commonly produced in Australia but are limited to certain cross sectional configurations. Most of these sections have depth of hollow flange, d_f, equal to one third the width of the flange, b. In addition, the depth between the two center lines of the hollow flanges, d_c, is equal to 0.375 of the total plate width forming the HFB section, L_p.

Many researchers investigated the behavior of rectangular HFBs either as axially loaded columns (Wilkinson et al. (2006)) or as flexure members (Avery et al. (2000), Mahendran & Mahaarachchi (2005a,b) & Poologanathan & Mahendran (2009)).

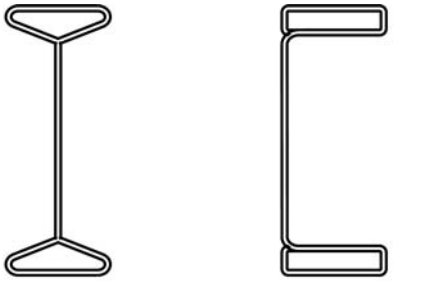

Figure 1. Different types of HFB.

Although the geometric configuration of HFB is the main parameter affecting its capacity, no researches have been done to optimize this configuration for best performance against LDB.

This paper presents the results of a finite element analysis carried out to explore the optimum cross sectional configurations that maximize the HFB bending strength. The paper also aims at examining the use of available standards equations to predict the strength of various cross sectional configurations of HFB.

2 FINITE ELEMENT MODELING OF HFB

Finite element analysis was performed using the commercial package ABAQUS. A finite element model (FEM) that takes into account geometric and material

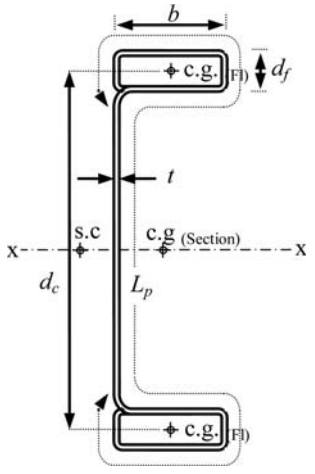

Figure 2. Geometric parameters of HFB.

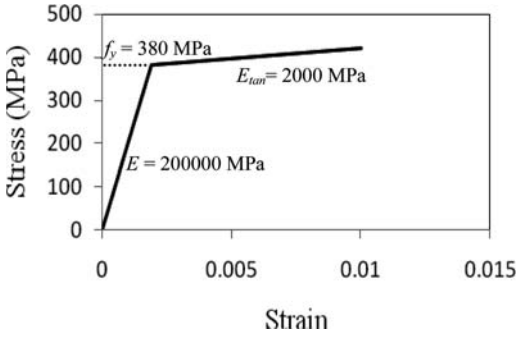

Figure 3. Bi-linear stress-strain curve.

non linearities, geometric imperfections, and residual stresses has been developed.

Two analyses were performed, namely, elastic buckling analysis and non-linear analysis.

Nominal center line dimensions were used to model the HFB sections. The corner radius was also neglected in the model for simplicity. Winatama & Mahendran (2008) reported that this simplification has an insignificant effect on the results obtained from the finite element model.

2.1 *Elements and material properties*

S4R5 shell element was selected for the FEM as it is capable of providing sufficient degrees of freedom to accurately model the buckling deformations. This element is a thin, shear flexible, isoparametric quadrilateral shell with four nodes, and five degrees of freedom per node with reduced integration. An element size of 5 mm × 10 mm was used to provide adequate accuracy (Mahendran & Mahaarachchi (2005a,b)).

A plasticity model based on a simplified bilinear stress-strain curve with strain hardening was assumed for modeling steel material, as shown in Figure 3.

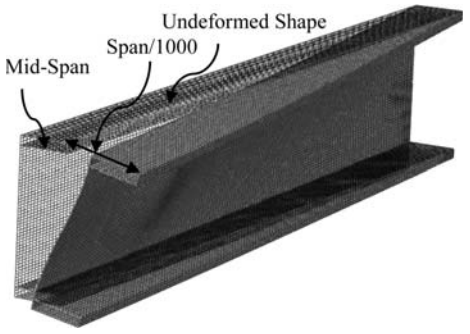

Figure 4. Geometric imperfection shape.

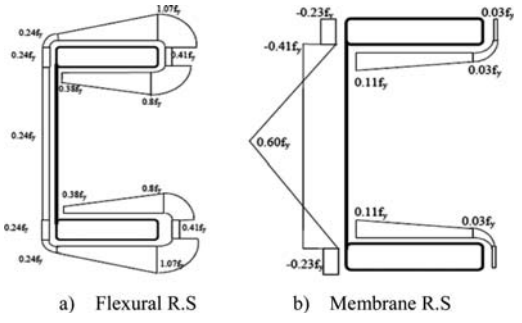

Figure 5. Idealized residual stress distribution for HFB sections (Seo et al. (2008)).

The mechanical properties were assumed based on the manufacturer's specifications (yield stresses of web $(f_y)_{web} = 380$ MPa, yield stress of flange $(f_y)_{flange} = 450$ MPa, Young's Modulus for steel $(E) = 200000$ MPa, and a Poisson's ratio $(\nu) = 0.25$).

2.2 *Initial geometric imperfections and residual stresses*

As shown in Figure 4, an initial geometric imperfection was modeled based on the buckling eigenvector obtained from the elastic buckling analysis. The imperfection for lateral distortional buckling includes lateral displacement, twist rotation, and cross section distortion at mid-span.

The mid-span cross section was modeled with the largest imperfection value of span/1000 being the Australian standards maximum allowed fabrication tolerance.

Both flexural and membrane residual stresses were introduced according to the ideal distribution proposed by Seo et al. (2008), as shown in Figure 5. The residual stress is expressed as a ratio of the virgin plate's yield stress (f_y) value of 380 MPa. Figure 6 shows the residual stress contours on the FEM.

2.3 *Loading and boundary conditions*

Figure 7 shows that four-point loading scheme is adopted in this study to develop pure moment on the

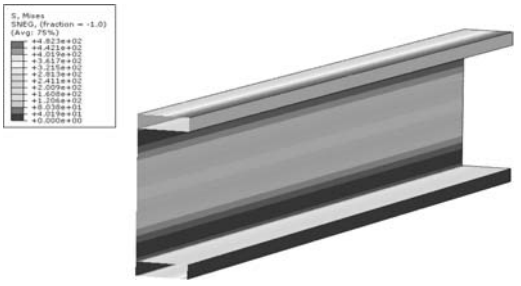

Figure 6. Residual stress contours for finite element modelling.

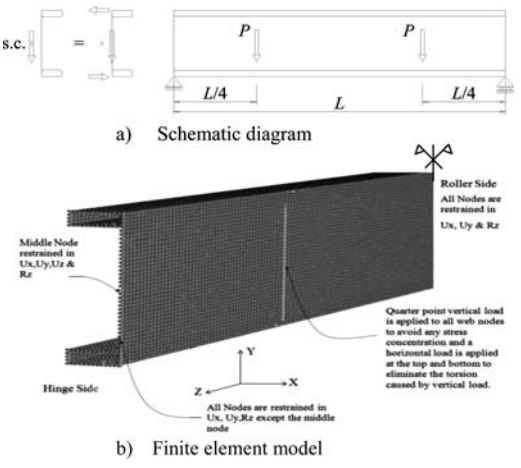

Figure 7. Loading and boundary conditions.

central half of the span. In addition, the loads are applied at the shear center to ensure that there is no additional torsion on the beam.

2.4 *Finite element model validation*

The finite element model was validated using three independent experimental studies (Mahendran & Mahaarachchi (2006), Anapayan & Mahendran (2009) & Winatama & Mahendran (2008)).

Table 1 shows the dimensions of eight specimens as well as a comparison between their experimental and predicted ultimate moments, M_{EXP} and M_{FEM}, respectively.

The variation between the FEM and experimental ultimate moments lies within a range of $\pm 10\%$, as shown in Figure 8. Table 1 shows an average ratio and its standard deviation value as 1.03 and 0.05, respectively.

3 PARAMETRIC STUDY

The validated model was used to carry out an extensive parametric study to evaluate the effect of different cross sectional parameters on the flexural strength of

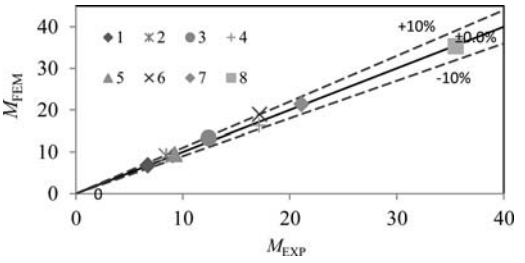

Figure 8. Comparison between experimental and FEM results.

HFB. All specimens were chosen to have a constant thickness of 2 mm.

A total of 84 specimens were used in this research to study the following parameters:

1. The ratio between the depth of the hollow flange and its width [$d_f/b = 0.2$ to 1.0].
2. The ratio between the depth between the two centerlines of the hollow flanges to the overall plate width [$d_c/L_p = 0.3$ to 0.5].
3. The overall width of the plate forming the beam cross section [$L_p = 360$, 480, and 650 mm].
4. The span of the beam [$L = 4000$, 6000, and 8000 mm].

Two analysis methods were used with each FEM specimen, namely, elastic buckling analysis and nonlinear analysis. The elastic buckling analysis is used to determine the critical buckling moment, M_{od}, as well as the buckling eigenvector for imperfections modeling, while the non linear analysis is used to determine the ultimate moment, M_u.

4 RESULTS

Table 2 lists the values of both (M_u) and (M_{od}) for all specimens. The following sections discuss the effect of each parameter of d_f/b, L_p, L, and d_c/L_p on the bending strength of the HFB.

4.1 *Effect of flange aspect ratio, d_f/b, on the strength of HFB sections*

One of the main parameters in this study is the aspect ratio of the flange. Values ranging from 0.2 to 1.0 were given to the flange depth-to-width ratio, d_f/b. The lowest value was taken equal to 0.2 to allow for rolling and welding operations, while the highest value was taken not exceeding 1.0 to simulate the practical cases.

Figures 9, 10, and 11 show curves illustrating the relationship between the flange depth-to-width ratio, d_f/b, versus the normalized ultimate moment, M_u/M_y, where M_y is the moment initiating yielding at the extreme tension/compression fibers of the full section ($M_y = S_x \text{ x} f_y$).

The results are plotted for specimens spanning 4000 mm and having web depth-to-plate width ratio, d_c/L_p, equal to 0.375 and 0.423.

Table 1. Comparison between experimental results and FEA results.

ID	Reference	Section Dimensions (mm) d_c	d_f	b	t	L (mm)	M_{FEM} (kN.m)	M_{EXP} (kN.m)	M_{FEM}/M_{EXP}
1	Mahendran & Mahaarachchi (2006)	135	15	45	1.6	3000	6.82	6.72	1.01
2		135	15	45	2.0	3000	9.09	8.45	1.08
3		180	20	60	2.0	3500	13.30	12.41	1.07
4		180	20	60	2.5	4000	16.30	17.13	0.95
5	Anapayan & Mahendran (2009)	185	15	45	1.6	3000	9.46	9.24	1.02
6		280	20	60	2.0	4000	18.89	17.17	1.10
7	Winatama & Mahendran (2008)	230	20	60	2.0	3500	21.40	21.10	1.01
8		230	20	60	2.0	3500	35.30	35.50	0.99
							Average	1.03	
							S.D.	0.05	

Table 2. Results of finite element analyses.

M_u/M_{od} (kN.m) / L_p(mm)	L(mm) / d_c/L_p / d_f/b*	4000					6000		8000	
		0.300	0.375	0.400	0.423	0.500	0.375	0.423	0.375	0.423
360	0.20	7.55/8.10	5.58/5.18	5.04/4.68	5.18/4.96	3.65/3.10	4.92/3.43	–	–	–
	0.33	9.63/11.44	7.89/8.45	6.58/6.73	6.34/6.50	4.72/4.71	6.08/5.82	–	–	–
	0.50	10.50/13.45	9.06/10.03	8.12/8.75	7.51/7.46	5.15/5.24	7.11/7.05	–	–	–
	0.67	10.90/13.90	9.28/10.26	8.40/9.04	7.69/8.15	5.35/5.46	7.32/7.25	–	–	–
	0.80	10.90/13.50	9.08/9.99	8.30/8.94	7.60/8.04	5.43/5.32	7.17/7.06	–	–	–
	1.00	10.90/13.32	8.87/9.96	8.15/8.60	7.45/7.81	4.96/5.03	6.99/6.83	–	–	–
480	0.20	–	13.40/14.72	–	11.30/12.03	–	10.40/10.23	–	8.94/7.80	–
	0.33	–	15.80/18.58	–	13.00/14.44	–	12.90/13.64	–	10.87/10.64	–
	0.50	–	16.90/20.58	–	14.30/16.30	–	14.37/15.52	–	12.27/12.30	–
	0.67	–	17.10/20.73	–	14.50/16.72	–	14.66/15.85	–	12.59/12.63	–
	0.80	–	17.20/20.63	–	14.50/16.48	–	14.79/15.83	–	12.67/12.63	–
	1.00	–	16.60/19.72	–	14.20/15.98	–	14.20/15.11	–	12.12/12.05	–
650	0.20	–	24.10/30.83	–	22.41/26.96	–	–	19.18/20.84	–	16.40/16.63
	0.33	–	26.38/34.61	–	23.71/29.06	–	–	21.30/23.96	–	18.80/19.83
	0.50	–	27.20/35.92	–	23.80/29.76	–	–	22.10/25.52	–	20.17/21.68
	0.67	–	27.50/36.60	–	23.74/29.80	–	–	22.45/25.77	–	20.45/22.03
	0.80	–	27.40/36.18	–	23.67/29.68	–	–	22.56/25.85	–	20.69/22.23
	1.00	–	26.60/34.91	–	22.89/29.23	–	–	22.50/25.43	–	20.24/21.53

* d_f/b values are approximated. Actual values may be slightly different to avoid modeling fractions of millimeters.

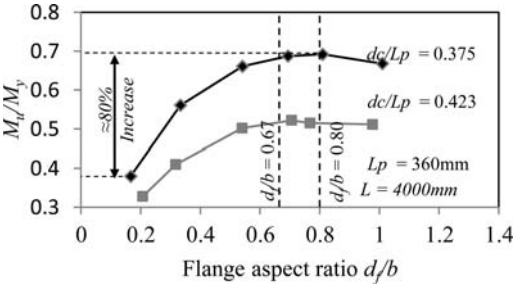

Figure 9. Flange aspect ratio, d_f/b, versus normalized ultimate moment, M_u/M_y, for models with $L_p = 360$ mm.

Figures 9, 10 and 11 show that as the flange aspect ratio, d_f/b, increases M_u/M_y increases until it reaches a nearly constant region at d_f/b values ranging from 0.67 to 0.8. The beams' capacity starts to slightly decrease afterwards.

4.2 *Effect of web depth-to-plate width ratio, d_c/L_p, on the strength of HFB sections*

Another main parameter is considered in this sudy which is the web depth-to-plate width ratio, d_c/L_p. This ratio is assumed to range from 0.3 to 0.5. The lowest value of 0.3 was considered because values less than 0.3 will lead to a great loss in the major inertia about x-x axis that will affect the serviceability of the beam. The highest value of 0.5 was taken because any value above 0.5 will lead to a more slender web.

Figure 12 shows the relationship between web depth-to-plate width ratio, d_c/L_p, versus the normalized ultimate moment, M_u/M_y, for L_p equals 360mm and L equals 4000 mm.

Figure 12 shows that the normalized ultimate moment of beams decreases with the increase of the beam d_c/L_p ratio. This decrease is due to the decrease in the lateral stiffness of the flanges. The figure shows that the ultimate capacity of the beam deteriorates

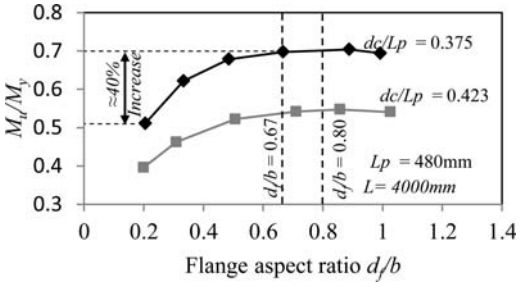

Figure 10. Flange aspect ratio, d_f/b, versus normalized ultimate moment, M_u/M_y, for models with $L_p = 480$ mm.

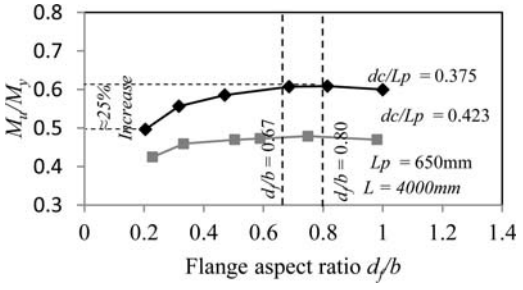

Figure 11. Flange aspect ratio, d_f/b, versus normalized ultimate moment, M_u/M_y, for models with $L_p = 650$mm.

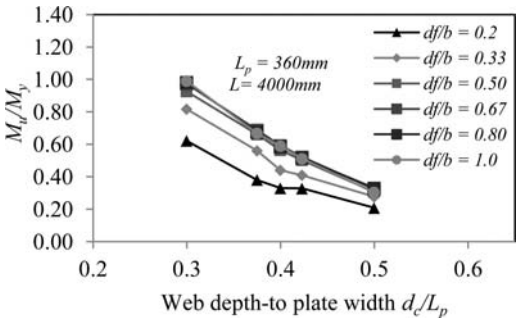

Figure 12. Web depth-to-plate width ratio, d_c/L_p, versus normalized ultimate moment, M_u/M_y.

down to less than 40% of its yielding moment at d_c/L_p equal to 0.50.

4.3 *Effect of plate width, L_p, on the strength of HFB sections*

Table 2 indicates that increasing the plate width, L_p, increases the beam ultimate moment, for all the spans investigated in this study. However, figures 9 to 11 show that the increase in M_u/M_y of HFB gained by increasing d_f/b decreases as L_p increases. For the same d_c/L_p (equal to 0.375), the percentage increases in flexural capacity are 80%, 40%, and 25% for L_p equal to 360, 480, and 650, respectively. This decrease is mainly due to the reduction in the web stiffness

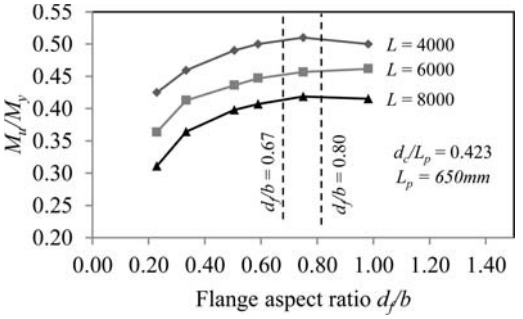

Figure 13. Flange aspect ratio, d_f/b, versus normalized ultimate moment, M_u/M_y.

in supporting the lateral buckling of the flange by increasing L_p.

4.4 *Effect of beam span, L, on the strength of HFB sections*

To ensure that all HFBs follow the same behavior discussed in the previous sections despite having different spans, L, the d_f/b were plotted versus the normalized ultimate moment, M_u/M_y, as shown in Figure 13. For three beams having d_c/L_p equal to 0.423, L_p equal to 650mm, and having three different spans and the same behavior can be recognized.

5 FAILURE MODES

There are three modes of failure for any HFB section according to its slenderness, λ_d, (AS/NZS-4600 (2005)), These modes are clearly indicated by three zones, as shown in Figure 14, and can be described as follows:

- Yielding associated with local buckling for short spans.
- Lateral distortional buckling for intermediate spans.
- Lateral torsional buckling for long spans.

Figure 14 indicates that the slenderness of HFB (λ_d) is a very important characteristic in predicting their failure modes. The slenderness of HFB can be calculated according to the current design rules of AS/NZS-4600 (2005) as follows:

$$\lambda_d = \sqrt{\frac{M_y}{M_{od}}} \qquad (1)$$

The Finite element results of all specimens investigated at this study are also plotted in figure 14. It is clear that the specimens lie mostly in the intermediate region, where the lateral distortional buckling is the predominant mode of failure. While few specimens experienced lateral torsional buckling (λ_d>1.7), no specimens succeeded to reach the yielding zone.

In the following sections, the effects of both d_f/b and d_c/L_p on the slenderness value are discussed.

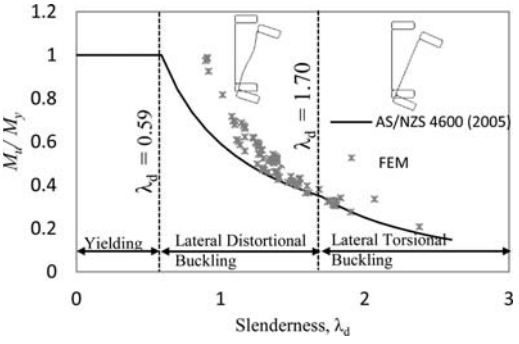

Figure 14. Comparison between FEM results & AS/NZS4600.

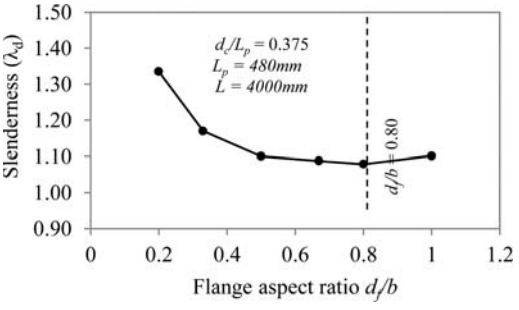

Figure 15. Flange aspect ratio, d_f/b, versus the slenderness of HFB, λ_d.

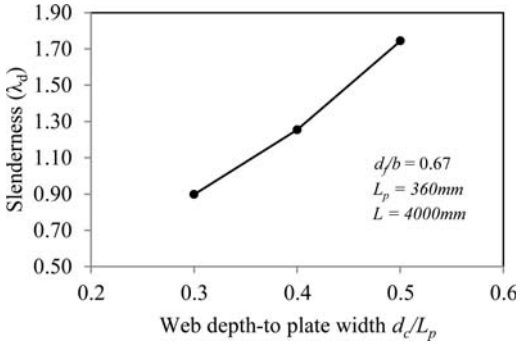

Figure 16. Web depth-to-plate width ratio, d_c/L_p, versus the slenderness of HFB, λ_d.

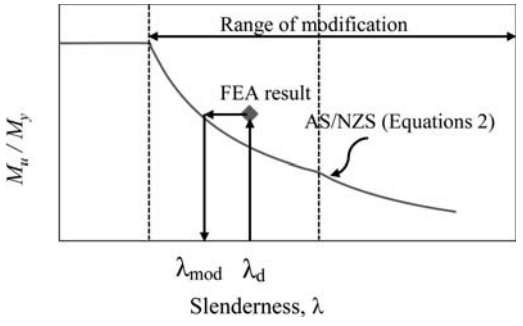

Figure 17. Modification process for slenderness value.

5.1 *Effect of d_f/b on the slenderness of HFB*

Six specimens were investigated having L_p equals 480 mm, d_c/L_p equal to 0.375, L equal to 4000 mm, and d_f/b ranging from 0.2 to 1.0.

The slendernesses of these specimens were plotted against the flange aspect ratio, d_f/b, as shown in Figure 15. It is clear that a value of 0.8 for the aspect ratio of the flange is corresponding to the lowest slenderness value.

5.2 *Effect of d_c/L_p on the slenderness of HFB*

Three specimens were investigated having L_p equals 360 mm, L equals 4000 mm, d_f/b equal to 0.67, and d_c/L_p equal to 0.3, 0.4, and 0.5, respectively.

The slenderness values of these specimens were plotted against the web depth-to-plate width ratio, d_c/L_p, as shown in Figure 16. It is clear that as the web depth-to-plate width ratio increases the slenderness of HFB increases.

6 REVIEW OF AS/NZS-4600 (2005) DESIGN EQUATIONS

Most of the current standards set design equations for the common C or Z cold formed sections. These design equations account for beams failure due to local buckling, distortional buckling, or lateral torsional buckling. The Australian/New Zealand Standards (AS/NZS-4600 (2005)) was found to be the only standards that accounts for the failure mode of lateral distortional buckling. These standards are used in this study to calculate the critical moment of HFB as these sections are susceptible mainly to lateral distortional buckling. The AS/NZS-4600 (2005) standards provide the following equations to calculate the beams critical moment, M_c:

$$\text{For } \lambda_d \le 0.59 \quad : \quad M_c = M_y \qquad (2a)$$

$$\text{For } 0.59 < \lambda_d \le 1.70 : \quad M_c = M_y \left(\frac{0.59}{\lambda_d} \right) \qquad (2b)$$

$$\text{For } \lambda_d > 1.70 \quad : \quad M_c = M_y \left(\frac{1}{\lambda_d^{\,2}} \right) \qquad (2c)$$

6.1 *Proposed modification for the calculation of HFB slenderness values*

Figure 14 shows that the current design rules applied for HFB are conservative and need to be modified to reflect the actual behavior of HFB with different geometric parameters.

Two approaches may be followed to adjust the observed conservation of the AS/NZS standards. The first approach is to modify equations (2b) and (2c), which is currently under investigation by the authors. The second approach is to keep the standards equations

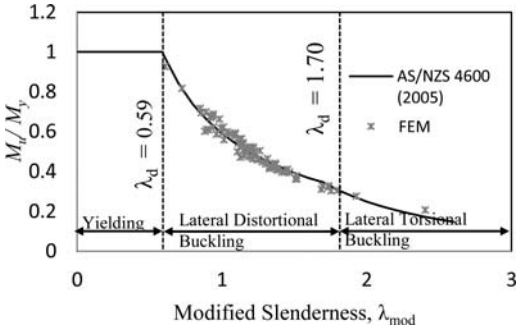

Figure 18. Comparison between modified plot of FEM results (using λ_{mod}) and AS/NZS 4600(2005).

while utilizing modified slenderness values (λ_d). The second approach is adopted in this study as described below.

For calculating the critical moment, M_c, (using equations 2) a modified slenderness, λ_{mod}, is used instead of the slenderness, λ_d, this modification is proposed as a function of the geometric configuration of the HFB.

The modified slenderness is calculated using Equations 2b and 2c by replacing M_c with M_{FEM}.

Figure 17 shows a schematic representation for the process adopted to modify the slenderness values to be applied for HFB sections according to the (AS/NZS-4600 (2005)) equations.

This modified slenderness, λ_{mod}, takes into account the geometric parameters presented in this study (d_c/L_p& d_f/b). A non-linear regression analysis between λ_{mod} and three independent variables (d_c/L_p, d_f/b, and λ_d) was carried out to introduce a formula for calculating, λ_{mod}, as follows:

$$\lambda_{mod} = 1.872\,(d_c/L_p) - 0.133\,(d_f/b) + 0.939(\lambda_d) - 0.744 \quad (3)$$

The slenderness, λmod, is calculated using equation (1) and M_{od} can be calculated using finite strip method or simplified equation suggested by PI & Trahair (1997).

The relation between the modified slenderness, λ_{mod}, and the variables d_c/L_p, d_f/b, and λ_d has a coefficient of multiple determination (R^2) equal to 0.96 and a standard error of 0.064. These values prove the high reliability of the newly introduced equation for slenderness, λ_{mod}.

Figure 18 shows that using the modified slenderness in the current design rules (AS/NZS 4600 (2005)) can accurately predict the bending capacity of HFB with different geometric configurations.

7 CONCLUSIONS

This paper presents a detailed investigation to study the best geometric configurations for the HFBs. The flange aspect ratio is found to be the most important parameter affecting the behavior of HFB sections. The lowest slenderness associated with the highest bending strength of the HFBs was achieved when the hollow flange aspect ratio equals to 0.8. For flange aspect ratio with values higher than 0.8, it was found that the lateral moment of inertia of the compression flange decreases and no further increase in the bending strength is recognized. It was, however, found that values for the flange aspect ratio ranging from 0.67 to 0.80 achieve reasonably high bending strength and thus recommended. Another parameter affecting the behavior of HFB sections is the web depth-to-plate width ratio. It is found that the lower the d_c/L_p ratio the higher the beam bending strength. The lowest practical web depth-to-plate width ratio that does not violate the deflection requirements is found to be 0.30.

Finally, slenderness modification that takes into account various cross sectional parameters is proposed based on the results of the FEM. This slenderness modification can accurately predict the bending strength of HFBs.

REFERENCES

Anapayan, T., & Mahendran, M. 2009. Improvements to the design of Litesteel Beams undergoing lateral distortional buckling. *9th International Conference on Steel Concrete Composite and Hybrid Structures* .

AS/NZS-4600. 2005. *Austalia/New Zealand Standard for Cold Formed Sections.*

Avery, P., Mahendran, M., & Nasir, A. 2000. Flexural Capacity of Hollow Flange Beams. *Journal of Constructional Steel Research* .

Design Capacity Tables For LiteSteel Beams. 2007. LiteSteel Technologies.

Mahendran, M., & Mahaarachchi, D. 2006. Development, Behavior & Design of LiteSteel Beams. *4th International Symposium on Steel Structures ISSS '06* .

Mahendran, M., & Mahaarachchi, D. 2005a. Lateral Buckling Tests of LiteSteel Beam Sections. *Report No.1, Queensland University of Technology* .

Mahendran, M., & Mahaarachchi, D. 2005b. Section Capacity Tests of LiteSteel Beam Sections. *Report No.2, Queensland University of Technology* .

PI, & Trahair. 1997. Lateral Distortional Buckling of Hollow Flange Beams. *Journal of Structural Engineering* .

Schafer, B., & Pekoz, T. 1998. Computational Modeling of Cold-formed Steel. *Journal of Constructional Steel Research*.

Seo, J. K., Anapayan, T., & Mahendran, M. 2008. Initial Imperfection Characteristics of Mono-Symmetric LiteSteel Beams for Numerical Studies. *Proceedings 5th International Conference on Thin-Walled Structures : ICTWS 2008* .

SIMULIA. *Abaqus 6.9 Documentation.*

Wilkinson, T., Zhu, Y., & Yang, D. 2006. Behaviour of Hollow Flange Channel Sections Under Concentrated Loads. *Tubular Structures XI- Packard & Willibald (eds)*, (pp. 187-194).

Winatama, C., & Mahendran, M. 2008. Effect of Moment Gradient on The Strength of LiteSteel Beams. *Eleventh East Asia-Pacific Conference on Structural Engineering & Construction (EASEC-11)* .

Winatama, C., & Mahendran, M. 2009. Elastic Lateral Buckling of Simply Supported LiteSteel Beams Subject to Transverse Loading. *Thin-Walled Structures* .

Tubular Structures XIV – Gardner (Ed.)
© 2012 Taylor & Francis Group, London, ISBN 978-0-415-62137-3

First order elastoplastic GBT analysis of tubular beams

M. Abambres, D. Camotim & N. Silvestre
Department of Civil Engineering and Architecture, ICIST, Instituto Superior Técnico, Technical University of Lisbon, Lisbon, Portugal

ABSTRACT: This paper aims to present an original formulation of Generalised Beam Theory (GBT) intended to perform first order elastoplastic analysis of thin-walled members, made of isotropic non-linear material and subjected to arbitrary deformation. The J_2-flow theory is used to model plasticity in conjunction with the Euler-Backward return-mapping algorithm. After presenting the formulation, its application is illustrated by means of the first order analysis of beams with (i) Rectangular Hollow Section (RHS) and (ii) LiteSteel section, made of an elastic-perfectly plastic material and subjected to distributed and point loading, respectively. The GBT results, which include equilibrium paths, displacement profiles, stress diagrams, 3D stress/displacement contours and deformed shapes, are compared with the ones obtained by ABAQUS code using a shell finite element model. GBT and ABAQUS results display a very good agreement.

1 INTRODUCTION

Materials with non-linear behaviour (e.g. metals) are widely used in construction industries, like civil, mechanical and aeronautical engineering. This use is due to the fact that these materials are able to simultaneously assure outstanding properties such as strength, stiffness, ductility and tenacity. These high performance properties often lead to the design of structural elements displaying thin walls and rather slender cross-sections and exhibiting high susceptibility to local deformations. One very interesting thin-walled steel member is the LiteSteel beam (LSB), which has a channel section combining two hollow flanges and a slender web. This shape has proven to be very competitive in comparison with hot rolled profiles.

The numerical determination of accurate collapse loads of structural members has been only possible by means of shell finite element (FE) analyses using non-linear constitutive laws and incremental-iterative techniques. Since this task requires time-consuming procedures, a very promising alternative to this approach is the use of one-dimensional models (beam FE) based on Generalised Beam Theory (GBT). Currently, GBT is widely recognized by the scientific community as a powerful, versatile, elegant and efficient thin-walled beam theory. It is valid for prismatic bars only and its elegance arises from the fact that the displacements field is obtained as a linear combination of cross-section deformation modes, which can be carefully determined and whose amplitudes along the longitudinal axis are the problem unknowns. Until the end of last century, GBT was developed to perform first order and linear stability analysis. Since 2002, GBT has attracted the interest of several researchers, which led to the development of new formulations and applications. In this regard, *Camotim et al*. (2010) successively developed, validated and illustrated the application of GBT to (i) stability and vibration analyses of orthotropic members, and (ii) post-buckling analyses of isotropic members. The theory has been extensively upgraded at the Technical University of Lisbon (*Camotim et al*. 2010) and has been applied to distinct materials (steel, steel-concrete, FRP). In these contributions, the material was always assumed elastic, with no degradation (plasticity) involved. The first physically non-linear GBT formulation was presented by *Gonçalves and Camotim* (2004), in the context of elastoplastic bifurcation analysis. Recently, *Gonçalves and Camotim* (2011a, b) proposed a finite element based on the J_2-flow plasticity theory in the context of GBT.

Abambres et al. (2011a) developed a GBT first order formulation for the elastic-plastic analysis of members undergoing only global (axial, bending, torsion) deformation. In order to overcome this limitation, the formulation presented in this paper (i) is valid for a non-linear isotropic material subjected to arbitrary (local and/or global) deformation, and (ii) is based on the J_2-flow plasticity theory. Although this plasticity theory was already considered in the aforementioned work of *Gonçalves and Camotim* (2011a, b), the GBT formulation presented herein is based on different types of deformation modes (see section 2). In order to illustrate the application of this formulation, analyses of RHS and LSB fixed-pinned beams made of elastic-perfectly plastic material were performed. In section 3, GBT equilibrium paths and several displacement/stress results are compared with the ones

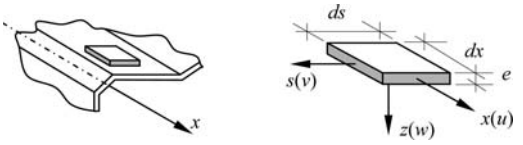

Figure 1. Local coordinates at each section wall.

yielded by ABAQUS software (*Simulia* 2004) using a shell FE model.

2 BRIEF OVERVIEW OF GBT FORMULATION

Due to space limitations, the GBT formulation is briefly presented in this section. The interested reader is referred to detailed information in *Abambres et al.* (2011a, b). A GBT analysis of a structural element consists of two main stages: (i) a cross-section analysis followed by (ii) a member analysis. One of the features that better characterize this theory is its modal nature, since the displacement field is obtained as a linear combination of cross-section deformation modes. These modes approximate the displacements along the cross-section mid-line (*s* coordinate). Fig. 1 illustrates the local coordinates and displacements used in GBT. The cross section analysis considered in this work is based on the approach developed by *Silva et al*. (2008), which consists of (i) 4 deformation mode families obtained via different eigenvalue problems and (ii) 4 dof per cross-section node (three displacements and one transverse flexural rotation). Although these mode families are considered in the present formulation, the initial (elementar) deformation modes are based on a set of 5 degrees-of-freedom (dof) per cross-section node[1] . Besides the usual 4 dof per node, the present formulation also includes a rotation corresponding to a vector contained in the cross-section plane, which is an original contribution of the present work. This new dof, called warping rotation, is used in each node and wall direction, making it possible to approach the warping profile u(s) by means of piecewise Hermite cubic polynomials, instead of usual piecewise linear functions (*Abambres et al.* 2011a).

The GBT equilibrium equation states that

$$\delta V = \delta U + \delta \Pi = 0 \tag{1}$$

It is well known that the achievement of a non-linear equilibrium path requires the use of an incremental-iterative strategy. Consider a generic bar FE and its incremental relation of an arbitrary point of the equilibrium path

$$\Delta f^{\,\mathrm{int}} = \Delta f \Leftrightarrow K_{\tan}\Delta d = \Delta\lambda\,\bar{f} \tag{2}$$

where f^{int} is the internal force vector, λ is the load parameter and K_{tan} is the tangent stiffness matrix at the equilibrium point. Due to use of a non-linear constitutive law σ (ε), the stress-displacements relations σ (d) are non-linear. Thus, the relation expressed by (2) can be determined based on the "linearization" of relations $\sigma(d)$, such that

$$\Delta\sigma_{mn} = \frac{\partial\sigma_{mn}}{\partial d_i}\Delta d_i \tag{3}$$

where σ_{mn} is a generic 2nd Piolla-Kirchhoff stress component. Since (i) these components depend on the deformation components ε, (ii) ε depend on the longitudinal deformations χ (*Abambres et al.* 2011a), and (iii) χ depend on the generalized displacements d(unknowns of the FE method), relation (3) can be rewritten as

$$\Delta\sigma_{mn} = \left(\begin{array}{l} \dfrac{\partial\sigma_{mn}}{\partial\varepsilon_{xx}}\dfrac{\partial\varepsilon_{xx}}{\partial\chi_{(xx)k}}\dfrac{\partial\chi_{(xx)k}}{\partial d_i} + \\ \dfrac{\partial\sigma_{mn}}{\partial\varepsilon_{ss}}\dfrac{\partial\varepsilon_{ss}}{\partial\chi_{(ss)k}}\dfrac{\partial\chi_{(ss)k}}{\partial d_i} + \\ \dfrac{\partial\sigma_{mn}}{\partial\gamma_{xs}}\dfrac{\partial\gamma_{xs}}{\partial\chi_{(xs)k}}\dfrac{\partial\chi_{(xs)k}}{\partial d_i} \end{array} \right)\Delta d_i \tag{4}$$

where k and i are indexes related with the deformation mode k and the component i of displacements vector d (satisfying the summation convention). The gradients $\partial\varepsilon/\partial\chi$ are given by the sectional deformations E (*Abambres et al.* 2011a) and $\partial\chi/\partial d$ depend on the type of approximation chosen for the FE. In this work, it is based on the Hermite cubic polynomials (Ψ_H) and is given by

$$\zeta_k^{\,v,w\neq 0}(x) = \Psi_H(x)\,d_k \tag{5}$$

$$\zeta_{k,x}^{\,v,w=0}(x) = \Psi_H(x)\,d_k \tag{6}$$

where $k$denotes the deformation mode k, Eq. (5) is related to all the modes k with in-plane displacements ($v, w \neq 0$), Eq. (6) is related to axial and warping shear modes only ($v, w = 0$) and d_k is the elementar displacements vector (4×1). Once defined the FE approximation, the insertion of Eqs. (4)–(6) in Eq. (1) gives rise to the incremental equilibrium relation

$$\begin{aligned} &K_{\tan}\Big|_j \Delta d = \Delta\lambda\,\bar{f} \\ &K_{ik,\tan}\Big|_j = K_{ik,\tan}^{xx} + K_{ik,\tan}^{ss} + K_{ik,\tan}^{xs} \end{aligned} \tag{7}$$

where the component $i-k$ of the tangent stiffness matrix is a 4×4 sub-matrix related to modes $i$and k and is defined in *Abambres et al.* (2011b) for the equilibrium point j. However, it is important pointing out that expressions presented in that work are not valid for axial and warping shear modes. The way to obtain the components $i-k$ due to those modes consists in replacing the correspondent vectors Ψ and their derivatives

[1] Every node defined in the cross-section (natural or intermediate) will be designated in this paper as "section node".

by vectors with an order of differentiation reduced by 1 (check Eqs. (5)–(6)).

In order to complete the definition of all the variables needed to perform an incremental-iterative procedure, it is also necessary to define the vector of internal forces for a generic point at the equilibrium path, which arises from the first member of Eq. (1), if Eqs. (5)–(6) are taken into account. For all modes displaying in-plane displacements, the component k (4×1 sub-vector) of the elementar (FE with length L_e) internal force vector at the jth equilibrium point is obtained by

$$f_k^{\text{int}}\Big|_j = \int_{L_e} \left\{ \begin{array}{l} F_{(xx)k}\left(\Psi^k_{H,xx}\right)^T + F_{(ss)k}\left(\Psi^k_{H}\right)^T + \\ F_{(xs)k}\left(\Psi^k_{H,x}\right)^T \end{array} \right\} dx \quad , \tag{8}$$

$$F_{(mn)k} = \int_b \int_e \mathrm{E}_{(mn)k}\, \sigma_{mn}\Big|_j dz ds$$

The way of defining the components related to axial and warping shear modes is identical to the aforementioned procedure regarding tangent stiffness matrix.

Concerning the plasticity model, it was considered a J_2-flow theory with associated flow rule (*Borst and Sluys* 2007). In order to compute the tangent stiffness matrix presented in Eq. (7), the consistent elastoplastic constitutive matrix D^{ep*} was used (*Abambres et al.* 2011b), which is known to reduce the computational cost of the incremental-iterative procedure when compared to the conventional constitutive matrix (*Borst and Sluys* 2007).

In order to compute the tangent stiffness matrix and the internal forces vector defined in Eqs. (7)–(8), one must be able to update stresses and the plastic proportional factor at any point and any equilibrium instant. For that purpose, a robust return-mapping scheme should be used for those points that undergo plastic flow during a deformation increment. In this work, the Euler-backward method based on a Newton-Raphson scheme was considered (*Borst and Sluys* 2007). The GBT formulation was implemented using MATLAB (R2010a) software (*MathWorks* 1998).

3 ILLUSTRATIVE EXAMPLES

Next, two illustrative examples are presented and the GBT results are compared with the ones yielded by ABAQUS (*Simulia* 2004) using S4 shell FE model. The cross-section dimensions are referred to section mid-line. The material behavior is linear elastic-perfectly plastic and isotropic (Young modulus $E = 200000\ \text{N/mm}^2$, Poisson ratio $\nu = 0.3$, uniaxial nominal yield stress $\sigma^y = 450\text{N/mm}^2$). In order to perform an effective comparison between GBT and ABAQUS results, 3 points of the equilibrium path ($\lambda - \delta$ curve) were selected, namely: (A) elastic, (B) elastoplastic and (C) plastic. In order to make a correct comparison between GBT and ABAQUS stress results, it is worth pointing out that all GBT normal stress outputs were transformed to true stresses in post-processing. However, GBT Von Mises stresses were based on nominal stress components as those were the ones used when implementing J_2-flow theory. The stresses distributions and displacements profiles are obtained at $z = 0$ and correspond to membrane type (see Fig. 1).

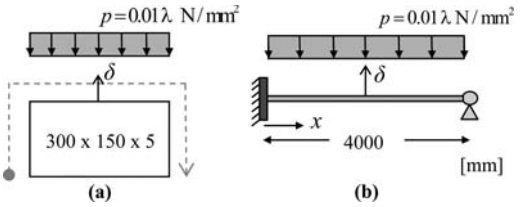

Figure 2. (a) Section dimensions, loading and (b) structural mode.

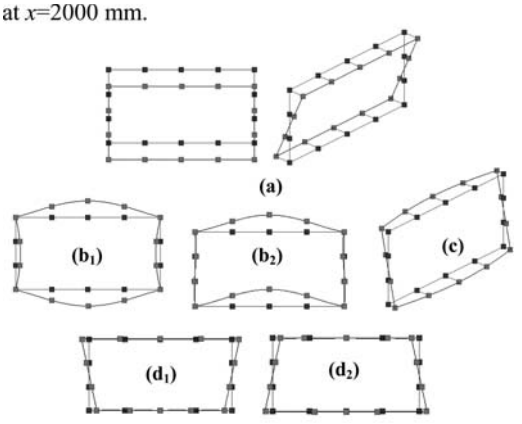

Figure 3. Some GBT relevant modes: (a) global, (b_1; b_2) local, (c) warping shear, (d_1; d_2) transverse extension.

3.1 *RHS beam*

Consider the RHS fixed-pinned beam depicted in Fig. 2. The beam has a length $\mathrm{L} = 4000$ mm and is acted by an uniformly distributed load $p = 0.01\lambda\ \text{N/mm}^2$ (Fig. 2(b)) applied at the top flange (Fig. 2(a)). Only 17 (out of 74) modes were used in the GBT analysis. The RHS node discretization used in GBT, as well as some of the most relevant modes, are represented in Fig. 3. Regarding FE models, (i) 16 beam FE's were used in GBT model (6 FE's in $x \leq$ 0.15L and 10 FE's in $x >$ 0.15L) and (ii) 160 "transverse rows" of 36 shell FE's were used in ABAQUS model. For the numerical integration purposes, (i) 5 Gauss points were used in all directions (s, z, x) of the GBT model and (ii) 5 Gauss points were used in through-thickness direction of the ABAQUS FE model. All stress diagrams presented in this example are referred to the section located at $x = 1996$ mm (see Fig. 2(b)) and to the section path depicted by the arrowed line in Fig.2(a).

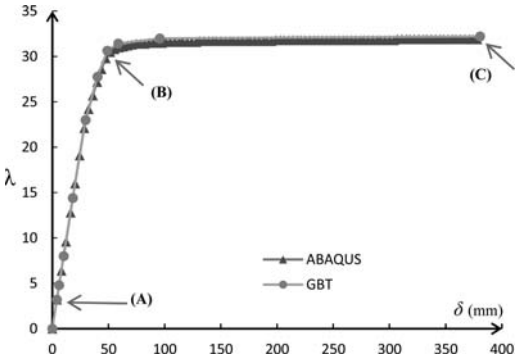

Figure 4. Load-displacement equilibrium path.

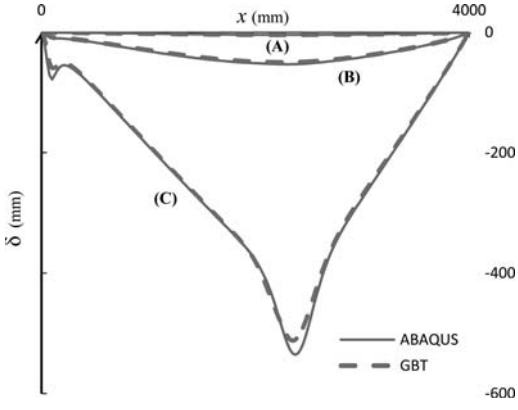

Figure 5. Displacement profiles for points A, B and C.

In Fig. 4, the equilibrium paths $\lambda(\delta)$ obtained by GBT and ABAQUS are presented, where δ is the monitoring displacement represented in Fig. 2 and located at $x = 2000$ mm.

It is observed that the$\lambda(\delta)$ curves yielded by GBT and ABAQUS compare very well, with the maximum difference never exceeding 1.6%. The 3 equilibrium points chosen to compare the results correspond to the following load parameters (see Fig.4): (A) $\lambda_{GBT} = 3.20$, $\lambda_{ABQ} = 3.20$, (B) $\lambda_{GBT} = 0.63$, $\lambda_{ABQ} = 30.50$ and (C) $\lambda_{GBT} = 32.21$, $\lambda_{ABQ} = 31.90$.

Fig. 5 depicts the displacement profiles $\delta(x)$ of section node indicated in Fig. 2(a) and show a very satisfactory agreement between ABAQUS and GBT. Regarding point C, the difference at the maximum absolute displacement is about 4.5%. In Fig. 6. the axial stress diagrams for points A and C are presented. Whereas for point A there is a quite satisfactory agreement between GBT and ABAQUS for the whole domain of the cross-section, for point there are notorious similarities along the top flange ($150 \leq s \leq 450$ mm) but relevant differences at the webs ($0 \leq s \leq 150$ mm and $450 \leq s \leq 600$ mm). However, one should bear in mind that point C is the one where load parameter λ has greater difference between ABAQUS and GBT, and the results regarding

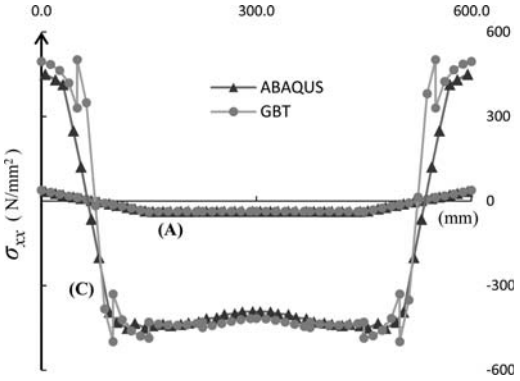

Figure 6. Axial stresses ($x = 1996$ mm) for points A and C.

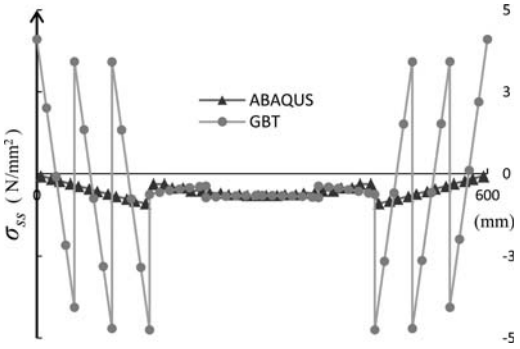

Figure 7. Transverse stresses ($x = 1996$ mm) for point A.

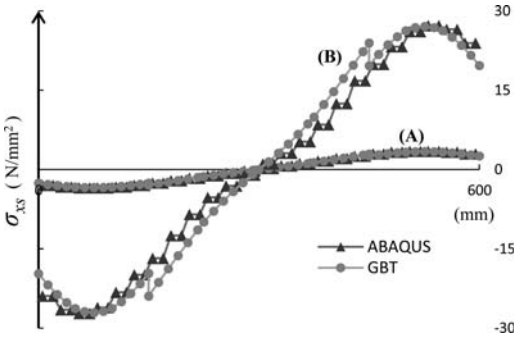

Figure 8. Shear stresses ($x = 1996$ mm) for points A and B.

the plastic response are more susceptible to numerical errors.

Fig. 7 depicts the transverse stress diagrams for point A, where the resemblance is quite satisfactory along the top flange ($150 \leq s \leq 450$ mm), but there are huge discrepancies along the webs ($0 \leq s \leq 150$ mm and $450 \leq s \leq 600$ mm). Despite these dissimilarities, it can be noticed that the mid-points of GBT lines are very close to ABAQUS diagram. The existence of these notorious discrepancies may be attributed to the use of linear functions to approximate the transverse (v) displacements between section nodes. Additionally, the

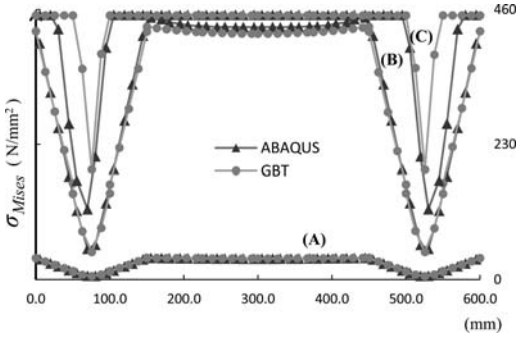

Figure 9. Mises stresses ($x = 1996$ mm) for points A, B and C.

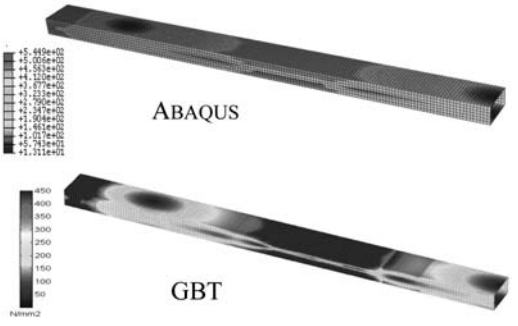

Figure 10. Mises stress (σ_{Mises}) contours for point C.

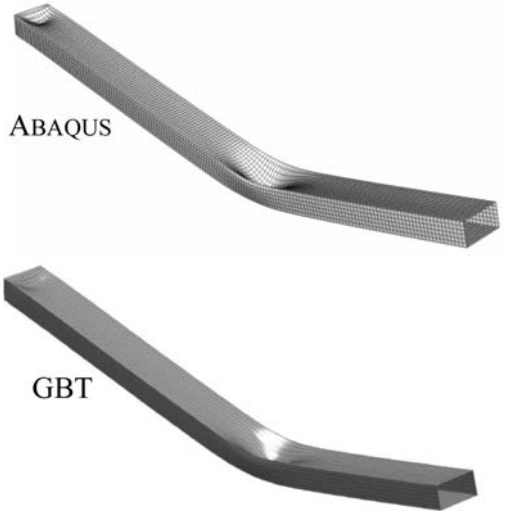

Figure 11. Deformed shape for point C – plastic collapse.

GBT analysis adopted only two nodes in the web (see Fig. 3) while the ABAQUS analysis used five.

Fig. 8 shows quite satisfactory results regarding the shear stress diagrams for points A and B, although some important differences are seen in the top flange for point B. However, one should bear in mind that

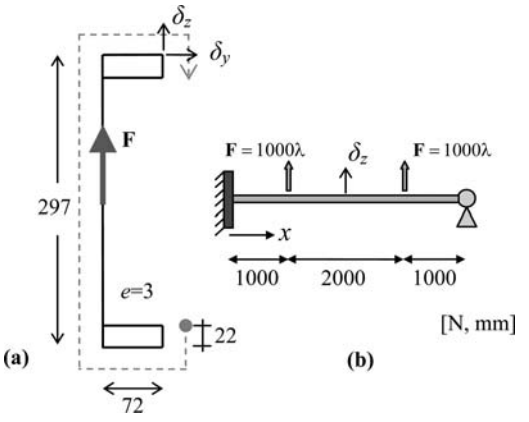

Figure 12. (a) Section dimensions, loading and (b) structural model.

GBT and ABAQUS load parameters coincide for point A but do not for point B (see Fig. 4).

Concerning Mises stress diagrams, and taken into account the differences between GBT and ABAQUS load parameters, Fig. 9 shows that results from both analyses are very close. Because point C is the one where discrepancies are bigger, Von Mises stress contours for that point are shown in Fig. 10. It can be noted that the spread of plasticity in ABAQUS and GBT exhibit a very good agreement. Lastly, Fig. 11 displays the collapse deformed shape for both analyses: it is evident that local deformation takes place where plastic deformation is bigger. Moreover, it is also notorious the existence of shear deformation at clamp's vicinity.

3.2 *LiteSteel beam*

Now, consider the fixed-pinned LSB with length L = 4000 mm depicted in Fig. 12. The beam is loaded at L/4 (x = 1000 mm) and 3L/4 (x = 3000 mm) by two vertical concentrated loads F = 1000 λ N located in the middle of the web, as illustrated in Fig. 12. In this case, 70 (out of 93) GBT modes were used in the analysis. The cross-section discretization and some of the most relevant modes used in GBT are represented in Fig. 13. Regarding the FE models, (i) 40 beam FE's were used in GBT model (6 in $0 < x < 0.2$L, 12 in $0.2\text{L} \leq \text{x} \leq 0.3\text{L}$, 4 in $0.3\text{L} \leq \text{x} \leq 0.7\text{L}$, 12 in $0.7\text{L} \leq \text{x} \leq 0.8\text{L}$ and 6 in $\text{x} > 0.8\text{L}$) and (ii) 184 "transverse rows" of 28 shell FE's were used in ABAQUS model. For the numerical integration, (i) 5 Gauss points in s and x directions were adopted in the GBT model and (ii) 7 Gauss points in through-thickness direction were used in both ABAQUS and GBT models. All the stress diagrams presented in this example are referred to the section located at x = 2000 mm (see Fig.12(b)) and to the section path depicted by the arrowed line in Fig. 12(a).

In Fig. 14, the equilibrium paths $\lambda(\delta_z)$ obtained by means of GBT and ABAQUS are presented, where δ_z is the monitoring displacement represented in Fig.12

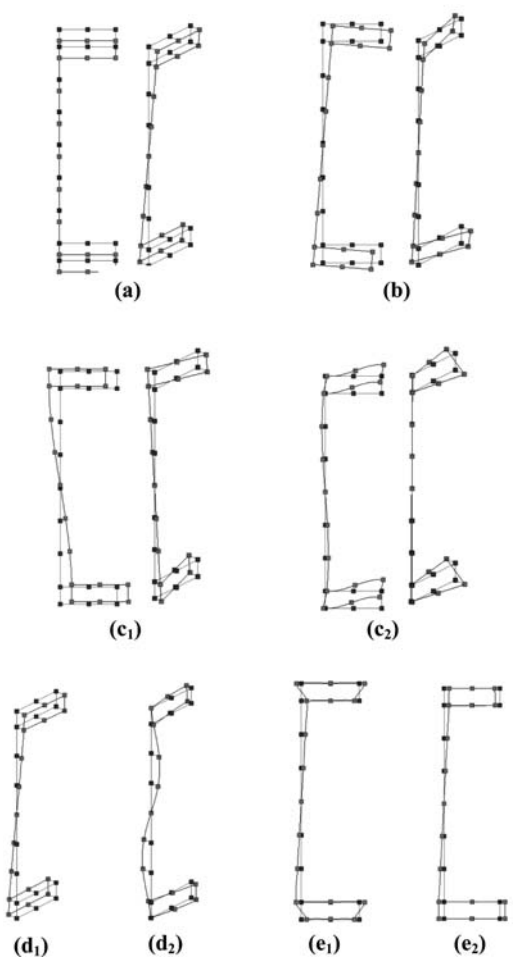

Figure 13. Some GBT relevant modes: (a) global, (b) cell (torsion), (c_1; c_2) local, (d_1; d_2) warp.shear, (e_1; e_2) transv.extension.

and located at $x = 2000$ mm. The curves yielded by both analyses compare very well, with a maximum difference of 2%. The 3 equilibrium points chosen to the comparison of results correspond to the following load parameters (Fig. 14): (A) $\lambda_{GBT} = 17.25$, $\lambda_{ABQ} = 17.20$, (B) $\lambda_{GBT} = 98.90$, $\lambda_{ABQ} = 97.00$ and (C) $\lambda_{GBT} = 112.65$, $\lambda_{ABQ} = 111.00$.

In the bottom part of Fig. 14, the modal participation diagram is displayed. In accordance with the modal participation definition used in this work[2], one can conclude that modes 2 (major axis bending – Fig. 13(a)), 4 (torsion – Fig. 13(b)) and 5 (local – Fig. 13(c_1)) are the most relevant ones

[2] In this work, the participation of a given mode is defined as the ratio between the displacement due to that mode in a particular section (where the member displays the maximum total displacement) and the sum of displacements due to all modes. This definition normally results in low participations for warping shear and transverse extension modes, although they are crucial to obtain accurate results.

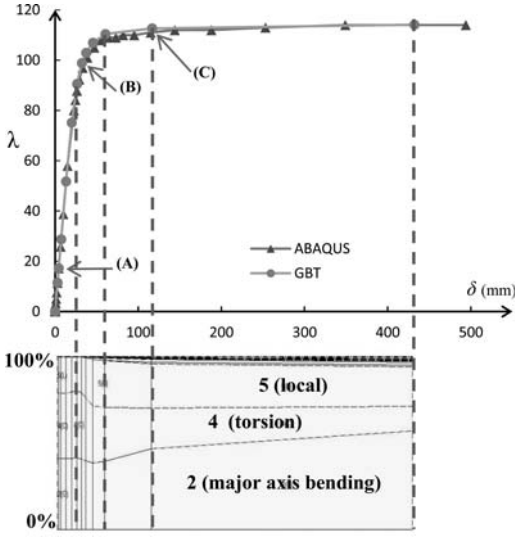

Figure 14. Load-displacement equilibrium path and GBT modal participation diagram.

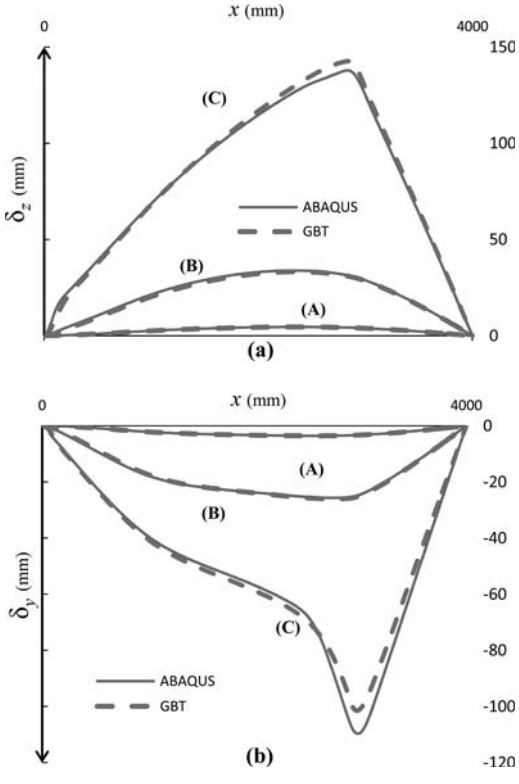

Figure 15. Displacement profiles (a) $\delta_z(x)$ and (b) $\delta_y(x)$.

(participation $\geq 5\%$). In the spread of plasticity phase (after yielding and before the horizontal plateau), it is seen that modes 2 and 4 decrease their participation while the contribution of mode 5 clearly increases. Within the horizontal plateau, the participation of

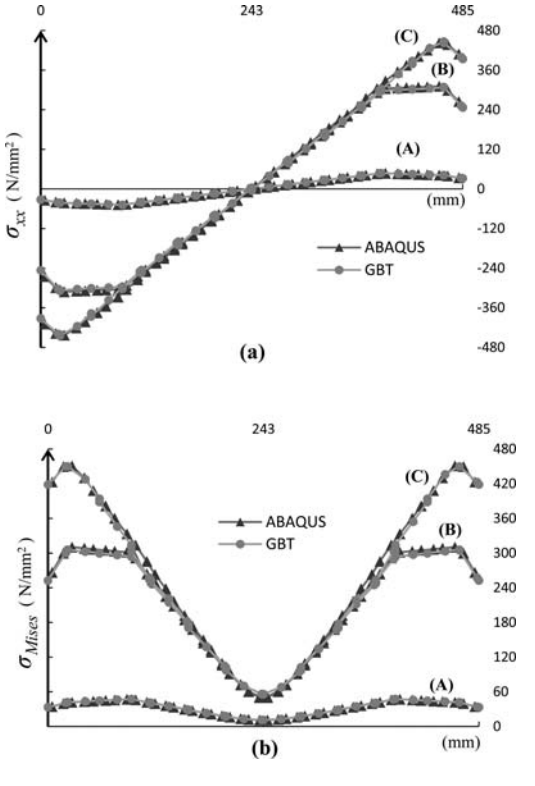

Figure 16. (a) Axial and (b) Mises stresses ($x = 2000$ mm) for points A, B and C.

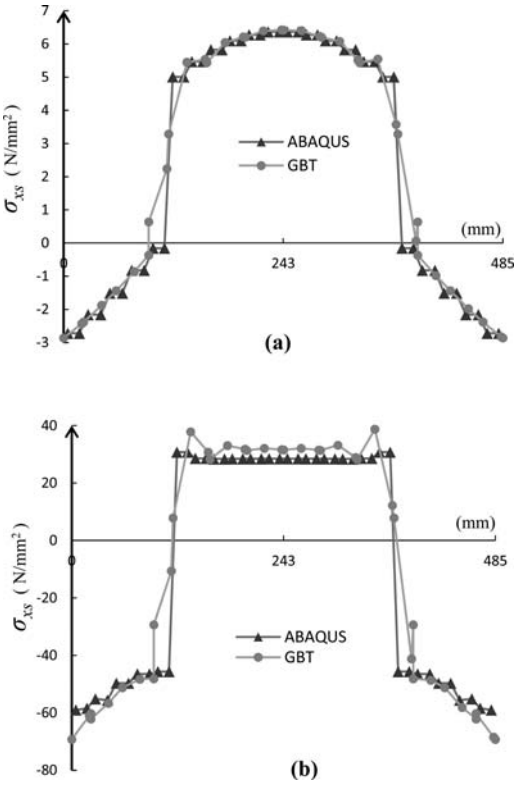

Figure 17. Shear stresses ($x = 2000$ mm) for points (a) A and (b) C.

modes 2, 4 and 5, increase, decrease and remain uniform, respectively.

The displacement profiles $\delta_z(x)$ and $\delta_y(x)$ of the node indicated in Fig. 12(a) are depicted in Fig. 15 and the comparison between GBT and ABAQUS results display an excellent agreement for points A and B. In the case of point C, GBT and ABAQUS profiles show a maximum difference in the section where the maximum absolute displacement takes place, with differences about 4.5 and 8.5%, respectively for $\delta_z(x)$ and $\delta_y(x)$. However, one should bear in mind that point C doesn't correspond to the same displacement in GBT and ABAQUS (see Fig. 14).

Figs. 16(a) and 16(b) show axial and Von Mises stresses diagrams, respectively. Once again, the similarities between GBT and ABAQUS results are notorious. Fig. 17(a) and 17(b) depicts the variations of shear stresses for points A and C, respectively. It is seen that the shear stresses in the web evolve from quadratic variation (point A – elastic) to an almost uniform profile (point C – plastic). There is also a good resemblance between both GBT and ABAQUS results.

The Von Mises stress and axial displacement contours for point B are presented in Figs.18 and 19, respectively, where the results are qualitatively and quantitatively fairly good. Lastly, similar collapse deformed shapes yielded by GBT and ABAQUS are depicted in Fig. 20 and it can be seen that most of the deformation occurs close to the load at x = 3000 mm.

Figure 18. Mises stress (σ_{Mises}) contours for point B.

4 CONCLUSIONS

A GBT formulation to analyse the first-order elasto-plastic behaviour of thin-walled members was presented and applied to illustrate the behaviour of

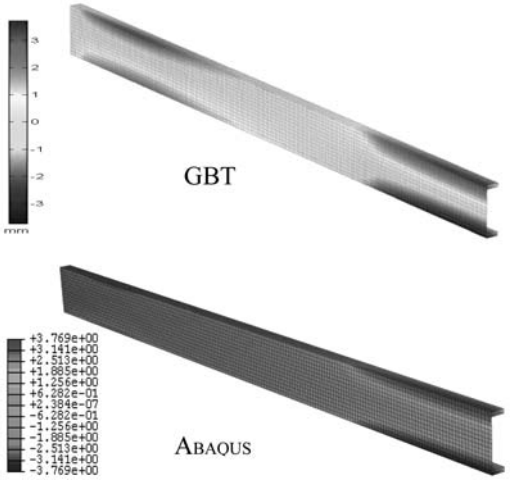

Figure 19. Axial displacement (u) contours for point B.

Figure 20. Deformed shape for point C – plastic collapse.

RHS and LSB fixed-pinned beams subjected to distributed and concentrated loading, respectively. The GBT results were compared with the ones obtained from ABAQUS (*Simulia* 2004) code using shell FE's. Equilibrium paths, displacement profiles, stress diagrams, stress / displacement 3D contours, as well as 3D deformed shapes were compared and a very good agreement was found for all results. Finally, it is important to highlight that the number of dof used in each ABAQUS model was 65.1 (RHS beam) and 5.3 (LSB beam) times higher than in GBT.

REFERENCES

Abambres, M., Camotim, D., Silvestre, N. (2011a). Elasto-plastic Analysis of thin-walled bars in the context of Generalised Beam Theory (in Portuguese), CD-ROM Proceedings of the Congress on Numerical Methods in Engineering (CMNE), Coimbra, Portugal, June 14–17th.

Abambres, M., Camotim, D., Silvestre, N. (2011b). Physically Non-Linear Analysis of Steel Beams in the context of Generalised Beam Theory (in Portuguese), Proceedings of the VIII Congress on Steel and Composite Construction (CMM), Guimarães, Portugal, November 24–25th.

Borst, R. de., Sluys, L.J. (2007). Computational Methods in Non-linear Solid Mechanics, Koiter Institute, Delft University of Technology, The Netherlands.

Camotim, D., Basaglia, C., Bebiano, R., Gonçalves, R., Silvestre, N. (2010). Latest Developments in the GBT Analysis of Thin-Walled Steel Structures, Proceedings of International Colloquium on Stability and Ductility of Steel Structures (SDSS'Rio 2010), E. Batista, P. Vellasco, L. Lima (Eds.), Federal University of Rio de Janeiro, Rio de Janeiro, pp. 33–58 (Vol. 1), September 8–10th.

Gonçalves R, Camotim D (2004). GBT local and global buckling analysis of aluminium and stainess steel columns, Computers and Structures, 82(17–19), 1473–1484.

Gonçalves, R., Camotim, D. (2011a). Generalised beam theory-based finite elements for elastoplastic thin-walled metal members, Thin-Walled Structures, 49, p.1237–1245.

Gonçalves, R., Camotim, D. (2011b). Geometrically Non-Linear Generalised Beam Theory for Elastoplastic Thin-Walled Metal Members, Thin-Walled Structures, in press.

MathWorks (2010). MATLAB – The Language of Technical Computing.

Silva, N., Camotim, D., Silvestre, N. (2008). GBT Cross-Section Analysis of Thin-Walled Members with Arbitrary Cross-Sections: A Novel Approach, Proceedings of the Fifth International Conference on Thin-Walled Structures, Brisbane, Australia.

Simulia Inc, DS. (2004). ABAQUS Standard (version 6.5).

Tubular Structures XIV – Gardner (Ed.)
© 2012 Taylor & Francis Group, London, ISBN 978-0-415-62137-3

GBT buckling analysis of thin-walled steel tubular members with regular polygonal cross-sections

R. Gonçalves
UNIC, Civil Engineering Dept., FCT, Universidade Nova de Lisboa, Caparica, Portugal

T. Patricio
Civil Engineering Dept., FCT, Universidade Nova de Lisboa, Caparica, Portugal

D. Camotim
Civil Engineering Dept., ICIST, Instituto Superior Técnico, TU Lisbon, Lisbon, Portugal

ABSTRACT: This paper concerns the application of Generalised Beam Theory (GBT) to analyse the buckling behaviour of thin-walled steel members with single-cell regular polygonal cross-section, such as those employed to build transmission line structures, antennas and masts. First, the most relevant local and distortional cross-section GBT deformation modes are obtained and examined. Then, the buckling (bifurcation) behaviour of uniformly compressed members (columns) and members subjected to pure torsion is assessed with the help of GBT-based semi-analytical formulae and beam finite elements. Attention is paid to both local and distortional (flattening) buckling phenomena. For comparison and validation purposes, some results obtained are compared with values yielded by standard finite strip and shell finite element analyses.

1 INTRODUCTION

Generalized Beam Theory (GBT), which was first proposed by Schardt (1966, 1989) in the context of linear elastic isotropic thin-walled members, may be viewed as an extension of Vlasov's thin-walled prismatic bar theory that accounts for cross-section in-plane and out-of-plane (warping) deformations. In a GBT analysis, the member deformed configuration is expressed as a combination of pre-determined cross-section deformation modes, whose varying amplitudes along the member axis are the problem unknowns. This quite unique modal nature renders GBT analyses considerably more versatile and efficient than equivalent (similarly accurate) finite strip or shell finite element analyses and it has been widely demonstrated that GBT constitutes a powerful, elegant and clarifying tool to solve a wealth of structural problems involving thin-walled members (*e.g.*, Camotim et al. 2010a, b).

This paper concerns the application of GBT to analyse the buckling behaviour of single-cell thin-walled steel members with *n*-sided regular (equiangular and equilateral) convex polygonal cross-section, such as those widely employed to build transmission line structures, antennas and masts. In section 2, the GBT cross-section analysis procedure is employed to obtain the shapes and characteristics of the most relevant local and distortional deformation modes for increasing *n* values (number of walls). In section 3 the local and distortional buckling (bifurcation) behaviour of uniformly compressed members is assessed using a GBT-based semi-analytical approach and the previously determined deformation modes. In particular, the local buckling behaviour of even and odd-walled members is investigated. Moreover, attention is paid to the distortional (flattening) buckling phenomenon occurring in members with high wall numbers. Finally, a GBT-based finite element is employed to investigate the member buckling behaviour under torsion.

For validation purposes, the GBT-based results are compared with values determined by means of buckling (linearised) analyses performed using (i) the finite strip code CUFSM (Schafer, 2003) or (ii) ADINA (Bathe, 2010) shell finite element models.

2 GBT DEFORMATION MODES

2.1 *Brief review of the GBT cross-section analysis*

Consider the arbitrary thin-walled prismatic member depicted in Fig. 1, which shows also the mid-surface local axes (x, y, z) for each wall. Adopting Kirchhoff's assumption, which states that fibres located initially along z remain undeformed and perpendicular to the member mid-surface, the wall displacement components are given by

$$\begin{aligned} U_x &= u - zw_{,x} \\ U_y &= v - zw_{,y} \\ U_z &= w \end{aligned} \qquad (1)$$

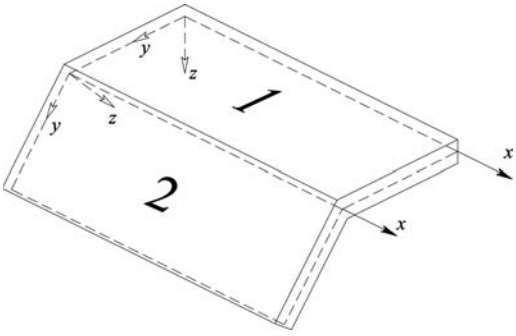

Figure 1. Arbitrary thin-walled member local coordinate systems.

where u, v and w are the wall mid-line displacement components along x, y and z, respectively, and the comma indicates partial differentiation.

The displacement components of the wall mid-line are further expressed as

$$\begin{aligned} u(x,y) &= \overline{u}_k(y)\phi_{k,x}(x) \\ v(x,y) &= \overline{v}_k(y)\phi_k(x) \\ w(x,y) &= \overline{w}_k(y)\phi_k(x) \end{aligned} \tag{2}$$

where (i) the summation convention applies to subscript k, (ii) functions $\overline{u}_k(y)$, $\overline{v}_k(y)$, $\overline{w}_k(y)$ contain the mid-line displacement components associated with each of the cross-section deformation modes and (iii) $\phi_k(x)$ are the corresponding (modal) longitudinal amplitude functions, which constitute the problem unknowns. It should be mentioned that the differentiation with respect to x appearing in u is necessary to enforce the null membrane shear strain hypothesis, commonly designated as "Vlasov's hypothesis".

The most unique feature of a GBT analysis is the preliminary identification of the cross-section *deformation modes*, *i.e.*, the determination of the shapes of the functions $\overline{u}_k(y)$, $\overline{v}_k(y)$, $\overline{w}_k(y)$. These function shapes are obtained through the performance of the so-called "GBT cross-section analysis", a sequential procedure consisting of two main steps (Gonçalves et al. 2010a):

(i) Cross-section discretisation by means of "cross-section nodes" and generation of an initial set of deformation modes (shape functions). Each initial deformation mode is obtained by imposing a unit displacement (u, v or w) at a single cross-section node, while keeping all the remaining nodal displacements null. The in-plane deformed configuration of the cross-section associated with each mode requires solving a statically indeterminate folded-plate problem, which can be done, for instance, by viewing it as a 2D frame subjected to imposed nodal displacements. The frame analysis is then carried out by using any suitable method of structural analysis (*e.g.*, direct stiffness, direct displacement or beam finite element methods).

(ii) Performance of an appropriate change of base in the space spanned by the initial set of deformation modes, by sequentially solving a series of eigenvalue problems, in order to a final set of deformation modes that are both structurally meaningful and hierarchically ordered.

For instance, for the particular case of the deformation modes involving transverse wall bending (*i.e.*, the local and distortional modes), the relevant eigenvalue problem is defined by

$$(\mathbf{B} - \lambda\mathbf{C})\mathbf{v} = \mathbf{0} \tag{3}$$

where (i) matrix **B** concerns wall transverse bending and (ii) matrix **C** takes into account longitudinal bending and the wall warping. Their components read

$$\begin{aligned} B_{ij} &= \int_S \frac{Et^3}{12(1-\nu^2)} \overline{w}_{i,yy}\overline{w}_{j,yy}dy \\ C_{ij} &= \int_S Et\,\overline{u}_i\overline{u}_j dy \end{aligned} \tag{4}$$

where the integrations are performed over the cross-section mid-line S, t is the wall with, E is Young's modulus and ν is Poisson's ratio.

It is worth mentioning that the authors have recently discussed and extended the scope of the GBT cross-section analysis procedure, making it possible (i) to perform more rational analyses of cross-sections with arbitrary shapes, namely those combining closed cells with open branches and even (ii) to take into account internal and external constraints (Gonçalves et al. 2010a).

2.2 *Distortional modes*

For closed single-cell cross-sections, it was shown by two of the authors (Gonçalves et al. 2010a) that, assuming (i) the in-plane inextensibility of the cross-section walls and (ii) null membrane shear strains (the Vlasov's hypothesis), the number of warping deformation modes (*i.e.*, modes involving axial displacements) equals the number of cross-section nodes – in this particular case, it also equals the number of cross-section walls. Note, however, that the null membrane shear strain assumption leads to unacceptable errors in capturing the member torsional behaviour, which can only be eliminated if a "uniform shear flow deformation mode" is included in the analysis (Schardt 1989).

When only the warping modes are considered, the performance of a GBT cross-section analysis leads to (i) three "rigid-body" (global) deformation modes (axial extension and major/minor axis bending) and (ii) $n-3$ distortional modes. Therefore, the simplest single-cell cross-section, the triangle (either regular or irregular), exhibits no distortional modes – moreover, it is possible to conclude that torsion may not involve warping.

In many cases of practical interest the configuration of some (or all) distortional modes may be easily determined from symmetry and anti-symmetry

considerations, following the principle that the warping functions associated with each deformation mode must be mutually orthogonal (including those concerning the "rigid-body" modes). For instance, in a rectangular hollow cross-section, one has $n-3=1$ and the warping function corresponding to the (single) distortional mode must be anti-symmetric with respect to the axes of symmetry of the cross-section.

Regular (equiangular and equilateral) convex n-sided polygons exhibit rotational symmetry of order n, thus leading to some noteworthy peculiarities exhibited by their deformation modes. First of all, any centroidal axis is also a principal axis of inertia and, therefore, the "rigid-body" bending deformation modes may be related to any orthogonal pair of such axes.

These cross-section shapes are characterised by $n-3$ distortional modes, which can be obtained directly from the solution of the eigenvalue problem defined by Equation (3). Notably, this procedure leads to eigenvalues with multiplicity 2, which means that these distortional eigenvalues are associated with a pair of distortional deformation modes not unambiguously defined (like the "rigid-body" bending deformation modes). Figure 2 shows the distortional deformation modes obtained for cross-sections with $n=4$ to $n=7$, characterised as follows:

(i) The square ($n=4$) has only one eigenvalue and one distortional mode.
(ii) The pentagon ($n=5$) has one eigenvalue with multiplicity 2, associated with modes 1 and 2.
(iii) The hexagon ($n=6$) has two eigenvalues, where the first has multiplicity 2 and is associated with modes 1 and 2, whereas the second corresponds to a single mode (mode 3).
(iv) The heptagon ($n=7$) has two eigenvalues with multiplicity 2, which are associated with two pairs of deformation modes ($1+2$ and $3+4$).

2.3 *Local modes*

Concerning the GBT cross-section analysis, the local deformation modes are obtained by subdividing the cross-section walls by means of "intermediate nodes". The initial set of local modes is obtained by imposing lateral (normal to the wall mid-line) unit displacements at each intermediate node. Like for the distortional modes, the local deformation mode set is obtained by solving Equation (3). Clearly, the number of local modes equals the number of intermediate nodes.

Figure 3 shows sets of local deformation modes concerning the four regular polygons depicted in Figure 2, which are determined on the basis of wall subdivisions into two equal wall segments (a single mid-width intermediate node per wall), thus implying that the total number of local modes obtained is equal to n.

Once more, the solution of Equation (3) leads to eigenvalues with multiplicity 2, even if the picture is now somewhat different for cross-sections consisting of even-sided and odd-sided polygons. In the case

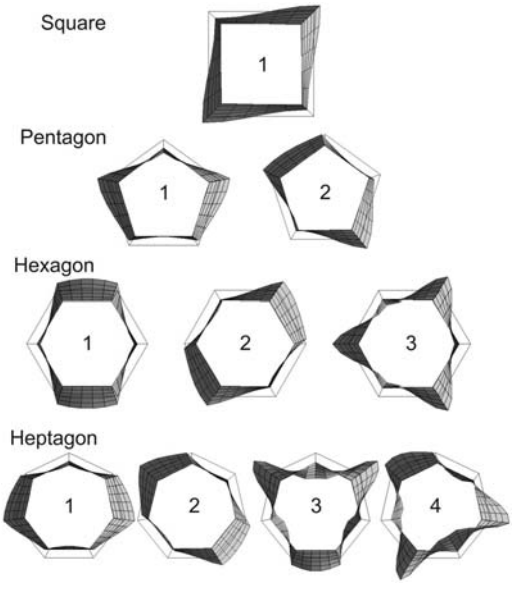

Figure 2. GBT distortional deformation modes of cross-sections consisting of convex regular polygons with 4 to 7 sides (walls).

of even-sided polygons, the first and last deformation modes are always "isolated" (*i.e.*, not associated with eigenvalues exhibiting multiplicity) and the pairs are formed by the intermediate modes, sequentially ordered: $2+3$ for the square ($n=4$) and $2+3$, $4+5$ for the hexagon ($n=6$). For the odd-sided polygons, only the last deformation mode is "isolated" and the pairs concern the remaining deformation modes, again sequentially ordered: $1+2$, $3+4$ for the pentagon ($n=5$) and $1+2, 3+4, 5+6$ for the heptagon ($n=7$).

3 BUCKLING BEHAVIOUR

For uniformly compressed simply supported members, the exact solutions of the GBT buckling (bifurcation) analysis equations correspond to sinusoidal amplitude functions of the form

$$\phi_k(x) = \overline{\phi}_k \sin\left(\frac{m\pi x}{L}\right) \tag{5}$$

where (i) $\overline{\phi}_k$ is the maximum amplitude value for deformation mode k, (ii) m is the buckling mode longitudinal half-wave number and (iii) L is the member length.

Inserting Equation (5) into the bifurcation equations leads to a semi-analytical approach, in which the buckling loads λ_b are obtained by solving (*e.g.*, Schardt 1994, Gonçalves et al. 2010b)

$$\det\left(\left(\frac{m\pi}{L}\right)^2\mathbf{C}+\mathbf{D}+\left(\frac{L}{m\pi}\right)^2\mathbf{B}+\lambda_b\mathbf{X}\right)=0 \tag{6}$$

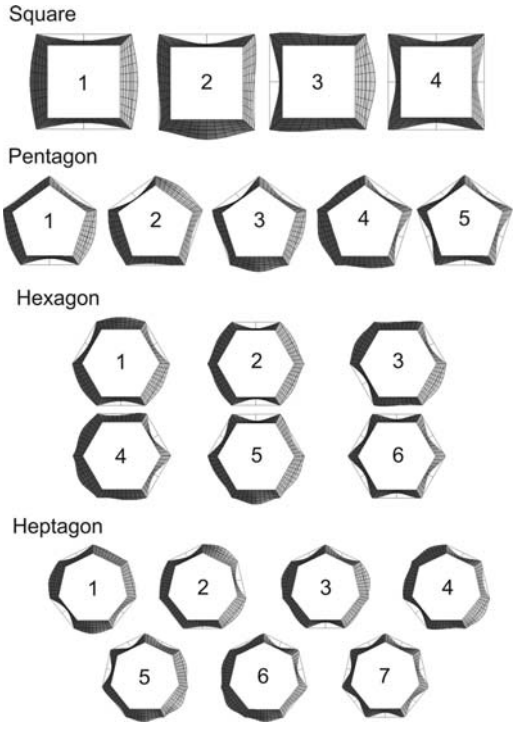

Figure 3. GBT local deformation modes of cross-sections consisting of convex regular polygons with 4 to 7 walls, each of them exhibiting a mid-width intermediate node.

where **C** and **B** are the previously discussed modal matrices, **D** is a modal matrix associated with torsion and longitudinal/transversal bending coupling, and **X** is the modal geometric matrix, with components

$$D_{ij} = \int_S \frac{Gt^3}{3} \overline{w}_{i,y} \overline{w}_{j,y} dy - \\ - \int_S \frac{\nu E t^3}{12(1-\nu^2)} \left(\overline{w}_{i,yy} \overline{w}_j + \overline{w}_{j,yy} \overline{w}_i \right) dy \\ X_{ij} = \int_S \sigma_{xx} t (\overline{v}_i \overline{v}_j + \overline{w}_i \overline{w}_j) dy \tag{7}$$

where σ_{xx} are the pre-buckling longitudinal normal stresses and$G$ is the shear modulus.

For non-simply supported members, the above equation may still be employed (approximately) to assess the distortional or local buckling behaviour of long columns, for which the effect of the boundary conditions is negligible. In more general cases, it is obviously preferable to employ GBT-based beam finite elements (*e.g.*, Silvestre & Camotim 2003 or Gonçalves & Camotim 2012), which are still computationally quite "economic", particularly when compared with similarly accurate standard shell finite element models.

3.1 *Local buckling under uniform compression*

Provided that adequate bracing against flexural buckling is provided, the instability of thin-walled members with closed cross-sections is primarily governed by local buckling. The calculation of critical local buckling loads is rather straightforward and, in most cases, it is sufficiently accurate (and conservative) to analyse the most slender wall (that having the highest width-to-thickness ratio b/t) as if it were simply supported on all edges. Therefore, the classic expression providing the critical buckling stress of uni-axially loaded plates can be readily applied. It reads (*e.g.*, CEN 2006)

$$\sigma_{cr} = \frac{k\pi^2 E}{12(1-\nu^2)} \left(\frac{t}{b} \right)^2 \tag{8}$$

where k is the buckling coefficient, which depends on the applied stress distribution and plate support conditions. For uniformly compressed simply supported plates one has $k = 4$, which also constitutes the exact value for regular convex polygons with an even number of walls under uniform compression – this is due to the "pure" anti-symmetric nature of the buckling mode shape. For irregular polygons, regular polygons with an odd number of walls and/or non-uniform loading, the use of $k = 4$ naturally leads to errors that may be more or less significant for a specific case. In order to obtain more accurate critical buckling stress, it is indispensable to resort to numerical procedures, such as GBT-based finite elements.

Table 1. Buckling coefficients for even-sided polygonal columns.

Int. nodes	Square	Hexagonal	Octagonal
1	4.0171	4.0171	4.0171
2	4.0023	4.0023	4.0023
3	4.0006	4.0006	4.0006

Even-sided polygonal columns are first analysed and Table 1 provides the buckling coefficients associated with the critical local buckling stresses for $n = 4$, 6 and 8, obtained with Equation (8) and considering up to 3 intermediate nodes per wall. The numerical results presented concern columns with $r = 100$ mm (cross-section circumradius), $t = 2$ mm, $E = 210$ GPa and $\nu = 0.3$. The configurations of the critical buckling modes obtained for the three polygonal columns are displayed in Figure 4 – note that the deformed shape of each wall closely resembles that of a simply supported plate.

In this case, $k = 4$ is the exact result for the three columns and it is clear that GBT already leads to a nearly perfect match with just a single intermediate node per wall (less than 0.4% differences are obtained). Moreover, the buckling mode shapes shown in Figure 4 confirm that the critical mode always corresponds to the first local deformation mode depicted in Figure 3.

Next, attention is turned to the analysis of odd-sided polygonal columns, for which the value $k = 4$ provides a more or less considerable underestimation of the real critical local buckling stress. For these cross-section shapes, the local buckling stresses are associated with

Figure 4. Critical local buckling mode shapes of even-sided polygonal columns.

Table 2. Buckling coefficients for odd-sided polygonal columns.

Int. nodes	Triangular	Pentagonal	Heptagonal
1	4.7536	4.3000	4.1633
2	4.7162	4.2775	4.1447
3	4.7108	4.2747	4.1424
Finite Strip	4.7043	4.2695	4.1477

pairs of buckling mode shapes, *i.e.*, they correspond to eigenvalues with multiplicity 2 – this means that the buckling modes are not uniquely defined, since any linear combination of the two competing shapes is still a buckling mode (one has a "buckling mode plane").

Table 2 shows the buckling coefficients for odd-sided polygonal columns with $n = 3$, 5 and 7 and $r = 100$ mm, $t = 2$ mm, $E = 210$ GPa and $\nu = 0.3$ (as before). Figure 5 shows the corresponding critical buckling mode shapes. For comparison and validation purposes, critical buckling coefficients and mode shapes determined with the finite strip (FS) code CUFSM (Schafer 2003) are also presented. The following conclusions can be drawn:

(i) As expected, the buckling coefficient k decreases as the number of sides grows and gradually approaches the exact value 4.0.
(ii) The comparison between the GBT and FS buckling coefficients shows that the accuracy achieved by the former is still quite high considering just a single intermediate node per wall. However, 2 intermediate nodes are required in the triangular column to ensure that the difference, with respect to the FS value, is kept below 1% (only one intermediate node leads to a difference slightly higher).
(iii) There is no perfect match between the buckling mode shapes provided by the GBT and FS analyses (although some of these modes appear to be related by rigid-body rotations), which is due to the fact that these critical modes are not uniquely defined. Nevertheless, both the GBT and FS buckling mode pairs can be used as a possible base of the same vector space.

3.2 *Distortional buckling under uniform compression*

For cross-sections with low b/t ratios, local buckling ceases to govern and distortional buckling may

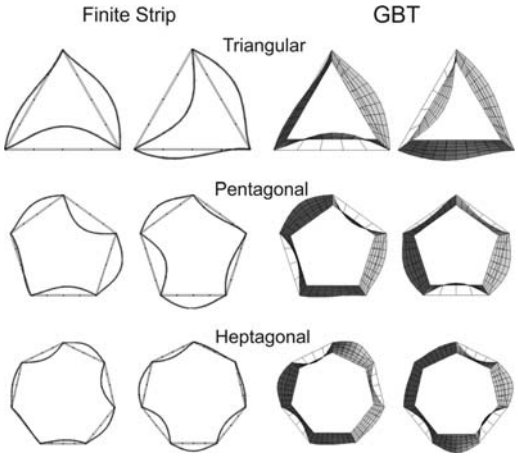

Figure 5. Critical local buckling modes for odd-sided polygonal columns.

become critical. Note that a low b/t value does not necessary imply a "thick-walled" cross-section, since the same distortional buckling relevance occurs as n increases, *i.e.*, the polygon approaches a circle. In the limit case of $n = \infty$, *i.e.*, for a thin cylindrical shell under uniform compression, the critical distortional buckling stress is given by (Timoshenko & Gere 1963)

$$\sigma_{cr} = \frac{3}{5}\frac{E}{\sqrt{3(1-\nu^2)}}\frac{t}{r} \tag{9}$$

It is worth noting that Silvestre (2007) developed a GBT formulation aimed at performing buckling analyses of thin-walled circular tubes. This formulation makes it possible to recover Equation (9) and further leads to the following analytical expression for the associated critical length (L_{cr}) values

$$L_{cr} = \frac{\pi}{2\sqrt{3}}\frac{r}{t}\sqrt{rt}\sqrt[4]{12(1-\nu^2)} \tag{10}$$

Since the GBT-based approach developed in this work is based on the assumption of straight walls, it is obviously not capable of recovering the above analytical expressions. Nevertheless, as n grows, the solutions obtained by means of these equations should be approached. By equating the expressions given by Equations (8) and (9), one is led to (assuming $\nu = 0.3$)

$$k = 1.661\frac{r}{t}\sin^2(\pi/n) \tag{11}$$

Table 3 shows the critical buckling coefficients and lengths (L_{cr}) for several icosagonal ($n = 20$) columns with $r = 100$ mm, $E = 210$ GPa, $\nu = 0.3$ and variable t (thickness). Once more, the critical buckling stresses

Table 3. Icosagonal column distortional buckling coefficients and critical lengths.

	k			L_{cr} (mm)	
t (mm)	GBT	Finite Strip	Eq. (11)	GBT	Eq. (10)
1	3.9939	3.9457	4.065	1600	1649
2	2.0158	1.9696	2.032	1150	1166
3	1.3577	1.3101	1.355	950/900	952
4	1.0289	0.9812	1.016	825/800	824
5	0.8315	0.7832	0.813	725/800	737

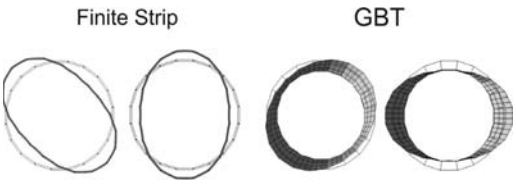

Figure 6. Icosagonal column critical distortional buckling modes.

correspond to eigenvalues of multiplicity 2 and the associated buckling modes are depicted in Figure 6. It is possible to draw the following conclusions:

(i) Although the differences between GBT and FS critical distortional buckling loads remain quite small, they are nevertheless higher than their local counterparts. Such differences vary from 1.2% ($t = 1$ mm) up to 6.2% ($t = 5$ mm) and, moreover, they do not decrease if additional intermediate nodes are included in the GBT analyses.

(ii) All the buckling coefficients obtained by means of both the GBT and FS analyses are lower than 4 (but $k \approx 4$ for $t = 1$ mm), which means that distortional buckling is critical in all cases.

(iii) Equation (11) provides values that are practically coincident with the GBT (and FS) ones. The differences are always below 2.2% (for $t = 5$ mm).

(iv) The L_{cr} values obtained with the analytical Equation (10) are also remarkably close to the numerical GBT values. In this case the differences fall always below 3%.

3.3 *Buckling under uniform torsion*

The last illustrative example concerns the buckling behaviour of polygonal members subjected to pure uniform torsion. Because the walls of closed cross-section members are subjected to pure shear, they invariably undergo critical shear buckling. Moreover, due to the polygonal cross-section shape, distortional deformation modes are also involved, which means that the longitudinal edges connecting adjacent walls do not remain straight in the column buckled configuration.

Table 4. Hexagon torsional buckling loads.

No. FE	T_{GBT}(kNm)	T_{Shell} (kNm)	%
2	47.18	−3.1	
3	45.26	1.1	
4	45.23	45.78	1.2
5	45.16	1.4	
6	45.12	1.4	

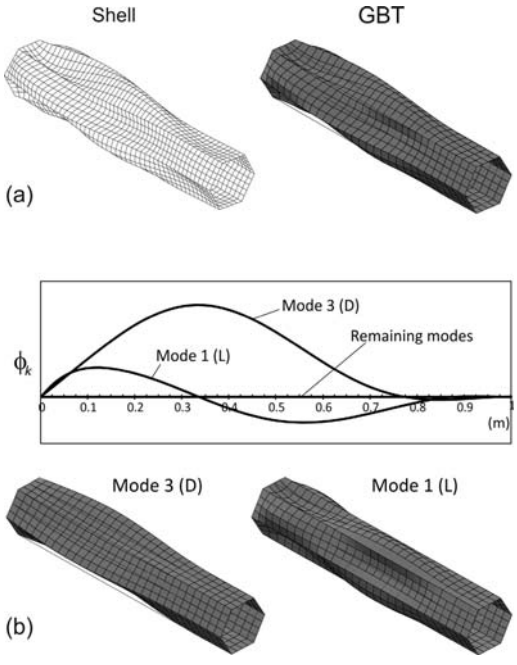

Figure 7. Hexagonal member subjected to torsion: (a) critical mode shapes and (b) GBT modal decomposition (amplitude functions and configuration of the most relevant modes).

Because Equation (5) no longer constitutes a exact solution for simply supported members, it is necessary to employ a GBT-based finite element approach to obtain accurate buckling torsional moments. On the other hand, the code CUFSM is not able of handling pre-buckling shear stresses and, thus, ADINA (Bathe 2010) shell finite models are used for comparison purposes.

The numerical results presented and discussed next concern the particular case of an hexagonal ($n = 6$) member characterised by $L = 1000$ mm, $r = 100$ mm, $t = 2$ mm, $E = 210$ GPa and $\nu = 0.3$. At one end, all member walls are "locally" simply supported, a boundary condition that fully restrains torsional rotations but does not preclude warping. At the other member end a torsional moment is applied and a rigid diaphragm is introduced to simulate a realistic/feasible boundary condition that restrains warping and plate bending at this member end. The GBT model is fully consistent with its shell counterpart, as far as all boundary conditions are concerned.

The GBT analyses are based on the consideration of a single intermediate node in each wall, which means that 3 distortional (Fig. 2) and 6 local (Fig. 3) deformation modes are included in the analysis.

Table 4 shows the critical torsional moments obtained through (i) the GBT analyses, adopting member discretisations into up to 6 equal-length beam finite elements, and (ii) a standard ADINA shell model. A rather accurate value is achieved with only two GBT finite elements (overestimation of about 3%) and the consideration of additional elements brings the GBT critical torsional moment very close to the shell model value – GBT provides underestimates with differences around 1-1.5%, which end up growing slightly when the number of finite elements increases.

Figure 7(a) makes it possible to compare the configurations of the GBT and ADINA (shell model) critical buckling modes, and a virtually perfect match is observed. The GBT modal amplitude functions are shown in Figure 7(b) and one readily concludes that only two deformation modes are relevant: the distortional mode 3 (see Fig. 2) and the local mode 1 (see Fig. 3). This finding shows that it is indispensable to include distortional deformation modes in the GBT buckling analyses of polygonal members subjected to uniform torsion.

4 CONCLUDING REMARKS

This paper presented the application of Generalised Beam Theory (GBT) to analyse single-cell thin-walled steel members exhibiting regular convex polygonal cross-sections. The identification and characterisation of the GBT distortional and local deformation modes were first addressed. One interesting feature unveiled was the presence of deformation modes with multiplicity 2.

Concerning the buckling behaviour of uniformly compressed members (columns), it was shown that both local buckling (for small n) and distortional buckling (for large n) may be critical and that critical buckling modes with multiplicity 2 are obtained in all cases.

Finally, the member buckling behaviour under uniform torsion was also investigated and it was found that the inclusion of distortional deformation modes in the GBT buckling analyses is essential to obtain accurate critical torsional moments.

For validation purposes, the GBT-based critical buckling stresses/moments and corresponding buckling mode shapes where compared with similar results obtained by means of standard finite strip (buckling behaviour under uniform compression) and shell finite element (buckling behaviour under uniform torsion) analyses carried in the codes CUFSM and ADINA, respectively. An excellent agreement, concerning both the values of the critical buckling stresses/moments and the configurations of the corresponding buckling modes was found in all cases.

ACKNOWLEDGEMENTS

The financial support provided by *Fundação para a Ciência e Tecnologia* (FCT – Portugal), through project PTDC/ECM/108146/2008 ("Generalised Beam Theory (GBT) – Development, Application and Dissemination"), is gratefully acknowledged.

REFERENCES

Bathe, K.J. 2010. *ADINAsystem*. ADINA R&D Inc.

Camotim D., Basaglia C., Bebiano R., Gonçalves R., Silvestre N. 2010a. Latest developments in the GBT analysis of thin-walled steel structures. E. Batista, P. Vellasco, L. de Lima (eds), *Stability and Ductility of Steel Structures*; *Proc. Int. Col., Rio de Janeiro, 8–10 September 2010*: 33–58.

Camotim D., Basaglia C., Silva N.F., Silvestre N. 2010b. "Numerical analysis of thin-walled structures using Generalised Beam Theory (GBT): recent and future developments. In B.H.V. Topping et al. (eds), *Computational Technology Reviews, Vol. 1*: 315–354. Stirlingshire: Saxe-Coburg.

CEN (Comité Européen de Normalisation) 2006. *Eurocode 3 – Design of Steel Structures – Part 1–5: Plated Structural Elements*. Technical Committee CEN/TC250, Brussels.

Gonçalves R., Ritto-Corrêa M., Camotim D. 2010a. A new approach to the calculation of cross-section deformation modes in the framework of Generalized Beam Theory. *Computational Mechanics*, 46(5): 759–781.

Gonçalves R., Le Grognec P., Camotim D. 2010b. GBT-based semi-analytical solutions for the plastic bifurcation of thin-walled members, *International Journal of Solids and Structures*. 47(1): 34–50.

Gonçalves R., Camotim D. 2012. Geometrically non-linear Generalised Beam Theory for elastoplastic thin-walled metal members. *Thin-Walled Structures*, 51: 121–129.

Schafer B. 2003. *CUFSM 2.6, Finite Strip Buckling Analysis of Thin-Walled Members*. Civil Engineering Dept., Johns Hopkins University, Baltimore (www.ce.jhu.edu/bschafer).

Schardt R. 1966. Eine erweiterung der technischen biegetheorie zur berechnung prismatischer faltwerke. *Stahlbau*, 35:161–71 [in German].

Schardt R. 1989. *Verallgemeinerte Technische Biegetheorie*. Berlin: Springer Verlag [in German].

Schardt R. 1994. Generalized Beam Theory – an adequate method for coupled stability problems. *Thin-Walled Structures*, 19(2–4): 161–80.

Silvestre N. 2007. Generalised beam theory to analyse the buckling behaviour of circular cylindrical shells and tubes. *Thin-Walled Structures*, 45(2): 185–198.

Silvestre N., Camotim D. 2003. GBT buckling analysis of pultruded FRP lipped channel members. *Computers and Structures*, 81(18–19): 1889–1904.

Timoshenko S.T., Gere J.M. 1963. *Theory of Elastic Stability*. McGraw-Hill International.

Tubular Structures XIV – Gardner (Ed.)
© 2012 Taylor & Francis Group, London, ISBN 978-0-415-62137-3

Advanced analysis and design of structures composed of concrete-filled hollow sections

S.L. Chan, Y.P. Liu & S.W. Liu
Department of Civil and Structural Engineering, The Hong Kong Polytechnic University, Hong Kong, China

R. Chu
Meinhardt (Hong Kong) Limited, Hong Kong, China

ABSTRACT: Structures composed of concrete-filled steel hollow sections are widely used to-date due to their structural efficiency and economy. This paper proposes a second-order design method which requires only section capacity check without need of assuming an effective length and using prescriptive formulae in different codes and the shape of the member cross section can be arbitrary. The member-based design by the linear analysis and the effective length assumption is abandoned and replaced by the second-order analysis utilizing an incremental-iterative nonlinear process. Using a curved element allowing for member P-δ effects and initial imperfections, the non-linear response of individual members and a frame can be captured directly and used for structure resistance checks. The proposed method could be used for generation of failure surfaces of the arbitrary shaped cross sections and the stress distribution along the concrete component is considered by segments with the entire structural steel section meshed into small fibres for determination of section capacity. Verification of the proposed analysis method is carried out by comparison against examples. It is believed that the proposed approach will be the next-generation design method for modern structures made of members of concrete filled sections of any shape and the new design method is also being implemented in design of composite structures in the consultant firm of the last author.

1 INTRODUCTION

Apart from the strength check, the stability check is also included in the design procedures. Although the descriptions for the stability check in Bare Steel (BS), Reinforced Concrete (RC) and Steel-Concrete Composite (SCC) codes may be different, the requirement for consideration of second-order effects such as P-Δ and P-δ effects is conceptually the same because it is the true behaviour of a structure. It is noted that only the P-Δ but not P-δ effect is commonly considered in most previous researches and therefore the tedious member buckling strength design by codes is still needed. In this paper, the Pointwise-Equilibrium-Polynomial (PEP) element (Chan & Zhou 1994), which could allow for both the P-Δ and P-δ effects and imperfections at element level, and a robust nonlinear incremental-iterative procedure are used. Thus, this method fulfils the requirements of modern design codes such as AISC(2010), Eurocode 3 (2006), CoPHK(2005). Furthermore, the proposed approach takes into account for various factors affecting the structural behaviour and as a result it can be directly used for safety check without member design. This unified design method eliminates need of tedious and unreliable individual member check to various codes and carries out design for structures made of different materials in a consistent manner. As the internal forces and moments obtained from the proposed second-order analysis have already included the P-Δ and P-δ effects, a simple cross sectional capacity check is therefore adequate for the safety check of a structure. The cross sectional capacity is generally described by the failure surface, which is also usually named as the full yield surface. A major consultant firm in Hong Kong has also applied successfully the design concept to design of a mega composite truss in a project in Hong Kong.

2 GEOMETRIC NONLINARITY & ELEMENT FORMULATION

Most finite element approaches for frame structures are based on the cubic Hermite element with the addition of geometric stiffness matrix to the linear stiffness matrix to allow for the geometric nonlinearity. The limitation of the use of cubic element received many debates and it is mainly due to the assumed straightness in the element formulation that the authors consider the cubic element as unsuitable for second order analysis. This inability of modelling change of curvature when element is under load and in the presence of initial

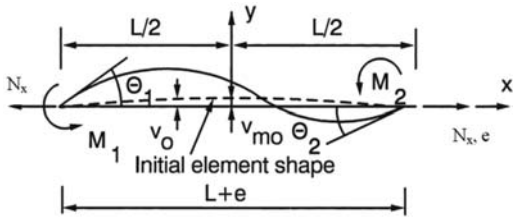

Figure 1. Basic forces vs. displacements relations in an element.

member imperfection are unacceptable in the second-order design and advanced analysis, like Eurocode 3 (2006) and Eurocode 4 (2005) which require the input of initial curvature in members and does not permit the use of straight members in a practical second-order design. To overcome this drawback of the conventional beam-column element, Chan & Zhou (1994) developed a Pointwise Equilibrating Polynomial (PEP) element with initial curvature as shown in Figure 1. They also refined the element with different features to simplify the analysis procedure and make the advanced analysis practical and reliable against numerical divergence (Chan & Zhou 1995; Chen & Chan 1995; Zhou & Chan 1996; Zhou & Chan 1997; Chan & Zhou 1998; Chan & Zhou 2000). A brief introduction of the PEP element is given here, and more details can be referred to the original paper Chan & Zhou (1994).

In the PEP element, six conditions are imposed on the evaluation of the displacement function. They are the compatibility conditions at the two end nodes and the equilibrium conditions at mid span. Mathematically, these conditions can be stipulated as follows.

For compatibility,

$$\text{At } x = \pm\frac{L}{2};\ v = 0 \tag{1}$$

$$\text{At } x = -\frac{L}{2};\ \dot{v} = 0 \tag{2}$$

$$\text{At } x = +\frac{L}{2};\ \dot{v} = 0 \tag{3}$$

For equilibrium,

$$EI\,\ddot{v} = N_x(v + v_0) + \frac{M_1 + M_2}{L}\left(\frac{L}{2} + x\right) - M_1 \tag{4}$$

$$EI\,\dddot{v} = N_x\dot{v} + \frac{M_1 + M_2}{L} \tag{5}$$

A polynomial function of fifth power is further assumed for the fulfilment of the aforementioned six constrained equations, i.e.

$$v = a_0 + a_1x + a_2x^2 + a_3x^3 + a_4x^4 + a_5x^5 \tag{6}$$

The coefficients are then eliminated from the equations above and final displacement can be written as:

$$v = (N_1 N_2)(L\theta_1 L\theta_2)^T \tag{7}$$

in which N_1 and N_2 are shape functions given by

$$N_1 = \frac{A}{H_1} + \frac{B}{H_2} \tag{8}$$

$$N_2 = \frac{A}{H_1} - \frac{B}{H_2} \tag{9}$$

with

$$A = -20\frac{x}{L} + (80 - q)\left(\frac{x}{L}\right)^3 + 4q\left(\frac{x}{L}\right)^5 \tag{10}$$

$$B = 6 - \frac{1}{2}(48 - q)\left(\frac{x}{L}\right)^2 - 2q\left(\frac{x}{L}\right)^4 \tag{11}$$

$$H_1 = 80 + q \tag{12}$$

$$H_2 = 48 + q \tag{13}$$

$$q = \frac{N_x L^2}{EI} \tag{14}$$

The shape function of the PEP element will be converted to the cubic Hermite function when the axial load parameter q is zero. The discrepancy between the cubic and the present higher-order element increases when the axial load is large.

The remarkable advantage of the proposed advanced analysis by PEP element lies on its automatic computation of primary linear and secondary nonlinear stresses such that the assumption of K-factor or effective length factor is avoided and the element itself could detect buckling and second-order stresses. The change on member stiffness in the presence of axial load is also allowed for in the stress computation and analysis and this feature is considered in order to compute internal forces and moments in elements accurately since member stiffness is affected by initial stresses or internal forces. When using the cubic Hermite element for modelling of slender braces, the error could be considerable, leading to a wrong prediction of force distribution between the tension and compression braces.

3 CONSTITUTIVE RELATIONSHIP

Various constitutive models in codes or obtained from laboratory can be adopted in the proposed second-order analysis. In this paper, the stress-strain relationship of steel is assumed as elastic-perfectly-plastic, while the material constitutive model of concrete is taken from Eurocode 2 (1999) and can be expressed as,

$$\sigma_c = f_c\left[1 - \left(1 - \frac{\varepsilon_c}{\varepsilon_0}\right)^n\right] \quad \text{for} \quad 0 \le \varepsilon_c \le \varepsilon_0 \tag{15}$$

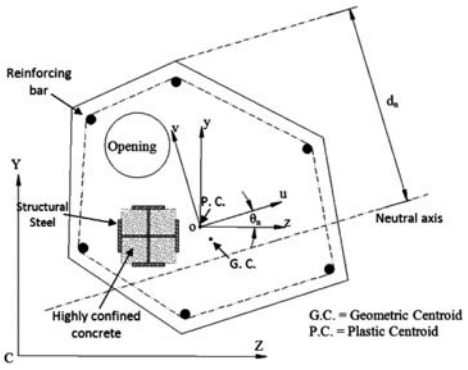

Figure 2. Arbitrary shape composite cross-section.

$$\sigma_c = f_c \qquad \text{for} \quad \varepsilon_{c0} \le \varepsilon_c \le \varepsilon_{cu} \qquad (16)$$

where f_c is the peak compressive design strength of concrete; ε_0 and ε_{cu} are the strain at reaching the maximum strength and the ultimate respectively; n is the exponent which can be conventionally taken as 2.0 for normal strength concrete.

The confinement effect of concrete can be taken into account by modifying the stress-strain relationship stated in Eurocode 2 (1999) as,

$$f_{c,c} = f_c(1.000 + 5.0\sigma_2 / f_{ck}), \text{ for } \sigma_2 \le 0.05 f_c \qquad (17)$$

$$f_{c,c} = f_c(1.125 + 2.50\sigma_2 / f_c), \text{ for } \sigma_2 > 0.05 f_c \qquad (18)$$

$$\varepsilon_{c0,c} = \varepsilon_{c0}(f_{c,c} / f_c)^2 \qquad (19)$$

$$\varepsilon_{cu,c} = \varepsilon_{cu} + 0.2\sigma_2 / f_c \qquad (20)$$

in which, σ_2 is the effective lateral compression due to confinement; $f_{c,c}$ is the peak compressive strength of confined concrete; $\varepsilon_{0,c}$ and $\varepsilon_{cu,c}$ are the confined concrete strains at the maximum and the ultimate strength respectively.

3.1 *Cross-sectional analysis for RC and SCC sections*

In this section, the sectional analysis for arbitrary shape sections, which may consist of four types of components, namely as unconfined and confined concrete, rebar, structural steel and openings, is discussed. An arbitrarily shaped cross section with arbitrary arrangement of reinforcing bars and structural steels subjected to biaxial-eccentric load is shown in Figure 2.

3.1.1 *Reference loading axes*

As shown in Figure 2, the location of the neutral axis can be determined by two variables, i.e., orientation angle θ_n and the depth d_n of neutral axis Brondumnielsen (1985) and Yen (1991) used a quasi-Newton method to find the θ_n and the d_n, which was claimed to be effective and efficient in dealing with cross section with regular shape. They adopted the geometric centroid as the origin of the reference loading axes which can be calculated as,

$$Z_{gc} = \frac{A_c Z_c + A_r Z_r + A_s Z_s - A_o Z_o}{A_c + A_r + A_s - A_o} \qquad (21)$$

$$Y_{gc} = \frac{A_c Y_c + A_r Y_r + A_s Y_s - A_o Y_o}{A_c + A_r + A_s - A_o} \qquad (22)$$

in which, A_c, A_r, A_s and A_o are the area of concrete, reinforcing bars, structural steels and opening respectively; $Z_c, Y_c, Z_r, Y_r, Z_s, Y_s, Z_o$ and Y_o are respectively the centroidal coordinates of each component; Z_{gc} and Y_{gc} are the coordinates of geometric centroid of the whole section.

However, Chen et al. (2001) reported that this technique did not always converge when it is applied to irregularly shaped cross section, especially when the arrangement of reinforcing rebar and structural steels is highly eccentric. They further proposed that, by using the plastic centroid as the origin of the reference loading axes, the aforementioned convergence problem can be overcome and meanwhile the number of iterations for convergence can be reduced. For an arbitrarily shaped composite cross section, the plastic centroid may be determined as (Roik & Bergmann 1990),

$$Z_{pc} = \frac{A_c Z_c f_c / \gamma_c + A_r Z_r f_r / \gamma_r + A_s Z_s f_s / \gamma_s - A_o Z_o f_c / \gamma_c}{A_c f_c / \gamma_c + A_r f_r / \gamma_r + A_s f_s / \gamma_s - A_o f_c / \gamma_c} \qquad (23)$$

$$Y_{pc} = \frac{A_c Y_c f_c / \gamma_c + A_r Y_r f_r / \gamma_r + A_s Y_s f_s / \gamma_s - A_o Y_o f_c / \gamma_c}{A_c f_c / \gamma_c + A_r f_r / \gamma_r + A_s f_s / \gamma_s - A_o f_c / \gamma_c} \qquad (24)$$

in which, f_c, f_r and f_s are the characteristic strengths of concrete, reinforcing bars and structural steels respectively; γ_c, γ_r and γ_s are the corresponding partial safety factors; Z_{pc} and Y_{pc} are the coordinates of plastic centroid of the whole section.

It should be further noted that, due to the Euler-Bernoulli hypothesis assumed in the beam-column element analysis, the generalized force and moments should correspond to the origin of the geometric centroid and therefore, the moment capacities calculated at the plastic centroid should be transferred to the geometric centroid for consistency. The transformation of the moments is described in the followings.

3.1.2 *Coordinate systems*

Three coordinate systems are adopted to describe the analysis procedure: ZCY, zoy and uov. The ZCY system is to describe the cross section defined by designers. The zoy and uov systems have the same origin as the plastic centroid of the cross section. Both the geometrical and plastic centroid can be readily determined. So the whole iterative process involves only coordinate transformation twice, as the global ZCY system to the load-reference zoy system and then to the uov system of which the u-axis is parallel to the neutral axis.

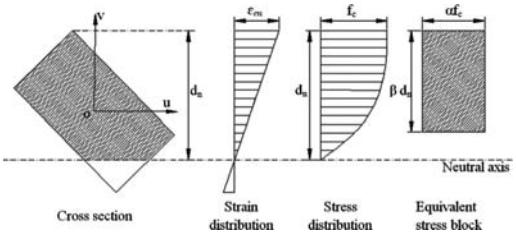

Figure 3. Stress resultants by equivalent stress block method.

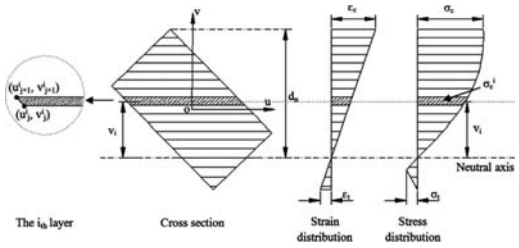

Figure 4. Stress resultants by elaborated integration method.

Their coordinate transformation formulae can be written respectively below as,

$$z = Z - Z_{pc}, \quad y = Y - Y_{pc} \tag{25}$$

$$u = z\cos\theta_n + y\sin\theta_n, \quad v = y\cos\theta_n - z\sin\theta_n \tag{26}$$

in which Z and Y, z and y, u and v are the coordinates in ZCY, zoy and uov systems respectively.

3.1.3 *Stress Resultants in concrete by equivalent stress block method*

In the calculation of the stress resultant of concrete under ultimate crushing state, the Whitney's stress block (Whitney 1965) (see Fig. 3) is introduced for the integration of the parabola stress-distribution, which is adopted in many national concrete codes. It should be pointed out that the strain of the most external fibre is taken as the crushing strain ε_{cu} and the tensile strength is usually ignored at the ultimate state.

The equivalent stress block method is limited to the generation of the stress resultant under the ultimate failure state. The stress resultants of other limit states can be obtained by more elaborated segments integration approach. The difference between the equivalent stress block method and elaborated segments integration method for calculating the stress resultant of the concrete under ultimate failure state is small as to be demonstrated in the verification examples in this paper. Due to simplicity and efficiency, it is more suitable to calculate the stress resultant of the concrete under ultimate limit state by using the equivalent stress block method. The mathematical expressions for calculation of stress resultants are shown as follows.

$$N_{xc} = \left|\sum_{i=1}^{n_c} N_{xci}^e\right| = \left|\sum_{i=1}^{n_c}\int_{u_i}^{u_{i+1}}\int_0^{\bar{v}(u)} \alpha f_c \, du d\bar{v}\right| \tag{27}$$

$$M_{uc} = \rho\sum_{i=1}^{n_c} M_{uci}^e = \rho\sum_{i=1}^{n_c}\int_{u_i}^{u_{i+1}}\int_0^{\bar{v}(u)} [-\alpha f_c(\bar{v}+v_n)] du d\bar{v} \tag{28}$$

$$M_{vc} = \rho\sum_{i=1}^{n_c} M_{vci}^e = \rho\sum_{i=1}^{n_c}\int_{u_i}^{u_{i+1}}\int_0^{\bar{v}(u)} \alpha f_c u \, du d\bar{v} \tag{29}$$

in which n_c is the number of vertices of the compression zone; $\bar{v}(u)$ is the linear equation of boundary line equal to $v(u) - v_n$ with v_n being the coordinate of the neutral axis in v-axis; ρ is equal to $+1$ when $N_{zc} > 0$ and equal to -1 when $N_{zc} < 0$.

3.1.4 *Stress Resultants in concrete by elaborated integration method*

As aforementioned, for more accurate integration of the stress in concrete component, the concrete zone will be divided into several segments as shown in Figure 4. Due to the stress and strain distribution are the same under the same vertical level in the rotated local axis, the strains in fibres in each layer segments are the same, and the method of layer segments division is more efficient than the conventional sectional fibre discretization. The complete concrete zone should be divided into a number of sub zones and the tension zone of concrete will be ignored.

The proposed layer segments integration approach can be applied to generate any kinds of yielding or controlling surfaces through adjusting the strain value at the most extreme fibre and its extended application will be discussed other publications by the authors. Moreover, the stress-strain model should be used for the determination of stress distribution. An adequate number of segments are required for acceptable accuracy. The mathematical formulas are given by,

$$N_{xc} = \sum_{i=1}^{n_L} N_{xci}^L = \sum_{i=1}^{n_L}\sum_{j=1}^{n_v(i)}\int_{u_j^i}^{u_{j+1}^i}\int_0^{\bar{v}(n)} \sigma_c^i \, du d\bar{v} \tag{30}$$

$$M_{uc} = \rho\sum_{i=1}^{n_L} M_{uci}^L = \rho\sum_{i=1}^{n_L}\sum_{j=1}^{n_v(i)}\int_{u_j^i}^{u_{j+1}^i}\int_0^{\bar{v}(n)} [-\sigma_c^i(\bar{v}+v_n)] du d\bar{v} \tag{31}$$

$$M_{vc} = \rho\sum_{i=1}^{n_L} M_{vci}^L = \rho\sum_{i=1}^{n_L}\sum_{j=1}^{n_v(i)}\int_{u_j^i}^{u_{j+1}^i}\int_0^{\bar{v}(n)} \sigma_c^i u \, du d\bar{v} \tag{32}$$

in which n_L is the number of the sectional layers; $n_v(i)$ is the number of intersection points in the corresponding layers.

3.1.5 *Stress Resultants in steel*

Each rebar is treated as an individual fibre, while the structural steel will be meshed into a number of fibres with rectangular areas. The stress resultants of steel section and reinforcement can be computed as,

$$N_{xs} = \sum_{j=1}^{n_r}\sigma_{rj}A_{rj} + \sum_{k=1}^{n_s}\sigma_{sk}A_{sk} \tag{33}$$

$$M_{us} = -\sum_{j=1}^{n_r} \sigma_{rj} A_{rj} v_{rj} - \sum_{k=1}^{n_s} \sigma_{sk} A_{sk} v_{sk} \tag{34}$$

$$M_{vs} = \sum_{j=1}^{n_r} \sigma_{rj} A_{rj} u_{rj} + \sum_{k=1}^{n_s} \sigma_{sk} A_{sk} u_{sk} \tag{35}$$

where A_{rj} and A_{sk} are the areas of discrete fiber and reinforcing bar respectively; σ_{rj} and σ_{sk} are the corresponding stresses.

3.1.6 *Opening area*

The negative area approach is used to remove the voids occupied by the steel components and the openings in the section.

3.1.7 *Total force and moments*

The bending moments obtained from the above equations are summed up and then transformed to the xoy system by the following transformations. The moments generated from the cross-section analysis are based on the origin of the plastic centroid, which should be transferred to the reference loading axes, i.e. the origin of geometric centroid.

$$N_x = N_{xc} + N_{xs} - N_{xo} \tag{36}$$

$$\begin{cases} M_u = M_{uc} + M_{us} - M_{uo}, \\ M_v = M_{vc} + M_{vs} - M_{vo} \end{cases} \tag{37}$$

$$\begin{cases} M_{pz} = M_u \cos\theta_n - M_v \sin\theta_n, \\ M_{py} = M_u \sin\theta_n + M_v \cos\theta_n \end{cases} \tag{38}$$

$$\begin{cases} M_z = M_{pz} + N_x (Z_{gc} - Z_{pc}), \\ M_y = M_{py} + N_x (Y_{gc} - Y_{pc}) \end{cases} \tag{39}$$

3.1.8 *Iteration scheme*

By rotating the orientation θ_n of neutral axis from 0° to 360° with the change of depth d_n, the section capacity can be precisely determined. The Regula-Falsi numerical method is utilized to satisfy the equilibrium, compatibility, and constitutive relationships.

The axial force capacity N_x is iterated with respect to d_n by the following equation with θ_n kept unchanged.

$$d_{n,k} = d_n + \frac{d_n^{'} - d_n}{N_x^{'} - N_x} (N_{xd} - N_x) \tag{40}$$

where $d_{n,k}$ is the depth of updated neutral axis; d_n and d_n' are the depth of neutral axis with the axial capacity being smaller and greater than the design value respectively; N_x and N_x' are the axial force capacity calculated at d_n and d_n' and N_{xd} is the current design axial loading.

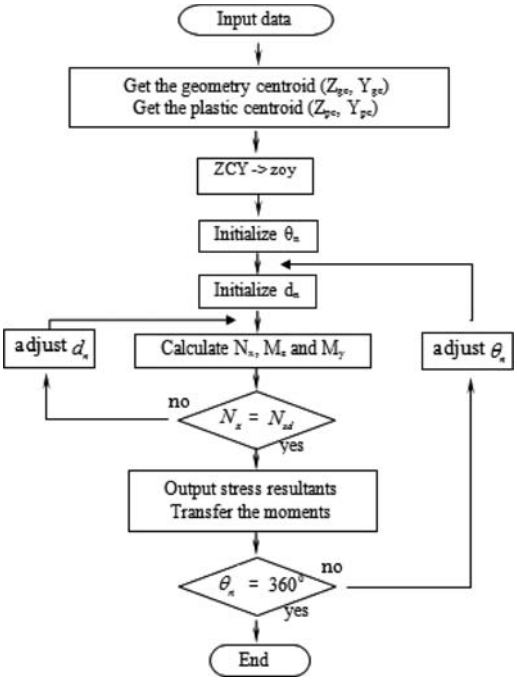

Figure 5. Generation the yield surfaces under given axial load.

The whole procedure of sectional analysis is illustrated in Figure 5.

3.1.9 *Section strength check*

To check the member adequacy, the section capacity factor ϕ_f defined in Eq. (41) is used to identify the failure condition:

$$\varphi_f = \frac{\sqrt{(M_y + N_x\Delta_y + N_x\delta_y)^2 + (M_z + N_x\Delta_z + N_x\delta_z)^2}}{\left|M_p^{\chi}\right|} \tag{41}$$

where Δ is the second-order displacement due to nodal coordinate change which includes out-of-plumpness frame imperfections and sway induced by loads in the frame; δ is the displacement due to member curvature and bowing induced by initial imperfections and load at ends and along the length of a member; M_p^{χ} is the moment capacity with the same orientation angle as applied moments under same axial force. If $\phi_f > 1$, the section capacity check fails and it implies that the section has reached its ultimate capacity.

In practice of the first-plastic hinge design, a geometrically nonlinear analysis is carried out and the load causing the formation of the first plastic hinge, detected by computation of section capacity factor ϕ_f along any member being greater than or equal to unity, is taken as the design load. In other words, in the incremental-iterative procedure, any member attaining a section capacity factor ϕ_f greater than unity is

considered as failure of the member and the load causing the failure of this member is taken as the resistant design load.

3.2 *Flexural stiffness modeling*

For the conventional design procedure, which is mainly based on the first order linear elastic theory, it is common to assume the effective moment of inertia for the concrete component by the empirical values or the code-specified reduction factors. Generally, it uses half of the gross moment of inertia for beams and the whole moment of inertia for columns. Many design codes and guidelines give approximate reduction factors for cracking effects on the flexural stiffness of the concrete components. For example, FEMA 356 (2000) suggests the gross moment of inertia of the highly and modestly loaded columns are respectively reduced to 30% and 50% of their uncracked values. The New Zealand Standard code (1995) gives a more detailed estimation of the effective moment of inertia for the concrete component under different loading conditions and magnitudes for an elastic analysis.

For design of high-rise buildings, the overall lateral deformation and internal storey drift sometimes govern in place of the strength criteria at elemental level and hence an accurate estimation of the flexural stiffness is crucial in design of this structural form. As the cracking effect of concrete component is quite different when under various loading conditions, codes give the conservative value which may over-estimate the cracking effect in most cases. For more elaborated representation of the gradual cracking effect within the concrete component, the modelling of gradual cracking will be presented in the companion paper. In the conventional design practice, this reduction factor specified in codes should be taken.

4 CASE STUDY

Two examples are chosen to demonstrate the application of the proposed second-order analysis and cross sectional analysis of a concrete filled steel tube section by methods.

4.1 *Elastic geometrically nonlinear analysis of deep toggle frame – Basic test of software for second-order analysis*

Many research studies claimed their success of using one element per member in a second-order analysis but their example is only on frames with members under small axial force at buckling. For example, the shallow William toggle frame is widely used but the snap through load of the William toggle is far below the member buckling load. When the axial force is large, many of these formulations are invalid that divergence will occur or the solution is not accurate. The deep toggle frame with depth increased by 10 times from

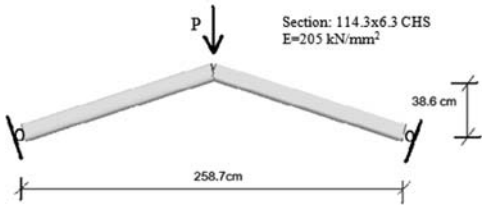

Figure 6. Deep toggle frame modeled by 1 element per member.

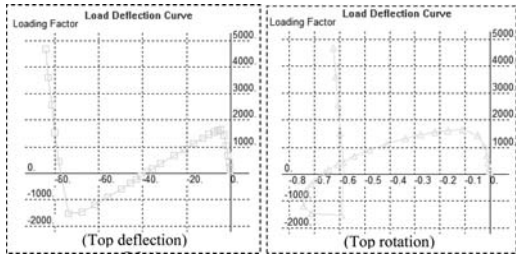

Figure 7. Vertical top deflection and rotation at tip of deep toggle.

the William toggle frame is shown in Figure 6 below and used to test the efficiency and reliability of software for a pure elastic analysis. Material yielding is not considered in order to check the part for geometrically nonlinear analysis.

The elastic load vs. deflection plots of the frame are shown in Figure 7 above. It can be seen that the frame buckles elastically at a load about 1600 kN at which the frame snaps-through.

4.2 *Typical concrete filled hollow section*

A rectangular concrete filled section is used to verify the accuracy of the proposed approach. The layout and section properties of the two sections are shown in Figure 8a. While, the failure surfaces of major and minor axes obtained from the proposed method are compared with those designed by Eurocode 4 (2005) are shown in Figure 8b.

The axial force vs. moment interaction curves from the proposed methods is also very close to the result calculated by code, as can be seen in Figure 8. From above, the proposed cross-sectional analysis technique is noticed to be accurate and efficient. For beam-columns of other and irregular sections, the results are reported in other publications by the authors due to limitation in page number of this paper.

4.3 *Discussions*

By using the proposed second-order analysis approach, which considers initial imperfections of the individual members and the whole frame, the effective length assumption is eliminated and therefore a

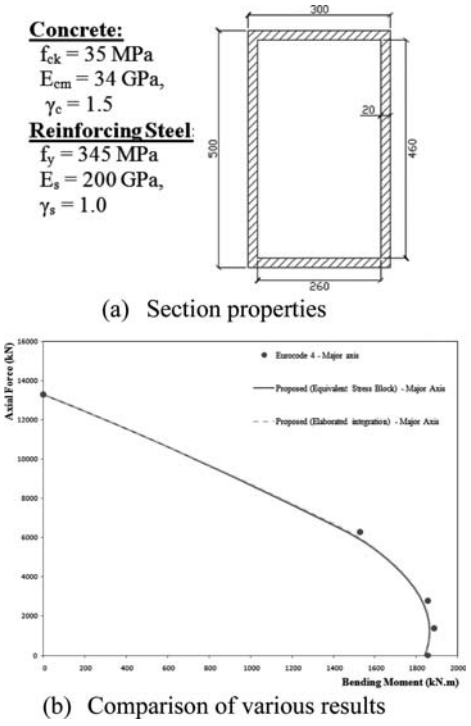

Figure 8. Sectional analysis of a concrete filled hollow section.

safe and economical design can be achieved. Thus, all types of structural members can be designed in a unified way with safety ensured by the simple section capacity check.

5 CONCLUSIONS

In this paper, an advanced analysis and design approach is proposed for the design of structures composed of concrete-filled hollow sections. By using an initially curved beam-column element in the robust nonlinear incremental-iterative procedure, the second-order effects of individual members and of the structural system can be modelled. Further, a divergence-proof iterative procedure is used to exactly calculate the strength interaction surfaces of arbitrary concrete-filled hollow sections subjected to biaxial bending. Thus, the proposed method checks the stability and sectional strength in the process of structural analysis without additional individual member design. The remarkable advantages include the abandon of the assumption of effective length for member check and the consideration of the effects of stiffness variation due to loads on columns. It is believed that the proposed approach will be the next-generation design method for modern structures made of members of concrete filled sections of any shape. The application of the second-order direct analysis is especially suitable for hollow sections where buckling is seldom controlled by local plate and lateral-torsional buckling which nevertheless could still be handled by the second-order analysis with modest increase in analysis and design effort.

ACKNOWLEDGEMENT

The authors acknowledge the financial support by the Research Grant Council of the Hong Kong SAR Government on the projects “Collapse Analysis of Steel Tower Cranes and Tower Structures (PolyU 5119/10E) and “Stability and second-order analysis and design of re-used and new scaffolding systems (PolyU 5116/11E)”.

REFERENCES

American Institute of Steel Construction 2010. Specification for Structural Steel Buildings.

Brondumnielsen, T. 1985. Ultimate Flexural Capacity of Cracked Polygonal Concrete Sections under Biaxial Bending. Journal of the American Concrete Institute 82(6): 863–869.

Buildings Department of Hong Kong SAR Government 2005. Code of Practice For The Structural Use of Steel 2005.

Chan, S. L. & Zhou, Z. H. 1994. Pointwise Equilibrating Polynomial Element for Nonlinear-Analysis of Frames. Journal of Structural Engineering-ASCE 120(6): 1703–1717.

Chan, S. L. & Zhou, Z. H. 1995. 2Nd-Order Elastic Analysis of Frames Using Single Imperfect Element Per Member. Journal of Structural Engineering-ASCE 121(6): 939–945.

Chan, S. L. & Zhou, Z. H. 1998. On the development of a robust element for second-order ‘nonlinear integrated design and analysis (NIDA)’. Journal of Constructional Steel Research 47(1–2): 169–190.

Chan, S. L. & Zhou, Z. H. 2000. Non-linear integrated design and analysis of skeletal structures by 1 element per member. Engineering Structures 22(3): 246–257.

Chen, S. F., Teng, J. G., et al. 2001. Design of biaxially loaded short composite columns of arbitrary section. Journal of Structural Engineering-ASCE 127(6): 678–685.

Chen, W. F. & Chan, S. L. 1995. 2Nd-Order Inelastic Analysis of Steel Frames Using Element with Midspan and End Springs. Journal of Structural Engineering-ASCE 121(3): 530–541.

Federal Emergency Management Agency 2000. Prestandard and Commentary for the Seismic Rehabilitation of Buildings (FEMA356). Building Seismic Safety Council, Washington, D.C, FEMA.

New Zealand Standard 1995. Concrete structures standard: part 2 – Commentary on the design of concrete structures. New Zealand.

Roik, K. & Bergmann, R. 1990. Design Method for Composite Columns with Unsymmetrical Cross-Sections. Journal of Constructional Steel Research 15(1–2): 153–168.

The European Committee for Standardization (CEN) 1999. Eurocode 2: Design of concrete structures.

The European Committee for Standardization (CEN), 2005. Eurocode 4: Design of composite steel and concrete structures. (DD ENV 1994-1-1:2004).

The European Committee for Standardization (CEN), 2006. Eurocode 3 : Design of steel structures. (DD ENV 1993-1-3:2006).

Whitney, C. S. 1965. Plastic theory of reinforced concrete design. Emmitsburg, MD, National Emergency Training Center.

Yen, J. Y. R. 1991. Quasi-Newton Method for Reinforced-Concrete Column Analysis and Design. Journal of Structural Engineering 117(3): 657–666.

Zhou, Z. H. & Chan, S. L. 1996. Refined second-order analysis of frames with members under lateral and axial loads. Journal of Structural Engineering-ASCE 122(5): 548–554.

Zhou, Z. H. & Chan, S. L. 1997. Second-order analysis of slender steel frames under distributed axial and member loads. Journal of Structural Engineering-ASCE 123(9): 1187–1193.

Tubular Structures XIV – Gardner (Ed.)
© 2012 Taylor & Francis Group, London, ISBN 978-0-415-62137-3

Strength and stability of High-Strength Steel tubular beam-columns

A.E. Pournara & S.A. Karamanos
Department of Mechanical Engineering, University of Thessaly, Volos, Greece

J. Ferino & A. Lucci
Centro Sviluppo Materiali (CSM) S.p.A, Rome, Italy

ABSTRACT: In this study, the structural behavior of high-strength steel tubular CHS seamless structural members under combined loading of axial compression and bending is examined. The work is mainly numerical supported by a series of tests. Eight full-scale combined loading tests on short seamless tubular specimens are performed and are used to calibrate the finite element tools. Furthermore, initial imperfection and residual stress measurements are conducted and taken into account in the numerical analyses. Using the numerical tools, stability curves for high-strength steel (TS590) tubular members are obtained. Subsequently, combined loading analyses are conducted on high-strength steel tubular members, so that interaction diagrams are developed, showing the interaction between axial load and bending moment. Both stability curves and interaction diagrams are compared with existing beam-column design provisions of relevant European and American specifications. The comparison shows that the current EN 1993, API RP 2A and AISC specifications, provide reasonable, yet conservative, estimates for the ultimate strength of high-strength steel tubular CHS seamless beam-columns.

1 INTRODUCTION

The use of Circular Hollow Sections (CHS) has recently had a significant development both for their excellent structural and architectural properties. In particular, High-Strength Steel (HSS) CHS members have become commercial about 3 decades ago, but their use is still limited in the construction industry, despite the growing demand for high-strength lightweight structural systems; the use of high strength steel, with yield strength from 460 to 690 MPa, could provide cost efficiency in column and beam CHS member design because of the higher structural strength resulting in structures with a good strength-to-weight ratio.

The buckling behavior of high-strength steel tubular members constitutes an issue of particular interest. One should note that the stress-strain behavior of HSS is considerably different from that of mild steel, exhibiting considerably lower material ductility and higher levels of strain hardening. Previous studies on the buckling behavior of HSS members referred mainly to H, I and box sections (Rasmussen & Hancock 1995; Beg 1996; Sivakumaran & Bing 1998; Johansson & Collin 2008) and indicated that they perform quite well compared with ordinary steel structural members, while the existing design rules for normal-grade steel (e.g. EN 1993) can be used as a conservative approach. The good buckling behavior of HSS is attributed to the smaller influence of geometric imperfections and residual stresses (Jiao & Zhao 2003).

The present study is mainly numerical, supported by experimental testing on short columns and imperfection measurements. It is a part of an extensive European research effort with the aim at developing structural design guidance for high-strength steel CHS members, compatible with the current provisions of EN 1993. Special emphasis is given to possible revisions of strength and buckling predictions for predicting the ultimate capacity of high-strength steel CHS elements under axial and bending loading, in terms of stability curves and interaction diagrams, as well as revising the current slenderness limits for CHS member classification for the case of HSS. It should be noted that the EN 1993-1-12 standard, which specifies the use of high-strength structural steel, does not impose any restriction on the use of EN 1993-1-1 rules for CHS beam-column design, but this subject needs more in-depth investigation.

The present paper refers to stability curves and interaction diagrams for high-strength steel CHS members, whereas the corresponding cross-sectional classification is examined in detail in the companion paper of Pappa *et al*. (2012).

2 CURRENT SPECIFICATIONS

The structural design of tubular members under axial compression, bending and combined loading conditions is covered by the current provisions of EN-1993-1-1 (EN 1993), in sections 6.2 and 6.3, officially applicable for steel grade up to 460 MPa.

Two other specifications are considered in the present study. The AISC specification for hollow sections (AISC 1999) contains rules for structural steel tube design. In addition, the API RP2A – LRFD rules, Chapter D, have been developed for the design of tubular for offshore steel platforms. Both specifications do not cover the case of high-strength steel. Finally, the CIDECT provisions (CIDECT 1992) are based on the old provisions of ENV 1993-1-1 and, therefore, they are not considered in the present study.

3 EXPERIMENTAL INVESTIGATION

3.1 *Specimen description and set-up*

The experimental investigation consists of eight (8) full-scale tests on 1.5-meter-long tube specimens of 12-inch and 14-inch nominal diameter. The tubes are seamless, made of TS590 high-strength steel material (nominal yield stress equal to 590 MPa), and have been produced by Tenaris Dalmine. The corresponding cross sectional dimensions are Ø355.6/12.5 (referred to as "section A"), and Ø323.9/10 (referred to as "section B"). The specimens are tested under combined-loading conditions of thrust and bending.

Initial imperfection measurements have been conducted in several specimens before testing, in terms of thickness variation, initial wrinkling of the tube wall to be used in the finite element simulations. In addition, residual stress measurements have been obtained. All those measurements are presented in the next paragraph.

Uniaxial tension tests on coupon strip specimens have been conducted for obtaining the real material properties of the steel material. The tests have indicated that yield stress σ_y and ultimate stress equal to 723 MPa, and 805 MPa respectively. Following a small plastic plateau after yielding, strain hardening of the material started at 0.5% engineering strain. Furthermore, the ultimate stress of 805 MPa occurred at a value of engineering strain equal to 7%, indicating a rather low ductility, typical for high-strength steel.

The combined loading tests on the tubular specimens are conducted with the use of the testing rig shown in Figure 1. The specimens are simply supported, with the use of two hinges that allow rotation on the horizontal plane. This equipment can accommodate tubular specimens of length up to 5 meters, with diameters ranging from 8 to 20 inches. The maximum tensile and compressive load capacity of the testing machine is 25,000 kN and 30,000 kN, respectively, whereas the maximum bending moment capacity is 3,000 kNm.

The connection of the specimen ends to the testing machine is made through a 40-millimeter-thick connecting flange, bolted to the machine ends with eigthteen M30 12.9 bolts. To avoid local buckling at the two ends, 20-mm-thick stiffeners are welded around the circumference. The total specimen configuration with the end stiffeners is shown in Figure 2. The stiffened ends of the tubular specimens are connected

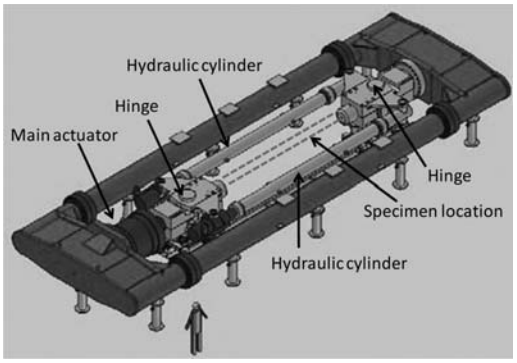

Figure 1. CSM experimental set-up for large scale testing.

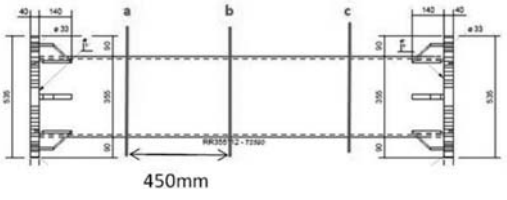

Figure 2. Final drawing of beam-column specimens.

to the hinges of the testing device through the 2.22-meter-long very thick tubes, which remain practically undeformed during the test (Fig. 1).

The combined loading conditions are considered through a $N \rightarrow M$ loading sequence. More specifically, axial compressive loading is applied first through the main actuator, at a prescribed level. Subsequently, while the axial load is kept constant, bending moment is gradually applied through the free hinges by means of rotation-controlled conditions, activating the two hydraulic cylinders, as shown in Figure 1. During the testing procedure, bending strain gauges are implemented on circumferential positions, along the tubular axis at cross sections a, b, c as shown in Figure 2. Moreover, 4 LVDTs are instrumented around the tube circumference parallel to the tubular axes, in order to measure the tube deflection.

3.2 *Imperfection Measurements*

Thickness measurements indicated that the actual thickness of the tested specimens varies between 12.1 mm and 13.83 mm for specimens A, while for specimens B the thickness values range between 9.90 mm and 11.59 mm. Thickness variation is measured at 8 points around several cross-sections along the specimen longitudinal axis via an ultrasonic technique.

Initial wrinkling measurements were also performed prior to the experimental procedure via special-purpose equipment. Each specimen was placed horizontally on the manual measuring device as shown in Figure 3 and the tube wall wrinkling was measured at specific points along 8 equally-spaced

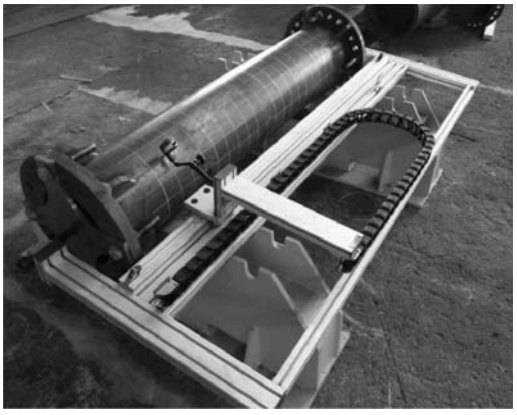

Figure 3. Imperfection measuring device.

generators. The maximum value of wrinkling amplitude, recorded by the machine, is measured equal to 3.62% of the tube thickness (Pappa *et al.* 2012).

Residual stress measurements were also performed in both the axial and the circumferential direction. The measurements in the hoop direction follow the "splitting ring" method, as specified in ASTM E1928-99, and resulted in an opening ring deformation (gap) of 1.7 mm, corresponding to a maximum hoop stress equal to 122 MPa (about 17% of the yield stress). Furthermore, to estimate the residual stresses in the axial direction, longitudinal strips have been extracted from the tubes, and their curvature has been measured, resulting in a maximum stress of 26 MPa, which is only 4% of the yield stress (Pappa *et al*. 2012).

3.3 *Experimental results*

The experimental results are tabulated in Table 1. As expected, the bending moment capacity is decreased with the increase of axial loading. Moreover, section A specimens present higher bending capacity than section B specimens due to the larger value of their cross sectional area. Indicative buckling shapes of both groups are compared with the failure modes of the finite element models as shown in the following session.

Table 1. Experimental results.

Specimen	D_{nom} (mm)	t_{ave} (mm)	N (kN)	M (kNm)
A1	355.6	–	1345.0	891.5
A2	355.6	12.63	2563.5	701.0
A3	355.6	12.74	5127.0	382.4
A4	355.6	12.62	7690.5	104.0
B1	323.9	–	1003.0	575.8
B2	323.9	10.86	1990.3	500.7
B3	323.9	10.86	3980.5	208.5
B4	323.9	10.79	5970.8	76.4

4 FINITE ELEMENT SIMULATION OF TESTS

Nonlinear finite element tools have been employed to simulate the above combined loading experiments. The main purpose of this numerical simulation is the calibration of the finite element models, to be used in the extensive parametric study, described in the next session.

The simulations are conducted with FE program ABAQUS, and the finite element models are capable of describing large displacements and strains, as well as inelastic effects through a J_2 (von Mises) flow plasticity model. The tube is simulated with four-node reduced-integration shell elements, which have shown to perform very well in nonlinear analysis problems involving large inelastic deformations of relatively thick-walled steel cylinders. Based on thickness measurements, the tubes have been assumed with uniform thickness equal to 12.5 mm and 10.26 mm for sections A and B respectively.

Initial wrinkling is considered in the form of buckling mode obtained through an eigenvalue analysis of the specimen under bending conditions. The amplitude of initial wrinkling is assumed equal to 2.6% of the tube wall thickness, as a representative value in accordance with the wrinkling measurements (Pappa *et al*. 2012). Furthermore, residual stresses in hoop direction have been considered as initial stresses of the model in the form of a linear anti-symmetric distribution through the tube thickness with a maximum value of 122 MPa. Residual stresses in the longitudinal direction are quite small and are neglected in the numerical model.

The stiff tube segments which connect the specimen ends to the machine hinges are simulated as rigid members using appropriate beam elements. The shape of the buckle may not be symmetric with respect to both the middle-section and the plane of bending, therefore, the entire tube is simulated, without any symmetry considerations.

The numerical analysis allows for the calculation of bending strength under several levels of axial load, in accordance with the experimental procedure; axial load is applied first up to a certain prescribed level and, subsequently, keeping the axial load constant, bending is applied through an arc-length continuation algorithm (Riks) until a maximum bending moment is reached. Upon buckling formation, bending load is continued in the post-buckling range to obtain the buckled shape and compare with the experiments.

The end sections of the 1.5-meter-long tubular specimen (sections C1 and C2 in Figures 4 & 5) are bolted with the tubular member. Therefore, a "kinematic coupling" technique is adopted, relating the degrees of freedom of the shell nodes around a specific section with the degrees of freedom of a fictitious node, referred to as the "reference node," located at the centroid of the section under consideration. The entire finite element configuration is simply supported at both ends of the rigid segments D1 and D2.

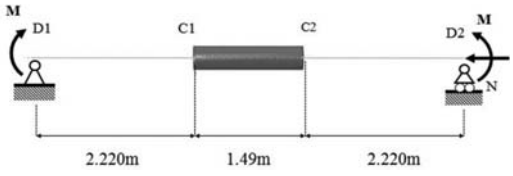

Figure 4. Schematic configuration of the numerical model that simulates the experiments.

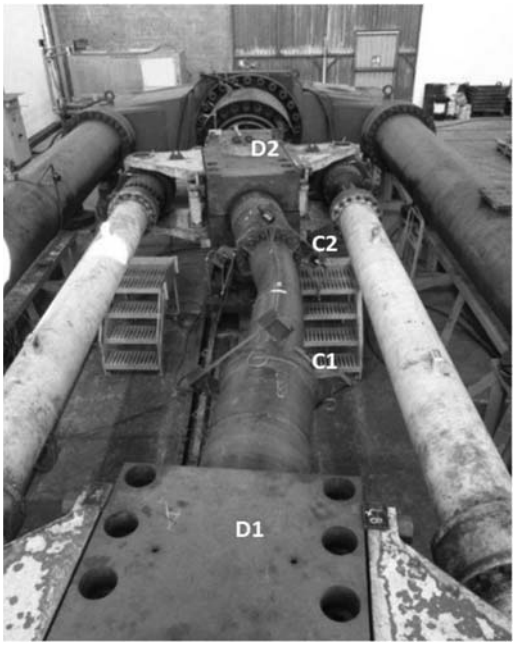

Figure 5. Test set-up and post-buckling configuration of specimen A1.

The finite element results are compared in Figure 6 with the experimental data, in terms of thrust-bending interaction curves. The comparison shows that the numerical models provide very good predictions of the axial-bending combined capacity of the high strength steel tubular columns. Furthermore, the buckled shapes of the specimens obtained numerically compare very well with the corresponding buckled shapes observed in the experiments, as shown in Figures 7 & 8.

It should be noted that for the purpose of conducting a consistent comparison between the numerical and experimental results, the axial force and bending moment (Figure 6) applied at the end hinges of the experimental set-up through the testing machine, are considered in the present simulations.

5 NUMERICAL PARAMETRIC STUDY

Finite element analysis has been conducted in order to obtain buckling curves and interaction diagrams of compression and bending. The geometric properties

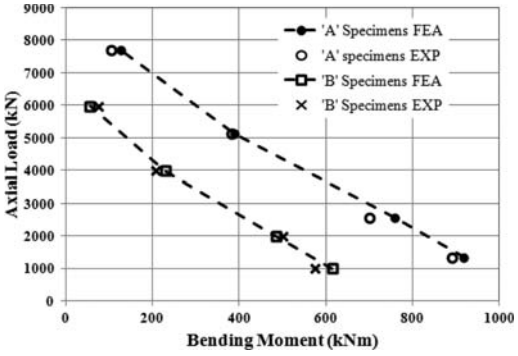

Figure 6. Interaction diagrams; numerical results in comparison with the experimental data.

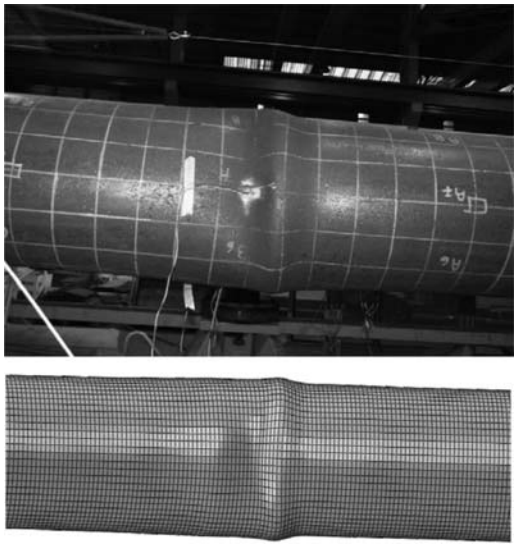

Figure 7. Buckled shape for the A4 specimen and FE simulation.

of the tubular cross sections under consideration are presented in Table 2 and the member length L ranges from 1 to 14m. The tubular member is assumed simply supported. The material stress-strain curve used in the present analysis represents a bilinear elastic-plastic curve with yield stress equal to 590 MPa and a post-yield modulus equal to $E/40$, as measured in the high strength steel coupon tests (Pappa *et al*. 2012). The results are compared with the current design provisions of EN-1993, API 2A-LRFD and AISC-LRFD. Safety factors are excluded.

5.1 *Stability curves*

The buckling strength N_u of beam-columns in terms of their flexural or column slenderness,

$$\lambda_C = \frac{L}{\pi r}\left(\frac{\sigma_y}{E}\right)^{0.5} \quad (1)$$

Table 2. Geometric-mechanical properties.

Section	Outer Diameter D (mm)	Thickness t (mm)	D_0/t	σ_y (MPa)	Class*
AA	355.6	8	44.5	590	4
AB	355.6	12.5	28.5	590	3
AC	355.6	16	22.2	590	2

*According to EN-1993-1-1 classification.

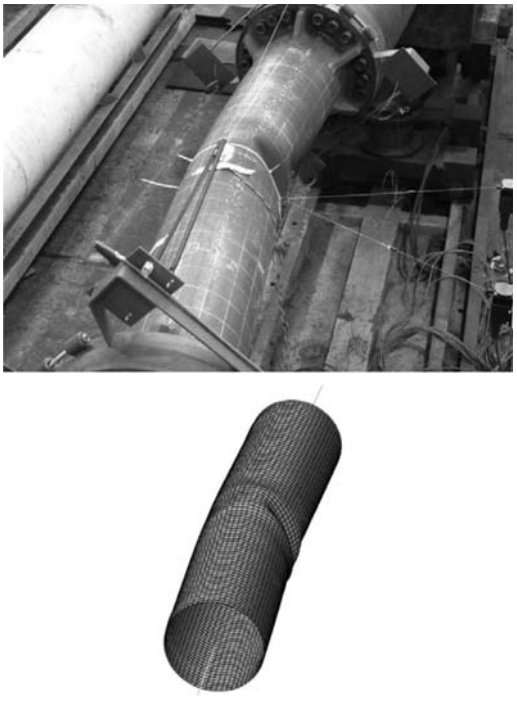

Figure 8. Buckled shape for the B4 specimen in comparison with the FE model.

where r is the radius of cross section inertia, so that

$$N_u = \chi(\lambda_C)\sigma_y A \tag{2}$$

where $\chi(\lambda_C)$ = the buckling reduction function and A = the cross sectional area.

Considering tube length between 1m to 14m, the corresponding member slenderness ranges between 0.13 and 2. A combination of initial imperfections has been imposed according to the measurements reported in session 3; the wrinkling amplitude is considered equal to 2.6% of the tube thickness, and the residual stresses are imposed with amplitude of ±122 MPa, linearly distributed through the thickness. Finally, initial out-of-straightness of $L/750$ is assumed according to EN 1090-2.

The ultimate buckling load N_u is depicted in Figures 9-11. The buckling load is normalized by $Ny = A\sigma y$. The stability curves are compared with the provisions

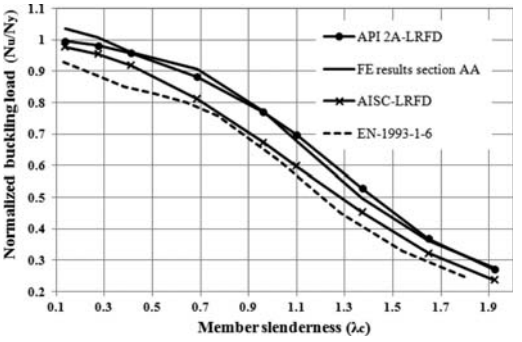

Figure 9. Finite element stability curve for section AA in comparison with European and American provisions.

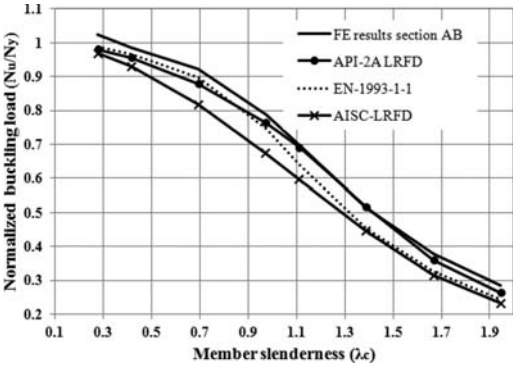

Figure 10. Finite element stability curve for section AB in comparison with EN and American provisions.

of EN 1993, API RP-2A and AISC-LRFD. It should be noted that according to EN 1993-1-1, the cross section AA is classified as class 4 and therefore, EN 1993-1-6 has been used to obtain the cross-sectional strength σ_{xRk}; the value of σ_{xRk} replaces the yield stress σ_y in equations (1) and (2). Because of the very small values of initial wrinkles measured throughout the experimental investigation, as reported in Section 3.2, excellent fabrication conditions have been assumed (quality factor (Q) equal to 40).

It appears that EN 1993-1-6 equations penalize significantly section AA. The results are well correlated with the stability curve proposed by API standard, while the AISC is conservative by over 20% for all slenderness values.

The stability curves of AB and AC sections compare reasonably well with the EN 1993 and API predictions. For large values of member slenderness ($\lambda \geq 1$) EN 1993-1 underestimates by over 10% the buckling strength. On the other hand, for intermediate values of member slenderness, AISC seams to penalize the buckling strength significantly.

As a conclusion, the EN 1993 and API provisions appear to provide reasonable yet conservative estimates for the buckling load of high strength steel CHS columns.

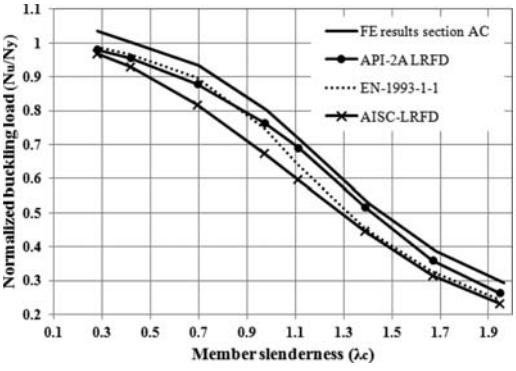

Figure 11. Finite element stability curve for section AC in comparison with European and American provisions.

Figure 12. Buckled shape of 1m-long (stub) tube of section AA under axial compression.

Figure 13. Buckled shape of 5m-long tube of section AA under axial compression.

Furthermore, indicative buckled shapes due to axial compression for short and long tubular members of section AA are depicted in Figures 12–13.

It is observed that, in short members ($0.1 \leq \lambda_C \leq 0.3$), local buckling occurs progressively while plastic deformation is accumulated at the most critical region of the tube wall. The member does not deviate from the longitudinal axis until the tube wall has been excessively deformed. For intermediate and large values of member slenderness, global (Euler type) buckling occurs, and the member is suddenly deflected laterally from the initial straight position.

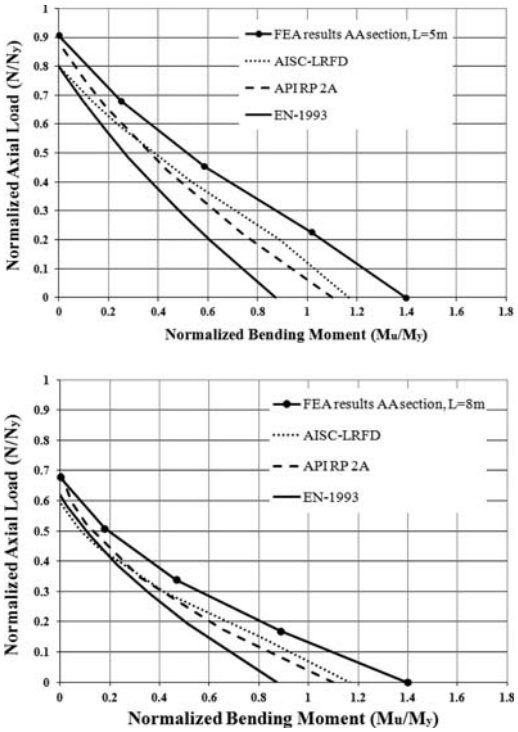

Figure 14. Interaction diagrams for AA section in comparison with current provisions.

As it is shown in Figure 13, in the case of long tubular members ($\lambda_C > 0.5$) the buckle shape commonly consists of a single inward buckle perpendicular to the longitudinal axis of the member.

5.2 *Interaction diagrams*

Interaction diagrams are developed for 5m and 8m-long beam-columns under combined loading conditions to obtain showing the ultimate moment capacity of the tubular member M_u in terms of the level of axial force$N$. The reported values of moment correspond to the moments applied at the two ends of the tubular beam-column. The initial imperfections, the geometrical and material properties adopted for this analysis are similar to the ones described previously.

The axial load and bending moment values are normalized with the values $N_y = A\sigma_y$ and $M_y = W_{el}\sigma_y$, where W_{el} is the elastic modulus of the cross-section, representing the compressive and bending strength of the cross section respectively.

The interaction diagrams are compared with the curves proposed by design specifications as shown in Figures 14 and 15. EN 1993 provisions (employed herein with beam-column method 1) significantly penalize the bending capacity of the tubular member so that the bending strength is underestimated by approximately 35% for both AA and AB sections. The reason is that these CHS members are classified as class 4 and 3, respectively, but the finite element results

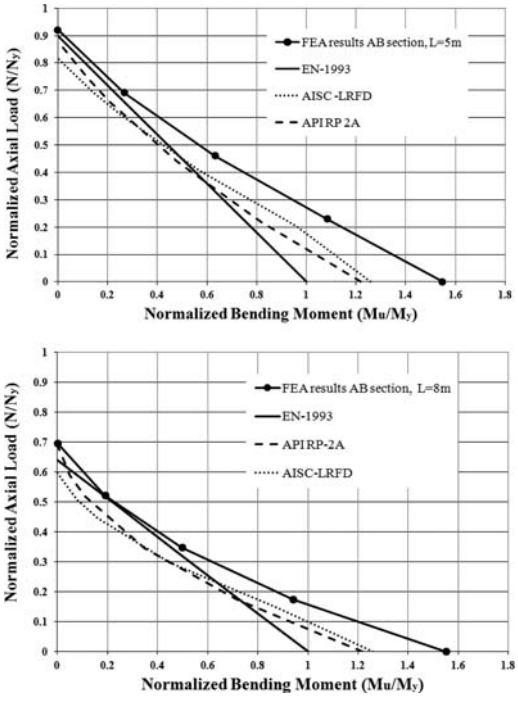

Figure 15. Interaction diagrams for AB section in comparison with current provisions.

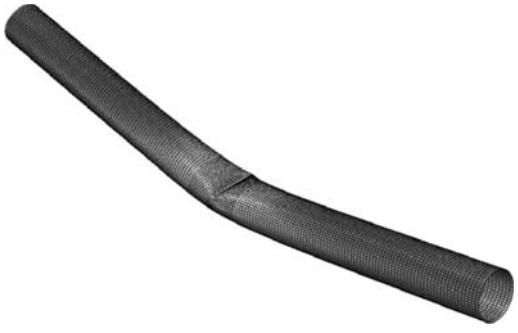

Figure 16. Buckled shape of 5m-long tube with section AB under combined compression and bending.

indicate that the sections are capable of undergoing significant inelastic deformation before reaching an ultimate moment capacity. Moreover, AISC penalizes the bending strength by over 15%. Similarly, the bending capacity is underestimated by API by more than 18%. In addition, representative buckled shapes obtained from the finite element models AA and AB are shown in Figures 16 & 17.

It can be concluded that the current standards appear to be rather conservative, especially the EN 1993 predictions mainly due to the "penalizing" classification of CHS cross sections in EN 1993-1-1 (Pappa *et al*. 2012).

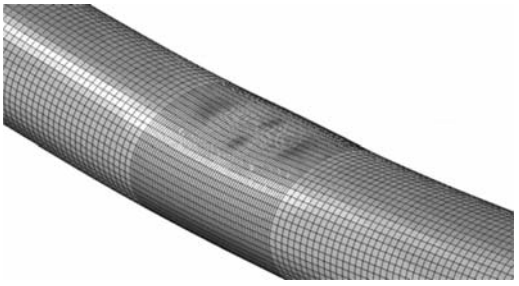

Figure 17. Buckle development in an 8m-long model with section AA under combined loading.

6 CONCLUSIONS AND RECOMMENDATIONS

Using advanced numerical tools, supported by key experimental data, the high-strength steel CHS beam-column behavior has been examined, and compared with current design practice.

Stability curves from EN 1993-1-1, API RP 2A, provide reasonable yet conservative predictions for design. On the other hand, AISC provisions for CHS beam-columns appear to be more conservative. The EN 1993 provisions penalize the buckling capacity of high-strength steel CHS members of relatively small thickness because they are classified as class 4, referring to EN 1993-1-6 rules. This implies that the current EN 1993 classification should be re-examined for high-strength steel CHS sections.

Furthermore, the axial load-bending interaction curves obtained by the finite element analyses indicate significantly higher ultimate capacity with respect to the design rules of the above specifications. In particular, EN 1993 rules penalize by a substantial amount the pure bending strength mainly due to the conservative classification limits when applied to high-strength steel CHS sections.

The above classification limits for axial and bending loading in high-strength steel CHS sections are examined in detail in the companion paper (Pappa *et al*. 2012).

ACKNOWLEDGEMENTS

This work has been carried out with financial support from the Research Fund for Coal and Steel of the European Commission, within ATTEL project: "Performance-Based Approaches for High Strength Steel Tubular Columns and Connections under Earthquake and Fire Loadings", Grant No RFSR-CT-2008-00037.

REFERENCES

AISC-LRFD 2000. *Load Resistance Factor Design Specification for steel hollow structural sections*. American Institute of Steel Construction, Chicago, Illinois.

American Petroleum Institute 1993. *Recommended Practice, Designing and Constructing Fixed Offshore Platforms-Load and Resistance Factor Design*. Recommended practice 2A-LRFD, 1st Edition. Washington.

Beg, H. 1996. *Slenderness limit of Class 3 I cross-sections made of high strength steel*. Journal of Constructional Steel Research,Volume 38, Number 3, pp. 201–217.

CEN EN 1993-1-1 2005. Eurocode 3: *Design of steel structures. Part 1–1: General rules and rules for buildings.* European Committee for Standardization, Brussels.

CEN EN 1993-1-6, 2007. Eurocode 3: *Design of steel structures. Part 1–6: Strength and Stability of Shell Structures.* European Committee for Standardization, Brussels.

CEN EN 1993-1-12, 2006. Eurocode 3: *Design of steel structures. Part 1–12: Additional rules for the extension of EN 1993 up to steel grades S 700.* European Committee for Standardization, Brussels.

CEN EN-1090-2 2008. *Execution of steel structures and aluminium structures – Part 2: Technical requirements for steel structures.* European Committee for Standardization, Brussels.

CIDECT 1992. *Structural Stability with Hollow Sections*. CIDECT design guide No. 2, Springer-Verlag.

Jiao H. and Zhao X.-L. 2003. Imperfection, residual stress and yield slenderness limit of very high strength (VHS) circular steel tubes. *Journal of Constructional Steel Research,* Volume 59, Number 2, pp. 233–249.

Johansson B. & Collin P. 2005. *Eurocode for high strength steel and applications in construction*. Luleå University of Technology, Sweden.

Pappa, p., and Karamanos, S. A. 2012. Buckling of High-Strength Steel CHS Tubular Members Under Axial Compression and Bending. 14th International Symposium on Tubular Structures, Paper No. 104, London, UK.

Rasmussen G. J and Hancock K. 1995. Test of High Strength Steel Columns. *Journal of Constructional Steel Research*, Volume 34, pp. 27–52.

Sivakumaran K.S. and Bing Y. 1998. Slenderness limit and ductility of high strength steel sections. *Journal of Constructional Steel Research*, Volume 46, Number 1, pp. 149–151.

Materials and section forming

Tubular Structures XIV – Gardner (Ed.)
© 2012 Taylor & Francis Group, London, ISBN 978-0-415-62137-3

Direct forming versus continuous forming, for cold-formed square hollow sections

M. Sun & J.A. Packer
University of Toronto, Toronto, Canada

ABSTRACT: This paper compares the geometric and mechanical properties of square hollow sections manufactured in North America by direct forming and continuous forming production methods. Square 152 × 152 mm sections, produced by direct forming, continuous cold forming, and also with the latter subsequently stress-relieved by heat treatment in accordance with Canadian standards, are the basis of the comparison. The mechanical properties compared are the overall compressive behaviour (via stub column tests), tensile behaviour and ductility in the flats and corners (via tension coupon tests), and notch toughness in the flats and corners as a function of test temperature (via Charpy V-notch impact tests). It is shown that direct-forming, or "folding", generally leads to more favourable mechanical performance than continuous-forming, for square/rectangular hollow sections.

1 INTRODUCTION

Cold-formed structural hollow sections are most commonly manufactured internationally by a "continuous forming" or "round-to-square" method, whereby steel plate or coil strip is progressively bent into a circular shape by passage through a series of pressure rolls, then welded into a tube by means of an induction heating process. Further shaping of the tube into square or Rectangular Hollow Sections (RHS) is then achieved by additional flattening and cold-working, using still more rolls. The final square or rectangular hollow section contains high levels of residual stress throughout its entire cross-section. An alternative production process for cold-formed square and rectangular hollow sections, practiced in some parts of the world, is the so-called "direct forming" method, whereby steel plate is bent only at four discrete points to form the corners of the section and the shape is again closed by a continuous longitudinal seam weld. The cold-working in this case is concentrated at the four corners.

In North America, Europe, Japan and Australia the continuous forming process is used almost exclusively (one exception being Bull Moose Tube in the US which uses the direct-forming method). Recently, a research project carried out by Shanghai Institute of Iron and Steel Technology on high performance cold-formed RHS resulted in the direct forming technique becoming the dominant manufacturing method of large size, cold-formed RHS in China. Mass production by this method started from 2005, with maximum dimensions of 500 × 500 × 19 mm, a maximum tensile strength of 630 MPa and a yield-stress-to-tensile-strength ratio less than 0.8. Production was 14,758 tons in 2005, and these RHS have been successfully used in the construction of Olympic stadiums, railway stations, power plants and bridges (MOST 2006).

With cold-formed RHS, depending on the amount of cold working, the mechanical properties are sometimes substantially different from those of the steel strip before forming. Cold working causes strain hardening of the steel material hence its yield stress and tensile strength increase while its ductility decreases. RHS of nominally similar geometries may exhibit different structural behaviours due to different strain histories and thermal actions experienced during production. The influence of cold working on the mechanical properties of structural steel and stainless steel sections has been studied extensively in the past and models have been developed to estimate the change in the material properties, but direct comparisons between cold-formed RHS produced by different manufacturing methods are scarce. In this paper, the mechanical properties of RHS manufactured in North America by these direct forming and continuous forming methods are compared through a series of investigations.

2 TEST SPECIMENS

An experimental study comprising geometric measurements, stub column tests, tensile coupon tests and Charpy V-notch impact tests on material from various locations around RHS specimens has been carried out at the University of Toronto Structural Testing Facilities and a metal testing laboratory in Ontario. The nominal sizes and manufacturing standards for the four RHS examined are summarized in Table 1. Specimens DF#2, CF#1 and CF#2 have the same nominal dimensions to enable the effects of cold-working on their corner (and overall) properties to be directly compared. CF#1 and CF#2 were made from the same steel material, while CF#2 was subsequently stress-relieved

Table 1. Manufacturing information for test specimens.

RHSID	RHS designation	Manufacturing standard/grade	Manufacturing method
DF#1	152 × 152 × 8 mm	N/A (Domex)	Direct-forming
DF#2	152 × 152 × 13 mm	CAN/CSA-G40.20-04/G40.21-04 Gr. 50W Class C	Direct-forming
CF#1	152 × 152 × 13 mm	CAN/CSA-G40.20-04/G40.21-04 Gr. 50W Class C	Continuous-forming
CF#2	152 × 152 × 13 mm	CAN/CSA-G40.20-04/G40.21-04 Gr. 50W Class H	Continuous-forming and heat treated

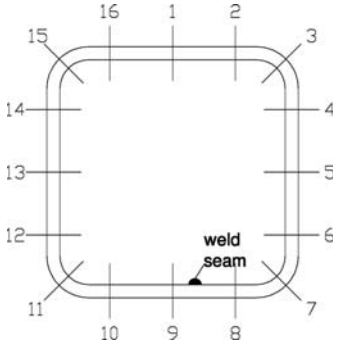

Figure 1. Thickness and corner radius measurement locations.

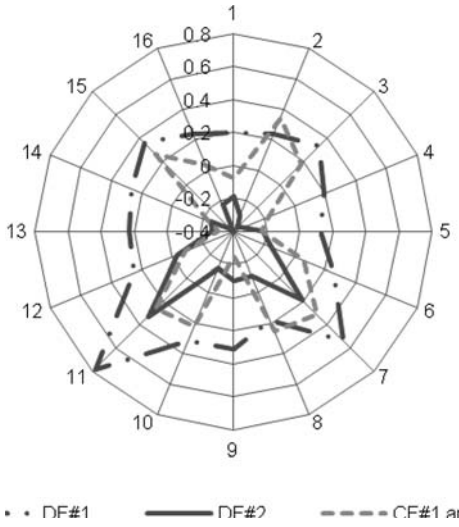

Figure 2. Measured and nominal thickness difference (mm).

by heat treatment in accordance with Canadian standards for "Class H" finishing (heated to a temperature of 450°C or higher, followed by cooling in air) (CSA 2004). The inclusion of DF#1 (direct-formed, thin-walled, high-strength RHS) enabled a comparison of its mechanical properties with the other three RHS with different wall thicknesses and strength properties. Also, the effect of residual stresses due to direct-forming could be further demonstrated, in conjunction with DF#2.

3 GEOMETRICAL MEASUREMENTS

One stub column from each of the four RHS was made, in accordance with accepted criteria for the preparation of stub columns (Ziemian 2010). The lengths of the stub columns were chosen to be 0.5 metres so that they were sufficiently short to preclude global member buckling when compressed, but sufficiently long to contain the same initial residual stress pattern as a much longer member cut from the same stock. Prior to testing the specimens, each was subject to careful geometrical measurement. For each specimen, the width of all four sides, the thickness at 16 different locations, and the outside and inside corner radii of all four corners of the section were measured. The measurement locations of thickness and corner radius are shown in Figure 1. The differences between the measured and nominal thickness for the four RHS are shown in Figure 2. The average measured width, the average measured thickness and the measured cross-sectional area were recorded and these are compared to the nominal values in Table 2. The cross-sectional area of each stub column was obtained by weighing and using a steel density of 7850 kg/m^3 (CISC 2010). The cross-section of each specimen was scanned and put into AutoCAD so that three-point arcs could be drawn to fit the outside and inside surfaces all corners, and the corner radii were then determined by measuring the radii of these arcs. The measured outside corner radii and inside corner radii of all four specimens are normalized to their corresponding average measured thicknesses in Table 3. The dimensions of CF#1 and CF#2 are the same since they were cut from the same tube.

Table 2. Nominal and measured dimensions of RHS specimens.

Specimen ID	d_{nom} mm	d_{avg} mm	t_{nom} mm	t_{avg} mm	A_{nom} mm^2	A mm^2
DF#1	152	153.5	7.95	8.252	4430	4662
DF#2	152	152.4	12.7	12.54	6680	6678
CF#1 &#2	152	151.9	12.7	12.73	6680	6565

According to Figure 2, there is considerable variation in thickness among different locations on the cross-section of the RHS examined. The continuous-formed RHS (CF#1 and #2) have regular thickness variation patterns around the section with corners being thicker than the flat faces, while for the two direct-formed RHS (DF#1 and #2) the two corners adjacent to the weld seam are thicker than the rest of the section.

Table 3. Normalized corner radii.

Specimen ID	Location 3		Location 7		Location 11		Location 15		Average	
	r_o/t_{avg}	r_i/t_{avg}	r_o/t_{avg}	r_i/t_{avg}	r_o/t_{avg}	r_i/t_{avg}	r_o/t_{avg}	r_i/t_{avg}	r_o/t_{avg}	r_i/t_{avg}
DF#1	2.20	1.28	1.65	1.13	1.87	0.74	1.85	1.30	1.89	1.11
DF#2	1.84	0.73	1.99	0.42	2.04	0.65	1.89	0.95	1.94	0.69
CF#1&#2	2.97	1.61	2.29	1.34	2.26	1.13	1.73	1.07	2.31	1.29

*Measurement locations as per Figure 1.

In Table 3, the "average r_o/t_{avg}" values for all RHS, ranging from 1.89 to 2.31, are within the typical scatter previously found for cold-formed sections in North America (Packer & Frater 2005). In general, the two direct-formed RHS have lower "measured corner radius/measured thickness" values than those of the two continuous-formed RHS. For some particular corners (e.g. location 7 of DF#2), the inside surfaces were severely cold-worked to very small corner radii and the centres of curvature for the inside and outside radii were found to be far from each other when measured in AutoCAD. The fact that location 7 of DF#2 was bent to such a small r_i/t_{avg} value of 0.42 is likely to cause the local mechanical properties to differ from other parts of the section and hence invite corner-cracking problems, especially evident if subjected to hot-dip galvanizing.

4 COMPRESSION BEHAVIOUR

Stub column compression tests were performed on each RHS in accordance with accepted international standards (Ziemian 2010). Each stub column was instrumented with 5 mm long strain gauges oriented longitudinally at the mid-height of each tube face and Linearly Varying Displacement Transducers (LVDTs) to ensure proper alignment.

The stress-strain curves, together with their proportional limits, for all four stub column specimens, are shown in Figures 3–6. The stress-strain curves of the three RHS with the same nominal wall thickness of 12.7 mm (DF#2, CF#1 and CF#2) are then normalized by their "2% offset yield stress" for comparison in Figure 7. Table 4 summarizes the test results.

The stress-strain curves in Figure 7 and the data in Table 4 show that:

1. The continuous-formed Class C RHS, CF#1, starts to yield (reaches its proportional limit) at a very early stage (27% of yield load) since it has the highest level of residual stress among the three RHS, due to the severe cold-working throughout its entire section.
2. The direct-formed RHS, DF#2, contains an intermediate level of residual stress since the cold-working is concentrated only at the four corners, and the proportional limit is at 47% of the yield load.

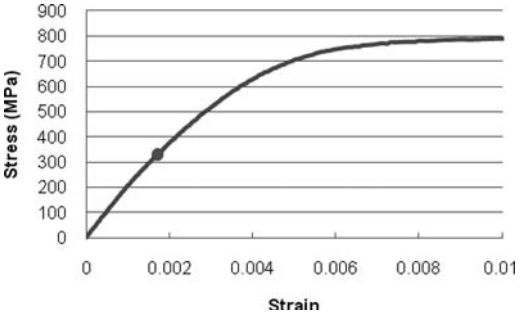

Figure 3. Stub column test results for DF#1 (Direct-formed; high strength steel).

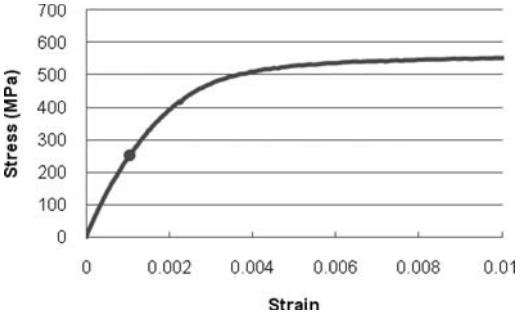

Figure 4. Stub column test results for DF#2 (Direct-formed; Class C).

3. The continuous-formed Class H RHS, CF#2, has the lowest level of residual stress, and the proportional limit is at 69% of the yield load.
4. The continuous-formed Class C RHS, CF#1, has a clear strain-hardening stage which also indicates that it experienced the largest amount of cold-working during the manufacturing process.
5. The "direct forming" or folding manufacturing process produces a square/rectangular hollow section with a compression capacity which is mid-way between that of a "continuous-formed" cold-formed section (CSA Class C) and a "continuous-formed" cold-formed + stress-relieved section (CSA Class H). Note that DF#2 and CF#1/#2 were chosen so that the "corner area" represented a significant portion of the gross area, to emphasize the corner properties.

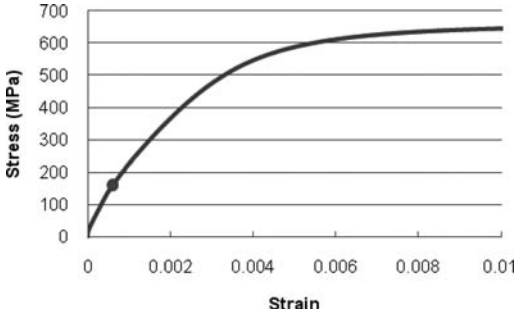

Figure 5. Stub column test results for CF#1 (Continuous-formed; Class C).

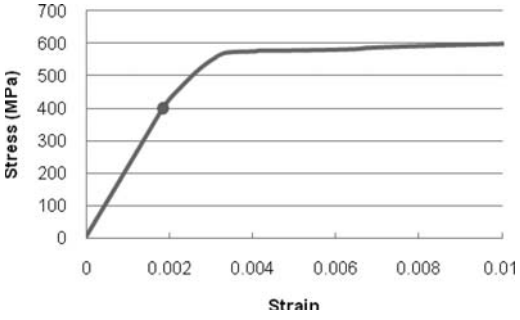

Figure 6. Stub column test results for CF#2 (Continuous-formed; Class H).

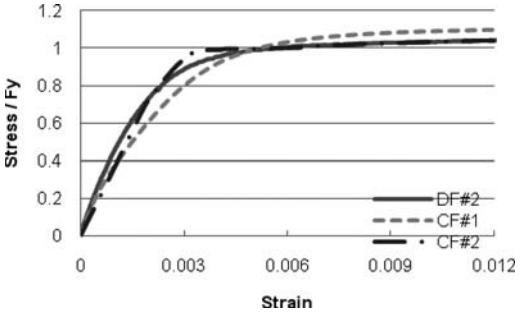

Figure 7. Normalized stub column test results for DF#2, CF#1 and CF#2.

5 TENSILE BEHAVIOUR

The tensile behaviour and ductility of the investigated direct-formed and continuous-formed RHS were obtained through tensile coupon tests. The coupons had a gauge length of 50 mm and the tests were performed in accordance with ASTM A370 (ASTM 2009). For each of the four RHS, three tensile coupons were machined from the three flat faces away from the weld (from locations 1, 5 and 13 in Figure 2) and three corner coupons were also extracted (from locations 3, 7 and 11 in Figure 2) in order to examine the influence of the highly localised cold work. The cross-sectional area of the test region in the coupons from the corners was determined by weighing and using a steel density of 7850 kg/m^3 (CISC 2010).

The tensile coupons curved after being cut from the RHS since the residual stresses due to longitudinal continuity were relieved. Of all the tensile coupons, those from the continuous-formed Class C RHS (CF#1) curved the most since they contained the highest level of residual stress. The curved coupons were straightened forcibly for the purpose of: (i) fitting them into the universal testing machine, and (ii) restoring their original straight shape so that their in-situ tensile behaviours could be studied.

The average elongations of the flat coupons and corner coupons at failure are shown in Figure 8. The tensile stress-strain curves are shown in Figures 9 to 12. In all cases the two highest curves represent the

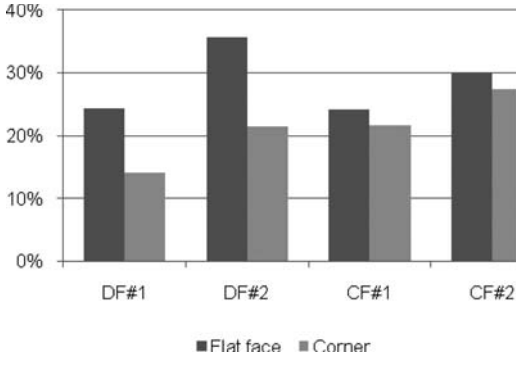

Figure 8. Average elongation of tensile coupons at failure.

Table 4. Stub column test results.

	Nominal	Measured			
Specimen ID	Min. specified yield stress MPa	Stress at 0.2% strain MPa	Max. stress MPa	Proportional limit MPa	(Proportional limit) / (stress at 0.2% strain)
DF#1	690	766	801	330	0.43
DF#2	345	530	580	250	0.47
CF#1	345	590	659	160	0.27
CF#2	345	580	614	400	0.69

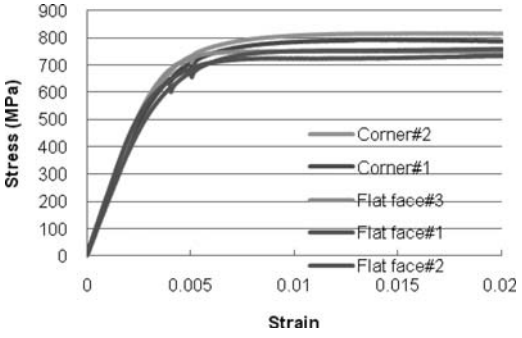

Figure 9. Tensile coupon test results for DF#1 (Direct-formed; High strength steel).

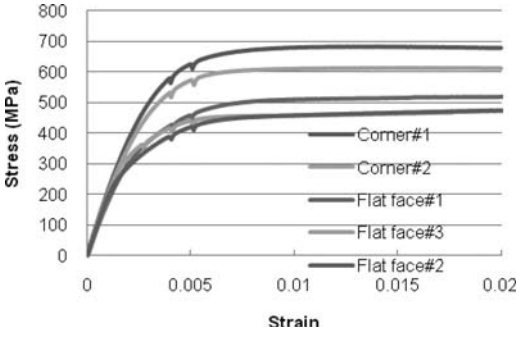

Figure 10. Tensile coupon test results for DF#2 (Direct-formed; Class C).

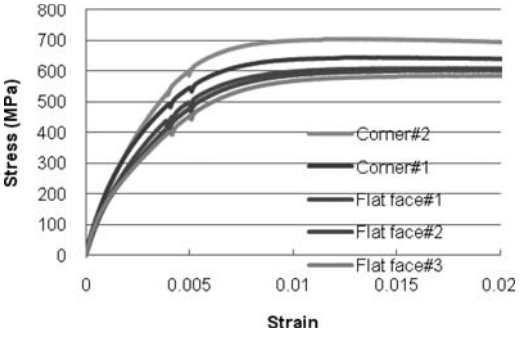

Figure 11. Tensile coupon test results for CF#1 (Continuous-formed; Class C).

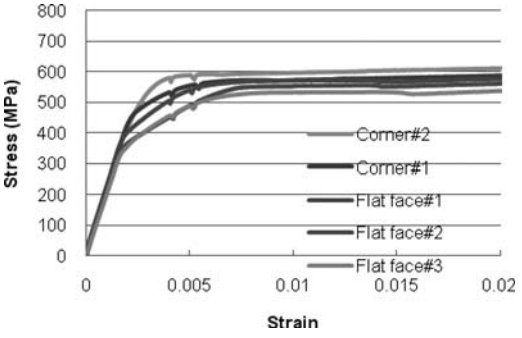

Figure 12. Tensile coupon test results for CF#2 (Continuous-formed; Class H).

Table 5. Tensile coupon test results.

Specimen ID	$F_{y,nom}$ MPa	$F_{u,nom}$ MPa	$F_{yavg,f}$ MPa	$F_{uavg,f}$ MPa	$F_{yavg,c}$ MPa	$F_{uavg,c}$ MPa
DF#1	690	N/A	723	779	770	807
DF#2	350	450	427	522	615	649
CF#1	350	450	457	599	590	676
CF#2	350	450	483	606	570	637

two corner test locations. Key results from all tensile coupon tests are summarized in Table 5. The yield stress is determined by the 0.2% strain offset method. It can be seen from the test results that:

1. From Figure 8, the flat face is much more ductile than the corner for direct-formed RHS (DF#1 and #2), while for continuous-formed RHS (CF#1 and #2) the difference is minor. Also, the heat treatment is effective in bringing back the ductility of the cold-formed RHS.
2. Similar post-yield stress-strain relationships were observed for the corner coupons from the two cold-formed regular strength RHS (DF#2 and CF#1) in Figures 10–11 as expected, since the final effective strain in the corner from the continuous-forming method is theoretically the same as that from the direct-forming method, although the former is accumulated from two steps (flat sheet to circular section, then to square section). Unlike DF#2, the stress-strain curves of the flat coupons are close to those of the corner coupons for CF#1 since the whole section experienced a similar amount of cold-working during the continuous-forming process.
3. According to Figures 11–12, the heat treatment was effective in relieving the residual stress. The proportional limits of all five tensile coupons from the Class H RHS (CF#2) are much higher than those from its Class C counterpart (CF#1). The tensile coupons from CF#1 reached their proportional limits at such early stages since they curved longitudinally the most of all coupons, thus they were already highly stressed in flexure before loading due to the straightening process.

6 CHARPY V-NOTCH IMPACT BEHAVIOUR

Another very important material property is the notch toughness, which is defined as the ability of a material to absorb energy in the presence of a sharp notch, often when subjected to an impact load. Notch toughness can be measured by a variety of test methods. The Charpy V-notch (CVN) impact test procedure is one of the most widely used and it can bring out the notch

behaviour (brittle versus ductile) of a test specimen by applying a single overload of stress. The low cost and simplicity of the CVN test have made it a common requirement in international codes and standards for dynamically loaded structures.

Charpy V-notch investigations on manufactured hollow structural steel sections have also been conducted to establish methods for the choice of ductile material to avoid brittle fracture and CVN toughness requirements have been made more explicit in some hollow section manufacturing specifications (CEN 2006; CSA 2004). For RHS, it is usually specified that the standard CVN specimen shall be taken from the flat face of the section, away from the weld, and that the orientation shall be longitudinal to the RHS. However, according to previous research (Kosteski et al. 2005; Wardenier et al. 2010), CVN specimens with this standard orientation generally lead to the most optimistic notch toughness result for the cross section. It has been suggested that alternate specimen locations should be considered for dynamic loading situations where notch toughness is a design criterion. Hence, a comparison of CVN test results of specimens from the four examined RHS has been made. The objective was to generate the complete toughness-temperature transition curves between −30°C and 20°C, for specimens sampled from various cross-section locations (flat face, corner and weld seam) with different specimen orientations (longitudinal and transverse) and notch face exposures (interior and exterior face of RHS).

A total of 216 full-sized (10 × 10 × 55 mm) and 54 sub-sized (10 × 5 × 55 mm) rectangular beam-type specimens, with a 2 mm deep machined notch of specified geometry as per ASTM A370 (ASTM 2009), were made from the four RHS. For the three RHS with a nominal wall thickness of 12.7 mm (DF#2, CF#1 and CF#2), full-sized specimens with a notch parallel to the RHS surfaces were made, since specimens with a through thickness notch orientation would not effectively exploit the toughness difference between the flat face versus the corner of the RHS, according to previous research (Dagg et al. 1989; Soininen 1996). For the RHS with a nominal wall thickness of 8 mm (DF#1), sub-sized specimens were made since the RHS is not thick enough for full-sized specimens, and the notches are perpendicular to the RHS surface because the notches have to be on the narrow face of the sub-sized CVN specimens according to the ASTM specification (ASTM 2009). The cutting locations and orientations of the specimens are listed in Table 6.

A pendulum-type "Riehle" impact tester with a 325 J direct reading scale was used to perform all the CVN impact tests. The tester passed the Charpy machine qualification program conducted by the National Institute of Standards and Technology (NIST) before the tests. In order to further ensure the quality of actual tests, 10 self-verification specimens (five low-energy ones and five high-energy ones) supplied by NIST were used to check the calibration of the tester and the results were consistent with the expected values provided by NIST. The specimens were cooled by a "Revco" freezer and an additional thermometer was used to ensure the accuracy of the intended temperature.

Table 6. Sampling locations and notch orientations of CVN specimens.

Location	Sub-sized specimens	Full-sized specimens
A	Flat face	Flat face
B	Corner – notch through thickness	Corner – notch out
C	Weld HAZ – transverse	Weld HAZ – transverse
D	N/A	Corner – notch in

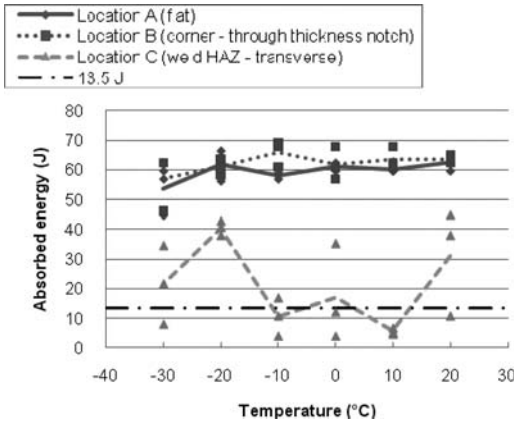

Figure 13. Charpy test results for DF#1 (Direct-formed; High strength steel).

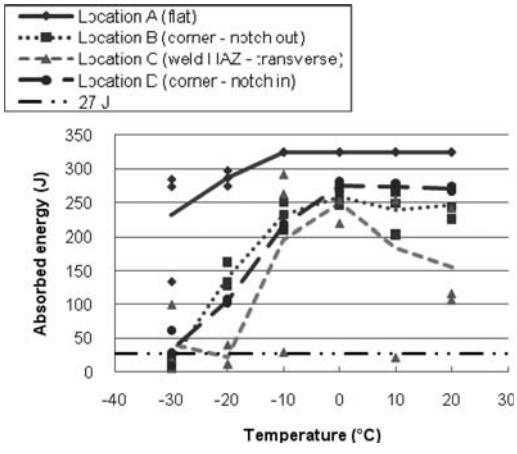

Figure 14. Charpy test results for DF#2 (Direct-formed; Class C).

Figures 13–16 give the toughness-temperature transition curves for the four RHS. The 27 J energy absorption requirement for full-sized Charpy specimens specified by EN 10219 grade S355J2H (CEN

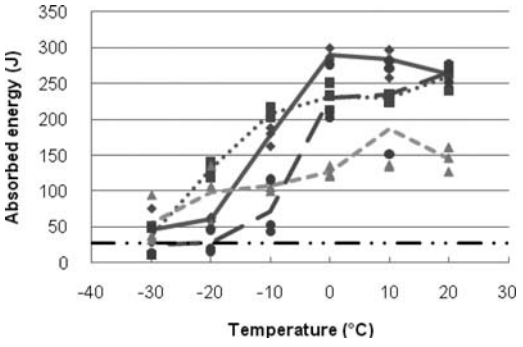

Figure 15. Charpy test results for CF#1 (Continuous-formed; Class C).

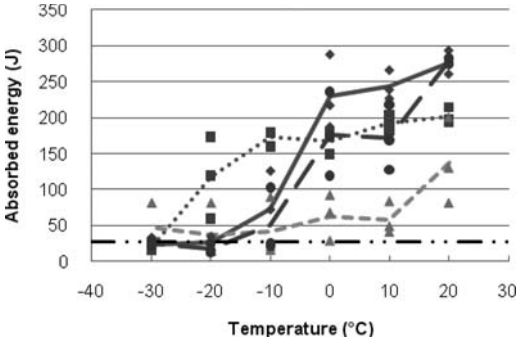

Figure 16. Charpy test results for CF#2 (Continuous-formed; Class H).

2006) is shown in Figures 14–16 for reference purposes. The 13.5 J line is used in Figure 13 since the sub-sized specimens have half of the cross-section of the full-sized ones.

Three replicate specimens were tested at each target temperature and the average result was used to plot the toughness-temperature point because of the inherent scatter of CVN test results. Some specimens from DF#2 did not break at 20°C (room temperature), 10°C, 0°C and −10°C, therefore the tester capacity (325 J) has been used to plot these points. It can be seen on these figures that:

1. The Charpy results from the flat face and corner of DF#1 are similar in Figure 13. It is possible that since the notches of the sub-sized specimens have to be perpendicular to the RHS surface, as per specification, that this notch characterizes the average through-thickness material properties of the RHS and thus does not effectively capture the toughness differences between the flat face versus the corner.
2. Comparing the two cold-formed regular strength RHS with the same nominal thickness, a large difference between the Charpy results from the flat face and the corner of DF#2 was observed in Figure 14, especially when the testing temperature was low, since the flat face of DF#2 experienced little cold-working during the direct-forming manufacturing process. As expected, CF#1 does not have such a difference in Figure 15. Also, direct-forming produces somewhat better corner Charpy values than continuous-forming, at low test temperatures. For the two corners (locations B and D) below −20°C, the energy absorption values are 145 J and 105 J for DF#2, and 130 J and 27 J for CF#1. Due to the material properties in the heat-affected zone (HAZ) and the sampling orientation (transverse to the direction of rolling), the Charpy results for location C have a wider scatter than the other locations and some extremely low values can be seen at relatively high temperatures. The Charpy curve of the HAZ of CF#1 is relatively smooth while that of DF#2 has a sudden drop when the temperatures are low.
3. Each of the 10×10 mm CVN specimens taken from the middle of the wall thickness at location B of DF#2, CF#1 and CF#2 has the 2 mm deep notch facing the outside surface of the RHS, thus it contains more compressive residual strain over the critical cross-section (8 x 10 mm) of the specimen due to cold-forming. Likewise, CVN specimens from location D of DF#2, CF#1 and CF#2 contain more tensile residual strain over their critical cross-sections. It seems that tensile residual strain has a negative effect on the Charpy impact toughness property since the test results from CVN specimens with the notch facing the inside surface are in general higher than those of the specimens with notch on the opposite side. This phenomenon was observed in the continuous-formed RHS (CF#1, CF#2) tested herein and in a previous investigation (Kosteski et al. 2005), but was not as significant in the direct-formed RHS (DF#2) possibly due to: (i) the inherent scatter of CVN test results, or (ii) the fact that the direct-forming process may produce better corner Charpy values than continuous-forming.
4. According to Figure 15–16, moderate heat treatment can reduce the Charpy toughness of a cold-formed section.

7 CONCLUSIONS

This paper performed geometrical measurements on RHS manufactured by different cold-forming methods and the compression, tensile and Charpy V-notch impact behaviours of these RHS were examined. The following conclusions, which are limited to the RHS tested so far, are drawn from this work:

1. The continuous-forming method produces RHS with a regular thickness variation pattern in which the corners are thicker than the flat faces, while the direct-forming method produces RHS with the two corners adjacent to the weld seam thicker than the rest of the section. The corner radii of direct-formed RHS are generally smaller than those of continuous-formed ones.

2. Direct-formed RHS has a compression behaviour mid-way between continuous-formed Class C (cold-formed) and Class H (cold-formed + stress-relieved) sections. The difference in compression behaviour between direct- and continuous-formed Class C RHS members may become greater as the b/t ratio increases. The authors are conducting further work to investigate this hypothesis.
3. The flat face of direct-formed RHS has better ductility than that of continuous-formed Class C and Class H sections. The corners of direct-formed and continuous-formed Class C RHS have similar tensile behaviours.
4. Except for the weld HAZ, direct-formed RHS has better Charpy toughness around the section than continuous-formed Class C and Class H sections.

8 NOTATIONS

A	measured cross-sectional area
A_{nom}	nominal cross-sectional area
d_{nom}	nominal width of RHS
d_{avg}	average measured width of RHS
$F_{yavg,c}$	average yield stress of corner of RHS
$F_{uavg,c}$	average ultimate stress of corner of RHS
$F_{yavg,f}$	average yield stress of flat face of RHS
$F_{uavg,f}$	average ultimate stress of flat face of RHS
$F_{y,nom}$	nominal yield stress of RHS
$F_{u,nom}$	nominal ultimate stress of RHS
r_i	inside corner radius
r_o	outside corner radius
t_{avg}	average measured wall thickness of RHS
t_{nom}	nominal wall thickness of RHS

REFERENCES

ASTM 2009. Standard test methods and definitions for mechanical testing of steel products. *ASTM A370-09a*, West Conshohocken, U.S.A.

CEN 2006. Cold formed welded structural hollow sections of non-alloy and fine grain steels – Part 1: Technical delivery conditions. *EN 10219-01: 2006*, Brussels, Belgium.

CISC 2010. Handbook of steel construction, 10th. edition, Canadian Institute of Steel Construction, Toronto, Canada.

CSA 2004. General requirements for rolled or welded structural quality steel/structural quality steel. *CAN/CSA-G40.20-04/G40.21-04*, Toronto, Canada.

Dagg, H. M., Davis, K. & Hicks, J. W. 1989. Charpy impact tests on cold formed RHS manufactured from continuous cast fully killed steel. *Proc. of the Pacific Structural Steel Conf*., Queensland, Australia.

Kosteski, N., Packer, J. A. & Puthli, R. S. 2005. Notch toughness of internationally produced hollow structural sections. *Journal of Structural Engineering* 131(2): 279–286.

MOST 2006. Application of new large dimension rectangular hollow sections and connections. *http://www.most.gov.cn/ztzl/863cj/863cjxcl/200603/t20060320_34162.htm*, Beijing, China.

Packer, J. A. & Frater, G. S. 2005. Recommended effective throat sizes for flare groove welds to HSS. *Engineering Journal* 42(1): 31–44.

Soininen, R. 1996. *Fracture behaviour and assessment of design requirements against fracture in welded steel structures made of cold formed hollow sections*. Tieteellisiä Julkaisuja Research Papers 52, Lappeenranta University of Technology, Lappeenranta, Finland.

Wardenier, J., Ritakallio, P., Iglesias, G., Puthli, R. S., Packer, J. A., Krampen, J., Feldmann, M., Eichler, B., Kühn, B., Stranghöner, N., Dahl, W., Langenberg, P., Kouhi, J., Pope, R. & Sedlacek, G. 2010. *Choice of steel material to avoid brittle fracture for hollow section structures – Addition to EN 1993-1-10.* Brussels, Belgium.

Ziemian, R. D. 2010. *Guide to stability design criteria for metal structures*. Hoboken: John Wiley & Sons.

Tubular Structures XIV – Gardner (Ed.)
© 2012 Taylor & Francis Group, London, ISBN 978-0-415-62137-3

Avoidance of brittle fracture of cold-formed hollow sections by appropriate choice of steel material

B. Eichler, M. Feldmann & G. Sedlacek
Institute for Steel Structures, RWTH Aachen University, Germany

ABSTRACT: European cold-formed hollow sections in general exhibit better toughness properties than required by EN 10219. However, limits in applying the toughness related rules for the choice of steel material in EN 1993-1-10 to cold-formed hollow sections still constitute barriers to free marketing. By requests from European producers a conservative assessment procedure has been developed which is based on toughness measurements and a concept using effective strains. Due to the cold-forming process such plastic strains may occur in the bent areas of the profiles associated with a noticeable reduction in material toughness. For the degradation of these toughness properties an appropriate temperature shift ΔT_{cf} has been derived for both circular and rectangular hollow sections. In order to guarantee the proper application of this temperature shift Table 2.1 in EN 1993-1-10 had to be extended to lower temperatures down to −120°C.

1 INTRODUCTION

The design rules in EN 1993 for steel structures are based on ductile material behavior that is controlled by the upper-shelf toughness behavior of steels in the toughness-temperature diagram. However, brittle failure of steels may be possible where triaxial stress states, for instance stemmed from sharp notches like flaws or cracks, extremely low temperatures and stresses from external loads and internal restraints come together and form an accidental fracture mechanical limit state scenario. Therefore, EN 1993-1-10 provides rules for the choice of steel material to avoid brittle failure of steel structures. Sufficient reliability of these rules is achieved by a mathematical model using a fracture mechanics approach calibrated to large-scale fracture tests of plated specimens.

The rules for cold-formed steel given in EN 1993-1-10 are limited and not sufficient for the specific case of cold-formed hollow sections. High degrees of plastic strain arise in the bent areas of the sections throughout the production process and result in a noticeable reduction of toughness. Due to the absence of experiments representing the fracture mechanical behavior of welded hollow sections at low temperatures this drawback was overcome by introducing a conservative approach.

The selection of an adequate steel grade is based on an appropriate temperature shift ΔT_{cf} to account for the loss of material toughness and thus required the extension of Table 2.1 in EN 1993-1-10 to temperatures down to −120°C. Two different methods have been examined and revealed reasonably consistent temperature shifts for circular and rectangular cold-formed hollow sections:

- A non-experimental method using the concept of effective strains (approach no. 1) where the cold-forming effects are determined on the basis of the procedure in EN 1993-1-10 for base material delivered according to EN 10025.
- An experimental method using the results of Charpy-V-impact tests (approach no. 2) carried out with cold-formed hollow sections delivered according to EN 10219 taking account of the production of hollow sections and the location of test specimen.

The evaluation of the results of the experimental tests exposed a significant influence of the toughness quality of the parent material used for cold-forming. It was revealed that the toughness quality of the evaluated European steel is far better than required by EN 10219. Moreover, the measured toughness data matches the statistical background of the fracture mechanics test population on which EN 1993-1-10 is based. As approach no. 2 was verified for a limited test population of S355J2H-steel, its primary purpose was to confirm the results of approach no. 1 that turned out to be the relevant one applicable to all sizes and steel grades.

The paper is based on the JRC-Report “Choice of Steel Material to avoid Brittle Fracture for Hollow Section Structures – Addition to EN 1993-1-10” (Feldmann et al. 2011) prepared by RWTH Aachen University, Institute for Steel Structures.

Steel grade	Sub-grade	Charpy energy CVN at T [°C]	Charpy energy CVN J_{min}	Reference temperature T_{RE} [°C]																	
				10	0	-10	-20	-30	-40	-50	10	0	-10	-20	-30	-40	-50	10	0	-10	-20	-30	-10	-50
				$\sigma_{Ed} = 0{,}75\,f_y(t)$							$\sigma_{Ed} = 0{,}50\,f_y(t)$							$\sigma_{Ed} = 0{,}25\,f_y(t)$						
S235	JR	20	27	60	50	40	35	30	25	20	90	75	65	55	45	40	35	135	115	100	85	75	65	60
	J0	0	27	90	75	60	50	40	35	30	125	105	90	75	65	55	45	175	115	135	115	100	85	75
	J2	-20	27	125	105	90	75	60	50	40	170	145	125	105	90	75	65	200	200	175	155	135	115	100
S275	JR	20	27	55	45	35	30	25	20	15	80	80	55	50	40	35	30	125	110	95	80	70	60	55
	J0	0	27	75	65	55	45	35	30	25	115	115	80	70	55	50	40	165	145	125	110	95	80	70
	J2	-20	27	110	95	75	65	55	45	35	155	155	115	95	80	70	55	200	190	165	145	125	110	95
	M,N	-20	40	135	110	95	75	65	55	45	180	180	130	115	95	80	70	200	200	190	165	145	125	110
	ML,NL	-50	27	185	160	135	110	95	75	65	200	200	180	155	130	115	95	230	200	200	200	190	165	145
S355	JR	20	27	40	35	25	20	15	15	10	65	55	45	40	30	25	25	110	95	80	70	60	55	45
	J0	0	27	60	50	40	35	25	20	15	95	80	65	55	45	40	30	150	130	110	95	80	70	60
	J2	-20	27	90	75	60	50	40	35	25	135	110	95	80	65	55	45	200	175	150	130	110	95	80
	M,N	-20	40	110	90	75	60	50	40	35	155	135	110	95	80	65	55	200	200	175	150	130	110	95
	ML,NL	-50	27	155	130	110	90	75	60	50	200	180	155	135	110	95	80	210	200	200	200	175	150	130
S420	M,N	-20	40	95	80	65	55	45	35	30	140	120	100	85	70	60	50	200	185	160	140	120	100	85
	ML,NL	-50	27	135	115	95	80	65	55	45	190	165	140	120	100	85	70	200	200	200	185	160	140	120
S460	Q	-20	30	70	60	50	40	30	25	20	110	95	75	65	55	45	35	175	155	130	115	95	80	70
	M,N	-20	40	90	70	60	50	40	30	25	130	110	95	75	65	55	45	200	175	155	130	115	95	80
	QL	-40	30	105	90	70	60	50	40	30	155	130	110	95	75	65	55	200	200	175	155	130	115	95
	ML,NL	-50	27	125	105	90	70	60	50	40	180	155	130	110	95	75	65	200	200	200	175	155	130	115
	QL1	-60	30	150	125	105	90	70	60	50	200	180	155	130	110	95	75	215	200	200	200	175	156	130
S690	Q	0	40	40	30	25	20	15	10	10	65	55	45	35	30	20	20	120	100	85	75	60	50	45
	Q	-20	30	50	40	30	25	20	15	10	80	65	55	45	35	30	20	140	120	100	85	75	60	50
	QL	-20	40	60	50	40	30	25	20	15	95	80	65	55	45	35	30	165	140	120	100	85	75	60
	QL	-40	30	75	60	50	40	30	25	20	115	95	80	65	55	45	35	190	165	140	120	100	85	75
	QL1	-40	40	90	75	60	50	40	30	25	135	115	95	80	65	55	45	200	190	165	140	120	100	85
	QL1	-60	30	110	90	75	60	50	40	30	160	135	115	95	80	65	55	200	200	190	165	140	120	100

Figure 1. Maximum permissible values of element thickness in [mm], Table 2.1 from EN 1993-1-10.

2 SELECTION OF STEEL MATERIAL

2.1 *Basics of EN 1993-1-10*

The design rules for the choice of steel material in order to avoid brittle fracture given in Eurocode 3, Part 1–10 are related to welded structures made of plates, hot rolled profiles and rolled sections according to EN 10025. The main conclusion of this standard is Table 2-1 which is reprinted in Figure 1. This table allows to choose the base material for fabrication with adequate toughness by limiting an admissible plate thickness depending on

- the steel grade and minimum T_{27J}-value,
- the applied temperature T_{Ed} down to $-50°C$ and
- the utilization rate σ_{Ed}/f_y, where σ_{Ed} is the service stress under the "frequent" load combination.

The background of Table 2.1 is a fracture mechanics analysis where the fracture toughness is related to the Charpy energy CVN by using Wallin's Master Curve Approach (Wallin 1999) and the Sanz-correlation (Marandet & Sanz 1976), by which the temperature T_{27J} is correlated to the temperature T_{K100} where a fracture toughness of $100\,\mathrm{MPa}\cdot\mathrm{m}^{1/2}$ is reached in a small-scale fracture mechanic test.

Pre-straining effects from cold-forming can be accounted for by applying an appropriate temperature shift ΔT_{cf} to the reference temperature. A safe sided estimation for ΔT_{cf} is computed according to equation (1) where ε_{cf} is the plastic strain resulting from the degree of cold-forming. In EN 1993-1-10 equation (1) is limited to plastic strains $\varepsilon_{cf} \leq 10\%$.

$$\Delta T_{cf} = 3 \cdot \varepsilon_{cf} \tag{1}$$

For plastic strains ε_{cf} smaller than 2% no temperature shift ΔT_{cf} has to be applied. In case of stress relief heat treatment equation (2) can be used.

$$\Delta T_{cf} = 1{,}5 \cdot \varepsilon_{cf} \tag{2}$$

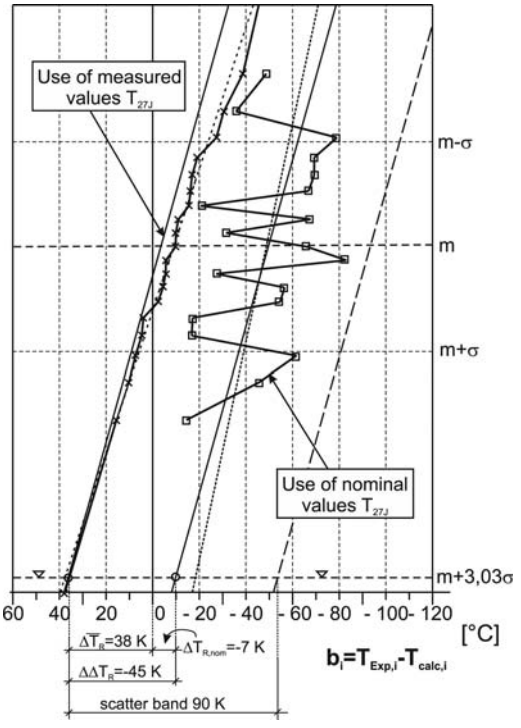

Figure 2. Determination of the safety element ΔT_R for DECT-plates (double edge cracked plate tension specimen).

The complete temperature based verification format in EN 1993-1-10 reads:

$$\underbrace{T_m + \Delta T_r + \Delta T_\sigma + \Delta T_R + \Delta T_{\dot{\varepsilon}} + \Delta T_{cf}}_{T_{Ed}} \geq \underbrace{T_{27J} - 18 + \Delta T_{27J}}_{T_{Rd}} \tag{3}$$

2.2 *Validation of the fracture mechanics model*

Table 2.1 in EN 1993-1-10 contains an inherent safety element $\Delta T_{R,nom} = -7\,K$ which has been evaluated by a large number of tests with pre-cracked specimens calibrated to nominal values f_y and T_{27J} according to the material standard EN 10025.

In Figure 2 the probability distribution of the differences b_i between the temperature $T_{exp,i}$ and the temperature $T_{calc,i}$ are plotted on Gaussian paper with $T_{exp,i}$ designating the test temperature at which the failure of test specimen was brittle and $T_{calc,i}$ indicating the computed temperature determined from the fracture mechanics model to predict failure of the test specimen with input from measured material data. The following conclusions can be drawn:

1. The calculable and experimental values fit well. The tangent to the dotted distribution line nearly hits the point (b = 0, m). Hence, for measured material data the theoretical model can be used with the safety element $\Delta T_{R,meas} = 0\,K$ to determine the expected (mean) values of temperature for fracture.

2. In applying the Eurocode definition of design values the safety element for ULS-verification related to the use of measured values T_{27J} and f_y is obtained on the level

$$R_d = m + 3{,}03 \cdot \sigma \quad (4)$$

which gives a safety element $\Delta\bar{T}_R = +38$ K.

3. When material data from product standards are used the evaluation shows a scatter band of deviations from nominal values in the range of ~90 K. The material's high quality is revealed by a temperature shift of about $\Delta\Delta T_R = -45$ K representing the positive effect of differences between actual values and nominal values for T_{27J} and f_y as specified in EN 10025.
4. Therefore, the safety element ΔT_R related to the use of nominal values of T_{27J} and f_y is $\Delta T_{R,nom} = -45\,K + 38\,K = -7\,K$.
5. $\Delta T_{R,nom} = -7$ K has also been justified by the evaluation of further test results with welded details and thus has been adopted for any fracture mechanical assessment related to nominal material properties.

Further background information can be taken from (Sedlacek et al. 2008).

2.3 *Basis for extending the method in EN 1993-1-10 to cold-formed hollow sections*

The method in EN 1993-1-10 to cope for effects of cold-forming is limited to the following:

- The linear relationship given in eq. (1) and eq. (2) respectively is limited by a certain degree of cold-forming $DCF_{max} = \varepsilon_{cf} = 10\%$.
- The validity of the Master-Curve-Concept is calibrated by standard Charpy-V-test-samples of $10 \times 10 \times 50$ mm.
- The distribution of the degree of cold-forming across the section of the test specimen is assumed to be constant.

The basis for the extension of the existing rules to cold-formed hollow sections is:

- Evaluations on structural steel S355J2 indicate no significant change of the notch impact energy with increasing degree of cold-forming higher than 15% (Steel 1992), see Figure 3.
- In the case of cold-forming by bending the strain distribution varies over the cross section from tension to compression, see estimation for ε_{pl} in Figure 4.

Furthermore, it is assumed that

- strains from tension and compression have equal effects to temperature shifts ΔT_{cf} because of the increase of dislocation density and
- the effect of unequal strain distribution over the critical cross section of the sample for notch impact tests is equivalent with the effect of the mean strain value of the distribution, see Table 1.

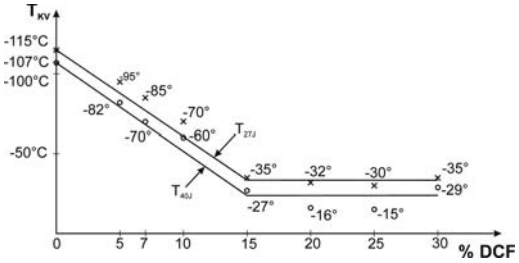

Figure 3. Change of T_{27J}- and T_{40J}-values by cold-forming for S355J2 (DCF = degree of cold-forming).

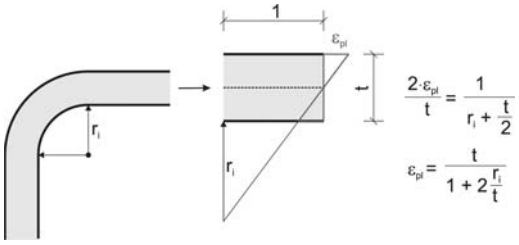

Figure 4. Geometrical definition of ε_{pl} by cold-forming, linear approach.

Table 1. Derivation of ε_{ff}.

t [mm]	ε-distribution	ε_{eff}
≥ 20	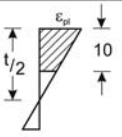	$\varepsilon_{pl}\left(1-\frac{10}{t}\right)$
10 ≤ t < 20	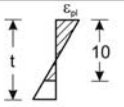	$\frac{\varepsilon_{pl}}{2}\left\{\frac{t}{20}+\frac{(20-t)^2}{20t}\right\}$
< 10	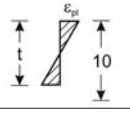	$\frac{\varepsilon_{pl}}{2}\cdot\frac{t}{10}$

3 METHODS TO DETERMINE THE ADMISSIBLE PLATE THICKNESS OF HOLLOW SECTION STRUCTURES

The minimum toughness values specified in EN 10219 are identical with the values given in EN 10025. Anyhow, Table 2.1 of EN 1993-1-10 cannot be directly applied to cold-formed welded hollow sections according to EN 10219 as the distribution of these material properties is not sufficiently specified to determine an admissible plate thickness. For circular cold-formed sections the minimum toughness values are guaranteed along the whole perimeter of the cross section, for rectangular sections the toughness values are guaranteed

in the flat parts only. As material tests in the cold-formed (bent) area are not provided in EN 10219-1 in section 5.2 – Options, a deeper look into magnitudes and distributions of material properties of the products of EN 10219 is required.

Rectangular and circular tubes in general are produced from hot-rolled strip delivered to EN 10025, EN 10111 or EN 10149 by continuous roll-forming in combination with electric welding or submerged arc welding. The major production process for circular tubes is "direct forming" where the properties of the roll-formed and welded product are influenced by the degree of cold-forming. For rectangular sections "universal forming" is applied by most producers. This two-part process involves the forming and welding of a round tube with equivalent diameter followed by the shaping of the round tube to the desired rectangular cross section in a second step. In this case the degree of cold-forming at the flat face is roughly 2x the degree of cold-forming for the equivalent round tube.

Actually, fracture mechanics tests with welded large-scale test specimens according to the procedure as carried out for justifying EN 1993-1-10 would be recommended for the determination of the toughness related effects due to cold-forming. Since such tests are not available two different approaches shall clarify the following questions:

1. Is the statistics of differences between the measured material data T_{27J} and the nominal values T_{27J} as specified in EN 10219 different to the statistics related to the values in EN 10025 or does $\Delta\Delta T_R = -45$ K also apply to material according to EN 10219 that give the safety element $\Delta T_R = -7$ K, cf. section 2.2?
2. Is it necessary to apply the temperature shift $\Delta T_{cf} = -3 \cdot \varepsilon_{cf}$ or is the temperature shift ΔT_{cf} already included in the difference $\Delta\Delta T_R$ determined by testing the material properties of the finished cold-formed profiles, which include already all effects of cold-forming?

Approach no. 1 does not consider any material testing of cold-formed sections and is a safe-sided estimate on the basis of properties of the parent material according to EN 10025. $\Delta\Delta T_R = -45$ K and $\Delta T_{cf} = -3 \cdot \varepsilon_{cf}$ are applied together with the concepts of effective strains to consider the various steps of the production process. It is assumed that the mean value of strain in the critical cross section of the Charpy-V-specimen is the effective strain (see Table 1) equivalent to a uniformly distributed strain as supposed in the formula for ΔT_{cf}. Approach no. 1 is used to compare the results with the more convenient approach no. 2

Approach no. 2 considers material data from Charpy-impact tests of cold-formed sections to derive the temperature shift ΔT_{cf} necessary to apply Table 2.1 of EN 1993-1-10. Such data were used to establish a relationship between the measured T_{27J}-values at the critical corners and the nominal values of T_{27J} in the flat face of the cross-sections as specified in EN 10219. Since the data in the corner regions and also the data in the flat face region both contain a certain amount of cold-forming, only the differences of the measured data between those regions can be identified. Therefore, measured toughness properties including cold-forming effects need corrections to eliminate impacts of the strain gradients across the wall thickness, of the position of the CVN-test specimen in the wall and of the change of triaxiality of the stress state when sub-sized Charpy-specimens have been used.

Table 2. Effective strain ε_{eff} [%] for different r_i/t-ratios for circular cold-formed hollow sections.

t [mm]						
r_i/t [–]	6	10	16	20	30	40
5	2,73	4,55	3,86	4,55	6,06	6,82
10	<2	2,38	2,02	2,38	3,17	3,57
15	<2	<2	<2	<2	2,15	2,42
≥20	<2	<2	<2	<2	<2	<2

Table 3. Temperature shift ΔT_{cf} [K] for different r_i/t-ratios.

t [mm]						
r_i/t [–]	6	10	16	20	30	40
5	8	14	12	14	18	20
10	0	7	6	7	10	11
15	0	0	0	0	6	7
≥20	0	0	0	0	0	0

4 CIRCULAR SECTIONS

Since there are no toughness data for circular cold-formed hollow sections, only approach no. 1 has been applied. The maximum plastic strain ε_{pl} for circular hollow sections can be taken from equation (5), cf. Figure 4.

$$\varepsilon_{pl} = 1 / \left(1 + 2\frac{r_i}{t}\right) \tag{5}$$

where r_i is the inner radius and t is the plate thickness. According to the criterion $\varepsilon_{pl} \leq 2\%$ given in EN 1993-1-10 cold-forming effects could roughly be neglected for circular sections with $r_i/t \geq 25$. In this case Table 2.1 may be used without modifications.

More accurate limits are determined considering the combination of equation (5) and the equations for ε_{eff} as given in Table 1. The resulting values for ε_{eff} and the temperature shifts ΔT_{cf} calculated by equation (1) for various material thickness t and r_i/t-ratios are given in Table 2 and Table 3. For cross sections with $r_i/t > 15$ cold-forming effects may be neglected, otherwise the

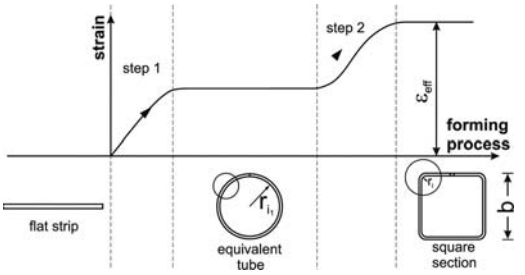

Figure 5. Steps of cold-forming in the corner parts of the rectangular cross section produced by the "universal forming" process.

ΔT_{cf}-values are in the range of 6 K to 20 K depending on the plate thickness t.

5 RECTANGULAR SECTIONS

5.1 *Approach no. 1*

Correction factors ΔT_{cf} for the feed material have been determined for both the flat and the bent areas of the rectangular sections. As the ΔT_{cf}-factors in the bent areas are relevant the evaluation of the analogous values for the flat parts is not presented here. The strain-time history of the cold-forming process for the corners is given in Figure 5.

It is obvious that the effective strain in the corner area from "universal forming" is accumulated from two steps and has the same amount as from "direct forming". According to Figure 4 the maximum ε_{pl}-values at the surface can be computed with the specifications in EN 10219-2, Annex B.3 for the inner radius r_i and the plate thickness t in the corners. The effective strains may be determined with the definitions in Table 1 and the temperature shifts ΔT_{cf} are calculated by using equation (1), see Table 4. Conservative temperature shifts ΔT_{cf} are obtained when lower bound values for the inner radii r_i from exploiting tolerances are used. These results are illustrated in Figure 6 together with the data from Table 4.

For nominal values of r_i and $t \leq 16$ mm the mean value ΔT_{cf} is 30 K. A safe-sided value $\Delta T_{cf} = 35$ K has been chosen to have a constant value without considering thickness effects within the given limits. The most conservative value for all thicknesses considering tolerances would be $\Delta T_{cf} = 45$ K. This preliminary temperature shift requires the extension of Table 2.1 of EN 1993-1-10 which is limited to temperatures +10°C/−50°C. Anyhow, the new input temperature T_{Ed}* to Table 2.1 could be determined according to equation (6)

$$T_{Ed}^{*} = T_{Ed} - \Delta T_{cf} \tag{6}$$

This new temperature shift will be verified by the experimental approach no. 2.

Table 4. Plastic strain ε_{pl} [%], effective strain ε_{eff} [%] and temperature shift ΔT_{cf} [K] for nominal radii in the corner regions of rectangular hollow section acc. to EN 10219.

t [mm]	r_i	ε_{pl} (Figure 3)	ε_{eff}	ΔT_{cf}
$t \leq 6$	$1{,}0 \cdot t$	$t/(2t+t) = 33{,}3\%$	10% (t = 6)	30,0
$6 < t \leq 10$	$1{,}5 \cdot t$	$t/(3t+t) = 25{,}0\%$	10% (t = 8)	30,0
$6 < t \leq 10$	$1{,}5 \cdot t$	$t/(3t+t) = 25{,}0\%$	12,5% (t = 10)	37,5
$t > 10$	$2{,}0 \cdot t$	$t/(4t+t) = 20{,}0\%$	8,7% (t = 12)	26,0
$t > 10$	$2{,}0 \cdot t$	$t/(4t+t) = 20{,}0\%$	10% (t = 20)	30,0
$t > 10$	$2{,}0 \cdot t$	$t/(4t+t) = 20{,}0\%$	15% (t = 40)	45,0

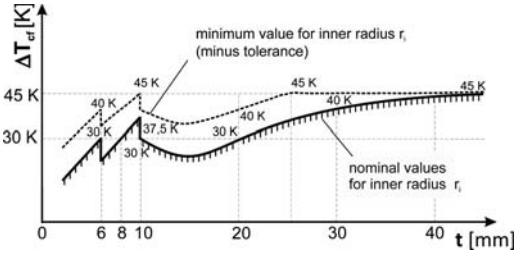

Figure 6. Dependency of ΔT_{cf} on plate thickness t.

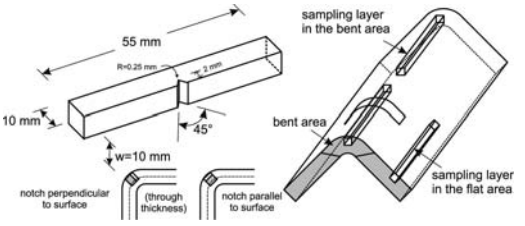

Figure 7. Standardized Charpy-V-sample and position of Charpy-samples.

5.2 *Approach no. 2*

5.2.1 *Evaluation of T_{27J}-temperature*

The data basis of approach no. 2 is 25 sets of full impact toughness-temperature-curves of cold-formed hollow sections made of steel S355 in the flat and bent parts of the cross sections according to EN 10219 provided by CIDECT (Puthli et al. 2004 & Kosteski et al. 2003), a producer (Ritakallio 2010) and from further researchers (Dagg et al. 1989 & Soininen 1996). Figure 7 illustrates the sampling of the specimens from the flat and the bent parts of the sections on the basis of CIDECT-report 1A (Puthli et al. 2004). The notch of the CVN-sample was parallel to the surface.

As an example the impact energies KV for a rectangular section of S355J2H (micro-alloyed fine grain steel) with the dimensions $100 \times 100 \times 10$ mm are shown in Figure 8 for the flat parts and in Figure 9 for the bent parts of the cross section. The inner radius of the section was $r_i = 12$ mm.

The toughness properties T_{27J} were evaluated by fitting an adequate mathematical curve to the measured impact data. As the measured data points were

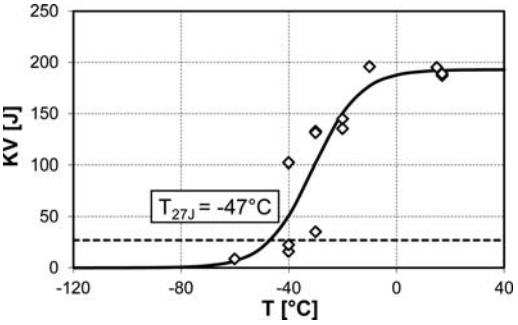

Figure 8. Impact energies KV in the plane (cold-formed) areas measured for sample no. 4 (RHS 100 × 100 × 10 mm, S355J2H acc. to EN 10219).

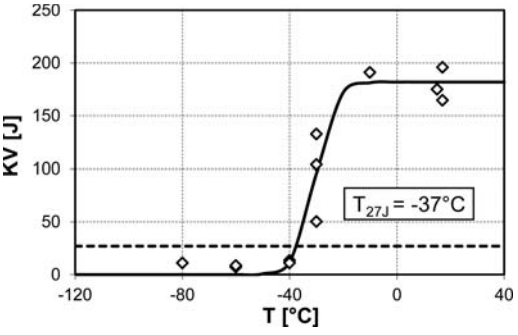

Figure 9. Impact energies KV in the bent (cold-formed) areas measured for sample no. 4 (RHS 100 × 100 × 10 mm, S355J2H acc. to EN 10219).

uniformly distributed along the temperature-axis the KV-T-data pairs could be approximated by the tanh-function according to equation (7)

$$KV = A \cdot \left(1 + \tanh \frac{T - B}{C}\right) \tag{7}$$

with A, B and C representing fitting coefficients to be determined by the least squares method.

Figure 8 and Figure 9 indicate a small displacement of the KV-T-curve to the right without significant changes in upper shelf toughness. Moreover, the gradient in the transition zone steepens for cold-formed material. With equation (7) a $T_{27J,plane}$-value of $-47°C$ for the plane areas of the hollow section and a value of $T_{27J,bent} = -37°C$ for the bent areas was evaluated. This example indicates the general tendency of a loss in toughness when pre-straining effects like cold-forming are experienced. Due to the inelastic deformations the increase of dislocation density results in a translation of the KV-T-curve towards the lower shelf range where cleavage fracture prevails, see Figure 10.

Measured data as documented from Charpy-V-tests from cold-formed sections shall be comparable with measured data that have been used for developing the assessment procedure in EN 1993-1-10. To achieve

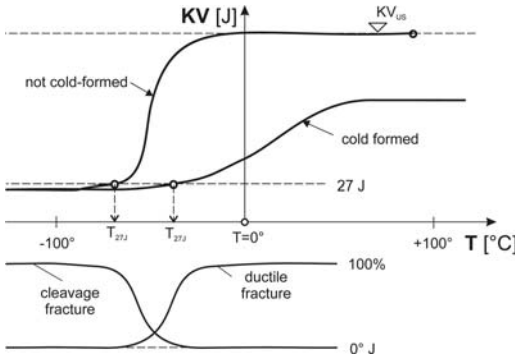

Figure 10. Impact of cold-forming on the KV-T-relationship.

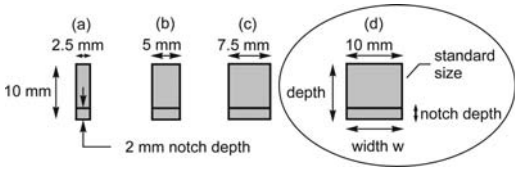

Figure 11. Undersized Charpy impact test specimens according to ASTM E23.

compliance the following corrections of measured data are introduced.

1. Corrections for undersized specimen with a width $w < 10$ mm.
2. Corrections due to the position of the impact test specimen that does not include the maximum strain ε_{pl} as assumed in averaging the strain distribution for the test specimen.
3. Corrections of measured values of T_{27J} in the flat part of the cold-formed sections to link the material properties of feed material for cold-forming.

5.2.2 *Effects of undersized impact samples*

For plate thickness $t < 11$ mm undersized samples with $w < 10$ mm ($w = t - 2 \cdot 0{,}5$ mm for machining) are applied, cf. Figure 11. With decreasing width w such samples exhibit a favorable toughness effect associated with a modification of the triaxiality of the stress state. It may be estimated in terms of an additional temperature shift ΔT_{ss} by equation (8) established within the SINTAP-procedure (Zerbst et al.).

$$\Delta T_{ss} = -51{,}4 \cdot \ln\left[2 \cdot \left(\frac{w}{10}\right)^{0{,}25} - 1\right] \tag{8}$$

It is recommended not to apply the formula for thicknesses t below 5 mm. The temperature corrections ΔT_{ss} are summarized in Table 5 for $6 \text{ mm} \leq t \leq 10$ mm. With regard to the impact data evaluation the range from 8 mm to 10 mm was relevant.

Table 5. Temperature shift ΔT_{ss} due to undersized specimens.

t [mm]	Charpy width w [mm]	ΔT_{ss} [K]
6	5	19,7
7	6	14,1
8	7	9,6
9	8	5,9
10	9	2,7

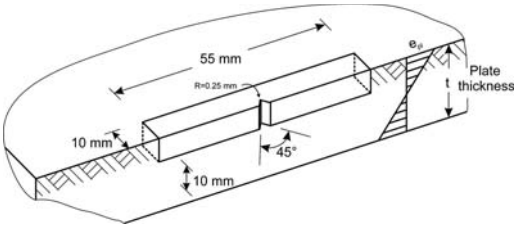

Figure 12. Definition of strains along the depth of the Charpy-V-sample.

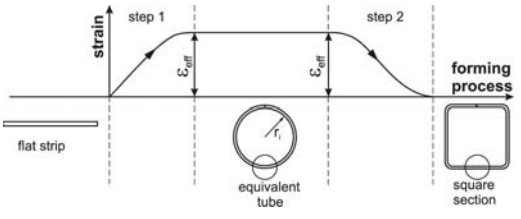

Figure 13. Steps of cold-forming in the flat parts of the rectangular cross section produced by the "universal forming" process.

5.2.3 *Effects of position of sample and strain gradient*

Two sampling positions are distinguished for Charpy-V-notch-specimens taken at the outside or at the inside of the radius:

- a position close to the surface with a maximum strain value ε_{pl} and a notch perpendicular to the surface and
- a position close to the surface with the notch parallel to the surface.

Therefore, a temperature shift ΔT_{pos} (eq. 8) for the location of the impact test specimen is applied to transform the results to the reference case in Figure 12. The correction is performed conservatively with $\Delta T_{cf} = 3 \cdot \varepsilon_{cf}$ with $\varepsilon_{cf} = \Delta\varepsilon = \varepsilon_{eff} - \varepsilon_{pos}$. For the calculation details of ε_{pos} see (Feldmann et al. 2011).

$$\Delta T_{pos} = 3 \cdot \Delta\varepsilon = 3 \cdot \left(\varepsilon_{eff} - \varepsilon_{pos}\right) \tag{9}$$

5.2.4 *Link between the measured values T_{27J} in the flat parts to the feed material properties*

It is assumed that all cold-formed sections for which measured data exist have been produced according to

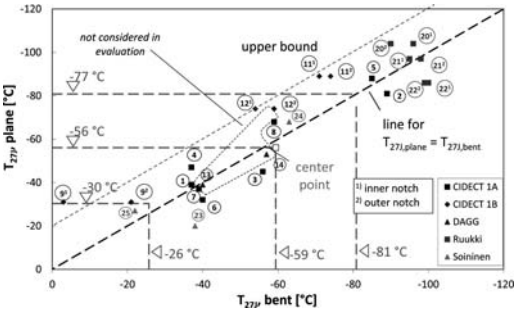

Figure 14. Ratios between $T_{27J,plane}$ and $T_{27J,bent}$ of cold-formed rectangular sections.

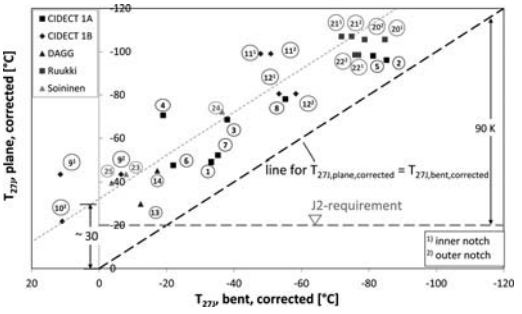

Figure 15. Ratios between corrected values of $T_{27J,plane,corr}$ and $T_{27J,bent,corr}$ of cold-formed rectangular sections.

the "universal forming" process. The flat parts of the sections have undergone an effective straining that follows from Figure 13. The temperature shift ΔT_{cf} is computed with equation (1) and ε_{cf} being the effective strain $\Sigma\varepsilon_{eff} = 2 \cdot \varepsilon_{eff}$, see equation (10).

$$\Delta T_{cf} = 3 \cdot \sum \varepsilon_{eff} \tag{10}$$

5.2.5 *Evaluation of test data*

The evaluation considers the results of Charpy-tests with longitudinal orientated specimens. Beside T_{27J}-values also the upper shelf behavior ($KV_{US} - T_{US}$) of the cold-formed sections was investigated. The population of the evaluated data revealed high quality steels, that even after cold-forming exceed the toughness requirements for any steel grade in EN 10219 by far.

As already demonstrated in the example with test specimen no. 4, cf. Figure 8 and Figure 9, only a small decrease in upper shelf toughness is recognized for the majority of the data between the plane and the corner areas of the sections. Some results appear to contradict this tendency which may be caused by an inevitable large scatter of the CVN-test results. Upper shelf mean values for the plane area are $KV_{US,plane} = 190$ J and $T_{US,plane} = -28°C$, for the bent areas $KV_{US,bent} = 184$ J and $T_{US,bent} = -38°C$. The distribution of the transition temperature is shown in Figure 14, mean values

Table 6. Extract of the extended Table 2.1 according to EN 1993-1-10 for $\sigma_{Ed} = 0{,}75 \cdot f_y$ and S355, see Figure 1.

Steel grade	Sub-grade	Charpy energy CVN		Reference temperature T_{Ed} [°C]														
				10	0	−10	−20	−30	−40	−50	−60	−70	−80	−90	−100	−110	−120	
		at T [°C]	J_{min}	$\sigma_{Ed} = 0{,}75 \cdot f_y(t)$														
S355	JR	20	27	43	35	29	24	20	16	14	11	10	8	7	6	5	5	
	J0	0	27	63	52	43	35	29	24	20	16	14	11	10	8	7	6	
	J2	−20	27	92	76	63	52	43	35	29	24	20	16	14	11	10	8	
	M,N	−20	40	109	91	75	62	51	42	35	28	23	19	16	13	11	9	
	ML,NL	−50	27	155	131	110	92	76	63	52	43	35	29	24	20	16	14	

for T_{27J} are almost identical: $T_{27J,plane} = -56°C$ and $T_{27J,bent} = -59°C$.

For the determination of the temperature shift ΔT_{cf} due to cold-forming corrections to obtain T_{27J}-values for the feed material and T_{27J}-values representing the effects of effective strain (see section 5.2.2, 5.2.3 and 5.2.4) must be applied. For the bent corner region the measured T_{27J}-values are shifted to the right side of the KV-T-diagram where the position of the sample (ΔT_{pos}) in the bent area and the triaxiality of the undersized specimen (ΔT_{ss}) gave favorable values, equation (11).

$$T_{27J,bent,corr} = T_{27J,bent} + \Delta T_{pos} + \Delta T_{ss} \quad (11)$$

For the plane region the measured values may contain cold-forming effects from production ΔT_{cf}, see equation (11), so that they should be shifted to the left in the KV-T-diagram. Favorable results due to the stress triaxiality give a further shift ΔT_{ss} to the right side. It is assumed that test specimens have been sampled closely from the surface in the plane areas so that no ΔT_{pos} is taken into account, eq. (12).

$$T_{27J,plane,corr} = T_{27J,plane} - \Delta T_{cf} + \Delta T_{ss} \quad (12)$$

The ratios between the corrected values of T_{27J} are given in Figure 15. The values $T_{27J,plane,corr}$ may be considered as estimates of the T_{27J}-values for the feed material for cold-forming and $T_{27J,bent,corr}$ may be used as an estimate of the T_{27J}-values in the corner area in compliance with EN 1993-1-10. The following conclusions can be drawn from Figure 15:

- The scatter of all T_{27J}-values for the feed material is about 90 K. This corresponds to the situation in Figure 2 with $\Delta\Delta T_R = -45$ K.
- The mean value of $T_{27J,bent,corr}$ in the corner region is in the mean about 30 K higher than the T_{27J}-value for the feed material ($T_{27J,plane,corr}$). This results in $\Delta T_{cf} = 30$ K, see approach no. 1.

6 CONCLUSIONS

A procedure in conformity with EN 1993-1-10 for the choice of steel material for cold-formed hollow sections according to EN 10219 was introduced. It was validated by a large data set of Charpy-values determined from S355J2H-steel corresponding to the statistical situation of fracture mechanics tests in EN 1993-1-10. The value ΔT_{cf} for a temperature shift was determined to be adopted with Table 2.1 of EN 1993-1-10.

Two different approaches resulted in identical safe-sided values for rectangular and circular cold-formed sections. As the experimental test population was limited with regard to sizes and steel grades approach no. 1 using the concept of effective strains turns out to be the decisive one. For rectangular hollow sections the adjustment for all steel grades and sizes of cross sections reads eventually:

- $\Delta T_{cf} = -35$ K for $t \leq 16$ mm and
- $\Delta T_{cf} = -45$ K for $t > 16$ mm

For circular cold-formed hollow sections the maximum value may be taken as

- $\Delta T_{cf} = -20$ K.

For more precise calculations equation (1) with $\varepsilon_{cf} = \varepsilon_{eff}$ in relation to Table 1 can be applied for the determination of ΔT_{cf}. Therein, ε_{eff} is defined as the average value of plastic strain of a Charpy-V-test specimen with longitudinal position in the cold-formed corner.

Therefore, Table 2.1 in EN 1993-1-10 requires an extension with regard to low temperature (down to −120°C) and should be replaced by the new table, see Table 6.

ACKNOWLEDGEMENTS

The authors would like to thank the members from CIDECT and the experts from CEN/TC 250 for the valuable contributions and comments while preparing the JRC-document "Choice of Steel Material to avoid Brittle Fracture for Hollow Section Structures – Addition to EN 1993-1-10" on which the present paper is based.

REFERENCES

ASTM E23. 2007. Standard Test Methods for Notched Bar Impact Testing of Metallic Materials.

Dagg et al. 1989. Charpy Impact Tests on Cold-Formed RHS Manufactured from Continuous Cast fully Killed Steel. Proceedings from the Pacific Structural Steel Conference, Australian Institute for Steel Construction, Queensland, Australia.

EN 1993-1-10. 2010. Eurocode 3: Design of Steel Structures – Part 1-10: Material Toughness and Thickness-Properties.

EN 10025. 2004. Hot Rolled Products of Structural Steels.

EN 10219. 2006. Cold-formed Welded Structural Hollow Sections of Non-Alloy and Fine Grain Steels.

Feldmann et al. 2011. Choice of Steel Material to avoid Brittle Fracture for Hollow Section Structures – Addition to EN 1993-1-10. JRC Scientific and Technical Report.

Kosteski et al. 2003. Notch Toughness of Cold-Formed Hollow Sections. Final Revision 2, Report to CIDECT on Programme 1B, CIDECT Report 1B-2/03.

Marandet, B., Sanz, G. 1976. Étude par mécanique de la rupture de la ténacité d'aciers à résistance moyenne fournis en forte épaisseur. Revue de Métallurgie, pp. 359–383.

Puthli et al. 2004. Welding in Cold-Formed Areas of Rectangular Hollow Sections. Draft Final Report on Programme 1A, CIDECT-Report 1A-05/04.

Ritakallio, P. 2010. Ruukki Cold-Formed Hollow Sections – Grade S355J2H – Random Samples. Private Communication.

Sedlacek et al. 2008. Commentary and Worked Examples to EN 1993-1-10 "Material Toughness and Through-Thickness Properties and other Toughness oriented Rules in EN 1993". JRC Scientific and Technical Report, EUR 23510.

Soininen, R. 1996. Fracture Behaviour and Assessment of Design Requirements against Fracture in Welded Steel Structures made of Cold-Formed Hollow Sections. Tieteellisiä Julkaisuja Research Papers 52, Lappeenranta University of Technology, Lappeenranta, Finland.

Steel. 1992. A Handbook for Material Research and Engineering Volume 1: Fundamentals. Springer Verlag, Verlag Stahleisen mbh Düsseldorf.

Wallin, K. 1999. The Master Curve Method: A new Concept for Brittle Fracture. International Journal of Materials and Product Technology, Vol. 14, No. 2/3/4, pp. 342–354.

Zerbst et al. 2007. Fitness-for-Service Fracture Assessment of Structures containing Cracks. A Workbook based on the European SINTAP/FITNET Procedure. 1st edition.

Tubular Structures XIV – Gardner (Ed.)
© 2012 Taylor & Francis Group, London, ISBN 978-0-415-62137-3

Experimental study on strength and ductility of steel tubular stub columns filled with Geopolymeric Recycled Concrete

X.S. Shi & Q.Y. Wang
College of Architecture and Environment, Sichuan University, Chengdu, P.R. China

X.L. Zhao & F. Collins
Department of Civil Engineering, Monash University, Clayton, Australia

ABSTRACT: Geopolymeric Recycled Concrete (GRC) is a new construction material which takes environmental sustainability into account, by using alkali solution and fly ash to completely substitute Portland cement as well as by replacing natural coarse aggregate with recycled coarse aggregate. GRC could be used together with steel hollow sections to form composite section. There is very limited study on such GRC filled tubular sections. This paper presents an experimental study on GRC filled tubular stub columns. A total of 12 specimens were tested. The main parameters varied in the tests are: (1) two section sizes of square hollow sections (B × t) with 200 mm × 6 mm and 150 mm × 5 mm; (2) different concrete types: GRC and Recycled Aggregate Concrete (RAC); (3) different Recycled Aggregate (RA) replacement ratios of 0%, 50% and 100%. The relationship of load versus axial strain was recorded and analysed to compare the ultimate strength and failure mechanism. Meanwhile, the ductility of the columns was investigated by a ductility index (DI). The results show that the ultimate strength decreased with increasing RA contents for both GRC and RAC filled columns. The influence of RA content on the strength was greater in GRC than that in RAC. The effect of RA content on the ductility of the columns was further investigated. Simulation method for predicting load versus strain relationship is discussed for RAC and GRC filled steel tubular columns with different RA replacement ratios.

Keywords: Geopolymeric Recycled Concrete (GRC); tubular stub column; recycled aggregate replacement ratio; strength; ductility

1 INTRODUCTION

With the development of the human society, the problems of natural resources reduction, environmental pollution and greenhouse effect are getting more and more pressing. Nowadays, as the awareness of environmental protection is strengthened, the concept of "low carbon" is becoming the theme of all the human's activities. The infrastructure construction is a main part of all the human's performances which result in the need of concrete all over the word is second only to water. However, it is estimated the production of Ordinary Portland Cement (OPC) contributes approximately 7% of global man-made CO_2 emissions (Meyer 2009). In order to reduce the CO_2 emission effectively, to find an alternative binder in the concrete is a way to make environmental friendly concrete. Geopolymer is cement-like binder, which is a new type of inorganic polymer material generally synthesized by alkali activation of industrial aluminosilicate waste materials such as fly ash, granulated blast furnace slag, construction waste and contaminated soil. The research on fly ash based geopolymer concrete show that, given appropriate mixture design and formulation development, the concrete could exhibit superior chemical and mechanical properties to OPC, with high compressive strength, very little brittle drying shrinkage, low creep, good bond with reinforced steel, and also good resistance to acid sulphate and fire (Sumajouw et al. 2007, Sofi et al. 2007, Duxson et al. 2007a,b, Hardjito et al. 2004, 2005, Swanepoel & Strydom 2002). Using recycled aggregate (RA) to replace the natural aggregate in the geopolymer concrete partially or totally to form Geopolymeric Recycled Concrete (GRC), is a new type of green concrete. In GRC, CO_2 emission could be reduced due to without cement, as well as waste concrete could be reused which shows a great potential to be used as sustainable construction material. According to author's previous experimental studies, the mechanical properties of GRC present some advantages compared with OPC and corresponding recycled aggregate concrete (RAC) (Shi et al. 2011). However, the structural properties of such GRC are barely studied.

Concrete filled steel tube is widely studied and used because of its smart combination of both steel tube

and inside concrete (Zhao et al. 2010). At present, some research show that, the mechanical properties and structural behavior of RAC filled steel tube could be improved, indicating higher loading capacity and better ductility compared with ordinary concrete filled steel tube (Konno et al.1997, 1998, Yang & Han 2006, Chen et al. 2010a,b). Some theoretical calculations and numerical analysis methods were proposed for predicting the load and strain relationship (Zhong 1994, Yang 2007, Han 2007).

This paper describes a series of axial compression tests carried out on 12 concrete filled square section steel tubular columns, including 6 RAC filled steel tubes (RACFST) and 6 GRC filled steel tubes (GRCFST) with different RA replacement ratios of 0%, 50% and 100%. The structural behaviors, compressive strength and failure modes of such columns under axial compressive load are analyzed.

2 EXPERIMENTAL PROGRAM

2.1 *Material properties*

Cold-formed C350L0 Square Hollow Sections (SHS) were used in the testing program. The mechanical properties of steel were obtained by tensile coupon tests according to Australian Standard AS1391 (2007).

Table 1. Mechanical properties of steel.

Steel hollow section (mm)	Elastic modulus E (GPa)	Yield stress f_y (Mpa)	Ultimate tensile strength f_u (Mpa)
150 × 150 × 5	197	486	558
200 × 200 × 6	199	467	544

Table 2. Densities and water absorption of aggregates (SSD = saturated surface dry).

Aggregate type	Apparent density (t/m^3)	Dry density (t/m^3)	SSD density (t/m^3)	Water absorption (%)
NA	2850	2819	2908	1.08
RA	2433	2304	2645	5.60

The coupons were cut from the flat face of the SHS along the longitudinal direction of the section. The dimensions and test results of the steel are listed in Table 1.

All the recycled aggregates were supplied by Alex Fraser P/L and the fine particles smaller than 4.75 mm were removed from the RA by sieving in the laboratory. The nominal size of RA and Natural Aggregate (NA) were 20 mm and 14 mm, respectively. The densities and water absorption of RA and NA were presented in Table 2. The concrete mixture proportions were based on aggregates in Saturated Surface Dry (SSD) conditions.

Fly ash (ASTM Class F) was used as the main aluminum and silicate source for synthesizing of geopolymeric binder. It is mainly glassy with some crystalline inclusions of mullite, hematite and quartz.

Sodium silicate solution (Na_2SiO_3) with specific gravity of 1.53 and sodium hydroxide (NaOH) flakes of 98% purity were supplied by PQ Australia. The chemical composition of the sodium silicate solution was $Na_2O = 14.7\%$, $SiO_2 = 29.4\%$ and water = 55.9% by mass. Sodium hydroxide was dissolved using distilled water to provide 8 molarity alkaline solutions. Na_2SiO_3 and NaOH solutions were prepared one day prior to usage.

Six mixtures were designed to compare the influence of different RA replacement ratios on RAC and GRC concrete. The concrete mixture proportions are summarized in Table 3. W/G is the ratio of total water to geopolymeric binder solids.

2.2 *Specimens*

An electric vibration pole was used while the concrete was poured into the steel tube. The specimens of RACFST columns were cured under polyethylene sheets in the laboratory ambient environment. The GRCFST columns were cured under polyethylene sheets at 80°C for 24 hours in the oven, and then moved out into laboratory ambient environment. In order to make sure the loading was applied evenly, the surfaces of the columns were polished. At the same time, 3 cylinders were made for each type of concrete for testing the compressive strength of the inside concrete.

In total, 12 steel tubular columns were manufactured. The dimensions and the experimental results were summarized in Table 4. The total length of the columns was 750 mm. The square

Table 3. Summary of concrete mixture proportions (kg/m^3).

Mixture	RA ratio	RA/NA	Cement	Sand	Fly ash	NaOH solution	Na_2SiO_3 Solution	Added Water	W/G Ratio
RC0	0%	0/1294	364	554	–	–	–	182	0.50
RC50	50%	647/647	364	554	–	–	–	182	0.50
RC100	100%	1294/0	364	554	–	–	–	182	0.50
GRC0	0%	0/1294	–	554	368	53	131	0	0.50
GRC50	50%	647/647	–	554	368	53	131	0	0.50
GRC100	100%	1294/0	–	554	368	53	131	0	0.50

hollow sections of 200 mm × 200 mm × 6 mm and 150 mm × 150 mm × 5 mm were labeled as "S1" and "S2", respectively. 0, 50 and 100 refer to the RA replacement ratio of the inside concrete are 0%, 50% and 100%.

2.3 *Experimental procedure*

Specimens were tested on AMSLER500 in Civil Engineering Laboratory at Monash University. One longitudinal strain and one transverse strain were attached in the middle of the column on each side to record the deformation of the steel tubular columns. Two LVDTs were set up between loading and bottom plates diagonally to measure the displacement of the columns. The test set up is shown in Figure 1.

The loading process was controlled by hydraulic valve manually. The load, strains and displacements were recorded during the loading process.

3 RESULTS AND DISCUSSIONS

3.1 *Load capacity*

The ultimate loads of the specimens are listed in Table 4. The confinement factor is defined as $\xi = A_s f_y / A_c f_{ck}$ which can indicate the constraining effect of the outer steel tube to the inner concrete. The load capacity of the columns decreased with the increasing RA replacement ratio. In Figure 2, the results show that the ultimate strength of the columns decreased much more for GRCFST50 compared with GRCFST0 of both sectional types.

Here, in order to compare the influences of RA contents on the column's strength, the strength index SLI is proposed and defined as:

$$SLI = \frac{N_{e0} - N_{e,r}}{N_{e0}} \quad (1)$$

where N_{e0} = experimental results of concrete filled steel tubular columns with 0% RA replacement ratio; and $N_{e,r}$ = experimental results of concrete filled steel tubular columns with r% RA replacement ratio. The results were listed in Table 4. Obviously, with more RAs, the load capacity is weaker. The strength of GRCFST columns with 100% RA replacement ratio decreased about 24% compared with GRCFST columns without RAs. However, the reduction for RACFST columns is only about 10% in this case. It can be inferred that the RA contents has greater influence on GRCFST columns than that on RACFST columns.

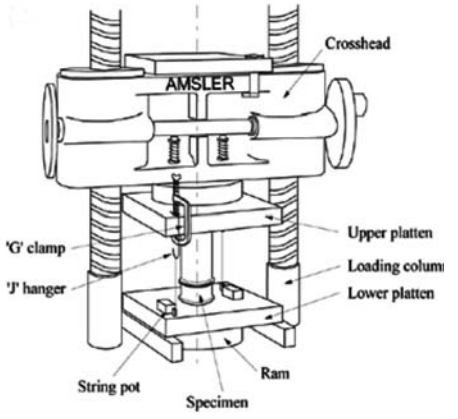

Figure 1. Test set up (Elchalakani 2002).

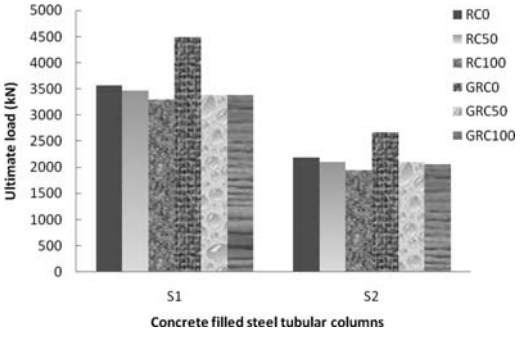

Figure 2. Load capacities of different columns.

Table 4. Summary of the specimens and measured properties.

Specimens	B (mm)	t (mm)	L (mm)	As/Ac	fc (MPa)	fy (MPa)	ξ	Fmax (kN)	DI	SLI (%)
S1RC0	200	6	750	0.132	68	467	1.08	3561	2.70	–
S1RC50	200	6	750	0.132	57	467	1.30	3466	3.00	2.7
S1RC100	200	6	750	0.132	49	467	1.49	3297	3.04	7.4
S1GRC0	200	6	750	0.132	69	467	1.07	4497	1.89	–
S1GRC50	200	6	750	0.132	56	467	1.32	3380	3.39	24.8
S1GRC100	200	6	750	0.132	44	467	1.68	3376	2.74	24.9
S2RC0	150	5	750	0.148	68	486	1.26	2184	2.83	–
S2RC50	150	5	750	0.148	57	486	1.52	2100	3.36	3.9
S2RC100	150	5	750	0.148	49	486	1.75	1947	4.83	10.9
S2GRC0	150	5	750	0.148	69	486	1.25	2676	1.64	–
S2GRC50	150	5	750	0.148	56	486	1.54	2100	2.87	21.5
S2GRC100	150	5	750	0.148	44	486	1.97	2057	3.07	23.1

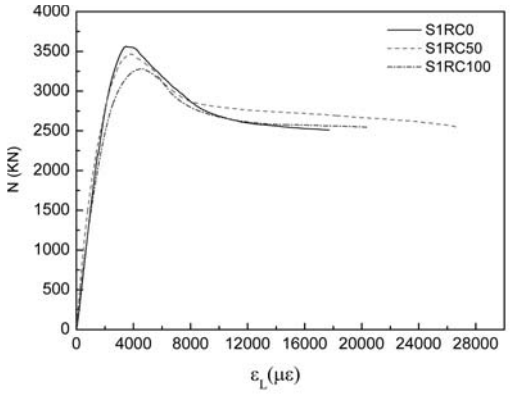

(a) RACFT columns of S1

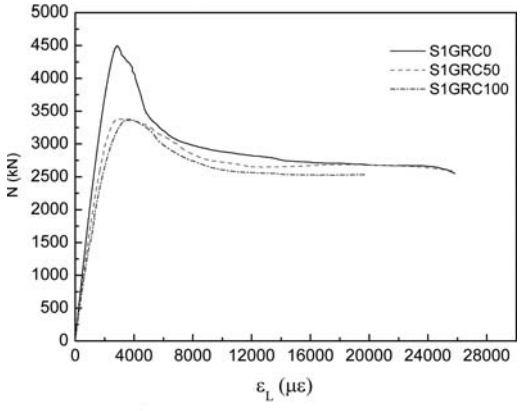

(b) GRCFT columns of S1

Figure 3. The load versus longitudinal strain ($N \sim \varepsilon_L$) curves of S1 columns.

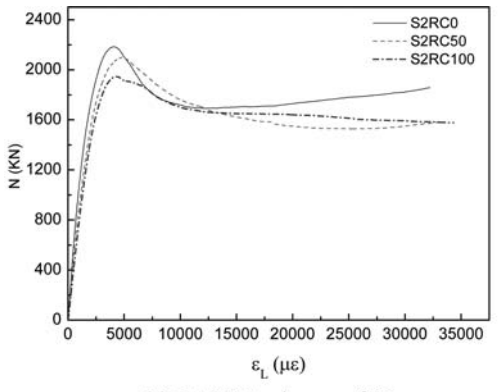

(a) RACFT columns of S2

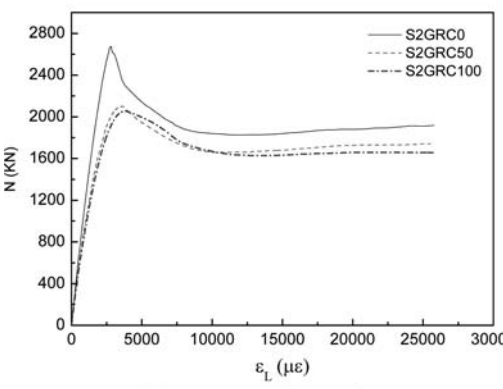

(b) GRCFT columns of S2

Figure 4. The load versus longitudinal strain ($N \sim \varepsilon_L$) curves of S2 columns.

3.2 *$N \sim \varepsilon$ curves and ductility*

The load versus strain ($N \sim \varepsilon$) curves of the steel tubular columns indicate the relationship of bearing load and strain during the loading process, which present the structural behavior of the columns. The axial load versus longitudinal strain ($N \sim \varepsilon_L$) curves are shown in Figure 3 and Figure 4 for two different sectional columns.

The results in Figure 3 and Figure 4 show that, with the increasing of RA replacement ratio, the ultimate strength of the columns decreased, while the ultimate strain increased slightly for both S1 and S2. For RACFST columns, the deduction of the strength and the increment of the ultimate strain changed almost homogeneously. However, for GRCFST columns, the changes of strength and ultimate strain are greatly influenced by RA contents with 50% replacement ratio. But with much more RA contents, the changes are trailed off, such as the comparison of GRCFST columns with 50% and 100% RA replacement ratios. After the peak point of the curves in the figures, the curves drop more slightly with more RA contents for both RACFST and GRCFST columns. Especially for GRCFST columns, the declining period of the curves drop very sharply for the columns with GRC0, but much more slightly for the columns with GRC50 and GRC100. These indicate that the ductility of the columns is improved with RAs for both RACFST and GRCFST columns. In order to study the ductility quantitatively, the ductility index DI is used according to the method for ordinary concrete filled steel tubular columns, which is defined as (Han 2002, Tao et al. 2008):

$$DI = \frac{\varepsilon_{85\%}}{\varepsilon_y} \tag{2}$$

Where $\varepsilon_{85\%}$ = longitudinal strain when the load falls to 85% of the ultimate load; $\varepsilon_y = \varepsilon_{75\%}/0.75$, $\varepsilon_{75\%}$ = axial strain when the load attains of 75% the ultimate load in the pre-peak stage. The results of DI for each column are listed in Table 4. It can be seen from Figure 5, with more RAs in the columns, the DI values are higher overall. The ductility of the columns are improve by 12%, 45%, 70% and 87% for S1RACFST, S1GRCFST, S2RACFST and S2GRCFST between 100% and 0% RA replacement ratio, respectively. This

indicates that the influence of RA contents on ductility for the columns with GRC is greater than that with RAC. On the other hand, the confinement factor ξ of S1 is lower than that of S2. It can be inferred that with better confinement effect, the ductility could be greater improved.

3.3 *Failure mechanism*

During the loading process, there is no obvious deformation at the beginning of the loading for all the columns. With the load being applied near to the ultimate load, some crack noises could be heard. Then, the local buckling on the columns appeared. The configurations of the columns after the testing are shown in Figure 6. For S1 columns, the local buckling firstly appeared near the middle of columns. While the load went up, the bulges also happened on the top part of the column. The bulges on the each side of the column gradually connected together to form the typical "roof" type failure mode. For S2 columns, the local buckling mostly started from the top or the bottom of the column. The bulges appeared on the diagonally sides of the column as the load carrying on. The failure mechanism is similar to S1 columns. At the end of the loading, the bulges were measured as about 2 ~ 3 cm above the steel tube surface.

During the deformation process, they were found that with more RAs and larger confinement factor, the failure mode presents a trend of transferring from shear type to drum type. It can be seen in Figure 6 that the bulges on RC0 and GRC0 columns are in greater angle on the cross. While, on the RC100 and GRC100 columns, the bulges almost appeared on the same level around the column. This is also found out by Han (2007). That is with larger confinement factor, the failure is generally happened with drum failure mode; while, with smaller confinement factor, the failure is always shear broken mode.

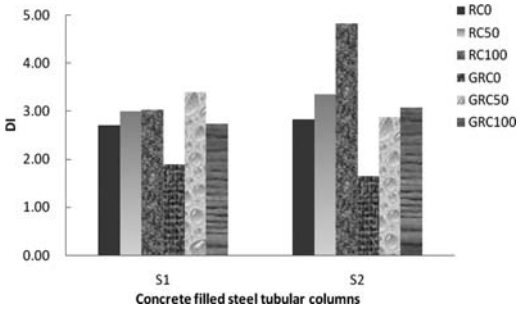

Figure 5. The ductility index (DI) of different columns.

4 THEORETICAL ANALYSIS

According to the numerical analysis method for ordinary concrete filled steel tube on load and strain relationship, the numerical analysis method for such GRCFST columns is discussed based the constructive relationships of steel and the core concrete.

4.1 *Constructive relationships*

4.1.1 *Steel*

For cold formed steel, the ideal constructive relationship could be described as elastic-plastic strain-stress relationship based on multilinear isotropic strain hardening rule (Chen & Han 1988) as shown in Figure 7.

So, the relationship can be expressed as:

$$\sigma_s = \begin{cases} E\varepsilon & \varepsilon \le \varepsilon_1 \\ f_P + E_{T1}(\varepsilon - \varepsilon_1) & \varepsilon_1 < \varepsilon \le \varepsilon_2 \\ f_{ym} + E_{T2}(\varepsilon - \varepsilon_1) & \varepsilon_2 < \varepsilon \le \varepsilon_3 \\ f_y + E_{T3}(\varepsilon - \varepsilon_1) & \varepsilon_3 < \varepsilon \end{cases} \quad (3)$$

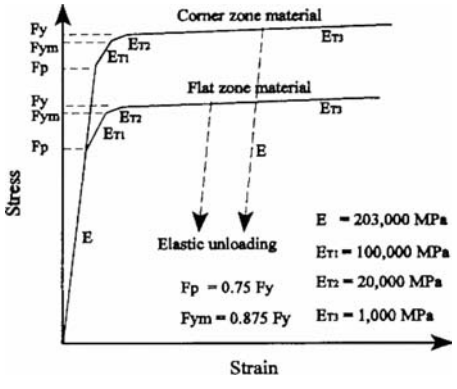

Figure 7. Strain-stress curve of cold-formed steel.

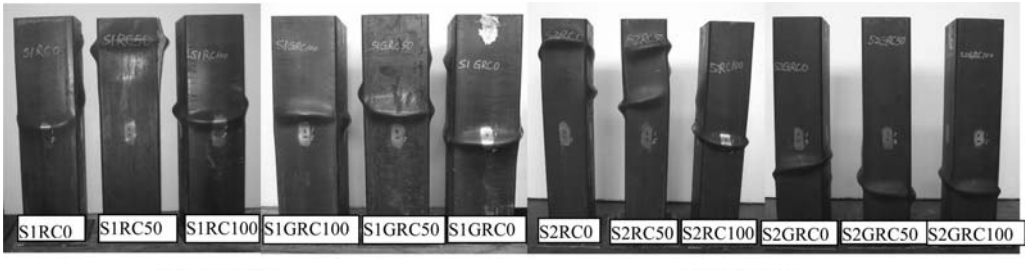

Figure 6. The failure modes of the columns.

where, f_y = yielding strength of the steel; E = 2.00×105 MPa; $E_{T1} = 0.5E, E_{T2} = 0.1E, E_{T3} = 0.05E$; $f_p = 0.75f_y$, $f_{ym} = 0.875f_y$; $\varepsilon_1 = 0.75f_y/E$, $\varepsilon_2 = \varepsilon_1 + 0.125f_y/E_{T1}$, $\varepsilon_3 = \varepsilon_2 + 0.125f_y/E_{T2}$.

4.1.2 *Core concrete*

In the Concrete Filled Steel Tubular (CFST) structure, the stress state of the core concrete is different from concrete in the free state due to the confinement effect of the outer tube. When the CFST column is under axial compressive load, the steel tube and the core concrete carry the load together at the initial period. The transverse deformation of the steel tube is larger than that of core concrete due to its greater Poisson's ratio, so the core concrete is under axial compression. As the load being applied, the deformation of concrete is increasing. When the transverse deformation of the core concrete becomes larger than that of steel tube, the confinement effect of the steel tube on the core concrete works, and then, the core concrete is under triaxial compression stress state. Accordingly, Han (2007) proposed the constructive relationship of core concrete. Based on Han's study and the RAC properties, Yang (2007) revised this mode for RAC's strain-stress relationship. Considering the influence of the RA replacement ratio on the RAC's compressive strength and peak strain (Xiao 2005), for square sectional RACFST, the constructive relationship of core RAC can be described as:

$$y = \begin{cases} 2x - x^2 & (x \le 1) \\ \dfrac{x}{\beta(x-1)^{\eta} + x} & (x > 1) \end{cases} \tag{4}$$

where, σ_0 = maximum stress of the concrete; ε_0 = peak strain of the concrete; $x = \frac{\varepsilon}{\varepsilon_0}$; $y = \frac{\sigma}{\sigma_0}$;

$$\sigma_0 = \left[1 + (-0.0135\xi^2 + 0.1\xi)\left(\frac{24}{f_c}\right)^{0.45}\right] f_c(1 - 0.3r + 0.13r^2)$$

$$\varepsilon_0 = \left\{\varepsilon_{cc} + \left[1330 + 760\left(\frac{f_c}{24} - 1\right)\right]\xi^{0.2}\right\} \bullet \left(1 + \frac{r}{\beta'}\right) \quad (\mu\varepsilon)$$

$$\beta' = 65.715r^2 - 109.43r + 48.989;$$

$$\varepsilon_{cc} = 1300 + 12.5f_c;$$

$$\eta = 1.6 + 1.5/x;$$

$$\beta = \begin{cases} \dfrac{f_c^{0.1}}{1.35\sqrt{1+\xi}} & (\varepsilon \le 3.0) \\ \dfrac{f_c^{0.1}}{1.35\sqrt{1+\xi(\xi-2)^2}} & (\varepsilon > 3.0) \end{cases}$$

Considering the different compressive strength properties of GRC, the relationship of RA replacement ratio and compressive strength can be expressed as Equation 5 based on previous studies.

$$F_G^r = F_G^n(1 - 0.26r - 0.1r^2) \tag{5}$$

So, the maximum stress of core GRC is:

$$\sigma_0 = \left[1 + (-0.0135\xi^2 + 0.1\xi)\left(\frac{24}{f_c}\right)^{0.45}\right] f_c(1 - 0.26r - 0.1r^2)$$

4.2 *$N/N_{max} \sim \varepsilon_L$ curves*

Based on the definition of materials constructive relationship, the load and deformation relationship of RACFST and GRCFST columns under axial loading could be investigated by setting up equilibrium and deformation-coordination conditions, as well as the load-deformation relationships for steel and core concrete could be identified respectively. According to "Fiber Model" method, in order to compare the bearing load proportion, $N/N_{max} \sim \varepsilon_L$ curve is used to describe the load-deformation relationship. The hypotheses of the calculation are:

(1) no sliding between steel tube and core concrete;
(2) the constructive relationships of RAC and GRC could be expressed as Equation (4) and (5);
(3) only consider the longitudinal equilibrium and deformation-coordination relation;

The equilibrium equation of the columns gives:

$$N = N_s + N_c \tag{6}$$

The deformation-coordination condition gives:

$$\varepsilon_{sl} = \varepsilon_{cl} \tag{7}$$

where, N = external load; N_s = axial load on the steel tube; N_c = axial load on the core concrete; ε_{sl} = longitudinal strain of the steel tube; ε_{cl} = longitudinal strain of the core concrete.

Synthesis method is adopted to realize the calculation. Firstly, appoint one train value (ε_1), and the corresponding σ_s and σ_c can be defined by Equation (4); and then, the axial load (N_1) could be calculated by adding $N_s = A_s\sigma_s$ and $N_c = A_c\sigma_c$. In the same way, the second point (ε_2) can figure out N_2. So, we can get the typical $N/N_{max} \sim \varepsilon_L$ curves for RACFST and GRCFST columns, as seen in Figure 8 and Figure 9.

In Figure 8, the curves for columns demonstrate similar configuration. As the RA contents increase, the calculated results are better. During the loading process, when the load added to about 70% ~ 80% of the maximum load, the columns got into plastic state from the initial elastic state, which can be found by the reduction of the curves' slope. The columns with more RA contents came into plastic state much earlier. The curves of steel and core concrete show that, in the elastic period, the elastic modulus of the steel is larger than that of the core concrete. As the RA replacement ratio increasing, the load carried by steel tube would get larger.

In Figure 9, overall the developing trend of the load-deformation relationship is similar to the curves in Figure 8. However, the calculated peak strains of the

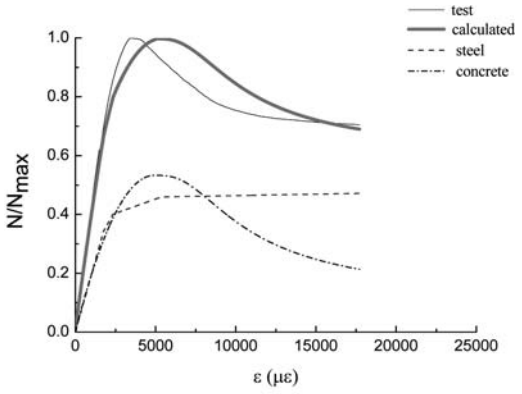

(a) S1RC0，ξ=1.08

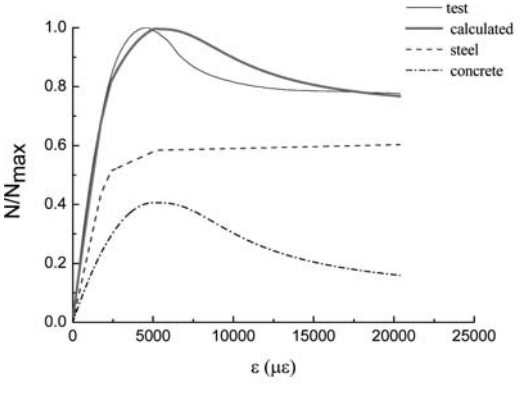

(b) S1RC100，ξ=1.49

Figure 8. Typical $N/N_{max} \sim \varepsilon_L$ curves of RACFST columns.

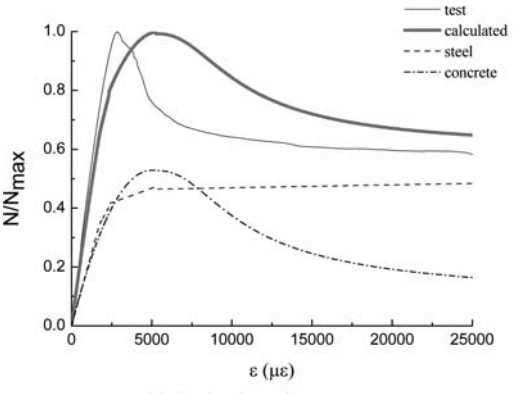

(a) S1GRC0，ξ=1.07

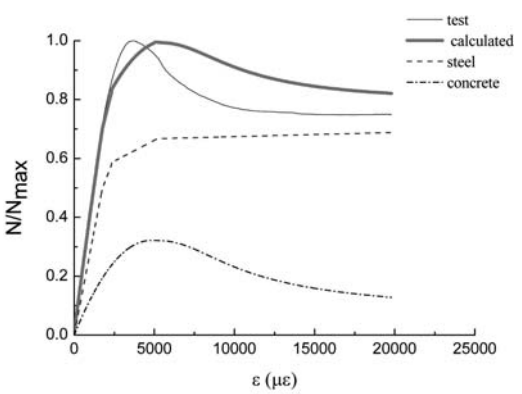

(b) S1GRC100，ξ=1.68

Figure 9. Typical $N/N_{max} \sim \varepsilon_L$ curves of GRCFST columns.

columns are significant larger than the experimental results. This is because the predicted peak strain model of GRC is not close to the practical situation due to the different constructive relationship of GRC from RAC, especially for the post-peak period. For example, in Figure 8(a), the curves declined very sharply indicating very poor ductility, which is quite different from RACFST. With more RAs in the columns, the peak strain is larger and the ductility of the columns gets much better. Overall, the simulation of GRCFST according to the method for RACFST should be revised and improved based on more specific core GRC constructive relationship.

5 CONCLUSIONS

The structural behaviors of geopolymeric recycled concrete, which is a new sustainable material, filled in steel tubular columns under axial loading were investigated by testing 12 concrete filled columns. By comparison with RACFST and different RA replacement ratios, it can be found that the RA replacement ratios play greater effect on the strength and ductility to GRCFST than that to RACFST. The strength of GRCFST columns decreased more obviously with RAs. The ductility of columns could be improved with greater RA contents. The failure mechanisms are similar for both RACFST and GRCFST columns. The simulation method for predicting load-deformation curves, which based on materials constructive relationships, is feasible for RACFST columns. However, for GRCFST columns, such method is expected to be improved by considering more specific strain-stress relationship of core GRC. Overall, the applications of GRC in structures show prospective future.

ACKNOWLEDGEMENTS

Authors gratefully acknowledge the support from Chinese Scholarship Council, Monash-Sichuan University Strategic Fund for sponsorship to provide the study resources for this research work. The efforts and assistance with the laboratory work provided by Long Kim Goh, Jeff Doddrell, Kevin Nievaart, Mark Taylor are also gratefully acknowledged.

REFERENCES

Chen, W.F & Han, D.J. 1988. Plasticity for structural engineers. New York: Springer-Verlag New York, Inc.

Chen, Z.P., Liu, F., Zheng, H.H., Xue, J.Y. 2010. Research on the bearing capacity of recycled aggregate concrete-filled circle steel tube column under axial compression loading. *2010 International Conference on Mechanic Automation and Control Engineering, MACE2010*, June 26, 2010 – June 28, 2010. Wuhan, China: IEEE Computer Society; 1198–1201.

Chen, Z.P., Chen, X.H., Ke, X.J., Xue, J.Y. 2010. Experimental study on the mechanical behavior of recycled aggregate coarse concrete-filled square steel tube column. *2010 International Conference on Mechanic Automation and Control Engineering, MACE2010*, June 26, 2010 – June 28, 2010. Wuhan, China: IEEE Computer Society; 1313–1316.

Duxson, P., Provis, J.L., Lukey, G.C., Van Deventer, J.S.J. 2007. The role of inorganic polymer technology in the development of 'green concrete'. *Cement and Concrete Research*. 37:1590–1597.

Duxson, P., Fernandez-Jimenez, A., Provis, J., Lukey, G., Palomo, A., van Deventer, J. 2007. Geopolymer technology: the current state of the art. *Journal of Materials Science* 2917–2933.

Elchalakani, M., Zhao, X.L., Grzebieta, R. 2002. Tests on concrete filled double-skin (CHS outer and SHS inner) composite short columns under axial compression. *Thin-Walled Structures*. 40:415–441.

Hardjito, D., Wallah, S.E., Sumajouw, D.M.J., Rangan, B.V. 2004. On the development of fly ash-based geopolymer concrete. *ACI Mater J* 101(Compendex):467–472.

Hardjito, D., Wallah, S.E., Sumajouw, D.M.J., Rangan, B.V. 2005. Fly Ash-Based Geopolymer Concrete. *Australian Journal of Structural Engineering* 6(1):77–86.

Han, L.H. 2002. Tests on stub columns of concrete-filled RHS sections. *Journal of Constructional Steel Research* 58:353–372.

Han, L.H. 2007. Concrete filled steel tube—theory and practice (2nd edition). Beijing: Sicenice and technology press; (in Chinese)

Konno, K., Sto, Y., Kakuta, Y. 1997. The property of recycled concrete column encased by steel tube subjected to axial compression. *Transactions of the Japan Concrete Institute* 19:351–358.

Konno, K., Sato, Y., Uedo, T. 1998. Mechanical property of recycled concrete under lateral confinement. *Transactions of the Japan Concrete Institute* 20:287–292.

Meyer, C. 2009. The greening of the concrete industry. *Cement & Concrete Composites* 31(8):601–605.

Sumajouw, D.M.J., Hardjito, D., Wallah, S.E., Rangan, B.V. 2007. Fly ash-based geopolymer concrete: study of slender reinforced columns. *Journal of Materials Science* 42(Copyright 2008, The Institution of Engineering and Technology):3124–3130.

Sofi, M., van Deventer, J.S.J., Mendis, P.A., Lukey, G.C. 2007. Engineering properties of inorganic polymer concretes (IPCs). *Cement and Concrete Research* 37(Compendex):251–257.

Swanepoel, J.C., Strydom, C.A. 2002. Utilisation of fly ash in a geopolymeric material. *Applied Geochemistry* 17(8):1143–1148.

Shi, X.S., Collins, F.G., Zhao, X.L., Wang, Q.Y. 2011. Experimental study on geopolymeric recycled concrete using as sustainable construction material. *International conference on advances in construction materials through science and engineering, RILEM*. Hong Kong SAR, China.

Xiao, J.Z., Li, J.B., Zhang, C. 2005. Mechanical properties of recycled aggregate concrete under uniaxial loading. *Cement and Concrete Research* (35):1187–1194.

Yang, Y.F. & Han, L.H. 2006. Experimental behaviour of recycled aggregate concrete filled steel tubular columns. *Journal of Constructional Steel Research* 62:1310–1324.

Yang, Y.F. 2007. Theoretical research on load-deformation relations of recycled aggregate concrete filled steel tubular members. *Industrial Construction* 37(12):1–7. (in Chinese)

Zhao, X.L., Han, L.H. and Lu, H.(2010) Concrete filled tubular members and connections, Taylor and Francis, London.

Zhong, T., Han, L.H., Wang, D.Y. 2008. Strength and ductility of stiffened thin-walled hollow steel structural stub columns filled with concrete. *Thin-Walled Structures* 46:1113–1128.

Zhong, S.T. 1994. The unified theory of concrete filled steel tube (CFST). *Journal of Harbin University of Civil Engineering and Architecture* 27(6):21–27. (in Chinese)

Tubular Structures XIV – Gardner (Ed.)
© 2012 Taylor & Francis Group, London, ISBN 978-0-415-62137-3

Rotation capacity and ductility of square hollow sections: A comparison between cold-formed and hot-finished sections

S. Terada
Nippon Steel & Sumikin Metal Products Co., Tokyo, Japan

K. Ochi & T. Nagaoka
Kumamoto University, Kumamoto, Japan

ABSTRACT: Bending tests under cyclic loads were carried out on cold-formed (200 mm diameter × 12.0 and 12.5 mm thickness) and hot-finished sections (180 mm diameter × 12.5 mm thickness) of steel grade S355J2H (EN) in order to investigate fracture at welded corner and rotation capacity. The specimens of the tensile coupon test and Charpy V notch impact test were carried out of the flat areas and corner areas of cold-formed and hot-finished hollow sections. Using the material properties, the material constants of the modified Ramberg-Osgood curves are presented. Finite element analyses were carried out to examine the effects of the yield ratio on the load-deformation curves of bending tests of cold-formed sections.

1 INTRODUCTION

Rectangular hollow sections are used in building structures as beam-columns. Plastic design can be applied in frames which resist loads predominately by bending. There must be sufficient material ductility of the steel to avoid fracture.

The rotation capacity and ductility of plastic hinges are affected by the process of manufacturing cold-formed, hot-rolled and hot-finished square hollow sections. The strain hardening capacity and the toughness at the corners part of cold-formed columns decrease due to strain aging. The seismic design for building construction requires sufficient deformability in structural members before clear loss of loading capacity, caused by local buckling or brittle fracture. In order to assure the safety usage of cold-formed sections as frame building members, it is important to study the brittle fracture characteristics on their corners.

The aim of this paper is to compare the ductility, notch toughness and rotation capacities of cold-formed, hot-rolled and hot-finished square hollow sections as obtained from a number of tests and FE analyses.

2 EXPERIMENTAL STUDY

2.1 *General*

An experimental programme of consisting of bending tests, tensile coupon tests and Charpy V notch impact tests, was designed to evaluate the difference between the hot-rolled sections, the hot-finished sections and cold-formed sections. Table 1 shows the manufacturing process and origins of materials. Sectional dimensions and steel grades are shown in Table 2.

Table 1. Material properties.

Material no.	Manufacturing process	Origin	Standard
1	hot-rolled	UK	EN10210
2	hot-finished	China	EN10210
3	cold-formed	Malaysia	EN10219
4	cold-formed	Japan	EN10219

Table 2. Sectional dimensions.

Material no.	Dimensions	Steel grade
1	180 × 180 × 12.5	S355J2H
2	180 × 180 × 12.5	S355J2H
3	200 × 200 × 12	S355J2H
4	200 × 200 × 12	S355J2H

2.2 *Tensile coupon tests*

Four coupons according to both EN and Japanese Industrial Standards (JIS) were taken from the center of the flats of each tube. Corner coupons according to JIS were cut from selected a corner of SHS. The coupons were prepared and tested in accordance with

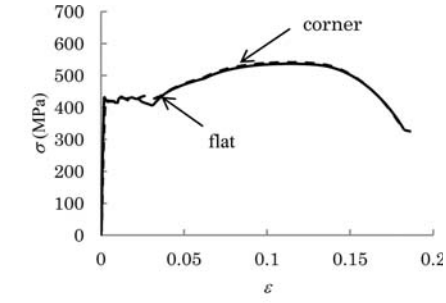

(a) hot-rolled No.1.

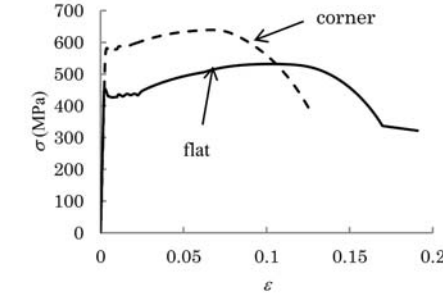

(b) hot-finished No.2.

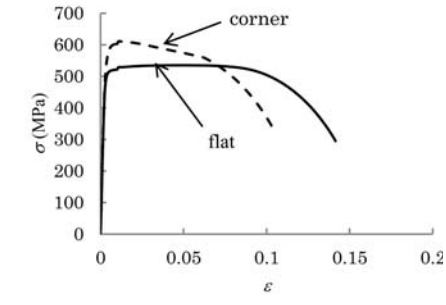

(c) cold-formed No.3.

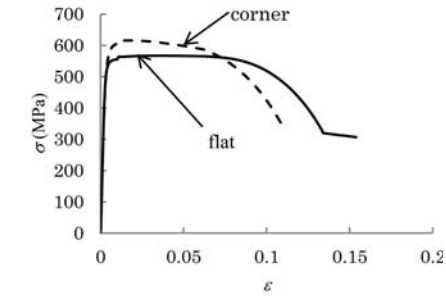

(d) cold-formed No.4.

Figure 1. Comparison of stress-strain curves.

EN and JIS. Typical stress-strain curves obtained for the test specimens (JIS) are shown in Figure 1. Yield strength and ultimate tensile strengths obtained from coupon testing are summarized in Table 3.

Table 3. Material properties of coupon tests.

Material No.		YS MPa	TS MPa	YR %	
1	flat	416	537	77.5	JIS
	flat	416	523	79.5	EN
	corner	421	540	78.0	JIS
2	flat	435	532	81.8	JIS
	flat	458	527	86.9	EN
	corner	562	625	89.9	JIS
3	flat	511	535	95.5	JIS
	flat	461	521	88.5	EN
	corner	564	597	94.5	JIS
4	flat	542	569	95.3	JIS
	flat	515	569	90.5	EN
	corner	573	620	92.4	JIS

YS = yield strength; TS = tensile strength; YR = yield ratio.

For the hot-rolled sections (No. 1), the material has a distinct yield plateau and there is no significant difference in stress-strain relations between the flat faces and the corners of SHS as shown in Figure 1 (a) and Table 3.

Because of the non-linearity of the stress-strain curves for the cold-formed sections (No.3 and 4) as shown in Figure 1 (c) and (d), 0.2 per cent proof stress was used for yield strength of cold-formed sections. The yield strengths obtained from the corner coupons were on average 10 % higher than that of the flat faces. Cold- formed steel has higher yield stress and tensile stress but less ductility than hot-rolled steel.

For the hot-finished section (No. 2) as shown in Figure 1 (b), the material has a yield plateau, but there are difference in stress-strain relations and the values of yield strength, tensile strength and yield ratio between the flat faces and the corners as shown in Table 3 and Figure 1 (b), The behaviours of hot-finished materials are between the cold- formed and hot-rolled sections.

The difference in shapes of specimens between EN and JIS affect the results of coupon test. The average of the yield stress of EN specimens from the flat faces was used in the determination of plastic moment.

2.3 *Charpy V-notch Impact tests*

Standard full-size $10 \times 10 \times 55$ mm test pieces were cut from SHS on the surface. For each tube type, Charpy V-Notch (CVN) test coupons were taken from flats faces and corners around the cross-section at the longitudinal direction. The coupons had a through-thickness notch orientation.

Figure 2 shows the test results for the four tube types sampled with CVN test specimens at temperatures of $-40°C$, $-20°C$ and $0\,°C$. Because of the inherent scatter of CVN test results, either three replicate specimens from flats face and four specimens from corners were tested at each target temperature. In total, 84 CVN specimens have been machined and impact tested.

Figure 2 (a) shows the toughness-temperature results of the hot-rolled tube (No. 1). There is no significant difference in absorbed energy of CVN test results between the flat faces and the corners.

The results of hot-finished tube (No. 2) are shown in Figure 2 (b). The difference in absorbed energy between the flat faces and corners are significant. The corner regions of the hot-finished SHS produce lower CVN toughness values than the flat faces.

Figures 2 (c) and (d) show the relations of test results between toughness and temperature of the cold-formed tubes. There is no significant difference in absorbed energy of CVN test results between the flat faces and the corners. Toughness properties of cold-formed test results exceed the requirements at all locations around the cross-section. The effect of the properties of parent steels on toughness may cause the difference in toughness between No.3 and No.4.

All the test results accord with requirements of EN10210 or EN10219. Specimens of cold-formed SHS showed much higher value than the other two, while the values of hot-formed and hot-finished SHS are closing to each other.

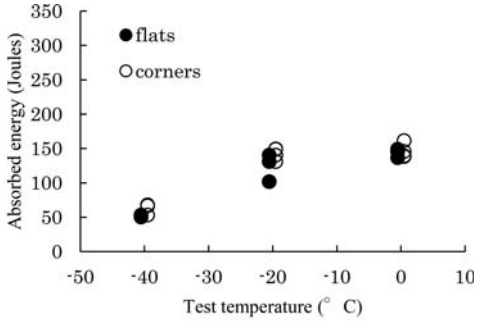

(a) hot-rolled No.1.

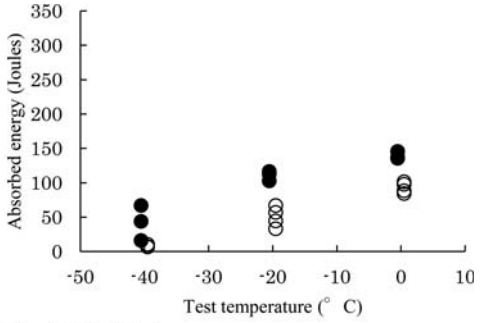

(b) hot-finished No.2.

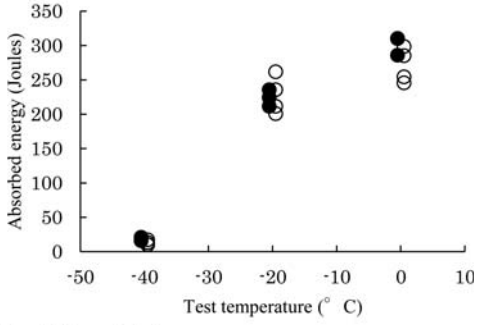

(c) cold-formed No.3.

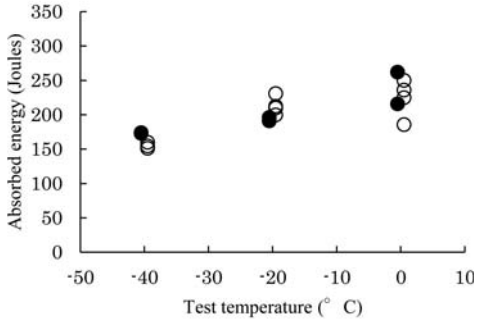

(d) cold-formed No.4.

Figure 2. Plots of Charpy toughness-temperature.

2.4 *Bending tests*

A diagram of the test set-up is shown in Figure 3. The three point bending arrangement provide triangle bending moment distribution at a half part of the specimen. Specimens were supported on mechanical rollers which simulated a set of simple supports. Because of the decision of maximum bending stress at the corner of the sections, the sections of specimen are 45 degrees around the member axis.

Figure 4 shows the number of cycles and displacements corresponding beam rotation at the mid span. The rotation is calculated by dividing the displacements of the mid span by the half span length of the beam. The cyclic loadings were applied at the mid span.

The results of the cyclic bending tests are presented in Figure 5. The rotation capacities of hollow sections for seismic design are estimated by the skeleton curves using the cyclic tests results as shown in Figure 6. Figure 5 and 6 shows the relations of M/M_p and θ/θ_p. M_p is the plastic moment of the section based on the measured dimensions and the mean of yield stress of the flat faces. The moment is normalized with respect to M_p. The rotation is normalized with respect to θ_p, where θ_p is the elastic rotation at the M_p. The decrease in moment is usually associated with an inelastic local buckle or fractures.

The specimens have the CPJ welded joints between the steel plate at the load point and SHS member. The corner at the maximum bending stress of the specimen has weld. All specimens experienced initial ductile cracks at the deformations ($\theta/\theta_p = 4$). There was no unloading associated with the ductile cracks. The hot-rolled (No.1) and cold-formed specimens (No.3, No.4) experienced local buckling which produced a slowly shedding of load with increased deflection at larger

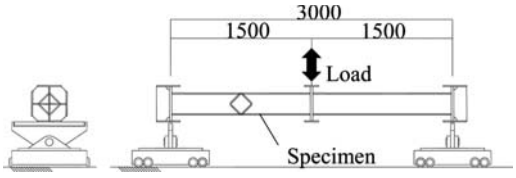

Figure 3. Test set-up.

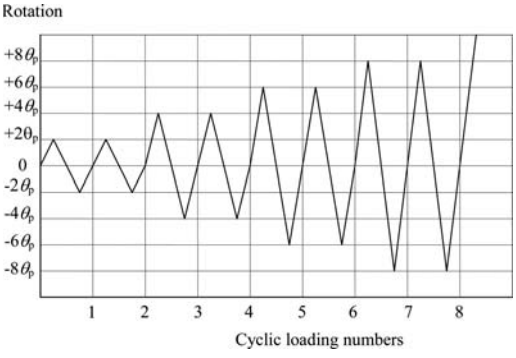

Figure 4. Loading procedure.

deformations as shown in Figure 7. The hot-finished specimen (No.2) failed through ductile fracture of the weld at the corner. Hot-rolled specimen (No.1) exhibited large deflections and an inelastic local deformation was observed at high rotations (θ/θ_p) greater than 15 as shown in Figure 6.

There was no sudden unloading associated with the local buckles and fractures as shown in Figure 5 and 6. No specimen failed due to insufficient material ductility. All of the sections failed to reach the plastic moment and have plastic rotation capacity ($\theta/\theta_p > 5$) sufficient for plastic design as shown in Figure 6.

The relation between moment and deformation of the hot-rolled section is considerable lower moment than the hot-finished and cold-formed sections as shown in Figure 6.

The yield ratio of the cold-formed sections (No.4) coincide with limit of the material ductility requirement (1/YR = 1.1) of Eurocode 3 for plastic design. However local buckling was the failure mode of the both hot-rolled and cold-formed sections. The limitation on cold-formed SHS for plastic design on reduced material ductility may need reconsiderations.

3 FEA FOR BENDING TESTS OF COLD-FORMED SHS

3.1 *Material stress-strain models*

Cold-formed stress-strain curves with showing a smooth elastic-plastic transition obtained from the test specimens are shown in Figure 1 (c) and (d).

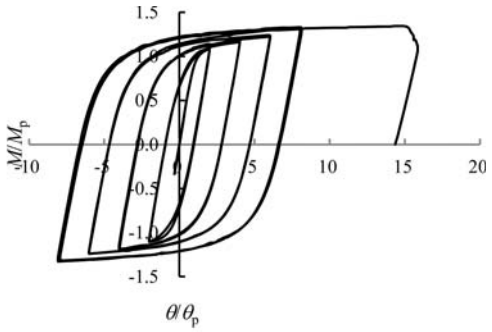

(a) hot-rolled No.1.

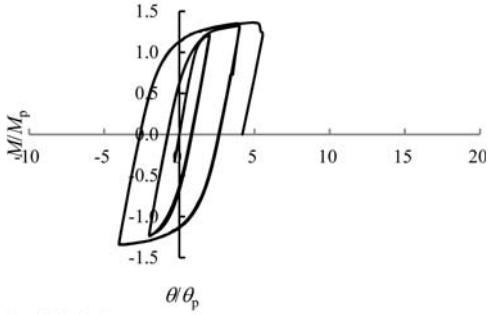

(b) hot-finished No.2.

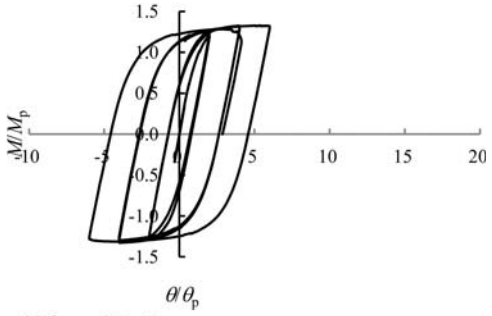

(c) cold-formed No.3.

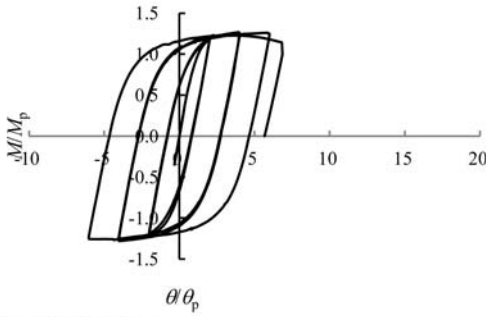

(d) cold-formed No.4.

Figure 5. Moment vs. rotation relations of beams.

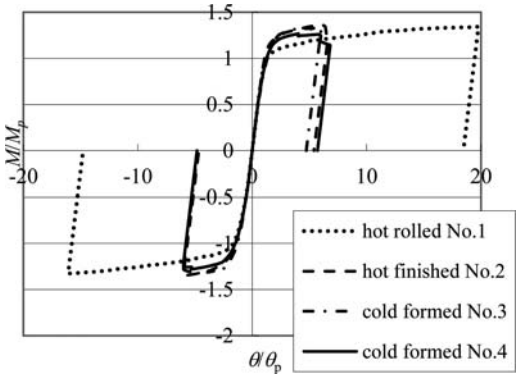

Figure 6. Skeleton curves of cyclic test results.

The Ramberg-Osgood equation, expressed in terms of strain, is:

$$\varepsilon = \frac{\sigma}{E} + 0.002\left(\frac{\sigma}{\sigma_y}\right)^n \tag{1}$$

where ε = logarithmic strain; σ = true stress; σ_y = yield stress (yield strength); E = elastic modulus and n = material constant.

$$\sigma_u = \left(\frac{1}{c \cdot e \cdot n}\right)^{1/n} \tag{2}$$

in which $e$is the mathematical constant.
where:

$$c = \frac{0.002}{\sigma_y^n} \tag{3}$$

Equation 2 is used for determining the material constant (n) in Equation 1 (Ochi 2010). The true stress-true strain curves generated by the Ramberg-Osgood equation using the yield strength and tensile strength of the JIS specimens in Table 3 are shown in Figure 8.

3.2 *Results of FEA*

The numerical analyses were performed using finite element code ANSYS (2010). Because of symmetry at the mid span of specimens, the FEA model only considered half of the specimen. A shell finite element model is used to the plastic and local buckling behaviours of cold-formed sections. The multi-linear true stress-true strain relations fitted with equation 1 as shown in Figure 8 were used. Residual stresses were neglected in the models.

Figure 9 shows load-deformation relations obtained from tests and the FE analyses. The maximum strength of the tests are seen to be in close agreement with the results of the FEA. The load rotation relations predicted by FEA models were extremely close to the experimental skeleton curves at ultimate behaviour including local buckling.

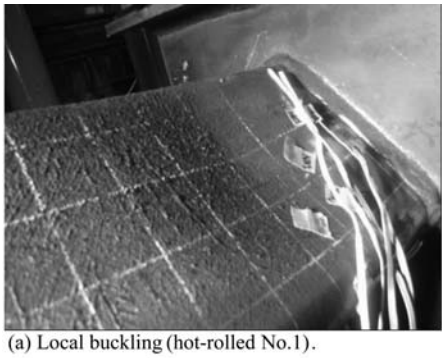

(a) Local buckling (hot-rolled No.1).

(b) Local buckling (cold-formed No.4).

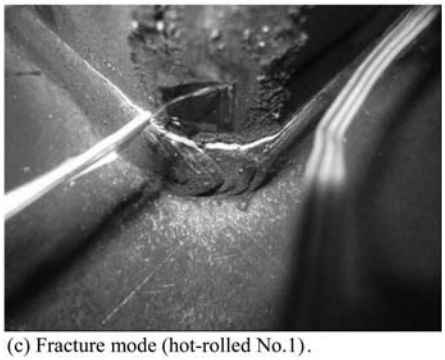

(c) Fracture mode (hot-rolled No.1).

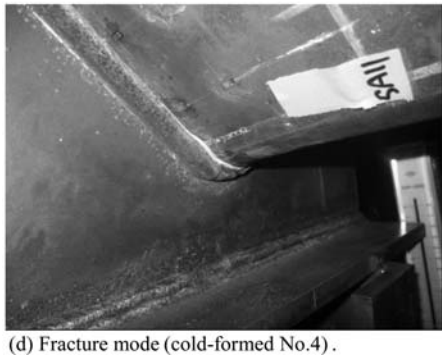

(d) Fracture mode (cold-formed No.4).

Figure 7. A comparison of failure modes with hot-rolled section and cold-formed section.

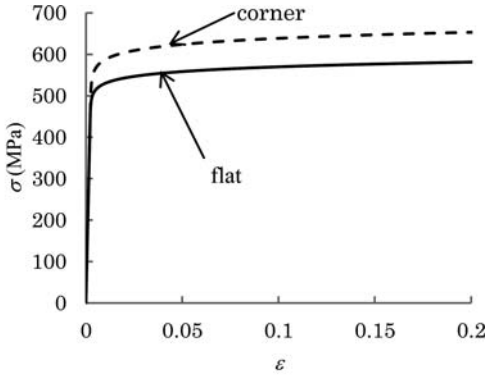

flat: $n = 35.5$, corner: $n = 31.3$
(a) cold-formed No.3.

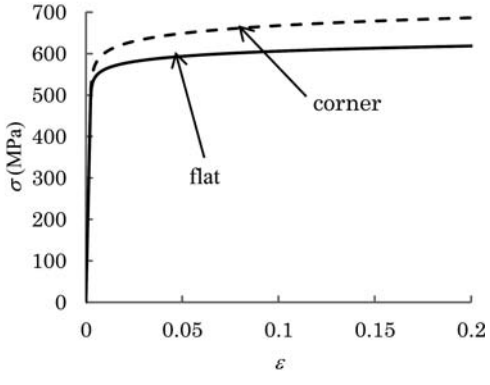

flat: $n = 34.8$, corner: $n = 25.5$
(b) cold-formed No.4.

Figure 8. Ramberg-Osgood true stress-true strain curves.

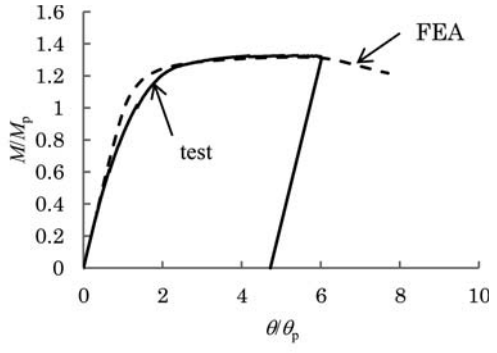

(a) cold-formed No.3.

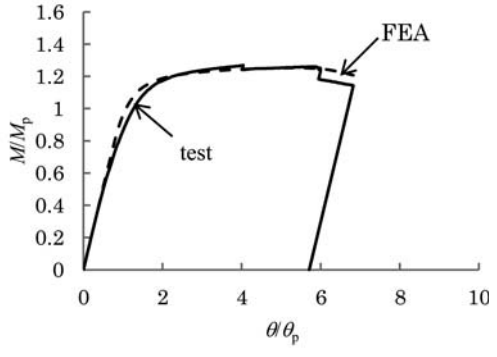

(b) cold-formed No.4.

Figure 9. Experimental skeleton curve and FEA for bending tests of cold-formed sections.

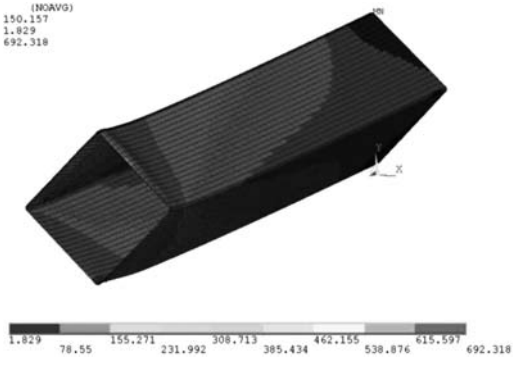

Figure 10. Example of FEA deformed shape and von Mises stress.

Figure 10 shows the distribution of the Von Mises equivalent stress and deformations generated by the finite element models at the ultimate strength. In Figure 10, the areas of stress concentration and local buckling shapes at the corner of tube end agree well with the location of cracks and local buckling shown in Figure 7.

The FEA model using stress-strain relations with cold-formed high yield ratio demonstrate their ability to provide close predictions of the ultimate behaviour of local buckling.

4 CONCLUSIONS

The results from bending tests under cyclic loads are presented. The effects of the forming process such as cold-formed, hot-finished and hot-rolled sections are examined. All of the sections failed to reach the plastic moment and have plastic rotation capacity sufficient for plastic design.

The specimens of the tensile coupon test and Charpy V notch impact test were carried out of the flat areas and corner areas of cold-formed, hot-finished and hot-rolled hollow sections. All the test results accord with the steel specifications. Specimens of cold-formed SHS showed much higher value than the other two, while the values of hot-formed and hot-finished SHS are closing to each other.

Using the cold-formed material properties, the material constants of the modified Ramberg-Osgood curves are presented. Finite Element (FE) analyses

were carried out to examine the effects of the yield ratio on the load-deformation curves of bending tests of cold-formed sections.

REFERENCES

CEN 2005. Eurocode 3: Design of steel structures-Part 1.1: General rules and rules for buildings. *EN 1993-1-1: 2005*, European Committee for Standardization, Brussels, Belgium.

CEN 2006a. Hot finished structural hollow sections of non-alloy and fine grain steels-Part 1: Technical delivery conditions. *EN 10210-1: 2006(E)*, European Committee for Standardization, Brussels, Belgium.

CEN 2006b. Cold formed welded structural hollow sections of non-alloy and fine grain steels-Part 1: Technical delivery conditions. *EN 10219-1: 2006(E)*, European Committee for Standardization, Brussels, Belgium.

Kosteski, N., Packer, J.A. & Puthli, R.S. 2005. Notch toughness of internationally produced hollow structural sections. *ASCE Journal of Structural Engineering* 131 (2): 279–286.

Ochi, K. 2010. Material properties of cold formed tubular sections with high yield strength steels. *Proc. 13th Intern. Symp. on Tubular Structures*, Hong Kong, China, Tubular Structures XIII: 429–434.

Tubular Structures XIV – Gardner (Ed.)
© 2012 Taylor & Francis Group, London, ISBN 978-0-415-62137-3

Comparative study on cold-formed, hot-formed and hot-finished structural hollow sections

S.P. Chiew & M.S. Zhao
School of Civil and Environmental Engineering, Nanyang Technological University, Singapore

ABSTRACT: A comparative study on the influence of different manufacturing process on physical, chemical and mechanical properties of cold-formed, hot-formed and cold-formed with subsequent heat treatment steel square structural hollow sections manufactured to Grade S355J2H of BS EN 10219 and BS EN 10210 was carried out. Physical properties were checked against the corresponding production standards. Chemical composition test using optical emission spectrometer was employed to analyze their differences in chemical contents, while tensile test, sectioning test and hole-drilling test were carried out to analyze the difference in mechanical properties such as yield stress, tensile stress, ductility, impact toughness and locked-in residual stress. The study concluded that mechanical properties are greatly affected by their manufacturing process, and hot-finished sections are not the same as hot-formed sections although they shared the same production standard.

1 INTRODUCTION

Structural Hollow Sections (SHS), especially rectangular sections, are widely used in welded steel frames due to their advantages in both efficiency and aesthetics. Such tubular members are efficient under axial compression, bending and torsion about any axis. Meanwhile, for architectural reasons, the clean lines of a closed section are aesthetically pleasing, and minimize the amount of surface area for dirt, corrosion, or other fouling (Marshall 1992). Currently, SHS are classified into two major groups based on their manufacturing method: hot-finished and cold-formed SHS (EN 10210: 2006 and EN 10219: 2006 respectively), in which hot-finished hollow sections consist of two types, i.e. hollow sections formed hot and formed cold with subsequent heat treatment (hot-formed and hot-finished). Hot-finished hollow sections are treated as the same as the hot-formed in mechanical properties, provided that the hollow sections formed cold are fully annealed in subsequent heat treatments.

Although the steel grades for the three types of SHS may be the same, e.g. S355J2H, the different manufacturing processes result in several key differences from physical to mechanical properties. First, cold-formed SHSs have larger corner radii than hot-formed due to the high degree of cold working in the corner region. Second, the mechanical properties of cold-formed hollow sections are inhomogeneous around the perimeter due to strain hardening during cold forming (Salmi 2006 and Gardner et al 2010). Besides, the potential for micro cracks at the corners and large amount of residual stresses due to cold forming make cold-formed sections more unsuitable for dynamic and fatigue applications (George 1961 and Puthli 2004). As a result, although cold-formed SHSs are easier to manufacture and more economical, they are often treated unfavorably compared with hot-formed/hot-finished SHSs.

2 EXPERIMENTAL INVESTIGATION

In this study, the influence of different manufacturing process on physical, chemical and mechanical properties of cold-formed, hot-formed and hot-finished square steel structural hollow sections manufactured to Grade S355J2H of BS EN 10219 and BS EN 10210 was investigated. The hot-formed and hot-finished hollow sections investigated were of dimensions 180 mm × 180 mm × 12.5 mm, while cold-formed hollow section was of dimensions 200 mm × 200 mm × 12.5 mm. It is a pity that the cold-formed hollow section was in different sizes, but non-geometrical parameters were used to minimize the influences. Physical properties check was carried out first against their corresponding production standards. Subsequently, Optical Emission Spectrometer (OES) was employed in chemical composition analysis to compare the physical differences, while tensile test, sectioning test and hole-drilling test were carried out to analyze the difference in mechanical properties such as yield stress, tensile stress, ductility, impact toughness and locked-in residual stress.

2.1 *Physical properties test*

The surface delivery conditions and dimensional tolerances for cold-formed steel and hot-formed/hot-finished hollow sections were checked against EN 10219-2: 2006 and EN 10210-2:2006 respectively.

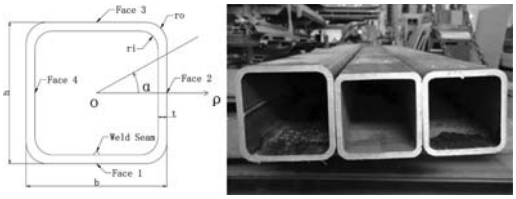

Figure 1. The three hollow section specimens.

a. Test Gun b. Analyzer

Figure 2. Chemical test using OES.

Surface discontinuities in terms of imperfections and defects were checked against the depth of representative surface discontinuities defined by the corresponding product standards, and the following geometrical dimensions were measured, width b, height h, wall thickness t at each side of the sections, inner corner radii (r_i) and outer corner radii (r_o) at all corners, as shown in Figure 1. Based on the mean values of the measured dimensions, the non-geometrical parameters were calculated, including b/t, outer corner radii related to wall thickness r_o/t and inner corner radii related to wall thickness r_i/t.

2.2 *Chemical composition test*

Chemical composition analysis was carried out using the Optical Emission Spectrometer, a universal metal components analyzer widely used in metal producing, processing and recycling industries, which is shown in Figure 2. The specimens were 100 mm long and wide, with depths of 12.5 mm, and all were cut from the surfaces without weld seam, which were the same positions for tensile test coupons, as shown in Figure 3. On each specimen, three tests were carried out after surface polishing. A complete chemical analysis of the following elements has been done: C, Mn, Cu, P, S, Al, Ti, Si, Cr, Mo, V, Ni, and CE.

2.3 *Mechanical properties test*

Specimens for tensile test and charpy v-notch impact test were designed and tested according to EN 10002 and EN ISO 148 respectively.

In tensile tests, three coupons tests were carried out for each hollow section. Both strain gauge and

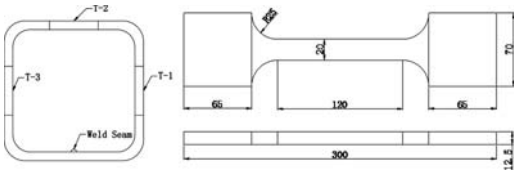

Figure 3. Sources and dimensions of tensile test specimens.

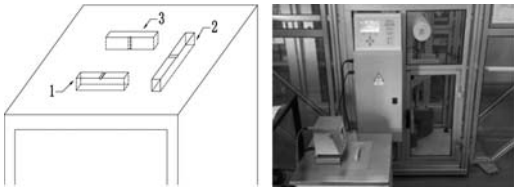

Figure 4. Location of specimens and impact test machine.

extensometer were employed to record the strain-elongation data. The sources and dimensions of the specimen are shown in Figure 3. Non-proportional gauge length of 80 mm was employed as the original gauge length. For conversion of elongation values from non-proportional gauge length to the proportional gauge length, $5.65\sqrt{S_o}$, the conversion tables from BS EN 2566-1 were used.

In charpy v-notch impact test, standard test specimens were cut from the surface opposite to that with weld seam. Three specimens were tested for each hollow section: the first specimen was cut from the transverse direction and had V-notch on the outside surface; the second one was cut at the longitudinal direction, and had V-notch on the outside surface; the third one was cut from the transverse direction and had V-notch at the normal direction of the SHS, as shown in Figure 4. The specimens were 55 mm long and of square section with widths of 10 mm. A standard V-notch which had an included angle of 45°, a depth of 2 mm, and a root radius of 0.25 mm was cut in the centre of each specimen. Finally, the test tests were carried out at −20.0°C with temperature precision of ±0.1°C.

2.4 *Residual stresses measurement*

The residual stress in cold-formed, hot-formed and hot-finished SHS was measured by Sectioning test and hole-drilling strain gauge method (ASTM E837-08). Sectioning test was done first as qualitative measurement, and subsequently hole-drilling strain gauge test as quantitative measurement. In the sectioning test, specimens with length of 200 mm were cut from the tubes. There were 3 cuts with equal spacing on each side and depth of 170 mm. The cutting positions on hot-formed/hot-finished specimens are shown in Figure 5 as example.

The hole-drilling method, which can identify in-plane residual stresses within the boundaries of the drilled hole on the work piece material, was employed to measure the locked-in residual stresses along

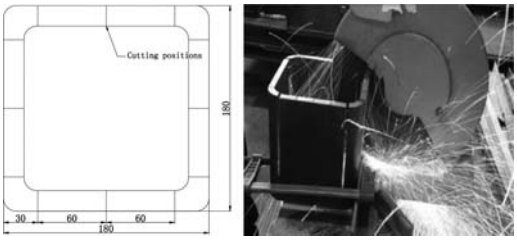

Figure 5. Sectioning test.

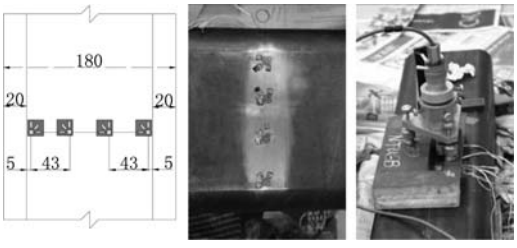

Figure 6. Hole-drilling test.

the perimeters of the hollow sections. This test is often described as a type of semi-destructive residual stresses measurement because the damage that it causes is localized and often does not significantly affect the usefulness of the work piece (ASTM E837-08 2008). In the hole-drilling test, specimens with lengths of 1m were cut from the tubes which are long enough to eliminate the influences of stress relieving caused by cutting, and the center loop of the specimen was chosen as the test area. RS200 milling guide and electric strain gauge FRAS-2-11 were employed to measure the residual stresses within the depth of 2 mm. During the test, a 2 mm deep hole was drilled in the center of the special strain gauge rosette in several steps depending on the required calculation method and precision. The released strains at each step were recorded for further residual stress calculation using the formulas provided by ASTM E837-08.

As the hollow sections are usually loaded longitudinally in practice, the measurement was focus on the residual stresses in the longitudinal direction (perpendicular to the section). Further study about the residual stresses in the transverse direction (shear stresses along the perimeter) is under processing up to now, and thus will not be published in this paper. Test positions were arranged with equal distance along the perimeter, and extra test points were added at corners and weld seam. The test positions on the hot-formed and hot-finished hollow sections are shown in Figure 6.

3 TEST RESULTS

3.1 *Physical properties check results*

As the surfaces of all the hollow sections were elaborately treated by the manufacturers, no surface discontinuities which were not allowed in BS EN 10210 and BS EN 10219 were found. The measured mean geometrical dimensions as well as the non-geometrical parameters are shown in Table 1. Although the thicknesses of the three sections were the same and the widths of the square hollow sections were comparable, their radii at the corners differ remarkably. Cold-formed hollow section had the biggest inner radius and outer radii, followed by hot-finished and then hot-formed hollow sections.

Table 1. Geometrical dimensions.

Sample	b (mm)	t (mm)	r_o (mm)	r_i (mm)	b/t	r_o/t	r_i/t
Cold-formed	200.5	12.8	30	22	15.7	2.35	1.71
Hot-formed	180.3	12.7	25	12	14.2	1.97	0.95
Hot-finished	180.3	12.9	27	14	14.0	2.08	1.09

3.2 *Chemical test results*

The chemical compositions of hot-formed, cold-formed and hot-finished square hollow sections are listed in Table 2. All the elements contents were strictly within the ranges required by BS EN 10210 and BS EN 10219. Generally, it is shown that the compositions of the three sections are similar to each other, although they share different product standards. Small differences were observed in the contents of C, Mn and Cu and so on among the three types of hollow sections, which may be the result of adjustment for manufacturing purposes. However, the slight variance in certain elements accumulates to a difference in CE which was calculated according to the AWS CE equation, and eventually weldability. Cold-formed hollow sections turned out to have the lowest CE value, followed by hot-finished S355J2H and hot-formed, which is out of expectation. Although the CE values satisfied the requirement from EN 10210 and EN 10219, the AWS states that for CE value above 0.4 there is a potential for cracking the heat affected zone on flame cut edges and welds (AWS D1.1 2008), which put the investigated hot-formed hollow section in question. Although the tested tubes could not represent all the sections in each kind, it is proven that cold-formed SHS can obtain good weldability as hot-formed or hot-finished SHS.

3.3 *Mechanical test results*

Although the studied hot-formed, hot-finished and cold-formed square hollow sections consist of similar contents of elements, they differ remarkably in mechanical properties, as shown in Table 3–4 and Figure 7. In tensile test, Hot-formed and Hot-finished steels showed typical high tensile stress-elongation curve with obvious yield stage but cold-formed steel

Table 2. Chemical composition of cold-formed, hot-finished and hot-formed SHS.

	C	Mn	Cu	P	S	Al	Ti	Si	Cr	Mo	V	Ni	CE
Cold-formed	0.07	0.97	0.022	0.031	0.005	0.02	<0.001	0.16	0.026	0.008	0.004	0.020	0.270
EN 10219-1	≤0.2	≤1.6	≤0.35	≤0.04	≤0.04	≥0.02	≤0.05	≤0.6	≤0.3	≤0.2	≤0.05	≤0.8	≤0.45
Hot-formed	0.14	1.330	0.034	0.031	0.009	0.045	<0.001	0.340	0.033	0.008	0.006	0.026	0.432
Hot-finished	0.12	1.300	0.017	0.033	0.006	0.029	<0.001	0.170	0.024	0.010	0.009	0.016	0.360
EN 10210-1	≤0.2	≤1.6	≤0.35	≤0.04	≤0.04	≥0.02	≤0.03	≤0.6	≤0.3	≤0.1	≤0.2	≤0.8	≤0.45

Table 3. Tensile test results.

Sample (S355J2H)	f_y (MPa)	f_u (MPa)	Stress ratio	Elongation on $5.65\sqrt{S_o}$ GaugeLength (%)
Cold-formed	526	563	1.07	22
Hot-formed	412	536	1.30	31
Hot-finished	454	546	1.20	27
EN 10210 & EN 10219	Min. 355	Min. 470 Max. 630		Min. 22

Table 4. Charpy impact test results.

Samples and Positions		Energy (J)	Average (J)	EN 10210 & EN 10219
Cold-formed S355J2H	1	168.6	172.8	
	2	255.4		
	3	94.4		
Hot-formed S355J2H	1	56.9	127.4	Min. 27 J
	2	280.2		
	3	45.0		
Hot-finished S355J2H	1	143.1	135.1	
	2	190.5		
	3	71.7		

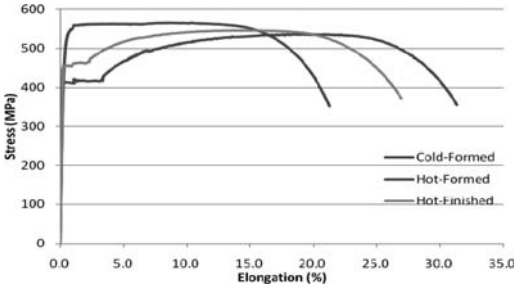

Figure 7. Stress-elongation curves of cold-formed, hot-formed and hot-finished specimens.

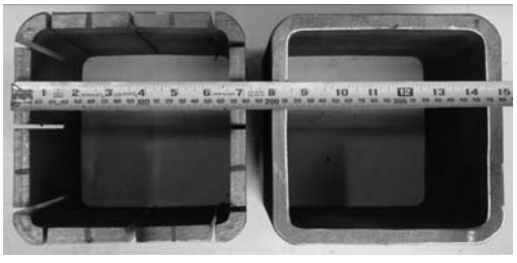

Figure 8. Sectioning test of the hot-formed hollow section.

did not. Specifically, cold-formed S355J2H showed the highest yield and tensile strength but the worst ductility in terms of tensile ratio and elongation. On the contrary, hot-formed steel showed the lowest strength yet the best ductility. Hot-finished S355J2H behaved intermediately between the other two in both strength and ductility, i.e. intermediate strength and ductility.

The toughness values of the tested specimen varied with their original positions and cut directions on the tubes. Specimens from position 2 have the highest toughness values which are much more than the values required by EN 10210 and EN 10219, while the values of specimens from position 3 showed much lower values than the other two though they are still in the safe range. However, it should be mentioned that the toughness at the flat area of hot-finished SHS distributed in the same pattern as cold-formed SHS, with clear three stages. The toughness at positions 1 and 3 of the hot-formed SHS were both low, but that at position 2 was extremely high. Overall, cold-formed S355J2H showed the best toughness, while that of hot-formed and hot-finished S355J2H were comparable. Although it may be too soon to conclude that the concern for brittle fracture at the flat area on the sections seems to be redundant for cold-formed SHSs, but it is proven that cold-formed SHS can obtain good toughness comparable to hot-formed and hot-finished SHSs at least.

3.4 *Residual stress measurement*

After stress relieving by sectioning for depths of 170 mm, the width of cold-formed SHS increased from 200 mm to 210 mm (5%); that of hot-formed SHS remained the same (180 mm); that of hot-finished SHS increased from 180 mm to 186 mm (3.3%). From the contrast of sectioned and original specimen, it can be conclude that cold-formed SHS contained the largest amount of residual stresses, and hot-finished SHS contained median, while hot-formed SHS contained the least, as shown in Figure 8–10.

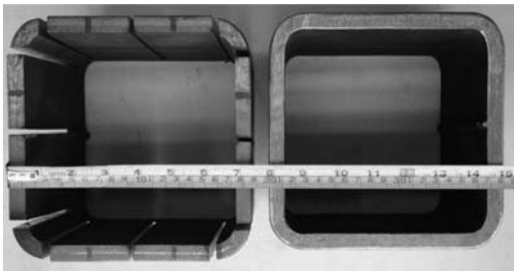

Figure 9. Sectioning test of the hot-finished hollow section.

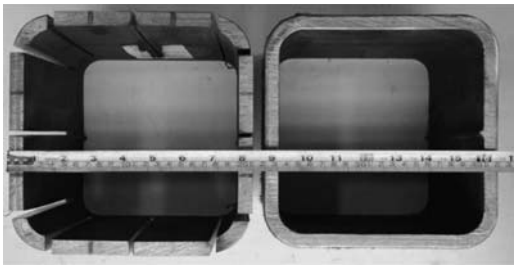

Figure 10. Sectioning test of the cold-formed hollow section.

Quantitative measurement of residual stress was provided by hole-drilling strain gauge method precisely. In accordance with geometrical symmetry, axial stresses normal to the section were generally symmetrical, as presented in Figure 11. However, residual stresses fluctuate distinctly at locations near the weld and corners. The summary of residual stress distribution is presented in Figure 11(d), in which the values measured residual stress values were divided by the corresponding actual strengths listed in Table 3, i.e. f_t/f_y, and the angle values corresponding to the coordinate system shown in Figure 1. For cold-formed hollow section, the largest longitudinal stress was 414.9 MPa, locating at the weld seam, which already exceeded the nominal yield stress (355 MPa) as much as 16.9%. Compared with cold-formed hollow section, hot-formed SHS obtained much smaller residual stresses and most parts were even in small compression. The distributions of residual stresses in hot-finished SHS were extremely similar to those in the cold-formed, particularly from 135° to 360°, but the values were much smaller, especially those near weld seam and corners.

From the comparison of average residual stresses on the flat areas presented in Table 5, it can also been seen that the hot-formed SHS have the least locked-in residual stresses, followed by the hot-finished and cold-formed SHS. In addition, the residual stress distribution patterns of hot-formed and hot-finished SHSs are totally different, i.e. the residual stress distributions of hot-finished are more similar to that of the cold-formed SHS.

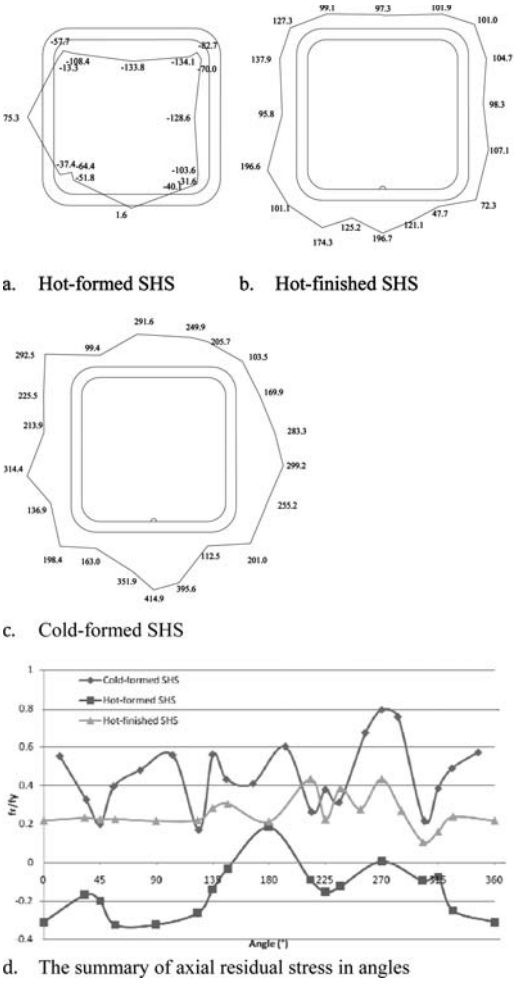

Figure 11. Longitudinal residual stresses in the tested SHSs.

Table 5. The average residual stresses on each faces (MPa).

Samples	Face 1	Face 2	Face 3	Face 4
Cold-formed	359.5	282.8	211.6	222.7
Hot-formed	−30.1	−107.7	−125.4	8.2
Hot-finished	133.0	102.1	99.4	143.4

4 CONCLUSIONS

A comparative study on the influence of different manufacturing process on physical, chemical and mechanical properties of cold-formed, hot-formed and hot-finished steel square structural hollow sections was carried out. Physical examination and chemical analysis were carried out while tensile test, sectioning test and hole-drilling test were carried out to analyze the difference in mechanical properties such as yield stress, tensile stress, ductility, impact toughness and locked-in residual stress. While the three sections are

able to comply fully with their production standards, they are very different mechanically. Specifically, hot-formed and hot-finished hollow sections have different mechanical properties although they shared the same production standard.

In the tests, the cold-formed SHS showed the highest strength but the lowest ductility; the hot-formed SHS had the lowest strength but the best ductility, while the hot-finished SHS was somewhere in between. The highest toughness at −20°C was showed by cold-formed S355J2H, but the values of all three different sections are much higher than those required by the corresponding product standards. Although the tested tubes may be insufficient to represent all the sections in each kind, it is proven that cold-formed SHS can obtain good weldability and toughness as hot-formed or hot-finished SHS. However, there were large amount of longitudinal residual stresses locked in the cold-formed SHS, especially the locations near the weld seam and corners. This is the main reason why cold-formed sections are treated differently in all design codes. Besides, hot-finished hollow sections are treated the same as hot-formed hollow sections in design codes such as BS 5950 and EN 1993 yet they still have much residual stresses distributed similar to those in the cold-formed hollow section and their mechanical properties have been shown to be different from hot-formed hollow sections. This is an area of concern since structural safety may be compromised and it is recommended that both production standard EN 10210 and design codes such BS 5950 and EN 1993 should be tightened to address this concern.

REFERENCES

ASTM International. (2008). "Standard Test Method for Determining Residual Stresses by the Hole-Drilling Strain Gauge Method." ASTM E837-08.

American Welding Society. (2008). "Structural Welding Code – Steel". 21st Edition. AWS D1.1.

British Standards Institution (BSI). (2001). "Tensile Testing of Metallic Materials – Part 5: Method of Test at Ambient Temperatures." BS EN 10002-5: 2001.

British Standards Institution (BSI). (1999). "Steel – Conversion of elongation values – Part 1: Carbon and low alloy steels." BS EN 2566-1.

British Standards Institution (BSI). (2010). "Metallic Materials – Charpy Pendulum Impact Test, Part 1: Test Method." BS EN ISO-148.

British Standards Institution (BSI). (2006). "Hot-Finished Structural Hollow Sections of Non-alloy and Fine Grain Steels." BS EN 10210-1&2: 2006.

British Standards Institution (BSI). (2006). "Cold-Formed Structural Hollow Sections of Non-alloy and Fine Grain Steels." BS EN 10219-1&2: 2006.

Gardner, L., Saari, N. & Wang, F. (2010). "Comparative Experimental Study of Hot-rolled and Cold-formed Rectangular Hollow Sections." Thin-Walled Structures, Vol. 48, pp. 495–507.

George, E. & Dieter. (1961). "Mechanical Metallurgy." McGraw-Hill Book Company, Inc. New York.

Marshall, P.W. (1992). "Design of Welded Tubular Connections – Basis and Use of AWS Code Provisions". Elsevier.

Puthli, R., Herion, S., Boellinghaus, T. & Florian, N.W. (2004). "Welding in Cold-formed Areas of Rectangular Hollow Sections." Final Report. University of Karlsruhe, Germany.

Salmi, P. & Kouhu, J. (2006). "Design rules for cold-formed structural hollow sections." EUR ISSN 1018-5593. European Commission.

Tubular Structures XIV contains the latest scientific and engineering developments in the field of tubular steel structures, as presented at the 14th International Symposium on Tubular Structures (ISTS14, Imperial College London, UK, 12-14 September 2012). The International Symposium on Tubular Structures (ISTS) has a long-standing reputation for being the principal showcase for manufactured tubing and the prime international forum for presentation and discussion of research, developments and applications in this field.

Various key and emerging subjects in the field of hollow structural sections are covered, such as: special applications and case studies, static and fatigue behaviour of connections/joints, concrete-filled and composite tubular members and offshore structures, earthquake and dynamic resistance, specification and standard developments, material properties and section forming, stainless steel and aluminum structures, fire resistance, castings and fabrication innovations. Research and development issues presented in this topical book are applicable to buildings, bridges, offshore structures, entertainment rides, cranes, trusses and towers.

Tubular Structures XIV is thus a pertinent reference source for architects, civil and mechanical engineers, designers, steel fabricators and contractors, manufacturers of hollow sections or related construction products, trade associations involved with tubing, owners or developers of tubular structures, steel specification committees, academics and research students all around the world.

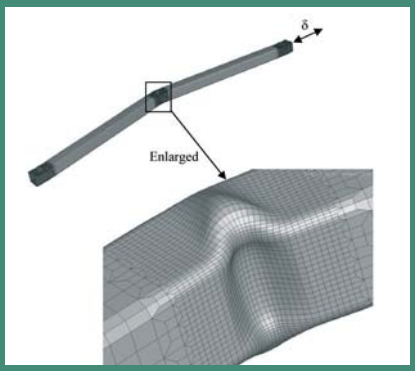

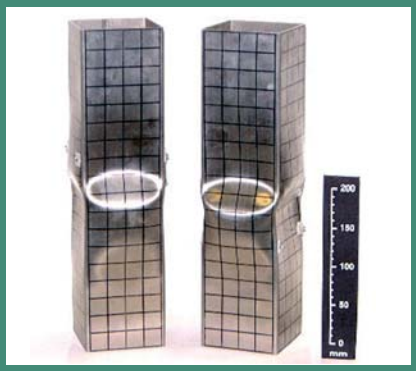

ISBN 978-0-415-62137-3
9 780415 621373

CRC Press
Taylor & Francis Group
an informa business
www.crcpress.com

6000 Broken Sound Parkway, NW
Suite 300, Boca Raton, FL 33487
Schipholweg 107C
2316 XC Leiden, NL
2 Park Square, Milton Park
Abingdon, Oxon OX14 4RN, UK

an informa business